Ouk-40468-1-C81849

Proceedings of the International Conference on

Control, Instrumentation and Information Communication

306/1

December 13-15, 2001
The Science City, Kolkata, India

Editors
Asit K. Datta
Anish Deb
Samarjit Sengupta

CALCUTTA UNIVERSITY ★ CENTRAL LIBRARY.

Organized by
Department of Applied Physics
University of Calcutta

621·381
P 941

Editors
Asit K. Datta
Anish Deb
Samarjit Sengupta
Department of Applied Physics
University of Calcutta
92, Acharya Prafulla Chandra Road
Kolkata 700 009, India

Copyright © 2001, University of Calcutta

All rights reserved. No part of this publication may be reproduced, stored in a retrieval system or transmitted in any form or by any means, electronic, mechanical, photocopying, recording or otherwise without prior permission of the publisher

All export rights for this book vest exclusively with the University of Calcutta.

This book is printed from the camera ready text provided by the authors, subject to editorial modifications.

Price – Rs. 500
$ 50

Published By
A. Basuray, Head of the Department of Applied Physics
University of Calcutta
92, Acharya Prafulla Chandra Road
Kolkata 700 009, India

Printed by
Pradip Kumar Ghosh
Calcutta University Press
48, Hazra Road, Kolkata 700 019

BCU 2824
GS1849

BCU
1181

International Advisory (Technical) Committee

E. M. Abed, University of Maryland, USA

S. T. Ali, Concordia University

S. P. Bhattacharyya, Texas A & M University, USA

B. K. Bose, University of Tennessee, USA

Anajan Bose, Washington State University, USA

M. S. Baptista, Inst. Di Fisica, Brazil

A. K. Chattapadhyay, BE College, India

Ashoke Chandra, MHRD, Govt. of India, New Delhi

J. D. N. Cheeke, Concordia University, Canada

George Giaskos, Akron University, Ohio, USA

D. P. Kothari, Indian Institute of Technology, Delhi, India

D. Crischen, University of Manchester, UK

C. L. Karr, University of Alatamn, USA

I. Kale, University of Westminister, UK

S. K. Pal, Indian Statistical Institute, Calcutta, India

D. Popovic, University. of Bremen, Germany

J.L.R. Marrero, University Pontifica Comillas, Spain

G. P. Rao, UNESCO, Abu Dhabi, UAE

B. S. Sonde, Goa University, India

R. S. Sirohi, Indian Institute of Technology, Delhi, India

N. K. Sinha, McMaster University, Canada

G. S. Sanyal, Indian Institute of Technology, Kharagpur, India

N. Viswanadham, National University of Singapore

W. M. Wonham, University of Toronto, Canada

Y. Yan, University of Greenwich, UK

T, Yatagi, University of Tsukuba, Japan

D. K. Basu, University of Calcutta, India (Chairman)

Acknowledgements

Financial support provided by the following agencies is gratefully acknowledged

University of Calcutta

Defence Research and Development Organization, Govt. of India

Council of Scientific and Industrial Research, Govt. of India

Indian National Science Academy, New Delhi

Department of Science and Technology, Govt. of India

Ministry of Information Technology, Govt. of India

Ministry of Human Resource Development, Govt. of India

Atomic Energy Commission, Govt. of India

Research Centre Imarat, Hyderabad

Department of Science and Technology, Govt. of West Bengal

West Bengal Industrial Development Corporation Ltd, Kolkata

West Bengal Electronics Industry Development Corporation Ltd, Kolkata

PATROT Automation Projects Ltd (Caltiger.com)

IEEE, (Calcutta Chapter)

IEE, (Calcutta Chapter)

Optical Society of India

PREFACE

The technologies of control, instrumentation and information communication are becoming a potent force in shaping the industrial revolution of twenty first century. The span of the impact is wide, affecting not only the way people live, learn, work and interact, but also the technologies have become a vital engine for the industrial growth of a country.

To discuss the rapid and new developments in the areas of control, instrumentation and information communication, the Department of Applied Physics, University of Calcutta has organized an international conference from December 13 to 15, 2001. This conference is a part of the platinum jubilee celebration of the Department, where speakers from all over India and abroad have presented their original research works.

Over 130 research papers including 12 review papers authored by eminent scientists, technologist and research workers are included in this proceedings. The areas covered are,

- Control Theory,
- Control of Power System
- Power Electronic Control and Drives
- Process Control and Instrumentation
- Signal Processing
- Image Processing and Pattern Recognition
- Information Processing and Communication
- Optical Sensors and Systems.

The editors would like to express their gratitude to Prof. A. K. Banerjee, Vice Chancellor and Prof. Surabhi Banerjee, the Pro-Vice Chancellor (Academic), the University of Calcutta for their whole-hearted support and guidance. We are also thankful to Prof. H. K. Banerjee, Pro Vice-Chancellor (B A & F) University of Calcutta and Prof. A. Basuray, Head of the Department of Applied Physics, for their keen interest and encouragement for the publication of this volume. Members of the international advisory committee and national organizing committee have contributed significantly for this publication. The editors are grateful to the reviewers of the papers who have made tremendous effort to maintain the time schedule and standard of the publication.

We thank authors for their timely submission of manuscripts and also to the Calcutta University press for their cooperation. It is our pleasure to acknowledge the technical assistance provided by Ms. Madhura Datta, a student of our computer science department. Perhaps she is better known to the most of the authors through her email correspondences. Ms. Soumika Munshi, a research scholar of this Department also has helped at various stages during the preparation of this volume for the press.

Editors

Contents

Preface
Acknowledgements

General

An Evolutionary Model For A Class Of Mathematical Concepts And Representations (Invited paper) 1
Ganti Prasada Rao

Recent Trends In Electric Energy Systems Research (Invited paper) 9
D. P. Kothari

Control Theory

A New Three Level Output Feedback Sliding Mode Control For Discrete System 13
B. Bandyopadhyay and Chakravarthini M. Sajj

Identification Of Time Varying Dynamical Systems: A Neural Network Approach 19
S. V. Dudul, A. A. Ghatol, S. S. Salankar and V. R. Mankar

Adaptive Parameter Estimation Of Robust Kalman Filter Frequency Tracker 25
K. Aadhi Vairava Sundaram and M. J. Nigam

Dynamic Fuzzy Logic System (DFLS) Based Identification Of Chaotic System 31
O V Ramana Murthy, R. K. P. Bhatt and N. Ahmed

Identification Of Transfer Function Model For Unstable System With A Zero 37
R. Padma Sree and M. Chidambaram

Self-oscillation Quenching By Injecting Dither In Nonlinear Two Dimensional Control System 41
B. B. Pati and K. C. Patra

Reduction Of Large Scale MIMO Interval Systems Using Routh Approximants 45
G. V. K. R. Sastry and P. Mallikarjuna Rao

A New Algorithm For Analysis And Design Of High Order Non-linear Systems Using Frequency Response Modelling Technique 51
G. V. K. R. Sastry, K. B. Madhu Sahu and G. S. Kalyan

A Simplified Method For Large Scale Discrete Systems Modelling Using Bilinear Transformation And CFE 57
G. V. K. R. Sastry and G.Raja Rao

Biased Model Reduction For Multivariable Systems Using Simplified Polynomial Derivative Technique 61
G. V. K R. Satry and G. Raja Rao

Study of unstable plant with no poles 65
S. K. Nagar, Abhishek Sharma and Salil K. Jain

Embedded Simulation Of FOPTD And Second Order Systems 67
J. J. Barve and K. P. Detroja

Control And Synchronization Of Chaotic System 73
Biswapriya. Mukhopadhyay, Prodyot Kumar Roy and Syamal Kumar Dana

A Complementary Pair Of Orthogonal Triangular Function Sets And Its Application To The Analysis Of SISO Control Systems 81
Anish Deb, Gautam Sarkar and Anindita Dasgupta

Control Of Power Systems

Artificial Intelligence Techniques For Monitoring And Control Of Power System 91
R. C. Bansal, T. S. Bhatti and D. P. Kothari

A Fuzzy Approach To Handle Parameter And Control Uncertainties In Power System Bifurcation Analysis. 97
P. K. Satpathy, D. Das and P. B. Dutta Gupta

Optimal Scheduling Of Short-Term Thermal Generation Using An Annealing Neural Network 101
C. Christober Asir Rajan, M. R. Mohan and K. Manivannan

Maintenance Scheduling Of Generating Units Of A Captive Thermal Power Plant Using Intelligent Computational Technique 109
D.K. Mohanta, T. Ghosh, R. C. Jha, B. M. Karan and T. Mohanta

Solution Of Economic Generation Scheduling Of Thermal Units Using Genetic Algorithm 115
T. Ghosh, R. C. Jha, I. Alam and S. K. Goswami

A Fuzzy Expert System For Service Restoration Of Primary Distribution System 121
T. Ananthapadmanabha, A. D. Kulkarni, W. M. Shivakumar, N. Nagendra, S. B. Shivakumar and M. S. Nagaraj

Unit Commitment: A Neural Hybrid Algorithm Integrating the EP, SA And NN 127
T. Aruldoss Albert Victoire, Thomas Joseph and Sishaj P. Simon

Computer Aided Analysis Of Thermal Generating Unit Commitment By Tabu Search 133
C. Christober Asir Rajan, M. R. Mohan and K. Manivannan

A Multi-Objective Bi-Directional Search Algorithm For Distribution Network Optimization 139
T. Ananthapadmanabha, W. M. Shivakumar, A. D. Kulkarni, N. Nagendra, N. S. Nagaraj and S. B. Shivakumar

Actual Reactive Capability Assessment Of Large Alternator 143
K. K. Saxena and R. S. Mahajan

New Automated Control Logic For Parallel Valve Operation For Power System Transient Stability Enhancement 149
Ramnarayan Patel, T. S. Bhatti and D. P. Kothari

Controllability And Observability Of Large Tandem-connected Systems 155
A. Gupta and S. Kumar

Development Of Simulation Technique To Facilitate Control And Improvement Of Voltage Stability Of Power Transmission Systems Using Fast Decoupled Load Flow (FDLF) **161**
A. Chakrabarty, C. K. Chanda, S. Dey, P. N. Das and A. K. Mukhopadhyay

Neuro Controller For Power Plant Generator Excitation System **167**
N. S. Bhuvaneswari, T. R. Rangaswamy And S Nagarajan

An Algebraic Criteria For Robust Stability Of Voltage Controller Under Convex Optimization Technique **173**
S. C. Konar and A. S. Chaudhuri

A Double Order Reactive Power And Voltage Input Signals SVS Auxiliary Controller For Suppressing The Sub-synchronous Resonance In A Power Systems **179**
Sushil Kumar Gupta, A. K. Gupta and Narendra Kumar

A New Approach To Power System Frequency Estimation Using Least Mean Square Technique **187**
A. K. Pradhan, M. K. Patel and A Routray

An On-Line Microprocessor Based Generation Frequency And Voltage Regulator Using LFC And SVC **191**
Arabinda. Das, T. K. Sengupta and A. K. Mukhopadhyay

Detection, Classification And Location Of Transmission Line Faults Using Radial Basis Function Based Artificial Neural Network **199**
R. N. Mahanty and P. B. Dutta Gupta

Distribution System Fault Location Using Expert System And Automatic Location **203**
A. D. Kulkarni, T. Ananthapadmanabha, W. M. Sshivakumar, S. B. Shivakumar, M. S. Nagaraj and P. Venkataramu

A Frequency Domain Technique For Fault Signal Detection And Isolation In Distributed Systems **209**
K. A. Gopala Rao

Web Based Substation Automation **215**
P. Anbalagan, V. Vasantharathna, S. Santthosh Babu And R. K. Manimozhian

A Simple Method For Load Flow Solution Of Unbalanced Radial Distribution Networks **219**
Smarajit Ghosh

Methods For Branch Conductors Optimization Of Radial Distribution Networks **223**
Smarajit Ghosh

Interaction Between Insulation Coordination And Pollution **227**
R. P. Singh

Power System Stability Using Functional Approach **231**
A. K. Singh and S. Agrawala

Forecasting Of Monthly Peak Electric Load Demand Using An Artificial Neural Network **237**
S. G. Bhirud and T. K. Basu

Optimum Operating Condition Of A Series Capacitor Compensated EHV Transmission Line For Its Enhanced Efficiency **243**
S. Sengupta, Utpal Maji, Netai Pal and A. K. Mukhopadhyay

Power Electronic Control and Drives

High Power High Performance Industrial AC Drives and Their Control (Invited Paper) **249**
Ajit K. Chattopadhyay

Statistical Analysis of Chaotic Systems: Applications to Power Converters (Invited paper) **259**
José Luis Rodríguez Marrero

Next Generation Power Electronic Systems (Invited paper) **263**
Sudip K. Majumder

Design Compensation Through Experimentation and Sensitivity Analysis in n-Channel MOSFET Based Controlled Power Circuits **269**
Y. Singh and P. S. Bimbhra

Implementation of An Active Load Sharing Scheme For AC-DC Converter System **273**
B. K. Dubey and S. B. L. Saxena

IGBT Based Chopper **279**
A. Srinivasa Rao

The Design Of Microprocessor Based Series Resonant Inverter For A New Generation Contamination Free Induction Heated Medicinal Plant **285**
P. K. Sadhu, S. K. Mukherjee, R. N. Chakrabarti, S. P. Choudhury and B. M. Karan

Transient Stability Study Of The Series Generator -Series Motor Drive **293**
K. L. Barui and B. Bhattacharya

A Digital Controller For Diode Rectifier With Sinusoidal Input Current **299**
M. R. Vikraman and A Kandaswamy

A New Single Phase High Power Factor AC-DC Buck Converter **303**
Mahadev S. Patil, Vinayak N. Shet and Victor P. Sundarsingh

An Innovative Method For Turn-Off Of SCR And Power Factor Improvement Of Controlled Converter **307**
Vinayak N. Shet and Victor P. Sundarsingh

A PC Based Speed Control System For A Switched Reluctance Motor **311**
Rajat Bhattacharjee

Process Control and Instrumentation

Sensors in Instrumentation (Invited paper) **315**
D. Patranabis

Supervisory Control Of Discrete-event Systems (Invited paper) **321**
W. M. Wonham

Spatial Control Of Large Nuclear Reactor By Three Different Approaches (Invited paper) **331**
B. Bandyopadhyay and A. P. Tiwari

Distributed Control System To Field Bus **339**
M. D. Desai

Real Time Level Control Using Fuzzy Logic **345**
R. Abdul Matheen , D Najumnissa Jamal and Abdullah

Nonlinear PI Controller For Buffered Acid Base System **351**
A. Arvind Kumar, M. Chidambaram, V. S. R Rao and Rainer Pickhardt

Design Of Automatic Control System To Supply Fuel Gas With Suitable Calorific Value Utilizing The Available By-product Gases In Iron And Steel Plant **355**
G. Karmegam and S. B. L. Saxena

Implementation Of A Suitable Process Controller Along With A Contamination Detector In A Novel See-Saw Bioreactor For Achieving Very High Yield From Animal Cell Line Culture **359**
Gautam Saha, Partha Sarathi.Pal, Alok Barua and Satyabroto Sinha

Design Of Convex Controller For Insulin Delivery System With Optimization Of Parameter λ **365**
A. Sutradhar, G. C. Ray and A. S. Chaudhuri

Design of Robust Controller For Robot Joint With Computer Torque **371**
K. A. Gopal Rao

A New Lead Wire Compensation Method For Existing Two Wire Resistance Temperature Detectors (RTDs) **375**
S. K. Sen

Fault Tolerant Three Phase Real Power Measurement Using Microprocessor **379**
S. Sengupta, Gautam Sarkar, Arghya Sarkar and A. K. Mukhopadhyay

Algorithm For Digital PID Redesign Of An Existing Analog Controller **385**
S. K. Bharadwaj and S. K. Nagar

Analytical Structures For Fuzzy Controllers **389**
J. S. Saini, M. Gopal and A. P. Mittal

Dynamics Of Driven Colpitts Oscillator **397**
Prodyot Kumar Roy, Syamal Kumar Dana, Biswapriya Mukhopadhyay and Arijit Basuray

An Approach To The Design Of A Low Cost PID Controller Combined With Inverse Derivative Control Action **401**
S. C. Bera and S. Chattopadhyay

PC Based Position Control System Of A Motorised Valve In A Process Plant **407**
S. C. Bera and J. K. Ray

Design Of A Novel Bridge Type Flowmeter For A Conducting Liquid **413**
S. C. Bera

Study Of A Low Noise Head Mounted Temperature Transmitter **419**
S. C. Bera and J. K. Ray

Signal Processing

MS Excel Spreadsheet Simulation Of Logic Functions Using Function-specific MSI Circuits 425
S. K. Sanyal And R. Nandi

Simulation Of Fuzzy Combinational Functions Using Microcontroller 431
S. Chattopadhyay, S. K. Sanyal and R. Nandi

Digital Tuning Of Analog Wave Processor 437
R. K. Nagaria, P. Venkateshwaran, S. K. Sanyal And R. Nandi

DPLL- Operation and Circuit Simulation 443
Shubhra Verma and S. K. Kak

On Noise Segmentation And Filtering 447
P. Praveen and Vinod Kumar

A New Generation Microprocessor Based Interlocking Device 453
R. Swaroop, P. K. Sadhu, S. K. Mukherjee, R. Chakraborti and B. M. Karan

A Low Noise Multiplexed Analog Digital Signal Processor For Dimuon Spectrometer Of ALICE 459
S. Sarkar, J. C. Santiard, V. Sharma. J. N. Roy and S. K. Sen

An Automated Data Acquisition System And Frequency Response Of 12 Lead ECG Signal 463
M. Mitra and Sucharita Mitra

A PC Based Bio-feedback System For Correcting Paraplegia 467
Puvvada Ramesh

Labview Based Communication Protocol For Interfacing Spirometer With Personal Computer 472
A. Kanadaswamy, C. Sathish Kumar And T. Vamsee Kiron

DSP Based Online Air-Gap Torque Monitor For Detection Of Squirrel Cage Rotor Fault 475
Vinod V. Thomas, Krishna Vasudevan and V. Jagadeesh Kumar

A Microprocessor Based Protection Scheme For The Alternator Rotor Winding 481
Konika Das (Bhattacharya), Debashis Ghosh and Dipten Dasgupta

Application Specific Fuzzy Switching 485
Pradeep Chatterjee, Rajpal Singh, B. M. Karan and P. K. Sinha

Image Processing and Pattern Recognition

Soft Computing Pattern Recognition: Principle, Integration and data Mining (Invited Paper) 491
Sankar K. Pal

Human Face Recognition Using Radial Basis Function Neural Network 503
M. V. Raghunadh, N. S. Murthy and K Kishan Rao

Face Recognition Using Fractal Measure On Colour Images 509
U. R. Jena, M. Das Gupta, M. Mondal And A. K. Mondal

Face Recognition Using Eigenfeatures 517
Narottam Chand

3 Dimensional Fractal Measures For Texture Similarity 521
A. K. Mondal, M. Dasgupta, M. Mondal and U. R. Jena

Digital Image Watermarking: A Technique For Secure Transmission 527
Santi P. Maity and Malay K. Kundu

Document Skew Detection Algorithm 531
M. V. Raghunadh, N. S. Murthy And K. Kishan Rao

RLS Algorithm Based Sub-Band Decomposition And Application To Reduced Memory Image Compression 537
Suprava Patnaik

Vector Image Encapsulation 543
Deepak Bhushan and S. K. Kak

A Robust Edge Detector 547
B. L. Narayan and C. A. Murthy

Speech Feature Extraction For Speaker Identification Using Artificial Neural Network 551
Anupam Shukla, A. S. Zadgaonkar and Ritu Tiwari

Neural Network Model Of Vertebrate Retina 555
Soumika Munshi and Asit. K. Datta

Information Processing and Communication

Application of Wavelet Transform Towards The Optimization Of Signal Parameters Of An Optical Wireless Local Access Network (WLAN) (Invited paper) 561
N. Patnekar, G. C. Gaiskas, L Fraiwan

Word Matching Algorithm In Information Processing 565
Vadali Srinivasa Murty and S. Raman

Framing Strategy For Congestion Control In BISDN/ATM 571
S. K. Singhai, K. K. Saxena and N. P. Singh

Performance Evaluation Of Handover Initiation Algorithm For Microcellular Systems 575
Brahmjit Singh and K. K. Aggarwal

A Statistical Method For Characterizing Network Traffic 581
Narottam Chand, Ajay Guleria and D. R. Rana

A Mathematical Model For The Specification of Sliding Widow Protocol 585
Awadhesh Kumar Singh and Anup Kumar Bandyopadhyay

Non Uniform Sampling And On Line Estimation Of Local Bandwidth Of A Nonstationary Signal 589
Sumeet Goyal and Pradip Sarkar

Frequency Selective Rayleigh Faded HF Channel Using Multipath Propagation- A Model Based Approach 595
S. Sri Gowri, B. Prabhakara Rao and P. V. Subbaiah

Some Studies On Open Slot And T-Junction Radiators 599
K. Chandra Bhushana Rao, K. Padma Raju, G. S. N Raju and K. R. Gottumukkala

A New Approach For Implementing A Robust Synchronous Optical CDMA Network 603
Abhinav Roongta, Saurabh Sood and Subrat Kar

Automatic Categorical Modularization Of Computer Network Protocols 607
A. K. Daniel

40 Khz Signal Amplitude In Relation To Solar radio Emission At 2800 MHz 611
Barin Kumar De and Pinaki Pal

Propagation of ELF Radio Wave In Relation To Geomagnetic Storms 615
Barin Kumar De, Samarjit Sengupta and Pinaki Pal

Compression And Decompression Of Information By Using 2D Cellular Automata 619
Amal K. Ghosh, Pabitra Pal Choudhury, Kajal Dihidar and Amitabha Basuray

Optical Sensors and Systems

MEMs /Porous Silicon-Based Smart Sensors And System-On-Chip (Invited paper) 621
H. Saha

Development Of System On Chip (SOC) Based On A Porous Silicon Humidity Sensor 625
H. Saha, S. Dey and J. Das

Effects Of Structural Parameters On Threshold Current Density In VCSEL 631
M. C. Srivastava and B. D. Shinde

Optical Feedback Noise Reduction In Vertical Cavity Surface Emitting Lasers (VCSEL) Using Diffused Quantum Well Structure 633
M. C. Srivastabha and B. D. Shinde

Wave Length Shift Evaluation In Fibre Bragg Grating For Strain Measurement 635
Y. K. Jain and Sanjeev Jain

Improvement Of Defocusing Error 641
Dola Roy Choudhury, Kallo Bhattacharyya and A. K Chakraborty

COLDII: A Software Package For Computer Optimization Of Lens Design 647
Jaya Basu and Lakshminarayan Hazra.

Near Field Diffraction Of Gaussian Beams By Radial Walsh Filters 653
R. Sen Sarma and L. N. Hazra

Application Of Genetic Algorithm In Structural Design Of Cemented Triplets With Prespecified Aberration Targets 659
S. Chatterjee and L. N. Hazra

Computerized Fringe Analysis For The Measurement O F Refractive Index Profile Of GRIN Glasses Of Different Geometry **665**
M. Ray (Shah), A, Datta, S. K. Sarkar and A. Basuray

Indigenously Developed Optical Computer **671**
Asit K. Datta and Soumika Munshi

Laser Beam Shaping Using Phase-Only Filter At Fractional Fourier Transform Plane **679**
K. N. Dey, S. Sanyal and Ajay Ghosh

Post Dated Papers

Network Sensitivity Relations From Dee Bee's Invariant Product Theorem **685**
D. Basu and Bhaskar Bhattacharya

Simulation And Performance Analysis Of FDDI Based Network Designed For Movement Of Trains In Sections **687**
Vikas jain and Vinod Chandra

Virtual Wavelength Path Algorithm For Design Of WDM Network Exploiting Combined Wavelength And Optical Code Conversion (Invited Paper) **693**
R. Gangopadhyay

System Design of Night Vision Devices (Invited paper) **699**
P. K. Datta

An Electric Field Induced Single Mode Fiber Optic Polarization Controller **705**
S. Chakraborty, S.K. Ghosh, and S. K. Sarkar

Study Of A Fiber-Optic Non-Contact Rotation Sensor For Calibration Of Energy Meter **711**
S. K. Ghosh, A. Rakshit, S. Chakraborty and S. Mondal

Control And Communication For The Power Grid In A Restructured Power Industry (Invited paper) **717**
Anjan Bose

A new approach to designing PID controller (Invited paper) **719**
S. P. Bhattacharyya

Author Index **721**

An Evolutionary Model for a Class of Mathematical Concepts and Representations

Ganti Prasada Rao
UNESCO-EOLSS Joint Committee
PO Box 2623, Abu Dhabi, UAE.

Abstract

This paper attempts to model the process of evolution of a class of mathematical concepts and representations. It examines at first the process of evolution of numbers and number systems referring to the contributions by the ancient Hindus. Some aspects of the spiritual philosophy of the Hindus are outlined to support an understanding of how the profound concept zero (and infinity) could become a natural product of the Hindu mind and shape the structure of number systems. The paper then shows how the number concept itself may be seen is the genesis of the process of evolution of a class of mathematical concepts in which the structure of expressions is surprisingly the same as that of the sum-of-products (SOP) form of the number systems while the rich diversity of our modern mathematical concepts and expressions is due to the elements of this structure taking various forms that occur at various stages in the process of evolution of numbers from positive integers to complex variables.

Indexing terms – Mathematical expressions, number concept, zero and infinity, function representation, integral transforms, operations, signals and systems

INTRODUCTION

Standard historical accounts of development of mathematical concepts are usually chronological. Discussions on the relationships among developments in time and space are generally limited to the recent times. The earliest mathematical concepts are as old as humans themselves and date back to antiquity. The systems of counting and numeration, which represent the beginning of mathematics, cannot be precisely dated. In contrast, developments in mathematics in recent history are well documented. Several mathematical techniques that are in regular use today are attributed only to developments in relatively recent times and attempts to trace them to their true origin in early history are rare. A close study suggests that many of our modern mathematical concepts and the related expressions seem to have actually evolved on the basis of the earliest foundations laid down in antiquity. Most new developments are extensions or generalizations of what already existed although the connections with the past may not be readily apparent or may have not received adequate attention by historians. In this paper we briefly review the evolution of the number concept and systems of number representation. With zero (and infinity), argued as the product(s) possibly of the unique tenets of the spiritual philosophy of the Hindus, the general structure of the number systems became so robust that there seems to be little scope for any change or need for further improvement. Furthermore, this structure seems to have become the basic format for a class of our modern mathematical expressions. We will show how the generalization of the number concept and its insertion into the basic structure of number representation yields a host of modern mathematical concepts and representations. The present discussion will be centered mainly on analytical and descriptive aspects without reference to geometry.

EXPRESSION

Let us begin with a simple definition of a mathematical expression:

> *A 'constant' or a 'variable' is an expression.*
> *A pair of expressions connected by an operator is an expression. This is a recursive definition.*

The structure of the language of mathematical description

may be broadly characterized by expressions in two forms:
(a) sum of products (SOP), and
(b) product of sums (POS)
in which the terms sum and product are operations that are more general than their arithmetic counterparts. These happen to be the basis of synthesis and realization of binary expressions with the sum and product respectively denoted by the operators OR and AND.

Some expressions contain certain specially designated expressions such as $\sin x$, $\tan x$, etc. An expression in SOP may be represented in POS form or in mixed form. The 'sum' or the 'product' may be finite or infinite.

$$\text{SOP: } \Sigma\,(L.R),$$
and
$$\text{POS: } \Pi(L+R),$$

in which L and R denote the left and right parts respectively of product or sum.

The build up of the structure of expressions starts with the elementary entities such as constants and variables. Let us first consider constants as numbers the evolution of which is of interest in the context of the present discussion.

THE I-R-C COURSE OF DEVELOPMENT OF THE NUMBER CONCEPT

The main thesis of this paper is that the number concept in its basic form has influenced much of the SOP structure of mathematical expressions. The **I-R-C** course of evolution of the number concept has likewise influenced the course of evolution of various mathematical developments associated with the SOP structure. The following represent the various stages in the course of development of the number concept: **I**: Integer; **R**: Real; **C**: Complex. These developments are shown in Fig. 1. Visualized in a space, **I** and **R** are associated with a line (uni-dimensional space) and **C** is with a two dimensional space. The **I-R-C** course of development of the number concept is characterized by two distinct stages. The first is a generalization of the real part, i.e., from discrete to continuous form and the second is the addition of another dimension to represent the 'imaginary' part. Fig.2 shows a geometric representation of the general number space **C** in its final form of evolution. The number when further generalized, takes the form of a variable.

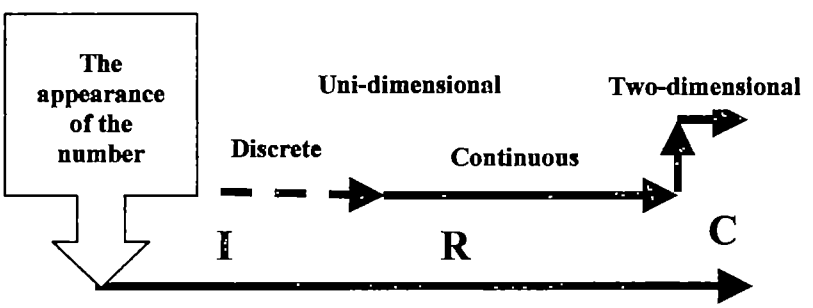

Fig 1 The I-R-C course of evolution of the number concept

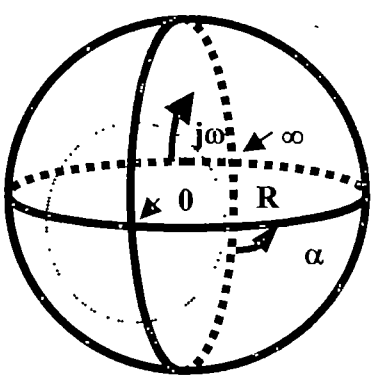

Fig 2 The complex number space as the surface of an infinite sphere, the great equatorial circle of which happens to be R that contains the discrete set I .

Table 1: Various ancient systems of denoting numbers

Babylonian	Y	YY	YYY	YYY Y	YYY YY	YYY YYY	YYY YYY Y	YYYY YYYY	YYYY YYYY Y	<	
Egyptian	I	II	III	IIII	III II	III III	IIII III	IIII IIII	III III III	∩	
Greek	A	B	Γ	Δ	E	F	Z	H	θ	I	
Roman	I	II	III	IV	V	VI	VII	VIII	IX	X	
Ancient Chinese	一	二	三	四	五	六	七	八	九	十	
Mayan	.	..	...	....	—	. —	.. —	... —	.... —	— —	∩ ∪
Hindu	1	2	3	4	5	6	7	8	9	10	0

NUMBER EXPRESSION

The ancient human communities in the various parts of the world used different forms or systems to express numbers. Table 1 shows the symbols used by different people. For example, "twelve" was written as follows in the systems used by various communities:

Babylonian <YY
Roman XII
Egyptian ∩II
Mayan
Greek(Attic) ΔII
Greek(Ionian) ιβ
Hindu 12

Despite certain defects and/or disadvantages in some of them, all these forms of expression served the needs of those times. They are the forerunners of the SOP form.

The aim of representation or expression in the case of a number is to express the multitude in terms of a much smaller number of symbols. The choice of the basis was most probably influenced by human anatomy. Fingers and toes played a significant role not only in counting but also in forming bases such as five and ten. The Babylonians used sixty as the basis and had two symbols which looked like 'Y' (standing for one) and '<' (representing ten). Although there is grouping in 'tens', the radix or base of their system was 'sixty', which seems to arise out of their commendable work in astronomy. In their system, forty two was written as

<<<< YY

The square root of two was computed and represented as

Y << YY <<<<< < Y

to be read as 'ONE -TWENTYFOUR-FIFTYONE-TEN'. In the decimal system this appears as 1.414213, which is an impressive estimate. The way we read numbers is inherently linked to the decimal system. Reading the Babylonian numbers was probably arduous but the Babylonians were skilled in the use of such a large base. The common people were to wait until a simple and perfect system came from the Hindus. The Babylonians were the earliest people known for the use of the place value which is an important characteristic of the SOP structure. They did not consider 'zero' seriously. Consequently their notation never distinguished 620 from 62000. A 'true zero' came from India and brought numeration and arithmetic into the reach of the common people. The Mayans of Central America also were using zero.

Mathematicians acknowledge and admire the introduction of zero as one of the greatest achievements [1]. The introduction of zero rendered the decimal system of numeration sound and flawless. It is an epoch-making

event in the history of mathematics. We take up the issue of zero in some detail in the following.

THE *VALUE* OF ZERO

Despite being a symbol to denote nothing, zero is regarded as a profound contribution by the Hindus to the world of mathematics. On the surface this accreditation seems mysterious. Consideration of some aspects of Indian philosophy will help clear the mystery. Indian spiritual philosophy holds certain concepts that are remarkably in harmony with the concept of zero and infinity. Indian mathematicians occasionally darted into the world of their spiritual philosophy deviating briefly from their normal mathematical path.

The ancient mathematical works of the Hindus were in a poetic style for aesthetic appeal and convenience in memorisation - the latter process being the major means of preserving knowledge for posterity. To avoid monotony, synonyms were used to mean the same thing at different places to fit the rhyme and the rhythm. The synonyms for zero according to *Sankhya Nighantu* (Books of synonyms for numbers), an attachment to *Muhurthadarpanam* (Mirror of the auspicious moments), a book of astrology, are given by the following:

Aakaasham gaganam shuunyam antariksha-
maruthpatham.

The author of this paper found a rare copy of this old book in his father's personal collection. The particulars of this publication were lost along with the first few pages of this copy and it is very unlikely that the book is publicly accessible. Most scholars including the author's father memorized all such texts with little attention to the publication details. Certainly, the publishers of the book do not exist today.

Shuunyam means vacuum and it is the only word that is close to the commonly understood meaning of zero today. *Aakasham* and *gaganam* both mean the sky, *antariksham* means outer space and *maruthpatham* may be literally translated as air-path. Bhaskara the Indian mathematician refers to zero as *kha* that also means sky. The latter set of words seems to signify some sense of vastness that is associated with the Indian concept of zero. Vastness reflects the sense of infinity. Thus zero and infinity possess certain common properties that are supernatural. There is a non-duality (*Advaita*) concept in Indian spiritual philosophy that considers two entities, which are believed to be the same and at the same time distinctly different. These concepts are somewhat difficult to understand in the physical context.

Although zero is often the focal point of many mathematical discussions, its inseparable companion 'infinity' should also be considered in the light of the mysticism of the Hindu thinking. In fact, zero and infinity do not belong to the real physical world. They had to be invoked from outside the physical world to render our world of mathematics sound and eternally robust.

Infinity (∞) is unique as is Parabrahma, the Supreme Being. It is the diametrically opposite point on the great ball. It is relative to the origin of our world (Jagat/ Universe/ Creation / Maya). Polytheism instead of being explained as a diversity property of the Unique Thing, misleading interpretations are often given. The multitude of the deities are manifestations of the unique Supreme Being which is referred to as Anantham, Achyutam, Parabrahmam, etc. relative to ones own world of reference. Let us consider the prayers addressed to the Supreme Being in 'Srimahabhagavatham' (Chapter 8, Section 3) by the renowned Telugu poet Bammera Potana:

73
By whom the universe is created;
Within whom it remains absorbed;
The Supreme Lord,
Who is the root cause;
Who is devoid of origin, middle and end;
Who happens to be everything;
In such a One, the Self-Created; I seek refuge.
74
I think of the One
That is the universe both exclusive and inclusive of Himself,
The eternal witness to all events, The Spotless and The Untarnished,
The Self-created.

Bhaskaracharya discusses the relationship between zero and infinity in mathematical terms as follows:

*Any number * Shuunyam (zero) = Shuunyam (zero)*
Any number / Shuunyam (zero) = Khahaaram (Infinity)

These two apparently separate statements in fact propose

$$x / \delta x = \infty$$

or

$$x = \infty \bullet \delta x$$

only one non-dual statement.
Anatham (Parabrahma) * Shuunyam (Kha or maaya) = Physical World.

The Physical World is not a novel entity. It is an element of the countless values of Khahaaram (Infinity). Likewise, the Physical World which is the result of the relationship between Brahma and Maaya can not be different from the true Parabrahma. For this reason Bhaskaraachaarya refers to Infinty as 'Anantham' and Achyutham', two synonyms of Brahma or Parabrahma. This is based on the concept that Parabrahma remains invariant despite the creation of the Physical World or the integration of the countless physical entities in itself.

Brahma (Sat) is often referred to also as 'Ekam' in the ancient Indian scriptures. This is not characterized by a numerical value (half of two, one quarter of four, etc.). It is the Infinity into which all numbers dissolve and lose their individual identities. Bhaskara concludes his *'Leelavathi'* with an expression of great reverence to Parabrahma. In the 11th poem of Beejaganitham Bhaskara refers to Parabrahma as Anantham (limitless) and Achyutham (that can not be replaced).

The Hindu choice of the symbol for zero also seems to have significance. A circle represents an endless line. Anantham also signifies endlessness.

The common feature between 'Zero' and 'Infinity' is termed as *'poornam'*, meaning fullness. A reference to this feature may be found in the following hymn:

Poornamadah poornamidam poornaat
poornamudachyatey
Poornasya poornamaadaya poornameva-avasishyatey

This describes some features of the Supreme Entity called as *Brahma* referred to by the pronoun 'That'. The other entity is the universe referred to by the pronoun 'This'. The above hymn means literally as follows:

That is full. This is full.
The fullness of this is created by the fullness of that.
If fullness is taken away from fullness, what remains is only fullness.

Mathematically speaking, zero and infinity satisfy the property

$$f - f = f \qquad (0)$$

that is beyond the scope of any physical entity. The Hindu mysticism appears to have played a positive role in fixing the concept of zero (and infinity) leading to a perfect number system and elegant methods of computation that are greatly admired in the world of mathematics.

THE GENERAL STRUCTURE OF THE HINDU NUMBER SYSTEM

The number expression in the Hindu system of numeration $d_{k-1}\ \ d_{k-2}\ \ \ldots\ \ d_1\ \ d_0$ is evaluated as

$$n = \sum_{0}^{k-1} d_k.(10)^k . \qquad (1)$$

This gave rise to the general formula

$$n = \sum_{0}^{k-1} d_k.(r)^k . \qquad (2)$$

in which r, the radix or base of the number system, may be any positive integer > 1 and $d_k \in B$, $B=[0, 1, 2, r-1]$. This gave rise to the generic structure in the SOP form as shown in Fig.3. A considerable number of mathematical expressions may be seen to fit into this structure in which the various components were generalized in distinct stages. This process of generalization too appears to be strongly correlated with the various stages of development of the number concept itself from positive integers through real numbers to complex numbers, while the generic structure seems to have played host to a variety of mathematical expressions as will be apparent from the following discussion.

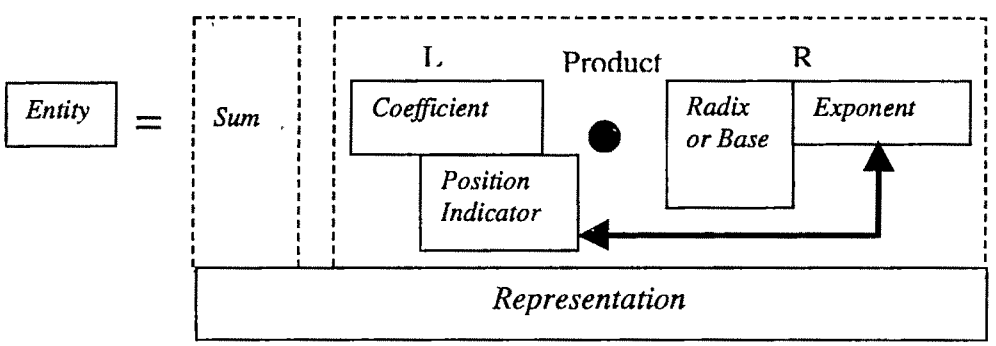

Fig 3 The generic SOP structure suggested by the number system

At its first appearance, the SOP form (1) served as a formula to give the numerical value of a number expression. All components of the structure belong to the discrete domain of positive integers. The 'sum' and the 'product' represent numerical addition and multiplication respectively. The 'coefficient' is in B. The 'radix' or 'base' is a positive integer $r \geq 2$, that is equal to the cardinality of B. The 'position indicator' k attached to the coefficient and the 'exponent' k of the radix are the same integers. The digits in a number representation may be evaluated as

$$d_k = Integer\ part\ of\left[\frac{n}{r^k}\right] - Integer\ part\ of\left[\frac{n}{r^{k+1}}\right].r \qquad .(3)$$

As the coefficient becomes real and the radix a real function while all others in the generic structure remain as in the case of the number representation, function representation in power series SOP form becomes apparent. That is,

$$f(t) = \sum_k f_k . t^k , \qquad (4)$$

in which

$$f_k = \frac{1}{k!}\left[\frac{d^k f(t)}{dt^k}\right]_{t=0} . \qquad (5)$$

Next, as the radix assumes the status of an imaginary function, the discrete Fourier series representation of a periodic function emerges as:

$$f(t) = \sum_k f_k \left[\exp(j\omega t)\right]^k , \qquad (6)$$

where

$$f_k = \frac{\Omega}{2\pi}\int_{-\pi/\Omega}^{\pi/\Omega} f(t).\exp(-jk\Omega t)dt . \qquad (7)$$

When the position indicator and the exponent of the SOP form become continuous, the sum becomes an integral. The Dirac delta function acts as the radix in the expressed for the realization of a generalized function whose shift (continuous) is directly indicative of its position without the need to be realized through an exponent.

$$\varphi(\tau) = \int_{-\infty}^{\infty} \varphi(t)\delta(t-\tau)dt . \qquad (8)$$

The Laplace trnasform definition arises out of a further generalization of the structure with real and continuous entities. The radix happens to be the complex special function *exp(-s)*. It could be an exponent of any positive real number and the whole study of linear time invariant dynamical systems is possible with such a transform, but it would require a scale factor that is reduced to unity by choosing the base of Naperian logarithms and the transform is normalized.

$$F(s) = \int_0^{\infty} f(t).\exp(-st)dt . \qquad (9)$$

$$f(t) = \frac{1}{2\pi j}\oint F(s).\exp(ts)ds . \qquad (10)$$

The z-transform is the result of discretizing the Laplace transform *with* $z = exp(sT)$, where T is the discretization interval. In this case the radix is the complex variable z^{-1} and the position indicator k that is equal to the exponent represents the position.

$$F(z) = \sum_{k=0}^{\infty} f_k . \left[z^{-1}\right]^k . \qquad (11)$$

$$f_k = \frac{1}{2\pi j}\oint F(z).z^{k-1}dz . \qquad (12)$$

Fourier transform:

$$F(\omega) = \frac{1}{2\pi}\int_{-\infty}^{\infty} f(t).\exp(-j\omega t)dt . \qquad (13)$$

$$f(t) = \frac{1}{2\pi}\int_{-\infty}^{\infty} F(\omega).\exp(j\omega t)d\omega . \qquad (14)$$

Mellin Transform:

$$F(m) = \int_0^{\infty} f(t).t^{m-1}dt . \qquad (15)$$

$$f(t) = \frac{1}{2\pi}\oint F(m).t^m dm . \qquad (16)$$

Consider the expression defining integral transforms in general

$$F(s) = \int f(t).K(s,t)\,dt . \qquad (17)$$

Here the kernel $K(s,t)$ is a position descriptor that literally means 'at t'. The inverse formulas

$$f(t) = \oint F(s).K^{-1}(s,t)\,ds \qquad (18)$$

may also be interpreted in the same way by interchanging the roles of t and s.

Table 2 summarizes the relationships among the various forms of mathematical expression with reference to the generic SOP form identified in this paper. Thus the

Table 2: Evolution of various SOP forms of mathematical expression from the Hindu system of number representation

Expression → Features ↓	Number system	Function as power series	Discrete Fourier series of a periodic function	Generalized function	Laplace transform	Fourier transform	z-transform	Mellin transform
Radix (Base)	*Positive integer* $r \geq 2$	*Real, t*	$exp(j\Omega t)$	$\delta(t)$	$exp(-s)$	$exp(-j\omega)$	z^{-1}	*Real, t*
Coefficient	$0 \leq d_k \leq r-1$	*Real,* f_k	f_k	*Generalized function*	*Real, f(t)*	*Real, f(t)*	*Real,* f_k	*Real, f(t)*
Position index (Exponent)	*Integer k*	*Integer, k*	*Integer, k*	*Real,* τ	*Real* $t \in [0, \infty[$ *continuous*	*Real* $t \in [0, \infty[$ *continuous*	*Positive integer,k*	t
Position value	r^k	t^k	$exp(j\Omega t)^k$	$\delta(t-\tau)$	$[exp(-s)]^t$	$[exp(-j\omega)]^t$	$(z^{-1})^k$	t^{s-1}
Remarks	*Word length: Number of digits in the number expression*		*Discrete spectrum: The set of coefficients*	*Natural positioning along t*	*In general* α^t *is also possible.* $\alpha=e$ *normalizes*	*Continuous spectrum*	*Positioning natural*	

evolution of a class of mathematical expressions is traced back to the Hindu number system with which it shares a common structure. The development of the number concept seems to have also driven the process in which mathematics moved from numbers through functions to integral transforms.

VII. Concluding Remarks

In view of these observations, the following statements seem to make sense.

- Terms such as $exp(j\Omega t)$, $\delta(t)$, $exp(-s)$, z^{-1}, belong to the same species as the radix of a number system with reference the generic SOP form.
- The string of digits in a number or for that matter, any discrete sequence of quantities or function representing the 'coefficients' in the SOP form, is in the sense of a 'spectrum'. Consequently 'bandwidth' or 'word length' are in the same spirit.
- The inverse formula for the evaluation of the 'coefficients' is in the sense of tuning.
- An interesting feature of the SOP form is the duality between 'product' and 'convolution'. In fact the popular method of multiplication of numbers is by convolution of the digital representations.

Let us consider two numbers M and N each of three digits

$$M = m_2 r^2 + m_1 r + m_0,$$
$$N = n_2 r^2 + n_1 r + n_0,$$

whose product

$$M.N = m_2 n_2 r^4 + (m_1 n_2 + m_2 n_1) r^3 + (m_0 n_2 + m_1 n_1 + m_2 n_0) r^2 + (m_0 n_1 + m_1 n_0) r + m_0 n_0 .$$

This may be computed using the convolution formula

$$M.N = \sum_{j=-(k-1)}^{k-1} \sum_{i=0}^{k-1} m_i r^i n_{i-j} r^{i-j}, \quad k = 3$$

as illustrated in Table 3:

The result shown in the last row is the value of the product and not its representation in the r-based number system. The above illustration also looks exactly like one for multiplication of polynomials. The product of any two entities that are subject to the present generic SOP structure can be evaluated by the same convolution procedure. The SOP structure happens to be the backbone of matrix operations in terms of which several computations are realized in the well-known Matlab system.

Table 3: Multiplication by convolution

		m_2	m_1	m_0			
n_2	n_1	n_0					
		$m_2 n_0 r^2$					$j=-2$
		m_2	m_1	m_0			
	n_2	n_1	n_0				
		$m_2 n_1 r^3$	$m_1 n_0 r$				$j=-1$
		m_2	m_1	m_0			
		n_2	n_1	n_0			
		$m_2 n_2 r^4$	$m_1 n_1 r^2$	$m_0 n_0$			$j=0$
		m_2	m_1	m_0			
			n_2	n_1	n_0		
			$m_1 n_2 r^3$	$m_0 n_1 r$			$j=1$
		m_2	m_1	m_0			
				n_2	n_1	n_0	
				$m_0 n_2 r^2$			$j=2$
$m_2n_2 r^4+(m_1n_2+m_2n_1)r^3+(m_0n_2+m_1n_1+m_2n_0)r^2+(m_0n_1+m_1n_0)r+m_0n_0$							

A characteristic feature of the generic SOP structure that makes such procedure applicable is the positioning descriptor that appears also as the exponent over a radix. When the positioning is artificial as in the case of number representation, a value equal to r^k is associated with the position but when the positioning is natural, no such value is applicable; the term with an exponent denotes an operator merely signifying the position. Thus there are good reasons to suspect that the SOP structure of mathematical expressions was triggered by the ancient Hindu number system and the creation of the class of modern mathematical concepts considered in this paper was influenced by the process of generalization of the number concept itself.

DEDICATION

This work is dedicated to the loving memory of Sri Ganti Venkatappadu, the author's father, who until his last journey to Kolkata on 20 December 1998 provided inspiration and information on the ancient Indian literature.

REFERENCE

[1] RASHED R., and MORELON R., (Ed.): *Encyclopedia of the History of Arabic Science, vol.2, Mathematics and Physical Sciences*, Routledge, London &NY, 1996.

Recent Trends in Electric Energy Systems Research

D.P. Kothari
Department of Electrical Engineering, Centre for Energy Studies
Indian Institute of Technology -Delhi, New Delhi 110 016, India

Abstract

This paper throws light on recent trends in electric energy systems research. Main areas discussed are unit commitment, maintenance scheduling economic dispatch, emission dispatch, stability, security etc. This will help to initiate research work and further studies in these areas by new researchers and students.

Index terms: Recent trends, electric energy systems, research area

INTRODUCTION

The rapid development in computer technology and power electronics during the last three decades has ushered in a new era in electric energy systems management and control as with most other fields of science and engineering. The growth in the power sector and stringent demands on quality, reliability and economy has spurred new studies and analysis especially in the developed countries. Computers are extensively used offline for load forecasting, systems planning, stability studies and energy management. Computers are used online for SCADA, state estimation, Unit commitment, security and economic load dispatch etc. Although much of these technologies are not yet implemented in the Indian power sector, it is imperative that they are used and it is essential that electric energy systems engineers from utilities, industries and academic institutions are introduced to the latest developments.

The increasing complexity of electric power networks and interconnections to other infrastructures, vulnerabilities to cascading power failures, interactive and large scale nature of these networks, coupled with advances in modeling, computational methods, software technologies, simulations, control of networks and economic aspects, have stimulated the interest of power community in this area. With the advent of deregulation, unbundling and competition in electric power industry, new ways are being sought to improve the efficiency of that network without seriously diminishing its reliability.

ELECTRIC ENERGY SYSTEMS: BRIEF HISTORY

Electric energy system is around 100 years old. It has now grown enormously in size and complexity. Hence as already said earlier, it is necessary to monitor and control power system operation using computers. For India, the total generating installed capacity of 1300 MW in 1947 has now become 100,000 MW today (2001). For carrying optimal loading, a special purpose slide-rule was devised by Kirchmayer. Till 1950's analog controllers were used for economic dispatch and load frequency control. In 1957, first load flow program was written. July 1974, Dec 87 and Feb 2000 special issues of Proc. IEEE have documented in an excellent manner the advances in power system research.

OPTIMAL OPERATION SCHEDULING

Operation scheduling in electric power industry involves the scheduling of utility's generating facilities. It includes the solution of three sub-problems: maintenance scheduling, unit commitment and economic dispatch. The main objective is to find which of the generating units, available for generation, should be committed (on-line) and how much load they will carry. The type of fuel to be use d is also to be decided for the units that can burn multiple fuels. Nits on maintenance are not available for generation.

During the last decade, large-scale optimization methods have been applied for solving the hydro-thermal scheduling problems. Various techniques used so far are maximum principle, dynamic programming, gradient method (NLP), ANN fuzzy, genetic algorithm etc. Implementation of various methods that can effectively handle practical constraints for real-world problems need to be further addressed. Modeling is another area which needs more attention. More work needs to be done in the area of commitment of hydro units. Recent trends are to develop better coordination methods, which should result in better secured and economic operation

MAINTENANCE SCHEDULING

Several mathematical techniques such as integer programming, integer linear programming, dynamic programming, branch and bound etc. have been used in the past to solve the generator maintenance scheduling. Several heuristic search algorithms have also been tested. Recent trend is also to use multi-objective programming method, which takes care of conflicting objectives. More flexible methods are being developed to make it practically applicable.

UNIT COMMITMENT

UC problem can be defined as the scheduling of production of electric power generating unit's area over a daily to weekly time horizon in order to accomplish some objective subject to various constraints. Problem is a large-scale non-linear mixed integer program. The recent trend is to evaluate the functions that UC modules should perform in restructured markets. Other features that may be considered include distributed generation, transmission network, emissions modeling and particular stochastic methods for modeling reliability, uncertainty, and variability.

ELECTRIC POWER QUALITY

Electric Power quality means different things to different people. Electric power is the only entity, which is consumed at the instant of its production. So long as its use is restricted to heating, lighting and motor applications, very limited quality constraints were sufficient and acceptable all over the world. With proliferation of electronics, number of inadequacies of electrical power were exposed and new quality norms evolved in advanced countries. Main focus is now on harmonics, noise, filtering and communications interfacing power systems. This will guide the user on selection installation and usage of power conditioning equipment.

DISTRIBUTION AUTOMATION

Power distribution systems in India are characterized by increased power loss, poor voltage profile, inadequate metering, frequent failures of major equipment mainly due to non-availability of their loading information and lack of proper monitoring and coordinated controls. Distribution automation DA is getting worldwide attention to overcome these problems. GTD have increased in size and complexity. There are huge T & D losses. Expansion of distribution system has been mostly in an unplanned way in India. This has resulted in non-optimal routing, inadequate conductor size, highly stressed operation of equipment and lengthy low Voltage feeders. These have led to the following problems: increased system losses, poor quality and reliability of supply, increased peak demands and unbalanced loads and poor return of revenue.

The objectives of DA are conservation of energy and solution/ mitigation of above problems, deferral of new construction etc. The EMS (70's) and DMS(90's) have been developed over years as two distinct branches of control centers that work on a SCADA platform. Dispersed generation has further complicated already complex distribution system. The international electrical industry is undergoing a radical transformation from essentially regulated as monopolistic industry to an industry made uncertain within impending deregulation functions and the advent of competitive forces. Captive power plants, specific industrial loads, power quality aspects are to be considered. Computer assisted fault location and service restoration, intelligent sensing devices etc. are other recent areas.

STATE ESTIMATION

State estimation in power systems is a function used to determine the system operating states (V & delta) by filtering the noise, which is usually present in telemetered measurements acquired through data acquisition system. The output of the estimator is used as infeed to various advanced functions of EMS or DMS. A state estimator can smooth out small random errors in meter readings, detect and identify gross measurement errors, and fill-in meter readings that have failed due to communication failures. The new modeling needs associated with the introduction of new control devices and the changes induced by emerging energy markets are making state estimation and its related functions more important than ever. New developments are taking place in areas such as observability analysis, bad data processing, network topology processing, topology estimation and parameter estimation.

LOAD FORECASTING

Latest trend is to find innovative methodological issues and techniques in addressing the problem of forecasting daily loads and prices in the new competitive power markets. Neural networks are preferred for forecasting the demand side and strategic simulation using artificial agents for the supply side.

Forecasting electricity loads have reached a comfortable state of performance in the years preceding the recent waves of industry restructuring. Adaptive time-series techniques based on ARIMA, kalman filtering or special methods were sufficiently accurate in the short term for operational purposes, achieving errors of 1-2% [1,2]

Implications of the new competitive environments for forecasting

- Forecast errors have significant implications for profits, market shares and ultimately shareholder value.
- Day ahead, weather-based forecasting is becoming the most crucial activity
- Information is becoming proprietary
- Distributed and embedded generation may increase

We need further research and integration with conventional time-series methods to provide a more precise forecasting, rather than general descriptive focus.

EMISSION DISPATCH

Because of the increased public awareness of the environmental situation and the plea for clean air, emission dispatch is gaining more importance. Therefore in order to obtain a more meaningful and practical optimal schedule of operation for power system, a study on economic load dispatch is conducted in multi-objective framework (even some objectives may be conflicting) where loss minimization emission objective (NO%, CO, CO_2, SO_2) voltage control, cost are undertaken simultaneously. Optimal hydro-thermal scheduling with multiple conflicting objectives with due consideration of uncertainties in production cost data, system load demand and inflows has become necessary in the present context.

POWER SYSTEM STABILITY

The development of fast acting exciters and electronic voltage regulators overcame to a large extent the transient stability and steady state stability problems. A parallel development in high-speed operation of circuit breakers and reduction of the fault clearing time and reclosing, also improved stability The regulation of frequency has led to the development of turbine and speed governors which enable rapid control of frequency and power output of the generator, with minimum deadband. In well developed and highly interconnected power systems the tie line frequency control (also termed as automatic generation control, AGC) has assumed major importance.

Over last 25 years, the problems of low frequency power oscillations have assumed importance. The frequency oscillations are in the range of 0.2 to 2 Hz. The lower the frequency, the more widespread are the oscillations (called inter-area oscillations) the presence of these oscillations is traced to fast voltage regulation in generations and can be overcome through supplementary control employing power system stabilizers (PSS). The design and development of effective PSS is an active area of research.

Another major problem faced by modern power systems is the problem of voltage collapse or voltage instability, which is a manifestation of steady state instability Historically steady state instability, has been associated with angle stability and slow loss of synchronism among generators. The slow collapse of voltage at load buses under high loading conditions and reactive power limitations is a recent phenomenon.

Power transmission bottlenecks are faced even in countries with large generation reserves. New control devices such as Thyristor controlled series compensation (TCSC) and static phase shifters are under development. The multiplicity of controllers present challenges in their design and coordinated operation. Many intelligent systems are being proposed to deal with this task.

The advent of digital computers has not only resulted in the introduction of complex equipment models but also the simulation of large scale systems. The realistic models enable the simulation of systems over a longer period than previously feasible. However the real time dynamic simulation is not yet feasible even with super computers.

Voltage instability has become a major threat for the operation of many stems during past two decades. In the prevailing open access environment, it is a actor leading to limit power transfers. More work is going on about implementation of countermeasures, getting the sensitivities of margin to collapse and oscillatory stability margin with respect to different controls. New methods are being developed for voltage security analysis and enhancement using intelligent techniques.

FLEXIBLE AC TRANSMISSION SYSTEMS

Flexible AC transmission Systems (FACTS) is the name given to the application of power electronics devices to the control of flows and other quantities in power system. Various configurations of FACTS devices can be developed. While the cost of FACTS devices remain quite high, they may be the best option when new generation and transmission facilities can not be built because of environmental reasons.

CONCLUSION

This paper has thrown light on recent trends in Electric energy systems in 10 main areas of power systems. A large number of references are also given. It is envisaged that this paper should be helpful for students and researchers in the area of electric energy systems

In future, there will be increased use of distributed resources, higher use of power electronics in loads. The customers will expect higher reliability, lower cost and better quality. Rates will depend on the performance.

REFERENCES

1. I.J. Nagrath and D.P. Kothari, "Power system engineering", Tata McGraw Hill, New Delhi 1994
2. I.J. Nagrath and D.P. Kothari, "Electric Machines" ,2nd edition, Tata McGraw Hill New Delhi 1997
3. A.K. Mahalanabis, D.P. Kothari and S.I. Ahsow, "Computer aided power system analysis", Tata McGraw Hill New Delhi 1998
4. T.V. Custem and C. Vournas, "Voltage stability of electric power systems", Norwell M.A. Kluwer 1998
5. P.W. Sauer and M.A. Pai, "Power system dynamics and stability" Englewood cliffs, NJ Prentice Hall 1997
6. P. Kundur, "Power system stability and control", McGraw Hill New York, 1994
7. A. Montecelli "State estimaiton in electric power systems- A generalised approach", Norwell, MA: Kluwer, 1999
8. A Chakrabarti, D.P. Kothari and A.K. Mukhopadhyay, "Performance operation and control of EHV power transmission systems: Wheeler, New Delhi 1995
9. D.P. Kothari and J.S. Dhillon, "Optimal power sytem scheduling:" Prentice Hall of India
10. Proc. IEEE special issue of June 1974, Dec 1987 and Feb 2000
11. L. Phillipsm and H Lee Wills, "Understanding electric utilities and deregulaiton", Marcel Dekkar Inc. New York 1999

A New Three Level Output Feedback Sliding Mode Control For Discrete System

B. Bandyopadhyay and Chakravarthini M. Saaj
Systems and Control Engineering, Dept. of Electrical Engineering,
Indian Institute of Technology, Mumbai-400076, India.
E-mail: bijnan@ee.iitb.ac.in

Abstract

This paper presents a new approach for sliding mode control of discrete-time systems using a three stage switching control implemented using the fast output sampling feedback technique. Our proposed control scheme does not require the system states as it makes use of only the output samples for designing the controller. This method provides a good solution to chattering elimination. Finally, we show, in simulations, that the fast output sampling sliding motion similar to that obtained using state feedback.

Key words: Sliding mode control, Three stage switching, Fast output sampling.

INTRODUCTION

In recent years a considerable amount of effort has been put in to obtain a systematic definition of the concepts of Digital Sliding Mode (DSM) and controller design Techniques have been carried out [1]-[4]. In [2], Furuta presents a stable discrete sliding mode control insensitive to the choice of sampling interval. The control system design is designed on the basis of a discrete Lyapunov function and a sufficient condition of the control gain to make the system stable is given. This method ensures stability and at the same time avoids chattering. Gao [3] has used the " reaching law approach " to design the controller for a discrete-time system using state feedback. The digital implementation requires a certain sampling interval which brings not only chattering along the predesigned sliding mode but also possible instability with a large gain [4]. A few research works are available which deal with VSC design using output feedback [5]-[11] The static output feedback problem is one of the most investigated problems in control theory and application [8]. However no results are available till today, which shows that complete pole, assignment is possible using static output feedback.

Output feedback can be realized using fast output makes it possible to arbitrarily assign the system poles. Unlike static output feedback, fast output sampling feedback always guarantees sampling [9] or by periodic output feedback [10]. In [9] Werner has used the fast output sampling (FOS) feedback which has used the features of static output feedback and the stability of the closed loop system. In [11], we developed a new approach for sliding mode control of discrete-time systems using the reaching law approach in [3] together with the fast output sampling feedback proposed in [9].

In this paper, we present a new algorithm for the three-stage output feedback discrete sliding mode control using the results proposed in [2]. The outline of this paper is as follows: A brief review of the preliminary results is presented. The new design procedure using the proposed method is illustrated, followed by a numerical example to illustrate the advantages of the method. Concluding remarks are drawn.

PRELIMINARIES ON DISCRETE-SLIDING MODE CONTROL

Consider the SISO discrete-time system

$$x(k+1) = \phi_\tau x(k) + \Gamma_\tau u(k),$$
$$y(k) = C\,x(k), \qquad (1)$$

where τ is the sampling period, x is the n-dimensional state vector, u is a scalar, y is the output vector and ϕ_τ, Γ_τ, C are matrices of appropriate dimensions. Let the switching plane be

$$s(k)=c^T x(k)=0.$$

where c^T is a constant $(1 \times n)$ matrix. The following type of two level switching control is considered in [2]

$$u(k) = (F_{eq} + F_D)x(k), \qquad (2)$$

where

$$F_{eq} = -(c^T\Gamma_\tau)^{-1}c^T(\phi_\tau - I).$$

F_D is the discontinous control law. The absolute value of the i-th element of F_D , f_i is a constant for all time amd the same for all i , i.e.,

$$|f_i^+| = |f_i^-| = f_0 , \; i=1,2,3.....n$$

Thus

$$\begin{aligned} f_i &= f_0 \text{ for } (c^T\Gamma_\tau)s(k)x_i(k) < -\delta_i, \\ &= 0 \text{ for } -\delta_i \le (c^T\Gamma_\tau)s(k)x_i(k) \le \delta_i, \\ &= -f_0 \text{ for } (c^T\Gamma_\tau)s(k)x_i(k) > -\delta_i , \end{aligned} \qquad (3)$$

where $x_i(k)$ is the element of x(k) and δ_i is defined as

$$\delta_i = \frac{1}{2}\sum_{j=1}^{n} |x_i(k)||x_j(k)| f_0 (c^T\Gamma_\tau)^2$$

with f_0 limited by

$$0 < f_0 < \left| \frac{2}{c^T\Gamma_\tau \sum_{j=1}^{n} |t_{1j}|} \right| , \qquad (4)$$

t_{1j} being the i-th element of t_1 satisfying

$$c^T t_1 = 1 , \; c^T t_i = 0, \; t_i \perp t_j \; (i \neq j).$$

ROBUSTNESS ANALYSIS

Here the design is done under plant uncertainty [2]. The plant is known to be represented by

$$\begin{aligned} x(k+1) &= \phi_{\tau 0} x(k) + \Gamma_\tau u(k), \\ y(k) &= Cx(k). \end{aligned} \qquad (5)$$

The actual system matrix ϕ_τ is related to $\phi_{\tau 0}$ by

$$\phi_\tau = \phi_{\tau 0} + \Delta\phi_\tau .$$

The equivalent control is designed as

$$F_{eq} = -(c^T\Gamma_\tau)^{-1} c^T(\phi_{\tau 0} - I).$$

The i-th element f_i of the control law F_D of equation (2) is

$$\begin{aligned} f_i &= f_0 \text{ for } (c^T\Gamma_\tau)s(k)x_i(k) < -\delta_i', \\ &= 0 \text{ for } -\delta_i' \le (c^T\Gamma_\tau)s(k)x_i(k) \le \delta_i', \\ &= -f_0 \text{ for } (c^T\Gamma_\tau)s(k)x_i(k) > -\delta_i', \end{aligned} \qquad (6)$$

where

$$\delta_i' = \frac{1}{2}(c^T\Gamma_\tau)^2 \sum_{j=1}^{n} |x_i(k)||x_j(k)| (f_0 + \bar{d})$$

so f_0 satisfy

$$\bar{d} < f_0 < \left| \frac{2}{c^T\Gamma_\tau \sum_{j=1}^{n} |t_{1j}|} \right| - \bar{d} \qquad (7)$$

FAST OUTPUT SAMPLING SLIDING MODE CONTROL

In fast output sampling period τ is subdivided into N subintervals

$$\Delta = \tau/N,$$

Let (ϕ, Γ, C) be the system obtained from (1) by sampling at the rate $1/\Delta$. let ν denote the observability index of (ϕ, Γ). N is chosen to be greater than or equal to ν. The last N output samples are measured at time instants $t = l\Delta$, l=0,1,....N-1 and a constant control signal is applied over a period τ. The control signal is constructed as a linear combination of the last N output samples [9] and is given as

$$u_k = [L_0 \; L_1 \; ..... \; L_{N-1}] \begin{bmatrix} y(k\tau - \tau) \\ y(k\tau - \tau + \Delta) \\ . \\ . \\ y(k\tau - \Delta) \end{bmatrix} , \qquad (8)$$

where the block L_i represent the output feedback gains. The control law (8) can be interpreted as a static output feedback

$$u_k = Ly_k .$$

Then a representation for the system (1) is

$$\begin{aligned} x_{k+1} &= \phi_\tau x_k + \Gamma_\tau u_k , \\ y_{k+1} &= C_0 x_k + D_0 u_k , \end{aligned} \qquad (9)$$

where

$$C_0 = \begin{bmatrix} C \\ C\phi \\ . \\ C\phi^{N-1} \end{bmatrix} , \; D_0 = \begin{bmatrix} 0 \\ C\Gamma \\ . \\ . \\ C\sum_{j=0}^{N-2} \phi^j\Gamma \end{bmatrix} \qquad (10)$$

Let F be an initial state feedback gain such that the closed loop system $[\phi_\tau + \Gamma_\tau F]$ has no eigen values at the origin. Then one can define a fictitious measurement matrix.

$$C(F,N) = (C_0 + D_0F)(\phi_\tau + \Gamma_\tau F)^{-1}, \quad (11)$$

which satisfies the fictitious measurement equation

$$y_k = Cx_k.$$

Let L to realize the effect of F it must satisfy

$$LC = F. \quad (12)$$

An important relation for evaluating the switching function in terms of the output samples y_k is

$$s(k) = c^T C^{-1} y_k . \quad (13)$$

For the inverse of C to exist we select N to be equal to the order of the system [11].

THREE LEVEL OUTPUT FEEDBACK SLIDING MODE CONTROL

In this section as an extension of the state feedback sliding mode control in [2], the fast output controller is developed. The new control algorithm using fast output sampling is given below:

Step 1: Discretize the given continous-time system for a sampling period τ to get the discrete system (ϕ_τ, Γ_τ, C) in (1). Select the number of output samples N=n, where n is the order of the system and construct the fictitious system (ϕ, Γ, C) of sampling period Δ where $\Delta = \tau/N$.

Step 2: Determine the switching surface parameter c to evaluate the initial value of the switching function

$$s(0) = c^T x(0).$$

Step 3: Obtain the equivalent state feedback gain F_{eq} and the switching gain F_D by testing the conditions listed in (4).

Step 4: In fast output sampling initially a state feedback control of the form

$$u(0) = Fx(0)$$

is to be applied. Here the initial state feedback control applied to the system is

$$u(0) = (F_{eq} + F_D)x(0).$$

Step 5: The control generates a trajectory and measure the fast output samples y_k at the next sampling instant $t = k\tau$, $k = 1,2,\ldots$. Evaluate the switching function

$$s(k) = c^T C^{-1} y_k .$$

Here we see that we compute the switching function in terms of the fast output samples thereby eliminating the need to measure the system states.

Step 6: Now test the conditions given in equation (4) and then fix the value for the switching gain f_i as f_0 , 0 or $-f_0$. Let us express the state feedback gain as

$$F = F_{eq} + F_D$$

Here it is to be noticed that F is not a fixed gain. It takes three different values as F_D switches between the f_0 , 0 or $-f_0$

Step 7: Construct the fictitious measurement matrix C and compute the output feedback gain L using the expression

$$L = FC^{-1}.$$

Here again L takes three different values depending upon F and C.

Step 8: The output feedback sliding mode control to be applied is

$$u_k = Ly_k .$$

Repeat steps 5 to 8 in order to get sliding mode motion using fast output sampling. Similar algorithm is applied in the case of perturbed plant making use of (8) through (10) for evaluating the equivalent control F_{eq} and the switching control F_D.

NUMERICAL EXAMPLE

The same example as cited in [2] is considered here to illustrate how output feedback gives the same results as obtained with state feedback. Consider the linear system

$$\dot{x} = \begin{bmatrix} 0 & 1 \\ -1 & -2 \end{bmatrix} x + \begin{bmatrix} 0 \\ 1 \end{bmatrix} u,$$
$$y = [1 \quad 0]x.$$

Let the initial conditions be

$$x(0) = [1 \quad 0].$$

Now sample the above system with sampling period τ = 0.1 to derive the following discrete system

$$\ddot{o}_\tau = \begin{bmatrix} 0.9953 & 0.0904 \\ -0.0904 & 0.8143 \end{bmatrix}, \tilde{A}\delta = \begin{bmatrix} 0.0046 \\ 0.0904 \end{bmatrix},$$
$$C = [1 \quad 0].$$

Since the order of the system is 2, let us select N=2. Therefore $\Delta = 0.05$. The discrete system obtained by sampling at the rate $\Delta = 0.05$ is

$$\phi=\begin{bmatrix}0.9988 & 0.0476\\ -0.0476 & 0.9037\end{bmatrix},\ \Gamma=\begin{bmatrix}0.0012\\ 0.0476\end{bmatrix},$$
$$C=\begin{bmatrix}1 & 0\end{bmatrix}$$

and

$$C_0=\begin{bmatrix}1 & 0\\ 0.9988 & 0.0476\end{bmatrix},\ D_0=\begin{bmatrix}0\\ 0.0012\end{bmatrix}.$$

Let the switching surface (a line in this case) be

$$s(k) = [1 \quad 1]x(k).$$

Case a: Nominal plant

For the nominal plant the equivalent state feedback gain is

$$F_{eq} = [1 \quad 1].$$

Here f_0 is chosen as 5. Determine the values of F_D using (3). Then the discrete state feedback gain is

$$F= [1 \quad 1] + [f_1 \quad f_2].$$

The fictitious measurement matrix C and L using (11) and (12) and the switching surface is

$$s(k) = [1 \quad 1]C^{-1}y_k.$$

Then the output feedback sliding mode control is

$$u(k) = Ly_k.$$

Case b: Perturbed plant

Let the upper bound of perturbation be

$$\bar{d} = 1(i = 1,2)$$

and

$$D=[0.1 \quad -0.5].$$

Therefore the uncertainty of the nominal plant ϕ_τ is

$$\Delta\phi_\tau = \begin{bmatrix}0.0005 & -0.0023\\ 0.009 & -0.0452\end{bmatrix}$$

and the perturbed plant $\phi_{\tau 0}$ is

$$\phi_{\tau 0} = \begin{bmatrix}0.9949 & 0.0928\\ -0.0995 & 0.8596\end{bmatrix}.$$

Here it is assumed that the system is supposed to be modeled to give the equivalent control

$$u_{eq} = 0,$$

i.e.,

$$F_{eq} =[0 \quad 0],$$

Then the state feedback gain is

$$F=[f_1 \quad f_2].$$

Here again f_0 is chosen as 5. The values of f_1 and f_2 are selected using (6). Then C and L are evaluated obtained using (11) and (12).

The simulation results of the second order discrete system are shown in Figure 1 and 2. The results are satisfactory. Figure 1 show the response of the nominal system. Figure 2 show the response of the perturbed system. The plot of the switching function shown in Figure 1(a) decreases towards zero form the initial value and stays within a band of decreasing amplitude. Figure 1(b) show the response of the states. The control function plot in Figure 1(c) settles to zero because no reference input is applied. The phase portrait in Figure 1(d) show the sliding motion and the trajectory stays within a thin region along the neighborhood of the sliding mode.

Figures 2(a) through (d) show the responses of the perturbed system. The state responses are shown in Figure 2(a). The behavior of the switching function vector is depicted in Figure 2(b). Initially due to the presence of parameter uncertainties, the value of s(k) is large but after this initial transient s(k) remains near zero.

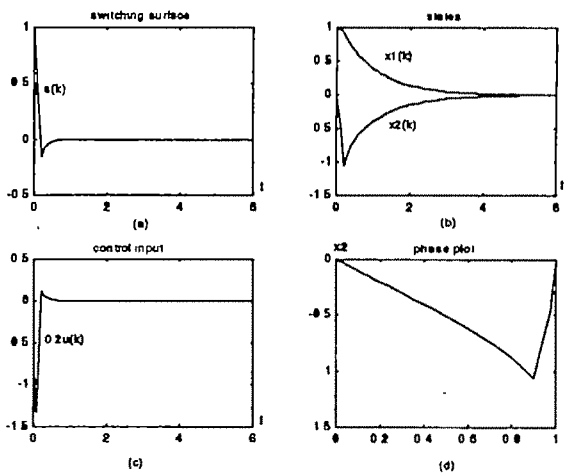

Figure 1. Response of the nominal plant

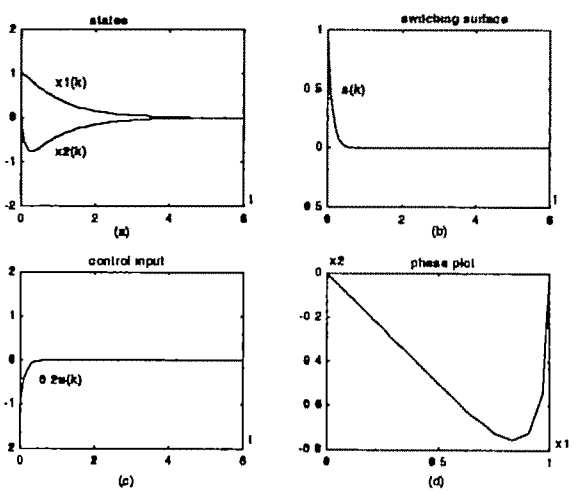

Figure 2. Response of the perturbed plant

The effect of the uncertain parameter is evident in the transient. The state variables go to zero despite the perturbation. Figure 2(c) shows the control input. We see that even without using the equivalent control, satisfactory results can be obtained by considering the uncertainty. The phase plot is shown in Figure 2(d). the simulation results clearly demonstrate the robustness of the system with respect to the parametric perturbation.

CONCLUSION

A new approach for the design of a three stage output feedback sliding mode control for linear discrete-time systems has been presented in this paper. The key advantage of this method is that we do not use the system states for feedback purpose. In this method large output feedback coefficients are applied outside the switching region, and in the neighborhood of the sliding mode, the equivalent linear control is used. The switching control gain takes values of three levels only. Since the control input does not switch so frequently chatter response is obtained is obtained. Moreover, the discrete sliding mode control is insensitive to the choice of sampling interval. The proposed method is straightforward and can also be applied to the system subjected to disturbance. The results in this paper help to design a new output sampling sliding mode with good performances. This can make output feedback sliding control a viable alternative to state feedback and estimated state feedback for many practical applications of variable structure systems in the near future.

REFERENCES

[1] S. Z. Sarpturk, Y. Istefanopulos, and O. Kaynak, "On the stability of discrete-time sliding mode systems", IEEE *Trans. Automat Contr.*,vol. 32, no.10, pp. 930-932, 1987.

[2] K. Furuta, "Sliding mode control of a discrete system", *Syst. and Contr. Lett.*, vol.14, pp. 145-152, 1990.

[3] W. Gao, Y. Wang and A. Homaifa, "Discrete-Time Variable Structure Control Systems", IEEE *Trans. Ind. Electron.*, vol. 42, no. 2, pp.117-122, 1995.

[4] V. I. Utkin, J. Guldner and J. Shi, *Sliding mode control in electromechanical systems*, London: Taylor and Francis Ltd., pp. 155 -169, 1999.

[5] S.H. Zak, S. Hui, "On Variables Structure Output Feedback Controllers for Uncertain Dynamic Systems", IEEE *Trans Automat. Contr.*, vol 38, no.10, pp. 1509 -1512, 1993.

[6] S. H. Zak, S. Hui, "Output Feedback Variable Structure Controllers and State Estimators for Uncertain/Nonlinear Dynamic Systems", IEE *Proc* D, vol.140, no.1, pp. 41-50, 1993.

[7] S. K. Bag, S. K. Spurgeon, C. Edwards, "Output Feedback Sliding Mode Design for Linear Uncertain Systems," IEE *Proc. Contol Theory Appl.* vol. 144, no.3, pp. 209 - 216,1997.

[8] V. L. Syrmos, P. Abdallah, P. Dorato K.Grigori adis, "Static Output Feedback: A survey"Atomatica, vol. 33, no. 2, pp. 125 - 137,1997.

[9] H. Werner, "Multimodel Robust Control by Fast Output Sampling – An LMI Approach", *Automatica*, vol. 34, no. 12, pp. 1625 - 1630, 1998.

[10] H. Werner, K. Furuta, "Simultaneous Stabilzation by Piecewise Constant Periodic Output Feedback", *Control Theory and Advanced Technology* vol. 10, no. 4, Part 4, pp.1763-1775, 1995.

[11] B. Bandyopadhyay, Chakravarthini M. Saaj and H. Unbehauen, "A new algorithm for discrete-time sliding mode control using fast output sampling feedback", under revision in IEEE *Trans.*on Industrial Electronics.

Identification Of Time Varying Dynamical Systems: A Neural Network Approach

S. V. Dudul[1], A. A. Gahtol[2], S. S. Salankar[3] and V. R. Mankar[4]
[1]PG Department of Applied Electronics, Amravati University, Amravati 444 602, India
[2]Govt. college of Engineering, Pune
[3]Department of Electronics, B. D. College of Engineering, Sevagram, Wardha, India
[4]Department of Electronics, Govt. Polytechnic, Amravati, India

Abstract:

In this paper, we deal mainly with the identification of linear time-varying discrete time dynamical systems. It is presumed that such systems are represented by transfer function characterizations. As the behavior of the system changes, the neural network keeps track of the changes in the characteristics and parameters. Thus, at any instant of time, it correctly simulates the given time-varying system, despite the significant changes in system's property. A system transforms a given input signal to some output signal in accordance with its parameters and characteristics. The excellent approximating capability of the neural network is used to identify the relationship between system variables and parameters. In essence, a neural network perfectly mimics and identifies the actual physical system. It is shown that a simple neuronal model containing a single neuron fairly accurately simulates the adaptive system under consideration, which may be of Auto-Regressive or Moving-Average or Auto-Regressive Moving-Average type.

Key words- Dynamical system, neural networks, adaptive system identification

INTRODUCTION:

In adaptive system identification, the true output and the model output are compared, and the error is fed back to a learning element, which modifies the model in an attempt to reduce the error. This behavior is exactly the same as what the neural network does. However, the neural network combines both the model and the learning element in a single entity. It learns to adjust itself. When learning concludes, the network identifies and simulates the system. System identification deals with building models of systems and signals from observed data. It is a vital problem in many fields of signal processing such as automatic control, communication systems, power spectrum estimation, and seismic processing [1,2]. It is mainly concerned with the determination of input-output mapping of the system. Such an identification allows one to predict the system outputs and as a result, this problem has a considerable impact on the applications mentioned above, where forecasting is of extreme importance.

System identification is the experimental approach to the modeling of a process or a plant of unknown parameters. It involves experimental planning, selection of a model structure, parameter estimation and model validation. The procedure of system identification, as pursued in practice, is iterative in nature in that one may have to go back and forth between these steps until a satisfactory model is built. In this paper, we suppose that we have an unknown linear dynamical plant, and the requirement is to build a suitably parameterized identification model for it. The identification procedure is based on an input-output model, which hinges on prior information of the inputs and observable of the system. We suppose that the unknown plant is accessible through its output. Let the system be of single input, single output kind. Let $y(n)$ denote the output of the system due to the input $u(n)$ for varying discrete-time n. Then, the difference between the actual output and the estimated actual output (error) is used to adjust the synaptic weights of the neural network so as to minimize the error in some statistical sense.

System identification is a task of approximating the behavior of the system using a neural network or other learning methods. It can be distinctly helpful in achieving the desired output signal of the system. The issue of identification is perhaps of even greater importance in the field of adaptive control systems.

Since, the plant in an adaptive control system varies in operation with time, the adaptive control must be adjusted to account for the plant

variations. In simple identification problem, one usually assumes that the model has general mathematical form and then its unknown parameters are estimated [3].

The design of any system requires knowledge of its dynamic characteristics. While a simple system may be built with only an intuitive feeling about its behavior, its proper operation depends on a choice of parameters suitable to the characteristics of the particular system. These characteristics must usually be determined by measurements on the system inputs and outputs. A system can be considered to be a transformation of an input into an output. Identification then implies the determination of this transformation based on measurements of the input and the output.

In this paper, we deal primarily with the identification of linear time-variant systems on the basis of normal operating records. We assume a transfer function characterization of the system. Thus the characterization is parametric, so that the problem essentially reduces to one of identifying certain parameters in the system. Here, simple neural networks are trained to adaptively model a linear or near-linear system. Incremental training is used for neural networks, so that when behavior or parameters of the system changes neural network model changes. Thus, at any instant of time, neural network always correctly identifies the parameters of linear time-varying systems.

ADAPTIVE SYSTEM IDENTIFICATION:

A dynamical system with the unknown mathematical characterization is considered in the present paper. What is available on the system is a set of labeled input-output data generated by the system at discrete instants of time at some uniform rate. Specifically, when an m-dimensional stimulus $x(i)$ is applied across m input nodes of the system, the system responds by producing a scalar output $d(i)$, where $i = 1, 2, \ldots, n, \ldots$.

Thus, the external behavior of the system is described by the data set

$$\Gamma : \{x(i), d(i); i = 1,2, \ldots, n, \ldots\} \qquad (1)$$

where $x(i) = [x_1(i), x_2(i), \ldots, x_m(i)]^T$

The samples comprising Γ are identically distributed according to an unknown probability law. The dimension m pertaining to the input vector $x(i)$ is referred to as the dimensionality of the input space. It is assumed that the m elements of $x(i)$ denote the set of present and $(m-1)$ past values of some excitation that are uniformly spaced in time. Now, we attempt to design a multiple input-single output (MISO) model of the unknown dynamical system by building it around a single linear neuron. The neuronal model (adaptive filter) functions under the influence of an algorithm that controls necessary adjustments to the synaptic weights of the neuron. Its operation consists of two continuous processes: 1. Filtering process: which involves the computation of two signals: An output, denoted by $y(i)$, and an error signal, denoted by $e(i)$, and 2. Adaptive process: which involves the automatic adjustment of the synaptic weights of the neuron in accordance with the error signal $e(i)$.

Thus, the combination of these two processes working together constitutes a feedback loop acting around the neuron. Since the neuron is linear, the output $y(i)$ is exactly the same as the induced local field $v(i)$; that is,

$$y(i) = v(i) = \sum_{k=1}^{m} w_k(i)x_k(i) \qquad (2)$$

where $w_1(i), w_2(i), \ldots, w_m(i)$ are the m synaptic weights of the neuron, measured at time, i. In matrix form, $y(i)$ is expressed as an inner product of the vectors $x(i)$ and $w(i)$ as follows:

$$y(i) = x^T w(i) \qquad (3)$$

where $w(i) = [w_1(i), w_2(i), \ldots, w_m(i)]^T$

The neuron's output $y(i)$ is compared to the corresponding output $d(i)$ received from the unknown system at time i. Typically, $y(i)$ is different from $d(i)$; hence, their comparison results in the error signal:

$$e(i) = d(i) - y(i) \qquad (4)$$

The manner in which the error signal $e(i)$ is employed to control the adjustments to the neuron's synaptic weights is determined by the cost function used to derive the adaptive filtering algorithm of interest. This issue is closely related to that of optimization [4].

As system changes its behavior, a neural network also changes its architecture, so that at any time, it correctly simulates the given time-varying dynamic system. Such adaptive neural network model of a system can be used to obtain a great deal of information. For instance, the adaptive model can be analyzed at any given time to determine characteristics of the actual system. Moreover, it might be monitored so as to give a warning that its parameters were approaching values that would result in instability. Another use for an adaptive linear model is evident by its ability to find a minimum sum-squared error linear estimate of a nonlinear system's behavior.

NEURAL NETWORK APPROACH:

In dynamic system identification, if neural networks are used, the objective is to determine an adaptive algorithm or rule which adjusts the parameters of a network, based on given set of input-output pairs. The ability of the neural network to approximate large classes of nonlinear functions sufficiently accurately

BCU 2824 BU 1189 621·381 P941

make them prime candidates for using dynamic models for the representation of nonlinear plants. The fact that static and dynamic backpropagation can be used for the adjustment of their parameters, also makes them attractive in identifiers [5].

Neural networks used for identification typically have multilayer feedforward architecture and are trained using the error backpropagation technique. The purpose of the identification is to find the neural network with response *'o'* that matches the response *'y'* of the system for a given set of inputs *'x'*. During the identification, the norm of the error vector $||d-o||$ is minimized through a number of weight adjustments. To account for system dynamics, the input to the neural network may consist of various past inputs to the system. This can be produced by inserting the delay elements at the system inputs. Neural network tries to model the mapping of the system input to output measured at the time, since the trained neural network is feedforward and instantaneous.

For neural network based identification, there are two main issues. One is the choice of the model architecture to be adopted for system identification and the other is the choice of the learning algorithm. A static neural network and a linear dynamic system are interconnected to form an identification model [6]. From a systems theoretic point of view, multilayer networks represent static nonlinear maps while recurrent neural networks are represented by nonlinear dynamic feedback systems. The problem of identification consists of setting up suitably parameterized identification model and adjusting the parameters of the model to optimize the performance function based on the error between the plant and the identification model outputs. Neural networks hold the promise of solving problems that have here-to-fore proven extremely difficult for traditional digital computers [7].

In this paper, identification of linear time-variant MA, AR, and ARMAX system is carried out using a two-layer feed-forward neural network with a single hidden layer having only one neuron. The proposed network, having a single neuron with a linear transfer function, elegantly simulates the given system.

SIMULATION:

We consider linear time-varying dynamic systems with AR (Auto Regressive), MA (Moving Average), or ARMAX (Auto Regressive Moving Average with Exogenous inputs) models for identification. All-pole filter system (AR) is suitable for representing spectra with narrow peaks (resonance). Secondly, the AR model results in very simple linear equations for the AR parameters. On the other hand, MA (All-Zero) model may require many more coefficients to represent a narrow spectrum. Consequently, it is rarely used by itself as a model for spectrum estimation. It is used to detect the trend of a fast-changing movement. By combining poles and zeros, the ARMAX model provides a more efficient representation, from the viewpoint of the number of model parameters of the spectrum of a random process or system.

Various kinds of input signals given by the following mathematical expressions are presented to finite impulse response linear systems that are causal, stable and minimum phase. The input signal time series lasts for a period of 6 seconds at 5 ms interval. AR, MA, and ARMAX systems are considered for simulation. A digital system can be defined in terms of either a transfer function $H(Z)$ or a standard difference equation. The relationship between the output signal y_n and the input signal x_n is described by the difference equation. We assume that

$$y_n = \sum_{k=0}^{N_2} b_k x_{n-k} - \sum_{k=1}^{N_3} a_k y_{n-k} \qquad (5)$$

which also corresponds to the following transfer function form,

$$H(Z) = \frac{B(Z)}{A(Z)}; \qquad (6)$$

where $B(Z) = b_0 + b_1 z^{-1} + b_2 z^{-2} + \ldots + b_n z^{-n}$ and

$A(Z) = a_0 + a_1 z^{-1} + a_2 z^{-2} + \ldots + a_n z^{-n}$, (7)

where $\{b_k\}$ and $\{a_k\}$ are the system coefficients that determine the location of the zeros and poles of $H(Z)$, respectively. Thus, $H(Z)$ is causal, stable, and minimum phase linear system.

The output of the system is then computed on the basis of the parameters like $B(Z)$, $A(Z)$, and the given input signal. The neural network then makes an attempt to predict the system's output given the current and past two input signal samples from input signal, X. The neural network needed to simulate the given system has only one neuron because the system produces only one output. Moreover, this neuron must have three inputs to accept the current and two delayed values of the input signal samples. Such a neuron is designed with the help of function "newlin". This function calculates the weight W and bias B values for a neural network with a linear layer from inputs, P and targets, T according to mean square error (mse) minimization criteria.

It appears that the neural network performs a perfect job of modeling the system. This is further verified by examining a plot of the difference between the neural network output and given system's output (error) with respect to time.

IDENTIFICATION RESULTS:

CASE 1: An input signal time series, X (where X =sin(sin(time*2).*time*4) is applied to the AR system

GS1849

over a period of six seconds with a sampling rate of 200 samples per second. After 4 seconds, the transfer function of the dynamical system changes from $H(Z) = 1/(1.5 - 0.5Z^{-1})$ to $H(Z) = 1/(8.0-Z^{-1})$. It is evident that the system behaves differently in the intervals before and after the fourth second. The linear neuron is adaptively trained using Widrow-Hoff rule to model this system and produces nearly the same output as the actual system. The neuronal model estimates the system's output from the last two values of the input signal. Input signal applied to the system, the output signal generated, the estimated output of the neuronal model and the error between the actual output and the estimated output are plotted in Fig. 1. The error plot reveals that the neuronal model needs 2.5 seconds to track the model with a very high accuracy. Then at four seconds, when the system changed suddenly, another 0.5 seconds were required for the neural network to properly model it again.

CASE 2: An input signal time series, X (where X =sin(sin(time*3).*time*6) has been applied to the MA system over a period of six seconds with a sampling rate of 200 samples per second. After 4 seconds, the transfer function of the dynamical system changes from $H(Z) = (2.5 - 0.5Z^{-1})$ to $H(Z) = (1.9 - 0.6Z^{-1})$. Here again examination of error plot shows that the neuronal model needs about 3.5 seconds to track the model with a very high accuracy. Then at four seconds, when the system changed suddenly, another 0.2 seconds were required for the neural network to properly model it again.

CASE 3: An input signal time series, X (where X =sin(sin(time*2.5).*time*5) has been applied to the ARMAX system over a period of six seconds with a sampling rate of 200 samples per second. This input signal is supposed to be contaminated by a zero-mean Gaussian white noise sequence with variance of 0.01. The seed value of 999 is used to generate this noise. After 4 seconds, the transfer function of the dynamical system is changed from $H(Z) = (2 + 2Z^{-1})/(3 + Z^{-1})$ to $H(Z) = (1 - Z^{-1})/(4 + 2Z^{-1})$. Again examination of error plot shows that the neuronal model needs about 3 seconds to track the model with a very high accuracy. Then at four seconds, when the system changed suddenly, another 1 second was required for the neural network to properly model it again.

In order to obtain the simulation results, MATLAB version5.2 is used on an Intel PIII 800 MHz computer. For each case, the input signal and the actual system output are demonstrated in the accompanying graphs. Also, the difference between the actual system's output and neural network's output (error) is plotted against time. From the various plots, it is evident that a linear neural network correctly identifies the given MA, AR or ARMAX system.

CONCLUSIONS:

The recent emergence of the neural network paradigm as a powerful tool for learning complex input, output mappings has stimulated many studies in using neural network models for identification of systems. From the results presented above, it is clear that linear neural networks may be used for modeling and identification of real systems. Despite the variations in the transfer function realization of the system with respect to time, a simple neuronal model mimics the given system with fair elegance and perfection. If the real system is linear or approximately linear, then the neural network comprising of a single neuron with linear transfer function can act as a zero or a low error model. The neural network designed produces same output as the system under consideration is expected to produce.

REFERENCES:

1. M.D. Srinath, P.K.Rajasekaran, and R. Viswanathan, "Introduction to Statistical Signal Processing with applications", Prentice-Hall of India Pvt. Ltd., 1996.
2. K. Mehrotra, C.K.Mohan, and S. Ranka, "Artificial Neural Networks", Penram International Publishing (India), 1997.
3. Jacek M. Zurada, "Introduction to Artificial Neural Systems", Jaico Publishing House, 1997.
4. Simon Haykin, "Neural Networks a Comprehensive Foundation", Pearson Education Asia, 1999.
5. K.S.Narendra and K.Parthasarathy, "Identification and Control of Dynamical Systems Using Neural Networks", IEEE Trans. On Neural Networks, Vol. 1, No. 1, March 1990, pp. 4-27.
6. S. J. Orfanindis, "Optimum Signal Processing: An Introduction", 2nd Ed., McGraw-Hill Book Co., 1990.
7. LiMin Fu, "Neural Networks in Computer Intelligence", McGraw-Hill, Inc., 1994.

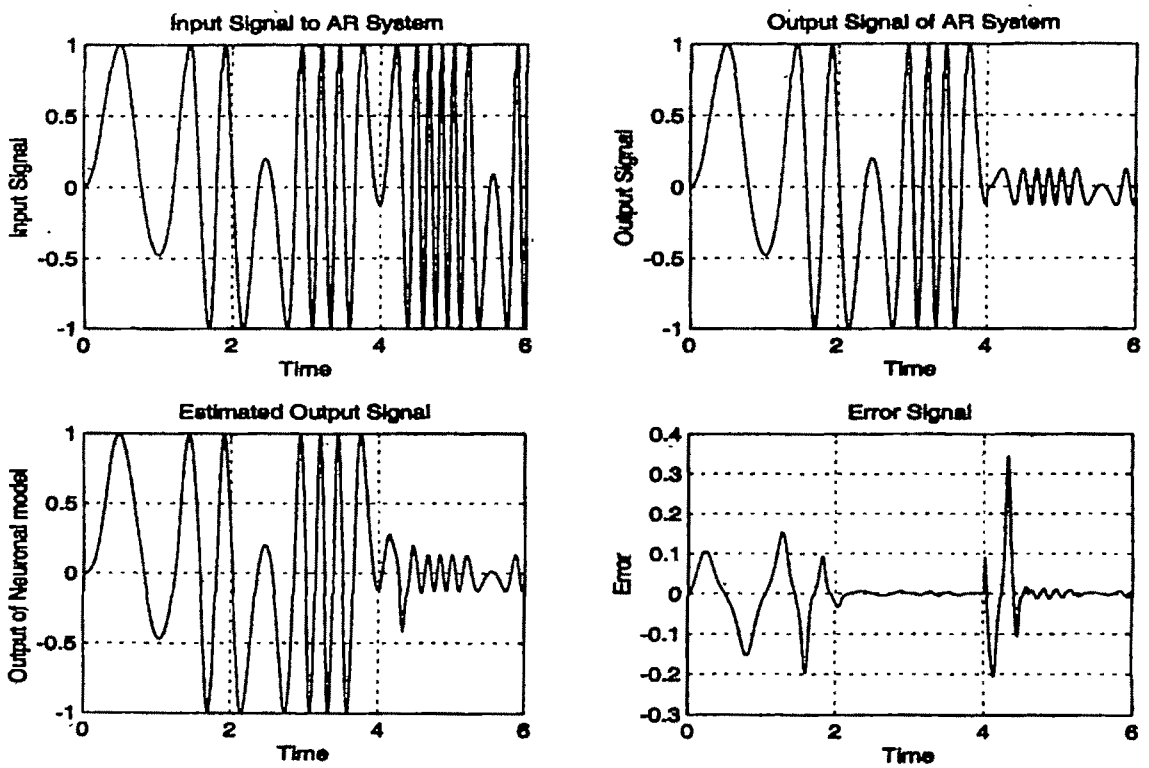

CASE 1: Identification of AR System

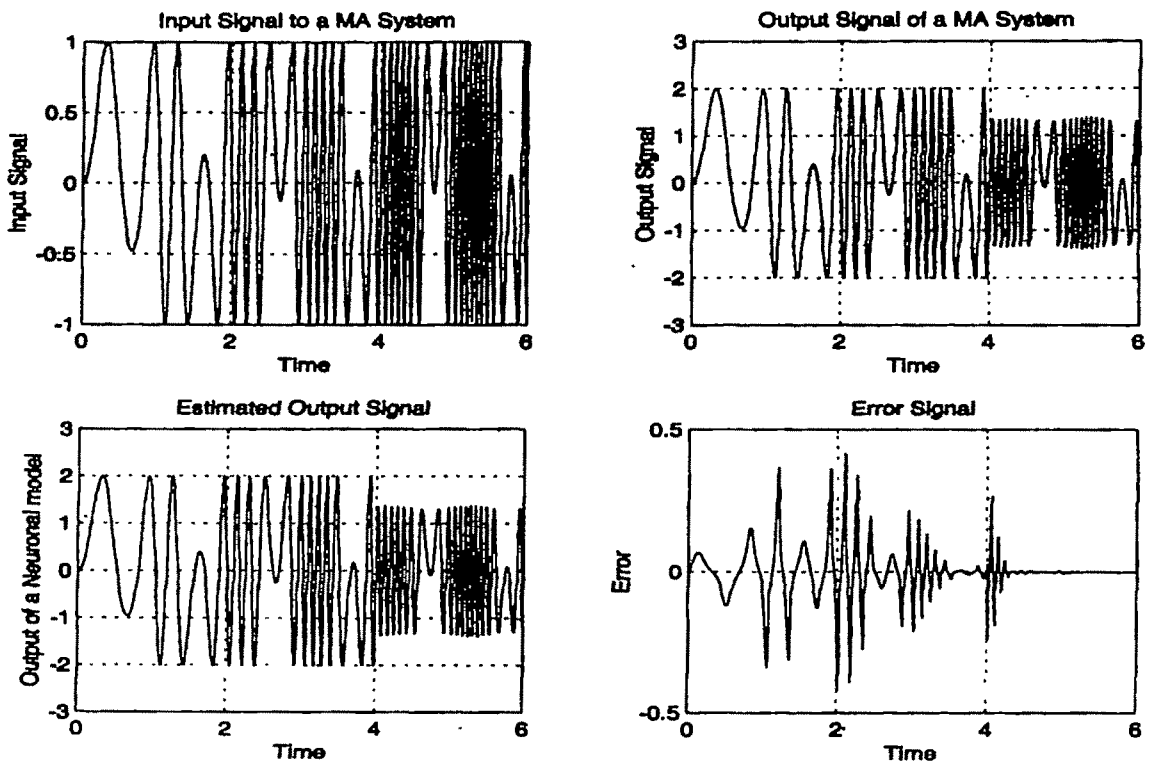

CASE 2: Identification of MA System

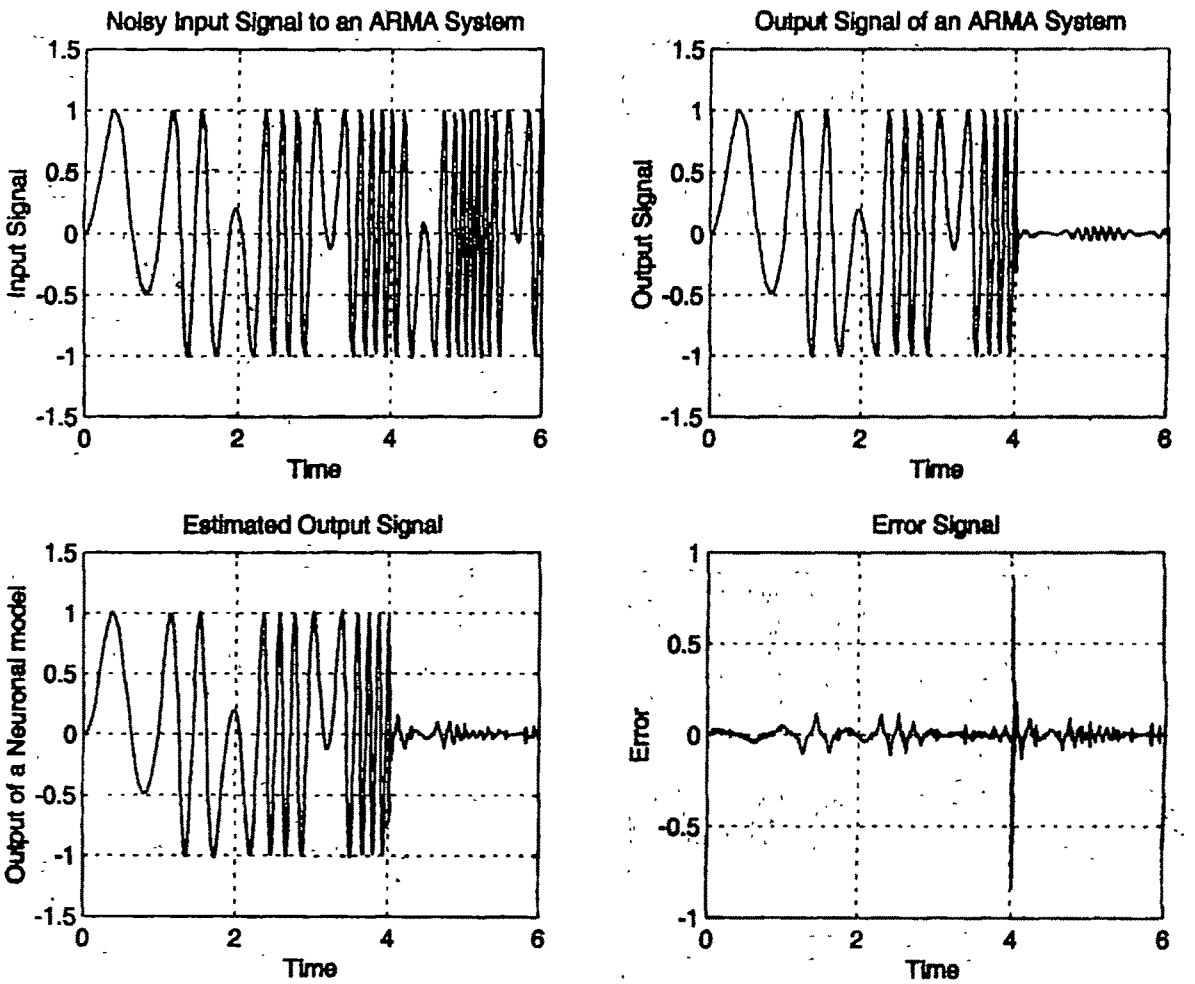

CASE 3: Identification of ARMA System

Adaptive Parameter Estimation Of Robust Kalman Filter Frequency Tracker

K. Aadhi Vairava Sundaram[+*], M. J. Nigam[+]

[+] Electronics and Computer Engineering, Indian Institute of Technology Roorkee, Roorkee, 247667

E-mail of corresponding author [*]:- k_aadhivs@rediffmail.com

aadhipec@isc.rurkiu.ernet.in

ABSTRACT

In this paper the problem of estimating the frequency of a harmonic signal, given its noisy measurement (corrupted by impulsive noise) is considered. Recently robust kalman filter with variable forgetting factor was proposed for impulsive noise cancellation. However, it is assumed that the parameter ε is known apriori, which should be estimated from the noisy signal. An algorithm based on adaptive neural network for the estimation of the parameter and estimation of frequency using the robust kalman filter with variable forgetting factor is proposed. To support our proposed method, simulation results are also provided in this paper, which indicate that the filter is extremely useful for noise reduction.

Key words: Parameter Estimation, Kalman Filter, Impulsive noise, Robust, Variable Forgetting factor, Frequency estimation.

INTRODUCTION

Frequency estimation is a problem frequently encountered in real-world applications, especially in the field of signal processing and adaptive control. Here attempt is made to estimate the frequency in the presence of Impulsive noise. Impulsive noise is short impulses occurring because of adverse channel environments in a communication system, mouse clicks, surface degradation of CD tracks etc. The typical method for removing it is median filter, which introduces a great deal of processing distortion by modifying even a genuine signal. The Robust Kalman filter with Variable forgetting factor [1] effectively tackles the propagation of the estimation error of the impulsive noise by introducing the Huber's min-max function and variable forgetting factor. Important point to be noted is that [1] have added noise to the desired performance but here the noise is added to the input signal itself. It has been demonstrated in [2] the working of the algorithm for frequency estimation without noise. Another approach used for estimating the frequency of a signal is using Extended Kalman filter [3]. It is computationally complex because of the need to compute the jacobian.

The signal under consideration is non-stationary, so the kalman filter used is based on the random- state walk model. The kalman filter for non-stationary inputs differs from the normal one in two basic assumptions. The state transition matrix equals the identity matrix and the process noise have zero mean and correlation matrix hence the weight vector varies about the mean value. The robust kalman filter with variable forgetting factor tackles the impulsive noise using Huber's min-max approach named M-estimation and reduces the error propagation using variable forgetting factor.

The impulsive noise is modeled as follows

$$n_i = (1-\varepsilon)N\left(0,\sigma_1^2\right)+\varepsilon N\left(0,\sigma_2^2\right) \qquad (1)$$

where $N(.m,\sigma^2)$ is the Gaussian distribution with mean m and variance σ^2. The parameter ε is usually not known. We estimate the parameter from the noisy signal adaptively using Neural network. This inturn increases the adaptation of the algorithm to filter the signal itself instead

of the desired performance. It's assumed that if the impulsive noise is not present at any instant then gaussian noise is present. This signifies equation (1). This type of generating the noise is called as composition method (also called as "mixture" method) [4] in which the parameter ε is the probability that impulsive noise occurs and the error signal is assumed to be gaussian when there is no impulsive noise. If a multiplicative model [5]-[6] is used then the parameter is c.

MODIFIED ROBUST KALMAN FILTER WITH VARIABLE FORGETTING FACTOR

The robust kalman filter with variable forgetting factor is used to tackle the impulsive noise. The kalman filter with Variable forgetting factor [2] is used to estimate the frequency. This filter is a modified form of time-weighted error kalman filter [7]. So combining both of them we get the equation for the filter to tackle impulsive noise and estimate the frequency. The artificial neural network is used to obtain an estimate of the parameter ε. The equation of the modified robust kalman filter with variable forgetting factor is given here. The robustness is achieved by using Huber's min-max function and tracking ability is provided by the variable forgetting factor.

Sp(*j-1*) is an n-dimensional parameter vector of past observation represented by $[s(j-1),\ldots,s(j-n)]^T$ where s represents the signal value. $R^{-1}(j)$ is the variance of measurement noise. $\lambda(k)$ is the Variable Forgetting Factor. P(*k*) is the error covariance.

$$e(k) = s(k) - Sp^T(k-1)a(k-1 \mid k-1) \tag{2}$$

where the prediction error is used instead of residual error.

$$\hat{\sigma}_e^2(k) = \frac{\underset{i}{\text{med}}\left(\left|e^2(i) - \underset{i \neq j}{\text{med}}\left(e^2(j)\right)\right|\right)}{0.6745} \tag{3}$$

med(.) is the median operator. This is the median absolute deviation method to calculate the estimated standard deviation of the error signal, where *i,j= k,k-1,....k-N+1*, where N is the length of block data window.

$$R(k) = E\left\{\hat{\sigma}_e^2(1:k)\right\} \tag{4}$$

The influence function of Huber's function is given by

$$\emptyset_H(x) = \begin{cases} x, & |x| \le \hat{\sigma}, \\ \hat{\sigma}\ \mathrm{sgn}(x), & |x| > \hat{\sigma}, \end{cases} \tag{5}$$

where sgn(x) is the signum function and τ is given by

$$\tau = \mathrm{erf}^{-1}(1-\varepsilon) * \sqrt{2}\hat{\sigma}_e(k) \tag{6}$$

τ is used to control the robustness against the impulsive noise. Because ε is used in computing the robustness factor it affects the filter performance. Using this equation $\hat{e}(k)$ is calculated.

$$\hat{e}(k) = \Psi_H(e(k)) \tag{7}$$

where $\hat{e}(k)$ is the restricted prediction error given by Huber's function.

$$\lambda(k) \approx 1 - \frac{R^{-1}(k)}{E_1}\hat{e}^2(k)[1 - Sp^T(k-1)K(k)]^2 \tag{8}$$

where λ(k) is the variable forgetting factor and K(k) is the kalman gain given by

$$K(k) = \frac{P(k \mid k-1)Sp(k-1)}{\lambda(k-1)R(k) + Sp^T(k-1)P(k \mid k-1)Sp(k-1)} \tag{9}$$

where P(k) is the inverse of the correlation matrix.

$$P(k \mid k-1) = \frac{1}{\lambda(k)}[\Phi^T(k,k-1)P(k-1 \mid k-1)\Phi^T(k,k-1)] \tag{10}$$

where Φ(k,k-1) is the time-varying parameter transition matrix. a(k) is the required parameter vector.

$$a(k \mid k) = a(k \mid k-1) + K(k)\hat{e}(k) \tag{11}$$

$$a(k \mid k-1) = \Phi(k,k-1)a(k-1 \mid k-1) \tag{12}$$

$$P(k \mid k) = [1 - K(k)S^T(k-1)]P(k \mid k-1) \tag{13}$$

The equations are not necessarily computed in the given order.

NEURAL NETWORK MODEL

Neural network is a massively parallel distributed processor made up of simple processing units, which has a natural propensity for storing experiential knowledge and making it available for use. The knowledge is acquired through a learning process and interneuron connection strengths known as synaptic weights are used to store the acquired knowledge. They are inspired by the neurons found in the brain. The neural network used here is of competitive network. It is of self organizing type. The neurons in a competitive layer distribute themselves to recognize frequently presented input vectors [8]. The architecture for the competitive network is shown in Fig.1.

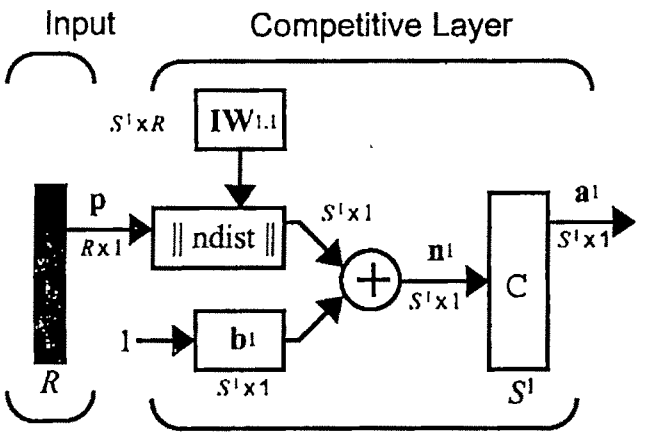

Fig.1. Architecture of the competitive network.

The || **ndist** || block accepts the input vector **p** and input weight matrix $\mathbf{IW^{1,1}}$ and produces a vector having $\mathbf{S^1}$ elements. The elements are the negative of the distances between the input vector and vectors $_i\mathbf{IW^{1,1}}$ formed from the rows of the input weight matrix. The net input $\mathbf{n^1}$ of a competitive layer is computed by finding the negative distance between input vector **p** and the weight vectors and adding the biases **b**. If all biases are zero, the maximum net input a neuron can have is 0. This occurs when the input vector **p** equals that neuron's weight vector. The competitive transfer function accepts a net input vector for a layer and returns neuron outputs of 0 for all neurons except for the winner, the neuron associated with the most positive element of net input $\mathbf{n^1}$. The winner's output is 1. If all biases are 0 then the neuron whose weight vector is closest to the input vector has the least negative net input, and therefore wins the competition to output a 1.

The difference between the self organizing maps and competitive learning is that the former learns the topology along with the classification. In the self organizing maps along with the winning neuron its neighbor's are updated. The competitive layer has two learning rules one for weight learning (Kohonen learning rule) and the other bias learning rule. The weights of the winning neuron (a row of the input weight matrix) are adjusted with the Kohonen learning rule. Supposing that the i th neuron wins, the i th row of the input weight matrix are adjusted as shown below.

$$ {}_i\mathrm{IW}^{1,1}(q) = {}_i\mathrm{IW}^{1,1}(q-1) + \alpha\left(p(q) - {}_i\mathrm{IW}^{1,1}(q-1)\right) \quad (14) $$

where α is the learning rate.

The Kohonen rule allows the weights of a neuron to learn an input vector. The neuron whose weight vector was close to the input vector is made even closer so that when an input vector similar to that is given the neuron responds to that. In some cases some of the neurons may never win the competition if they start very far from any input vectors which are called as dead neurons. To counter this problem a positive bias is added to the negative distance, which makes a distant neuron more likely to win. This is called as the bias update. The second advantage of biases is that they force each neuron to classify roughly the same percentage of input vectors. Thus, if a region of the input space is associated with a larger number of input vectors than another region, the more densely filled region will attract more neurons and be classified into smaller subsections.

Fig.2 shows the block diagram of the system. It depicts the prediction of the parameter and working of the filter.

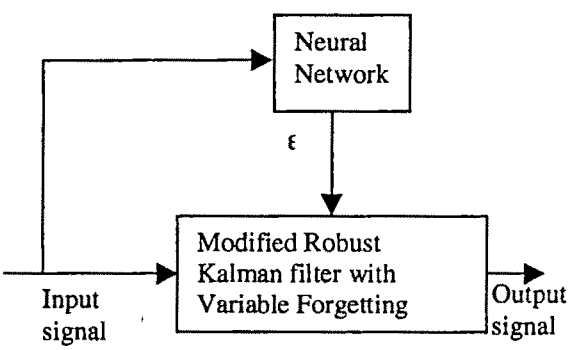

Fig.2. Block diagram of the system

CONSTRUCTION OF INPUT SIGNAL

The input signal consists of 500 samples of which the frequency remains constant for the first 100 samples and increases linearly to a certain frequency for the next 100 samples. It remains constant in that frequency for the next 100 samples and decreases for the remaining 100 samples. After that it remains constant for the remaining 100 samples. The signal to noise ratio is kept at 20dB.The

following formula is used to calculate the signal-to-noise ratio.

$$SNR = 10 * \log\left(\frac{V^2_{max.peak-to-peak of signal}}{mean^2 of noise + variance of noise}\right) \quad (15)$$

The noise is generated using a ε–contaminated gaussian model, in which ε has been varied from 0.008 to 0.1 as along with $\sigma^2_2 = 200\sigma^2_1$ in which $\sigma^2_1 = 1$ Thus the noise is generated and added to the signal for forming the noise-corrupted signal.

The algorithm starts with initial values being specified as follows.

$P(I)=100 * I$; a (0|0)=1; R (*I*)=1,λ (*I*)=1,Φ(k,k-1)=I.

The neural network is trained by varying the ε between 0.008 and 0.05. The frequency is estimated using a second order AR model which is updated at each sample.

IMPLEMENTATION

The simulation of the proposed approach is done in MatlabV5.2.0.3084 and the graphs were plotted. The simulation runs on a Pentium II 400 MHz PC. Some of the functions in the neural network toolbox of Matlab were used. The test signal generated is a chirp signal defined by $s(k)=\sin(\beta\pi k^2/N)$ where N is the number of samples.

CONCLUSION

The proposed approach can track a fast time varying signal and to very low signal-to-noise ratio (15 db). Once trained the neural network is capable of tracking between the whole ranges. The estimated parameter takes some minimum number of samples depending upon the parameter itself. The graph in next page shows the result. The Fig.3. shows the signal after adding noise. It can be observed that gaussian noise is also there in addition to impulsive noise. The Fig.4 shows the estimated frequency of the test signal against impulsive noise. If the parameter ε is estimated by conventional methods, then the error accumulated in that perturbs into the kalman filter which degrades the performance seriously. Thus by calculating the parameter adaptively the algorithm works for noise corrupted signal with less modification.

REFERENCES

1. Han Su Kim, Jun-Seok Lim, Seong Joon Baek, and Koeng-Mo Sung, "Robust Kalman Filtering with Variable Forgetting Factor against Impulsive Noise," IEICE Trans. Fundamentals, Vol E84-A, (2001) p 363-366
2. S.-W.Lee, J.-S. Lim, S.J.Baek, and K.-M. Sung, "Time-varying signal frequency estimation by VFF kalman Filtering," Signal Processing, vol.31, no.5., (1999), p343-347.
3. Sergiio bittani and Sergio M.savaresi, "On the parameterization and design of an extended kalman filter frequency tracker," IEEE Transactions on automatic control, vol.45, NO.9. (2000).
4. Peterson, A. V., Jr., and R.A. Kronmal, "On Mixture methods for the Computer Generation of Random Variables," Am. Statistician, 36 (1982), p 184-191.
5. J.Chambers, "A robust mixed-norm adaptive filter algorithm," IEEE Signal Processing Letters, vol.4no.2, (1997) p.46-48.
6. G.A. Williamson, P.M.Clarkson and W.A.Sethares, " Performance Characteristics of the median LMS adaptive filter," IEEE Transaction on Signal Processing, vol.41 (1993), p667-680.
7. G.A.Mack and V.K.Jain, "Speech parameter estimation by time-weighted error kalman filtering," IEEE Trans. Acoust. Speech Signal Process.ASSP-31 (1983), p1300-1303
8. Kohonen, T.Self-Organization and Associative Memory, 2nd Edition, Berlin: Springer-verlag, 1987.
9. C.J.Marseliez, "Approximate non-gaussian filtering with linear state and observation relations," IEEE Transactions on Automatic Control, AC-20 (1975) , p 107-111.
10. S.Haykin, "Adaptive Filter Theory," 2nd edition, Prentice Hall, Englewood Cliffs, NJ, 1991.
11. Robert Grover Brown, "Introduction to Random signal Analysis And Kalman Filtering," John Wiley & Sons, NewYork, 1983.

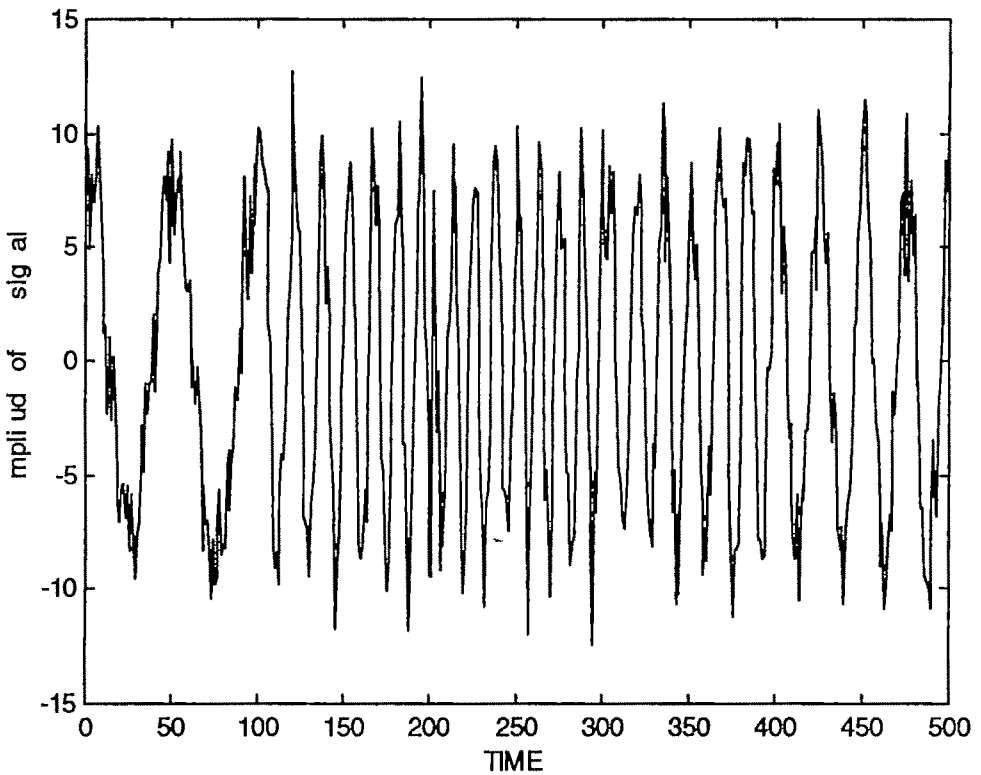

Fig.3. Signal Corrupted with noise

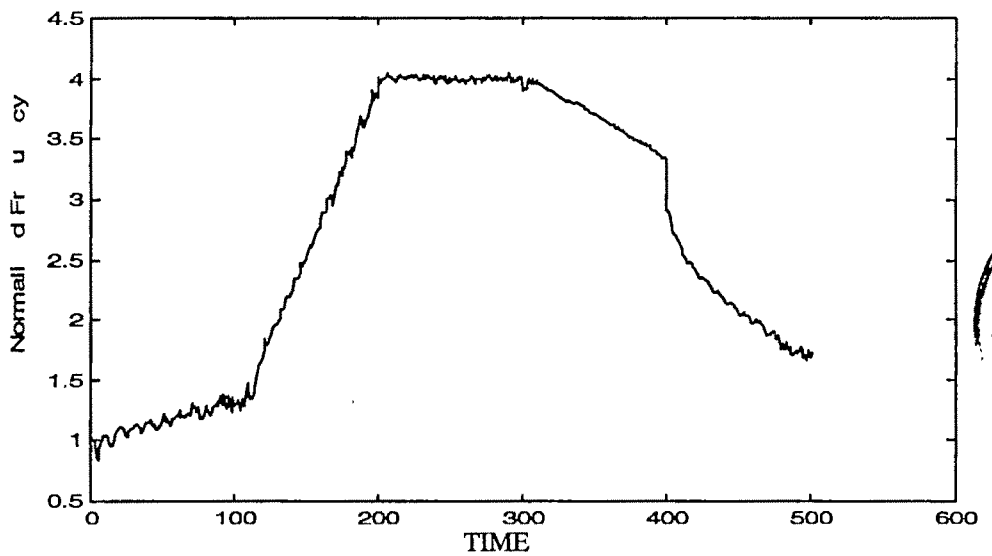

CALCUTTA UNIVERSITY
CENTRAL LIBRARY.

Fig.4. Estimated frequency of the test signal through the proposed approach.

Dynamic Fuzzy Logic System (DFLS) based Identification of Chaotic System

O. V. Ramana Murthy*, R. K. P. Bhatt, N. Ahmed
Department of Electrical Engineering,
Indian Institute of Technology, Delhi, Hauz Khas, New Delhi-110016, India.
*omurthy@yahoo.com

Abstract

The Dynamic Fuzzy Logic System consists of static fuzzy logic system added with a dynamic element –the integrator- with a feedback constant α .It was shown to possess the important universal approximation capability. Further, based on the DFLS, a stable identification scheme, developed via a Lyapunov synthesis approach has been successfully applied to single link flexible robot arm by J.X.Lee et al. In this paper, the procedure for identification scheme is generalized and investigated successfully on chaotic system-Duffing's equation

INTRODUCTION

Although impressive results have been achieved both practically and theoretically by FLSs for identification of complicated systems, the FLS used to date are static in nature. Motivated by the fact that the physical systems of interest are generally dynamic, this suggests that one might include dynamic elements into the fuzzy systems, which would themselves then be more naturally integrated into dynamic systems and take advantage of these intrinsic dynamics. This would provide new tools in identification of dynamic systems. Hence the DFLS. This paper is briefly organized as follows. *DFLS, DFLS as Identifier, identification of chaotic system and results.* Each part is described below

DYNAMIC FUZZY LOGIC SYSTEM

The DFLS consists of two parts-the static fuzzy logic system and a dynamic element with positive feedback constant as in Fig(1). Both are described below.

The fuzzy logic system

The FLS consists of four major components, namely, *a fuzzy interface, a fuzzy rule base, a fuzzy inference engine* and *a defuzzification interface.* Because multi-input, multi-output (MIMO) system can often be decomposed into group of multi-input, single-output (MISO) systems, only MISO fuzzy logic systems will be considered in this paper.

In Fig(1), for p=1...P,

$z_p \in U_p \subset R$ is an input variable, $y_F \in V \subset R$ is the output, U_p is the universe of discourse of the variable z_p, V is the universe of discourse of the variable y_F, R is the set of real numbers, Z_p is the fuzzy set generated from the crisp input z_p by a corresponding fuzzifier and Y is the fuzzy set induced by the fuzzy inference engine.

The fuzzification interface is composed of a set of fuzzifiers, each of which corresponds to an input variable. It transforms the crisp input vector, $z = \{z_1, z_2, \ldots z_P\}^T$, into a corresponding fuzzy vector, $Z = \{Z_1, Z_2 \ldots Z_P\}^T$. The singleton fuzzifier is used in this work.

All the input variables are pre filtered properly and brought into a common UOD. This UOD is divided uniformly into i_p p=1,2,...P Gaussian-type membership functions.

The Fuzzy rule base is defined by a collection of IF-THEN rules of the form

$$F^i : \text{IF } [(z_1 is U_1^{i_1}) \text{ AND } \ldots\ldots \text{AND } (z_p is U_1^{i_P})]$$
$$\text{THEN } [y_i \text{ is } V^i] \; i = 1,2,\ldots\ldots l \qquad (1)$$

where F^i, i =1,.....l, stands for the i th rule, l is the total number of rules in the rule base.

$U_p^{i_p}$, i_p= 1...i_P, p=1,2....P is a primary fuzzy set defined in the universe of discourse U_p. V^i is a primary set defined in the universe of discourse V.

Further V is partitioned into J primary fuzzy sets, $V^j \in \{V^j ; j=1,\ldots\ldots,J\}$. The name primary fuzzy set is used to distinguish these sets from the fuzzy sets obtained via fuzzifiers.

Each IF-THEN rule of Eq (1) defines a fuzzy implication,

$$F^l = (U_p^{l_1} \text{ X} \ldots\ldots\ldots \text{X } U_p^{l_p} \rightarrow V^l)$$
$$= (U_p^{l_1} \text{ X} \ldots\ldots\ldots \text{X } U_p^{l_p} \text{ X } V^l)$$

which is fuzzy set defined in the Cartesian product space $F = U_l$ X ..... U_p X $V \subset R^{P+1}$, and characterized by a membership function

$$\mu_{F^l}(z, y_F) = \mu_{U_1^{l_1} \times \ldots U_p^{l_p} \times V^l}(z, y_F).$$

R^{P+1} represents the $(P+1)$- dimensional Euclidean space. The specific manner of evaluating $\mu_{F^l}(z, y_F)$ from the constituent membership functions $\mu_{U_p^{l_p}}(z_p)$ and $\mu_{V^l}(y_F)$ is the particular *operation rule of fuzzy implication*. The *product rule of fuzzy implication* will be applied. i.e., $\mu_{F^l}(z, y_F)$ is evaluated as

$$\mu_{F^l}(z, y) = \mu_{U_p^{l_1}}(z_1) . \mu_{U_p^{l_2}}(z_2) \ldots\ldots$$
$$\ldots \mu_{U_p^{l_p}}(z_P) . \mu_{V^l}(y_F) \qquad (2)$$

where "." Represents algebraic product.

The fuzzy inference engine is the decision making logic which, based on the fuzzy rule base, induces an output fuzzy set Y from fuzzy vector Z.

Each individual IF-THEN rule induces a component of Y, Y^l, i = 1,.....l. Y is the union of Y^l, i.e.,

$$Y^l = Z \text{ o } F^l, \quad Y = \bigcup_{l=1}^{l} Y^l \qquad (3)$$

where "o" represents composition. Y^l is characterized by a membership function,

$$\mu_{Y^l}(z, y_F) = \mu_z(z, y_F) \circ F^l(z, y_F).$$

Evaluation of this expression is based on a particular *compositional rule of inference*. In this work, we use the *Sup-product compositional rule of inference* i.e.,

$$\mu_{Y^l}(z, y_F) = \sup_{z \in U} \{\mu_z . \mu_{F^l}(z, y_F)\}, \qquad (4)$$

where $U = U_1$ X .....X U_P denotes Cartesian product, is given inEqn (2), and $\mu_z(z)$ is evaluated by the product rule.

$$\mu_z(z, y_F) = \mu_{Z_1}(z_1) . \mu_{Z_2}(z_2) \ldots \mu_{Zp}(z_p) \qquad .(5)$$

where $\mu_{Zp}(z_p)$ is the grade of the membership characterizing the fuzzy set Z_p, which is the fuzzified crisp input z_p.

The defuzzification interface is a defuzzifier which transforms the fuzzy output set Y into a crisp output, y_F. The centroid defuzzifier is used here, i.e.

$$y = \frac{\sum_{l=1}^{l} \bar{y}_l \prod_{p=1}^{P} \mu_{F^l}(z, \bar{y}_l)}{\sum_{l=1}^{l} \mu_{F^l}(z, \bar{y}_l)}$$
$$= \frac{\sum_{l=1}^{l} \bar{y}_l \prod_{p=1}^{P} \mu_{u_p^{lp}}(z_p)}{\sum_{l=1}^{l} \prod_{p=1}^{P} \mu_{u_p^{lp}}(z_p)}$$

where $\bar{y}_l$ is the point of support in V^l at which $\mu_{V^l}(y)$ achieves its maximum value (=1).

Defining

$$\Phi_l(z) = \frac{\prod_{p=1}^{P} \mu_{U_p^{l_p}}(z_p)}{\sum_{l=1}^{l} \prod_{p=1}^{P} \mu_{U_p^{l_p}}(z_p)} \quad i = 1, \ldots l \qquad (7)$$

Eqn (6) is rewritten as

$$y_F = \sum_{l=1}^{l} \bar{y}_l \Phi_l(Z) = \Phi^T \bar{Y} \qquad (8)$$

where $\bar{Y} = \{\bar{y}_1 \ldots\ldots\ldots \bar{y}_l\}^T$ and $\Phi = \{\Phi_1, \qquad \Phi_l\}^T$.

Eqn (8) shows that Φ is characterized by the number of input fuzzy sets, $\{U_1^1, U_2^1 \ldots\ldots U_P^1, U_1^2, U_2^2 \ldots\ldots\ldots U_P^{lp}\}$, as well as the position and shape of the membership function for each input fuzzy set. If we fix these parameters and leave only, $\bar{y}_l$ i=1,.....,l, as adjustable parameters, it makes the above expression linear in it's parameters.

DYNAMIC FUZZY LOGIC SYSTEM

Consider the Dynamic Fuzzy Logic System (DFLS) illustrated in Fig(1) below, it can be represented by the following differential equation of the form

$$\dot{y} = -\alpha y + \Phi^T(Z)\bar{Y} \qquad (9)$$

where y is a scalar variable and feedback coefficient α is positive. The second term on the right hand side of the

above equation is the output of standard fuzzy logic system, y_F, described by above eqn (8).

DFLS AS A SYSTEM IDENTIFIER

Consider a general dynamic system of form

$$\dot{X} = F(X,U) \qquad (10)$$

i.e. $\dot{x}_k = f_k(X,U)$ k = 1,2,....N, where X and U are the state vector and external input vector of the physical process, respectively.

To identify the kth state x_k , k$\in$ {1,.....N}, we use a DFLS in the form

$$\dot{y}_k = -a_k y_k + \Phi_k^T(X,U)\bar{Y}_k,$$
$$a_k > 0, k \in \{1,2...N\} \qquad (11)$$

where $\bar{Y}_k = \{\bar{y}_{k1}.....\bar{y}_{kl}\}^T$ and

$\Phi_k = \{\Phi_{k1}.....\Phi_{kl}\}$.

This formulation implicitly assumes that all the states are available. Following the well-known Lyapunov synthesis approach, the training law for $\bar{Y}_k$ has been developed in [4] such that the identification error, $e_k = y_k - x_k$, is uniformly bounded, and even asymptotically approaches zero under certain conditions.

The training law is

$$\dot{\bar{Y}}_k = - H_k \Phi_k(X,U)\, e_k - S_k \beta_k H_k \bar{Y}_k$$
$$k \in 1,2,.....i_P \qquad (12)$$

where H_k is a constant positive definite symmetric matrix
e_k is error defined by $e_k = y_k - x_k$ and
S_k is a switch defined as

$$S_k = \begin{cases} 0, \text{ if } \| \bar{Y}_k \| < M_k^y, \\ \quad \text{or } \| \bar{Y}_k \| = M_k^y \text{ and } \Phi^T{}_k H_k \bar{Y}_k\, e_k \geq 0; \\ \quad \text{or } \| \bar{Y}_k \| > M_k^y \text{ and } \Phi^T{}_k H_k \bar{Y}_k e_k > 0; \\ 1, \text{ Otherwise} \end{cases}$$

M_k^y is bound on parameter vector $\bar{Y}_k$

β_k(effective only when $S_k = 1$) is a positive design parameter which satisfies

$$\beta_k \geq -\frac{\Phi_k^T H_k \bar{Y}_k}{\bar{Y}_k^T H_k \bar{Y}_k} e_k, if \| \bar{Y}_k \| = M_k^y$$
$$and \Phi_k^T H_k \bar{Y}_k e_k \geq 0$$
$$> -\frac{\Phi_k^T H_k \bar{Y}_k}{\bar{Y}_k^T H_k \bar{Y}_k} e_k, if \| \bar{Y}_k \| > M_k^y$$
$$and \Phi_k^T H_k \bar{Y}_k e_k \leq 0$$

During simulation β_k can take a value of

$$-\left(\frac{\Phi_k^T H_k \bar{Y}_k}{\bar{Y}_k^T H_k \bar{Y}_k} + \Delta\right) e_k \quad , \Delta \text{ is small value}$$

IDENTIFICATION OF CHAOTIC SYSTEM

The above described DFLS based identification is now applied to identify the states of a chaotic system

Chaotic system formulation and solution

Consider the following type of Duffing's equation, which exhibits chaotic behavior.

$$\ddot{x} + 0.25\dot{x} + x^3 - x = 0.3\cos t \qquad (13)$$

Let $x_1 = x$ and $x_2 = \dot{x}$ then equation in state space form is :

$$\dot{x}_1 = x_2$$
$$\dot{x}_2 = x_1 - x_1^3 - 0.25x_2 + 0.3\cos t \qquad (14)$$

Using the generalized identification algorithm described above, two DFLS identifiers F_1 and F_2 are used for identification of x_1 and x_2 respectively. The present state $x(t) = (x_1(t)\ x_2(t))^T$ is fed as input to each identifier and the next state $x(t+dT)$ is identified.

$$x_1(t+dT) = F_1(x_1(t)\ x_2(t))$$
$$x_2(t+dT) = F_2(x_1(t)\ x_2(t))$$

SIMULATION DETAILS AND RESULTS

In F_1 and F_2 each universe of discourse is partitioned uniformly into five fuzzy sets whose membership functions are defined over [–2 2]. For all the membership functions, the spread was taken as 0.45. Each identifier has 25 rules. The sampling rate is set at 10Hz. For k=1,2, the parameters to be trained, $\overline{Y}_k$, each containing 25 elements, are initially assigned uniformly distributed random numbers in [-1,+1], $\alpha_k = 11$, the gain matrices H_k are diagonal with elements 40. The bound on parameter vector M_k^y is taken as 10^4. It is assumed that the system to be identified is initially at rest, i.e. $x(0)= \{0\ 0\}^T$. The initial 5 estimates of the identifier are set to zero. The training lasts for 100 secs for the each identifier.

Fig(2a) shows training of F_1 for initial condition $x(0)= \{0\ 0\}^T$. Fig(3a) shows training of F_2 for initial condition $x(0)= \{0\ 0\}^T$.

Choice of initial conditions has significant effects on the dynamics, particularly of chaotic systems. So the trained identifiers are tested against a different initial condition, $x(0) = \{1\ 3\}^T$. Mean square error was taken as performance index(PI). PI for F_1 was 0.1095 and for F_2 it was 0.1185. The results were satisfactory. Next we train the identifiers for several initial conditions from combination of $x_1(0)=\{-2\ -1\ 0\ 1\ 2\}$ and $x_2(0)=\{-2\ -1\ 0\ 1\ 2\}$ i.e. for 25 different initial conditions near to it's chaotic attractor. For each initial condition the training lasts for 100secs. At the end of the above-described training, again the trained identifier was used to identify the system for initial condition $x(0) = \{1\ 3\}^T$ Fig(2b) shows the identification by F_1 for initial condition $x(0)=\{1\ 3\}^T$. Fig(3b) shows the identification by F_2 for initial condition $x(0)=\{1\ 3\}^T$. It has been observed that when more training was done using many different initial conditions, the PI showed a drastic improvement. Fig(4a) shows PI versus number of number of initial conditions for x_1. It can be clearly seen that by training the identifier for more initial conditions, PI improves drastically. PI for F_1 was 0.0032 and PI for F_2 was 0.0004.The equivalent graph for x_2 is shown in Fig(4b).

The original system is found to have a chaotic attractor. The phase plane obtained by our identifier also has almost the same type of attractor as the original one. The initial five estimates of the identifier were set to zero. So the performance slowly improved and good identification of the attractor was achieved. Fig(5a) shows the attractor for the original system. Fig(5b) shows the attractor identified by the DFLS identifiers.

CONCLUSION

The DFLS based identification scheme has been successfully used to identify the states of a chaotic system. The DFLS structure described in this work can be taken as initial guess for identification of any other system. Then appropriate scaling of input-data and slight variations in parameters of membership functions (spread, center), α, H, M^y can yield good result.

REFERENCES

1. T. Takagi and M. Sugeno "Fuzzy identification of systems and it's application to modeling and control", IEEE Transactions Systems, Man, Cybernetics, vol 15, pp 116-132,1985.
2. L. X. Wang, "Fuzzy Systems are Universal approximators," Proc .IEEE Int.Conference Fuzzy Systems. San Diego,CA,1992,PP 1163-1170.
3. M. Sugeno and T. Yasukawa , "A fuzzy logic based approach to qualitative modeling", IEEE Transactions in Fuzzy Systems vol1, pp 7-31, 1993.
4. Lee J. X and G. Vukovich, "The Dynamic fuzzy logic system: Nonlinear system identification and application to robotic manipulators", Journal of Robotic Systems, 14(6), 1997, 391-405 .
5. Hans-Walter Lorenz, 1993, Nonlinear Dynamical Economics and chaotic motion, second edition, pp182-192, Springer-Verilag.

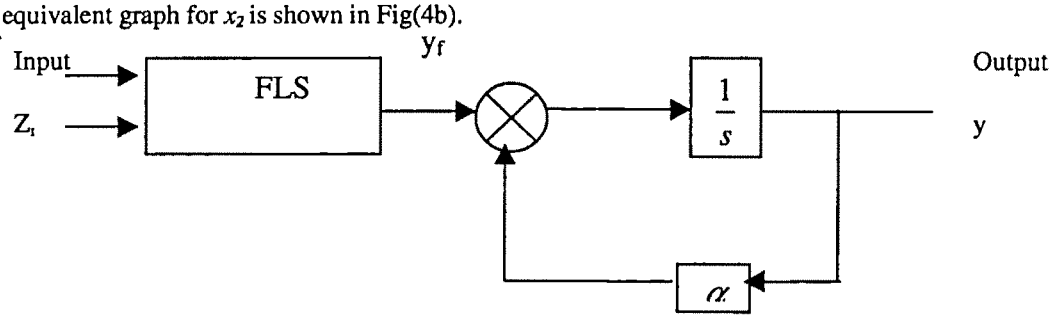

Fig 1 Dynamic Fuzzy logic structure

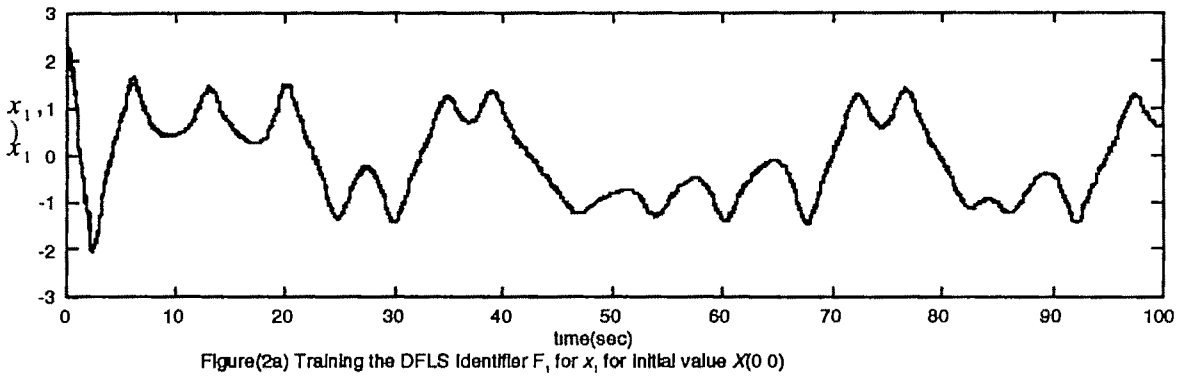

Figure(2a) Training the DFLS identifier F_1 for x_1 for initial value $X(0\ 0)$

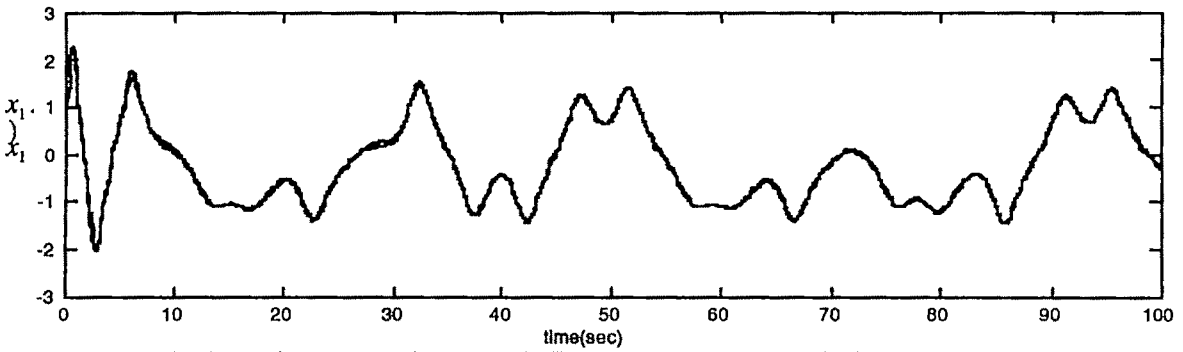

Figure(2b) Identification of x, using already trained DFLS identifier F, with an initial value $X(1\ 3)$

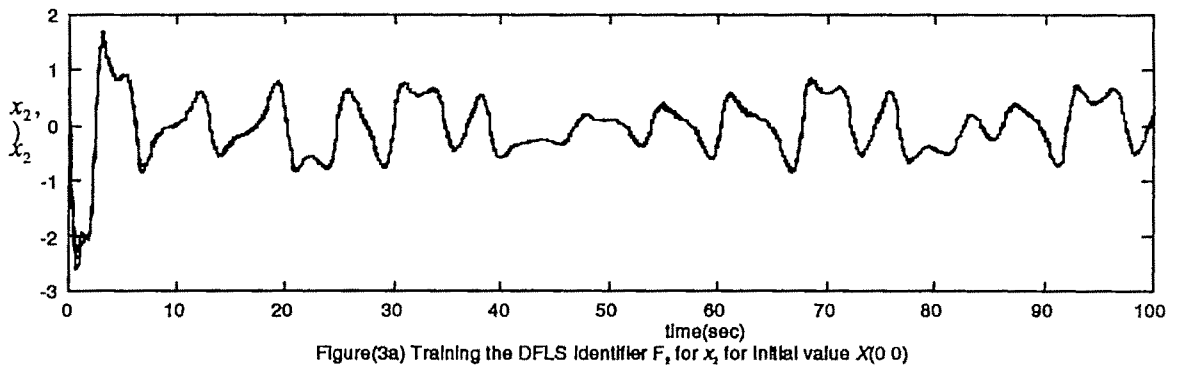

Figure(3a) Training the DFLS identifier F_2 for x_2 for initial value $X(0\ 0)$

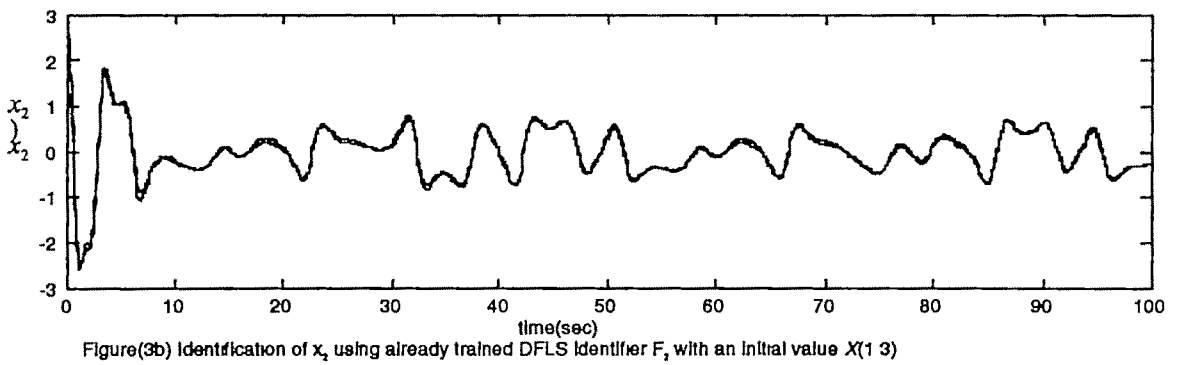

Figure(3b) Identification of x_2 using already trained DFLS identifier F_2 with an initial value $X(1\ 3)$

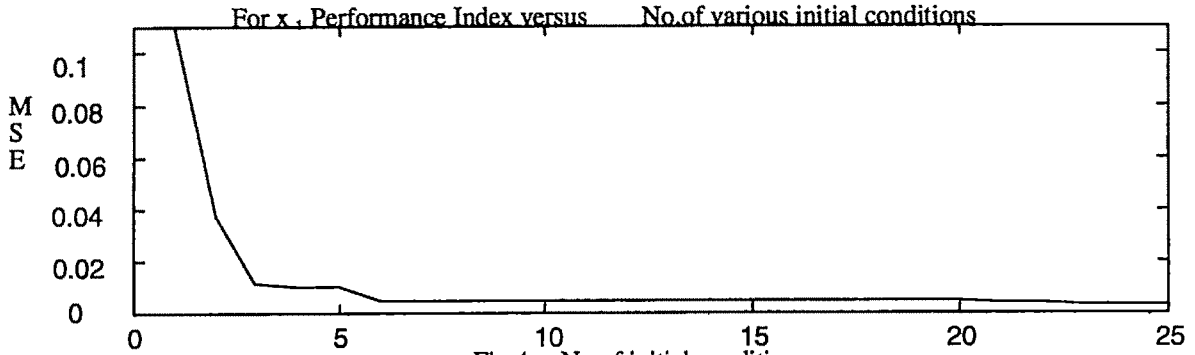

Fig 4 a No of initial conditions

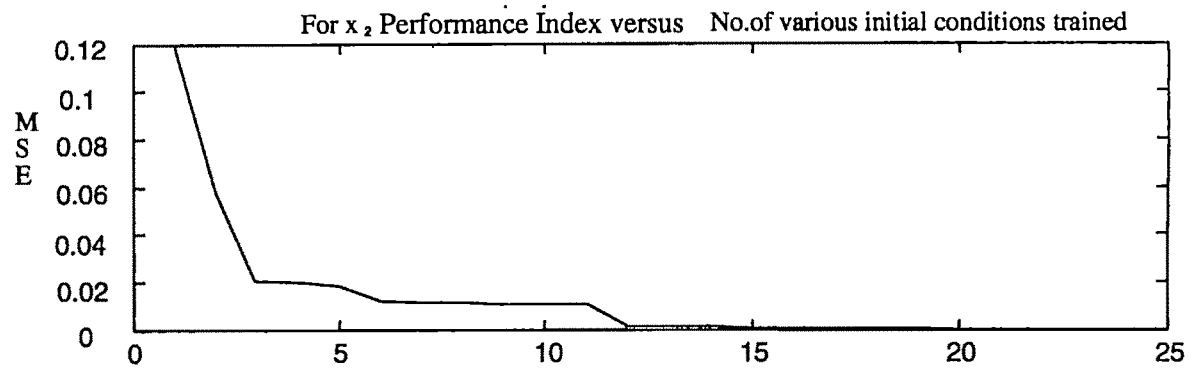

Figure(4a) No of initial conditions

Fig 5a Chaotic attractor for X(1 3)

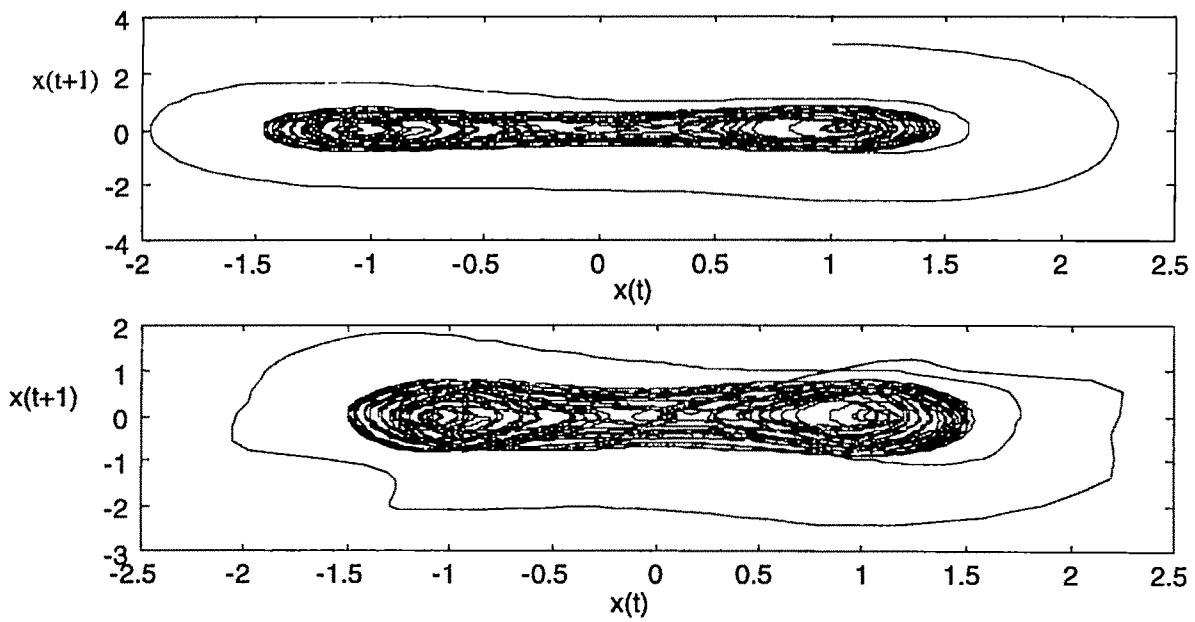

Fig 5b chaotic attractor for x(1 3) initial condition by estimator

Identification Of Transfer Function Model For Unstable System With A Zero

R. Padma Sree and M. Chidambaram
Department of Chemical Engineering
Indian Institute of Technology , Madras, India
Chennai 600 036, India

Abstract

A method of identifying first order plus time delay model with a zero (FOPTDZ) for an unstable system is proposed. The method is based on a single experiment on a closed loop system with a step change in the set point of a PI controller. The step response data and the derived algebraic equations using the characteristic equation are used to calculate the steady-state gain, time constant, zero and the process delay. Simulation results are given for assumed transfer function models. The responses of the identified model parameters are compared with that of the actual systems. A simulation study on a chemical reactor with a non ideal mixing model is given to identify a suitable unstable FOPTD with a zero transfer function model.

Key words: identification, unstable model, transfer function , zero, closed loop

INTRODUCTION

Kavdia and Chidambaram [1] have extended the method proposed by Yuwana and Seborg [2] for stable systems to identify an unstable first order plus time delay (FOPTD) model. Basically the method first identifies a second order plus time delay model for the closed loop system using the response obtained for a step change in the set point of a proportional controller. From the identified closed loop model, the open loop transfer function is derived. For unstable plus time delay systems, a large off set is obtained by using a proportional controller. Hence, a method is required to obtain the model parameters by using the closed loop step response using a PI controller. Recently Ananth and Chidambaram [3], have proposed a time domain method to identify an unstable FOPTD transfer function model. However, in this method, the process delay is assumed as that of the closed loop delay which is noted from the response. Padma Sree and Chidambaram [4] have proposed a modification of this method so as that an additional equation is derived to calculate the time delay also. There are systems which are to be identified as an unstable first order plus time delay with a zero (FOPTDZ) transfer function model. The zero may be a positive or a negative one. In the present work, a closed loop time domain method is proposed to identify an unstable FOPTDZ transfer function model.

PROPOSED METHOD

Case study 1: The transfer function to be identified is $k_p (1+b_1 s)/(\tau s-1)$. A PI controller is used to get a response for a unit step change in the set point. From the step response, the peak values y_{p1}, $y_{p,2}$, $y_{m,1}$ and the corresponding times $t_{p,1}$, $t_{p,2}$ are noted. We can then calculate the damping coefficient (ζ) and the effective time constant (τ_e) from the equations given by Ananth and Chidambaram [3]. The closed loop transfer function, on Laplace inverse gives the servo response as:

$$y(t) = 1 + K \exp(-\zeta t/\tau_e) [-\cos(qt/\tau_e) + [\{(b_3/\tau_e)-\zeta\}/q] \sin(qt/\tau_e)] \quad (1)$$

where $q=(1-\zeta^2)^{0.5}$ (2a)

$$K = [1-(b_1\tau_I/\tau K_c^2)] \quad (2b)$$

$$b_3 = [b_1 + \tau_I - (2\zeta\tau_I b_1/\tau_e)]/K \quad (3)$$

By substituting t=0 in Eq(1), we get

$$b_1 = y_0\tau_c^2/\tau_1 \quad (4)$$

Hence, by noting the initial jump response (y_0) and using the values of ζ and τ_c, we can calculate b_1 from Eq(4). From the values of ζ and τ_c , the roots of the characteristic equation is calculated. By equating these roots with that of the derived closed loop system, we get the following equations:

$$\tau = (b_1 + \tau_1 - 2\zeta\tau_c)/(\tau_c^2 - b_1\tau_1) \quad (5)$$

$$k_p = \tau\tau_1 / (\tau_c^2 - b_1\tau_1) \quad (6)$$

It is to be noted that for systems with a positive zero, the initial jump will be in the reverse direction of that of the final steady-state response. For systems with a negative zero, the initial jump in the response will be in the same direction as that of the final steady-state.

Simulation example 1: Let the transfer function is (1-0.5s)/(s-1) and the PI settings used are k_c =1.292 and τ_1 =11.6. The closed loop servo response is shown in Fig.1. From Fig 1, we note the initial response y_0 as -1.8 and the values of peaks and valleys and the corresponding times are noted as y_{p1}=3.79, $y_{m,1}$ =0.7274 and $t_{p,2}$=2.79. By using these values in the equations given by Ananth and Chidambaram [3], we calculate the damping coefficient as ζ=0.594 and τ_c =1.781. The value of b_1 is calculated from Eq(4) as –0.492 and the values of gain, time constant are calculated from Eqs (5) and (6) as k_p=0.999 and τ=0.988. These parameters values are close to the actual values. The closed loop response of the identified model with the same settings of the PI controller are shown in Fig.1. The matching is good.

Case study 2: Let us consider the transfer function considered in Case study I with time delay: k_p $(1+b_1s)$ $\exp(-Ls)/(\tau s-1)$. A PI controller is used. From the closed loop servo response the initial peak (y_0) [for positive zero, this would be the first valley whereas for the negative zero, this will be the first peak], the peak values and the valley values ($y_{p,1}$, $y_{p\,2}$,$y_{m,1}$) and the corresponding times ($t_{p,1}$, $t_{p,2}$) are noted. From these values, the damping coefficient (ζ) and the effective time constant (τ_c) of the closed loop system are calculated. From the Laplace inverse of the closed loop dominant second order system, we get the following equation:

$$(y_{p,1} - 1)/v_1 = Kd\,[\exp(-\zeta/q)\,\{\tan^{-1}(r_1) - \pi\}] \quad (7)$$

$$\text{where } K = 1 - (b_1\tau_1/\tau_c^2) \quad (8)$$

$$d = [1 - (2\,b_3\zeta/\tau_c) + (b_3/\tau_c)^2]^{0.5} \quad (9)$$

$$r_1 = (-b_3\,q/\tau_c)/\,[1-(b_3\zeta/\tau_c)] \quad (10)$$

$$v_1 = (1-y_0)/(y_{p,1}-1) \quad (11)$$

Substituting the calculated two roots of the dominant second order system in the derived closed loop transfer function we get:

$$X_1(\alpha^2 - \beta^2) - X_2\alpha + \exp(-L\alpha)\,[C_1\cos(L\beta) + C_2\sin(L\beta)] = 0 \quad (12)$$

$$2X_1\alpha\beta - X_2\beta + \exp(-L\alpha)\,[C_2\cos(L\beta) - C_1\sin(L\beta)] = 0 \quad (13)$$

where

$$X_1 = \tau\tau_1 / k_p k_c \quad (14a)$$

$$X_2 = X_1/\tau \quad (14b)$$

$$C_1 = 1 + \alpha(\tau_1 + b_1) + b_1\tau_1(\alpha^2 - \beta^2) \quad (15a)$$

$$C_2 = \beta(\tau_c + b_1) + 2\,b_1\tau_1\,\alpha\beta \quad (15b)$$

We have to calculate four parameters (k_p, b_1, L,τ) of the transfer function model. We have already formulated a separate equation for b_1 [Eq.7]. We have so far formulated only 2 equations to calculate the remaining 3 parameters. Now let us formulate one more relation. Let y(s) be the response in Laplace domain for a unit step change in y_r. From the time response, we calculate y(s) as follows:

$$y(s) = \int_0^\infty y(t)\exp(-st)\,dt \quad (16)$$

We can evaluate the above value at $s=s_1$. We use s_1 =$8/t_s$, where t_s is the settling time (to reach 98% of the final response) of the response. We can also formulate an equation for y(s) from the closed loop transfer function model as:

$$y(s) = K(1+b_1s)(1+\tau_1 s)\,\exp(\_Ls)/\{[\tau_c s(\tau s-1) + K\exp(-Ls)(1+\tau_1 s)(1+b_1 s)](s)\} \quad (17)$$

This function can be evaluated at the same value of $s=s_1$. By equating the resulting expression with value of y(s) calculated from Eq(16) we can formulate the third equation. Solutions for the nonlinear algebraic equations give the model parameters k_p, L and τ. The initial guess for the parameters k_p , τ, and L are obtained as follows: (i) the open loop time constant is assumed as that the closed loop system. The closed loop time constant is calculated as: $t_s/8$, (ii) the process gain is calculated from the proportional

controller tuning formula[5]: $k_p = (\tau/L)^{0.5}$ $(1/k_c)$ and (iii) the process delay is noted from the closed loop response.

Simulation example 2: Let us consider a system (1+0.25s) exp(-0.25s)/ (s-1). The PI settings are k_c =1.4 & τ_I =14. The closed loop servo response is obtained and shown in Fig 2. From the Fig. 2, we get $y_{p,1}$=2.5812, $t_{p,1}$ = 4.39, $y_{m,1}$ =0.8824, $y_{p,2}$=1.0087, $t_{p,2}$=30. 3. Using these data, we get for the closed loop system : ζ=0.6376, τ_c = 3.1769. Solving Eq(7) by using *fsolve* of **MATLAB**,, we get the value of b_1 as 0.2761. Using the closed loop servo response, we calculate he integral in Eq(16) as 7.5627. Now we have to solve the eqs(12) and (13). From the steps given earlier, the initial guesses for model parameters are : τ=(35/8)=4.375, k_p=2.988 and L=0.25. The numerical solution of Eqs(12) to (13) give : τ=0.9962, k_p=0.9999 and L=0.2797. The closed loop response of this identified model with the PI controller and that of the actual process are shown in Fig 2. The matching is good.

Simulation example 3: Let us consider a system (1-0.25s) exp(-0.25s)/ (s-1). The PI settings are k_c =1.3 & τ_I =12. The closed loop servo response is obtained and shown in Fig 3. From the Fig. 3, we get y_0 = 0.3138, $y_{p,1}$ = 4.1806, $t_{p,1}$ = 3.125, $y_{p,2}$=1.0435, $t_{p,2}$=14.79. Using these data, we get for the closed loop system : ζ=0.5647, τ_c = 1.5584. Solving Eq (7) by using *fsolve* of **MATLAB**, we get the value of b_1 as –0.298. Using the closed loop servo response, we calculate he integral in Eq. (16) as 7.5627. Now we have to solve the eqs (12) and (13). From the steps given earlier, the initial guesses for model parameters are : τ=(40/8)=2.5, k_p=2.4325 and L=0.25. The numerical solution of Eqs (12) to (13) give : τ=0.9962, k_p=0.9999 and L=0.2797. The closed loop response of this identified model with the PI controller and that of the actual process are shown in Fig 2. The matching is good.

Simulation example 4: Control of a Chemical reactor

We consider an isothermal CSTR with the reaction rate given by $-k_1c/(1+k_2c)^2$. The nonideal mixing is described by Chollets model. Here n is the fraction of the reactant feed that enters the zones of the perfect mixing and m is the fraction of the total volume of the reactor where the reaction occurs [i.e., (1-m) fraction of the volume is a dead zone]. The transient equation for the reactor is given by [6,7] as:

$$dc/dt = (nq/mV)(c_f - c) - k_1c/(1+k_2c)^2 \quad (18)$$

$$nc + (1-n)c_f = c_0 \quad (19)$$

$$\text{at } t=0,\ c=c_0. \quad (20)$$

Here c is the concentration of the reactant in the well mixed reactor zone and c_e is the concentration of the reactant in the exit stream. The controlled variable is c_0 and the manipulated variable is the feed concentration (c_f). For the present simulation study, we consider n=m=0.75, k_1=10 s^{-1}, k_2 =10 *mol*/s^{-1}, V=1 *l*. For c_f =3.222 *mol*/*l*, we get c_0 = 1.8 *mol*/*l*. and c=1.304. We have assumed a measurement delay of 20 secs. A PI controller with the settings k_c = 1 and τ_I =40, the closed loop servo response of c_e for a step change in c_f from 18 to 1.9 is evaluated. The response (in terms of deviation variable) is shown in Fig 4. From the response y_{p1}, $y_{m,1}$, $y_{p,2}$, $t_{p,1}$, $t_{p,2}$ are noted as: 1.6702, 0.8207, 1.0557, 84, 205.4, 322.6 respectively. From these values the value for damping coefficient and the effective time constant of the closed loop system are calculated as: ζ=0.3776 and τ_c =35.1491. The value of b_1 is obtained from Eq( ) as 16.8292. The value of the integral [eq (16)] is obtained as 80.3562. The initial guess for the model parameters are calculated a s: k_p = 2.091, L=20, and τ =87.5 . The numerical solution equations are obtained by *fsolve* of MATLAB routine as: τ=191.07, L=24.23 and k_p=4.6267. The response oft hie identified model with the same PI settings are evaluated and compared with that of the actual system. The response is show in Fig 4. The matching is good and hence the identified model is a representation of the system.

CONCLUSIONS

A method to identify a first order plus time delay with a zero transfer function model is proposed in time domain. The closed loop data for a step change in the set point is obtained using a PI controller. From the closed loop servo response, the characteristic equation's parameters and from the definition of Laplace transform, the value of y in Laplace domain is calculated. From the initial jump of the response, the value of the system zero is calculated. Three algebraic equations are derived for the calculations of the time constant, time delay and the process gain. Simulation results show that the proposed method gives a good fit when compared with that of the actual system with the same PI settings.

REFERENCES

1. Kavdia, M. and M.Chidambaram, On-line controller tuning for unstable systems, Comp & Chem. Eng., 20, 301-305 (1996).
2. Yuwana, M. and D.E.Seborg, A new method for on-line controller tuning, AIChE J., 28, 434- 440 (1982).

3. Ananth, I. and M.Chidambaram, Closed loop identification of unstable systems, Jl Franklin Institute, 36, 1055-1061 (1999).
4. PadmaSree , R. and M.Chidambaram, Closed loop identification of unstable systems, CHECON 2001, Dec-2001, Chennai.
5. DePaor, A.M and M. O'Malley, Controllers of Ziegler-Nichols type for unstable processes with time delay, Int. J. Control, 41, 1025- 1036 (1989)
6. Liou, C.T. and Y.S.Chien, The effect of nonideal mixing on input multiplicity, Chem. Eng. Sci., 46, 2113-2116 (1991).
7. Chidambaram,M. and G.P. Reddy, Nonlinear control of systems with input and output multiplicity, Comp & Chem. Eng., 20,295 -299 (1997)

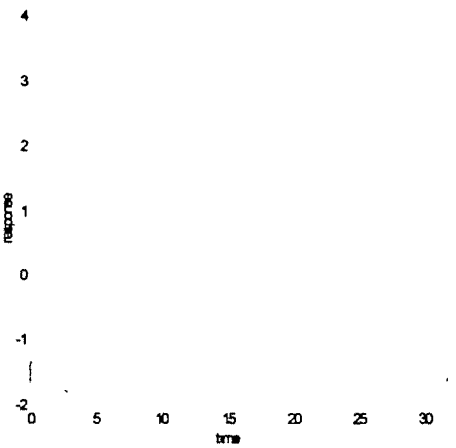

Fig 1 Comparison of closed loop response of the system and identified model for case study 1

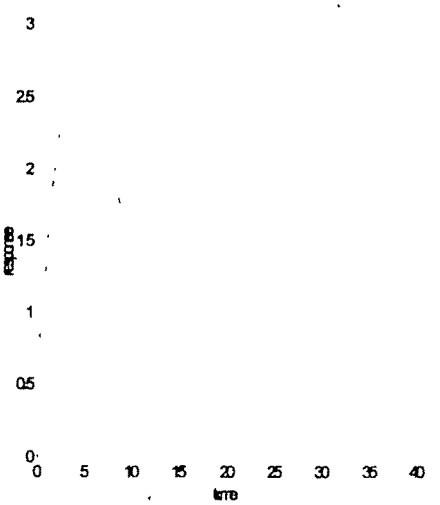

Fig 2 Comparison of closed loop response of the system and identified model for case study 2

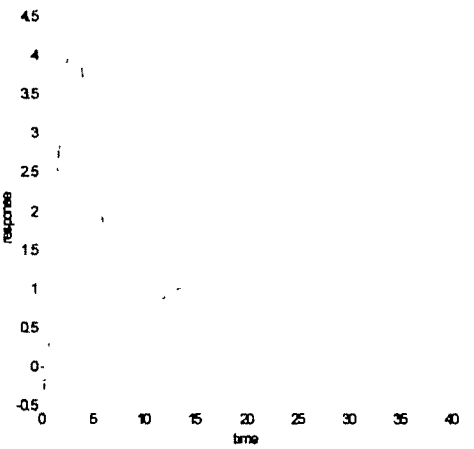

Fig 3 Comparison of closed loop response of the system and identified model for case study 3

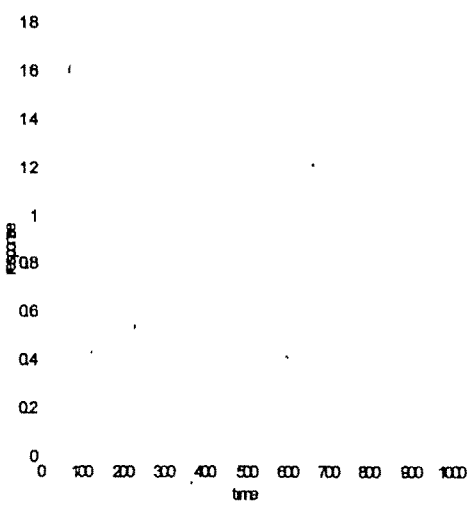

Fig 4 Comparison of closed loop response of the system and identified model for case study 4

Self-oscillation Quenching by Injecting Dither in Nonlinear Two Dimensional Control System

B. B. Pati and K. C. Patra
Department of Electrical Engineering, I.G.I.T. Sarang, Dhenkanal, Orissa-759146, India.
Email:-bbpati@hotmail.com,

Abstract

A nonlinear multidimensional (Two input two output) control system exhibiting limit cycle in autonomous mode is studied here. The effects of high frequency dither subjected at one or both of its input locations are analyzed. The phenomena of synchronization and de-synchronization are also studied using the principle of harmonic balance technique.

Keywords-Limit cycle, Nonlinear, Dither, Signal stabilization, Describing function.

INTRODUCTION

Most of the real systems, invariably possess significant nonlinear characteristics exhibiting various interesting phenomena such as limit cycles, sub-harmonic oscillations, jump resonance, asynchronous excitation etc..

Investigation of the behaviour of non-linear systems therefore is a very interesting and important field of study. The use of signal stabilization as a mean of stabilizing nonlinear systems has been known for a long time. In sixties, it was suggested that the injection of a dither at the input to the nonlinear element serves as an effective method of quenching limit cycle. Typically a dither is a periodic or stationary random function whose power spectrum lies above the system cutoff frequency, and is filtered out before reaching the output.

Although no truly significant results have been obtained in recent years for multidimensional system, the study of limit cycle prediction and signal stabilization thereof are of evident importance and hence addressed here.

The uniqueness and difficulty of obtaining solutions to nonlinear problems led many investigators in the fifties to examine approximate methods which might be applied with some generality to a large class of engineering systems. The result was liberalization methods and the most widely accepted method describing function (DF) method.

Harmonic balancing is a way of looking for periodic solutions in nonlinear systems by trying to fit a truncated Fourier series and choosing the frequency, amplitudes and phases so that any error only occurs in the discarded harmonics. In this attention is directed to find out the frequency and magnitude of oscillation for non-linear multivariable system, using the harmonic balance method analytically.

The authors have considered a general two-dimensional system derived from the fundamentals and used earlier[1,2]. The authors would like to mention that from oscillation point of view, nothing is gained by complicating the situation by overemphasizing the importance of system structure, other than considered here[1,2].

SYSTEM STRUCTURE

This structure of Fig.1 represents a general class of two dimensional system developed by the author [2] considering the coupling effect between subsystems and relationships between individual parameters of significance within the subsystem and used for limit cycle prediction in the earlier reported works. As shown in Fig.1, there exists a nonlinear element in the feedback loop of each subsystem. From limit cycle and signal stabilization point of view, this system claims to be more suitable for analysis, and almost all practical 2x2 system can be reduced to this general form. The system of Fig.1 exhibits self-oscillation or limit cycle at a frequency of ω_s rad/s in the autonomous state[2]. We now examine the possibility of quenching the limit cycle by injecting a high frequency (ω_f rad/s) deterministic signal. The dither can be injected at both the inputs simultaneously or at any one location U_1 or U_2. With the injection of dither, the system would exhibit complex oscillations. The signals at various points in the system would then be composed of signals of frequency (ω_f), signals of frequency of limit cycle (ω_s) and the combination frequencies, $k_1\omega_f \pm k_2\omega_s$ where k_1 and k_2 assume various integer values. However,

with the increase of the dither amplitude B, the frequency of limit cycle would also gradually change. For a certain amplitude of dither, the limit cycle would vanish and the system would exhibit forced oscillation at dither frequency(ω_f). The analysis of such oscillation is exceedingly complex even in a relatively simple two dimensional system containing memory-less odd non-linearity.

DITHER AT BOTH POINTS

For analysis of forced oscillation the system of Fig.1 can be represented by Fig.2 where both the subsystem nonlinear elements are substituted by their equivalent dual input describing function(DIDF)[3].

It may be noted that for a possible limit cycle in the system the following conditions must be fulfilled for ensuring a harmonic balance[1-5].

(i) The Phase Condition : $\theta_{c1}+\theta_{c2} = 180^o$

where

$\theta_{c1}=Arg[(N_1G_1(j\omega))/(1 + N_1G(j\omega))]$ and $\theta_{c2} = Arg[(N_2G_2(j\omega))/(1 + N_2G_2(j\omega))]$ (1a)

(ii) The Gain Condition: $(C_1/R_1).(C_2/R_2) = 1$ where

$(C_1/R_1)= [(N_1G_1(j\omega))/(1 + N_1G_1(j\omega))]$ and

$(C_2/R_2)= [(N_2G_2(j\omega))/(1 + N_2G_2(j\omega))]$.(1b)

(iii) The Amplitude Ratio Condition :

$[X_2/X_1]= | 1/(1+N_2G_2(j\omega)) |$ (1c)

Eqns.1 constitute a set of three independent equations that can be solved for three unknown quantities say ω, N_1 and N_2 yielding the required solution[1,4].

The following example will illustrate the procedure clearly.

EXAMPLE 1

Consider the system shown in Fig.1 with $G_1(s) =2/[s(s+1)^2]$, $G_2(s) =1/[s(s+4)]$ and the two nonlinear elements having ideal relay characteristics with $D_1 =1.0$ and $D_2 = 1.126$[5]. This configuration is not uncommon as many control systems are two dimensional and they employ relays or use controllers that operate in a relay type mode[4].

By utilising the proper phase, gain and amplitude ratio condition, of eqn.1, the expression for N_{1eq}, N_{2eq} and amplitude ratio can be written in a form as:

$N_{1eq}=[(\omega^2-1)N_{2eq}/8]+[(9\omega^2-\omega^4)/8$.(2)

$N_{2eq} = [(11-3\omega^2)\omega^2 \pm \sqrt{[(11-3\omega^2)^2\omega^4 - 8(\omega^2+16)(1-\omega^2)^2\omega^2]}]/[4(1-\omega^2)]$ (3)

$X_2/X_1 = [2N_{1eq}\sqrt{(\omega^2+16)}]/[(1+\omega^2)\ [\omega^2(\omega^2+16-2N_{2eq})+N_{1eq}^2]]$ (4)

The expressions of N_{1eq} and N_{2eq} are functions of B_1 and B_2. Keeping B_2 constant, the oscillation parameters are noted for various values of B_1 following the sequential steps:

(a) A certain value of ω is assumed;

(b) Equation 3 yields a value of N_{2eq};

(c) Consequently Eqn.2 yields N_{1eq};

(d) Subsequently Eqn.4 yields a value of X_1/X_2 ;

(e) For the N_{2eq} and N_{1eq} obtained in steps (b) and (c) above and for a particular value of B_1 an alternative ratio X_1/X_2 can be obtained from DIDF expressions [3,4].

(f) The steps (a) to (e) are repeated for several assumed values of ω, while keeping the value of B_1 a fixed number.

The frequency at which both the results of step (d) and (e) are same is the frequency of forced oscillation at a particular B_1. With B_2 kept at zero the variation of oscillation parameters were studied by varying B_1[1]. The point of synchronization is determined. The expressions of N_{1eq} and N_{2eq} are functions of B_1 and B_2. For various B_2 also the parameters are determined and given in Table.1-3. For each case the point of des-synchronization (using the concept of IDF) and synchronization were determined. These results have been substantiated with that of Simulink 1.3 toolbox use(cf.Table.1-3). Fig.3 shows the variation of oscillation parameters with variation of dither amplitude B_1 for a particular value of dither. (The first three curves in its legend represent the results of analytical method and second three that of simulation results). The synchronization and de-synchronization boundaries in B_1/B_2 plane is also determined and is shown in Fig.4 concisely.

CONCLUSION

Comparison of analytical results with the results of simulation using simulink tool box use of the example considered, shows that the simplifying assumptions made in the analysis leads to results of acceptable accuracy.

Concluding it can be said that prediction of oscillation using harmonic balance technique as suggested here is very systematic and can be applied to any complex structure system without loss of generality. The credibility of the DF is enhanced by this systematic method which entice the designer for use in complex or higher order

system. However, the inept handling of system equations may lead to no solution.

REFERENCES

1. K.C. Patra, and B.B. Pati, "An investigation of forced oscillation for signalstabilisation of two-dimensional nonlinear system," *Jour. of Systems and Control Letters*, Netherlands, vol.35, pp.229-236, 1998.
2. K.C.Patra, B.B.Pati, and J. Kacprzyk, "Prediction of Limit Cycles in Nonlinear Multivariable Systems" Archives of Control Science, Vol.4, No.3-4, pp.281-297, 1995.
3. D.P. Atherton, *Nonlinear Control Engineering-Describing function Analysis and Design*, Von Nostrand-Reinhold, London, 1975.
4. B.B. Pati, *Signal Stabilisation of Multivariable Nonlinear control system*, Ph.D.Thesis,UtkalUniversity,2000.
5. K.C. Patra, and Y.P. Singh, "Graphical method of prediction of limit cycle for multivariable nonlinear system,"*IEE Proc. Control Theory Appl.* Vol.143m pp.1-6,1996.

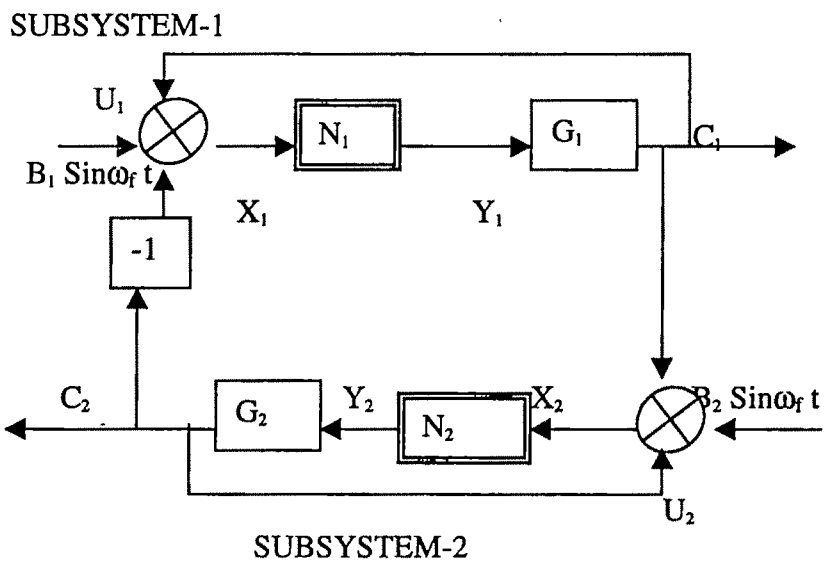

Fig.1 A generalized two dimensional nonlinear system[1,2]

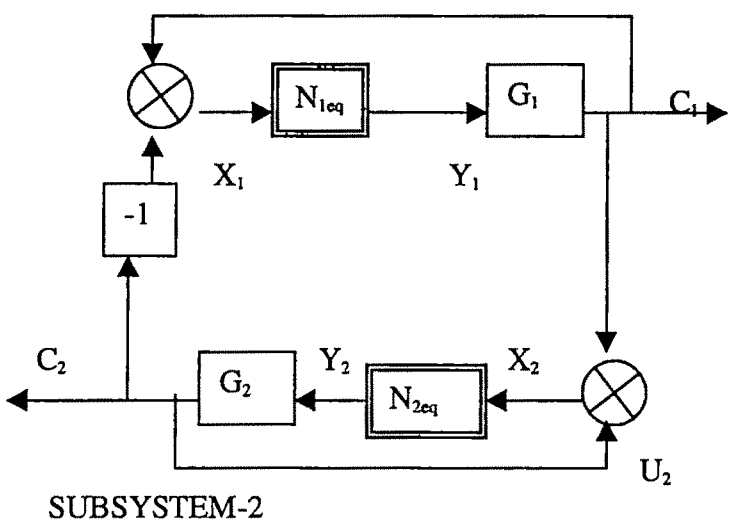

Fig.2 Linearised version of the system of Fig.1[3,4]

Table.1 Variation of Forced Oscillation Parameters for B_2=0.5

Method	B_1	0	0.25	0.5	0.75	1.0	1.25	1.5	1.75	1.95
Analytic Method	ω_s	0.80	0.8	0.8	0.8	0.8	0.78	0.77	0.68	
	C_1	1.93	1.92	1.89	1.88	1.86	1.78	1.59	0.91	
	C_2	0.43	0.43	0.42	0.41	0.43	0.43	0.43	0.42	
Simulink Method	ω_s	0.76	0.77	0.77	0.78	0.77	0.76	0.75	0.67	0.67
	C_1	2.05	2.08	2.08	2.0	1.98	1.88	1.88	0.90	0.70
	C_2	0.53	0.53	0.49	0.52	0.52	0.49	0.48	0.46	0.36

Table.2 Variation of Forced Oscillation Parameters for B_2=0.75

Method	B_1	0	0.25	0.5	0.75	1.0	1.25	1.55
Analytic Method	ω_s	0.8	0.81	0.81	0.8	0.79	0.78	
	C_1	1.94	1.92	1.88	1.85	1.80	1.73	
	C_2	0.43	0.43	0.42	0.41	0.43	0.43	
Simulink Method	ω_s	0.78	0.77	0.76	0.76	0.76	0.77	0.76
	C_1	2.02	2.06	2.07	2.0	1.98	1.89	1.09
	C_2	0.46	0.47	0.47	0.48	0.46	0.47	0.46

Table.3 Variation of Forced Oscillation Parameters for B_2=1.0

Method	B_1	0	0.25	0.5	0.75	1.0	1.25	1.45
Analytic Method	ω_s	0.81	0.8	0.8	0.8	0.79	0.79	0.77
	C_1	1.88	1.89	1.86	1.82	1.76	1.66	1.59
	C_2	0.41	0.40	0.40	0.4	0.4	0.40	0.43
Simulink Method	ω_s	0.78	0.77	0.76	0.76	0.78	0.76	0.78
	C_1	2.05	2.08	2.07	2.0	1.8	1.68	1.58
	C_2	0.45	0.53	0.47	0.45	0.44	0.42	0.38

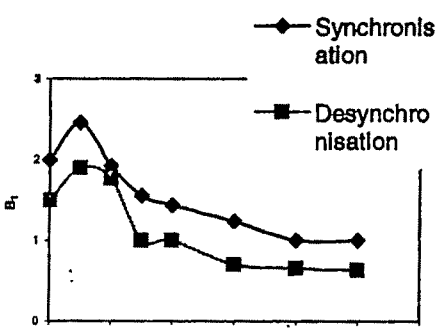

Fig. 4. Synchronisation/Desynchronisation values depicting stability information

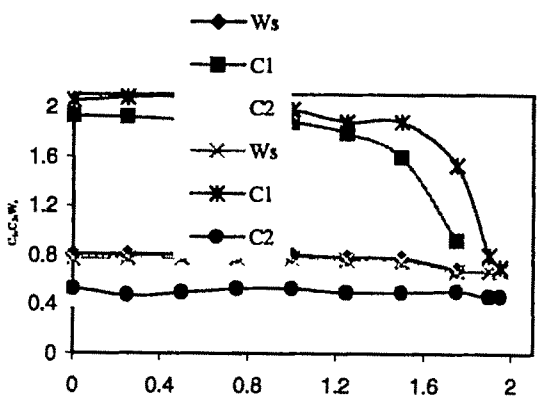

Fig.3 Variation of Outputs and frequency with B_1 at B_2=0.5

Acknowledgement: The authors wish to thank Dr. S. C. Mishra, Principal, and dept of Electrical Engg. IGIT, Sarang for providing necessary facilities for the work. The authors wish to thank AICTE govt. of India for funding the research work through MODROB project.

Reduction Of Large Scale MIMO Interval Systems Using Routh Approximants

G. V. K. R. Sastry and P. Mallikarjuna Rao
Department of Electrical Engineering, College of Engineering, Andhra University,
Visakhapatnam-530003, (A.P), India.

Abstract

A new method for the reduction of order of Large Scale MIMO Interval Systems based on Routh Approximation technique is proposed in this paper. This method is computationally simple and efficient as it requires only γ-table and avoids the necessity of formulation of both γ - δ tables and evaluation of time moments of original system beforehand unlike other methods. It always generates low-order models, which retain the stability and initial time-moments of the original high-order MIMO interval system. Typical numerical examples illustrate the proposed method.

Key words: Control Systems, Model Reduction, Large Scale MIMO Systems Modelling, Interval Systems

INTRODUCTION

Physical Control Systems possess high order transfer functions whose prototypes cannot be easily proposed. An attempt to investigate the behaviour of such systems with their high order transfer functions increases complexity and the methods which deal with such cases are out of scope. To overcome this problem, usually Large scale system reduction technique is to be used. The reduced order models obtained by the modelling techniques are expected to satisfy the constraints and approximate the behaviour of the original practical systems. Two factors influence in any model reduction technique, are viz., its simplicity and its accuracy. If a system model is over simplified, presumably for computational effectiveness, incorrect conclusions may be drawn from it is representing the actual system. On the otherhand, a highly detailed model would lead to a great deal of unnecessary complications and should a feasible solution be attainable, the extent of resulting details become so vast that further investigations of the system behaviour would become impossible with questionable practical values. Even though many methods are available in literature for High order continuous SISO systems reduction, only few methods are available in literature for the modelling of Large Scale Interval systems, particularly for Large Scale MIMO Interval systems.

Recently, some methods are suggested by Bandhopadhyay et,al., for reducing Interval systems [2,3]. "The Routh-Pade Approximation method for Interval systems"[2] is indirect and involves much complex computations in calculation of time-moments of the original high order system beforehand. "The γ -δ Routh Approximation method for Interval systems"[3] needs the formulation of both γ and δ tables which increases the complexity of the reduction procedure involving considerably more computational effort.

This paper presents a new and computationally simple method for the reduction of Large Scale MIMO Interval Systems. New algorithms are proposed to develop the denominator and numerator polynomials of the reduced order models by using Routh Approximants, avoiding the necessity of finding time moments of original system beforehand. The proposed method needs the formulation of only γ -Table unlike the other methods [2, 3]. The first 'k' time-moments of the original high order system will be retained in the k^{Th} order reduced model.

PROPOSED REDUCTION METHOD:

Let the n^{th} order Original MIMO Interval system be defined as,

$$G(s) = \frac{1}{D_n(S)} \begin{vmatrix} g_{11}(s) & g_{12}(s) & \ldots & g_{1j}(s) \\ g_{21}(s) & g_{22}(s) & \ldots & g_{2j}(s) \\ \ldots & \ldots & \ldots & \ldots \\ g_{i1}(s) & g_{i2}(s) & \ldots & g_{ij}(s) \end{vmatrix} \quad \begin{matrix} ; i=1,2,3\ldots\ldots \\ \quad j=1,2,3\ldots \end{matrix}$$

where, $D_n(s)$ is a Scalar polynomial represented as,

$$D_n(s)= \sum_{L=0}^{n} [Q_L^-, Q_L^+]\, s^L \quad \text{and} \quad g_{ij}(s) = \sum_{L=0}^{n-1} [P_{ij}^-, P_{ij}^+]_L\, s^L$$

Hence,

$$G_{ij}(s) = \frac{\sum_{L=0}^{n-1} [P_{i,j}^-, P_{i,j}^+]_L\, s^L}{\sum_{L=0}^{n} [Q_L^-, Q_L^+]\, s^L}$$

Then the k^{th} order reduced MIMO model is defined as,

$$R(s)= \frac{1}{D_k(S)} \begin{vmatrix} N_{11}(s) & N_{12}(s) & \ldots.. & N_{1j}(s) \\ N_{21}(s) & N_{22}(s) & \ldots.. & N_{2j}(s) \\ \ldots\ldots\ldots\ldots & & & \\ N_{i1}(s) & N_{i2}(s) & \ldots.. & N_{ij}(s) \end{vmatrix} \quad \begin{matrix} ; \ i = 1,2,\ldots.. \\ \quad j = 1,2,\ldots.. \end{matrix} \qquad (2)$$

where,

$$R_{ij}(s) = \frac{\sum_{L=0}^{k-1} [p_{i,j}^-, p_{i,j}^+]_L\, s^L}{[1,1]s^k + \sum_{L=0}^{k-1} [q_L^-, q_L^+]\, s^L} = \frac{N_{ij}(s)}{D_k(s)}$$

Denominator $D_k(z)$:

The new algorithms proposed for the reduced denominators of models with $k \le n$ are;

$$\text{For } k=1;\ D_1(s)= [1,1]s + \frac{[\gamma_1^-,\gamma_1^+]}{[Q_0^-, Q_0^+]}\, [Q_0^-,Q_0^+]$$

$$\text{For } k=2;\ D_2(s)= [1,1]s^2 + \frac{[\gamma_1^-,\gamma_1^+][\gamma_2^-,\gamma_2^+]}{[Q_0^-, Q_0^+]}\, \{[Q_0^-,Q_0^+]+[Q_1^-,Q_1^+]s\}$$

and in general,

$$D_k(s) = [1,1]s^k + \frac{[\gamma_k,\gamma^+_k]\ !}{[Q^-_0, Q^+_0]}\, \{[Q_0^-,Q_0^+] + [Q_1^-,Q_1^+]s + \ldots\ldots\ldots + [Q_k^-,q_k^+]s^{k-1}\} = [1,1]s^k + \sum_{L=0}^{k-1} [q_L^-, q_L^+]\, s^L \qquad (3)$$

Numerator $N_K(z)$:

The new algorithms proposed for the reduced numerators of models with $k \le n$ are;

$$\text{For } k=1;\ N_1(s)= [1,1]s + \frac{[\gamma_1^-,\gamma_1^+]}{[Q_0^-,Q_0^+]}\, [P_{1,j}^-, P_{1,j}^+]_0$$

$$\text{For } k=2;\ D_2(s)= [1,1]s^2 + \frac{[\gamma_1^-,\gamma_1^+][\gamma_2^-,\gamma_2^+]}{[Q_0^-, Q_0^+]}\, \{[P_{i,j}^-, P_{i,j}^+]_0 + [P_{i,j}^-, P_{i,j}^+]_1 s\}$$

and in general,

$$N_{i,j}(s) = \sum_{L=0}^{k-1} [p_{i,j}^-, p_{i,j}^+]_L\, s^L \qquad (4)$$

The Interval coefficients $[\gamma_k^-,\gamma_k^+]$ with k=1,2, —n are obtained from the proposed $[\gamma^-,\gamma^+]$

Routh type Discrete Interval table.

$[\gamma^-,\gamma^+]$ TABLE:

$$[\gamma_1^-,\gamma_1^+] = \begin{cases} [Q_0^-,Q_0^+]\ [Q_1^-,Q_1^+]\ [Q_2^-,Q_2^+]\ldots \\ [Q_1^-,Q_1^+]\ [Q_2^-,Q_2^+]\ldots\ldots\ldots \end{cases}$$

$$[\gamma_2^-,\gamma_2^+] = \begin{cases} [C_1^-,C_1^+]\ [C_2^-,C_2^+]\ [C_3^-,C_3^+]\ \ldots \\ [C_2^-,C_2^+]\ [C_3^-,C_3^+]\ldots\ldots\ldots \end{cases}$$

$$[\gamma_3^-,\gamma_3^+] = \begin{cases} [D_1^-,D_1^+]\ [D_2^-,D_2^+]\ldots\ldots\ldots \\ [D_2^-,D_2^+]\ldots\ldots\ldots \end{cases} \qquad (5)$$

and,

$[\gamma_1^-,\gamma_1^+] = [Q_0^-,Q_0^+]/\ [Q_1^-,Q_1^+]$,

$[\gamma_2^-,\gamma_2^+] = [C_1^-,C_1^+]/\ [C_2^-,C_2^+]$ ...and so on....

For i = odd

$$[C_i^-,C_i^+] = [Q_i^-,q_i^+]\ ;\ i=1,3,5....$$
$$[D_1^-,D_1^+] = [C_2^-,C_2^+]$$
$$[D_i^-,D_i+] = [Q_{i+1}^-,q_{i+1}+]\ ;\ i=3,5\ ....$$

(6)

For i = even

$$[C_i^-,C_i^+] = [Q_i^-,q_i^+] - \{[Q_{i+1}^-,Q_{i+1}^+] [Q_0^-,Q_0^+]\} / [Q_1^-,Q_1^+]$$

$$[D_i^-,D_i^+] = [C_{i+1}^-,C_{i+1}^+] - \{[C_1^-,C_1^+] [C_{i+2}^-,C_{i+2}^+]\} / [C_2^-,C_2^+]$$

NUMERICAL EXAMPLES

Example1: Consider the Original MIMO interval system given as,

$$G(s) = \frac{1}{D(s)} \begin{vmatrix} g_{11}(s) & g_{12}(s) \\ g_{21}(s) & g_{22}(s) \end{vmatrix}$$

Where, $D(s) = [0.537464, 1.537464]s^2 + [1.379131, 2.379313]s + [1,2]$

$g_{11}(s) = [0.622, 1.622]s + [1.00721, 2.00721]$
$g_{12}(s) = [462.6,463.6]s + [715.2653, 716.62653]$
$g_{21}(s) = [3.563, 4.563]s + [4.8589, 5.8589]$
$g_{22}(s) = [610.435,611.435]s + [1000.5485,1001.5485]$

Interval $[\gamma^-, \gamma^+]$ – Table:

$[\gamma_1^-, \gamma_1^+]$		
	[1,2]	[1.379131,2.379131] [0.537464,1.537464]
	[1.379131,2.379131]	[0.537464,1.537464]

The interval $[\gamma, \gamma^+]$- parameter for the first output using eqn.5 is obtained as,
$[\gamma_1^-, \gamma_1^+] = [0.42, 1.45]$

The denominator $D_1(s)$ of the reduced order model using eqn.3 is obtained as,

$D_1(s) = [1, 1]s + [0.2, 2.0]$.

The numerator polynomial, $N_{11}(s)$ for the first output of the reduced order model using eqn.4 is obtained as,

$N_{11}(s) = [0.2115, 2.0]$

The first order reduced MIMO model obtained by the proposed method is,

$$R_1(s) = \frac{1}{D_1(s)} \begin{vmatrix} [0.2115, 2.9] & [150.206, 1038.58] \\ [1.0204, 8.49] & [210.12,1452.24] \end{vmatrix}$$

where, $D_1(s) = [1, 1]s + [0.2, 2.9]$

The first order reduced MIMO model obtained by applying the " Routh-Pade Approximation method for Interval systems" of Bandhopadhyay et, al., [2] is,

$$R_B(s) = \frac{1}{D_B(s)} \begin{vmatrix} [0.2922, 6.93] & [207.3, 2471.8] \\ 1.425, 20.22] & [290,3456.344] \end{vmatrix}$$

where,
$D_B(s) = [1.379313, 2.379313]s + [0.5797, 3.451]$

The step responses for first output of the original high order system and models obtained by the proposed method and method of Bandhopadhyay, et.al., [2] are compared in fig.1 and fig.2.

Example2: Consider the MIMO Interval system as,

$$G(s) = \frac{1}{D(s)} \begin{vmatrix} g_{11}(s) & g_{12}(s) \\ g_{21}(s) & g_{22}(s) \end{vmatrix}$$

where,
$D(s) = [1,2]s^6 + [41,42]s^5 + [571,572]s^4 + [3491,3492]s^3 + [10060,10061]s^2 + [13100,13101]s + [6000,6001]$

$g_{11}(s)=[2,3]s^5+[70,71]s^4 + [762,763]s^3 + [3610,3611]s^2 + [7700,7701]s + [6000,6001]$

$g_{12}(s)=[1,2]s^5+[38,39]s^4 + [459,460]s^3 + [2182,2183]s^2 + [4160,4161]s + [2400,2401]$

$g_{21}(s)=[1,2]s^5+[30,31]s^4 + [331,332]s^3 + [1650,1651]s^2 + [3700,3701]s + [3000,3001]$

$g_{22}(s)=[1,2]s^5+[42,43]s^4 + [601,602]s^3 + [3600,3601]s^2 + [9100,9101]s + [6000,6001]$

The second order reduced MIMO model obtained by the proposed method is,

$$R_2(s) = \frac{1}{D_2(s)} \begin{vmatrix} N_{11}(s) & N_{12}(s) \\ N_{21}(s) & N_{22}(s) \end{vmatrix}$$

where,
$N_{11}(s) = [1.1716,0.9105]s + [0.9129,0.7095]$
$N_{12}(s) = [0.6329,0.492]s + [0.365,0.2839]$
$N_{21}(s) = [0.5629,0.4376]s + [0.4565,0.3548]$
$N_{22}(s) = [1.3846,1.0761]s + [0.9129,0.7096]$

and,
$D_2(s) = [1,1]s^2 + [1.9932,1.549]s + [0.9129,0.7095]$

It can be observed that, the above reduced order models obtained by the proposed method are same as those obtained by "γ - δ Routh Approximations for Interval Systems" method of Bandhopadhyay et,al.,[3].

CONCLUSIONS

A new, simple and direct method for the model reduction of Large Scale MIMO Interval Systems is proposed. The method is based on Routh Approximants and computationally superior to the existing methods in literature as it requires only [γ ,γ^+] table and avoids necessity of calculating the time moments of original high order system beforehand and matrix multiplications.

REFERENCES

1. B.Ross Barmish, "A Generalisation of Kharitonov's Four Polynomial Concept for robust stability problem with linearly dependent coefficient perturbations", IEEE Trans. on Automatic Control, Vol.34, No.2, PP.157-163, 1989.

2. B.Bandhopadhyaya, U.Ismail and R.Gorez,"Routh-Pade Approximation for Interval Systems", IEEE trans. Automatic Control, Vol. 39, PP.2454-2456, 1994.

3. B.Bandhopadhyaya," γ - δ Routh Approximations for Interval Systems", IEEE trans. On Automatic Control,Vol.42, No.8, PP.1127-1130, 1997.

APPENDIX

The rules of Interval arithmetic have been defined as:

Addition : [p,q] + [l,m] = [p+l, q+m]

Subtraction : [p,q] – [l,m] = [p-m, q-l]

Multiplication: [p,q][l,m] = [min(pl,pm,ql,qm), max(pl,pm,ql,qm)]

Division : [p,q] / [l,m] = [p,q] [1/m,1/l];
[p,q] /[p,q] = 1.0

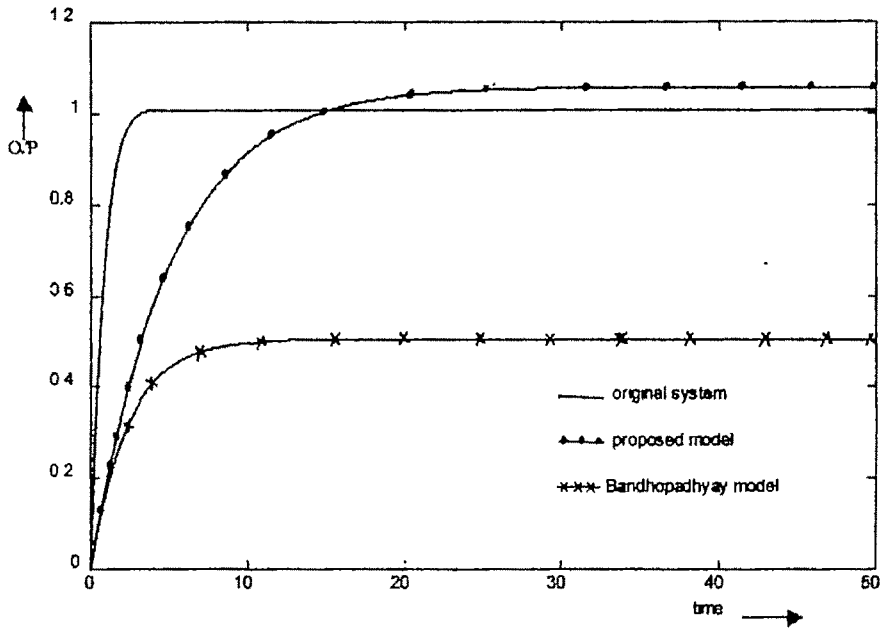

Fig.1 : Comparison of Step responses of Ex.1. 1st output (Lower Limits)

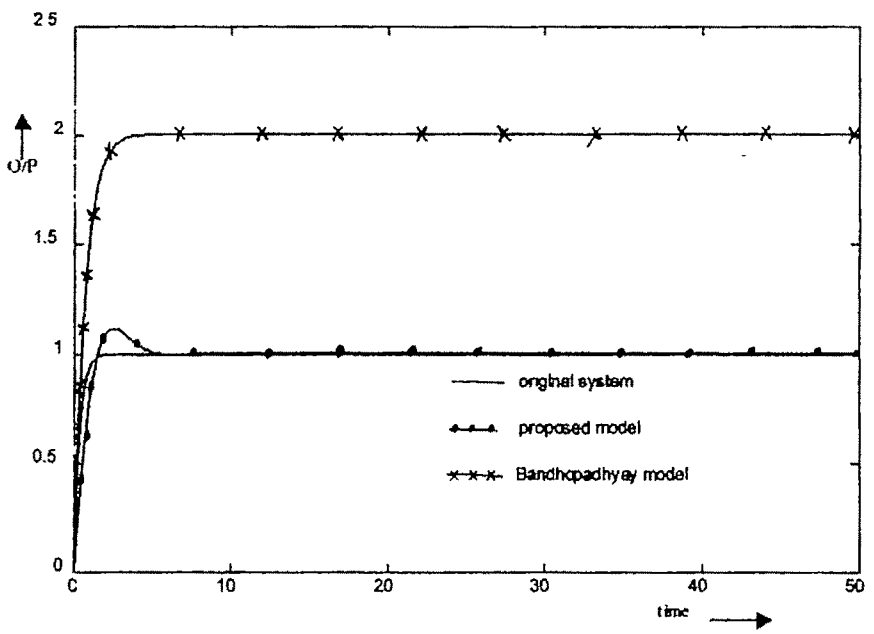

Fig.2 : Comparison of Step responses of Ex.1, 1st output(Upper Limits)

A New Algorithm For Analysis And Design Of High Order Non-linear Systems Using Frequency Response Modelling Technique

G. V. K. R.Sastry*, K. B. Madhu Sahu and G. S. Kalyan****
*Dept. of Electrical Engg., Andhra University, Visakhapatnam, 530003, India
**Dept. of Electrical Engg., GMR Institute of Tech., Rajam, 532127,India
E-mail for corresponding author: profgvkrsastry@yahoo.com

Abstract

A new algorithm is proposed for the stability analysis and design of a class of high-order Non-Linear Systems. The proposed method involves three important stages namely Stability Analysis using Popov-criterion, Modelling technique based on frequency response matching to save computational effort and the Design procedure to realise a compensator to make the system stable if found unstable. The algorithm suggested, is for stability analysis and design of compensator making use of the reduced order system which is expected to make high-order Non-Linear system stable. Therefore much computational effort and computer time can be saved. The method is digital computer oriented.

Key words: Control Systems, Non-Linear Systems, Large Scale System Modelling.

INTRODUCTION

We know that there are very few methods available for the stability analysis of non-linear systems unlike for linear systems and Popov-criterion is one of the graphical methods available for this purpose. When applied to high-order non-linear systems i.e. non-linear systems with high order linear plants, it is always preferable to make use of large scale system modelling to save much computational effort involved in dealing with original high order system directly. It is also very useful to suggest a procedure to design a compensator to make a high-order non-linear system stable if found unstable.

The proposed method involves three important stages namely the Application of Popov criterion for stability analysis, Modelling Technique based on frequency response matching to save computational effort and the Design procedure to realise a compensator to make the system stable if found unstable. These three important aspects are discussed in detail in the following text.

PROPOSED METHOD

Modelling procedure steps 1.Consider the given original high order non-linear system with non-linear element [0,k] and high order linear part G(s) as shown in Fig. 2(a).

2.Reduce G(s) to second order model using Simplified Routh Approximation Method (SRAM) and compute gain cross over frequency ω_p analytically as follows:
Let the given high order linear part G(s) of the original high order non-linear system be:

$$G(s) = \frac{B_0 + B_1 s + \ldots + B_{n-1} s^{n-1}}{A_0 + A_1 s + \ldots + A_n s^n}$$

Using SRAM the second order model is defined as:

$$R_2(s) = \frac{\alpha_1 \alpha_2 (B_0 + B_1 s)}{s^2 + \alpha_1 \alpha_2 (A_0 + A_1 s)}$$

where $\alpha_1 = A_0 / A_1$
and $\alpha_2 = A_1^2 / (A_1 A_2 - A_0 A_3)$

By definition, the gain cross over frequency ω_p, can be calculated as

$$\left| R_2 (j\omega_p) \right| = 1$$

3.Consider the transfer function of original high order linear system given by

$$G(s) = \frac{A_{2,1} + A_{2,2} s + A_{2,3} s^2 + \ldots + A_{2,n} s^{n-1}}{A_{1,1} + A_{1,2} s + A_{1,3} s^2 + \ldots + A_{1,n+1} s^n}$$

4.The reduced r-th order model which retains the gain margin of the original n-th order system is defined as:

$$(\omega_1,\omega_2, \ldots\ldots\ldots, \omega_m)\ R\ [r\text{-}1,r]^i_j\ (s) = \frac{d_0 + d_1 s + d_2 s^2 + \ldots + d_{r-1} s^{r-1}}{c_0 + c_1 s + c_2 s^2 + \ldots + c_r s^r}$$

where r and r-1 represent the number of poles and zeros of R(s) respectively.
i and j are the number of times of the continued fraction expansion of G(s) about s=0 & s=infinity respectively.
$\omega_1,\omega_2, \ldots\ldots\ldots, \omega_m$ are the frequencies at which the frequency response of original high-order system G(s) is to be matched by the response of reduced system $R_k(s)$.

5.Expand G(s) about s=0 for i (even number) times, i.e.,

$$G(s) = \frac{1}{A_{1,1} + A_{1,2}\, s + A_{1,3}\, s^2 + \ldots + A_{1,n+1}\, s^n \ \Big/\ A_{2,1} + A_{2,2}\, s + A_{2,3}\, s^2 + \ldots + A_{2,n}\, s^{n-1}}$$

$$= [h_1 + [h_2 / s + [\ldots + [h_i / s + H_N(s) / H_D(s)]^{-1}]^{-1}]^{-1}]^{-1} \qquad (1)$$

where $h_i = A_{1,1} / A_{i+1,1}$
and $H_N(s)$ & $H_D(s)$ are calculated using the equations

$$H_N(s) = A_{i+2,1} + A_{i+2,2}\, s + \ldots + A_{i+2,\,n-i/2}\, s^{n-1-i/2}$$
$$H_D(s) = A_{i+1,1} + A_{i+1,2}\, s + \ldots + A_{i+1,\,n+1-i/2}\, s^{n-i/2}$$

6.Reverse the polynomial sequence in equations $H_N(s)$ and $H_D(s)$ and continue to expand Eqn. 1 about s=infinity for j (even number) times. The expression for $H_N(s)/H_D(s)$ when expanded about s=infinity for j times is given by

$$H_N(s)/H_D(s) = [E_1 s + [E_2 + [\ldots + [E_j + F_N(s)/F_D(s)]^{-1}]^{-1}]^{-1}]^{-1} \qquad (2)$$

where $F_N(s)$ and $F_D(s)$ are calculated by using the below equations:

$$F_N(s) = A_{i+j+2,\,n-[(i+j)/2]}\, s^{n-1-[(i+j)/2]} + \ldots + A_{i+j+2,2}\, s + A_{i+j+2,1}$$
$$F_N(s) = A_{i+j+1,\,n+1-[(i+j)/2]}\, s^{n-[(i+j)/2]} + \ldots + A_{i+j+1,2}\, s + A_{i+j+1,1}$$

7.Replace $F_N(s) / F_D(s)$ in Eqn. 2 by $T_N(s)/T_D(s)$, which is given by

$$T_N(s)/T_D(s) = \frac{Y_{m-1}s^{m-1} + Y_{m-2}s^{m-2} + \ldots + Y_1 s + Y_0}{X_m s^m + X_{m-1}s^{m-1} + \ldots + X_1 s + X_0}$$

With $Y_{m-1} = 1$

8.Calculation of $Y_{m-2}, Y_{m-3}, \ldots, Y_1, Y_0, X_m, \ldots, X_1, X_0$ is as follows:

$$\text{Let } T_N(s)/T_D(s)\ \Big|_{s=j\omega_K} = F_N(s)/F_D(s)\ \Big|_{s=j\omega_K} = r_K + jm_K \qquad (3)$$

where K=1,2,....,m and r_K & m_K are the real and imaginary parts of $F_N(s)/F_D(s)$ for $s=j\omega_K$ respectively.

9.Separating the real part and the imaginary part in Eqn. 3, a pair of simultaneous independent equations is obtained. Therefore, the 2m unknowns $Y_{m-2}, Y_{m-3}, \ldots, Y_1, Y_0, X_m, \ldots, X_1, X_0$ are obtained by solving the 2m simultaneously independent equations.

10.After replacing $F_N(s)/F_D(s)$ with $T_N(s)/T_D(s)$, invert the continued fraction and the reduced model is obtained i.e.,

$$(\omega_1,\omega_2, \ldots\ldots\ldots, \omega_m)\ R\ [r\text{-}1,r]^i_j\ (s)$$

$$= [h_1 + [h_2/s + [\ldots + [h_i/s + [E_1 s + [E_2 + [\ldots + [E_j + T_N(s)/T_D(s)]^{-1}]^{-1}]^{-1}]^{-1}]^{-1}]^{-1}]^{-1}]^{-1}$$

The order of the denominator of the reduced model is r=m+(i+j)/2 . If both i&j are odd numbers then the foregoing equations have some minor differences.

APPLICATION PROCEDURE

Stability Analysis:

1.Consider the non-linear element, represented by its sector values [0,k].
2.Consider the linear plant G(s) of the original high-order non-linear system.
3.Reduce the high-order linear plant G(s) of the uncompensated non-linear system into a 4th order system $R_4(s)$ using the proposed modelling procedure, retaining gain margin of G(s) with $\omega_1=0$ & $\omega_3=\omega_p$ and $0<\omega_2<\omega_3<\omega_p$.
4.Obtain the frequency response plots on S-plane i.e., Popov plot of linear plant $R^*(j\omega)$ and the Popov line of non-linear element, where system plot is the modified Nyquist plot of $R(j\omega)$, i.e., $R^*(j\omega)=[\mathrm{Re}\ R(j\omega) + j\omega x \mathrm{Im} R(j\omega)]$ for different values of 'ω' and the Popov line of non-linear element passes through (-1/k , j0).
5.If there is any intersection between non-linear Popov line and the Popov plot of $R^*(j\omega)$, the system is said to be undergoing limit cycle condition and hence unstable otherwise stable.
6.The number of intersections of the two plots signifies number of limit cycle conditions.

Compensator Design Steps:

Making use of the compensator $G_c^*(j\omega)$ obtained using only low order system(model), the original high-order non-linear system (originally unstable) is expected to become stable. A compensator with the transfer function $G_c^*(s)$ will be designed to make an unstable non-linear system stable using the following steps.
1.Plot the Popov locus of the linear part $G(j\omega)$ of uncompensated non-linear system i.e., plot between Re $G(j\omega)$ and ωxIm $G(j\omega)$ for w=0 to infinity.
2.The initial intersection point of Popov locus $G^*(j\omega)$ with Popov line representing non-linear element is considered.

3.The frequency at which the initial intersection of the Popov locus occur with the Popov line is considered as ω_c. The corresponding values of real and imaginary of $G^*(j\omega)$ are (x,y).

4. Let the compensator be defined as :

$$G_c^*(s) = \frac{1 + T_2(s)}{1 + T_1(s)}, \quad T_1 > T_2$$

5.To find T_1 and T_2:

The Popov locus of the compensator will be a line P0P1 as shown in fig.1 where the coordinates of the point P0 & P1 are defined as $(-1/k_2, 0)$ and (x_1, y_1) respectively with

$$x_1 = \frac{x}{x^2 + y^2} \quad \text{and} \quad y_1 = \frac{-y}{x^2 + y^2}$$

6.Then the value of

$$T_1 = \frac{1/k_2 + x_1}{y_1}$$

The value of T_2 is calculated by solving the following equations :

$$x^1 = \frac{1 + w_c^2 T_1 T_2}{1 + w_c^2 T_1^2} \quad \text{and} \quad y^1 = \frac{w_c^2 (T_2 - T_1)}{1 + w_c^2 T_1^2}$$

where $x^1 = -x_1/k_2$ and $y^1 = -y_1/k_2$

EXAMPLE

Consider a non-linear system with the single valued non-linearity characteristic (N) in cascade with the linear plant G(s) as shown in fig.2(a).The linear plant is represented by its transfer function given as

$$G(s) = \frac{s^5+32.5s^4+380s^3+2070s^2+5424s+2240}{s^7+15s^6+124s^5+630s^4+2144s^3+4600s^2+5856s+2880}$$

The non-linear characteristic is bounded by the sector values [0, 1.5].

It is required to analyze the stability of the system and design a compensator to stabilize the system if found unstable using the proposed method.

The uncompensated system Popov plot and the Popov –line of the Non-Linear characteristic are shown on modified S-Plane in fig.3 by simulating the example on digital computer using the computer algorithm developed for the proposed method. It can be observed that there is an intersection between the system plot and the Non-Linear (Popov Line)plot. Therefore the system is found to be unstable.

Design of Compensator for the original high-order system (without modelling):

Using the proposed design procedure, the compensator $G_c(s)$ is designed to make the system stable using G(s).

The transfer function of the compensator will be

$$G_c(s) = \frac{1 + 0.0702s}{1 + 0.9124s}$$

The modified transfer function of the compensated linear part of the system is

$$G_c(s)G(s) = \frac{0.0702s^6+3.282s^5+59.184s^4+525.359s^3+2450.884s^2+5581.297s+2240}{0.9124s^8+14.6874s^7+128.149s^6+698.87s^5+2586.389s^4+6341.477s^3+9943.57s^2+8483.985+2880}$$

(without modelling)

The Popov plots of the compensated system are shown in fig.4 it can be observed that the intersection between the plots is eliminated using the compensator hence the system is found to be stable.

Design using Modelling :

The 4th order reduced system is obtained for the original high-order system using the proposed modelling procedure, which retains gain margin of the original system.

The transfer function of reduced model is obtained as

$$R_4(s) = \frac{s^2+26.575s+13.263}{s^4+3.927s^3+15.529s^2+27.549+17.053}$$

The Popov plots of reduced order system and the non-linear elements are shown in fig. 5. It is found that the system is unstable representing the stability of original uncompensated system.

A Compensator is designed for the reduced order system using the proposed algorithm. The transfer function of the compensator is

$$G_c^*(s) = \frac{1 + 0.1191s}{1 + 1.424s}$$

The transfer function of compensated reduced order system will be

$$R_4(s)G_c^*(s) = \frac{0.1191s^3+4.1651s^2+28.1546s+13.263}{1.4242s^5+6.5928s^4+26.0434s^3+54.7643s^2+51.83588s+17.053}$$

The Popov plots of the compensated system (reduced) shown in fig. 6 confirm that the reduced order system is stable. The original uncompensated high-order system is compensated using the compensator designed for the reduced order system.

Then the transfer function of the compensated original high-order system is given by

$$G(s)G_c^*(s) = \frac{0.1191s^6+4.87075s^5+77.758s^4+626.537s^3+2715.9984s^2+5690.784s+2240}{1.4242s^8+22.363s^7+191.6008s^6+1021.246s^5+3683.4848s^4+8695.32s^3+12940.1152s^2+9957.696s+2880}$$ (with modelling)

The Popov plots of the compensated system (using modelling) are shown in fig. 7. It can be observed that the intersection between the plots is eliminated using the compensator hence the system is said to be stabilized by using the compensator designed for the reduced order system.

CONCLUSIONS

An algorithm for the stability analysis and design of high-order Non-Linear system, which is based on Popov – Criterion and Frequency response matching to save computational effort is proposed. The method is digital computer oriented.

REFERENCES

[1].Hutton, M.F., And Friendiand, B., "Routh Approximations for the reduced order of linear, time-invariant systems", IEEE Trans, Automatic Control, pp.329-337, 1975.

[2].G.V.K.R.Sastry And V.Krishna Murthy, "Relative Stability using Simplified Routh Approximation Method (SRAM)", Journal of IETE, Vol.35, No.3, pp.99, May 1987.

[3].Hsia, T.C., "On the simplification of linear systems", IEEE Trans, Automatic Control, AC-17, pp.3723-374, 1972.

[4].J.M.Lin And K.W.Han, "Model Reduction for Keeping Gain Margin and Phase Margin Unchanged", IEEE Transactions on Industry Applications, Vol.1A-22, No.1, pp.51, Jan/Feb 1986.

[5].C.Hwang And Ying-Chinlee, "Multi frequency pade approximation via Jordan type continued fraction expansion", IEEE Trans. On Automatic Control, Vol. AC-34, No.34, pp.444-446, 1989.

[6].Hu.Xiheng, "F.F.-Pade Method of model reduction in frequency domain", IEEE Trans. On Automatic Control, Vol. AC-32, No.3, pp.243-246, 1987.

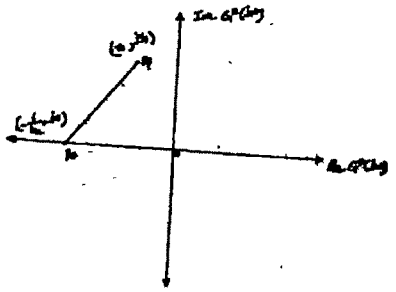

Fig 2.:- Root Locus of Compensator

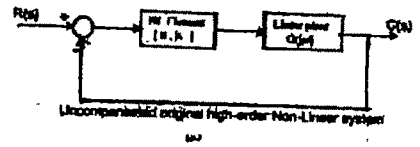

Uncompensated original high-order Non-Linear system

(a)

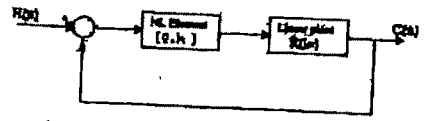

Unacompensated reduced low-order Non-Linear system

(b)

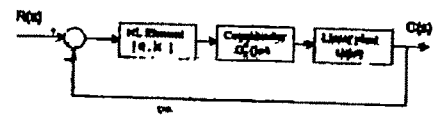

Compensated original high-order Non-Linear system using compensator designed for the reduced low order model

(c)

FIG-3L

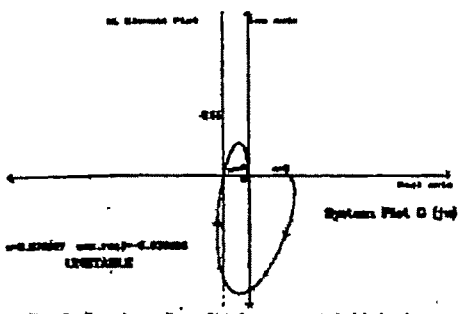

Fig. 3 Example Popov Plot of uncompensated original system

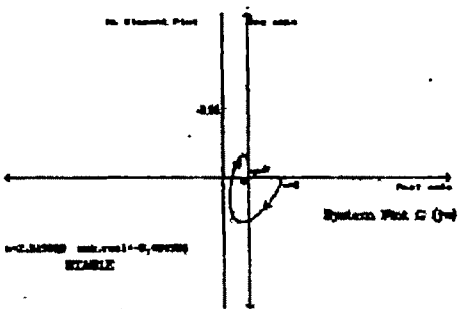

Fig. 4 Example Popov Plot of compensated original system (without overshoot)

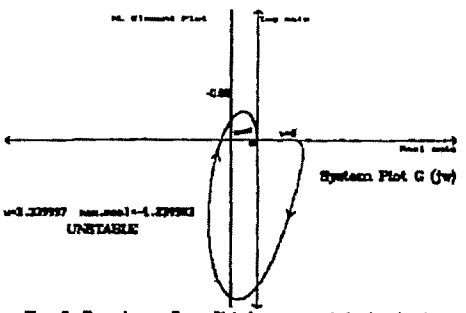

Fig. 6 Example . Popov Plot of uncompensated reduced system

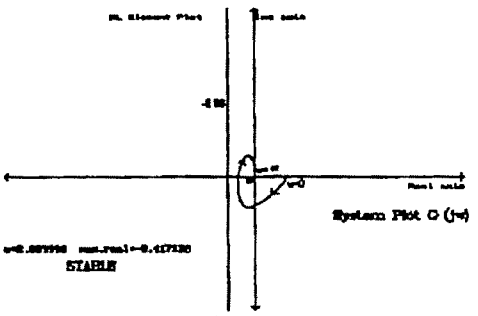

Fig. 8 Example Popov Plot of compensated reduced system

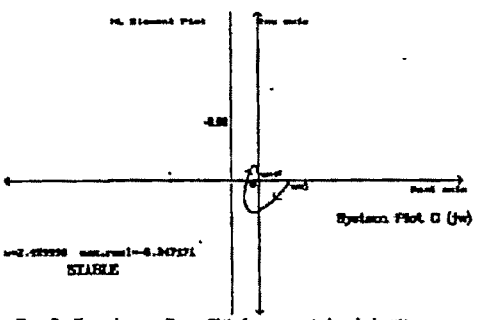

Fig. 7 Example . / Popov Plot of compensated cycled system (with modelling)

A Simplified Method for Large Scale Discrete Systems Modelling using Bilinear Transformation and CFE

G. V. K. R. Sastry* and **G. Raja Rao****
*Department of Electrical Engineering, College of Engineering, Andhra University, Visakhapatnam, Andhra Pradesh – 530 003,India.
**Department of Electrical & Electronics Engg., S.R.K.R.Engg. College, Bhimavaram, Andhra Pradesh – 534 204
E-mail: raja_guntu@yahoo.com

Abstract

The authors present a new method for modelling of large-scale discrete systems using bilinear transformation and Continued-Fraction Expansion (CFE) technique. The proposed method is an extension of continuous time CFE technique. The CFE is applied at $\omega = 0$ and $\omega = a$ in ω - domain. The proposed method always generates unique stable low order models for stable original discrete systems. The method is computationally simple and direct as it overcomes the major limitations or drawbacks of existing methods like necessity of reciprocal transformation and need to evaluate the time moments of the original system in advance. Typical numerical examples illustrating the proposed method are provided.

Key words: Control Systems, Discrete Systems, Bilinear Transformation, Modelling.

INTRODUCTION

Owing to the ever-present demand for modelling of large-scale control systems of complex dynamic processes, it is more often becomes necessary to use reduced order models at some stage of the analysis and design. In recent years, many efforts are being made in the field of large-scale systems modelling.

Several mixed methods have been proposed for modelling of large-scale systems during the last two decades. Some of the discrete system reduction methods [1] have a serious deficiency in that the model produced may be unstable, even though the original discrete system is stable. Few of the continuous time modelling methods have been extended to discrete systems based on stability equation method [2] and modal methods.

In this paper, a new, simple and direct method is proposed for the reduction of large-scale discrete systems based on continuous time CFE about two points i.e., $\omega = 0$ and $\omega = a$. The method is computationally efficient as it gives a straightforward procedure for the selection of value of general point 'a' and avoids necessity of reciprocal transformation, unlike other existing methods [3]. The method is computer oriented and always generates unique stable low order models for stable original high order discrete systems.

PROPOSED REDUCTION PROCEDURE

Consider an n^{th} order discrete time single-input single-output (SISO) system given as,

$$G_n(z) = \frac{N_m(z)}{D_n(z)}$$

$$= \frac{A_{2,m+1}z^m + A_{2,m}z^{m-1} + ... + A_{2,2}z + A_{2,1}}{A_{1,n+1}z^n + A_{1,n}z^{n-1} + ... + A_{1,2}z + A_{1,1}} \qquad (1)$$

with, $m < n$.

where, m is the order of the numerator polynomial and n is the order of the denominator polynomial.

For this original system, the proposed reduced order model of order 'r' ($r \leq n$) is defined as,

$$R_r(z)=\frac{N_r(z)}{D_r(z)}=\frac{B_{2,r}z^{r-1}+.....+B_{2,2}z+B_{2,1}}{B_{1,r+1}z^{r}+.....+B_{1,2}z+B_{1,1}} \tag{2}$$

The following procedural steps are used to obtain the above model:

Step 1: Convert $G(z)$ into $G(\omega)$ by using bilinear transformation as given :

$$\left.\begin{aligned} N_m(z)\Big|_{z=(1+\omega)/(1-\omega)} &= N_m(\omega)/(1-\omega)^m=0 \\ D_n(z)\Big|_{z=(1+\omega)/(1-\omega)} &= D_n(\omega)/(1-\omega)^n=0 \end{aligned}\right] \tag{3}$$

This yields, $G_n(\omega)=\dfrac{N_m(\omega)}{D_n(\omega)}$

$$=\sum_{j=1}^{m+1}a_{2,j}.\omega^{j-1}\Big/\sum_{j=1}^{n+1}a_{1,j}.\omega^{j-1}$$

$$=\frac{a_{2,m+1}.\omega^{m}+a_{2,m}.\omega^{m-1}+.....+a_{2,1}}{a_{1,n+1}.\omega^{n}+a_{1,n}.\omega^{n-1}+.....+a_{1,1}} \tag{4}$$

The reduced order model in ω-domain for this is then defined as,

$$R_r(\omega)=\frac{N_r(\omega)}{D_r(\omega)}$$

$$=\sum_{j=1}^{r}b_{2,j}.\omega^{j-1}\Big/\sum_{j=1}^{r+1}b_{1,j}.\omega^{j-1} \tag{5}$$

Step 2: The r[th] order model in ω-domain which retains the first 't' terms about $\omega = 0$ and $(2r - t)$ terms about $\omega = a$ is obtained using the arrays given by Lucas [4] with the value of 'a' selected by the proposed new algorithms as given below:

$$a=\frac{\sum_{i=1}^{r1}|p_i|+\sum_{j=1}^{r2}|p_{(n-j+1)}|}{r(n-m)^t};\quad r=(r_1+r_2) \tag{6}$$

where, r_1 = integer part of $r/2$; r_2 = integer part of $(r+1)/2$

$$\left.\begin{aligned} &\text{If,} && (n-r)\le r \quad \& \quad (n-m)=1 \\ &\text{then,} && t=(r-1); \\ &\text{otherwise,} && t=r. \end{aligned}\right\} \tag{7}$$

$|p_i|\ (i=1,2,.....,n)$ are the magnitudes of the real parts of the factors of the denominator polynomial of the original system in ω-domain with

$|p_1|<|p_2|<|p_3|<.....<|p_n|$.

Step 3: Convert $R_r(\omega)$ into $R'_r(z)$ by using the reverse bilinear transformation as given below:

$$\left.\begin{aligned} N_r(\omega)\Big|_{\omega=(z-1)/(z+1)} &= N'_r(z)/(z+1)^{r-1}=0 \\ D_r(\omega)\Big|_{\omega=(z-1)/(z+1)} &= D'_r(z)/(z+1)^{r}=0 \end{aligned}\right] \tag{8}$$

where, $R'_r(z)=\dfrac{N'_r(z)}{D'_r(z)}$

$$=\frac{B'_{2,r}z^{r-1}+.....+B'_{2,2}z+B'_{2,1}}{B'_{1,r+1}z^{r}+.....+B'_{1,2}z+B'_{1,1}} \tag{9}$$

Step 4: To remove the steady state error, if any, between the original system and the above model outputs (for Unit step input) multiply $R'_r(z)$ with the gain correction factor, K_g, as given below,

$$R_r(z)=K_g.R'_r(z)$$

$$\text{with,}\qquad K_g=G_n(z)/R'_r(z)\Big|_{z=1} \tag{10}$$

NUMERICAL EXAMPLES

To demonstrate the computational simplicity, accuracy and usefulness of the proposed method, the following typical numerical examples are considered.

Example 1:Consider an 8[th] order discrete system given by [5],

$$G_8(z)=\frac{N_7(z)}{D_8(z)}$$

$$=\frac{1.682z^7+1.116z^6-0.21z^5+0.152z^4-}{8z^8-5.046z^7-3.348z^6+0.63z^5-0.456z^4+}$$

$$\frac{0.516\,z^3-0.262\,z^2+0.044\,z-0.006}{1.548\,z^3+0.786\,z^2-0.132\,z+0.018}$$

Using bilinear transformation and the proposed new algorithms, given in equations (6 & 7), for a 3rd order model in ω-domain,

$$t = 3 \quad \text{and} \quad a = 2.415$$

Then the model in ω-domain is obtained as:

$$R_3(\omega) = \frac{N_3(\omega)}{D_3(\omega)}$$

$$= \frac{-0.06655\,\omega^2 + 1.4599596\,\omega + 0.2664473}{\omega^3 + 13.258131\,\omega^2 + 1.1935123\,\omega + 0.2664473}$$

Using reverse bilinear transformation as given in equation (8 & 9), the reduced order discrete model is obtained as:

$$R_3'(z) = \frac{N_3'(z)}{D_3'(z)}$$

$$= \frac{0.1056017z^2 + 0.0423712z - 0.0801663}{z^3 - 0.9075706z^2 - 0.6777096z + 0.7208933}$$

The final 3rd order reduced discrete model, after removing the steady state error, as given in equation (10), is obtained as:

$$R_3(z) = \frac{0.2112034\,z^2 + 0.0847424\,z - 0.1603328}{z^3 - 0.9075706\,z^2 - 0.6777096\,z + 0.7208933}$$

The step response of original discrete system $G_8(z)$ and the proposed 3rd order model $R_3(z)$ are compared in Fig. (1).

Example 2: Consider an 8th order discrete system given by [6],

$$G_8(z) = \frac{N_7(z)}{D_8(z)}$$

$$= \frac{280.333z^7 + 186z^6 - 35z^5 + 25.33z^4 -}{666.66z^8 - 280.33z^7 - 186z^6 + 35z^5 -}$$
$$\frac{86z^3 - 43.66z^2 + 7.333z - 1}{25.33z^4 + 86z^3 + 43.66z^2 - 7.333z + 1}$$

Using bilinear transformation as given in equation (3), the original system in ω-domain is:

$$G_8(\omega) = \frac{N_7(\omega)}{D_8(\omega)}$$

$$= \frac{-1.5E-06\,\omega^7 + 1.22\,\omega^6 + 6.964\,\omega^5 +}{\omega^8 + 9.22\,\omega^7 + 33.744\,\omega^6 + 62.568\,\omega^5 +}$$
$$\frac{13.532\,\omega^4 + 15.544\,\omega^3 + 11.564\,\omega^2 + 4.5\,\omega + 0.5}{72.012\,\omega^4 + 52.02\,\omega^3 + 20.936\,\omega^2 + 4\,\omega + 0.5}$$

Using the proposed new algorithms, given in equations (6 & 7), for a 3rd order model,

$$t = 3 \quad \text{and} \quad a = 2.165$$

Then the model in ω-domain is obtained as:

$$R_3(\omega) = \frac{N_3(\omega)}{D_3(\omega)}$$

$$= \frac{-0.1882046\,\omega^2 + 3.3838138\,\omega + 0.6237682}{\omega^3 + 13.733834\,\omega^2 + 2.760045\,\omega + 0.6237682}$$

Using reverse bilinear transformation, the reduced order discrete model is obtained as:

$$R_3'(z) = \frac{N_3'(z)}{D_3'(z)}$$

$$= \frac{0.21081\,z^2 + 0.08963\,z - .162728}{z^3 - 0.66799\,z^2 - 0.64151\,z + 0.58493}$$

The final 3rd order reduced discrete model, after removing the steady state error, as given in equation (10), is obtained as:

$$R_3(z) = \frac{N_3(z)}{D_3(z)}$$

$$= \frac{0.42162\,z^2 + 0.179266\,z - 0.325456}{z^3 - 0.66799\,z^2 - 0.64151\,z + 0.58493}$$

The 3rd model obtained by the stability equation method given by Prasad [6] is:

$$P_3(z) = \frac{0.351766z^2 - 0.250187z - 6.68436E-03}{z^3 - 1.99004z^2 + 1.433258z - 0.348324}$$

The step response of original discrete system, the proposed 3rd order model and the model obtained by the stability equation method given by Prasad [6] are compared in Fig. (2).

CONCLUSIONS

A new and simple method for the model reduction of large-scale discrete systems is proposed. The new algorithms for CFE technique of continuous time systems have been extended to discrete systems. The method is computationally superior over many existing methods, in literature, as it avoids the necessity of application of reciprocal transformations and finding the time moments of the original system before hand.

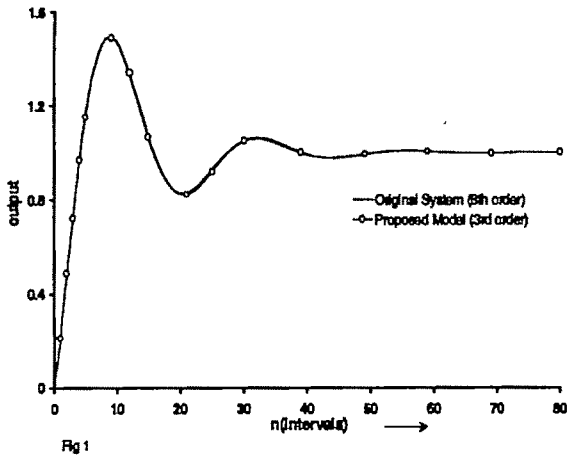

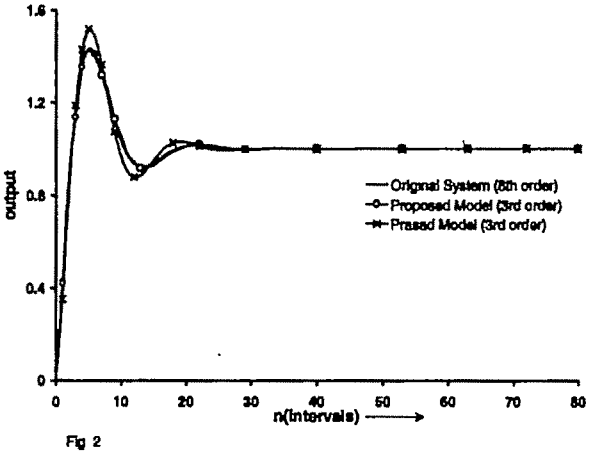

Figs. 1 & 2: Comparison of Step Responses.

REFERENCES

1. K. Warwick, A new approach to reduced order modelling, IEE Proceedings, part D, Control theory & Application, Vol. 131, No. 2, pp. 74 – 78, 1984.
2. R. Prasad, Order reduction of discrete time systems using stability equation method and weighted time moments, Institution of Engineers (India) – Electrical, Vol. 74, pp. 94 – 99, 1993.
3 M. Farsi, K. Warwick and M. Guilandoust, 'Stable reduced order models for discrete time systems', IEE Proceedings, part D, Vol. 133, No. 3, pp. 137 – 141, 1986.
4. T.N. Lucas, 'Efficient algorithm for reduction of continued-fraction expansion about s = 0 and s = a', Electronics Letters, Vol. 19, pp. 991 – 993, 1993.
5. Y. Bistritz, 'A discrete Routh stability method for discrete system modelling', System and control letters, Vol. 2, No. 2, pp. 83 – 87, 1982.
6. R. Prasad, 'Analysis and design of control systems using reduced order models', *Ph.D. Thesis*, 1990, University of Roorkee, India.

Biased Model Reduction for Multivariable Systems using Simplified Polynomial Derivative Technique

G. V. K. R. Sastry* and G. Raja Rao**
*Department of Electrical Engineering, College of Engineering, Andhra University, Visakhapatnam, Andhra Pradesh – 530 003, India
**Department of Electrical & Electronics Engg., S.R.K.R.Engg. College, Bhimavaram, Andhra Pradesh – 534 204, India
E-mail: raja_guntu@yahoo.com

Abstract

The authors present a new method for generating low order models for large-scale multivariable continuous time systems using simplified polynomial derivative technique. The method is computationally simple and overcomes the major limitations or drawbacks of existing methods like necessity of matrix multiplications & inversions, reciprocal transformations, formation of long Routh-type differentiation arrays and calculation of time moments of the original system beforehand. It always generates unique and stable biased models for stable original system. The proposed method retains the initial Markov parameter and (r – 1) time moments of the original system in an r^{th} order model thus improving the time response approximation. Typical numerical example, available in literature, illustrating the proposed method is provided.

Key words: Control Systems, Large-scale systems, Multivariable systems, Model reduction.

INTRODUCTION

It is a well-known fact that it is always useful to reduce the original high order multi-input multi-output (MIMO) systems into low order systems so that much computational effort can be reduced for the analysis and synthesis of these systems.

Recently, Prasad and Pal proposed methods based on stability equation [1] and polynomial derivatives technique [2]. Lucas also proposed methods based on differentiation technique [3],[4]. These methods have major limitations like necessity of reciprocal transformations, matrix multiplications and inversions which make the method more complex and tedious and generate non-unique models [1],[2] and need to form long Routh-type differentiation arrays involving much computational effort [3],[4]. These methods [1]-[4] also have another significant draw back of always retaining only one initial time moment of the original system in the reduced order models which results in poor approximation in time response.

To overcome the limitations of the existing methods [1],[4] based on differentiation technique, new simple and direct algorithms are proposed to generate low order models whose denominator polynomials are same as the methods [2],[3]. The proposed reduced order model retains the stability and the initial Markov parameter and (r – 1) time moments of the original system thus improving the time response approximation.

PROPOSED REDUCTION PROCEDURE

Let the original high order q-input p-output MIMO system be given by its transfer matrix as,

$$G(s)=\left[G_{i,j}(s)\right]=\frac{B_0+B_1s+B_2s^2+.....+B_ms^m}{A_0+A_1s+A_2s^2+.....+A_ns^n} \qquad (1)$$

with i=1,2,...,p; j=1,2,...,q.
where, $m \le n$; B_i (i = 0,1,.....,m) are matrix coefficients of numerator polynomial and A_i (i = 0,1,.....,n) are scalar coefficients of the common denominator polynomial.

For this original system, the proposed reduced order model of order 'r' ($r \le n$) is defined as,

$$\left[R_r(s)\right]=\frac{N_r(s)}{D_r(s)}=\frac{b_0+b_1s+b_2s^2+.....+b_{r-1}s^{r-1}}{a_0+a_1s+a_2s^2+.....+a_rs^r} \qquad (2)$$

The scalar coefficients of the numerator and denominator polynomials of the reduced order model are obtained as given below:

Denominator $D_r(s)$: The reduced order denominator polynomial $D_r(s)$ (for r ≤ n) is obtained by the following newly proposed algorithms:

For r = 1,

$$D_1(s) = \left(\frac{{}^{n-1}C_{n-1}}{{}^{n}C_{n-1}}\right)A_1 s + \left(\frac{{}^{n}C_{n-1}}{{}^{n}C_{n-1}}\right)A_0$$

For r = 2,

$$D_2(s) = \left(\frac{{}^{n-2}C_{n-2}}{{}^{n}C_{n-2}}\right)A_2 s^2 + \left(\frac{{}^{n-1}C_{n-2}}{{}^{n}C_{n-2}}\right)A_1 s + \left(\frac{{}^{n}C_{n-2}}{{}^{n}C_{n-2}}\right)A_0$$

and in general,

$$D_r(s) = \left(\frac{{}^{n-r}C_{n-r}}{{}^{n}C_{n-r}}\right)A_r s^r + \sum_{j=1}^{r}\left(\frac{{}^{n-j+1}C_{n-r}}{{}^{n}C_{n-r}}\right)A_{j-1}s^{j-1} \quad (3)$$

with, ${}^{P}C_{Q} = \frac{P!}{Q!\,(P-Q)!}$ and ${}^{P}C_{P} = 1$

After proper normalization, the reduced order common denominator is obtained as,

$$D_r(s) = \sum_{i=0}^{r} a_i s^i \; ; \qquad \text{with } a_r = 1.$$

Numerator $N_r(s)$: The reduced order numerator polynomials are obtained using the proposed new algorithms as given below,

For r = 1, $N_1(s) = T_0$

and in general, for r = 2, 3, ..., n.

$$N_r(s) = M_0 s^{r-1} + \sum_{i=0}^{(r-2)} T_i s^i \quad (4)$$

with $M_0 = \frac{B_m}{A_n}$ and for i = 0,1,2,.....

$$T_i = \frac{a_0}{A_0}B_i + \frac{B_0}{A_0}\left\{a_i - \frac{a_0}{A_0}\times A_i\right\} + \sum_{j=1}^{i-1}(-1)^j\left\{\frac{A_j \times b_j}{A_0} - \frac{B_j \times a_j}{B_0}\right\} \quad (5)$$

NUMERICAL EXAMPLE

To ascertain the flexibility and effectiveness of the proposed method, the following typical numerical example available in literature is considered.

Consider the 6th order multivariable system given by transfer matrix [2],

$$\mathbf{G}(s) = \frac{\begin{bmatrix}3\\2\end{bmatrix}s^5 + \begin{bmatrix}108\\72\end{bmatrix}s^4 + \begin{bmatrix}1221\\932\end{bmatrix}s^3 + \begin{bmatrix}5792\\5310\end{bmatrix}s^2 + \begin{bmatrix}11860\\12800\end{bmatrix}s + \begin{bmatrix}8400\\9000\end{bmatrix}}{s^6 + 41s^5 + 571s^4 + 3491s^3 + 10060s^2 + 13100s + 6000}$$

Then the 3rd model for the above original system is defined as,

$$\mathbf{R}_3(s) = \frac{\mathbf{N}_3(s)}{D_3(s)} = \frac{\begin{bmatrix}g_1(s)\\g_2(s)\end{bmatrix}}{D_3(s)}$$

Denominator $D_r(s)$: Applying the proposed method the 3rd order reduced model common denominator is obtained as given below,

$$D_3(s) = \left(\frac{{}^{3}C_{3}}{{}^{6}C_{3}}\right)3491\,s^3 + \left(\frac{{}^{4}C_{3}}{{}^{6}C_{3}}\right)10060\,s^2 + \left(\frac{{}^{5}C_{3}}{{}^{6}C_{3}}\right)13100\,s + \left(\frac{{}^{6}C_{3}}{{}^{6}C_{3}}\right)6000$$

$$= 174.55s^3 + 2012s^2 + 6550s + 6000$$

After proper normalization, the reduced order common denominator is,

$$D_3(s) = s^3 + 11.52678s^2 + 37.52506s + 34.37411$$

Numerator $N_r(s)$: The scalar coefficients of the numerator polynomial of the reduced biased model which retain initial Markov parameter and two initial time moments i.e., M = 1 and T = 2, are obtained as,

$$g_1(s) = M_0 s^2 + \sum T_i s^i \; ; (\mathrm{i} = 0,1) \quad \text{with}$$

$$M_0 = \frac{3}{1} = 3\,; \; T_0 = \frac{a_0}{A_0}B_0 + \frac{B_0}{A_0}\left\{a_0 - \frac{a_0}{A_0}\times A_0\right\}$$

$$= \frac{34.3741}{6000}\times 84000 + \frac{8400}{6000}\left\{34.3741 - \frac{34.3741}{6000}\times 6000\right\}$$

$$= 48.1238 \quad \text{and}$$

$$T_1 = \frac{a_0}{A_0}B_1 + \frac{B_0}{A_0}\left\{a_1 - \frac{a_0}{A_0}\times A_1\right\}$$

$$= \frac{34.3741}{6000}\times 11860 + \frac{8400}{6000}\left\{37.5251 - \frac{34.3741}{6000}\times 13100\right\}$$

$$= 15.4111$$

Similarly, $g_2(s) = M_0 s^2 + \sum T_i s^i$; (i = 0,1)
with, $M_0 = 2$; $T_0 = 51.5612$ and $T_1 = 17.0439$
Thus yielding a 3rd order biased model as,

$$R_3(s) = \frac{\begin{bmatrix}3\\2\end{bmatrix}s^2 + \begin{bmatrix}15.4111\\17.0439\end{bmatrix}s + \begin{bmatrix}48.1238\\51.5612\end{bmatrix}}{s^3 + 11.52678s^2 + 37.52506s + 34.37411}$$

with M = 1 and T = 2.

The third order model obtained by the Polynomial Derivatives method suggested by Prasad *et al* [2] is,

$$P_3(s) = \frac{\begin{bmatrix}7.679\\5.743\end{bmatrix}s^2 + \begin{bmatrix}41.159\\37.391\end{bmatrix}s + \begin{bmatrix}48.1238\\51.5612\end{bmatrix}}{s^3 + 11.52678s^2 + 37.52506s + 34.37411}$$ with

M = 0 and T = 1.

The third order model obtained by the Differentiation method given by Lucas [3] is,

$$L_3(s) = \frac{\begin{bmatrix}3.318\\3.042\end{bmatrix}s^2 + \begin{bmatrix}27.178\\29.333\end{bmatrix}s + \begin{bmatrix}48.1238\\51.5612\end{bmatrix}}{s^3 + 11.52678s^2 + 37.52506s + 34.37411}$$

with M = 0 and T = 1.

It can be observed from figs. 1 & 2 that the model obtained by the proposed method gives better approximation over the other methods.

It can also be observed that the models due to [2], [3] match only the first time moment resulting in poor time response approximation. Further the Integral Square Error (ISE) due to step or impulse response will be much less for the model obtained by the proposed method than that of the models given by methods [2], [3].

CONCLUSIONS

A simple and direct method for the model reduction of large-scale multivariable systems is proposed. The method is based on polynomial derivative technique and is computationally superior over many existing methods in literature as it avoids the necessity of application of reciprocal transformations, formation of long Routh-type differentiation arrays and finding the time moments of the original system before hand.

REFERENCES

1. R. Prasad and J. Pal, Stable reduction of linear systems by continued fractions, Institute of Engineers (India) Journal-Electrical, Vol. 72, pp. 113 – 116, 1991.
2. R. Prasad, J. Pal and A.K. Pant, Multivariable systems approximation using polynomial derivatives, Institute of Engineers (India) Journal-Electrical, Vol. 76, pp. 186 – 188, 1995.
3. T.N. Lucas, Some further observations on the differentiation method of model reduction, IEEE Trans. Autom. Control, Vol. 37, No. 9, pp. 1389 – 1391, 1992.
4. T.N. Lucas, Differentiation reduction method as a multi-point Pade approximant, IEE Electronics Letters, Vol. 24, pp. 60 – 61, 1988.

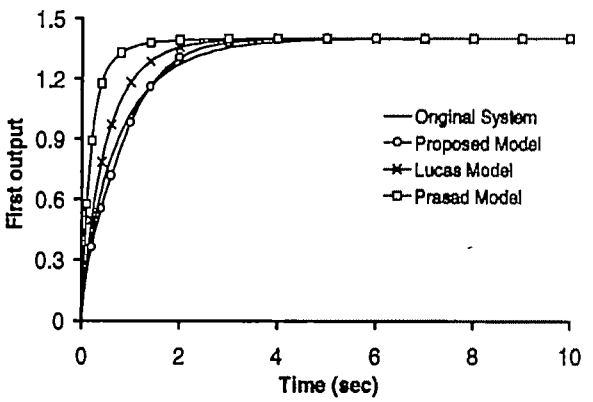

Fig 1 Comparison of step responses

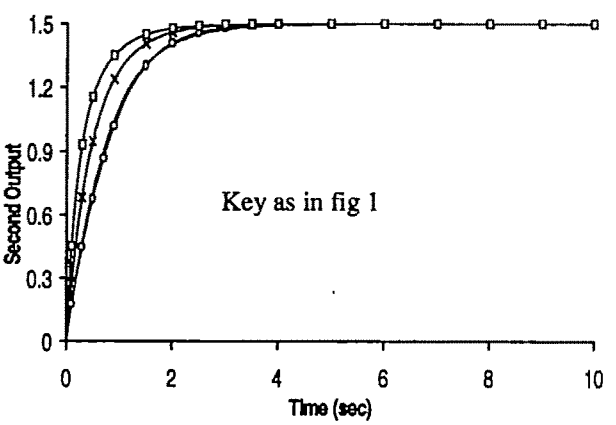

Fig 2 Comparison of step responses

Study Of Unstable Plant With No Poles

S. K. Nagar[1], Abhishek Sharma[2] and Salil Kr Jain[2]
[1]Department of Electrical Engineering
[2]Department of Electronics Engineering
Institute of Technology, banaras Hindu University, Varanasi 221 005, India

***Abstract*— In this paper stability of bounded input/bounded-output (BIBO), single input/single output (SISO) plant has been studied with a novel approach. The adopted approach has been displayed by virtue of an example of a bounded input/bounded-output (BIBO) unstable plant given by convolution with a causal locally integrable impulse response whose transfer function is evarywhere analytic in finite plane.**

***Index Terms*— Poles, stability, transfer function, series solution.**

I. Introduction

It is well known for rational plants, bounded - input / bounded - output (BIBO), presence of poles the transfer function in the right half plane always signals an instability of the plant.

In this paper a study is done on such functions which do not have any singularities at all in the finite plane but they are unstable in nature. The transfer functions F(s) of plants given by convolution with impulse response like these functions as proposed in the paper, results in instability.

As is well known, BIBO stability for plant given by convolution with a causal locally integrable impulse response f(t) is easily characterizable in the time domain; the resulting exactly when

$$\int_0^\infty |f(t)|dt < \infty \qquad (1)$$

a consequence of the closed graph theorm - see the proof in [1, p.163]. But the time - domain characterization of stability for a *general* convolution plant is not so simple - *the stable plants are those given by convolution with the generalized derivative of an ordinary signal of bounded variation* [2]. Unstable plant with an everywhere analytic transfer function illustrate that a frequency domain characterization of stability is impossible on the basis of singularity alone.

Singularity at ∞ shed no light on stability - any nonrational transfer function (stable or not) with no singularities in the finite plane will of course possess an essential singularity at ∞.

There are well known examples of unstable semigroups whose generators have no right - hand plane spectrum [3]. The goal here is to achieve, once and for all an example of a classical single - input/single - output (SISO) unstable plant with no singularities in the finite plane. This example has been extracted from Korner's book [4]. No such example exist for discrete time since a z - transform without finite singularities is zero.

II. The Unstable Plant

Our example plant has the (causal locally interable) impulse response

$$f(t) = \begin{cases} a\sin\left(\frac{t^2}{2}\right) + b\cos\left(\frac{t^2}{2}\right), & \text{if } t \geq 0 \\ 0, & \text{if } t < 0 \end{cases} \qquad (2)$$

It is known that for this class of functions have improper Reimann integral exists [5], yet its Lebesgue integral does not (since f is not absolutely integrable). Thus by (1) convolution with f is not BIBO stable.

In full details, note that

$$\int_0^\infty |f(t)|dt = \int_0^\infty \left|a\sin\left(\frac{t^2}{2}\right) + b\cos\left(\frac{t^2}{2}\right)\right| dt$$

It can be written as

$$\int_0^\infty \left|\sqrt{a^2+b^2}\,\sin\left(\frac{t^2}{2}+\phi\right)\right| dt$$

where $\phi = \tan^{-1}\frac{b}{a}$

$$= \sum_{n=0}^{\infty} \int_{n\pi}^{(n+1)\pi} \frac{\left|\sqrt{a^2+b^2}\,\sin(x+\phi)\right|}{\sqrt{2x}} dx$$

$$\geq \sum_{n=0}^{\infty} \int_{n\pi+\pi/4}^{(n+1)\pi-\pi/4} \frac{dx}{2\sqrt{x}}$$

In full detail, we have

$$\geq \sum_{n=0}^{\infty} \frac{\Pi/4}{\sqrt{(n+1)\Pi - \Pi/4}} = 0$$

and so convolution with $f(t)$ is unstable.

It can also be seen that conditions need to be imposed on a, b i.e. a and b can not be zero simultaneously, as in that case ϕ = undefined.

III. The Analytiicity of the Transfer Function

The causal bounded impulse response (2) has Laplace transform,

Dr. S.K. Nagar is with the Department of Electrical Engineering, Institute of Technology, Banaras Hindu University, Varanasi - 221 005 (Email: sknagar@banaras.ernet.in).

Abhishek Sharma and Salil Kumar Jain are with the Department of Electronics Engineering, Institute of Technology, Banaras Hindu University, Varanasi - 221 005 (Email: abhishek.sharma@angelfire.com, salil_d@yahoo.co.in).

$$F(s)=\int_0^{\infty}\left[a\sin\left(\frac{t^2}{2}\right)+b\cos\left(\frac{t^2}{2}\right)\right]\exp(-st)dt \qquad (3)$$

It can be written as

$F(s) = I_1(s) + I_2(s)$

where $I_1(s)=\int_0^{\infty} a\sin\left(\frac{t^2}{2}\right)\exp(-st)dt$

$$I_2(s)=\int_0^{\infty} b\cos\left(\frac{t^2}{2}\right)\exp(-st)dt$$

It can be seen that because of the dominance of the exponential weighting, converges $F(s)$ (thus $I_1(s)$ & $I_2(s)$) absolutely and uniformly on each right half plane Re $s \geq \varepsilon > 0$ and hence converges to an analytic function on the open right half - plane Re $s > 0$. Thus, we may differentiate $I_1(s)$ & $I_2(s)$ separately and integrate by part to see that

$$I_1'(s)=-a\int_0^{\infty} t\sin\left(\frac{t^2}{2}\right)\exp(-st)dt$$

$$=a\exp(-st)\cos\left(\frac{t^2}{2}\right)\Big|_0^{\infty}+as\int_0^{\infty}\exp(-st)\cos\left(\frac{t^2}{2}\right)dt$$

$$=-a+as\int_0^{\infty}\exp(-st)\cos\left(\frac{t^2}{2}\right)dt \qquad (4)$$

Differentiating again by the product rule and integration by parts

$$I_1''(s)=a\int_0^{\infty}\exp(-st)\cos\left(\frac{t^2}{2}\right)dt-as\int_0^{\infty} t\cos\left(\frac{t^2}{2}\right)\exp(-st)dt$$

$$=a\int_0^{\infty}\exp(-st)\cos\left(\frac{t^2}{2}\right)dt-as\sin\left(\frac{t^2}{2}\right)\exp(-st)\Big|_{t=0}^{\infty} \qquad (5)$$

$$-as^2\int_0^{\infty}\sin\left(\frac{t^2}{2}\right)\exp(-st)dt$$

Combining (4) and (5) and assuming a = 1, we see that $I_1(s)$ satisfies the following second order differential equation

$$sI_1''(s)-I_1'(s)+s^3I_1(s)=1 \qquad (6)$$

everywhere on the open right half - plan Re $s > 0$

Consider the following ordinary differential equation

$$sw'' - w' + s^3w = 1 \qquad (7)$$

now by knowledge of theory of solution of differential equation we can solve the above differential equation by the method of series solution of the following form

$$w=\sum_{n=0}^{\infty} c_n s^n \qquad (8)$$

about $s = 0$, where c_0 and c_2 is freely chosen

where $c_1 = -1$, $c_3 = 0$ and

$$c_{n+4}=-\frac{c_n}{(n+4)(n+2)} \qquad (9)$$

Now considering $I_2(s)$ separately as determined in [6] from there

$$sy'' + y' + s^3y = s^2 \qquad (10)$$

$$y=\sum_{n=0}^{\infty} k_n s^n \qquad (11)$$

about $s = 0$, k_1 = arbitrary, $k_2 = 0$, $k_3 = 1/9$,

$$k_{n+4}=\frac{k_n}{(n+4)^2} \qquad (12)$$

Now combining the two results (8) and (11) we get

$$z=\sum_{n=0}^{\infty}\left(c_n s^n + k_n s^n\right) \qquad (13)$$

By analysing we can find that because of the recursion (9) & (11) there is a factorial growth in the denominators of the coefficients, it is clear that such a series solution (13) has an infinite radius of convergence and converges to an entire (everywhere analytic) function. Since all the other points $s_0 \neq 0$ are ordinary point of both (7) & (10), each solution of (7) & (10) near $s = s_0$ is the sum of a fixed particular solution (8) & (11) plus linear combination of fixed independent homogeneous solutions - all of which can be supplied by the series solution (13) about $s = 0$. Thus our transfer function $z = F(s)$, itself is a solution to (13) on the open right half - plane, has a unique analytic extension to the entire complex plane.

IV. Summary

There exist BIBO - unstable SISO plants whose transfer functions have no singularities in the finite plane.

References

[1] C.R. MacCluer, *Industrial Mathematics*. Upper saddle river NJ: Prentice Hall 2000

[2] "Stability from an operational viewpoint" IEEE *Trans. Automatic Control* vol 33, May 1988

[3] M. Miklavcic, *Applied Functional Analysis and Partial Differential Equations*, Singapore: World Scientific, 1998, p.180

[4] T.W. Korner, *Fourier Analysis*, Cambridge, U.K.: Cambridge University Press, 1988, p.406

[5] C.R. MacCluer, *Boundary value Problems and Orthogonal Expansions*, New York: IEEE Press, 1994, p.280

[6] S.K. Nagar, Abhishek Sharma and Salil Kumar Jain, *Unstable Plant with No Poles*. National Symposium on Systems, Sept. 2001 IIT Madras

Embedded Simulation Of FOPTD And Second Order Systems

J. J. Barve and K. P. Detroja
Instrumentation & Control Engineering Department
D. D. Institute of Technology, Nadiad- 387 001 Gujarat, India

Abstract

We have developed and implemented the embedded software for simulation of the standard mathematical models used in the analysis and design of the control systems. The simulation is carried out using assembly language programming (ALP) of microcontroller 8051. The main feature is software implementation of the floating-point arithmetic in ALP without using math co-processor. The work can be applied for developing embedded model predictive controllers, soft-sensors etc. and can be easily extended to embedded robust controllers.

INTRODUCTION

Recently, the use of advanced control algorithms based on the model of the process (system) has become popular for better performance of the control systems. For example, Internal Model Control (IMC), Model Predictive Control (MPC) --Dynamic Matrix Control (DMC) and Generalized Predictive Control (GPC), Model Reference Adaptive Control (MRAC), Self-tuning PID controllers, etc. [1, 2, 3, 4]. Similarly, in the field of measurement a concept of soft sensor is becoming popular. Soft sensing enables the online measurement of many process variables (mainly the quality variables e.g. MFI and density of a polymer), which are otherwise not measurable on-line. This enables the online feedback control of such important quality variables resulting in better quality control [17]. Such advanced control algorithms and soft-sensors are normally implemented on the personal computers, because their implementation requires simulation of mathematical models of the system. Hence, such controllers are costly and are inconvenient to be used in the field instrumentation. Hence, they are used only at the supervisory control level and for the complex systems.

In our work we have tried to avoid this practical limitation by developing and implementing the embedded simulation program for two most popular forms of the model approximations i.e. first order and second order transfer functions. This is done in the assembly language program of micro-controller 8051, which is available at low cost and is one of the popularly used microprocessor in field instrumentation. Such embedded system can be used in developing the model based embedded controllers for real-time advanced process control of simple and small SISO systems represented by the FOPTD or second order transfer function models. Many simple LTI, SISO systems are represented using these models. Many complex systems having higher order mathematical models are also usually represented using one of these two forms after approximation. These models are simple but still form basis for several advanced control algorithms. For example, Generalized Predictive Controllers (GPC) or Self-tuning PID controllers often use FOPTD model. The first order models can be generally found in the applications like tank level control, temperature control systems, electronic home appliances etc. Whereas, the second order models are generally used in servomechanisms and power electronics [7,8,9,10].

Thus, our work is aimed towards facilitating the implementation of advanced control and measurement techniques on low cost hardware i.e. embedded systems. The main features of our work are -- a) embedded simulation and b) implementation of the simulation using real floating-point arithmetic and nearest rounding on 8-bit micro-controller.

BACKGROUND

Consider the standard first order plus time delay transfer function given in (1).

$$\frac{C(s)}{R(s)} = \frac{Ke^{-Ls}}{Ts+1}; \qquad (1)$$

where, K is the process gain, T is the time constant, L is time delay and C(s) & R(s) are Laplace transforms of the input and output signals of the system.

The conventional derivative terms in the differential equation are replaced using the discrete derivative i.e.

$$\frac{dx}{dt} = \frac{x(k+1) - x(k)}{t_s}$$

where t_s is a sampling time of discretization. The difference equation for the first order transfer function is derived below for illustration.

First order transfer function part of (1) can be converted into differential equation $T\frac{dc}{dt} + c(t) = K\, r(t)$ by simplifying and using inverse Laplace transform, which can then be reduced to the difference equation (2) making use of discrete derivative term.

$$T\,\frac{c(k+1) - c(k)}{t_s} + c(k) = K\, r(k)$$

$$c(k+1) = \frac{Kt_s}{T}\, r(k) + \left(1 - \frac{t_s}{T}\right) c(k) \qquad (2)$$

The difference equation for the first order system is given in equation (2), where t_s represents the sampling time and k the current sample or point of simulation. If we consider t_s as unity, equation (2) can be reduced to the simpler equation (3)

$$c(k+1) = \frac{K}{T}\, r(k) + \left(1 - \frac{1}{T}\right) c(k) \qquad (3)$$

Now, the time delay part of (1) can be included just shifting the terms in (3) by $\frac{L}{t_s}$ and equating the first $\frac{L}{t_s}$ term to zero as given in (4).

$$c(i) = 0; \qquad \text{for } i \le \frac{L}{t_s}$$

$$c(i) = \frac{K}{T}\, r(i-1) + \left(1 - \frac{1}{T}\right) c(i-1); \text{ for } i > \frac{L}{t_s} \qquad (4)$$

The standard second order transfer function is given in (5). Which can be converted into the difference equation (6).

$$\frac{C(s)}{R(s)} = \frac{\omega_n^2}{s^2 + 2\zeta\omega_n s + \omega_n^2} \qquad (5)$$

$$c(k+2) = \omega_n^2\, r(k) + 2\,(1 - \zeta\omega_n)\, c(k+1) - (1 - 2\zeta\omega_n + \omega_n^2)\, c(k) \qquad (6)$$

The difference equation (4) and (6) are implemented by iterations using the ALP of micro-controller 8051. Important feature of our method is development of the *floating-point arithmetic* in ALP without using any floating-point math processor. Due to this the simulation parameters and variables are more accurately represented even in 8-bit microprocessor. We have used the floating-point representation of the real numbers using 13 bits for abscissa (1 sign bit, 4-bit integer and 8-bit fraction) and 9 bits for mantissa (1 sign bit and 8-bit integer). Hence, the range of real numbers covered is -9.99e99 to +9.99e99, whereas the smallest positive number that can be defined (i.e. the machine precision number) is 1.00e-99.

PROPOSED METHOD

First we describe the main components of the considered embedded system on which the developed simulation procedure is to be implemented. The embedded system consists of 8-bit micro controller of family MCS-8051 [11]. The considered micro controller of the family MCS-8051 consists of 4-MB EPROM and 128 bytes of RAM on-chip. The internal EPROM can store the program, whereas the internal RAM is used for storage of temporary data as well as the model and simulation parameters. The micro controller of the considered embedded system is required to be interfaced with an external RAM of required size (maximum 64 KB) interfaced with 8051, in which the result data is to be stored. The size of an external RAM can decide the maximum number of simulation samples that can be stored in the system. The embedded system can also have a facility to transmit/ receive data to/ from remote computer through on-chip facility of serial communication. This can be useful in avoiding the restriction on the maximum number of simulation samples.

Now, we give the procedures for the embedded simulation of the FOPTD and second order systems using the assembly language programming (ALP) of 8051 – the 8-bit micro controller.

PROCEDURE

FOPTD Model

INPUTS:

Model parameters: K, T and L as real number; *Simulation parameters:* Total simulation time T_{sim}, sampling time t_s, starting (base) address – $ADDR_0$ in external RAM from where the result data are to be stored.

OUTPUTS:

Simulation result: List of real numbers representing the simulated output variable at the sampling instant $i \in \{0,1,2,\ldots,N_{sam}\}$, where N_{sam} is an integer number obtained by truncating the number $N_{sam} = T_{sim}/t_s$.

PROCEDURE:
(Initialization)

Step-1: Compute coefficients $\frac{K}{T}$ and $(1-\frac{1}{T})$ given in (4) and store them in appropriate memory locations of internal RAM of micro controller 8051.

Step-2: Store c(-1) and r(-1) as 0. Store input values r(i) as per the test input signal (e.g. for step input r(i) = 1 $\forall$ i $\geq$ 0) in appropriate memory locations of internal RAM of 8051. Initialize i = 0, and result pointer register DPTR as the base address $ADDR_0$.

(Iterative Solution of Difference Equation)

Step-3:

(a) Compute c(i) using equation (4) or (6) appropriately.
(b) Store c(i) appropriately from the locations given by DPTR.
(c) Make i = i +1.
(d) Update pointer DPTR appropriately.

Step-4: If i <= i_{max} GOTO Step-3
Else GOTO Step-5.

(Termination)

Step-5: Terminate.

Second Order Model:

The procedure for simulation of the second order transfer function model is similar to the procedure for the FOPTD model, excepting the model parameters, the difference equation and the difference equation coefficients used are as given in equations (5) and (6).

IMPLEMENTATION

We have implemented the necessary real arithmetic operations in an assembly language of the micro-controller MCS-8051.

The real numbers are represented in the form of 22-bit floating-point number [14] defined as given below. The floating-point number consists of two components -- Abscissa and Mantissa. The abscissa consists of a sign (+ or -), one digit integer number and four digits to represent a fraction. Similarly, mantissa consists of a sign and two digits integer. For example the real numbers -12.334, 0.4567 and 1.2045 can be represented respectively as –1.23e+01, +4.57e-01 and +1.20e+00 in the form of floating point numbers, where –1.23, +4.57 and +1.20 are called abscissa and +01, -01 and +00 are called mantissa components.

While implementing in the embedded system based on MCS-8051, these numbers can be represented using binary numbers as follows:

Abscissa: (13 bits) 1-bit for sign (0 for positive and 1 for negative number), 4-bits to represent an integer as 1-BCD♦ digit, and 8-bits to represent fraction as 2 BCD digits.
Mantissa: (9 bits) 1 bit for sign and 8-bits to represent integer using 2 BCD digits.

Hence, the range of real numbers that can be used is from -9.99e99 to +9.99e+99, whereas the smallest positive number (called the machine precision number) is 1.00e-99. This range and precision are enough for most applications.

The simulation result at each sampling instant consists of the real numbers approximating the actual response. For storing each real number, 5 bytes of the external RAM are used as defined below:

1) 1-byte: 00 or FF according to Abscissa sign-bit 0 or 1
2) 1-byte for storing one BCD digit of Abscissa integer
3) 1-byte for storing two BCD digits of Abscissa fraction
4) 1-byte: 00 or FF according to mantissa sign bit 0 or 1
5) 1-byte for storing two BCD digits of Mantissa integer

For example, -1.23e+01 is stored in five consecutive memory locations as FF, 01, 23, 00, and 01. Similarly the other two numbers (i.e. +4.57e-01 and +1.20e+00) can be stored as 00, 04, 57, FF, 01 and 00,01,20,00,00, respectively. Hence, each real number occupies five memory locations.

As the simulation results are stored in the external RAM and MCS-8051 can address maximum external RAM of about 64KB (i.e. 65,536 bytes), the number of simulation points that can be stored is 13106 -- sufficient for most real time simulation application.

The embedded simulation program is tested on several example transfer functions by computing response to different test signals e.g. step, ramp, pulse etc. Their results are compared with those obtained on the personal computer using MATLAB. The results are found to be in agreement.

NUMERICAL EXAMPLES

We implemented our procedures on the system based on micro-controller 8051 and tested on several example transfer functions by changing the system and simulation parameters. The simulation results are compared with those obtained on the personal computer by using the MATLAB [15]. The results for two examples are given below.

Example-1: Consider the FOPTD system represented by the transfer function –

$$\frac{Y(s)}{X(s)} = \frac{Ke^{-Ls}}{Ts+1}$$, where

System parameters are:
K = 5, T = 10, and L = 6

♦ BCD means Binary Coded Decimal

Simulation Parameters are:

$t_s = 1$, $N_{sim} = 100$

We carried out the simulation runs for three standard test signals: step, pulse and ramp inputs.

First the step response results are discussed. The test results of the simulation runs are obtained – 1) on embedded system using the proposed procedure 2) on personal computer using real mathematics compiler (MATLAB) The results are shown in Fig-1.

The results obtained by the proposed procedure of embedded simulation satisfactorily match with the true response. The small amount of mismatch is due to the use of only 8-bits (i.e. 2 BCD digits) to represent the abscissa fraction. This, along with rounding, restricts the smallest possible jump in the abscissa fraction to 0.01. This error can be reduced, if more bits (e.g. 16-bits instead of 8-bits) are used to represent the abscissa fraction. In fact, we used 16-bit fraction in case of the second order example (example-2) to reduce the effect of such error.

Next, we carried out the simulation runs using the standard the unit ramp and unit pulse (of duration starting from sample-0 to sample-20) as test inputs. For these test inputs, the results obtained by the proposed procedure are compared with those obtained on PC using MATLAB (See Fig-2 to 3 respectively).

Example-2: Consider the standard second order system represented by the transfer function –

$$\frac{C(s)}{R(s)} = \frac{\omega_n^2}{s^2 + 2\zeta\omega_n s + \omega_n^2},$$

where, the system parameters are:

$\omega_n = 0.1$, $\zeta = 0.5$

Simulation Parameters are:

$t_s = 1$, $N_{sim} = 100$

We carried out the simulation runs using the standard step input as a test signal.

In Fig. 4, the results obtained by the proposed procedure and those obtained on PC using MATLAB are compared The results are found to be matching satisfactorily.

CONCLUSION

The simulation results obtained on the embedded system based on micro-controller 8051 satisfactorily match with the results obtained on the personal computer. Thus, the use of proposed procedures enable the embedded systems in providing the low cost solution for simulation of the FOPTD and second order systems. Hence, the proposed simulation procedure can be used in developing the on-line model based embedded controllers. There exists the scope of extending this work towards simulation of the parametric uncertain systems [5,6] making use of the interval arithmetic [12,13]. The authors have already worked in this direction and obtained successful results for uncertain FOPTD models [16].

REFERENCES

1) C. R. Cutler and B. L. Ramaker, *Dynamic Matrix Control – A computer control algorithm*, Houstan Texas, 1979, AIChE
2) C. E. Garcia and M. Morari, *Internal Model Control 1. A unified results and some new results*, Ind. Eng. Chem. Proc. Des. Dev., 21 (1982), pp-308-323
3) D. W. Clarke, C. Mohtadi and P. S. Tuffs, *Generalized Predictive Control*, Automatica, 23 (1987), p 137.
4) K. J. Astrom and B. Wittenmark, *Adaptive Control*, Reading, Massachusetts, Addison-Wesley Publishing Company, 1989.
5) P. Dorato, *Robust Control*, IEEE Press, NY, 1987.
6) S. P. Bhattacharya, H. Chapellat and L. H. Keel, *Robust Control – The parametric approach*, Prentice Hall, NY, USA, 1995.
7) P. Harriot, *Process Control*, Publishers, Englewood Cliff, NY, USA, 1994
8) W. L. Luyben, *Process Modelling, Simulation and Control for chemical Engineers*, McGraw Hill, NY, 1990.
9) I. J. Nagarath and M. Gopal, *Control System Engineering – 2nd Edition*, Wiley Eastern, 1995.
10) K. Ogata, *Modern Control Engineering*, PHI Publishers, Englewood Cliff, NY, USA, 1970
11) K. J. Ayala, *The 8051 Micro controller- Architecture, Programming and Applications – 2nd Edition*, Penram International Publishing (India), 1996.
12) R. E. Moore, *Interval Analysis*, Prentice Hall, Englewood Cliffs, New Jersey, USA, 1966.
13) R.E. Moore, *Methods and Applications of interval analysis*, SIAM, Philadelphia, 1979.
14) M. Morris Mano, *Digital Logic and Computer Design*, Prentice Hall India, New Delhi, 1987.
15) *MATLAB user guide version 5.3*, The Mathworks Inc., MA, USA, 2000.
16) J. J. Barve and K. P. Detroja, *Embedded Simulation of Uncertain FOPTD system*, Accepted for publication in international conference -- ICQRC-2001 -- to be held at IIT, Bombay, India during December 26-28, 2001.
17) J. J. Barve *"Modelling, Simulation and Control of Polymerization reactor"*, MTech Dissertation, Systems & Control Engineering, IIT Bombay, India, 1998.

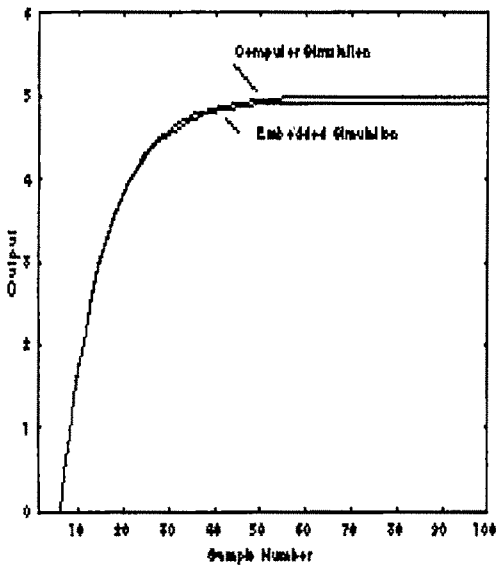

Fig 1 Comparison of embedded and computer simulation for the step response of FOPTD system

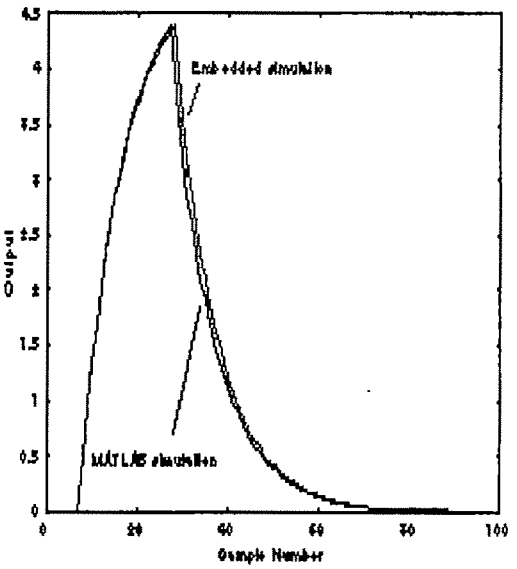

Figure 2: Comparison of Embedded and Computer simulation for the pulse response of FOPTD system

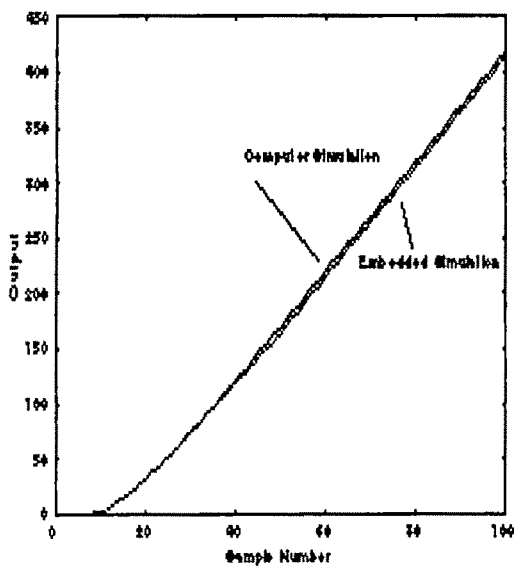

Figure 1: Comparison of Embedded and Computer simulation for the ramp response of FOPTD system

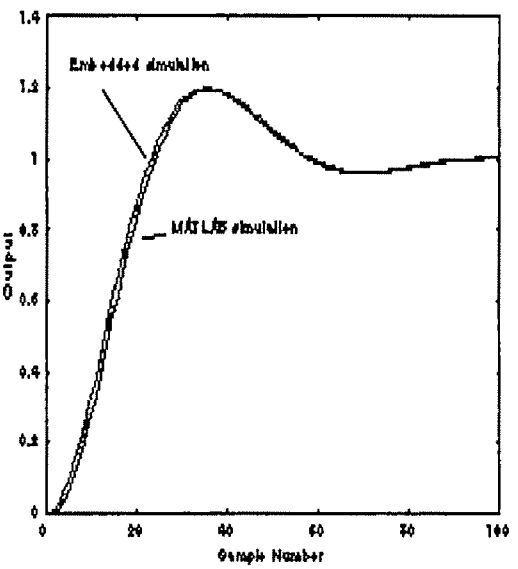

Figure 3: Comparison of Embedded and Computer simulation for the step response of the standard second order system

Control and Synchronization of Chaotic systems

Biswapriya Mukhopadhyay, Prodyot Kumar Roy, Syamal Kumar Dana, *Member, IEEE*

Abstract- **An overview of control and synchronization of chaotic systems is given here. The major techniques of controlling chaos and synchronization has been elaborated with examples. The seminal work on control of chaos, namely, OGY method is described. Synchronization of identical chaotic circuits as driver-response system as proposed by Pecora and Carroll has been described. Phase synchronization phenomena is explained with the results of studies on phase synchronization in Chua circuit made by the authors is reported.**

I. INTRODUCTION

The interest on nonlinear dynamics leading to chaos dates back to 1963, when Lorenz first proposed [1] a 3-D model system to explain the unpredictability of chaos. The trajectory of its time evolution is unpredictable since it is highly sensitive to initial conditions. He observed rich dynamics in his model, which is called a strange attractor in state space. The strange attractor is composed of densely populated unstable periodic orbits but it is bounded to a particular space. The dynamics appears random yet there is an inherent order. In 1990, Ott-Grebogi-Yorke (OGY) first proposed [2] a technique of how to control a chaotic attractor. Controlling chaos means fixing the systems to a particular unstable periodic orbit embedded within the attractor. It opens the flood gate of an enormous amount of research interest from many branches of science as physics, mathematics, chemistry, biology, ecology.

B. Mukhopadhyay is with the Jadavpur Vidyapith, Jadavpur, Kolkata 700032
P.K.Roy is with the Department of Physics, Presidency College, Kolkata 700073 (pkpresi@yahoo.com)
S.K.Dana is with the Instrument Division, Indian Institute of Chemical Biology, Jadavpur, Kolkata 700032 (sdana_ecsu@yahoo.com)

All natural systems are nonlinear. Any nonlinear dynamical system behaves chaotically, in a particular parameter space, but even then maintains a definite pattern and synchrony. Controlling such chaotic behaviour opens up possibilities of challenging technologies like self-correction of cardiac arrhythmia and chaotic digital communication. Synchronization of chaotic systems has been investigated by Pecora and Carroll [3] for the purpose of digital communication. Chaotic oscillators are, unlike periodic oscillators used in conventional communication system, are simple in design and moreover, the security of message is more assured. Chaotic oscillation has a broad spreading in frequency spectrum which is more useful in hiding the message as it appears as noise in the power density distribution within the spread spectrum. Complete synchronization, in the form amplitude and phase in chaotic systems is still a challenge. In this context, phase synchronization of chaotic oscillators has been investigated recently.

In this paper, a brief introduction of chaos is given in the next section. Techniques of controlling chaos are described in section III. Synchronization of chaotic system is discussed in section IV. Phase synchronization in chaotic system is elaborated in section V with results of studies made by the authors phase synchronization in forced Chua circuit. The authors tried to discuss only the major works that generates tremendous interest in chaos and its possible applications.

II. CHAOTIC DYANMICS

Chaotic dynamics is briefly introduced here taking the example of Lorenz system. Any dynamical system is governed by a system of differential equations. Lorenz system is described by a system of three nonlinear differential equations given in eq.(1), where x,y,z

are the state variables and r, b and σ are the system parameters.

$$\frac{dx}{dt} = \sigma(y - x) \qquad (1a)$$

$$\frac{dy}{dt} = rx - y - xz \qquad (1b)$$

$$\frac{dz}{dt} = -bz - xy \qquad (1c)$$

This system of equations has three equilibrium points at (0, 0, 0), (6√2, 6√2, 27) and (-6√2, -6√2, 27) for r=28, σ=10 and b=8/3. The eigen values for the three equilibrium points are given as (-22.8, 11.8, -2.6), (-13.85, 0.094+10.195i, 0.094-10.195i) and (-13.85, 0.094+10.195i, 0.094-10.195i) respectively. The equilibrium point (0,0,0) is a saddle with one positive and two negative real eigenvalues while other two symmetric equilibrium points has one negative real and two complex pair of eigenvalues with positive real part. The eigenvalues near the equilibrium points indicate the stability of the system. The trajectory is decided by their corresponding eigenvectors. The time evolution of x is shown in Fig.1a, while the phase portrait of x and z is shown in Fig.1b which is called the Lorenz attractor.

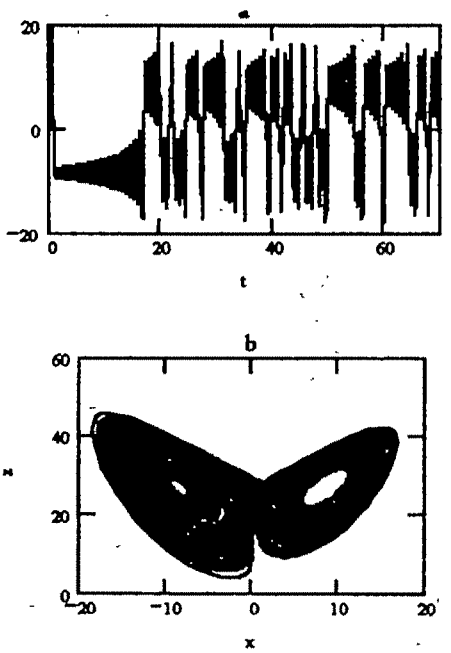

Fig.1 Chaotic dynamics in Lorenz system (a) time domain plot of x (b) phase portrait of x and z [r=28, σ=10 and b=8/3].

The time evolution shows aperiodic or chaotic behavior. It appears as random but the phase portrait is still bounded to a particular region. The phase portrait is the 2-D projection of the 3-D structure. It shows a definite order in this randomness. The system is sensitive to initial conditions as may be observed in Fig.2.

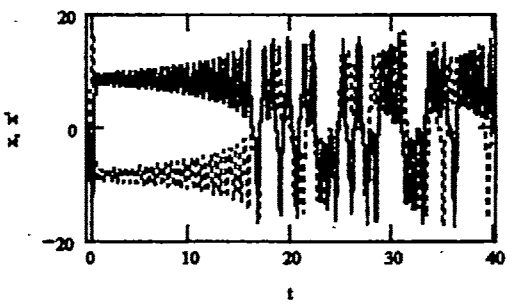

Fig.2 Chaotic trajectories of Lorenz system with different initial conditions: solid line for x with initial condition (0.1, 0.1,0.1) and dotted curve for x' (-0.1, -0.1, 0.2).

The two trajectories finally reach to two different points, far apart from each other. Even for a very small distance between two initial points they evolves into large distance apart. The Lyapunov exponent gives a measure of sensitive dependence upon the initial conditions. The

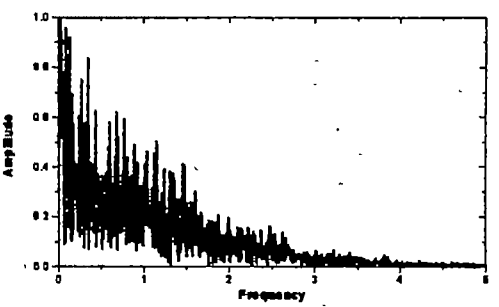

Fig.3 Fourier spectrum of Lorenz system Parameters: [r=28, σ=10 and b=8/3]

Lyapunov exponent gives a measure of the average rate of divergence from a small difference in initial conditions. If it is positive, two trajectories starting from two slightly different initial conditions will diverge exponentially, the motion is then chaotic. The negative values of this exponent indicate stable motion, when two trajectories will ultimately converge. Another signature of chaos is the

broad spreading in frequency spectrum. The Fourier spectrum of chaotic Lorenz system in Fig.3 shows a broad spreading in frequencies.

III. CONTROL OF CHAOS

An infinitely large number of unstable periodic orbits (UPO) are embedded within a chaotic attractor. The trajectory of the system moves through different UPO, but never terminates to a particular orbit. The techniques of controlling chaos attempts to set the trajectory of a chaotic system to any of the UPO embedded within the attractor. Once set, the trajectory remains on that UPO, never goes out of that orbit. It must be robust to external noise. The first method of control of chaos was proposed by Ott-Grebogi-Yorke, which is better known as OGY method [2]. They used standard methods of control theory, and achieved control over any selected UPO. The fundamental idea is to apply a perturbation to one of the system parameter whenever the trajectory nearly completes a periodic orbit and before it goes far away from it. The trajectory is continuously monitored and the perturbation feedback to system parameter is applied in such a way that the final trajectory is pushed towards the stable manifold and the trajectory completes a periodic orbit exactly when it moves along the stable manifold. This is very tedious process but still successfully experimented in different systems, physical [4], biological [5], chemical [6]. Pyragas proposed a different method [7] of controlling chaos using time delay feedback but the authors restrict this paper to describe the OGY method only.

A. Ott-Grebogi-Yorke method

This method is based on small perturbation in a single parameter, as mentioned earlier which necessitates one of the system parameters to be accessible for measurements. The dynamics of any system can be described by a n-dimensional map of the form as given by

$$X_{n+1} = F(X_n, p) \qquad (2)$$

This map can be constructed from Poincare surface of section of system trajectories. p is the accessible system parameter which can be changed in some small neighborhood from its nominal value p_o. For a specific value of p_o, one can select an arbitrary UPO within the attractor around which the system may be stabilized. One can assume X_0 as a fixed point for parameter p_0 and that the dynamics is linear around the vicinity of this fixed point. This concept can be expressed by

$$X_{n+1} - X_0 = M(X_n - X_0) \qquad (3)$$

The elements of the matrix M can be calculated from the measures of time series of the system. The eigenvalues λ_s, λ_u and eigenvectors e_s, e_u of this matrix can also calculated. The eigenvectors determine the stable and unstable directions of motion in the neighborhood of the fixed point. A small parameter variation $|p_n - p_0|$ in so chosen that, using linear approximation,

$$X_{n+1} = p_n g + [\lambda_u e_u f_u + \lambda_s e_s f_s][X_n - p_n g] \qquad (4)$$

where f_s, f_u are the contravariant eigenvectors ($f_s e_s = f_u e_u = 1$, $f_s e_u = f_u e_s = 0$) and

$$g = \frac{\partial X_0(p)}{\partial p}\Big|_{p+p_0}$$

To control any UPO, X_{n+1} has to be pushed to the stable manifold of X_0 by changing the parameter from p_0 to p_n such that $f_u X_{n+1} = 0$, when

$$p_n = \frac{\lambda_u X_n f_n}{(\lambda_u - 1)\, g\, f_u} \qquad (5)$$

p_n gives an estimate of parameter shift from p_0 so that X_{n+1} falls on the stable manifold of the fixed point. The basic scheme of OGY algorithm is shown in Fig.4

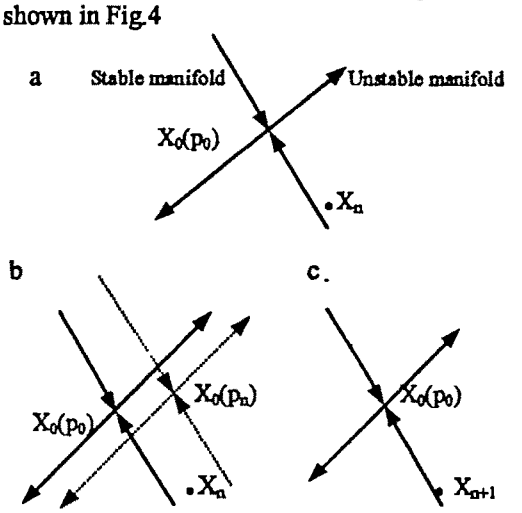

Fig.4 Schematic illustration of OGY scheme
(a) nth iterate X_n falls near the fixed point for p_0
(b) Fixed point moves for change in p_0 to p_n
(c) X_{n+1} iterate falls onto stable manifold of X_0

The fixed point of a chaotic map $X_0(p_0)$ for control parameter p_0 (accessible parameter) is shown in Fig.4a. The nth iteration of the map X_n falls outside both the stable and unstable manifold. For a small change in parameter from p_0 to p_n the fixed point shifts to $X_n(p_n)$ shown in dotted line in Fig.4b while the nth iteration X_n is found between the stable manifolds of nominal parameter p_0 and changed parameter p_n. If the accessible parameter is so changed that the next iteration X_{n+1} falls (Fig.4c) on the stable manifold of the changed parameter p_n, the successive iterations X_{n+2}, X_{n+3} ... moves along the stable manifold. The trajectory remains on the closed UPO for ever. The estimate of the shift in parameter p is given by eqn.(5). OGY method of controlling chaos is mathematically more rigorous. It has been experimented with different systems like laser [4], cardiac chaos [5], chemical [6] and electronic circuits [8]. The critical factor that decides the success of any control technique is its robustness to external noise.

IV. SYNCHRONIZATION OF CHAOS

Synchronization in chaotic systems has been addressed by many researchers [9] to understand the behaviors of natural system that consists of a large ensemble of similar systems. The authors avoided the vast premises of large systems and restricted the discussions here only to the methods of synchronization between two chaotic systems that can act as transmitter and receiver for the purpose of secure communication. For conventional communication systems, the synchronization between two identical systems is no problem since they are assumed periodic. But it is difficult to achieve synchronization when the systems are chaotic even if they are assumed identical. Pecora and Carroll [3] first proposed a technique where a chaotic system is split into two systems called as driver-response systems. One of the measurable state variables of the driver is fed to the response system and they observed perfect synchronization in both phase and amplitude. Perfect synchronization is difficult to achieve since no two systems are identical in nature. For non-identical chaotic systems, a more generalized framework of synchronization has been proposed [10-11]. Recently, several studies revealed that phase synchronization [12-14] is possible between a driven chaotic oscillator and the periodic forcing and, also between two chaotic oscillators even in the absence of any identical synchronization.

A. Pecora and Carroll Method

Synchronization between the transmitter and the receiver is essential for sending an encoded message from the transmitter and its recovery or decoding at the receiver end. For the purpose of communication using chaotic oscillators, different investigators addressed [15-16] the problem of synchronization between two identical chaotic oscillators as transmitter and receiver. The technique of identical synchronization or complete synchronization between two identical chaotic oscillators as proposed by Pecora and Carroll [3] has been described here. Pecora and Carroll used a dynamical system with x_1, y_1 and z_1 state variables as driver system. It may be used as a transmitter. They took another identical system and split its y_2 and z_2 variables into a second part to form the response system, called as receiver. x_1 signal of the transmitter drives the receiver as shown in Fig.5.

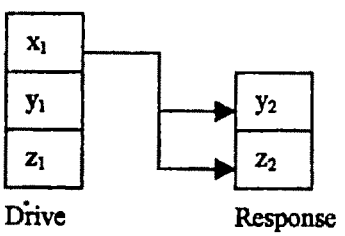

Fig.5 Drive-response synchronization scheme

A 5-dimensional driver-response system is thus built up, using Lorenz model, as given by,

$$\frac{dx_1}{dt} = \sigma(y_1 - x_1) \tag{6a}$$

$$\frac{dy_1}{dt} = rx_1 - y_1 - x_1 z_1 \tag{6b}$$

$$\frac{dz_1}{dt} = -bz_1 - x_1 y_1 \tag{6c}$$

and

$$\frac{dy_2}{dt} = rx_1 - y_2 - x_1 z_2 \tag{6d}$$

$$\frac{dz_2}{dt} = -bz_2 - x_1 y_2 \tag{6e}$$

where x_1 replaces x_2 in eqn.(6d-e)

The condition for synchronization is that the response system must be stable, which is characterized by its negative conditional Lyapunov exponent. This ensures that the trajectory of response system converges to the trajectory of driver system as $t \to \infty$, when $y_1 = y_2$ and $z_1 = z_2$.

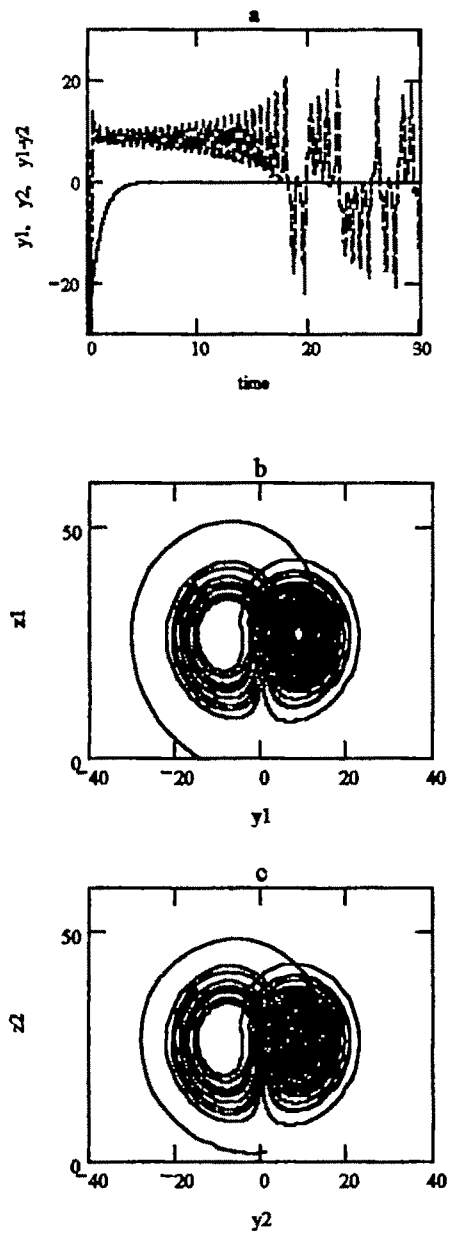

Fig.6 Dynamics of the drive-response system
(a) trajectories of y_1, y_2 and y_1-y_2
(b) phase portrait of driver y_1 and z_1
(c) phase portrait of response y_2 and z_2

The initial conditions for the drive and response systems are assumed here as (-1, -2, -5) and (1, 2) respectively. The trajectories of drive and response, although differ initially, they converge exponentially with time as shown in Fig.6a. Trajectories of y_1 and y_2 plotted in dotted and dashed line respectively converge with time but the initial difference is not so clear. But the difference (y_1-y_2) in solid line clearly indicates the exponential convergence of y_1 and y_2.

The chaotic attractors of drive and response systems in Fig.6b&c respectively show similarity in geometry, although the trajectories start from different initial (y,z) coordinates. The phase plot of z_1 and z_2 in Fig.7 is a straight line ($z_1 = z_2$) with a slope of 45^0, which confirms synchronization between driver and response systems. The initial divergence in the phase plot between z_1 and z_2 is reflected in the deviations from the straight line.
Fig.7 Phase plot of z_1 and z_2 showing identical

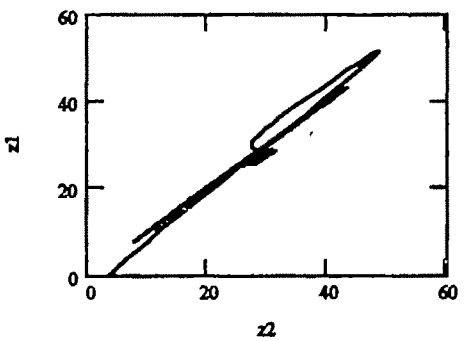

synchronization of drive-response system

In reality, no two physical systems are identical. Afraimovich et al [10] addressed this problem while studied synchronization between two chaotic oscillators. In this situation, two state variables of the driver and response cannot converge with time, but the state of the response system becomes a function of the state of the driver system. Several attempts [10-11] have been made to establish this concept of generalized synchronization.

B. Phase Synchronization

In absence of any identical or generalized synchronization between two chaotic oscillators, a correlation between their phases may have been established. Pikovsky et al [12] first reported this phenomena in driven chaotic circuits as phase synchronization. Phase synchronization is defined as a "particular kind of collective dynamics: chaotic oscillations in all subsystems follow the common pace but other characteristics remain uncorrelated". In this

section, the concept of phase synchronization of chaotic systems has been briefly introduced and finally results of some investigations by the authors on phase synchronization in periodically forced Chua circuit have been described.

The phase $\phi(t)$ of a stable periodic or limit cycle of time period T is described as

$$\frac{d\phi}{dt} = \omega_0 \quad \text{where } \omega_0 = \frac{2\pi}{T}$$

But the phase of a chaotic oscillator is directly not available, it has to be reconstructed from experimental or numerical data. One of the commonly accepted method of quantifying phase of any arbitrary signal s(t) based on analytical signal concept using Hilbert transform. The analytical signal $\zeta(t)$ is a complex function of time defined as

$$\zeta(t) = s(t) + j\hat{s}(t) = A(t)\, e^{j\phi} \qquad (7)$$

where

$$\hat{s}(t) = (1/\pi).PV\int_{-\infty}^{\infty} s(\tau)/(t-\tau)d\tau \qquad (8)$$

$\hat{s}(t)$ is the Hilbert transform of s(t), *PV* means that the integral is taken in the sense of Cauchy principal value. The instantaneous phase $\phi(t)$ and amplitude A(t) of signal s(t) are thus uniquely obtained.

The phase can also be obtained by transforming (x, y, z) coordinates to spherical coordinates (r, θ, ϕ) where ϕ is the phase as given by

$$\begin{aligned} r &= (x^2+y^2+z^2)^{1/2} \\ \theta &= \arccos[z/(x^2+y^2+z^2)^{1/2}] \\ \phi &= \arg(x+jy) \end{aligned} \qquad (9)$$

But the most popularly used technique of measuring phase of chaotic signal is to consider the projection of the chaotic attractor on a plane as smeared circles. A surface of section assumed as Poincaré plane is so chosen that the trajectory of the motion in a particular direction pierce the Poincaré plane just one time for each unstable periodic orbit of the attractor. The phase on each periodic revolution increases by 2π.

The main concern of phase synchronization is to compare the phase of two oscillators. We restrict our system of study sinusoidally forced Chua circuit. A particular Poincaré plane is assigned to the 3-D Chua attractor. A "orbit turn" of an attractor is defined as a segment of orbit between two consecutive return on the prescribed surface. The phase increases by 2π on each orbit turn. At any instant inside the orbit turn, the phase $\phi(t)$ is defined as

$$\phi(t) = 2\pi k + 2\pi\frac{t-t_k}{t_{k+1}-t_k} \qquad (10)$$

where $t_k < t < t_{k+1}$

t_k and t_{k+1} are the kth and (k+1)th piercing on the Poincaré plane. The mean frequency ω of the chaotic motion is defined as the grwoth rate of the phase as

$$\omega = \lim_{N\to\infty}\frac{2\pi N}{t(N)} \qquad (11)$$

where t(N) denotes the amount of time required to complete N orbit turns.

Based on this concept of phase in any chaotic systems, phase synchronization between periodic forcing and driven Lorenz system [13] and also between coupled chaotic oscillators [14] has been investigated recently. It has been observed that perfect phase synchronization in a periodically forced Lorenz system is possible when the return time onto Poincaré plane of all possible orbit turn in an attractor has a narrow band. In case of broad band of return time, imperfect phase synchronization have been observed where occasional phase slips occur with alternation in phase locking ratios.

The authors investigated the phenomena of phase synchronization in sinusoidally driven Chua circuit. The equations governing the driven Chua circuit [17] are given, in dimensionless form, as

$$\frac{dx}{d\tau} = \alpha(y-x) - \alpha f(x) + A\sin(\omega\tau) \qquad (12a)$$

$$\frac{dy}{d\tau} = x - y + z \qquad (12b)$$

$$\frac{dz}{d\tau} = -\beta y \qquad (12c)$$

where

$$f(x) = bx + 1/2(a-b)[\,|x+1| - |x-1|\,]$$

f(x) is piecewise linear approximation of the nonlinear resistance in the circuit, which has a slope a in the inner region and slope b in the outer region as shown in Fig.8.

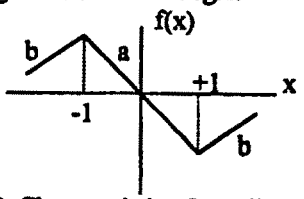

Fig.8 Characteristic of nonlinear resistance

For selected parameters α=10.215, β=16 and a = -8/7, b = -5/7, the dynamics shows a double scroll attractor in Fig.9 without any external forcing (autonomous). When the Chua circuit (no circuit diagram is given, enormous amount of literature is available in ref.[17]) is forced by sinusoidal signal with its frequency chosen as the natural frequency of the circuit, imperfect phase synchronization with phase slips are found. The amplitude of the forcing signal is arbitrarily chosen.

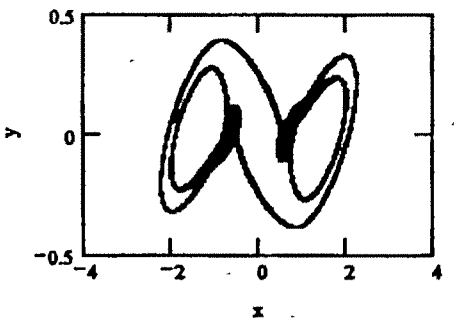

Fig.9 Double scroll attractor of Chua circuit

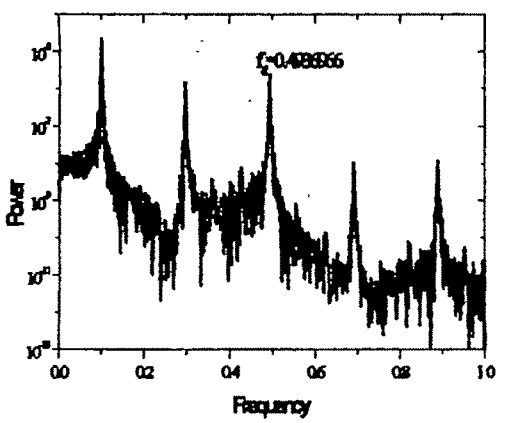

Fig.10 Power spectrum of Chua circuit

The power spectrum of x state variable in Chua circuit (autonomous) in Fig.10 shows spreading of frequency spectrum with several peak but the peak at f=0.4936966 is identified as the natural frequency of the circuit for the selected parameters. When the Chua circuit is driven by the sinusoidal signal of amplitude A=0.35 and $f=f_d$=0.4936966, the chaotic oscillation of the driven circuit shows synchronization of phase with occasional slips as shown in Fig.11a. The difference in instantaneous phases of the both of them is shown in Fig.11a. The time evolution of chaotic oscillation in driven Chua circuit is shown shown in Fig.11b. The phase difference is defined as N(T)-ωT/2π where ω=2πf, f is the driving signal frequency. N(T) is number of penetration on the Poincaré plane by the chaotic oscillation in time T when the phase of sinusoidal signal is ωT. The Poincaré plane is

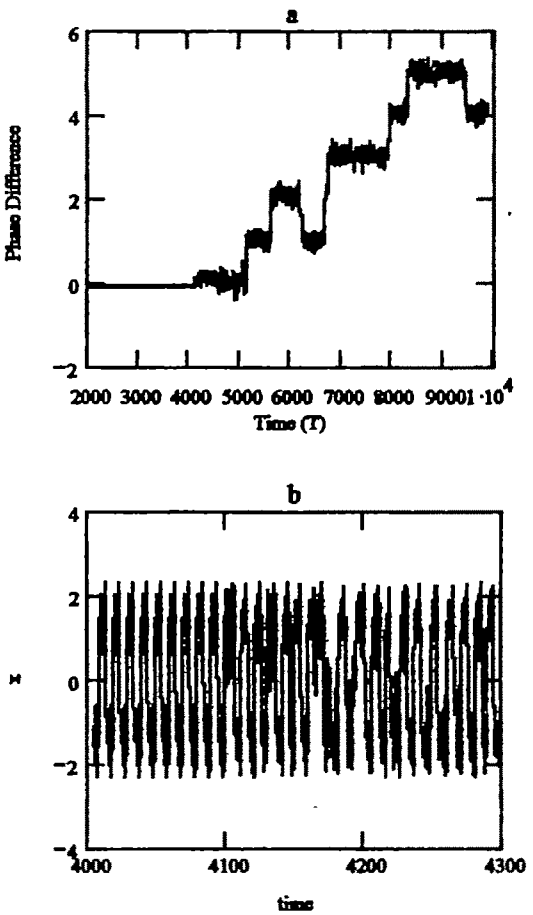

Fig.11 Phase synchronization in Chua circuit
(a) Difference of instantaneous phases of chaotic oscillation and sinusoidal driving signal (b) time evolution of chaotic oscillation

chosen at x+z=0. The system on each orbit turn pierce the Poincaré plane only once when its phase gains by 2π. Hence its phase increases by 2πN(T) at N orbit turns. It may be observed (cf.Fig.11a-b) that the system is periodic, initially, till T≈4000 when the phase difference remain a straight line. The circuit dynamics and the periodic forcing synchronized. Near T≈4100, the system becomes chaotic when the phase difference follows a straight line but fluctuates. Again it jumps occasionally by unit step (2π) in subsequent times. The phase difference is not a

straight line now but appeared as noisy. It is due to error in definition of phase of chaotic signal. Along the horizontal regions of phase difference the chaotic signal and sinusoidal signal are locked in particular locking ratio. At each 2π jump (unit step), the phase of the chaotic signal leads the sinusoidal signal by unit cycle and then maintains a different phase-locking ratio. Thus the chaotic signal switches to different phase locking ratios. This situation is called as imperfect phase synchronization between the chaotic system and driving periodic signal.

V. CONCLUSION

A chaotic dynamical system behavior is briefly introduced here with its possible applications. The major techniques of control and synchronization in chaotic systems are described with examples. Studying chaos and its control is a subject of great interest, in present time, for its application in secure communication and in biological systems. Different other controlling techniques are already available to suit variety of situations and they are experimentally verified in many systems. Synchronization of chaotic systems is most essential for digital communication, which problem is yet to be resolved. It is difficult to go into details of control and synchronization of chaos in this brief paper. The authors tried to explain, in brief, and in simplified language the essence of chaotic dynamical behaviour and their possible applications to encourage others.

REFERENCES

[1] C.Sparrow, An introduction to the Lorenz equations, *IEEE Trans.Cir.Systs.*, Vol.CAS-30, no.8, pp.533-541, 1983

[2] E.Ott, C.Grebogi and J.A.Yorke, Controlling chaos, *Phys.Rev.Lett.*, Vol.64, no.11, pp.1196-1199, 1990

[3] T.L.Carroll, L.M.Pecora, Synchronizing chaotic circuits, *IEEE Trans.Cir.Systs.*, Vol.38, pp.453-456,1991

[4] R.Roy, T.W.Murphy, T.D.Maier, Z.Gills, E.R.Hunt, Dynamical control of a chaotic laser:Experimental stabilization of a globally coupled system, *Phys.Rev.Lett.*, Vol.68, pp.1259-1262, 1992

[5] A.garfinkel, M.L.Spano, W.L.Ditto, J.N.Weiss, Controlling cardiac chaos, *Science*, Vol.257, pp.1230-1235, 1992

[6] V.Petrov, V.Gaspar, J.Masere, K.Showalter, Controlling chaos in Belousov-Zhabotinsky reaction, *Nature*, Vol.361, pp.240-243, 1991

[7] K.Pyragas, Continuous control of chaos by self-controlling feedback, Phys.Lett. A, Vol.107, pp.421-428, 1992

[8] M.J.Ogorzalek, Taming chaos:Part II-Control, *IEEE Trans.Cir.Systs-I*, Vol.40, no.10, pp.700-706, 1983

[9] L.M.Pecora, T.L.Carroll, G.A.Johnson, D.J.Mar, Fundamentals of synchronization in chaotic systems, concepts, and applications, *Chaos*, Vol.7, no.4, pp.520-543, 1997

[10] V. S. Afraimovich, N. N. Verichev, M. I. Rabinovich, Stochastic synchronization of oscillations in dissipative systems, Radiophys.Quantum electron, Vol.29, pp.795-803, 1986

[11] N.F.Rulkov, M.M.Sushchik, L.S.Tsimring, Generalised synchronization of chaos in directionally coupled chaotic systems, Phy.Rev.E, Vol.51, no.2, pp.980-994, 1995

[12] A.Pikovsky, M.Rosenblum, G.Osipov, J.Kurths, Phase synchronization of chaotic oscillators by external driving, *Physica D*, Vol.104, pp.219-238, 1997

[13] E.H.Park, M.A.Zaks, J.Kurths, Phase synchronization in the forced Lorenz system, *Phys. Rev.E*, vol.60, pp.6627-6638, 1999

[14] M.G.Rosenblum, A.S.Pikovsky, J.Kurths, Phase synchronization in driven and coupled chaotic oscillators, *IEEE Trans. Cir. Systs. CAS-I*, vol.44, no.10, pp.874-881, 1997

[15] K. Cuomo, A.V.Oppenheim Circuit implementation of synchronized chaos with application to communications, *Phys.Rev.Lett.*, Vol.71, p.65, 1993

[16] S.Hayes, C.Grebogi, E.Ott, A.Mark, Experimental control of chaos for communication, *Phy.Rev.lett.*, Vol.73, no.13, pp.1781-1784., 1994

[17] M.P.Kennedy, Three steps to chaos-Part II: A Chua's circuit primer, *IEEE Trans. Cir. Systs. CAS-I*, vol.40, no.10, pp.657-674, 1993

A Complementary Pair of Orthogonal Triangular Function Sets and its Application to the Analysis of SISO Control Systems

Anish Deb[1], Gautam Sarkar[1] and Anindita Dasgupta[2]

[1]DEPARTMENT OF APPLIED PHYSICS, UNIVERSITY OF CALCUTTA
92 A P C Road, Kolkata 700 009, India
[2]NORTH CALCUTTA POLYTECHNIC
15 Gobinda Mandal Lane, Cossipore, Kolkata 700 002, India
E.mail of corresponding Author : anishdeb@cucc.ernet.in

Abstract

The present work proposes a complementary pair of orthogonal triangular function (TF) sets derived from the well-known block plse function (BPF) set. The operational matrices for integration in TF domain have been computed and their relation with the well-known BPF domain integral operational matrix is shown. It has been established with illustration that the TF domain technique is more accurate than the BPF domain technique as far as integration is concerned, and it provides with a piecewise linear solution.

As a further st\udy, the newly proposed sets have been applied to the analysis of dynamic systems via convolution. The results prove the fact that it introduces less mean integral squared error (MISE) than the staircase solution obtained using BPF.

Keywords : Orthogonal functions, triangular functions, operational matrices, dynamic systems, convolution

INTRODUCTION

Piecewise constant basis functions (PCBF) have been around in the literature for about nine decades. An organized search for such functions started with the introduction of Haar function in 1910 [1]. The most striking feature of this function set was its piecewise constant nature which was quite different from sine-cosine set of orthogonal functions enjoying immense popularity at that time. Specialty of this new kind of function was noticed by researchers and eventually other functions of similar nature, e. g., Walsh functions, block pulse functions (BPF), slant functions etc. followed [2].

Of all such PCBF's, block pulse functions turned out to be the most fundamental [2] and efficient for analysis as well as synthesis of control systems and various related applications [3-8]. Also, this function set was used to generate its pulse-width modulated (PWM) version which proved to be advantageous for efficient applications [9]. A few interesting variants of BPF were also introduced by Deb et al [10, 11] one of which was the well known delta function set — merely samples of block pulse functions.

These facts represent the overwhelming influence of block pulse and related functions during the past two decades.

In this work, efforts have been made to present a complementary pair of orthogonal triangular function (TF) sets and their subsequent application to the analysis of dynamic systems. Triangular functions evolved from a simple dissection of block pulse functions and they can easily be normalized [12]. Also, when these sets are used in a fashion similar to that of block pulse functions, they yeild a piecewise linear solution of dynamic systems with less mean integral squared error (MISE).

The main objectives of the present work are :

(i) To present a complementary pair of orthogonal triangular function (TF) sets and compare their basic properties with that of BPF set.

(ii) To derive operational matrices of integration, namely **P1** and **P2**.

(iii) To compare the effectiveness of integration in the BPF domain and TF domain.

(iv) To analyse a liner SISO system via triangular functions and compare the resultas with its BPF domain solution.

BRIEF REVIEW OF BLOCK PULSE FUNCIONS (BPF) AND THE RELATED OPERATIONAL MATRICES [2]

A set of block pulse function $\psi_{(m)}(t)$ containing m component funcitons in the semi-open interval [0, T) is given by

$$\psi_{(m)}(t) = [\psi_0(t) \;\; \psi_1(t) \ldots \psi_i(t) \ldots \psi_{m-1}(t)]^T \quad (1)$$

where $[...]^T$ denotes transpose.

The i–th component $\psi_i(t)$ of the BPF vector $\psi_{(m)}(t)$ is defined as

$$\psi_i(t) = \begin{cases} 1 & iT/m < t \le (i+1)T/m \\ 0 & \text{otherwise} \end{cases}$$

where i = 0, 1, 2, ... (m−1).

A square integrable time function f(t) of Lebesgue measure may be expanded into an m-term BPF series in $t \in [0, T)$ as

$$f(t) \simeq [c_0 \; c_1 \; c_2 \ldots c_i \ldots c_{m-1}]\psi_{(m)}(t) = c^T\psi_{(m)}(t) \quad (2)$$

The constant coefficients c_i's in equation (2) are given by

$$c_i = (1/h) \int_{ih}^{(i+1)h} f(t)\,dt \quad (3)$$

where h = T/m is the duration of each component BPF along time scale.

In the m-term BPF domain, an opeartional matrix for integration $P_{(m)}$ has been derived by Chen et al. [13] as the following triangular matrix.

$$P_{(m)} = h \, [\![\tfrac{1}{2} \;\; 1 \ldots \ldots \ldots 1]\!]_{m\times m} \quad (4)$$

where, $[\![a \;\; b \;\; c]\!] = \begin{bmatrix} a & b & c \\ 0 & a & b \\ 0 & 0 & a \end{bmatrix}$.

The matrix $P_{(m)}$ performs as an integrator in the BPF domain and it is pivotal in any BPF domain analysis.

Thus, approximate integration of a function f(t), using equations (2) and (4), is

$$\int f(t)\,dt \simeq C^T.P.\psi_{(m)} \quad (5)$$

where, C, P, $\psi_{(m)}$ all are of order m.

FROM BLOCK PULSE FUNCTIONS TO A NEWLY DEFINED COMPLEMENTARY SET OF TRIANGULAR FUNCTIONS

Though block pulse functions are effective for analysis and synthesis of various control systems, it is not a baseless hunch to think that a staircase solution provided by the BPF domain analysis may introduce relatively more error than an equivalent piecewise linear solution.

In the following, we have dissected a block pulse function (say, the first member $\psi_0(t)$ of an m-set BPF) into two triangular functions as shown in figure 1.

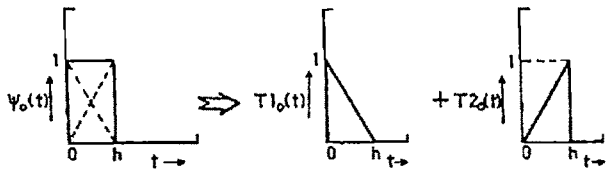

Figure 1 : Dissection of BPF into two triangular functions

Thus, we have

$$\psi_0(t) = T1_0(t) + T2_0(t)$$

For the whole set of BPF, $\psi_{(m)}(t)$, we can thus generate two sets of orthogonal triangular functions (TF), namely $T1_{(m)}(t)$ and $T2_{(m)}(t)$ such that

$$\psi_{(m)}(t) = T1_{(m)}(t) + T2_{(m)}(t)$$

Figures 2(a) and 2(b) show the orthogonal triangular function sets, $T1_{(m)}(t)$ and $T2_{(m)}(t)$, where m has been chosen arbitrarily as 8. It could be said that these two sets are complementary to each other as far as block pulse functions are considered. For convenience, we call $T1_{(m)}(t)$ the left handed triangular function (LHTF) vector and $T2_{(m)}(t)$ the right handed triangular function (RHTF) vector.

Now, following equation (1), we can express the m-set triangular function vectors as

$$T1_{(m)}(t) = [T1_0(t) \; T1_1(t) \; T1_2(t) \ldots T1_i(t) \ldots T1_{m-1}(t)]^T$$

and $T2_{(m)}(t) = [T2_0(t) \; T2_1(t) \; T2_2(t) \ldots T2_i(t) \ldots T2_{m-1}(t)]^T$

where $[\ldots]^T$ denotes transpose.

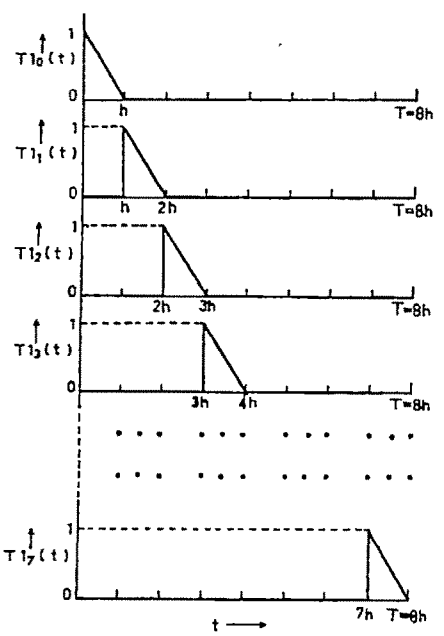

Figure 2 : (a) A set of LHTF $T1_{(m)}(t)$

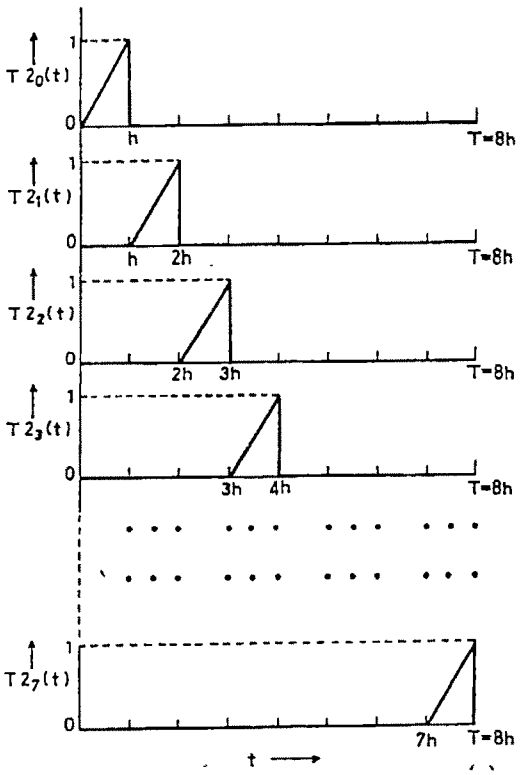

Figure 2 : (b) A set of RHTF $T2_{(m)}(t)$

The i-th component of the LHTF vector $T1_{(m)}(t)$ is defined as

$$T1_i(t) = \begin{cases} 1 - (t - ih)/h, & ih < t < (i+1)h \\ 0 & \text{otherwise} \end{cases} \quad (6)$$

and the i-th component of the RHTF vector $T2_{(m)}(t)$ is defined as

$$T2_i(t) = \begin{cases} (t - ih)/h, & ih < t < (i+1)h \\ 0 & \text{otherwise} \end{cases} \quad (7)$$

where, $i = 0, 1, 2, ..., (m-1)$.

A square integrable time function f(t) of Lebesgue measure may be expanded into an m-term TF series in $t \in [0, T)$ as

$$f(t) \simeq [\, c_0\ c_1\ c_2 \ldots c_i \ldots c_{m-1}\,]\, T1_{(m)}(t) + [\, d_0\ d_1\ d_2 \ldots d_i \ldots d_{m-1}\,]\, T2_{(m)}(t)$$

$$\triangleq C^T.T1_{(m)}(t) + D^T.T2_{(m)}(t) \quad (8)$$

The constant coefficients c_i's and d_i's in (8) are given by

$$c_i = f(ih) \text{ and } d_i = f[(i+1)h] \quad (9)$$

The following relation between c_i's and d_i's are also noted.

$$c_{i+1} = d_i \quad (10)$$

It may be noted that, the coefficients c_i's and d_i's in (9) are *not optimal* in the sense that they do not help in approximating f(t) in a least square manner. This would essentially imply that the mean integral squared error (MISE) is not *minimized*. However, the advantage of choosing c_i's and d_i's as different samples of f(t) for obtaining a piecewise linear solution, instead of conventional integration formula, is obvious. It is apparent from equations (3) and (9) that unlike BPF's, the TF representation does not need any integration to evaluate the coefficients, thereby reducing a lot of computational burden. In a sense, we can call these c_i's and d_i's of (9) to be *non-optimal*.

TABLE 1

Basic properties of BPF's and TF's

Property	BPF	TF
Piecewise constant	Yes	No
Orthogonal	Yes	Yes
Finite	Yes	Yes
Disjoint	Yes	Yes
Orthonormal	Can easily be normalized	Can easily be normalized
Implementation	Easily implementable	Easily implementable
Coefficient determination of f(t)	Involves integration of f(t) and scaling	Needs only samples of f(t)
Accuracy of analysis	Provides staircase solution with more error than TF analysis in most of the cases	Provides piecewise linear solution having less error than BPF analysis in most of the cases

The basic properties of BPF's and TF's are tabulated in Table 1 to provide a qualitative appraisal. In the following, a quantitative assessment is presented to unravel the power of the newly proposed triangular functions.

Approximation of a time function f(t) by BPF and TF

To compare the effectiveness of TF with that of BPF, let us consider the function

$$f(t) = \exp(-2t)$$

For T = 1 s and m = 4, the BPF representation of f(t), using equation (2) and (3) is

$$f(t) \simeq [\ 0.7869387\ \ 0.4773024\ \ 0.2894986\ \ 0.1755898]\psi_{(4)}(t) \quad (11)$$

Similarly, using equation (8) and (9), triangular function

representation of f(t) is given by

$$f(t) \approx [\,1 \quad 0.6065307 \quad 0.3678794 \quad 0.2231302]\mathbf{T1}_{(4)}(t) + [\,0.6065307 \quad 0.3678794 \quad 0.2231302 \quad 0.1353353]\mathbf{T2}_{(4)}(t) \quad (12)$$

It is only apparent that TF representation is superior to BPF representation.

OPERATIONAL MATRICES FOR INTEGRATION IN THE ORTHOGONAL TRIANGULAR FUNCTION DOMAIN

Similar to the BPF domain technique, we now derive the operational matrix for integration in the orthogonal triangular function domain.

We integrate $T1_0$ of figure 2(a) and express the result in terms of an m-set triangular functions using equation (8) and (9). That is, dropping the argument t for simplicity, we have

$$\int_0^t T1_0\, d\tau = \int_0^t (1-\tau/h)\, d\tau = t - \frac{t^2}{2h}$$

$$\approx \frac{h}{2}.T2_0 + \frac{h}{2}\left[(T1_1 + T2_1) + (T1_2 + T2_2) + \ldots + (T1_{(m-1)} + T2_{(m-1)})\right]$$

$$= \frac{h}{2}[0 \;\; 1 \;\; 1 \;\ldots\; 1 \;\; 1]\mathbf{T1}_{(m)} + \frac{h}{2}[1 \;\; 1 \;\; 1 \;\ldots\; 1 \;\; 1]\mathbf{T2}_{(m)} \quad (13)$$

It is obvious that integration of other members of the LHTF set will yield the same result, only the integrated curves will have different delays depending upon the respective delays of different component functions. Figure 3(a) shows integration of the function $T1_0$.

Considering the above mentioned delays and using equation (13), we can write down the relation between the first integration of the LHTF set $\mathbf{T1}_{(m)}$ and the pair of triangular function sets $\mathbf{T1}_{(m)}$ and $\mathbf{T2}_{(m)}$ as

$$\int_0^t T1_{(m)}\, dr = \frac{h}{2}[\![0 \;\; 1 \;\; 1 \;\; 1 \;\ldots\; \ldots \;\; 1 \;\; 1]\!]_{m\times m}\mathbf{T1}_{(m)} + \frac{h}{2}[\![1 \;\; 1 \;\; 1 \;\; 1 \;\ldots\; \ldots \;\; 1 \;\; 1]\!]_{m\times m}\mathbf{T2}_{(m)}$$

$$\approx \mathbf{P1}_{(m)}\,\mathbf{T1}_{(m)} + \mathbf{P2}_{(m)}\,\mathbf{T2}_{(m)} \quad (14)$$

where we call the matrices $\mathbf{P1}_{(m)}$ and $\mathbf{P2}_{(m)}$ the operational matrices for integration in triangular function domain.

It is easy to see that, $\mathbf{P} = \mathbf{P}_1 + \mathbf{P}_2$

Now we integrate $T2_0$ to obtain the curve of figure 3(b).

Since integration is a linear operator, it is obvious that

$$\int_0^t T1_0\, d\tau + \int_0^t T2_0\, d\tau = \int_0^t (T1_0 + T2_0)\, d\tau = \int_0^t \psi_0\, d\tau$$

This is illustrated in figure 3 where the curve of figure 3(c) is obtained by adding the curves of figures 3(a) and 3(b).

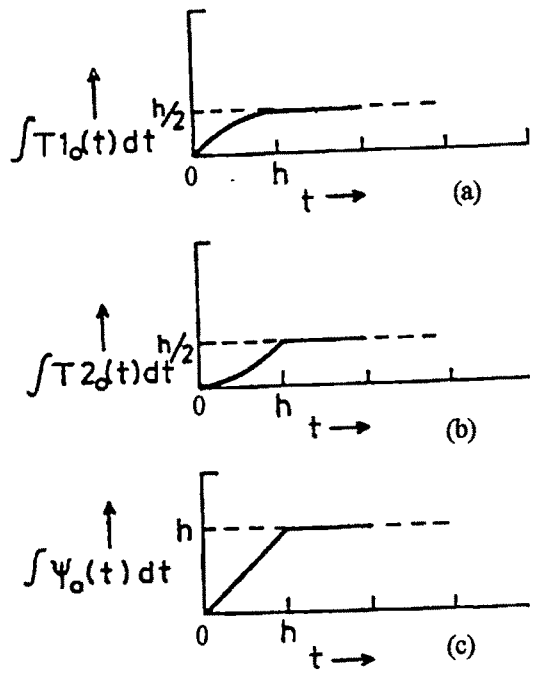

Figure 3 : (a) First integration of the triangular function $T1_0$, (b) First integration of the triangular function $T2_0$ and (c) their relation to the first integration of block pulse function

Proceeding in a similar manner as for **T1**, we find that

$$\int_0^t \mathbf{T2}\, d\tau = \mathbf{P1}_{(m)}\,\mathbf{T1}_{(m)} + \mathbf{P2}_{(m)}\,\mathbf{T2}_{(m)} = \int_0^t \mathbf{T1}\, d\tau \quad (15)$$

Now we attempt to integrate a square integrable function f(t) in $t \in [0, T)$. Considering m component functions and a sampling period of h seconds, we can write, using equations (8) and (9)

$$f(t) \approx [\,f(0) \; f(h) \; f(2h) \ldots f((m-1)h)\,]\mathbf{T1}_{(m)} + [\,f(h) \; f(h) \; f(2h) \; f(3h) \ldots f(mh)\,]\mathbf{T2}_{(m)}$$

$$= \mathbf{C}^T.\mathbf{T1}_{(m)} + \mathbf{D}^T.\mathbf{T2}_{(m)} \quad (16)$$

Hence

$$\int_0^t f(\tau)\, d\tau \approx \mathbf{C}^T \int_0^t \mathbf{T1}_{(m)}\, d\tau + \mathbf{D}^T \int_0^t \mathbf{T2}_{(m)}\, d\tau$$

$$\approx (\mathbf{C} + \mathbf{D})^T\mathbf{P1}.\mathbf{T1}_{(m)} + (\mathbf{C} + \mathbf{D})^T\mathbf{P2}.\mathbf{T2}_{(m)} \quad (17)$$

Knowing **C** and **D**, which are in fact (m+1) number samples of f(t) from 0 to T, we can determine approximate integration of f(t).

Integration of a time function f(t) in BPF domain and TF domain

Let us consider the function f(t) = exp(–2t).

Considering T=1 s and m=4, we have, from equations (2) – (5), the BPF domain representation of

$$\int_0^t f(t)\,dt \simeq [\,0.7869387 \;\; 0.4773024 \;\; 0.2894986 \;\; 0.1755898\,]P_{(4)}.\Psi_{(4)}$$

$$= [\,0.0983673 \;\; 0.2563975 \;\; 0.3522476 \;\; 0.4103837\,]\Psi_{(4)} \quad (18)$$

Considering T=1 s and m=4, TF domain representation of f(t), using equations (8) and (9), is

$$f(t) \simeq [\,1 \;\; 0.6065307 \;\; 0.3678794 \;\; 0.2231302\,]T1_{(4)} + [\,0.6065307 \;\; 0.3678794 \;\; 0.2231302 \;\; 0.1353353\,]\,T2_{(4)}$$

$$= C1^T.T1_{(4)} + D1^T.T2_{(4)}$$

Using equation (17)

$$\int_0^t f(t)\,dt \simeq [\,0 \;\; 0.2008163 \;\; 0.3226176 \;\; 0.3964938\,]T1_{(4)} + [0.2008163\;0.32226176\;0.3964938\;0.4413020]T2_{(4)} \quad (19)$$

Figure 4 shows BPF and TF domain representations of $\int f(t)\,dt$, while Table 2 compares the efficiency of integration in BPF and TF domain and computes percentage error in the TF domain.

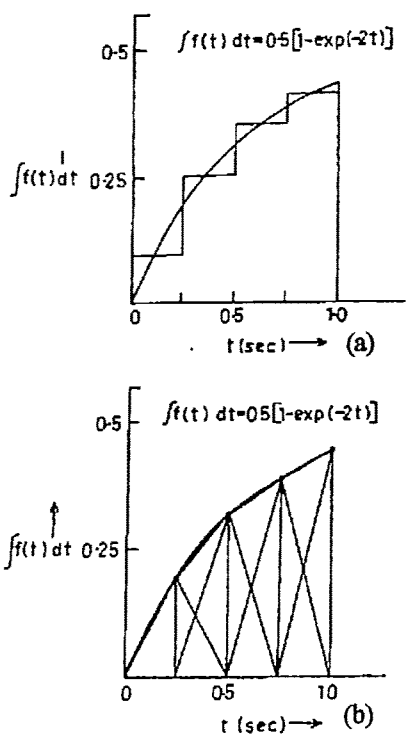

Figure 4 : (a) BPF domain representation of $\int f(t)\,dt$,

(b) TF domain representation of $\int f(t)\,dt$

TABLE 2

Comparison of BPF and TF domain integration for the function f(t) = exp(–2t)

Time t(sec)	Samples of $\int_0^t \exp(-2t)\,dt$	BPF domain solution [Eq. (18)]	TF domain solution [Eq. (19)]	% Error
0	0		0	–
		0.0983673		
0.25	0.1967347		0.2008163	–2.07452
		0.2563975		
0.5	0.3160603		0.3226176	–2.07470
		0.3522476		
0.75	0.3884349		0.3964938	–2.07471
		0.4103837		
1.0	0.4323324		0.4413020	–2.07470

CONVOLUTION PROCESS INVOLVING TRIANGULAR FUNCTIONS FOR CONTROL SYSTEM ANALYSIS

Having established the orthogonal triangular function sets, it is worthwhile to determine the convolution of two real valued functions, say, $f_1(t)$ and $f_2(t)$, in triangular functions domain.

If two functions $f_1(t)$ and $f_2(t)$ are defined and continuous for all t, then their convolution is given by the well-known integral

$$CV12(t) = \int_{-\infty}^{\infty} f_1(\tau)\, f_2(t-\tau)\,d\tau \quad (20)$$

Obviously, it is assumed that the integral given by equation (20) exists.

For convolution of two functions, one function may be considered to be the static function or say, STF (in our case, $f_1(t)$), and the other can be termed as the scanning function or say, SCF (in our case $f_2(t)$).

If $f_1(t)$ and $f_2(t)$ are to be convolved in triangular function domain, the first task is to expand the functions $f_1(t)$ and $f_2(t)$ in terms of triangular functions. Then we need the results of convolution of component triangular functions and use the same to determine the final result, namely CV12(t).

The following algorithm is presented for better clarity :

1. Express $f_1(t)$ in terms of TF.
2. Express $f_2(t)$ in terms of TF.

3. Convolve $T1_p(t)$ and $T1_q(t)$ [(p+1) – th and (q+1) – th members of the LHTF set] each having a different scaling factor, say $c1_p$ and $c2_q$.
4. Express the result in TF domain.
5. Convolve $T2_p(t)$ and $T2_q(t)$ [(p+1) – th and (q+1) – th members of the RHTF set] each having a different scaling factor, say $d1_p$ and $d2_q$.
6. Express the result in TF domain.
7. Convolve $T1_p(t)$ [(p+1) – th member of the LHTF set] and $T2_q(t)$ [(q+1) – th member of the RHTF set] in the same fashion as in step 3.
8. Express the result in TF domain.
9. Convolve $T2_p(t)$ [(p+1) – th member of the RHTF set] and $T1_q(t)$ [(q+1) – th member of the LHTF set] in a manner similar to step 7.
10. Express the result in TF domain.
11. Use the results of steps 4, 6, 8 and 10 to determine the final result CV12 in TF domain.

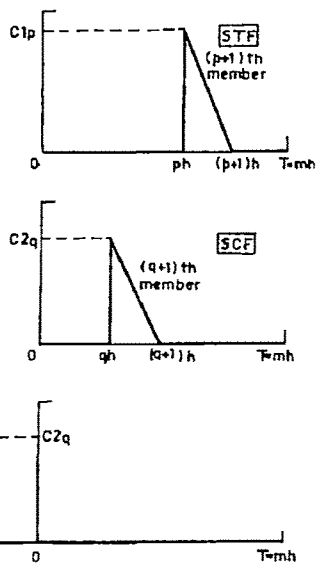

Figure 5 : Convolution of two members of the LHTF, namely $T1_p$ and $T1_q$

Convolution of $T1_p$ and $T1_q$ in TF domain

The convolving functions are shown in figure 5. Since, for generality, the functions have different amplitudes and delays, the convolution result $CV11_{pq}(t)$ is given by

$$CV11_{pq}(t) = \begin{cases} 0 \quad \text{for } 0 \le t < (p+q)h \\ c1_p c2_q \left[t - t^2/h + t^3/(6h^2) \right] \\ \qquad \text{for } (p+q)h \le t < (p+q+1)h \\ c1_p c2_q \left[4h/3 - 2t + t^2/h - t^3/(6h^2) \right] \\ \qquad \text{for } (p+q+1)h \le t < (p+q+2)h \end{cases} \quad (21)$$

The resulting function is shown in figure 6.

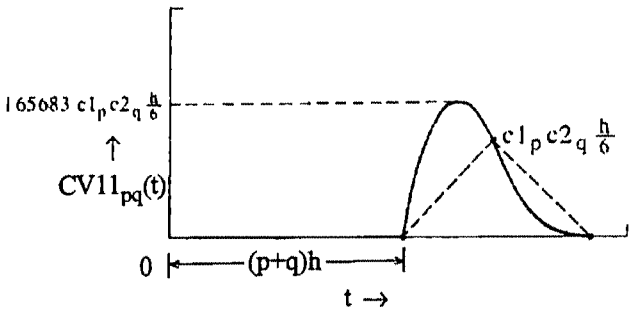

Figure 6 : A typical curve showing the result of convolution of two members of LHTF (having unit amplitude each, i.e., $c1_p = c2_q = 1$) and its TF domain approximation

To express the result in TF domain we need to take samples of $CV11_{pq}(t)$ at (p+q)h, (p+q+1)h and (p+q+2)h. Thus, from figure 6, we have

$$CV11_{pq}(t) = \left[\underbrace{0\ 0 \ldots 0}_{(p+q)\text{ zeros}}\ 0\ c1_p c2_q \frac{h}{6}\ \underbrace{0 \ldots 0\ 0}_{\{m-(p+q+2)\}\text{ zeros}} \right] T1_{(m)} + \left[\underbrace{0\ 0 \ldots 0}_{(p+q+1)\text{ zeros}}\ c1_p c2_q \frac{h}{6}\ 0\ \underbrace{0 \ldots 0\ 0}_{\{m-(p+q+3)\}\text{ zeros}} \right] T2_{(m)} \quad (22)$$

Convolution of two triangular function trains in TF domain

Now, we extend our ideas to convolution of two triangular function trains comprised of four component functions (m=4), having different amplitudes.

To do this, we take two trains of T1 (say, $T1_1$ and $T1_2$) basis as shown in figure 7. Following the approach shown above, the result of convolution, expressed in matrix form. is

$$CV11_{(4)}(t) = h/6[c2_0\ c2_1\ c2_2\ c2_3]\ [\![0\ c1_0\ c1_1\ c1_2]\!]T1_{(4)} + h/6[c2_0\ c2_1\ c2_2\ c2_3]\ [\![c1_0\ c1_1\ c1_2\ c1_3]\!]T2_{(4)} \quad (23)$$

With other combinations of traingular function trains (e. g. T1*T2, T2*T1 and T2*T2) similar convolution results may be obtained.

Convolution of two time functions in TF domain

Referring to equation (8), we now express $f_1(t)$ and $f_2(t)$ in TF domain having m basis functions. Thus

$$f_1(t) = [c1_0\ \ c1_1\ \ c1_2 \ldots c1_{(m-1)}]\,T1_{(m)} + [d1_0\ \ d1_1\ \ d1_2 \ldots d1_{(m-1)}]\,T2_{(m)} = C1^T.T1_{(m)} + D1^T.T2_{(m)} \quad (24)$$

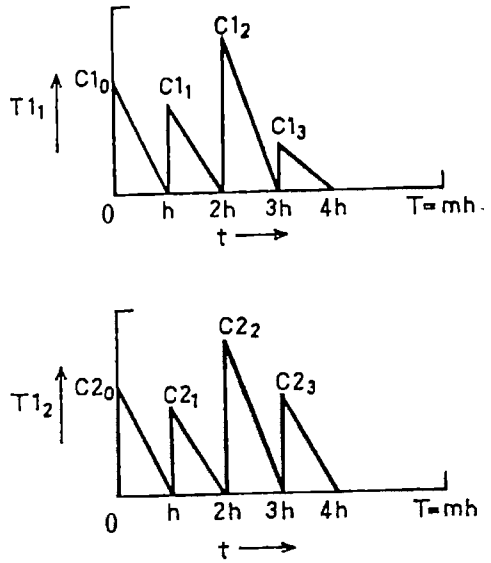

Figure 7 : Two trains of triangular functions, $T1_1$ and $T1_2$, of the T1 basis.

$$f_2(t) \approx [\, c2_0 \;\; c2_1 \;\; c2_2 \;\ldots\; c2_{(m-1)} \,]\, \mathbf{T1_{(m)}} + [\, d2_0 \;\; d2_1 \;\; d2_2 \;\ldots\; d2_{(m-1)} \,]\, \mathbf{T2_{(m)}}$$

$$\approx \mathbf{C2^T.T1_{(m)}} + \mathbf{D2^T.T2_{(m)}} \qquad (25)$$

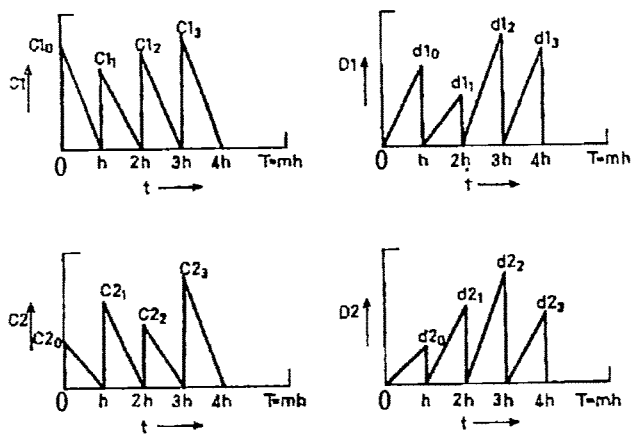

Figure 8 : Time diagram of the vectors **C1, D1, C2** and **D2** resulting from TF domain expansion of the functions $f_1(t)$ and $f_2(t)$

In figure 8, the vectors **C1, D1, C2** and **D2** are shown. Convolution of $f_1(t)$ and $f_2(t)$ of (24) and (25) will involve convolution of four sets of triangular function trains. The component results thus obtained are to be conglomerated (step 11 of Algorithm) to compute the final result. That is

$$\mathbf{CV12(t)} \approx (\mathbf{C1^T.T1} * \mathbf{C2^T.T1}) + (\mathbf{C1^T.T1} * \mathbf{D2^T.T2}) + (\mathbf{D1^T.T2} * \mathbf{C2^T.T1}) + (\mathbf{D1^T.T2} * \mathbf{D2^T.T2}) = \mathbf{C^T.T1} + \mathbf{D^T.T2}$$

Thus, as elaborated in the foregoing, the result of convolution **CV12(t)**, in TF domain, for two functions having m-terms each, is given by

$$\begin{aligned}\mathbf{CV12(t)} \approx\; & \tfrac{h}{6}[c2_0\, c2_1 \ldots c2_{(m-2)}\, c2_{(m-1)}]\, [\![0\, c1_0\, c1_1 \ldots c1_{(m-2)}]\!]\mathbf{T1_{(m)}} \\ & + \tfrac{h}{6}[c2_0\, c2_1 \ldots c2_{(m-2)}\, c2_{(m-1)}]\, [\![c1_0\, c1_1 \ldots c1_{(m-1)}]\!]\mathbf{T2_{(m)}} \\ & + \tfrac{h}{3}[d2_0\, d2_1 \ldots d2_{(m-2)}\, d2_{(m-1)}]\, [\![0\, c1_0\, c1_1 \ldots c1_{(m-2)}]\!]\mathbf{T1_{(m)}} \\ & + \tfrac{h}{3}[d2_0\, d2_1 \ldots d2_{(m-2)}\, d2_{(m-1)}]\, [\![c1_0\, c1_1 \ldots c1_{(m-2)}]\!]\mathbf{T2_{(m)}} \\ & + \tfrac{h}{3}[c2_0\, c2_1 \ldots c2_{(m-2)}\, c2_{(m-1)}]\, [\![0\, d1_0\, d1_1 \ldots d1_{(m-2)}]\!]\mathbf{T1_{(m)}} \\ & + \tfrac{h}{3}[c2_0\, c2_1 \ldots c2_{(m-2)}\, c2_{(m-1)}]\, [\![d1_0\, d1_1 \ldots d1_{(m-1)}]\!]\mathbf{T2_{(m)}} \\ & + \tfrac{h}{6}[d2_0\, d2_1 \ldots d2_{(m-2)}\, d2_{(m-1)}]\, [\![0\, d1_0\, d1_1 \ldots d1_{(m-2)}]\!]\mathbf{T1_{(m)}} \\ & + \tfrac{h}{6}[d2_0\, d2_1 \ldots d2_{(m-2)}\, d2_{(m-1)}]\, [\![d1_0\, d1_1 \ldots d1_{(m-1)}]\!]\mathbf{T2_{(m)}} \end{aligned} \qquad (26)$$

NUMERICAL EXPERIMENT

Consider a first order plant having a transfer function [14]

$$G(s) = (s+1)^{-1}$$

For a input r (t) = u (t), the output is given by

$$C(s) = \mathcal{L}^{-1}\,[s(s+1)]^{-1}$$

Thus $c(t) = r(t) * g(t)$

where, $g(t) = \exp(-t)$, for $t \geq 0$

Exact solution for plant response is

$$c(t) = 1 - \exp(-t), \text{ for } t \geq 0 \qquad (27)$$

Triangular function expansion of r(t) and g(t), for T=1 s and m = 10, following equation (9) yields

$$r(t) \approx [\, 1\;1\;1\;1\;1\;1\;1\;1\;1\;1 \,]\, \mathbf{T1} + [\, 1\;1\;1\;1\;1\;1\;1\;1\;1\;1 \,]\, \mathbf{T2}$$

$$g(t) \approx [\, 1 \;\; 0.9048375 \;\; 0.8187308 \;\; 0.7408182 \;\; 0.6703200 \;\; 0.6065307 \;\; 0.5488116 \;\; 0.4965853 \;\; 0.4493290 \;\; 0.4065696 \,]\, \mathbf{T1} + [\, 0.9048375 \;\; 0.8187308 \;\; 0.7408182 \;\; 0.6703200 \;\; 0.6065307 \;\; 0.5488116 \;\; 0.4965853 \;\; 0.4493290 \;\; 0.4065696 \;\; 0.3678794 \,]\, \mathbf{T2}$$

The output, according to equation (26), is

$$c(t) \approx [\, 0 \;\; 0.0952419 \;\; 0.1814203 \;\; 0.2593978 \;\; 0.3299547 \;\; 0.3937972 \;\; 0.4515643 \;\; 0.5038342 \;\; 0.5511299 \;\; 0.5939248 \,]\, \mathbf{T1} + [\, 0.0952419 \;\; 0.1814203 \;\; 0.2593978 \;\; 0.3299547$$

0.3937972 0.4515643 0.5038342 0.5511299

0.5939248 0.6326473] **T2** **(28)**

However, direct TF domain expansion of C(t) in (27), for m=10 and T=1 s, is

$$c(t) \simeq [\,0\ 0.0951625\ 0.1812692\ 0.2591818\ 0.3296800\ 0.3934693\ 0.4511884\ 0.5034148\ 0.5506710\ 0.5934304\,]\ \mathbf{T1}$$

$$+\,[\,0.0951625\ 0.1812692\ 0.2591818\ 0.3296800\ 0.3934693\ 0.4511884\ 0.5034148\ 0.5506710\ 0.5934304\ 0.6321206\,]\ \mathbf{T2} \quad (29)$$

Comparing equations (28) and (29), it is observed that the coefficients are very close indicating efficiency of the method.

Minimum integral squared error (MISE) in TF domain and its comparison with BPF domain solution

Let us consider (m+1) sample points of the function f(t), having a sampling period h, denoted by f(ih), i=0, 1, 2, ... , m. Then piecewise linear representation of the function f(t) by triangular functions is obtained simply by joining these sample points. The equation of one such straight line in the i-th interval is given by

$$f(t) = m_i t + f(ih) - im_i h \quad (30)$$

$$\text{where, } m_i = \frac{f[(i+1)h] - f(ih)}{h} \quad (31)$$

Then minimum intergral squared error (MISE) in the i-th interval is given by

$$[\epsilon_i]^2 = \int_{ih}^{(i+1)h} \left[\, \hat{f}(t) - f(t) \,\right]^2 dt \quad (32)$$

To compute the MISE for the result obtained in (28), we naturally make use of equation (32). The coefficients of (28) form the function $\hat{f}(t)$, while f(t) is the exact analytical expression of c(t).

The MISE in the interval [0,1) for m = 10, is found to be 2.5732038×10^{-7}.

A similar analysis is of special interest in the BPF domain to judge the efficiency of the TF domain solution against its BPF counterpart. Following Kwong and chen [15], the BPF domain solution for the output of the same plant via convolution is

$$c(t) \simeq [\,0.0475813\ 0.1382159\ 0.2202255\ 0.2944309\ 0.3615746\ 0.4223288\ 0.4773015\ 0.5270429\ 0.5720507\ 0.6127755\,]\ \Psi_{(10)}$$

Following (32), the MISE in the BPF domain is 3.6021721×10^{-4}.

Thus $\dfrac{\text{MISE}_{\text{BPF}}}{\text{MISE}_{\text{TF}}} = 1399.8782551$ (33)

This establishes the superiority of the TF domain analysis over the BPF domain.

CONCLUSION

The present work proposed a complementary pair of orthogonal triangular function (TF) sets and established its effectiveness for piecewise linear approximations of time functions of Lebesgue measure. Further, operational matrices for integration in the TF domain, namely **P1** and **P2**, have been derived and their relation with the well-known block pulse function domain integral operational matrix **P** is shown. It has also been established with illustration that integration of time functions with **P1** and **P2** are more accurate than that in the BPF domain.

The newly proposed sets have been applied to determine the convolution of two triangular function trains and the result was used to compute the output of a linear SISO control system via an operational technique. The estimated minimum integral squared error (MISE) is found to be much less than the alternative staircase solution obtained from BPF domain technique.

The analysis technique presented herein is based upon non-optimal determination of the expansion coefficients to enjoy the advantages of using function samples as the coefficients like in [10, 11].

ACKNOWLEDGEMENT

The third author is grateful to Mr Samiresh Mukherjee, Principal, North Calcutta Polytechnic, for allowing her to carry on part time research work in the Department of Applied Physics, Calcutta University.

REFERENCES

1 Haar, A., Zur theorie der orthogonalen funktionensysteme, Math. Annalen, Vol. 69, pp. 331-371, 1910.

2 Deb, Anish, Sarkar, G. and Sen, S. K., Block pulse functions, the most fundamental of all piecewise constant basis functions, Int. J. Sys. Sci., vol. 25, no. 2, pp. 351-363, 1994.

3 Tzafestas, S. G. (Ed), *Walsh functions in signal and systems analysis and design*, Van-Nostrand Reinhold Co., New york, 1985.

4 Jiang, J. H. and Schaufelberger, W., *Block pulse functions and their applications in control systems*, LNCIS-179, Springer-Verlag, Berlin, 1992.

5 Sannuti, P., Analysis and synthesis of dynamic systems

via block-pulse functions, Proc. IEE, vol. 124, no. 6, pp. 569-571, 1977.

6 Deb, Anish, Sarkar, Gautam, Bhattacharjee, Manabrata and Sen, Sunit K., All-integrator approach to linear SISO control system analysis using block pulse functions (BPF), J. Franklin Instt., vol. 334B, No.2, pp. 319-335, 1997.

7 Chi-Hsu, Wang, Generalized block pulse operatational matrices and their applications to operational calculus, Int. J. Control, vol. 36, pp. 67-76, 1982.

8 Jiang, Z. H. and Schaufelberger, Recursive block pulse function method, in *Identification of continuous-time systems*, N. K. sinha and G.P.Rao (ed.), Kluwer Academic Publishers, Dordrecht, pp. 205-226, 1991.

9 Deb, Anish, Sarkar, Gautam and Sen, Sunit K., Linearly pulse-width modulated block pulse functions and their application to linear SISO feedback control system identification, IEE Proceedings — Control Theory & Applications, vol. 142, no. 1, pp. 44-50, 1995.

10 Deb, Anish, Sarkar, Gautam, Bhattacharjee, Manabrata and Sen, Sunit K., A new set of piecewise constant orthogonal functions for the analysis of linear SISO systems with sample-and-hold, J. Franklin Inst., vol. 335B, No.2, pp. 333-358, 1998.

11 Deb, Anish, Sarkar, Gautam, Bhattacharjee, Manabrata and Sen, Sunit K., Analysis of linear discrete SISO control systems via a set of delta functions, IEE Proceedings — Control Theory & Applications, vol. 143, no. 6, pp. 514-518, 1996.

12 Sansone, G., *Orthogonal functions*, Interscience, New York, 1959.

13 Chen, C. F., Tsay, Y. T. and Wu, T. T., Walsh operational matrices for fractional calculus and their application to distributed systems, J. Franklin Instt., vol. 303, no. 3, pp. 267-284, 1977.

14 Ogata, K., *Modern control engineering* (3rd ed.), Prentice-Hall of India Ltd., New Delhi. 1997.

15 Kwong C.P. and Chen, C. F., Linear feedback system identification via block pulse functions, Int. J. Sys. Sci., vol. 12, pp. 635-642, 1981.

Artificial Intelligence Techniques for Monitoring and Control of Power Systems: An Overview

R.C. Bansal[1], T.S. Bhatti[2], D.P. Kothari[3]

[1]Electrical & Electronics Engg. Department, Birla Institute of Technology & Science, Pilani, (India)

[2, 3]Centre for Energy Studies, Indian Institute of Technology, Delhi, Hauz Khas, New Delhi - 110016 (India)

[3]E-mail of Corresponding Author: dkothari@ces.iitd.ernet.in

Abstract

Power system optimization problems are very difficult to solve because power systems are very large, complex, and geographically widely distributed and are influenced by many unexpected events. It is therefore necessary to employ most efficient optimization methods to take full advantages in simplifying the formulation and implementation of the problem. This paper presents the overview of important artificial intelligence techniques used in power optimization problems. Applications of hybrid systems in power systems have also been presented in this paper.

Key words: artificial intelligence, artificial neural network, expert systems, fuzzy systems, genetic algorithm

INTRODUCTION

Mathematical optimization (algorithmic) methods have been used over the years for many power system planning, operation, and control problems. Mathematical formulations of real-world problems are derived under certain assumptions and even with these assumptions, the solutions of large-scale power systems are not trivial. On the other hand, there are many uncertainties in power system problems because power systems are large, complex, geographically widely distributed systems. More recently deregulation of power utilities has introduced new issues into the existing problems. Solution of the problem should be optimum globally, whereas solution searched by mathematical optimization is optimum locally. These facts make it difficult to effectively deal with many power system problems through strict mathematical formulation alone. Therefore intelligent techniques, which promise a global optimum solution, such as expert systems, artificial neural network, genetic algorithm, fuzzy logic, have emerged in recent years in power systems as a complement tool to mathematical approaches. The real beginning of AI is often quoted as 1958 when John McCarthy coined the phrase [1]. This paper presents the overview of important artificial intelligence techniques used in power optimization problems. Review of artificial techniques e.g. expert systems, fuzzy logic, artificial neural network, genetic algorithm, ant colony search, tabu search for their application in power system have been have been presented in this paper. Complex power system problems can be dealt by integrating the two or more techniques in order to combine their different strengths and overcome each other's weaknesses to generate hybrid solutions. Applications of hybrid systems in power system have also been discussed in this paper.

EXPERT SYSTEMS

Expert System (ES) was first introduced by Feigenbaum et al. in the early 1970 [4]. ES is a knowledge-based or rule based system, which uses the knowledge and interface procedure to solve problems that are difficult enough to require human expertise for their solution. Main advantages of ES are (i) It is permanent and it is consistent; (ii) It can be easily transferred or reproduced; (iii) It can be easily documented. Main disadvantage of ES is that it suffers from a knowledge bottleneck by having inability to earn or adapt to new situations. For the past twenty years, a great deal of ES applications has been developed to help plan, analyze, manage, control and operate various aspects of power generation, transmission and distributions systems. A bibliographic survey of expert systems in power system is presented in reference [6-8]. Lu et al. [9-11] have done considerable work on the applications of expert systems in power systems. ES has been applied to various areas of power systems, including [12]:

- Planning (power system planning)
- Operation (alarm processing/fault diagnosis, substation automation, load forecasting, power

system restoration, reactive power management and voltage control, stability, unit commitment, energy management system)
- Analysis (analysis and control, protection coordination).

ARTIFICIAL NEURAL NETWORKS

The starting point of artificial neural network (ANN) was the training algorithm proposed by Hebb in 1949, which demonstrated how a network of neurons could exhibit learning behaviour [13] Neural networks are categorized by their architecture (number of layers), topology (connectivity pattern, feed forward or recurrent etc.), and learning regime. Most of the applications in the power system use multi-layered feed forward network. The main advantages of ANN technology are [14-16]:

- It is fast
- It possesses learning ability
- It is robust
- It adapts to the data
- It is appropriate for non-linear modeling.

These advantages suggest the use of ANNs for voltage security monitoring and control. Though the neural network training is generally computationally expensive, it takes negligible time to evaluate voltage stability once the network has been trained. Despite the advantages of the ANN method, some disadvantages [14-16] of this technology are:

- Its large dimensionality
- Selection of the optimum configuration
- Convergence difficulties
- The choice of training methodology
- The 'black-box' representation of ANNs – they lack explanation capabilities and so decisions are not audible
- The fact that results are always generated even if the input data are unreasonable.

General information on neural network and their applications in power systems has been presented in [17-19] Vankayala et al. [20] have presented a bibliographical survey of neural network and their applications to power systems. Neural network has been mainly used in following area of power systems [12]:

- Planning (long term load forecasting, capacitor placement/voltage control)
- Operation (economic dispatch/unit commitment, short-term load forecasting, fault diagnosis, load flow, static and dynamic security assessment, generator scheduling, transient stability)
- Analysis (analysis and control, power system stabilizer).

FUZZY LOGIC PROGRAMMING

Fuzzy logic was developed by Lotfi Zadeh in 1964 to address uncertainty and imprecision which widely exist in the engineering problems [24]. The advantages of fuzzy theory are (i) The fuzzy sets more accurately represent the operational constraints of power systems; (ii) Fuzzified constraints are softer than traditional constraints [25].

A detailed introduction to fuzzy logic and their applications in power systems has been presented in [26-28] Mamoh et al. [29] have presented the overview and in-depth literature survey of fuzzy set theory in different areas of power systems i.e. power systems planning and scheduling, power systems operation, power system diagnosis, power system control, etc. Fuzzy systems has been used in many areas of power systems, including [12]:

- Planning (reliability and security analysis)
- Operation (voltage and reactive power control, state estimation, hydro-thermal/generation/maintenance scheduling, stability, unit commitment, fault diagnosis).
- Analysis (power system stabilizer, various control systems design).

EVOLUTIONARY COMPUTING

Evolutionary Programming is based on the Darwin's 'survival of the fittest strategy'. An evolutionary algorithm begins by initializing a population of candidate solutions to a problem. New solutions are then created by randomly varying those of the initial population. All solutions are measured with respect to how well they address the task. Finally, a selection criterion is applied to weed out those that are below par. The process is iterated using the selected set of solutions until a specific criterion is met. The advantages of evolutionary programming are adaptability to change and ability to generate good enough solutions quickly. Evolutionary computing can be subdivided into genetic algorithm, evolution strategies, evolutionary programming, genetic programming, classified systems and simulated annealing. Over 95% of all the papers published in power systems are based on genetic algorithm [12]. GA and simulated annealing have been discussed in this section.

A. Genetic Algorithms

Genetic Algorithms (GA) is a global search technique based on mechanics of natural selection and genetics. It is general-purpose optimization algorithms that are distinguished from conventional optimization by the use of concept of population genetics to guide the optimum search. A GA operates on a random population of individuals each

representing a solution to the problem at hand. In recent years GA is gaining popularity for its easy searching process, global optimality, independence of searching space and probabilistic nature. GA does its searching process based on its mechanics of natural genetics. Instead of point-to-point search, GA searches from population to population. Each member of population is a randomly selected binary string of definite length called cromosome. New population is evolved from older one through three operations i.e. reproduction, crossover and mutation. Reproduction is the probabilistic selection of two parent strings from the population of strings. The task of crossover between two individual chromosomes between two individual chromosomes is done by crossing over the bits around a randomly selected bit position to generate two child strings. Mutation is the process of complementing the 0's and 1's of the newly born child strings probabilistically in order to introduce variety in the child strings. A complete search at all the members of the population constitutes the generation. At every generation, the quality of the population is judged by its fitness function as such only good string gets the right access to the next generation.

The advantages of GA over traditional techniques are; (i) It needs only rough information of the objective function and places no restriction; (ii) The method works with a set of solutions from one generation to the next and not a single solution, thus making it less likely to converge on local minima; (iii) The solutions developed are randomly based on the probability rate of the genetic operators such as mutation and crossover; the initial solutions thus would not dictate the search direction of a GA. Disadvantage of GA method is that it requires tremendously high time.

Alander [32] has presented an extended bibliography of genetic algorithm in power systems. Following are the major applications of GA in power systems [12]:

- Planning (transmission expansion planning capacitor placement)
- Operation (voltage/reactive power control, unit commitment/economic dispatch, hydrothermal scheduling, maintenance scheduling, power system stabilizer).

B. Simulated Annealing

Simulated Annealing (SA) techniques based on thermodynamics were originally inspired by the formation of crystals in solids during cooling. The advantages of SA are its general applicability to deal with arbitrary systems and cost functions, its ability to refine optimal solution, and its simplicity of implementation even for complex problems. The major drawback of SA is repeated annealing. This method cannot tell whether it has found optimal solution [33]. Some other method (e.g. branch and bound) is required to do this. Simulated Annealing has been used in various power systems applications e.g. transmission expansion planning, unit commitment, generator maintenance scheduling, etc.

ANTI COLONY SEARCH

The first Anti Colony Search (ACS) system was introduced by Marco Dorigo in 1992 [33]. ACS techniques take inspiration from the behavior of real ant colonies and are used to solve function or combinational problems. ACS algorithms, to some extent, mimic the behavior of real ants. As we know, real ants are capable of finding shortest path from food sources to the nest without using visual cues. They are also capable of adapting to changes in the environment, for example finding a new shortest path once the old one is no longer feasible due to some obstacle. Such capabilities are essentially due to 'pheromone trails', which ants use to communicate information among individuals regarding path and to decide where to go. The main characteristics of ACS are positive feedback for recovery of good solutions, distributed computation, which avoids premature convergence, and the use of a constructive greedy heuristic to find acceptable solutions in the early stages of the search process. Poor computational of the ACS is the main drawback of this technique.

TABU SEARCH

Tabu Search (TS) is an iterative improvement procedure that starts from some initial solution and attempts to determine a better solution in the manner of a 'greatest descent neighborhood'. search algorithm. Basic components of TS are the moves, tabu list and aspiration level. TS is a metahuristic search to solve global optimization problem, based on multi-level memory management and response exploration [33]. Tabu search has been used in various power system applications e.g. feeder route location/transmission planning, optimal capacitor placement, unit commitment, hydrothermal scheduling, fault diagnosis' alarm processing, reactive power planning' etc.

HYBRID SYSTEMS

The real life power system problems may neither fit the assumptions of a single AI technique nor be effectively solved by the strengths and capabilities of single technique. One approach to deal with these complex real world problems is to integrate the use of two or more techniques in order to combine their different strengths and overcome each other's weaknesses to generate hybrid solutions. The hybrid techniques can be developed in variety of ways e.g.

combination, integration, fusion, and association. Various hybrid systems used in power systems are fuzzy expert systems, neural expert systems, fuzzy neural network systems, neuro-fuzzy systems, genetic algorithm neural network hybrid systems, genetic algorithm fuzzy hybrid systems, etc [12] With the benefits offered by hybrid systems, their applications to power system have been increasing rapidly. Table 1 lists the different hybrid techniques that have been applied to various power systems problems.

Table 1 Application areas of hybrid systems in power system problems

Hybrid systems	Application areas/power system problems
Fuzzy neural network systems	Generation and distribution, relaying, fault diagnosis, load forecasting, reactive power control, generator maintenance scheduling
Fuzzy genetic systems	Stability, Power system control, economic dispatch
Fuzzy expert systems	Power system planning
Fuzzy/ neural/expert/genetic systems	Load forecasting electric industry, power system stabilizer
Simulated annealing with fuzzy/genetic/expert systems	Reactive power planning, generator maintenance scheduling

CONCLUSIONS

This paper has shed some light on the important artificial intelligence techniques used in power system applications. Various hybrid techniques used in power system have also been discussed. Major areas in which particular AI technique has been used have also been highlighted. In the light of the overview presented in this paper, the following are the significant points of conclusions.

AI relies heavily on good problem description and extensive domain knowledge. Expert system, which is a knowledge-based system, suffers from a knowledge bottleneck by having an inability to learn or to adapt to new situations. Knowledge-based systems can enhance the capabilities of a power system. Whereas ANN can acquire knowledge through adaptive training and generalization. ANN, fuzzy, and ES suffer from the same requirement of expert user in their design and implementation. They also suffer from a lack of the formal model theory and mathematical rigors and so are vulnerable to the experts' depth of knowledge in problem definition. Fuzzy theory with its of realistic description of power system problems and ANN with its promise of adaptive training and generalization deserves scope for further study. GA, by contrast, access deep knowledge of system problem by well-established models. GA has much more potential in power system analysis and are also latest entry into the AI fields and are getting most of the current attention. GA needs to be understood in relation to the computation requirements and convergence properties. The application of hybrid systems in power system problems is a novel development, which represents a definite future trend in power system research.

REFERENCES

1. John McCarthy," Programs with Common Sense," Proc. National Physics Lab., HMSO, London, 1958.
2. Yong-Hua Song," Modern Optimization Techniques in Power Systems," Kluwer Academic Publishers, London, UK, 1999,
3. Malcolm R. Irving, Yong-Hua Song," Optimization Methods for Electric Power Systems, Part 1, Mathematical Optimization Methods," IEE Power Engineering Journal, Vol. 14, No. 5, October 2000, pp. 245-254.
4. B.G. Bucannan, E.A. Feigenbaum," DENDRAL and METADENDRAL: Their Applications Dimension," Artificial Intelligence, pp. 5-24, November 1978.
5. T.J. Dillon, MA. Laughton," Expert System Application in Power Systems," Prentice Hall, 1990.
6. Z.Z. Zhang, G.S. Hope and O.P. Malic," Expert Systems in Electric Power Systems – A Bibliographic Survey, " IEEE Transactions on Power Systems, Vol. PWRS – 4, No. 4, November 1989, pp. 1355-1362.
7. N.J. Balu, R.A. Adapa, G. Cauley, M. Lauby, D.J. Maratukulam," Review of Expert Systems Planning and Operations," Proceedings of IEEE, Vol. 80, No. 5, May 1992.
8. CIGRE Task Force 38-06-02," Survey on Expert System in Alarm Handling," Electra, Vol. 139, pp. 133-151, 1991.
9. C.C. Liu," Special Issue on Knowledge-Based Systems in Electric Power Systems, " Proceedings of IEEE, Vol. 80, No. 5, May 1992.
10. C.C. Liu, T.K. Ma, K.L. Liou, M.S. Tsai, " Practical Use of Expert Systems in Power Systems," International Journal on Engineering Intelligent Systems, March 1994, pp. 11-22.
11. C.C. Liu," Practical Use of Expert Systems in Planning and Operation of Power Systems," Electra, February 1993, pp. 31-67.
12. Kelvin Wardwick, Arthur Ekwue, Raj Aggarwal," Artificial Intelligence Techniques in Power Systems," IEE, London, UK, 1997.
13. P.D. Wasserman," Neural Computing: Theory and Practice," Van Nostrand Reinhold, New York, 1989.

14. D. Niebur, T.S. Dillon (editors)," Neunal Network Applications in Power Systems," CRL Publishing Ltd. U.K. 1996.
15. D.P. Kothari," Application of Neural Networks to Power Systems," (Invited paper), Proc. Int. Conference, ICIT 2000, Jan. 2000, pp. 621-626.
16. B.L. Dhikshatulu, B. Mannan, R. Krishnan," Introduction to Neural Networks," Journal of Institution of Electronics and Telecommunication Engineers, Paper No. 186-D, pp. 561-571, 1991.
17. R.K. Aggarwal, Y.H. Song," Artificial Neural Networks in Power Systems: Part 1 General Introduction to Neural Computing," IEE Power Engineering Journal, Vol. 11, No.3, pp. 129-134, 1997.
18. R.K. Aggarwal, Y.H. Song," Artificial Neural Networks in Power Systems: Part 2 Types of Artificial Neural Networks," IEE Power Engineering Journal, Vol. 12, No.1, pp. 41-47, 1998.
19. R.K. Aggarwal, Y.H. Song," Artificial Neural Networks in Power Systems: Part 3 Examples of Applications in Power Systems," IEE Power Engineering Journal, Vol. 12, No. 6, pp. 279-287, December 1998.
20. V.S.S. Vankayala and N.D. Rao," Artificial Neural Networks and Their Applications to Power Systems – A Bibliographical Survey," Electric Power Systems Research, Vol. 28, pp. 67-79, 1993.
21. P.S. Kulkarni, A.G. Kothari, D.P. Kothari," Combined Economic Dispatch Unit Using Economic Improved Back Propagation Neural Network," Electric Machines and Power Systems, Vol. 28, No. 8, January 2000, pp. 31-44.
22. P.S. Kulkarni, A.G. Kothari and D.P. Kothari," Adaptive BP NN Approach to Emission Constrained Economic Dispatch," Proc. CBIP Int. Conference, New Delhi, Dec. 1999, pp. viii-1-10.
23. P.S. Kulkarni, A.G. Kothari, D.P. Kothari," Combined Economic and Emission Dispatch Using Improved Back Propagation Neural Network," International Journal of Electric Machines and Power Systems, vol. 28, no.1, Jan. 2000, pp. 31-43.
24. L.A. Zadeh," Fuzzy Sets," Information and Control, Vol. 8, pp. 338-353, 1965.
25. Shankar K. Pal, Deba Prasad Mandal," Fuzzy Logic and Approximate Reasoning: An Overview," Journal of Institution of Electronics and Telecommunication Engineers, Paper No. 186-C, pp. 548-559, 1991.
26. Y.H. Song, A.T. Johns," Applications of Fuzzy Logic in Power Systems: Part 1 General Introduction to Fuzzy Logic, IEE Power Engineering Journal, Vol. 11, No.5, pp. 219-222, 1997.
27. Y.H. Song, A.T. Johns," Applications of Fuzzy Logic in Power Systems: Part 2: Comparison and Integration with Expert Systems, Neural Networks and Genetic Algorithms," IEE Power Engineering Journal, Vol. 12, No. 4, pp. 185-190, 1998.
28. Y.H. Song, A.T. Johns," Applications of Fuzzy Logic in Power Systems: Part 3," IEE Power Engineering Journal, Vol. 12, No.6, p. 97, 1998.
29. J.A. Mamoh, X.W. Ma, K. Tomsovic," Overview and Literature Survey of Fuzzy Set Theory in Power Systems," IEEE Transactions on Power Systems, Vol. 10, No. 3, pp. 1676-1690, August 1995.
30. J.S. Dhillon, S.C. Parti and D.P. Kothari, "Fuzzy Decision Making in Multi objective Long-term Scheduling of Hydrothermal system", International Journal of Electric Power and Energy Systems, vol.23, no1, Jan. 2001,pp 19-29.
31. David B. Fogal," What is Evolutionary Programming? ," IEEE Spectrum, pp.26-32, February 2000.
32. J.T. Alander," An Indexed Bibliography of Genetic Algorithm in Power Engineering," Report Series 94-1, Power, 21 February 1996, ftp://ftp.uwasa.fi/cs/report94-1/gaPOWERbib.ps.Z.
33. Yong-Hua Song, Malcolm R. Irving," Optimization Methods for Electric Power Systems, Part 2, Heuristic Optimization Methods," IEE Power Engineering Journal, Vol. 15, No. 3, June 2001, pp. 151-160.
34. M. Dorigo, V. Maniezzo and A. Colorni," The Ant System: Optimization by a Colony of Co-operating Agents," IEEE Transactions on Systems, Man and Cybernetics, 1995.
35. Y H Song, C S Chou," Application of Ant Colony Search Algorithms in Power System Optimization," IEEE Power Engineering Review, Vol.18, No.12, 1998, pp.63-64
36. F. Glover, M. Laguna," Tabu Search," Kluwer Academic Publishers, Boston, USA, 1997.
37. F. Glover, M. Laguna, E. Tallard and D.de Werra (eds)," Tabu Search," Science Publishers, Basel, Switzerland, 1993.
38. F. Glover," Tabu Search – Part 1," ORSA Journal on Computing, Vol. 1, No. 3, 1989, pp. 190-206.
39. F. Glover," Tabu Search – Part 1," ORSA Journal on Computing, Vol. 2, No. 1, 1990, pp. 4-32
40. Y.H. Song," Hybrid Systems-the Next Generation of Intelligent Techniques," Journal of Power System Technology, Vol. 20, No. 2, pp. 32-34, 1996.
41. I.J. Nagrath, D.P. Kothari," Modern Power Systems Analysis," Second Edition, Tata McGraw-Hill Publishing Company Limited, New Delhi, 1989.
42. I.J. Nagrath, D.P. Kothari," Power Systems Engineering," Tata McGraw-Hill Publishing Company Limited, New Delhi, 1994.
43. A.K. Mahalanabis, D.P. Kothari, S.I. Ahson," Computer Aided Power System Analysis and Control," Tata McGraw-Hill Publishing Company Limited, New Delhi, 1994.

A Fuzzy Approach to Handle Parameter and Control Uncertainties in Power System Bifurcation Analysis

P. K. Satpathy, D. Das and P. B. Dutta Gupta

Department of Electrical Engineering
Indian Institute of Technology, Kharagpur-721302(WB), India

Abstract

So far, all sorts of analyses related to power system problems are coordinated with crisp parameter values. However, such systems being physically complex and geographically widely distributed are subject to credible uncertain events. The bifurcation analysis provides a standard platform for studying the underlying dynamics of these systems. In this paper, the possibility of incorporating a fuzzy approach to handle parameters and control uncertainties in bifurcation analysis of power systems is proposed. Results include identification of critical busbars and operating margins to maintain voltage stability within the network. Simulation study on standard IEEE 14-bus test system validates the proposed scheme.

Key Words: Uncertainty, Fuzzy Sets, Membership function, Bifurcation, Voltage Stability and Power Systems.

INTRODUCTION

It is observed that the present day operating conditions for the power systems are more stressed than was usual in the past. As a result, maintaining stable voltage operation within the network has become a matter of great concern for the utilities. One important aspect of the voltage stability problem, which makes its understanding and solution more difficult, is that the phenomena involved are truly nonlinear [1].

There exist two major techniques viz., static approach and dynamic approach for this analysis. The solutions obtained using static approach are based on several implicit assumptions on the steady state behaviour of dynamic components, for which they fail to describe the actual system behaviour during transients. In such cases, dynamic simulation of a linearized system (small-disturbance analysis) or complete time domain dynamic simulation (large-disturbance analysis) may be called upon.

Here comes the bifurcation theory [2] that plays a key role in dealing with dynamics of nonlinear systems. In either case, the analysis requires a set of input values describing the several states (voltage magnitudes and angles), parameters (real and reactive power injections) and control settings (generator excitation, speed governor settings, load tap of transformers) for finding the desired solution.

Use of crisp numbers for the specified voltage magnitudes, angles, scheduled power injections at buses and control settings is the most common occurrence in the literature reported so far. But, in real practice, a lot of uncertainties may always be associated in the selection of these input parameters for their implementation in any analytical method. These facts make it difficult to effectively deal with many power system problems through strict mathematical formulations alone. Fuzzy set theory on the other hand, is a natural choice and seems to be promising. It is felt that these uncertainties can be properly modeled with the help of fuzzy set theory and fuzzy reasoning [3].

In this paper, the voltage stability problem is studied within the framework of bifurcation analysis through an application of fuzzy set theory. This objective is accomplished by suitably modeling the parameters and control variables as fuzzy members with appropriate membership function assigned for each. The following

sections of this paper highlight the basic facts about fuzzy set theory and fuzzy modeling aspects of input parameters. The general bifurcation procedure is also highlighted and simulation results for the case study conducted on standard IEEE 14-bus test system are presented with proper validation.

BASIC FACTS OF FUZZY SET THEORY

Zadeh [4] reported that the imprecise knowledge and perception of human beings could be modeled in a more natural way to generate meaningful probability distributions with the application of fuzzy sets. A fuzzy set $\tilde{A}$ in the universe of discourse (U) can be defined as a set of ordered pairs, where each subset includes some element (x) and its membership function $\mu_{\tilde{A}}(x)$. Otherwise stated, each element (x), which is a member of a given fuzzy set $\tilde{A}$, may be assigned a membership function, better known as the degree (or grade) of membership of (x) in $\tilde{A}$. This membership grade is denoted by $\mu_{\tilde{A}}(x)$, which indicates the degree or extent that (x) belongs to $\tilde{A}$ as in (1).

$$\tilde{A}=\left\{\left(x,\mu_{\tilde{A}}(x)\right)\middle|\, x\in U\right\} \qquad (1)$$

There are several membership functions (MF) described in the literature viz. triangular MF, trapezoidal MF, exponential MF etc. A proper selection of a particular MF is highly crucial for a specific objective. In this work, an L-R type trapezoidal MF [5] seems to best fit the modeling requirement of the input functions. A further explanation of this membership function is described in the next section.

FUZZY MODELING OF INPUT PARAMETERS

In this paper, the uncertainties in the input parameters are modeled with the help of L-R type trapezoidal membership functions, **Fig 1.** A fuzzy number is defined to be of the L-R type if there are L-R shape functions in association with positive scalars α (left spread) and β (right spread). Such a membership function is usually expressed by the characteristic points a_1, a_2, a_3 and a_4 such that the fuzzy number under study can assume any value between a_1 and a_4, but values within the range a_2 and a_3 are most likely to take place. All the values within the range a_2 and a_3 have a membership value (μ_x=1) that indicates complete membership for the event. However, the values within ranges (a_1-a_2) and (a_3-a_4) have memberships values ($0\le\mu_x\le1$), indicating partial membership values. Any value outside the range of a_1 and a_4 has membership values (μ_x=0) indicating non-membership for the parameter.

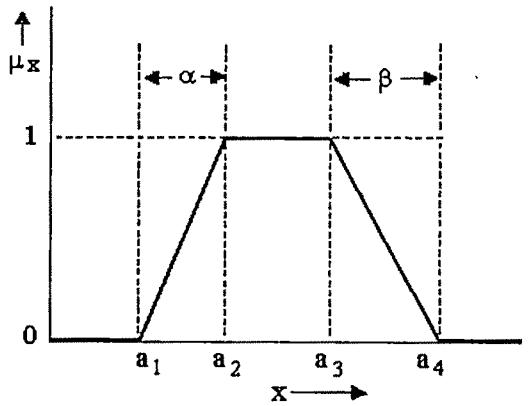

Fig 1: Schematic representation of a trapezoidal L-R type fuzzy membership function.

A specific relationship for the element 'x' and its degree of membership 'μ_x' for the L-R trapezoidal membership function is presented in (2-4).

$$\mu_{\tilde{A}}(x)=\begin{cases}L(x) & \text{for } a_1\le x\le a_2\\ R(x) & \text{for } a_3\le x\le a_4\\ 0 & \text{otherwise}\end{cases} \qquad (2)$$

$$\text{where, } L(x)=\left.\frac{x-(a_2-\alpha)}{\alpha}\right|_{\alpha\ge0} \qquad (3)$$

$$\text{and} \quad R(x)=\left.\frac{(a_3+\beta)-x}{\beta}\right|_{\beta\ge0} \qquad (4)$$

A judicious selection of characteristic values a_1, a_2, a_3 and a_4 renders an appropriate modeling of the input parameters under consideration.

BIFURCATION ANALYSIS

The term bifurcation originates from the concept of different branches of equilibrium points intersecting each

changes in system response arising from smooth, continuous parameter variations.

The mathematical interpretation of bifurcation is considered as the migration of the linearized system eigenvalues from one complex half plane to the other. Starting from a stable equilibrium point one can lead to locate the bifurcation point by increasing the parameter values monotonically.

Two common forms of bifurcation are; Saddle node bifurcation and Hopf bifurcation. In saddle node bifurcation (**Fig 2**), a real eigenvalue crosses the origin along the real axis of the complex plane resulting in an aperiodic instability. In Hopf bifurcation (**Fig 3**), two complex eigenvalues cross the imaginary axis thus producing an oscillatory instability. The analysis in this paper is based on the Hopf bifurcation theory.

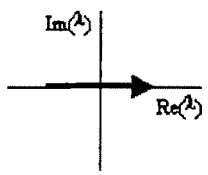

Fig 2: Mechanism of Saddle Node Bifurcation.

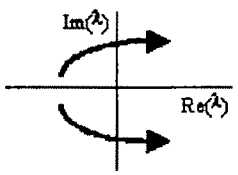

Fig 3: Mechanism of Hopf Bifurcation.

The power system is modeled with algebraic and differential equations (5) and (6), where the parameters and control variables are considered to have fuzzy distribution. In the first step, an equilibrium point is solved for (x_0, y_0, ξ_0).

In the next step, the system equations are linearized as described by equation (7) and (8). A complete Jacobian (9) is formed with these submatrices representing the dynamic Jacobian (J_{dyn}). The eigenvalues (λ) of equation (9) are formed from the solution of the characteristic equation (10) for further study and detection of the bifurcation point.

$$\dot{x} = f(x, y, \tilde{\xi}) \tag{5}$$

$$0 = g(x, y, \tilde{\xi}) \tag{6}$$

$$\Delta\dot{x} = J_{fx}\Delta x + J_{fy}\Delta y \tag{7}$$

$$0 = J_{gx}\Delta x + J_{gy}\Delta y \tag{8}$$

$$J_{dyn} = \begin{vmatrix} J_{fx} & J_{fy} \\ J_{gx} & J_{gy} \end{vmatrix} \tag{9}$$

$$\det\left(J_{dyn} - \lambda \begin{vmatrix} I & 0 \\ 0 & 0 \end{vmatrix} \right) = 0 \tag{10}$$

where, x is the dynamic state vector, y is the vector of algebraic variables representing complex node voltages, ξ is the parameter variation component, J_{fx} , J_{fy} , J_{gx} , J_{gy} are the Jacobian submatrices for each case and I is the identity matrix.

CASE STUDY AND NUMERICAL RESULTS

A case study on IEEE 14-bus test systems is conducted and results thus obtained, are presented in this section. A single line diagram of the IEEE 14-bus test system is shown in **Fig 4**. This system has 14 nodes and 20 lines. Bus-1 is treated as the slack bus and busbars 2-5 are considered as voltage control (PV) buses. Other buses are treated as load (PQ) buses. The bus data and line data for the IEEE 14-bus test system are obtained from [6].

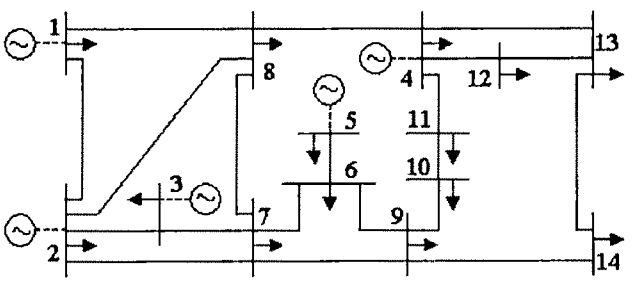

Fig 4: Single line diagram of IEEE 14-bus test system.

The numerical values used for fuzzy modeling of parameters and control variables can be assigned independent characteristic values or all may have same values. In this paper the later assignment is followed, (i.e. a_1=-0.25p.u., a_2=-0.20p.u., a_3=-0.12p.u., and a_4=-0.07 p.u.). The fuzzy based bifurcation analysis results are obtained for a variety of membership values and the loading level at the bifurcation point or point of collapse is noted for each membership grade.

It has been observed that all state variables namely voltage magnitudes and angles, (viz. V_6 through V_{14} and δ_6 through δ_{14}) indicate trapezoidal membership distributions at the point of collapse. Results for voltage angles (δ_6 through δ14) for various left and right side membership grades are presented in **Table 1** and **Table 2** respectively

Similarly, the results for voltage magnitudes (V_6 through V_{14}) for various left and right side membership grades are presented in **Table 3** and **Table 4** respectively.

Table 1: Voltage angles for Left membership values.

States	Fuzzy Membership'μ_x' ; L : Left side value			
	0.0 (L)	0.2 (L)	0.4 (L)	1.0 (L)
δ_6	-0.5440	-0.5375	-0.5311	-0.5117
δ_7	-0.5226	-0.5169	-0.5112	-0.4939
δ_8	-0.9806	-0.9675	-0.9545	-0.9153
δ_9	-1.2039	-1.1903	-1.1766	-1.1352
δ_{10}	-1.3257	-1.3113	-1.2968	-1.2529
δ_{11}	-1.3873	-1.3727	-1.3580	-1.3135
δ_{12}	-1.4268	-1.4120	-1.3972	-1.3521
δ_{13}	-1.4035	-1.3889	-1.3742	-1.3296
δ_{14}	-1.4622	-1.4473	-1.4321	-1.3859

Table 2: Voltage angles for Right membership values.

States	Fuzzy Membership'μ_x' ; R : Right side value			
	1.0 (R)	0.7 (R)	0.3 (R)	0.0 (R)
δ_6	-0.4605	-0.4510	-0.4384	-0.4290
δ_7	-0.4480	-0.4394	-0.4280	-0.4195
δ_8	-0.8130	-0.7943	-0.7694	-0.7509
δ_9	-1.0254	-1.0052	-0.9781	-0.9579
δ_{10}	-1.1355	-1.1137	-1.0846	-1.0627
δ_{11}	-1.1946	-1.1726	-1.1432	-1.1212
δ_{12}	-1.2321	-1.2099	-1.1803	-1.1581
δ_{13}	-1.2110	-1.1891	-1.1599	-1.1380
δ_{14}	-1.2603	-1.2368	-1.2052	-1.1814

Table 3: Voltage magnitudes for Left membership values.

States	Fuzzy Membership'μ_x' ; L: Left side value			
	0.0 (L)	0.2 (L)	0.4 (L)	1.0 (L)
V_6	0.7876	0.7898	0.7919	0.7984
V_7	0.7901	0.7927	0.7953	0.8030
V_8	0.7463	0.7467	0.7471	0.7487
V_9	0.6246	0.6238	0.6232	0.6216
V_{10}	0.5952	0.5939	0.5927	0.5896
V_{11}	0.7381	0.7370	0.7359	0.7329
V_{12}	0.8494	0.8483	0.8473	0.8445
V_{13}	0.8414	0.8403	0.8392	0.8361
V_{14}	0.5056	0.5028	0.5002	0.4929

Table 4: Voltage magnitude for Right membership values.

States	Fuzzy Membership'μ_x' ; R : Right side value			
	1.0 (R)	0.7 (R)	0.3 (R)	0.0 (R)
V_6	0.8150	0.8180	0.8219	0.8248
V_7	0.8229	0.8264	0.8311	0.8346
V_8	0.7533	0.7542	0.7554	0.7563
V_9	0.6190	0.6187	0.6184	0.6183
V_{10}	0.5835	0.5826	0.5816	0.5809
V_{11}	0.7267	0.7257	0.7245	0.7237
V_{12}	0.8381	0.8371	0.8358	0.8349
V_{13}	0.8294	0.8283	0.8270	0.8261
V_{14}	0.4769	0.4743	0.4712	0.4691

CONCLUSIONS

In this paper, the principles of fuzzy set theory has been exploited and successfully applied for fuzzy modeling of the parameters and control variables. Later, this is applied for the purpose of bifurcation analysis of voltage stability problem. A case study on IEEE 14-bus test system is conducted with proper validation of the proposed scheme. The critical results reveal that the voltage magnitudes/angles, power generations, power losses, and load parameter ξ at the bifurcation point also follow clear trapezoidal membership distributions. Thus it is concluded that in voltage stability bifurcation analysis of power systems the fuzzy logic can be successfully applied in modeling the imprecision and uncertainty offered by the system parameters and control variables to understand the system behavior in a more realistic manner.

REFERENCES

1. C. W. Taylor. Power System Voltage Stability. Mc Graw-Hill (1993).
2. V. I. Arnol'd. Catastrophe Theory, Springer Verlag (1986).
3. L. A. Zadeh, Fuzzy Sets, I J Information and Control. Vol.8, p.338-353 (1965).
4. L. A. Zadeh. Fuzzy Sets as a Basis for a Theory of Possibility, I J Fuzzy Sets and Systems, Vol.1, p.3-28 (1978).
5. D. Dubois and H. Prade, Fuzzy Real Algebra, Some Results, I J Fuzzy Sets and Systems, Vol.2, p.327-348 (1979).

Optimal Scheduling Of Short – Term Thermal Generation Using An Annealing Neural Network

C. Christober Asir Rajan[+], M. R. Mohan[*], K. Manivannan[+]
[+]Faculty of Electrical Engineering Department, Pondicherry Engg. College, Pondicherry – 605014
[*]School of Electrical Engineering, Anna University, Chennai – 600025, India.
E-mail: asir_70@hotmail.com

Abstract

This paper presents an annealing neural network algorithm to solve the optimal short - term thermal unit commitment. In power systems, the major goal of the generating unit commitment is to minimize the total fuel cost of the thermal units subject to some practical constraints. This also means that it is desirable to find the optimal generating commitment in the power system for the next H hours. The annealing neural network combines good solution quality for simulated annealing with rapid convergence for artificial neural network. The extended mean field annealing neural network is used to find short-term thermal unit commitment. By doing so, it can help in finding the optimum solution rapidly and efficiently. The effectiveness of the proposed approach is demonstrated by thermal unit commitment of Neyveli Thermal Power System. It is concluded from the results that the proposed approach is very effective in reaching proper unit commitment.

Keywords: Unit Commitment, Artificial Neural Network, Simulated Annealing

INTRODUCTION

Unit commitment is the problem of selecting the generating units to be put into service during a scheduling period and for how long. The committed units must meet the system load and reserve requirements at minimum operating cost, subject to a variety of constraints. Unit commitment is an important optimization task in the daily operating planning of power system. The solution of Unit Commitment problem (UCP) is really a complex optimization problem. It can be considered as two linked optimization problems, the first is a combinatorial problem of generating units, which could be a very huge number.

A survey of literature on the problem reveals that various numerical optimization techniques have been employed to approach the complicated unit commitment problem. More specifically, there are priority list method, dynamic programming method, Lagrangian relaxation method, mixed integer programming method, simulated annealing method, fuzzy theorem, artificial neural network and so on. Among theses methods, some are simple and fast but the quality of the final solution is rough, others may be have good quality of the final solution but they often take time to finish.

In this paper, an extended mean field annealing neural network is applied to solve the unit commitment problem. This algorithm is based on the annealing neural network has the advantages which combine both good solution quality for simulated annealing and rapid convergence for artificial network. The extended mean field annealing neural network also combines many features of the simulated annealing and the neural network that exhibits the rapid convergence of the neural network while preserving the solution quality afforded by stochastic simulated annealing. In the application on Neyveli Thermal Power System Unit – II shows that we can find the optimal solution effectively.

PROBLEM FORMULATION

The objective is to find the generation scheduling such that the total operating cost can be minimized, when subjected to a variety of constraints. In the unit commitment problem under consideration, an interesting solution would be minimizing the total operating cost of the generating units with several constraints being satisfied. The major component of the operating cost, for thermal and nuclear units, is the power production cost of the committed units and this is given in a quadratic form is given in equation (1).

$$F_{it}(P_{it}) = A_i P^2_{it} + B_i P_{it} + C_i \quad \text{Rs./ hr} \qquad (1)$$

Where

A_i, B_i, C_i ~ the cost function parameters of unit i (Rs./MW hr.,Rs./MW hr.,Rs./ hr.)
$F_{it}(P_{it})$ ~ production cost of unit i at a time t (Rs.hr.)
P_{it} ~ output power from unit i at time t (MW)

The start up cost depends upon the down time of the unit, which can vary from a maximum value, when the unit i is started from cold state, to a much smaller value, if the unit i is turned off recently. The start up cost calculation depends upon the treatment method for the thermal unit during down time periods. The entire procedure for the calculation of start up cost is formulated in the appendix section. The overall objective function of the UCP is given in equation (2).

$$F_T = \sum_{t=1}^{T} \sum_{i=1}^{N} (F_{it}(P_{it}) U_{it} + S_{it} V_{it}) \text{ Rs./ hr.} \qquad (2)$$

Where

U_{it} ~ unit i status at hour t = 1 (if unit is ON) = 0 (if unit is OFF)
V_{it} ~ unit i start up / shut down status at hour t =1 if the unit is started at hour t and 0 otherwise.
F_T ~ total operating cost over the scheduled horizon
S_{it} ~ start up cost of unit i at hour t

Constraints

Depending on the nature of the power system under study, the unit commitment problem is subjected to many constraints the main being the load balance constraints and the spinning reserve constraints. The other constraints include the thermal constraints, fuel constraints, security constraints etc.

1] Load Balance Constraints

The real power generated must be sufficient enough to meet the load demand and must satisfy the following equation given in (3).

$$\sum_{i=1}^{N} P_{it} U_{it} = PD_t \qquad (3)$$

Where

PD_t ~ system peak demand at hour t (MW)
N ~ number of available generating units

2] Spinning Reserve Constraints

The spinning reserve is the total amount of the real power generation available from all synchronized units minus the present load plus the losses. The reserve is considered to be a pre specified amount or a given percentage of the forecasted peak demand. It must be sufficient enough to meet the loss of the most heavily loaded unit in the system. This has to satisfy the equation given in (4).

$$\sum_{i=1}^{N} P\max_i U_{it} >= (PD_t + R_t);\ 1<=t<=T \qquad (4)$$

Where
T ~ scheduled time horizon (24 hrs.)

3] Thermal Constraints

The temperature and pressure of the thermal units vary very gradually and the units must be synchronized before they are brought online. A time period of even 1 hour is considered as the minimum down time of the units. There are certain factors, which govern the thermal constraints like minimum up time, min. down time and the crew constraints.

a] Minimum Up Time:

If the units have already been shut down, then there is a minimum time before which they can be restarted.

$$Ton_i >= T up_i$$

Where
Ton_i ~ duration for which unit i is continuously ON
Tup_i ~ unit i minimum up time

b] Minimum Down Time:

If all the units are running already, then they cannot be shut down simultaneously.

$$T off_i >= T down_i$$

Where
$T down_i$ ~ unit i minimum down time
$T off_i$ ~ duration for which unit i is continuously OFF

c] Must Run Units:

Generally in a power system, some of the units are given a must run status in order to provide voltage support for the network.

UNIT COMMITMENT BY EXTENTED MEAN FIELD ANNEALING NEURAL NETWORK

When we use extended mean field annealing neural network to solve the unit commitment problem, our objective function is to minimize the total operating cost. The resultant schedule should minimize the system operating cost during the study periods while simultaneously satisfying the load demand, spinning reserve, physical and operational constraints of the individual unit.

First, we want to decide the energy function of the neural network. Many combinational optimization problems can be mapped onto neural network by constructing suitable energy functions and then transforming the problem of their minimization into associated systems of differential or difference equations. In general, such an energy function can be written in the form of two terms:

E = 'cost' + 'global constraints'

These two terms of the energy function compete with each other; as a result the function E may have many local minima. We attempt to minimize the 'cost' function while simultaneously maximizing the number of 'global constraints' that are satisfied. Mathematically the computational energy function can often be expressed as:

$$E(X) = E_c(X) + \sum_j k_j E_j(X) \qquad (5)$$

where

$E_c(X)$: the cost (objective) function

$E_j(X)$: penalty function terms representing constraint violations

k_j : penalty factors which are positive numbers

$X = [x_1, x_2, x_3, \ldots x_n]^T$: the design vector with discrete values which is expressed the binary states of neutral states

For a wide class of optimization problems the computational energy function in eqn. (5) can be transformed into or approximated by the quadratic energy function. This is also called the Liapunov equation:

$$E(X) = \frac{1}{2}\sum_{j=1}^{n}\sum_{q=1}^{n} w_{j,q} x_j x_q - \sum_{j=1}^{n} \Theta_j x_j \qquad (6)$$

where

$w_{j,j} = 0$

$w_{j,q} = w_{q,j}$

$$w_{j,q} = -\frac{\partial^2 E(X)}{\partial x_j \partial x_q} \qquad (7)$$

$$\Theta_j = -\frac{\partial E(X)}{\partial X_j}\Big|_{X=0} \qquad (8)$$

when we use the artificial neural network to solve the unit commitment problem, the energy function can be expressed as:

E = 'cost' + 'global constraints'

$$= \sum_{k=1}^{H}\sum_{i=1}^{N} F_i(P_{i,k}) * V_{i,k} + \sum_{i=1}^{N} C_{st,i} + k_1 * \sum_{k=1}^{H}\left(\sum_{i=1}^{N} P_{i,k} * V_{i,k} - D_k\right)^2 - k_2 * \sum_{k=1}^{H} \min\{0, SR_k\} - k_3 * \sum_{i=1}^{N} \min\{0, UP_i\} - k_4 * \sum_{i=1}^{N} \min\{0, DW_i\} \qquad (9)$$

where

$$SR_k = \sum_{i=1}^{N} P_{i,\max} * V_{i,k} - (D_k + R_k) \geq 0 \quad for \quad k = 1,2,\ldots 24 \qquad (10)$$

$$UP_i = \sum_{k=ku}^{kd-1} V_{i,k} - MU_i \geq 0 \quad for \quad i = 1,2,\ldots N \qquad (11)$$

$$DW_i = \sum_{k=kd}^{ku-1} V_{i,k} - MD_i \geq 0 \quad for \quad i = 1,2,\ldots N \qquad (12)$$

k1,k2,k3,k4: penalty factors which are positive numbers

The extended mean field-annealing algorithm to solve the unit commitment problem can be expressed as follows:

Step 1: Initialize the parameters

First, initialize the parameters as the initial temperature T_0, frozen temperature T_f, cooling rate β, and the number of the iterations at each temperature. The initial values of the neutron states often affect the result of the unit commitment significantly. Some poor initial values of the neurons often mean that we must take time to finish the optimal process or it will converge to the local minimum. So must decide the initial values of the neuron states cautiously. The energy function E contains a large number of the local minimum on the vertex of the hypercube $\{0,1\}^n$. Some of these local minima can be avoided by replacing the binary neurons with the signum function by analog neurons with a smooth sigmoid activation function where digital neurons with two binary states $x_j = 0$ or 1 are replaced by analogue neurons with

continuous output u_j constrained between 0 and 1. So, our initial values of neurons are decided by the mean field theorem as follows:

$$u_{j,initial} = 1/2 + \delta \qquad for \quad j = 1,2,...n \qquad (13)$$

where δ is a random number between –0.1 and +0.1. u_j is state value of the j^{th} neuron. $V_{j,k}$ is the state value of the j^{th} generating unit at period k. The relations of the state values of the neurons and generating units are shown below:

(a) Correlation:

$$u_1 \rightarrow V_{1,1}, u_2 \rightarrow V_{1,2}, u_3 \rightarrow V_{1,3}, ... u_n \rightarrow V_{N,H}$$

where n = N*H

(b) when $u_j \geq 0.5$, $V_{j,k} = 1$: when uj < 0.5, $V_{j,k} = 0$

Minimizing the energy function E with $u_j \in [0,1]$ ($0 \leq u_j \leq 1$) instead of E with $x_j \in \{0,1\}$ considerably decreases the probability of being trapped in local minima since the function E has effect of smoothing local minima. During the optimization process the output variable u_j of the neurons may traverse through the interior of a hypercube $\Omega \in \{0, 1\}^n$ but the desired discrete final state {0,1}is not guarantied. To force the analogue neurons, many discrete values 0 and 1, an auxiliary penalty term is added to the energy function E.

$$E_p = \sum_{j=1}^{n} u_j * (u_j - 1) \qquad (14)$$

which is equal to zero only if all u_j take the binary values {0,1}.

Step 2: Stopping Criterion

When the annealing temperature T is higher than frozen temperature T_f, repeat the following steps until the annealing temperature T is smaller than the frozen temperature T_f. If frozen condition is signaling then set the system to be frozen and stop the formula and print out the solution of the final unit commitment.

Step 3: Update the State Values

Let the state u_j has a continuous value from 0 to 1, then the state average $\langle u_j \rangle$ can be derived as follows:

$$\langle u_j \rangle = \sum_{u_j \in [0,1]} u_j * \Pr\{u_j\}$$

$$= \frac{(u_m = 0) * \exp(-E_0/T) + (u_m = 0+\epsilon) * \exp(-(E_0+\epsilon)/T) + ... + (u_m = 1) * \exp(-E_1/T)}{\exp(-E_0/T) + \exp(-(E_0+\epsilon)/T) + ... + \exp(-E_1/T)}$$

$$= \int_0^1 u_l * \exp(-E_l/T) du_l \Big/ \int_0^1 \exp(-E_l/T) du_l \qquad (15)$$

It is difficult to calculate the state average represented by eqn. 11 owing to the computational floating-point overview. To circumvent this difficulty, a method called perturbation scheme is used in this paper described as follows:

Select a neuron at random and perturb,

$$u_{j,new} = u_{j,old} + \alpha * \zeta \qquad (16)$$

Here, α is the maximum allowed displacement, ζ is a random number between –1 to +1.

This perturbation scheme is included in the extended mean field field-annealing algorithm when the mean field-annealing algorithm calculates the special state average. Then the average value will be replaced by a new equilibrium neuron state value u_j. When we update our neuron states, this mechanism is similar to conventional simulated annealing but there is a difference. In the case of conventional simulated annealing, all neuron states are perturbed to find thermal equilibrium. But in the algorithm, only one state is selected, perturbed and updated. Therefore, this mechanism can be applied to all neuron states in parallel. By the new neuron states, we can obtain the new generating unit states. When we obtain the new generating unit states, we can calculate the new energy function E_{new} And find out the value $\Delta E = E_{new} - E_{old}$.

Step 4: Acceptance Test

If the perturbed state u_j decrease the energy value, then the new state will be accepted. Otherwise the probability that will accept this state is calculated by the following:

If $\Delta E \leq 0 \rightarrow$accept new state u_j,

If $\Delta E>0 \rightarrow$ if random [0,1]<exp $(-\Delta E/T) \rightarrow$ accept new state u_j, otherwise reject.

Step 5: Decrease the perturbed temperature T

We determine the number of iteration under this temperature has arrived. If it does not arrive at the specified number of iteration at the temperature, go back to Step 3 and update the new state values. If it has arrived at the specified number of iteration, decrease the perturbed temperature $T = \beta T$. In this paper, β is set to 0.95. After decreasing the perturbed temperature, go back to Step 2. In the extended mean field-annealing algorithm, we can see that when the neuron state u_j is updated, it is different from the conventional simulated annealing.

In the extended mean field-annealing algorithm it perturbs only one neuron state, while conventional simulated annealing perturbs all neurons to find a new state.

SIMULATION RESULTS

In this work, the Neyveli Thermal power station Unit – II is considered as case study and tested using the extended mean field annealing neural network in the unit commitment problem to prove that the algorithm is feasible and effective. In this paper, the extended mean field-annealing program was coded in Borland C++ and implemented on a compatible personal computer. The parameters of operating units are provided in Table 1.

Table 1. Unit Characteristic, Load Pattern and Initial Status

Unit	Max (MW)	Min (MW)	Incremental heat rate (Btu / kWh)	No-load cost ($/h)	Full-load average cost ($/MWh)	MU (h)	MD (h)
1	215	186	7980	884.75	19.00	8	5
2	209	190	9870	710.40	21.79	6	3
3	204	185	10540	684.74	22.43	5	3
4	199	107	11450	585.35	23.65	4	2
5	213	199	8540	800.34	20.34	8	5
6	185	130	12540	490.95	28.00	1	1
7	212	192	8730	780.35	21.10	7	4

Unit	Initial conditions hours off-line (-) or on-line (+)	Start-up costs		Cold start (h)
		Hot ($)	Cold ($)	
1	7	160	600.00	8
2	4	170	700.00	6
3	4	500	1300.00	5
4	-6	120	500.00	4
5	6	300	1100.00	8
6	-5	0	0 02	0
7	7	200	1000.00	7

Load Pattern

Hour	Load(MW)	Hour	Load(MW)
1	1125	6	1164
2	1138	7	1178
3	1135	8	1159
4	1135	9	1169
5	1148	10	1207

The simulation results of the extended mean field annealing (EMFA) neural network compared with those of simulated annealing (SA) and mean field annealing (MFA) algorithm are given in Table 2 based on the same initial temperature, decreasing rate β, and frozen temperature. In these fifteen times simulation tests, the initial neuron states are selected random. It is found from Table 2 that many cases have the same total costs, but their execution times are different from the EMFA, MFA, and SA. This is because that they have different initial neuron states. A poor initial value may take much time to reach the optimal solution.

Table 2. : The results of fifteen times simulation tests from EMFA, MFA, and SA

Unit	EMFA		MFA		SA	
	Total cost ($)	Time (sec)	Total cost ($)	Time (sec)	Total cost ($)	Time (sec)
1	94018.1	5.0	94109.9	3.0	94109.9	61.0
2	94018.1	10.0	94109.9	8.0	94018.1	51.0
3	94018.1	3.0	94018.1	4.0	94018 1	46.0
4	94018.1	2.0	94018 1	4.0	94109.9	166.0
5	94018.1	4.0	94837.9	7.0	94018.9	71.0
6	94018.1	2.0	94837.9	2.0	94018.1	39.0
7	94109.9	4.0	94837.9	5.0	94018 1	67.0
8	94018.1	7.0	94837.9	3.0	94018.1	74 0
9	94018.1	3.0	94837.9	2.0	94018.1	36.0
10	94018.1	6.0	94837.9	4.0	94036 5	78.0
11	94018.1	3.0	94837.9	4.2	94036.5	68.7
12	94018.1	2.0	94837.9	7.0	94036.5	78 9
13	94018.1	4.0	94837.9	4.0	94018.1	80.0
14	94018.1	7.0	94837.9	4.1	94018.1	97.8
15	94015.7	3.0	94837.9	4 0	94020.2	101.2

For comparing the performance of the three algorithms, the total cost and execution time are listed in Table 3 and 4 respectively.

Table 3. Comparison of the total costs from EMFA, MFA and SA

Total cost ($)	Algorithm		
	EMFA	MFA	SA
Best cost	94018.12	94018.12	94018.12
Worst cost	94109.89	94357.99	94109.89
Average cost	94027.30	94179.54	94036.47

In Table 3, the average cost is the average value of total cost of three fifteen times simulation results, respectively. It is observed from Table 3 that the best costs are the same from EMFA, MFA, and SA, but the worst costs are not all the same. In particular, in the

average cost from EMFA, MFA and SA, we can see that the EMFA has better convergence than the other two.

In Table 4, the average execution time is the average value of execution time of these fifteen times simulation tests. The shortest execution time and longest execution time are the shortest and longest execution time of these fifteen times simulation tests, respectively. It is observed from Table 4 that the difference in execution time between EMFA and MFA is not obvious. This is because that theses two algorithms have a high convergence speed and the test system is too small to compare the difference. It is also from Table 4 that the SA algorithm needs considerable time to reach the optimal solution than the other two.

Table 4. Comparison of the execution time from EMFA, MFA and SA

Time (sec)	Algorithm		
	EMFA	MFA	SA
Shortest execution time	1.2	1.2	27 0
Longest execution time	1.0	0.8	163.0
Average execution time	4.3	4.7	61.7

Tables 5 - 7 show that the neuron states during iterations for solving the unit commitment problem from EMFA. In which, Table 5 represents typical initial neuron states, Table 6 represents typical neuron states during iterations, and Table 7 represents final neuron states. It is noted that the neuron states will be converged to 0 and 1 at sufficiently low temperature.

Table 5. Typical initial neuron states of unit commitment problem from EMFA

Unit	Hour									
	1	2	3	4	5	6	7	8	9	10
1	0.7	0.8	0 7	0 6	0.7	0.7	0.8	0.7	0.7	0.7
2	0.7	0.6	0.6	0.8	0 6	0 8	0.7	0.7	0.6	0.6
3	0.6	0.8	0.7	0 7	0 8	0 6	0.7	0 7	0.7	0.7
4	0.7	0.8	0.6	0.8	0.7	0.7	0.8	0 8	0 6	0.6
5	0.6	0.7	0.5	0.7	0.6	0.6	0.7	0.7	0.5	0.7
6	0.5	0.6	0.4	0.6	0.5	0.5	0.6	0.6	0.4	0.7
7	0.4	0 5	0.3	0.5	0 4	0.4	0.5	0.5	0.3	0.8

Table 6. Typical neuron states during iterations of unit commitment problem from EMFA

Unit	Hour									
	1	2	3	4	5	6	7	8	9	10
1	0.5	0.2	1.0	0.7	0.7	1.0	0.2	0.0	0.5	0.2
2	1.0	0.8	0.9	0.7	0.6	0.7	0.6	0.9	0.8	1.0
3	1.0	1.0	1.0	1.0	1.0	1.0	1.0	1.0	1.0	1.0
4	0.2	0.2	0.4	0.2	0.9	0.5	0.3	0.2	0.2	0.2
5	0.0	0.2	0.9	0.2	1.0	0.7	0.6	1.0	0.2	0 0
6	0.9	0.3	0.2	0.2	1.0	1.0	0.7	0.9	0.3	0.9
7	1.0	0.5	0.4	1.0	1.0	0.2	0.6	1.0	0.5	1.0

Now we specially compare with the convergence speed of EMFA, MFA, and SA to the unit commitment problem as in given Figure 1. Figure 1 shows the characteristic convergence speed from EMFA, MFA and SA. These results are the average value of the fifteen times simulation results.

Table 7. Final neuron states of unit commitment problem from EMFA

Unit	Hour									
	1	2	3	4	5	6	7	8	9	10
1	0.0	0.0	1.0	1.0	1.0	1.0	0.0	0.0	0.0	1.0
2	1.0	1.0	1.0	1.0	0.0	0.0	0.0	1.0	0.0	1.0
3	1.0	1.0	1.0	1.0	1.0	1.0	1.0	1.0	1.0	1.0
4	0.0	0.0	0.0	0.0	1.0	0.0	0.0	0.0	0.0	1.0
5	0.0	0.0	1.0	1.0	1.0	0.0	0.0	1.0	0.0	1.0
6	1.0	0.0	1.0	1.0	1.0	1.0	0.0	1.0	1.0	1.0
7	1.0	1.0	0.0	1.0	1.0	0.0	0.0	0.0	0.0	0 0

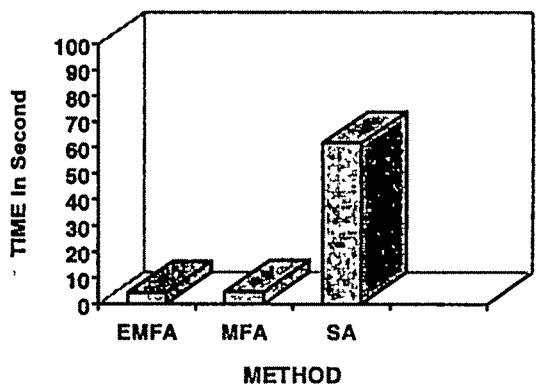

Figure 1: Comparison of the characteristic of the convergence speed from EMFA, MFA, and SA

It is noted that the unit commitment problem is first formulated as an optimization problem which is then solved by the extended mean field annealing neural network to determine the on off states of generating units. The practical constraints such as minimum up/down time of units, etc. have been considered already.

It is observed from the above results that the proposed extended mean field annealing network approach is attractive for the optimization problem because the solution is determined in a very short time. Results from numerical simulations indicate that extended mean field annealing neural network provides a useful alternative to traditional approaches for optimization problems

CONCLUSION

In this paper, an extended mean field annealing neural network has been proposed to solve the optimal unit commitment problem. First, the unit commitment

problem was described into a numerical formulation. Next, an extended mean field annealing neural network was presented for solving unit commitment and the feasibility of this algorithm for solving unit commitment problem was proved by example. The numerical results show that the extended mean field-annealing algorithm can reach the optimal solution of unit commitment problem.

Therefore, we believe that the extended mean field annealing neural network has good performance and has the ability to determine the global optimal solution in short time in a lsarge scale electric power systems.

REFERENCES

1. Wood.A.J. And Woolenberg.B.F. : "Power Generation and control" (Jhon Wiley and Sons. New York, 1996, 2nd Edn.)
2. Pang.C.K. And Chen.H.C.: "Optimal short - term thermal unit commitment", IEEE Trans. 1976, PAS-95, pp. 1336-1341.
3. Mantamy.A.H.: "Optimal Scheduling of Thermal Generation in Electric Power System", A Master Thesis, Ain Shams University, Cario, Egypt.
4. Zhuang.F., F.D.Galiana,: "Unit Commitment by Simulated Annealing", IEEE Trans. On Power Systems, Vol.5, No.1, 1990, pp. 311-318.
5. Shokri.Z., Selim And K.Alsultan, "A Simulated Annealing Algorithm for the Clustering Problem", Pattern Recognition, Vol. 24, No. 10, 1991, pp. 1003-1008.
6. Nieva.R., Inda.A., And Guillen.I, : "Lagrangian reduction of search range for large scale unit commitment", IEEE Trans., 1987, PWRS-2, PP. 465-473.
7. A. Turgeon , " Optimal Scheduling of Thermal Generating Units" , IEEE Transactions on Automatic Control , Vol. AC -23 , No:6 , 1978 ,.
8. C.K.Prag , G.B.Sheble , F.Albuyeh , " Evaluation of Dynamic Programming Based Methods and Multiple Area Representation for Thermal Unit Commitment ", *IEEE Transactions on PAS*, Vol.6 , No.3 , 1981, pp1212-1218.
9. Cohen.A.I.Sherket.V.R., "Optimization - Based Methods for Operations scheduling", Proceedings of the IEEE, Vol. 75, No. 12, Dec. 1987, pp. 1574-1581.
10. Glover, F.: 'Future paths for integer programming sand links to artificial intelligence ', Comput. Oper. Res., Vol.13, No:5, 1986, pp.533-549.

Maintenance Scheduling Of Generating Units Of A Captive Thermal Power Plant Using Intelligent Computational Technique

D. K. Mohanta, T. Ghose, R. C. Jha, B. M. Karan and T. Mohanta[+]
Dept of Electrical and Electronics Engineering,
Birla Institute of Technology,Mesra, Ranchi-835215, India
[+]Hewlett-Packard, Bangalore.
E-Mail of corresponding Author - d_mohanta@yahoo.com

Abstract

For the reliable operation of power system, the effective maintenance scheduling of generating units plays a vital role. Since such scheduling problem is concerned with several complicated factors and uncertainties even in a small system or an isolated system, the solution is always confronted by the "curse of dimensionality". The captive power plants posses certain unique attributes as far as their operation is concerned. This paper is an attempt to solve such complex maintenance scheduling of thermal generating units of a captive power plant exploiting the advantages of intelligent computational technique known as simulated annealing.

Keywords: *Maintenance scheduling, captive thermal power plant, curse of dimensionality, intelligent computational technique, simulated annealing.*

INTRODUCTION

The objective of this paper is to obtain effective solution to problem of maintenance scheduling of thermal generating units in Captive Power Plants using simulated annealing. The maintenance scheduling of thermal generating units in captive power plants in power system is a long-term scheduling problem of planned outages for regular maintenance [1]. Thermal units take relatively longer duration for maintenance, and it is crucial to maintain a proper level of reserve margin between available generation capacity and forecasted load demand keeping the system reliability in view. Particularly the captive power plants are intended for catering the power demand of power intensive utilities such as Aluminum smelters or blast furnaces in steel plants etc. In such utility services the interruption of power causes solidification of molten metal.

The overall goals of the given maintenance scheduling problem are to increase the system reliability as well as economic benefits, to extend generator lifetime, to reduce and (or) postpone installation of new units. The above goals must be met as a consequence of peculiarity of power system, as quoted by Kralj and Petrovic [2].The traditional methods developed in the past such as heuristic search algorithms [3,4], mathematical programming techniques [5,6,7] etc have been used in practice but better ones need to be developed for taking into account the stochastic, non-linear, large scale and multi objective nature of the problem. In addition, captive power plants have their own system requirements. Therefore this paper is a maiden attempt to implement the general principles of maintenance scheduling to meet with specific milieu of captive power plants. This maintenance scheduling problem is solved as a constrained optimization problem using intelligent computational technique such as simulated annealing

PROBLEM FORMULATION

There are normally two categories of objective function in power system maintenance, i.e., Minimization of the system operating cost, i.e., cost (or economic) objective function & maximization of system reliability, i.e., reliability objective function. In order to make the maintenance plan feasible certain constraints have to be considered according to real life conditions of power system.

Operation constraints are power system operation constraints and include reserve margin constraints; generation demand balance and generation constraints and the maintenance constraints include maintenance window,

maintenance man power and maintenance capacity constraints.

List of symbols used:

i : index of thermal generating unit
maxunit : maximum number of generating units
j : index of period
J : total number of periods
P [i][j] : generating capacity of unit i in period j
nm : maintenance count in the planning horizon
Q_{min} [i] [nm] : the earliest starting period of maintenance for unit i for nm^{th} maintenance
Q_{max} [i] [nm] : the latest starting period of maintenance for unit i for nm^{th} maintenance
Q [i][nm] : starting period of maintenance for unit i for nm^{th} maintenance
S [i] [nm] : type of maintenance for unit i during for nm^{th} maintenance count(For class D,S,M maintenance ,S[i] [nm]=1,2 and 3 respectively)
M [S [i][nm] : duration of maintenance for a particular type of maintenance
F [i] [nm] : maximum available extension terms for i^{th} unit for nm^{th} maintenance.
R[j] : reserve for j^{th} period
Ro : minimum reserve requirement
PM [i] [j] : power loss due to maintenance for unit i during period j.
PD [j] : power demand during period j.

OBJECTIVE FUNCTION

The objective function (F) is formulated to minimize the sum of squares of reserve generation as appended.

$$F = \sum_{j=1}^{J} \sum_{i=1}^{maxunit} \left\{ P[i][j] - PM[i][j] - PD[J] - R_O \right\}^2 \quad \text{---- (1)}$$

Subject to the constraints such as, Starting Period of Maintenance, Maximum Permissible Period Constraint, and Minimum Reserve Requirement Constraint. Keeping statutory safety regulations in view, the thermal units must be maintained within a maximum permissible period Qmax [i] [nm]. The earliest staring period Q_{min} [i] [nm] is chosen from the general consideration that the thermal unit maintenance must commence within one year plus or minus one month (48 weeks) from last maintenance.

$$Q_{min}[i][nm] \le Q[i][nm] \le Q_{max}[i][nm]$$
$$Q_{min}[i][nm] = Q[i][nm-1] + M[(S[i][nm])] + 48 \quad (2)$$

Simplified maintenance for boiler and generator must be completed within 1.5 years (turbine within 156 weeks). No extensions are permitted before or after minor maintenance. The maintenance class adopted before or after the minor maintenance must be a detailed one.The minor maintenance cannot be adopted continuously for the same unit. The minor maintenance is carried out so that more time-consuming maintenance can be postponed.The maintenance durations for the three classes of maintenance, namely, detailed (class D), simplified (class S) and minor (class M) have been considered as 10,6 and 3 weeks.From the above criteria, the maximum permissible maintenance period is determined as follows.

$$Q_{max}[i][nm] = Q_{min}[i][nm] + F[i][nm] \quad (3)$$

The extension term F [i] [nm] is dependent on previous maintenance classes.

All the time reserve requirement $R[j] \ge Ro$ (4)
where Ro is the minimum reserve requirement.

For this maintenance scheduling problem, the objective function (1) is minimized under constraints (2) to (4).

INTELLIGENT COMPUTATIONAL TECHNIQUES (SIMULATED ANNEALING)

The concepts of simulated annealing method are based on a strong analogy between the physical annealing process of solid and the problem of solving large combinatorial optimization problems [8,9]. In a physical multi-particle system, "annealing" is a thermal process for obtaining low energy states of a solid in a heat bath. Frist the temperature of heat bath is increased to a maximum value at which the solid melts, and then the temperature of the heat bath is decreased carefully until the particles arrange themselves in the ground state of solid. Solutions in combinatorial optimization problem are equivalent to states (rearrangement of particles) of a physical problem.

Step 0: Initialization
Initialize the iteration count K = 0, and the temperature T^o to be sufficiently high find an initial feasible solution (X_o) belonging to set of feasible solutions (X_i)
Step –1: Repeat for each temperature T^KExecute steps 2-4 until an equilibrium criterion is satisfied.
Step-2: Neighborhood solution
Create a trial solution X^{K+1} in the neighborhood of current solution X^K.

Step-3: Acceptance criterion (Metropolis criterion)
The acceptance criterion is described below in a nutshell.
Let $\Delta = f(X^{K+1}) - f(X^K)$
and r is a random number uniformly distributed over [0,1].
If $\Delta < 0$ (i.e., the solution is improved), the trial solution is accepted. Otherwise, the trial solution is accepted with the probability exp. $(-\Delta/T^K) > r$
Step–4: Equilibrium criterion
If the number of generated solutions becomes sufficiently large, go on to step 5. Otherwise, go back to step 2 and generate a new solution.
Step 5: Cooling schedule
Gradually decrease the value of the temperature T^K by
$T^{K+1} = \rho * T^K$ where $0 < \rho < 1$
Step 6: Convergence check
If the freezing point is reached and the algorithm is terminated. Otherwise set K = K+1 and go to Step-1.

IMPLEMENTATION OF SIMULATED ANNEALING TO CAPTIVE POWER PLANTS WITH EXAMPLE

The proposed algorithm is applied in three stages, as depicted below.

STAGE 1
Step1: From the information of the previous two maintenances, the $[Q_{min}$ (i, nm)] i.e., earliest maintenance starting time for the i^{th} unit for the first maintenance in the planning horizon (nm=3) is calculated using equation 2.
Step 2: If the initial solution does not satisfy the reserve constraint, the shifting of the starting period of the units under maintenance is done corresponding to the periods violating the reserve constraints. If still the feasible solution is not obtained, then the class M maintenance is employed as depicted in stage 2.

STAGE 2
Class-M maintenance is introduced only when there is no feasible solution available by the combination of class-D and class-S maintenance. The class-M maintenance is introduced to take care of reserve constraints.
Step-1 An interval with largest reserve constraint violation is chosen.
Step-2 A set of generating units whose maintenance period is included in the above chosen interval is chosen.
Step-3 Class-M maintenance is used for generating units chosen in step-2 for a feasible solution.

STAGE 3
For global optimization using simulated annealing, the steps given in Fig. 1 are employed.

RESULTS AND DISCUSSION

The performance of the proposed method is examined through long- term real scale captive power plant (6 units, 208 weeks). The load demand has been realistically considered and its magnitude varies between 400 MW to 450 MW.

OPTIMAL SOLUTION

The algorithm for the technique of simulated annealing for maintenance scheduling has been developed in C language (Turbo C). The flow chart has been incorporated in figure 2.

CONCLUSION

A relatively simple algorithm has been formulated to solve the complex formulated to solve the complex maintenance scheduling problem dealing with various maintenance classes and a planning horizon spanning over so many years. The statutory safety requirements for power plant maintenance have been incorporated as mathematical formulations that indicate the earliest and latest starting period of maintenance. The proposed method shows the reasonable combination of local and global search using shifting of starting time of maintenance as well as introducing minor class maintenance. The introduction of class –M is restricted to only those cases where a feasible solution is not found using D and S classes of maintenance. As a result the reliability level of maintenance scheduling required for the captive power plants is retained.

REFERENCES

1. A.J. Wood and B.F. Wollenburg, Power Generation, Operation, and Control, John Wiley and Sons, New York, 1984.
2. Kralj, B.L. and Petrivic, R., 1988, "Optimal Preventive Maintenance Scheduling of Thermal Generating Units in Power System, A Survey of Problem Formulation and Solution Methods", European Journal of Operation Research, Vol. 35, pp. 1-15.
3. Graver, L.L., 1972, Adjusting Maintenance Scheduling to Levilize Risk, IEEE Transactions on Power Apparatus and Systems, Vol. PAS-91, No. 5, September/October, pp. 2057-2063.
4. Stremel, J.P., 1981, Maintenance Scheduling for Generating System Planning, IEEE Transactions on Power Apparatus and Systems, Vol. PAS-100, March, pp. 1410-1419.

5. Rao, S.S., Engineering Optimization, Theory and Practice, New Age International (P) Limited, Publishers, New Delhi.
6. Yamayee, Z.A., Sidenblad, K., and M. Yoshimura, 1983, A Computationally Efficient Optimal Maintenance Scheduling Method, IEEE Transactions on Power Apparatus and Systems, Vol. PAS-102, pp. 330-338.
7. Mukherjee, R., Merrill, H.M., Erickson, B.W., Parker, J.H., and Friedman, R.E., 1991, Power Plant Maintenance Scheduling Optimizing Economics and Reliability, IEEE Transactions on Power Systems, Vol. 6, May, pp. 476-483.
8. Kim, H., Hayashi, Y., and K. Nara, 1996, An Algorithm for Thermal Unit Maintenance Scheduling Through Combined Use of genetic algorithm, SA and TS, 96 WM 291-5-PWRS
9. .S. Kirkpatrick, C.D. Gelatt, Jr., and M.P. Vecchi, "Optimization by Simulated Annealing", Science, Vol. 220, pp. 671-680, 1883.

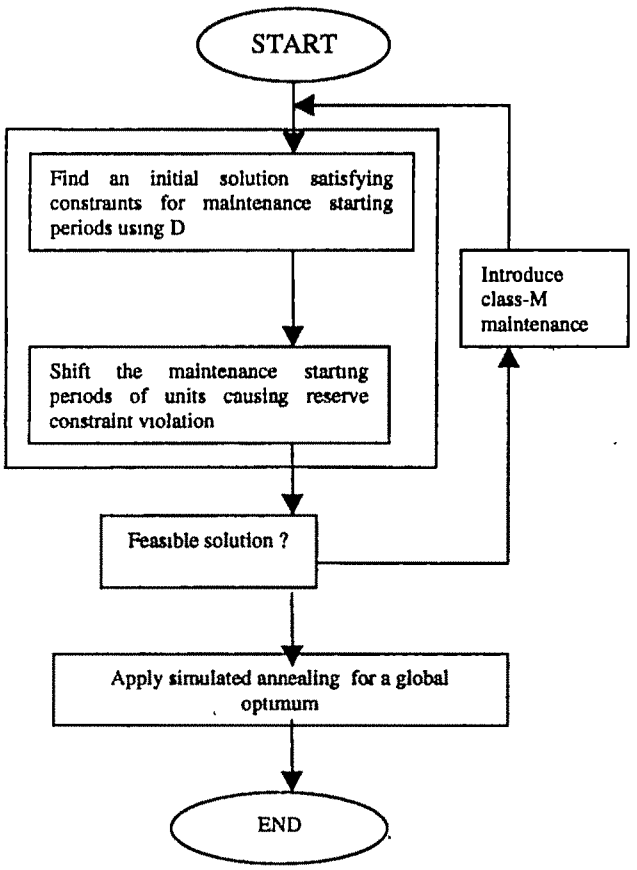

Fig 2

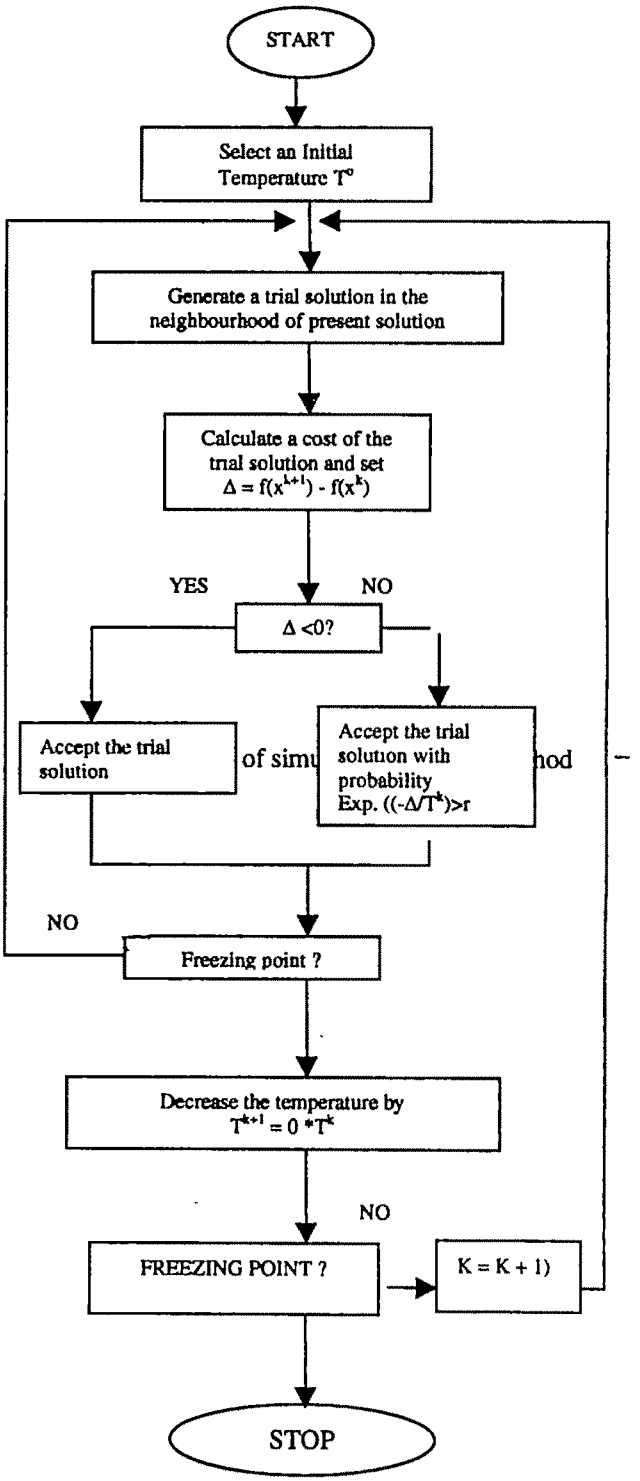

Table 1 Determination of F[I][nm]

$(nm-2)^{th}$ maintenance class	$(nm-1)^{th}$ maintenance class	Gap between two maintenances	Present nm^{th} maintenance	Extention F[I][nm] in weeks
D or S	D or S	≥78	D	29
D or S	D or S	<78	D	59
D or S	D or S	<78	S	29
D	M	<78	D or S	10
S	M	<78	D	10

Table 2 Data for generating units

Unit No	Capacity (MW)	Main duration in weeks			Status of previous maintenances			
		D	S	M	nm=1	Type	nm=2	Type
1	120	10	6	3	74	D	4	S
2	120	10	6	3	103	S	34	D
3	120	10	6	3	94	D	19	S
4	120	10	6	3	93	S	54	S
5	120	10	6	3	63	S	1	D
6	120	10	6	3	103	D	14	D

UNIT	NM	TYPE	QMIN	QMAX	Q
1	1	1	0	0	-74
1	2	2	0	0	-4
1	3	1	50	109	109
1	4	3	167	196	186
2	1	2	0	0	-103
2	2	1	0	0	-34
2	3	2	24	53	53
2	4	1	107	166	166
3	1	1	0	0	-94
3	2	2	0	0	-19
3	3	1	35	94	94
3	4	1	152	181	181
4	1	2	0	0	-93
4	2	2	0	0	-54
4	3	1	59	59	59
4	4	1	146	146	146
5	1	2	0	0	-63
5	2	1	0	0	-1
5	3	2	57	86	86
5	4	1	140	199	196
6	1	1	0	0	-115
6	2	1	0	0	-14
6	3	1	44	73	73
6	4	1	131	160	160

Table 3 Q data for generating units

Solution Of Economic Generation Scheduling Of Thermal Units Using Genetic Algorithm

T. Ghose[1], R. C. Jha[1], I. Alam[1] and S. K. Goswami[2]
[1]*Department of Electrical and Electronics Engg.*
Birla Institute of Technology, Mesra, Ranchi – 835215
[2]*Department of Electrical Engg, Jadavpur University*
Calcutta 700 032
E-mail of the corresponding author : tirtha_ghose@yahoo.com

Abstract

This paper reports Genetic Algorithm (GA) based solution of the economic generation scheduling of thermal units. The objective of the solution is to select a combination of available units at various times of operation so as to meet the load demand in such a manner that the overall cost becomes minimum. The present work also incorporates economic load sharing among the committed units. The paper reports the results of a optimal commitment scheduling of five thermal units.

INTRODUCTION

The scheduling problem in a power system involves the start-up and shut-down schedules of generating units to be used to meet forecasted demand over a future short-term (24-168 hours) period. The objective is to minimize total production costs while observing a large set of operating constraints. The solution of the problem justifies the running schedule of all the available units for generation because of it is neither economical nor technically feasible to run all the available units for all the time. It is obvious that various combinations of units can meet a certain demand. But fuel cost saving can be achieved by selecting the proper combination.

Several mathematical programming techniques have been proposed to solve these time-dependent unit-commitment problems. They typically include complete priority ordering (CPO) and heuristic methods, dynamic programming (DP), the method of local variations, mixed integer programming, Lagrangian relaxation, the branch and bound method, bender decomposition [2-12]. The main problem with these methods is that the solution obtained is only local optimal .Genetic Algorithm is used for the problem [13] but economic generation is not considered.

In the present work,GA has been used to solve the present problem . The mechanism of GA is such that it has the capability to get rid of the stacking with local optima. Another motivation to apply a Genetic Algorithm to the problem is that it can completely replace classical mathematical programming methods, and it is easy to implement as a search procedure.

PROBLEM FORMULATION

The objective of the scheduling problem is the minimization of the total production costs comprises of fuel cost, start-up cost and shut-down cost over the scheduling horizon. Fuel costs, called as running costs, are calculated using unit heat rate and fuel price information. Besides the running costs, an additional cost appears in the problem for starting the units. Because the temperature and pressure of a thermal unit moves slowly, a certain amount of energy must be expensed to bring the unit on-line. This energy does not result in any MW generation from the unit and is brought into the scheduling problem as start-up cost. The start-up cost is a time dependent cost as it depends on the time for which the unit has been kept shut down. The star-up cost can vary from a maximum ***cold start*** value to a much smaller value if the unit was only turned off recently and is still relatively close to normal temperature. There are two approaches to treating a thermal unit during its down period. One approach of calculating the star-up cost by assuming the cost curve is exponential depends on thermal time constant of the unit. The second approach adopted here is simplified time-dependent The start-up cost will be hot start cost when the down time is less than or equal to defined cold start hours for the unit. The down time is the hours the unit was in idle before going to start. Hot start

cost and cold start cost are given for each individual unit along with other input data.

Start –up cost = hot start cost, if down-time<= cold start hours
= cold start cost, otherwise

Shut down costs are defined as the fixed rupees amount for each unit per shut down.

The purpose of the scheduling problem is to gain in economy but certainly the commitment must satisfy the some constraints. In the present work, the objective function is subjected to the following constraints :

(i) System power balance,
(ii) Unit minimum up and minimum down time,
(iii) Unit initial status and status restrictions,
(iv) Unit high and low MW limits,

The first two constraints concern all the units of the system and are called system constraints. In general, the system constraints must take into account the possible transmission bottlenecks in the allocation of the demand and the reserves to the generating units. The other constraints are related with individual units and are called local constraints.

For the purpose of security it is necessary that the committed capacity should always be more than or at least equal to the load plus the specified spinning reserve. The commited capacity of every generator should be the economic generation.This is firstly due to the unavoidable uncertainty in demand prediction i.e. load forecasting and secondly due to any unforesee outage of loaded units. Spinning reserve must be specified using certain rules like it must be a given percentage of forecasted peak demand.

In the operation of units, engineering considerations or manufacturer specification normally reaquires that a unit be running for at least a certain length of time before it is shut down and vice-versa. This gives the need for minimum up & minimum down time.

THE OBJECTIVE FUNCTION

The short-term commitment is considered with 12 hour time horizon, which may be repeated using the load profile of each day. Since the system load varies substantially over a 12 hour period and the cost of operation over this time span depends on the timing and frequency of the unit's start-ups and shunt-downs. This commitment problem is generally viewed as a multiperiod problem in which the commitment horizon is divided into a number of periods of shorter length. The scheduling of the units at every hour is solved i.e. a one hour commitment interval is considered.

Economic Generation Scheduling Problem is the multi-modal optimization problem of determining the schedule of generating units under various operating constraints.

U_i^t as : $U_i^t = 0$, if unit i is off-line during period t
$= 1$, if unit i is on-line during period t

The objective function is considered :

$$F_T = \sum_{t=1}^{T} \sum_{i=1}^{N} [F_i(P_i^t) + SU_i^t + SD_i^t] U_i^t \qquad (1)$$

where, T and N are total hours and total number of units respectively, F_i is the fuel cost per MWh is the function of generation P of i^{th} unit at t^{th} hour and SU_i^t & SD_i^t are start up & shut –down cost respectively

This objective function (eqn. 1) is subjected to three constraints:-

$$\sum_{i=1}^{N} P_i^{max} \geq R^t + L^t$$

where,
P_i^{max} is the maximum capacity of unit i,
L^t is the demand and
R^t is the spinning reserve in time period t.

At transition period,
Up-time ≥ specified up-time for i^{th} unit
Down-time ≥ specified down-time for i^{th} unit

The major component of the operating cost is the power production cost (F) of the committed units. It is given as,

$$F_i = A_i P_i^2 + B_i P_i + C_i \quad \text{Rs./hour} \qquad (2)$$

where, A_i, B_i, C_i are the cost funciton parameters of unit i.

As in the commitment problem, the cost function is optimtzed so P_i is calculated from the λ method based the solution of Econmic load dispatch problem discussed in earlier section.

Start–up cost depends upon the down time of the units. A simplified time dependent start-up cost is as:

Start-up cost = hot start cost, if down-time ≤ cold start hours
= cold start cost, otherwise

IMPLEMENTATION OF GENETIC ALGORITHM (GA)

For the application of GA to the UC problem a simple binary alphabet was chosen to encode a solution. If N represents the no. of units and H the scheduling periods in hours, then with the assumption that at every hour a certain unit can be either ON or OFF, an H-bit string is needed to

describe the operating schedule of a single unit. In such a string, a `1' at a certain location indicates that the unit is `ON' at this particular hour while a `0' indicates that the unit is `OFF'. As the time horizon is twelve hours then twelve bit string (i.e. H=12) corresponds the status of every unit at every hour.

First of all, a number of M initial binary coded solutions (genotype) are produced at random to form the initial population. Then, each genotype is evaluated, and its fitness value calculated as follows:-

a) GA is applied to the maximization problem while the UC problem is a minimization problem. So, the following fitness function is introduced here:

$$\text{Fitness Function} = \frac{1}{F_T + 10^6 * \text{Penalty}} \qquad (3)$$

where F_T is total operational cost including start-up/shut-down cost, calculated from eqn. (1) and penalty represents the number of time periods when operational constraints are violated.

b) The total fuel cost is computed as the sum of the hourly fuel costs by economically dispatching the load demand to the operating units for every hour t, of the scheduling period. If for some hour t, due to the operating limits of the on line units, the power balance equation is not satisfied, a penalty term is added to the fitness function.

c) Time- dependent start up costs and shut down costs, can be easily computed from the information contained in the genotype and the initial state (continuous up or down time) of the units.

d) For every violated constraints (e.g. minimum up time) a penalty term proportional to the amount of constraint violation is added to the fitness function. The penalty multiplier is chosen sufficiently large to discourage the selection of solution with violated constraints.

After the evaluation of the initially randomly generated population the GA begins the creation of the new generation of the solutions. Two genotypes are selected using roulette wheel parent selection algorithm that selects a genotype with a probability proportional to the genotype's relative fitness within the population. Then, a new offspring genotype (new solution) is produced by means of the two basic genetic operators:

1. **Crossover** : This operator is applied with a certain probability. When applied, the parent genotypes are combined (exchange bits) to form two new genotypes that inherit solution characteristics from both parents. This means the offspring are identical replications of their parents.
2. **Mutation** : With a small probability, randomly chosen bits of the offsprings genotypes change from `0' to `1' and vice versa.

The above procedures are repeated until M new genotypes are produced which are considered as the new generation of solutions. The new generations totally replaces the parents.

AN ADOPTED METHOD FOR ECONOMIC LOAD DISPATCH

In the present work, the scheduling is also satisfied the economic generation by developing an optimization technique by Lagrangian multiplier method.

The economic load dispatch problem is defined as,

$$\frac{dF_n}{dP_n} = F_{nn}P_n + f_n, Min\ F_T = \sum_{n=1}^{N} F_n$$

$$subject\ to\ P_D = \sum_{n=1}^{n} P_n$$

where F_T is total fuel input to the system, F_n the fuel input to nth unit, P_D the total load demand and P_n the generation of nth unit.

By making use of Lagrangian multiplier the auxiliary function is obtained as

$$F = F_T + \lambda\left(P_D - \sum_{n=1}^{N} P_n\right)$$

where λ is the Lagrangian multiplier.

Differentiating F with respect to the generation P_n and equating to zero gives the condition for optimal operation of the system.

The condition for optimum operation is,

$$\frac{dF_1}{dP_1} = \frac{dF_2}{dP_2} = \ldots\ldots = \frac{dF_n}{dP_n} = \lambda$$

Here dF_n / dP_n is the incremental production cost of plant n in Rs. Per MWhr. The incremental production cost of a given plant over a limited range is represented by,

$$DF_n / dP_n = F_{nn} P_n + f_n$$

where, F_{nn} = slope of incremental production cost curve
f_n = intercept of incremental production cost curve

The optimal condition suggests that the machines be so loaded that the incremental cost of production of each machine is same.

The following iterative method is used :

1. Assume a suitable value of λ^0. The value should be more than the largest intercept of the incremental cost characteristics of the various generators.
2. Compute the individual generations P_1, P_2, ... Pn corresponding to incremental cost of production. In case generation at any of the buses is violated, the generation of that generator is fixed at the limit violated during that iteration and the remaining load is distributed among the remaining generators.
3. Check if the equality is satisfied.

$$P_D + R = \sum_{n=1}^{n} P_n$$

4. If not, make a second guess λ and repeat the above steps. The selection of λ in this step must of course be guided by the result in step 3.
5. If equality is satisfied, the generation as calculated in step 2 give the optimum operating strategies.

The flowchart for the solution of the Economic Scheduling is shown in Fig. 1.

SIMULATION RESULTS

The programs based on simple GA for the solution of UC problem is developed in C^{++} and is applied to an example problem which consists of 5 thermal units. We have considered short term scheduling where the time horizon is 12 hours and a typical load profile for this 12 hours is taken. The data consisting of characteristics of the thermal units and the initial status of the individual unit is shown in Table-1. The hourly demand for the 12 hours is given in another Table-2. The experiment is conducted with a population size of 30 using different crossover and mutation probability. Each run was allowed to continue up to 500 generations. Crossover probability of 60% and a mutation probability of 3% were found best.The state of the units at optimum cost is given in Table 3 where 1 is used to indicate that a unit is committed and 0 to indicate that a unit is not committed. The economic generation for the committed units is given in Table 4. The optimum cost is found US $ 152342.00 at 168 generation.

CONCLUSION

A genetic algorithm solution to the short-term economic generation scheduling has been presented. Genetic Algorithm is found very effective and simple to implement to the highly non-linear, multi-modal objective function like the present problem. The major advantages of using genetic algorithms are that they can replace the shortcomings of mathematical programming approaches more efficiently. That is, for each of the subsets of the total number of units that are to be tested, are operated in optimum economic fashion. It is observed that the computational time is required very high for including the economic load dispatch problem as sub problem but since genetic algorithms can be efficiently implemented in a highly parallel fashion, this drawback becomes less significant with its implementation in a parallel machine environment.

REFERENCES

1. A.J. Wood and B. F. Wollenberg, Power Generation Operation and Comtrol, 1984, John Wiley, New York.
2. Happ H. H., R. C. Johnson, W.J. Wright, " Large scale hydro-thermal unit commitment method and Results", IEEE Trans. On PAS, Vol. PAS-90,pp. 1373-1383, 1971.
3. Baldwin C. J., K. M. Dale, R. F. Dittrich," Study of Economic Shut down of generating units in daily dispatch", AIEE Tras. On PAS, Vol. 78, 1960, PP.1272-1284.
4. C.K. Pang, H.C. Chen, " Optimal Short term Thermal Unit Commitment" , IEEE Trans. On PAS, Vol. PAS-95, No. 4., 1976, Pp. 1336-1346.
5. C.K. Pang, G. V. Shebele, F. Albuyeh, " Evaluation of Dynamic Programming Based Methods and Multiple Area presentation For thermal unit commitments", IEEE Trans. On PAS-100, 1981, pp. 1212-1218.
6. W.J. Hobbs, G. Hermon, S. Warmer, G.B. Shebel, " An Enhanced Dynamic Programming Approach For Unit commitment" , IEEE Trans. On power systems, 1988, pp. 1201-1205.
7. Lauer G.S.,D.P. Bertsekas ,N.R. Sandell, Jr.,T.A. Posbergh, "Solution of large-scale optimal unit commitment problems",IEEE Trans. On PAS,1982,pp.79-86.
8. A Merlin and P. Sandrin , "A New method for unit commitment at Electricite De France",IEEE Trans.on PAS ,vol. PAS-102.No.-5.
9. K.Aoki, T.Satoh,M. Itoh, "Unit Commitment in a large scale power system including fuel constrained

thermal and pumped-storage hydro", IEEE Trans. On Power systems, 1987,pp. 1071-1083.
10. F.N. Lee, "A Fuel constrained Unit Commitment method",IEEE Trans. On power systems,1989,pp.691-698.
11. T.S. Dillon ,"Integer programming Approach to the problem of optimal unit commiyment with Probabilistic Reserve Determination ",IEEE Trans. On PAS 1978,pp. 2154-2164.
12. A.I. Cohen,M. Yoshimura, " A branch and bound algorithm for unit commitment", IEEE Trans. On PAS ,1983,pp. 444-451.
13. S. Kazarilis A. Bakirtzis, V.Petridis, " A Genetic Algorithm solution to the unit commitment problem ",IEEE Trans. On Power systems, 1996,pp. 83-92.

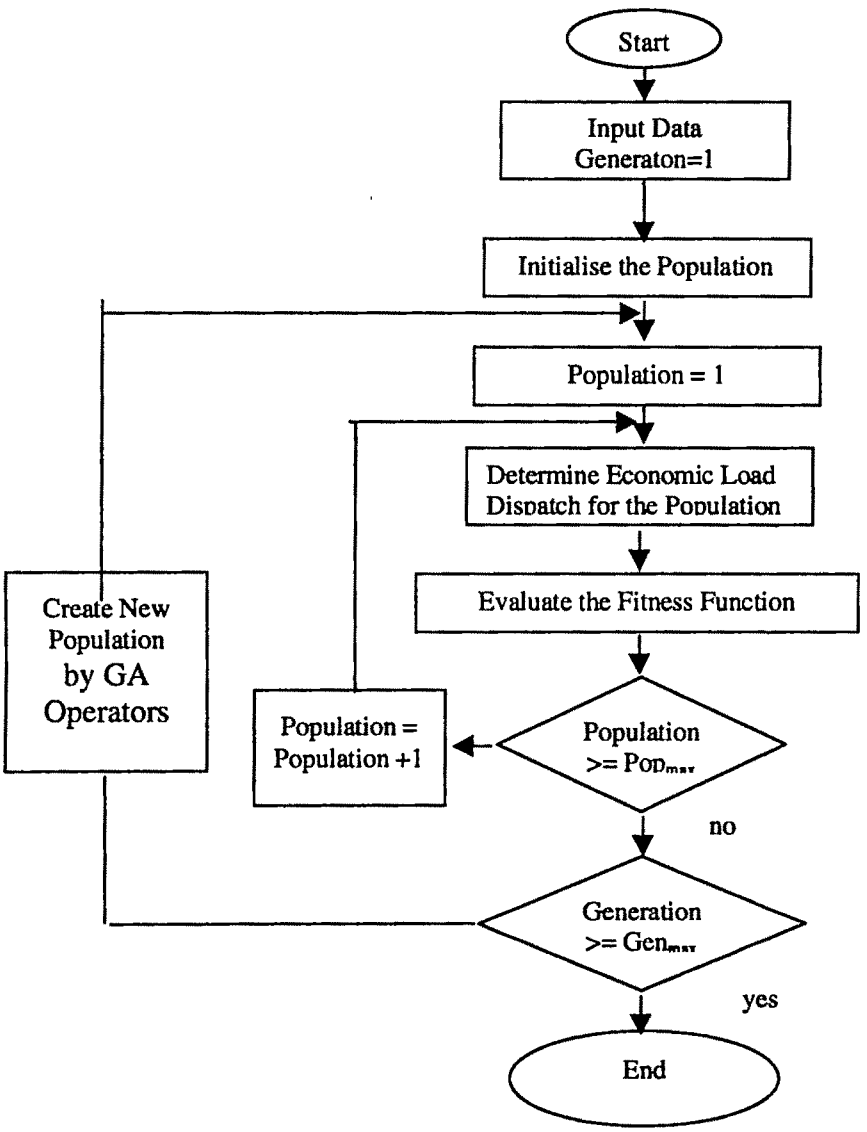

Fig 1 Flow chart for the implementation of the genetic algorithm

TABLE 1: Problem data for the 5-unit s.

	Unit 1	Unit 2	Unit 3	Unit 4	Unit 5
P_{max} (MW)	455	330	330	120	100
P_{min} (MW)	150	20	20	20	55
A ($/h)	1000	700	680	370	660
B ($MWh)	16.19	16.60	16.50	22.26	25.92
C ($MW^{2}h)	0.00048	0.002	0.00211	0.00712	0.00413
Min up (h)	3	3	2	2	1
Min dn (h)	3	3	2	2	1
Hot start cost ($)	4500	550	560	170	30
Cold start cost ($)	9000	1100	1120	340	60
Cold start hrs (h)	5	4	4	2	0
Initial status (h)	3	-3	-2	-2	-1

table 2: Hourly load demand

Hour	Demand (MW)	Hour	Demand (MW)
1	400	7	480
2	450	8	500
3	480	9	420
4	500	10	450
5	530	11	480
6	450	12	400

TABLE 3 : Optimum scheduling of 5-units solved by the developed technique.

	Status Of The Units At Each Hour											
Unit	1	2	3	4	5	6	7	8	9	10	11	12
1	0	0	0	0	0	0	1	1	1	1	0	0
2	1	1	1	1	1	1	1	0	0	0	1	1
3	1	1	1	0	0	1	1	1	1	1	1	1
4	1	1	1	1	1	1	1	1	1	0	0	1
5	1	0	0	1	1	0	0	1	0	1	1	1

TABLE 4: Power Generation of the units on Optimum Scheduling

			Generation of the Units (MW)		
Hour	1	2	3	4	5
1	0	156.34	171.89	20	55
2	0	208.3	221.14	20	0
3	0	225.76	237.69	20	0
4	0	330	0	111.61	55
5	0	330	0	120	76.18
6	0	208.3	221.14	20	0
7	426.3	20	23.52	20	0
8	409.02	0	20	20	55
9	391.76	0	20	20	0
10	374.53	0	20	0	55
11	0	203.95	217.02	0	55
12	0	156.35	171.9	20	55

Fuzzy Expert System for Service Restoration of Primary Distribution System

T. Ananthapadmanabha[1], A.D Kulkarni[1], W.M Shivakumar[2], N.Nagendra[3], S. B Shivakumar[5], M.S Nagaraj[4]

[1] The National Institute of Engineering, Mysore, Karnataka, India.
[2]Karnataka Power Transmission Corporation Ltd., Bangalore, Karnataka, India
[3]Power Research and Development Consultants Pvt. Ltd., Bangalore, Karnataka, India
[4]Bapuji Institute of Engineering and Technology, Davangere, Karnataka, India
[5]Sri Jagadguru Murugarajendra Institute of Technology, Chitradurga, Karnataka, India.

Abstract

A simple and effective method for selecting feasible plan during a service restoration process using fuzzy expert system is presented in this paper. The constraints faced while selecting a suitable restoration plan among the feasible plans obtained satisfying basic requirements will be solved to a greater extent, as these are treated as fuzzy variables rather than Boolean or crisp. The process begins with selection of restoration plans using single feeder / multiple feeder configuration technique to generate the required fuzzy sets. These sets will be subjected to fuzzy criteria and will be evaluated based on the heuristic inference provided by the operator. Final Restoration scheme is selected by ranking the restoration schemes depending on the performance index obtained. The Restoration scheme, which possesses highest performance index, will be selected to energise the outage zones.

INTRODUCTION

Service restoration is one of the most important functions in a Distribution Automation System in case of a fault on the primary feeder. Service restoration after a fault usually referred to, as emergency service restoration should be achieved quickly to shorten blackout. However, the reconfiguration problem is too complicated and the outcome should be feasible in all respects. The critical constraints while resolving a service restoration problem includes lesser number of switching operations, proper feeder–load balance, better voltage regulation, less overloading on the power system components etc. Thus Service Restoration is a problem of multiple objectives.

Earlier studies by Yaun-Yih Hsu and Han Ching Kuo [5] highlighted Fuzzy Reasoning approach for distribution system service restoration. The method takes into account the basic requirements to be satisfied for service restoration. In addition, the technique also considers some special requirements needed for certain distribution authority that is responsible for electricity distribution. Seung-Jae Lee [6] et.al. presented an improved method for service restoration using fuzzy logic / reasoning techniques. He suggested the use of different restoration schemes to generate candidate set of feasible restoration plans from which the best plan will be selected based on fuzzy reasoning approach.

This paper highlights the development of a fuzzy expert system for service restoration process. By providing a number of constraints to be satisfied for selecting the best plan, restoration process can be carried out with minimal amount of time ensuring the customer better quality supply during emergency states also.

METHODOLOGY

The proposed methodology can be divided into two sections namely,

1). Selection of feasible restoration plans using single and multiple feeder configuration technique.
2). Application of fuzzy expert system to determine the final restoration strategy.

Restoration schemes obtained using the above technique will be subjected to basic constraint: availability of feeder spare. Set of plans satisfying this basic constraint are termed as feasible restoration plans. From this set of feasible restoration plans, fuzzy criteria in terms of physical values namely Number of switching operations, Feeder loading, Backup margin and Voltage deviation will be found out. The second half involves the evaluation of these fuzzy criteria using fuzzy expert system. The whole process of obtaining the solution through fuzzy expert system is explained below:

Under *fuzzification*, the membership functions defined on the input variables are applied to their actual values, to determine the degree of truth for each rule premise.

Under *inference*, the truth-value for the premise of each rule is computed, and applied to the conclusion part of each rule. This results in one fuzzy subset to be assigned to each output variable for each rule. In the proposed technique Minimum and Maximum inference is applied to obtain final membership value.

Under *defuzzification*, using centroid method, the crisp value of the output variable (performance index) of each plan is computed by finding the center of gravity of the membership functions defined by the set of fuzzy criteria.

SELECTION OF FEASIBLE RESTORATION PLANS

Selection of alternative feeders to restore the outage zone is one of the preliminary requirements to search for the possibilities of a feasible plan. Suitable search technique can be employed to determine the alternative feeders. While selecting the feeder, basic constraint namely availability of feeder margin (FM) is tested. If the feeder satisfies this constraint, then this will be put under feasible restoration scheme. The following algorithm arrives at selection of feasible feeders

1. Start with identifying single feeder that has a direct path to the outage zones
2. Check if FM > ΣLoad (outage Zones)
3. If 'yes', select the feeder. If 'no' search for next alternative feeder.
4. If no more single feeder configuration is possible, select multiple feeders that have a direct path to outage zone. In this case suitable break-point has to be found out in order to maintain radiality.
5. Go to step 2 for checking the basic constraint.
6. The process is repeated until the selection of a set of feasible plans is obtained.

DETERMINATION OF FUZZY VARIABLES

Five Fuzzy variables namely, Number of switching (NS), Feeder Loading (FL), Backup Margin (BM), Line Loading (LL), Voltage Deviation (VD) are calculated for each of the feasible plans. Calculations of these variables are as follows

$$Feeder\ Loading = \sum_{NF} \frac{S'_{FL}}{S'_{Rated}} \qquad (1)$$

where; S_{FL} *= Loading of* i^{th} *feasible Feeder*

$$Line\ Loading = \frac{\sum_{NL} S_{LL}}{NL} \qquad (2)$$

where; S_{LL} = *Line Loading*

NL = Number of lines coming under feasible feeder

$$Voltage\ Deviation = \frac{\sigma}{\bar{x}} \times 100 \qquad (3)$$

where ; σ *= Standard deviation of the voltages*

$\bar{x}$ *= mean of the voltages*

APPLICATION OF FUZZY RULES

The following rules are applied to evaluate each restoration scheme.

Number of Switching (NS) (figure 1)

If NS is L[#]	Then PLAN is GOOD
If NS is M	Then PLAN is MEDIUM
If NS is H	Then PLAN is POOR

Feeder Loading (FL) (figure 2)

While energising the outage zones it is necessary to ascertain that the backup feeder, which is participating in the restoration process, should not get loaded critically. Lower the loading on the backup feeder, better is the system performance.

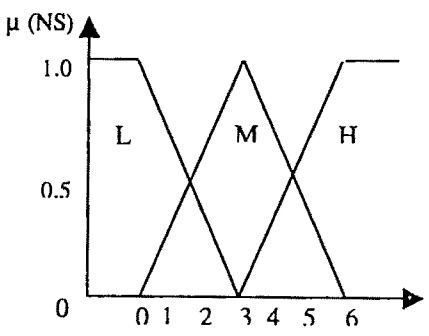

Figure 1 Number of switching rule

[#] L: LOW, M: MID, H: HIGH

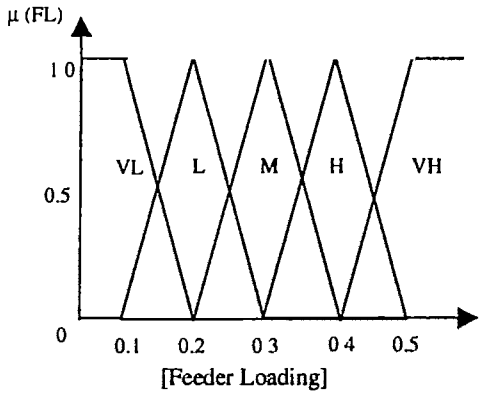

Figure 2 Feeder loading rule

If FL is V_L *	Then PLAN is V_G
If FL is L	Then PLAN is G
If FL is M	Then PLAN is M
If FL is H	Then PLAN is P
If FL is V_H	Then PLAN is V_P

Line Loading (LL) (figure 3)

Line loading is an important factor in determining the capability of the network to remain in the emergency configuration. Higher the line loading, greater the chances of line exceeding their thermal limit, ultimately leading to breakdown of the line.

IF LL is L	Then plan is GOOD
If LL is M	Then plan is MEDIUM
If LL is H	Then plan is POOR

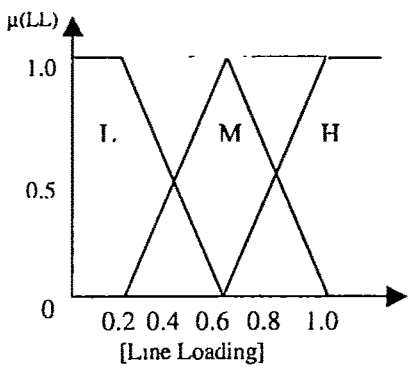

Figure 4 Line loading rule

* V_L VERY LOW, V_G . VERY GOOD
V_H VERY HIGH, V_P: VERY POOR

Voltage Deviation [VD] (figure 5)

Voltage deviation is one among the major factor in deciding the ability of the post restoration scheme. Voltage deviation should be minimal to avoid collapse of the system due to voltage drop induced by heavy loading.

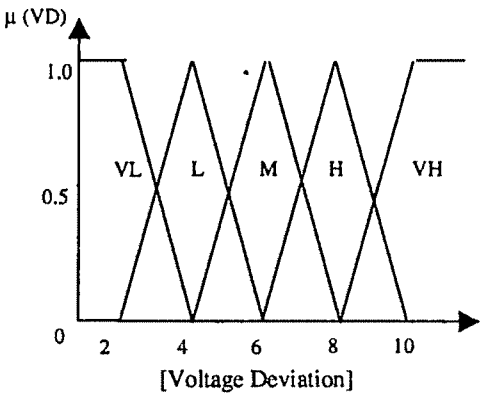

Figure 5 Voltage deviation rule

If VD is V_L	Then PLAN is V_G
If VD is L	Then PLAN is G
If VD is M	Then PLAN is M
If VD is H	Then PLAN is P
If VD is V_H	Then PLAN is V_P

CALCULATION OF PERFORMANCE INDEX

Performance Index (PI) under Defuzzification is calculated based on the weight factors provided for each of the fuzzy criteria.

$$\frac{W_{NS} \times M_{NS} + W_{FL} \times M_{FL} + W_{LL} \times M_{BM} + W_{VD} \times M_{VV}}{M_{NS} + M_{FL} + M_{LL} + M_{VD}}$$

where:

W_{NS}, W_{FL}, W_{LL}, W_{VD} are the weight factors assigned to fuzzy criteria and

M_{NS}, M_{FL}, M_{LL}, M_{VD} are the membership values obtained for each fuzzy criteria.

SYSTEM STUDIED

The proposed method has been successfully tested on a practical 11 kV distribution system comprising of 5 feeders and 40 zones. Figure 5 presents the network configuration.

The solid line indicates the presence of permanent connection between the zones and the feeder. The dotted line indicates tie line connecting adjacent feeders, which are normally kept open.

A. Single Feeder Configuration

With single feeder configuration (SFC), the feeders identified for alternative supply are F1, F3, F4 and F5. These feeders are first subjected to basic constraint, namely feeder spare. In this case as the feeders have sufficient spare, all the feeders are identified as under feasible restoration scheme. As each feeder can handle the outage load with their remaining spare capacity, these four set of alternative plans are selected for further evaluation namely, Number of switching, Feeder loading, Voltage deviation and Line Loading. Table I presents output values for the single feeder configuration scheme. Table II presents the fuzzy evaluation results performed on the crisp values obtained. From Table II it is found that feeder-2 has the highest performance index with weightage factors
NS =0.4; FL = 0.3; L =0.15; VD =0.15.

Table I: Single Feeder configuration

Feeder	NS	FL	LL	VD
1	1	0.956	0.42	3.43
2	1	0.640	0.21	6.77
3	1	0.592	0.35	11.53
4	1	0.712	0.3	10.93

Table II: Fuzzy evaluation for SFC

Feeder	NS	FL	LL	VD	PI
1	0.66	0.50	0.82	0.84	0.66
2	0.66	0.55	0.90	0.85	0.69
3	0.66	0.50	0.60	0.50	0.58
4	0.66	0.60	0.67	0.90	0.68

B. Multiple feeder configuration

Using multiple feeder configuration (MFC) technique where the outage loads can be distributed between two possible feeders, the feeder pairs identified are F1-F3, F1-F4, F1-F5, F3-F4, F3-F5 and F4 -F5. Table III presents the output results and table IV presents fuzzy evaluation and performance index of each plan

Table III: Multiple Feeder Configuration

Feeder	NS	FL	LL	VD
1	3	0.82	0.162	3.82
2		0.24	0.083	1.77
1	3	0.59	0.162	3.82
3		0.24	0.124	1.46
1	3	0.89	0.168	3.53
5		0.26	0.140	1.42
3	3	0.53	0.20	5.30
4		0.20	0.104	1.50
3	3	0.24	0.090	1.74
5		0.57	0.320	8.00
4	3	0.24	0.118	1.46
5		0.57	0.320	8.00

Table IV: Fuzzy evaluation of MFC

Feeder	NS	FL	LL	VD	PI
1	0.92	0.80	0.90	0.93	0.71
2		0.98	0.98	0.99	0.79
1	0.92	0.70	0.90	0.93	0.68
3		0.98	0.91	0.99	0.78
1	0.92	0.81	0.98	0.9	0.73
5		0.98	0.69	0.99	0.75
3	0.92	0.86	0.60	0.65	0.65
4		0.98	0.98	0.99	0.79
3	0.92	0.98	0.98	0.99	0.79
5		0.90	0.99	0.99	0.77
4	0.92	0.98	0.98	0.99	0.79
5		0.90	0.99	0.99	0.77

C. Selection of final restoration plan

Selection of final restoration plan among the generated plans mainly depends on the weightage factors selected. Weightage factors will be selected based on the operator's heuristic and practical considerations. With the weightage factors as mentioned above for this particular case, feeder - 2 in single feeder configuration technique is found to be the best alternative supply feeder to energize the outage zones. In Multiple feeder configuration, feeder pairs 3,5 and 4,5 come out to be best alternative supply to energise the outage zones.

ACKNOWLEDGEMENTS

The Authors greatly acknowledge the suggestions made by Prof. K Parthasarathy, Chief Technical Consultant, PRDC, Bangalore and Dr. R Nagaraja, Managing Director, PRDC Bangalore.

CONCLUSIONS

The proposed technique presents a Fuzzy expert system to solve the uncertainty faced while selecting a feasible plan during restoration process. The main highlights of the proposed techniques are summarised ,

- Basic restoration schemes are generated using single/ multiple feeder configuration technique, taking into consideration all the feasible restoration plans that can exist for a specific problem.
- Heuristic rules will be arrived at with the operator's past experience and decision making ability that he possesses. These rules will be treated as guidelines to solve the restoration problem.
- Once the rules are set, the fuzzy reasoning technique will be able to decide the most preferable plan very quickly and faithfully.

- As the technique is well proven and takes into consideration all the practical constraints in arriving at a feasible solution, it can be applicable to systems of varying complexity.
- There is a possibility to increase the number of fuzzy sets and membership functions to evaluate the restoration scheme more accurately.

REFERENCES

1. K. Aoki, K. Nara, M.Itoh, T. Satch and H. Kuwabara "A new algorithm for service restoration in distribution systems ", IEEE Trans. PD, Vol-4, No3, July 1989.
2. C. C Liu, S.J Lee and S.S Venkata, "An expert system operational aid for restoration and loss reduction of distribution system", IEEE Trans. P S, Vol-3, No 2, May 1988.
3. T. Ananthapadmanabha et.al. 8th National Power Systems Conference, "Knowledge base heuristic expert system for service restoration and system reconfiguration in distribution system", New Delhi, India, December 1994.
4. W.M Shivakumar, T.Ananthapadmanabha, K. Parthasarathy, N. Nagendra, A. D Kulakarni, N. Kumar, " Artificial neural network approach to service restoration in distribution system through network reconfiguration" 11th NPSC, IISc, Bangalore INDIA. December-2000.
5. Y.Y Hsu and H.C. Kuo, "A heuristic based fuzzy reasoning approach for distribution system service restoration", IEEE Trans. PD, Vol-9, No-2, pp. 948-953, April-1994
6. Seung Jae Lee, et.al,"Service Restoration of primary distribution system based on Fuzzy evaluation of multi criteria ", IEEE, Trans. PS Vol-13, No. 3, August 1998.

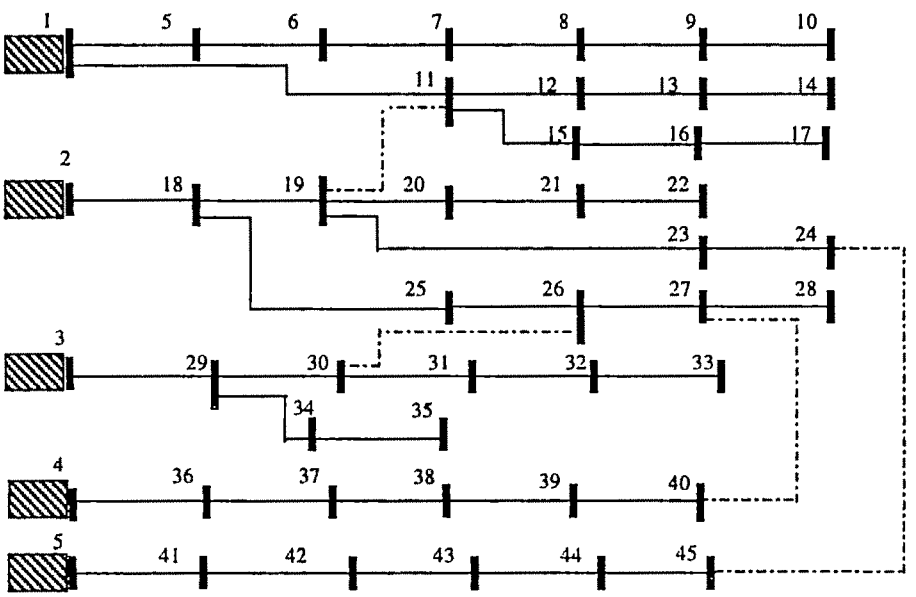

Fig 5 Practical Distribution system

Unit Commitment: A Novel Hybrid Algorithm Integrating the EP, SA and NN

T. Aruldoss Albert Victoire, Thomas Joseph and Sishaj P. Simon
Department of EEE, Karunya Institute of Technology, Coimbatore – 641 114

Abstract

Problems associated with the unit commitment have generally been difficult to solve because of the uncertainty of particular aspects of the problem. Various inconsistencies in the problem also affect the overall economic operation of the electric power system. Unit commitment Problem (UCP) is a complex decision making process because of multiple constraints which must not be violated while finding the optimal or near optimal commitment schedule. This paper discusses a new hybrid algorithm based on integrating the Evolutionary Programming (EP), Simulated Annealing (SA) and Neural Network (NN) methods to solve the Unit commitment problem. . The problem has two sub problems: a combinatorial optimization problem that is solved using combined EP and SA techniques and a nonlinear programming problem is solved using NN technique. It is demonstrated through a numerical example that the proposed algorithm achieves a feasible economical cost of operation of the power system.

INTRODUCTION

The solution of the unit commitment problem is really a complex optimization problem, with different constraints such as fuel constraints, power balance constraints, security constraints and other operating constraints [1]. Because of tremendous expense involved in unit commitment, the utility must determine which generators are the most economical to operate and the combinations of units that should be committed to meet the given load demand. The solution of UCP is really a complex optimization problem [2]. The economics of generation must be based on the variable costs of all generating units having a lower variable cost getting high priority in generation. The exact solution of the UCP can be determined by complete enumeration of all feasible combinations of generating units. Basically the high dimension of the possible solution space is the real difficulty in solving the problem.

Unit commitment is a very difficult optimization problem that includes a number of inequality as well as equality constraints. Major solution methods proposed [3] so far may be classified as:,

(1) Dynamic programming ,
(2) Branch and bound Method ,
(3) Mixed integer programming, and
(4) LaGrangian relaxation.

In the above, methods (1) -(3) are not practical since computational burden and storage requirement dramatically increase with the number of generators. Although the last method is effective to a large power system, it does not necessarily yield an optimal solution and moreover needs fairly long computation time.

Artificial Intelligence tools such as EP, SA, and NN are combined to solve the UCP. EP [4] is capable of determining the global or near global solution. It is based on the basic genetic operation of human chromosomes. It operates with the stochastic mechanics, which combine offspring creation based on the performance of current trial solutions and competition and selection based on successive generations, form a considerably robust scheme for large-scale real-valued combinational optimization.

SA [5] is a powerful technique for solving the combinatorial optimization problems. It has the ability of escaping the local minima by incorporating a probability function in accepting or rejecting new solutions. A main advantage of SA is that it does not need large computer memory. A simple cooling schedule has been used to simplify and speed up the computation.

A NN [6] is trained such that the application of a set of inputs produces an output with respect to the target vector in minimizing the objective function. Here Hopfield

network can be used either as an associative memory for optimization. Here it acts as an optimizer. This network is a fully connected recurrent NN consisting of N neurons. The weights W are placed on the lateral connections between the input and the output of the neuron.

PROBLEM DESCRIPTION

Operating in the present competitive environment, unit commitment has become increasingly important in the power industry, because significant savings can be accrued from sound commitment decisions. To do this a scheduler must indicate which of the generating units are to be committed (on or off) in every time interval during the scheduling time horizon [7]. This decision must take into account load forecast information and the economic implications of the start-up or shutdown of various units. The transition between their commitment states must satisfy the operating (minimum up and down time) constraints. Therefore, there are two types of constraint associated with unit-commitment problems. The first type is the global one, which results from load requirements that couple all the generating units during each time period. The second type of constraint is local, and it represents the different operating restrictions of the individual unit. To maintain a certain degree of reliability, some standby capacity is necessary, that can immediately take over when a running unit breaks down or an unexpected load occurs. Hence the amount of spinning reserve is an important factor in ensuring an uninterrupted power supply. There are several spinning reserve policies that have usually been adopted: a fixed percentage of the fore-cast peak demand at every time period; a variable reserve; a reserve slightly greater than the output of the most heavily loaded unit; or a probabilistic reserve constraint known as unit-commitment risk may be used to ensure better system reliability. However, there should be no significant excess of reserve capacity in an economic commitment. However, spinning reserve constraints only provide the lower bound, since the total capacities of the committed units may not exactly match the load and spinning reserve.

PROBLEM STATEMENT

The overall objective function of the UCP [2] of N generating units for the scheduling time horizon T, is

$$F_T = \sum_{t=1}^{T} \sum_{I=1}^{N} (U_{It}F_{It}(P_{It}) + V_{It}S_{It}) \qquad (1)$$

where,

U_{It} : is status of unit I at hour t.

V_{It} : start-up/shunt-down status of unit I at hout t.

P_{It} : is the output power from unit I at hour t.

F_{It} : is the production cost in a quadratic form.

S_{It} : is the start up cost.

The production cost $F_{It}(P_{It})$, of a committed unit i, is conventionally taken in a quadratic form :

$$F_{It}(P_{It}) = A_i P^2_{It} + B_i P_{It} + C_i \qquad (2)$$

where A_i, B_i, C_i : are the cost function parameters of unit i.

The start up cost S_{It} is a function of the down time of unit i :

$$S_{It} = So_i [\, 1 - D_i \exp(-Toff_i / Tdown_i)] + E_i \qquad (3)$$

where, So_i : is unit i cold start up cost and D_i E_i : are start up cost coefficients for unit i.

The constraints that have been taken into consideration in this work, may be classified into two main groups :

(i) System constraints :

a- load demand constraints:

$$\sum_{i=1}^{N} U_{It}P_{It} = PD_t \text{ ; for all t} \qquad (4)$$

where PD_t : is the system peak demand at hour t (MW).

b- Spinning Reserve

Spinning reserve, R_t, is the total amount of generation capacity available from all units synchronized (spinning) on the system minus the present load demand.

$$\sum_{i=1}^{N} U_{it}Pmax_i \geq (PD_t + R_t) \text{ ; for all t}$$

(ii) Unit constraints :

The constraints on the generating units are

a- generation limits

$$U_{It}Pmin_i \bullet P_{It} \bullet Pmax_i\, U_{it}, \text{ for all t.}$$

where $Pmin_i$, $Pmax_i$ is minimum and maximum generation limits of unit i, respectively.

b- Minimum up/down time

$Toff_i \geq Tdown_i$ for all i,

$Ton_i \geq Tup_i$ for all i,

where $Toff_i$, $Tdown_i$ are unit i minimum up/down time.

Ton_i , Tup_i ,are time periods during which unit i is continuously ON/OFF.

APPLICATION OF SA TO COMBINATORIAL OPTIMIZATION PROBLEM

It is of great advantage to make use of the analogy between the annealing process and the optimization problem. Hence by it is possible for us to solve the combinatorial optimization problem using the SA technique. Following is the test procedure of transition from equilibrium state to another state reaching minimum energy of the system [5].

The analogy of transition is briefed as follows; Solutions in the combinatorial optimization problem are equivalent to the states or configurations of the physical systems. Also the cost of the solution is equivalent to the energy of the state. A control parameter is introduced to play the temperature role in the annealing process.

In applying the SA method to solve the combinatorial optimization problem, the basic idea is to choose a feasible solution at random and then get a neighbor to this solution. A move to this neighbor is performed if either it has a better objective value or, in case the neighbor has a higher objective function value. The effect of decreasing the control parameter is that the probability of accepting an increase in the objective function value decreased during the search.

EVOLUTIONARY PROGRAMMING

The following are the operators of the EP to solve Combinatorial optimization problem [4].

Vector representation : The real valued variables to determined in the EP algorithm are represented as a trial n – dimensional vector p that is associated with the extremum of an objective functional $f(p) : R^n$. Each vector p is an individual of the population to be evolved.

Initialization: An initial population of parent individual p_i $i=1,2,....N_p$, is selected randomly from a feasible range in each dimension. Typically, the distribution of initial trials is uniform.

Creation of offspring : Equal number of offspring p_i , $i=1,2,...N_p$ is generated by adding a gaussian random variable with zero mean and preselected standard deviation to each component of p_i . Therefore the individuals including parents and offspring exist in the competing pool.

Competition and selection : Each individual in the competing pool must stochastically strive against other members of the pool based on the functions $f(p_i)$ and $f(p_i')$. The N_p individuals with the best function values are selected to form a survivor set according to decision rule. The individuals in the survivor set are new parents for the next generation.

Stopping rule : The process of generating new trials and selecting those with the best function values are continued until the function values are not obviously improved or the given count of total generations is reached.

PROPOSED ALGORITHM

The problem is classified into two categories one is a combinatorial optimization problem and the other the nonlinear programming problem. The combinatorial optimization problem is done using the combined EP and SA technique and the nonlinear programming problem is done using the Neural Network method. The flowchart for the Economic Dispatch using NN is shown in fig. 2. Here the objective function is considered to be the energy function of the Hopfield NN. The dynamic equation of the network can be solved using the efficient algorithm, until the network attains a tolerance in error. The algorithm as follows,

(a) Generate the Initial population randomly such away that the individuals should be a feasible solution from the feasible region.
(b) The Economic Dispatch Problem eqn (2) routine using the Neural Networks.
(c) Initiate the weights of the network and input bias.
(d) Calculate output vector with discrete time step.
(e) Update the output vector such a way to force the input variables into the feasible region.
(f) Check for the violation of constraints.
(g) If the constraints are violated then force the slack variables into feasible region & repeat from step (c).
(h) If the constraints are not violated then
(i) Check the cost function values by looking at the present and the immediate previous values. If the difference is below the tolerance level terminate. Otherwise
(j) Recalculate the change in time with new values to the output vector and continue from step (b).
(k) Apply the Evolutionary Programming operators to generate a new set of population by copying the best solution from the current.
(l) Use the SA technique to generate the few new members in the new population as neighbors to randomly selected in the new population.
(m) Determine the fitness function for (1) of each individual in the population.
(n) Terminate when the number of iteration performed since the best solution last changed is greater than a pre-specified number.

The flowchart for the above-proposed algorithm is shown in fig. 1.

NUMERICAL RESULTS

The proposed Integrated Novel algorithm using the NN and EP was tested for the systems with four units [1] and ten

units [2] .The total cost of scheduling of generators obtained with the proposed algorithm is compared with the scheduling costs obtained using the other methods like Dynamic Programming, Fuzzy Logic, SA and GA [1,8-10] . The results obtained using the developed algorithm seems to be efficient and optimal. The results obtained using the proposed algorithm is shown in table 1.

Table 1

Method	System with 4 Units	System with 10 Units
Dynamic Programming	74773.86	-
Fuzzy Logic Analysis	75267.51	-
Genetic Algorithms	-	537686
Simulated Annealing	-	536622
Hybrid EP/SA & NN	74663.63	535723.34

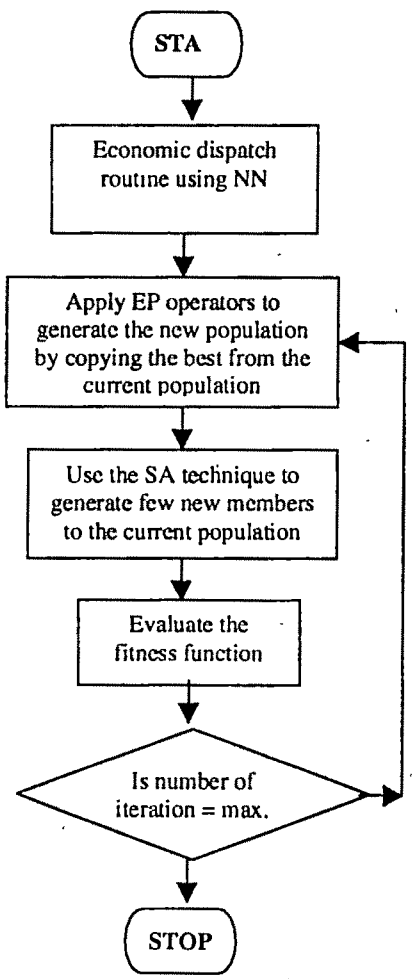
STA
Economic dispatch routine using NN
Apply EP operators to generate the new population by copying the best from the current population
Use the SA technique to generate few new members to the current population
Evaluate the fitness function
Is number of iteration = max.
STOP

Fig 1 Flowchart for the proposed algorithm

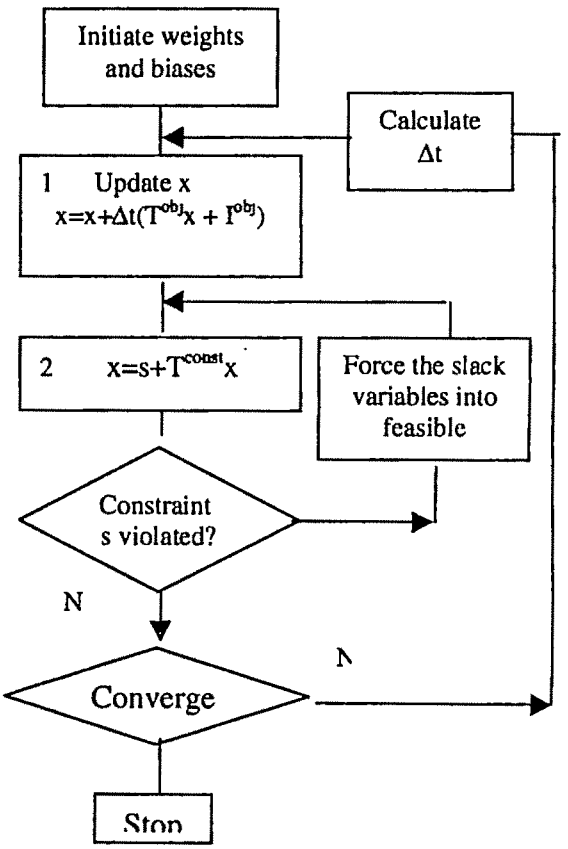

Fig 2 Flowchart for economic dispatch problem using neural network

CONCLUSION

Thus the proposed Hybrid Algorithm is implemented and tested for sample systems. The numerical results show the efficiency of the algorithm. The artificial intelligence techniques NN, EP and SA are combined together to form an efficient algorithm that provides a much faster unit commitment results. Further the algorithm shall be extended for large system with more number of units.

REFERENCE

1. A J. Wood and B. F. Woolenberg " *Power Generation, Operation and control*" –, 1996, John Wiley and Sons, New York.
2. A.H.Manatwy, Youssef L.Abdel-Magid, Shokri Z.Selim "Integrating GA,TS, and SA for the Unit Commitment Problem ", IEEE Trans on PWRS, Vol. 14, Aug '99. pp 829-836.

3. H. Sasaki, M.Watanabe, R.Yokoyama "A solution method of Unit commitment by Artificial Neural Networks",, IEEE Trans. on PWS, Vol. 7, No. 3, August 1992.
4. Davis B. Fogel and Lawrence J. Fogel, "Guest editorial Evolutionary computation", IEEE Trans. On Neural Networks, Vol.5.No.1.Jan 1994.
5. S. Kirkpatrick, C. D. Gelatt and M. P.Vecchi, "Optimization by Simulated Annealing", Science, 1983. page (671-680).
6. A.H.Gee, S.V.B.Aiyer and R.W.Prager "An Analytical Framework for optimizing Neural Networks, Neural Networks Vol. 6, pp 79-97, 1993
7. T. Yalcinoz and M.J. Short "Neural networks Approach for Solving Economic Dispatch Problem with Transmission capacity Constraints", IEEE Trans. on PWS. Vol.13, No.2, May '98.
8. S. Saneifard, N.R. Prasad, H.A. Smolleck "A Fuzzy Logic Approach to Unit Commitment" , IEEE Trans on PWRS, Vol.12, No. 2, May 97.pp 988-995.
9. A.H. Manntawy, Youssef L. Abdel-Magid, and Shokri Z. Selim "A Simulated Annealing Algorithm for Unit Commitment", IEEE Trans. on Power Systems, Vol.13, No. 1, February 1998, pp. 197-204.
10. S.A. Kazarlis, A.G. Bakirtzis, and V. Petridis, "A Genetic Algorithm Solution to the Unit Commitment Problem" IEEE Trans. on Power Systems, Vol.11, No.1, Feb. 1996, pp.83-92

Computer Aided Analysis Of Thermal Generating Unit Commitment By Tabu Search

C.Christober Asir Rajan[+], M. R. Mohan[*], K. Manivannan[+]
[+]Faculty of Electrical Engineering Department, Pondicherry Engg. College, Pondicherry – 605014
[*]School of Electrical Engineering, Anna University, Chennai – 600025, India.
E-mail: asir_70@hotmail.com

Abstract

AN application of the tabu search (TS) method to solve the unit commitment problem (UCP) is presented. The TS seeks to counter the danger of entrapment at a local optimum by incorporating a memory structure that forbids or penalizes certain moves that would return to recently visited solutions. New rules for randomly generating feasible solutions for the UCP are introduced. The problem is divided into two sub - problems: a combinatorial optimization problem and a non-linear programming problem. The former is solved using the tabu search algorithm (TSA) while the latter problem is solved via a quadratic programming routine. Numerical results show an improvement in the solution cost compared to previously obtained results. The effectiveness of the proposed approach is demonstrated by thermal unit commitment of Neyveli Thermal Power Station in Tamil Nadu. It is concluded from the results that the proposed approach is very effective in reaching proper unit commitment.

Keywords: Unit commitment, tabu search

INTRODUCTION

Unit commitment is the problem of selecting the generating units to be put into service during a scheduling period and for how long. The committed units must meet the system load and reserve requirements at minimum operating cost, subject to a variety of constraints. Unit commitment is an important optimization task in the daily operating planning of power system. The economic dispatch problem (EDP) is to optimally allocate the load demand among the running units while satisfying the power balance equations and unit operating limits.

TS is a powerful optimization procedure that has been successfully applied to a number of combinatorial optimization problems. It has the ability to avoid entrapment in local minima. TS employ a flexible memory system (in contrast to 'memory less' systems, such as SA and GA, and rigid memory system such as in branch - and - bound). Specific attention is given to the short - term memory component of TS, which has provided solutions superior to the best obtained with other methods for a variety of problems. TS also has many strong features including:

- Finding a high quality solution that does not strong depend on the choice of the initial solution
- Not needing a complicated mathematical model of the problem under study. Hence, problems that are difficult to formulate can be easily implemented
- Ability to start with any given solution and try to improve it. This feature could be utilized to improve solution output from other sub - optimal or heuristic methods.

In this paper we propose a new UCP algorithm based on the TS method. New rules for randomly generating feasible solutions are also introduced. The combinatorial optimization sub - problem is solved using the TSA while EDP is solved via a quadratic programming routine. Different criteria for constructing the tabu list restrictions for the UCP are implemented and compared. Several examples are solved to test the developed computer model. The results show an improvement in the quality of obtained solutions compared with previous results. In the application on Neyveli Thermal Power System Unit – II shows that we can find the optimal solution effectively.

PROBLEM FORMULATION

The objective is to find the generation scheduling such that the total operating cost can be minimized, when subjected to a variety of constraints. In the unit commitment problem under consideration, an interesting solution would be minimizing the total operating cost of the generating units with several constraints being satisfied. The major component of the operating cost, for thermal and nuclear units, is the power production cost of

the committed units and this is given in a quadratic form is given in equation (1).

$$F_{it}(P_{it}) = A_i P^2_{it} + B_i P_{it} + C_i \quad Rs./hr \qquad (1)$$

Where
A_i, B_i, C_i ~ the cost function parameters of unit i (Rs./MW hr.,Rs./MW hr.,Rs./ hr.)
$F_{it}(P_{it})$ ~ production cost of unit i at a time t (Rs.hr.)
P_{it} ~ output power from unit i at time t (MW)

The start up cost depends upon the down time of the unit, which can vary from a maximum value, when the unit i is started from cold state, to a much smaller value, if the unit i is turned off recently. The start up cost calculation depends upon the treatment method for the thermal unit during down time periods. The entire procedure for the calculation of start up cost is formulated in the appendix section. The overall objective function of the UCP is given in equation (2).

$$F_T = \sum_{t=1}^{T} \sum_{i=1}^{N} (F_{it}(P_{it}) U_{it} + S_{it} V_{it}) \; Rs./hr. \qquad (2)$$

Where
U_{it} ~ unit i status at hour t = 1 (if unit is ON) = 0 (if unit is OFF)
V_{it} ~ unit i start up / shut down status at hour t =1 if the unit is started at hour t and 0 otherwise.
F_T ~ total operating cost over the scheduled horizon
S_{it} ~ start up cost of unit i at hour t

Constraints

Depending on the nature of the power system under study, the unit commitment problem is subjected to many constraints the main being the load balance constraints and the spinning reserve constraints. The other constraints include the thermal constraints, fuel constraints, security constraints etc.

1] Load Balance Constraints

The real power generated must be sufficient enough to meet the load demand and must satisfy the following equation given in (3).

$$\sum_{i=1}^{N} P_{it} U_{it} = PD_t \qquad (3)$$

Where
PD_t ~ system peak demand at hour t (MW)
N ~ number of available generating units

2] Spinning Reserve Constraints

The spinning reserve is the total amount of the real power generation available from all synchronized units minus the present load plus the losses. The reserve is considered to be a pre specified amount or a given percentage of the forecasted peak demand. It must be sufficient enough to meet the loss of the most heavily loaded unit in the system. This has to satisfy the equation given in (4).

$$\sum_{i=1}^{N} P_{max_i} U_{it} >= (PD_t + R_t); \; 1<=t<=T \qquad (4)$$

where
T ~ scheduled time horizon (24 hrs.)

3] Thermal Constraints

The temperature and pressure of the thermal units vary very gradually and the units must be synchronized before they are brought online. A time period of even 1 hour is considered as the minimum down time of the units. There are certain factors, which govern the thermal constraints like minimum up time, min. down time and the crew constraints.

a] Minimum Up Time:

If the units have already been shut down, then there is a minimum time before which they can be restarted.

$$Ton_i >= T up_i$$

Where
Ton_i ~ duration for which unit i is continuously ON
Tup_i ~ unit i minimum up time

b] Minimum Down Time:

If all the units are running already, then they cannot be shut down simultaneously.

$$T off_i >= T down_i$$

Where
$T down_i$ ~ unit i minimum down time
$T off_i$ ~ duration for which unit i is continuously OFF

c] Must Run Units:

Generally in a power system, some of the units are given a must run status in order to provide voltage support for the network.

TABU SEARCH

A. Over view

In general terms, tabu search (TS) is an iterative improvement procedure that starts from some initial feasible solution and attempts to determine a better solution in the manner of a greatest – decent algorithm. However, Ts is characterized by an ability to escape local optima by using a short-term memory of recent solutions. Moreover, TS permits backtracking to previous solutions, which may ultimately lead, via a different direction, to better solutions. The main two components of a TSA are the tabu list (TL) restrictions and the aspiration level (AL) of the solution associated with these restrictions.

B. Tabu List Restrictions

TS may be viewed as a 'meta-heuristic' superimposed on another heuristic. The approach is designed to transcend local optimality by the strategy of forbidding certain moves. The purpose of classifying certain move as forbidden is basically to prevent cycling. Moves that hold tabu status are generally a small fraction of those available, and a move loses its tabu status to become once again accessible after a relatively short time.

The choice of appropriate types of tabu restrictions list, TL, depends on the problem under study. A fraction that utilizes historical information from the search process, extending up to 'Z' iterations in the past, where 'Z' can be fixed or variable depending on the application or stage of search. The TL restrictions could be stated directly as a given change of variables or indirectly as a set of logical relationships or linear inequalities. Use of these two approaches depends on the size of TL for the problem under study.

TLs are managed by recording moves in the order in which they are made. Each time a new element is added to the bottom of a list, the oldest element on the list is dropped from the top. The TL is designed to ensure the elimination of cycles of length equal to the TL size. Empirically, TL sizes that provide good results often grow with the size of the problem and stronger restrictions are generally coupled with smaller lists.

The way to identify a good TL size for a given problem class and choice of tabu restrictions is simply to watch for the occurrence of cycling when the size is too small and the deterioration in solution quality when the size is too large. Best sizes lie in an intermediate range between these extremes. In some applications a simple choice of 'Z' in a range centered on 7 seems to be quite effective.

C. Aspiration Criterion

Another key issue of TS arises when the move under consideration has been found to be tabu. The tabu status of a move is not absolute, but can be overruled if certain conditions are met, expressed in the form of aspiration level (AL). If appropriate aspiration criterion is satisfied, the move will be accepted in spite of the tabu classification. Roughly speaking, AL is designed to override tabu status if a move is 'good enough'. Different forms of aspiration criteria are used in the literature. The one we use in this study is to override the tabu status if the tabued move yields a solution, which has better objective function than the one obtained earlier for the same move. Consequently, the AL associated with each move in the TL is equal to the value of the objective function obtained when performing that move. The effectiveness of using aspiration criterion is to add some flexibility in the tabu search by directing the search towards the attractive moves.

D. Stopping Criterion

There may be several stopping criterions for the search. For this implementation the search is stopped if the following conditions are satisfied:

- The load balance constraints are satisfied
- The spinning reserve constraints are satisfied

TABU SEARCH ALGORITHM FOR UNIT COMMITMENT

A. Overview

In solving the UCP, two types of variables need to be determined. The unit's status variables U and V, which are integer variables and the units, output power variables P that are continuous variables. The problem can then be decomposed into two sub problems, a combinatorial problem in U and V and a non linear optimization problem in P. TS is used to solve the combinatorial optimization and the nonlinear optimization is solved via a quadratic programming routine. The proposed algorithm contains three major steps:

- First, generating randomly feasible trail solutions
- Second, calculating the objective function of the given solution by solving the EDP
- Third, applying the TS procedures to accept or reject the solution in hand.

B. Tabu Search Algorithm for UCP

Step(0): By optimum allocation find the initial feasible solution (U_i, V_i).

Step(1): Demand is taken as the control parameter.
Step(2): Generate the trial solution.
Step(3): Calculate the total operating cost, F_t, as the summation of running cost and Start up – shut down cost.

C. Generating Trial Solution

Step(1): Generate randomly a unit i ~ UD(1,N), and a time instant t ~ UD(1,T).
Step(2): If unit i at time t is OFF, then go to Step(3) to consider switching it ON starting from t.
Step(3): Perform the following sub steps:
- **a]** Move backward in time, to find the nearest shutdown instant, $Tshut_i$.
- **b]** Move forward in time, to find the nearest start up instant, $Tstart_i$.
- **c]** If $Toff_i = Tdown_i$, set $L = Toff_i$ and set $t = Tshut_i$. Go to (f).
- **d]** If $Toff_i > Tdown_i$, then
  - ¬ Generate L ~ UD (1, $Toff_i - Tdown_i$), and set $t = Tshut_i$.
  - ¬ If $L = Toff_i - Tdown_i$, then set $L = Toff_i$. Go to (f).
- **f]** Turn unit i ON for the times t + k, k = 0,1,.....L-1

Step(4): Perform the following sub steps:
- **a]** Move forward in time, to find the nearest shutdown instant, $Tshut_i$.
- **b]** Move backward in time, to find the nearest start – up instant, $Tstart_i$.
- **c]** If $Ton_i = Tup_i$, set $L = Ton_i$ and set $t = Tstart_i$. Go to (f).
- **d]** If $Ton_i > Tup_i$, then
  - ¬ Generate L ~UD (1, $Ton_i - Tup_i$), and set $t = Tstart_i$.
  - ¬ If $L = Ton_i - Tup_i$, then set $L = Ton_i$. Go to (f).
- **f]** Turn unit i OFF for the times t+k, k=0,1,.....L-1

Step(5): Check the reserve constraints, load demand constraints for each hour.
- **a]** If satisfied, go to the next hour for Checking the same.
- **b]** Else, decrement the demand for that instant and again generate the trial solution from this instant of time.

Step(6): Trace the optimal schedule.

D. Generating an Initial Solution

The TSA requires a starting feasible schedule, which satisfies all the system and units constraints. This schedule is randomly generated. The following algorithm is used for finding this starting solution:

Step(1): Set U = V= P = 0, Set t = 1
Step(2): Do the following sub steps:
Generate randomly a unit i, i ~ UD (1,N) If the unit i at hour t is OFF then go to Step(3), otherwise go to Step(1) to choose another unit
Step(3): Follow the procedure in Step(4), to consider switching this unit ON starting from hour t
Step(4): If t = T, go to Step(50, otherwise set t = t+1 and go to Step(2)
Step(5): Check the reserve constraints for all hours. Repeat the steps (2) and (3) for the hours at which the constraints are not satisfied

E. Operating Cost Calculation

Once a trail solution is obtained, the corresponding total operating cost is determined. Since the production cost is a quadratic function, the EDP is solved using a quadratic programming routine. The start – up cost is then calculated for the given schedule.

CASE STUDY

In order to test the model, the Neyveli Thermal Power station Unit - II in Tamil Nadu has considered as case study. It contains 7 units. The scheduling time horizon for the case is 24 hours. Based on the TSA and the proposed rules for generating random that solutions, a computer program has been written. The program offers different choices for finding trail solutions, e.g. completely random, pseudo random, and a mix of both with certain probabilities. To illustrate the convergence trend in the TS method a plot of the current and best solutions with the iteration number for the case study is given in Fig. 1. As shown, the current solution has no trend, as the TS criterion is to accept any non - tabu solution regardless of its objective function value. Basically this is the main idea behind the ability of the TS method of escaping local minima.

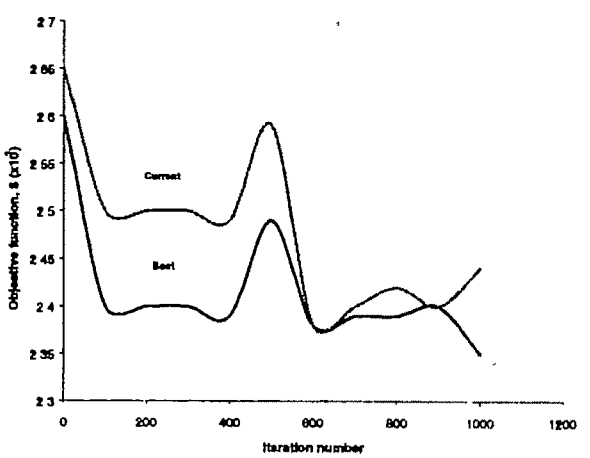

Fig. 1. Best and Current solutions versus iteration number

On the other hand the best solution is improving very fast at the beginning of the search while the improvement becomes slower at the end of the search. Table 1 shows the daily operating costs for the proposed four approaches of TL types as applied to case study. In all cases we started with the same initial feasible solution and the same random seed. It is obvious that the results of approach 4 are best. The reason is that the attributes of moves are fully recorded; hence the search becomes more precise which prevents cycling during the age of tabu list.

Table 1. Comparison of different approaches of TL types using TL size of 7

Approach No.	1	2	3	4
TL dimension	ZX1	ZX2	ZX3	ZX4
Cost $	240387	240112	240025	239450

Table 2 shows the daily operating costs obtained, using approach 4, at different tabu sizes starting with the same initial solution. The best results for this case are obtained at a tabu size value of 7 as shown in the table. Hence for the rest of the presented results the TL is created according to approach 4 and of size 7.

Table 2. Comparison of different tabu list sizes using approach 4

TL size	9	11	25	35	45
Cost $	249476	238490	239470	239022	240230

Table 3 presents the comparison of results for case study solved by Legrangian relaxation (LR), integer programming (IP), and the TSA. The results show the improvement achieved by TSA algorithm over both IP and LR results.

Table 3. Comparison of different algorithms with the proposed TSA

Solution Type	TSA	LR	IP
Total Cost ($)	239430	240952	306570
% Saving	0.575	0	-
No. of Iterations	840	-	-

Tables 4, 5 & 6 show detailed results for the case study. Table 4 presents the initial starting solution for the results in Tables 5 and 6, in which all units are ON for most of the time. It is obvious that this initial schedule is very far from the optimal one. The cost of this initial schedule is $ 407483.93, whereas that of the final solution obtained is $ 239430. Table 5 shows the load sharing among the committed units in the 24 hours and it is found that unit III is OFF all hours. Table 6 gives the hourly load demand, and the corresponding committed capacities, economic dispatch costs, start-up costs, and total operating cost. The optimal unit commitment table for the case study is shown in Table 7 along with the load demand and the hourly operating costs.

Table 4. Power sharing (MW) of the initial schedule

Hour	Unit Number						
	1	2	3	4	5	6	7
1	186	204	149	193	209	130	203
2	186	206	147	192	207	145	202
3	188	205	150	192	200	154	196
4	188	207	150	191	203	151	195
5	195	207	150	192	205	154	195
6	191	202	150	193	208	175	195
7	194	203	147	195	211	176	199
8	186	200	150	190	209	180	194
9	202	201	150	194	211	154	207
10	198	208	150	197	207	185	212
11	201	202	142	199	202	184	212
12	197	209	139	198	199	178	205
13	193	208	146	191	207	178	207
14	198	202	142	195	210	178	210
15	202	205	139	191	210	176	209
16	205	199	150	186	208	174	205
17	204	203	148	153	210	164	192
18	202	204	142	107	212	172	212
19	197	203	150	110	208	170	209
20	194	194	150	177	210	170	202
21	207	199	150	193	210	170	206
22	210	203	139	186	213	177	210
23	201	190	150	189	206	175	210
24	215	194	149	192	202	175	210

Table 5. Power sharing (MW) of the final schedule

Hour	Unit Number					
	1	2	4	5	6	7
1	186	0	0	209	0	203
2	186	0	0	207	0	202
3	188	0	0	200	0	196
4	188	0	0	203	0	195
5	195	0	0	205	0	195
6	191	202	0	208	0	195
7	194	203	195	211	0	199
8	186	200	190	209	180	194
9	202	201	194	211	154	207
10	198	208	197	207	185	212
11	201	202	199	202	184	212
12	197	209	198	199	178	205
13	193	208	191	207	178	207
14	198	202	195	210	178	210
15	202	205	191	210	176	209
16	205	199	186	208	174	205
17	204	203	153	210	164	192
18	202	204	107	212	172	212
19	197	203	110	208	170	209
20	194	194	177	210	170	202
21	207	0	193	210	170	206
22	210	0	0	213	177	210
23	201	0	0	206	175	210
24	215	0	0	202	175	0

Table 6. Load (MW), capacities (MW), hourly costs ($)

Hour	Load	Capacity	ED - cost	ST - cost	T – cost
1	598.0	620.0	7670.0	-	7670.0
2	595.0	620.0	7540.0	-	7540.0
3	584.0	615.0	6345.0	-	6345.0
4	586.0	615.0	6124.0	-	6124.0
5	595.0	620.0	8458.3	-	8458.3
6	796.0	840.0	11445.0	-	11445.0
7	1002.0	1050.0	17504.0	-	17504.0
8	1159.0	1200.0	19050.1	-	19050.1
9	1169.0	1200.0	21475.0	-	21475.0
10	1207.0	1250.0	23785.0	-	23785.0
11	1200.0	1245.0	25478.0	-	25478.0
12	1186.0	1225.0	26242.0	-	26242.0
13	1184.0	1224.0	24965.0	-	24965.0
14	1193.0	1230.0	19607.0	-	19607.0
15	1193.0	1230.0	17592.0	1050.0	18642.0
16	1177.0	1205.0	15918.0	-	15918.0
17	1126.0	1050.0	17401.0	2150.0	19551.0
18	1109.0	1040.0	22503.0	2250.0	24753.0
19	1097 0	1135.0	23119.0	-	23119.0
20	1147.0	1195.0	18347.0	2222.0	20569.0
21	986.0	1100.0	12748.0	8475.0	21223.0
22	810.0	985.0	10497.0	-	10497.0
23	792.0	840.0	9545.0	-	9545.0
24	592.0	615.0	9420.0	-	9420.0

Table 7. UCT, load demand (MW), hourly cost ($)

Hour	Load	Unit Number							T – cost
		1	2	3	4	5	6	7	
1	598.0	1	0	0	0	1	0	1	7670.00
2	595.0	1	0	0	0	1	0	1	7540.00
3	584.0	1	0	0	0	1	0	1	6345.00
4	586.0	1	0	0	0	1	0	1	6124.00
5	595.0	1	0	0	0	1	0	1	8458.30
6	796.0	1	1	0	0	1	0	1	11445.0
7	1002.0	1	1	0	1	1	0	1	17504.0
8	1159.0	1	1	0	1	1	1	1	19050.1
9	1169.0	1	1	0	1	1	1	1	21475.0
10	1207.0	1	1	0	1	1	1	1	23785.0
11	1200.0	1	1	0	1	1	1	1	25478.0
12	1186.0	1	1	0	1	1	1	1	26242.0
13	1184.0	1	1	0	1	1	1	1	24965.0
14	1193.0	1	1	0	1	1	1	1	19607.0
15	1193.0	1	1	0	1	1	1	1	18642.0
16	1177.0	1	1	0	1	1	1	1	15918.0
17	1126.0	1	1	0	1	1	1	1	19551.0
18	1109.0	1	1	0	1	1	1	1	24753.0
19	1097.0	1	1	0	1	1	1	1	23119.0
20	1147.0	1	1	0	1	1	1	1	20569.0
21	986.0	1	0	0	1	1	1	1	21223.0
22	810.0	1	0	0	0	1	1	1	10497.0
23	792.0	1	0	0	0	1	1	1	9545.0
24	592.0	1	0	0	0	1	1	0	9420.0

CONCLUSION

We proposed new TS - based algorithm for the UCP. The problem is highly combinatorial. Even moderate size problems are currently being solved with great difficulty. The proposed algorithm is based on the short - term memory procedure of the TS method. TS are characterized by its ability to escape local optima by using a short - term memory of recent moves. Moreover, TS permits backtracking to previous solutions, which may ultimately lead, via, a different direction, to better solutions.

Different approaches for constructing the tabu list for the UCP are presented and tested. Different tabu list sizes are tried to find the most reasonable one for the case study. The successful implementation presented in this paper highlights the importance of tabu search approach as a powerful tool for solving difficult combinatorial optimization problems. Better solutions are also expected when employing sophisticated tabu search procedures. These include the use of intermediate and long - term memory, which could lead to new unexplored solutions to the problem. Probabilistic tabu search procedures could also be used. Further work in this area may include parallel processing of the TS, thus reducing the computation time, or exploring a wider solution space.

REFERENCES

1. Wood.A.J. And Woolenberg.B.F. : "Power Generation and Control", John Wiley and Sons. New York, 1996, 2nd Edn.
2. Tong, S.K., Shahidepour, S.M. and Ouyang.Z. : "a Heuristic Short - Term Unit Commitment", IEEE Trans. Power Syst., 1991, 6, (3), pp. 1210-1216.
3. Ouyang.Z., and Shahidepour, S. M. : " Short - Term Unit Commitment Expert System", Electr. Power Syst. Res., 1990, 20, pp. 1-13.
4. Bard, J.F.: "Short - Term Scheduling of Thermal - Electric Generators using Lagrangian Relaxation", Oper. Res. 1988, 36, (5), pp. 756-766.
5. Pang.C.K. And Chen.H.C.: "Optimal Short - Term Thermal Unit Commitment", IEEE Trans. 1976, PAS-95, pp. 1336-1341.
6. Ayoub, A.K., And Patton, A.D.: "Optimal Thermal Generating Unit Commitment", IEEE Trans. 1971, PAS-90, (4), pp. 1752-1756.
7. Mantamy.A.H.: "Optimal Scheduling of Thermal Generation in Electric Power System", A Master Thesis, Ain Shams University, Cario, Egypt.
8. A. Turgeon , " Optimal Scheduling of Thermal Generating Units" , IEEE Transactions on Automatic Control , Vol. AC -23 , No:6 . 1978 ,.
9. C.K.Prag . G.B.Sheble , F.Albuyeh , " Evaluation of Dynamic Programming Based Methods and Multiple Area Representation for Thermal Unit Commitment ", *IEEE Transactions on PAS*, Vol.6 , No.3 , 1981, pp1212-1218.
10. Cohen.A.I.Sherket.V.R., "Optimization - Based Methods for Operations scheduling", Proceedings of the IEEE, Vol. 75, No. 12, Dec. 1987, pp. 1574-1581.

A Multi Objective Bi-Directional Search Algorithm for Distribution Network Optimization

T. Ananthapadmanabha[1], W. M. Shivakumar[2], A. D. Kulkarni[1], N. Nagendra[3], M. S. Nagaraj[4], S. B. Shivakumar[5]

[1]The National Institute of Engineering, Mysore, Karnataka, India

[2]Karnataka Power Transmission Corporation Ltd, Bangalore, Karnataka, India

[3]Power Research and Development Consultants Pvt. Ltd., Bangalore, Karnataka, India.

[4]Bapuji Institute of Engineering and Technology, Davangere, Karnataka, India

[5]Sri Jagadguru Murugarajendra Institute of Technology, Chitradurga, Karnataka, India

Abstract

In this paper, a Multi Objective Bi-directional Algorithm is developed for determining a restoration plan for radial distribution system by network optimization. The proposed algorithm is based on the concept of local network using relaxation technique and multi-solution reconfiguration algorithm through bi-directional search. Feeder-load matrix minimum technique is utilised to determine the basic and composite variants of alternate supply depending on the number of switching. These variants are ranked according to the specific criteria. The outcome of the algorithm will be in the form of ranked list of alternate supply variants based on which the operator can select the best plan for restoring the network.

INTRODUCTION

Power system is becoming increasingly complex with increasing power demand. However, the generation is not sufficient to meet the increasing demand. The transmission & distribution loss in Karnataka (India) is about 26% out of which 10-15 % is contributed from the distribution system. Although electric utilities constantly strive to maintain the stability and integrity of the power system, absolute security can never be guaranteed. A catastrophic sequence of events that defeats the preventive measures and overcome the corrective actions will occasionally unfold and cause a collapse of the entire power system. If such a black out occurs, electrical service must be restored as soon as possible to minimise the economic losses, inconvenience to the customers and the direct cost to the supply authority. The main objective in distribution system management is to ensure safer, cheaper and more reliable electrical power to the customer and for this purpose service restoration and network reconfiguration have become important to power engineers.

Various techniques have been proposed to solve the problem of service restoration. Karen Nan Miu [1] proposed fast restoration for large scale distribution system. He suggested three phase power flow analysis with ranking indices to determine the final restoration strategy. Expert system approach to service restoration [2] by Chen-ching Liu discussed the implementation of group restoration and zone restoration. As the problem of determining restoration plan for a distribution network is multi-objective, Dragan .S Popovic and Rade M. Ciric [3] presented a multi-objective algorithm, that produces a number of high quality variants of alternate supply.

This paper proposes a bi-directional search technique with feeder load matrix minimum technique to obtain the desired plan very quickly decreasing the restoration time to a minimum extent.

PROPOSED METHODOLOGY

The proposed methodology starts with reducing the dimension of the problem by determining local network using relaxation technique. This network represents a part of the distribution system where possibility of restoration is to be investigated.

Within the local network defined, a selection of variants of alternate supply is made using multi - solution reconfiguration algorithm The algorithm is based on a decision tree using a bi-directional search. Here a feeder load (FL) matrix is developed in which the shortest path from adjacent feeder to all the zones of the network is

determined. The size of the matrix depends upon the number of feeders and the number of zones in the distribution system. The spare capacity (in MVA) of all feeders and load in each zone (in MVA) are incorporated in FL matrix. Using matrix minimum technique the FL matrix can be effectively analysed to decide the possibility of energizing all the effected load points, through various feeders having sufficient spare capacity. Here as opposed to other algorithms, which renders a solution involving one basic radial configuration, the proposed algorithm produces a specified number of "high quality" radial configuration which is having least deviation from the basic radial configuration.

After obtaining a set of variants of alternate supply, ranking list of selected variants is made according to the user specified criteria. The choice of the criteria is directly dependent on the problem, on which the restoration is supported to overcome. The final output of the algorithm is a ranking list of alternate supplies in distribution system and switching operation plans for their performance. In addition, the algorithm also takes account of unsuccessful switching operation in performing chosen variants. Ranking of all variants is done based on user criteria or one of the combinations as below

a) Switching operation cost.
b) Critical power reserve of the transformer
c) Critical current reserve of the supply transformer
d) Critical voltage drop.

LOCAL NETWORK FORMATION

The term local network refers to the network surrounding the outage area. The main idea in determining the size of the local network is to access the number of feeders necessary to take over the load from the outage zones. Determination of feeders belonging to the local network is done in iterative circles. In the first circle, all the feeders, which have normally open (NO) switches towards outage area, are included in the network. These feeders form the primary feeders for supplying the outage loads. The proposed bi-directional search algorithm is applied to find these feeders forming the first circle. The procedure continues to the next circle which comprises of tie switches, that can feed the outage load through the primary ties.

By expanding the local network, it is possible to choose a variety of alternate supplies, which is carried out at a higher switching operation cost. However, in certain cases it is more efficient to use a variant with a smaller number of switching operations along with a small reduction of load in outage zone.

SEARCH ALGORITHM

The algorithm called as " The maximum paths algorithm "[5] finds a set of paths for the source node (feeder) to the terminal node (zone). This algorithm incorporates " bi-directional search technique" to find the individual candidates for various paths. A bi-directional search technique is one that emanates from source and destination nodes simultaneously.

Step 1: Read the network and form the adjacency matrix [G_{st}] .The adjacency matrix is formed as follows G[i][j] =G[j][i] =1, if i^{th} node is connected to the j^{th} node else , G[i][j] =G[j][i] =0

Step 2: Identify the source node 's' and terminal node 't': s= F_i for i =1,2...m, where m= total number of feeders. t= Z_i for i= 1,2...n (Total number of zones)

Step 3: Formation of T_k and S_k, where k= number of intermediate nodes. T_k consists of nodes corresponding to the non-zero elements of row 's' in G_{st} and $T^i_k(p)$ denotes element p of list i in T_k where, 1<=p<k. S_k consists of nodes corresponding to non-zero elements of the column 't' and $S^j_k(p)$ denotes element p of list 'j' in S_k where 1<=p<k.

Step 4: Put k =1 and compare the sets T_k and S_k; If $T^i_k(1) = S^j_k(1)$ for some i and j then there is a path of length 2 defined by P = [s, $t^i_k(1)$,t] ELSE go to next step.

Step 5: Increment k and form the sets T_{k+1} and S_{k+1}: On the observation of the corresponding rows and columns of the respective elements of sets T_k and S_k, the subsets of subsequent sets T_{k+1} and S_{k+1} are formed

Step 6: Compare the sets T_{k+1} and S_k: For path of length 3 if $T^i_{k+1}(2) = S^j_k(1)$ for some i and j then there is a path defined by,

$$P = [s, T^i_k(1), T^i_{k+1}(2), t]$$

Step 7: Compare the sets T_{k+1} and S_{k+1} :
IF $T^i_{k+1}(2) = S^j_{k+1}(1)$ for some i and j, then path of length 4 is defined by,

$$P = [s, T^i_{k+1}(1), T^i_{k+1}(2), S^j_{k+1}(2)\ t].$$

Step 8: This path finding sequential procedure is continued until the path of maximum length is obtained having k intermediate nodes.

Step 9: Selection of optimal set of paths: The length of each path is found out by adding individual zone lengths. These paths are stored in the F-L matrix.

FEEDER -LOAD MATRIX

Feeder - Load Matrix is m x n matrix with 'm' feeders and n zones. Table I presents the feeder load matrix. The element NS_{ij} of the F- L matrix represents the number of switching operations required to feed the outage zone j from feeder i. Number of switching = 1, indicates the primary feeders or the feeders which are adjacent to the outage load which are termed as basic variants of alternative supply.

The technique starts with selection of the feeder with minimum switching operation. These feeders will be evaluated based on the ranking index as suggested. Once the basic variant search is completed, 2^{nd} order variants

(Number of switching > 1) will be selected which represents the tie switches which encircles the basic variants.

Table I: Feeder Load Matrix

Zone / Feeder	Z1	Z2	Zj	Zn	Feeder Spare
F_1	NS_{11}	NS_{12}	...	NS_{1n}	FS_1
F_2	NS_{21}	NS_{22}	...	NS_{2n}	FS_2
.					
.					
.					
Fi	NS_{i1}	NS_{i2}	...	NS_{in}	FS_i
.					
Fm	NS_{m1}	NS_{m2}	...	NS_{mn}	FS_m
Zone Load	ZL_1	ZL_2	...	Z_n	

RANKING OF VARIANTS

(1) Switching operational costs: It is defined by the following expression

$$IC^h_{sw} = \Sigma N_{si} \times C_{si} \qquad (1)$$

where, C_{si} is the cost of i^{th} switching operation. The cost of each switching operation can be introduced fictitiously depending on whether it is a remotely operated switch or not.

(2) Critical power reserve of the supply transformer
It is defined for the h^{th} variant as,

$$I^h_{CPR} = \frac{S_{Rated} - S_{Actual}}{S_{Rated}} \qquad (2)$$

where,
S_{Rated} = Rated capacity of the primary feeder
S_{Actual} = Loading of the feeder after energizing the outage loads

(3) Critical current reserve of the feeder in the h^{th} variant is given by,

$$I^h_{CCR} = \frac{I_{Rated} - I_{Actual}}{I_{Rated}} \qquad (3)$$

where,
I_{Rated} = rated current of the feeder
$I_{Ractual}$ = actual current in the feeder
The expression (3) is defined as reciprocal value of the minimum relative values of the margin between the nominal and real current of the feeder. Lower values of index indicate greater current reserve in the feeder, meaning higher security in the operating state.

(4) Critical voltage drop: This is defined by the following expression

$$I^h v_{CVD} = \underset{k=1,..i_n}{} \left(\frac{V_S - V_{ik}}{V_S} \right) \qquad (4)$$

where,
V_s = Voltage at the root (source) and
V_{ik} =Actual voltage of k^{th} distribution transformer at the i^{th} feeder in the h^{th} variant.
Expression (4) is defined as the value of the maximum relative voltage drop between the root and one of the distribution transformer. Lower value of index indicated a lower voltage drop meaning a higher quality voltage profile.

CALCULATION OF RESULTANT INDEX

Resultant Index (IR) is calculated by the following expression

$$IR = IC_{SW} \times w_1 + I_{CPR} \times w_2 + I_{CCR} \times w_3 + Iv_{cvd} \times w_4$$

Where, w_1, w_2, w_3, w_4 are the weightage factors for each index. The variant, which has the lowest index, will be selected to energise the outage zones.

SYSTEM STUDIED

The proposed method has been successfully tested on a practical 11 kV distribution system with 41 zones and 5 feeders. The network diagram is shown in Figure -1. With fault at section-19 - 20, the outage zones identified are Z19 -Z28. Using bi-directional technique, from the outage zones possible paths to the adjacent tie switches (1st circle - basic variants) were found out and incorporated in Feeder - Load matrix. In the present case the basic variants are 13 -18, 7-24, 25-32 and 25- 32 (closing of normally open switch/line). The search is continued to the next circle to find alternate plans to energize the outage loads.

Using matrix minimum technique, a search is made for the variant, which has least number of switching operations. These variants are subjected to ranking indices to determine the optimum solution. Table II presents the ranking list of variants for the above-mentioned fault.

Table II: Ranking indices

Variant	IC_{SW}	I_{CPR}	I_{CCR}	Iv_{CVD}
13 - 18	0.8	0.85	0.4	0.5
7 -24	0.8	0.8	0.5	0.4
25 -32	0.9	0.5	0.23	0.35
41 -28	0.9	0.6	0.48	0.45

For each of the ranking index, weightage factor will be given based on the operator's knowledge and customer's requirements. In the present case IC_{sw} = 0.35, I_{CPR} = 0.25, I_{CCR} = 0.20, Iv_{CVD} =0.20. The resultant ranking is presented in table III and it is found that feeder - 4 is the best alternative to energize the outage zones, which has low resultant index indicating greater reliability. This is accomplished by closing tie line 41 - 28.

Table III: Ranking list of variants

Feeder	Variant	IR
1	13 - 18	0.67
2	7 -24	0.66
4	25 -32	0.55
5	41 -28	0.65

ACKNOWLEDGEMENTS

The authors greatly acknowledge the suggestions made by Prof. K Parthasarathy, Chief Technical Consultant, PRDC, Bangalore and Dr. R Nagaraja, Managing Director, PRDC Bangalore.

CONCLUSIONS

In this paper, a multi - purpose, interactive, efficient and robust algorithm to determine the restoration plan of radial distribution network supply is presented. The proposed algorithm is based on the concept of local network, which reduces the size of the problem. Fast bi-directional search technique has been introduced to find out the variants of alternate supply.

The variants so obtained will be stored in Feeder - Load matrix and are ranked according to the set constraints. The variant, which has the lowest ranked value, will be selected for the restoration process. The proposed algorithm can be used to solve service restoration problem effectively in large distribution system.

REFERENCE

1. Karen Nan Miu, Hsiao -Don.-chiang et al "Fast service restoration for large scale distributions systems with priority customers and constraints ", IEEE Transactions on power systems VOL 13, No 3, August 1998
2. Chen - Ching - Liu , Seung Jae Lee et al.,"An expert system operational aid for restoration and loss reduction of distribution systems " IEEE Transactions on power systems VOL 3, No 2, May 1988
3. Dragan S. Popovic , Rade M Ciric,"A Multi -objective algorithm for distribution network restoration " IEEE Transactions on power delivery VOL 14, No 3, July 1999
4. K. Aoki, K Nara, M. Itoh,"A New algorithm for service restoration in distribution systems" IEEE Transactions on power delivery VOL 4, No 3, July 1999
5. Don Torrieri ,"Algorithms for finding an optimal set of short disjoint paths in a communication network" IEEE Transactions on communication VOL 40, No 11, November 1992
6. Seung Jae Lee, Bok-Shin Ahn et al, "Service restoration of primary distribution systems based on fuzzy evaluation of multi- criteria" IEEE Transactions on power systems Vol. 13, No 3, August 1998
7. N.D.R Sarma, S.Ghosh, "Real time service restoration in distribution networks - A practical approach", IEEE Transactions on PWRD, Vol 9, No.4, October 1994

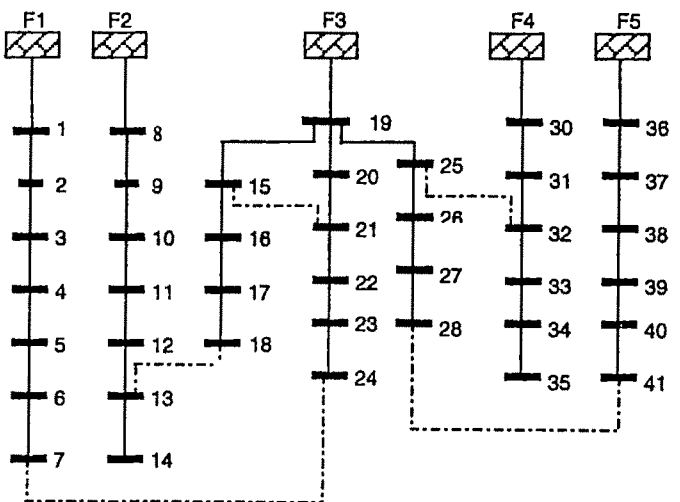

Figure -1: 11 kV Practical distribution system

Actual Reactive Capability Assessment Of Large Alternator

K. K. Saxena and R. S. Mahajan
Department of Electrical Engineering, G.E.C. Bilaspur, India.

Abstract

Achievable generator reactive capability (GRC) is generally much less than what indicated by manufacturers reactive capability curves due to constraints imposed by plant auxiliaries and power system itself. Hence actual determination of generator reactive capability is very important. In this paper for the above said purpose, the limits which are incorporated are (1) Voltage dependent reactive power limits and (2)Reactive power limits considering plant and system constraints.

Keywords: Overexcitation, underexcitation, reactive capability, excitation limitation, reactive requirement.

INTRODUCTION

During the restoration of power system ,when long high voltage transmission lines are energized, there is a sudden increase in positive reactive generation (line charging),which if not neutralized, produced sustained over voltages. Generator's under excitation reactive capability can play a very important role in compensating for positive reactive generation.

Generator's over excitation reactive capability is very important for power system voltage stability consideration and prevention of voltage collapse under highly stressed conditions.

Hence assessment of generators actual reactive capability becomes very important. GRC Curves supplied by manufacturers and used in operation planning, typically have a greater range than can be realized in practice. Generally these curves are strictly a function of synchronous m/c design parameters and don't consider plant and system operating conditions as limiting factors.

Here the limits which are incorporated in load flow are strictly a function of synchronous m/c design parameters and don't consider plant and system operating conditions as limiting factors.

Here the limits which are incorporated in load flow are
(1) Voltage dependent reactive power limits .
(2) Reactive power limits considering plant and system constraints.

VOLTAGE DEPENDENT REACTIVE POWER LIMITS

(1) Maximum and minimum reactive limits with respect to maximum allowable stator currents are given by

$$Q_{GS.max/min} = \pm[V_t^2 I_{max}^2 - P_G^2]^{1/2}$$

I_{amax} = maximum allowable stator currents.
P_G = Real Power generation.

(2) Maximum reactive power generation with respect to maximum allowable rotor current is given by

$$Q_{Grmax} = (-V_t^2/X_d)/X_d \pm [V_t^2 E_{Qmax}^2/X_d^2 - P_G^2]^{1/2}$$

where E_{Qmax} is maximum internal voltage with respect to maximum rotor current.

(3) Minimum rotor current limiter, the purpose of which is to avoid very small rotor currents since these could cause problems for excitation system is of particular interest for synchronous compensators. If minimum internal voltage corresponding to minimum rotor current is denoted by E_{Qmin} and the active power generation is set to zero, the minimum rotor current limit becomes

$$Q_{Grmax} = [-V_t^2 + V_t E_{Qmin}]/Xd$$

(4) The under excitation limiter will limit the maximum angle between voltage vector of external system and the quadrature axis i.e. the internal voltage vector. When this limiter goes into action, it will try to reduce the above angle difference by increasing the level of excitation to avoid the generator from loosing synchronizing.

The minimum limit for 'QG' set by under excitation limiter is given by

$$Q_{Gumin} = P_G/\tan\delta_{max} + V_t^2/X_q$$

REACTIVE LIMITS CONSIDERING PLANT AND SYSTEM CONSTRAINTS

A typical arrangement for supplying power plant auxiliaries and services in a generating station is composed of many major components and subcomponents that operate as a system to supply power to the power system. Each component is designed to operate continuously within certain electrical and mechanical limits specified by the manufacturer. Any component may have operating limits imposed on voltage, current, frequency or a combination of these such that MVA, Volt/Hz and stability.. These limitation reduces the reactive capability of alternate to below the designed ranges.

Let the system representation considered is the one, which is shown in the figure1. The generators reactive capability 'Q_G' can be written as ,

$$Q_G=[\{(E_tE_g)/(X_tT_t)\}^2-P_t^2]^{1/2}-[(E_t/T_t)^2/X_t]$$

The maximum and minimum auxiliary voltages Eamx and Eamn respectively, when reflected to generator terminal buses are

$$Eg' = (Eamx + j\ Ia * Xa) * Ta.$$

and

$$Eg'' = (Eqmn + j\ Ia * Xa) * Ta$$

If $Eg' > Egmx$ then Egmx is the over excitation limiting factor and if $Eg'' > Egmn$ then Egmn is the under excitation limiting factor. Similarly when Eg_1 and Eg_2 are the maximum and min. system voltages, reflected to generator terminal bus, then when $Eg_1 > Egmx$, Egmx is the over excitation limiting factor and when $Eg_2 > Egmn$, Esmn is the under excitation limiting factor.

Thus the alternators, reactive capability $\pm Q_G$ can be determined as a function of real power output 'Pg', from minimum generation Pgmn to maximum generation Pgmx, for a given main and auxiliary transformer tap positions Tt and Ta and for system voltage schedule Es.

CONCLUSION

Voltage dependent reactive power limits are included in NR load flow as against the ordinary load flow which incorporates constant reactive power limits at the PV busses. The reactive limits are shown in table no. 1&2 and the corresponding graph is shown in figure 2. It is shown that the realizable reactive capacity, considering plant and system constraints (for which the reactive limits are shown in table no 3&4 and the corresponding graph is shown in figure 3), is much less than that is obtained by incorporating only voltage dependent reactive power limits. Standard IEEE 5 bus system is used for the purpose. Further it is shown that the realizable reactive capacity can be step up by slightly increasing the auxiliary transformer tap positions and hence the best overall GRC under prevailing high and low system voltage conditions can be obtained.

REFERENCE

1) Say M.G.: The performance and design of alternating current machines; Pitman and son, second edition 1949.
2) P. A. Lof, G. Anderson and D. J. Hill: Voltage dependent reactive power limits for voltage stability studies; IEEE Transactions on power systems, vol. 10, no. 1, Feb. 1995, pp.220-228.
3) Furnham S. B. et al: Field excitation in relation to machine and system operation; AIEE , Fall GM, Nov 1953, Kansas city , pp. 1215-1221.
4) A Panvini, T. J. Yohn: Field assessment of Generator reactive capability; IEEE Transactions on power systems, vol. 10, no. 1, Feb. 1995, pp. 288-296.
5) N. E. Nilson, J. Mercurio: Synchronous generator capability curve testing and evaluations; IEEE Transactions on power delivery , vol. 9, no. 1, Jan. 1994, pp. 414-421.
6) A. capasso, E. Mariani: Influence of generator capability curve representation on system voltage and reactive power control studies; IEEE Transactions on power systems, vol. PAS-97, no. 4, Jul/Aug. 1978, pp. 1036-1041.
7) Nagy I. : Analysis of minimum excitation limits of synchronous machines; IEEE Transactions, vol. PAS-86, no. 7, Jul/Aug 1970, pp. 1001-1008.
8) M. M. Adibi, D. P. Milanicz: Reactive capability limitations of synchronous machines; IEEE /PES winter meeting, Columbus, January 31 to February

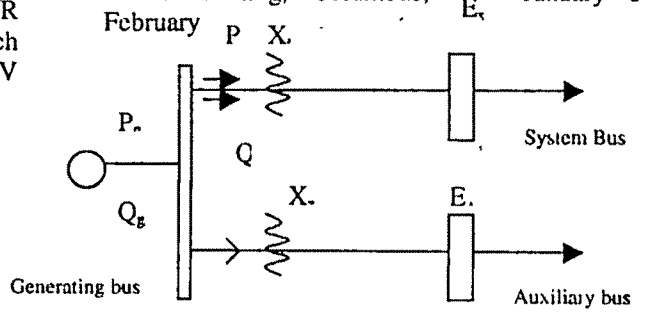

Figure 1 : Schematic diagram of bus structure →

Table 1
Incarporation Of Voltage Dependent Reactive Power Limits
IEEE 5 Bus System Under Excitation Condition

Real Power Gen. (PG2)	QGS_{min}	QGR_{min}	QGV_{min}	QG_{min}	No. of Iteration	
					Limits (reactive) Independent of Voltage	Q limits depending on voltage
0.1	-1.4966	-0.5	-0.7929	QGR_{min}	4	7
0.2	-1.486607	-0.5	-0.7525	QGR_{min}	4	7
0.3	-1.4696	-0.5	-0.7121	QGR_{min}	4	7
0.4	-1.4456	-0.5	-0.6717	QGR_{min}	4	7
0.5	-1.4142	-0.5	-0.6313	QGR_{min}	4	7
0.6	-1.3747	-0.5	-0.5909	QGR_{min}	4	7
0.7	-1.326	-0.5	-0.5505	QGR_{min}	4	7
0.8	-1.2688	-0.5	-0.5101	QGR_{min}	4	7
0.9	-1.20	-0.5	-0.4697	QGV_{min}	4	9
1.0	-1.1180	-0.5	-0.4292	QGV_{min}	4	9
1.1	-1.1098	-0.5	-0.3888	QGV_{min}	4	9
1.2	-0.9	-0.5	-0.3484	QGV_{min}	4	9
1.3	-0.7485	-0.5	-0.3080	QGV_{min}	4	9
1.4	-0.5385	-0.5	-0.2674	QGV_{min}	5	9

Table No.2
Incarporation Of Voltage Dependent Reactive Power Limits
IEEE 5 Bus System Over excitation Condition

Real Power Gen. (PG2)	QGR_{max}	QGS_{max}	QG_{max}	No. of Iteration	
				Q Limits Independent of Voltage	Q limits depending on voltage
0.1	1.33083	1.4966	QGR_{max}	8	10
0.2	1.3233	1.4866	QGR_{max}	8	10
0.3	1.3107	1.4696	QGR_{max}	8	10
0.4	1.2929	1.4457	QGR_{max}	8	11
0.5	1.2698	1.4142	QGR_{max}	8	11
0.6	1.2412	1.3747	QGR_{max}	8	11
0.7	1.2068	1.3267	QGR_{max}	8	11
0.8	1.1664	1.2689	QGR_{max}	7	11
0.9	1.1193	1.20	QGR_{max}	7	11
1.0	1.0654	1.1181	QGR_{max}	7	11
1.1	1.00379	1.02	QGR_{max}	7	13
1.2	0.9333	0.90	QGS_{max}	7	15
1.3	0.8532	0.7485	QGS_{max}	7	15

* Generation and loads are appropriately scaled.

Table 3

Reactive Limits Considering Plant And System Constraints
IEEE 5 Bus System Under excitation Condition

Real Power Gen. (PG2)	Variable 'Q' Limits		Gen. Terminal Voltage Constraint	No. of Iteration			
	System Trans Tap (1.0)	System Trans Tap (1.02)		Q Limits Independent of Voltage		Q limits depending on voltage	
				Tap (1.0)	Tap (1.02)	Tap(1.0)	Tap(1.02)
0.25	-0.3289	-0.2046	Gen. Terminal L.V.limit	4	4	11	13
0.30	-0.3270	-0.2026	,,	4	4	11	13
0.40	-0.3220	-0.1976	,,	4	4	11	13
0.50	-0.3155	-0.1909	,,	4	4	13	13
0.60	-0.3073	-0.1825	,,	4	4	13	13
0.70	-0.2976	-0.1726	,,	4	4	13	13
0.80	-0.2862	-0.1610	,,	4	4	13	13
0.90	-0.2732	-0.1478	,,	4	4	13	13

Table .4
Reactive Limits Considering Plant And System Constraints
IEEE 5 Bus System Over excitation Condition

Real Power Gen. (PG2)	Variable 'Q' Limits		Gen. Terminal Voltage Constraint	No. of Iteration			
	System Trans Tap (1.0)	System Trans Tap (1.02)		Q Limits Independent of Voltage		Q limits depending on voltage	
				Tap (1.0)	Tap (1.02)	Tap(1.0)	Tap(1.02)
0.25	0.3748	0.5121	Gen. Terminal H.V.limit	6	6	27	25
0.30	0.3771	0.5145	,,	6	6	27	25
0.40	0.3828	0.5203	,,	6	5	27	25
0.50	0.3899	0.5275	,,	6	5	25	25
0.60	0.3985	0.5363	,,	5	5	25	23
0.70	0.4085	0.5465	,,	5	5	25	23
0.80	0.4200	0.5582	,,	5	5	25	23
0.90	0.4329	0.5714	,,	5	5	25	23

** Generation and Loads are appropriately scaled.

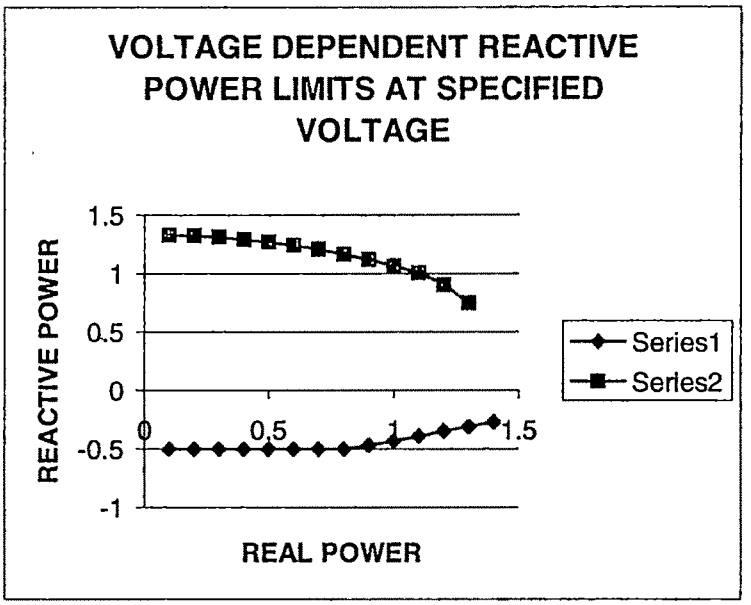

Figure 2 Reactive limit considering plant and system constraints

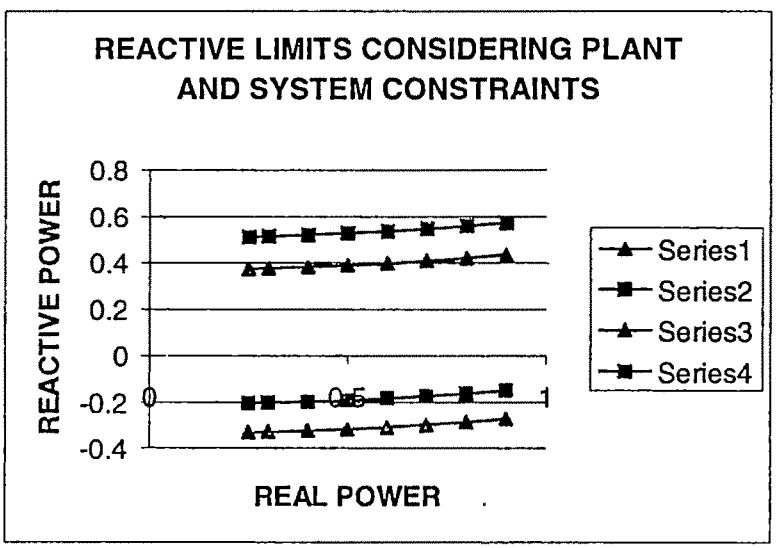

Figure 3 Voltage dependent reactive power limits at specified voltages

New Automated Control Logic for Parallel Valve Operation for Power System Transient Stability Enhancement

Ramnarayan Patel[1], T.S. Bhatti[2] and D.P. Kothari[3]
Centre for Energy Studies, Indian Institute of Technology,
Hauz Khas, New Delhi, 110016 (India)
[3]E-mail of the corresponding author: dkothari@ces.iitd.ernet.in
Tel. 91 – 11 – 6591250, Fax: 91 - 11 – 6862037

Abstract

A new automated control logic has been developed to operate the parallel valves in fast valving scheme in order to improve the transient stability performance of power systems. Fast valving scheme using parallel valves is a new concept, which overcomes many of the limitations of the conventional scheme. The proposed control logic for operating these valves has been applied to a typical single machine infinite bus system. Single as well as multiple stroke operations for controlling the turbine power output has been studied implementing the new control sequence. It gives very encouraging results over the conventional scheme of fast valving. A multiple stroke operation mode, though effective in damping the rotor angle swing over a longer period of transient, may also give rise to system instability.

Key words: Transient stability, Fast valving, Contorl logic

INTRODUCTION

Fast valving is one of the effective and economic means of improving the stability of a power system under large and sudden disturbances. Fast valving schemes involve rapid closing and opening of turbine valves in a prescribed manner to reduce the generator acceleration following a severe fault [1]. For maximum gains with fast valving, the turbine driving power should be reduced as rapidly as possible. Fast valving techniques have been applied as early as 1929, but they have been extensively used during the decades of 1970's and 1980's all over the world [2].

Fast turbine valving can be classified into two general categories – temporary and sustained [1]. To accomplish either type of fast valving, the control and/or intercept valves must be closed rapidly. With temporary valving, the control and/or intercept valves are permitted to reopen to their original operating position, allowing the driving power to return to the pre-fault value very shortly after a predetermined minimum is achieved. For sustained valving on the other hand, after the initial closure of the control valves, the opening of the valves is adjusted so that the post-fault driving power is reduced to a new unit level [3]. In addition, boiler controls must be adjusted to maintain system pressure and temperature within acceptable limits. In one of the commonly used schemes, only the intercept valves are rapidly closed and then re-opened after a short time delay. Since the intercept valves control nearly 70% of the total unit power [1, 4-7], this method results in a fairly significant reduction in turbine power. Sustained fast valving (SFV) necessarily associates with the partial closure of control valves and may give rise to some extra complications and problems. It should be noted that fast valving is applicable only to thermal generating units.

Conventional schemes of fast valving generate a fixed valve stroke sequence for the control of turbine valves under transient conditions. A typical valve stroke characteristic curve for a whole cycle of fast valving operation is depicted in Fig. 1. The conventional scheme suffers the problem of poor adaptability for different fault conditions and at different loading levels of a power system [8]. During the past two decades various schemes have been proposed to improve upon the generalisation capability of fast valving techniques.

Some of the primary limitations of the conventional fast valving schemes include the valve opening and closing rate constraints and valve dead time, which is not adjustable to very low values.

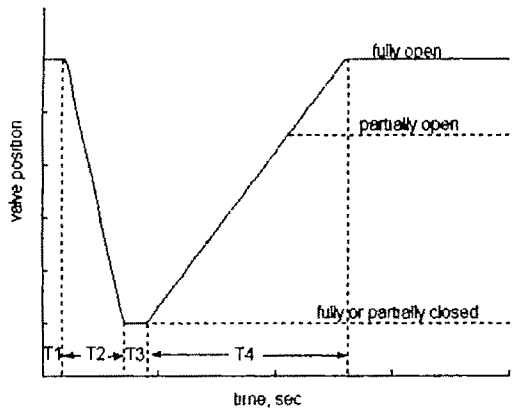

T1 = delay between time of initiation and the time when Valve begins to close
T2 = valve closing time
T3 = time during which the valve remains closed
T4 = valve-opening time

Fig. 1: Valve stroke characteristic curve

The influence of these factors may lead to instability of the system during the second or subsequent rotor angle swings. Hassan et al. [9] propose the use of two parallel valves, each installed on a separate steam piping branch to the low pressure (LP) turbine. A variety of combinations for the reciprocal operation of parallel valves (ROPV) were studies in order to ensure the optimum system response for a particular fault case. The variations include the decision of the valve opening and closing instants as well as the number of desired closing and opening, known as valve strokes. The approach for selecting the best closing/opening instant was decided by the method of trial and error. Fast decision-making is the prime criterion in transient stability studies. Moreover, the control logic should also be capable of making the necessary changes in the valve control sequence as the fault location and/or the loading levels change. The present work defines the criterion for desired closing and opening of the valves. The control logic can adjust to the system requirements for different values of fault clearing time (F.C.T.). The proposed control logic is universally applicable for any case of fault and loading of the power systems.

ILLUSTRATIVE SYSTEM EXAMPLE

The single machine infinite bus system of Fig. 2 has been considered for the present study. The system also appears in the references [10-13]. The system data are given in the appendix – I, for immediate reference.

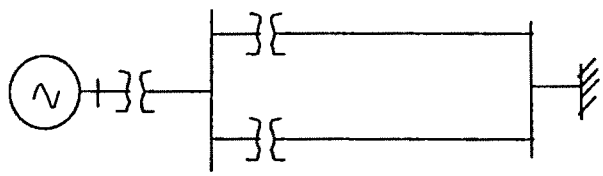

Fig. 2: Line diagram of the example system

The associated governor is of electro-hydraulic type. The governor and turbine are modelled as in reference 1.

PROPOSED CONTROL LOGIC

Generator accelerating power and the rotor angular speed deviation are the two most commonly used signals, in power system transient stability controls. In the control of dynamic braking resistors (concerning power system transient stability enhancement), many researchers have used the rate of change of kinetic energy (RACKE) of the rotor mass and the rotor angular speed deviation signal, to decide the most effective insertion and removal times of the brakes [14-15]. However, the dynamic brake usually connected to the generator bus bars, is rendered ineffective for a fault close to generator terminal. This is due to the low bus voltage profiles during the fault on period. Thus the first insertion of the brake is done only when the fault is cleared. This affects the overall stability of the power system.

The swing equation can be written in its simplest form as following:

$$\frac{2H}{\omega_0}\frac{d^2\delta}{dt^2} = P_m - P_e \qquad \text{.... (1)}$$

where,
P_m = mechanical driving power input, in pu
P_e = electrical power output, in pu
H = inertia constant, in MW-s/MVA
ω_0 = nominal speed, in electrical radian/sec.
δ = rotor angle, in electrical radian

From equation (1), it is apparent that the decrease in the mechanical driving power has the same impact on the rotor angle swings as that of increase in the electrical power output. This gives the motivation to extend the control logic for braking resistors, to the fast valving schemes. Here the added advantage is that the fast valving can be applied from the very beginning of the fault period unlike the dynamic brake. This results in a more effective control over the rotor acceleration.

The strategy based on rate of change of kinetic energy and rotor angular speed deviation, as applicable to the fast valving schemes can be summarized as follows:

Valve Closing Criterion:

$(RACKE)_i = 0$ and $\omega_i = 0 \pm\uparrow$ (2)

where,

ω_i is the angular speed of the rotor of generator i and $0 \pm\uparrow$ means that the variable is zero while changing sign from negative to positive.

Valve Opening Criterion:

$(RACKE)_i = 0$ and $\omega_i = 0 \pm\downarrow$ (3)

where,

$0 \pm\downarrow$ means that the variable is zero while changing sign from positive to negative.

The power system model and the associated control logic have been simulated using Matlab/Simulink. A typical variation of the angular speed and RACKE is shown in Fig. 3.

A close look of Fig. 3 reveals that the frequency of variation in RACKE is twice that of the agular speed variation. Thus for all practical purposes the angular speed deviation can be used to guide the opening and closing of the turbine valves. This will be apparent with the careful look into the guiding equations (2) and (3). Nevertheless, the RACKE signal can be used to ensure the positive acceleration while valve closing and vice versa. When the acceleration is within a certain lower limit, the operation of the fast valving scheme may not be necessary, as it is meant only for the severe faults. Devices like power load unbalance relay and acceleration detector are employed for this purpose [1].

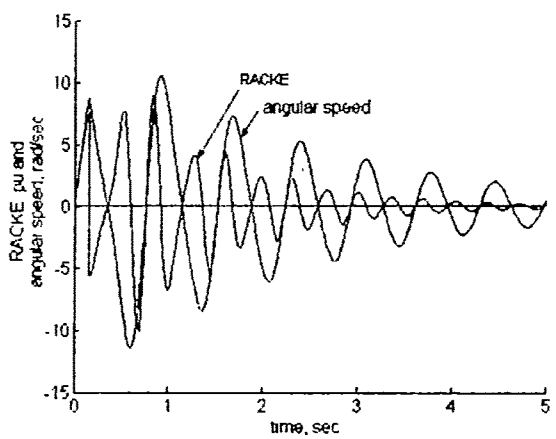

Fig. 3: RACKE and rotor angular speed

OPERATION OF PARALLEL VALVES

A detailed description of the parallel valve operations can be found in reference 9. Here only a short description is given with the point of view of the proposed control logic. One detail to be noted here that the full opening of the intercept valves is not recommended in a number of fault cases and load levels [1, 8]. Thus the ROPV logic suggested by Hassan et al. [9], gives the sub-optimal result in many situations. The optimal values of the valve dead time and the final valve positions are case specific. The proposed control logic has the capability to adjust to the system requirements.

Figs. 4 and 5 give a typical case of 2-strokes and 4-strokes operation of the two parallel valves. The angular speed deviation signals are scaled down by a factor of 10 for the sake of clarity. In 2-stroke operation the first valve starts closing upon receiving a positive angular speed deviation signal under the delay time and closing rate constraints given by Fig. 1. The second valve, in a parallel steam-piping branch, is closed at this point and can be initiated to open prior to or after the full closing of the first valve. Thus the ROPV scheme can overcome the constraint due to inherent dead time of a single valve. The second valve starts opening upon receiving a negative angular deviation signal. Valve closing and opening operations are guided by the proposed control logic. This facilitates automatic selection of valve dead time and final positions of the valves. The four-stroke operation as given by Fig. 5, is self explanatory in the light of the above explanation. In a similar fashion, the valves can be operated for many cycles when required. Fig. 6 gives the variation in the mechanical power input to the generator for different schemes of valve operation.

RESULTS AND DISCUSSION

The studies were conducted for the power system given by Fig. 2. A symmetrical three-phase fault on the high-tension side of a line transformer, is cleared by opening of the corresponding line.

Fig. 7 shows the system response for fault clearing time (FCT) of 0.15 sec. Various schemes of fast valving have been applied. The results show that the sytem with no fast valving control results in highest first swing in rotor angle. The conventional schemes of fast valving as well as the fast valving schemes with proposed control are effective in reducing the first swing. At the second swing stage, the proposed 2-strokes scheme is more effective than the conventional scheme and the 4-strokes scheme is yet more effective.

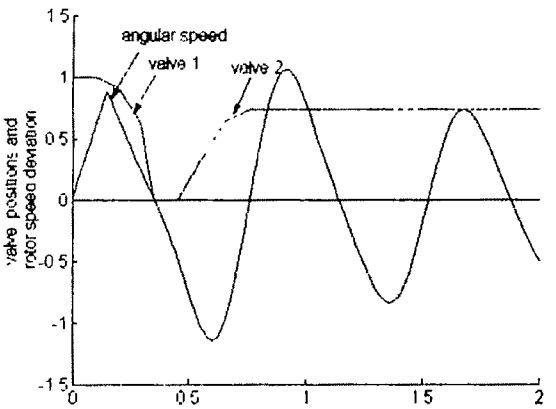

Fig. 4: 2-strokes fast valving scheme

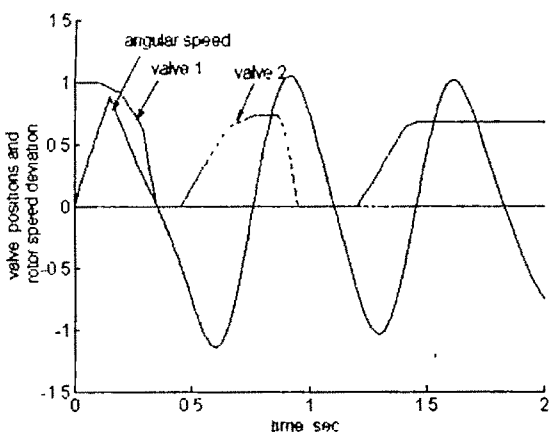

Fig. 5: 4-strokes fast valving scheme

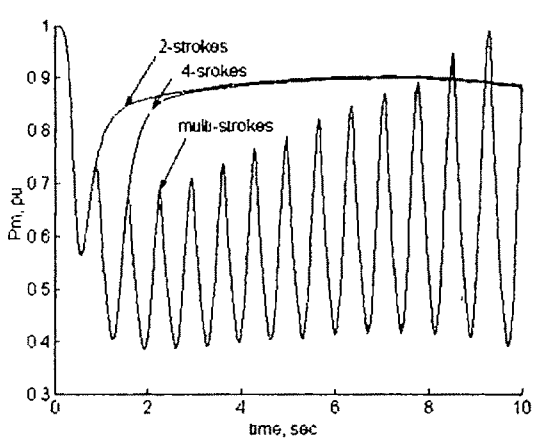

Fig. 6 Mechanical power variations for different fast valving schemes

It is interesting to note at this point that at the stage of third swing in rotor angle, the 2-stroke scheme performs better than the 4-stroke fast valving scheme. This holds good for all other higher order swings. Thus the more number of strokes, although more effective during the initial periods, may result in loss of synchronism in long run due to excessive control action. The mechanical stress considerations and boiler transients also may not permit the frequent closing and opening of the valves.

Further, it was observed that the generator looses synchronism for FCT value of 0.16 sec., with no control. The conventional fast valving scheme remains effective up to this point. When the FCT is increased to 0.17 sec., the proposed control scheme runs fine due to its good adaptability, whereas the conventional scheme fails to maintain synchronism as shown in Fig. 8. It is also clear from the figure that the multiple strokes operation is most effective up to third positive swing, but fails to maintain the overall stability, as discussed earlier in this section. To clarify the point further, an observation for FCT value as low as 0.1 sec. is shown in Fig. 9. The system is stable without fast valving control, but the frequent closing and opening of the valves leads to instability. The two-stroke operation is found to be quite competent for most of the cases and at the same time it can avoid the undesirable stress at the turbine and boiler stages. It is advisable to give some time gap after one cycle of closing and opening operation, so that the transients can settle down.

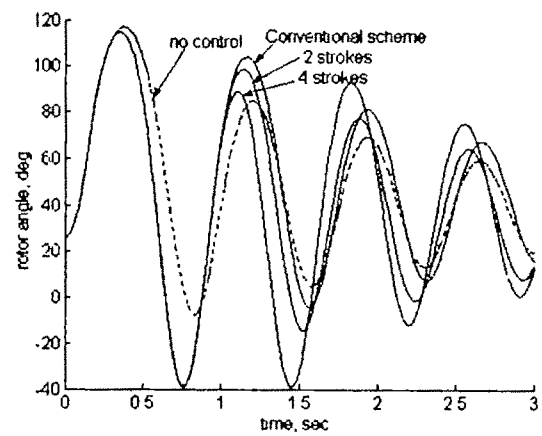

Fig. 7: Rotor angle variation with different fast valving schemes, for F.C.T. = 0.17 sec.

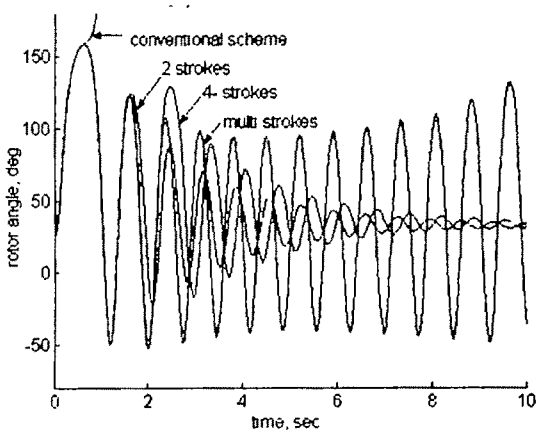

Fig. 8: Rotor angle variation with different fast valving schemes, for F.C.T. = 0.17 sec.

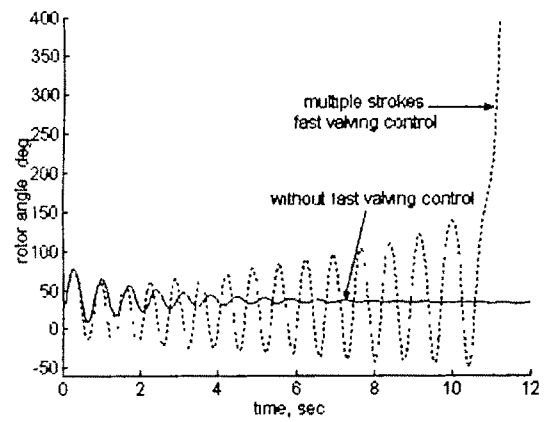

Fig. 9: Rotor angle variation with no control and multiple stroke fast valving, for F.C.T. = 0.1 sec.

CONCLUSIONS

The Simulation results show that the proposed control logic for the operation of the parallel valves in the fast valving scheme improves the transient stability performance of the power system significantly. It not only overcomes the limitations of the conventional scheme, but also facilitates the multiple stroke operation to obtain desired valve characteristic. Normally the 2-stroke scheme gives the best performance. Higher number of valve strokes can be used to damp the higher order swings, but it jeopardizes the stability in long run and may also result in undue stress in turbine and boiler sections. The proposed control logic automatically decides the desired valve closing and opening times. The generated valve control sequence is adjustable to the varying system requirements unlike the conventional schemes of fast valving.

REFERENCES

1. P. Kundur, "Power System Stability and Control", McGraw -Hill, Inc., 1994.
2. Ramnarayan Patel, T.S. Bhatti and D.P. Kothari, "Improvement of Power System Transient Stability Using Fast Valving: A Review", Electric Power Components and Systems, Vol. 29, No. 10, pp. 927-938, Oct. 2001.
3. L. Edwards, J.D. Gregory, D.L. Osborn, J.H. Doudna, B.M. Pasternack and W.G. Thompson, Report of a panel discussion sponsored jointly by the IEEE DISCOS Working Group and ASME/ IEEE Power Plant/ Electrical System Interacting Working Group, "Turbine Fast Valving to Aid System Stability; Benefits and Other Considerations", IEEE Transactions on Power Systems, Vol. PWRS-1, No. 1, pp. 143-153, Feb. 1986.
4. I.J. Nagrath and D.P. Kothari, "Power System Engineering", Tata McGraw-Hill,1994.
5. K.R Padiyar, "Power System Dynamics Stability and Control", Interline Publishing Pvt. Ltd., 1999.
6. E.W. Cushing, G.E. Drechsler, W.P. Killgoar, H.G. Marshall and H.R. Stewart, "Fast Valving as an Aid to Power System Transient Stability and Prompt Resynchronization and Rapid Reload after Full Load Rejection", IEEE Transactions on Power Apparatus and Systems, Vol. PAS-91, pp. 1624-1636, July/Aug. 1972.
7. J. Vandegrift, J.R. Woodall and J.T. Beckham, "Fast Intercept Valving Aids Unit Stability", Electrical World, July 13, 1970.
8. Y. Han, Z. Wang, Q. Chen and S. Tan, "Artificial-neural-network-based Fast Valving Control in a Power-generation System", Engineering application of Artificial Intelligence, Vol. 10, No. 2, pp. 139-155, 1997.
9. F.F. Hassan, R. Balasubramanian and T.S. Bhatti, "Fast Valving Scheme using Parallel Valves for Transient Stability Improvement", IEE Proc.-Generation Transmission and Distribution, Vol. 146, No. 3, pp. 330-336, May 1999.
10. A.H.M.A. Rahim and D.A.H. Alamgir," A Closed Loop Quasi-Optimal Dynamic Braking Resistor and Shunt Reactor Control Strategy for Transient Stability", IEEE Transaction, PWRS-3, No. 3, pp. 879-886, Aug. 1988.
11. A.H.M.A. Rahim and A.I.J. Al-Sammak,"Optimal Switching of Dynamic Braking Resistor, Reactor or Capacotor for Transient Stability of Power Systems", IEE Proceedings-C, Vol. 138, No.1 pp. 89-93, January 1991.

12. A.H.M.A. Rahim, A.M. Al-Sheri and A.I.J. Al-Sammak,"Optimum Control Strategies for Transient as well as Oscillatory Instability of Power Systems", IEEE Transactions, PWRS-8, No. 2, pp. 491-496, May 1993.
13. A.H.M.A. Rahim and S.A. Al-Baiyat, "Dynamic Brake Switching Strategies for stabilization of Power Systems using Artificial Neural Networks", Expert Systems with applications, vol 18, Iss.-2, pp. 101-109, Feb. 2000.
14. F.J. Al-Azzawi and F. Omar, "Direct Approach to the Switching of Shunt Elements used for Multimachine Power System Transient Stability Augmentation", Vol. 6, Proc. 5th Sci. Conference/SRC, Iraq Baghdad, pp77-89, Oct.1989.
15. F.J. Al-Azzwi, N.M. Al-Wafi, A.K. Jassim and F. Omar, "Braking Resistor Size, Switching Instants and Assessment of Power System Transient Stability by Direct Methods", Journal of Institution of Engineers (India), Vol. 76, pp. 175-180, November 1995.

APPENDIX – I

Parameters of the Single Machine System

H = 3.0	E_i = 1.15 pu
f = 60 Hz	X_d' = 0.2 pu
P_m = 1.0 pu	D = 0.051 pu

Other reactances are
Generator transformer = 0.1 pu
Line transformer, each = 0.1 pu
Line reactance, each = 0.3 pu

Controllability and Observability of Large Tandem-connected Systems

A.Gupta and S. Kumar
Birla Institute of Technology and Science, Pilani-333 031, India

Abstract

This paper presents the necessary and sufficient conditions of controllability and observability of large composite system, consisting of a large number of tandem-connected linear time-invariant subsystems, following Gilbert's method and using a new approach of step-by-step diagonalization. These conditions are expressed in the form of recursion relations. Controllability and observability conditions of multi-input-single-output systems are also derived. The method has been illustrated for a two-reach river problem to find the condition of controllability of biological oxygen demand in the river water to control the water quality.

Key words: Controllability, observability , tandem-connected composite system, SISO, MISO

INTRODUCTION

The concept of controllability and observability was introduced by Kalman [1] and has been utilized by others [2-4] to study the problems of optimal control. Gilbert [5] derived the necessary and sufficient conditions for controllability and observability of composite systems consisting of two subsystems in Jordan canonical form with distinct eigenvalues.

In the present paper, the conditions of controllability and observability have been derived for a general case of tandem-connected large composite system using a new approach of step-by-step diagonalization. The subsystems are considered in Jordan canonical form having distinct eigenvalues. In this approach [6], starting from a system with two series connected subsystems, a large system is built up by adding subsystem one by one through tandem-connection. The system is transformed into normal form by diagonalizing the system matrix following Gilbert's[5] method at each stage of addition of a subsystem. Matrix elements of transformation matrices are obtained as function of matrix elements of the input-connection and system matrices. Input- and output-connection matrices of the large tandem-connected system are thus obtained in normal form.

The conditions of controllability (observability) of a series-connected system are obtained in the form of a set of recursive relations. This method is equivalent to Kalman's method. The recursive relations are derived both for Single-Input-Single-Output (SISO) and Multi-Input-Single-Output (MISO) systems.

The controllability of biological oxygen demand (BOD) and dissolved oxygen (DO) in a two-reach river system [7] is presented as an illustrative example. This method reduces the computational time.

METHDOLOGY

A general n-th order multi-input linear-time-invariant system is represented as

$$S: \quad \dot{X} = AX + BU \qquad (1a)$$

$$Y = CX + DU \qquad (1b)$$

where $X \in R^n$, $U \in R^m$ and $Y \in R^r$. The system matrix A, input-connection matrix B, the output-connection matrix C and the transmission matrix D have appropriate dimensions. Consider the large system to be consisting of N series connected subsystems (S_i , i =1,2,...N). For the ith subsystem, system matrix A_i is $n_i \times n_i$, B_i is $n_i \times m_i$, C_i is $r_i \times n_i$ and D_i is $r_i \times m_i$. n is given by

$$n = \sum_{i=1}^{N} n_i \qquad (2)$$

The necessary but insufficient condition[5] for controllability (observability) of such a series connected

system is that each subsystem should be controllable (observable). The resulting system may still have uncontrollable (unobservable) coordinates arising due to series connection. Using Kalman test or Gilbert's method the controllability and observability can be checked for subsystems. To ensure the controllability (observability) of the series-connected system a set of recursive relations has been derived.

SINGLE-INPUT-SINGLE-OUTPUT SYSTEM

Let us consider Single-Input-Single-Output (SISO) tandem-connected subsystems, each of which is controllable (observable), Fig.I. To start with, two controllable (observable) LTI systems are considered in normal form which are represented by

$$S: \dot{x}_i = A_i x_i + B_i u_i \qquad (3a)$$

$$y_i = C_i x_i + D_i u_i \qquad (3b)$$

and where A_i (i = 1,2) are in diagonalized form with distinct characteristic roots λ_{ij}'s, j = 1, ... n_i; and x_i's , u_i's , y_i's are n_i -dimensional state vectors, one-dimensional input and one-dimensional output respectively, for ith subsystem. Hence B_i is a column matrix and C_i is a row matrix of appropriate dimensions. The matrix equation, after tandem-connection, is

$$\dot{X}_{(2)} = A_{(2)} X_{(2)} + B_{(2)} u_1, \qquad (4a)$$

$$y_2 = C_{(2)} X_{(2)} + D_{(2)} u_1 \qquad (4b)$$

$$\text{where } X_{(2)} = \begin{bmatrix} x_1 \\ x_2 \end{bmatrix} \text{ and } A_{(2)} = \begin{bmatrix} A_1 & 0 \\ B_2 C_1 & A_2 \end{bmatrix},$$

$$B_2 = \begin{bmatrix} B_1 \\ B_2 D_1 \end{bmatrix}, C_{(2)} = [D_2 C_1 \;\; C_2]$$

$$\text{and } D_{(2)} = D_2 D_1$$

The coupling elements B_2C_1 in the system matrix, arising out of tandem-connection, are given by $(B_2\ C_1)_{ij} = b_{2i}c_{1j}$, where b_{2i} is ith element of B_2 column matrix and c_{1j} is the jth element of C_1 row matrix. We can express the system equation in normal form as

$$\dot{\underline{X}}_{(2)} = \underline{A}_{(2)} \underline{X}_{(2)} + \underline{B}_{(2)} u_1 \qquad (5a)$$

$$y_2 = \underline{C}_{(2)} \underline{X}_{(2)} + D_{(2)} u_1 \qquad (5b)$$

$$\text{where } \underline{A}_{(2)} = T_2^{-1} A_2 T_2$$

$$= \begin{bmatrix} I_1 & 0 \\ -\Phi_{21} & I_2 \end{bmatrix} \begin{bmatrix} A_1 & 0 \\ B_2 C_1 & A_2 \end{bmatrix} \begin{bmatrix} I_1 & 0 \\ \Phi_{21} & I_2 \end{bmatrix}$$

Since $\underline{A}_{(2)}$ is diagonalized , the ijth element of Φ_{21} is given by

$(\Phi_{21})_{ij} = -b_{2i}\, c_{1j} / (\lambda_{2i} - \lambda_{1j})$ for all i,j values. (5c)

The subscript '2' in Φ and T matrices as well as '(2)' in A, B, and C are used, when the system is consisting of two tandem-connected subsystems. The state vector in normal form is given by $\underline{X}_{(2)} = [\, x_1 \;\; -\Phi_{21}x_1 + x_2]^T = [\underline{x}_1 \;\; \underline{x}_2]^T$. The input-connection matrix in the normal form is given by

$$\underline{B}_{(2)} = T_2^{-1} [\, B_1 \;\; B_2 D_1 \,]^T = [\, B_1 \;\; -\Phi_{21}B_1 + B_2 D_1 \,]^T$$
$$= [\, \underline{B}_{(2)1} \;\; \underline{B}_{(2)2} \,]^T \qquad (6)$$

Since the subsystem S_1 is controllable, $B_1 = \underline{B}_{(2)1}$ has nonvanishing rows; so for controllability of this tandem-connected system, $\underline{B}_{(2)2}$ ($=-\Phi_{21}B_1 + B_2D_1$) should have nonvanishing rows. Similarly, for observability all the columns of the output connection matrix $\underline{C}_{(2)}$ in normal form are nonvanishing, where

$$\underline{C}_{(2)} = [D_2C_1 \; C_2]\, T_2$$
$$= [D_2C_1 + C_2\Phi_{21}C_2] = [\underline{C}_{(2)1} \underline{C}_{(2)2}] \qquad (7)$$

Since C2 ($= \underline{C}_{(2)2}$) has all the columns nonvanishing, the observability condition of tandem-connected system requires nonvanishing of all the columns of $\underline{C}_{(2)1}$ ($=D_2C_1 + C_2\Phi_{21}$).

In this way, a system with tandem-connected N-subsystems can be brought to normal form, by using the technique of step-by-step-diagonalization where at first step a tandem-connected system consisting of two subsystems is chosen. Then the subsystems are added one by one and normalization is done at each step. For such a system the state equation in normal form is given by

$$\dot{\underline{X}}_{(N)} = \underline{A}_{(N)} \underline{X}_{(N)} + \underline{B}_{(N)} U, \;\; U = u_1 \qquad (8a)$$

$$y_N = \underline{C}_{(N)} \underline{X}_{(N)} + D_{(N)} U \qquad (8b)$$

$$\underline{X}_{(N)} = [\underline{x}_1, \underline{x}_2, \underline{x}_3 \ldots\ldots \underline{x}_i \ldots\ldots \underline{x}_N]^T,$$

where

$$\underline{x}_1 = x_1 \text{ and } \underline{x}_i = x_i - \sum_{j=1}^{i-1} \Phi_{ij} \underline{x}_j, \; i > 1$$

$\underline{B}_{(1)1} = B_1$ and $\underline{B}_{(p)i} = \underline{B}_{(i)i}$

for p=2,3,...N, and i=1,2,3....(p-1)

$$\underline{B}_{(p)P} = \sum_{k=1}^{p-1} \Phi pk \underline{B}_{(p-1)k} + B_p D_{(p-1)} \qquad (9)$$

$\underline{C}_{(p)j} = D_p \underline{C}_{(p-1)j} + C_p \Phi_{pj}$ and $\underline{C}_{(p)p} = C_p$

for p=2,3,...N, and j=1,2....(p-1) (10)

$D_{(1)} = D_1$ and $D_{(p)} = D_p D_{(p-1)}$ (11)

$(\Phi_{pq})_{ij} = -b_{pi}\, \underline{C}_{(p-1)qj}/(\lambda_{pi} - \lambda_{qj})$

for p=2,3,...N, and q= 1,2...,p-1 (12)

If $\underline{B}_{(p)s}$ has sth row having all zero elements, then the input u has no influence on the sth mode of the system. The mode is said to be uncontrollable, and a system having one or more such modes is uncontrollable. The system is said to be unobservable, if all the elements of one or more columns of $\underline{C}_{(p)}$ are zero.

MULTI-INPUT-SINGLE-OUTPUT SYSTEM

DECENTRALIZED INPUT

MISO system is represented in Fig. 2 . The matrix equation for each subsystem S_i is represented by

$$S_i : \dot{x}_i = A_i x_i + B_{i1} y_{i-1} + B_{i2} u_i \qquad (13a)$$

$$y_i = C_i x_i + D_{i1} y_{i-1} + D_{i2} u_i \qquad (13b)$$

Each subsystem S_i has two inputs u_i and y_{i-1} which is output from S_{i-1}. The input u_i's and y_{i-1}'s are 1-dimensional, and $u_o = y_o$; B_{i1} and B_{i2} are n_i x 1 input-connection matrices, C_i's are 1x n_i output-connection matrices and D_{i1} and D_{i2} are input-output coefficients; all other symbols are same as defined in case of SISO system. When p subsystems are tandem-connected, the resulting system after normalization is represented as given in (11a) and (11b) where $U = U_{(N)} = [\, u_0\, u_1\, u_2 \ldots\ldots u_N]$. Using $B_{(1)11} = B_{11}$ and $\underline{B}_{(1)12} = B_{12}$, the generalized expression for the elements of input connection matrices in normal form for p=2,3,...N are

$$\underline{B}_{(p)ij} = \underline{B}_{(p-1)ij} \quad ; \; i= 1,2,..(p-1) \; ; \; j=1,2,..p$$

$$= 0 \quad ; \; i= 1,2,...(p-1) \; ; \; j=p+1$$

$$\underline{B}_{(p)\,pj} = B_{p1}\, D_{(p-1)j} - \Sigma\, \Phi_{pk}\, \underline{B}_{(p-1)kj}$$

$$; \; j= 1,2,...p \; ; \; k=1,2...(p$$

$$= B_{p2} \quad ; \; j=p+1 \qquad (14a)$$

The generalized expression for elements of output connection matrix $C_{(p)}$ which is a row matrix, using

$$\underline{C}_{(1)1} = C_1, \; \underline{C}_{(p)j} = D_{p1}\, \underline{C}_{(p-1)j} + C_p \Phi_{pj}$$

$$; \; j=1,2,...(p-1) \;\&\; \underline{C}_{(p)p} = C_p \qquad (14b)$$

Similarly, using $D_{(1)1} = D_{11}$, we obtain

$$D_{(p)j} = D_{p1}\, D_{(p-1)j}$$

$$; \; j=1,2.....p \quad \& \quad D_{(p)p+1} = D_{p2} \qquad (14c)$$

The ij-th matrix element of Φ_{pq} is expressed as

$$(\Phi_{pq})_{ij} = -b_{p1i}\, \underline{C}_{(p-1)qj} / (\lambda_{pi} - \lambda_{qj})$$

$$; \; q= 1,2...,(p-1). \qquad (14d)$$

where b_{p1i} and $\underline{C}_{(p-1)qj}$ are matrix elements of B_{p1} and $\underline{C}_{(p-1)q}$, respectively.

If $B_{(p)s}$ has qth row having all zero elements, then the input u has no influence on the qth mode of the system. The mode is said to be uncontrollable, and a system having one or more such modes is uncontrollable. The system is said to be unobservable, if all the elements of one or more columns of $\underline{C}_{(p)}$ are zero.

CENTRALIZED INPUT

The tandem-connected systems with centralized input are represented in Fig. 3. The matrix equations for N tandem-connected subsystems are given by (11a) and (11b), where the input connection matrix $\underline{B}_{(N)}$ is a Nx2 super matrix in normal form.

Using $\underline{B}_{(1)11} = B_{11}$ and $\underline{B}_{(1)12} = B_{12}$,the generalized expressions for matrix elements in normal form for p= 2,3,..N are

$$\underline{B}_{(p)ij} = \underline{B}_{(p-1)ij} \quad ; \; i= 1,2,...(p-1) \text{ and } j=1,2$$

$$\underline{B}_{(p)p1} = B_{p1} D_{(p-1)1} - \Sigma \Phi_{pk} \underline{B}_{(p-1)k1} \; ; \; k=1,2...(p-1)$$

$$\underline{B}_{(p)\,p2} = B_{p1}\, D_{(p-1)2} - \Sigma \Phi_{pk}\, \underline{B}_{(p-1)k2} + B_{p2}$$

$$; \; k=1,2..(p-1) \qquad (15a)$$

The generalized expression for elements of output connection matrix $\underline{C}_{(p)}$ is:

$$\underline{C}_{(p)j} = D_{p1}\, \underline{C}_{(p-1)j} + C_p \Phi_{pj} \quad ; \; j=1,2,...(p-1)$$

$$\underline{C}_{(p)p} = C_p \qquad (15b)$$

using $\underline{C}_{(1)1} = C_1$.

Similarly, $D_{(p)}$ is a row super matrix, using $D_{(1)1} = D_{11}$ and $D_{(1)2} = D_{12}$, the matrix elements of $D_{(p)}$ are

$$D_{(p)1} = D_{p1}\, D_{(p-1)1}$$

$$D_{(p)2} = D_{p1} D_{(p-1)2} + D_{p2} \qquad (16a)$$

The ij-th matrix element of Φ_{pq} is expressed as

$$(\Phi_{pq})_{ij} = (b_{p1i}\, \underline{C}_{(p-1)qj}) / (\lambda_{pi} - \lambda_{qj})$$

$$; \; q= 1,2...,p-1. \qquad (16b)$$

where b_{p1i} and $\underline{C}_{(p-1)qj}$ are matrix elements of B_{p1} and $\underline{C}_{(p-1)q}$, respectively.

If $\underline{B}_{(p)}$ has qth row having all zero elements, then the input u has no influence on the qth mode of the system. The mode is said to be uncontrollable, and a system having one or more such modes is uncontrollable. The system is said to be unobservable, if all the elements of one or more columns of $\underline{C}_{(p)}$ are zero.

ILLUSTRATIVE EXAMPLE

Consider the example of two-reach river system, where we shall check the controllability conditions of the level of BOD and DO. The mass balance equations are:

$$BOD: \dot{M}_i = -K_1 M_i + f_{i-1} M_{i-1} - f_i M_i + (1-p) m \eta_i \qquad (17a)$$

$$DO: \dot{D}_i = -K_1 M_i + K_2 (D_i^s - D_i) + f_{i-1} D_{i-1} - f_i D_i + d\eta_i \qquad (17b)$$

where M_i is the mass of BOD in the ith reach, K_1 is the rate of decay of BOD (per day), D_i is the mass of DO in the ith reach, D_i^s is the saturation mass of DO in the ith reach, K_2 is the rate of reaeration of DO (per day), f_{i-1} is the fraction of BOD of (i – 1)th reach that flows to ith reach per day; m is the mass of BOD in the effluent to be discharged to the river per day out of which p is the fraction of BOD removed from the effluent during treatment before it falls; d is the mass of DO in effluent discharge to the river per day. The fraction of effluent discharged after treatment to the ith reach is η_i . Let us consider

$${}_iX_1 = M_i,\ {}_iX_2 = D_i,\ {}_iA_{11} = -K_1 - f_i,\ {}_iA_{22} = -K_2 - f_i,\ {}_iA_{21} = -K_1$$

$$u_i = (1-p_i),\ B_{i1} = m_i\eta_i,\ \alpha_{i1} = f_{i-1}M_{i-1},$$
and $\alpha_{i2} = f_{i-1}D_{i-1} + K_2 D_i^s + d\eta_i$

The state equations of reaches are

$$\begin{bmatrix} {}_1\dot{X}_1 \\ {}_1\dot{X}_1 \end{bmatrix} = \begin{bmatrix} {}_1A_{11} & 0 \\ {}_1A_{21} & {}_1A_{22} \end{bmatrix} \begin{bmatrix} {}_1X_1 \\ {}_1X_2 \end{bmatrix} + \begin{bmatrix} B_{11} \\ 0 \end{bmatrix} u + \begin{bmatrix} \alpha_{11} \\ \alpha_{12} \end{bmatrix}$$

for reach 1

$$\begin{bmatrix} {}_2\dot{X}_1 \\ {}_2\dot{X}_2 \end{bmatrix} = \begin{bmatrix} {}_2A_{11} & 0 \\ {}_2A_{21} & {}_2A_{22} \end{bmatrix} \begin{bmatrix} {}_2X_1 \\ {}_2X_2 \end{bmatrix} + \begin{bmatrix} B_{21} \\ 0 \end{bmatrix} u + \begin{bmatrix} \alpha_{21} \\ \alpha_{22} \end{bmatrix}$$

for reach 2

These equations are brought into normal form using the diagonalizing matrix T_i,

$$T_i = \begin{bmatrix} I & 0 \\ \Psi^i & I \end{bmatrix}$$

where i indicates the ith reach . From the condition of diagonalization, (8c), the ψ^i is found to be the same for both the reaches and so superscript i dropped , i.e. ψ is given as,

$$\psi = K_1 / (K_1 - K_2)$$

After tandem connection of the two reaches, we obtain

$$\begin{bmatrix} {}_1\dot{X}_1 \\ -\Psi_1\dot{X}_1 + {}_1\dot{X}_2 \\ {}_2\dot{X}_1 \\ -\Psi_2\dot{X}_1 + {}_2\dot{X}_2 \end{bmatrix} = \begin{bmatrix} {}_1A_{11} & 0 & 0 & 0 \\ {}_1A_{21} & {}_1A_{22} & 0 & 0 \\ f_1 & 0 & {}_2A_{11} & 0 \\ 0 & f_1 & {}_2A_{21} & {}_2A_{22} \end{bmatrix}$$

$$\begin{bmatrix} {}_1X_1 \\ -\Psi_1X_1 + {}_1X_2 \\ {}_2X_1 \\ -\Psi_2X_1 + {}_2X_2 \end{bmatrix} + \begin{bmatrix} B_{11} \\ -\Psi B_{11} \\ B_{21} \\ -\Psi B_{21} \end{bmatrix} u + \begin{bmatrix} \alpha_{11} \\ -\Psi\alpha_{11} + \alpha_{12} \\ \alpha_{21} \\ -\Psi\alpha_{21} + \alpha_{22} \end{bmatrix}$$

The system equation can be brought into normal form using diagonalizing matrix $T_{(2)}$,

$\begin{bmatrix} I_1 & 0 \\ \Phi^{(2)} & I_2 \end{bmatrix}$, where $\Phi^{(2)} = \begin{bmatrix} \Phi_{31} & 0 \\ 0 & \Phi_{42} \end{bmatrix}$;

and $\Phi_{31} = \Phi_{42} = f_1 / (f_2 - f_1)$

Controllability condition requires $\Phi_{31} \neq \eta_2 / \eta_1$ i.e., $f_1 / (f_2 - f_1) \neq \eta_2 / \eta_1$

If the above methodology is extended for j number of reaches each of which gets discharges from the same effluent removal plant, the controllability conditions will become

$f_{i-1} / (f_i - f_{i-1}) \neq \eta_i / \eta_{i-1}$ for i =2,3,....j

In case the effluent removal plant discharges only in one of the reaches, and there is discharge in other reaches, the controllability condition is always satisfied. To demonstrate some numerical results we use some typical values of f_i's as f_1 =0.45, f_2 = 0.5, f_3 = 0.55 etc., which give us the controllability conditions as

$\eta_2/\eta_1 \neq 9$, $\eta_3/\eta_2 \neq 10$

REFERENCES

1. R.E. Kalman, On the general theory of control systems, *Proc. First Int. Cong. Of Automatic Control*, Moscow, USSR,1960.
2. R. E. Kalman, Y.C.Ho,and K.S. Narendra, *Controllability of linear dynamical systems, Contributions to Differential Equations*, vol 1, John Wiley, New York1961.
3. W. A. Wolovich and H. L. Huang, Composite system controllability and observability of composite systems, *IEEE Trans. Automat. Contr.*, vol AC-18, pp. 74-75,1973.
4. E. Kreindler and P.E. Sarachik, On the concepts of controllability and observability of linear systems, *IEEE Trans. Automat. Contr.*, vol AC-9, pp. 129-136, April 1964.

5. E.G. Gilbert, Controllability and observability in multivariable control systems,*SIAMJ. Contr.*, vol 2, pp. 128-151, 1963.
6. A.Gupta, *Systems Analysis: Concepts and Applications,* CBS Publishers& Distributors, Delhi, 1993.
7. H. Tamura, A discrete dynamical model with distributed transport delays and its hierarchical optimization for preserving stream quality, *IEEE Trans. Systems, Man and Cybernatics,* vol, SMC-4, pp.424-431, 1974.

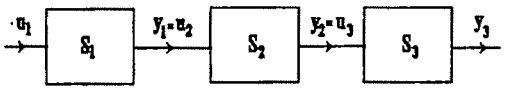

Fig.1Representation of tandem-connected Subsystems

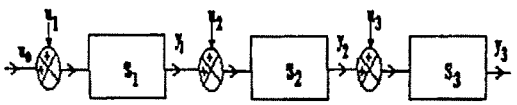

Fig. 2 Representation of Multi-input single output tandem-connected system

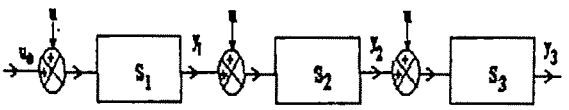

Fig. 3. Representation of n number of tandem-connected subsystems with centralized input

Development of a Simulation Technique to Facilitate Control and Improvement of Voltage Stability of Power Transmission Systems Using Fast Decoupled Load Flow (FDLF)

A. Chakrabarti[1], C. K. Chanda[1], S. Dey[2] and P. N. Das[1] and A. K. Mukhopadhyay[3]
[1]Deptt. of Electrical Engineering, B. E. College (D. U.), Howrah- 711 103, India
[2]J.I.S. College of Engg. P. G. Research.
[3]Deptt. of Applied Physics, Calcutta University, India.

Abstract

A methodology of equivalencing of a multi-bus power system to a two bus radial system being developed in this paper using the 'Fast Decoupled Load Flow' technique, attempts have been made in order to highlight the simplification achieved in simulation, control and enhancement of the voltage stable states of a typical 'weak' as well as a robust multi-bus system using this developed technique.

Key words : *Load flow in LPS system, Transmission planning, Voltage stability, Power system equivalency.*

INTRODUCTION

Fast decoupled load flow technique [1] is widely accepted in load flow algorithm and is suitable in the planning and operation studies of a multi-bus power system. The primary objective in this method is to check whether the solution offered is well within the permissible operating limits. However, in an actual power system, the system configuration and/or loads may change constantly causing the violation of secured limits of operation. Fast decoupled load flow technique can even be well utilised in order to check the system performance including system stability on off-line basis [3,4].

Continuous interconnections have made a power network more vulnerable to stability and associated problems [5,6]. Voltage stability of a multi-bus power system being the question of the day [7,8,9,10], researches reveal successful use of standard load flow techniques for predicting or analysing the voltage stable performance of a power transmission system [8].

In this paper a simple extension has been proposed in order to apply the conven-tional and well tested FDLF technique in a multi-bus power system (a typical 6 bus weak and robust 16 bus) to obtain an equivalent two bus radial network. It then becomes easy to simulate and analyse the performance of the original multi-bus network in the equivalent domain.

A BRIEF REVIEW OF FDLF [1]

The decoupled load flow equations are given by

$$\Delta P = H\Delta\delta \quad .. \quad (1)$$

$$\Delta Q = L\left[\frac{\Delta|V|}{|V|}\right] \quad .. \quad (2)$$

where the elements of the submatrices H and L can be represented as

$$H_{ij} = V_i V_j \left(G_{ij} Sin\ \delta_{ij} - B_{ij} Cos\ \delta_{ij}\right),\ i\neq j \quad (3)$$

$$H_{ii} = B_{ii}|V_i|^2 - Q_i\ ,\ i=j \quad .. \quad (4)$$

$$L_{ij} = V_i V_j \left(G_{ij} Sin\ \delta_{ij} - B_{ij} Cos\ \delta_{ij}\right) = H_{ij}\ ,\ i\neq j \quad (5)$$

$$L_{ii} = B_{ii}|V_i|^2 + Q_i\ ,\ i=j \quad (6)$$

Even though this decoupled load flow method reduces the memory storage requirements considerably, it still requires significant amounts of computational effort. This problem had been sorted by developing the Fast Decoupled Load Flow Method (FDLF) with the following assumptions:

i) The power systems have high x/r ratios

$$\therefore G_{ij} Sin\ \delta_{ij} \leq B_{ij} \quad (7)$$

ii) The difference between adjacent bus voltage angles is very small;

$$\left.\begin{aligned} \therefore Sin\ \delta_{ij} &= Sin(\delta_i - \delta_j) \equiv (\delta_i - \delta_j) = \delta_{ij} \\ Cos\ \delta_{ij} &= Cos(\delta_i - \delta_j) \equiv 1.0 \end{aligned}\right\} \quad (8)$$

iii) Also, $Q_i \le B_{ii}|V_i|^2$ .. (9)

Thus equations (1) and (2) can be further approximated as

$$\Delta[P] = [|V|B'|V|][\Delta\delta] \quad .. (10)$$

$$\Delta[Q] = [|V|B''|V|]\left[\frac{\Delta|V|}{|V|}\right] \quad .. (11)$$

Here, the elements of the matrices B' and B'' are the elements of matrix B.

$$\therefore B'_{ij} = -\frac{1}{x_{ij}}, \quad i \neq j \quad .. (12)$$

$$B'_{ii} = \sum_{j=1}^{N}\frac{1}{x_{ij}}, \quad i = j \quad .. (13)$$

$$B''_{ij} = -B_{ij} \quad .. (14)$$

The decoupling process in the FDLF has been further modified based on this simplified assumption as

$$\left.\begin{aligned}\frac{\Delta P}{|V|} &= B'\Delta\delta \\ and, \frac{\Delta Q}{|V|} &= B''\Delta|V|\end{aligned}\right\} \quad .. (15)$$

DEVELOPMENT OF EQUIVALENT TWO BUS RADIAL NETWORK CONCEPT

With reference to the proposed two bus network shown in Fig.-1,

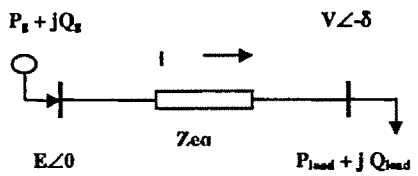

Fig.-1 : Equivalent Two Bus System

$$\left.\begin{aligned}P_{loss} &= \frac{R_{eq}(P_g^2 + Q_g^2)}{E^2} \\ \text{and } Q_{loss} &= \frac{X_{eq}(P_g^2 + Q_g^2)}{E^2}\end{aligned}\right\} \quad (16)$$

However, for the multi-bus power system, following the principle of energy conservation, energy generated = energy consumed + energy lost ; thus we can write,

$$\left.\begin{aligned}\Sigma P_{loss} &= \Sigma P_g + \Sigma P_{load} \\ \Sigma Q_{loss} &= \Sigma Q_g + \Sigma Q_{load}\end{aligned}\right\} \quad .. \quad (17)$$

The two bus system shown in Fig.-1 can be treated to be a equivalent model of a multi-bus system provided following equality is satisfied; i.e.,

ΣP_{loss} (For multi-bus system)

$= P_{loss}$ (For two bus system)

ΣQ_{loss} (For multi-bus system)

$= Q_{loss}$ (For two bus system)

This equality yields, for the two bus equivalent network,

$$\left.\begin{aligned}R_{eq} &= \frac{\frac{P_g - P_{load}}{(P_g^2 + Q_g^2)}}{E^2} = \frac{P_g - P_{load}}{(P_g^2 + Q_g^2)} \\ X_{eq} &= \frac{\frac{Q_g - Q_{load}}{(P_g^2 + Q_g^2)}}{E^2} = \frac{Q_g - Q_{load}}{(P_g^2 + Q_g^2)}\end{aligned}\right\} .. \quad (18)$$

[Here the sending end bus voltage magnitude has been assumed to be unity, i.e., at nominal p.u. values]

Zeq, the impedance of the equivalent line being given by

$$Z_{eq} = R_{eq} + jX_{eq},$$

From above, we can write

$$V = E - \frac{Z_{eq}(P_g - jQ_g)}{E} \quad .. (19)$$

[Since $V = E - Z_{eq}i$ and $i = \frac{S^*}{E^*} = \frac{S^*}{E}$]

Expression (19) provides the receiving end bus voltage of the equivalent two bus system.

[The validity of the developed equivalencing technique has been checked by the following method:

Let $dP = \Sigma P_{loss}$ in the multi-bus system obtained from conventional load flow method $- P_{loss}$ in the equivalent two bus system using the proposed method;

$dQ = \Sigma Q_{loss}$ in the multi-bus system obtained from conventional load flow method $- Q_{loss}$ in the equivalent two bus system using the proposed method.

If dP or $dQ \le \varepsilon$, a tolerance, then it can be reasonably concluded that the proposed method representing an equivalent two bus model of the multi-bus system.]

The flowchart of the proposed method is displayed below :

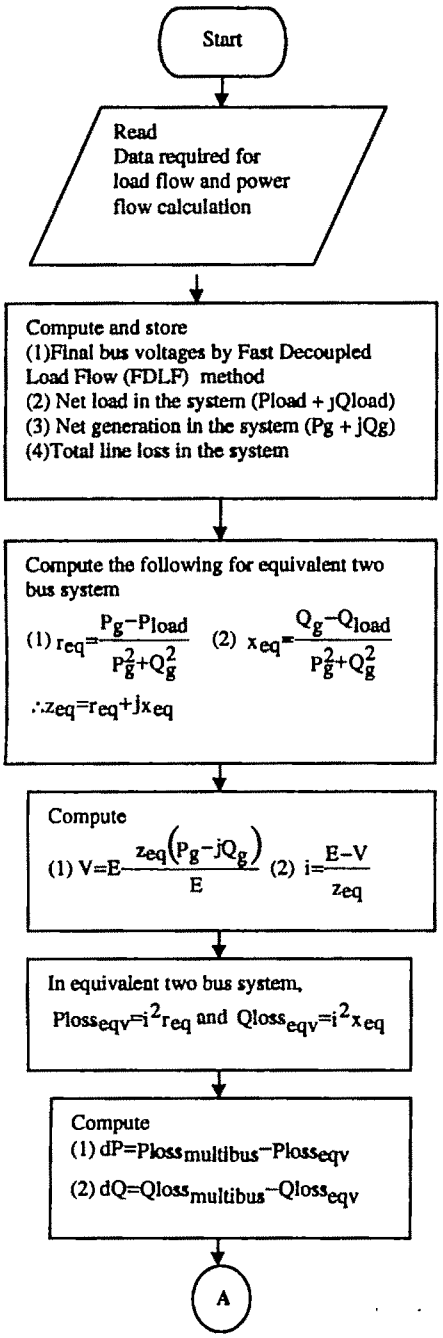

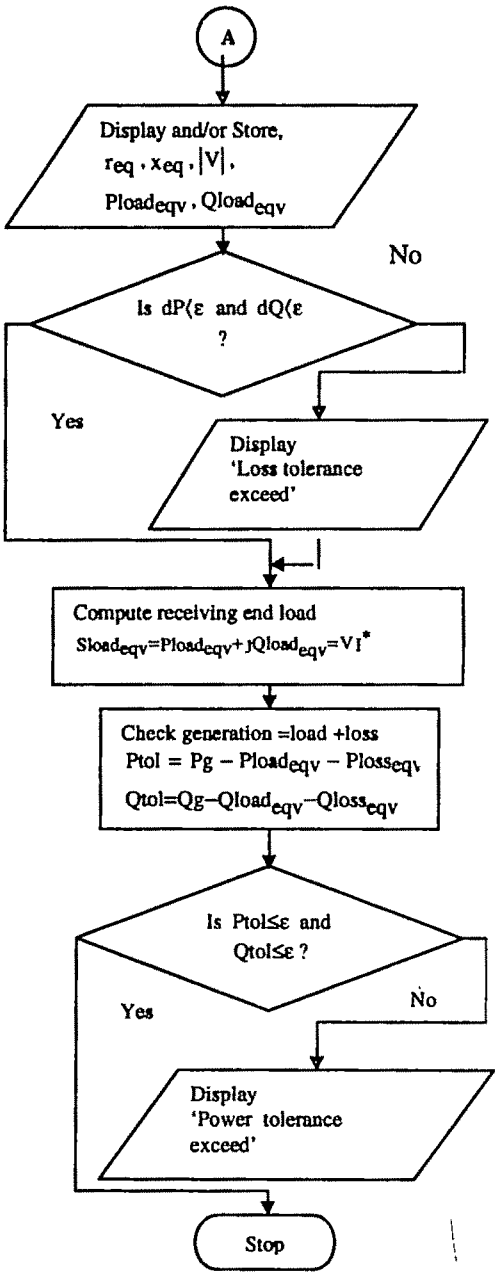

SIMULATION

A longitudinal type six bus power system (Fig.A-1) as well as another system similar to sixteen bus power system (Appendix-A) [11] have been simulated for application of the proposed theory in order to derive respective equivalent models for studying the voltage stable states of the original multi-bus system. Table-1 shows the computed values of dP

and dQ for the six bus and sixteen bus network justifying the validity of the proposed equivalencing technique.

Table 1 : dP and dQ values

Type of System	dP	dQ
Six bus system	-0.001790	0.009
Sixteen bus system	-0.002570	0.000589

The flexibility of the equivalent model can be observed from the text part of the simulation where any load bus of the proposed system is 'dynamically loaded' (i.e., the load bus voltage in the load flow possesses the initial guess being same as the final iterative voltage value of previous step) and the profile of the equivalent model receiving end voltage has been plotted against power loading of that particular bus (Fig.-2). The stable operating states of the load buses would thus be obtained from the upper part of the respective profiles. The maximum power (S_{max}) that the load bus could cater can also be determined.

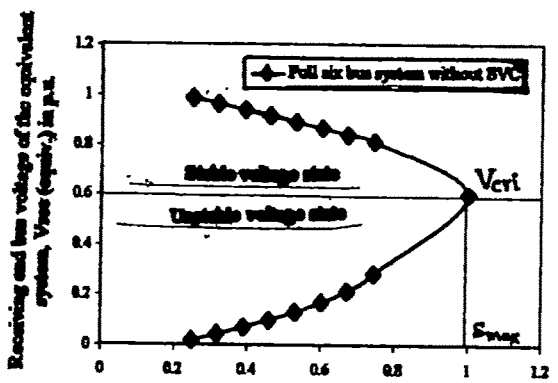

Fig.-2 : Simulated voltage stable states in the equivalent system

Next, in the simulation a static var compensator (SVC) [3] is applied at one of the load buses and the voltage profiles of the receiving end system of the two bus equivalent model of the six bus system are plotted [Fig.-3], Improvement of voltage stability being observed, it becomes evident that for any change of circuit configuration or load status, the equivalent model reorients itself and provides the simulated voltage stable states for the entire system in the equivalent domain. The line contingency has also been attempted for given system and the conducted simulation highlights the improvement of voltage stability using SVC at the affected bus (Fig.-4).

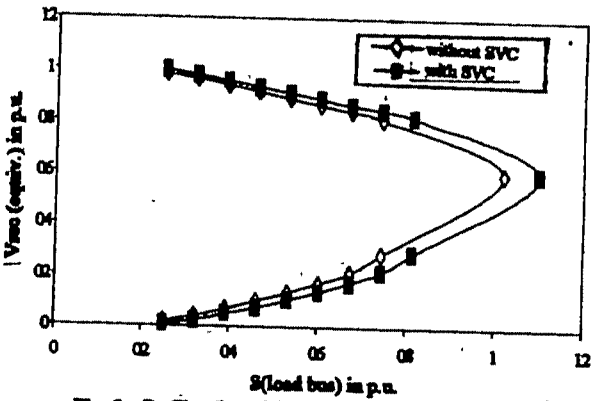

Fig.-3 : Profile of receiving end bus voltage vs. complex power with and without SVC at load bus for the equivalent simulated model of six bus system [Bsvc = 0.01 p.u.].

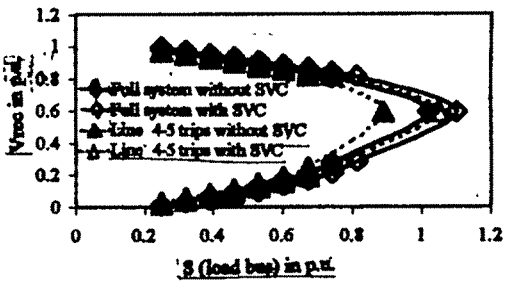

Fig.-4 : Profile of receiving end bus voltage for full system and during line contingency with and without SVC for the equivalent simulated model of six bus system [Bsvc = 0.01 p.u.].

Though the presented simulations have been performed on the six bus power system, same exercise has been conducted for the sixteen bus system also and the simulations gave satisfactory results.

CONCLUSION

The investigation reveals that a simple extension performed on the standard 'Fast Decoupled Load Flow' technique provides an equivalent two bus radial network model which is easily computable for determining the voltage stable states of any multi-bus power network against any contingency or load reallocation. The operator thus gets a global picture of the voltage stable states of the entire network through the equivalent two bus model.

ACKNOWLEDGEMENT

This work has been financed by the UGC, Govt. of India, New Delhi under a major project scheme under Dr. A. Chakrabarti, Professor, Electrical Engg., in the Deptt. of Electrical Engineering, B. E. College (A Deemed University), Howrah-3.

REFERENCES

1. Stott, B. and Alsac, O. : "Fast Decoupled Load Flow". IEEE Trans.,1974, PAS-93.
2. Laughton, M. A., Humphrey Davis, M. W. : "Numerical Technique in the Solution of Power System Load Flow Problems". IEE Proc., 1964, III, (9).
3. Aboytes, F et al. : "Application of Static Var Compensators in Longitudinal Power Systems". IEEE Trans. On PAS, Vol.-102, No.-10, 1983.
4. Chakrabarti, A. and Mukhopadhyay, A. K. : "Voltage Stability of Longitudinal Power System". Jl. Of Electrical Engg., Institution of Engineers (India), Vol.-71, Aug'90.
5. Brian, J. and Rastgoufard, P. : "Power System Voltage Stability and Security Assessment". Electric Power System Research., No. 30, 1994.
6. Chanda, C. K., Dey, S. and Chakrabarti, A : "Effect of Shunt Susceptance at Load Bus of Longitudinal Power Supply System on its Operational Security". National Conference on Power System : Recent Advances and Prospects in 21st Century, Feb'2001, Jaipur, India.
7. Melo, A. C. G. et al : "The Effects of Voltage Collapse Problems in the Reliability Evaluation of Composite Systems". IEEE PES Winter Power Meeting, 96 WM 316-0-PWRS.
8. Nagao, T., Taneka, K. and Takeneka, K: "Development of Static and Simulation Programs for Voltage Stability Studies of Bulk Power System". IEEE PES Winter Power Meeting, 96 WM 279-0-PWRS.
9. Mohammed A. and Jasmon. : "A New Clustering Technique for Power System Stability Analysis". Elect Machines and Power Systems, Vol. 23, No.- 4.
10. Zulapa R. R and Corey B. J. : "Reactive Reserve Management". IEEE Procedings on Gen., Trans. And Dist., Vol.142, Jan'1995.
11. Gross C. A. (Book) : "Power System Analysis (Second Edition)", Published by Jhon Weiley & Sons, 1986.

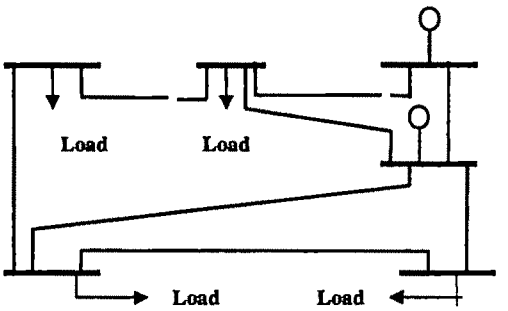

Fig.A1 :.Six bus test system

Table 2 : Impedance and line charging of six bus sample system :

Bus-code p-q	Line impedance Z_{pq}	Line Charging $Y_{pq}/2$
1-2	0.04 + j0.30	j0.010
2-3	0.03 + j0.20	j0.010
3-4	0.04 + j0.20	j0.010
3-5	0.04 + j0.20	j0 010
4-5	0.03 + j0.15	j0.010
5-6	0.06 + j0.30	j0.010

Table 3 : Transformer data of six bus sample system

Bus-code p-q	Transformer impedance Z_{pq}	Off-nominal tap ratio of transformer
1-2	0.0 + j0.40	1.05 + j0.0
2-6	0.0 + j0.20	1 02 + j0.0

Table 4 : sixteen bus test system
Impedance and line charging of sixteen bus test system :

Bus-code p-q	Line impedance Z_{pq}	Line Charging Y_{pq}
4-6	(0.006650+ j0.035190)	j0.074580
8-10	(0.006650+ j0.035190)	j0 074580
10-11	(0.009980+ j0.052790)	j0.111900
2-4	(0.016640+ j0.087980)	j0.186440
2-11	(0.016640+ j0.087980)	j0.186440
5-7	(0.008302+ j0.045550)	j0.008129
15-16	(0.027680+ j0.151800)	j0.027100
11-12	(0.006656+ j0.035192)	j0.074576
13-14	(0.052100+ j0.177300)	j0.003707

Table 5 :Transformer data of sixteen bus test system

Bus-code p-q	Transformer impedance Z_{pq}	Off-nominal tap ratio of transformer
1-2	(0.0035+ j0.035)	(1.0 + j0.0)
15-2	(0.002722+ j0.032670)	(1.0 + j0.0)
13-12	(0.002083+j0 041670)	(1.025 + j0.0)
3-4	(0.003846+ j0.038460)	(1.0 + j0.0)
5-6	(0.001667+ j0.041670)	(1.0 + j0.0)
7-8	(0.001667+ j0.041670)	(1.0 + j0.0)
9-10	(0.0012+ j0.024)	(1 0 + j0.0)

Neuro Controller for Power Plant Generator Excitation System

N.S. Bhuvaneswari, T.R. Rangaswamy, S.Nagarajan
Department of Instrumentation & Control Engineering
Crescent Engineering College, Vandalur, Chennai – 48.

Abstract

In a thermal power station, Boiler is used to produce steam. The steam is fed in to turbine to rotate the shaft. The shaft is coupled with the generator which is used to produce electricity. Every generator in power plant equipped with an automatic voltage regulator to control the voltage within prescribed limits. The three-phase output voltage is compared with a reference and the error signal is fed into the rotor excitation system to control the stator output voltage. The control of excitation output leads to the control of the main generator voltage. This paper deals with a Neural Network Controller to maintain the output voltage of the generator at constant value.

Keywords: Neural Network, firing angle, SCR control circuit, Back propagation, error.

INTRODUCTION

Every generator in power plant, equipped with an automatic voltage regulator to control the voltage within prescribed limits. The three-phase output voltage from the stator is compared with a reference voltage and the error voltage is fed into the rotor excitation system to control the stator output voltage. The control of excitation output leads to the control of the main generator voltage. This paper deals with a Neural Network Controller to maintain the output voltage of the generator at constant value. Modular based hardware design consists of CPU, input-card, output card, control & protection card and communication card. Software design consists of data acquisition, back propagation algorithm and output data processing using C++ language. All the input signals, controls & interlocks were simulated using computer and the outputs were studied. Actual Neural network setup with one miniature dc generator using thyristor module was fabricated and tested with the actual data collected from the power station. The inputs considered for the neural network are error voltage i.e. the difference between the reference voltage and actual stator voltage. The output from the neural net is the firing angle to the thyristor control circuit to control the rotor excitation voltage which in turn control the stator output voltage. The response was found to be satisfactory when compared with the conventional system. The advantages of this system are 1. Fast response 2. High reliability 3.Maintenance free performance 4. Elimination of overloading the rotor 5. Self learning techniques.

CONVENTIONAL CONTROL SYSTEM

Static excitation system has been used in 200 MW unit in order to furnish a significant improvement in the overall system stability. This system controls the generator voltage by direct variation of the excitation current. .In thermal power station, every generator is equipped with an automatic voltage regulator to get the voltage within prescribed limits. The automatic voltage regulator(AVR) is the most important unit of the excitation system. The actual value of a.c. generator voltage is tapped by means of a P.T.C.T's are used to tap the load current. The resultant voltage is rectified and applied to one terminal of control amplifier. This voltage acts as actual or sensed voltage. A reference voltage is applied to this amplifier by means of a motor potentiometer. The control amplifier compares actual signal with the reference and produces an output voltage as an error signal. This voltage is the main control voltage which controls the firing pulses generated in the gate control circuit. These firing pulses determine the final output voltage of the thyristor bridge which is applied to the field winding of the generator. Thus the AVR controls the generator voltage and tries to keep it constant by adjusting its own output voltage.

Gate control unit

This unit generates pulses in a definite cycle sequence which causes firing of the thyristors arranged in bridge configurations. The output control signal of AVR is applied to each of the gate control unit. Simultaneously an a.c.voltage is also applied by filters to this unit , which

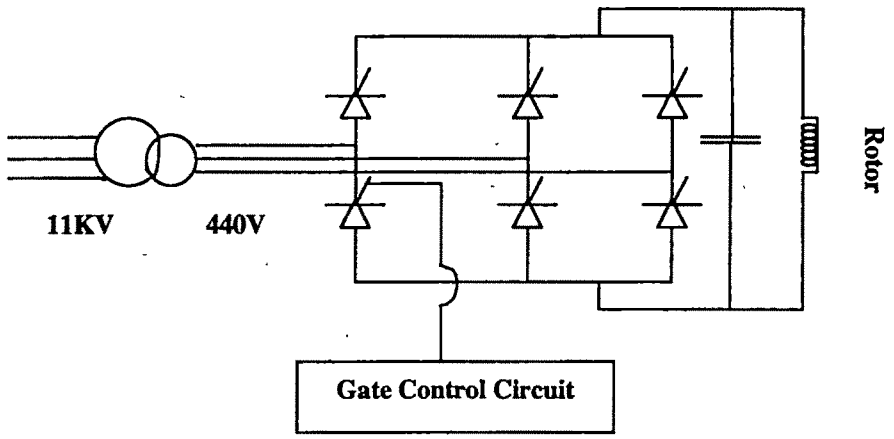

Fig. 1. Conventional SCR Control Circuit

acts as synchronous reference voltage. The combination of these two voltages produces a row of rectangular pulses by means of an operational amplifier. The positions of the firing pulses are shifted according to the magnitude of a.c. or d.c. voltages. The output voltage of thyristor bridge depends on the firing angle of these trigger pulses. Whenever the generator output voltage is deviated due to the load disturbances, from the desired value, error voltage is created. This error voltage thus produced, changes the time delay of the pulse in the SCR control circuit, which inturn changes the triggering instant of SCR. Once the triggering instant varies, it changes the output voltage of the SCR control circuit. Therefore the output voltage produced is in proportion with the error voltage produced. This output voltage is given to the rotor winding of the three phase generator. When the voltage given to the rotor winding changes, it changes the magnitude of the flux and in turn brings the generator output voltage to the desired value. So whenever error occurs, the SCR control circuit takes action such that to vary the rotor excitation voltage and brings the generator output to the prescribed value. The circuit used is shown in Fig. 1. To avoid overloading and to minimize the time consumption for taking control action, neuro control is employed here by replacing the conventional control circuit.

NEURO CONTROL SYSTEM

In this control, the conventional control circuit is completely eliminated. Instead of that neuro-control system is employed. The function of the conventional control circuit is that, it gets the error signal and accordingly varies the time delay in the SCR control circuit and hence varies the firing angle to trigger the SCR. This operation is done by neural network in this proposed method. For that, the neural-network is trained for generating the optimum firing angle to trigger the SCR control circuit for the given error and hence to produce optimum voltage to be given to the rotor winding of the three phase generator. Once the optimum voltage excitation is given to the rotor, the stator generates optimum controlled, desired output voltage.

For training the neural network, a set of training data's were collected from the thermal power plant i.e. for each error voltage created, how much is the firing angle to trigger the SCR control circuit to be given and hence to produce optimum rotor excitation voltage. The data's were collected from the thermal plant. About 50 data's were collected. A few data's are given in the table.1.

Error In Volts	Firing angle in deg
25	90
50	85
75	80
100	75
125	70
150	65

Table. 1 Training Data

The above data's are trained by using popular back-propagation algorithm considering an input node (error, e) and an output node (firing angle, α) and one hidden layer with three hidden nodes. The network architecture used for the training is shown in the Fig.2. Popular paradigm of learning called learning with the teacher supervised learning involves modification of the synaptic weights of Neural networks by applying a set of labeled samples or task examples. The training of the network is repeated for many examples in the set until the network reaches a steady state where there no further significant changes in the synaptic weights. The previously applied training session executed in a different order. Thus the network learns from the examples by constructing an input-output mapping for the problem at hand.

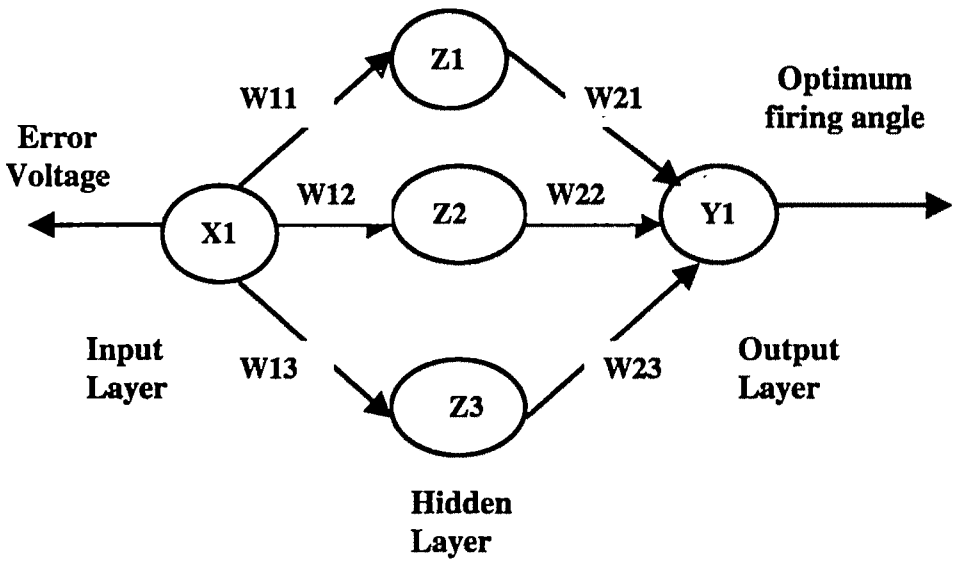

Fig. 2. Neural-network architecture

Neural networks have a built-in capability to adapt their synaptic weights to changes in the surrounding environment. In particular, a neural network trained to operate in a specific environment can be easily retrained to deal with minor changes in the operating environmental conditions. A neural net work can be designed to changes its synaptic weights in real time. As a general rule, It may be said that the more adaptive we make a system, all the time ensuring the system remains stable. The more robust its performance will likely be when the system required to operate in a non stationary environment. It should be emphasized, however, that adaptivity does not always lead to robustness.

The feedforward backpropagation network is a very popular model in neural networks. It does not have feedback connections, but errors are back propagated during training. Least mean square error is used. Many applications can be formulated for using a feedforward backpropagation network, and the methodology has been a model for most multilayer neural networks. Errors in the output determine measures of hidden layer output errors which are used as a basis for adjusting the two sets of weights between the input and hidden layers. Adjusting the two sets of weights between the pairs of layers and recalculating the outputs is an iterative process that is carried on until the errors fall below a tolerance level. Learning rate parameters scale the adjustments to weights. A momentum parameter can also be used in scaling the adjustments from a previous iteration and adding to the adjustments in the current iteration. The feedforward backpropagation network maps the input vectors to output vectors. Pairs of input and output vectors are chosen to train the network first. Once training is completed, the weights are set and the network can be used to find outputs for new inputs.

BACK-PROPAGATION ALGORITHM

Adjustment of link weights in the network is carried by calculating the error function and then back propagating the error from one layer to the previous layer .The weight matrix is adjusted in the steepest descent direction until minimum error is achieved.

Defining the error (Ep) to be proportional to the square of the difference between the actual output(tpj) and desired output (opj).

$$Ep=1/2\Sigma(tpj-opj)2 \quad (1)$$

Learning rule:

$$Wij(t+1)=wij(t)+\eta*\delta pj.Xpi \quad (2)$$

For the branches connecting input and hidden nodes,

$$Wij(t+1)=Wij(t)+\delta pi.Xpi \quad (3)$$

For branches connecting hidden and output nodes,

$$Wkj(t+1)=Wkj(t)+\eta*\delta pk.ipk \quad (4)$$

Adding momentum parameter,

$$Wkj(t+1)=Wkj(t)+\eta*\delta pk.ipk+ \propto[Wkj(t)-Wkj(t-1)] \quad (5)$$

where

Error	:Ep
Actual output	:Tpj
Desired output	opj
Weight	w
Node in the input layer	:i
Node in the hidden layer	:j
Node in the output layer	:k
Instant of iteration	:t
Learning rate	:η
Momentum parameter	:$\propto$

After the training, testing is done by applying an input from the training dataset and the output is calculated from the architecture.

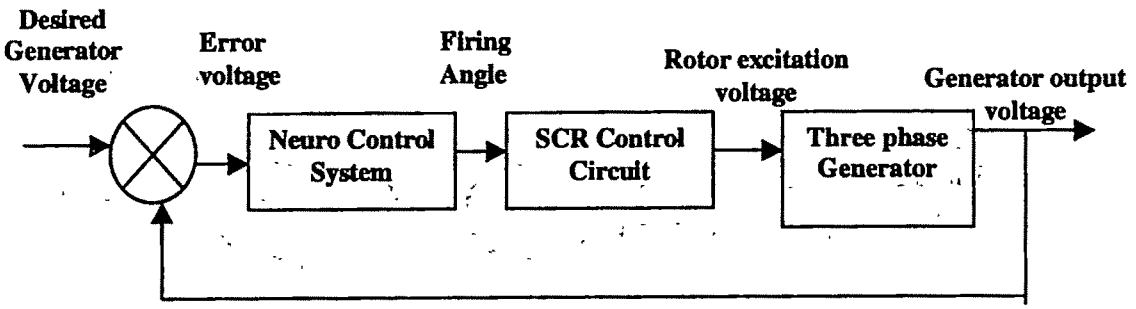

Fig. 3. Block Diagram Using Neuro Control System

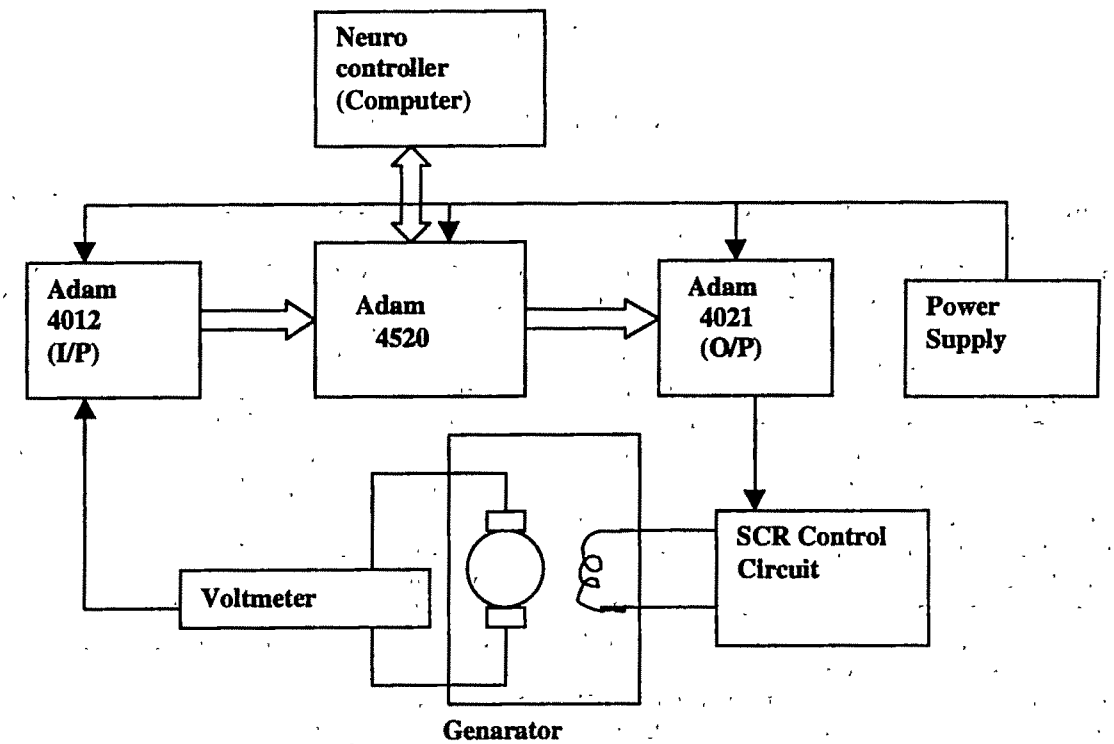

Fig.4. Setup diagram

The calculated output will be equal to the output data available in the dataset corresponding to that input data. The untrained input data i.e. error value (not available in the dataset) also can be given as the input. Now, the designed network will now generate the correct output i.e. firing angle (∝).

SELECTION OF HIDDEN NODES

The number of hidden nodes is selected by trial and error method. For that various number of hidden nodes were assumed. The training was carried out for different hidden nodes assumed. The error is noted down after each training. The number of hidden nodes yielding the lowest error is chosen as the optimum number of hidden nodes.

In this case, three hidden nodes were found to be optimum. It is given in the table.2

No of hidden Nodes	Iteration	Max error
2	1,85,00,000	0.028737
3	5,16,00,000	0.013672
4	1,15,00,000	0.029208
5	1,50,00,000	0.032500
6	1,17,00,000	0.037681
7	1,17,00,000	0.039680
8	96,00,000	0.03541

Table.2 Selection of hidden nodes

IMPLEMENTATION OF NEURAL-NETWORK

The actual three phase generator output voltage is measured and compared with the desired reference generator voltage. If there is any deviation, it produces error signal. The error signal is given as the input of neuro control system. The neural network is already trained for generating the optimum firing angle for the given error. This firing angle changes the triggering instant of SCR circuit and hence changes the SCR control circuit voltage. This voltage is given to the input of the rotor winding of the three-phase generator. Once the excitation voltage changes, it brings the stator three phase voltage to the desired, controlled value as shown in the fig.3.

The laboratory setup was carried out in real time using one miniature dc generator, fabricated thyristor module and ADAM modules as shown in the fig.4. The actual generator output voltage was measured by dc voltmeter and it is given to the input ADAM module 4012 which is configured in voltage mode. Then this voltage enters the computer where setpoint, desired voltage is entered through keyboard. Then program is written for computing the error voltage. Already neural network was trained in the PC. The error voltage thus produced is given as the input of the trained neural network which finds the optimum firing angle to be changed in the SCR control circuit. The firing angle to be changed is given to the control circuit through the output ADAM module 4021. The output from the control circuit is applied to the field winding of the generator. Now the field current and hence the output voltage is brought to the desired value. So whenever error voltage is created, the designed neural network will give the optimum firing angle and generator output voltage is brought to the desired value. Thus changes in the firing angle brings the stator output voltage to the desired normal value. Neural network architecture trained with the actual data collected from the thermal power station and tested for the untrained data. The result was found to be satisfactory.

CONCLUSION

The Neuro based scheme describes to control AVR gives a flexible design by which a wide range of operating conditions are made available. The response of the system is excellent compared to the conventional control system using dedicated hardware and software. Further more dangers of overloading of rotor is eliminated. The major advantages of the system are the 1. Fast response 2. High reliability 3.Maintenance free performance 4. Elimination of overloading the rotor 5. Self learning techniques. The neuro controller was able to keep the generator voltage in the optimum range whenever the load disturbance made. Neurocontrollers are most robust, user friendly and easier to construct than other existing controllers. The stator output voltage is brought to the normal value within less time where as the conventional control takes much larger time.

REFERENCES

1. Bark Kosko University of Southern California, 1997, Neural Networks and Fuzzy Systems, Prentice Hall of India Pvt. Ltd., New Delhi.
2. Dennis. J. Gausell, Henry. T. Darlington, "Supervisory Control and data acquisition" Special issue on computer in power operations, IEEE Proceedings, Dec. 1987, pp 1645-1658.
3. S. Renganathan, Ranganathan Muthu, National Symposium on "Role of Fuzzy logic Neural Netowrks and Genetic Algorithms in Process Control" Tutorials, MIT, Anna University, Chennai, 1998.
4. Soon Chung Hong, Min Ho Park, "Microprocessor based high efficiency drive of a DC motor" IEEE Transsaction on Industrial Electronics, vol IE34, No.4, Nov. 87, pp 433-440.
5. Thermal Training Instituite U.P. State Electricity Board, Operating Instructions Manual for 200/210 MW thermal power units.

An Algebraic Criteria for Robust Stability of Voltage Controller Under Convex Optimization Technique

S. C. Konar and A. S. Chaudhuri
Department of Electrical Engineering,
Bengal Engineering College (D. U.), Botanic.Garden, Howrah-711103, INDIA
su_ch_konar@hotmail.com , aschaudhuri@hotmail.com

Abstract

This paper gives a presentation of the analysis and design of a family of voltage controllers based on numerical convex optimization. The family of controllers is then tested for stability by the method of Kharitnov's Stability Theorem. The step–response, Bode plot, root-locus, and Nyquist curves for different values of single parameter (λ) are drawn.

Key words : Controller, Convex Optimization, Kharitonov's Criteria, Step Response, Stability.

INTRODUCTION

The goal of control engineering is to improve, or in some cases enable the performance of a system by addition of sensors, which measure various signals in the system and external command signals. Control processors processed the measured signals to drive actuators which affect the behavior of the system. A schematic diagram of a general control system is shown in Fig.1. The use of the sensed response of the system in the computation of the actuator is called feedback control. So, the control processor is responsible to generate the actuator signals. The control processor designs the controller, which may involve mechanical design, analog and digital circuit design, and software design.

The problem of controller design for a restricted set of systems and a restricted set of design specifications has been truckled by using the method of convex optimization, as outlined in [1], [2]. In [2], the convex combination of the finite set of points $x_1, x_2, \ldots, x_n$ in n-dimensional or n-component (either row or column vectors) Euclidean space(R^n) is a point x given by

$$x = \lambda_1 x_1 + \lambda_2 x_2 + \ldots\ldots\ldots\ldots + \lambda_n x_n .$$

where λ_i's are real and ≥ 0, for i =1 , 2 , ... , n and

$$\sum_{i=1}^{n} \lambda_i = \lambda_1 + \lambda_2 + \ldots + \lambda_n = 1.$$

So, the convex combination [2],[5] of two points x_1 and x_2 is given by, $x = \lambda_1 x_1 + \lambda_2 x_2$, such that $\lambda_1 , \lambda_2 \geq 0$ and $\lambda_1 + \lambda_2 = 1$ or by $x = \lambda x_1 + (1-\lambda) x_2$, $0 \leq \lambda \leq 1$. Thus, if X is a convex set, then every point x given by $x = \lambda x_1 + (1-\lambda) x_2$, $0 \leq \lambda \leq 1$, $x_1, x_2 \in X$, is also a point of the set X. A convex set may be bounded or unbounded. The first quadrant of the two dimensional plane is an example of an unbounded convex set whereas a circle is a bounded convex set.

In [1], convex optimization has been used to show that if two controllers, which stabilizes a plant, are obtained then we can obtain an infinite number of controllers which stabilize the plant by varying a single parameter λ. The family of controllers thus designed has been tested for robust stability using Kharitonov's Theorem.

Section-2 deals with voltage controller design by convex optimization technique. It outlined the main principles behind the design and also provides essential formula(s).

Section-3 incorporates with step response analysis of the modified system after using the controllers.

Section-4 describes the stability of the system tested by Kharitonov's theorem.

Section-5 deals with the Bode, root-locus, Nyquist plots for different values of λ

LINEAR CONTROLLER DESIGN BY CONVEX OPTIMIZATION

The problem of controller design for a restricted set of systems and for a restricted set of design specifications by the method of convex optimization [1] is used. Here we assume that the plant, P, and controller, K, are linear time

invariant (LTI), and lumped. It often occurs that a controller designed on the basis of a linear model of a non-linear plant, will work well with the nonlinear plant, even if the linear model of the plant is not particularly accurate. A subset of a vector space is said to be affine when two distinct points are in the set, so that the entire lines passing through them. More preciously, C∈ V is affine [1] for any two points v_1, $v_2 \in C$, and any $\lambda \in R$, such that $\lambda v_1 + (1-\lambda) v_2 \in C$, whereas a subset of a vector space is convex whenever two points are in the set, so is the entire line segment between them. More preciously, C∈ V is convex if for any $v_1, v_2 \in C$, and any $\lambda \in [0,1]$, $\lambda v_1 + (1-\lambda) v_2 \in C$ [1].

All affine sets are convex. Geometrically, we may think of a convex combination of two points are being on the line segment between the points. The design specifications must be closed-loop convex. Wide class of performance specifications, e.g., limits on RMS regulation or tracking errors, actuator authority, rise-time, and overshoot are closed-loop convex. A controller, which has two order is easily implemented, achives an RMS regulation error only 10% above the minimum achievable by any linear controller, is a very strong point in favor of the design. LTI controller design is based on two categories.

A rational transfer function is stable if it has no more zeros than poles and if each pole has negative real part. A transfer matrix is stable if all of its entries are stable transfer functions.In 1975, Desoer and Chan [3] proposed a formal definition of internal stability. It makes use of two auxiliary signals v_1 and v_2, injected as shown in Fig.1. The signal v_1 is an actuator referred plant noise and v can be interpreted as a sensor noise.

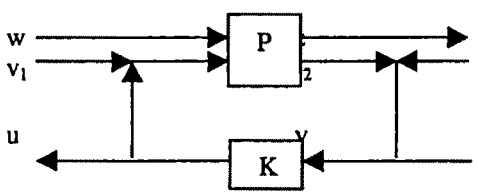

Fig.1 : Representation of sensor & actuator noises

According to definition, the four closed-loop transfer matrices from v_1 and v_2 to w_1 and y are

$$H_{uv1} = K(I - P_{yu}K)^{-1}P_{yu},$$
$$H_{uv2} = K(I - P_{yu}K)^{-1},$$
$$H_{yv1} = K(I - P_{yu}K)^{-1}P_{yu},$$
$$H_{yv2} = K(I - P_{yu}K)^{-1},$$

and are stable.

It prohibits a very small (bounded) actuator or sensor noise from having very large (unbounded) effect on u or y and therefore z. Assumption is that P and K have no unstable hidden modes, that is, mode uncontrollable from u or unobservable from y.

By including v_1 and v_2 as parts of the exogenous input w and including y as a part of the regulated output z, the four transfer matrices of the Desoer – Chan [3] definition appear as blocks within the overall closed – loop transfer matrix H. Assuming the realization of P and K, that have no unstable hidden modes, with the inclusion of signals in w and z, the satisfaction of the Desoer – Chan conditions are equivalent to stability of H. In fact, we must include u and y in z and sensor and actuator noises (v_1 and v_2) in w. The four transfer matrices in the definition of closed-loop stability are closed-loop transfer matrices and so they should appear in H. Thus the whole issue of internal stability can be seen as arising when one considers as H that is too "small". In classical control, the designer must concentrate on the input /output (I/O) transfer function ($P_o K$) /($1-P_o K$). However, the transfer function can be acceptable or desirable but the design will work because another important closed-loop transfer function is unstable. So the designer must simultaneously consider all closed-loop transfer function matrices achieved by controllers that stabilize the plants are now considered. If K and $\bar{K}$ each stabilizes P and yield closed-loop transfer matrices H and $\bar{H}$, respectively, then for each $\lambda \in R$, there is some controller K_λ that stabilizes P and yields closed - loop transfer matrix, $H_\lambda = \lambda H + (1-\lambda)\bar{H}$. Thus if we can find two controllers that stabilize P, we can find entire one parameter family of controllers that stabilize P.

An important point is that, the controller K_λ that yields closed - loop transfer matrix H_λ is generally not $K_\lambda = \lambda K + (1-\lambda)\bar{K}$. In algebraic notation,

$$K_\lambda = (A + \lambda B)^{-1}(C + \lambda D),$$

Where,
$$A = I + \bar{K}(I - P_{yu}\bar{K})^{-1}P_{yu},$$
$$B = K.(I - P_{yu}K.)^{-1}P_{yu} - \bar{K}(I - P_{yu}\bar{K})^{-1}P_{yu},$$
$$C = \bar{K}(I - P_{yu}\bar{K})^{-1},$$
$$D = K.(I - P_{yu}K.)^{-1} - \bar{K}(I - P_{yu}\bar{K})^{-1},$$

By this method, we can get an infinite number of controllers, each of which makes the system stable by varying a single parameter. This parameter λ can take on any value between 0 and 1 and corresponding to each value we get a controller, K_λ, which make the system stable.

STEP RESPONSE ANALYSIS

Let us consider the general n [th] – order transfer function.

$$M(s) = \frac{b_{n+1}s^n + b_n s^{n-1} + \ldots\ldots\ldots\ldots + b_2 s + b_1}{s^n + a_n s^{n-1} + \ldots\ldots\ldots\ldots + a_2 s + a_1}$$

The "state" of a system refers to the past, present and future of the system. It represents all the information that one cares to know about the behavior of the system. The state variables of a linear system may be defined as a minimal set of variables [7], $x_1(t), x_2(t), \ldots\ldots\ldots, x_n(t)$. Here c (t) is the output and r (t) is the input. By trial and error, the state variables are defined as follows:

$$x_1(t) = c(t) - h_0(t)$$
$$x_1(t) = x_2(t) - h_1 r(t)$$
$$x_2(t) = x_3(t) - h_2 r(t)$$
$$\vdots$$
$$x_{n-1}(t) = x_n(t) - h_{n-1} r(t)$$
$$x_n(t) = -a_1 x_1(t) - a_2 x_2(t) - \ldots\ldots - a_n x_n(t) + h_n r(t)$$

Where, $h_0, h_1, h_2, \ldots\ldots\ldots, h_n$ are determined from

$$h_0 = b_{n-1}$$
$$h_1 = b_n - a_n b_{n+1}$$
$$h_2 = b_{n-1} - a_{n-1} b_{n+1} - a_n h_1$$
$$h_3 = b_{n-2} - a_{n-2} b_{n+1} - a_{n-1} h_1 - a_0 h_2$$
$$\vdots$$
$$h_n = b_1 - a_1 b_{n+1} - a_2 h_1 - a_3 h_2 - \ldots\ldots\ldots\ldots a_n h_{n-1}$$

The different state variables are then computed using Runga – Kutta (5[th] – order) method with initial condition and step input . This is finally checked using simulation technique of MATLAB.

STABILITY ANALYSIS

The set of monic n[th] – degree characteristic polynomial after using the controller is of the form,

$$f(s) = s^n + a_{n-1}s^{n-1} + a_{n-2}s^{n-2} + \ldots\ldots\ldots\ldots + a_0$$

for all $a_0, \ldots\ldots\ldots, a_{n-1}$ such that $\underline{a}_k \le a_k \le \bar{a}_k$, $k = 0, 1, \ldots\ldots\ldots, n-1$, then we define the four polynomial [7], [9] (where $\underline{a}_n = \bar{a}_n := 1$) as follows

$$g_1(s) := \underline{a}_0 + \bar{a}_2 s^2 + \underline{a}_4 s^4 + \ldots\ldots = \sum_{k=0,even}^{n} j^k .\min.(j^k \underline{a}_k , j^k \bar{a}_k) . s^k .$$

$$g_2(s) := \bar{a}_0 + \underline{a}_2 s^2 + \bar{a}_4 s^4 + \ldots\ldots\ldots = \sum_{k=0,even}^{n} j^k .\max.(j^k \underline{a}_k , j^k \bar{a}_k) . s^k .$$

$$h_1(s) := \underline{a}_1 s + \bar{a}_3 s^3 + \underline{a}_5 s^5 + \ldots = \sum_{k=0,odd}^{n} j^{k-1} .\min.(j^{k-1} \underline{a}_k , j^{k-1} \bar{a}_k) s^k$$

$$h_2(s) := \bar{a}_1 s + \underline{a}_3 s^3 + \bar{a}_5 s^5 + \ldots = \sum_{k=0,odd}^{n} j^{k-1} .\min.(j^{k-1} \underline{a}_k , j^{k-1} \bar{a}_k) s^k$$

Finally, we define the Kharitonov polynomials [9],[10].

$k_k \lambda(s) := g_k(s) + h\lambda(s)$, where $k, \lambda = 1, 2$.

If the Kharitonov's four polynomials are Hurwitz then the characteristic polynomials are Hurwitz, i.e., the system is stable in the given perturbation range.

NUMERICAL EXAMPLE

The system shown in Fig.1 has been analyzed by [5] , [8] using the procedure described inthis chapter. The function is given by $P_0 = \frac{1}{2(s+1)}$. The two Proportional Integral (PI) controllers are : $K(s) = 1.5 + \frac{1}{s}$, and $\bar{K}(s) = 2 + \frac{55}{s}$, each stabilizes P_0 With K in the loop, the transfer matrix from w to $[z_1 z_2]^T$ is

$$H(s) = \begin{pmatrix} \frac{1.5s+2}{2s^2+3.5s+2} \\ \frac{3s^2+7s+4}{2s^2+35s+2} \end{pmatrix} \quad \text{,and } \bar{H}(s) = \begin{pmatrix} \frac{s+27.5}{2s^2+4s+55} \\ \frac{2s^2+57s+55}{2s^2+4s+55} \end{pmatrix}$$

For every $\lambda \in R$, there is a controller K_λ that stabilizes P_0 and yields a closed-loop transfer matrix of

$$H_\lambda(s) = \lambda H(s) + (1-\lambda)\bar{H}(s)$$

For $\lambda = 0.5$,

$$H_{0.5}(s) = \begin{pmatrix} \frac{3.5s^3+63.5s^2+143.5s+110}{4s^4+15s^3+128s^2+200.5s+100} \\ \frac{7s^4+134s^3+414s^2+507s+220}{4s^4+15s^3+128s^2+200.5s+110} \end{pmatrix}$$

It is analytically seen that,

$$\lim_{s \to 0} \; s \cdot \frac{1}{s} \; H_\lambda(s) = 1$$

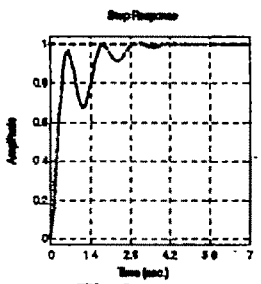

Fig.2

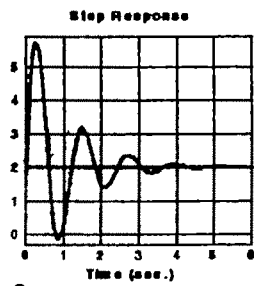

Fig.3

Which means that the steady state step response [11] at $t \to \alpha$ is unity for unit step input. The controller transfer function is

$$K_{0.5}(s) = \frac{3.5s^3 + 63.5s^2 + 143.5s + 110}{2s^3 + 3.75s^2 + 28.5s}$$

The step responses [6], [7], [13], [14] from w to z_1 of K, and from w to z_2 of $\bar{K}$ for $\lambda = 0.5$ are shown respectively in Fig.2, and Fig.3. Similarly, Body - Plot, root -locus, Nyquist diagrams for

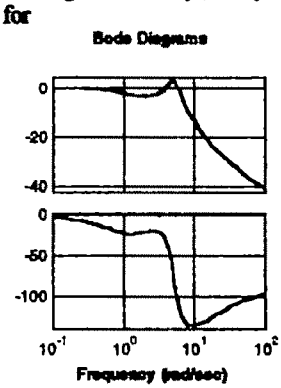

wz_1 for K : $\lambda = 0.5$

Fig.4

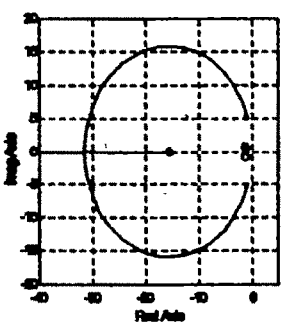

Root-Locus : wz_1 for K

Fig.5 : $\lambda = 0.5$

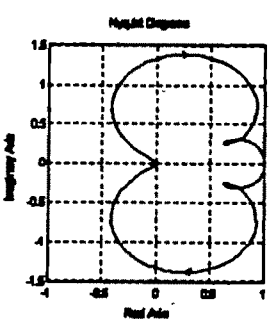

Nyquist-Plot : wz_1 for K :

Fig.6 : $\lambda = 0.5$

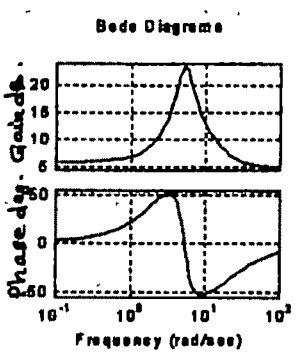

Bode-Diagram : wz_2 for $\bar{K}$

Fig.7 : $\lambda = 0.5$

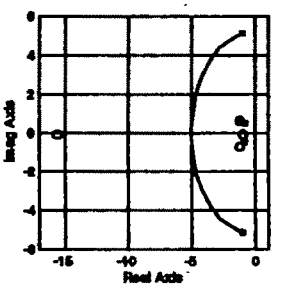

Root-Locus : $wz_{2\ \text{for}}\ \bar{K}$

Fig.8 : $\lambda = 0.5$

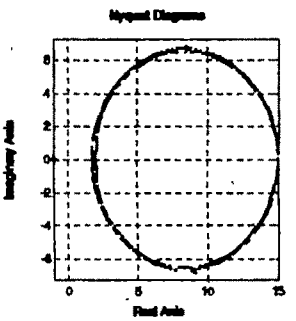

Nyquist-Plot : $wz_{2\ \text{for}}\ \bar{K}$

Fig.9 : $\lambda = 0.5$

$\lambda = 0.5$ for wz1 and wz_2 i.e., for controllers K and $\bar{K}$ are being drawn to Fig.4 through Fig.9 . The step-response of the designed controller for $\lambda = 0.5$ also gives the satisfactory results. The characteristic polynomial for $\lambda = 0.5$ is tested for stability using Kharitonov's polynomials. The characteristic equation when $\lambda = 0.5$ is

$$s^4 + 3.75s^3 + 45s^2 + 50.125s + 27.5 = 0$$

$$\rho(p^0) = \min\{s_1, r_w, r\} = \min\{2705642, 4.011289, 325.05692\} = 4.031189$$

$\mu(x) := \dfrac{\rho(p^0)}{\|c(x)\|_2} \rightarrow$ The stability margin [7], [12] of the system with the given controller.

The magnitude of the stability margin $\mu(x)$ is calculated and its value $\mu(x) = 0.020795$

Therefore, Kharitonov's four polynomials [9] , [10] are :

$k_{11}(s) : = 27.479202 + 50.104202s + 45.020798s^2 + 3.770798s^3 + s^4$
$k_{12}(s) : = 27.479202 + 50.145798s + 45.020798s^2 + 3.729202s^3 + s^4$
$k_{21}(s) : = 27.520798 + 50.104202s + 44.979202s^2 + 3.770798s^3 + s^4$
$k_{22}(s) : = 27.520798 + 50.145798 + 44.979202s^2 + 3.729202s^3 + s^4$

So, first column of Routh's Hurwitz [4] of Kharitonov's polynomials (4-nos.) are all positive. Hence Kharitonov's polynomials i.e., $k_{11}(s)$, $k_{12}(s)$, $k_{21}(s)$, $k_{22}(s)$ are Hurwitz . Thus we conclude, that the entire class of polynomials are Hurwitz. The example has been tested for other values of λ between 0 and 1 , and the result shows that the whole family of controllers which yields the closed-loop transfer matrix, $H_\lambda = \lambda H + (1-\lambda)\ \bar{H}$ makes the system stable.

CONCLUSION

In this chapter a closed-loop transfer matrix H has been formed. The closed-loop transfer matrix H should include every closed-loop transfer function necessary to evaluate a candidate controller or compare completing designs without

unsaturated requirements on transfer functions not appearing in H. It is useful to associate with each design specification, the set of transfer matrices that meet the design specification. Many design specifications are closed-loop convex. An infinity number of controllers can be designed when the design specifications are closed-loop convex. In this chapter each controller thus designed as been tested by Kharitonov's theorem. One numerical example has been described. Bode, Root-Locus, and Nyquist plots for w to z_1 and for w to z_2 of $\lambda = 0.5$ have been drawn, but for other values of $\lambda = 0.0, 0.3, 1.0$ have been tested. It has also been noted that the real part of the roots of the characteristic equations are all negative and therefore found satisfactory results about stability of the system. It has been shown rather heuristically that the criteria on robustness are concurrent with that of convex controller design.

REFERENCES

1. S. Boyd, C. Barratt, and S. Norman, " Linear Controller Design Limits of Performance Via Convex Optimization, " IEEE Proc., Vol. 78, No.3, March 1990.
2. A.Mukherjee, *Fundamental Treatise on Linear Programming Numerical Methods and Computer Programming in Fortran*, 1995, Pub. S. Bandyopadhyay, India.
3. C.A.Desoer, and W. S. Chan, "The Feedback International of Lumped Linear Time–Invariant Systems, " J. Franklin Inst., Vol. 300, pp.-335 – 351, Nov. – Dec1975..
4. B.C.Kuo, *Automatic Control Systems*, Second Edition, 1974, Prentice - Hall of India Private Limited, New Delhi.
5. M. Athans, and P. L. Falb, *Optimal Control : An Introduction to the Theory and its Applications* , 1966, McGraw – Hill Book Company.
6. Saadat Hadi, *Power System Analysis*, 1999, McGraw-Hill International Editions
7. L. H. Keel, S. P. Bhattacharyya, and J. W. Howze, " Robust Control with Structured Perturbations, " IEEE Trans. of Automatic Control, Vol. 39, No. 1, January 1988.
8. Katsuhiko Ogata, *Modern Control Engineering*, 1992, Prentice-Hall of India Private Limited.
9. B. Ross Barmishn, " A Generalization of Kharitonov's Four-Polynomial Concept for Robust Stability Problems with Linearly Dependent coefficient Perturbations," IEEE Transactions on Automat. Contr., Vol. AC.34, No.2 , pp.157-165, Feb. 1989.
10. R. J. Minnichelli, J. J. Anagnost, and C.A. Desoer, "An Elementary Proof of Kharitonov's Stability Theorem with Extensions," IEEE Transactions on Automat. Control, Vol. AC. 34, No. 9, pp. 995-998, Sept. 1989.
11. Joseph A. Edminister, Schaum's *Outline of Theory and Problems of Electric in SI Units* , 1965, McGraw- Hill International Book Company, New York.
12. Barmish, B. R., Kang, H. I., "A survey of extreme point results for robustness of control systems" , *Automatica* Vol. 29, 1, pp. 13-35, January, 1993.
13. Cevik, M. K. K., Schumacher, J. M., "The regulator problem with robust stability" *Automatica* Vol. 31, 10, pp. 1393-1406, October, 1995.
14. Qu,Zhihua, Kamen, E. W., Dorsey, J. F., "Continuous I/O robust control of SISO time-varying systems" *Automatica* Vol. 33, 4, pp.533-550, April, 1997.

A Double Order Reactive Power And Voltage Input Signals SVS Auxiliary Controller For Suppressing The Sub-Synchronous Resonance In A Power Systems

Sushil Kumar Gupta[1], A. K. Gupta[1] and Narendra Kumar[2]
[1]C. R. State College of Engineering. Murthal (Sonepat) India
[2]Delhi College of Engineering. Delhi, India

Abstract

This paper describes an investigation of a double order SVS auxiliary controller using reactive power and voltage signals as state variable feedback to suppress subsynchronous resonance of the power systems. The analysis is applied to the first benchmark model proposed by the IEEE Power Engineering Society task force on subsynchronous resonance. The results demonstrate that this controller is successful as a SSR countermeasure. The special feature of the controller is that a change in the capacitive compensation level in the transmission line does not affect the performance of the controller.

Keywords: SSR, SVS

INTRODUCTION

The problem of subsynchronous resonance (SSR) in power systems has received much attention since the two incidents of turbine generator shaft failure at Mohave Power Station in Nevada, U.S.A. [1]. Previous investigations [1-9] have shown that, unless precautionary steps are taken, unstable SSR oscillations could occur if the transmission system is to be operated at a modest level of series capacitor compensation.

Any perturbance in the system produces the oscillations of the natural frequency ($f_n=f_0\sqrt{(X_C/X_L)}$ of the system. Flux component produced by the current component of this frequency in the stator of the generator runs slower than the rotor thereby producing a negative slip component and, hence, at the same time generator acts as the induction generator causing the self-excitation [2].

This effect is called induction generator effect. The frequency of the rotor current (or torque) because of this natural frequency component is given by $s.f_n$, which comes out to be $(50-f_n)$, where 's' is the slip and power frequency is 50 Hz. If this torque frequency $(50-f_n)$ coincides with or is close to a rotational modal frequency f_m of the shaft system, or we can say if f_n is the complement of the shaft system frequency, a resonance called subsychronous resonance takes place causing enhanced subsynchronous electrical torque and growing oscillations. With these growing oscillations the turbine generator shaft will break with disastrous consequences. Even if the oscillations are not unstable, system disturbance can result in transient shaft torque of high magnitude, causing loss of fatigue life of the shaft. This phenomenon is called torsional interaction effect. The following control strategies have been reported in the literature as a means of suppressing unstable subsynchronous oscillations: a) using Shunt Reactor Control, b) using SIMO Controllers, c) using Controlled Excitation System d) using Controlled Series Compensation. H. M. A. Hamdan [3] presented a study for enhancing the SSR damping using excitation control proves cheaper but less effective for transient stability. K. R. Padiyar and R. K. Verma [4] presented an investigation on damping torque analysis of static VAR system controller. J. R. Smith and D. A. Pierre [5] investigated two controllers for power system damping. But all of these [4,5] methods are based on a linearized power system model around a nominal operating point. However, the high degree of non linearity of power systems and continuous change in operating points make it very difficult to achieve a good controller design using only single nominal model.

Narendra Kumar and M. P. Dave [6] developed a combined reactive power and frequency auxiliary controller for the SVS located at the middle of the transmission line, which stabilized all the torsional mode oscillations. The results of this study show that mode 4 is marginally stabilized and the compensation of the transmission line is done at a fixed level of 25%. The applicability of the controller at different levels of compensation has not been shown. This paper describes the design and application of a double order reactive power and voltage signals based SVS auxiliary controller for suppressing the subsynchronous resonance. It presents the mathematical model of the system. The results demonstrate the effectiveness of the controller.

THEORY

In order to investigate the nonlinear power system, it is necessary to describe each system element by the mathematical model. The differential equations describing the generator, excitation, transmission, SVS system and mechanical system are considered. The theory related to the proposed controller is given in succeeding section.

Mechanical system

The mechanical system consists of a four stage turbine, a generator and an exciter as shown in figure 1 and is represented as six inertia interconnected by five connecting shafts. Each major rotating element is considered as a lumped mass represented by its inertia while every shaft is considered as a mass-less torsional spring with its stiffness expressed by the spring constant. Viscous damping of each mass and shaft segment is represented by a dash-pot damping.

Generator Model

The detailed mathematical model of the synchronous machine used is as given in [7]. The model includes the field winding and a damper winding along the d-axis and two damper windings along the q-axis.

Excitation System Model

An IEEE type–I excitation system with continuously acting system has been considered here [8].

Transmission Line Model

The transmission line is modeled by a single lumped parameter π-circuit equivalent of a long line. Figure 2 below shows the α-axis representation of the AC network. SVS is connected at the receiving end, and the line is compensated at sending end side.

SVS Model

The static compensator is an adjustable shunt susceptance. Thyristor Controlled Reactor with fixed capacitor (TCR-FC) includes a closed loop voltage regulator and thyristor gating angle control system as shown in figure 3. These control posses a slightly delayed time response in correcting the change in SVS bus voltage resulting from disturbances on the transmission system. SVS has been employed to an increasing extent in the modern power systems due to its capability of VAR generation and absorption. SVS can maintain the voltage deviation within a close tolerance and causes enhancement of dynamic performance of the system. A worthwhile improvement in transient stability is possible with SVC of limited size [9]. The block diagram representations of static VAR model is shown below in figure 4.

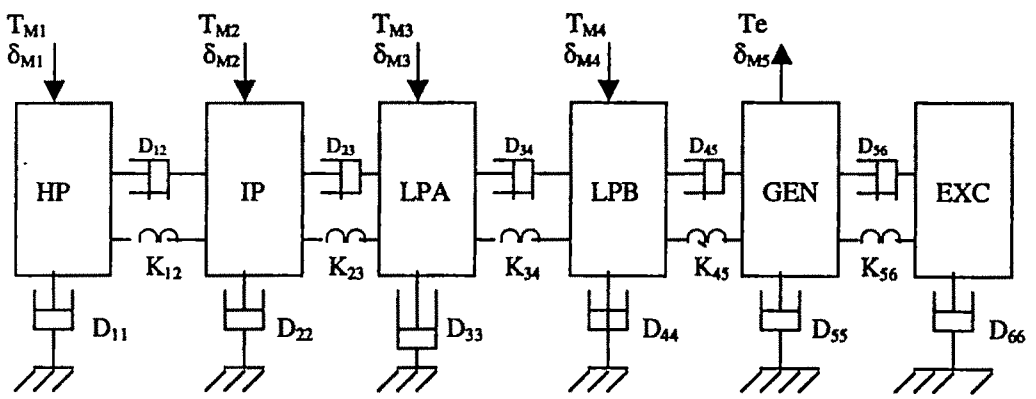

Fig. 1 Mechanical System

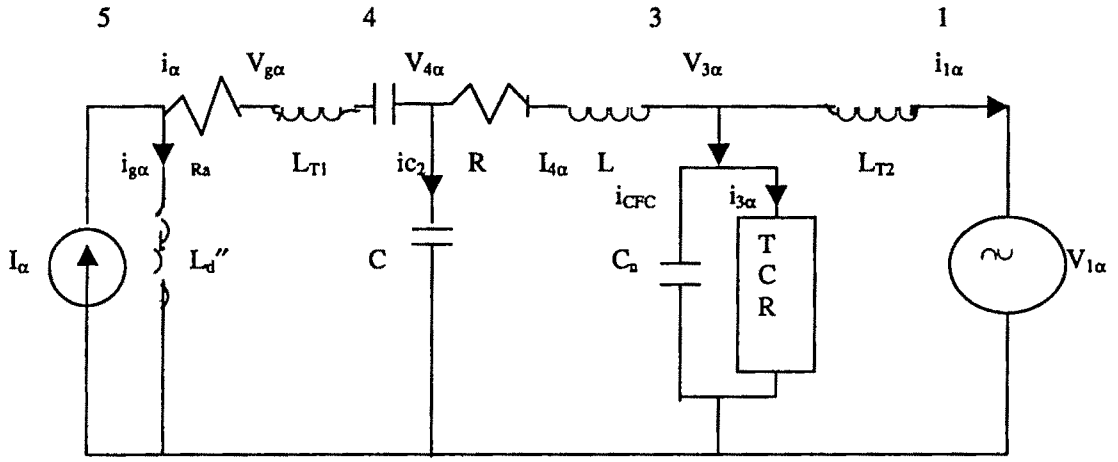

Fig. 2 α-axis representation of the AC network

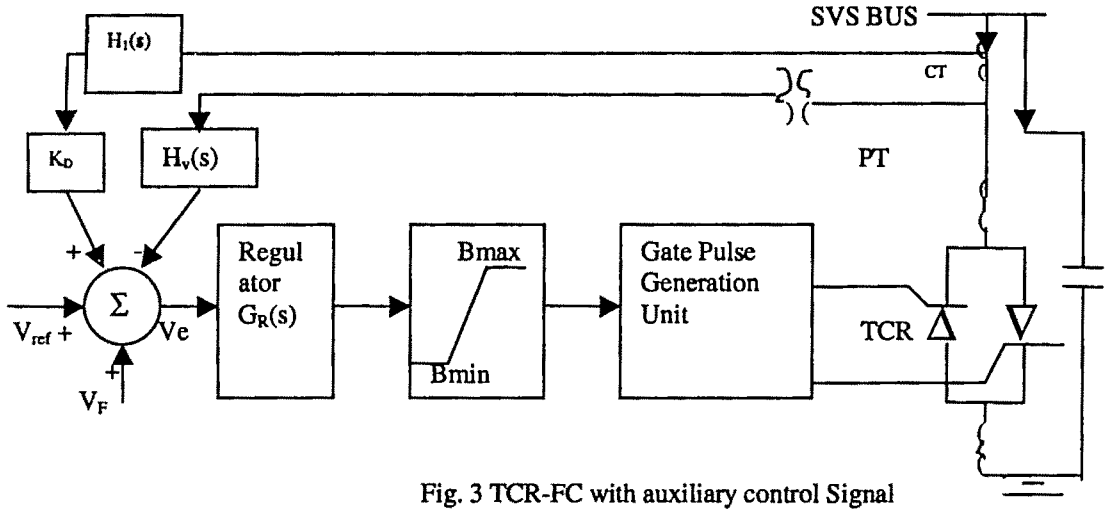

Fig. 3 TCR-FC with auxiliary control Signal

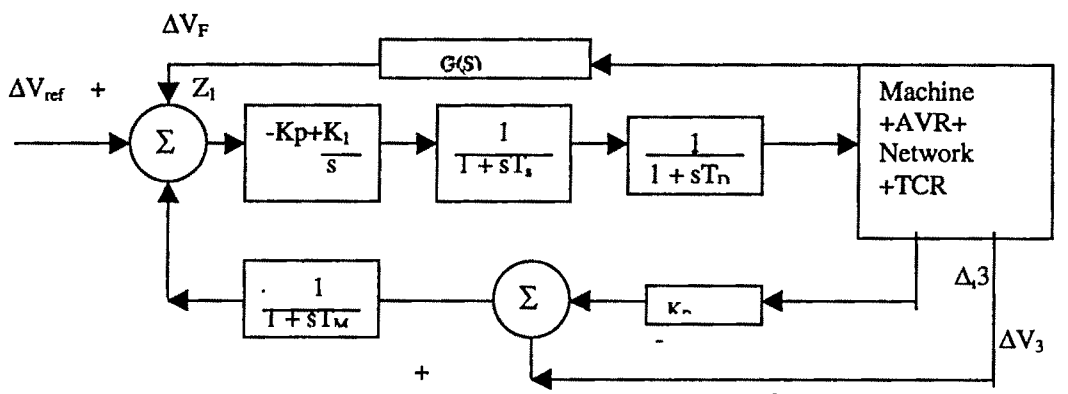

Fig. 4 SVS model

Auxiliary Controller

The compensators are generally used to improve the transient performance of the system. Feedback compensation often provides greater stiffness against disturbance. The auxiliary controller's transfer function G(S) should have an appropriate phase compensation circuit to compensate for the phase lag between the SVS input and output susceptance. This phase lag is because of the delay associated with SVS controller and measurement units. To make the SVS control system more effective the reactive power (Q_3) at the SVS bus and SVS bus voltage are used as auxiliary input signals and are applied through a double order controller as shown in figure 5. The linear blocks composed of the constants x, α, ω_d and G are expected to offer the required phase lead to the selected stabilizing signals. The controller parameters, given in table 1, are optimally found from the locus of the results obtained by the recursive technique.

The auxiliary controller adds two poles and two zeros in the system. The parameters are optimized such that the effects of these additional poles on the system is minimum while the effect of additive zeros is to counter balance the effect of unstable torsional modes of the system.

Here, $y=(\alpha^2+\omega_d^2)/x$

$p = ((x-\alpha)^2+\omega_d^2)/(y-x)$

$q =((y-\alpha)^2+\omega_d^2)/(x-y)$

Reactive Power (RP) and voltage signals (V_S) at the SVS bus are being used as the auxiliary input signals, the set of differential equations of it is as under:

$RP=V_{3D}(i_{4Q0}-i_{4Q})+i_{4Q}(V_{3D0}-V_{3D})-V_{3Q}(i_{4D0}-i_{4D})-i_{4D}(V_{3Q0}-V_{3Q})$

$V_S=(V_{3D}/V_{30})(V_{3D0}-V_{3D})+(V_{3Q}/V_{30})(V_{3Q0}-V_{3Q})$

$U_c=RP+G_v.V_S$

$\Delta V_F=G.Uc+Z_{c1}+Z_{c2}$

$dZ_{c1}/dt=-x.Z_{c1}+p.Uc$

$dZ_{c2}/dt=-y.Z_{c2}+q.Uc$

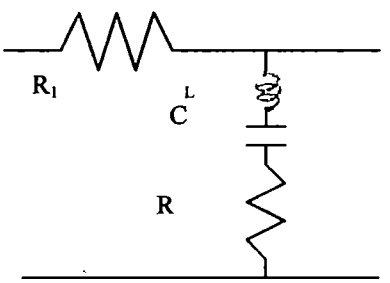

Fig. 6 Realization of circuit for the controller of figure 5

Where, $R_1 = -L(p+q)/G$

$a = x+y+(p+q)/G$

$C = 1/L(\omega_d^2+a^2)$

$R = 2.a.L$

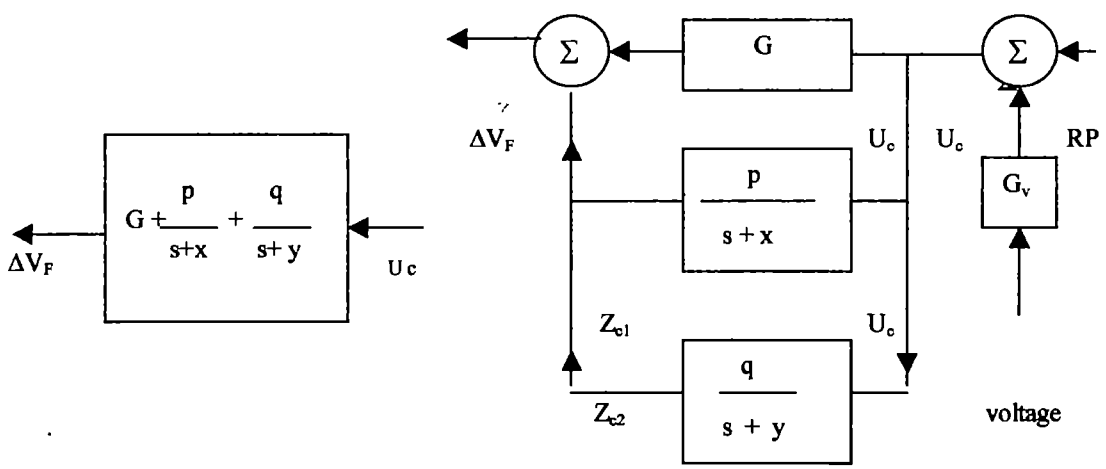

Fig. 5 Auxiliary controllers block diagram

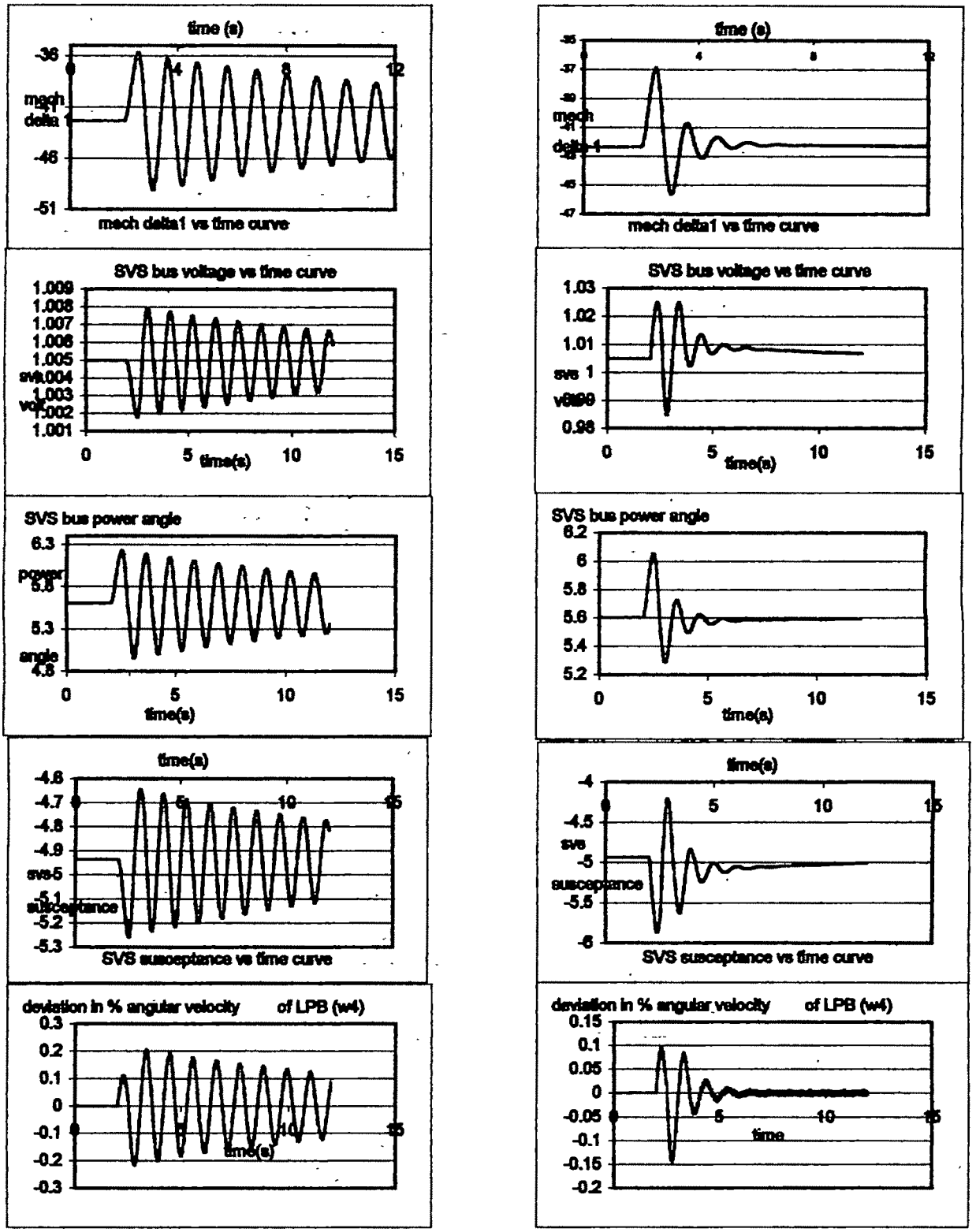

Fig. 7 variations in HP Shaft angle, in transmission system states and in angular velocity.
due to 25% increase in mechanical torque for 0.5 seconds.
(a). Response curves without auxiliary controller (b). Response curves with auxiliary controller

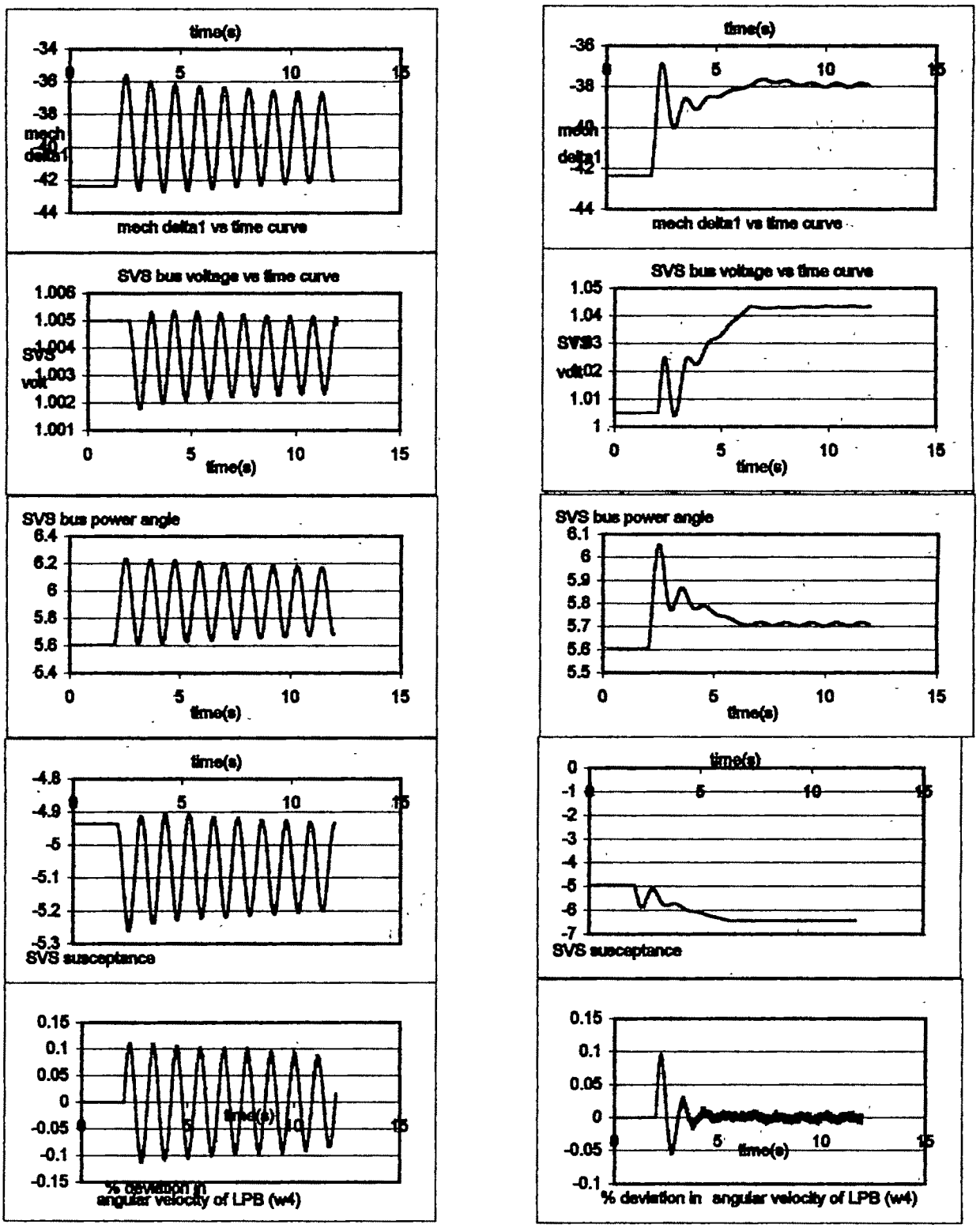
time(s)
mech delta1 vs time curve
SVS bus voltage vs time curve
SVS bus power angle
SVS susceptance
% deviation in angular velocity of LPB (w4)

Fig.8 Variation in angular position of inertias due to sustained disturbance of 25% in input torque. (a). Response curves withoutauxiliary controller (b). Response curves with auxiliary controller

TRANSIENT PERFORMANCE

The study system consists of a 22kV, 1110 MVA synchronous generator supplying power to an infinite bus over a 400kV, 600km long series compensated single circuit transmission line. The other data are given in [6]. The study is carried out at 10%, 25%, 40%, 55% and 70% series compensation levels of transmission line, as at these levels of compensations different modes are found more prominent. The loadflow study is carried out for calculating the operating point at normal running conditions. Time-domain computer simulation study has been performed for solving the nonlinear system differential equations by fourth order Runga Kutta method. Disturbance is simulated by 25% increase in input torque for 0.5 seconds. The figures 7 show a set of response curves for the system consisting SVS with and without auxiliary controller at 55% of series compensations. Similar curves are also obtained at other levels of series compensations. The system's natural damping is considered to be zero to see the damping effect of proposed controller exclusively. The response curves of sustained faults of same magnitude are also been plotted as shown in figure 8 with and without auxiliary controller.

RESULTS AND CONCLUSION

In this paper, a reactive power and voltage input signals based SVS auxiliary controller is proposed for suppressing the torsional oscillations in the power systems. For evaluating the performance of double order auxiliary controller under large disturbance conditions the digital simulation study has been carried out using the non-linear system model. Figures 7 show the variations of HP turbine shaft angle, SVS bus voltage, SVS bus power angle, SVS susceptance and deviation in angular velocity of LPB turbine, when a disturbance of sudden increase of 25% input torque for 0.5 seconds is applied. It is seen from the response curves that the responses are highly oscillatory without the application of auxiliary controller. And these responses are effectively stabilized on application of the proposed controller. Figures 8 show the variation in same parameters when step increase of 25% input mechanical torque is applied. Response curves show the large amplitude oscillations without the application of the controller. Large amplitude oscillations are suppressed effectively on application of the proposed controller as shown. The controller is applicable for wide range of series compensation of the transmission line and for wide range of load variations. It does not suffer from any limitation.

REFERENCES

1. SSR Task Force, Analysis and control of Subsynchronous Resonance, IEEE Publ. 76 CH10660-PWR, 1976.
2. IEEE subsynchronous Resonance Working Group, Terms, definations and symbols for subsynchronous oscillations, IEEE Transactions on PAS, 104, 1985, 1326-1334.
3. H. M. A. Hamdan, SSR in power system comprising two identical generators, Electric Machines and Power Systems, 27,1999, 53-62.
4. K. R. Padiyar R. K. Verma, Damping torque analysis of static VAR system controller, IEEE Transactions on Power Systems, 6(2), May 1991, 450-465.
5. J. R. Smith et al, An enhanced LQ adaptive VAR unit controller for power system damping, IEEE Transactions on Power Systems, 4(2), May 1989, 443-451.
6. Narendra Kumar and M. P. Dave, Application of an auxiliary controlled static VAR system for damping SSR in power systems, EPSR, 37, 1996, 189-201.
7. R. S. Ramshaw and K. R. Padiyar, Generalized system model for slipring machines, IEE proceedings, 120(6), June 1973.
8. P .M. Anderson et al, Subsynchronous resonance in power systems, IEEE Press Edition 1989.
9. N. G. Hingorani and Laszio Gyugyi, Understanding FACTS: Concepts and technology of flexibl ac transmissionsystems, (IEEE Press, Piscataway 2000).

A new approach to Power System Frequency Estimation using Least Mean Square technique

A. K. Pradhan[!], M. K. Patel[+] and A. Routray[*]
[!]Department of Electrical Engineering,
[+]Department of Computer Sc. & Engineering,
University College of Engineering, Burla, Orissa-768018
[*]Department of Electrical Engineering, I.I.T., Kharagpur-721302
E-mail of corresponding author: akp@uceb.ren.nic.in

Abstract

Frequency is an important parameter in power system monitoring, control and protection. A least mean square (LMS) algorithm based frequency estimation technique is presented in this paper. The three phase voltage signals are converted to a complex form for processing of the filter. The performance of the filter is studied through simulations at different situations of the power system.

Keywords: Frequency estimation, LMS algorithm

INTRODUCTION

In a power system as the frequency varies dynamically the conventional phasor estimation techniques based on constant frequency modeling are affected significantly. Further the deviation in system frequency from its nominal value results in component-reactance change, which influences different relay functionality. Frequency, therefore, is an important parameter in power system relaying, monitoring, operation and control using digital technologies. A large number of numerical methods available for frequency estimation from digitized samples of system voltage. Conventional methods assume that the power system voltage waveform is purely sinusoidal and therefore, the time between two zero crossing is an indication of system frequency [1-2]. An extended complex Kalman filter for dynamic frequency estimation is proposed in [3]. It is simple from modeling point of view, but requires much computation. A simple and computationally efficient frequency estimation technique is proposed in this work where normalized least mean square estimation technique is used. Normalized LMS is a variant of most popular LMS algorithm where the constant term in the conventional LMS algorithm is replaced by a time varying equation for faster convergence. The LMS technique as such possesses the advantage of simplicity in its underlying structure besides extensive theoretical analysis and experimental verification of fundamental properties (convergence, tracking ability and robustness). The scheme uses three phase voltages to derive a complex signal for the LMS approach. The performance of such an estimator is adjudged through numerous examples.

LMS BASED FREQUENCY ESTIMATION

The discrete representation of three phase voltages of a power system is obtained as

$$\begin{aligned} V_{a_k} &= V_m \cos(\omega k\Delta T + \phi) + \in_{a_k} \\ V_{b_k} &= V_m \cos(\omega k\Delta T + \phi - 2\pi/3) + \in_{b_k} \\ V_{c_k} &= V_m \cos(\omega k\Delta T + \phi + 2\pi/3) + \in_{c_k} \end{aligned} \quad (1)$$

where V_m is the peak value of fundamental component, $\in_{a_k}, \in_{b_k}$ and $\in_{c_k}$ are noise terms that can be any combination of white noise and harmonics, ΔT is the sampling interval, k is the sampling instant (iteration count), ϕ is the phase fundamental component and ω is the angular frequency of the voltage signal ($=2\pi f_r$, f_r being the system frequency). The α-β components are obtained from the above discrete phase voltages as

$$\begin{bmatrix} V_\alpha \\ V_\beta \end{bmatrix} = \sqrt{\frac{2}{3}} \begin{bmatrix} 1 & -\frac{1}{2} & -\frac{1}{2} \\ 0 & \frac{\sqrt{3}}{2} & \frac{\sqrt{3}}{2} \end{bmatrix} \begin{bmatrix} V_{a_k} \\ V_{b_k} \\ V_{c_k} \end{bmatrix} \quad (2)$$

A complex voltage V_k is obtained from (2.2) as

$$V_k = V_{\alpha_k} + jV_{\beta_k} = Ae^{j(\omega k\Delta T+\phi)} + \xi_k \quad (3)$$

where A is amplitude of the signal V_k and ξ_k is its noise component.

The voltage can be modeled as

$$V_k = V_{k-1}e^{j\omega\Delta T} \quad (4)$$

This model is utilized in the proposed frequency estimation algorithm and the scheme that describes the method estimation process is shown in Fig.1.

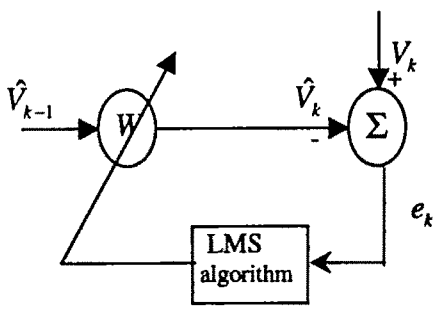

Fig.1 LMS based frequency estimation approach

In the above figure e_k stands for the error signal;

$$e_k = V_k - \hat{V}_k \quad (5)$$

where $\hat{V}_k$ is estimated value of voltage at the k^{th} instant. Further

$$\hat{V}_k = W_{k-1}\hat{V}_{k-1} \quad (6)$$

where the weight $V_k = e^{j\hat{\omega}_{k-1}\Delta T}$, $\hat{\omega}$ being estimated frequency.

Applying the normalized LMS algorithm,

$$W_k = W_{k-1} + \mu_k \hat{x}_k e_k$$

$$\text{where } x_k = \hat{V}_k \quad (7)$$

$$\mu_k = \alpha/(\beta + x_k^T x_k),\ \alpha \in (0,2), 0 \le \beta$$

The presence of β guarantees that the denominator never becomes zero, while α is a relation factor. The frequency is calculated as

$$\hat{f}_k = \frac{1}{2\pi\Delta T}\sin^{-1}[\mathrm{Im}(W_k)]$$

where Im stands for imaginary of a quantity.

SIMULATION RESULTS

The new technique is applied to estimate fundamental frequency during various power system operating conditions. In MATLAB programming environment with a sampling rate of 6.4 kHz different simulations are performed. In all cases the LMS parameters considered are μ=0.12,α=0.08 and β=0.01. Further to enhance the accuracy in the estimation process an averaging window of $1/4^{th}$ cycle width is used in the simulations.

Case 1: In presence of noise

Fig.2 shows a case of 50.5Hz fundamental frequency estimation in the presence of random white noise. Fundamental signal is contaminated with noise which is expected in a typical power system environment. The plot shows the fast and accurate frequency estimation capability of the new LMS based approach. The error in estimation within half a cycle of initialization falls within 0.005Hz.

Case 2 : In presence of harmonics

At 50.5 Hz fundamental frequency the input voltage signal of 1 p.u. is contaminated with the presence of 0.05 p.u. third harmonic, 0.001 p.u. fifth harmonic and 0.001 p.u. seventh harmonic. Fig. 3 presents the estimated frequency in such a situation. It is obseved that the error in estimation falls within 0.002Hz after inialization. It is obseved that the third harmonic component does not influence performance of the filter as the α-β transform eliminates it. Further for higher order harmonic components (fifth harmonic and above) accuacy in frequency estinmation is influenced significantly and therefore, a prefilter will be required in such situations.

Case 3 : With frequency jump up in the signal

The voltage signal is affected by step change in frequency from 50.5 Hz to 49.5 Hz at 0.04 s. It is observed from Fig. 4 that the accurate estimate is obtained within half a cycle after the inception of the change in frequency.

Case 4: With sudden amplitude change in the signal

The 50 Hz voltage signal is subjected to a sudden amplitude change of 0.01 p. u. at 0.04 s. The performance of the estimator is adjudged from Fig.5 and it is observed that accurate estimation is obtained within one cycle after initiation of the change.

CONCLUSION

The work proposes a new frequency estimation technique for power system environment. The LMS based approach using sampled values of three phase voltage signals is simple in its formulation. Test results show that the accuracy and speed of estimation is satisfactory even in the

presence of noise/ harmonics and during sudden changes in signal parameters.

REFERENCES

1. A. G. Phadke, J. Thorp and M. Adamiak, "A New Measurement Technique for Tracking Voltage Phasors, Local system frequency and Rate of Change of frequency" , IEEE Trans. on Power Apparatus and Systems, Vol. 102, No.5, 1983, pp.1025-1038
2. M. S. Sachdev and M. M. Giray, "A Least Square Technique for Determining Power System Frequency" IEEE Trans. on Power Apparatus and Systems, Vol.104, No.2, 1985, pp.437-443.
3. P. K. Dash, A. K. Pradhan and G. Panda, "Frequency Estimation of Distorted Power System Signals using Extended Complex Kalman Filter", IEEE Trans. on Power Delivery, Vol.14, No.3, 1999, pp.761-766.

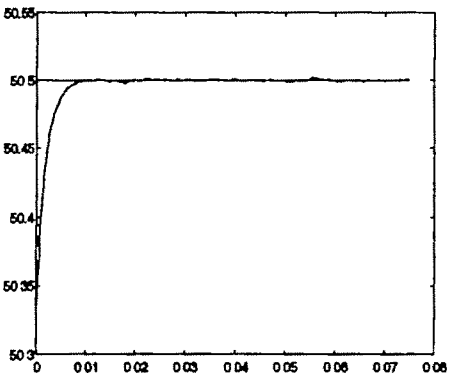

Fig.2 Frequency estimation in presence of noise

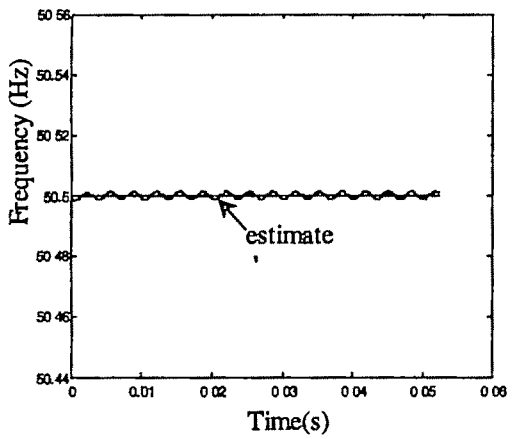

Fig.3 Frequency estimation in presence of harmonics

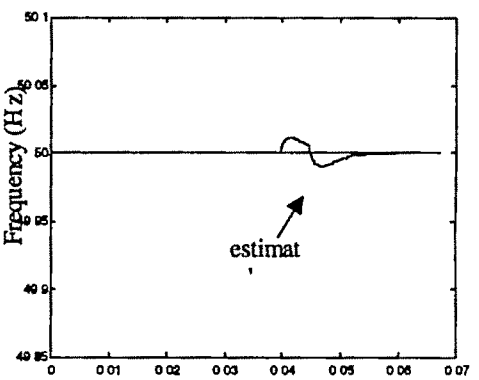

Fig.5 Frequency estimation with sudden amplitude change in the signal

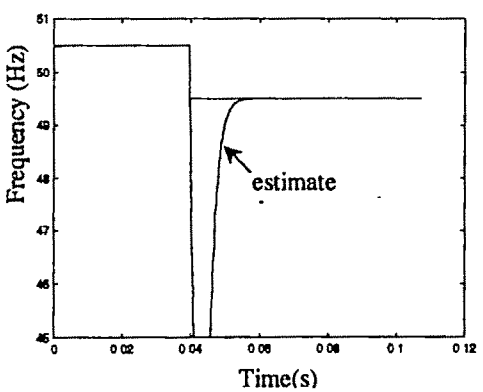

Fig 4 Frequency estimation during jump in system frequency

An On Line Microprocessor Based Generation Frequency And Voltage Regulator Using LFC And SVC

Arabinda Das[!], T. K. Sengupta[+], A. K. Mukhopadhyay[*]

[!] Electrical Engineering Department, Jadavpur University, Calcutta - 700 032, India
[+] General Manager (Tech.), Howrah Mills Co. Ltd, 493/C, G.T.Road (S), Howrah - 711102, India
*Sir R. B. Ghosh Professor, Department of Applied Physics, University of Calcutta,
92, A.P.C. Road, Calcutta - 700 009, India
e-mail : dr_arabinda@hotmail.com

Abstract

Fluctuation of load on alternator along with SVC at its generating end can be compensated by regulating frequency and reactive power. A microprocessor based digitally controlled controller has been developed to regulate the frequency and voltage by adjusting speed of prime mover and reactive power flow of FC-TCR type SVC, respectively. For accurate control of speed of prime mover and reactive power, the idea of parallel processing of microprocessor has been utilised. The software has been developed to control frequency and voltage by two Slave Processors guided by a Central Processor.

Key words : Load frequency and voltage control, Static VAR compensator, Microprocessor.

LIST OF SYMBOLS

Δ : prefix denoting a small change
Δf : frequency deviation (Hz)
ΔP_g : grnerated real power deviation (pu, Mw)
ΔX_g : deviation in govornor position (pu, Mw)
T_t, T_g : turbine and govornor time constant, sec.
R : regulator constant (Hz/pu Mw)
K_r, T_r : thyristor gain and time constant
K_w : washout time constant of the PI controller
ΔV_t : terminal voltage deviation
$\Delta\delta$: rotor angle deviation
ΔP_c : incremental change in speed change position
ΔP_d : deviation in demand
K_P, K_I : PI controller gains for the SVC
B : inductive suceptance of Static VAR compensator
T_a, K_a : voltage regulator time constant and gain
T_m : mechanical torque
T_e : electromagnetic torque
T_{do}' : d-axis armature winding transient open circuit time constant
M, D : inertia constant and damping co-efficient
$\Delta E_q'$: incremental change in voltage behind transient reactance
P, Q : active and reactive power of generator
ΔE_{fd} : incremental change in field voltage
ΔV_{SVC} : static VAR controller output voltage
K_s, T_s : generator gain and time constant
R_t, X_t : transmission line resistance and reactance
$\Delta\omega$: Change in rotor speed
X_d, X_q : d-axis and q-axis reactance
X_d' : d-axis transient reactance
K_1 - K_7 : constants of the linearised model synchronous machine

INTRODUCTION

In present day the demand of load frequency and voltage control at macro level is a major interest among power system researchers due to the power system environment, particularly while

unit sizes, unit capacity, system sizes, system interconnection etc. are increasing at faster rate. It is well known that during variation of load in a longitudinal power supply (LPS) system, the frequency as well as terminal voltage changes. This is harmful both for power apparatus as well as for power system. In interconnected system, the under frequency causes excess load on generator and finally cumulative effect on almost all generators and thereby further fall in frequency, result in system instability and blackout. However, the frequency deviation at generating end can be compensated by controlling the speed of the turbine / prime mover where as the voltage level can be regulated by controlling the excitation of the alternator.

Use of SVC (Static VAR Compensator) at distribution end of LPS system for controlling the voltage and also the power factor is not new [8 -12]. Refs. [5 - 6] describe a new application of SVC, where it is used at the generating end to dampen frequency oscillation. Literature [1 - 4] survey reveals that if SVC is used at generating end of the generator, the frequency and the terminal voltage deviation and hence the excessive power loading can be compensated by adjusting load angle of generator and by adjusting the reactive power generated by SVC, respectively. Also it may be mentioned that the regulation of terminal voltage at generating end and hence adjustment of reactive power relives excitation system from excessive loading, hazards and complicated operation.

In this paper a microprocessor based controller has been reported in which an algorithm suitable for an 8-bit microprocessor has been developed which generates control signal to control prime mover and to adjust reactive power depending on the deviation of frequency and voltage over recommended level, respectively. To justify the efficacy of the developed scheme, a prototype has been fabricated and the controller has been implemented on a separately excited dc motor - three phase alternator set with FC-TCR (Fixed Capacitor - Thyristor Controlled Reactor) type SVC connected at generating end.

A BRIEF REVIEW

Fig. 1 describes the block diagram of one area load frequency controller (LFC) system. Refs. [7-8] show that in LFC system the change in electrical output power of the machine is given by

$$\Delta P_e = K_7 \cdot \Delta\delta$$

where $\Delta\delta$ is the rotor power angle deviation and K_7 is the constant.

The block diagram of an SVC model combined with power system is shown in fig. 2. Refs. [7-8] show that deviation of rotor angle can be represented by

$$\Delta\delta = K_8 \cdot \Delta Q_{SVC} + K_9 \cdot \Delta f$$

Hence the change in electrical power output can be expressed as

$$\Delta P_e = K_7 K_8 \cdot \Delta Q_{SVC} + K_7 K_9 \Delta f$$

$$= K_{10} \Delta Q_{SVC} + K_{11} \Delta f$$

i.e., the excessive power can be compensated by adjusting frequency by means of controlling the speed of prime mover and also by controlling the reactive power by means of SVC.

THE PROPOSED SCHEME

Based on the above discussion, a control scheme for controlling frequency and voltage and hence to compensate the excessive loading, has been developed and presented in fig. 3. Here a typical LPS system for real time operation has been taken into consideration where a delta connected FC-TCR type SVC has been connected at generating end in which separately excited dc motor acts as a prime mover. The delta connection of SVC (fig. 4) is to eliminate the third harmonic. To create frequency and voltage deviation by means of load fluctuation loading arrangement has been provided at load bus.

To compensate frequency and voltage deviation, Master -Slave arrangement of microprocessor has been provided. In this

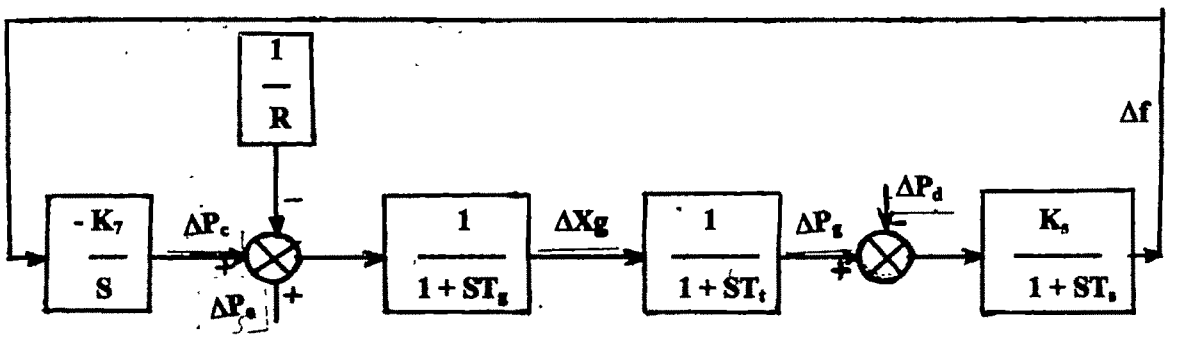

Fig. 1 Block diagram of power system control of one area system.

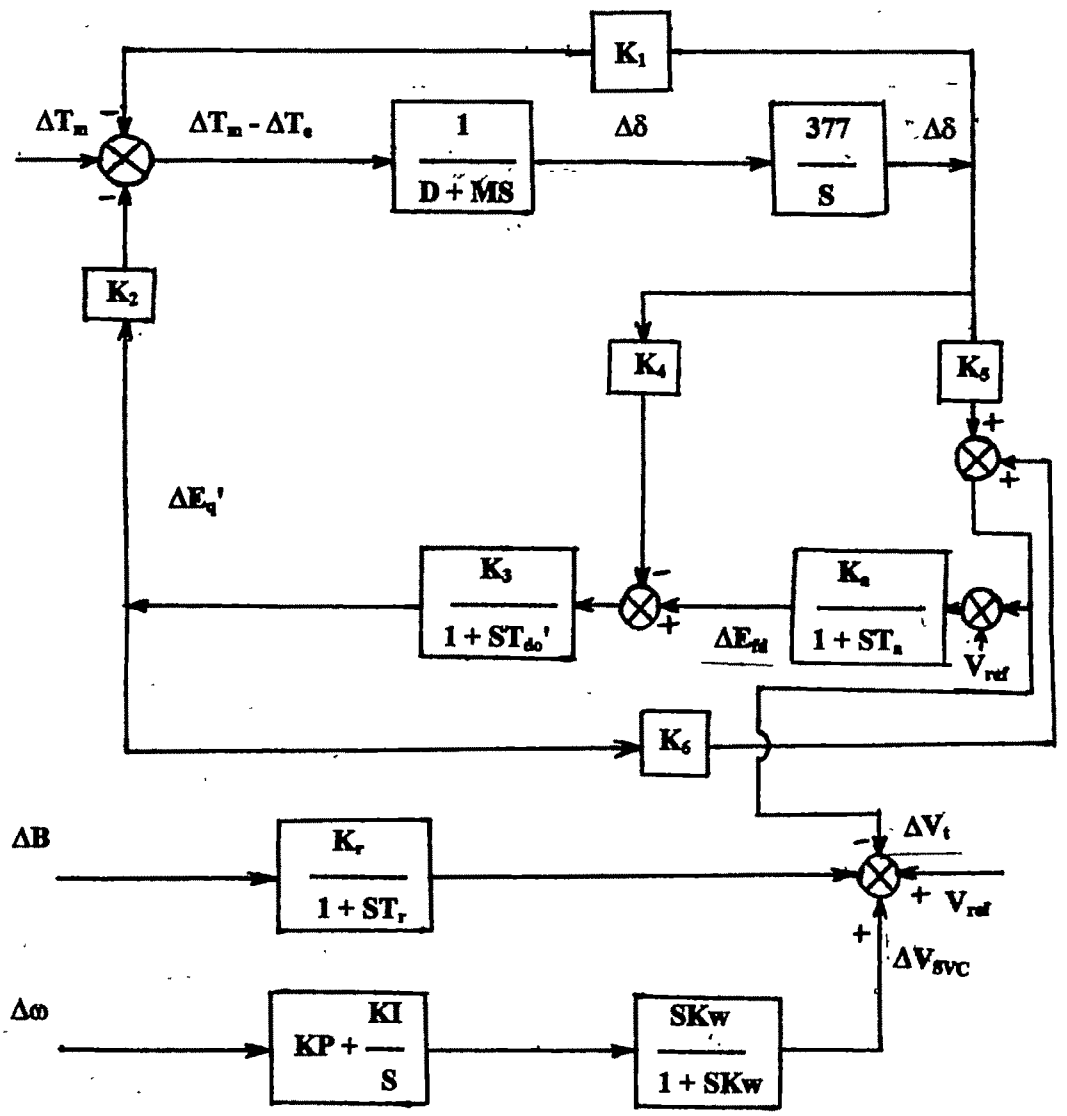

Fig. 2 SVC model combined with power system.

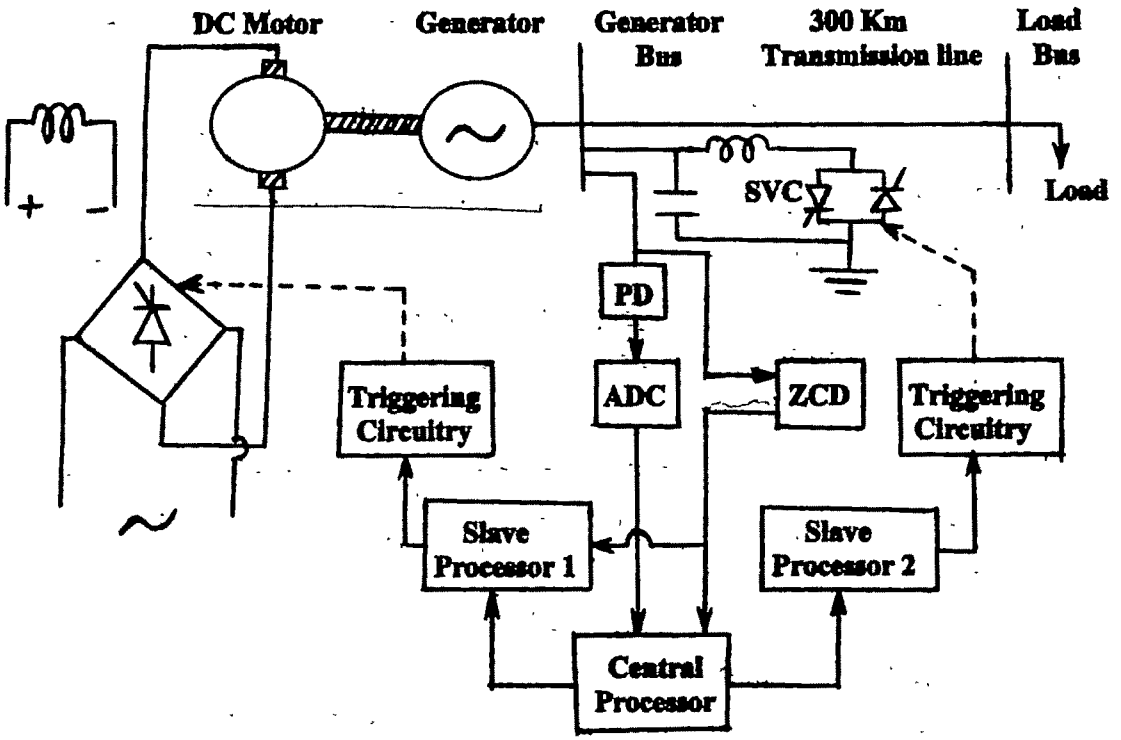

Fig. 3 Schematic Block diagram of the proposed scheme.

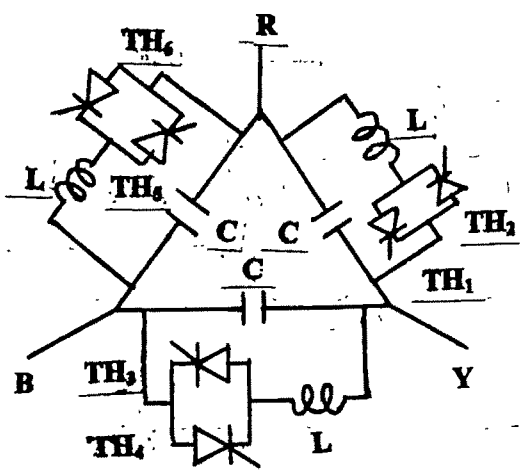

Fig. 4 The SVC module.

control scheme, Central Processor receives the train of square wave signal from Zero Crossing Detector (ZCD) based on IC LM-339 and detects the frequency deviation using the relation [14]

$$\Delta f = 50\,(N - N_{50})/N_{50}$$

where N and N_{50} be the count number for a small time interval over half cycle instantaneous and 50 Hz supply frequency, respectively.

Δf may be positive, negative or zero representing under, over and normal frequency respectively. After identifying the nature of Δf, Central Processor generates and transmits the signal 02, 01 or 00 to Slave Processor - 1 for the positive, negative and zero value of Δf. For receiving signal 02 from its master, the Slave Processor - 1 increases the speed of the separately excited dc motor by decreasing the trigger angle of the thyristor connected in full wave half controlled bridge. If the signal received by the Slave Processor - 2 is 01, then it decreases the speed of the prime mover by increasing the trigger angle of the thyristors where as for the signal 00, the Slave Processor - 2 continues its previous operation. It may be

mentioned here that after changing the triggering angle, microprocessor continues the same triggering operation for a number of cycles to stabilise the power system.

For controlling the reactive power, the Central Processor receives the signal through Peak Detector (PD) based on IC LM-324 and Analog to Digital Converter (ADC) based on IC ADC 0808. After receiving the voltage signal, it compares with the set value of voltage and generates and transmits the signal 20, 10 and 00 for over, under and normal voltage respectively to the Slave Processor - 2. For receiving the signal 20, the Slave Processor - 2 reduces the reactive power flow by increasing the triggering angle of the thyristors in steps whereas for the signal 10 it increases the reactive power flow by decreasing the triggering angle. In this case also after adjusting the trigger angle the processor repeats the same cyclic operation for a number of cycles to stbalise the power system.

SOFTWARE

Using the concept of parallel processing of microprocessor an intelligent software suitable for 8085A CPU based microprocessor has been developed. In this scheme, the Master Processor senses the frequency and voltage deviation through software execution from generating end and provides guidance to the two Slave Processors. After receiving the guidance, the Slave Processor 1 and 2 adjust the frequency by controlling the triggering angle in thyristor bridge and voltage by controlling the triggering angle of SVC, respectively. The developed software for Central and two Slave Processors has been presented in fig. 5 - 7.

EXPERIMENTATION

Based on the proposed scheme, a prototype model have been developed and tested in the laboratory. In this model a three phase, 415 V (L-L) generator coupled with a separately excited dc motor has been considered. The generator is connected with 300 Km transmission line simulator. To create the change in frequency and voltage through load variation, a mixed load consisting of induction motor, fixed inductor and resistor has been provided in load bus. Utilising the above discussed software, a controller has been developed and implemented in the laboratory. The experimentation shows that the power and voltage can be adjusted over the normal excitation with minimum oscillation.

DISCUSSION

The purpose of SVC used in this scheme is quite different from conventional SVC. Experimental results show that during excessive power deficit, the power can be adjusted by compensating the frequency and the reactive power. The SVC used in generating end serves two purposes. Firstly it provides reactive power compensation to maintain the terminal voltage and secondly it improves the dynamic performance in the transient state of the inception of disturbance. Since SVC itself is capable of damping dynamic power system oscillation [14], it provides damping during power oscillation arising during frequency adjustment.

REFERENCES

1. Golver J. D. and Schueppe F. C., "Advanced load frequency control", IEEE Trans. on Power Apparatus and Systems, Vol. PAS-91, No. 5, Pp. 2095 - 2102, Sept - Oct., 1972.

2. Kawabata H. and Kido M., A decentralize scheme of load frequency control of power system"' Elec. Engineering in Japan, Vol. 102, No. 4, Pp. 100 - 1065, 1982.

3. Miniesy S. M. and Bohn E. V, " Two level control of interconnected power plants", IEEE Trans. on Power Apparatus and Systems, Vol. PAS-90, No. 6, Pp. 2742 - 2747, 1971.

4. Hiyama T, "Design of decentralized load frequency regulators for interconnected power systems" IEE Proce., Vol. 129, Pt.c, No. 1, Pp. 17 - 23, Jan., 1982.

5. Yao-nan Yu, " Electric Power System Dynamic", Academic Press , INC, 1983.

6. EL-EMARY A.A and EL-SHIBINA M.A, "Application of static VAR compensation for

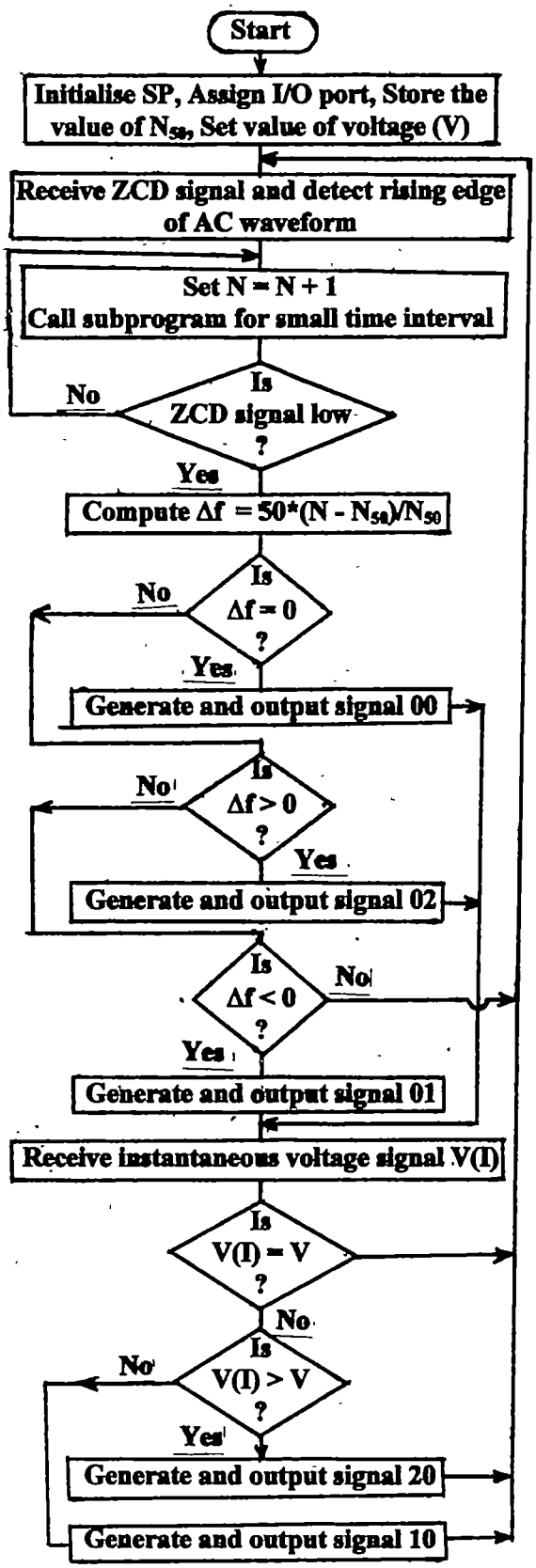

Fig. 5 Software for Central Processor

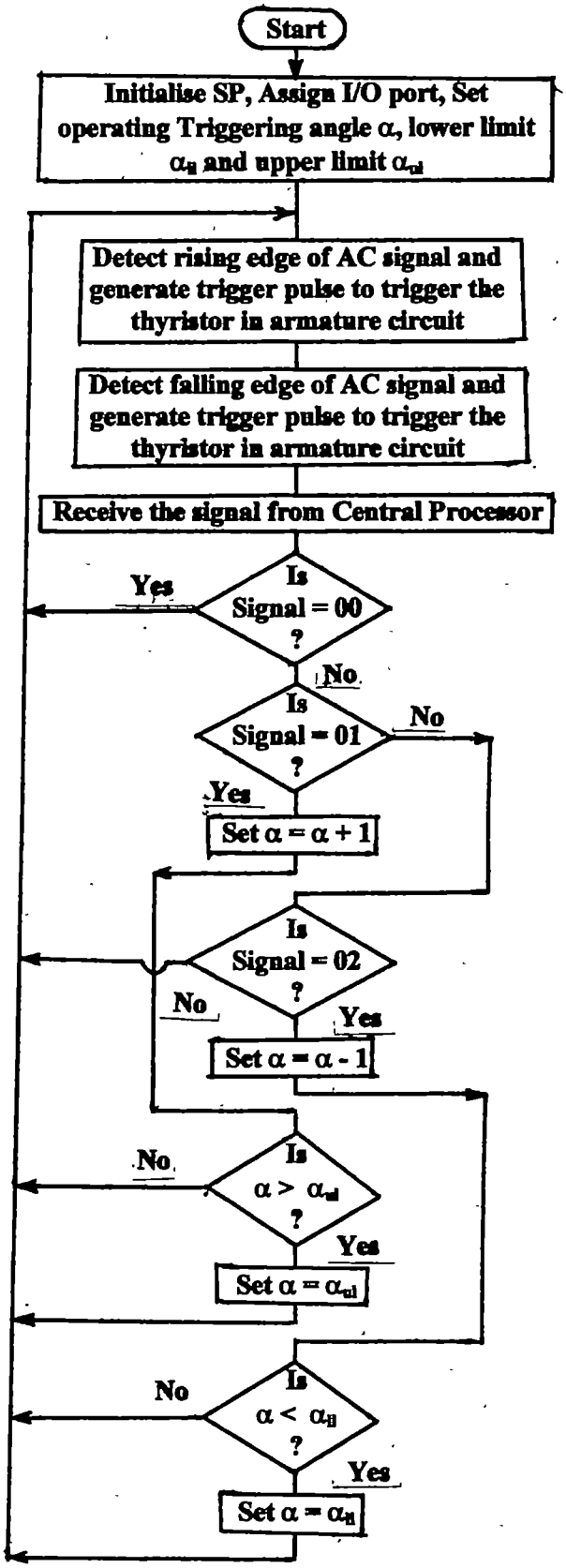

Fig. 6 Flowchart for Slave processor 1

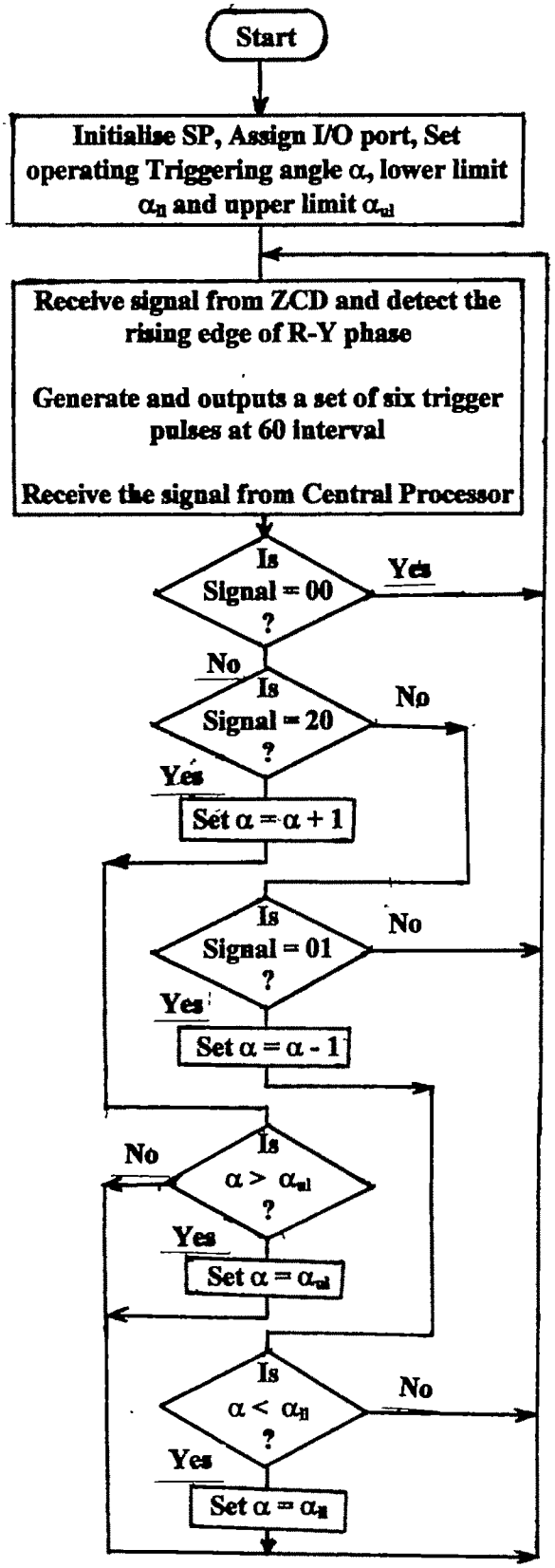
Start
Initialise SP, Assign I/O port, Set operating Triggering angle α, lower limit α_{ll} and upper limit α_{ul}
Receive signal from ZCD and detect the rising edge of R-Y phase
Generate and outputs a set of six trigger pulses at 60 interval
Receive the signal from Central Processor
Is Signal = 00 ?
Yes
No
Is Signal = 20 ?
No
Yes
Set α = α + 1
Is Signal = 01 ?
No
Yes
Set α = α - 1
Is α > α_{ul} ?
No
Yes
Set α = α_{ul}
Is α < α_{ll} ?
No
Yes
Set α = α_{ll}

Fig. 7 Flowchart for Slave processor 2

load frequency Control. Electric Machines and Power Systems", Vol. 25 Pp. 1009 - 1022, 1997.

7. Padiyar K.R and Varma R. K, "Damping Torque Analysis of Static VAR System Controllers", IEEE Trans. on Power Apparatus and System, Vol.6, No. 2, Pp. 458 - 465, May, 1991.

8. Cheng C.H. and Hsu Y.Y, "Application of a power System Stabilizer and Static VAR Controller to a multi machine power system.", IEEE Proe, Vol. 137, Pt . c, No. 1, Pp. 8 - 12, Jan., 1990.

9. Mukhopadhyay A. K and Chakraborti, "A Microprocessor Based Industrial Load Bus Static VAR Controller", Jour. Of Electric Machines and Power Systems, USA, Vol. 18, No. 5, 1990.

10. Wu. C. J. and Lee Y. S, "Damping of Synchronous generator by static reactive power compensator with digital contreoller", IEEE Proce., Vol. 138, Pt. C, No. 5 Pp. 427 - 432, Sep., 1991.

11. Das A and Mukhopadhyay A. K, "Development of an Industrial Load Bus Power Factor Regulator by using SVC and Parallel Processing of Microprocessor", Jour of IE(I), Vol. 77, Pp. 94 - 98, Aug., 1996.

12. Mukhopadhyay A. K and Das A, "Development of Parallel Processor based Power Factor regulator for Industrial Load Bus", Jour of IE(I), Vol. 82, Pp. 19 - 23, June 2001.

13. Chakraborti and Mukhopadhyay A. K, "Dynamic Damping of Power Swing and Improvement of Transient Voltage Stability with a Microprocessor based SVC at Load Bus of a Longitudinal Power System", Jour of IE(I), Vol. 82, Pp. 1 - 6, June 2001.

14. Mukhopadhyay A. K, "Text book on Microprocessor-based Laboratory Experiments and Projects" 2nd Edition, ISBN 81-7544-201-8, Wheeler Publishing, New Delhi, 2000.

Detection, Classification And Location Of Transmission Line Faults Using Radial Basis Function Based Artificial Neural Network

R. N. Mahanty and P. B. Dutta Gupta
Department of Electrical Engineering
Indian Institute of Technology, Kharagpur, India
E-mail of corresponding author: mahanty@ee.iitkgp.ernet.in

Abstract

A scheme for detection, classification and location of transmission line faults based on Radial Basis Function based Artificial Neural Network is presented. Whereas for fault detection and classification pre-fault and post-fault samples of three phase currents are considered, for fault location, post-fault current and voltage samples of three phases are considered. To validate the proposed scheme simulation studies have been carried out using EMTP and MATLAB on a three phase, 400 kV, 100 km transmission line, considering wide variations in fault inception angle, fault location and fault resistance.

eywords: Fault detection, classification and location, transmission line, Radial basis function, Neural Network.

INTRODUCTION

Power transmission lines are vital links in a power system, which provide the essential continuity of service from generating plants to the end users. Fast and accurate detection and classification of transmission line faults are required in order to maintain a reliable power system operation. Accurate location of the fault point is necessary to ensure quick service restoration.

Several fault detection and classification algorithms have been proposed in the past. Some of them are algorithms based on symmetrical components [1], [2], algorithms based on Clarke's components [2], [3], algorithms based on wavelet analysis [4], [5] and algorithms based on artificial neural network (ANN) [6]-[9]. The algorithms based on symmetrical components and those based on Clarke's components may misclassify faults and are particularly unsuitable under high impedance fault condition. The algorithms based on wavelet analysis and those based on artificial neural network are more effective than the other algorithms mentioned above and are accurate even under high impedance fault condition. The differential equation based algorithms [3], [10]-[12] and the Fourier analysis based algorithms [13], [14] are widely accepted for transmission line fault location. However, both are affected by the presence of fault resistance. Travelling wave based algorithms are capable of accurately locating faults but their implementation becomes complicated because of difficulty in accurate detection of signals.

The multilayer feedforward network with back propagation (BP) training algorithm is the most widely used neural network model for pattern classification applications. However, BP is not well suited for distance protection as the algorithm does not work satisfactorily when a case to be diagnosed falls in a region with no training data. The radial basis function (RBF) based neural network is well suited for such cases [8], [9].

A RBF neural network based scheme is presented. Whereas the previous researchers have used both current and voltage samples, the proposed scheme uses only current samples as inputs for detection and classification of faults. However, for location of fault point samples of both voltage and current are required. Large number of patterns has been generated by means of EMTP. Some of these have been used for training and some have been used for testing. Simulation studies have been carried out on a 400 kV, 100 km transmission line, considering wide variations in fault inception angle, fault location and fault resistance.

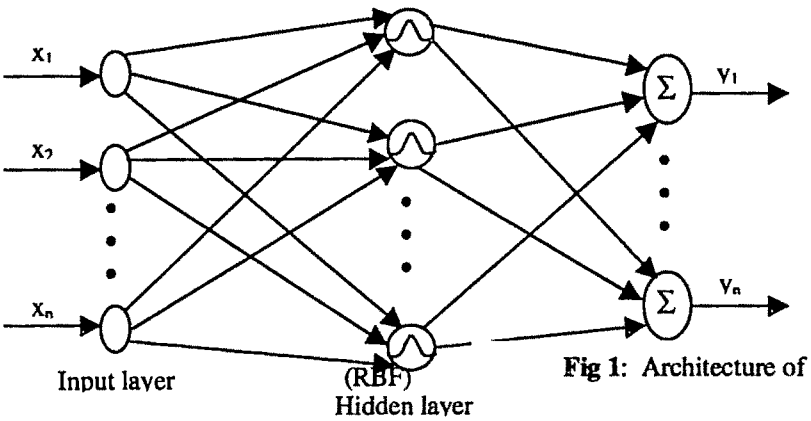

Fig 1: Architecture of RBFN

Four types of fault viz. line to ground, line to line, line to line to ground and three phase fault have been considered for simulation study.

RADIAL BASIS FUNCTION BASED A N N

The radial basis function network (RBFN) has three layers as shown in Fig 1. The input values are passed to the connecting arcs from the input nodes. The first layer connections are not weighted. Thus each hidden node receives each input value unaltered. The hidden nodes are the radial basis function units. The transfer function of the hidden nodes is non-monotonic in contrast to the monotonic sigmoid function of BP networks. The second layer of connections is weighed and the output nodes are simple summations. This particular architecture of RBFN has proved to directly improve training and performance.

SIMULATION STUDY

The equivalent circuit of a faulted line fed from both ends is shown in Fig 2, where R, L and C are the resistance, inductance and shunt capacitance of the line on which fault occurs. R', L' and C' are the same parameters for a second transmission line. Y_F and Y_T are equivalent admittances at the fault point and across the load terminals respectively. α is the fraction of line length up to the fault point. v_1, v_2, i_1 and i_2 are the terminal voltages and currents at the two ends. The line parameters and other relevant data are as shown below.

R_0=38.85 Ω, L_0=325.08 mH, C_0=0.845 μF

R_1=2.34 Ω, L_1=95.10 mH, C_1 =1.24 μF

R'=1.3 R, L'=1.3 L, C'=C

$v_{s1} = 400 \angle 0^0$ kV; $v_{s2} = 0.95\, v_{s1} \angle 20^0$ kV

$Zs_1 = (0.2 + j4.5)\ \Omega$, $Z_{s2} = (0.3 + j8)\ \Omega$

Load impedance $(Z_L) = 800 \angle 36.87^0\ \Omega$ per phase

The training and testing data are generated using EMTP [15] considering a sampling interval of 1ms. The fault detection and classification is carried out by a MATLAB program, which makes use of the 'Neural Network Toolbox' [16]. A similar program is used for fault location.

For detection and classification of faults, two separate

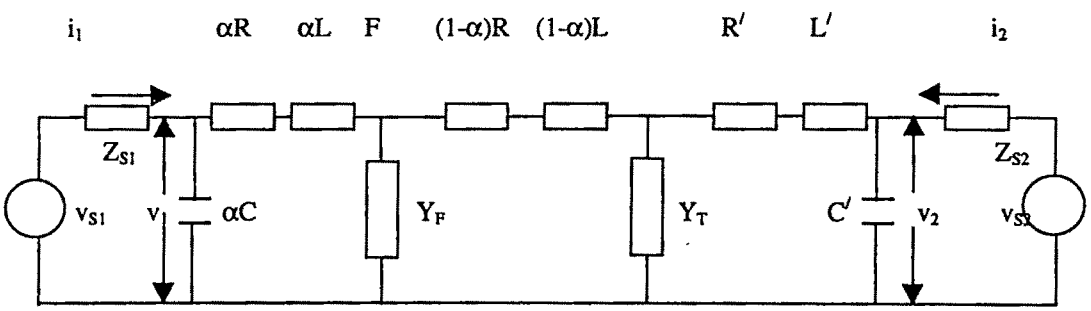

Fig 2: Equivalent circuit of a faulted transmission line fed from both ends

ANNs, one for faults involving earth and another for faults not involving earth, have been used. These two types of fault have been distinguished on the basis of the magnitude of the zero sequence component of current. Five pre-fault and five post-fault samples of each of the three phase currents are taken at one end of the line. Training data have been generated for fault resistance (R_F) of 5Ω, 50Ω and 200Ω considering fault at 5% of the line, the fault inception angle being 45^0. The input data, consisting of samples of three phase currents, I_{a1} ..I_{an}, I_{b1} I_{bn}, I_{c1} I_{cn} and the samples of zero sequence current, I_{01} I_{0n}, all normalized, are presented to ANN in the form of multiple input vectors as shown below. Corresponding to each input vector an output is obtained. The outputs have been termed as a, b, c and g.

$$P = \begin{bmatrix} I_{a1} & I_{b1} & I_{c1} & I_{01} \\ I_{a2} & I_{b2} & I_{c2} & I_{02} \\ . & . & . & . \\ . & . & . & . \\ I_{an} & I_{bn} & I_{cn} & I_{0n} \end{bmatrix} \quad \text{Inputs}$$

$$Q = [\, a \quad b \quad c \quad g \,] \quad \text{Outputs}$$

This type of batching operation is more efficient than the case when inputs are presented in the form of a single vector [16]. Any one of the outputs a, b, c approaching 1 indicates a fault in that phase. If g approaches 1, it indicates that the fault is connected to ground, e.g., Q =1001 indicates a-g fault. Similarly Q = 0110 indicates b-c fault and so on. The test results corresponding to a-g and b-c faults are shown in Tables 1 through 4. Similar results have been obtained for other faults.

Table 1: a-g fault (1001) at 10% of line

R_F=Fault resistance, FIA=Fault inception angle

R_F (Ω)	FIA (^{0})	a	b	c	g
0	0	0.990	0.182	0.248	0.996
	90	0.992	0.083	0.062	0.999
50	0	0.934	0.191	0.241	1.006
	90	0.957	0.055	0.029	0.983
200	0	0.674	0.203	0.238	1.005
	90	0.892	0.044	0.031	0.966

Table 2: a-g fault (1001) at 90% of line

R_F (Ω)	FIA (^{0})	a	b	c	g
0	0	0.829	0.244	0.232	0.993
	90	0.958	0.044	0.015	1.004
50	0	0.772	0.231	0.233	1.001
	90	0.919	0.045	0.017	0.993
200	0	0.601	0.218	0.235	1.012
	90	0.835	0.045	0.021	0.991

Table 3: b-c fault (0110) at 10% of line

R_F (Ω)	FIA (^{0})	a	b	c	g
0	0	0.266	0.912	0.945	-0.005
	90	0.104	1.009	0.999	-0.015
50	0	0.266	1.026	0.989	0.007
	90	0.104	0.984	0.991	0.002
200	0	0.266	0.993	0.899	0.001
	90	0.104	1.027	1.152	-0.003

Table 4: b-c fault (0110) at 90% of line

R_F (Ω)	FIA (^{0})	a	b	c	g
0	0	0.266	0.926	0.942	-0.002
	90	0.104	0.969	0.964	0.001
50	0	0.266	0.989	0.946	0.002
	90	0.104	1.006	1.010	0.001
200	0	0.266	0.993	0.861	0.001
	90	0.104	0.957	1.049	0.003

Table 5: a-g fault at 55% of line

α_e=Estimated fraction of line length up to fault point

R_F(Ω)	FIA(^{0})	α_e
0	0	0.5849
	45	0.5052
	90	0.4915
50	0	0.5513
	45	0.5972
	90	0.5524
200	0	0.5484
	45	0.5633
	90	0.5598

For the purpose of fault location separate ANNs have been used for each type of fault. Unlike in case of fault detection and classification, only post-fault samples have been considered for fault location. Ten such samples of

each of the three phase currents and voltages are taken at one end of line. The input data consists of samples of three phase currents and voltages and their squares, all normalized, which are presented in the form of a single input vector to ANN. Large number of training data have been generated considering fault at 10%, 20%, 30% ..... 80%, 90% of line for various values of fault resistance and fault inception angle. The test results corresponding to a-g fault occurring at 55% of the line for different fault inception angles and fault resistances are shown in Table 5. Similar results have been obtained for other cases.

CONCLUSION

A Radial Basis Function ANN based scheme for detection, classification and location of transmission line faults has been presented. Whereas for fault detection and classification pre-fault and post-fault samples of three phase currents are considered, for fault location post-fault samples of three phase voltages and currents are considered. The use of separate ANNs for faults involving earth and not involving earth has proved to be a convenient way of classifying faults. Simulation studies have been carried out considering wide variations in fault location, fault inception angle and fault resistance. The simulation results show that the proposed scheme is suitable for detection, classification and location of transmission line faults including the high impedance ones.

REFERENCES

[1] A. G. Phadke, T. Hlibka and M. Ibrahim. Fundamental basis for distance relaying with symmetrical components. IEEE Trans. Power Apparatus and Systems. Vol. 96, No. 2, p 635-646 (1977).

[2] A. G. Phadke and J. S. Thorp. Computer Relaying for Power Systems. Research Studies Press Ltd., Taunton, England (1988).

[3] W. D. Breingan, M. M. Chen and T. F. Gallen. The laboratory investigation of a digital system for the protection of transmission lines. IEEE Trans. Power Apparatus and Systems. Vol. 98. No. 2, p 350-368 (1979).

[4] J. Liang, S. Elangovan and J. B. X. Devotta. A wavelet multiresolution analysis approach to fault detection and classification in transmission lines. Elect Power & Energy Systems, Vol. 20, p 327-332 (1998).

[5] W. Zhao, Y. H. Song and Y. Min. Wavelet analysis based scheme for fault detection and classification in underground power cable systems. Electric Power Systems Research. Vol. 53, p 23-30 (2000).

[6] T. Dalstein and B. Kuliche. Neural network approach to fault classification for high speed protective relaying. IEEE Trans. Power Delivery. Vol. 10, No.2, p 1002-1011 (1995).

[7] F. Zahra, B. Jeyasurya and J. E. Quaicoe. High speed transmission line relaying using artificial neural networks. Electric Power Systems Research. Vol. 53, p 173-179 (2000).

[8] Y. H. Song, Q. Y. Xuan and A. T. Johns. Protection scheme for E H V transmission systems with thyristor controlled series compensation using radial basis function neural networks. Electric Machines and Power Systems. Vol. 25, p 553-565 (1997).

[9] P. K. Dash, A. K. Pradhan and G. Panda. Application of minimal radial basis function neural network to distance protection. IEEE Trans. Power Delivery. Vol.16, No.1, p 68-74 (2000).

[10] A. M. Ranjbar and B. J. Cory. An improved method for the digital protection of high voltage transmission lines. IEEE Trans. Power Apparatus and Systems. Vol. 94, No. 2, p 544-550 (1975).

[11] W. J. Smolinski. An algorithm for digital impedance calculation using a single pi section transmission line model. IEEE Trans. Power Apparatus and Systems. Vol. 98, No. 5, p 1546-1551 (1979).

[12] M. Akke and J. T. Thorp. Some improvements in the three phase differential equation for fast transmission line protection. IEEE Trans. Power Delivery. Vol. 13, No. 1, p 66-72 (1998).

[13] M. Ramamoorty. Application of digital computers to power system protection. Journal of Institution of Engineers, India. Vol. 52, No. 10, p 235-238 (1972).

[14] A. Wiszniewski. Accurate fault impedance locating algorithm. IEE Proc. C. Generation, Transmission and Distribution. Vol. 130, No. 6, p 311-314 (1983).

[15] Microtran Reference Manual. Transients analysis program for power and power electronic circuits. Microtran power system analysis corporation. Vancouver, Canada (1997).

[16] H. Demuth and M. Beale. Neural network toolbox for use with Matlab. The Mathworks, Inc., USA (1996).

Distribution System Fault Location using Expert System and Automatic Location

A.D. Kulkarni[1], T. Ananthapadmanabha[1], W.M. Shivakumar[2], S.B. Shivakumar[3], M.S. Nagaraj[4], P. Venkataramu[5]

[1]The National Institute of Engineering, Mysore, Karnataka

[2]Karnataka Power and Transmission Corporation Limited, Bangalore, Karnataka

[3]JMIT College, Chitradurga, Karnataka

[4]BIET College, Davanagere, Karnataka

[5]Vellore College of Engineering, Vellore, Tamil Nadu

Abstract

The fault location in the distribution network is a difficult and challenging task. On the secondary side of distribution system, no circuit breakers and relays are provided. Thus, for the fault event in this part of the distribution system, the dispatcher does not get any information about the fault. For the purpose of speedy repair and necessary maintenance work, it is necessary to locate the fault as quickly as possible. This paper proposes two methods for the location of faults and are applied to a sample practical distribution network of Karnataka, India.

Keywords: Expert systems, Fault location, Distribution system, Key customer,

INTRODUCTION

Electricity is modern man's most convenient and useful form of energy. The optimum utilization of this form of energy by the society is ensured by effective and efficient distribution system. In order to make the system more effective; it is necessary to minimize restoration time and to enhance the service reliability. It is essential for the dispatcher to locate the fault as quickly as possible. In current practice heuristic rules from system dispatchers, past experience are heavily relied on in identifying the fault locations.[1] Most of the expert systems developed so far employed information from the circuit breakers and relays.[2] Therefore they are suitable for fault location on transmission lines or primary feeders which are protected by relays and circuit breakers. But, on secondary side of distribution system (11KV/440V) no relays and circuit breakers are provided. In this paper two methods are proposed for the location of faults. They are:

1) Expert system approach
2) Automatic method of fault location

In expert system approach we make use of customer's data in finding the fault region. We receive a trouble call from interrupted customer and also his RR No. That number is fed to the computer. By performing backtracking exact fault location can be found out.

In automatic method we make use of hardware components like sensor and detector for fault location without receiving any trouble takes from the interrupted customer for fault location of fault. This method is also suitable for multiple fault location.

PROPOSED METHODOLOGY

EXPERT SYSTEM APPROACH

Fault is abnormal event that occurs frequently. The fault in this part of distribution system is identified only when the consumers inform to supply authority that consumers inform to supply authority about interruption of power. In order to locate the fault in this part of the distribution system without using any measuring devices, expert system asks the user to do some thing such as key in useful data. Here we make use of phone calls to obtain information from the customer and entered the feedback form the customer to the system.

The data collected for the customers include

1. Customer RR No.
2. The transformer from which the customer is supplied power
3. Phone number of the key customer
4. Address of each customer.

Key customer status is given to customers such as hotels, hospitals, multi-storied buildings and departmental stores. The purpose of giving key customer status is that it is assumed that they have their own technicians who are in-charge of electricity of the building, so that we can get information from them while reducing the fault region.

The distribution network is stored in the memory. The whole network is divided into number of branches. As said earlier, the key customer status is given to any hospitals, hotels, etc., If there is no key customer present in the branch then key customer status is given to any ordinary customer.

EXPLANATION ABOUT BACKTRACKING ALGORITHM

If there is any fault occurred between two poles, the interrupted customer makes a phone call to the distribution substation. The operator receives the call and takes the RRNO of the customer. This is entered and the customer record is found (Table 1). From customer record information about pole no (P) and branch no (Q) from which customer is supplied power is obtained. With this pole no and branch no as argument transformer no (T) from which customer is supplied is obtained. With P, Q, T as argument, a path is found from interrupted customer to transformer and next step is to reduce the fault region. For this algorithm starts checking the key customer in path from the interrupted customer's end. Phone number of the key customer is printed and operator has been asked to make a call to the key customer to confirm whether electricity is interrupted to him or not. If electricity is interrupted to him answer form key customer is 'Yes', otherwise 'No'. If answer is 'Yes' the operator enters 'Y'. Then the fault is from key customer poling no to interrupted customer pole no. If answer is from the key customer is 'No', then the operator enters 'N'. The fault path is from key customer pole no to transformer end. If there is key customer present in the path, the fault path is the entire path from the interrupted customer to the transformer end. Finally, fault path is printed along with the address of path. In graphical fault view the fault path is shown by change of color of line. The flowchart for this method is given in Fig. 1.

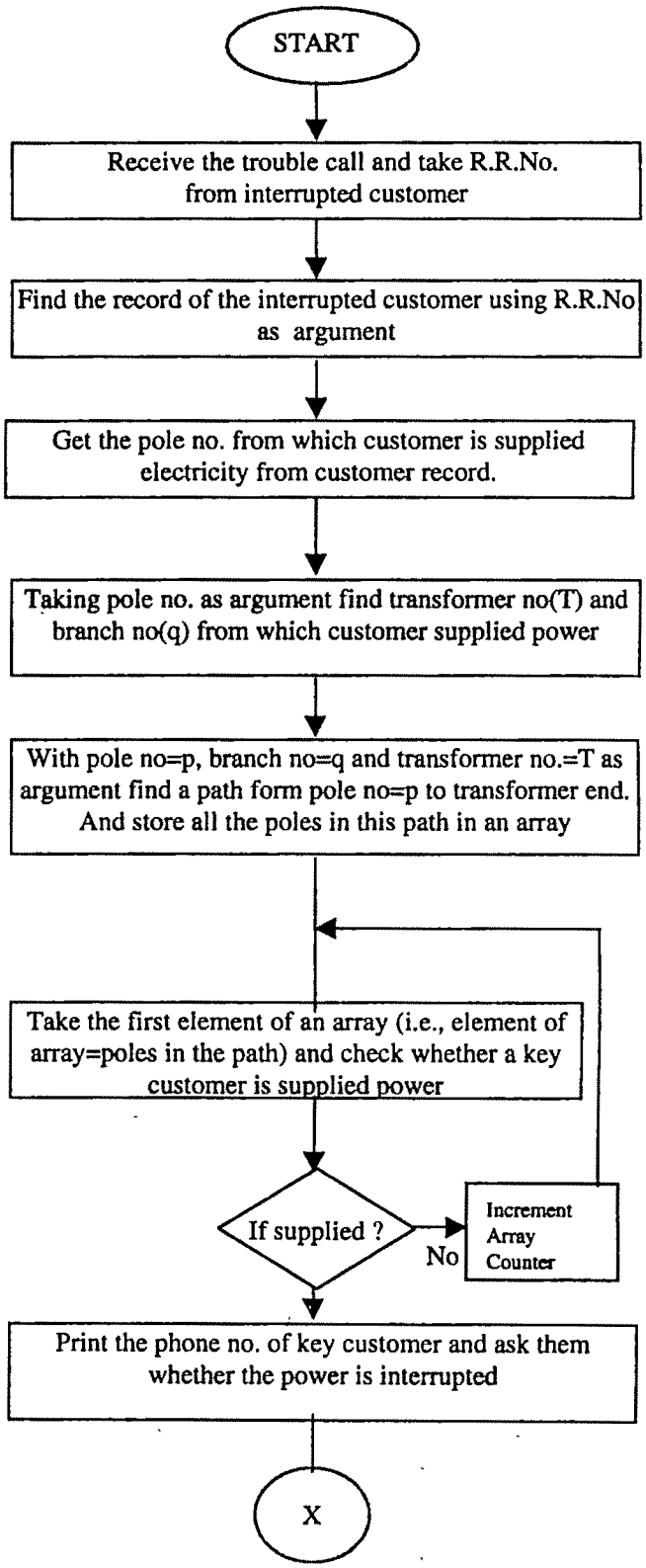
START
Receive the trouble call and take R.R.No. from interrupted customer
Find the record of the interrupted customer using R.R.No as argument
Get the pole no. from which customer is supplied electricity from customer record.
Taking pole no. as argument find transformer no(T) and branch no(q) from which customer supplied power
With pole no=p, branch no=q and transformer no.=T as argument find a path form pole no=p to transformer end. And store all the poles in this path in an array
Take the first element of an array (i.e., element of array=poles in the path) and check whether a key customer is supplied power
If supplied ?
No
Increment Array Counter
Print the phone no. of key customer and ask them whether the power is interrupted
X

Fig 1 Flow chart for expert system approach

(contd. next page)

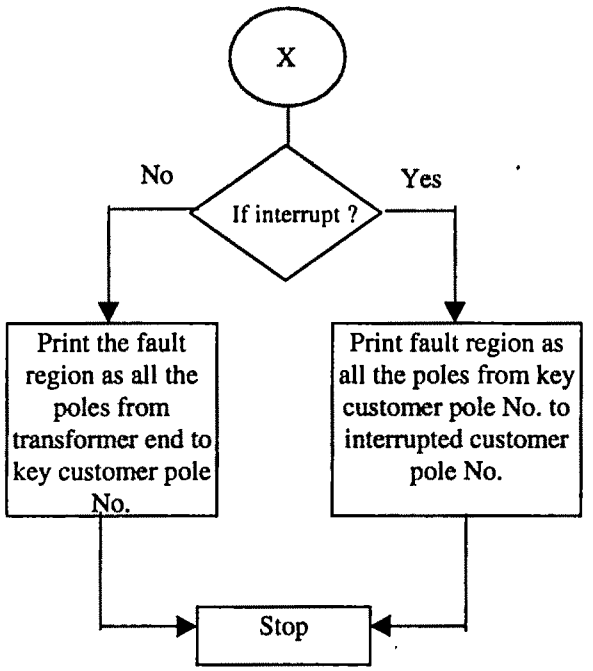
X
No
Yes
If interrupt ?
Print the fault region as all the poles from transformer end to key customer pole No.
Print fault region as all the poles from key customer pole No. to interrupted customer pole No.
Stop

AUTOMATIC FAULT LOCATION

In order to locate the fault automatically, it is necessary to measure electrical quantities like voltage; current, real or reactive power and information about the change in these quantities should be fed-back to the system, which locate the fault. In this method we make use of voltage sensor which under normal condition sends a signal of 5 volts (considers as logic 1) and under fault condition sends a signal logic of zero volts (considered as logic 0). The status of each sensor is stored in a file (error). The digital signal converted into analog signal using D/A converter provided at the transformer. This analog signal sends to the distribution station where it is converted again into a digital signal. This digital signal changes the contents of file (error) which stores the status of each sensor. When program runs, it scans the exact fault point.

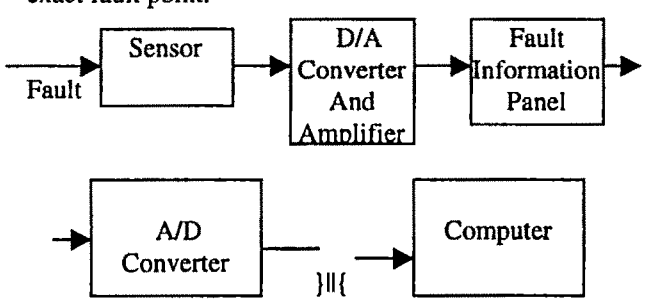

Fig 2 Block diagram for automatic fault location

In block diagram shown above a voltage sensor is provided at each pole. D/A converter and amplifier unit is provided at each transformer called detector. Since method is automatic, in order to get fault information for the operator, a v / amp is provided on fault information panel. A change over switch is also provided in fault information panel, which connects the incoming analog signal to A/D converter. In block diagram the disconnectivity is shown between A/D converter and computer because operator has to connect the incoming signal to the computer.

DETAILED EXPLANATION

Consider a fault between two poles. The sensor, provided at a point beyond the fault point, sends a signal of zero volts. This signal is passed through an inverter and then to the D/A converter. The analog signal is amplified by using operational amplifier and the signal is sent to the distribution substation. The signal, which comes to the station first, turns ON the lamp on fault information panel. Operator gets fault information. The operator changes the position of change over switch to incoming signal. This signal is interfaced with the computer and changes the contents of file, which stores the status of each sensor. Under normal condition it stores 0, under fault condition the zero is changed to 1. Once the program is compiled it scans the file and gives the exact fault point along with the address of fault point. In graphical view the fault point as shown by of pole. The circuit diagram of sensor and detector is shown in Figs. 3 and 4.

DATABASE

Expert system approach of locating fault mainly depends handling data in a database. The data, which is obtained by walk through survey, is converted into a formatted one, which is extremely necessary for the location of fault. Hence data should be properly stored in the database. The while distribution network of distribution system is drawn and stored in a system. The whole network is divided into number of branches and each branch is given a number. Customer details (viz. RR number, Pole number, Branch number and address) are created for storing data.

RR number is the number given by the supply authority for each customer and therefore this number is unique for each customer. Since the network is drawn and stored in a system, each pole in a network is given a number. The pole number in the customer details, corresponds to the pole to which the customer is supplied power.

As already said earlier network is divided into number of branches and thus the branch number in the customer details corresponds to branch form which the customer is supplied. Similarly address comes into play at the start operation of finding a path from the customer end to the transformer end.

The supply authority has given a number to each of the transformer. So, it is necessary to store the transformer number to identify the transformer from which customer is supplied power. Therefore another data field is created having {pole details, transformer number, pole number and branch number and key customer phone number }. One important field is the key customer phone number. Key customer status is given to customer such as hospital hotels, multistoried buildings, and departmental stores. A key customer status is given when the key customer have their own technician from whom we get some information for reducing the fault region. If there is no such customer exists, then key customer status is given to any ordinary customers. The pole number from the customer details is matched with the pole number in this field to find out the transformer number from which the customer is supplied. It is also necessary to obtain the information about whether the key customer is supplied power from the interrupted customer pole number or not. Branch number is mainly used for knowing the customer branches of a network from the corresponding transformer. The branch numbers are entered into branch number data or selected form branch number window. The two options, viz {To transformer, To branch} are given. If branch is directly connected to the transformer then the option "To transformer" is selected. If the branch is not directly connected to the transformer and if is connected to the transformer through another branches, then "To branch" is selected. When this option is selected we get the following field {To branch number, Branch pole number}. For example, if branch 2 is directly connected to transformer and branch 3 is connected to the transformer through pole number 6 of branch 2 then, the operator has to enter the information as {To branch number 2, Branch pole number 6}.

Thus the information which is collected through walk through survey is stored in an appropriate table, which is key for fault location. One important thing to be considers while giving number to pole in a network should be such that the numberings should be in prescribed manner that is either it should be in increasing or decreasing order towards the dead end of branch.

CASE STUDY AND RESULT

Expert system approach: Consider the part of the practical system as shown in Fig. 5. The above distribution network is the part of 440/230V lines from R.K. Nagar feeding to south sub-division, KPTCL, Kuvempunagar. In the above practical system shown whole distribution network as shown by dotted lines. The following table gives the key customer pole number:

BRANCH NO.	KEY CUSTOMER POLE NO.
1	Pole number = 3
2	Pole number = 10
3	Pole number = 15
4	Pole number = 21
5	Pole number = 28
6	Pole number = 31

Fault F1

Consider a fault in branch 2 between the pole number 7 and 8. Due to this fault, the customers supplied power from pole number: 8,9,10,11,12,13 are interrupted. Suppose one of the customers from pole number 9 makes a phone call to distribution substation and gives his RR number A32205. The operator enters this RR number and when he passes the "load pole" option, on the screen the following pole numbers are stored in an array.

LOAD POLE NO.	KEY CUSTOMER POLE NO.
9	0
8	0
7	0
6	0

Since there is no key customer present in the path when operator clicks onto "get message and load fault path" option then fault path are printed as 9-8-7-6. So the result will be as follows:

Nearest the fault path | 9 8 7 6 |

Address | 4th main, 1st cross, Knagar |

The graphical view of this path is shown by change of colour of the line from transformer end to pole number 9.

AUTOMATIC FAULT LOCATION

Here, we have assumed that voltage is provided at each pole. These sensors send a signal of 5 V under normal conditions and under a fault condition sends a signal of 0 volts. An error file is entered which stores the status of each sensor. Under normal condition it stores logic '0' for each sensor and under fault condition stores a logic '1'. The contents of this file under normal condition is given below:

Pole No.	1	2	3	4	5	6	7
Value	0	0	0	0	0	0	0
8	9	10	11	12	13	14	15
0	0	0	0	0	0	0	0

Multiple fault (F1 & F3)

Consider a fault F1 and F3 occurring simultaneously. Due to this fault, sensor at poles no 8 and 15. The content of the file (error) after fault is as follows:

Pole No.	1	2	3	4	5	6	7
Value	0	0	0	0	0	0	0
8	9	10	11	12	13	14	15
1	0	0	0	0	0	0	1

Once the program is run, the distribution network is displayed on the screen with pole no 8 and 15 is blinking. This indicates that fault has occurred between pole number 8 and 7 an pole number 14 and 15. We get the following result:

Fault at pole number: 8
Transformer number: RTK-17
Number of the loads connected:
a) A-31402 b) A-31468
Address: 4th main, 1st cross, Knagar
Fault at pole number : 15
Transformer number :RTK-17
Number of the loads connected :
a)A-32201 b) A-44467
Address: 4th main, 2nd cross, Knagar

Table 3

Branch number---------
- To transformer
- To branch

Fig. 5: Practical System

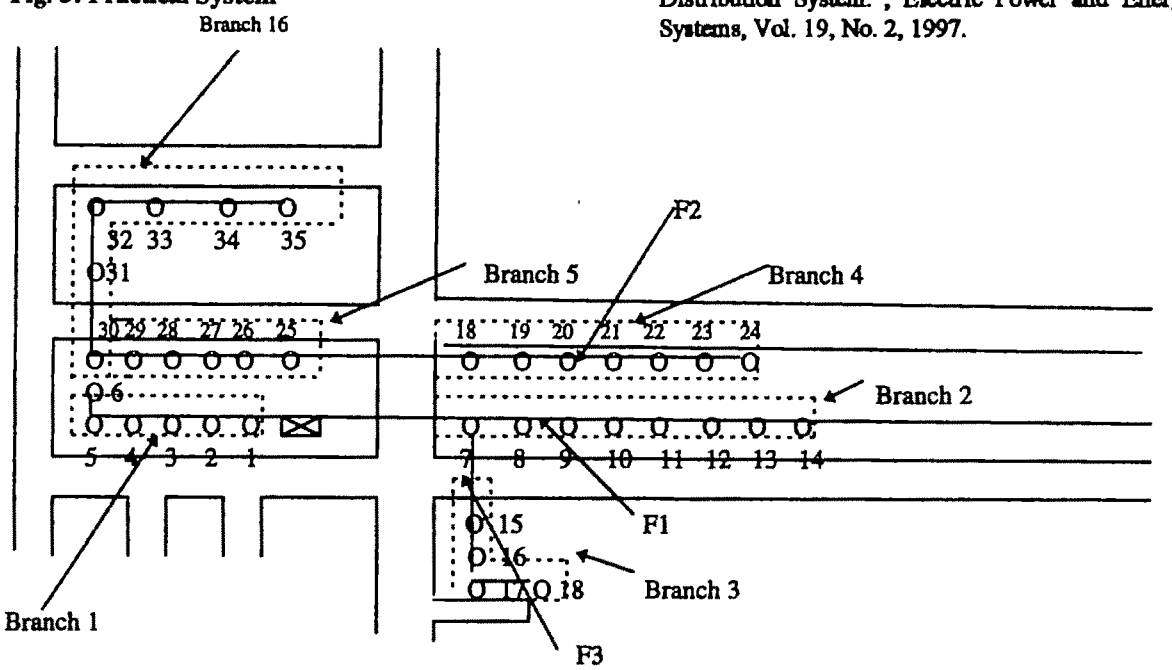

CONCLUSIONS

The expert system developed serves as a operational aid for the dispatcher. Both the methods are fast and reliable for fault location in a distribution system. The methods developed save the precious time and human effort and enhances the service reliability. Both the methods are most attractive in the field of distribution system. The effectiveness of the proposed method is demonstrated for the practical distribution network of Mysore City, Karnataka, India. The software has been developed using Visual Basic and 'C' Language, and both the methods are also applicable to primary side distribution system.

REFERENCES

1. Yuan-Yih Hsu, F.C. Lu and Y. Chien. "An Expert System for Locating Distribution System Faults". Dept. of Electrical Engg, National Taiwan University, TAIWAN.
2. K. Akoi, K. Nare, M. Itoh, T. Satoh and H. Kuwabara, "Outage State Optimal Load Allocation by Automatic Sectionalising Switches Operation in Distribution System." IEEE Trans. on Power Delivery, Vol. PWRD-2, No. 4, p. 1177-1185. 1989
3. N.D.R. Sarma, V.C. Prasad, K.S. Prakasa Rao and V. Sankar. "A New Reconfiguration Technique for Service Restoration in Distribution Networks". IEEE Trans. on Power Delivery, Vol. 5, No. 4, Oct. 1994.
4. T.Ananthapadmanabha, A. D. Kulkarni, K. Parthasarathy and K.R. Rao. "Knowledge Based Methodology for Sequence Switching, Fault Identification and Service Restoration of Distribution System.", Electric Power and Energy Systems, Vol. 19, No. 2, 1997.

Fig. 3: Sensor Circuit

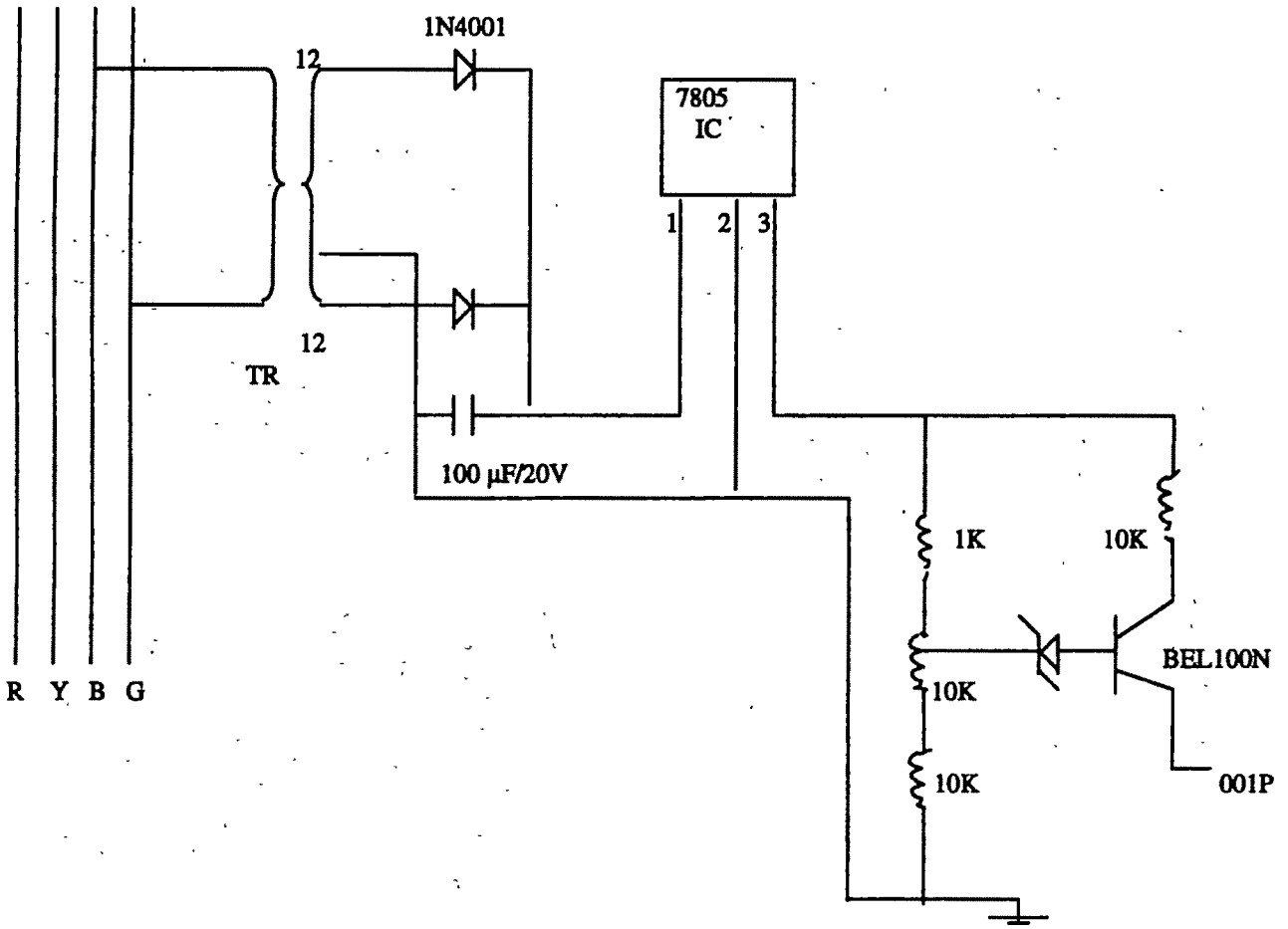

Fig. 4: Detector - Digital to Analog Converter

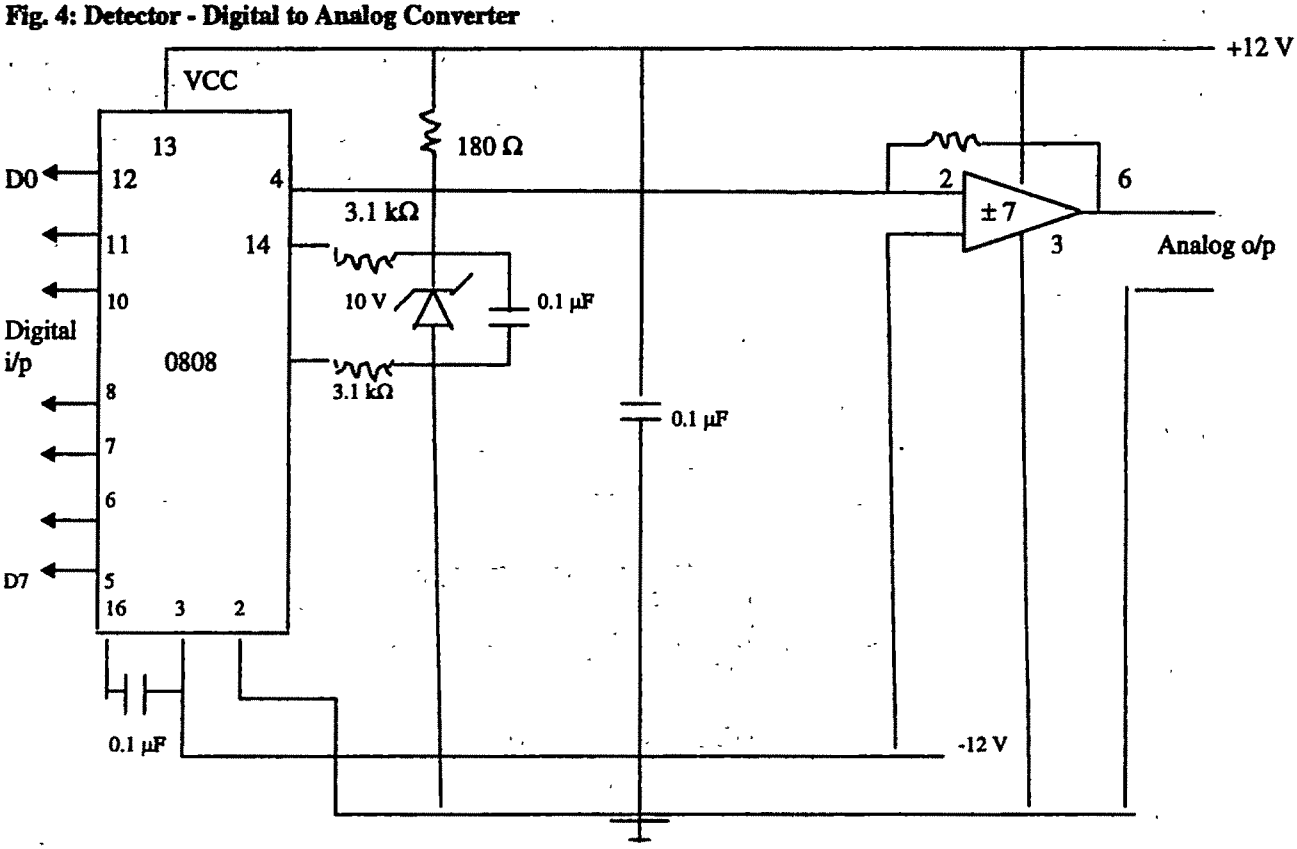

A Frequency Domain Technique For Fault Signal Detection And Isolation In Distributed Systems

K. A. Gopala Rao
Department of Electrical Engineering
Andhra University, Visakhapatnam, 530003, India

Abstract

In this paper, the decentralized fault detection (DFD) problem is formulated in frequency domain. Minimum length of widow for observation is determined. Also a technique has been established for the generation of all possible parity vectors from a given minimum order parity vectors. The methodology is illustrated with a numerical example.

INTRODUCTION

Fault detection and isolation (FDI) in dynamical systems deals with the problem of detecting deviations from normal behavior (we call them failure modes) in a specified complement of the system components (sensors, actuators etc.) and isolating the particular component that has failed. In recent years a wide variety of approaches to the problem of FDI in linear dynamical systems have been developed[1]. However, in these approaches the assumption is that all the information required for fault detection is available to the detector. This assumption does not hold in most practical situations, since for reasons of economy and reliability the information is spatially distributed. In many engineering systems the information available to the fault detectors is thus localized and each detector monitors a specified section of the large system. This makes the Decentralized Fault Detection (DFD) distinctly different and non standard and application of the centralized techniques to these problems is not straight forward.

However, some researchers [2,3] considered DFD problem with some kind of communication and made it possible to apply the algorithms developed for centralized situations. The present author, however, developed various approaches [4] to solve the DFD problem when there is no communication among the detectors. One among these approaches is the parity space approach.

The parity space approach as developed in [5], uses analytic redundancy for FDI. One of the key aspects of analytic methods of FDI is the use of information concerning the dynamic relationships among the measured inputs and outputs. This approach considers residuals generated from a window of observations over some interval of time. Then the "observation space" has dimension proportional to the length of this interval, and at its

simplest level, fault detection can be achieved by projecting the observations onto the orthogonal complement (parity space) of the subspace in which the observations should lie if there is no fault.

However, this idea raises additional questions which are of importance in implementation. Specifically, if we are given a linear, time-invariant system, how do we determine the minimum length of the window of observations that is required for detection? Can we generate all possible parity vectors from the given minimum order parity vectors? These questions are answered in a natural way considering the DFD problem formulation in the frequency domain in this paper. At the end we provide a numerical example to illustrate our methodology.

BACK-GROUND OF PARITY SPACE

Consider a linear, time-invariant, continuous time system described by

$$\dot{x}(t) = Ax(t) + Bu(t) \quad ...(1)$$
$$y(t) = Cx(t) \quad ...(2)$$

where x,y,u are n,m,q dimensional vectors respectively. As a first step we will focus on sensor and plant failure detection and not actuator faults. Thus without loss of generality we will assume $u=0$. Therefore the system equations we are dealing with can be written as

$$\dot{x}(t) = Ax(t) \quad ...(3)$$
$$y(t) = Cx(t) \quad ...(4)$$

Define the extended observation vector of length p to be

$$\bar{y}_p = [y^T, \dot{y}^T, .., (y^{(p-1)})^T]^T \quad ...(5)$$

obviously

$$\bar{y}_p(t) = \begin{bmatrix} C \\ CA \\ CA^{p-1} \end{bmatrix} x(t) \quad ...(6)$$

Let $q=mp$, then $\bar{y}_p \in \mathbb{R}^q$. Define

$$\bar{C}_p = [C^T, (CA)^T, .., (CA^{p-1})^T]^T \quad ...(7)$$

and the observation space (of length p) Z_p to be

$$Z_p = R(\bar{C}_p) \quad ...(8)$$

where $R(\bar{C}_p)$ is the range of $\bar{C}_p$. Define the detection space (of length p) G_p to be the orthogonal complement of Z_p, i.e.,

$$Z_p \oplus G_p = \mathbb{R}^q \quad ...(9)$$

Then for any vector $g \in G_p$, we have

$$\langle g, \bar{y}_p \rangle = 0 \quad ...(10)$$

Equation (10) (or more precisely, the left hand side of this equation) is called a parity check. We will call g a detection vector (of length p).

FREQUENCY DOMAIN FORMULATION

In this section we establish the link between the time dom in and frequency domain descriptions of the parity checks. Then we show that the frequency domain description of all possible parity checks is nothing more than the left nullspace of the polynomial matrix $[C^T, (sI-A)^T]^T$.

The observation space Z_p is a subspace spanned by the extended observation vector $\bar{y}_p(t)$ given in equn.(5). Assuming that there are no uncertainties, the detection space G_p is the orthogonal complement of Z_p. We also define a detection vector a_p to be

$$a_p^T = [a_{p0}^T, a_{p1}^T, ..., a_{pp-1}^T] \quad ...(11)$$

which satisfies

$$a_p^T \bar{y}_p(t) = 0 \qquad \ldots(12)$$

for some p =1,2,... Recall that the relationship (12) is called a parity check. It is obvious that $a_p \in \mathbb{G}_p$ and finding all possible parity checks of length p is equivalent to finding a basis for detection space $\mathbb{G}_p$.

Taking laplace transform of (12), we get

$$\sum_{i=0}^{p-1} a_{pi}^T s^i [y(s) - \sum_{j=0}^{i-1} y^j(0) s^{-j-1}] \qquad \ldots(13)$$

Using $y(s) = C(sI-A)^{-1}x_0$ and $y^p(0) = CA^p x_0$ and since (12) is valid for all initial conditions, we get

$$w^T(s)C(sI-A)^{-1} = r^T(s) \qquad \ldots(14)$$

where

$$w^T = \sum_{i=0}^{p-1} a_{pi}^T s^i \qquad \ldots(15)$$

and

$$r^T(s) = \sum_{i=0}^{p-1} a_{pi}^T \sum_{j=0}^{i-1} CA^j s^{i-j-1} \qquad \ldots(16)$$

Since (12) is nothing more than a parity check, (14) can be thought of as its frequency domain description, thus setting up a link between the frequency and time domains.

Now we will show that w(s) and r(s) span the left nullspace of the polynomial matrix $[C^T, (sI-A)^T]^T$. Here the left nullspace of some pxm rational matrix H(s) is defined as a subspace spanned by px1 rational vectors v(s)'s, which satisfy

$$v^T(s)H(s) = 0 \qquad \ldots(17)$$

Note that (14) can be written as

$$[w^T(s), -r^T(s)] \begin{bmatrix} C \\ (sI-A) \end{bmatrix} = 0 \qquad \ldots(18)$$

Define $[w^T(s), -r^T(s)]^T$ as detection vector and denote the left nullspace of $[C^T, (sI-A)^T]^T$ as $\mathbb{N}_{lc}$. Then from (18) we see that the polynomial parity vector $[w^T(s), -r^T(s)]^T \in \mathbb{N}_{lc}$. Therefore it is enough to know one polynomial basis of $\mathbb{N}_{lc}$ in order to generate all parity checks of all possible finite lengths.

PROBLEM FORMULATION

In this section, we formulate the decentralized fault detection problem. Consider the large interconnected system comprising of N- subsystems described by

$$\dot{x} = A_i x_i + B_i u_i + \sum_{\substack{j=1 \\ j \neq i}}^{N} A_{ij} x_j ; i = 1, 2, .., N. \qquad \ldots(19)$$

$$y_i(t) = C_i x_i ; \; i = 1, 2, .., N \qquad \ldots(20)$$

where x_i, u_i, y_i are n_i, m_i, P_i dimensional state, input output vectors of the i^{th} subsystem. Here we are concerned with the problem of designing N- local detectors for fault detection. The local detectors donot communicate among themselves. We have, available at each local detector, the following: measurements of the local input u_i and the local outputs y_i, the nominal values of the coefficient matrices C_i, A_i, B_i, A_{ij}.

In (19), if $A_{ij}=0$ or information about all x_j's is available at the i^{th} detector the problem is a classical one. Otherwise, each interaction term $A_{ij}x_j$ acts as an unknown input which makes the detection problem difficult to solve. By appropriately redefining various quantities, we can rewrite the term $\sum A_{ij}x_j$ as $E_i d_i(t)$ with E_i

having full coulmn rank q_i in all subsystems. Thus the i^{th} subsystem is

$$\dot{x}_i = A_i x_i + B_i u_i + E_i d_i \quad ...(21)$$

$$y_i(t) = C_i x_i(t) \quad ...(22)$$

we futher assume that $p_i > q_i$, and $C_i E_i$ is also of rank q_i.

Now we formulate the frequency domain version of the DFD problem. Since d_i is unmeasurable and only measurements available are y_i and u_i, the parity equation is given as

$$[\beta_i(s), -\alpha_i(s)] \begin{bmatrix} y_i(s) \\ B_i u_i(s) \end{bmatrix} = 0$$

or

$$[\beta_i(s), -\alpha_i(s)] \begin{bmatrix} C_i & 0 \\ (sI - A_i) & -E_i \end{bmatrix} = 0 \quad (23)$$

with the condition $p_i > q_i$ we can always find $[\beta_i(s), -\alpha_i(s)]$, such that equation (23) is satisfied. Hence the detection vector in the frequency domain is $[\tilde{\beta}_i(s), -\tilde{\alpha}_i(s)]$, where the '~' indicates the row vectors of β_i and α_i respectively. We rewrite the condition (23) to get two equivalent conditions as

$$\beta_i(s) C_i - \alpha_i(s)(sI - A_i) = 0 \quad (24)$$

$$\alpha_i(s) E_i = 0 \quad ...(25)$$

SOLUTION TO DETECTION PROBLEM

We now consider the problem of obtaining the solution to (24) and (25) To this end, we go through the following sequence of steps to recast (24)and (25) in a matrix pencil form[6], from which the desired solutions can be easily obtained.

Let R_i denote the left annihilator of E_i, i.e.

$$R_i E_i = 0 \quad ...(26)$$

where R_i has maximal row rank. From (25), we have then

$$\alpha_i(s) = \tilde{\alpha}_i(s) R_i \quad ...(27)$$

for some $\tilde{\alpha}_i(s)$. Then solving $\tilde{\alpha}_i(s)$ is equivalent to finding $\alpha_i(s)$, since rank α_i = rank $\tilde{\alpha}_i$ this follows from application of Sylvester's inequality to (27) and using the fact that R_i has full row rank. Substituting (27) in (24), we get

$$\tilde{\alpha}_i(s) R_i (sI - A_i) = \beta_i(s) C_i \quad ...(28)$$

Let Q_i = Ker C_i, i.e. $C_i Q_i = 0$, where Q_i has maximal column rank and let C_{iR} be the right inverse of C_i, i.e. $C_i C_{iR} = I$ Post multiplying (28) by Q_i and C_{iR} respectively, we get

$$\tilde{\alpha}_i(s)(sR_i Q_i - R_i A_i Q_i) = 0 \quad ...(29)$$

$$\tilde{\alpha}_i(s) R_i (sI - A_i) C_{iR} = \beta_i(s) \quad ...(30)$$

So, once $\tilde{\alpha}_i$ is obtained from (29), β_i can be directly computed using (30). Since $(sR_iQ_i - R_iA_iQ_i)$ is a singular pencil, the problem thus, reduces to obtaining the left nullspace of the matrix pencil. A simple way of obtaining the left nullspace of $(sR_iQ_i - R_iA_iQ_i)$ is by transforming it to the Kronecker canonical form and use the well established results on this form for finding the left nullspace. From Kronecker's theory, there exists nonsingular square matrices M and N such that the Kronecker canonical form can be obtained as

$M_i(sR_iQ_i - R_iA_iQ_i)N_i =$
Block diag$(O_{gxh}, L_e, L_r^T, D_a, (sI-J))$ ...(31)

where L_e, L_r^T, D_a and $(sI-J)$ have diagonal forms. Detailed discussion on this canonical form may be found in Gantmacher[6].

Now we show how in a simple way vectors of the left nullspace of a matrix pencil can be obtained when it is in the Kronecker canonical form. Consider the right hand side of (31). We note that in writing the above canonical form, we assumed that the pencil has minimal column indices $(e_1, e_2, \ldots, e_\eta)$ and minimal row indices $(r_1, r_2, \ldots, r_\tau)$. The D_a and J blocks correspond to finite and infinite elementary divisors respectively.

It is easy to see that the left nullspace of an operator with a block diagonal matrix representation is the direct sum of the left nullspaces of the operators corresponding to each of the diagonal blocks. Let

$W = \text{Block diag}(\Delta, \bar{P}, P, \theta, Z)$ ...(32)

where Δ, $\bar{P}$, P, θ and Z are the collection of vectors of the nullspaces corresponding to O_{gxh}, L_e, L_r^T, D_a and $(sI-J)$ blocks respectively. Note further, that in view of the structure of (31), $\bar{P}$, P, D and Z if they exist, are themselves block diagonal. Now we consider the components of W. From the dimensions of O_{gxh} block, it is evident that

$$\Delta = I_g \qquad \ldots(33)$$

Each of the components L_{e_i} of L_e has full row rank for all values of s and hence L_e has full row rank for all s. Consequently, $\bar{P}$ has the trivial solution

$$\bar{P} = 0 \qquad \ldots(34)$$

We have P = Block diag.$(P_{r_1}, \ldots, P_{r_\tau})$, where each P_{r_i} corresponds to the nullspace of $L_{r_i}^T$. The equation

$$\bar{P}_i(s) L_{r_i}^T = 0 \qquad \ldots(35)$$

has a solution of the for

$$\bar{P}_i(s) = (1, s, \ldots, s^{r_i}) \qquad \ldots(36)$$

As we are interested only in this solution, we donot consider other solutions of P. Next, since D_{a_i} (and hence D_a) has full row rank for all s, we have

$$\theta = 0 \qquad \ldots(37)$$

Finally we are interested in the solution of

$$z_{ij}(sI - J_{ij}) = 0 \qquad \ldots(38)$$

Observe that $s \neq \lambda_i$, where λ_i's are the eigenvalues associated with J_{ij} and $(sI-J_{ij})$ is nonsingular and hence (38) has only trivial solution $z_{ij}=0$. Thus, finally we have W as

$W = \text{Block diag}(I_g, 0, P, 0, 0)$...(39)

Observe that the solution W obtained above is precisely the solution that we want. Defining

$$W_i = \alpha_i M_i \qquad \ldots(40)$$

(29) can be put into the form (31) as

$$W_i(sM_iR_iQ_iN_i - M_iR_iA_iQ_iN_i) = \ldots(41)$$

If W_i is determined from (41), α_i can be computed from (27). Thus the original problem has reduced to one of finding W_i nothing more than that given by (39).

NUMERICAL EXAMPLE

To illustrate the technique described in the previous section here we consider a simple numerical example. Consider the observable system with A_i, B_i, C_i and E_i of station 'i' given by

$$A_i = \begin{bmatrix} -1 & 1 & 0 \\ -1 & 0 & 0 \\ 0 & -1 & -1 \end{bmatrix}; \quad B_i = \begin{bmatrix} 1 & 0 \\ 0 & 1 \\ 0 & 0 \end{bmatrix};$$

$$C_i = \begin{bmatrix} 1 & 0 & 0 \\ 0 & 0 & 1 \end{bmatrix}; \quad E_i = \begin{bmatrix} -1 \\ 0 \\ 0 \end{bmatrix}$$

Observe that $p_i=2$, $q_i=1$, i.e. $p_i>q_i$. By direct calculation it is true that

$$Q_i = \text{Ker. } C_i = \begin{bmatrix} 0 \\ 1 \\ 0 \end{bmatrix}; \quad R_i = \begin{bmatrix} 0 & 1 & 0 \\ 0 & 0 & 1 \end{bmatrix}$$

$$R_iQ_i = \begin{bmatrix} 1 \\ 0 \end{bmatrix}; \quad R_iA_iQ_i = \begin{bmatrix} 0 \\ -1 \end{bmatrix}$$

$(sR_iQ_i - R_iA_iQ_i) = \begin{bmatrix} s \\ 1 \end{bmatrix}$. Thus, with $M_i = \begin{bmatrix} 1 & 0 \\ 0 & -1 \end{bmatrix}$, the Kronecker form for the pencil is given by $\begin{bmatrix} s \\ -1 \end{bmatrix}$. Thus the pencil has only one block of the type L_r^1 with r=1. We note that

$$P_i(s)L_{r_1}(s) = [1, s]\begin{bmatrix} s \\ -1 \end{bmatrix} = 0$$

Thus P = [1, s], from which we get $\alpha_i(s)$ = [0, 1, -s] and $\beta_i(s)$ = [1, $-s-s^2$]So the parity equation in frequency domain is

$$[1, -s-s^2, 0, -1, s]\begin{bmatrix} y_i(s) \\ B_iu_i(s) \end{bmatrix} = 0$$

CONCLUSIONS

In this paper we have given a frequency domain formulation for the DFD problem. We established how naturally a minimal order parity vector and minimum length of the window of observations for fault detection can be derived.

REFERENCES

1. Willsky, A.S., "A survey of design methods for failure detection in dynamical systems", Automatica, Vol.12, No .1976, pp.601-611.

2. Singh, M.G. et al, "New approach to failur detection in large systems", Proc. IEEE Vol.-130, 1983, pp.243-249.

3. Hodzic, M. and Siljak, D.D., "Failure detection in large sparse systems" Large-Scale Systems, Vol.9, 1985, pp.83-100.

4. Gopala Rao, K.A., "Fault detection in linear dynamical systems", Ph.D. Thesis, I.I.Sc., Bangalore, 1986.

5. Chow, E.Y. et al, Issues inthe development of a general design algorithm for reliable failure detection", Proc IEEE conf. on Decision and Control, Dec.1980, pp.1008-1012.

6. Gantmacher, F.R., "the theory of Matrices", Vols. I & II, Chelsea, NewYork, 1959.

Web Based Substation Automation

P. Anbalagan, S. Vasantharathna, S. Santthosh Babu* and R. K. Manimozhian
Department of Electrical and Electronics Engineering
Coimbatore Institute of Technology.
Coimbatore – 641014 ,Tamil Nadu, India.
*e-mail s-babu@eth.net

Abstract

The World Wide Web (WWW) has become a convenient way to access information because the WWW browsers integrate different network services into a common easily accessible user-friendly interface. These features can be incorporated for a cost effective way of accessing information from SCADA systems (Supervisory Control and Data Acquisition). The paper describes a unique web based application, which is implemented based on the Embedded systems and client server architecture. The user can view the real time data super imposed on one-line diagrams generated automatically using the VLSI's placement and routing techniques. In addition, the user can also control the operation of a sub-station at the server site. The choice of JAVA offers unique and powerful features for design of the SCADA and Information Distribution systems.

Key words: One Line Diagram, VLSI routing, Embedded relays, Multithreading, Multiprocessor based relays, MMI, RMI

INTRODUCTION

The substation automation has become a major issue in recent years. Many web based automation techniques along with fault diagnosis via the expert systems have been developed. This paper presents an unique web based substation automation incorporating the advantages of client-server architecture and the multiprocessor systems. The proposed system has all the advanced functions such as the online automatic generation of oneline diagrams, fault diagnosis through expert systems, utilization of VLSI placement and routing algorithms, data preservation and security. Care is also taken in the design such that no one starve of data during the congestion time.

AUTOMATIC GENERATION OF ONE-LINE DIAGRAMS

Currently the generation of the one-line diagrams are done manually. The process is tedious, time consuming and error prone. This part of the work can be automated using placement and routing algorithms proposed for the VLSI design technology. This is shown in fig. 1. GUI (Graphical User Interfaces) of various complexities has been developed to simulate and display the dynamics of the power systems in the machine independent architecture. A typical distribution substation located at Peelamedu has two high voltage buses, three numbers of primary power transformers, few low voltage buses and number of circuit breakers. This system has been considered for the development of this paper [1].

CLIENT SERVER ARCHITECTURE

Traditional enterprise applications are for most part have limited access to one another's procedures and data so they are cumbersome to build and expensive to maintain because even simple functional changes require the entire code to be rewritten. But the Client Server architecture [1] provides scalability and robustness required to support mission critical applications in power systems and distribution. This architecture is

- 100 % Object oriented.
- Server based, Data Base driven.

A typical three tier Client Server architecture contains

- Service tier.
- Data store tier.
- Main Machine Interface tier (MMI).

NETWORK PROGRAMMING

Networking of substation terminals and the server enables programs to retrieve information stored in the Local Area Network (LAN) and can be expanded through the Internet. Networking of substation terminals and components is ideal for the SCADA distribution project for the following reasons

- Safe, easy to access – Proper level of authorization can be fixed to users in the network ensuring secure data processing.
- Low investment – All the user needs is a web browser to link to the WSDS server machine (As the features of the web browsers can be incorporated for networking).
- Extensive "*MULTITHREADING*" implications help us in a virtual parallel processing environment through which multiple SCADA systems can be managed by a single instance with an advent of multiprocessor based relays.
- The RMI (Remote Method Invocation [3]) ensures security in a dedicated network and in the Internet. Marshalling at the transmission level and Unmarshalling at the receiving end is done to ensure a data safe transmission.

JAVA PROGRAMMING LANGUAGE

The substation automation system should be simple, secure, portable, robust, Multitasking, generalized to run on different architectures, should render high performance.

Java programming language provides ample features for the system. The objects powerful graphical user interface for the automation system that runs on almost any operating system. Any automation system should handle multiple processes at a time. Multithreading feature of Java helps us to enhance the system capability, by allowing us to allocate different threads for each component in the substation rather than creating individual objects, this feature helps us to handle memory more efficiently and track processes individually. The Java Runtime Environment system provides elegant yet sophisticated solution for multiprocess synchronization that enable smoothly running interactive threads. Multithreading also allows dealing about the specific behavior of a component of the substation rather than total substation itself.

DATA BASE PROGRAMMING

The database is the most crucial and important part of the information processing in the automation of substation. Conventional Data Base Management Systems (DBMS) are less efficient compared to the Relational DBMS. The new technology helps us to provide proper level of data access to the queries made by the clients through the SQL (Structured Query Language) a common standard for the database management systems. The SQL queries are embedded in the software developed for the automation so that the tool is user friendly and reliable.

The automation system should be liable to handle multiple operating systems and databases form various vendors, hence compatibility at the programming level should be ensured. Open Data Base Connectivity is used to interface applications developed using the programming languages with the Open Source Data Bases. The ODBC driver is not compatible with the UNIX based RDBMS (MYSQL) hence a common utility service that handles all types of RDBMS is necessary.

Java finds apt position in handling variety of databases through the common data base utility JDBC (Java Data Base Connectivity) Query and DB Management operations are carried out through the JDBC- ODBC (Java Data Base Connectivity – Open Data Base connectivity) driver from the JDK 1.x development kit for windows based systems and JDBC directly interacts with the SQL drivers in case of UNIX/LINUX based RDBMS. This helps the total system to be architecture-neutral (for example different data base servers such as ORACLE, MSSQL 7.x, SYBASE, MYSQL can be used in different parts of the same network [2]). Since the native data base connection is faster and efficient the system as a whole becomes faster and reliable.

To ensure the consistency of data through the database appropriate keys, triggers, transactions, procedures and cursors are used in the tables.

SYSTEM DESIGN DATA BASE

The database representation of the considered system is as follows:

- Representation of lines: transmission line or distribution line, substation name, r,x,c, capacity
- Representation of Bus: High voltage or low voltage bus, substation name, bus number, circuit breaker list
- Representation of transformers: substation name, Primary power transformer, Distribution transformer, transformer number, type capacity
- Representation of feeder lines:
- Circuit breaker: CB number, state, model, type
- Switch: State and number
- Relays: model, type, capacity, pickup value
- Automatic Reclosure devices: Number, state
- Lightning arrestors: location details
- And other fire fighting equipments and sub station components .

THE OVERALL NETWORK

The substation network is centralized through a server. The Database server and all the clients are connected to the central server. The clients are not directly connected to the Database server to ensure that there is no unauthorized tappings of data from the database sever. Each client has its own log of data about the particular line or the instrument connected it to. All the data from the client controllers are constantly uploaded to the Database server through the central server the level of authentication. Time slicing and multithreaded handling of various client terminals, Web based central administration is done in the central server. The information in the database server can be uploaded to the **web server** at constant intervals or to the Main Machine Interface computers. The queries from people across the globe can be answered through the Internet. Java Servlets Technology or the Java Server Pages (JSP) technology can be used to dynamically alter the web interface related to the queries made through the Internet. The centralized server and the web server can be placed in a single machine or different machines but if placed in different servers geographically separated proper firewall protection should be given too avoid illegal operations inside the servers.

SCADA AND JAVA CONNECTIVITY

For the Web based SCADA, the transmission delay should be reduced as much as possible. Hence SCADA can be designed on the basis of VLSI placement and routing algorithms [5]. Floor planning is a mapping between the logical description and the physical placement of components on the SCADA board. The prior step in system design should be connectivity between the SCADA system (based on the TCP/IP) and end user client sockets (end points of two way communication link between two programs running in the network). Multithreading is implemented in the connectivity and physical interrupted results such as line parameters, breaker status information, location of relays, transformer taps, etc., are passed on to the Web Server through the central server. Multiple threads are implemented to ensure the reliable connection between SCADA and the JAVA application, which is then transmitted to the central server.

The connectivity between the central server, the clients, DB server and the web server are carried in the socket level in Java using the variety of classes provided by the **java.net** package (ex: Authenticator, URL, URL Encoder, URL Decoder, URLStreamhandler, Server Socket, Socket, Inet Address). The network can also be provided with proxy servers at appropriate intervals to reduce network traffic. Different centralized servers can be connected to a powerful web server to form a large network.

The interruptions and emergency recovery commands from the central server can be taken to the terminal clients to perform forced operations in case of emergencies and breakdowns.

CLIENT AND MMI

The MMI (Main Machine Interface) is supported by auto- generation of one-line diagrams and GUI display systems. The auto generation and one line diagrams contains

I. Stream input data
II. Placement
III. Routing
IV. Dynamic Data Linkage
V. Graphics Editor

The stream input data supply the substation component information for creating the topology of the substation. The vertices of the topology of the substation, the vertices of the topology without the components will be placed using the VLSI's placement algorithm. Routing will route connections of all components according to some connectivity priorities. Routing of database incorporated in this paper is a kind of multilayer routing, where only the reserved clients (Load dispatch centers) has full control on the data and are given the highest priority. This avoids congestion to some extent. Dynamic Information such as voltage will be automatically linked to each component to display.

CONCLUSION

The VLSI, Embedded systems approach and the client / server module allow the user a great flexibility to dynamically interact with SCADA system. The one line diagrams can be accessed from any where in the world through the internet. No special hardware and software and application are required on the remote location. In addition to the information about the substation equipments, information regarding the power quality, fault studies can also be viewed from anywhere through the net.

REFERENCES

[1] Heung – Jae Lee, Bok – Shin Ahn, Young – Moon Park, "A Fault Diagnosis Expert Systems for Distribution Substations ", IEEE Transactions on Power delivery, Vol 15, No 1, Jan 2000, pp 92-97.

[2] Tan Loc Le, Michael Negnevitsky, " Expert System Application for Voltage and VAR control in power

transmission and Distribution systems, IEEE Transactions on Power delivery, Vol 12, No 3, Jul 1997, pp 1392-1397.

[3] —,"Black Book for Java Programming" Prentice Hall International Inc. 2000.

[4] Steven Holzner , JAVA 2,Swing, Servlets, JDBC & Java Beans PROGRAMMING, Dreamtech Press.

[5] B.Qiu, H.B.Gooi, " Web Based SCADA Display Systems For Access via Internet", IEEE transactions on Power Systems, Vol. 15, No.2,May2000,pp.681-686.

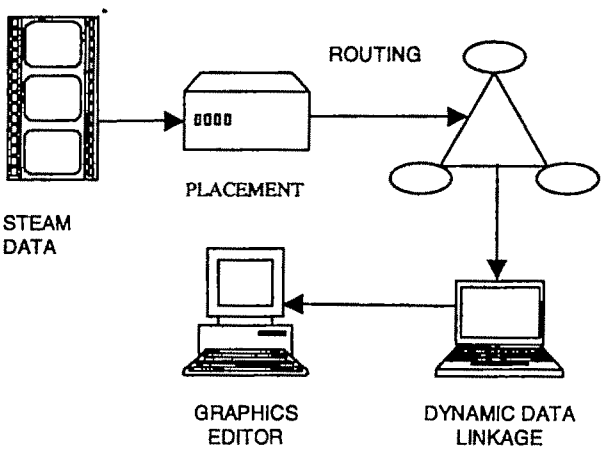

Fig 1 Process involved in the one-line diagram generation

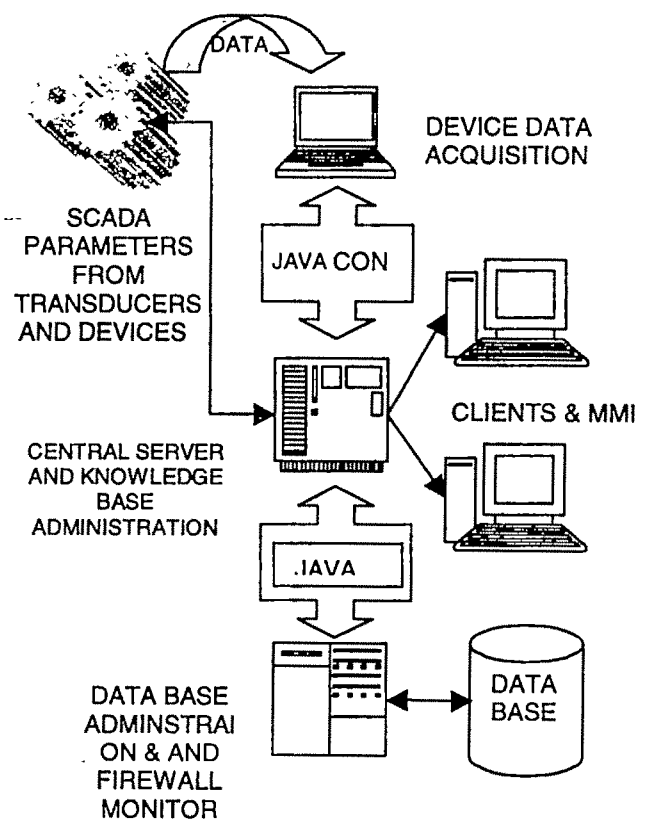

Fig 2 System Design

A Simple Method For Load Flow Solution Of Unbalanced Radial Distribution Networks

Smarajit Ghosh
Department of Electrical and Electronics Engineering
Birla Institute of Technology and Science, Pilani – 333 031, Rajasthan, India
e-mail : smarajitghosh@rediffmail.com

Abstract

A load flow technique for solving unbalanced radial distribution network is presented. The proposed method is computationally very efficient and stores all data in vector form. The effectiveness of the proposed method is demonstrated by an example.

INTRODUCTION

Little attention has been paid to load flow analysis of distribution systems. Load flow is an extremely important and fundamental tool for the analysis of any electric power and distribution system. It is well used in the operational as well as planning stages. Certain application particularly in distribution automation and optimization of power system require repeated load flow solutions. In these applications it is very important to solve the load flow problem as efficiently as possible. Since the invention and wide spread use of the digital computers, beginning in the 1950's and 1960's, many methods for solving the load flow problem have been developed. Generally, distribution networks are radial and R/X ratio is very high. For this reason, conventional Newton-Raphson [1] method and Fast-Decoupled Load Flow method[2] do not converge. Many researchers have suggested the modified versions of the conventional load-flow methods for solving power networks with high R/X ratio [3-5]. The methods [1-14] available in literature are only applicable for load-flow solution of balanced radial distribution networks because 1-φ, 2-φ, 3-φ loads and special treatment is necessary for solving such networks.

Berg et. Al. [15] have proposed method for solving unbalanced radial distribution network. In ref. [15] the backward sweep involves the computation o a driving point impedance equivalent at each bus and the forward sweep is used to update voltages and currents. The method proposed by Kersting and Philips [16] updates voltages and currents during the backward and forward sweep is a direct voltage correction. Goswam and Basu [17] have also suggested a method for solving unbalanced radial distribution networks based on Newton-Raphson method. The methods, however, suggested by the researchers ref. [15-17] are very cumbersome and large CPU time is required.

Therefore, the main target of the author is to develop an algorithm for solving the load flow solution of unbalanced radial distribution network. It is the extension of the work ref. [14].

SOLUTION METHODOLOGY

For the analysis of electric power transmission line two fundamental assumptions are generally made which are (i) balanced 3-φ system and (ii) complete transposition of conductors. However, distribution system does not lend itself to either of the two assumptions. Because of the dominance of 1-φ loads the assumption of balanced three phase current is not justified. Moreover, the distribution lines are never transposed nor can it be assumed that the conductor configuration is an equilateral triangle. It is very necessary to introduce a more sophisticated and accurate method of calculating line currents. The author has used Carson's equations [17] to three-phase four wire system. Carson's equations allow for the computation of conductor self impedances and mutual impedances between conductors above the ground. In this work line charging admittance is neglected at the distribution voltage level.

For a grounded neutral system, the Carson's equations can be written as

$$\begin{bmatrix} Z_{aa'} \\ Z_{bb'} \\ Z_{cc'} \end{bmatrix} = \begin{bmatrix} Z_{aa} Z_{ab} Z_{ac} \\ Z_{ab} Z_{bb} Z_{bc} \\ Z_{ca} Z_{cb} Z_{cc} \end{bmatrix} \begin{bmatrix} I_a \\ I_b \\ I_c \end{bmatrix} \qquad (1)$$

For exapmple in case of double-line consisting phase a and phase b, equation (1) may be written as

$$\begin{bmatrix} Z_{aa'} \\ Z_{bb'} \\ Z_{cc'} \end{bmatrix} = \begin{bmatrix} Z_{aa} & Z_{ab} & 0 \\ Z_{ab} & Z_{bb} & 0 \\ 0 & 0 & 0 \end{bmatrix} \begin{bmatrix} I_a \\ I_b \\ I_c \end{bmatrix} \quad (2)$$

Similarly, in case of single phase line involving phase b, equation (2) may be written as

$$\begin{bmatrix} Z_{aa'} \\ Z_{bb} \\ Z_{cc'} \end{bmatrix} = \begin{bmatrix} 0 & 0 & 0 \\ 0 & Z_{bb} & 0 \\ 0 & 0 & 0 \end{bmatrix} \begin{bmatrix} I_a \\ I_b \\ I_c \end{bmatrix} \quad (3)$$

If the returns through the neutral conductor in a single-phase line, a different procedures is followed. Fig. 1 shows a single-phase line consisting phase b and neutral n. The equation for voltage drop on phase b can be written as :

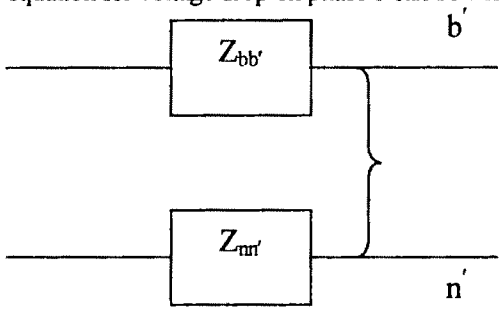

Fig. 1 : Single phase line section

$$V_{bb'} = V_{bn} - V_{b'n} \quad (4)$$

Also

$$V_{bn} = Z_{bb} * I_b + Z_{bn} * I_n \quad (5)$$

$$V_{b'n} = Z_{nb} * I_b + Z_{nn} * I_n \quad (6)$$

As all the phase current returns in the neutral conductor :

$$I_n = -I_b \quad (7)$$

Substitution equations (5),(6) and (7) in equation (4), we get

$$V_{bb'} = (Z_{bb} + Z_{nn} - Z_{bn} - Z_{nb}) * I_b \quad (8)$$

$$= Z_{b\varphi} * I_b \quad (9)$$

Therefore, for phase a

$$V_{aa'} = Z_{a\varphi} * I_a \quad (10)$$

Therefore for phase c

$$V_{cc'} = Z_{c\varphi} * I_c \quad (11)$$

In general equations for unbalanced radial distribution networks may be written as

$$\begin{bmatrix} V_a \\ V_b \\ V_c \end{bmatrix} = \begin{bmatrix} V_{a'} \\ V_{b'} \\ V_{c'} \end{bmatrix} + \begin{bmatrix} Z_{aa} Z_{ab} Z_{ac} \\ Z_{ab} Z_{bb} Z_{bc} \\ Z_{ca} Z_{cb} Z_{cc} \end{bmatrix} \begin{bmatrix} I_a \\ I_b \\ I_c \end{bmatrix} \quad (12)$$

If am, bm, cm are the sending-end nodes and a'm,b'm and c'm are the receiving-end nodes then we can write

$$\begin{bmatrix} V_{a'm} \\ V_{b'm} \\ V_{c'm} \end{bmatrix} = \begin{bmatrix} V_{am} \\ V_{bm} \\ V_{cm} \end{bmatrix} + \begin{bmatrix} Z_{aa}(j) Z_{ab}(j) Z_{ac}(j) \\ Z_{ab}(j) Z_{bb}(j) Z_{bc}(j) \\ Z_{ca}(j) Z_{cb}(j) Z_{cc}(j) \end{bmatrix} \begin{bmatrix} I_a \\ I_b \\ I_c \end{bmatrix} \quad (13)$$

In this work the loads are assumed to be fixed complex power (s=P+jQ) and wye connected and all double and single phase loads are connected line to neutral.

From figure 2, the following equation can be written as :

$$I_{xj} = \frac{P_{x'm} - jQ_{x'm}}{(V_{x'm})^*} \quad (14)$$

where x=a,b and c respectively. And $P_{x'm}$ and $Q_{x'm}$ are the total real power and reactive power fed through the nodes x'm respectively.

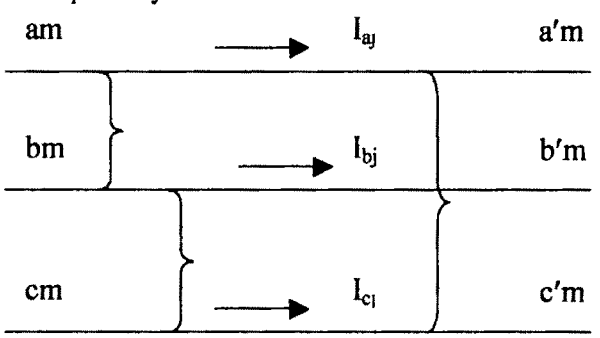

Fig. 2: Electrical Equivalent of phase a,b,c

The current fed by the node xm into the linee can be written as

$$I_{am,a'm} = \frac{V_{am} - V_{a'm}}{Z_{aa}(j)} + \frac{V_{am} - V_{bm}}{Z_{ab}(j)} + \frac{V_{am} - V_{cm}}{Z_{ac}(j)} \quad (15)$$

The power fed into the circuit from node am is given by

$$P_{am,a'm} = V_{am} * I^*_{am,a'm} \quad (16)$$

The real and reactive power losses in the line am-a'm can be written as

$$LP_a(j) = \mathrm{Re}al\{P_{am,a'm}(j) + P_{a'm,am}(j)\}$$

$$LQ_a(j) = \mathrm{Im}ag\{P_{am,a'm}(j) + P_{a'm,am}(j)\} \quad (17)$$

Similarly, for phases b and c the real and reactive power losses can be written as

$$LP_b(j) = \mathrm{Re}al\{P_{bm,b'm}(j) + P_{b'm,bm}(j)\}$$

$$LQ_b(j) = \mathrm{Im}ag\{P_{bm,b'm}(j) + P_{b'm,bm}(j)\} \quad (18)$$

$$LP_c(j) = \mathrm{Re}al\{P_{cm,c'm}(j) + P_{c'm,cm}(j)\} \quad (19)$$

$$LP_c(j) = \mathrm{Im}ag\{P_{cm,c'm}(j) + P_{c'm,cm}(j)\} \quad (20)$$

For obtaining the load flow solutions of unbalanced radial distribution networks, better starting values of currents are necessary. To achieve this, in very fast iteration, equation (14) are approximated as

$$I_{xj} = \frac{P_{x'm} - jQ_{x'm}}{(V_{xm})^*} \quad (21)$$

The algorithm as follows :

Step 1 : Start
Step 2 : Read System Data
Step 3 : Set iteration count IT=0 and DVMAX=0.0
Step 4 : Identify nodes beyond all he branches ref.[14]
Step 5 Calculate branch current and voltage at nodes a'm,b'm and c'm
Step 6 : Calculate DV(m2)=ABS|V(m2)-VV(m2)|
Step 7 : Jj=1
Step 8 : If DV(m20>DVMAX, DVMAX=DV(m2)
Step 9 : jj=jj+1
Step 10 : If jj ≤ LN1, go to step 8
Step 11 : If DVMAX ≤ ε, go to step 14
Step 12 : Set VV(m2)=V(m2)
Step 13 : IT=IT+1
Step 14 : If IT ≤ ITMAX, go to step 5
Step 15 : Print results
Step 16 : Stop

Example: A 4.16 kV unbalanced radial distribution network is taken from [16]. Power factor of the load is 0.8. Line and load data is available in ref [16]. It is assumed that the transfomer at the substation is balanced. Base voltage is chosen as 4.16 kV. Line charging admittances is neglected. System losses are :

Phase	Real Power Loss (kW)	Reactive Power Loss KVAr)
A	14.179	17.910
B	8.872	11.568
C	10.846	14.286

CONCLUSION

A new load flow technique for solving unbalanced radial distribution networks has been developed. Mutual coupling between the phases have also been considered in mathematical modeling. The proposed method is extremely simple as it solves simple recursive relationships of receiving-end and sending-end voltages. Hence the proposed method is computationally very efficient. Another advantage of the proposed method is that all the data can be stored in vector thus saving enormous amount of memory. The proposed method is tested successively through an example.

REFERENCES

1. W.F. Tinny, C.E. Hart," Power flow solution by Newton's like method," IEEE Transactions, 1967,Pas-67,pp.1449-1456.
2. B. Scott, O.Alsac,"Fast decoupled load flow", IEEE Transactions, 1974,Pas-93,pp.859-869.
3. D.Rajicic and Y. Tamura,"A modification to fast decoupled power flow by for networks with high R/X ratio," IEEE Transactions, 1988,PWRS-3, pp.743-746.
4. S.Iwamoto, Y.Tamura," A load flow calculation method for ill-conditioned power systems,"IEEE Transactions, 1981, Pas-100,pp.1736-1743.
5. S.C.Tripathy, G.Durgaprasad, O.P.Malik and G.S.Hope,"Load flow solution for ill conditioned power system by Newton like method," IEEE Transactions 1982, PAS-101,pp.3684-3657.
6. W.H.Kersting, D.L.Mendivee," An application of ladder network theory to the solution of three phase radial load flow problem," IEEE PES Winter meeting,New York, January 1976.
7. W.H. Kersting,"A method to design and operation of a distribution system," IEEE Transactions 1984,Pas-103, pp.1945-1952.
8. R.A. Stevens,D .T.Rizy, S.L.Purucker," Performance of conventional power flow routines for real distribution automation application, "Proceedings of 18 th Southeastern Symposium on System theory, 1986 (IEEE Computer Siciety), pp. 196-200.
9. D. Shirmohammadi, H.W.Hong, A.Semleyen, G.X. Luo," A compesation based power flow method for weakly meshed distribution and transmission network,"IEEE Transactions 1988, PWRS-3, pp.753-763.
10. M.E.Baran ,F.F.Wu," Optimal sizing of capacitors placed on a radial distribution system," IEEE Transactions, 1989,PWRD-2,pp.735-743.
11. H.D. Chiang, "A decoupled load flow method for distribution power network algorithms, analysis and convergence study," Electrical Power Energy System, 1991, 13(3), pp.130-138.
12. C.G. Renato, " New method for the analysis of distribution networks,"IEEE Transactions, 1989, PWRD-2,pp.735-743.

13. D.Das, H.S. Nagi , D.P.Kotahri,"Novel method for solving radial distribution networks," IEE Proceedins Part C(GTD), Vol.141,No.4, Nov.,pp.291-298,1994.
14. S.Ghosh, D.Das,"Method for load flow solution of radial distribution networks," Proceedings IEE Part C (GTD), Vil.146, No.6, Nov 1999.
15. R. Berg et. Al.,"Mechanical calculation of unbalanced load flow on radial distribution circuits," IEEE Transactions on Pas, Vol. Pas-86,No.4,April 1967, pp.415-421.
16. W.H. Kersting and W.H. Philips,"A three-phase power flow program for the PC,"Presented at 1987 Frontriers Power Conference, Stillwater, Oklahama, Oct.1987.
17. S.K.Goswami and S.K.Basu,"Direct solution of distribution systems,"IEEE Proceedings Part C(GTD), 188(1),pp.78-88.
18. J.R. Carson,"Wave propagation in overhead wires with ground return,"Bell Systems Technical Journal,Ocyt. 1926,Vol5.

Method For Branch Conductors Optimization Of Radial Distribution Networks

Smarajit Ghosh
Department of Electrical and Electronics Engineering
Birla Institute of Technology and Science, Pilani – 333 031, Rajasthan, India
smarajitghosh@rediffmail.com

Abstract

A simple and efficient method for optimal conductor selection of radial distribution networks is presented. The proposed method also shows that selection of optimum conductors reduces losses instead of selecting uniform conductors. The usefulness of the proposed method is demonstrated by one example.

INTRODUCTION

Distribution losses account for the bulk of the system losses and the capital investment of the distribution network is a considerable fraction of the total capital investment. Therefore, considerable attention has been focused on optimal distribution system planning over the last few years. The distribution feeders have been assumed to be uniform cross-section in the methods ref. [1-3]. The most important characteristic of the distribution networks is that they are radial and load carried by different feeders segments are different.

In 1950's Funk Houser et. al. [4] have proposed a method of optimal conductor grading. This method is based on the assumption of uniform load distribution for the feeders. Ponnavaikko and Rao [5] have proposed a model (PPR model) for optimal conductor selection of radial distribution networks. Their model is flexible and can handle the variations of load growth rate, load factor, cost of energy etc. over a plan period. The PPR model considers the conductor grading problem as an optimization of minimizing the sum of feeder cost and present worth of feeder energy loss costs. The main drawback of this method [5] is that it cannot handle the lateral branches. Tram and Wall [6] have developed a computer algorithm for optimum selection of conductors of radial distribution networks. They have also explored the possibility using a regulator instead of reconductoring the feeder segments to resolve the voltage problems. Ponnavaikko and Rao [7] have proposed a new technique for distribution system planning through optimal conductor gradation. They have obtained the optimum cross-section of branch conductors by dynamic programming approach. However, their method is only suitable for main feeder and it cannot handle lateral branches. Nagendra Rao [8] have also proposed a technique for obtaining branch conductor cross-section. However, the main drawback of this method is that it cannot handle lateral branches.However, the methods [4-8] available in the literature are not based on any load flow techniques which is important for optimization branch conductors of radial distribution networks. Also it is very important to consider voltage constraint and maximum capacity of each type of conductor.

In this paper, the main target of author has been to develop a computer algorithm for optimal branch conductor selection of radial distribution feeders based on an efficient load flow technique developed in ref. [9]. The proposed method has the capability to consider lateral branches. It also considers the voltage constraint and the maximum current carrying capacity of each conductor.

ASSUMPTION

It is assumed that the three-phase radial networks are balanced and can be represented by their equivalent single-line diagram.

MODIFIED LOAD FLOW ALGORITHM

A fast load flow algorithm developed in ref. [9] is used for optimal branch conductor selection of radial distribution feeders with some modifications.

Fig. 1 of ref.[9] shows the single line diagram and table-1 gives the branch number, sending-end and receiving-end. Consider branch-1, the receiving-end node voltage of branch-1 can be written as

$$V(2,K)=V(1,k)-I(1,k)*Z(1,k) \quad (1)$$

where

V(1,k)	:	Substation voltage (constant for all k)
V(2,k)	:	Voltage of node 2 with k-type conductor of banch-1, k=1,2,....,Ntype
I(1,k)	:	Current of branch-1 with k-type conductor of branch-1, k=1,2,...,NTYPE
Z(1,k)	:	Impedance of branch-1 with k-type conductor of branch-1, k=1,2,...,NTYPE
NTYPE	:	Total number of conductors

Similarly for branch-2,

$$V(3,k)=V(2,k)-I(2,k)*Z(2,k) \quad (2)$$

Substation voltage V(1,k) is known. So if we know I(1,k) for k=1,2,.....,NTYPE, i.e., current of branch-1 for different type of conductors, we can easily calculate V(2,k) for k=1,2,.....,NTYPE from equation-1.

Once V(2,k) is known, we can easily calculate V(3,k) for k=1,2,.....,NTYPE from equation-2 if current through branch-2 i.e., I(2,k) is known for k=1,2,....,NTYPE. Similarly, voltage at nodes 4,5,.....,NB (total number of nodes) can be easily calculated for k=1,2,.....,NTYPE. Therefore, a generalize equation of receiving-end voltage, branch current and branch impedance is given below:

$$V(m2,k) = V(m1,k)-I(jj,k)*Z(jj,k) \quad (3)$$

where

jj	:	Branch number
m2	:	Receiving-end node of branch-jj
m1	:	Sending-end node of branch-jj

Equation-3 can be evaluated for jj=1,2,....., LN1(=NB-1) with different type of conductors. For developing the optimal branch conductor algorithm, charging currents are neglected.

Now current through the branch-1 is equal to the sum of the load currents of all nodes beyond branch-1. The general expression of branch current of k-type of conductor is given by

$$I(jj,k)=\sum_{k=1}^{N(jj)} IL\{IE(jj,k),k\} \quad (4)$$

The load current of node I is as follows :

$$IL(i,k)=\frac{PL(i)-jQL(i)}{V^*(i,k)} \quad (5)$$

where I=2,3,....NB and k=1,2.....,NTYPE

Equation (5) clearly shows that as the node voltages are different for different type of conductors, load currents are also different for different type of conductors.

Real and Reactive power losses of branch-jj with k-type conductor are given by:

$$LP(jj,k)=|I(jj,k)|^2 R(jj,k) \quad (6)$$

$$LQ(jj,k)=|I(jj,k)|^2 X(jj,k) \quad (7)$$

OBJECTIVE FUNCTION

The basic problem is that of selection a conductor type for each branch of a radial distribution feeder which will minimize the sum of the cost of capital investment and the cost of losses while maintaining an acceptable voltage.

The annual cost for the loss in branch-jj with k-type conductor can be calculated by,

$$L(jj,k)=K_p*LP(jj,k)+Lsf*LP(jj,k)*T*K_E \quad (8)$$

where

K_p	:	Annual demand cost of losses (Rs/kW)
K_E	:	Energy cost of losses (Rs/kW)
T	:	8670hrs
Lsf	:	Loss form

In equation (8), the loss factor is used because LP(jj,k) is peak real power loss of branch-jj with k-type conductor and Lsf*LP(jj,k) gives the average real power loss of branch-jj with k-type conductor.

The annual cost of capital for branch-jj with k-type conductor is

$$CC(jj,k) : \bullet *COST(k)*LEN(jj) \quad (9)$$

where

COST	:	Cost of k-type conductor (Rs/Km), K=1,2,.....,NTYPE
LEN(jj)	:	Length of branch-jj
$\propto$	:	Carrying charge current of feeders

Therefore, the objective function for branch-jj with k-type conductor can be written as

$$F(jj,k) : L(jj,k)+C(jj,k) \quad (10)$$

In this work optimal conductor selection is obtained by branch-wise techniques.

Constraints:

i) Feeder Voltage : The feeder voltage at every node in the feeder must be above the acceptable voltage level, i.e., $|V(i)| \geq V_{min}$ for all i.

ii) Maximum current carrying capacity: Current flowing through the branch-jj with k-type conductor should be less than the maximum current carrying capacity of k-type conductor.

COMPUTER ALGORITHM

Step 1 : Read Real System Data and assume a Flat Voltage Start

Step 2 : Identify Nodes Beyond all Branches Using Algorithm ref. [9]

Step 3 : IT=1 and DVMAX = 0.0

Step 4 : Compute L(jj,k), CC(jj,k) and F(jj,k) using equations (8), (9) & (10)

Step 5 : Test {VV(m2)>V_{min} & CII(jj)≤ CMAX(jj)

Step 6 : Calculate absolute change in voltage DV(m2) at node m2.

Step 7 : If DV(m2)≤ε, go to Step-10

Step 8 : IT=IT+1

Step 9 : If IT≤ITMAX, go to step 5

Step 10 : Print Results

EXAMPLE

In this section, the effectiveness of the proposed method is demonstrated by one example. In first case a physically existing rural distribution feeder is taken. The feeer is jeavily loaded during agricultural season. The basic objective is to examine whether branch conductors of this feeder are properly selected or not. Data of the conductors are given in Appendix-A. Line data and Load data for example are given in Appendix-B.

First a base case load flow is carried using the data given Appendix-B. The real and reactive power losses are 53.47 kW and 37.17 KVAr respectively. Minimum voltage at node 16 is |V(16)|=0.88670 p.u.

For the Optimization of branch conductors four different type of conductors are used (Appendix-A). Same load data in Appendix-B is used for the purpose of comparison. Limit of minimum voltage is taken as 0.90 p.u. Modifications of conductors depicted in Table –1.

Table –1 : Modifications of conductors

Branch No.	Existing Feeder	Modifications
	From	To
5-6	Rabbit	Raccon
9-10	Weasel	Raccon
11	Weasel	Rabbit
12-13	Squirrel	Rabbit
14	Squirrel	Rabbit

After modifications real and reactive power losses are 37.36kW and 35.15 KVAr respectively. Minimum voltage occurs at node 16 is |V(16)|=0.91533 p.u.

This clearly indicates the real power and reactive power losses are 16.11 kW and 1.98 KVAr respectively and also improvement of voltage.

CONCLUSION

In this paper, a method has been presented for selecting the optimal branch conductors of radial distribution feeders based on a load flow technique [9]. The proposed method selects the optimal branch conductors by minimizing an objective function which is the sum of capitalized feeder loss cost and the feeder cost. In addition, the proposed method keeps the minimum voltage within prescribed limit and the current flowing through each branch is less than the maximum current carrying capacity of the corresponding branch conductor. Effectiveness of the proposed method is demonstrated by an example.

REFERENCES

1. D.L. Wall, G.L. Thompson, J.E.D. Northcote-Green," An Optimization Model for Planning Radial Distribution Network," IEEE Transactions on PAS, Vol. PAS-98,1979, pp.1061-1067.
2. W.C. Kiran, R.B. Adler," A Distribution System Cost Model and its Application to Optimal Conductor Sizing," IEEE Transactions on PAS, Vol. PAS-101, Feb. 1982,pp. 1439-1442.
3. 3.M.Ponnavaikko, K.S.P. Rao,"Optimal Distribution System Planning," IEEE Transactions on PAS, June 1979, pp. 2969-2977.
4. 4.A.W. Funk Houser et. al.," A Method for Determining ASCR Conductor Sizes for Distribution System," AIEEE Transactions on PAS, June 1955.

5. 5.0M.Ponnavaikko, K.S.P. Rao," An Approach to Optimal Dsitribution System Planning through Conductor Gradation," IEEE Transactions on PAS, Feb. 1981, pp. 788-791.
6. 6.H.N. Tram and D.L. Wall," Optimal Conductor Selection in Radial Distribution Systems," IEEE Transactions on PAS, Vol. 3, No. 1, Feb. 1988, pp. 200-206.
7. 7.M.Ponnavaikko, K.S.P. Rao," An Approach to Optimal Dsitribution System Planning through Conductor Gradation," IEEE Transactions on PAS, Feb. 1982, pp. 1735-1742.
8. Nagendrao Rao, " An Extremely Simple Method of Determining Optimal Conductor Selections for Radial Distribution Feeders," IEEE Trans. On PAS, Vol.PAS-101, No. 6, 1985, pp.1439-1442.
9. 9.S. Ghosh , D.Das," Method for Load Flow Solution of Radial Distribution Networks," Proceedings IEE Part C(GTD),Vol. 146, No.6, Nov. 1999, pp. 641-648

Appendix-A
Table-2 : Data for Conductors

Type of Conductor	Area of Cross – section (mm^2)	Resistance (•/Km)	Reactance (•/Km)	Maximum current carrying capacity (Amps)	Cost of Conuctors (Rs/Km)
Squirrel	12.90	1.3760	0.3896	70.0	2889.0
Weasel	19.35	0.9108	0.3797	100.00	4338.0
Rabbit	32.36	0.5441	0.3673	148.0	7306.0
Raccon	48.39	0.3657	0.3579	200.0	10950.0

Appendix-B
Table-3 : Line and Load Data for Example

Branch no.	Type of conductor	Sending-end (m1)	Receving-end (m2)	Length(Km) LEN(jj)	Load at m2	
					KW	KVAr
1	Raccon	1	2	2.00	48.75	43.00
2	-do-	2	3	1.60	37.50	33.00
3	-do-	3	4	2.30	33.00	75.00
4	-do-	4	5	2.90	75.00	66.10
5	Rabbit	5	6	2.20	48.75	43.00
6	-do-	6	7	1.57	37.50	33.00
7	-do-	7	8	2.40	12.00	10.60
8	-d0-	8	9	4.00	37.50	33.00
9	Weasel	9	10	2.30	37.50	33.00
10	-d0-	10	11	2.50	75.00	66.10
11	-d0-	11	12	2.70	18.75	16.50
12	Squirrel	12	13	3.20	48.75	43.00
13	-do-	13	14	1.70	48.75	43.00
14	-do-	14	15	3.80	75.00	66.10
15	-do	15	16	2.00	37.50	66.10
Load KVA at node 1 is 0.0						

Interaction Between Insulation Co-Ordination And Pollution

R. P. Singh
Department of Electrical Engineering
NERIST, Itanagar(A.P.), India
E-Mail: rvps@neristernet.in

Abstract

Insulation co-ordination plays an important role in decision making for design optimization. At present due to increasing trends in wide variety of pollution levels and increase in voltage transmission level due to economic reasons, self restoring properties of the insulation is adversely affected . The conventional method of insulation co-ordination, the worst case method which involves the identification of the most severe voltage stress on the insulation and the minimum insulation strength attained by a particular insulation structure, some times becomes inadequate to reflect actual estimated performance. The paper comprises a critical review of insulation co-ordination in EHV systems and effect of pollution on its performance.

Keywords: *Insulation Co-ordination , Pollution, Insulator, Surge Arrester.*

INTRODUCTION

Detail and accurate knowledge about performance of insulation co-ordination for EHV system has become essential with the tremendous industrial growth and continuous increasing electrical power demand. On the other side , due to heavy investment and importance of reliability , all the components i.e. generation ,transmission and distribution networks of power system must achieve optimum performance without suffering from the any type of penalty either of conservative design or reduction in reliability level . With increase in the system voltage and cost involvement , it becomes uneconomical to provide insulation for withstanding the severest possible voltage stress that might occur . In such a case, the designer has to accept certain amount of risk of insulation failure. The basic objective of the insulation co-ordination is to minimize the extent of damage to the system in case of failure.

The co-ordination between the system voltage and the insulation should be in such a way that any failure would be confined to a place in the system where it would result in

-least damage
-be least expensive to repair and cause
-least hazard to the continuity of the supply

The insulation co-ordination becomes very much pronounced in the case if one of the component of the system happens to be protective device i.e. surge-diverter because insulation ones connected in a system behaves in a different way as compared to its individual behavior. That is to say that there is interaction between the fields across the components of the system and accordingly insulation behavior differs.

SYSTEM OVERVOLTAGES

Over voltages are the main cause of healthy insulation failure. There are two main causes of over voltages .

(i) Switching, faults and resonance are the main causes of internal over voltages. Switching surge over voltage, generally rises up to 2.5 per unit , but in severe conditions ,sometimes it may theoretically touch up to 4.0 per unit. Under sustained phase earth fault condition, temporary power frequency over voltage arise. Phase voltage of healthy phases at fault or arrester location rise from 80 to over 100% of line to line voltage depending upon the earthing arrangement of the system. Resonance over voltages may come up to 3-4 per unit. The fundamental frequency of stable ferro resonant state is the one which is potentially most dangerous in electrical distribution

networks. Generally, a ferro resonant circuit occurs when both the transformer and a length of cable are being single phase switched at the same time. Accordingly, ferro resonant conditions could be avoided by energizing the cable first and then the transformer and conversely, de-energizing the transformer first and then the cable.

(ii)Lightning discharges i.e. interclouds and cloud to line is the external causes of system over voltages. The protection against these voltages is provided by lightning arresters. For economical reasons, without loss of reliability, incorporating the proper available knowledge of over voltages and protective devices for these may reduce insulation levels of the equipments.

INSULATION CO-ORDINATION

The insulation requirement of a component of apparatus or system depends on the voltage stresses that it has to encounter in service. With increase in system voltage (EHV/UHV), it becomes uneconomical to provide insulation for withstanding the severest possible voltage stress that might occur. Therefore, the designer has to make a compromise between what one wants to have and how much one is willing to pay. In doing so , the designer has to accept certain amount of risk of insulation failure. At this stage , insulation co- ordination plays an important role . Its basic objectives are i.e. any failure would result in least damage, be the least expensive to repair and cause the least hazard to the continuity of service.

There is interaction between the components of a system and because of this, insulation connected in a system behaves in a different way as compared to its individual behavior. It was not before 1928 that the objective of insulation co-ordination was precisely defined. Perhaps the first paper detailing the objective of insulation co-ordination was published by Philip Sporn. It can also be observed from the literature that the progress in this direction was comparatively slow which can be attributed to the lack of

- data about over voltages on the systems
- knowledge of insulation characteristics
- adequate testing techniques

By early 1940, the impulse voltage levels (BIL) based on protective levels of surge diverters were standardized and adopted. The lightning over voltages became the main criterion for determining the insulation levels of the apparatus and systems. In 1960 's, with the increase in transmission voltage levels, it was recognized that switching over voltages required careful consideration in the practice of insulation co-ordination especially in the EHV systems . This special consideration for switching over voltage was given because of :

- the duration of these over voltages are more as compared to as lightning surge
- its magnitude is proportional to the system voltage
- more number of insulations are subjected to these over voltages simultaneously
- air insulation exhibits non-linear characteristics to these over voltages

Insulation levels for apparatus are determined by dielectric tests simulating the various stresses that occur in the system during service. From dielectric test point of view, the transmission system insulation can be classified in two categories.

- self-restoring (external insulation i.e. line insulators, isolators, bus bars, bushing etc.)
- non self -restoring (internal insulations i.e. between transformer windings etc.)

The strength of the self –restoring insulations is determined by 50% disruptive discharge test whereas the strength of non self-restoring insulation is verified by withstand test in which the test voltage is applied for limited number of times or for a limited duration. The conventional method of insulation co-ordination is also called as the worst case method , involves the identification of most severe voltage stress on the insulation and the minimum insulation strength attained by a particular insulation structure . Though this approach is workable and direct in concept but it has following disadvantages.

- The performance of the insulation greatly depends on the selection of proper set up of design conditions.
- The performance of the system can not be quantified and therefore there is no means of the comparison between two alternative designs.
- As the performance is not qualified, it is not possible to compare the estimated performance level with the system investment required to enable the optimum design to be involved and
- there may be cascading of safety factors which results in increased system investment.

As compared to the conventional method (the worst case method), the statistical method is more realistic but it involves complex calculations. To reduce the complexity, safety factors are generally taken in to account but it is not the optimum solution. Statistical methods of insulation co-ordination are mostly used for self re-storing insulation i.e. external insulation.

FACTORS INFLUENCING INSULATION CO-ORDINATION

Among the numerous factors associated with statistical methods of insulation co-ordination, following are some of the most important factors, which need careful consideration.

- Method of determining over voltage distributions.
- Method of determining insulation strength distributions
- Method of risk of failure evaluation.
- Effect of over voltage limiting devices.
- Weather variation along line length.
- Voltage profile along line length.
- Statistical aspects of surge diverters.
- Severity of pollution or contamination.

At present, due to tremendous industrial growth throughout the world, pollution is becoming severe and severe and on the other side power demand is increasing day by day. To fulfill bulk power demand, transmission voltage level is to go for EHV to UHV levels in order to economize the system. External insulation in the form of insulators, surge arresters, bushings etc are exposed in a variety of contaminants and pollutants as transmission lines pass through desert, sea shore, near fertilizer, cement and other chemical factories. Accordingly, concentration and variability of contaminants on insulation surface have its effects.

POLLUTION AND INSULATION

Generally, the pollution on an insulator surface or housing of the surge arresters do not cause serious problem under fair weather because in this condition, layers are substantially non–conducting. Lightly wetted layers start conducting significantly. Due to Joule heating, there will be uneven drying up of the wet layers. Thick layers can have, under wet condition, a very different conductivity than the superficial layers. So, it is obvious that drying of the wet conducting layer will also be non -uniform. Due to non-uniform drying of layers, current gets constricted to a few narrow paths, where, there may be intense heating giving rise to hot moisture, formation and growth of dry bands. The voltage across dry bands may rise to a very high value leading to arcing. If the drizzle is continuous, the dry band may again become wet and the arc may get quenched. So, formation and quenching of small arcs are known as scintillation. Scintillations are randomly located on the insulator surface or housing of the surge arresters.

In case, if there is flash over across the surface, the current is limited by the arc resistance and the source impedance. The arc resistance and dry band expansion depend on the several parameters and processes such as

- Dynamic arc current
-Scintillation phenomena, its development and quenching
-Constriction of current lines across the discharge root
-Voltage drops at the arc roots
-Energy lost to the immediate atmosphere
-Energy lost by the arc to the insulating substrate and to the terminal points
-Ambient conditions such as temperature, humidity, wind direction and velocity
-Presence of electric and magnetic fields
-Insulator profile

REVIEW OF SOME PUBLISHED PAPERS

According to IEC-Publication 71-2; Insulation Co-ordination Application Guide , pollution severity of sites has been divided in to four levels i.e. Light, Medium, Heavy, and Very heavy. With concentrating effects of pollutants on electrical transmission system

,- Corona also becomes more effective on the lines.

- Early corrosion on malleable iron caps, forged ball pins and stem of insulators, surge arresters and of other equipments takes place.

Insulations near a cement factory, face a little different types of problems. The cement particles, those come in contact with humid air, start setting in air itself. Before, they are permanently set, these cement particles are carried by winds and thrown on insulation surface and moist cement particles deposited get permanently set on the insulators themselves. These deposits are not soluble in water and rain. It is not possible to remove this coating by hand wiping or cleaning with water. These deposits are, however, found soluble in dilute hydrochloric acid [1].

Quantity, volume, density and conductivity of the snow falling on the insulator affect the AC/DC withstand voltage of insulator covered with snow. The snow, due to high current density, partly melts and snow falls down partially from the insulator string. This may cause non-uniform voltage distribution across the insulator string. If the resistance of remaining snow is low and the gap insulation is low, arc may occur between the gaps. If this process continues and fall of snow on the insulator increases, it may not cause flash over. Mitsuru Yasui et.al. [2] have reported that about 400 electrical faults on transmission lines of 275 kV or below were experienced by the Tokyo Electrical Power Co. during winter seasons in 20 years. Although such failures are rare, but ones it happens, it causes operational difficulties.

Surge arresters are the key equipments to protect costly generators, transformers and other installed equipments in substations against atmospheric as well as switching over voltages. Due to superior V-I characteristics and some other merits, Metal Oxide Arresters are extensively in use. But, in adverse atmospheric conditions, internal ionization and oxidation cause the decomposition of the medium surrounding the metal oxide (ZnO) element inside. The main constituent, oxygen content may greatly fall. In the arresters originally filled with dry air, internal chemical reaction uses oxygen and creates mainly CO, CO_2, NH_4 etc.

and in the arresters originally filled with SF_6 gas creates SO_2, H_2SO_4, SF_x etc.. Therefore, decreased percentage of oxygen may change the nonlinear property of the varistors. Presence of humidity, may also change the coupling capacitance between stack of varistors and housing of the arrester. Discharge products affect the conductivity of varistors surface and possibly its withstand ability also. Knobloch et.al. [3] have reported the case of a varistor in SF_6 medium, in which due to the decomposition of SF_6 a number of radical ions or neutral molecules are formed when fluorine atoms split off. With moisture, they produce HF, SO2, H_2SO_4 etc. whose corrosivity is well known.. Singh R.P. and Sinha J. N. [4] have reported that if voltage applied to ZnO varistor allows flow of small current for a long time, migration of ions is caused by the voltage and the physico chemical reaction changes accordingly. This is called Stress Degradation. Jean and Petit [5] also reported that typically, 7kJ/kV for a block size of 50 cm^2 can be absorbed by metal oxide disk which translates to some 180 J/ cm^3 once in a minute. Each rated energy discharge may translate into a sudden (adiabatic) temperature rise of the whole disk by about 60^0 C. If the energy exceeds beyond rated value, disk failure may result.

CONCLUSION

In order to improve the external electrical insulation performance by which a reliable design of the system be possible, research work in the following areas is going on

(i) Long term study of different types of insulations under natural pollution conditions by monitoring the surface leakage current or counting the frequency of flashovers etc. to judge the relative merits of the insulation.

(ii) Investigation of the flashover or the withstand characteristics of the insulation in the laboratory using artificial pollution test methods.

(iii) Investigations of the physical processes of the pollution flashover, either on model insulation or simulation studies on mathematical models.

(iv) Mathematical modeling of polluted insulators and surge arresters considering the dynamic variations in atmospheric conditions.

(v) Study of interaction between insulation and contaminants / pollutants deposited inside or outside.

REFERENCES

1. K.V. Rajaram, "Pollution Performance of Insulators near a Cement Factory". Proc.of ISPPISD-1983, IIT Madras, Paper no.3.03.
2. Mitsuru Yasui et. al., " AC Withstand Voltage characteristics of Insulator strings covered with snow", IEEE Trans. on Power Delivery , Vol.3, No. 2, April-1988, pp 828-838.
3. H.Knoblock et.al., " Influence of the surrounding medium and service behavior of Metal Oxide resisters for high voltage arresters", IEEE Trans. on Power Delivery, Vol. 6, No. 2, April-1991, pp 680-687.
4. R.P.Singh, J.N. Sinha, " Studies on Pollution Performance of Metal Oxide Arresters ", IE(I)-EL, Vol.-76, Feb.1996, pp 211-217.
5. G.S. Jean, A.Petit , " Metal Oxide Surge Arresters operating limits, defined by a temperature margin concept", IEEE-Trans on Power Delivery, Vol. 5, No.2, April 1990, pp 627-633.

Power System Stability Using Functional Approach

A. K. Singh and S. Agrawala
Electrical Engineering Department
Regional Institute of Technology, Jamshedpur 831014, India

Abstract

The input-output stability condition requires the system subloops to be stable, with a margin of boundedness, so that the overall system is stable, satisfying the positive definiteness of a test matrix. In this paper application of this approach to a linearized power system model is considered. This results in a bounded stability region. The results are validated through detailed analysis and graph.

Key words: Sub loops, Input-output stability, Loop-gains, Margin of roundedness, Conicity, Test-matrix.

INTRODUCTION

A number of interesting stability criteria for feedback system [6] heave been appeared in control theory literature. Out of these the method based on functional analysis appears to be more satisfactory one, in view of the essential simplicity of the intuitive nature of the results, i.e., the loop gain less than one and positivity conditions [8], and the fact that it unifies the various criteria such as the circle criteria and he Popov criteria [2,3,4,7,8]. The additional advantage of the method is that it is valid for all types of system may be linear, non-linear, time-varying and combinations.

A linearized model of synchronous machine with exciter system is considered [1]. This model is converted into block diagram form for input-output stability study. This system may be viewed as interconnection of several isolated subloops and called an interconnected system. In the input-output stability point of view for an interconnected system using functional approach, if each isolated subloop is stable within a sufficient margin of boundedness, then the overall system can be further tested. Using Michel's approach [3] for sector conditions, a stability test-matrix is formulated involving interacting operators, and analyzed for input-output conditions [1,2,3,7].

POWER SYSTEM MODEL

A linearized power system model [1] is considered and given in eq.(1)

$$T_{e\Delta} = K_1\delta_\Delta + K_2 E_{q'\Delta} \quad (1.a)$$

$$E_{q'\Delta} = \frac{K_3}{1+K_3\tau'_{do}\,s} E_{FD\Delta} - \frac{K_3K_4}{1+K_3\tau'_{do}\,s}\delta_\Delta \quad (1.b)$$

$$V_{t\Delta} = K_5\delta_\Delta + K_6 E_{q'\Delta} \quad (1.c)$$

where, $T_{e\Delta}$ is small change in electrical torque,

δ_Δ is small change in rotor angle,

$E_{FD\Delta}$ is small change in field winding,

$E_{q'\Delta}$ is small change in voltage proportional to the main field winding,

τ'_{do} is the d-axis open circuit time constant of the machine.

The constants K_1, K_2, K_3, K_4, K_5 and K_6 depends upon the network parameters and the quiescent operating conditions.

To complete the model the linearized swing equation is used i.e.

$$\tau j\omega_\Delta = Tm_\Delta - Te_\Delta \quad (2)$$

In the above equation the time is in p.u. to a base quantity of 1/377 s. T is the total torque to a base quantity of the three-phase machine power and $\tau j = 2H\omega_R$.

The combined block diagram of synchronous machine with exciter system with damper winding effect is shown in fig. 1 (with the subscript Δ omitted for convenience). The function $G_F(s)$ is the rate feedback signal and equal to $sK_F/(1+\tau_F s)$, with $K_F = 0.04$, $\tau_F = 1.0$ s and other parameters used in this block diagram are

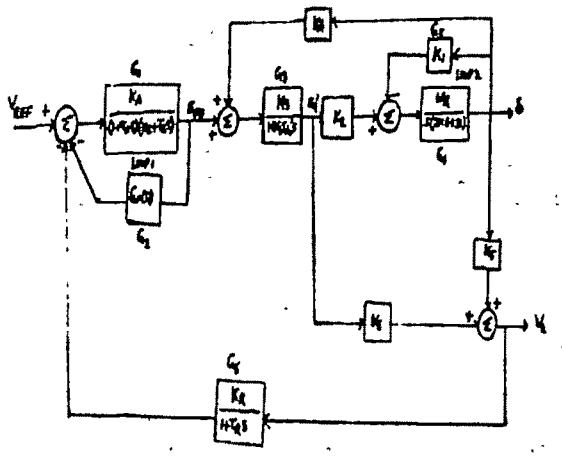

Fig.1. Reduced Combined Block Diagram of a Linear Synchronous Machine and Exciter

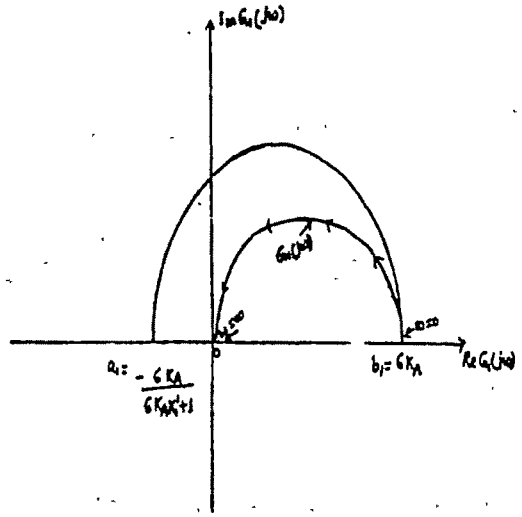

Fig.2. Nyquist Plot for $G_1(s) = K_A/[(1+\tau_A s)(K_E+\tau_E s)]$

The Exciter Data:

K_A=400, τ_A=0.05, K_E = -0.17, τ_E=0.95, K_R=1.0, τ_R=0.

The Machine Constants:

2H = 4.74 s, D = 2.0 & τ'_{do} = 5.9s

The Operating Points:

K_1 = 1.4479, K_3 = 0.3072, K_5 = 0.0294

K_2 = 1.3174, K_4 = 1.8052, K_6 = 0.5257

A brief discussion about the input-output stability using functional approach is shown in Appendix-A. Application of the function approach to the developed power system model is discussed in the next section.

APPLICATION OF INPUT-OUTPUT STABILITY TO POWER SYSTEM MODEL

Consider the block diagram in fig. 1, which may be viewed as interconnection of operator G_1, G_2, G_3, G_4, G_5 (=K_1, constant), G_6 and interconnecting element K_2, K_4, K_5 & K_6. There are two isolated sub-systems (i.e. loop1 & 2).

For the input-output stability of the system it is necessary to determine the conicity conditions, which give the sectors for the operators.

Select Do = {G_2, G_3, G_5, & G_6} and Co = {G_1, G_4}

Sector for each element

Consider each isolated sub-system.

Loop1: This loop contains two operators G_1 and G_2. Assume that operator G_1 is conic with constants (a_1, b_1) and the operator G_2 is conic with constants (a_2, b_2). From fig. 3 i.e. Nyquist plot of $G_2(s) = sK_F/(1+\tau_F s)$, its magnitude vary from 0 to ∞. Assume that operator G_2 is inside the sector (0, K'_1)

i.e. $a_2 = 0$, $b_2 = K_1'$ (non-negative real number),

$d_2 = -0.5(b_2+a_2) = -(K'_1/2)$

For a negative feedback, $c_1+d_2 = 0 \Rightarrow c_1=(K'_1/2)$

From fig. 2 i.e. the Nyquist plot of $G_1(s)$, $b_1 = 6K_A$ and using $c_1 = -0.5(1/a_1+1/b_1)$, we get,

$a_1=-6K_A/(6K_A K'_1+1)= -2400/(2400K'_1+1)$

Loop 2: This loop contains two operator G_4 and G_5. Assume that the operator G_4 is conic with constant (a_4, b_4) and operator G_5 is conic with constants (a_5, b_5). From fig. 4, i.e. the Nyquist plot of $G_4(s) = \omega_R/s(2Hs+D)$, which lies between 0 to infinity. Also assume that operator G_5 is inside the sector (0,K_2') i.e. $a_5 = 0$ and $b_5 = K_2'$. From fig. 4, it is clear that there is no possibility for satisfying the interior conicity for the operator G_4. Assume that $a_4 = -\epsilon$ (ϵ being small positive quantity) and using $d_5 = -0.5(b_5 + a_5) \Rightarrow d_5 = -K'_2/2$

Also using $c_4+d_5 = 0 \Rightarrow c_4 = K'_2/2$

Further, $c_4 = -0.5(1/a_4 + 1/b_4) = K'_2/2 \Rightarrow b_4 = \epsilon/(-\epsilon K'_2+1)$

Operator G_3: Operator G_3 is conic with constant (a_3,b_3). From fig.5, $a_3 = -0.3072$ and $b_3 = 0.3072$.

Operator G_6: Let us consider operator G_6 is conic with constant (a_6, b_6). Since $G_6(s) = K_R/(1+\tau_R s)$, using, $c_6 = -0.5(1/a_6 + 1/b_6)=0$, and taking K_R=1, τ_R=0, b_6=1, we get $a_6 = -1$.

Calculation for c_i, d_i and η_i for each operator:

All the operators c_i, d_i and η_i are computed following the procedures discussed in Appendix A

c_i & d_i for each operator

$c_i=0$ if $i \in D_o$ and $c_i=-0.5(1/a_i + 1/b_i)$ if $i \in C_o$.,

Also $d_i = 0$ if $i \in C_o$ & $d_i = -(b_i+a_i)/2$ if $i \in D_o$.

Using the above conditions, since $D_o = \{G_2, G_3, G_5, G_6\}$ and $C_o = \{G_1, G_4\}$,
We get $c_1 = K'_1/2$, $c_4 = K'_2/2$ and $c_2 = c_3 = c_5 = c_6 = 0$,
$d_1 = 0$, $d_2 = -K'_1/2$, $d_3 = 0$, $d_4 = 0$, $d_5 = -K'_2/2$, $d_6 = 0$.

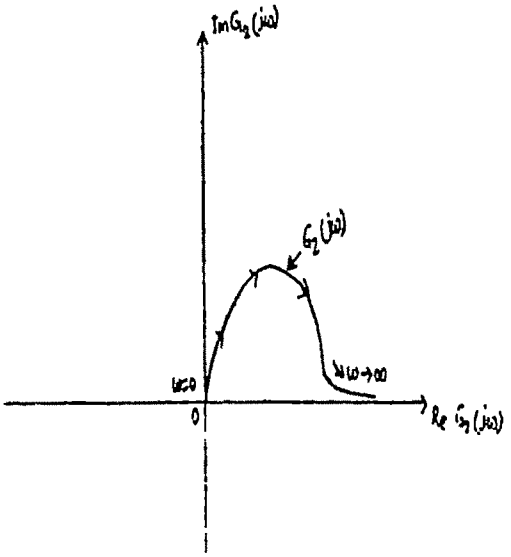

Fig.3. Nyquist Plot for $G_2(s) = sK_F/(1+\tau_F s)$

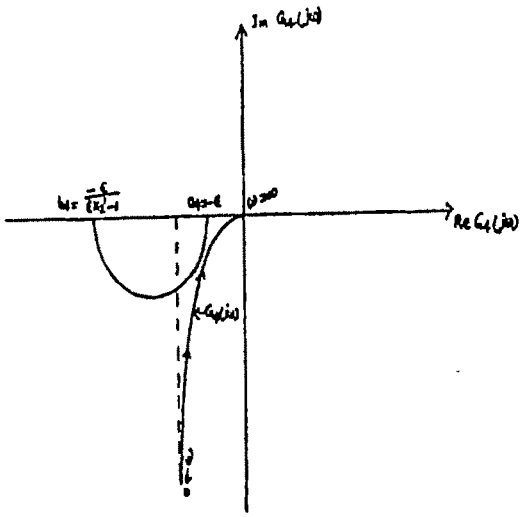

Fig.4. Nyquist Plot for $G_4(s) = \omega_R/s(2Hs+D)$

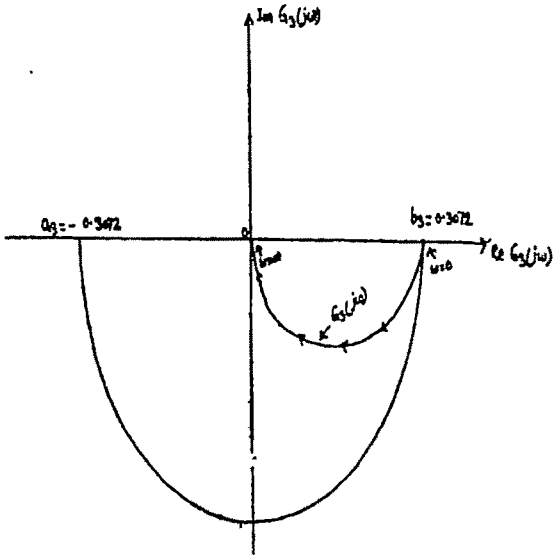

Fig.5. Nyquist Plot for $G_3(s) = K_3/(1+K_3\tau_{d'o}s)$

η_i for each operator.

$\eta_i = 0.5(b_i - a_i)$ if $i \in D_o$
and $\eta_i = -2a_i b_i/(b_i - a_i)$ if $i \in C_o$
using above expression, we get
$\eta_1 = 2400/(1200\,K'_1+1)$, $\eta_2 = K'_1/2$, $\eta_3 = 0.3072$
$\eta_4 = 2\epsilon/(-\epsilon K'_2+1)$, $\eta_5 = K'_2/2$, $\eta_6 = 1$

Calculation for δ_i (margin of bounded-ness) for each sub loop:
Loop 1: $\delta_1 = 1 - \eta_1 \eta_2 < 1 \Rightarrow K'_1 > 0$
Loop 2: $\delta_4 = 1 - \eta_4 \eta_{52} < 1 \Rightarrow \epsilon K'_2 > 0$

Formulation of test matrix

From the block diagram of fig 1, using the method discussed in Appendix A, the matrix B is in the form.

$$B = \begin{bmatrix} 0 & -1 & 0 & 0 & 0 & -1 \\ 1 & 0 & 0 & 0 & 0 & 0 \\ 1 & 0 & 0 & K_4 & 0 & 0 \\ 0 & 0 & K_2 & 0 & -1 & 0 \\ 0 & 0 & 0 & 1 & 0 & 0 \\ 0 & 0 & K_6 & K_5 & 0 & 0 \end{bmatrix}$$

Using $D = \text{diag.}\,(d_1, d_2, d_3, d_4, d_5, d_6,)$ with
$d_1 = d_3 = d_4 = d_6 = 0$,
$C = \text{diag.}\,(c_1, c_2, c_3, c_4, c_5, c_6)$ with $c_2 = c_3 = c_5 = c_6 = 0$
Using $B' = (I+BD)^{-1}(B+C) = [|\, b'_{ij} \,|]$,

Test matrix, $R = I - [|b'_{ij}|\,\eta_i|]$,

$$R = \begin{bmatrix} 1 & -\eta_2 & 0 & 0 & 0 & -\eta_6 \\ -\eta_1 & 1 & 0 & 0 & 0 & 0 \\ -\eta_1 & 0 & 1 & -K_4\eta_4 & 0 & 0 \\ 0 & 0 & -K_2\eta_3 & 1 & -\eta_5 & 0 \\ 0 & 0 & 0 & -\eta_4 & 1 & 0 \\ 0 & 0 & -K_6\eta_3 & -K_5\eta_4 & 0 & 1 \end{bmatrix}$$

The test matrix R is positive definite if the successive principal minors of R are all positive and in this case the conditions are.

$$(1-\eta_1\eta_2)\ (1-K_2K_4\ \eta_3\eta_4)>0 \quad (3)$$

$$(1-\eta_1\eta_2)\ [1-\eta_4\eta_5-K_2K_4\ \eta_3\eta_4]>0 \quad (4)$$

$$(1-\eta_1\eta_2)\ [1-\eta_4\eta_5-K_2K_4\ \eta_3\eta_4]+\eta_1\eta_6[K_2K_5\eta_3\eta_4 + K_6\eta_3(1-\eta_4\eta_5)]>0 \quad (5)$$

Substituting the value of all parameters in eq. (3), (4) & (5)

We get

$$1 > \epsilon(0.5\ K'_2+0.73) \quad (6)$$

$$1 > \epsilon(K'_2+0.73) \quad (7)$$

$$1 < \epsilon(K'_2+0.071) \quad (8)$$

The above three conditions are plotted and shown in fig 6. This gives the bounded region for the stability.

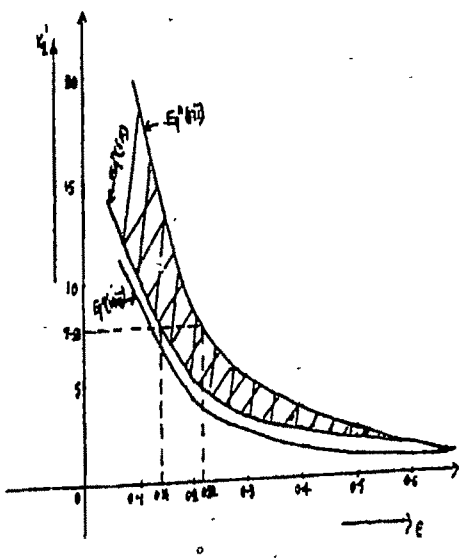

Fig.6. A Plot of ε Vs K'_2

RESULTS AND COMMENTS

Conditions obtained has been plotted and shown in fig.6. The common hatched portion shows the region of stability. For a particular value of operating point parameters, time response curve [1] is shown in fig.7. The slope of this curve gives the value of K'_2 i.e. tan θ= 7.59 and the corresponding value of ∈lies between 0.14 to 0.2. Since this value lies within the stability region, hence the system is said to be stable.

The parameters K_1 to K_6 of the linearized model are dependent on the operating point. If the parameter K_1 to K_6 changes then the slope K'_2 of the system response changes. If this value lies within the stability region then system is stable.

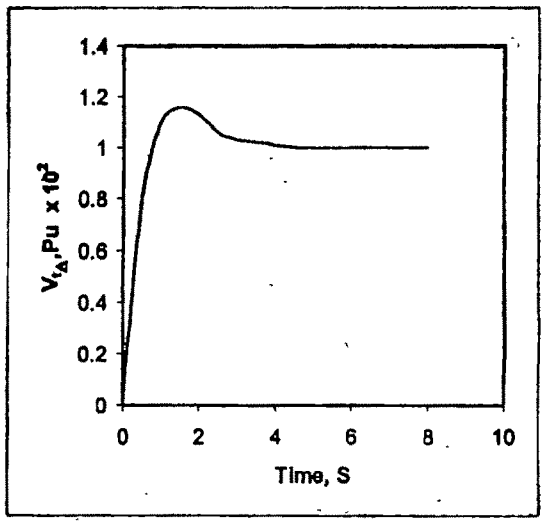

Fig.7. Time Response to a Step Change in V_{REF}

CONCLUSION

The input-input-output stability for linearized power system model using functional approach has been studied. This model has been analysed in terms of their sub-system and interconnecting structure. The stability conditions have been obtained in terms of sector condition (conocity) using the notion of extended space and margin of boundedness (δ). For a particular value of operating point, the system is said to be stable if its slope K'_2=tanθ of the system response lies within the stability region. In this way it is possible to get the limiting value of the operation of the power system, which it can tolerate.

APPENDIX- A

Input-Output Stability in Terms of Sector Conditions for a Single Loop [3]:

Consider a single loop system containing the two operators G_1 and G_2 in Hilbert space, and with loop transformation as shown in fig.8, for the positive feedback case. In general feedback may be positive or negative.

Loop transformation [7] is used to make loop-gain less than one. To get the sector condition using the result of Michel [3] , loop transformation is used so that the net transformation, from fig.8 is

$c_1 - d_2 = 0$, for positive feedback case. It follows that for negative feedback case, the net transformation with proper changes of signs in the fig. 8, will be $c_1 + d_2 = 0$

Margin of boundedness δ :

For a loop containing two operators G_1 and G_2, the maggin of boundedness δ is defined [3] as

$\delta = 1 - \eta_1 \eta_2 < 1$

Where η_1 is related to G_1 and η_2 is related to G_2.

Test Matrix of Michel [3] :

Consider the fig.9 of Michel. The inputs, errors, and outputs u_i, v_i, e_i, f_i, y_i, z_i all belongs, to the extended space $X_{i,e}$ the operator G_i maps X_{ie} into itself and the operator B_{ij} maps X_{je} into X_{ie}. Assume that G_i is conic with constants (a_i, b_i) where $b_i > a_i$ if $i \in D_0$ and $a_i b_i (b_i - a_i) < 0$ if $i \in C_0$ Here C_0 and D_0 be disjoint subsets of integers such that $C_0 \cup D_0 = 1, \ldots, l$. For each

$i = 1, \ldots, l$ pick constants d_i and c_i such that $c_i d_i = 0$, i.e. $d_i = 0$, if $i \in D_o$ and $c_i = 0$, if $i \in C_o$

Define,

$d_i = -(b_i + a_i)/2$; $i \in D_o$ & $d_i = 0$; if $i \in C_o$

$c_i = 0$; if $i \in D_o$ & $c_i = -(1/a_i + 1/b_i)/2$; $i \in C_o$

$\eta_i = (b_i - a_i)/2$; if $i \in D_o$ & $\eta_i = -2a_i b_i/(b_i - a_i)$ if $i \in C_o$

Define $B' = [I + BD]^{-1} (B+C)$

when $B' = [b'_{ij}]$ and $B = [b_{ij}]$ is an $l \times l$ matrix. B is called a structure matrix. B_{ij} represents a linear time invariant connection from the output of the j^{th} transfer system to the input of the i^{th} transfer-system, and B_{ii} represent, the connection from the output of the i^{th} transfer system with its own input. B matrix determines the structure of the system, which is the basis for input-output stability analysis, using sector condition.

Define,

$C \Delta$ diag. $[c_1, \ldots, c_l]$ and

$D \Delta$ diag. $[d_1, \ldots, d_l]$

If $B' = [|b'_{ij}|]$ has finite gain ie. $g(B'_{ij}) < \infty$ and if the successive principal minors of the test matrix $R\Delta\ 1 - [|b'_{ij}|]$ diag. $(\eta_1, \eta_2 \ldots, \eta_l)$ are all positive, then all of the input-output operators associated with system are bounded with respect to X_i.

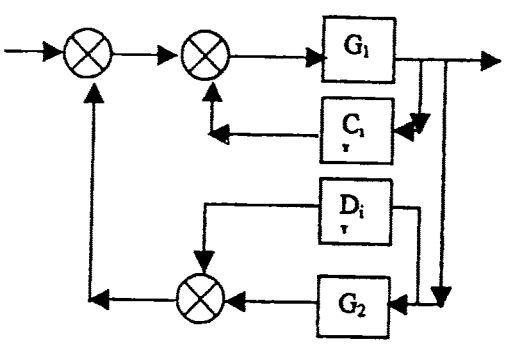

Fig 8 Feedback system with transformation

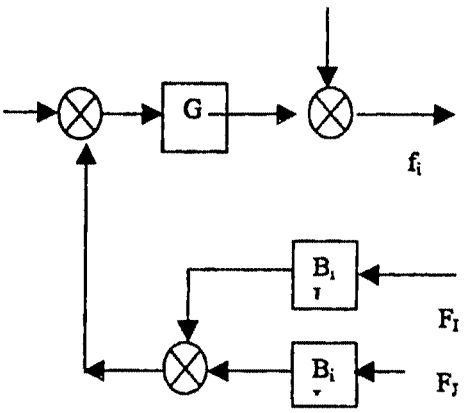

Fig 9 Block diagram of interconnected system

References

[1] Anderson, P.M. and Fouad, A.A, "Power System Control and Stability", The IOWA State Univ. Press, Ames, 1977.

[2] Michel, A.N., "Stability Analysis of Interconnected Systems", SIAM J. of Control, vol.-12, No.3, August 1974.

[3] Michel, A.N. and Miller, R.K., " Qualitative Analysis of Large Scale Dynamic System", Academic Press, New York 1977.

[4] Vidyasagar, M., "Input-Output Analysis of Large Scale Interconnected Systems".

[5] Vidyasagar, M., and Desoer, C.A., "Feedback Systems : Input-Output Properties", Springer-Verlag, Berline Heidelberg, New York, 1981.

[6] Willems, J.C., "Stability, Instability, Invertibility and Causality", SIAM J. Controlm 7(4), p.p. 645-671, 1969.

[7] Willems, J.C., "The Analysis of Feedback Systems", MIT Press, Cambridge, MA, 1971.

[8] Zames, G, "On the Input-Output Stability of Time-Varying Non-linear Feedback Systems – Conditions Derived Using Concepts of Loop Gain, Conicity and Positivity", IEEE Trans. Auto-Control, A.C.-11(2), pp. 228-238, 1966.

Forecasting Of Monthly Peak Electric Load Demand Using An Artificial Neural Network

S.G. Bhirud[1] and T. K. Basu[2]

[1]Department of Computer Technology, Veermata Jijabai Technological Institute, Mumbai- 400 019, India
(e-mail: sgbhirud@yahoo.com)

[2] Department of Electrical Engineering, Indian Institute of Technology, Kharagpur- 721 302, India
(e-mail: tkb@ee.iitkgp.ernet.in)

Abstract

This paper presents an artificial neural network (ANN) approach to monthly peak electric load forecasting. The ANN is used to learn the relationship amongst past, current and future loads. In order to provide the forecast load, the ANN interpolates the load data in a training data set. A multilayer neural network with a back-propagation algorithm to forecast the monthly peak load of the Tata Power Company, Mumbai has been used for different combinations of input and hidden variables. Eight different ANN models are proposed in which the input patterns are made up of the immediate past two to twelve months' peak load and the outputs have been considered for 1-step, 2-step or 12-step ahead forecast. The proposed ANN models have been applied to historical load for five years. Forecast results have been compared with the actual data for one year, for all the cases.

Index Terms--Load Forecasting, Neural Network

INTRODUCTION

One of the primary tasks for a system engineer in an integrated power system is to accurately predict load requirements at all times. For on-line control of an integrated system, a close tracking of the system load by system generation is a basic requirement. For economy of operation this must be accomplished over a broad spectrum of time intervals. While for short range of seconds or even minutes, the automatic generation function involving economic dispatch is used to ensure the matching of the load with economic allocation along the committed generation sources, the security of supply still depends on the availability of hot and cold reserves, which in turn, depends on the maintenance schedule and total load demand at any time [1-5]. The time range ahead of which the forecast is required has to be viewed from the standpoint of the functional areas of planning, operation and management. The time horizons commonly used by power system organization are

Short range forecasting (a few minutes to a few hours)
Medium range forecasting (one week to a few months)
Long range forecasting (a few months to a few years)

Short range forecasting deals with the continuous tracking of load and is aimed at on line dynamic voltage control, load flow studies to detect dangerous operating conditions and to analyze system contingencies (security checks), load dispatch for optimal allocation of generation and standby, exchange of power. Medium range forecasting are meant for preparation of maintenance schedule of unit auxiliaries and peaking stations and maintaining security constraints, the prediction of average hourly power demand of a day in a week helps (apart from maintaining security constraints) in minimizing the operation cost, in a deficient system, proper planning of load shedding can be maintained with such forecasts and system peaks can be reduced [6]. Long range forecasting concerns with general expansion planning (30 years or more) [7], transmission and distribution planning (8 to 15 years), strategy for energy conservation policy, financial planning, energy exchange policies between organizations, planning for peaking capacity plant, forecast for long term energy consumption (GWh), maintenance of major power plants

Various techniques for power system load forecasting have been proposed in the last few decades. Statistical techniques based on Box-Jenkins models, exponential smoothing, multiple regression, adaptive and weather models, state estimation, and Kalman filtering have been

proposed and applied with reasonable success for load forecasting [8-14]. The general problem with the statistical methods based on time-series analysis has their relative inaccuracy and numerical instability [15]. Statistical methods, furthermore, fail to provide accuracy when applied to longer-term forecasting.

In recent years, considerable attention has been given to developing electricity demand forecast models based on ANNs and expert systems [15-19]. ANNs have been successfully applied in electric load forecasting by many authors who have reported higher accuracy compared with other methods. However, applications have been limited to 1-hour to 24-hour ahead short-term load forecasting. Although short-term load forecasting is very useful in deciding system economic dispatch, spinning reserve and unit commitment, it does not provide any information on seasonal load variation and monthly energy use or peak demand (MW). These are extremely important from a utility's point of view when deciding monthly fuel requirement, scheduling maintenance of units, and system expansion planning.

In this paper a novel method employing ANN models have been suggested and implemented to forecast monthly peak load for various length of penetration. The model structures have been optimized by varying the number of variables in the hidden layer in each case of input output sets. The models are applied to the load demand data of Tata Power Company, Mumbai to forecast monthly peak load for the year 1996 using historical load data from 1991 to 1995.

THE ARTIFICIAL NEURAL NETWORK

The ANN proposed here is constructed with one input layer, one hidden layer and an output layer. For each neuron j in the hidden layer and neuron k in the output layer, the net inputs are given by

$$net_j = \sum_{i=1}^{NI} W_{ji} O_i \qquad j = 1, \Lambda\ , NJ \tag{1}$$

and

$$net_k = \sum_{j=1}^{NJ} W_{kj} O_j \qquad k = 1, \Lambda\ , NK \tag{2}$$

respectively.

The neuron outputs are given by

$$O_i = net_i \tag{3}$$

$$O_j = \frac{1}{1+e^{-(net_j+\theta_j)}} = f_j(net_j, \theta_j) \tag{4}$$

$$O_k = \frac{1}{1+e^{-(net_k+\theta_k)}} = f_k(net_k, \theta_k) \tag{5}$$

where net_i is the input signal from the external sources to node i in the input layer.

Let the connection weights W_{ji} and W_{kj} be updated after each presentation. They are changed after NQ input/output patterns (pairs) have been presented. Then for a presentation p, the sum of squared errors to be minimized is given by

$$E_p = \sum_{q=1}^{NQ} \sum_{k=1}^{NK} (t_{pqk} - O_{pqk})^2 \tag{6}$$

where t_{pqk} and O_{pqk} are the target output value and computed output value at output node k for the q^{th} input/output pair in presentation p, respectively.

By minimizing the error E_p using the technique of gradient descent, the connection weights between hidden unit j and output unit k can be updated [20].

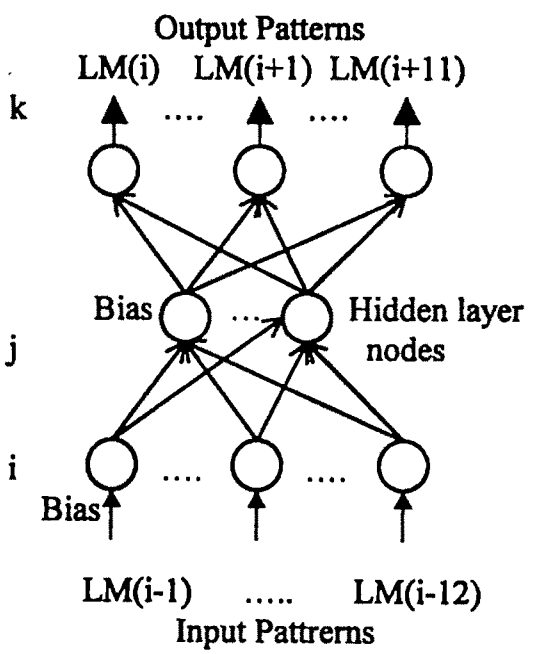

Fig. 1. Generalised diagram of ANN for eight cases

THE PROPOSED ANN MODELS

In the present study eight different ANN models have been considered and optimised and the forecast have been made for different ranges i.e. one month, two months and twelve months using different combinations of inputs and for each case the number of variables in the hidden layer has been varied from one to fourteen depending on the models and the optimum number of hidden nodes has been obtained.

$LM(i)$ denotes the monthly peak load of the i^{th} month. Forecast for $LM(i)$ to $LM(i+1)$, .. , $LM(i+11)$ for some cases has been made by using data at the input nodes with various combinations of $LM(i-1)$, $LM(i-2)$, ... , $LM(i-12)$. Table. I shows eight different cases of such combinations of input nodes, output nodes and hidden nodes. Similar combinations of input nodes have been tried for short range forecasting of hourly load by Barkirtzis *et al.* [21]. Fig. 1 shows the generalised diagram for the eight cases.

RESULTS AND DISCUSSION

For each case of the ANN models the monthly peak data from 1991 to 1995 have been used to train the models and forecast have been made and compared for the twelve month's peak loads of year 1996 (starting from January to December). Fig. 2 shows the actual and forecast load for the monthly peak demands for the eight different ANN models. The mean absolute percentage error (MAPE) and the root mean square error (RMSE) defined by the following equations are used to evaluate the performance of the forecast.

$$\text{MAPE} = \frac{1}{Nd}\sum_{i=1}^{Nd}\frac{|A_i - P_i|}{A_i}\times 100\% \qquad (7)$$

and

$$\text{RMSE} = \sqrt{\frac{\sum_{i=1}^{Nd}(A_i - P_i)^2}{Nd}} \qquad (8)$$

where, Nd : the number of predicted months,

A_i : actual peak load on i^{th} month,

P_i : predicted peak load on i^{th} month.

Table. II gives the details of the errors for all the cases. It appears from Table. II that case-7 gives minimum MAPE (1.0316%) and RMSE (22.6296MW). It shows that for short term forecast of lead time of one month, previous three month's data and the i^{th} month load of the previous year are sufficient by considering only three hidden nodes. Increase in the number of hidden nodes or the input nodes does not give a better forecast. In all the cases it has also been observed that the error is distributed.

CONCLUSION

In this paper ANN models with different combinations of inputs and outputs have been exploited for forecasting the monthly peak demand pattern of power system load using the previous five years load data for training. The results show that the forecasts match well with the actual demand in all the eight cases and the best result is obtained in case-7

ACKNOWLEDGMENT

The authors wish to thank the Tata Electric Power Company, Mumbai for their assistance in the collection of data. They also wish to thank the Director, I.I.T., Kharagpur and Principal, Veermata Jijabai Technological Institute, Mumbai for providing the necessary facilities.

REFERENCES

[1] J. S. Aiyar and S. C. Buch, "Power System Management with special reference to load dispatch control and protection," *Indian Journal of Power and River Valley Development, Power System Management, Annual Review,* 1985.

[2] K. Baden and P. Laja, "Computer Aided Short Term Operation Planning of Power Systems," *Brown Bovery Rev.,* Vol. 1, No. 2, pp. 25-28, 1983.

[3] A. B. Barker, "Load Forecasting for Scheduling Generation on a Large Interconnected System, in Comparative Models for Electrical Load Forecasting," *ed. D. W. Bunn and E. D. Farmer,* 1985.

[4] Discussion Report, "Prediction day-to-day Power Demand," *Electrical Times,* Vol. 5, No. 201 54 015, pp. 793-796, 1968.

[5] W. D. Liang and M. J. Metcalfe, "Computer assisted demand forecasting for power system control," *CEGB Res. (GB),* No. 18, pp. 28-36, 1986.

[6] S. Kaltio, "A method of time series analysis," *seminar on the medium and long term prospect of electric power industry, London, United Nations Economic Commission for Europe, Committee on Power, UNIB2,* 1981..

[7] P. J. Brown, "The synthesis of forecasting models in decision analysis," *Birkhauser, Basel,* 1978.

[8] G. E. Box and G. M. Jenkins, "*Time Series Analysis - Forecasting And Control,*" Holden - Day, San Francisco CA, 1976.

[9] W. R. Chiristiaanse, "Short-term load forecasting using exponential smoothing," *IEEE Trans.* PAS-90, pp. 900-910, 1971.

[10] P. Thompson, "Weather sensitive demand and energy analysis on a large geographical diverse power system: application to short-term hourly electric demand forecasting," *IEEE Trans.* PAS-95, pp. 384-393, 1976.

[11] P. Gupta and K. Yamada, "Adaptive short-term forecasting of hourly loads using weather information," *IEEE Trans.* PAS- 91, pp. 2085-2094, 1972.

[12] J. Toyoda and M. S. Chen, "An application of state estimation to short-term load forecasting, part 1 and 2," *IEEE Trans.* PAS-89, pp. 1678-1688, 1970.

[13] G. D. Frissari, S. E. Widergren and P. D. Yehsakul, "On- line load forecasting for energy control center application," *IEEE Trans.* PAS-101, pp. 71-78, 1982.

[14] T. K. Bhattacharya and T. K. Basu, "Medium range forecasting of power system load using modified Kalman filter and Walsh Transform", *Int. J. Electr. Power and Energy Syst.*, Vol. 15; No. 2, pp. 109-115, 1993.

[15] D. C. Park, M. A. El-Sharkawi, and R. J. Marks II, "Electric load forecasting using an artificial neural network," *IEEE Trans.* PAS- 6, No. 2, pp. 442-449, 1991.

[16] K. K. Ho, Y. Hsu, C. Liang and T. Lu, "Short-term load forecasting of Taiwan power system using a knowledge based expert system," *IEEE Trans.* PAS- 5, No. 4, pp. 1214-1221, 1990.

[17] S. Rahman and O. Hazim, "A generalized knowledge based short-term load forecasting technique," *IEEE Trans.* PAS-8, No. 2, pp. 508-514, 1993.

[18] C. N. Lu, H. T. Wu and S. Vemuri, "Neural network based short-term load forecasting technique," *IEEE Trans.* PAS- 8, No. 1, pp. 336-342, 1993.

[19] Sued. M. Islam, S. M. Alawi and K. A. Ellithy, "Forecasting monthly electric load and energy for a fast growing utility using an artificial neural network," *EPSR*, No. 34, pp. 1-9, 1995.

[20] Kun-Long Ho and Yuan-Yih-Hsu, "Short Term Load Forecasting Using A Multilayer Neural Network with an Adaptive Learning Algorithm," *IEEE Trans.* Power System. Vol. 7, No. 1, pp. 141-149, 1992.

[21] A. G. Bakirtzis, V. Petridis, S. J. Kiartzis and M. C. Alexiadis, "A Neural Network Short Term Load Forecasting Model for The Greek Power System," *IEEE Trans.* Power System. Vol. 11, No. 2, pp. 858-863, 1995.G. Eason, B. Noble, and I. N. Sneddon, "On certain integrals of Lipschitz-Hankel type involving products of Bessel functions," *Phil. Trans. Roy. Soc.* London, vol. A247, pp. 529-551, Apr. 1955.

TABLE I
DEFINITIONS OF ANN INPUTS AND OUTPUT

Case 1 : ANN input nodes = 12, hidden nodes = 8, output nodes = 12			
Inputs	Description	Output	Description
1-12	{LM(i-1), LM(i-2), ... LM(i-12)}	12	{LM(i),... M(i+11)}
Case 2 : ANN input nodes = 2, hidden nodes = 3, output nodes = 1			
Inputs	Description	Output	Description
1-2	{LM(i-1), LM(i-2)}	1	LM(i)
Case 3 : ANN input nodes = 3, hidden nodes = 4, output nodes = 1			
Inputs	Description	Output	Description
1-3	{LM(i-1), LM(i-2), LM(i-3)}	1	LM(i)
Case 4 : ANN input nodes = 4, hidden nodes = 3, output nodes = 1			
Inputs	Description	Output	Description
1-4	{LM(i-1), LM(i-2), LM(i-3), LM(i-4)}	1	LM(i)
Case5 : ANN input nodes = 3, hidden nodes = 4, output nodes =2			
Inputs	Description	Output	Description
1-3	{LM(i-1), LM(i-2), LM(i-3)}	2	{LM(i), LM(i+1)}
Case6 : ANN input nodes = 4, hidden nodes = 4, output nodes = 2			
Inputs	Description	Output	Description
1-4	{LM(i-1), LM(i-2), LM(i-3), LM(i-4)}	2	{LM(i), LM(i+1)}
Case7 : ANN input nodes = 4, hidden nodes = 3, output nodes = 1			
Inputs	Description	Output	Description
1-4	{LM(i-1), LM(i-2), LM(i-3), LM(i-12)}	1	LM(i)
Case8 : ANN input nodes = 5, hidden nodes = 5, output nodes = 1			
Inputs	Description	Output	Description
1-5	{LM(i-1), LM(i-2), LM(i-3), LM(i-4), LM(i-12)}	1	LM(i)

TABLE II
ERROR COMPARISION IN PEAK LOAD FORECASTING

Month in the Year 1996	Actual load (MW)	Case1		Case2		Case3		Case4		Case5		Case6		Case7		Case8	
		ANN forecast (MW)	MAPE %	ANN forecast (MW)	MAPE %	ANN forecast (MW)	MAPE %	ANN forecast (MW)	MAPE %	ANN forecast (MW)	MAPE %	ANN forecast (MW)	MAPE %	ANN forecast (MW)	MAPE %	ANN forecast (MW)	MAPE %
1	1631.4	1600.8	1.8752	1648.3	1.0388	1634.1	0.1651	1629.9	0.0891	1625.8	0.3435	1646.5	0.9239	1629.3	0.1282	1640.5	0.5597
2	1694.2	1648.5	3.1668	1651.6	2.5164	1654.6	2.3361	1649.8	2.6201	1644.0	2.9629	1708.9	0.8579	1691.8	0.1422	1667.8	1.5573
3	1729.1	1737.1	0.4604	1708.0	1.2224	1715.6	0.7831	1716.8	0.7116	1703.9	1.4589	1706.1	1.3310	1748.4	1.1159	1743.7	0.8439
4	1785.1	1763.0	1.2394	1729.9	3.0934	1744.3	2.2843	1742.3	2.3973	1738.4	2.6179	1733.6	2.8832	1787.6	0.1390	1779.8	0.2994
5	1748.7	1796.3	2.7204	1774.1	1.4551	1778.3	1.6931	1777.3	1.6333	1780.6	1.8229	1786.6	2.1692	1783.5	1.9879	1812.7	3.6591
6	1829.5	1831.2	0.0930	1734.8	5.1765	1744.8	4.6306	1742.3	4.7639	1736.8	5.1686	1739.5	4.9170	1799.6	1.6344	1803.1	1.4442
7	1804.3	1794.9	0.5236	1808.8	0.2471	1798.7	0.3122	1808.5	0.2110	1805.0	0.0387	1803.1	0.0691	1808.0	0.2025	1798.4	0.3273
8	1784.0	1803.9	1.0671	1778.1	0.3333	1786.5	0.1348	1782.9	0.0611	1789.7	0.3176	1789.3	0.2952	1797.7	0.7665	1785.0	0.0550
9	1752.5	1782.0	1.6812	1763.6	0.6324	1757.3	0.2746	1759.4	0.3939	1747.8	0.2693	1754.5	0.1134	1766.3	0.7869	1777.3	1.4163
10	1726.4	1816.9	5.2416	1738.3	0.6922	1735.5	0.5293	1739.6	0.7627	1722.3	0.2375	1728.1	0.0963	1745.9	1.1299	1760.9	1.9973
11	1650.4	1723.1	4.4076	1719.3	4.1742	1717.3	4.0546	1721.0	4.2805	1702.4	3.1490	1707.8	3.4781	1698.9	2.9376	1719.8	4.2038
12	1638.5	1645.7	0.4391	1654.9	1.0031	1661.0	1.3712	1654.1	0.9519	1694.2	3.3969	1686.0	2.9020	1661.6	1.4084	1684.3	2.7923
MAPE		1.9096		1.7987		1.5477		1.5730		1.8103		1.6705		1.0316		1.5963	

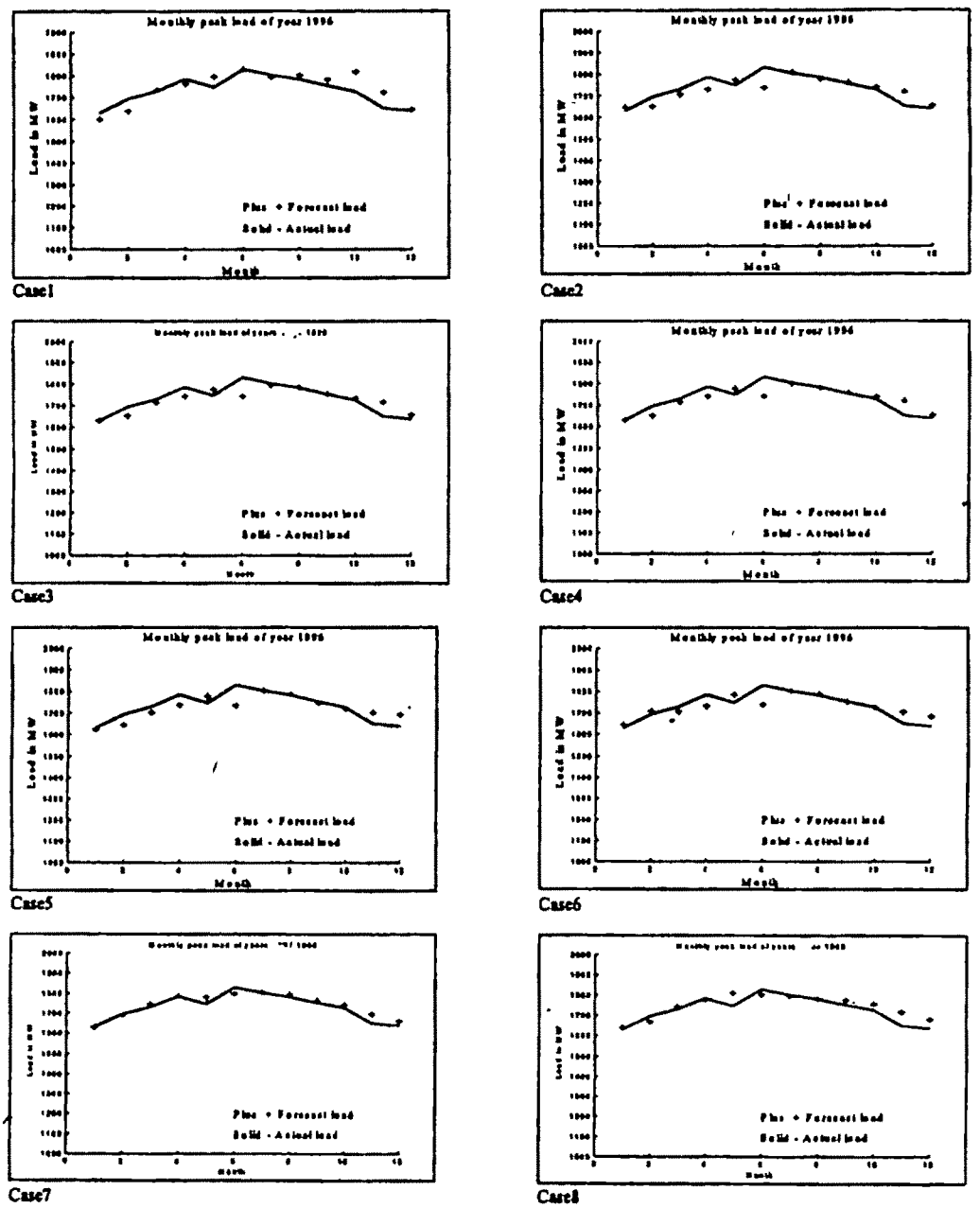

Fig. 2. Actual and forecast load for monthly peak demand for the year 1996 for the eight different ANN models (months 1 to 12 correspond to January and December respectively)

Optimum Operating Condition of A Series Capacitor Compensated EHV Transmission Line for Its Enhanced Efficiency

S. Sengupta* , Utpal Maji #, Netai Pal •, A. K. Mukhopadhyay •

* Department of Applied Physics 92, A. P. C. Road, Kolkata-700 009

Stock Holding Corporation of India Ltd, 125/1, Park Street Kolkata-700 017

• Asansol Engineering College Kanyapur, Satellite Township, Asansol-713304

Abstract

Series capacitor compensation of EHV transmission lines is very useful in enhancing the efficient operation of a transmission line which substantially increases the loadability of EHV transmission system and offers an economic means of increasing the power transfer. But there are certain practical limitations in enhancing the power transfer through such an EHV transmission line. In this paper, a study of the performance of a series capacitor compensated EHV transmission line has been made for its efficient operation. Theoretical developments have been presented first and then the results of computer simulation have been provided. From the results, some specific operating conditions have been obtained for enhancing the efficiency of the capacitor compensated transmission line.

Key words: series compensation, transmission efficiency

INTRODUCTION

The structure of power systems is directly related to the industrial and urban developments. Generating sources are normally away from the main load centres and a medium and long EHV lines carry power to the load. Frequent imbalances in generation and demand also need bulk power transfer from one place to the other preferably through EHV lines. Series compensation is one of the powerful tools to improve the performance of EHV transmission lines although it may invite a number of problems.

Researches in the field of series capacitor compensation have been reported since long [1], [2]. Literature survey reveals that the optimum location of the series capacitor is at the centre of the line for maximum loadability [3], [6]. Effect of series compensation on the performance of power transmission has been reported in the references [3], [6]. Indulkar et. al. [4], [5] investigated the series capacitor compensation regarding enhancement of loadability and power transfer capability of reactive power constrained lines.

In this paper, performance of a series capacitor compensated transmission line has been investigated theoretically. From the computer simulations, some specific conditions have been evolved for efficient operation of the transmission line.

THEORETICAL BACKGROUND

The schematics diagram of a long transmission line have been shown in Fig. 1 in which the following nomenclature has been used:

z = series impedance / unit length / phase
  = r + jwL
y = shunt admittance / unit length / phase
  = g + jwC
r = resistance / unit length / phase.
g = shunt conductance / unit length / phase.
L = inductance / unit length / phase.
C = capacitance / unit length / phase to neutral.
l = transmission line length
Z = l.z = total series impedance / phase.
Y = l.y = total shunt admittance / phase to neutral.
Subscript 's' stands for sending end quantity and `r ' for receiving - end quantity.

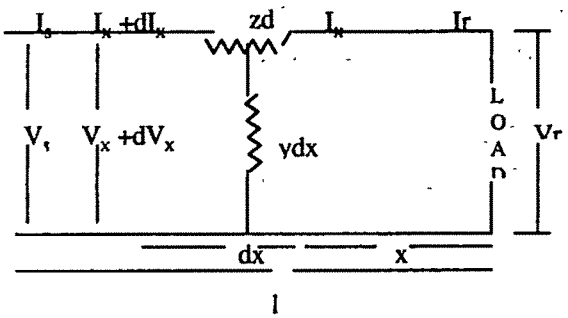

Fig 1: Schematic diagram of a long transmission line

The transmission line equation can be written as,

$$\begin{bmatrix} V_s \\ I_s \end{bmatrix} = \begin{bmatrix} A & B \\ C & D \end{bmatrix} \begin{bmatrix} V_r \\ I_r \end{bmatrix} \quad (1)$$

Where,

$$A = D = 1 + YZ/2 \quad (2)$$

$$B = Z(1 + YZ/6) \quad (3)$$

$$C = Y(1 + YZ/6) \quad (4)$$

and $A = |A|\angle\alpha$, $B = |B|\angle\beta$, $D = |D|\angle\alpha$ (5)

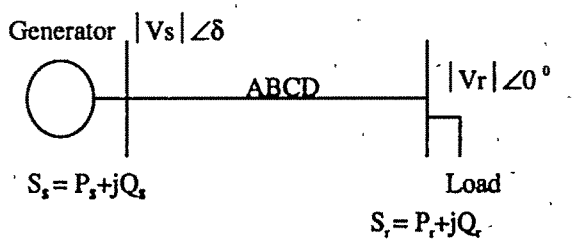

Fig. 2 Schematic diagram of a Two Bus System

Power flowing through the uncompensated line from sending end to receiving end as shown in Fig. 2 can be written as

$$P_r = \frac{|Vs||Vr|}{|B|}\cos(\beta - \delta) - \frac{|A|}{|B|}|Vr|^2\cos(\beta - \alpha) \quad (6)$$

$$Q_r = \frac{|Vs||Vr|}{|B|}\sin(\beta - \delta) - \frac{|A|}{|B|}|Vr|^2\sin(\beta - \alpha) \quad (7)$$

where receiving end voltage $V_r = |V_r|\angle 0^0$ is considered as reference and sending end voltage
$V_s = |V_s|\angle\delta$, δ being the frequency angle.
It is seen from (6) that the receiving end power P_r will be maximum at $\delta = \beta$ such that

$$P_{rm} = \frac{|Vs|^2}{|A||B|\sqrt{[2\{1 + \cos(\Phi - \beta + \alpha)\}]}} - \frac{|Vs|^2\cos(\beta - \alpha)}{2|A||B|[1 + \cos(\Phi - \beta + \alpha)]} \quad (8)$$

The corresponding Q_{rm} (at P_{rm}) is obtained from (7) as

$$Q_{rm} = -\frac{|Vs|^2\sin(\beta - \alpha)}{2|A||B|[1 + \cos(\Phi - \beta + \alpha)]} \quad (9)$$

Thus the load must draw Q_{rm} amount of leading MVAR in order to receive the maximum real power.
The values of A B C D constants in terms of line parameters can be derived as

$$A = D = a + jb \quad (10)$$

$$\text{where, } a = \frac{2 + GR - B_1X_L}{2} \quad (11)$$

$$\text{and} \quad b = \frac{B_1 R + G X_L}{2} \tag{12}$$

where, G = total shunt conductance / phase
and B_1 = total shunt suceptance / phase

$$B = p + jq \tag{13}$$

$$\text{where } p = \frac{6R + G(R^2 - X_L^2) - 2B_1 R X_L}{6} \tag{14}$$

$$\text{and} \quad q = \frac{6X_L + B_1(R^2 - X_L^2) - 2GRX_L}{6} \tag{15}$$

If a series capacitor having capacitive reactance X_C is inserted in the line, the net series impedance becomes,

$$Z = R + j(X_L - X_C)$$

Then modified A B C D constants for a capacitor compensated transmission line change which can be obtained by replacing X_L by $(X_L - X_C)$ in (11), (12), (14), (15) and then substituting in (10) and (13) to yield as follows,

$$A_{mod} = D_{mod} = a_{mod} + jb_{mod} \tag{16}$$

$$\text{where, } a_{mod} = \frac{2 + GR - B_1(X_L - X_C)}{2} \tag{17}$$

$$\text{and } b_{mod} = \frac{B_1 R + G(X_L - X_C)}{2} \tag{18}$$

$$B_{mod} = p_{mod} + j\, q_{mod} \tag{19}$$

where, p_{mod} =

$$\frac{6R + G[R^2 - (X_L - X_C)^2] - 2B_1 R(X_L - X_C)}{6} \tag{20}$$

and q_{mod} =

$$\frac{6(X_L - X_C) + B_1[R^2 - (X_L - X_C)^2] + 2GR(X_L - X_C)}{6} \tag{21}$$

By substituting the modified expressions for A, B, C, D from (16) to (21) for a series capacitor compensated transmission line, modified values of real and reactive powers can be obtained.

COMPUTER SIMULATION

Specifications of the Transmission Line used for Simulation

Specifications of the transmission line considered for simulation in this paper are as follows:
Length of the transmission line , l = 500 KM, Sending end voltage, Vs = 136.25 KV, Receiving end voltage, Vr = 220 KV, Frequency of supply, f = 50 Hz, The line parameters for this line:R = 0.074 ohm / KM / phase, L = 0.001212 H / KM / phase, C = 0.009577 microfarad / KM / phase, G = 0, Load angle (δ) = 22.3°

Program for Calculations

The real power and reactive power have been calculated with inserted series capacitor using C compiler. The values of maximum real power and reactive power have also been calculated for various conditions.

Discussions on Characteristics Obtained

Fig.3 shows the variation of P_r and Q_r with increase of s ($=X_L / X_C$, degree of compensation) wherein it is seen that the rate of increase of Q_r is much higher than P_r imposing a limitation on compensation. Fig. 4 shows maximum real and reactive power flow through an uncompensated transmission line whereas Figs. 5 to 9 show those for a compensated transmission line for different degree of compensation. From these it is seen that the magnitude of maximum values of real and reactive powers increase in a compensated line. From Figs. 5 to 9 it is seen that for s = 0.4 to 0.7, P_{rm} and Q_{rm} start increasing beyond a load power factor of 0.7 but rate of rise decreasing with of ` s ' whereas for s = 0.8, P_{rm} and Q_{rm} remain almost constant over a wide power factor range. Figs. 10 to 14 show variation of P_{rm} and Q_{rm} with s for various values of load power factor. A close inspection of the characteristics show that range of variation of P_{rm} remains almost the same over the power factor range considered whereas the range of variation of Q_{rm} becomes narrower as the load power factor approaches unity. In all the characteristics, symbol γ represents real power and symbol ν represents reactive power.

CONCLUSION

From the results obtained for a particular transmission line, the following conclusions can be drawn for enhancing the efficiency of a series capacitor compensated transmission line:

Degree of compensation should be chosen in such a way that Q_r is not predominant in the line. For a particular line, there will be a value of ` s ' at which P_{rm} and Q_{rm} remain almost constant over a wide power factor range. Range of variation of P_{rm} remains almost the same over a specific power factor range whereas the range of variation of Q_{rm} becomes narrower as the load power factor approaches unity.

Accordingly on-line control of ` s ' and load power factor can be implemented to increase the efficient operation of a series capacitor compensated line.

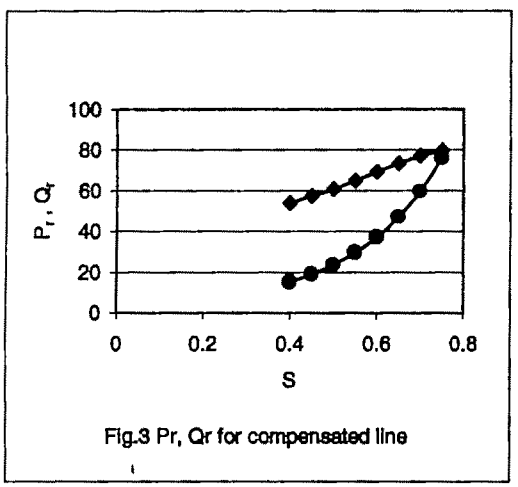

Fig.3 Pr, Qr for compensated line

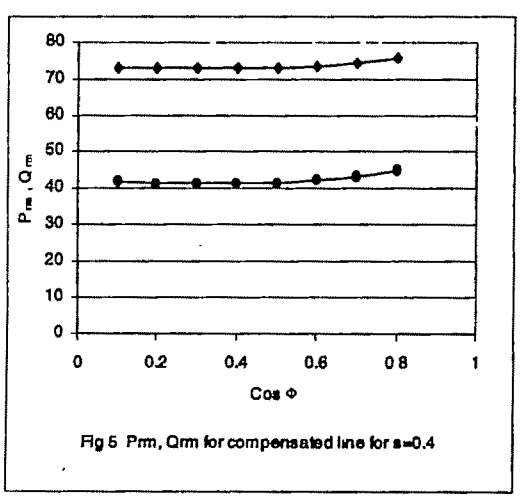

Fig 5 Prm, Qrm for compensated line for s=0.4

REFERENCES

[1] Breuer G.D., Rustebakke, H. M., Gibley, R. A. and Simmons, H. O. " Use of series capacitor to obtain maximum EHV transmission capacity" Trans. AIEE, Nov. 1964, Pp. 1090

[2] Purakayastha, G. P. and Desikachar, K. V. "Determination of optimum value of the series compensation of a transmission line and its experimantal verification" Jour. IEI, Sept. 1996.

[3] Ashok Kumar, B. S. et al " Effectiveness of series capacitor in long distance transmission lines " IEEE Trans. On PAS, Vol. PAS-80, Pp.941, 1970.

[4] Indulkar C.S. and Viswanathan, B. " Series compensation in EHV transmission lines" JIE (I), Vol. 65, pt-EL-2 , 1984, Pp. 85 – 88.

[5] Indulkar C.S., Viswanathan, B. and Venkata S. S. " Reactive power constrained loadibility limits of series capacitor compensated EHV transmission lines" IEEE Trans. On Power Sys., vol. PWRS-2, no.3, Aug. 1984, Pp585 –91.

[6] Bellarmine G.T. and Srikrishna K. " Optimum compensation with series capacitor at centre of a transmission line" JIE (I), Vol. 60, pt-EL-2 , June 1980.

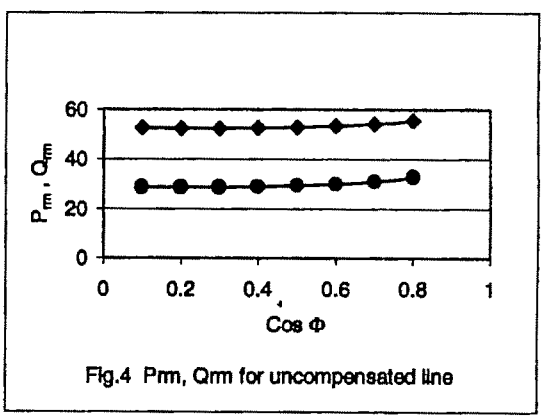

Fig.4 Prm, Qrm for uncompensated line

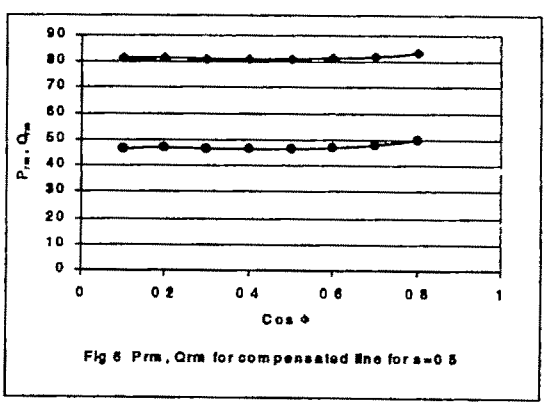

Fig 6 Prm, Qrm for compensated line for s=0.8

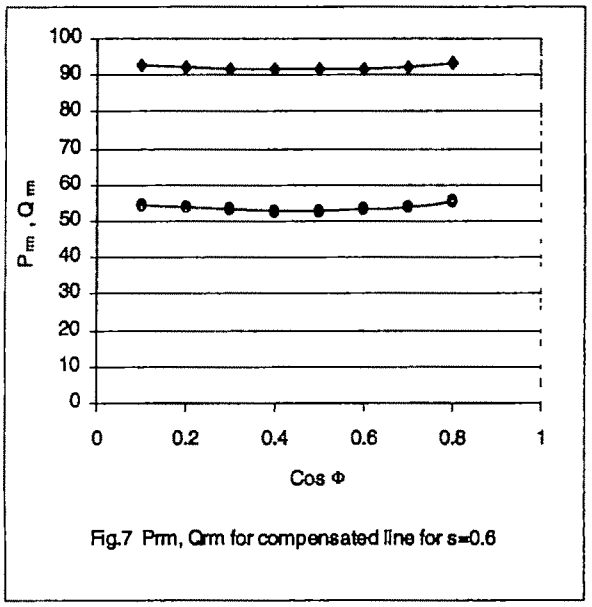

Fig.7 Prm, Qrm for compensated line for s=0.6

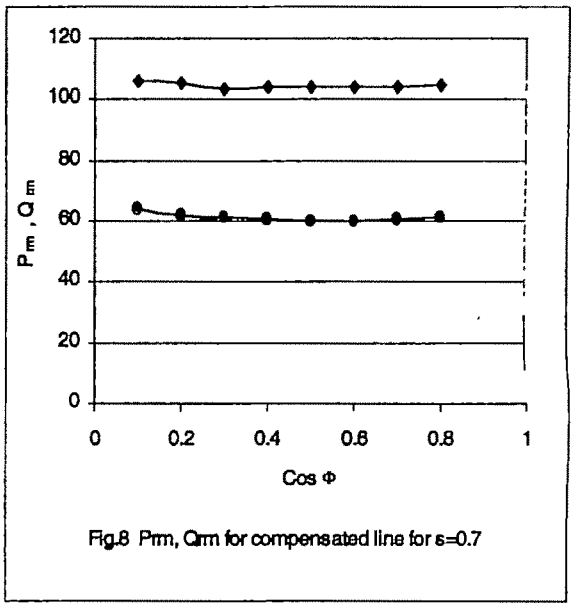

Fig.8 Prm, Qrm for compensated line for s=0.7

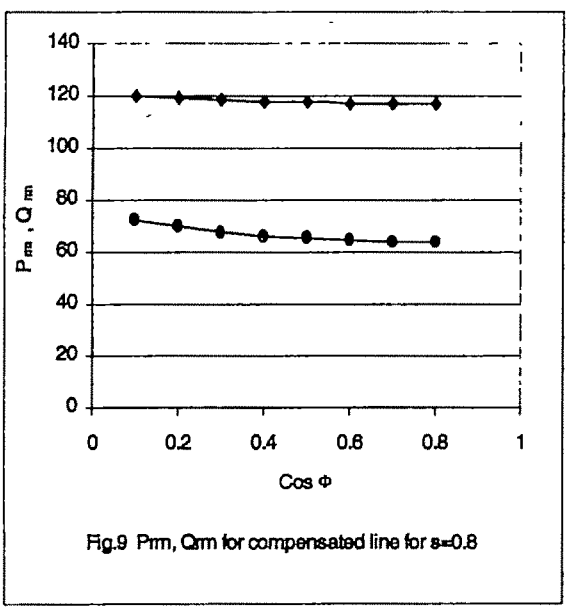

Fig.9 Prm, Qrm for compensated line for s=0.8

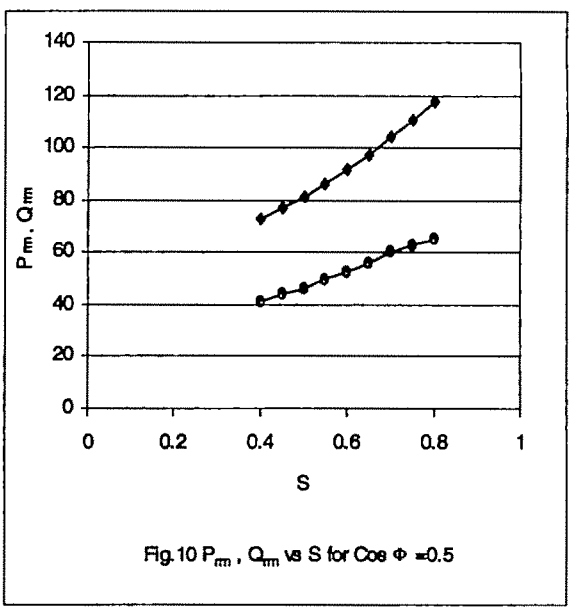

Fig.10 P_m , Q_m vs S for Cos Φ =0.5

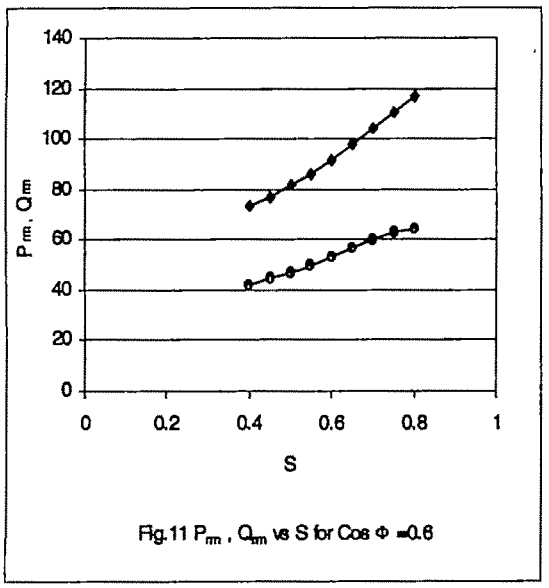

Fig.11 P_m , Q_m vs S for Cos Φ =0.6

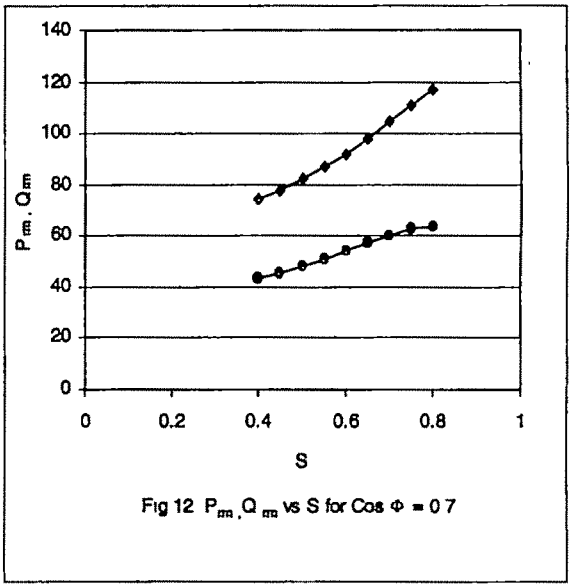

Fig 12 P_m , Q_m vs S for Cos Φ = 0 7

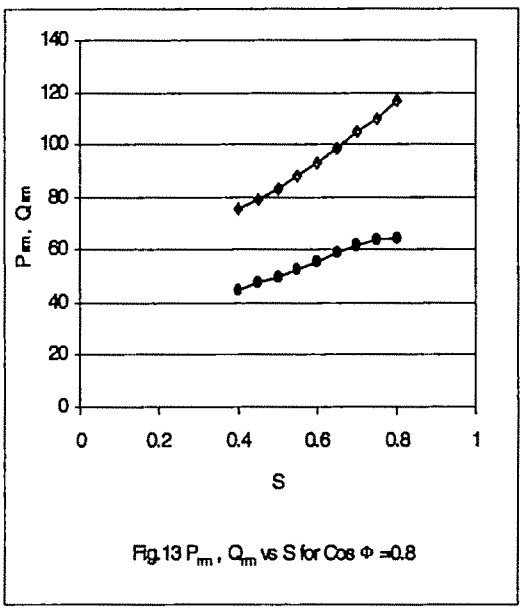

Fig.13 P_m , Q_m vs S for Cos Φ =0.8

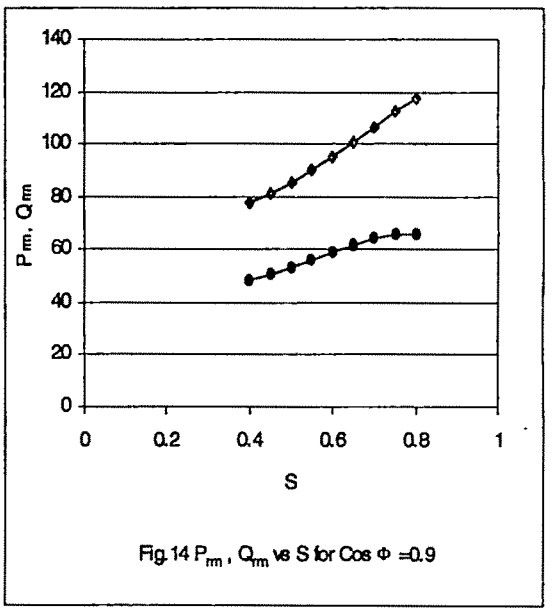

Fig.14 P_m , Q_m vs S for Cos Φ =0.9

High Power High Performance Industrial AC Drives and Their Control

Ajit K. Chattopadhyay

Electrical Engineering Department, Bengal Engineering College (D.U.), Howrah-711 103, India
E-mail: akcee@hotmail.com

Abstract

With the rapid developments of power electronic technologies, microprocessor/digital signal processor based control and estimation techniques and introduction of high power semi-conductors, high power high performance ac drives using either induction or synchronous motors with inverters or cycloconverters have become viable alternatives to the earlier dc drives for wide industrial applications. In this paper, a brief review on the state-of-the-art control technologies for such drives which include vector control and the direct torque control methods is presented

Keywords: *Induction Motor Drives, Synchronous Motor Drives, Vector Control, Direct Torque Control, High Performance Drives, High Power Converters , Field Orientation Control ,inverters, cycloconverters*

I. INTRODUCTION

The power ratings of large industrial drives range between few hundred kilowatts to a few tens of megawatts. The upper limit is decided by the requirements of the applications rather than by the technology of the converters and machines. The available speed range lies from 10 rpm for low speed machines (e.g. Cement mills) 1500/3000 rpm for normal speed drives to even 18000 rpm for very high speed drives (compressors). The limits for the dc motors such as cost, size, commutator problems and inability to operate satisfactorily in a dirty and explosive environment have called for ac motor drives for high power applications. Major technical breakthroughs have occurred in both the power conversion and in control areas of variable-voltage variable-frequency (VVVF) ac drives to meet the exacting requirements of ac drives using direct ac/ac cycloconverters or ac/dc/ac link inverters which feed either induction or synchronous motors.. The machine may be excited by a voltage source or a current source. Synchronous motor drives have the advantages over the induction motor drives in that, with separate field excitation, these can be operated at any power factor--leading, lagging and unity. The operation near unity power factor reduces armature copper loss and permits inverter size reduction with simplicity of commutation with thyristors as switches. Further, a synchronous motor runs at a precisely set speed independent of load and voltage fluctuations unlike an induction motor.

Recent trends are to use PWM (Pulse Width Modulated) VSI (Voltage Source Inverters) or CSI (Current Source Inverter) with self-commutated devices like Power Transistors (for low power drives only), IGBTs (Insulated Gate Bipolar Transistors) ,GTOs (Gate Turn Off Thyristors) and IGCTs (Integrated Gate Commutated Thyristors) for efficient VVVF control with harmonic reduction. The development of new high power semiconductors such as 3.3/4.5 kV IGBTs and 4.5/5.5kV IGCTs with the introduction of *three* level topologies in contrast to earlier *two* level ones have led to an increased application of PWM controlled Voltage Source Converters (VSC) ranging from 0.5MVA to 10 MVA [1].CSI fed dives with simplified regeneration control and microcomputer controlled drives to implement novel concepts like *field orientation* or *vector control* with either inverter or cycloconverter -fed induction or synchronous motors by which dc machine-like performance can be obtained are now finding increasing acceptance in *high performance* industrial drives for applications such as steel mills, paper mills, servos, cement kilns and electric vehicles [2].The converters for these drives meeting the *high performance* requirements of such applications must

- Generate smoothly variable frequency and voltage
- produce nearly sinusoidal current waveforms throughout the operating range to avoid undesirable torque oscillations
- permit highly dynamic control both in motor and braking applications
- provide as nearly as possible equivalent performance to the dual converter-fed dc drives as regards cost, service reliability and harmonic effect on the system.

The technology is vast and the objective of this paper is to present a state-of-the-art review of these high power high performance industrial drives and their control technologies.

II. INDUCTION MOTOR DRIVES WITH SCALAR CONTROL

A. PWM VSI-Induction Motor Drive

For high power drives, the configuration of such a drive is invariably as shown in Fig. 1 with a line side PWM rectifier using either IGBTs or GTOs feeding a well regulated dc voltage with little ripple and at a high power factor to a load side PWM inverter also using IGBTs or

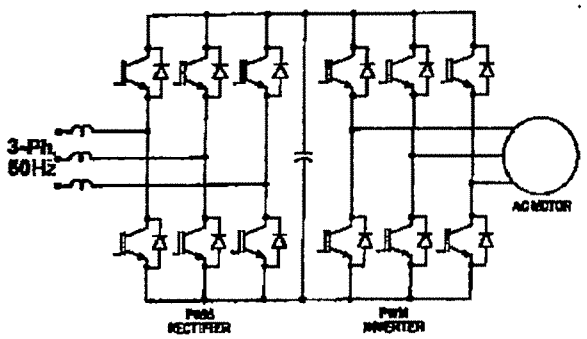

Fig. 1 PWM rectifier-PWM VSI inverter induction motor drive

GTOs. The classical flux regulation control scheme for an SCR-rectifier-inverter fed drive with simple *constant V/f ratio or scalar control* for the constant torque region with

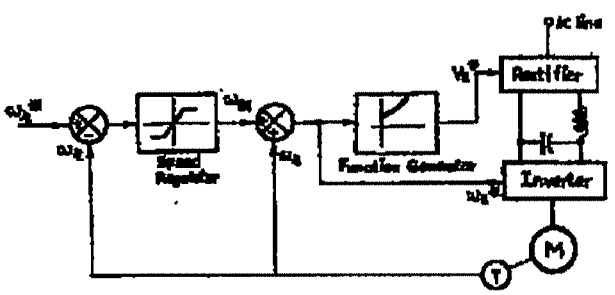

Fig. 2 Constant V/f or scalar control of a rectifier-inverter induction motor drive with slip regulation

slip regulation is shown in Fig 2 [3]. The slip frequency ω_{sl} which is proportional to torque is regulated by the speed loop error. The ω_{sl} signal is added to w_r to generate the inverter frequency ω_e. The voltage control signal V_c is generated from ω_e through a function generator so as to maintain the air-gap flux nearly constant. The drive accelerates with the clamped value of slip corresponding to the maximum torque and then settles down to a value as dictated by the load torque. If the commanded speed ω_r is reduced at steady state, the slip becomes negative and the drive system goes into the dynamic or regenerative braking mode. Instead of regulating the slip, it can be maintained constant and the speed loop error may control the dc link voltage. The variation of V/f ratio causes the variation of air-gap flux and correspondingly the developed torque is regulated. The open loop scalar control is popular in the industry when a small drift in speed and air-gap flux due to fluctuation are of no significance.

A simple and most common sinusoidal PWM method of *2-level* voltage control is shown in Fig.3 An isoseles triangle carrier is compared with the sine wave signal and the crossover points determine the points of switching. Except at low frequency range, the carrier is synchronized with the signal and an integral ratio (multiple of three) is maintained to improve harmonic content. The fundamental output voltage can be varied by variation of the modulation index (the ratio A_r/A_c). Various PWM techniques like

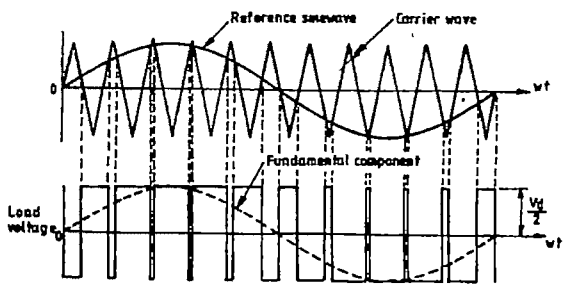

Fig.3 2-level sinusoidal pulse width modulation

selected harmonic elimination method, uniform sampling method, current controlled or regulated hysteresis PWM, space vector PWM etc have been developed which can be implemented with the help of microcomputers

B. Two/Three Level IGBT/GTO Inverter Drive

Fig 4 shows a *3-phase 3-level* PWM inverter (also known as Neutral Clamped Converter (NPC)) using IGBTs/GTO's In *two level* inverters the output voltages consist of pulses of either $+V_d/2$ or $-V_d/2$ whereas with a 3-level inverter these may be $+V_d/2$, 0 and $-V_d/2$. For high power high speed drives three level inverters have been preferred as they can be operated with twice the rated voltage without any series or parallel circuit and therefore with twice the rated power with significantly improved output voltage waveform when compared to a 2-level inverter. However,

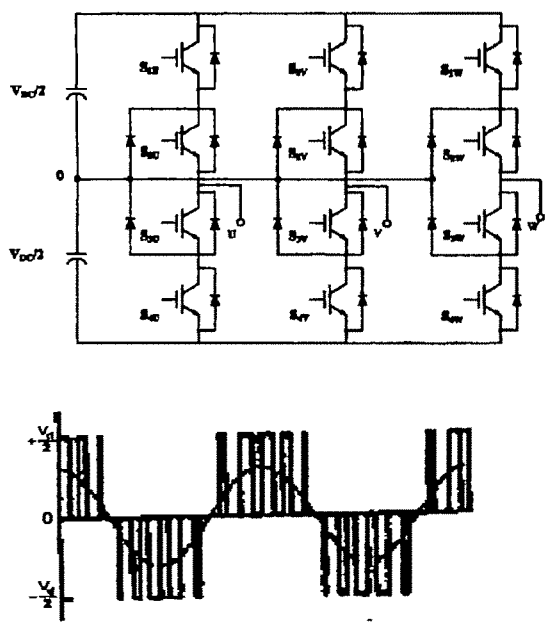

Fig. 4 3-level PWM inverter(a) circuit diagram, (b) output voltages

a 3-level inverter consists of 12 IGBTs/GTOs – 4 IGBTS/GTOs per phase. Here, the connection in each phase may be represented by a three point changeover switch, the output of which can be connected to the positive pole, zero or the negative pole of the dc supply. One 3-level inverter can be regarded as an inverter which can be operated with two independent pulse patterns. Rated power and frequency of today's GTO-VSIs are limited to about 2 MW/60 Hz for 2-level VSIs and 4 MW/130 Hz for 3-level VSIs [4]. Siemens has recently introduced new SIMOVERT-ML drive with 3-level converters of MW range with vector control for application to synchronous or induction motor

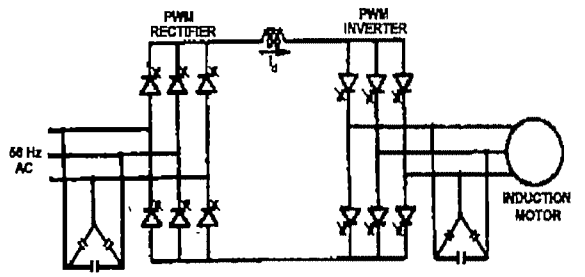

Fig.5 CSI-PWM rectifier-PWM inverter fed drive

drives [5]. Hitachi Ltd., Japan has also developed 3-level GTO-based 6.4 MW inverter induction motor drive for steel rolling mills recently [6]. The synchronous motor is often the most cost-effective solution for applications with a wide field weakening range and for high surge load requirements

C *Current Source Inverter-Induction Motor (CSI-IM) Drive*

A schematic diagram of a *dual PWM* current source inverter (CSI)-fed drive using GTOs [7] is shown in Fig.5. The system is a dual of the PWM -VSI Rectifier-Inverter system in Fig.1. The PWM rectifier provides sinusoidal input

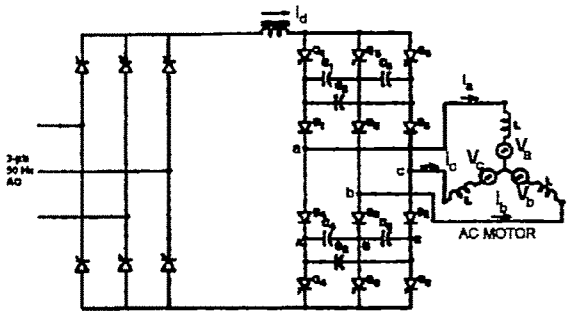

Fig. 6 Auto-sequential commutated inverter (ASCI) fed Induction motor drive

current at unity power factor. This scheme has replaced the earlier phase-controlled rectifier fed auto-sequentially commutated inverter (ASCI) using SCRs with capacitors and series diodes as commutation elements (Fig.6) [8]. The variable dc voltage is converted to a current source by connecting a large inductor in series eliminating the filter capacitor of the VSI. The freewheeling diodes, typical of VSI, are absent in CSI as when supplied by a current source, current in any half-leg of the inverter cannot change in polarity and can only flow through the power switches. A method of speed control with CSI in which the slip ω_{sl} is varied as a function of the I_d (pre-computed for given parameters of the machine) to maintain constant air-gap flux (as in the V/f control of the VSI-fed drive) is shown in Fig. 7.[8]. The full 4-quadrant capability of the drive can be obtained.

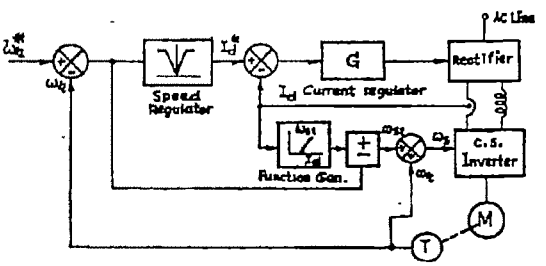

Fig.7 CSI-drive with slip-frequency control

D. Cycloconverter-Induction Motor Drive

A cycloconverter converts ac line power from one frequency to that in another directly (AC/AC) in contrast to the dc link inverter (AC/DC/AC). Fig.8 shows a 3-phase 3-pulse cycloconverter induction motor drive using 18 thyristors and phase voltage and current waveforms. For large drives, 6 or 12 pulse converter bridges are used requiring 36 or 72 thyristors in total respectively. Like dual converters, the cycloconverters can be operated in the circulating current-free mode where no circulating current is permitted between the P- and N- groups by appropriate logic control. The circuit operates in phase control line commutation mode and the firing angles are modulated to synthesize a mean sine wave voltage. The bridge which conducts the current generates the voltage. Due to line commutation, its output frequency is limited to, typically, 1/3 to 1/2 of the line frequency and is suitable for low speed high power drives, with easy four quadrant operation.

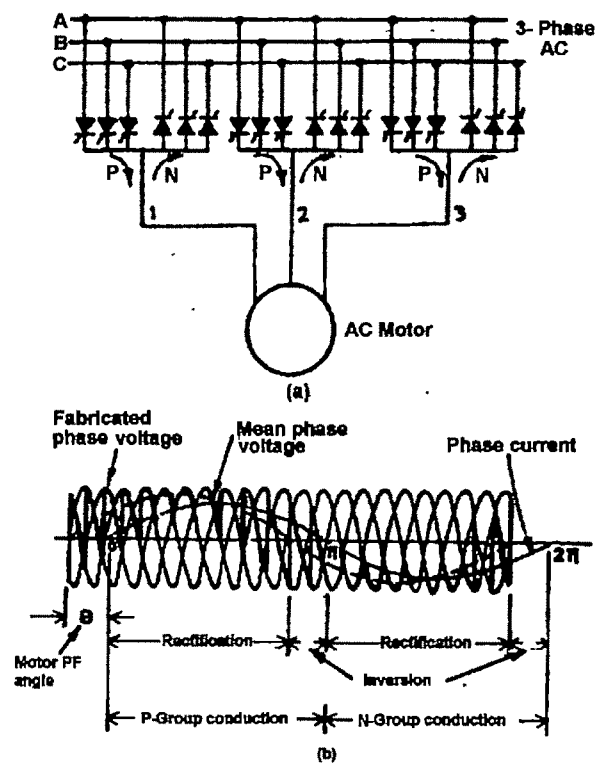

Fig. 8 3-phase 3-pulse cycloconverter induction motor drive (a) power circuit (b) waveforms

The output voltage of a cycloconverter contains a complex harmonic pattern given by $k_1nf_i \pm k_2f_o$ where f_i= output frequency, f_o= output frequency, n= pulse number and k_1, k_2 are integers. A 3-pulse cycloconverter may contain sub-harmonics of lower frequency than the output frequency which may be reduced by modifying the cosine firing control technique. Because of the phase control principle, the cycloconverter presents lagging reactive power at the input irrespective of the power factor of the load and various schemes to improve this power factor have been developed including fast current control loop or trapezoidal modulation.

The control method concepts discussed with VSI and CSI can be extended to cycloconverter drives. The cycloconverter-fed induction motor drives have been used for low speed multi-motor driven steel mill roller tables and with *vector control*, recently, in rolling mill drives as discussed in section V.

III. SYNCHRONOUS MOTOR DRIVES WITH SCALAR CONTROL

A. Self-synchronous or Commutator-less Motor

The synchronous motor drives have essentially two different modes of operation. One is the true synchronous mode in which the machine is controlled by inverter or cycloconverter through an independent oscillator just like the V/f control of an induction motor drive. The other mode is the self-synchronous mode which is known as *Commutator-less motor* (CLM) mode (Fig.9) where the inverter or cycloconverter firing signals are derived from a rotor shaft position sensor (dc -CLM) when supplied from

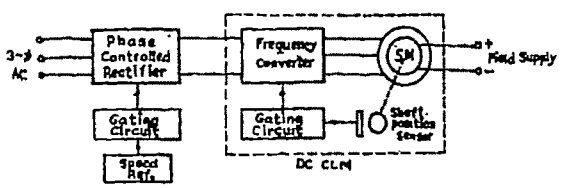

Fig. 9 Commutator-less dc motor

an inverter and ac-CLM when supplied from a cycloconverter . In the self-synchronous mode, the synchronous motor acts exactly like a dc motor– the

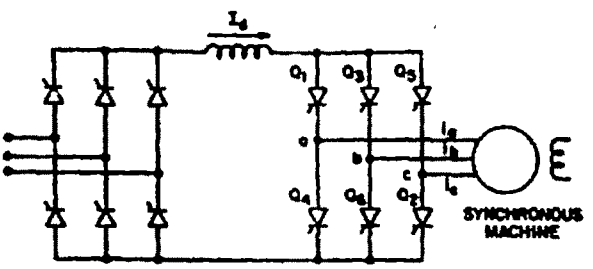

Fig.10 LCI-fed synchronous motor drive

mechanical brush system being replaced by the shaft position sensitive converter. Here, the frequency is slaved to the speed and not vice-versa. Therefore, there is no risk of pull out. Any slow down of the motor, no matter sudden causes a corresponding drop in frequency. The magnitude of the dc current supplied to the static commutator (for dc CLM) determines the torque and the speed.

B. Load-Commutated Inverter (LCI)-Synchronous Motor Drive

An important feature of the synchronous machine is that it can be operated in the leading power factor and when supplied by a CSI, load commutation can be used. Fig.10 shows the power circuit for such a drive. With a normal synchronous motor , the inverter is not capable of load commutation below a certain speed (typically 10%) because of inadequate counter emf. Special starting arrangements with forced commutation through fourth leg or 'current pulsing' are to be made at starting /low speed running.

LCI-fed drives in CLM mode are widely used in high power drives such as pumps, compressors, pumped storage hydro- and gas turbine start-up applications besides continuous rolling mills and traction drives.

C. Cycloconverter-Synchronous Motor (ac-CLM) Drive

Four quadrant torque-speed operation at a high power level with high torque at low speed are the drive requirements for which the cycloconverter-fed synchronous motor (Fig. 11) are best suited [11] :

- gear-less cement mill drives; the mill tube is driven from a low speed wrap around motor with higher number of poles [13],[14]
- drives for mine hoists with high power ratings [17]
- reversing rolling mill drives with high dynamic requirements for torque and speed reversal employing vector control [15], [16],[19], [20]
- icebreakers and other ships equipped with diesel generator-fed cycloconverter-fed synchronous motors with power rating up to about 20 MW rating per unit [18].

The cycloconverter is normally operated with line commutation but can have load commutation if the output frequency approaches or exceeds the line frequency. The firing pulses are derived from shaft position sensors and the machine terminal power factor is maintained at unity by field excitation control.

The method of driving the motor from a cycloconverter with the *transvector* control principle involving *field orientation control (FOC)* has been used by Siemens in Germany,for years, in very high capacity Cement Mills (> 8 MW) and also for Rolling Mills rated above 3 MW since 1978. A 4 MW (peak loading 10MW) Blooming Mill with a cycloconverter-synchronous motor drive having a speed of 60-120 rpm was commissioned in 1981 together with a

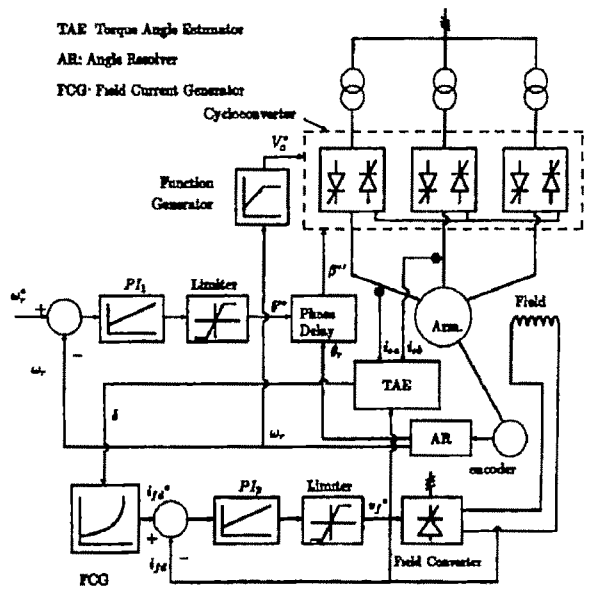

Fig. 11 Cycloconverter synchronous motor drive with scalar control (ac-CLM)

4MW roughing stand of a strip mill [15]. The control concept and relevant vector diagrams for field oriented operation with armature reaction is detailed in [14], 15] and discussed briefly in a later section..

IV. INDUCTION MOTOR DRIVES WITH VECTOR CONTROL

In a separately excited dc machine, use of power electronic converters with current feedback provides a direct control of the magnitude of the armature current and in proportion, the torque. For ac machine, however, this control is to be achieved in terms of both *amplitude* and *phase* which has led to the generic term *vector control*. In addition, unlike the dc machine, where the orientation of the field flux and the armature mmf is fixed by commutator and brushes, ac machine requires external control to fix this orientation without which the space angle between various fields vary with load (and during transients), giving rise to oscillatory dynamic response. *Field orientation control* (FOC) directly controls this space angle and, in particular, attempts to make it 90° between the specifically chosen field components so as to emulate a dc machine and provide a *de-coupling control*. The technique can be applied to either induction or synchronous motor fed from either CSI/ CRPWM VSI /VSI or cycloconverter. Early conceptual works on vector control were developed in Germany in the beginning of seventies and its implementation progressed

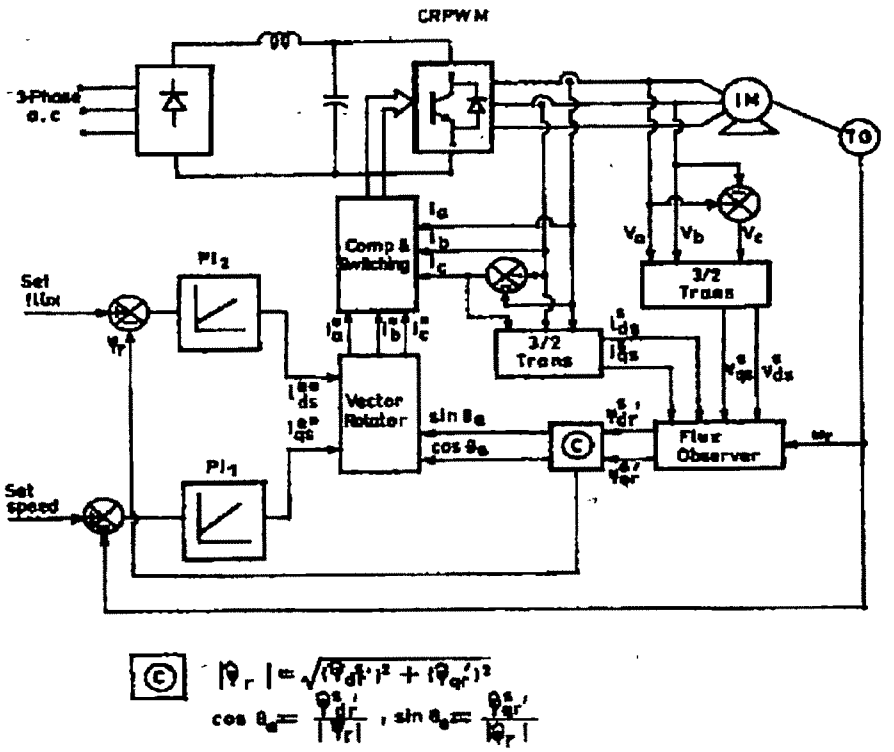

Fig. 12 Direct vector control scheme for a CRPWM-fed induction motor with a rotor flux observer

with the development of microprocessors in early eighties. In *vector control*, the currents i_{ds}^e and i_{qs}^e ,the d-axis and q-axis components respectively of the stator current in synchronously rotating reference frame are analogous to the field current I_f and to the armature current I_a of the dc machine and therefore the torque can be expressed as $T_e = K_t\psi_m i_{qs}^e = K'_t I_f I_a = K_t'' i_{qs}^e i_{ds}^e$. These two components can be independently controlled. For normal operation as in the dc machine, the current i_{ds}^e remains constant and the torque is varied by varying the i_{qs}^e component.

There are two basic methods of vector control based on the acquisition of the flux vector angle θ_e ($=\omega_e t$) which assures the alignment of i_{ds}^e with ψ_m and i_{qs}^e with the airgap voltage [3]. The *direct method* is based on the measurement or computation of the magnitude as well as the position of the flux vector and the *indirect method* uses a *slip relation* to compute θ_e as a sum of θ_r and θ_{sl} (corresponds to ω_r and ω_{sl} respectively).

A. Direct Vector Control (Flux Feedback)

Fig. 12 shows the block diagram of a direct vector control scheme for a Current Regulated PWM (CRPWM) inverter-fed induction motor drive [2]. The reference control signals i_{ds}^{e*} and i_{qs}^{e*} which are dc quantities are converted to a stationary reference frame by a *vector rotator* with the cos θ_e and sin θ_e signals generated from the flux signals followed by 2/3 phase transformation as shown. A flux feedback loop provides precision flux control. The speed control loop provides the torque command which generates the current reference.. The air-gap fluxes ψ_{dm}^s and ψ_{qm}^s can be measured directly by search coils /Hall probes or estimated (observed) from stator voltage and current signals. Though the air-gap or the *stator flux orientation* is attractive due to ease of flux measurement or computation it has been shown that they lead to instability and not a perfect de-coupling and the *orientation to rotor flux* is resorted to by synthesizing the rotor flux ψ_r from the directly sensed air-gap flux.

B. Indirect Vector Control (Flux Feed-forward)

An alternative to direct measurement or estimation of the flux position for application of vector control is to employ a slip relation derived from rotor voltage equations in a synchronously rotating reference system with rotor flux entirely in the d-axis [3],

$$\omega_{sl} = \frac{L_m}{\psi_r'^e}\left(\frac{R_r'}{L_r'}\right) i_{qs}^e \qquad (1)$$

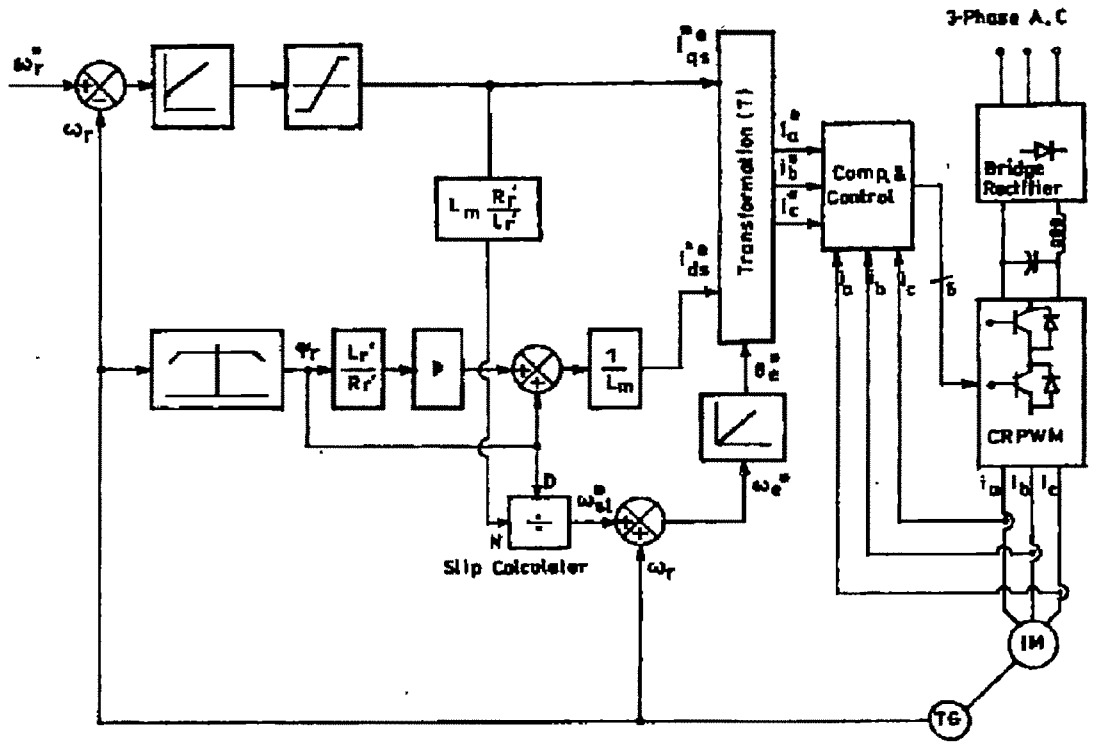

Fig. 13 Rotor flux oriented indirect vector control scheme for a CRPWM-fed induction motor

to compute the flux position relative to the rotor by summing a sensed rotor position signal with a commanded slip position signal

$$\theta_e^* = \theta_{sl}^* + \theta_r \qquad (2)$$

Fig. 13 shows the block diagram of the *indirect* vector controlled induction motor drive [2]. The commanded currents i_{qs}^{e*} and i_{ds}^{e*} are converted to stator referred reference currents by transformation as in the case of the direct field orientation. i_{qs}^{e*} is controlled according to the desired torque and constant rotor flux. $i_{ds}^{e*}$is obtained as ψ_{dr}^{e*}/L_m at the steady state.

Indirect vector control, also known as *flux feed-forward control*, has the limitation in the slip calculation which depends on the commanded machine parameters that may differ from the actual values during the running condition of the drive.

V. SYNCHRONOUS MOTOR DRIVES WITH VECTOR CONTROL

The control of synchronous motors is different from that of induction motors primarily due to the fact that, in the latter, the magnetizing current can be supplied from the field side independently of the armature current and the space position of the field is located by the position of the rotor. Additionally, the steady state slip between the rotor (field winding) and the controlled flux vector vanishes in the steady state. Therefore, the indirect or feed-forward type of vector control as used extensively for the induction motor does not seem obvious for a synchronous machine. For a self-synchronous or commutator-less motor with rotor position feedback and vector control, the implementation calls for control of the magnitude and the phase of the stator current with respect to the location of the field winding axis. The response of the field current is sluggish because of the large time constant and as a result, the response of a self-controlled synchronous machine is slow. The response can be improved considerably by using *vector control*, where the transient magnetizing current demand to maintain the rated flux can be temporarily supplied from the stator side.

A. Cycloconverter-fed Synchronous Motor Drive

Fig. 14 shows the block diagram of a stator flux oriented vector controlled cycloconverter drive as applicable to rolling mills [21] and the corresponding phasor diagram. This is an improvement on the Siemens' drives [12]-[15] as well as the Japanese one [19]. The implementation aims at a control that maintains a spatial orthogonality between the flux vector ψ_s and the armature current vector i_a as shown in the space phasor diagram. The reference speed and reference flux commands are given to the vector rotator that generates the reference analog voltages for the cyclocoverter (through the current controller) and the field converter. The stator flux is estimated by a closed loop

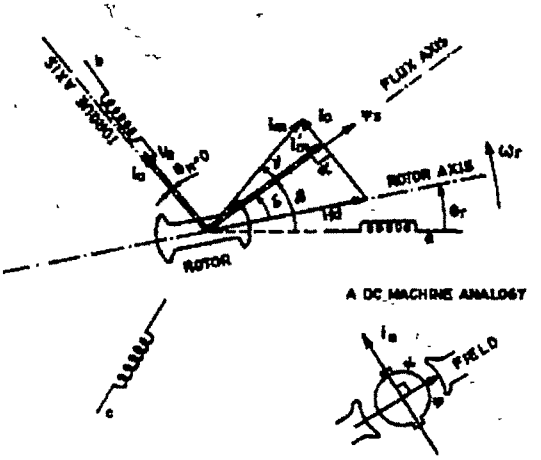

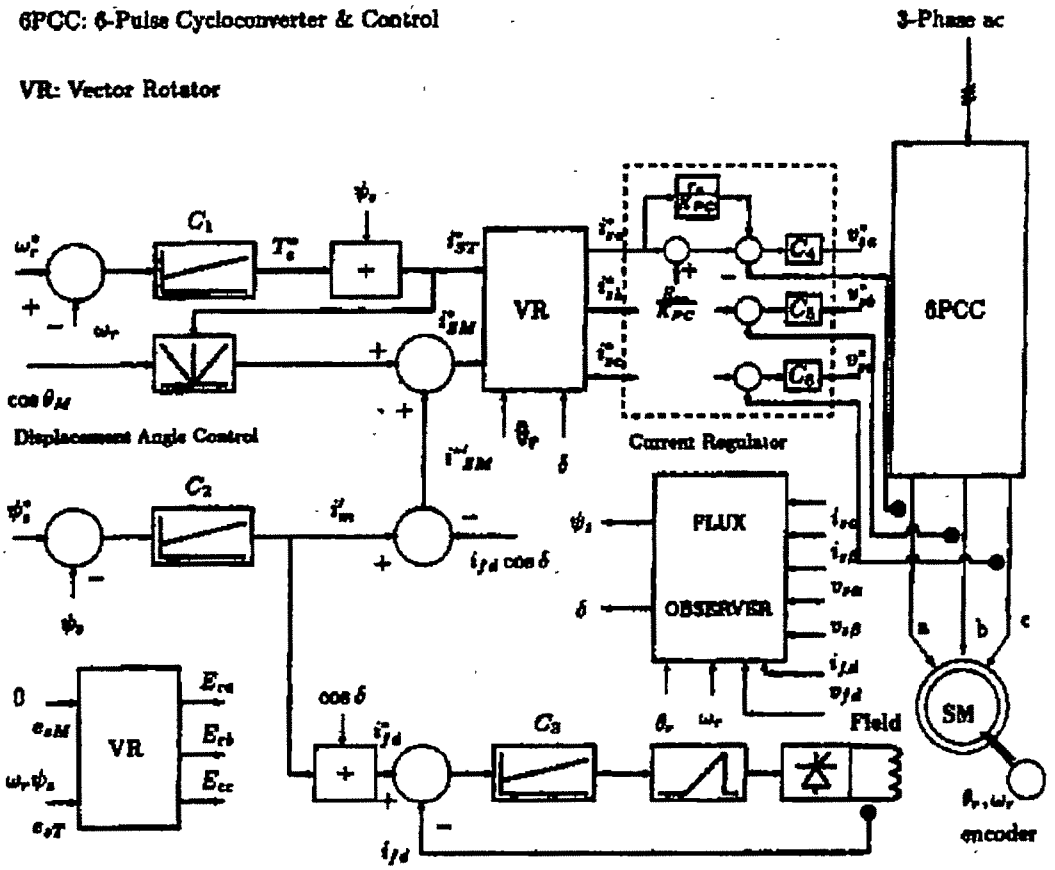

Fig. 14 Stator flux oriented flux-observer based vector controlled cycloconverter synchronous motor drive

reduced order observer. C_1 is the speed controller (PI) that generates the torque command which is divided by the stator flux to generate the torque component of current i_{sT}. The magnetization current along the flux axis i_m^* is obtained from a flux controller (PI) C_2. The transient stator flux component of current i_{sm} is obtained from the relationship, $I_{sm}^* = i_m^* - i_{fd} \cos\delta$, which decays down to zero in the steady state. The steady state displacement angle is decided by the displacement angle controller and the power factor can be maintained at unity. The set value of the field current is obtained from the relation, $i_{fd}^* = i_m^* / \cos\delta$. C_3 is the field current

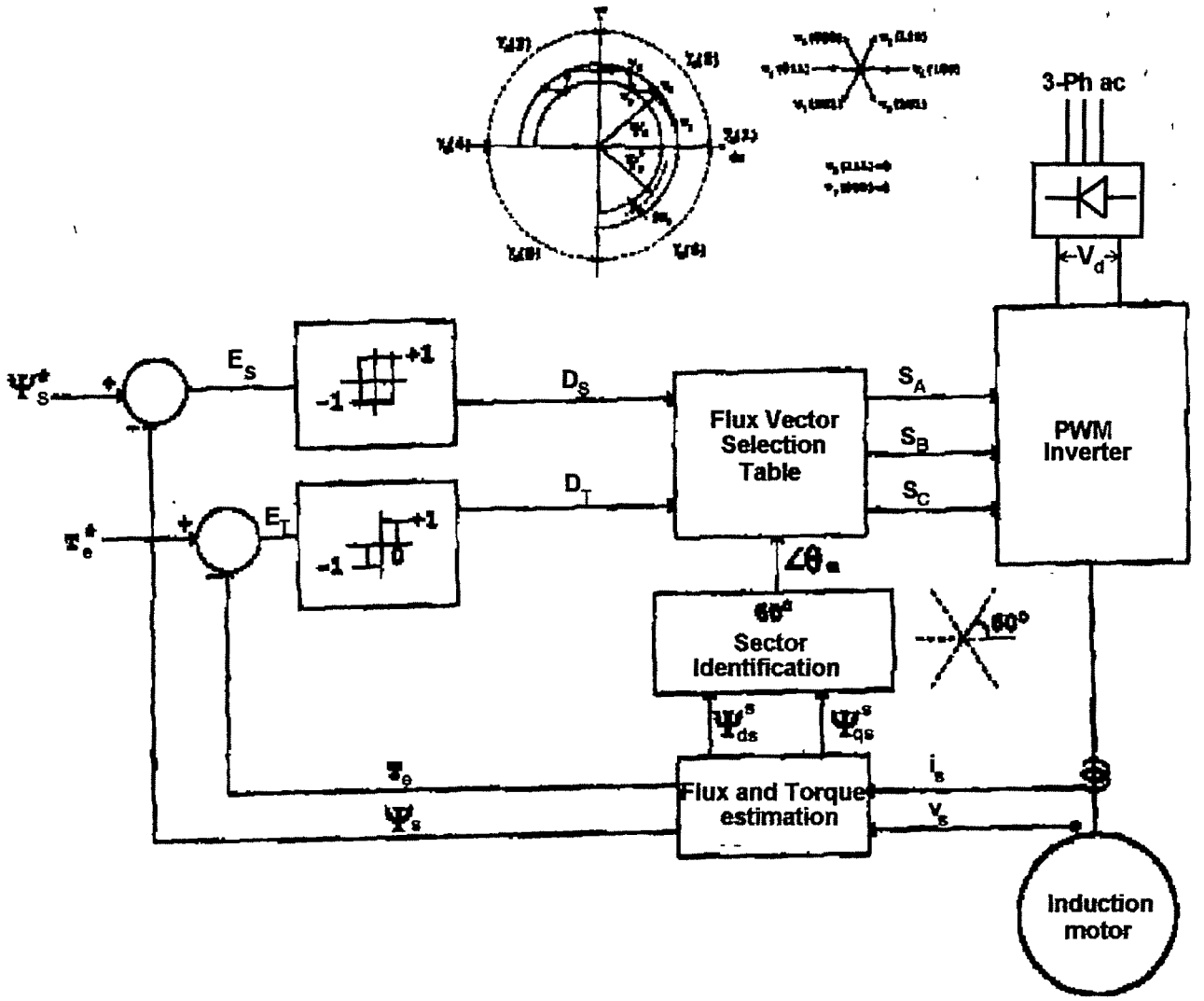

Fig.15 Direct torque and flux control (DTC) of an induction motor

controller (PI) that generates the control voltage for triggering the field converter. The vector rotator (VR) transforms the vector from two-axes flux-torque reference frame to abc stationary reference frame. two axes flux-torque reference frame to abc stationary reference frame. The observer and the control circuit design aspects together with the PC -based implementation are detailed in [21].

VI. INDUCTION MOTOR DRIVES WITH DIRECT TORQUE AND FLUX CONTROL (DTC)

A new concept to control the torque and flux in induction motor drives, popularly known as *Direct Torque Control (DTC),* which is basically a performance-enhanced *scalar* control was developed in the late eighties[22][23] and commercialised in the nineties by the ABB, Sweden [24].

With this scheme it is possible to obtain good dynamic control of the torque without any mechanical sensor on the shaft (*sensor-less).* The scheme is shown in Fig. 15 where both the flux ψ_s and the torque T_e are controlled by the hysteresis controllers in the outer loops as indicated. The machine voltages and currents are sensed to estimate the torque and the flux vector that gives information in one of the 60° sectors. The control loop errors E_S and E_T generate the digital signals D_S and D_T through the respective hystersis .-band comparators. The delays associated with the PWM stage is replaced by an optimal switching flux vector selection table (can be realized by an ASIC hardware) which selects the most appropriate voltage vector to satisfy the flux and the torque demands . The drive has a faster response than the field oriented /vector control and the absence of the closed loop current control, PI regulators,

vector transformation and conventional PWM algorithm simplifies the scheme. However, as the feedback signals are estimated from the machine terminals, the low speed limitation and the parameter variation problems are similar to the stator flux oriented direct vector control. In contrast to FOC, which is a linear control where the PWM and the static converter are modeled as a linear actuator, DTC is non-linear, which in turn exploits the discrete nature of the static converter for the sake of robustness and dynamics. Recently, a number of solutions of the inherent problems have been developed with the use of improved switching logic, discrete SVM techniques [25], three-level inverters and introduction of fuzzy and neuro-fuzzy techniques involving more computer power.

CONCLUSIONS

An overview of the high power high performance industrial ac drives, as available today, is presented along with their control strategies. These include both induction and synchronous motor drives with field oriented and direct torque control. However, many modern control concept strategies like *model referencing adaptive control (MRAC), sliding mode control (SMC), Neural Network Control (NNC)* or *Fuzzy Control (FC)* as proposed recently [26] for these high performance drives have been kept out of the scope of this paper as they have not yet gained full fledged industrial practice.

REFERENCES

1 S Bernett, 'Recent developments of high power converters for industry and traction applications', IEEE Trans on Power Electron, vol 15, no.6 Nov 2000, pp 1102-1117

2 A K Chattopadhyay, 'Advances in vector control of ac motor drives-a review', Sadhana (Journ of Ind, Acad. of Science), vol.22, Pt 6, December 1997, pp 797-820

3 B K Bose, 'Power Electronics and AC Drives', Prentice Hall, 1986

4 H Stemmler,'High Power Industrial Drives', Proc IEEE, August 1994, pp 1266-1285

5 T Salzmann,'Higher Quality Drives in Megawatt Range,' Engineering automation, Siemens, 19 (1-2), 1997, pp 38-40

6. M Tobisi et al, 'Inverter-Fed AC Drive Systems for Steel Rolling Mills Hitachi Review, Dec , 1996, 45(6), pp 299-304

7. A K Chattopadhyay, 'Current source induction motor drives-a state -of-the- art research review', IETE (I) Journal, 37 (1),1991, pp 34-36

8.G K Dubey, Power Semiconductor Controlled Drives' Prentice Hall, 1989

9 B K Bose, 'Adjustable Speed AC Drives-A technology status Review' Proc IEEE 70 (2), Feb., 1982, pp 116-135

10 J M D Murphy and F Turnbull, 'Power Electronic Control of AC Motors 'Pergamon Press, 1988

11 A K Chattopadhyay, ' Cycloconverters and cycloconverter-fed ac motor drives', Special Issue of Jour. of Ind Inst of Science, vol 77, no.5 Sept / Oct 1997, pp 347-419

12 K H Bayer et al, 'Field oriented close loop control of synchronous machine with the new Transvector control system', Siemens Review, 39, 1972, pp 220-223

13 D Richlen,'Gearless Drive for a Cement Mill' ,Siemens Review,38.9 Sept 1971, 398-401

14 T Salzmann, Cycloconverter and automatic control of ring motors driving Tube Mill,Siemens Review,XLV,1978,pp 3-8

15 W Timpe, 'Cycloconverter Drives for Rolling Mills, 'IEEE Trans IA-18, 41, July/August 1982, pp 401-404

16 K Sugi,Y Naito,R Kurosowa,Y Kano,' S Katyama, T Yoshida,'A microcomputer based high capacity cycloconverter drive for main rolling mill', Proc IPEC, Tokyo, March 1983, pp 744-755

17 M K Madiseti and M A Ramlu, 'Trends in the Electronic Control of Mine Hoists', IEEE Trans. IA-22, 6, Nov /Dec 1986, pp 1105-1112

18 W A Hill et al, 'A Vector Controlled Cycloconverter Drive for an icebreaker, 'IEEE Trans, IA-23, 6, Nov /Dec , 1987, pp 1030-1041

19 T Nakano et al,' A High Performance Cyclo- converter-fed Synchronous Machine Drive system,' IEEE Trans IA-20,5, Sept. /Oct 1984. Pp 1278-1284

20. K Ishihita et al. 'Application of New Drive systems for Plate Mill Drives, ' IEEE Trans Ia-22. 2, March /April, 1986, pp 345-351

21. S P Das and A K Chattopadhyay, 'Observer-based Stator Flux Oriented Vector Control of a Cyclocon- verter-fed Synchronous Motor Drive,'IEEE Trans IA-33, July/August,1997, pp 943-955

22. M Depenbrock,' Direct self control (DSC) of inverter-fed induction machine', IEEE Trans on Power Electron., vol 3, no.4, Oct. 1988, pp420-429

23 I Takahasi and N Noguchi,' A new quick response and high efficiency control strategy of an ac induction motor,' IEEE Trans on Ind Appl. Vol 22, Sept / Oct 1986. pp 820-827

24 J N Nash, 'Direct torque control, induction motor vector control without an encoder,' IEEE Trans on Ind Appl. Vol.33 no 2, Mar /Apr , 1997, pp 333-341

25 D Casadei,G Serra, A Tani, 'Improvement of direct torque control performance by using a discrete SVM technique,' Conf Rec PESC'98, Fukuoka, Japan, May, 1998, pp 997-1003

26 B K Bose, 'High performance control of induction motor drives', IEEE Ind Electronics Society Newsletter, vol 45, no 3, September, 1998, pp 7-11

Statistical Analysis of Chaotic Systems. Applications to Power Converters

José Luis Rodríguez Marrero

Abstract— **This paper reviews how to approach the analysis of physical systems in the chaotic regime, using a state densities approach. These ideas are applied to the analysis of the chaotic regime of DC-DC power converters.**

Keywords— **Chaos, power converters**

I. Introduction

THE erratic and complex behavior of physical systems is not always of random nature. This is in fact the case of certain deterministic nonlinear systems that operate in the chaotic regime. The dynamics of these systems can be described by one dimensional nonlinear models of the type

$$x_{n+1} = f(x_n) \quad (1)$$

$$y_n = g(x_n) \quad (2)$$

where x_0 is the initial state and f and g are real functions. Equation (1) describes the dynamics of the system, while (2) describes an *observable* of the state of the system. The function f is the *map* of the dynamical system. The evolution of the dynamical system is obtained by iterating (1) to generate a sequence of points, known as the orbit (or trajectory) of the initial state x_0. One of the objectives of studying (1) would be to determine the asymptotic behavior, or steady state, of the system for a given initial state. This is, in general, not possible. However, we can try answering the following questions:

- What portion of the state space does the system visit for large n?
- How often does the orbit visit certain subsets of the state space?

There are systems (1) described by certain maps, called *Markov maps*, for which we can answer this last question exactly. These maps generate chaotic signals (orbits). Although these signals are completely deterministic, they are in many ways similar to stochastic signals. Any particular trajectory is significantly altered by even a slight change in the initial state x_0. However, the distribution of points on the trajectory is not affected by the initial state. This fact suggests that the distribution of points visited on a trajectory constitute a more useful representation of the behavior of the system than knowledge of the exact orbit.

An important property of Markov maps is that its statistical properties can be determined in exact form [1], [2]. It has been shown that these maps are *ergodic*, which implies the existence of an invariant probability density function that governs the distribution of x_n, independent of the initial state. This probability density function can be used to compute time averages of physical quantities of the system by means of ensemble averages (*Birkhoff's ergodic theorem* [1]).

DC-DC converters under current-mode control provide an example of systems that, under certain assumptions, can be described by (1) and (2). For constant-frequency operation, a switch is turned on every T seconds but is turned off when the inductor current reaches a specified reference level, I_{ref}. This reference level is now the primary control variable; the duty ratio D becomes an indirectly controlled auxiliary variable. Steady-state operation with period T and with $D > 0.5$ (approximately) is impossible when $I_{\rm ref}$ is held constant, because this periodic solution is unstable, [3]. The waveforms for $D > 0.5$ under the condition that $I_{\rm ref}$ is constant assume complicated forms, corresponding either to periodic operation at some multiple of T (subharmonic operation) or to chaotic variation from cycle to cycle, see for instance [4], [5], [6], [7].

The spectral modifications associated with chaotic operation of DC-DC converters provide an important motivation for actual operation in this regime [8], [9], [10]. Conventional DC-DC converters generate electromagnetic interference (EMI) consisting of the switching frequency and many harmonics. Such interference gives rise to important electromagnetic compatibility (EMC) problems, which can be reduced by filtering (for conducted interference) and screening (for radiated interference). Other strategies for interference reduction are spectral shaping based on randomized modulation [11], and chaotic operation, which flatten the switching spectrum (at the expense of a corresponding broadening). Exploiting the random nature of the chaotic operation of DC-DC converters could provide a way of obtaining a prescribed power spectrum [12], [13], [14].

In Section II we review the role of densities in describing the chaotic regime of one dimensional non-linear maps, using a DC-DC converter as an example. In Section III we apply these ideas to compute the input-output gain, and various other averages of interest, for the chaotic regime of DC-DC converters under current-mode control and in continuous-conduction mode. Results are presented for the boost converter. Detailed analysis for this and other converters is given in [15].

II. Statistical analysis of the chaotic regime

The boost converter of Fig. 1 will be used as an example model of the ideas outlined above. It is assumed that the converter is operating in continuous-conduction mode. It is also assumed that the output voltage V_{out} is essentially

J. L. R. Marrero (marrero@dea.icai.upco.es) is with Universidad Pontificia Comillas, Alberto Aguilera 23, 28015 Madrid (Spain)

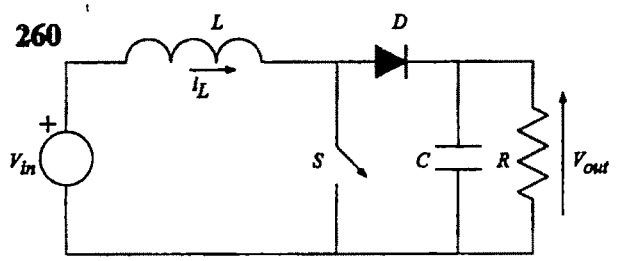

Fig. 1. Boost converter circuit

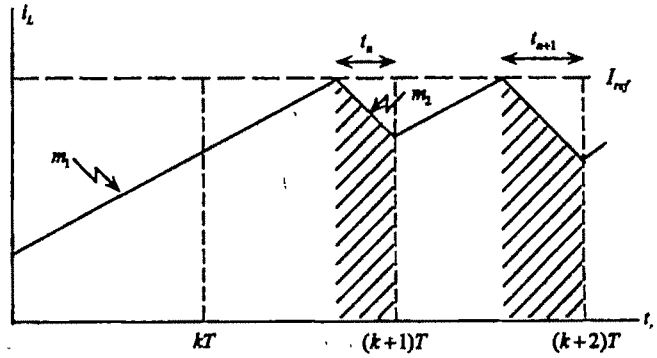

Fig. 2. Typical segment of inductor current for $\alpha > 1$

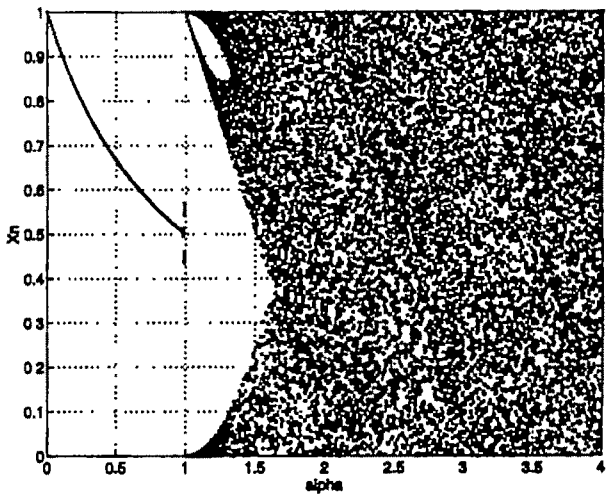

Fig. 3. Bifurcation map for (3)

constant and that the switching period is short enough for the inductor current to be essentially piecewise linear. Fig. 2 represents a typical segment of the inductor current variation with time for $\alpha > 1$. The shaded areas of the figure correspond to intervals when the switch is open; these are precisely the intervals when the diode current is non-zero, equal in value to the inductor current. Unlike in the case of $\alpha < 1$, where the diode current contains one pulse per clock period T, for $\alpha > 1$ there are some periods with no diode current. The ratio of clock periods with current and no current depends upon the value of α.

Under these assumptions, the dynamics of the converter are well described by the following map [8], [10]:

$$x_{n+1} = 1 - mod_1(\alpha x_n) \tag{3}$$

where: $mod_1(\ )$ denotes multiplication modulo 1 (hence simply the extraction of the fractional part); $x_n = t_n/T$ represents the normalized time from the n-th opening of the switch to the next closing of the switch, as marked in Figure 2; and α is the ratio of the slope magnitudes of the inductor current when the switch is open and closed, respectively:

$$\alpha = \frac{m_2}{m_1} = \frac{(V_{out} - V_{in})/L}{V_{in}/L} = \frac{V_{out} - V_{in}}{V_{in}} \tag{4}$$

The analysis of this equation shows that for $\alpha < 1$, which corresponds to $D < 0.5$, the equation has a nontrivial stable equilibrium point, corresponding to stable period-T operation of the converter. For $\alpha > 1$, or $D > 0.5$, the equation has no nontrivial stable equilibrium point or stable periodic solution, so stable operation of the converter with period T or any multiple of T is not possible (at least to the extent that the simplified model in (1) actually describes the circuit behavior). For $\alpha = 1$, the solution of the equation for most initial conditions has period 2, which implies the converter has a solution of period $2T$.

A qualitative, empirical analysis of the dynamics of the map (3) can be done as follows. Pick an arbitrary initial state $x_0 \in [0, 1]$. Iterate equation (3) to obtain a sequence of states, $x_1, x_2, x_3, \cdots$, called the *trajectory* or *orbit* emanating from or passing through x_0. Plotting these points (omitting the first few if the transient is not of interest) for a range of α values results in an empirical bifurcation diagram of the type shown in Figure 3. The figure shows that for $\alpha < 1$ the trajectory converges to a fixed state that is independent of the initial state chosen. This is consistent with the periodic behavior of the converter in this range of α: the switching cycle times are always the same in the periodic steady state. However, for $\alpha > 1$ and for most initial states, the trajectory does not converge to anything regular; it is erratic or chaotic. Moreover, the trajectory is significantly altered by a slight change in the initial state. It can be shown that all states are visited upon iteration for $\alpha \geq \alpha_0$, where $\alpha_0 = (1 + \sqrt{5})/2 \approx 1.618$ is the golden mean.

Although any particular trajectory for $\alpha > 1$ is very sensitive to even slight changes in the initial state x_0, the general appearance of the bifurcation diagram in Fig. 3 is hardly affected by picking different initial states. In other words, the distribution of points on the trajectory seems not to be much affected by the initial state. This fact suggests that the *distribution* of points visited on a trajectory may constitute a more useful representation of the behavior of the system than knowledge of the specific points. This is the idea that is elaborated on and exploited in the remainder of this section.

Suppose, for a given α, we pick the initial state x_0 *randomly* according to an arbitrary probability density function $f_\alpha^{(0)}(x)$. Then the next state x_1 will be random too, with a probability density function $f_\alpha^{(1)}(x)$, and similarly

at future time steps. Using the map (3), it is possible to track the evolution of probability densities from the initial density forward. It turns out, see [2], [13], that the properties of the map (3) ensure the densities will converge to a unique *invariant density* $f_\alpha(x)$. The reason for the label "invariant" is that if x_0 is distributed or picked according to this density, then all future x_n are also distributed according to this density.

The *operator* that transforms these density functions under the action of the map is called the *Frobenius-Perron* operator associated with the map. If we apply this operator to an initial density, the density will converge (subject to some conditions, see [1]) to an *invariant density*, one that does not change under application of the operator. The invariant density is thus the 'fixed point' of the Frobenius-Perron operator.

For certain special values of α the map (3) is what is known as a *Markov map*, for which the invariant density function can be found exactly. In this case the Frobenius-Perron operator can be easily obtained [2]. The corresponding invariant density turns out to be uniform for integer values of α ($\alpha > 1$), but more generally is piecewise constant, and can be computed in a systematic fashion [2], [15]. For example, the density for $\alpha = \alpha_0$ (the golden mean) is given by

$$f_{\alpha_0}(x) = \begin{cases} 1/(3-\alpha_0) & for \quad 0 \le x \le 2-\alpha_0 \\ \alpha_0/(3-\alpha_0) & for \quad 2-\alpha_0 < x \le 1 \end{cases} \tag{5}$$

The invariant density can then be used to replace time averages of functions of x_n ($\overline{Q}$) by ensemble (i.e., probabilistic) averages of these functions ($\langle Q \rangle$), computed with respect to the invariant density. This is a result of *Birkhoff's ergodic theorem* [1] that states that

$$\lim_{N\to\infty} \frac{1}{N} \sum_{n=0}^{N-1} Q(x_n) = \int_{[0,1]} Q(x) f_\alpha(x) dx \tag{6}$$

(for almost all x_0 —there are particular x_0, specifically those corresponding to the (unstable) periodic solutions, for which this is not true), where Q is an observable of the state of the system.

III. Analysis of a power converter in the chaotic regime

To calculate the output voltage V_{out} (assumed essentially constant) for $\alpha > 1$, we argue as follows. Consider the n-th switching cycle as the one that commences with the opening of the switch at the beginning of the interval marked t_n in Fig. 2, and ends at the next opening of the switch. During this cycle, the capacitor gets some charge through the diode and loses charge through the resistor. The charge through the diode in this cycle is just the shaded area under the interval marked t_n in Fig. 2. Under the assumption that V_{out} is essentially constant, this charge is given by

$$Q_D(n) = \left(I_{ref} - \frac{m_2 t_n}{2} \right) t_n \tag{7}$$

where $m_2 = (V_{out} - V_{in})/L$. Then, the time-average value of the diode current is obtained by dividing the charge through the diode over N switching cycles by the total length of time

$$\overline{I_D} = \lim_{N\to\infty} \frac{\sum_{k=0}^{N-1} Q_D(k)}{\sum_{k=0}^{N-1} T_k} = \lim_{N\to\infty} \frac{\frac{1}{N}\sum_{k=0}^{N-1} Q_D(k)}{\frac{1}{N}\sum_{k=0}^{N-1} T_k} \tag{8}$$

where $T_k = (1+\alpha)t_k$ is the time length of the k-th switching cycle.

Invoking the ergodicity of (3), we can use (6) to replace the time averages by ensemble averages computed with respect to the appropriate invariant density. Then, (8) becomes

$$\overline{I_D} = \frac{\langle Q_D \rangle}{\langle T \rangle} \tag{9}$$

In the case of integer α, the density $f_\alpha(x)$ is uniform, so the required calculation is easy. For this case, evaluating the above integral gives

$$\overline{I_D} = \frac{1}{1+\alpha}\left(I_{ref} - \frac{m_2}{3}\right) \tag{10}$$

The output voltage V_{out} is then $V_{out} = \overline{I_D} R$, which yields the constraint

$$I_{ref} = \frac{(1+\alpha)^2 V_{in}}{R} + \frac{\alpha V_{in} T}{3L} \tag{11}$$

For most non-integer values of α, the determination of the corresponding relationship becomes considerably more complicated. However, numerical experiments show that using (11) as an approximation for all $\alpha > 1$ yields very good results. To now find V_{out} in the chaotic regime for a given I_{ref}, we can use (11) to first compute α, and then (4) to determine V_{out}. Note that determination of this static characteristic in the periodic case, $\alpha < 1$, is much more direct [3]; the extension to chaotic operation is evidently non-trivial.

Fig. 4 shows a plot (solid line) of V_{out} in volts as a function of I_{ref} in amps, computed in this way for a particular example. The circuit parameters are $V_{in} = 10$ volts, $R = 20\Omega$, $T = 100\mu s$, $L = 1mH$ and $C = 500\mu F$. In Fig. 4 we also show a plot (dotted line) of the average output voltage obtained from computer simulations of the circuit. The major discrepancy occurs for $V_{out} = 20$ volts. Since $V_{in} = 10$ volts, this point corresponds to $\alpha = 1$, which is the onset of instability. For values of $\alpha > 1.4$, our approximate results are in excellent agreement with those obtained through numerical simulation of the circuit.

Another quantity of interest in the analysis of DC-DC converters is the *average switching frequency*, $\langle s \rangle$, defined as the average number of switch openings per clock period. For periodic operation $\langle s \rangle = 1$. However, for chaotic operation $\langle s \rangle < 1$, since there are clock cycles in which the switch does not open. For α integer ($\alpha > 1$) there are switching cycles of length T, $2T$,..., αT, all of them with the same probability. Invoking ergodicity, we can calculate this probability

$$\text{Probability } \{x \le 1/\alpha\} = 1/\alpha \tag{12}$$

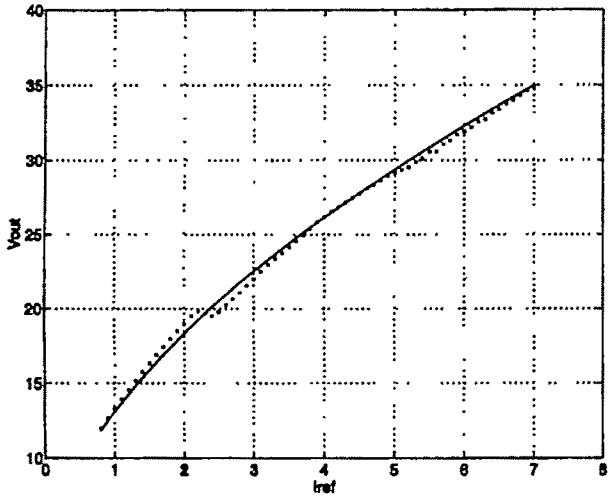

Fig. 4. V_{out} in volts as a function of I_{ref} in amps, for the boost converter parameters given in the text. The solid line corresponds to using our approximate expression (11), while the dotted line represents the results of simulations using the sampled-data model of (3)

Then, on the average, for every α switching cycles, there is one cycle of length T, another one of length $2T$, and so on up to one cycle of length αT. Hence

$$\langle s \rangle = \frac{\text{number of switching cycles}}{\text{number of clock periods}} = \frac{\alpha}{\sum_{k=1}^{\alpha} k} \qquad (13)$$

For α integer ($\alpha > 1$), this probability evaluates to $2/(\alpha + 1)$. For large α, therefore, the average switching frequency becomes small. This result may provide another motivation for chaotic operation of the converter, since switching losses — a primary factor in converter efficiency — are thereby reduced. However, it should be noted that the switching ripple will correspondingly increase.

IV. Conclusions

In this paper we have reviewed how to analyze physical systems in the chaotic regime using a state densities approach. This approach invokes the fact that the chaotic orbit of the system is *ergodic*, hence governed by a probability density, which permits time averages to be replaced by ensemble averages. A boost DC-DC power converter under current-mode control has been studied using this approach. Our results show very good agreement with numerical simulations of the model.

Acknowledgments

I would like to acknowledge the important contributions of José M. Font and Roberto Santos at different stages of this work. I am very grateful to George C. Verghese for his contributions, guidance and stimulating discussions during this work. I am also grateful for partial support by a grant from Comisión Interministerial de Ciencia y Tecnología of Spain (TIC97-0370)

References

[1] A. Lasota and M. C. Mackey, *Chaos, Fractals and Noise: Stochastic Aspects of Dynamics*. Springer-Verlag, 2nd ed., 1994.

[2] S. H. Isabelle, *A signal processing framework for the analysis and applications of chaotic systems*. PhD thesis, EECS Department MIT, February 1995.

[3] J. G. Kassakian, M. F. Schlecht, and G. C. Verghese, *Principles of Power Electronics*. Addison-Wesley, 1991.

[4] J. H. B. Deane and D. C. Hamill, "Chaotic behavior in a current-mode controlled dc-dc converter," *Electronics Letters*, vol. 27, pp. 1172–1173, 1991.

[5] J. H. B. Deane, "Chaos in a current-mode controlled boost dc-dc converter," *IEEE Transactions on Circuits and Systems*, vol. CAS-32, pp. 680–683, August 1992.

[6] C. K. Tse and W. C. Y. Chan, "Instability and chaos in a current-mode controlled Ćuk converter," in *IEEE Power Electronics Specialists Conference*, (Atlanta, USA), pp. 608–613, 1995.

[7] I. Zafrany and S. Ben-Yaakov, "A chaos model of subharmonic oscillations in current mode PWM boost converters," in *IEEE Power Electronics Specialists Conference*, (Atlanta, USA), pp. 1111–1117, 1995.

[8] J. L. R. Marrero, J. M. Font, and G. C. Verghese, "Analysis of the chaotic regime for DC-DC converters under current-mode control," in *IEEE Power Electronics Specialists Conference*, (Baveno, Italy), pp. 1477–1483, 1996.

[9] J. H. B. Deane and D. C. Hamill, "Improvement of power supply EMC by chaos," *Electronics Letters*, vol. 32, p. 1045, 1996.

[10] J. H. B. Deane, "Calculation of spectral peaks in a chaotic DC/DC converters," in *Nonlinear Phenomena in Power Electronics* (S. Banerjee and G. C. Verghese, eds.), IEEE Press, 2001.

[11] A. M. Stankovic, G. C. Verghese, and D. J. Perreault, "Analysis and synthesis of randomized modulation schemes for power converters," *IEEE Transactions on Power Electronics*, vol. 10, no. 6, pp. 680–693, 1995.

[12] L. O. Chua, Y. Yao, and Q. Yang, "Generating randomness from chaos and constructing chaos with desired randomness," *International Journal of Circuit Theory and Applications*, vol. 18, pp. 215–240, 1990.

[13] A. Baranovsky, A. Mögel, W. Schwarz, and O. Woywode, "Statistical analysys of a dc-dc converter," in *NDES*, (Ronne, Bornholm, Denmark), 1999.

[14] A. Baranovsky, A. Mögel, W. Schwarz, and O. Woywode, "Chaotic control of a dc-dc converter," in *IEEE International Symposium on Circuits and Systems*, (Geneva, Switzerland), 2000.

[15] J. L. R. Marrero, G. C. Verghese, R. Santos, and S. H. Isabelle, "Computations of averages under chaos," in *Nonlinear Phenomena in Power Electronics* (S. Banerjee and G. C. Verghese, eds.), IEEE Press, 2001.

Next Generation Power-Electronic Systems

Sudip K. Mazumder
Power Electronics Research Center
Department of Electrical and Computer Engineering, University of Ilinois
1020 SEO, Mail Code: 154, 851 South Morgan Street, Chicago, Illinois: 60607-7053, USA
Email: mazumder@ece.uic.edu

Invited Paper

Abstract

Power electronics is an area of enormous potential and growing importance. It already has or will have impact on almost every conceivable energy- and power-based industry and applications. The focus of this paper is on distributed power electronic systems (DPS), which is an emerging concept in power electronics. It is widely believed that, DPS will enable the transition of power-electronic designs from a modular to a system level in a cost-effective, re-liable, and efficient manner. This paper illustrates the concept of DPS using various applications and briefly outline some of the challenges in this field.

Keywords–Distributed power-electronic systems, power electronics building block, design, analysis, system integration.

INTRODUCTION

Utility restructuring, realization of the impending energy crisis, drive for improved harmonic standards, public environmental policy, need for re-liable and cost effective power-distribution systems for applications ranging from commercial and warfare aircrafts and ships to telecommunication power supplies to motor drives, and technological revolution are providing the impetus for distributed power-electronic systems (DPS) to become an important energy option in the coming years [1-17].

For example, with the growing need to deliver more power to mainframe, personal, and super computers at very low voltages and high currents, telecommunication power-supply companies are faced with a daunting task. Increasing the output power of the traditional centralized, stand-alone power supplies by increasing the input current, results in significant volt-age drops across the power switches and significant increase in their current stresses and switching losses. As such regulating the low output voltage at a high efficiency is not possible. A lower efficiency leads to a bigger heat sink. This is because a heat sink, which is connected to power switches, has to dissipate more heat due to increased switching losses. The size of a power conditioner is directly related to the size of its heat sink and hence, if the size of the heat sink increases, so will the size, weight, and cost of the power converter. Furthermore, because the total out-put power in a traditional power system is fed by a single power conditioner, its failure leads to a com-plete shutdown of the overall system. As such the reliability of the overall system is very low. One approach to avoid this problem is to build an auxiliary or back-up power module. However, the size, cost, and efficiency of this module will be comparable to the main module.

An alternate and improved solution to the above problem is obtained using the concept of DPS. It leads to improved fault tolerance, reliability, reconfigurability, and efficiency (depending on the demand of power some of the modules can be turned on or o .), reduced production cycle time, and lower cost. We illustrate the concept of DPS with four illustrations in the following paragraphs. The basic idea can be extended to numerous other applications.

Figure 1 shows a conceptual DPS for a telecommunication power supply [11]. The architecture of the power systems evolves around a primary dc bus (regulated at 400 V) and a secondary dc bus (regulated at 48 V). The power to the primary dc bus is typically fed by boost converters, which interface to a multi-phase utility. The high voltage on the primary bus is stepped down using front-end converters and their output is connected to the

secondary dc bus. The secondary bus serves as the source of power for all the loads. Figure 1 also shows that the front-end convert-ers are connected to a current-sharing bus. This bus enables the even distribution of load power among the N modules. The overall power supply is built using a modular building-block concept, which eliminates the need for a conventional centralized and bulky power supply.

Figure 2 shows a simplified Power Electronics Building Block (PEBB) based shipboard dc DPS [4-6]. The heart of the large-scale power-electronic system is a high-voltage (800 V) distributed dc bus to which various high-power source and sink (load) converters are connected. In Figure 1, the source converters are standalone and parallel bi-directional boost converters, which interface three-phase generators to the dc bus. The load converters are standalone dc-dc and standalone and parallel multi-phase dc-ac converters. Typical loads for the system could include motors, a secondary utility bus, pulsating loads, and nonlinear loads like uninterruptable power supplies (UPS). Comparing Figures 1 and 2, we observe that although the overall architectures of the two power systems are not much different, the applications of these two systems are vastly different. The power system shown in Figure 1 deals with a much higher power and voltage as compared to the one shown in Figure 2.

Next, we illustrate in Figure 3 a baseline power distribution system for a typical next generation transport aircraft [10]. The power distribution is built around a dual 270V/500kW dc bus with an auxiliary power unit (APU) and a battery-backup auxiliary bus. The starter/generator units (500 kW each) generate three-phase ac power at 110V and 400Hz. The bi-directional power converters (BDC) between a starter/generator unit and the corresponding dc distribution bus tightly regulate the bus at 270V even under feedforward and feedback disturbances. Typical loads that the dc bus has to supply include electric actuators, environmental control systems, and negative-impedance avionics etc.

Figure 4 shows a cascaded multilevel converter, which can be used to control the output voltage and frequency from renewable energy sources like fuel cell or photovoltaics [14]. Furthermore, the multi-level converter can also control the real and reactive power flows from a utility-connected renewable energy source. The DPS in Figure 4 is modular, easier to package, and has fast dynamic response. In addition, since it has multilevels, the switching frequency of the converter can be reduced significantly. The concept of DPS is also a prime candidate for areas of multi-axis drives, electric vehicles, photo-voltaic applications, and flexible ac transmission systems (FACTS).

THRUST AREAS AND CHALLENGES

The key emphasis of DPS are on reliability, compactness, efficiency, and high-performance. There are various stages in the developmental process of a DPS and the overall procedure is iterative and not sequential. With all of the advantages of DPS come increasing complexities related to their design, integration, analysis, and control and communication. In the following sections, we briefly review some of the major challenges in these thrust areas.

A. Design

The first step in that process is the conception of a converter design, which meets the specifications and requirements of a customer. Such a synthesis can be a single converter or a group of converters and accessories; for example an application for a motor drive or a hybrid converter.

Although, there are numerous papers in the area of topology for power-electronic converters, this field is still viable and growing. The topology of the converter varies primarily with the power level and application. The main challenges in the design of a topology are related to solving some of the following problems:

- high cost of many commercial power supplies
- poor reliability of many existing power supplies
- switching and conduction loss of power devices
- stresses of power devices and passive components
- reduced effects of electromagnetic interference (EMI).

As such, some of the following areas have emerged as the front runners to e .ectively deal with one or more of the above problems:

- multilevel converters
- hybrid converters
- parallel and cascaded converters
- integrated and single-stage converters
- soft-switched and multi-resonant converters.

B. Analysis

The recent trend in power electronics is to move towards a multi-module system-level implementation; DPS is one such approach. Development of a proto-type based on the conceptual design for such complex systems could be costly and time consuming. As such, the current trend is to do an analysis of the virtual system on 2D and 3D computer software platforms to determine the feasibility of these power-electronic systems. Using such platforms, one can conduct, with high degree of accuracy, thermal, reliability, stability, or even EMI analyses.

While computer-based analyses give a designer enormous degree of freedom and possibilities, such analyses should be meaningful and realistic. The major

challenges facing the analyses of distributed multi-module systems are related to the following:

- accurate models
- better stability criteria
- robust and high-performance numerical algorithms
- ensure compatability between new and commercially available softwares so that designers can conduct analysis of a complete system on a macro and micro level.

C. Devices and System Integration

Based on the preliminary evaluation of the de-sign of a power-electronic system, a decision is made regarding its effectiveness and feasibility. If the out-come is positive, the next step in the development process is transforming a design at a circuit level to a system level via integration of power converters and accessories on a micro and a macro level. Selection of appropriate power devices, which is a big part of this transformation process, yields an overall reliable and efficient system. Some of the challenging areas where the power-electronics industry is working actively are as follows:

- development of power devices capable of withstanding higher voltage, current, and temperature stresses and having low switching and conduction losses
- development of ultra and super capacitors for energy storage
- integration of passive components, sensors and power devices, and motors and power stages
- effectively distributing intelligence and protection between power stage and supervisory controllers
- intelligent, fault-tolerant, and sensor-less controls for converters, and drives
- communication protocols and architectures for communication between modules.

REFERENCES

1. B. Carsten, "Distributed power system of the fu-ture utilizing high frequency converter", High Frequency Power Conversion Conference, 1987.
2. N. G. Hingorani, "FACTS: flexible ac transmission systems", Electric Power Research Institute Conference on Flexible AC Transmission System, 1990.
3. J. Burns, J. Riel, and A. DiBene, "An intelligent, fault tolerant, high power, distributed power system for massively parallel processing computers" IEEE Applied Power Electronics Conference, pp.795-800, 1994.
4. C. Petry, "Shipboard electrical power architecture" Control Technology Workshop, pp. 100-110, 1995.
5. G. S. Thandi, R. Zhang, K. Xing, F. C. Lee, and D. Boroyevich, "Modeling, control and stability analysis of a PEBB based dc DPS", IEEE Trans-actions on Power Delivery, vol. 14, no. 2, 1999, pp. 497-505.
6. K. Xing ,F.C.Lee, D.Boroyevich ,Z.Ye,and S.K. Mazumder, "Interleaved PWM with discontinuous space-vector modulation", IEEE Transactions on Power Electronics, vol. 14, no. 5, 1999, pp. 250-256.
7. M. Batham, A. Bining, K. Birkinshaw, D. Hat-field, and A.J.Soinski, Draft plan for research in environmentally preferred advanced generation technologies, Report on Public Interest Energy Research submitted to California Energy Commission, 1999.
8. R. B. Alderfer and T. J. Starrs, Making connections: Case studies of interconnection barriers and their impact on distributed power projects, NREL/SR-200-28053, National Renewable Energy Laboratory, Colorado, 2000.
9. P. Barbosa, F. C. Canales, and F. C. Lee, "A front-end distributed power system for high-power applications", Proceedings of Industry Applications Society, pp. 2546-2551, 2000.
10. S. Chandrasekaran, Optimization tools for sub-system design in aircraft power distribution systems, Ph.D. Dissertation, Department of Electrical and Computer Engineering, Virginia Polytechnic Institute and State University, Blacksburg, Virginia, 2000.
11. S. K. Mazumder, Nonlinear analysis and control of standalone, parallel dc-dc, and parallel multi-phase PWM converters, Doctoral Dissertation, Virginia Polytechnic Institute and State University, Blacksburg, Virginia, 2001.
12. S. K. Mazumder, A. H. Nayfeh, and D. Boroye-vich, "Nonlinear analysis of power-electronic converters: towards stable distributed-power systems", Invited Paper, International Conference on Energy, Automation, and Information Technology, to be held at the Indian Institute of Technology, Kharagpur, December, 2001.
13. W. Bowman and C. Young, "Tools to design and evaluate the stability of highly complex distributed power architectures", Professional Seminar, IEEE Applied Power Electronics Conference, 2001.
14. L. M. Tolbert and F. Z. Peng, "Multilevel converters as a utility interface for renewable energy systems", Power Engineering Society Summer Meeting, pp. 1271-1274, 2000.
15. S. K. Mazumder, A. H. Nayfeh, and D. Boroye-vich, "Nonlinear dynamics and stability analysis of parallel dc-dc converters", IEEE Power Electronics Specialists Conference, 2001, pp. 1283-1288.
16. S. K. Mazumder, A.H. Nayfeh, and D. Boroyevich, "Robust control of parallel dc-dc buck converters by combing the concepts of integral-variable-structure- and multiple-sliding-surface control schemes", IEEE Transactions on Power Electronics, in press, to be published in January 2002.
17. S. K. Mazumder and K. Shenai, "Component reliability of a parallel dc-dc converter", To be presented at the Power Electronics Reliability Group meeting held at IBM, New York, 2001.

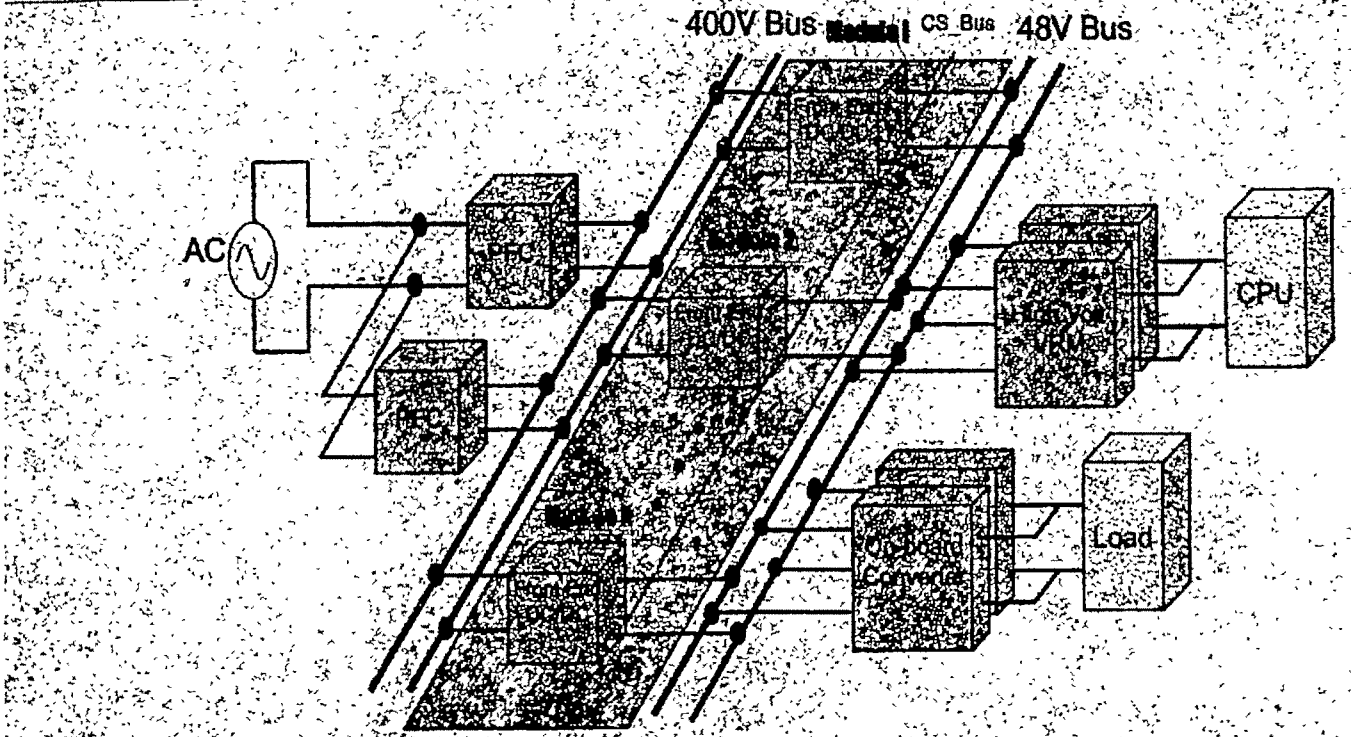

Fig. 1. A dc distributed power system for a telecommunication power supply.

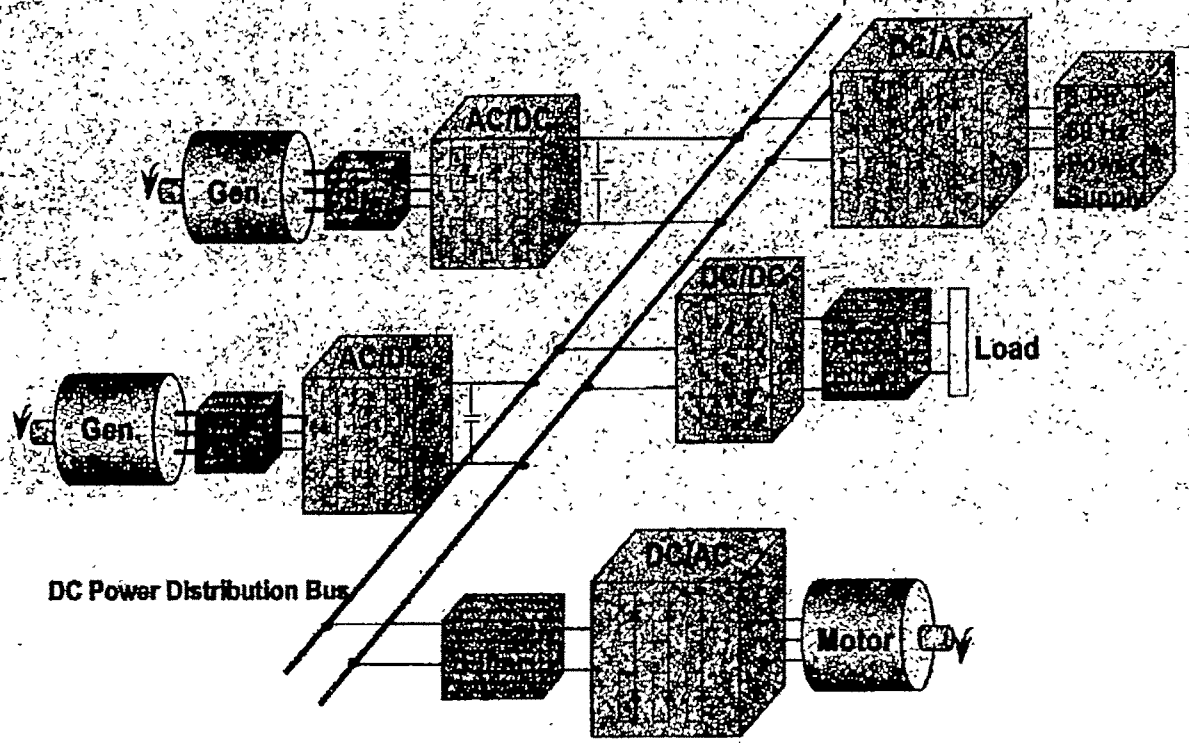

Fig. 2. A PEBB-based shipboard dc distributed power system.

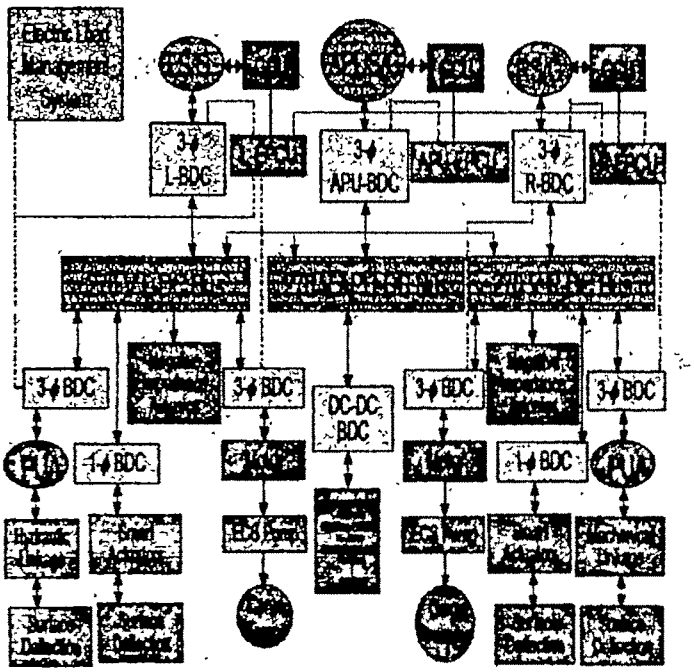

Fig. 3. A baseline power distribution system for a next generation transport aircraft.

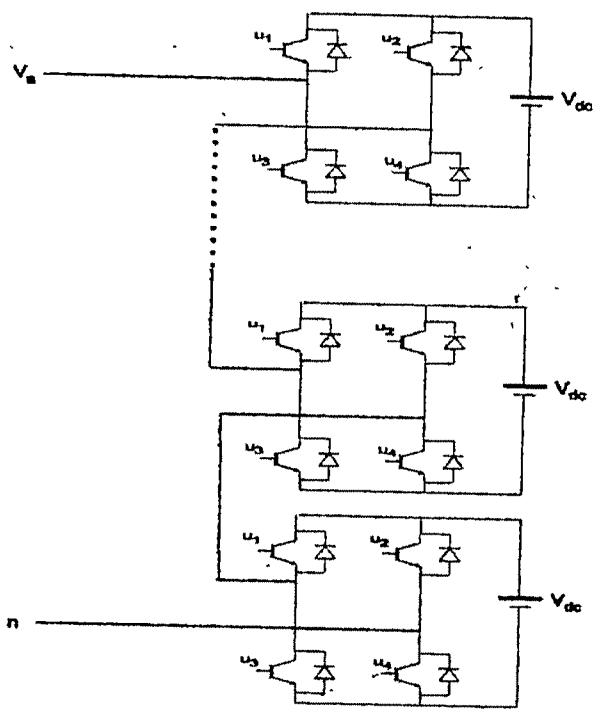

Fig. 4. A singl-phase structure of cascaded multilevel converter.

Design Compensation through Experimentation and Sensitivity Analysis in n-channel MOSFET based Controlled Power Circuits

Y. Singh* and **P. S. Bimbhra+**
* Dept. of Electrical & Electronics Engineering, T. I. E. T., Patiala
+ Dept. of Electrical & Electronics Engineering, T. I. E. T., Patiala
email: ysingh@tietp.ren.nic.in

Abstract

MOSFET is most important micro-electronic device in VLSI circuits because of it's high packing density, high yield and low power consumption. In this paper, several mathematical relationships and corresponding characteristics have been obtained for MOSFET and MOSFET based A.C.-to-D.C. power converters. For MOSFET, it has been shown that the threshold voltage exhibits non-linear temperature dependence and is less sensitive to temperature with increasing substrate bias. For MOSFET A.C.-to-D.C. power converter, output sensitivity has inverse non-linear variation with the device case temperature. The results have been obtained for it and they show that for case temperature (T_c), 0°C $\leq T_c \leq$ 25°C, the output sensitivity is constant ($\approx 4.5 \times 10^6$ %)and is independent of case temperature in this range. The case temperature range 0°C $\leq T_c \leq$ 25°C is recommended for device operation in precise application such as defence, space vehicles, navigational systems and sophisticated industrial drives.

Key words: Case temperature (T_c), surface potential (ψ_s),and temperature sensitivity ($S^M_{V_{DS}}$)

INTRODUCTION

MOSFETs are the most important micro-electronic device for memories & logic, VLSI circuits and high speed power conditioning in power circuits such as converters. The converters find their strategic application in variety of sophisticated low and high torque industrial drives, defence equipments, space and navigational systems. Due to change in operating temperature, the MOSFET parameters change resulting in in-accurate D.C. output from MOSFET A.C.-to-D.C. converter. Such variation in the output of converter spoils the performance of MOSFET based devices [1-3].

The temperature dependent study of MOSFET and it's devices is very topical and important as it determines the sensitivity of the parameters and enables optimization of process variables to obtain ultimate level of performance [9, 12] . In MOSFET, the temperature dependent parameters are the leakage current through drain / substrate junction, the carrier mobility and threshold voltage. Therefore it is very much essential to analyze and obtain relationships that describe the temperature dependence on these parameters. This study will determine the sensitivity of parameters and enabling optimization of process variables to obtain ultimate level of the device performance.

It has been reported in the past that MOSFET based power controlled devices (like MOSFET A.C.-to-D.C. converter) have failed to function reliably and accurately in the temperature variable environment. Thus there is need to make temperature vs. output sensitivity data available with the circuit designer so that beforehand compensation could be provided in the device at the design stage itself [4-6, 11]. In this paper, the authors have investigated the MOSFET and it's converter circuit. Certain novel inferences have been drawn. The relationship plots so obtained as shown in this paper prominently make out the suitable temperature ranges over which the device should be operated which in turn calls for suitable heat sink design and cooling methods.

PROCEDURE

In this paper, an effort has been made to develop simple and accurate model for MOSFET with as few parameters as possible. In defence, navigational systems and industrial drives, the MOSFET based systems are operated over wide temperature range (200 – 525°K). The advantages offered by the low temperature operation of MOSFETs have made it a subject of current interest at device, circuit and system level. Here MOSFET parameters dependency over the temperature has been investigated. The mathematical modeling of MOSFET has been carried out.

Further to investigate the temperature sensitivity (thermal stability) of MOSFET A.C.-to-D.C. converter, the converter mathematical modeling has been done under several assumptions and approximations. The MOSFET A.C.-to-D.C.converter output sensitivity $S_{V_{DS}}^{M}$ is obtained, where V_{DS} is drain-source voltage of MOSFET observed at various case temperatures during the device operation in open loop mode. The device details of MOSFET A.C.-to-D.C.converter which has been analysed here are as below,

MOSFET A.C.-to-D.C. converter

-Single crystal wafer 6H-SiC MOSFET with PC pad area 7, 85, 000 mil.^{2} with dia. of 1", device copper cladding thickness as 1.399".

-Thermal resistance " R_{thJA}" ≈ 72-78°C/W

-External cooling rate ≈ 50 ft./min.

-Tested MOSFET model no. IRFZ40 for switch characteristics

MATHEMATICAL ANALYSIS

The threshold voltage of MOSFET depends on a number of temperature sensitive parameters namely band gap (E_g), intrinsic carrier concentration (n_i), thermal potential and effective mass of hole and electron. The surface potential is derived here as under [7],

$$\psi_s = A + B \qquad .(1)$$

where

$$A = V_{GB} - V - V_{FB}$$

and

$$B = \gamma\sqrt{C + D_t} \;;\; C = (\Psi_s + V - V_t)$$

and $D = \{V_t \exp(\Psi_s - 2\varphi_b - V_{SB})/V_t\}$ where,

V_t : Thermal potential

φ_b : Bulk Fermi-potential

V: potential difference between the quasi-Fermi levels of electrons in the inversion layer and the source

γ: body effect coefficient

V_{SB}: source-to-bulk (substrate bias) voltage

V_{GB}: gate-to-bulk (substrate bias) voltage

V_{FB}: flat-band voltage

The parameter V_{FB} is derived as below,

$$V_{FB} = \Phi_{ms} - \frac{Q_{ox}}{C_{ox}} \qquad .(2)$$

where,

Φ_{ms}: metal to semi-conductor work function deifference

Q_{ox} : Fixed oxide charge density

C_{ox}: Gate oxide capacitance per unit area

Also Φ_{ms} is derived as under,

$$\Phi_{ms} = -(E_g/2) - \varphi_b \qquad .(3)$$

where,

E_g : Energy band gap

Figure 1-a shows the surface potential Ψ_s as a function of gate-to-substrate voltage V_{GS} for a given value of the MOSFET architecture. Under strong inversion, the threshold voltage can be re-written in the simple form as below [8],

$$V_T = \varphi_B + V_{FB} + \gamma\sqrt{\varphi_B + V_{SB}} \qquad (4)$$

Finding the temperature dependence of the MOSFET switch it is found that,

$$\frac{\partial V_T}{\partial T} = \frac{\partial V_{FB}}{\partial T} + R \qquad (5)$$

where

$$R = [1 + \frac{\gamma}{2\sqrt{(\varphi_B + V_{SB})}}]\frac{\partial \varphi_B}{\partial T}$$

Finally after certain suitable assumptions and approximations, the temperature dependence of threshold voltage is obtained as,

$$\frac{\partial V_T}{\partial T} = \frac{\partial V_{FB}}{\partial T} + (S \times T) \qquad (6)$$

where,

$$S = 2.2 \times \{1 + \frac{\gamma}{2\sqrt{\varphi_B + V_{SB}}}\}$$

and

$$T = \{\frac{\partial \varphi_b}{\partial T} - \frac{k}{2q}(3 + \frac{E_g}{kT} - \frac{1}{k} \times \frac{\partial E_g}{\partial T})\}$$

and the surface potential at the condition

$\varphi_B = 2.2 \times \varphi_b$ is obtained as below [10],

$$\frac{\partial \varphi_B}{\partial T} = 2.2\{\frac{\varphi_b}{T} - \frac{k}{2q}(3 + \frac{E_g}{kT} - \frac{1}{k}\frac{\partial E_g}{\partial T})\}$$

For sensitivity analysis of open loop n-channel MOSFET A.C.-to-D.C. converter after several mathematical derivations and substitutions, finally the below mentioned relationship is obtained,

$$\left| S^{M}_{V_{DS}} \right| = \frac{V_{DS}}{\sqrt{\{V_{DS}^2 + (5212.9 \times 10^4)^2\}}} \qquad (7)$$

where $M = \frac{V_o(s)}{V_i(s)}$ is the ratio of Laplace transformed output voltage V_o (s) (DC voltage) to Laplace transformed input voltage V_i (s) (AC voltage) of MOSFET A.C.-to-D.C. converter, and V_{DS} is drain-source voltage of MOSFET.

The relationship as obtained in eqn. 7 forms the basis for obtaining thermal stability characteristics of MOSFET A.C.-to-D.C. converter (as shown in fig. 2).

RESULTS AND DISCUSSION

Figure 2 shows the thermal stability characteristics of open loop n-channel MOSFET converter sensitivity after obtaining the values from equation 7. Figure 1 contains the plots of temperature dependence of surface potential and threshold voltage for a given structural parameters of the n-channel MOSFET. It has been inferred that the threshold voltage becomes progressively less sensitive with increasing substrate bias. The threshold voltage exhibits inverse non-linear temperature dependence.

Figure 2 shows that the output sensitivity of MOSFET A.C.-to-D.C. converter which has inverse non-linear variation with the device case temperature. The range 0°C $\leq T_c \leq$ 25°C is recommended for device operation in precise applications when temperature variation is same as considered over here. In this case the thermal resistance R_{thJA} (°C / W) of MOSFET is (≈) 72-78 °C / W. It has been calculated that it requires external cooling at the rate of (≈) 50 ft. / min.. Further, size of the device has to negotiated with heat sink design. As shown in figure 2, at low temperature ranges of T_c (case temperature) output sensitivity is high.

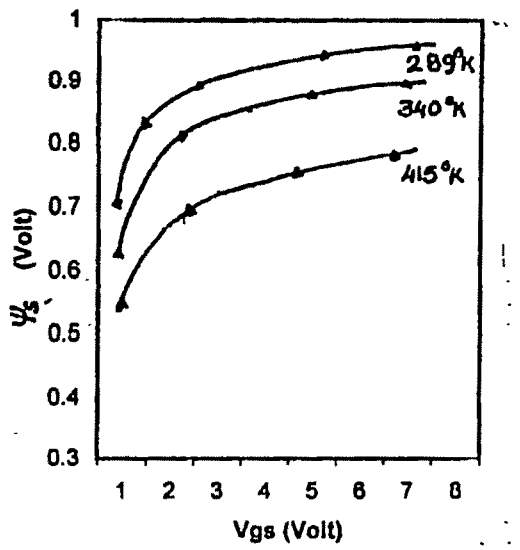

Fig. 1-a: Surface potential vs. gate- to- substrate potential at varying operating temperatures

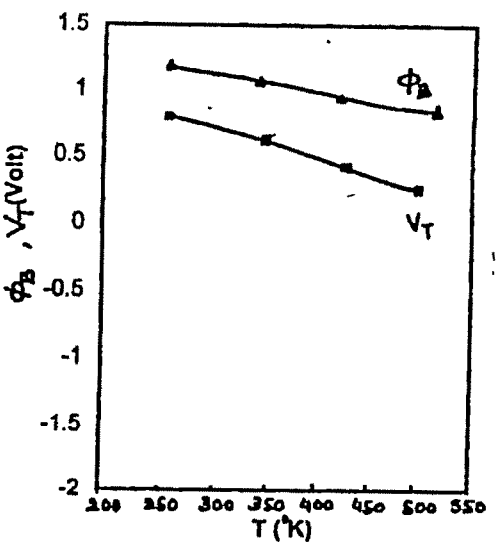

Fig. 1-b: Characteristics of temperature dependence for surface potential at strong inversion and threshold

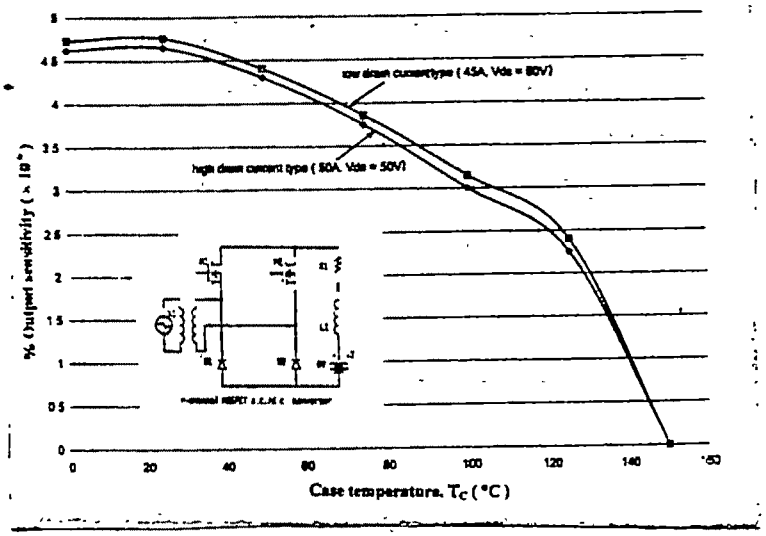

Fig. 2: Output sensitivity (%) vs. case temperature in single crystal wafer 6H-SiC MOSFET A.C.-to-D.C. converter in open loop

CONCLUSION

It can be concluded for the result data as shown in fig. 1, the threshold voltage decreases monotonically with temperature mainly due to decrease in the Fermi potential. The threshold voltage has linear temperature dependence and becomes progressively less sensitive to temperature with increasing substrate bias.

The single crystal wafer 6H-SiC MOSFET open loop converter provides thermally stable output in the range $0°C \leq T_o \leq 25°C$. The single crystal wafer of SiC, one inch in diameter are currently available and it is expected that large diameters will be available in the near future. The large diameters of semi-conductors limit the thermal resistance to a low value thus providing a better thermal stability in device operations. The range of case temperatures (T_o)as discussed above provide best thermal stability for MOSFET device which operated at an 1100V (at room temperature) with a breakdown of 460V.

Further linear control ranges have been determined for both type of converter devices for precise applications. The device performance can be constantly monitored with the help of data acquisition devices and controlled accordingly for linear and non-linear output dependencies w.r.t. switch parameters for the data as obtained in this paper.

Based on the above inferences and result data, beforehand compensation can be provided during the circuit design stage for the temperature dependent MOSFET parameters variation and it's reflection on the output of it's devices for higher accuracy of operations.

REFERENCES

1. J. Nishizawe, " Junction Field – Effect Devices", Semiconductor Devices for Power Conditioning, Rolland Sittig and P. Roggwiller (eds.) Plenum, New York, pp. 241-270, 1982
2. S. Clemente, B. R. Pelly and R. Uttonsha, "Current Ratings, Safe Operating Area and High Frequency Switching Performance of Power HEXFETs", Int. Rectrfier Appl. Note AN-949a (1984)
3. S. E. Laux, "Techniques for Small Signal Analysis of Semiconductor Devices", IEEE Trans. On Electron Devices, vol. E32, pp. 2028-2037, Oct., 1985
4. M. Lundstrom, "Fundamental of Carrier Transport ", vol. X, Modular Series on Solid State Devices, Reading, MA: Addison-Wesley, 1990
5. P. Habas, "A Physics based Analytical MOSFET Model with Accurate Field Dependent Mobility", Solid State Electronics, pp. 923-933, 1990
6. M. Bhatnagar, and B. J. Baliga, "Comparison of 6H-SiC, 3C-SiC and So for Power Devices" , IEEE Trans. On Electron Devices, vol. 40, No. 3, pp. 645-655, March 1993
7. N. Arora, "MOSFET Models for VLSI Circuit Simulation: Theory and Practice", New York: Springer-Verlag, pp. 210-219, 1993
8. S. Biesemans, S. Kubicek, and K. De. Meyer, "Analytical Calculation of a Figure of Merit for Novel MOSFET Architecture for the sub-0.25μm range" Tech. Dig. NUPAD V, pp. 11014, 1994
9. J. Burm, W. J. Schaff, L. F. Eastman, H. Amnao, and I. Akasaki, "75 A GaN Channel Modulation Doped Field Effect Transistors" , Applied Physics Lett., vol. 68, pp. 2849-2851, May 13, 1996
10. K. C. Liu, S. K. Ray, S. K. Oswal, and S. K. Banerjee, "A Deep sub-micron Si 1-x Gex Vertical P MOSFET Fabricated by Ge Ion Implementation" , IEEE Electron Devices Lett., vol. 19, pp. 13-15, Jan. 1998
11. K. De. Meyer, M. Caymax, N. Collaert, R. Loo, and P. Verheyen, "The Vertical Hetero-Junction MOSFET", Thin Solid Films, pp.299-305, Dec., 1998
12. Y. Wad, and M. Tamizawa, "Drain Avalanche Breakdown in Gallium Arsenide MOSFETs", IEEE Trans. On Electron Devices, vol.35, pp. 1765-1770, Nov., 1998

Implementation Of An Active Load Sharing Scheme For AC – DC Converter System

B. K. Dubey[2] and S. B. L. Saxena[1]
[1]Department of Electrical Engineering,
Regional Institute of Technology, Jamshedpur 831014, India
[2]NELCO Ltd

Abstract

In this work an analysis of converter system with load sharing concept has been presented to ensure uniform distribution of stress(load) and to enhance modularity to improve reliability of the proposed system. The converter architecture has achieved the desirable characteristics of individual converter to share the load current equally and stably.Distributed load sharing with master-slave scheme has been adopted here. The design and development of a practical eight-cell AC/DC Converter system has been done here. The results have been verified experimentally, on a superscalerRISC based controller.

Key words- Active load-sharing, i960, Super scalar, RISC (Reduced Instruction Set Computer), Master-slave, Cell (Single Converter), PLC (Programmable Logic Controller), CT(current Transformer).

Introduction

AC/DC Converters with load sharing provide advantages mainly in increased power processing capability, improved reliability due to more even distribution of the stresses and enhanced availability from the fault tolerance consideration. To ensure uniform distribution of stresses, the total load current should be shared appropriately among the converters. Variations of active current-sharing schemes include "democratic" scheme, where modules share currents in proportion to their ratings and the "master-slave" approach has been adopted in this work. In this scheme, converter carrying the highest value of current becomes the master and the other converters are regulated to relative output currents as that of the master converter and behave as slave.

The current-sharing behavior of the system is largely dependent on the manner in which the individual converters are controlled . Many converter systems use some form of global control in which a single, possibly redundant controller, directly regulates the load balance among the individual converter. However, to enhance modularity and improve reliability, it is more desirable to have the load-sharing control distribution among the converters. To implement a distributed load-sharing scheme, only a very limited amount of information needs to be shared among the individual cells, viz, average cell output current, rms cell current, weighted cell current stress, highest cell current and current of master cell for the master-slave mode of operation.

Load-Sharing information is generally shared and generated over a single interconnection between the converter cells. The interconnection system is designed so that when each cell generates a signal proportional to its output, the voltage on the interconnection bus is either the average or maximum of the individual signals. In the system under consideration, PLC has been used to monitor and share the required Load-Sharing information.

For a linear model it is necessary to assume constant field operation [12], as the field time constant is relatively much larger than that of armature time constant. If iron saturation, flux cross coupling and eddy-current damping are not considered, the DC machine may be represented by a set of analytic equations [10]. If the field is considered to be constant, then these equations are simple linear equations , which are used for the analysis under the load sharing scheme .

Analysis and design techniques for single converter are well established and extensively discussed in literature [10,11], but limited literature is available for the analysis of a system of converters. Analysis in [1] refering DC / DC converters has been successfully adopted here to analyze the present system .

The developed control algorithm here is very simple where a considerable fraction of processor time is available to perform on-line health monitoring role, thereby providing fail-safe functions in addition to the control strategy. The efficacy of the control algorithm has been tested on i960 super scalar RISC based controller.

The overall System description

The AC/DC converter based speed regulator system for a high-response reversible application may be designed with different configurations. The choice of the configuration depends upon operational readiness and availability, performance requirements and economic considerations. Circulating-current free systems i.e. a dual converter without circulating current two single three-phase double-way bridges are connected in an antiparallel mode is of practical importance in present work, used as a reversible armature power supply. It provides four-quadrant operation, motoring or generating in either direction of rotation. The present scheme incorporates direct digital control of the firing angle of the thyristors in the converters.

In the present microcomputer based control scheme, there is flexibility to change the software for different performance characteristics or to add extra control feature. It can also perform various desirable function: on/off of main power supply, start/stop of the drive, speed control, current control, monitoring the control variables, initiating protection and trip circuit, diagnostics for built-in-fault finding, and communication with a supervisory central computer.

The secondary voltage of the power transformer is chosen such that the converter voltage at a firing angle $\alpha=30^0$ is equals the rated voltage of the motor. Speed measurement is obtained using a digital tachogenerator with low ripple content.

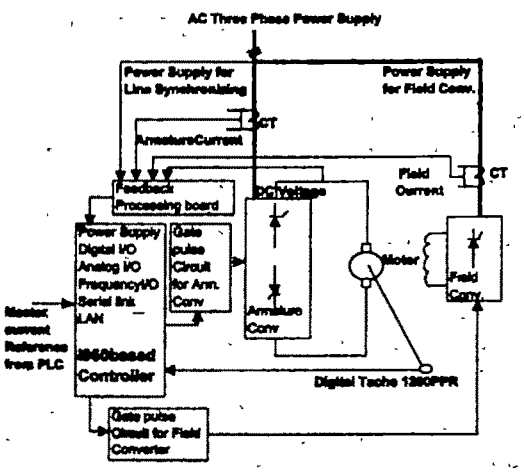

Fig.1 Schematic diagram of Four-quadrant DC drive (controlled by the Active load sharing scheme).

A schematic block diagram for hardware implementation of present work has been depicted in Fig.1. Both the armature and field currents are fed back into the controller. The current signal is fed into the controller through the feedback processing board, which converts the CT (with burden resistance across it) signal to the appropriate level. Additional health monitoring signals can be fed back, if necessary.

A Phase-lock signal is taken from the AC voltage source to the thyristor bridge to ensure that thyristor firing is synchronized with the mains frequency and a zero crossing detection circuit is used in the controller. All these feedback signals are converted into digital form (bit level) and memory mapped into the controller in the form of a system status register. When the status register is loaded into the condition code register of the processor, the complete control system is effectively monitored using a series of simple conditional branch instructions .The controller performs dual functions of gate-pulse generator and logic circuit. Gate pulse circuit provides the necessary isolation and produces gate pulses of required magnitude and duration.

Basic Control strategy

The basic control strategy adopted here are shown in Fig.2(a,b) . Active load sharing loop included in the system in addition to the conventional cascaded current loop and outer speed loop, Fig.2 (a). The choice between democratic or master-slave scheme is dependent on the choice of system designer on the basis of process requirement. Generally in a practical system there is a tendency for voltage overshoot to occur in response to a step input, this is prevented by imposing rate-of-change-of-speed (Ramp referencing block) reference limits. This Ramp reference block avoid the possibility of a large step demand. Current reference for the present master-slave scheme has been generated in the PLC, based on the logic as shown in Fig.3

Analysis and Modeling of the system

The present mathematical model has bee on the basis of [13] [15] [16].

Modeling of motor - A simplified model has been used to meet the requirement of the system design based on these assumptions-

1. The frictional torque is proportional to angular velocity and the friction [static] is negligible.
2. The voltage drop across brush is negligible,
3. The armature reaction is neglected, and
4. The Inductance & Resistance is constant.

The performance of dc motor with a constant field and armature voltage control is given as below-

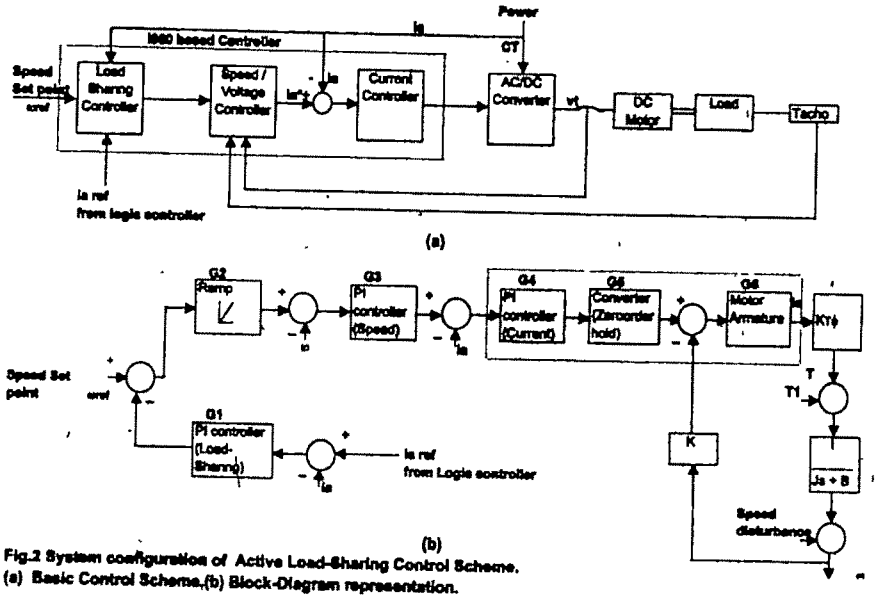

Fig.2 System configuration of Active Load-Sharing Control Scheme.
(a) Basic Control Scheme,(b) Block-Diagram representation.

$$V(i_a)=E+Ri_a+L\, di_a/dt \quad (1)$$

$$T= J\, d\omega/dt + T_l \quad (2)$$

$$E=K\omega \quad (3) \quad \text{and}$$

$$T=K_T i_a \quad (4)$$

The following state equation can be obtained

$$di_a/dt = -i_aR/L - Ke\omega/L + V(i_a)/L \quad (5)$$

$$d\omega/dt = K_T i_a/J - T_l/J \quad (6)$$

Where,
V;Converter output voltage , E;Back emf ,ia;Armature Current , T;Torque developed , T_l,Load Torque including friction , Ka;Motor Armature circuit constant, K=Kaϕ;Voltage constant for a given excitation(field), R;Armature resistance ,L;Armature inductance .
In terms of block-diagram the model has represented in Fig.2 (b) as a part of the system.

Modeling of Thyristor (AC/DC) Converter – While considering for the operation of converter we have to keep few points in mind. (1)Converter reverses the flow of power by reversal of voltage where as dc machine does so by reversal of current (2)The machine EMF is steady on the other hand the converter out put voltage is pulsating in nature . This causes problems associated with discontinuous current flow like poor speed regulation ; nonlinear transfer characteristic of the rectifier , and poor transient response . (3)Rectifier firing is a discrete process. As soon as there is any requirement to change the firing angle has been asserted the rectifier responded after a certain time which is the time interval between two consecutive firing instants (for a 50Hz three phase fully controlled rectifier it is 1/(50*12)=1.67ms).

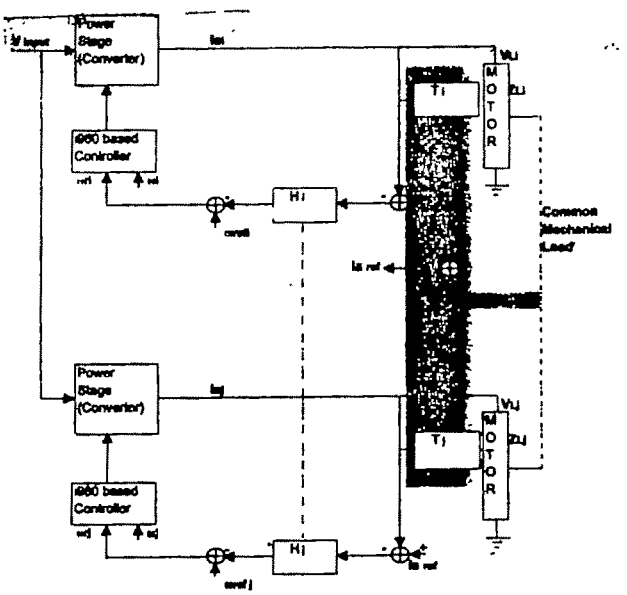

*For Democratic Current-Sharing Ti = - - - - - =Tj=1/n
*For Master-Slave Current-Sharing Ti =1 (For Master)
and for all others Ti= are zero .

Fig.3 Block Diagram of n no. of converters with active load sharing .

For conventional operation of three-phase rectifiers under continuous conduction, converter output voltage

$$V=(3V_{max}/\pi)\,Cos\alpha$$

Let us generate a reference timing wave $V_r=V_{rm}Cos\alpha$,and a firing pulse is produced when control voltage is equal to reference wave i.e. $V_c=V_r$, so $V_c=V_{rm}Cos\alpha$, since the firing angle α is an inverse cosine function of the control voltage Vc, hence the scheme is known as inverse cosine firing scheme .To ensure the firing of thyristors, Vc should always be less than Vrmax and α_{max} should be$(180-\delta)$,where δ is a positive angle required for the commutation.

Thyristor rectifier can be modeled as a zero order hold with transfer function $G5(s)=(1-e^{-sTs})/s$.

Discontinuous current model - The magnitude of the converter output current at which discontinuous current range start depends primarily as the motor armature inductance and the firing angle α (load) . Enough literature is available for the analysis of discontinuous current .For the present analysis of the system under consideration , it can be assumed that converters operate in the continuous current mode since these is always adequate load on the motor at steady state condition .

Stability analysis,Fast and optimum response

In the present work, the first approach is to determine system configuration, then to find out the stability boundary and afterwards to adjust regulatable parameters for fast response and optimum regulation. Since the stability of the system is of highest priority as compared to either fast response or optimum regulation. For the active load like DC motor the change in current is much faster than the armature voltage and speed, hence for the optimum process of the current control loop, the back emf and speed variation may be neglected.

For the analysis standard Z-transform is used since a digital computer is used to implement a control strategy, a calculation must be performed to calculate the new value of the controller output at every Ts (sampling interval) units of time. The computation of the controller output is made at each sampling instant and its value is held at a constant value until the next sampling instant occurs, during this time a new controller output is computed and held. This process of computation and holding is repeated at every T units of time

The inner loop i.e. Armature current loop Fig.2-b may be approximated as a current source supplying a load.

From which the Transfer function for inner (armature current) loop in the s-domain is given below;

$$\frac{I_a(s)}{I_r(s)} = \frac{G_4(s)\,G_5(s)\,G_6(s)}{1+G_4(s)\,G_5(s)\,G_6(s)} \qquad (7)$$

Stability analysis using Z-transform is as ;

$$\frac{I_a(z)}{I_r(z)} = \frac{G_4(z)\,G_5(z)\,G_6(z)}{1+G_4(z)\,G_5(z)\,G_6(z)} \qquad (8)$$

The expression of $G_4(z)\,G_5(z)\,G_6(z)$ is now substituting into the Transfer function as

$$G_4(z) = K_{p4}+K_{i4}(z/z-1) \qquad (9)$$

$$G_5\,G_6(z) = Z\left[\frac{1-e^{-sTs}}{S}\;\frac{K_{a1}}{1+sTa}\right] = (1-a)K_{a1}/(z-a) \qquad (10)$$

For a step response, i.e. $I_r(z)=z/(z-1)$ the characteristic equation is given by

$$F(z)=(z-1)(z-a)+[(z-1)K_{p4}+zK_{i4}](1-a)K_{a1} \qquad (11)$$

Hence the boundary conditions for the stability (Jury's criteria) of the system is,

$$F(1)>0,\ F(0)>-1 \text{ and } F(-1)>0 \qquad (12)$$

Hence the boundary condition is determined as

$$2K_{p4}+K_{i4}=2(1+a)/(1-a)K_{a1} \qquad (13)$$

For any change in the set point the new steady state value of the armature current is to achieve within one sampling interval then the current-time response is optimum.

From the restrictions imposed by fast and optimum response conditions the regulatable parameters is found as

$$K_{p4}=a/(1-a)K_{a1} \text{ and } K_{i4}=1/K_{a1} \qquad (14)$$

Calculated Values of $K_{p4}=0.4625$, $K_{i4}=0.0556$

Where,

Ir=Current reference, Ts=Sampling interval , Ta=Electrical time constant(L/R), K_{a1}=(Rated voltage / Rated current) / R and $a=e^{-Ts/Ta}$

The control system being represented as a pure delay element with delays T equal to the sampling interval. The system output will then follow the input within one interval. Since for a practical system there is normally more than one regulatable parameters hence the restrictive conditions on the fast response is not unique.

For speed loop there can never be a fast response for a large speed increment due to the load inertia and hence it is not necessary to implement fast and optimum response restrictions. The tuning of both the outer loop i.e. speed loop and Load sharing loop has been made by Ziegler-Nichols rule and has been further improved by

Ziegler-Nichols rule and has been further improved by applying step input and changing the parameters for the expected response. In practical industrial systems the torque disturbance is often encountered and it is generally less than the torque, which the system can deliver at rated current condition. The outer speed loop maintains the output speed close to the set point. Whenever there is a change in the torque demand the inner armature current loop gives a fast response and helps to keep the output speed constant. The outermost load sharing loop will constantly monitor the difference between reference current and the actual current drawn by the system and modified the set point itself accordingly.

The response of one drive is shown in Fig.4 and it can be concluded that presented scheme has increased the reliability of the system since Armature voltage is steady for fixed setpoint as well as Load-Sharing loop is consistently working for current equalization .

The experimental results as in Fig.5 shows the equal and steady current has been drawn by the drives control by the presented scheme.

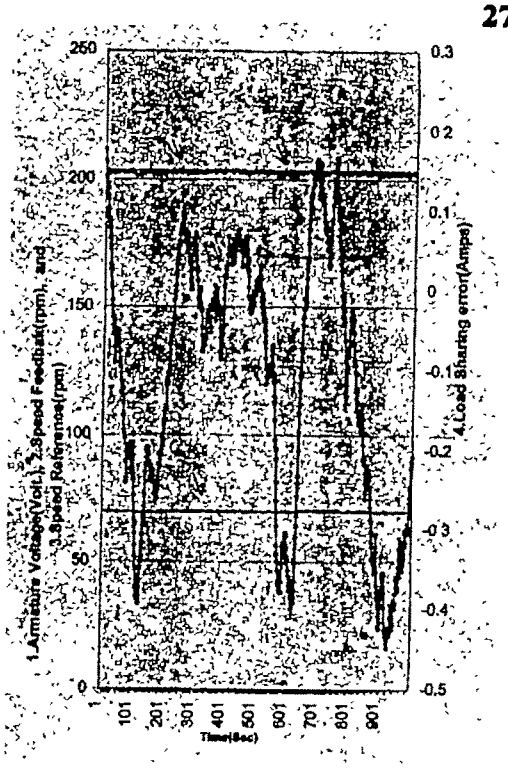

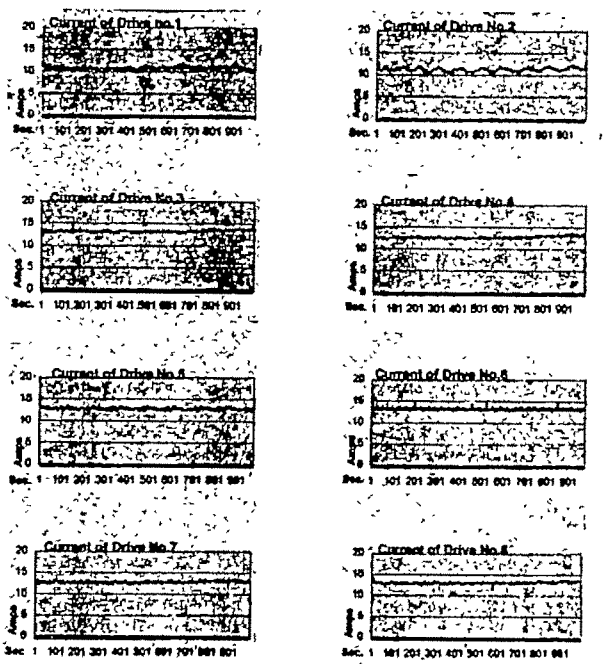
Current of Drive no.1
Current of Drive No.2
Current of Drive No.3
Current of Drive No.4
Current of Drive No.5
Current of Drive No.6
Current of Drive No.7
Current of Drive No.8

Fig.5 Experimental Results of Load-Sharing scheme implemented on eight no.of same rating Motor and converter system.

Conclusion

Drive calibration drift, different mechanical as well electrical constraints are the major factors for unequal currents / instability ,even with the same set point for all the drives . By equalizing the currents (equal load sharing) of all the drives driving a common mechanical load, the system reliability and stability can be improved.

Specifications and Ratings of major components used in present work : Motor=7.5KW , Armature Voltage=210VDC, Armature Amps=41ADC , RPM=670RPM , Field Volts=230VDC , Field Amps=2.2ADC , Armature CT=45:1 with burden resistance of 0.7Ω, Field CT=5:1 with burden resistance of 2Ω.

Acknowledgements

The authors wish to thank M/s NELCO Ltd. and concerned authourity of R.I.T.-Jamshedpur for providing necessary infra stucture to carry out the work.

References:

[1]"Analysis and control Design of paralleled DC/DC converter with current sharing"
-V.Joseph Thottuvelli and George C.Verghese.
IEEE Transactions on Power Electronics, Vol.13, No.4, July'1998
[2]"Frequency-Based Current-sharing Techniques for Paralleled Power converters"
-D J Perreault, R L Selders and J.G.Kassakian.
IEEE Transactions on Power Electronics, Vol.13, No.4, July'1998.
[3] "Control of Parallel Connected Inverters in Standalone ac Supply Systems"
-Mukul C.Chandorkar , Deepakraj M. Divan and Rambabu Adapa.
IEEE Transaction on Industry Applications, Vol IA-29, No 1, Jan/Feb'1993.
[4] "Parallel operation of bridge rectifiers without an interbridge reactor"
-J.K Hall , J.G.Kettleborough and A B.M.J Razak
IEE Proceddings , Vol.137 , Pt.B , No.2 ,March 1990
[5] "Computer-Aided Design of Electrical Machines for Variable Speed Applications"
-R.Krishnan , Aravind S.Bharadwaj and Peter N Materu.

IEEE Transaction on Industrial Electronics, Vol.35, No.4, Nov.'1988
[6]"Influence of Feedback Filter on system stability Area in Digitally contolled Thyristor converters"
-Fang L.Luo and Ronald J.Hill.
IEEE Transaction on Industry Applications, Vol.IA-22, No.1, Jan/Feb'1986.
[7]"Fast response and optimum regulation in digitally controlled Thyristor converters"
-Fong L.Luo and Ronald J.Hill.
IEEE Transaction on Industry Applications, Vol.IA-22, Jan/Feb'1986.
[8] "Analog and digital Speed Control of DC Drives using Proportional-Integral and Integral-Proportional Control Techniques"
-Pradeep K.Nandam and Paresh.C.Sen .
IEEE Transaction on Industrial Electronics, Vol.IE-34, No.2,May'1987
[9] "Digital controller for thyristor current source"
-F.L.Luo, R.D.Jackson and R.J.Hill
IEE Proceddings , Vol.132 , Pt.B , No.1 ,Jan 1985.
[10] "Response improvements in industrial DC drives derived from optimal analysis "
-B.J.Cardwell and C.J.Goodman
IEE Proceddings , Vol.131 , Pt.B , No.3 ,May 1984
[11] "Stability Analysis , Design ,and Simulation of a Closed-Loop Converter-Controlled DC Drive"
-P.B.Anajaneyulu ,S.S.Prabhu and G.K.Dubey
IEEE Transaction on Industrial Electronics, Vol.IE-31, No.2,May'1984
** Comment on"Stability Analysis , Design ,and Simulation of a Closed-Loop Converter-Controlled DC Drive"
-Philip S.M.Chin
IEEE Transaction on Industrial Electronics, Vol.IE-35, No.2,May'1988
[12] "A simple digital control scheme for a DC motor"
-B.A.White ,R.T.Lipczynski and A.R.Daniels
IEE Proceddings , Vol.130 , Pt.B, No.2, March 1983
[13] "Mathematical model and electric-circuit simulation of DC machines"
-R.S.Ramshaw and G.Xie
IEE Proceddings , Vol.130 , Pt.B , No.3 , May 1984
[14] "Automatic armature and field control of d.c. series motors"
-M.H.Rashid
IEE Proceddings , Vol.128 , Pt.B , No.1 ,Jan 1981
**"Correspondence - Automatic armature and field control of d.c. series motors-M.H.Rashid"
-B.O.Pantic
IEE Proceddings , Vol.128 , Pt.B , No.6 , Nov 1981
[15] "A simple digital control scheme for a DC motor"
-B.A.White ,R.T.Lipczynski and A.R.Daniels
IEE Proceddings , Vol.130 , Pt.B, No.2 ,March 1983
[16] "Mathematical model and electric-circuit simulation of DC machines"
-R.S.Ramshaw and G.Xie
IEE Proceddings , Vol.130 , Pt.B , No.3 , May 1984

IGBT Based Chopper

A. Srinivasa Rao
Department of Electrical Engineering
GITAM, Visakhapatnam
E.Mail : asrao47@yahoo.com

Abstract

The present paper deals with design and fabrication of DC – DC chopper with Insulated Gate Bipolar Transistor (IGBT) as switching device. This is a promising alternative for high speed ground transport with battery operated vehicles. This gives eco friendly and pollution free operation . The chopper circuit is designed, fabricated and experimentation has been done using permanent magnet DC motor as a load.The wave forms corresponding to all the four quadrants were observed on CRO

Key words: Chopper, IGBT,DC Motor

INTRODUCTION

In the age of information technology Eco friendly operation of vehicles has become very much essential. The present tendency is towards the battery operated vehicles. For operating these vehicles the electrical power needs to be processed and controlled with precision. Prior to the advent of power semiconductor devices the control of power is done by rotary converters. However these occupy a lot of space and they are expensive also. With the tremendous growth of power semiconductor devices the processing of power came to reality. The motive for using power semiconductor devices is to increase conversion efficiency to a high value. The era of power electronic devices stared with the birth of SCR in 1957. However SCR has it's own disadvantages because of need of separate circuits for turning on and turning off. Then came the era of hybrid power devices like IGBTs. IGBT is a new development in the area of power MOSFET technology. It combines in to it the advantages of both MOSFET & BJT.

The present paper deals with design, fabrication and operation of a chopper using IGBTs.

POWER CONVERSION

A power converter acts as an interface which accepts electrical power from existing source and converts it in a controlled manner into suitable form compatible with particular load. In some power systems there is need to transform dc power from one dc voltage level to either higher or lower dc level. For example in a public transport system a 4000V dc overhead line may be source to drive 300V dc motor in a bus. In the other case, a 12V battery may have to drive a device rated at 120V dc. In ac the voltage step up or step down can easily be done with a transformer. But in dc it is not possible. For so many years this is done by using electromechanical energy converters. These were however expensive, bulky, noisy and inefficient besides having poor dynamic response and needs periodical maintenance. But with the advent of power semi conductor devices dc – dc power conversion came to a reality. By using power semiconductor devices the main advantage is energy conservation and pollution free operation. Energy conservation refers to more efficient use of electrical energy. High level of productivity and enhancement in product quality could also be achieved.

CHOPPER

A chopper can be considered as dc equivalent of an ac transformer with continuously variable turns ratio. Chopper convert unregulated dc voltage to a regulated dc voltage at a different level. Choppers are widely used in applications like traction motor control in electric automobiles, trolley cars, trucks, mine locomotives and switched mode power supplies. Chopper circuits are designed and fabricated using the knowledge of power electronics. The era of power electronics started with birth of SCR in 1950's. In the last five decades there was a tremendous evolution in power semi conductor devices which form heart of modern power electronics. Prior to the advent of hybrid power devices Silicon Controlled

Rectifiers (SCR) are widely used in the chopper circuits. An SCR is basically is a 4 layer 3 junction device. This device is triggered in to conduction by a current pulse of short duration to the gate. But once the device starts conducting gate loses control over the device. Hence extra circuitry is needed to turnoff the device. Basically it is a unidirectional device. It also needs protection circuits to limit the values of high di/dt and high dv/dt. Due to the advancements in power semiconductor technology there is birth of hybrid power devices and Insulated Gate Bipolar Transistor(IGBT) is one among them.

IGBT

It is basically a hybrid MOS – gated turnon/off bipolar transistor that combines attributes of MOSFET, BJT and Thyristor.The device has high input impedance of a MOSFET but BJT like conducting Characteristics. IGBT's are ideal switching devices exhibiting fast switching speed, low forward voltage aswellas large SOA

SINGLE QUADRANT CHOPPER

Figure 1 represents the circuit diagram of a single quadrant chopper.The single phase 230 V ac is stepped down to 24 ac then rectified and applied to 24 V PMDC motor. The switching is done by a single IGBT. When IGBT is turned on by applying gating signals, the supply voltage is applied to the load with terminal a positive. A diode is connected in antiparallel across the load. When IGBT is turned off by removing the gating signal, the load current flows through the load in same direction through diode. Here both load voltage and load current are positive indicating I quadrant operation.

FOUR QUADRANT CHOPPER

Figure 2 represents the circuit diagram of a four quadrant chopper. The four quadrant chopper can be operated in two ways.

i)Unipolar switching
ii)Bipolar switching

i)Unipolar voltage switching operation:

Here the output voltage swings either from 0 to $+V_{dc}$ or 0 to $-V_{dc}$ Suppose initially devices T_1 and T_4 are turned on the load voltage is $+V_{dc}$ and load current flows through load from a to b. the path of load current is from source through T_1, load, T_4 and back to source. The load current and load voltage both are positive indicating operation in first quadrant. When devices are turned off the load current becomes zero. As soon as the load current becomes zero the devices T_3 and T_2 are turned on. Now the load current flows in load from b to a. The voltage across load is $-V_{dc}$.This represents operation in 3 quadrant. In unipolar voltage switching devices in each leg are controlled independently of other leg.

ii)Bipolar voltage switching operation:

Here the output voltage swings in both directions ie from $+V_{dc}$ to $-V_{dc}$. In bipolar switching mode (T_1, T_4) (T_3, T_2) are treated as two switch pairs and each pair are turned ON and OFF simultaneously. Initially the devices T_1, T_4 are switched on simultaneously. The load voltage is $+V_{dc}$ with terminal a positive. The load current flows in the motor from a to b. Here both load voltage and load current are positive indicating operation of the chopper in the I quadrant. Now the switches T_1, T_4 are turned off. Due to load inductance current can not change direction instantaneously. So load current flows through D3, dc source and D2. The load voltage is now $-V_{dc}$ as load terminal b is connected to positive of the source. So here load current is positive but load voltage is negative. Therefore the power is negative i.e. the power is being feedback to the source from load. This indicates operation of chopper in fourth quadrant. As soon as load current reaches zero the devices T_3, T_2 are turned on simultaneously by applying gating signals. The load voltage is $-V_{dc}$ and current flows from b to a. The load voltage and load current both are negative indicating operation of chopper in 3 quadrant. If the devices are turned off by removing gating signals the load voltage is positive and load current is negative indicating operation of chopper in second quadrant. The output wave forms are shown in fig 3 to 6 for unipolar and bipolar operations.

GENERATION OF GATING SIGNALS

Gating signals for turning on the IGBT's are produced by comparing a triangular carrier wave with control voltage level in a comparator. The output of the comparator is then isolated and amplified before applying to the gate driver circuit. The block diagram is shown here.

A triangular wave generator can be formed by connecting an integrator to a square wave generator. The frequency of square wave and triangular wave are same. The input to the integrator is a square wave while output is triangular wave. This triangular wave is compared with the control voltage obtained from a unity gain voltage follower using the comparator.Two control voltage levels $+V_c$ and $-V_c$ could be obtained by adjusting the potentiometer.These pulses are isolated from control power supply by means of high speed opto couplers. The outputs from these optoisolators are given

to two gate driver circuits which finally generate the gating signals required for turning on IGBTs.

CONCLUSIONS

In the present paper an attempt has been made to understand the capabilities of new hybrid device IGBT as switching device. The chopper operation is studied and observed using PMDC Motor as a load. The author feels that the IGBT becomes switch of the future in promising applications like battery operated vehicles as it has built in turnoff mechanism.

ACKNOWLEDGEMENTS

The author expresses his gratitude to University Grants Commission(UGC) for providing necessary financial assistance for doing the project.

REFERENCES

1. B.J.Baliga " Modern power Devices" John Wiley & sons, 1987
2. G.Busatto et al " Comparative Analysis of power bipolar devices" 21st IEEE Annual conference on Power Electronics pp. 147-153

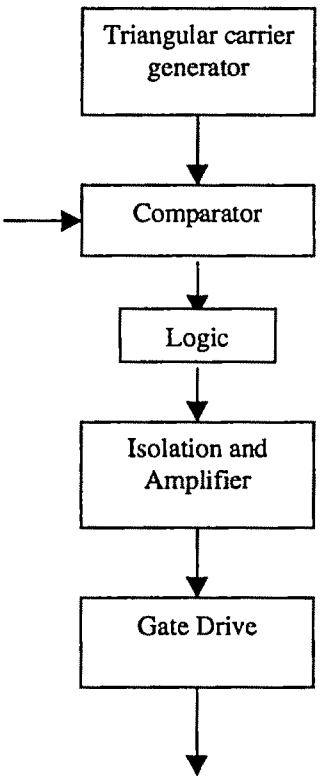

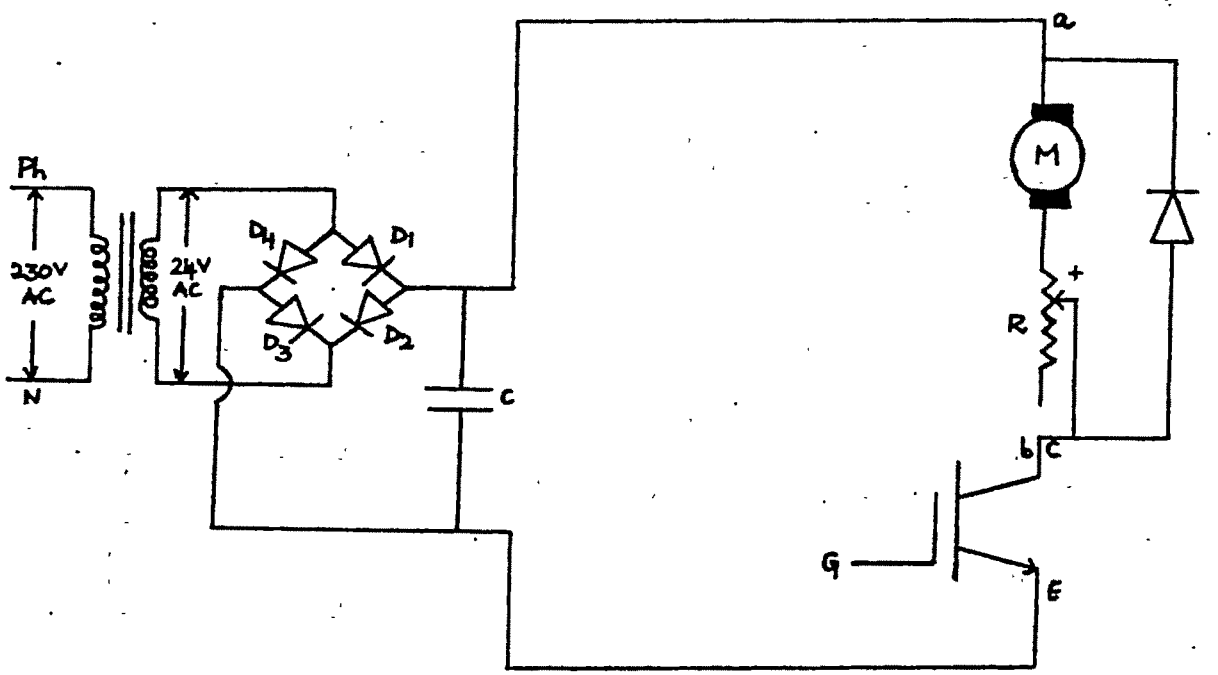
Ph
230V AC
N
24V AC
D4
D1
D3
D2
C
a
M
R
+
b
C
G
E

FIG. 1

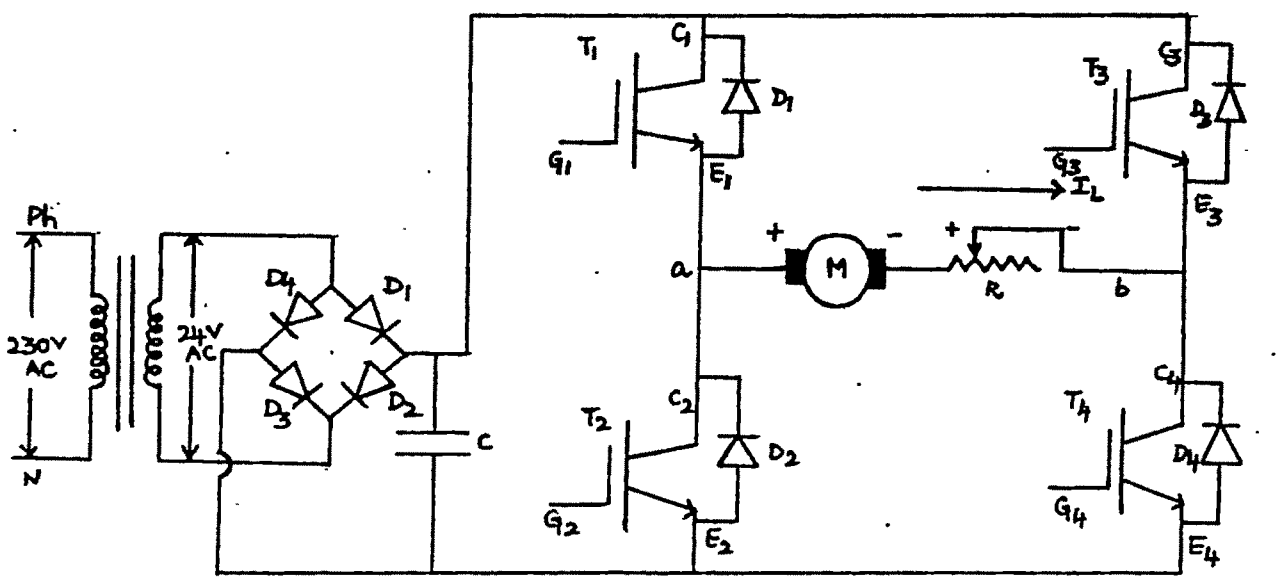
Ph
230V AC
N
24V AC
D4
D1
D3
D2
C
T1
C1
D1
G1
E1
T3
G3
D3
E3
IL
+
M
-
+
R
-
a
b
T2
C2
D2
G2
E2
T4
C4
D4
G4
E4

FIG. 2

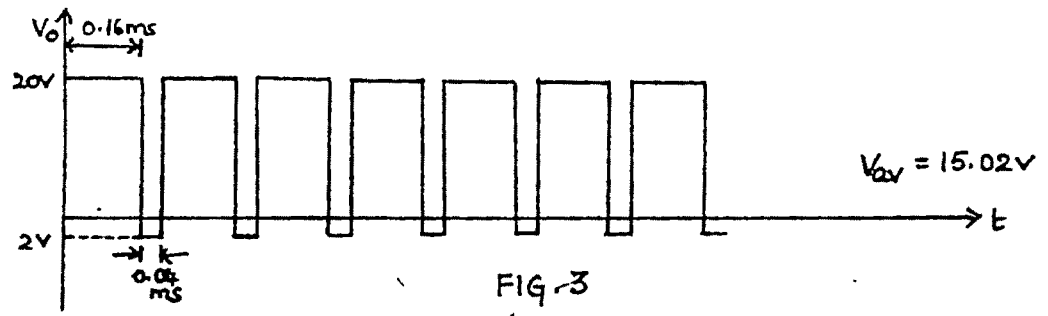

FIG-3

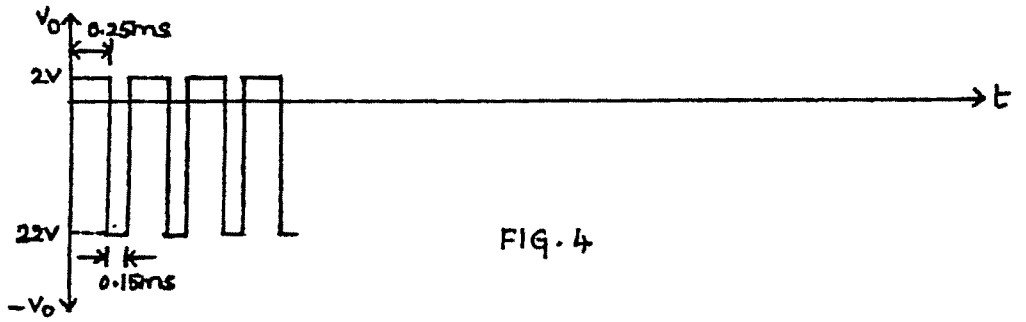

FIG. 4

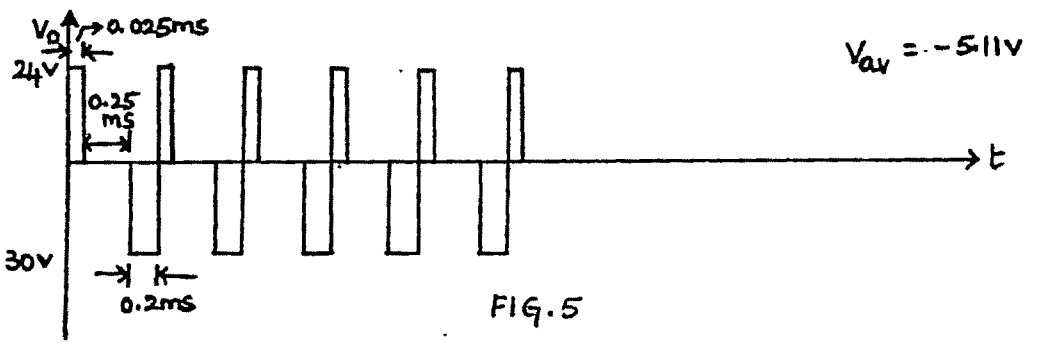

FIG. 5

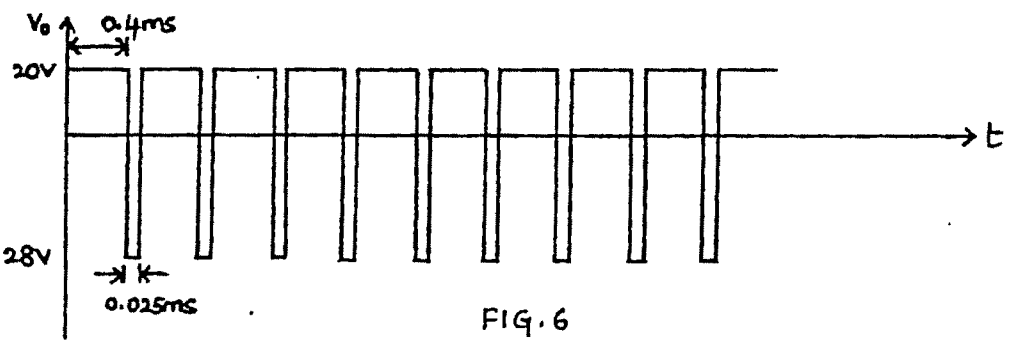

FIG. 6

The Design Of Microprocessor Based Series Resonant Inverter For A New Generation Contamination Free Induction Heated Medicinal Plant

P. K. Sadhu[1], S. K. Mukherjee[1], R. N. Chakrabarti[2] , S. P. Chowdhury[2] and B. M. Karan[1]
[1]Electrical & Electronics Engineering Department
Birla Institute of Technology, Mesra, Ranchi, India
[2]Electrical Engineering Department, Jadavpur University, Calcutta 700 032, India

ABSTRACT :

This paper presents some development in the process of electromagnetic induction heat flow through metallic package (stainless steel) in glass pipeline or vessel. The inverter fed fluid heating appliance is more acceptable than gas combustion method, steam heating method, electrical resistive heating method for better heat transfer and delivery processing under precise temperature management. This technology improved heat energy storage and heat exchange processing of tank fluid heating in the container or vessel or pipeline directly. The other advantage are contamination free heat production, good compactness , high-reliability, quick response, absence of combustion waste and absence of shock hazard in the boiling vessel. Besides enrouting water through specially designed metallic assemblies will permit eddy-current based heating through electromagnetic induction. In the case of steel vessel plant we shall produce heat directly on the vessel without heat conduction loss. In this article the series-resonant variable-frequency PWM I.G.B.T. inverter system are introduced as a new conceptional induction-heated pipeline fluid or vessel fluid heating for medicinal plant, sterilization plant and drier for surgical instruments. The salient feature of this inverter fed fluid heating appliance are presented and compared with the conventional electrical heating method.

Key words: PWM, IGBT, ZCS, kHz, series-resonant

INTRODUCTION:

In general, an induction heating is known as a contactless method of generating the heat energy in a magnetically-conductive work piece assembly by producing both eddy current losses and hysteresis losses in the work piece from an external high frequency alternating magnetic field produced by a high frequency PWM inverters using IGBT.The high-frequency magnetic field is usually established by a magnetic coil wrapped around the work piece or held parallel to the work piece surface. Resonant inverters are widely used for induction-heating over wide frequency ranges from 4 kHz to 500 kHz. The inverter operating frequency selected for a particular application is based on heat effectiveness and power conversion efficiency. The variable high-frequency resonant inverter circuits using IGBT appears more efficient, compact in size and of faster response as

compared to the conventional electrical heating method. In accordance with tremendous advances in power semiconductor switching devices, the authors have proposed an electromagnetic induction based fluid heating appliance using a current-fed high-frequency PWM resonant inverter using IGBT. The electromagnetic induction based fluid heating appliance using the high-frequency resonant inverter and its related system control technologies proposed by the authors seems to attract interest in the fields of medical, chemical, mechanical and consumer heat energy processing utilization in the pipeline system. Direct fluid heating based on electromagnetic induction principle can be done in two ways Viz. pipeline surface and wall skin effect heating and package-in-pipeline internal eddy current heating. The latter method seems a new and attractive concept proposed by authors. The eddy currents are induced in flow-through metallic package with a large number of heating surface incorporated into the non-metallic pipeline by means of an external working-coil connected to the high-frequency resonant inverter operated by PWM scheme. This paper presents a comparison between variable frequency phase-shifted PWM series load resonant inverter using IGBT modules and conventional electric heating to find out the most efficient fluid heating appliance.

INDUCTION HEATING SET-UP FOR MEDICINAL PLANTS :

The electromagnetic induction based fluid heating appliance using the high-frequency series resonant inverter and its related system control technologies proposed to attract interest in the fields of medical, chemical, mechanical and consumer heat energy processing utilization in the pipeline system. Direct fluid heating based on electromagnetic induction principle can be done in two ways Viz. pipeline surface and wall skin effect heating and package-in-pipeline internal eddy current heating. The latter method seems a new and attractive concept, which is incorporated in this topology. The eddy currents are induced in flow-through metallic package with a large number of heating surface incorporated into the non-metallic pipeline by means of an external working-coil connected either to the high-frequency series resonant inverter operated by PWM scheme whose 'OFF' time is more or less constant for different temperature response set and 'ON' time is increased with respect to quick temperature rise .

Fig. 1 shows a schematic system configuration of electromagnetic induction fluid heating appliance using a series resonant PWM inverter with an active power filter. The fluid-heating appliance used in the pipeline system is composed of a diode rectifier without smoothing filter so as to operate at a unity power factor. A specially-designed electromagnetic induction fluid heating assembly with a metallic package to achieve eddy current heating in the pipe line system is incorporated into the non-metallic vessel in addition to the working coil wrapped around for generating high-frequency flux. This appliance is highly acceptable for fluid heat-transfer and delivery processing plants as well as heats energy storage and heat exchange processing because of clean, compact, efficient and smart response. From practical viewpoint the above appliance seems cost effective for induction-heated wet sterilization plant.

Fig.2 indicates a specially designed eddy current heated metallic package developed, which is tightly incorporated into the non-metallic vessel or tank in the pipeline. The mechanically processed thin stainless-steel layer package with many spots and fluid channels for cylindrical induction-heated assembly is demonstrated in Fig.4. Internal structure of this metallic package to be heated by eddy current losses is indicated in Fig-3. When the fluid flows through the inherent package in the vessel or tank having a working coil connected to pipeline, the tabulant fluid is heated abruptly by eddy current losses generated inside the stainless-steel package.

Fig-4(a) & 4(b) show the comparison between the conventional electronic heater system and newly proposed prototype heater. In conventional system, at first electric heater heated the dowtherm or silicon oil. Then this heated dowtherm or silicon oil produces steam from water. Then this produced steam circulates in pipeline along distillatory tower. This so many stages are required for to eliminate the contamination of medicinal fluid in medicinal plant. But these cascading stages are offered lower or poor energy efficiency (35% to 40%). Our proposed plan will help to increase this efficiency to a value of 89.17%. In this case distillatory tower is directly heated through our induction heating process. This will save a lot of energy in the field of medicinal industry.

INDUCTION COIL ASSEMBLY:

From our previous experience we can say that in high frequency AC circuit, current penetration in the induction coil circuit is very difficult for higher diameter enameled copper wire due to skin-effect. The current flows through the upper layer of the enameled copper conductor. For this reason primary current is very less in the induction coil and as well as secondary flowing eddy current is very very less in the metal pans or vessels or

in metallic-packages. So, I_2^2 R is very less and there is no practicable heat generation in the objects. To avoid this difficulty we introduce a bundle enameled copper conductor for manufacturing the working induction coil. Inspite of using 10 S.W.G. enameled copper wire. The high frequency current capacity higher gauge wire is produced by twisting 16 numbers of 24 SWG copper enameled wire . This is shown in fig 6.

By means of this construction we shall penetrate the current in bundle conductors assembly but the current is passing through outer skin of the individual 24 SWG copper enameled wire but according to bundle conductor assembly current is passing throughout all cross sectional layers of equivalent higher gauge of conductor. Since the current penetrates in the primary winding of the induction coil, so the secondary current which is flowing in pan or vessel (eddy current) is very much higher. It gives fruitful result in practical induction heating equipment. Overall geometrical shape of the induction coil for better linking of magnetic flux with pan or vessel for home appliances is of spiral type like fig 7.

POWER SUPPLY UNIT FOR THE PRESENT SCHEME :

The voltage available in the laboratory or in the house is A.C 220 V,50 Hz .At first we take it from system bus and it has to be rectified to generate D.C voltage by full bridge rectifier before feeding to inverter circuit Before feeding to the inverter circuit ,the D.C output is filtered through an non-smoothing L-C filter circuit to get with ripple D.C supply .This non-smoothing filter works as a harmonics filter .When inverter operates then harmonics are generated .To avoid the harmonic injection in the system bus at the time of induction operation, this non-smoothing filter works as high pass filter through capacitor (C) in the figure 8.

IMPLEMENTATION OF TRIGGERING CIRCUIT :

The hard ware implementation was limited by the circuit constraint problem. Moreover, the hard ware implementation carried by the series resonant inverter with two I.G.B.T had the disadvantage that it draw very high peak circuit current from the source we require a necessary phase difference between the two I.G.B.T S firing which is difficult to implement Using a hardware approach. This approach as generating rectangular pulses with required phase difference is an easy task with the help of 8085 microprocessor .Here we designed the firing pulses through software as per the following table :

Temperature response setting	ON PERIOD (μ SEC)	OFF PERIOD (μ SEC)
Temperature set 1	5	25
Temperature set 2	8	22
Temperature set 3	12.6	22
Temperature set 4	16	21
Temperature set 5	19.6	21

INVERTER CIRCUIT FOR THE PRESENT SCHEME :

The present inverter circuit is developed in fig-9. The non-smooth D.C voltage is available in across A & B points in the above mentioned circuit .At first when we connect the inverter circuit with the D.C power supply of the system the capacitors C_1 and C_2 are charged when there are no gate pulses at G_1 and G_2. when we start high frequency A.C generation then we fed pulses from software control circuit alternatively in the gates of I.G.B.T –(1) and I.G.B.T-(2) . When the gate pulse is achieved in G_1 then I.G.B.T –(1) is in 'ON' state. So the charge of capacitor C_1 discharges through QRMN loop as well as C_2 charges through QRMNO path .By means of this operation current flow in the short circuit bar 'NM' from M to N .

On the next half of the operation the gate pulse is achieved in G_2 of the I.G.B.T- (2) then I.G.B.T- (2) is in 'ON' state. Before getting pulse in G_2 the gate pulse of G_1 is withdrawn to avoid the simultaneous conduction and the short circuit between D.C source. When I.G.B.T –(2) is in 'ON' state then C_2 discharges through NMPO loop as well as C_1 charges through QNMPO path .By means of this operation current flow in the short circuit 'NM' bar from N to M.

So by these gate pulses we generate alternating current in 'NM' bar. This alternating current frequency is in the range of radio-frequency like 33.33 kHz. At this high frequency the capacitor C across (A) & (B) terminals is working as very low impedance path for radio-frequency range [because capacitive impedance = $X_C = 1 / (2 \Pi f C)$]. So this alternating high frequency current flows through the (A), (Q), (R), (M), (N), (O), (B) loop in one half and in next half it will flow through

the (A), (Q), (N), (M), (P), (O), (B) loop .So the generated alternating current through the NM bar will also flow through the induction heating working coil 'L' which will generate alternating magnetic flux.

EXPERIMENTAL RESULTS FOR MEDICINAL PLANT :

SAMPLE EFFICIENCY CALCULATIONS FOR MEDICINAL PLANT FOR SET-II :-

Input no load current $=I_O=0.05$ amp
Input load current $= I_L=1.55$ amp
Input voltage $= V_I =200$ volt
Initial temperature of fluid (Ambient)$T_1 = 22.3\ ^oC$
Final temperature of fluid $T_2 =80.0\ ^oC$
Initial fluid mass (water) $m_i = 1.5$ Kg
Stainless steel package (bowl) weight $m_s =73.14$ g
Final mass of fluid after experiment $m_f = 1.337$ Kg
Mass of evaporated fluid $= m_{ev} = m_i - m_f = 1.5 - 1.337 = 0.163$ Kg
Total time taking for reaching final temperature = 2430 Sec
Taking L = 2256.9 KJ / Kg (some fluid will be evaporated which is nearer layer of steel plate)

Heat power transfer to fluid $P_o = \{m_f C_p(T_2 - T_1) + m_{ev}L\}$/ time in Sec = 739.5146 KJ/ 2430 Sec $=0.304327$ KW $= 304.327$ W
Input power taken from source $= P_I = V_I I_L \cos\phi$, here $\cos\phi = 1$

$= 200 \times 1.55 = 310$ W

Efficiency of the industrial setup system at temperature Set-II $= \eta_{i2} = 304.327 / 310 = 0.9817 = 98.17\ \%$

Temperature response settings	Efficiency of medicinal plant
Temperature set-I	57.56 %
Temperature set-II	98.17 %
Temperature set-III	97.4 %
Temperature set-IV	92.44 %
Temperature sat-V	95.1 %

CONCLUSION :

In this paper, an electromagnetic induction based fluid heating appliance has been proposed which is fed from a series load-resonant PWM high-frequency inverter using I.G.B.T. modules. The working principle of the proposed PWM control inverter topology has been described for modern induction heating. The proposed appliance is expected to be most cost-effective for induction-heated boiler heat exchanger and evaporator because of compactness in size, high-efficiency conversion, quick response and precise temperature control than the other method containing more harmonics in high frequency a.c. generation and more noise and also more loss in conventional electric heating. The authors believe that the proposed scheme will be quite useful for microwave oven and medical process in the near future.

REFERANCES :

1. J.P.Landis, " A static power supply for induction heating "- IEEE-Trans, IECI.Vol.17 No.4, P.P-313-320, setember,1970

2. Irving Gottlieb, " Solid-state high-frequency power"- Reston publishing company, INC, Prentice-Hall company, P.P31-41, 1989

3. M.Nakaoka, "A Phase-difference angle control-mode PWM high-frequency resonant inverters using static induction-transistors and thyristors"- Proceedings of IEEE-PESC 87,P.P 674-681, June1987

4. Y.Konishi & S.P.Wang M.Ishibashi,Y.L.Feng "Efficiency Ozonier using PDM and PWM controlled Resonant inverter and its performance evaluations" –Yamaguchi university, Yamaguchi, 755 Japan.

5. H.Fujita, H.Akagi, "Pulse-density-modulation power control of 4KHZ Voltage-source inverter for induction melting applications"- IEEE Transaction on industry applications.

6. J.Pforr, L.Hobon, "Resonant-switched mode preconverters for high-frequency induction heater"- Proceedings of power conversion international conference June 1991.

7. Ogiwara, watanate. J. nakaoka, " Fixed frequency mode phesor- shifting power control ZVS high - frequency inverter for induction heating using Sidevices."- Volume 393-398 1997., Pub: Industrial electronics 1997 ISIE,97 USA

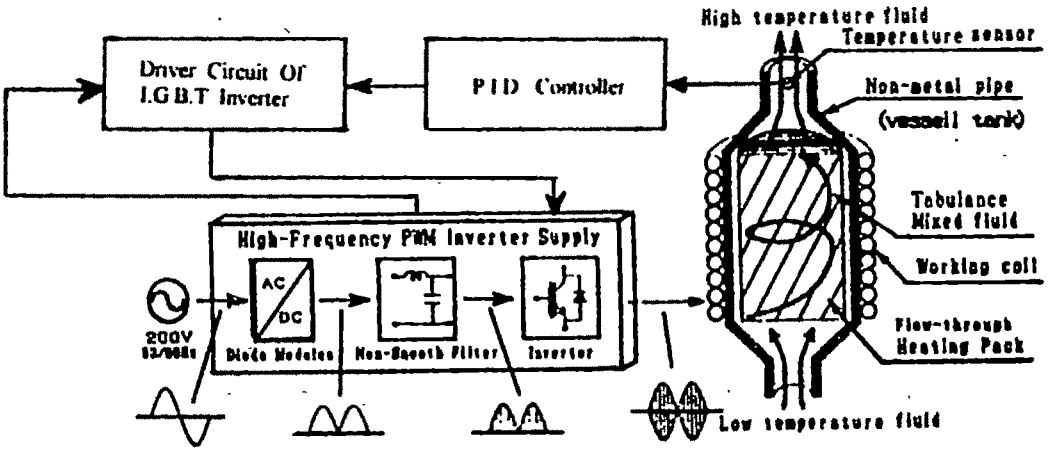

Fig-1 : New schematic induction-heated electrical energy conversion in non-metallic pipeline for industrial set-up.

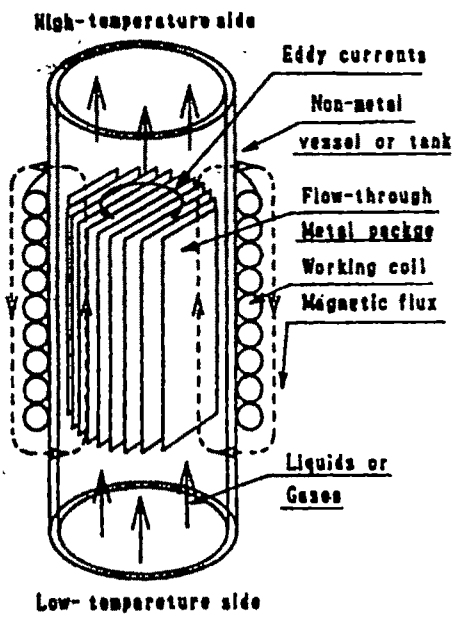

Fig-2 : Heating package in the vessel and tank in pipeline system.

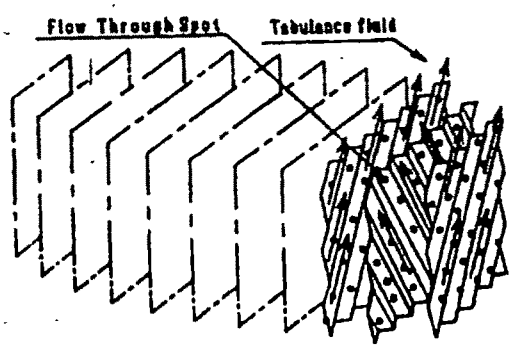

Fig-3 : Internal structure fluid-through Specially designed metal layer packing to generate tabulance fluid.

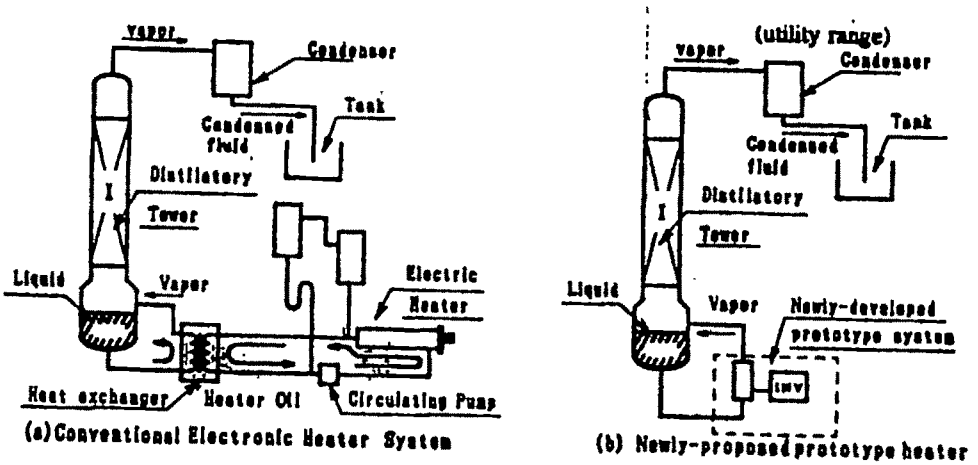

Fig-4 : Comparative feasible application between this induction heated systems and resistance heated appliance.

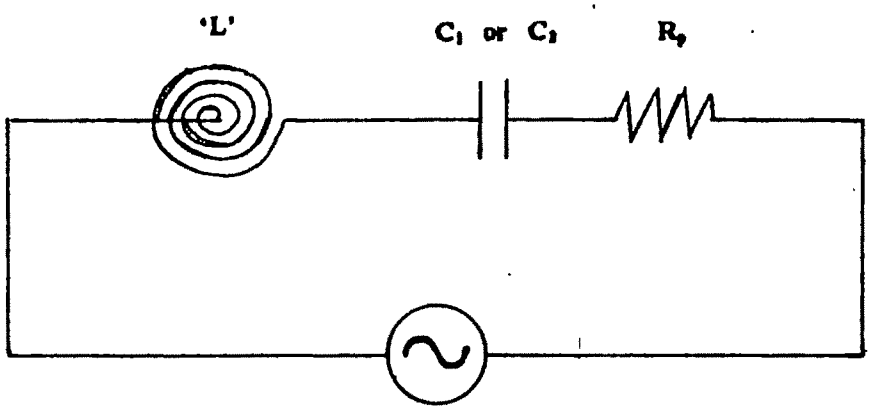

Fig-5 : Circuitry for determining series resonant.

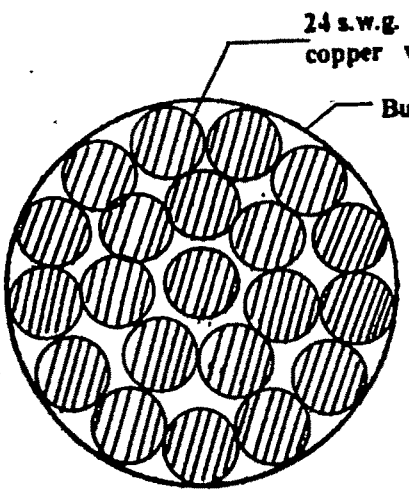

Fig-6 : Cross section of twisted bundle conductor of induction coil (Working coil).

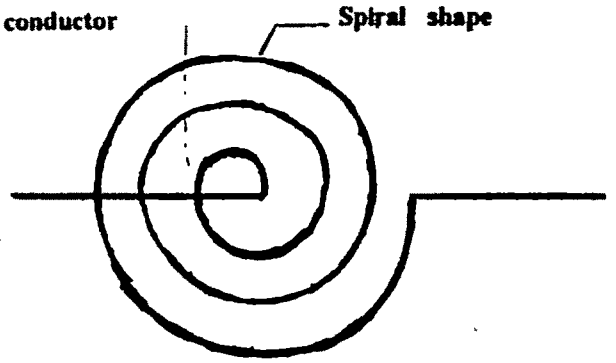

Fig-7 : Spiral shape induction coil.

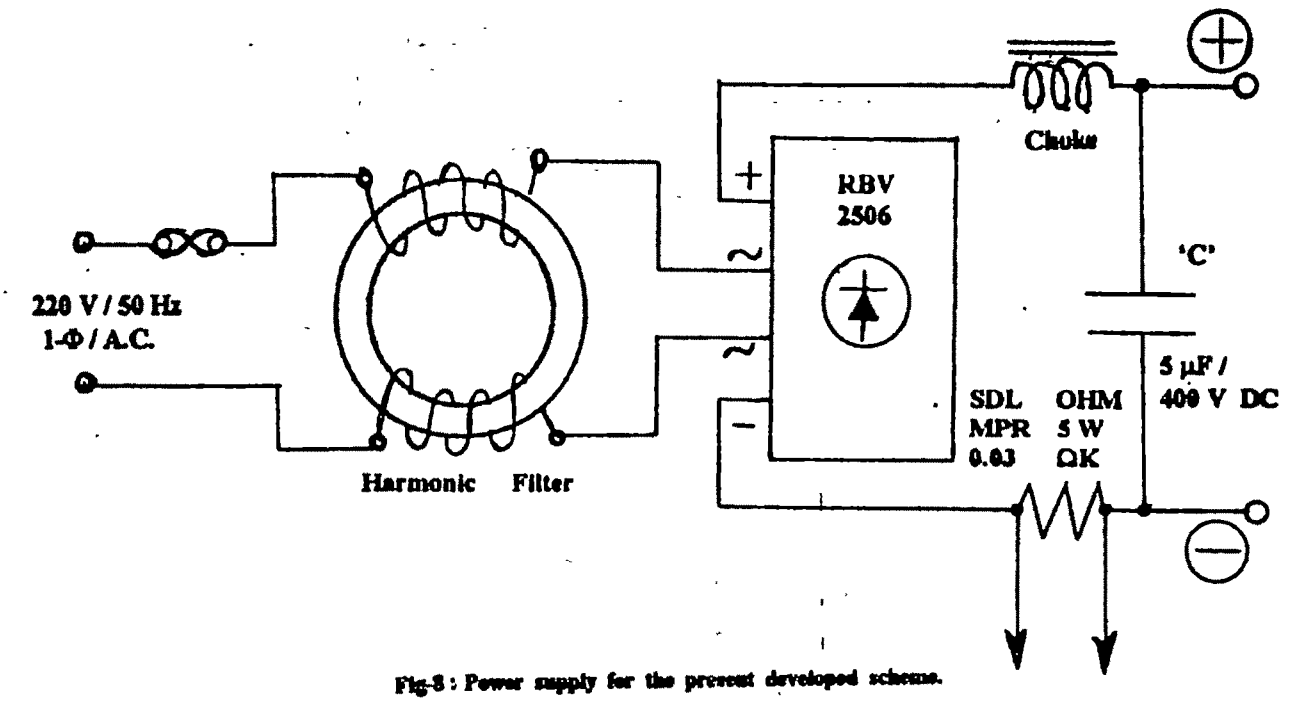

Fig-8 : Power supply for the present developed scheme.

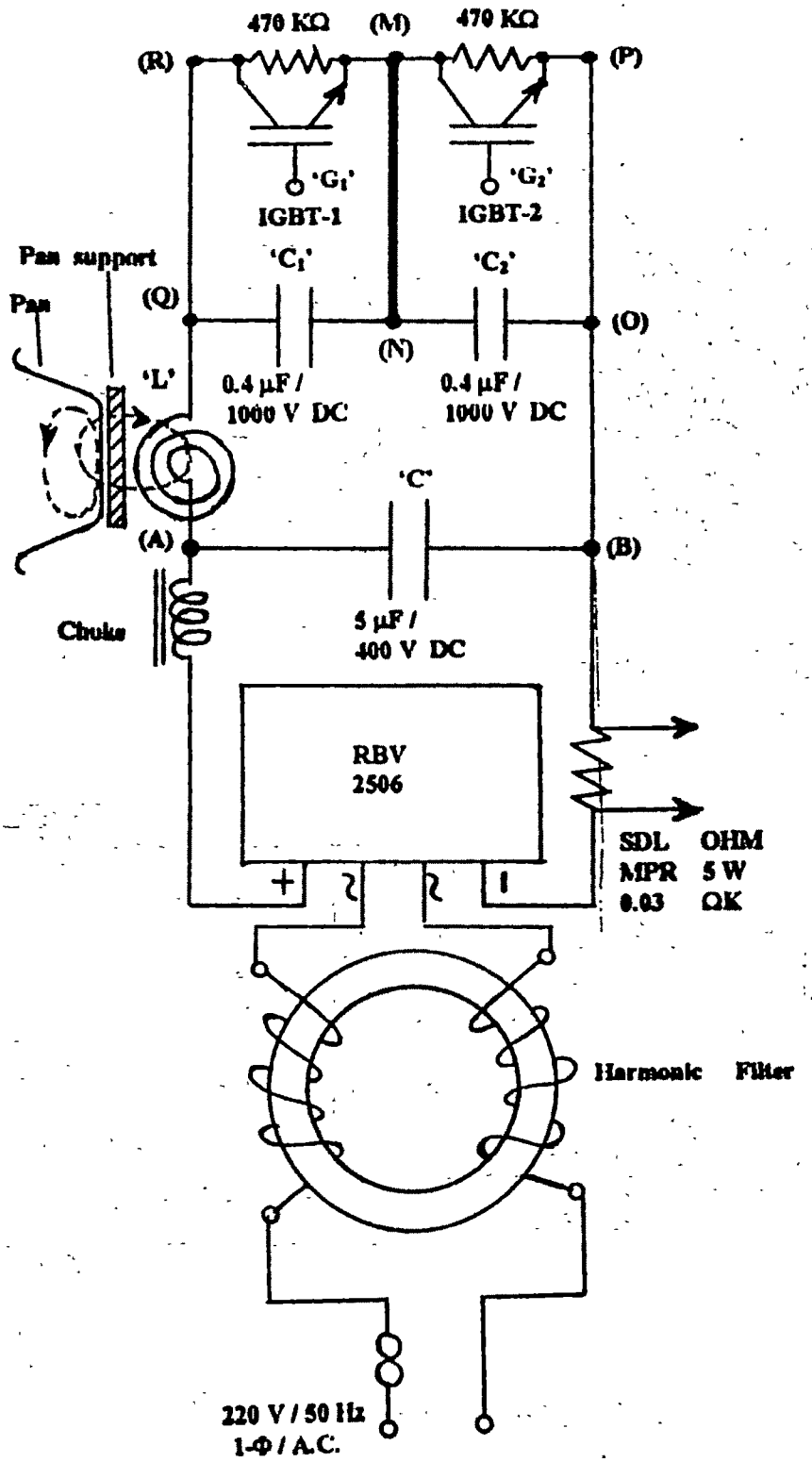

Fig-9 : Newly developed power inverter circuit.

Transient Stability Study of The Series Generator-Series Motor Drive

K. L. Barui [+] and B. Bhattacharya [*]
[+]National Test House, Alipore, Kolkata-700027
* Dept. of Applied Physics, University College of Technology, 92,A.P.C. Road, Kolkata-700009
E-mail of corresponding author: klb@nther.wb.nic.in

Abstract

In the present investigation, accounting the nonlinearities present in the loaded series generator-series motor drive, its conservative transient stability is rigorously analysed by the 2 nd method of Lyapunov. The system is found to be asymptotically stable in large provided it satisfies some parametric constraints. Its degree of stability depends on the proper choice of its positive damping factor.

Key words: d.c.Drive, Transient asymptotic stability, Lyapunov function, Damping factor.

INTRODUCTION

The d.c. series motor drive for the speed control, has various industrial utilities for the reasons of its economic and smooth speed control over a wide range and inherent stability in operation. The system has also high starting and accelerating torques and so relatively short settling time is required to obtain the desirable speed.

Many theoretical and practical investigations of this drive were presented in the literature for many years[1-5]. Jone & Meyer [6] took the loaded series motor drive electrically connected with a series generator operated at constant speed. Using the linearization technique for the nonlinear system, its stability behaviour was rigorously analysed by Lyapunov's 1st method – from where found out some parametric constraints helpful for designers [6,7].In the present investigation, the d.c. series generator-series motor drive is considered, where the motor is coupled with a versatile mechanical load operated over a wide range of speed. Considering the magnetisation characteristic of the machines as an idealised saturation function, the conservative transient stability of this non linear drive are analysed in the saturated and unsaturated operating portions of the magnetisation curve by the help of Lyapunov's 2nd method [8,9]. The suitable Lyapunov functions for both cases, are systematically generated by the Initiating function which was effectively applied for many engineering problems [10,11]. It is found that the system is globally asymptotically stable in the saturated zone of operation; whereas in the usual practical zone of operation i.e. in the unsaturated portion of the magnetisation curve, the series generator-series motor drive has transient asymptotic stability in large provided the drive has the positive damping. Effect of the damping to the system is critically assessed.

THE SYSTEM EQUATION

In this investigation, the d.c.drive system,as in Fig. 1, consists of a series motor coupled with a versatile load

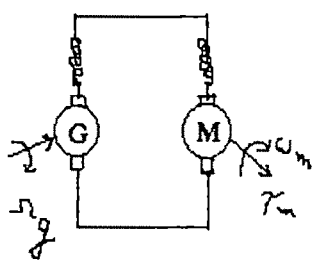

FIG.1 d.c. Drive system

operated over a wide range of speed. The motor is electrically connected with a series generator operated at a constant speed. Here the speed-load characteristic of motor and load is assumed to consist of a constant load component (C_L), a viscous damping component (F_L) and an inertial component (J_L).

The electrical equivalent circuit diagram of the series generator-series motor drive is presented in Fig.2[1,6]. Then considering the rated operating values of each machine as the base values, the normalised system equations of the drive are developed from the equivalent diagram and these are given as:

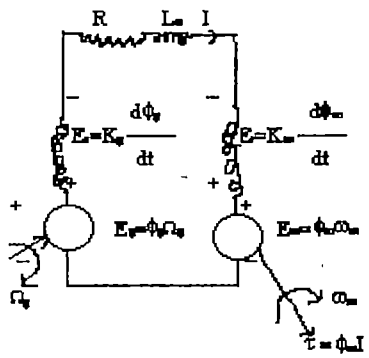

Fig.2 Equivalent circuit diagram

$$aj + T\frac{dj}{dt} = (N - \xi v)\,\psi - T_E\frac{d\psi}{dt} \qquad (1)$$

$$\psi j = d + bv + T_J\frac{dv}{dt} \qquad (2)$$

$$\psi = \psi(j) \qquad (3)$$

where the normalised paramerers and variables are

$\xi = \dfrac{E_{m0}}{E_{g0}}$ = ratio of the induced emf of the generator and motor under rated condition;

$a = \dfrac{RI_0}{E_{m0}}$ = armeture resistance voltage drop;

$b = \dfrac{F_L\Omega_{m0}}{\tau_{m0}}$ = damping factor of the load;

$d = \dfrac{C_L}{\tau_{m0}}$ = constant load component;

$T = \dfrac{L_a I_0}{E_{m0}}$ = armature inductance voltage drop;

$T_J = \dfrac{J_L\,\Omega_{m0}}{\tau_{m0}}$ = momentum component of the load;

$T_E = \dfrac{K_g}{\Omega_{g0}} + \xi\dfrac{K_m}{\Omega_{m0}}$ = proportionality constant;

$j = \dfrac{I}{I_0}$ = armature current;

$N = \dfrac{\Omega_g}{\Omega_{g0}}$ = generator speed;

$v = \dfrac{\omega_m}{\Omega_{m0}}$ = motor speed;

$\psi = \dfrac{\phi_g}{\phi_{g0}} = \dfrac{\phi_m}{\phi_{m0}} = \psi(j)$ = flux for the generator and motor.

Suffixes '0' stand for the rated values of the machines.

The mathematical relation of the magnetisation curve in equation (3), is not well established. Hence in the present investigation, one of the standard practices is to be assumed —where the nonlinear magnetisation curve is considered as an ideal normalised saturation type characteristic as in Fig.3.

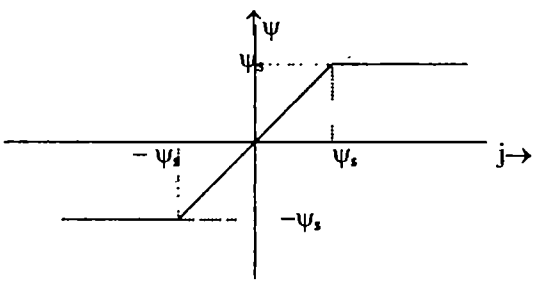

Fig.3 Normalised magnetisation curve

Here the equation (3) can be considered as

$$\psi = \text{Sat}\{i\} \quad \text{where } i = \frac{j}{\psi_s}$$

i.e. $\psi = i$ if $|i| \le 1$ [Case I]

$\psi_s = i$ if $|i| \ge 1$ [Case II]

where ψ_s = magnitude of the saturated (maximum) flux.

On the basis of this consideration, the normalised system equations will be

Case I : $\psi = i$ [For the linear incremental portion of the magnetisation curve]

$$(T + T_E)\frac{di}{dt} = -a\,i + (N - \xi v)\,i \qquad (4)$$

$$T_J\frac{dv}{dt} = i^2 - d - bv \qquad (5)$$

Case II : $\psi_s = i$ [For the saturated portion of the magnetisation curve]

$$T\frac{di}{dt} = -a\,i + (N - \xi v)\,\psi_s \qquad (6)$$

$$T_J\frac{dv}{dt} = \psi_s\, i - d - bv \qquad (7)$$

It is noted that the equations of Case I are nonlinear, whereas the equations of Case II are linear.

STATE DYNAMICAL EQUATIONS

Case I: The equilibrium points in the unsaturated portion of the magnetisation curve are

$$\begin{bmatrix} i_{10} \\ v_{10} \end{bmatrix} = \begin{bmatrix} 0 \\ -\frac{d}{b} \end{bmatrix}, \begin{bmatrix} \pm x_{10} \\ x_{20} \end{bmatrix} \qquad (8)$$

where $i_{10} = \left[d + \frac{b(N-a)}{\xi} \right]^{1/2}$ and $x_{20} = \frac{N-a}{\xi}$

First set of equilibrium points is physically absurd as the steady state current (i_{10}) is zero, i.e. the machines behave as the open – circuited condition.

Chosing the variation of the armature current and speed fluctuation as the state variables $x_1 = i - i_{10}$ and $x_2 = v - v_{10}$ the state dynamical equations of the system from the equations (4) and (5), will be

$$\dot{x}_1 = -\alpha_{11} x_2 - \alpha_{12} x_1 x_2 \qquad (9)$$

$$\dot{x}_2 = \alpha_{21} x_1 - \alpha_{22} x_2 + \alpha_{23} x_1^2 \qquad (10)$$

where $\alpha_{11} = \frac{\xi i_{10}}{T + T_E}$; $\alpha_{12} = \frac{\xi}{T + T_E}$; $\alpha_{21} = \frac{2 i_{10}}{T_J}$;

$$\alpha_{22} = \frac{b}{T_J}; \qquad \alpha_{23} = \frac{1}{T_J}.$$

Case II : The equilibrium point in the saturated portion of the magnetisation curve is

$$\begin{bmatrix} i_{20} \\ v_{20} \end{bmatrix} = \begin{bmatrix} x_{10}' \\ x_{20}' \end{bmatrix} \qquad (11)$$

where $x_{10}' = \frac{\psi_s [N b + d]}{a b + \xi \psi_s^2}$ and $x_{20}' = \frac{N \psi_s^2 - a d}{a b + \xi \psi_s^2}$

Choosing state variables as $x_1' = i - i_{20}$ and $x_2' = v - v_{20}'$ the state dynamical equations of the system from equations (6) and (7), will be

$$\dot{x}_1' = -\beta_{11} x_1' - \beta_{12} x_2' \qquad (12)$$

$$\dot{x}_2' = \beta_{21} x_1' - \beta_{22} x_2' \qquad (13)$$

where $\beta_{11} = \frac{a}{T}$; $\beta_{12} = \frac{\xi \psi_s}{T}$;

$$\beta_{21} = \frac{\psi_s}{T_J}; \qquad \beta_{22} = \frac{b}{T_J};$$

LYAPUNOV FUNCTION

Case I : From the state dynamical equations (9) and (10), the Lyapunov function V(X) and its time derivative, are developed by Initiating function method [10] as given in Table 1.

Table 1

Generation of V(X) and $\dot{V}(X)$

	$\dot{V}(X)$		
V(X)	x_1^2	x_2^2	$x_1 x_2$
$p_1 x_1^2$	$-2 p_1 \alpha_{12} x_2$		$-2 p_1 \alpha_{11}$
$p_2 x_2^2$	$2 p_2 \alpha_{23} x_2$	$-2 p_2 \alpha_{22}$	$2 p_2 \alpha_{21}$

For the evaluation of the constants p_1 and p_2, the condition is considered as

$$2 p_1 \alpha_{11} = 2 p_2 \alpha_{21}$$

Chosing $p_1 = 1$ (scale factor), $p_2 = \frac{\xi T_J}{T + T_E}$

Hence V(X) and $\dot{V}(X)$ functions are

$$V(X) = x_1^2 + \frac{\xi T_J}{T + T_E} x_2^2 \qquad (14)$$

$$\dot{V}(X) = -\frac{2b}{T + T_E} x_2^2 \qquad (15)$$

Case II : In the similar way, the Lyapunov function and its time derivative can be developed from the equations (12) and (13) as

$$V'(X') = x_1'^2 + \frac{\xi\psi_s}{a} x_2'^2 \qquad (16)$$

$$\dot{V}'(X') = -\frac{2a}{T} x_1'^2 - \frac{2b}{T_J}\frac{\xi\psi_s}{a} x_2'^2 \qquad (17)$$

CONDITIONS FOR ASYMPTOTIC STABILITY

Case I : It is seen from the equations (14) and (15) that

(i) $V(0) = 0$ at the origin $X = 0$, $V(X)$ is a continuous function of time and $V(X)$ is a positive definite function in the entire state space and $V(X) \to \infty$ as $||X|| \to \infty$.

(ii) $\dot{V}(0) = 0$ at the origin $X = 0$, $\dot{V}(X)$ is a continuous function of time and $\dot{V}(X)$ is a negative definite in the entire state space provided $x_2 \neq 0$ and b is a positive scalar.

Hence the system must be absolutely asymptotically stable in large except $x_2 = 0$ and for a positive damping.

Case II : From equations (16) and (17) it is seen that $V'(X')$ and $\dot{V}'(X')$ are continuous functions of time; $V'(0) = 0$, $\dot{V}'(0) = 0$ at the origin $X' = 0$ and $V'(X') > 0$ and $\dot{V}'(X') < 0$ in the entire state space except $X' = 0$. Hence the system is globally asymptotically stable.

NUMERICAL EXAMPLE

As an example, a practical system is considered with parametric values [6] as

$\xi = 1$, $N = 1$, $a = 0{\cdot}2$, $T = 0{\cdot}05$ s, $T_E = 0{\cdot}15$ s, $T_J = 0{\cdot}1$ s, $b = 0{\cdot}5$, $d = 0{\cdot}6$

From the equations (9) and (10) the state dynamical equations for the unsaturated zone of operation are

$$\dot{x}_1 = -(\pm)\, 5{\cdot}0\, x_2 - 5{\cdot}0\, x_1 x_2 \qquad (18)$$

$$\dot{x}_2 = (\pm)\, 20{\cdot}0\, x_1 - 5{\cdot}0\, x_2 + 10{\cdot}0\, x_1^2 \qquad (19)$$

$\dot{V}(X)$ and $\dot{V}(X)$ functions from the equations (14) and (15) are

$$V(X) = x_1^2 + 0{\cdot}5\, x_2^2 \qquad (20)$$

$$\dot{V}(X) = -10{\cdot}0\, b x_2^2 = -5{\cdot}0 x_2^2 \quad [\text{for } b = 0{\cdot}5] \qquad (21)$$

The Fig.4 shows the computed Lyapunov functions [$V(X) = 0{\cdot}5$, $1{\cdot}0$ and $2{\cdot}0$] in the state space. These are elliptical closed contours across the origin of the state space and the enclosed contour increases as $V(X)$ increases.

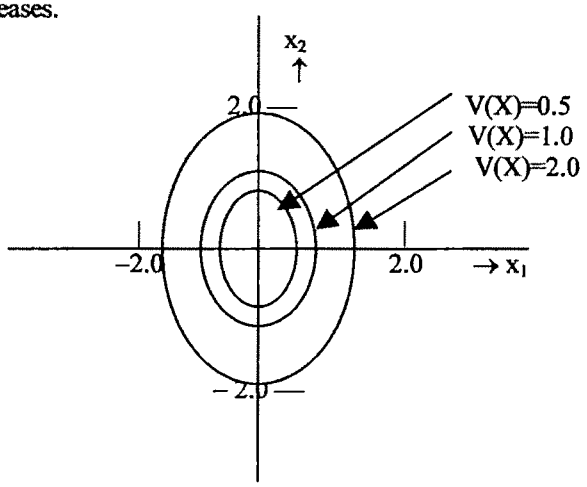

Fig.4 Closed contour of Lyapunov function V(X).

Fig.5 and Fig.6 show the decay times (t_1 and t_2) of $V(X) = 0.5$, 1.0 and 2.0 – where t_1 is computed by varying x_2 i.e. the speed fluctuation of this drive at constant damping factor $b = 0.5$ and t_2 is computed by varying b at constant $x_2 = 0.5$.

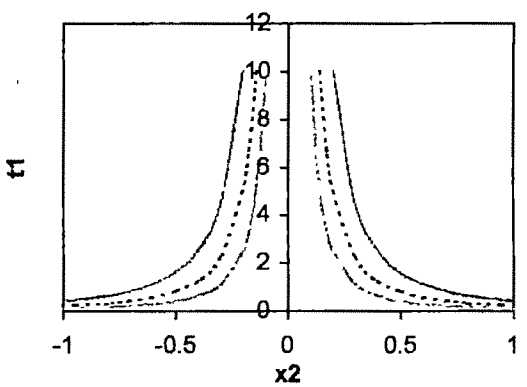

Fig.5 Decay time t_1 of V(X) vs x_2 for b= 0.5
—— V(X)=0.5, – – – V(X)=1.0, ·····V(X)=2.0

It is seen that the values of t_1 and t_2 are very large for small x_2 and b, but they decrease sharply for the increase

of x_2 and b. From the physical consideration of V(X) it can be postulated that the instantaneous built up restoring force by this drive due to the positive damping (b) and the speed fluctuation (x_2), is inversely proportional to each of these decay times t_1 and t_2. Hence this phenomenon

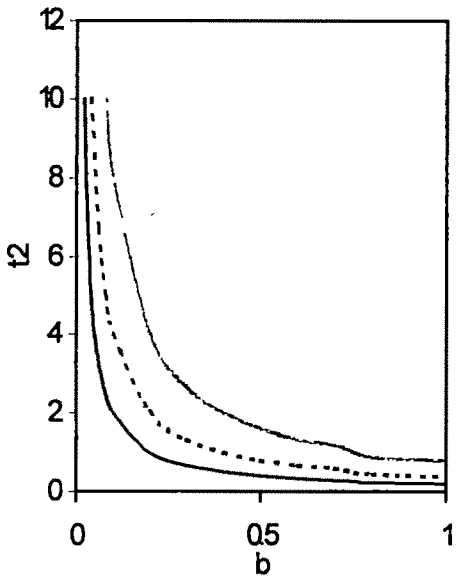

Fig.6 Decay time t_2 of V(X) vs b for x_2=0.5
—— V(X)=0.5, – – – V(X)=1.0, ·····V(X)=2.0

indicates that for larger values of x_2 and b, this drive can build up instantaneously larger restoring force which makes to settle the system at the steady state in reasonable time.

CONCLUSION

Under unsaturated zone of operation in the magnetisation characteristic, the series generator-series motor drive is a nonlinear system, but it has asymptotic stability in large as

seen from V(X) and V(X) in equations (14) and (15). This Lyapunov function shows one of the best possible choices for assessing the conservative stability of this drive. From the analysis it is seen that the system has transient asymptotic stability in large for the damping factor $b > 0$

and $\dot{V}(X) < 0$ except $x_2 = 0$. The physical interpretation of

$\dot{V}(X)=0$ for $x_2=0$ and $\dot{V}(X) < 0$ for $x_2 \neq 0$, are that for $b > 0$, when the speed of the drive remains at the rated operating speed (v_{10}), no restoring force is developed by the system, but if the drive faces a sudden speed fluctuation from the operating speed, whether small or large, the system builds up instantaneous restoring force for making correction and so the drive is strictly asymptotically stable in large.

Again the expression of V(X) is proportional to the product of the damping factor (b) and square of the sudden speed fluctuation (x_2) and is independent of its inertial factor (T_J). Hence the degree of its transient stability depends on the magnitude of b irrespective of the size of the machine and the instantaneous developed restoring motion is faster when a sudden larger speed variation is encountered by the drive. These phenomena are established from computed values of cited example (in Fig.5 and Fig.6).

For the theoretical interest if $b = 0$, then $V(X) = 0$ in the entire state space and so the system is critical one. In this case, there is every possibility of sustained limit cycle oscillation of the system. For negative damping factor ($b<0$), the system is absolutely unstable.

The study of Case II is only for the theoretical interest. In this case the drive is linear one and is globally asymptotically stable. This phenomenon is confirmed by the practical operation of this drive as: At the saturated zone of the magnetisation curve, the flux increases slightly by the sudden large increase of the circuit current and so the increase of the electro-magnetic torque is small. As a result, the speed of the motor is not changed much due to the sudden perturbation encountered by the system and so no question of the transient instability of the drive virtually arises.

For the practical drive of this type the operating zone is usually in the unsaturated portion of the magnetisation curve and the damping factor of the load is positive in nature. Hence from this analysis it can be concluded that any practical series generator-series motor drive of any machine size coupled with versatile load components, has inherent transient asymptotic stability in large and the degree of the stability depends on the proper choice of the damping factor.

REFERENCES

1. M.G.Say and E.O.Taylor, Direct current machine, 1st Edition (Pitman, London, 1980).
2. W.Leonhard, Control of electrical drive, 2nd Edition (Spinger Verlar, Berline, 1990).
3. N.R.Godfrey, L.S.Parkes and R.J.Wilkie,High performance speed regulation of rolling mill d.c. drives connected to common voltage bus, Proc I E Australia 4th Conf.,Control Engg.(1990),Aug, p 1.
4. P.C.Sen, Electric motor drive and control – past, present and future, IEEE Trans., Ind. Electron. (1990), vol. 37, Dec., p 562.
5. B.T.Boulter, Applying drive performance specifications to system applications, Part I. Speed performances, IEEE Trans., Ind. Applicant., (2001), Vol. 37, 4 (July / Aug), p 1082.

6. R.W.Jone and A.U.Meyer, Analysis of series motor-series generator drive, AIEE Trans., Part III (1960), Vol. 79, April , p 31.
7. J.C.Hsu and A.U.Mayer, Modern control principles and application, 1st Edition, (Mc-Graw Hill Book Comp., N.J., 1968), p 146.
8. R.E.Kalman and J.E.Bertrain, Control system analysis and design via 2nd method of Lyapunov, ASME J. Basic Engg. SecD,(1960),Vol 82,No2,p371.
9. K.Ogata, Modern Control Engg., 2nd Edition, (Prentice Hall of India Pvt, Ltd., N.D., 1991), p 772.
10. T.K.Mukherjee, B.Bhattacharya and A.K.Chaudhury, Transient stability of a doubly excited synchronous machine by the 2nd method of Lyapunov, Inst. J. System Scie., (1973), Vol. 4, No. 1, p 1.
11. B.Bhattacharya, Stability analysis of an industrial drive, National Sm. on Topics on App. Physics, C.U. (1979), Feb.

A Digital Controller for Diode Rectifier with Sinusoidal Input Current

M. R.Vikraman, A. Kandaswamy
PSG College of Technology, Coimbatore 641 004.
e-mail : mrvikraman@hotmail.com; kandaswamya@hotmail.com

Abstract

A diode rectifier draws non-sinusoidal current from the input ac source. This is highly undesirable. Many methods have been suggested to make the source current drawn by the diode rectifier sinusoidal. In this paper a digital controller which can incorporate a microprocessor or a PC for control action is described. First the theoretical part is explained and then a Simulink model of the whole system is derived. The derived model is simulated and the simulation results are also exhibited. The simulation results themselves explain the usefulness the system described in this paper.

Key words: Harmonics, Active Filters, Power Quality, Simulink

INTRODUCTION

The use of nonlinear loads such as controlled and uncontrolled rectifiers, variable speed drives and the like are increasing day by day. These nonlinear loads draw non-sinusoidal current from the utility. The non-sinusoidal current contains a number of harmonic components. These harmonics create problems to sophisticated instruments such as communication- and biomedical-equipment connected to the same utility. The common practice to reduce the effects of harmonics is to use passive filters. But, these passive filters are not sufficient to keep the utility clean. Use of active filters is an emerging idea in the field of power quality. An active filter consists mainly of semiconductor switches and a few energy storage devices. Here an active filter is incorporated to a diode bridge rectifier to tailor the source current drawn by the rectifier harmonics free. A digital control is used to control the switches of the active filter so that the active filter provides the harmonic requirements of the nonlinear load. Once this is achieved, the rectifier load will draw only the fundamental component of the load current, which is invariably sinusoidal, from the utility.

PRINCIPLE

The block schematic of the whole system is shown in Fig.1. Four controllable switches are also incorporated with the diode bridge rectifier circuit. These controllable switches are digitally controlled such that the current through the inductor at the ac side is sinusoidal. The current through this inductor and the dc side voltage are sensed and converted to digital signals using A/D converters. A PC is used as the controller here. This controller generates a sinusoidal reference current, which is synchronized with the line voltage. From the error between the actual and reference current waveforms, the pulse width required per sampling interval is calculated and applied to the appropriate switching devices.

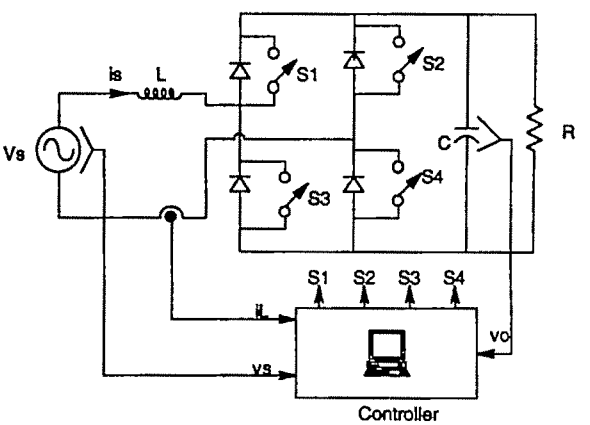

Fig.1 Block schematic of the whole system

Without any control, the current through the input side inductor L will be non-sinusoidal. The current through the inductor can be increased or decreased by controlling the voltage v_B. The voltage v_B can be controlled by the four switches S1, S2, S3 and S4. $v_B = 0$ when either S1 and S2 are ON or S3 and S4 are ON. $v_B =$

v_o when S1 and S4 are ON and $v_B = -v_o$ when S2 and S3 are ON.

MATHEMATICAL MODEL

Fig. 2 shows the waveforms of the input voltage $v_s(t)$, input current is(t) and the output voltage $v_o(t)$. The reference current $i_{ref}(t)$ should be proportional to $v_s(t)$. The

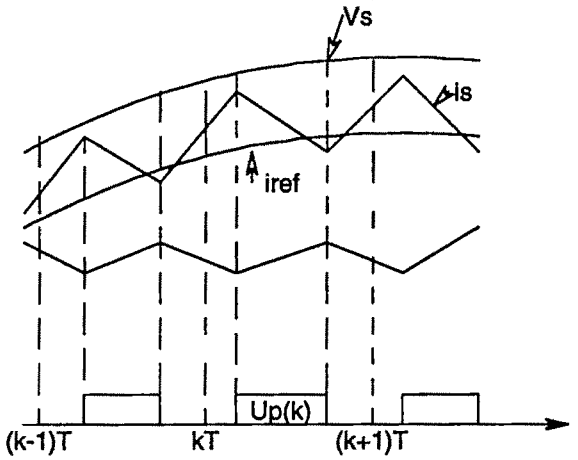

Fig.2 Different waveforms

time interval (k-1)T to kT is designated as the k^{th} period. $U_p(k)$ is a positive value and it gives the pulse width for the k^{th} period. This pulse width is assumed to be generated at the center of the corresponding period. The discrete time model of the system with source current, is and dc voltage, v_o as state variables is
when $v_B=0$

$$\begin{bmatrix} \dot{i}_s \\ \dot{v}_o \end{bmatrix} = \begin{bmatrix} 0 & \pm\frac{1}{L} \\ \pm\frac{1}{C} & -\frac{1}{RC} \end{bmatrix} \begin{bmatrix} i_s \\ v_o \end{bmatrix} + \begin{bmatrix} \frac{1}{L} \\ 0 \end{bmatrix} v_s \qquad (1)$$

and when $v_B=+-v_o$

$$\begin{bmatrix} \dot{i}_s \\ \dot{v}_o \end{bmatrix} = \begin{bmatrix} 0 & \pm\frac{1}{L} \\ \pm\frac{1}{C} & -\frac{1}{RC} \end{bmatrix} \begin{bmatrix} i_s \\ v_o \end{bmatrix} + \begin{bmatrix} \frac{1}{L} \\ 0 \end{bmatrix} v_s \qquad (2)$$

where L is the inductance on the ac side, C is the filter capacitor and R is the load resistance.
Equations (1) and (2) are digitized with a sinusoidal ac input voltage and the initial conditions $i_s(k)$ and $v_o(k)$. The resulting equations are given below.

$$\begin{bmatrix} i_s(k+1) \\ v_o(k+1) \end{bmatrix} = \begin{bmatrix} 1 & -\frac{U(k)}{L}e^{-(T/2RC)} \\ \frac{U(k)}{C}e^{-(T/2RC)} & e^{-(T/RC)} \end{bmatrix} \cdot \begin{bmatrix} i_s(k) \\ v_o(k) \end{bmatrix} + \begin{bmatrix} A \\ \frac{U(k)}{C}Be^{-(T/2RC)} \end{bmatrix} \frac{\sqrt{2}V_s}{\omega L} \qquad (3)$$

where

$$A = \cos(\omega kT) - \cos(\omega(k+1)T)$$

$$B = \cos(\omega kT) - \cos(\omega(k+\frac{1}{2})T$$

U(k) is a generalized pulse width that is either positive, negative or zero. The replacement of $U_p(k)$ with U(k) offers a difference equation for $v_B=0$ or $+-v_o$ in a reduced form. Since the ac side voltage is sinusoidal, the controller knows the reference current value $i_{ref}(k+1)$ at the end of the sampling period under consideration. Substituting $i_{ref}(k+1)$ into $i_s(k+1)$ of (3) gives the optimum pulse width U(k) to be applied within the k^{th} interval

$$U(k)=[L\{i_S(k)-i_{ref}(k+1)\}+\sqrt{2}V_S A/\omega]/[e^{-(T/2RC)}v_O(k)] \qquad (4)$$

This control law is a function of i_s, i_{ref} and v_o. i_s and v_o are measured and i_{ref} is generated by the controller.

SIMULINK MODEL

A model of the whole system was developed in Simulink. The Simulink model consists of a number of

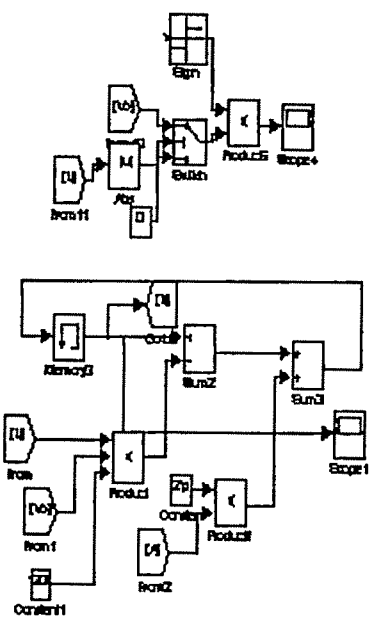

Fig.3 SIMULINK model(cont..)

functional blocks. In deriving the model, the digital equations and the system and the equation for optimum

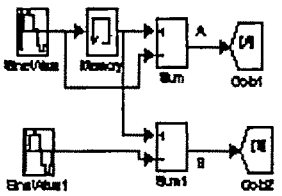

Fig.3 Simulink model(cont...)

pulse width were used. Using these equations smaller blocks were developed and interconnected them to form the whole system. The derived Simulink model is shown in Fig.3.

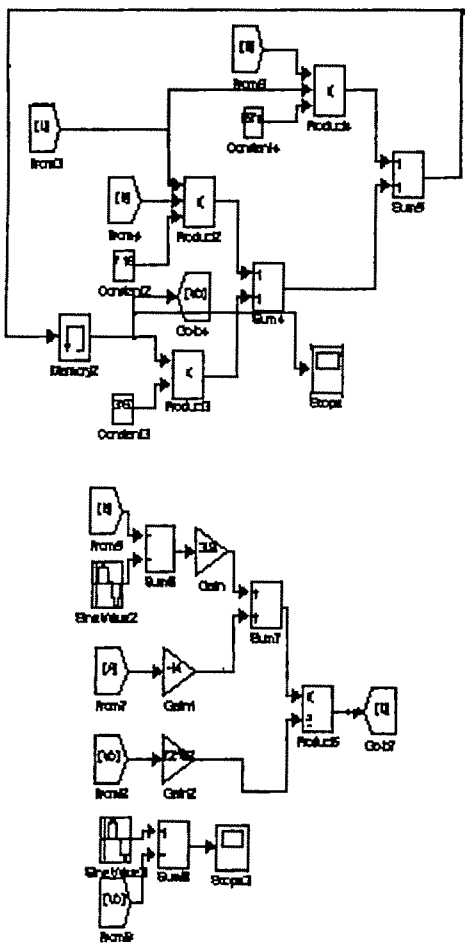

Fig.3 Simulink moel

SIMULATION RESULTS.

In order to view the results, a spectrum analyzer was developed in Simulink The performance of the rectifier with the proposed scheme was verified by simulation. Source current and its spectrum without any compensation are shown in Fig(4) The digital controller

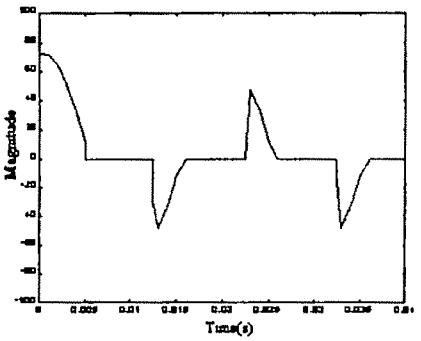

Fig.4.a Uncompensated current waveform

compensated source current and its spectrum are shown in

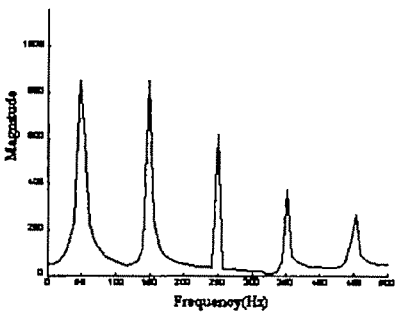

Fig4.b Spectrum of waveform in Fig.4.a

Fig.(5). From the figures we can see that the

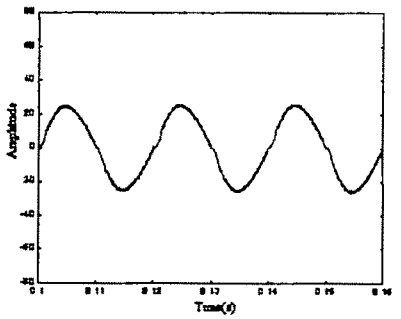

Fig.5.a Compensated current waveform

uncompensated source current contains a number of

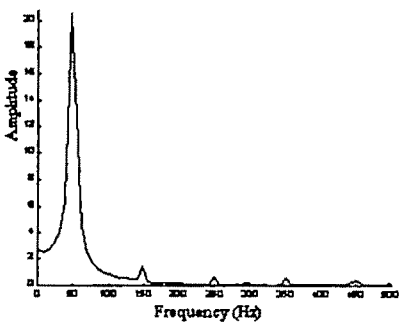

Fig.5.b Spectrum of compensated current

harmonics of the fundamental frequency component. Also, the magnitudes of the lower harmonic components are comparable. This leads to a high value of THD for the uncompensated system. The results also show that the

magnitudes of the harmonic components present in the compensated source current is negligibly small, which leads to a better value for THD.

CONCLUSION

The main problem with source current compensation is the extraction of a reference waveform. Here, the digital controller predicts the value of the source current and is compared with the actual source current. The controller to make the source current sinusoidal generates appropriate switching pulse widths and switching sequences. The controller improves the system power factor and considerably reduces the total harmonic distortion (THD)so that after compensation power factor and THD are within tolerance limits.

REFERENCES.

1. Ned Mohan, Tore M Undeland, William P Robin, "Power Electronics: Converters, Applications and Design", John-Wiley & Sons, New York, 1995
2. Muhammad Rashid, "Power Electronics, Circuits, Devices and Applications",Prentice Hall of India Pvt Ltd., New Delhi, 1998
3. Y.Nishida, O.Miyashita, T.Haneyoshi et al, "A Predictive Instataneous-Current PWM Controlled Rectifier with AC-side Harmonic Current Reduction", IEEE Trans. Inddus. Electron. Vol. 44, no. 3, June 1997, pp337-343.
4. M.R.Vikraman and.A.Kandaswamy, "A Simple Frequency Independent reference Current Generator for Active Power Filters", Proceedings of international conference, MS'2001, Ukraine(Lviv), pp 49-52., May 2001.
5. M.R.Vikraman and A.Kandaswamy, "Intelligent Controllers for Switched Capacitor Filters", Proceedings of national conference, NICE-2001, IETE Cochin center, pp 31-35, Feb 2001
6. M.R.Vikraman and A.Kandaswamy,"Educational Models of Power Electronic Systems Using Simulink", Proceedings of international conference, MS'2001, Lviv(Ukraine), pp 101-104, May 2001.
7. Matlab User's Guide, Math Works Inc, 1997
8. Simulink User's Guide, Math Works Inc, 1997
9. Hanselman.D and Littelfield.B, "Mastering Matlab", Prentice Hall, Englewood, Cliffs, NJ, 1996
10. Chee-Mun Ong, "Dynamic Simulation of Electric Machinery using Simulink and Matlab", Prentice Hall, New Jersey, 1998
11. W.Mack Grady, Robert. J Gilleskie, "Harmonics and how they Relate to Power Factor", Proceedings of EPRI Power Quality Issues & Opportunities Conference, San Diego, CA, Nov 1993,

A New Single Phase High Power Factor AC-DC Buck Converter

Mahadev S. Patil[1], Vinayak N. Shet[2] and Victor P. Sundarsingh[3]

[1]SES' College of Engineering, Kopargaon, Maharastra
[2]Goa Engineering College , Farmagudi, Ponda-Goa
[3]Indian Institute of Technology, Bombay, Mumbai,400 076, India
E-mail: mdvpat @yahoo.co.in ; vnshet@ee.iitb.ac.in ; vps@ee.iitb.ac.in

Abstract

A modified single-phase AC-DC buck converter having a high power factor is proposed in this paper. This converter is composed of controllable switches and fast switching diodes and functions in two operating modes. It has high power factor, sinusoidal input current, high input to output transformation ratio and is driven by a simple control strategy. The converter with the new control scheme was simulated in a computer and experiments were performed to check the validity. This converter has potential applications in telecom rectifier, battery charger and in DC motor drives

INTRODUCTION

The output voltage of a buck-type converter is lower than the peak of the input AC voltage,[1] and this significant feature is necessary in many applications requiring low DC voltage like UPS, DC motors etc. The delta modulation control (DMC) [2], which may also be called the capacitor voltage control (CVC), is being used for controlling the single phase AC-DC buck-type converter. This control scheme is sensitive to small perturbations in the circuit parameters and the control signal. On the other hand, inductor voltage control (IVC) method,[3] requires large inductors and the input to output transformation ratio is very low. Also, it uses complex control strategy. In this paper, we propose a simple control scheme to overcome these problems. It requires a few passive elements, comparatively small inductors and yet the input to output transformation ratio is high. At the same time, the power factor is near unity and the input current is almost sinusoidal.

PROPOSED CIRCUIT

The scheme with the simple control strategy is shown in Figure 1. The power circuit has four switches S_1-S_4. The switches (S_1, S_2) and (S_3, S_4) are switched in a complimentary fashion so that the output dc current is not interrupted. The inductor L_{in} and capacitor C_{in} act as an input H.F filter. The diodes D_1-D_4 are fast switching diodes. The capacitor C_o is selected depending on the ripple voltage requirement

OPERATING PRINCIPLE

The circuit operation can be explained in two modes.

MODE -I: During positive half cycle, switches S_1 and S_2 are first turned on. This will cause the inductor current to rise till the switches S_1 and S_2 are turned off.
MODE-II: As soon as the switches S_1 and S_2 are turned off, the switches S_3 and S_4 are turned on so that the inductor current decreases till the switches S_3 and S_4 are turned off. During the negative half cycle, switches S_3 and S_4 are first turned on. The inductor current again increases. As soon as the switches S_3 and S_4 are turned off, the switches S_1 and S_2 are turned on, ensuring that the inductor current decreases.

CONTROL CIRCUIT

The control circuit is designed in a manner such that it generates PWM pulses to turn ON and OFF the switches so that the output voltage can be controlled. The controller contains a zero crossing detector to identify the crossing of the positive half cycle to the negative half cycle of the input voltage. The output of the zero crossing detector is given to the switches A and C so as to turn them on during one half of the cycle. The complimentary pulses are fed to switches B and D, ensuring that they are turned on during the next half cycle. The PWM is generated by using a PWM generator. The output voltage of the converter and a DC reference voltage are the inputs to the proportional controller. The output of the proportional controller is given to the PWM generator, which controls the pulse width and

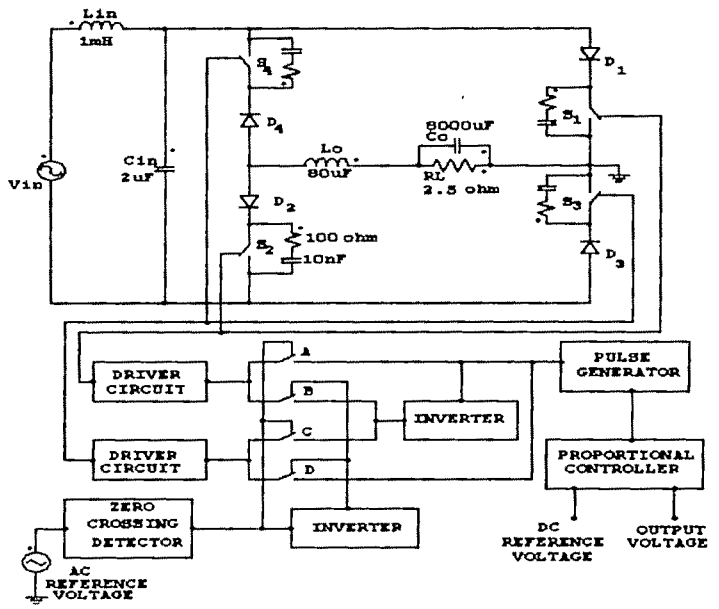

Fig 1 Proposed converter with simple control strategy

results in a close loop control. These pulses are then fed to the driver circuit through an optocoupler and then applied to the gates of the switches.

SIMULATION RESULTS

The proposed scheme is designed for 1kW power applications such as an UPS. The circuit is simulated for different conditions, using SABER simulation software [4]. In the simulation, generic switches offered by the SABER library were used. The designed circuit is simulated for a rated input voltage of 230V, for full load, half load and quarter load and also for an universal input voltages of 200V and 250V. The switching frequency is 20KHz. The output current is 20A and the output voltage is 52V, which is the float potential of a lead acid battery. The waveforms of the input current and the output voltage under full load condition are shown in Fig.2. It is observed that the input current is near sinusoidal and the power factor of the converter is 0.94 under full load condition. It is also observed that the input current waveform envelope improves if the input inductor filter value is increased. Also the circuit is simulated at 30KHz frequency and it is observed that the input current waveform remains sinusoidal.

EXPERIMENTAL RESULTS

The power circuit is fabricated and the entire circuit is tested in order to demonstrate the feasibility of the proposed scheme using IC 3524. Fig.3 shows the input voltage and the input current waveforms obtained experimentally. It is observed that the input current is near sinusoidal and is in phase with the input voltage. The experimental results were found to agree closely with the simulation results.

CONCLUSION

A new, single phase AC-DC buck converter having a simple control strategy has been proposed in this paper. This converter is capable of achieving a near sinusoidal input current and high power factor. It's features also include high input to output transformation ratio and there is no transformer in the scheme. The scheme was analyzed, simulated and the feasibility of the proposed converter was verified experimentally by implementing a 1KW prototype in the laboratory. This converter can be used in low and medium power applications where isolation is not required.

REFERENCES

1. Ramesh Oruganti and Ramesh Srinivasan, Single phase power factor correction-A Review, Sadhana,Vol. 22, Part 6, pp.753-780, December 1997.
2. Bakari M. M, Mwinyiwiwa, Patrica M. B and Boon-Teck Ooi, Delta Modulated Buck Type PWM Converter, IEEE Transactions on Industrial Application, vol. 28, No. 3, pp.552- 557, May/June 1992
3. Ramesh Oruganti and Moorthi Palaniapan, Inductor Voltage Control of Buck Type Single-Phase AC- DC Converter, IEEE Transactions on Power Electronics, vol. 15, No. 2, pp.411-417, March 2000
4. SABER and Power Express User's Guide, Analogy, Inc., 1993

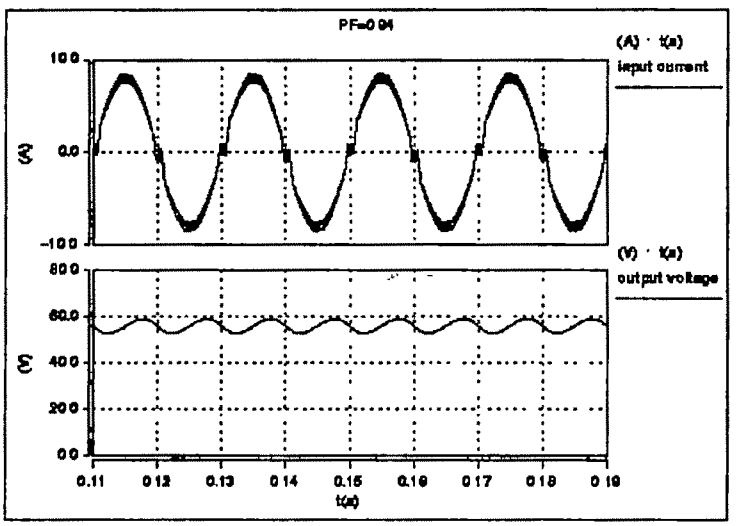

Fig 2 Input current and output voltage waveforms

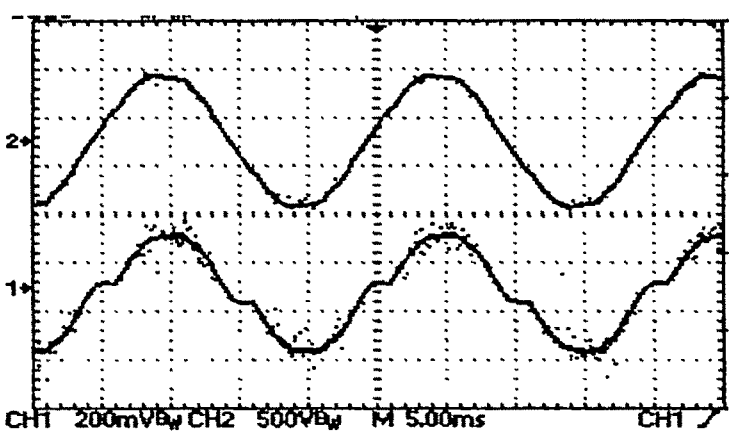

Fig 3 Experimental results of input voltage and input current

An Innovative Method for Turn-off of SCR and Power Factor Improvement of Controlled Converter

Vinayak N. Shet* and Victor P. Sundarsingh
Electrical Engineering Department
Indian Institute of Technology- Bombay, Powai, Mumbai 400 076, India
Email:vnshet@ee.iitb.ac.in ; vps@ee.iitb.ac.in

Abstract

Silicon controlled rectifier when used for an ac to dc converter results in poor power factor. However, they can be easily protected under overload condition, using a semiconductor fuse. In this paper, a novel scheme is incorporated, using which the SCRs can be subjected to sine weighted pwm switching. In addition, the power required to turn off the SCR is also sine weighted which results in the improvement of power factor from 0.4 to 0.9. Thus, good power factor along with rugged protection capability are achieved simultaneously. The scheme was simulated using SABER and experimentally verified.

INTRODUCTION

Any converter whose power factor is less than unity, absorbs apparent power higher than the real power it consumes, resulting in the loading of the power system. Most of the modern day power appliances and controllers, usually use a diode rectifier followed by a bulky LC filter to convert the ac voltage to a dc voltage. Because the conduction angle is small, especially when the ratio of the input voltage to the DC voltage is high, the input line current contains high harmonics, which pollute the power system and also interact with other equipments. In addition, power factor is low resulting in line losses. Switched-mode or pulse width modulated (PWM) rectifiers using instantaneous-value control are used for ac-to-dc power converter in inverters and uninteruptible power supplies to over come this problem [1]. Single stage, single switch power factor correction circuits are in the form of a cascade combination of discontinuous-mode Power Factor Converter (PFC) and a dc-dc converter, with the two converters sharing a single switch [2]. These PFC converters rely on the discontinuous-mode (DCM) of operation to provide higher power factor, while the dc-dc converter can operate in either mode [3]. Operating the dc/dc converter in DCM at constant frequency results in a constant voltage stress of the storage capacitor irrespective of the magnitude of the output load. However, these high-frequency switching pre-regulators considerably increase the cost and the complexity of the conversion unit and contribute to the generation of high-frequency electromagnetic interference, calling for the incorporation of suitable EMI filters in order to comply with the high-frequency emission limits. In addition, the harmonics current it produces deteriorate the quality of the power source. Because of these reasons, efforts to reduce the harmonics on the ac side and simultaneously realize near unity power factor of operation are being made. In addition, power factor correction circuits will become mandatory if more stringent requirements such as defined in the IEC-1000-3-2 standard or harmonic standard such as IEC 555-2 and IEEE 519 are imposed.

This paper presents a single-stage two switch converter topology having a regulated dc output voltage and a high input power factor.

OPERATING PRINCIPLES

The proposed power factor converter circuit for battery charging is shown in Fig.1. The converter has SCRs T_1 and T_2 as controlled switches and diode D_1 and D_2 as rectifying elements. Inductor L and a Capacitor C are used in the dc side as filter elements. To reduce the ripple current in the line, Inductor L_1 and C_1 are used as ac side H.F. filters. The SCRs are turned on in accordance with the PWM scheme and the PWM waveform is generated by comparing the reference sine wave with a generated triangular wave. The amplitude of the triangular wave generated is proportional to the difference between a reference and the output voltage. In order to turn-off the SCR, the switch Q_1, which was OFF, is turned-on by applying a signal to the base of

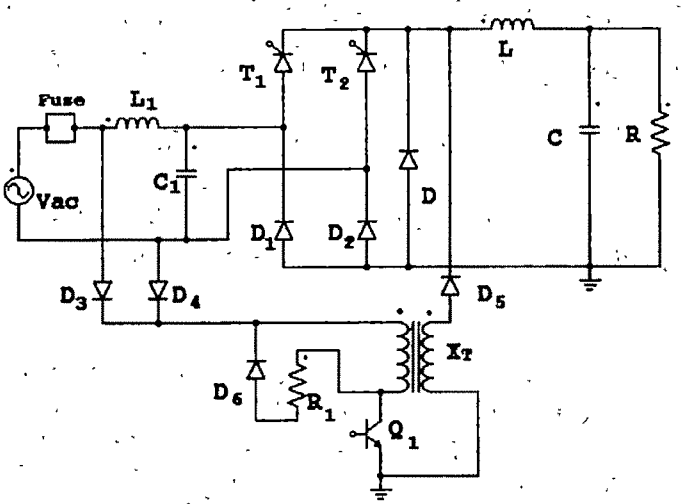

Fig 1 Proposed scheme for power factor control using SCR

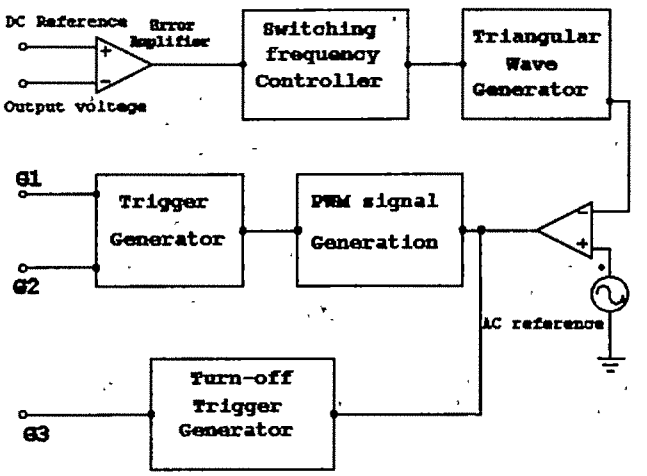

Fig 2 Control scheme used for controlling the converter

V_o	L_c	C_c	P.F. (Proposed)	Semiconverter (Conventional)	% increase (compared to conventional)
105.11	3mH	50μF	0.90	0.64	39
102.87	4mH	30μF	0.90	0.63	42
63.17	3mH	50μF	0.82	0.45	82
61.54	3mH	30μF	0.86	0.44	89
59.08	4mH	30μF	0.79	0.43	84
52.00	1mH	30μF	0.83	0.38	120

Table 1 Comparative performance of the proposed configuration with the conventional circuits

the transistor Q_1. The secondary to primary turns ratio is kept at 1.2 to 1.5 to ensure that at any instant the reverse voltage generated by the secondary of the transformer is greater than the mains input. This high voltage generated at the secondary of the transformer will turn off the already conducting SCR after t_q, the turn off duration of the SCR, by inducing a reverse voltage across the SCR. The voltage induced by the secondary of the transformer is for a duration slightly greater than the turn-off duration of the SCR namely t_q.

SIMULATION

This circuit is simulated on SABER. For this the reference voltage is applied to two switches, which are complementary to each other and are switched at half the switching frequency of the SCRs. The output voltage after the switch is integrated to generate a triangular wave, and then rectified. The rectified triangular voltage is compared with an ac signal taken as reference from the ac mains. The cross over points will generate the PWM waveform at the output of the comparator. The output of this comparator is then applied to the gate of the thyristor through a driver stage. To generate turn-off pulses, negative going edge of the PWM waveform is detected and transistor Q_1 is turned ON for 30μsec (t_q=20μsec) so that the SCR will turn off.

To obtain a high ac supply power factor and continuous input current conduction, ac side filtering is carriedout using L_1 and C_1 (High frequency). The values of the ac side inductor and the capacitor are selected to give maximum power factor. Table I shows the simulation results.

The main advantage of the scheme is that the commutation of the SCRs is independent of the commutating element, the charging voltage, and the current through these elements unlike the other conventional methods [4]. In the conventional method the performance deteriorates at low voltages and may results in a commutation failure. Further, in our scheme the transformer used to turn-off the SCR will be carrying current only during the turn-off period of the main SCR. Hence, the power rating and size will be minimal. Finally, the main advantage of this configuration is that the protection scheme calls for a simple HRC fuse. The comparative performance of the configuration is shown in Table I.

Here the conventional power factor is calculated using the formulae

$$\text{Semiconverter Power factor} = \frac{I_{s1}}{I_s}\cos\frac{\alpha}{2} = \frac{\sqrt{2}(1+\cos\alpha)}{[\pi(\pi-\alpha)]^{1/2}} \qquad (1)$$

In equation (1) α = firing angle of conventional controlled converter. I_s = input rms. current from the ac mains. I_{s1} =rms. value of fundamental current

From the table I it is seen that the performance improves considerably at low output voltages. It is clear that the battery charger which uses semicontrolled converter to deliver an output voltage of 52 volts has a power factor as low as 0.38. However, by using the proposed method the power factor can be increased to 0.83. The source current drawn by the converter follows the voltage and is a nearly sinusoidal with no phase shift and hence, high power factor is achieved. The simulation results of above proposed scheme is shown in Fig.3 which shows the voltage across the cathode of the main SCRs and the input line current drawn from the mains.

EXPERIMENTAL RESULTS

Based on the above principle a converter was designed for an output D.C voltage of 52 V and a power output of 1kW. It was tested under various input voltages from 170V to 250V and under various rated currents. The converter is operated at a switching frequency of 1.2khz and the scheme is shown in Fig.1.

The values of the component used are as follows: L_1=2mH, C_1=30uF, L=10mH C=10000uF. SCRs T_1, T_2 are BTW 30-800, switch Q_1 is BJT BUX 98A 3 nos.(in parallel), Diode D_1, D_2, D, D_3, D_4, D_5 are BYX 66-1000

The upper plot of Fig 4 shows the voltage across the cathode of the SCR and the lower plot shows that the input mains current is near sinusoidal having minimum ripple and negligible displacement. Finally, the output DC voltage is smooth having a ripple of 2%.

CONCLUSIONS

A single phase ac-dc converter having a conventional two SCR two-diode bridge is switched in a sine weighted pwm fashion using a new turn off scheme which also draws sinusoidal power. The scheme was simulated and experiments were conducted to evaluate its performance. The power factor was found to increase from 0.4 for a conventional bridge to 0.9 when new scheme is adopted. The scheme is easy to protect under overload and short circuit condition because of the inherent overload characteristic of SCR. Hence under short circuit the fuse fails without the device failure.

REFERENCES

1. Omar Stihi and Boon-teck Ooi, "A single-phase controlled-current PWM rectifier", IEEE Trans. on Power.Electronics. Vol. 3, No.4, 1998, pp.453-459.
2. Martin H.L. Chow, Yim-Shu Lee and et, "Single-stage

single-switch isolated PFC regulator with unity power factor, fast transient response, and low voltage stress", IEEE Trans. on Power Electronics, Vol. 15, No.1, Jan 2000, pp.156-163.

3. R. Redl, L.Balogh, and N.O. Sokal, "A new family of single-stage isolated power factor correctors with fast regulation of the output voltage," in IEEE Power Electronics Specialist Conf. Rec. , vol.2, June 1994, pp. 1137-1144.
4. M.H. Rashid, "Power Electronics", Prentice-Hall of India Pvt. Ltd., 1994.
5. V. N. Shet and V. P. Sundarsingh, "A Novel Power Factor Correction in Phase controlled Rectifier," *in IEEE International Conference on Harmonics and Quality of Power Proc.*, Oralndo, FL, Oct. 2000, pp. 560-563.

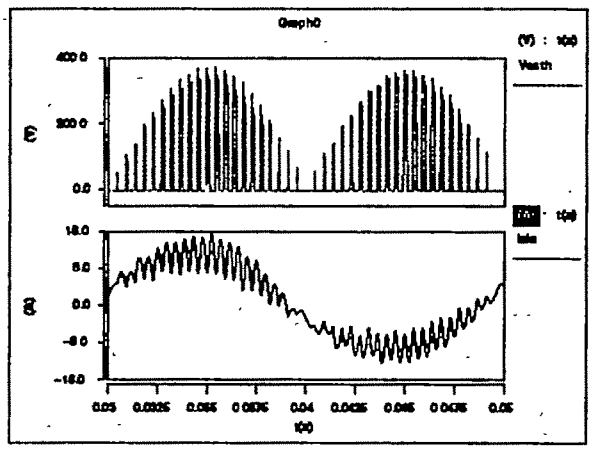

Fig.3 Simulation result for the proposed converter (i) Voltage across the cathode of converter SCR w. r. to ground (ii) line current from ac mains

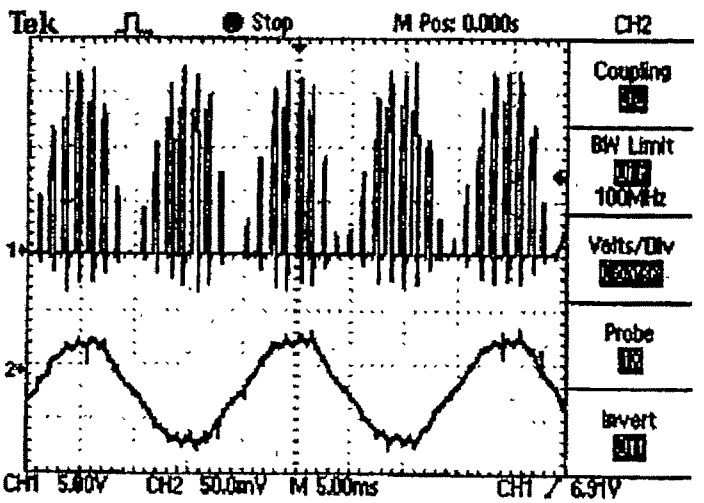

Fig.4 Experimental results of the proposed converter (i) upper plate cathode voltage across SCR w. r. to ground. (ii) lower plate line current drawn from the mains.

A PC based Speed Control System for a Switched Reluctance Motor

Rajat Bhattacharjee
Department of Electrical Engineering, Jadavpur University
Kolkata – 700 032, West Bengal, India.
E-mail : r_b@hotmail.com

Abstract

A PC based closed-loop speed control system of SR motor for variable speed drive system is presented in the paper. The PC function includes feedback speed control, computation of the feedback speed, sequencing, computation of the switching angles, control signal for current regulator and switching circuit. The complete control system was tested in the laboratory with a tailor-made 0.75 kW motor and the performance was found to be satisfactory.

INTRODUCTION

Recent interest in switched reluctance motor (SRM) drives has been expressed by many researchers because of the drives' cost advantages, ruggedness and ease of repair, which make it suitable for domestic and industrial applications [1]. In variable speed applications like fans, washing machine, machine tools and propulsion drives the preference of SRM is due to its advantages over competitive motors in manufacturing, reliability, robustness, high torque to inertia ratio as well as life-time. For special environments e.g. at high temperatures or in intense temperature variations operation of the SRM is possible.

SRM DRIVE

SRMConfiguration

The switched reluctance motor designed has six stator poles and four rotor poles. The cross-section of the motor is shown in Fig.1.

SRM Power Converter

The power electronic converter scheme used supplies for the opposite stator poles by a converter phase and the phase current is switched on and off in synchronism with the rotor position with the help of power transistors. The transistors conduct in sequence and the order of conduction depends on the direction of rotation. The flux in the switched reluctance motor is not constant but must be established from zero at every step. In motoring operation the build up is timed to coincide with the period when the rotor poles are approaching the stator poles of the phase that is due to be excited. The process is controlled by switching the supply voltage on at the turn-on angle and switching off at the commutation angle. In the converter circuit the chopping transistor of the current controller is working all the time whereas commutating transistor of the switching circuit have a duty cycle of one third, consequently the switching and conduction losses as well as mean and r.m.s currents in the chopping transistor are higher than commutating transistors. After commutation during the flux suppression period the stored field energy is returned to the supply. Freewheeling diode is used to suppress the flux when switched off due to volt-drop in the diode and winding resistance [5].

The current controller used in the converter circuit is a PWM switching type regulator in which constant current regulation is accomplished by using the LM 3524 regulating pulse width modulator IC. The operation of the PWM switching power supply is achieved by chopping the direct current (dc) input voltage into pulsed whose amplitude is the magnitude of the input voltage and whose duty cycle is controlled by a switching regulator controller. The power electronic controller used supplied unipolar current pulse to the stator and it regulates the magnitude and the wave shape of the current to fulfil the requirements of speed control and hence torque and to ensure safe operation of the motor and the power transistors.

CONTROL SYSTEM

The control system incorporates both hardware and system software written in C language using the interrupt facility of the PC. The software receives the angle commands from the feedback loop and translates them into transistor conduction angles which are synchronized with the rotor position. The machine has a rotor position encoder which consists of three optical sensors and an interrupting disc with the profile of the rotor stamping. The sensors are mounted at the right edge of each stator pole-pair. Optical sensors are connected to the sensing interface which transmits the angle command signal generated by optical interrupter disc via digital input interface to the PC. The system software compares the actual speed to the reference speed and depending on the error the analog output issues control signal to the current controller from the PC. Also the system software issues the signal to the base drives of the switching transistors of the switching circuit which supplies the stator phases and hence switching sequence task is also accomplished by the software.

LABORATORY TEST

The SRM used in testing has a nominal rating of 0.75 kW, design parameter of which was determined and accordingly the motor was fabricated. A dc load machine was coupled to the shaft to apply a variable load torque. The SRM was first tested open loop with the newly developed software based angle controller and then feedback control was incorporated. The drive system was tested for both steady-state and transient conditions and the performance was found to be satisfactory.

CONCLUSIONS

SR drives is capable of high levels of performance over a wide range of specifications in a robust form. This is achieved by sophisticated design of motors, power electronics and control strategies including closely integrated design of the motor and the controller. To achieve this many variables must be included in the design optimization. Soft switched drive circuits that use resonant circuits have been reported [6]. These circuits appear to produce less EMI and have lower switching losses in PWM action. The drive system should provide not only low switching losses and low EMI but also higher torque and higher efficiency. The development of new and improved control strategies is constantly improving its capabilities.

ACKNOWLEDGEMENT

This research work is a part of the research project sponsored by DOE, Government of India, New Delhi at the Jadavpur University, Kolkata. The author gratefully acknowledge the support received from the authority of the department of Electrical Engineering, Jadavpur University

REFERENCES

1. P.J. Lawrenson, J.M. Stephenson, P.T. Blenkinsop, J. Corda, and N.N. Fulton, "Variable speed switched reluctance motors", Proc. Inst. Elec. Engg., Vol.127, pt.B., no.4, pp 253-265, July (1980).
2. W.F. Ray et al, "High performance switched reluctance brushless drives", in Proc. IEEE-IAS Ann. Mtg., Oct. (1985), pp. 1769-1776.
3. B.K. Bose, T.J.E. Miller, P.M. Szczesny, W.H. Bicknell, "Micro-computer control of switched reluctance motor", IEEE Trans., Vol.IA-22, pp. 708 – 715, July/Aug (1986).
4. H. Moghbelli, G.E. Adams and R.G. Hoft, "Performance of a 10-h.p. switched reluctance motor and comparison with induction motors", IEEE Trans., Vol.IA-27, no.3, pp. 531 – 538, May/June (1991).
5. T.J.E. Miller, "Switched reluctance motors and their control", (1993) Oxford University Press.
6. Yoshihiro Murai, Ji Cheng and Masaharu Yoshida, "New soft-switched/switched – reluctance motor drive circuit", IEEE Trans. on Ind. Appl., Vol.35, no.1, Jan/Feb (1999).

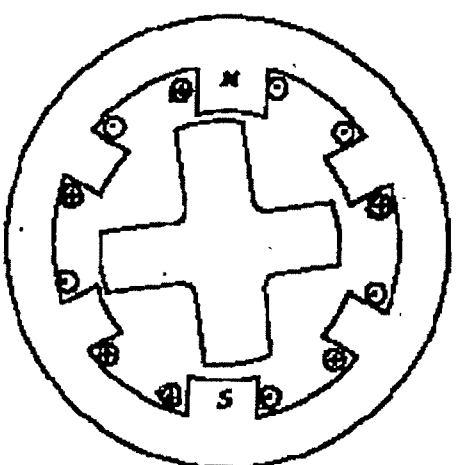

Fig.1 Cross-section of 6-4 pole SRM

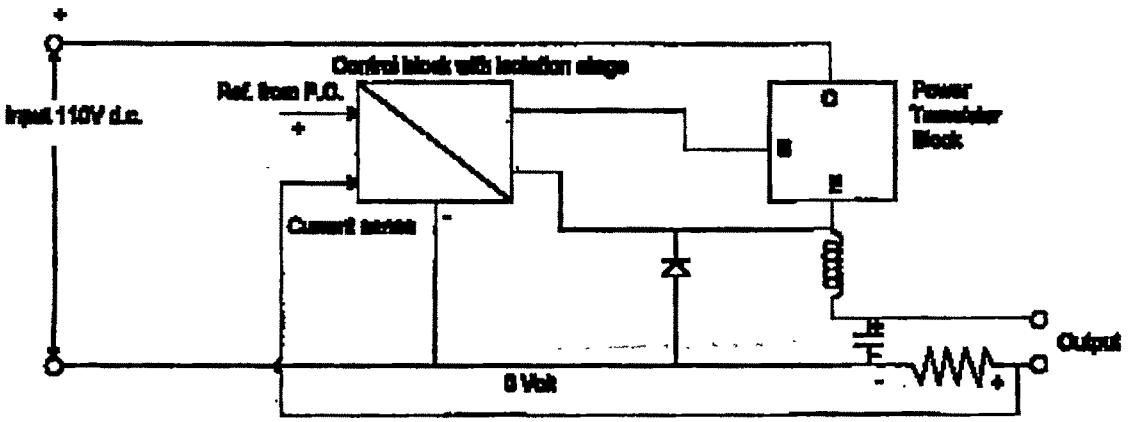

Fig.2.: Block diagram of Current Controller (SMPS)

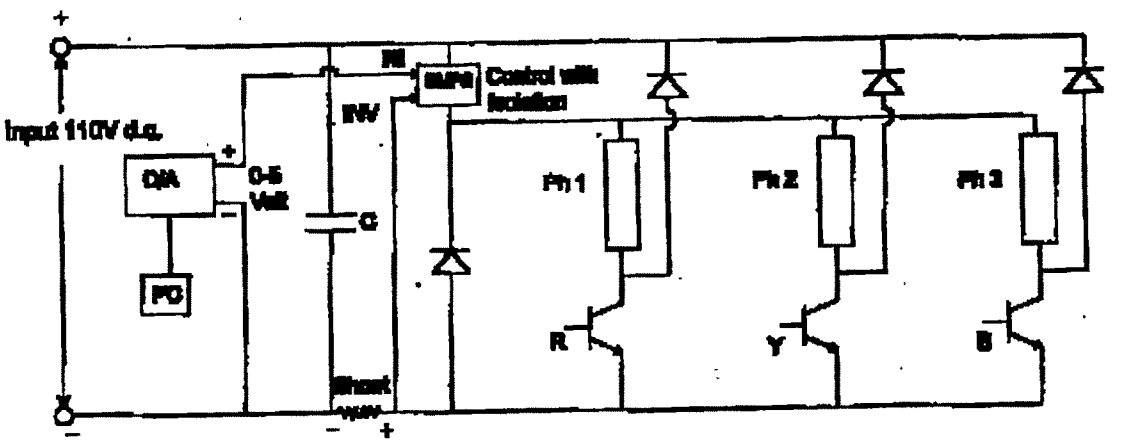

Fig. 3: Block diagram for the switching scheme used for the SRM

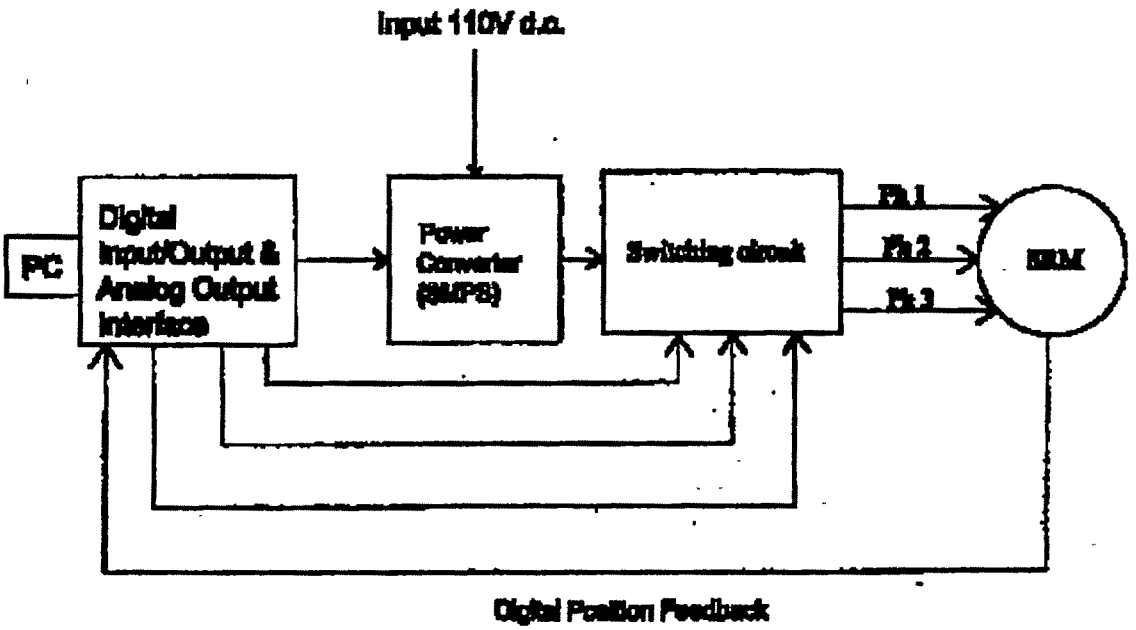

Fig. 4 : Block diagram of the SRM drive system

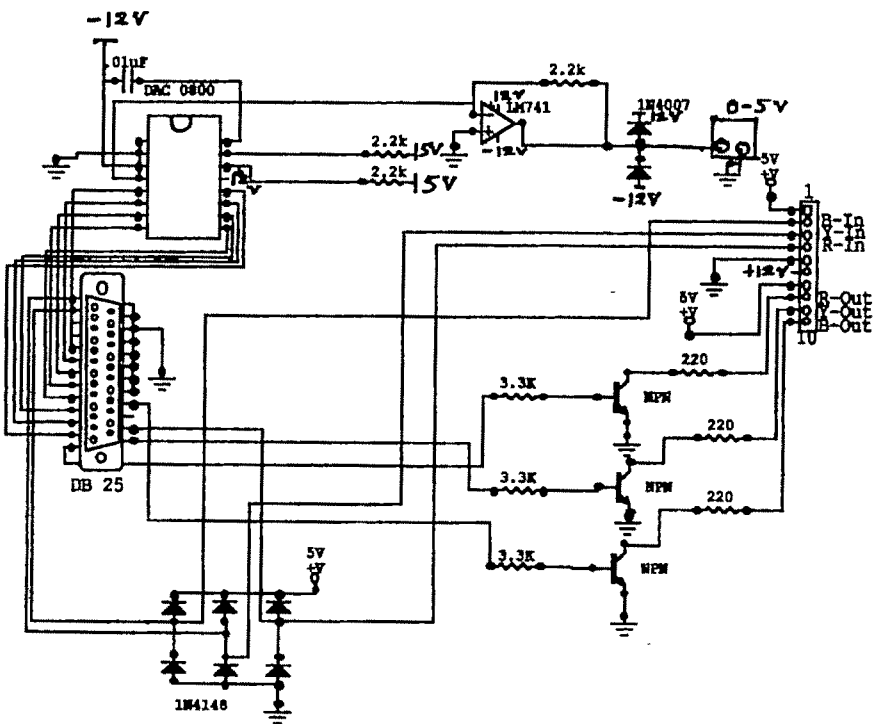

Fig.5 Digital Input/Output & Analog Output Interface Circuit

Sensors In Instrumentation

D. Patranabis
Department of Instrumentation Engineering
Jadavpur University, Calcutta 700 032

Abstract

Instrumentation in the present day state of the earth has converged into two components: (i) sensor and (ii) processor based outfit. In the latter networking, communication, fast computation and programmability have made the realization of the system quite comprehensive. While attempts are in the increase to integrate the sensors / transducers in this outfit leading to what is now known as virtual instrumentation, it is difficult to fully dispense with the traditional sensors at this stage. The presentation here gives minimal consideration to the second part of the system and attempts to cover the traditional as well as newly developed sensors in a perspective which may turn to be an appraisal.

INTRODUCTION

It is now a proverbial truth that the father of measurement science e Lord Kelvin, declared that only when something can be expressed in numbers it is understood properly and is said to be measured. Achievement in science and technology, in fact can be attributed to the human ability ascertain a physical system by measuring its state condition or characteristic – quantitatively and accurately.

Instrumentation science/ engineering/ technology is the present day terminology of the older time discipline Measurement science. It now includes not only measurement as such but also actuation, control analysis and telemetry. It is highly interdisciplinary in nature and deals with science and technology of instrumentation and variables in the area of physical science, life science, engineering and technology, and takes help of or supported by the electronics, communication, computers and networking which are themselves growing at faster rates.

A generalised instrumentation system would consist of a number of elements (Fig 1) and although there are some options in the items/blocks shown depending on the plants and processes, the mode (analog / digital) and the system requirement (local / remote) etc., it is certain that the basic measurement part is essentially needed in all centralised instrumentation system.

As seen from the figure 1, the major components in such a generalized instrumentation system are:
(sensor / transducer), (actuator and control valve), (analog system of control) / (digital system of control), telemetry system and analysers.

The sensor / transducer block is the primary block and is of our concern in the present discussion. A few relevant are thus made about sensor initiating the study to follow.

One notices in a typical sensor profile of a major process plant that it is still dominated by the traditional types, the other types are growing but yet not at pace expected at this point of time. The non-invasive microelectronic types are fast picking up but the areas covered are yet too limited.

Of the four process variables, flow pressure temperature and level, the order of population strength is temperature, flow and level with pressure coming in the sequel often as a monitoring parameter fro flow and level.
Solid state integrated type (IC) sensors are in increasing demand in the automotive industries and consumer applications areas are flushed with such sensors. Smart sensors are extension of such sensors where in-built compensation, calibration, data conversion, range change etc. are easily made using microprocessors.

Another category of newer type of sensors is the optical fibre variety which is gradually being commercialised for liquid level, flow, temperature, magnetic and electric fields, field rotation, acoustical field, strengths etc.

Analysis and hence analysers are very important for accuracy in process control and with the enhanced facilities of data analysis now, analysers have been able to find deep inroad into the production process. Besides, analytical instruments have widened the scope of pollution and environmental studies. Solid state sensors that are using materials and which have higher reliability, sensitivity and easy interfacing capabilities now being quite extensively

used in such studies in association with the microelectronic processing architecture.

GROWTH

Sensing and transducing elements which were developed early but are still in use are not uncommon. Along with however, newer types have been developed over the years and decades. We present a brief record of the major ones so developed in the century just ended.

- In the first two decades: the pneumatic types such as filled-in thermometers
- Third decade: flame analysers, UV detectors. electron microscope, precision RTD, thermistors, radiation incident detectors, piezo-sensors for vibration and acceleration, strain gauge and pneumatic displacement sensors etc.
- Fourth decade: humidity sensors, load cells, IR gas analysers, transistors (1948).
- Fifties: gas chromatography, magnetic flow meters, ultrasonic flow and level meter, capacitance pressure gauge.
- Sixties: fibre optics, fluidics, IC sensors.
- Seventies: LEE, VDU monitor, solid state pressure sensors, opto-isolators, cariolis mass flow meter, smart sensors.
- Eighties: Smart transmitter, communicators, area network
- Nineties: Environments fro process software, development in virtual instrumentation, intelligent I/O, nano-sensor technology.

Things obviously have not remained static and first development of newer techniques of information processing and dissemination is urging development of newer sensors as well as at least integration of the existing ones with these new techniques.

SENSORS AND TRANSDUCERS

Definition and standards

Sensors, as a term, is in use for over two decades now. Earlier to that no consideration was given separately to it from a generalized measurement system or instruments which, in turn, was considered as entity to gather information concerning physical, chemical, and biological environments. In fact, it was the 'human senses' and human intelligent put together that were being attempted to be followed to construct a technical analog after the capabilities of microprocessors were known. That time onward, instruments developed to measure physical, biological and chemical quantities were being designated as 'sensors' and obviously not very effectively.

In course of time, when instrumentation with its multidisciplinary functionality came to project itself as a separate discipline even in advanced technical courses of studies, definition of sensors started receiving attention but the wide spectrum of users and manufactures could not agree to a single expository definition. Obviously, several definitions appeared in the literature creating more confusion than comprehension. About that time another term appeared in the scene to signify the same thing. The diverse opinions seem not to destined to converge at all. This new term was derived from the principle of action of the elements followed conversion and / or transduction. However, it would be agreed by many, if not all, that sensor is the only the primary element of the instrumentation system. Transducer is perhaps, the same.

Going by the proposition of the ISA, transducer is considered to be a device which can provide an usable *output* in response to a specific *measurand* where the laster is a physical quantity, a property or r condition that is measured and the 'output' is to be an electrical quantity (ANSI MO 6.1, 1975) [1]. However, it should not be physical only, but biological and chemical as well.

Likewise usable output should not be limited to electrical only. It is suggested that all type of energy could from usable output – such as mechanical, chemical, thermal, magnetic, radiant and of course electrical.

In recent years, the primary element in an instrumentation system is called either a sensor or a transducer with preference for the latter as enunciated in the ANSI standard 1975. sensor, however, appears to be more popular in the bulk of literature. Transducer as a terminology is used by many in various other areas to designate other types of elements such as display elements that converts electrical energy into optical form, electro-acoustic devices that transmit or receive sonic or ultrasonic waves. However, transducers and sensors are synonymously used as far as measurement technology is concerned.

The International Electrotechnical Commission (IEC) has maintained that a sensor is the primary element of a measurement system [2] and it converts the input variables into a suitable form fo signal for measurement. There would not be any end of argument as to the appropriateness of this term for the purpose. We stick to the suggestions proposed by the Commission and ANSI which basically are the same.

Transduction principles are based on physical and chemical effects and transducers are developed using / exploiting these effects. There are more than 350 such effects, although all are not usable to form transducers. This is not the place to elaborate on these effects or at least the ones which are effectively utilized. However, a few of them are listed below stating the effect and the form of

conversion. The types are chosen to cover all forms at least once.

Table 1

Effect	Conversion
Acoustic (diaphragm)	Mechanical to mechanical
Electromechanical	Electrical to mechanical
Hall	Magnetic to electrical
Thermal conductivity	Chemical to thermal
Piezo-magnetic	Mechanical to magnetic
Electro luminescence	Electrical to radiant
Nuclear magnetic resonance	Chemical to magnetic
Doppler	Mechanical to radiant
Thermal expansion	Thermal to mechanical
Photovoltaic/photoconductive	Radiant to electrical
Piezoelectricity	Mechanical to electrical
Seebeck effect	Thermal to electrical
Thermopile/Bolometer	Radiant to thermal
Emission/ absorption spectroscopy	Chemical to radiant

Classification of sensors

Sensor classification is a very difficult process, as a single sensor may belong to a number of categories by adopting process of classification. However, classification may follow a compromise rule between principle of transduction and application. A very broad classification would look something like this: (i) mechanical and electromechanical (ii) Thermal (iii0 magnetic (iv) radiant (v) Electrochemical. Examples are as follows:

i. A piezoelectric element, a magneto-strictive sensor, an LVDT, a ferro magnetic plunger, etc.
ii. A resistance thermometer, i.e. an RTD, a thermocouple, a PTAT IC sensor, optical / total radiation pyrometer sensors.
iii. Yoke coil type (fro torque), magneto-strictive type, Hall effect type, Eddy cirrent type, synchros.
iv. Photoviltaic / photoconductive cells, photodiodes, phototransistors, X-ray, Gamma-ray sensors.
v. Hydrogen sensing electroded, membrane electrodes, ion-selective type and molecular selective electrodes, Chemical-FET.

SENSOR MARKET

Important sensors, specifically for process industries are flow, level, pressure and temperature which are supported by position, speed, chemical, flue gas and radiation (optical) sensors. With a recession in economy over the last five years there has been some decrease in the market growth. Earlier to that over the period of ten to fifteen yearsthe growth rate is quite high mainly because of the increased industrialization, consciousness of quality, competitiveness and availability of wide varieties and types including newer ones through break-through technology. Fig 2 shows the trends. .

Growth in application market

For better efficiency, comfort, economy of product output and enhancement of quality, sensors and transducers are covering all walk of life. The common areas in application volume can be listed as follows:

Table 2

Technologies	%
Industrial process and manufacturing technology	55
Building automation, safety and inspection	10
Automotive engineering	8
Medical, diagnostic, patient monitoring	8
Consumer products	6
Military and avionics	5
Agriculture	4
Pollution and ecology	4

R & D areas and laboratory activities are separately considered and have not been included in the list.

CERAMIC SENSORS

Ceramic sensors are a new class of sensors by themselves and are being increasingly used for sensing variables like gas composition, humidity, temperature, pressure, infra-red radiation and many others. The list (table 3) gives their present state and some application areas.

SINGLE AND MULTISENSORS

Single sensor is a term that is used to identify devices that include signal transformation and processing in a single sensor block. Smart sensor is a concept similar to it. It is a growing fast and is on its way to be standardized as well. Biological materials are becoming more useful in sensor development. Silicon, however remains the base material for single sensor system.

Multisensor system is a concept that has been utilized and is still in adoption stage to solve for (a) signal processing supported by integrated modular electronics at the place of measurement. (b) automatic signal processing by organized software (c) higher speed of signal processing and (d) standardization with sensor interface and ;;control systems.

REFERENCES

Electrical transducer nomenclature and terminology, ANSI standard No 6,1-1975, Research triangle park, New Connecticut, 1975

W. Gopel, J. Hasse and J. N. Zemel (ed), Sensors: A comprehensive survey, vol 1, VGH Verlagsgesdlschaft mbH, D 6940,Weinheim, Germany, 1989.

Table 3

Ceramic oxide sensor	Working principles	Applications
ZrO_2 Nasicon ($Na_{1+x}Zr_2Si_xP_{3-x}O_{12}$, $0<x<3$	Ion conductivity and Nerst equation	Oxygen and gas sensor
TiO_2 SnO_2 ZnO $SrTiO_2$, $BaTiO_3$, $SrSnO_3$,	Semiconductivity (conduction on temperature and gas pressure)	Oxygen Hydrocarbon gases Oxygen
ZrO-Y_2O_3, NiO-TiO_2,	N.T.C	Temperature
Doped $BaTiO_3$	P.T.C	Temperature
SiO_2, $ZnCr_2O_4$	Surface ionic conductivity	Humidity
$BaTiO_3$, $PbZrO_3$–$PbTiO_3$ (PZT®) PLZT+ ($Pb_{1-x}La_x$), (Zr_yTi_{1-y})$_{1-x, 3y}O_3$)	Piezo electricity	Pressure & refractive index
Quartz	Piezo electricity	Do
$PbTiO_3$, $LiTaO_3$, $SrNbO_3$	Pyro electricity	Infra red radiation

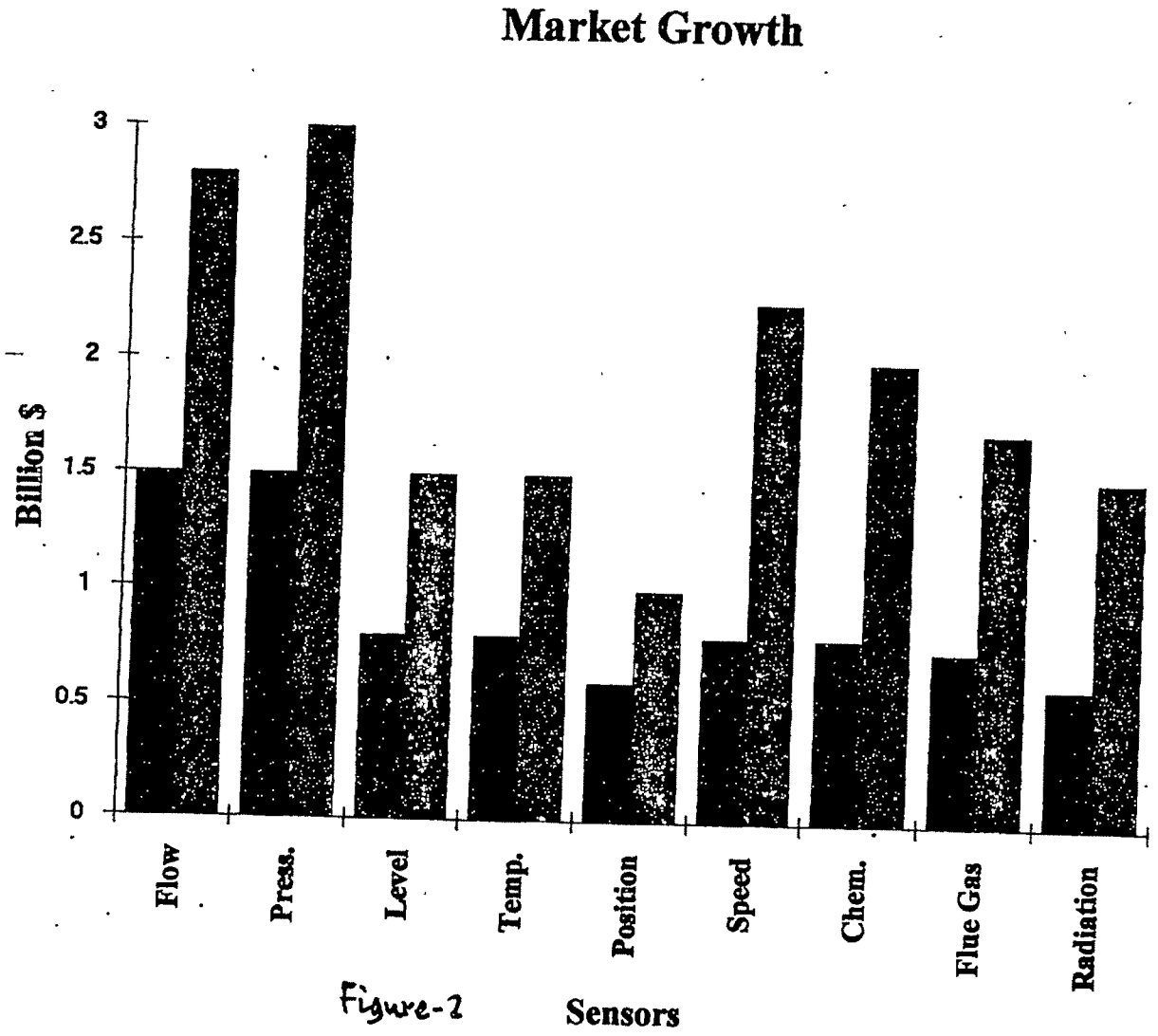

Figure-2

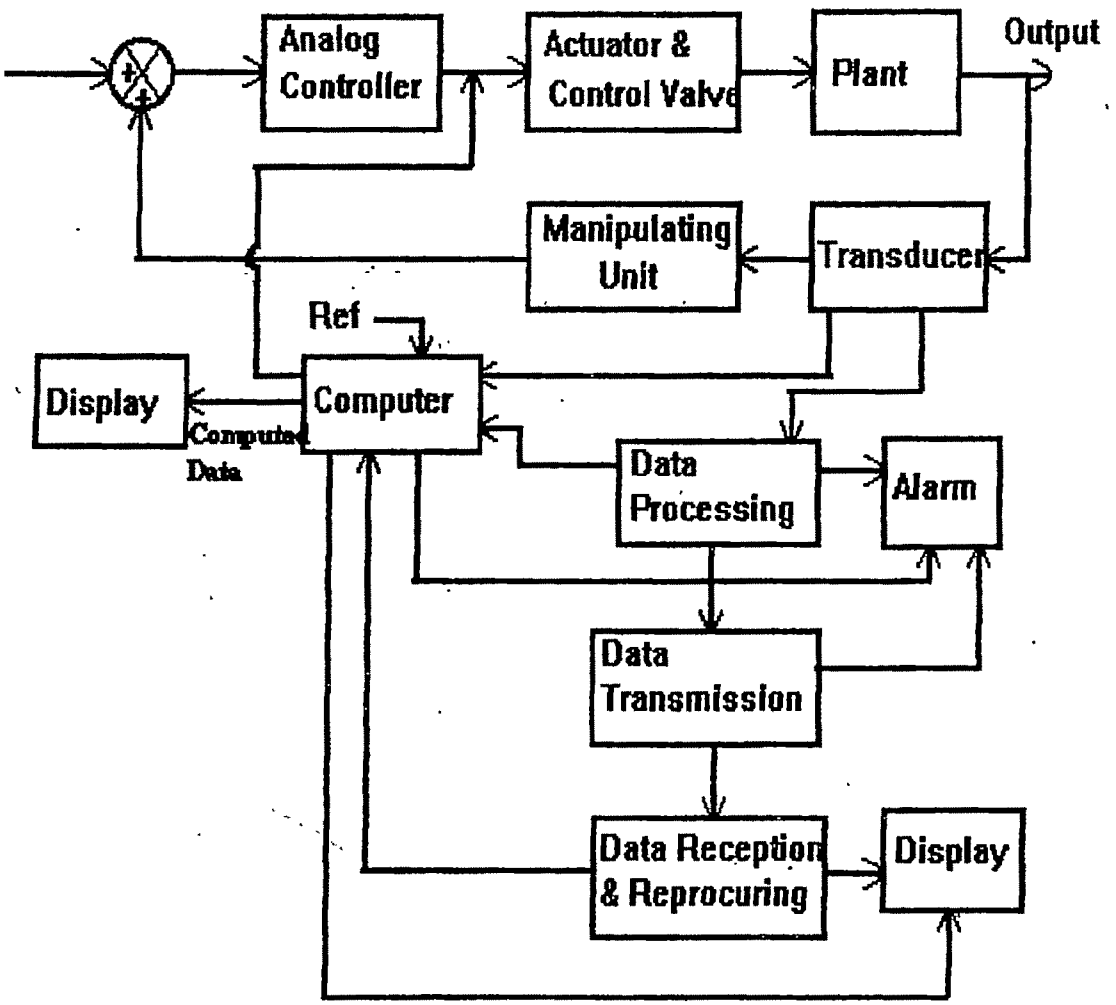
Analog Controller
Actuator & Control Valve
Plant
Output
Manipulating Unit
Transducer
Ref
Display
Computer
Computed Data
Data Processing
Alarm
Data Transmission
Data Reception & Reprocuring
Display

Figure 1.

SUPERVISORY CONTROL OF DISCRETE-EVENT SYSTEMS

W.M. Wonham
Systems Control Group
ECE Department, University of Toronto
wonham@control.utoronto.ca
http://www.control.utoronto.ca/

CIIC 2001 - 2001.12.13-15

ABSTRACT

This tutorial paper will introduce supervisory control theory (SCT) for discrete-event systems. After describing the framework and basic problems, we discuss how modular architecture (decentralized and hierarchical structures), combined with compact IDD representations for efficient computing, can effectively manage the complexity arising from potentially exponential state explosion. These approaches will be illustrated by industrial examples.

1 INTRODUCTION

This paper is concerned with discrete-event systems (DES), namely dynamic systems which live in a discrete state space, and change state in discrete jumps, at more-or-less random times. What come to mind are entities like manufacturing systems, traffic systems, push-button systems on automobiles, and so forth, modelled at a fairly high level of abstraction. We shall introduce the subject with a simple manufacturing workcell [1]; this will show what the control issues are. Then we shall cover some basic theory, in terms of languages and automata. This will lead to a formal problem statement, and a formal solution [2]. Next, we shall see that large systems lead to exponential state space explosion, but we shall also summarize an efficient computational technique based on so-called integer decision diagrams, or IDDs. These will be applied to much larger versions of our original small workcell problem [3].

Another way to investigate large systems is by way of suitable architecture. We shall indicate how our supervisory control theory accommodates hierarchical architecture [2].

Finally we conclude with a brief statement of what has already been accomplished, and what remains on the agenda for future research.

2 MANUFACTURING WORKCELL

The workcell model of Fig.1 consists of four machines and two robots. It runs two production streams concurrently, for Green parts and Red parts. The two streams share the machines and the robots. The first control requirement (Fig.2) called the "safety" specifications - is the obvious one of maintaining the correct sequencing in each of the two production streams, for Green and Red. Taking the two streams separately, this is easy to do.

But there can be a problem. In actual operation, the streams interleave in time, and thus have to share the machines and the robots. For instance, suppose Robot 1 has already loaded Machine 2 with a Green workpiece, and then unloads a Red workpiece from Machine 4. At that point the system is blocked, since in the model there is no mechanism for doing the required swap. Our control will have to prevent this sort of thing from happening. It will have to meet the second requirement, called nonblocking or "liveness".

This leads us to the general issues of supervisory control:

> Is there a control which enforces both safety and liveness and which is "maximally permissive"? That is, not overly constraining?
>
> If so, can the design of such a control be automated?
>
> And if so, what computing effort is required?

To answer these questions we need to look at the formal setup

3 SUPERVISORY CONTROL THEORY - BASICS

The base model is, first of all, just an automaton, like the MACHINE of Fig.3 with states Idle, Working, and Broken Down. The transitions are labeled $\alpha, \beta, \lambda, \mu$: these symbols make up the alphabet of events.

The control technology is very simple. Some transition arrows (α, μ) are controllable. The meaning is that the controllable transitions can be stopped, or disabled, by an external controller. If the machine is at Idle, we can keep it there by disabling the α transition. If the machine is broken down, we may need to leave it there (by disabling the repair event μ) until we can find a technician to repair it. Then we enable the event μ, so that eventually the machine can be successfully repaired and return to Idle.

The remaining transition arrows (β, λ) are the uncontrollable transitions. Uncontrollable transitions just happen if they want to. Thus, when our machine exits from the working state, it might either break down, or it might return successfully to Idle, ready to start a new work cycle. Which of these actually happens is outside our direct control.

In brief, our control technology partitions the total alphabet of events into controllable events and uncontrollable events.

It is very useful to think in "output" terms, in other words in terms of the symbol strings or languages which the machine can generate. The set of all such strings, starting from the initial state I, is called the machine's "closed behavior". The subset of those strings which finish up at a target or "marker" state, where there's an outgoing arrow, is called the machine's "marked behavior". In this case the marked behavior is just the strings corresponding to some integer number of production or breakdown/repair cycles.

In language terms it is easy to express our liveness or nonblocking property. All one needs to say is that the closed behavior is exactly the set of all prefix or initial strings of the marked behavior, in other words the prefix closure of the marked behavior. This says that no matter what state the machine reaches, it can always get home from there to a marker state (Fig.4).

What if our system is made up from a number of individual subplants?

In this case the full plant model is the so-called "synchronous product" of the components. This means cartesian product, but with synchronization of any common or shared events. An example is a Transfer Line (Fig.5) made up of two machines and a test unit, linked by buffers [4]. If a workpiece passes the test, it is released from the system. If it fails, it is sent back for reprocessing. The synchronous product of the two machines and the test unit provides the plant model.

Similarly we can form a complex specification as the synchronous product of individual partial specifications. For the Transfer Line, suppose the two buffers have capacities three and one. Their transition diagrams express the specifications that these buffers should not be allowed to overflow or underflow (Fig.6). The complete specification BUFFSPEC is their synchronous product.

We are now in a position to state the formal synthesis problem for Transfer Line. Let's say ConTL is the so-far unknown structure of TL under control. In language terms, we have, first, the safety requirement that the controlled marked behavior L_m (ConTL) be legal. Second, we must prevent blocking, so we have the prefix-closure condition for the liveness requirement. And third, we'd like to achieve both safety and liveness in the freest possible way, that is, with least constraint, or with maximal permissiveness.

The surprising and pleasant fact is that the problem just stated is solvable. The solution depends on the concept of a controllable language. As its name implies, a controllable language is one the system can be confined to, by appropriate enabling and disabling of controllable events.

Amazingly, there is always a unique largest, or supremal, controllable language for any given problem. One can think of this supremal controllable sublanguage, say K_{sup}, as the optimal solution. And K_{sup} can be effectively computed.

The conceptual picture, in terms of languages, can be displayed in a so-called "lattice diagram" (Fig.7). At the top, one has all possible strings over the alphabet of event symbols.

Then one has the data - the plant language and the specification language. The intersection of these two is the set of strings that are both physically possible and legally admissible. The optimization step picks out the largest sublanguage that is controllable, namely K_{sup}, our optimal solution.

While so far all of this is a bit abstract, the picture is simple and clear. Temporarily we are separating the issues of concept and implementation. Abstractly, everything is done in terms of languages, which are just sets of strings, though usually infinite sets. However, for the concrete implementation, we need to work with finite representations of these languages, namely our automata. While we begin and end with automata, the intermediate stage of abstract problem solving is done in languages. It would be a lot messier to do this intermediate stage directly using automata.

Let us turn to the automaton implementation.

This is easy. Assume that we have constructed models of the plant and the specification. What we need is a concrete automaton model of K_{sup}. Call this automaton "SUPER". There is a simple algorithm, called "supcon", which computes SUPER in polynomial time.

Then we put SUPER online with the plant - another synchronous product. SUPER will automatically provide the correct enabling and disabling control action. The resulting closed-loop system will generate exactly the language K_{sup} that we want.

4 SUPERVISORY CONTROL OF LARGE DES

Unfortunately, life may not be quite so simple as the basic paradigm of Sect.3 might suggest. What happens when we have many subplants and many partial specifications? Each time we synchronize, the old state size gets multiplied by the size of the new component. So, the total state size goes up exponentially with the number of components. For rather modest industrial systems, the state size is simply astronomical, as we shall see. Thus, we can't afford to be naive in the way we store and process data.

To confront this problem there are three techniques which, when combined together, seem to work very well.

The first is, retain cartesian product structure in the plant and spec, rather in the style of Petri nets. Unlike Petri nets, here we don't code everything into an integer vector addition system. We just keep the automaton structures as they are.

Second, express the required transition structures, in particular that of SUPER, as predicates on the product state space.

Third, instead of trying to represent these predicates as full "listings" of some sort, specify them as simple algorithms on tree-like structures called "integer decision diagrams".

Integer decision diagrams (IDDs) work like this. Suppose we have some function of discrete variables. Fig.8 shows a two-valued function f of two variables, $x1$ (taking 3 values) and $x2$ (taking 2 values). Imagine that f is represented as a tree. In general, this tree will be exponentially large in the number of variables, which is what we are trying to avoid. So our approach is to order the variables, in this case $x1, x2$, in a careful way. If we do it right, and are somewhat lucky, then the exponential tree partially collapses into something with a much smaller number of nodes. This is the IDD. It turns out that one can develop and manipulate these IDDs in the course of computation. We never actually have to form the original (exponential) tree, which of course would be self-defeating.

Fig.9 displays some results of this approach on the Manufacturing Workcell. What we did is increase the size by reduplicating each component - the machines and the robots - by a factor K, from $K = 1$ to $K = 30$. As shown, the state size goes up dramatically. However, the computing time increases much more modestly (to about 15 minutes for 10^{14} states) as does the memory for the computation, and the memory to store the control IDDs. Similar results were obtained for other large examples.

These results are recent, and still somewhat tentative, but quite encouraging. The computing time turns out to be some low-order power law in the node count - for the workcell, about power 1.5. In our examples, the node count depends on N, the number of distinct system components; on K, the reduplication factor; and on a measure C of internal coupling, which is typically rather small. The important observation is that the node count seems to grow linearly - not exponentially! - with N. In summary, the prospects are very good for turning this approach into an industrial strength design tool.

Fig.10 shows how the supervisor could be implemented. As the plant evolves from one product state to the next, new output events are generated, which drive the control automaton SUPER. The updated state of SUPER is fed into a parallel array of IDDs, one for each controllable event. The IDD will very quickly compute the enablement/disablement status of its event, which will then be enforced at the plant input, closing the feedback loop.

5 ARCHITECTURE - HIERARCHICAL LAYERING

Besides good computational technique, the key to dealing with large systems, in the long run, is control architecture. We now sketch a hierarchical architecture for supervisory control. In the familiar, classical, pyramidal hierarchy, there are a number of levels, linked by feedback loops. The people (or entities) at the top are slow to act but have wide scope. At the bottom the people are fast-acting but have limited scope. "Scope" can be defined in different ways, apparently without affecting the result very much. The scope ratio from one level to the next is typically rather small, say on the order of 5. So if one has 20,000 employees he might expect to have around seven levels. The reader may like to test this claim on his favorite organization.

The slogan is that hierarchy logarithmizes exponential complexity, so one is back to linear in the number of elements populating the hierarchy [5].

Fig.11 displays a two-level hierarchy. The high level is an abstract model of the low level. Planning decisions at the high level by a manager are implemented around the hierarchical loop, via the sequence "command", "low-level control", and "report". The manager's hope is that his plan actually gets executed around this loop. In that case, we apparently have a commutative diagram, in the sense of algebra. In the formal theory, it is exactly the commutativity of a suitable operator diagram that we try to achieve. This property is called "hierarchical consistency", and has recently emerged as a very fundamental systems concept. It is crucial, for instance, in hybrid systems too.

The formal setup is an extension of our basic one, but works in a similar way. Now one has two levels of language, over alphabets T and Σ. The "Report" map (Fig.11) is formalized as a suitable mapping from the low-level operator's language L to the high-level manager's language M. The "Command" map is just the inverse-image mapping of the Report map. Our main result is that, if one arranges things properly, he can get the right sort of operator diagram to commute. For this one needs a certain ordering condition on equivalence kernels (Fig.12). Roughly, the condition says that, if two low-level specification languages look the same to the manager, then the corresponding "K_{sup}" (supremal controllable sublanguages) will also look the same. This will guarantee that the manager can be equipped with a "control technology" of his own, which he can exercise to do his planning.

Arranging this so-called "kernel condition" is in general a complicated, but do-able, design process. If it succeeds, then one actually has the desired hierarchical consistency. Namely, the high-level plan gets implemented through the sequence Command, Control, and Report.

As an illustration, consider Transfer Line again (Fig.13). For hierarchical control, we choose a high-level alphabet of "significant events" for the manager. For instance, the event τ signals the return of a faulty workpiece for reprocessing by Machine 2. The state diagram (Fig.14) shows the behavior of the Transfer Line under low-level control, which guarantees that the buffers are protected from underflow or overflow. In this simplified version, both buffers have size 1. For the manager, the significant events are declared to be "input a workpiece", "test a workpiece", and either "return the tested workpiece for reworking", or "release the workpiece and input a new one." To implement this we have a so-called Moore machine, a state machine with state outputs. These are symbols from our high-level alphabet T. What we do is "vocalize" some of the states of our low-level controlled DES. The resulting high-level model, as seen by the manager, is then just a generator for the state-output high-level language. As an abstraction of the low-level model, it is much simpler.

Fig.15 shows what might be done with the high-level abstraction. One can pose a specification in terms of the high-level alphabet alone. Here "pass" and "fail" interpret the appropriate high-level symbols τ, etc. Then one can solve his synthesis problem using this specification and the high-level model. So one gets the high-level supervisor and the high-level controlled behavior. Now the theory guarantees that one can implement this behavior on the "real" low-level model, in a consistent way around the hierarchical loop. The benefit

is, that the design is done in the much more economical setting of the simple high-level model.

6 CONCLUSION

To finish up, let us review some of the achievements and challenges of supervisory control in this approach.

The achievements are fourfold: it is synthetic, it is correct, it is modular and it is easy.

It is "synthetic" in the same sense as standard optimal control, namely for a given plant model, specification, and design criterion, it generates an optimal control solution, uniquely defined (by the above data) whenever it exists. The criterion for existence is explicit - the supremal controllable sublanguage is nonempty.

It is "correct" in the same sense, again, as standard optimal control, namely the design criterion is always achieved (when that is possible) by actual construction, and therefore (in principle) no "cut-and-try" should be necessary.

It is "modular" in the sense that it admits horizontal (decentralized) and vertical (hierarchical) modular control architecture, as well as more general heterarchical configurations. Of course, this is crucial to the modelling and understanding of large complex systems.

Finally, it is "easy" in the sense of being (so far, at least) relatively nontechnical mathematically, and well supplied with learning materials on the Internet, e.g. [2].

Of the many challenges facing the researcher in this area, we single out two of the most salient.

First, there is the need, sometimes, to interpret what the optimal control is really doing, for psychological reassurance and engineering conviction. This is generally true of any optimal control approach. One has the answer before him, but is one prepared to fly in it? A good theory should provide windows on a complex system allowing its examination and testing from many points of view. Our theory, in this respect perhaps not very different from other control theories (at least nonlinear ones), deserves much further development as an effective development tool.

Secondly, from the system science point of view, we hope to pin down much better what the "laws" are of control system architecture: for instance, how the computational complexity of control synthesis depends on subsystem interconnection topology.

In summary, we need to understand in a much more precise way the relationships among structure, function, and complexity.

7 NOTES AND REFERENCES

[1] K. Barkaoui, I. Ben Abdallah. A deadlock prevention method for a class of FMS. Proc. IEEE Conf. on Systems, Man and Cybernetics 5, 1995, pp. 4119-4124. See also M. Seidl, G. Schmidt. Automatic high level controller design for flexible manufacturing systems. WODES'98, pp. 529-531.

[2] W.M. Wonham. Notes on Control of Discrete-Event Systems. Available on-line at http://www.control.utoronto.ca/ . Contains a bibliography and is accompanied by the software package CTCT.

[3] Z.-H. Zhang. Smart TCT: An Efficient Algorithm for Supervisory Control Design. M.A.Sc. Thesis, ECE Department, University of Toronto, April 2001. Available online at http://www.control.utoronto.ca/ .

[4] For the background reference to Desrochers & Al-Jaar, see [2].

[5] That is, if the number of elements is N, and the associated computational complexity in the absence of architecture (or state size of a flat model) is k^N, then organizing the system hierarchically could reduce computational complexity to $\ln(k^N) = N * \ln(k)$. The latter figure associates fixed computational effort $\ln(k)$ with each element, corresponding to the cost of "managing" a fixed number of subordinates m, say, where

$$(m^{L-1})/(m-1) = N$$

L being the number of hierarchical levels.

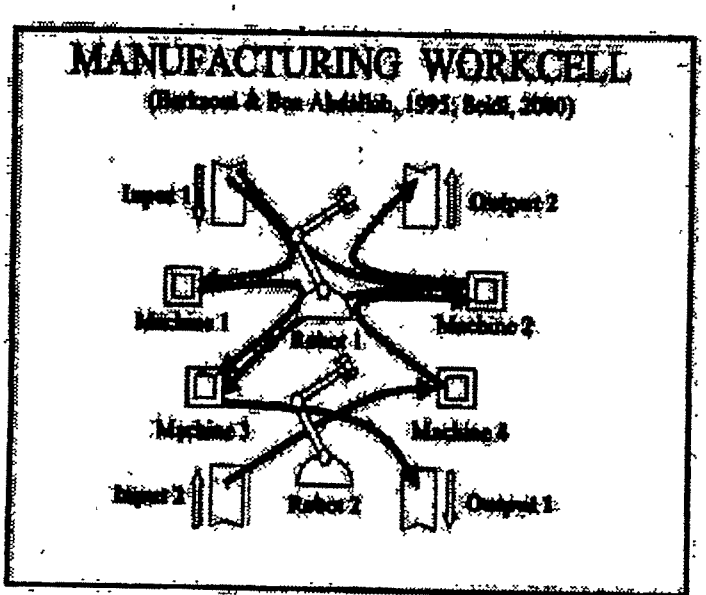

Fig. 1

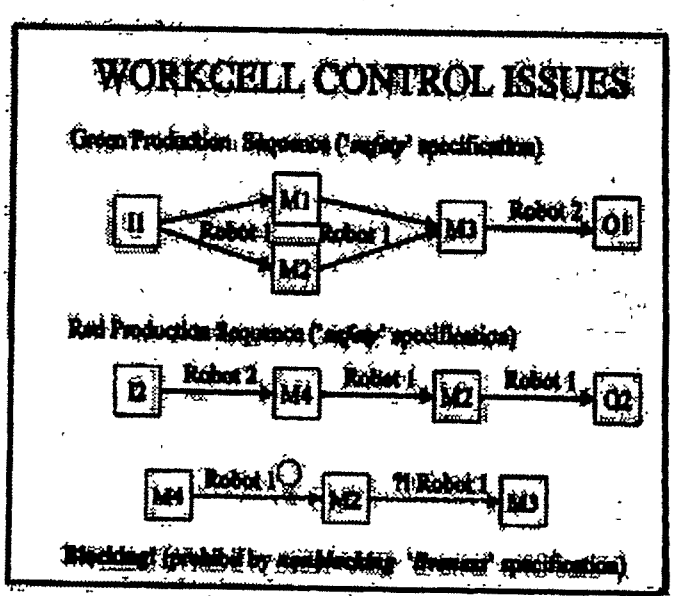

Fig. 2

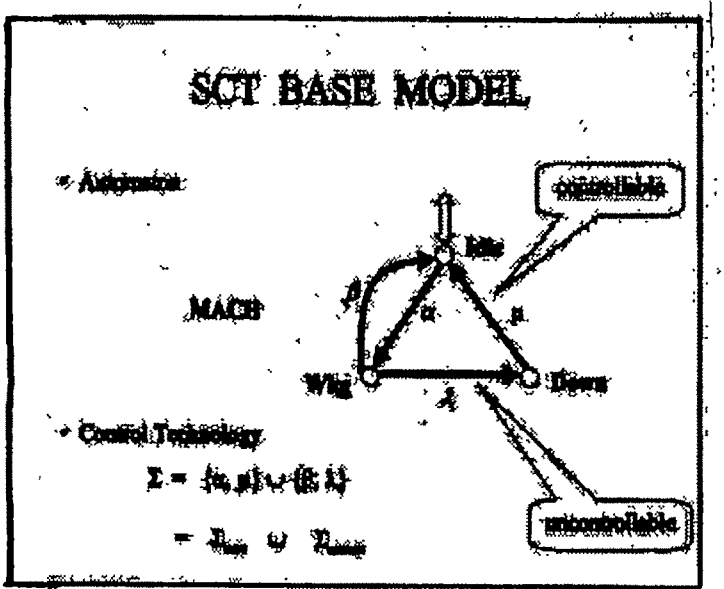

Fig. 3

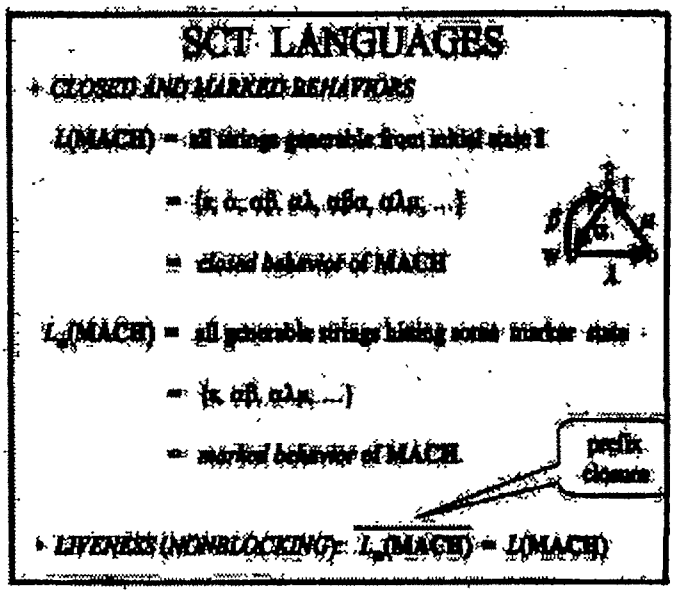

Fig. 4

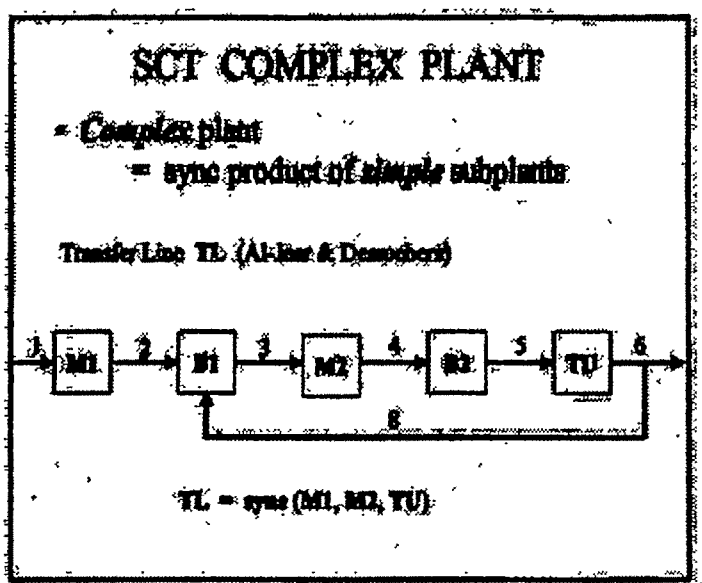

Fig. 5

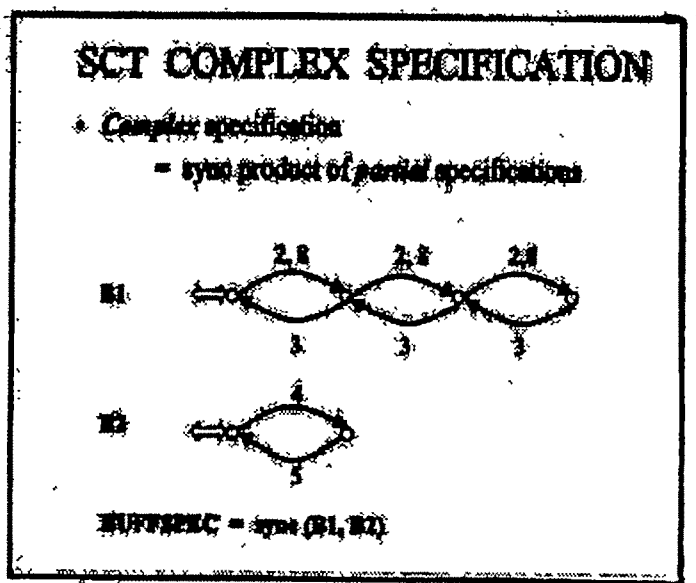

Fig. 6

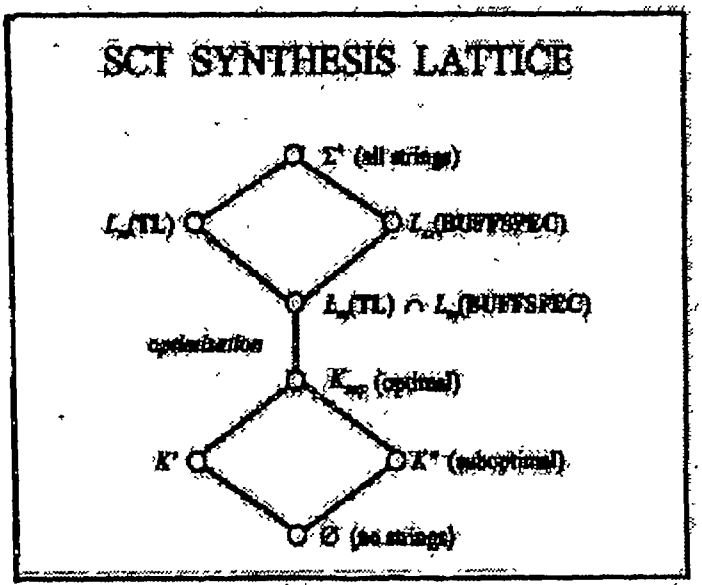

Fig. 7

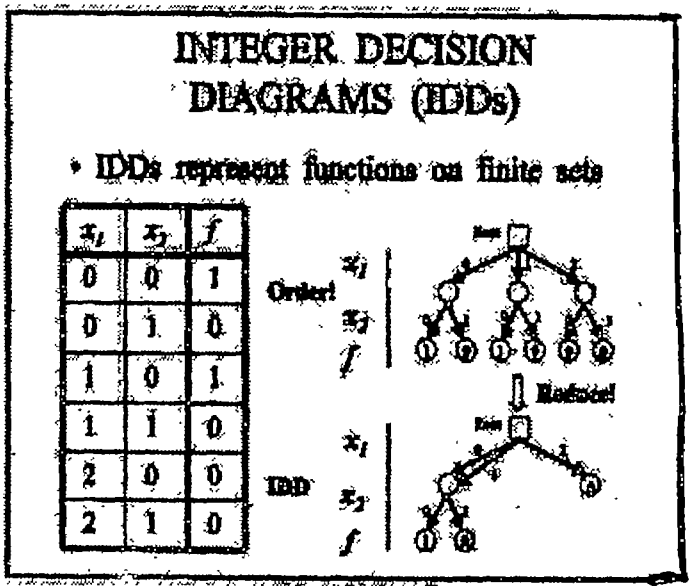

Fig. 8

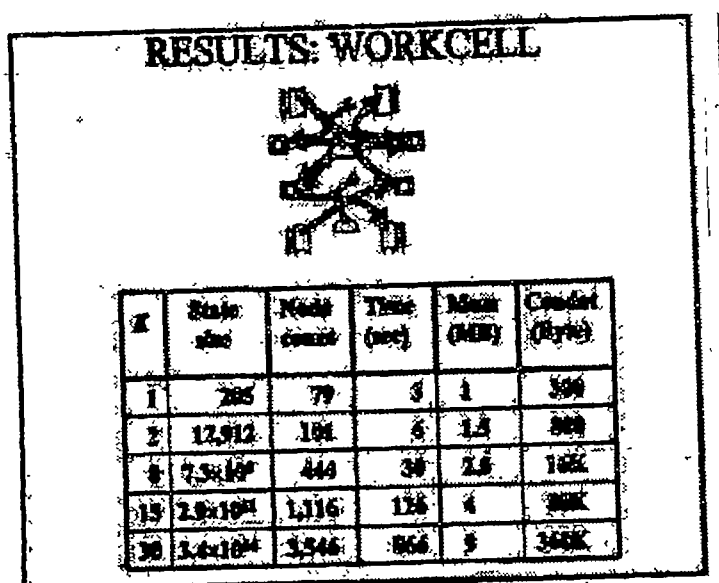

Fig. 9

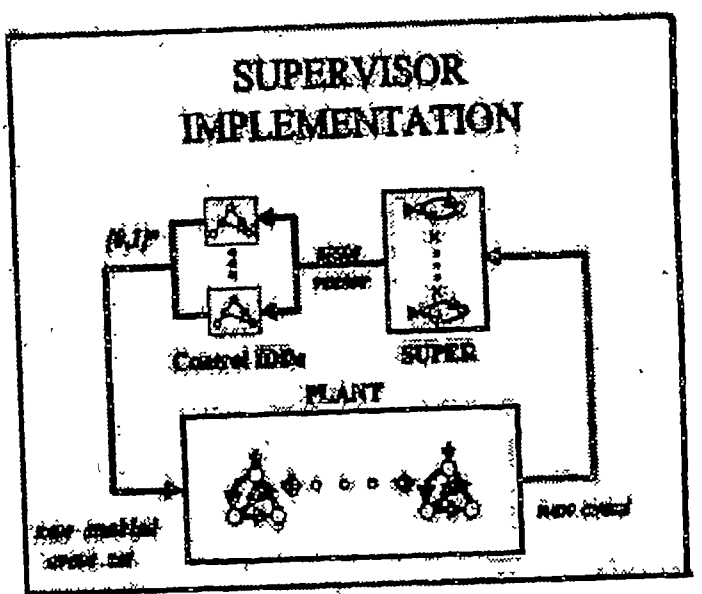

Fig. 10

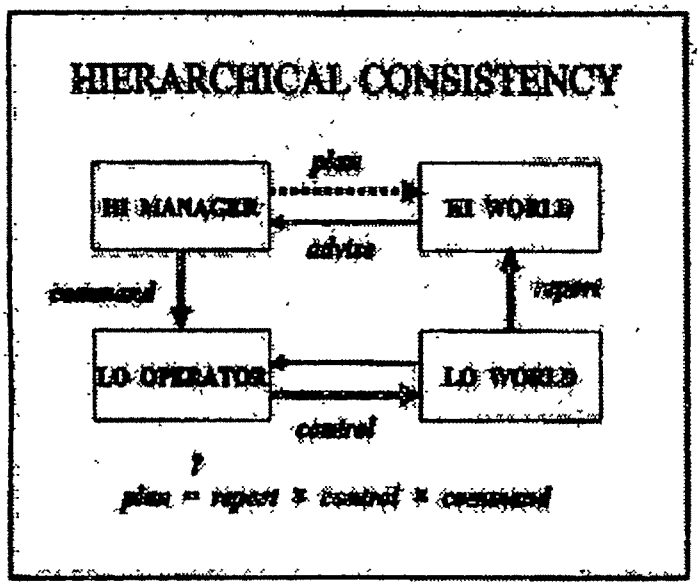

Fig. 11

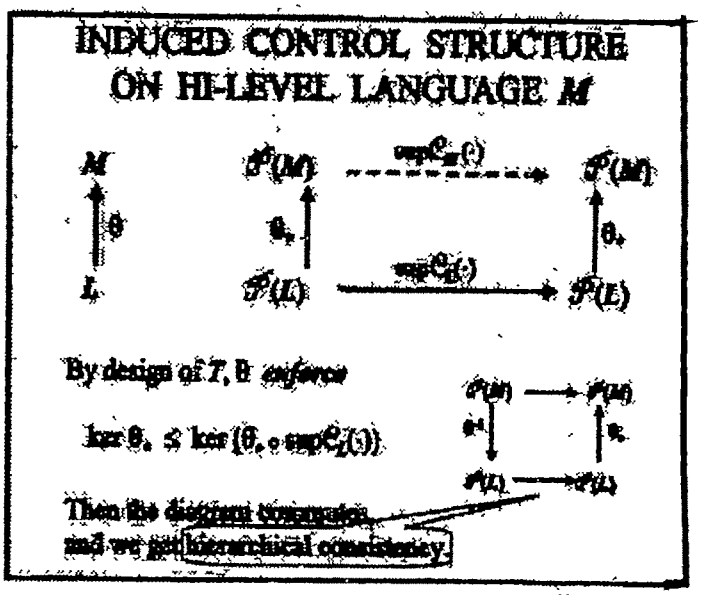
INDUCED CONTROL STRUCTURE
ON HI-LEVEL LANGUAGE M
By design of T, B enforces
Then the diagram commutes,
and we get hierarchical consistency.

Fig. 12

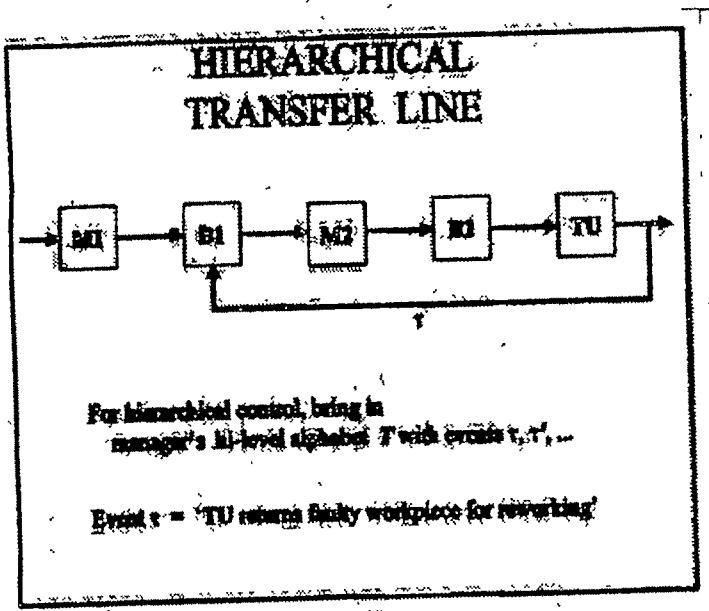

Fig. 13

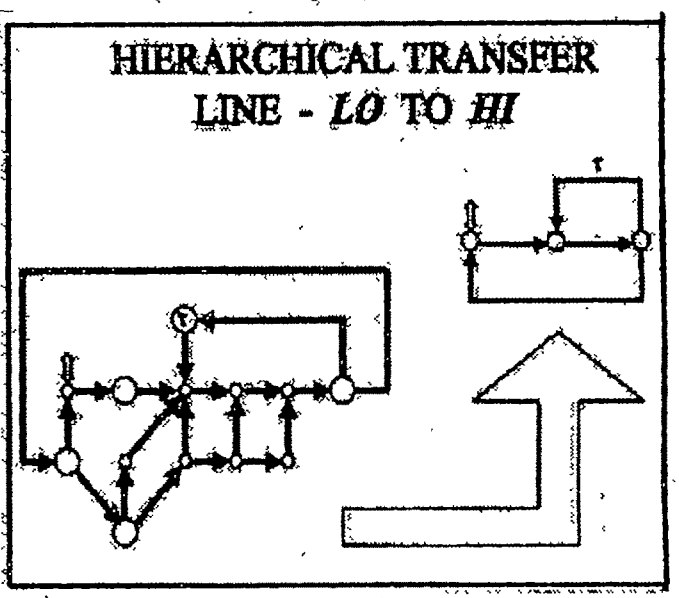

Fig. 14

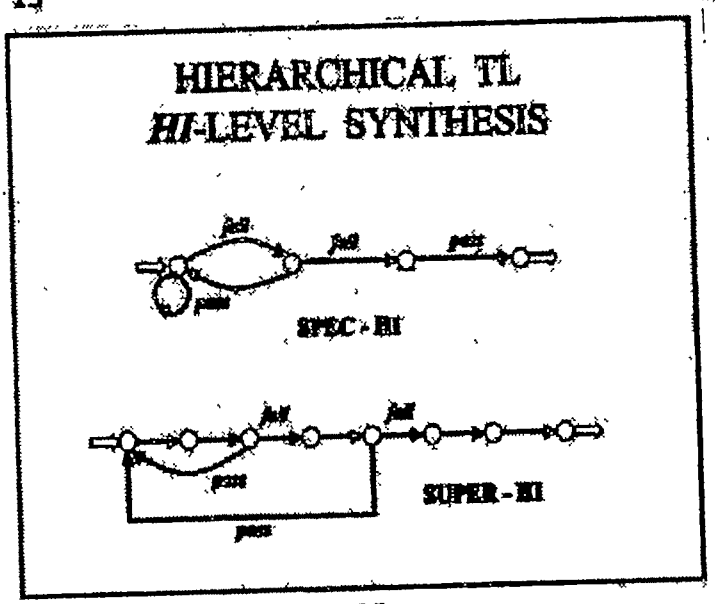

Fig. 15

Spatial Control Of Large Nuclear Reactor By Three Different Approaches

B. Bandyopadhyay* and A. P. Tiwari[1]
*Systems and Control Engineering, Dept. of Electrical Engineering,
Indian Institute of Technology, Mumbai – 400 076, INDIA.
Email: bijnan@ee.iitb.ac.in
† Reactor Control Systems Design Section
Bhabha Atomic Research Centre,Trombay, Mumbai-400 085 INDIA.
Email: aptiwari@apsara.barc.ernet.in

Abstract

The paper presents a nodal technique for modeling a large pressurized Heavy water Reactor (PHWR). Model equations are derived from the two group diffusion equation. A linear state space model has been obtained by linearising the non linear equations of the reactor over the equilibrium point. Three techniques, Aggregation , Periodic Output Feedback and Fast Output sampling methods have been discussed for the design of controllers. These techniques have been applied to a large Pressurized Heavy Water Reactor for the control of Xenon-induced spatial *oscillations.*

Keywords: Nuclear reactor, Spatial control, Aggregation technique, Periodic output feedback, Fast output sampling.

INTRODUCTION

Fission reactions taking in nuclear reactors can give rise to the formation of several nuclear species. However, the isotope ^{135}Xe requires special attention in operation and control of thermal reactors. A small fraction of this isotope is formed directly in fission but the major portion results from the radioactive decay of ^{135}I, with a half life of 6.7 hours. The ^{135}Xe has very large thermal neutron absorption cross-section, and it undergoes radioactive decay at a relatively slower rate than ^{135}I does . Hence, the immediate effect of an increase in neutron flux in the reactor is to cause a decrease in the concentration of ^{135}Xe , which in turn results into an increase in neutron flux. This continues for about 10 *hours* when the reverse starts taking place. Production of ^{135}Xe through the decay of ^{135}I becomes appreciable and the neutron flux starts decreasing due to increase in thermal neutron absorption by ^{135}Xe , resulting into further build up of concentration of ^{135}Xe .

In this manner , oscillations of the neutron flux are introduced by ^{135}Xe . Such oscillations induced by ^{135}Xe can be broadly classified in two categories :- fundamental mode or global power oscillations and higher mode or spatial oscillations. Generally speaking, global power oscillations are readily noticed and suppressed by control system while spatial oscillations are not. Here the global reactor power can remain constant so that no change in the coolant outlet temperature is effected, the oscillations being in spatial distribution of power inside the core. If the spatial oscillations in a reactor are not controlled, a serious situation known as "flux-tilting" may arise , i.e. one portion of the reactor may tend to produce more energy than the other portion does, and this can cause fuel in that region to exceed its thermal design limits. For this reason, spatial oscillations have received more attention in literature [1], [2].

Spatial control systems based on conventional concepts require the feedback of neutrons flux signal, derived from readings of several incore and excore detectors [3]. They are easy in implementation although there may be certain compromises in the overall closed loop system performance. Modern methods, on the other hand, are more promising as almost any specifications on the closed loop system response can be satisfied. However, the need for full state feedback is an obvious limitation inherent with these methods. A spatial control system based on the modern control methodologies would require the feedback of iodine and xenon concentrations besides the neutron flux or power. Several mechanisms are known for detection of neutron flux but instruments for measuring xenon and

iodine concentration in nuclear are not available. One method of overcoming this difficulty is to use observer based control laws or dynamic compensators but the resulting closed loop system has a complex structure that may require expensive hardware and processing networks. This paper presents the spatial control of a large Pressurized Heavy Water Reactor by means of Aggregation technique, Periodic output feedback method and Fast output sampling technique.

DERIVATION OF NODAL MODEL

Assuming two energy groups of neutrons, i.e. the fast and thermal neutrons fluxes ϕ_1 and ϕ_2, the neutron diffusion equation and the associated equation for precursor concentrations can be written explicitly in the following form :

$$\frac{1}{v_1}\frac{\partial\phi_1}{\partial t} = \nabla.D_1\nabla\phi_1 - \Sigma_{a1}\phi_1 + (1-\beta)[\nu\Sigma_{f1}\phi_1 + \nu\Sigma_{f2}\phi_2] - \Sigma_{12}\phi_1 + \sum_{i=1}^{m_d}\lambda_i\tilde{C}_i \,, \qquad (1)$$

$$\frac{1}{v_2}\frac{\partial\phi_2}{\partial t} = \nabla.D_2\nabla\phi_2 - \Sigma_{a2}\phi_2 + \Sigma_{12}\phi_1 \,, \qquad (2)$$

$$\frac{\partial\tilde{C}_i}{\partial t} = \beta_i(\nu\Sigma_{f1}\phi_1 + \nu\Sigma_{f2}\phi_2) - \lambda_i\tilde{C}_i \,, \qquad (3)$$

$i = 1,2,3\ldots m_d$.

It is assumed that fission reactions take place only due to thermal neutrons, all fission neutrons are generated as fast neutrons and neutron upscattering does not take place. It should be recognized that the neutron fluxes ϕ_1 and ϕ_2 are functions of both space co-ordinate and time. Also, the parameter D_1 , D_2 , Σ_{a1} Σ_{a2} , Σ_{12} , Σ_{f1}, and Σ_{f2} are different at different core locations. The spatial variation of diffusion co-oefficients D_1 and D_2 is small in the pressurized heavy water reactors and it can be ignored. Hence, the leakage term can be approximated as

$$\nabla.D_1\nabla\phi_1 = D_1\nabla^2\phi_1 \,. \qquad (4)$$

$$\nabla.D_2\nabla\phi_2 = D_2\nabla^2\phi_2 \,. \qquad (5)$$

Now consider dividing the reactor into a number of small coarse-mesh boxes in which the neutron fluxes and other neutronic parameters are represented by the respective average values integrated over its volume. Then the net rate of fast neutron flow from a box designated '*h*' to its neighbor designated by '*k*' can be written as

$$D_1\frac{d^2\phi_1}{dr^2}V_h = J_r A_{hk} \,, r = x, y, \text{or } z \,,$$

where V_h denotes the volume of box *h* and A_{hk} the area of interface between the boxes h and k , perpendicular to the direction of flow of neutron current. Using Fick's law, the above equation can be manipulated to obtain

$$D_1\frac{d^2\phi_1}{dr^2} = \frac{A_{hk}}{V_h}D_1\frac{d\phi_1}{dr} = \frac{D_1A_{hk}}{V_h\Delta_{hk}}[-\phi_{1h} + \phi_{1k}],$$

where Δ_{hk} denotes the centre to centre distance between two boxes. Based on the above, an approximation for the leakage terms in eqn. (4) and (5) could be

$$D_1\nabla^2\phi_1|_h = -\omega_{1hh}\,\phi_{1h} + \sum_{k=1}^{N_h}\omega_{1hk}\,\phi_{1k} \,, \qquad (6)$$

$$\text{and } D_2\nabla^2\phi_2|_h = -\omega_{2hh}\,\phi_{2h} + \sum_{k=1}^{N_h}\omega_{2hk}\,\phi_{2k} \,, \qquad (7)$$

where

$$\omega_{ihk} = \frac{D_iA_{hk}}{V_h\Delta_{hk}} \text{ and } \omega_{ihh} = \sum_{k=1}^{N_h}\omega_{ihk} \,, \qquad (8)$$

$i = 1,2.$

A mesh box has only up to six neighbors. Hence, the summations in equation (6) , (7) and (8) is not required over all mesh boxes because $\omega_{hk} = 0$ if the *k*th box is not a neighbor of the *h* box. Substituting the above values in eqn. (1) and (2), we have,

$$\frac{1}{v_{1h}}\frac{d\phi_{1h}}{dt} = -\omega_{1hh}\,\phi_{1h} + \sum_{k=1}^{N_h}\omega_{1hk}\phi_{1k} - (\Sigma_{a1h}+\Sigma_{a2h})\,\phi_{1h} + (1-\beta)[\nu\Sigma_{f1h}\phi_{1h} + \nu\Sigma_{f2h}\phi_{2h}] + \sum_{i=1}^{m_d}\lambda_i\tilde{C}_{ih} \,, \qquad (9)$$

$$\frac{1}{v_{2h}}\frac{d\phi_{2h}}{dt} = -\omega_{2hh}\phi_{2h} + \sum_{k=1}^{N_h}\omega_{2hk}\phi_{2k} - \Sigma_{a2h}\phi_{2h} + \Sigma_{12h}\,\phi_{1h} \,,$$

$(h = 1,2\ldots.Z).$ $\qquad (10)$

The eqn. (9) and (10) can be further simplified by employing the one and half group technique suggested by Hõld and Lupas [4] and using the relation between flux and power, the zonal power level equation can be put in the following form [5,6].

$$\frac{1}{v_h}\frac{dP_h}{dt} = -\omega_{hh}P_h + \sum_{k=1}^{N_h} \omega_{hk}V_h\Sigma_{fh}P_k/(V_k\Sigma_{fk}) - \Sigma_{ah}P_h + (1-\beta)\nu\Sigma_{fh}P_h + \sum_{i=1}^{m_d}\lambda_i\tilde{C}_{ih}E_{eff}\Sigma_{fh}V_h \,. \quad (11)$$

MODEL EQUATION

The power level equation along with the equation of concentrations of delayed neutron precursors, xenon and iodine in different regions or zones of the reactor are rewritten here as

$$\frac{dP_i}{dt} = \frac{\rho_i - \beta - \bar{\sigma}_{xi}X_i/\sum_{ai} - \alpha_{ii}}{\ell}P_i + \sum_{j=1}^{Z}\frac{\alpha_{ij}}{\ell}P_j + \sum_{h=1}^{m_d}\lambda_h C_{ih}\,, \quad (12)$$

$$\frac{dC_{ih}}{dt} = \frac{\beta_h}{\ell}P_i - \lambda_h C_{ih}\,, \quad (13)$$

$$\frac{dI_i}{dt} = \gamma_i\Sigma_{fi}P_i - \lambda_I I_i\,, \quad (14)$$

$$\frac{dX_h}{dt} = \gamma_x\Sigma_{fi}P_i + \lambda_I I_i - (\lambda_x + \bar{\sigma}_{xi}P_i)X_i\,. \quad (15)$$

The reactivity feedback through changes in temperatures of coolant, moderator, and fuel are generally small in case of a PHWR and only of minor significance in a discussion of spatial control. Hence, such effects have been ignored. The dynamics of sensor mechanism has also been neglected in the case study of spatial control. Furthermore, because the dynamics of xenon and iodine is much slower than the dynamics of precursors, only one effective group of delayed neutron precursors's is considered ,i.e. $m_d = 1$.

For small perturbations, the capability of liquid zone control system would be sufficient. Hence it would be only necessary to model the liquid zone control system, for study of xenon induced spatial oscillations. The reactivity, ρ_i , in a zone is directly proportional to the water level in the ZCC of that zone , as given by the following equations:

$$\rho_i = -\kappa_i(h_i - h_{i0}) \quad (16)$$

where

$\kappa_i = -3.5\times10^{-5}$ and $h_{i0} = 100.0\ cm\ \forall\ i = 1,2,.....Z.$

The instantaneous rate of change of water level in ZCC is directly proportional to the net water flow rate in the ZCC. The outflow from each zone, Q_0, is maintained constant and the variation of inflow is related to the instantaneous position of the control valve, which is generally governed by a second order dynamical equation. However, in case of the study xenon induced oscillations, the response of the LZC system is comparatively much faster than the time scales due to xenon and iodine dynamics. Hence, the following approximate equation can be used to describe the variation of water level as a function of input signal to control valves:

$$\frac{dh_i}{dt} = -m_i q_i \quad , \quad m_i = 2.0\,. \quad (17)$$

Substituting the value of h_i from eqn. (16) and (17) , we have

$$\frac{dP_i}{dt} = \frac{\kappa_i h_i - \beta - \bar{\sigma}_{xi}X_i/\sum_{ai} - \alpha_{ii}}{\ell}P_i + \sum_{j=1}^{Z}\frac{\alpha_{ij}}{\ell}P_j + \sum_{h=1}^{m_d}\lambda_h C_{ih}\,. \quad (18)$$

Equations (13)-(16), and (17) and (18) are the required equations governing the dynamics of a large PHWR, for the analysis of the spatial instabilities.

LINEARIZATION

Consider the operation of the reactor at steady state. It is represented by the condition in which total reactor power P_g is constant and the distribution does not vary in time. In terms of the modal equations (13)-(16), and (17) and (18) the steady state condition is achieved when zonal power levels are constant and the concentration of delayed neutron precursors, iodine and xenon are in equilibrium with the zonal power levels. Hence, from eqn. (13)-(16), and (17) and (18) the following steady state condition is obtained.

$$C_{i0} = \frac{\beta P_{i0}}{\lambda\ell},\ I_{i0} = \frac{\gamma_I P_{i0}}{\lambda_I}\Sigma_{fi}\,,$$

$$X_{i0} = \frac{(\gamma_x + \gamma_I)P_{i0}}{\lambda_x + \bar{\sigma}_{xi}P_{i0}}\Sigma_{fi}\,,\ h_{i0} = \frac{\bar{\sigma}_{xi}X_{i0}}{\kappa_i\sum_{ai}}\,. \quad (19)$$

Inserting these steady state values in eqn (18) and setting $dP_i/dt = 0$; we obtain the power distribution as

$$-\alpha_{ii}P_{i0} + \sum_{j=1}^{Z}\alpha_{ij}P_{j0} = 0; i = 1,2.....Z\,, \quad (20)$$

and

$$P_{g0} = \sum_{i=1}^{Z} P_{i0} \ , \qquad (21)$$

which form a redundant set. Therefore, they can be solved for $P_{i0} \neq 0$; i=1,2...Z to obtain the zonal power levels, corresponding to the global power P_{g0}.

Now consider an incremental change δ_{qi} in the input to the control valve. Let the resulting changes in zonal power levels, precursor, iodine and xenon concentrations, and ZCC water levels be δP_i , δC_i , δI_i , δX_i , and δh_i, respectively. Hence, in equations (13)-(16), and (17) and (18) we have

$$q_i = q_{i0} + \delta q_i \ ; P_i = P_{i0} + \ \delta P_i \ ; C_i = C_{i0} + \ \delta C_i \ ;$$

$$I_i = I_{i0} + \delta I_{i0} \ ; X_i = X_{i0} + \ \delta X_i \ ; h_i = h_{i0} + \ \delta h_i \ .$$

Equations (13)-(16), and (17) and (18) can be simplified neglecting the terms involving the products of incremental changes *e.g.* $\delta h_i \delta P_i$, and using eqn. (20) we obtain

$$\frac{d}{dt}\left(\frac{\delta P_i}{P_{i0}}\right) = -\frac{1}{\ell}\left(\beta + \sum_{j=1}^{Z} \alpha_{ij} \frac{P_{j0}}{P_{i0}}\right)\frac{\delta P_i}{P_{i0}} + \frac{1}{\ell}\sum_{j=1}^{Z} \alpha_{ij} \frac{P_{j0}}{P_{i0}} \frac{\delta P_j}{P_{j0}} + \frac{\beta}{\ell}\frac{\delta C_j}{C_{j0}} - \frac{\overline{\sigma}_x X_{i0}}{\ell \sum_m} \frac{\delta X_i}{X_{i0}} - \frac{\kappa_i \delta h_i}{\ell} \ , \qquad (22)$$

$$\frac{d}{dt}\left(\frac{\delta C_i}{C_{i0}}\right) = \lambda \frac{\delta P_i}{P_{i0}} - \lambda \frac{\delta C_i}{C_{i0}}, \qquad (23)$$

$$\frac{d}{dt}\left(\frac{\delta I_i}{I_{i0}}\right) = \lambda_1 \frac{\delta P_i}{P_{i0}} - \lambda_1 \frac{\delta I_i}{I_{i0}}, \qquad (24)$$

$$\frac{d}{dt}\left(\frac{\delta X_i}{X_{i0}}\right) = \left(\lambda_x - \lambda_1 \frac{I_{i0}}{X_{i0}}\right)\frac{\delta P_i}{P_{i0}} + \lambda_1 \frac{I_{i0}}{X_{i0}} \frac{\delta I_i}{I_{i0}} - (\lambda_x + \overline{\sigma}_{xi} P_{i0}) \frac{\delta X_i}{X_{i0}}, \qquad (25)$$

$$\frac{d\delta h_i}{dt} = -m_i \delta q_i \ . \qquad (26)$$

Equations (22) - (26) represent the linearized equations for the reactor. The following choice of state, control and output vectors is obvious from the above equations

$$\mathbf{x} = \left[Z_I^T \ Z_X^T \ Z_C^T \ Z_H^T \ Z_P^T\right]^T \ , \qquad (27)$$

$$\mathbf{u} = \left[\delta q_1 \ \delta q_2 \ ..... \delta q_Z\right]^T \ , \qquad (28)$$

$$\mathbf{y} = \mathbf{Z_p} \ , \qquad (29)$$

where $\mathbf{Z_I}$, $\mathbf{Z_x}$, $\mathbf{Z_C}$, $\mathbf{Z_p}$ are normalized state variables and $\mathbf{Z_H}$ is as

$$\mathbf{Z_H} = \left[\delta h_1 \ \delta h_2 \ ..... \delta h_Z\right]^T .$$

Now the system of equation (22) – (26) is expressed in standard state variable representation

$$\dot{\mathbf{x}} = \mathbf{Ax} + \mathbf{Bu} \ , \qquad (30)$$
$$\mathbf{y} = \mathbf{Cx} \ .$$

SUBOPTIMAL CONTROL VIA REDUCED MODEL

A system of high order can be numerically approximated to one of smaller by the Davison's method. The principle of the method is to neglect eigenvalues of the original system which are farthest from the origin and retain only dominant eigenvalues and hence dominant time constants of the original system in the reduced model. This implies that the original behavior of the approximate system will be very similar to that of the original system, since the contribution of the unretained eigenvalues to the system response are important only at the beginning of the response, where as the eigenvalues retained are important throughout the whole of the response.

Consider the linear transformation of states of eqn. (30)

$x = M\overline{x}$ or $\overline{x} = M^{-1}x$

such that the transformed model becomes

$$\dot{\overline{x}} = \overline{A}\overline{x} + \overline{B}u \ , \qquad (31)$$

$$y = \overline{F}\overline{x} \ , \qquad (32)$$

where

$$\overline{A} = M^{-1}AM \ ; \overline{B} = M^{-1}B \ ; \overline{F} = FM \ . \qquad (33)$$

$\overline{A}$ is in the diagonal form, i.e.,

$$\overline{A} = \mathrm{diag}\left[\Lambda_1, \Lambda_2, ... \Lambda_n\right] \ , \qquad (34)$$

and

$$\mathrm{Re}(\Lambda_1) > \mathrm{Re}(\Lambda_2) > \mathrm{Re}(\Lambda_3) ..... \mathrm{Re}(\Lambda_n) \ . \qquad (35)$$

Further assume that r eigenvalues are only dominant, i.e. the order of the reduced model is r, and partition the model as

$$\bar{x}_1 = \bar{A}_1\bar{x}_1 + \bar{B}_1u_1, \quad (36)$$

$$\bar{x}_2 = \bar{A}_2\bar{x}_2 + \bar{B}_2u_2, \quad (37)$$

$$y = \bar{F}_1\bar{x}_1 + \bar{F}_2\bar{x}_2. \quad (38)$$

Now because the contribution of modes represented by the eigenvalues $\Lambda_{r+1}, \Lambda_{r+2}, \ldots\ldots\Lambda_n$ is not significant, it may be assumed that $\bar{x}_2 = 0$, whereby we have

$$\begin{bmatrix} x_1 \\ x_2 \end{bmatrix} = \begin{bmatrix} M_{11} \\ M_{21} \end{bmatrix} \bar{x}_1, \quad (39)$$

where M_{11} and M_{21} are respectively $r \times r$ and $(n - r) \times r$ sub matrices obtained by partitioning of M and x_1 and x_2 are respectively r and n – r dimensional state vectors corresponding to the original state variables.

It follows from (39) that

$$\bar{x}_1 = M_{11}^{-1}x_1, \quad (40)$$

with which model in (36) can be transformed to

$$\dot{x}_1 = M_{11}\bar{A}_1M_{11}^{-1}x_1 + M_{11}\bar{B}_1u = A_rx_1 + B_ru, \quad (41)$$

$$y = \bar{F}_1M_{11}^{-1}x_1 = C_rx_1. \quad (42)$$

Thus the original n^{th} order model represented by (30) is reduced to an r^{th} order model given by (41) and (42). The state variables of the approximate model are the same as the first r state variables of the original high order model. The relation between the state vector of reduced model and original high order is given in the following

$$\begin{aligned} x_1 = M_{11}\bar{x}_1 &= M_{11}[I_r : 0]\bar{x} \\ &= M_{11}[I_r : 0]M^{-1}x \\ &= C_ax, \end{aligned}$$

where C_a is the Aggregation matrix.

Let $u = k_rx_1$ be an optimal control with some performance index control for the reduced model in eqn. (41). Then the control $u = k_rx_1 = k_rC_ax$ can serve as sub optimal control for the original high order system. It can be shown that the eigenvalues of the closed loop system are disjoint sum of the eigenvalues of the closed loop reduced model and the open loop eigenvalues of the original system which are not retained in the reduced model [7].

PERIODIC OUTPUT FEEDBACK

The problem of pole assignment by piecewise constant output feedback with infrequent observation was studied by Chammas and Leondes [8] for linear time invariant systems. They have shown that, by using periodically time-varying piecewise constant output feedback gains, the poles of the discrete time control system could be assigned arbitrarily (with natural restriction that they should be located symmetrically with respect to the real axis). Since the feedback gains are piecewise constant, their method could easily be implemented.

Consider the system in eqn. (30) with $x \in R^n$, $u \in R^m$, $y \in R^p$ and A, B, C are constant matrices. It is assumed that (A,B,C) is controllable and observable. Assume that output measurements are available from the system (30) at the time instants $t=k\tau$, where k= 0,1,2....Now construct a discrete time invariant linear system from these output measurements at the rate $1/\tau$, the system obtained so is

$$\begin{aligned} x(k+1)\tau &= \phi_\tau x(k\tau) + \Gamma_\tau u(k), \quad (43) \\ y(k\tau) &= C\,x(k\tau). \end{aligned}$$

Now design an output injection gain matrix G such that the eigenvalues of $(\phi_\tau + GC)$ are inside the unit circle. For the system (43) the control signal is generated according to

$$\begin{aligned} u(t) = K_l\,y(k\tau),\ & k\tau + l\triangle \le t < k\tau + (l+1)\triangle, \\ & K_{l+N} = K_l, \quad (44) \end{aligned}$$

for l = 0.1.2...N-1, where a sampling interval τ is divided into N subinterval $\triangle = \tau/N$. When the sequence of gain matrices $\{K_0, K_1, \ldots K_{N-1}\}$ substituted in equation (44) generates a time-varying piecewise constant output feedback gain K(t) for $0 \le t < \tau$. To see the relationship between the gain sequences $\{K_l\}$ and closed loop behavior, let $\{\phi,\Gamma,C\}$ denote the system sampled at rate $1/\triangle$ and collect the gain matrices K_l into one matrix

$$K = \begin{bmatrix} K_0 & \cdots & K_{N-1} \end{bmatrix}^T.$$

By applying a control input u(t) as calculated in equation (44), a state space representation for the system sampled at rate $1/\tau$ is

$$x(k+1)\tau = \phi^N x(k\tau) + \Gamma KC\, x(k\tau), \qquad (45)$$
$$y(k\tau) = C\, x(k\tau),$$

where

$$\Gamma = [\phi^{N-1}\ \Gamma \ldots\ldots \Gamma].$$

If $\{\phi,\Gamma\}$ system is controllable and $\{\phi_\tau,C\}$ is observable and N≥controllability index of the (ϕ,Γ) system, one can first choose an output injection gain G to place the eigenvalues of $(\phi_\tau + GC)$ in the desired locations and then compute the gain sequence $\{K_l\}$ such that

$$\Gamma K = G \qquad (46)$$

is satisfied.

The problem with controllers obtained in this way is that, although they are stabilizing, they may cause an excessive oscillation between sampling instants. Werner and Furuta [9] proposed a performance index so that $\Gamma K = G$ need not be forced exactly. This constraint is replaced by a penalty function, which makes it possible to enhance closed loop performance by allowing slight deviations from original design. The performance index is

$$J(k) = \sum_{l=0}^{\infty} \begin{bmatrix} x_l^T & u_l^T \end{bmatrix} \begin{bmatrix} \bar{Q} & 0 \\ 0 & R \end{bmatrix} \begin{bmatrix} x_l \\ u_l \end{bmatrix} + \sum_{k=1}^{\infty} (x_{kN} - x_{kN}^*)^T \bar{P} (x_{kN} - x_{kN}^*) \qquad (47)$$

where $R \in R^{m*m}$, $\bar{Q}$ and $\bar{P} \in R^{n*n}$ positive definite and symmetric weight matrices. The first term represents 'averaged state' and control energy and the second term penalizes deviation of the G.

FAST OUTPUT SAMPLING

A fast output sampling control law has been shown in [9] is explained briefly here. Consider again the system in eqn. 30.

A discrete time invariant linear system is obtained by sampling the system (30) at a sampling interval τ during which the control signal u is held constant. Now assume that output measurements are available from the system (30) at the time instants $t=l\Delta$, where l= 0,1,2....The sampling interval τ is divided into N subintervals with $\Delta=\tau/N$ and N is equal to or greater than the observability index (ν) of the discrete system obtained by sampling the system in eqn. (30) at the rate $1/\Delta$. The control signal u(t), which is applied during the interval

$k\tau \le t < (k+1)\tau$ is then generated according to

$$u(t) = [L_0\ L_1\ \ldots\ldots L_{N-1}] \begin{bmatrix} y(k\tau-\tau) \\ y(k\tau-\tau+\Delta) \\ . \\ . \\ y(k\tau-\Delta) \end{bmatrix} = Ly_k . \qquad (48)$$

where matrices L_j represent output feedback gains.

Let $(\phi_\tau,\Gamma_\tau,C)$, (ϕ,Γ,C) be the system obtained by sampling the system (A,B,C) at rate $1/\tau$ and $1/\Delta$. Consider the discrete-time system having at time $t=k\tau$ the input $u_k=u(k\tau)$, state $x_k= x(k\tau)$ and the output y_k is represented as

$$x_{k+1} = \phi_\tau x_k + \Gamma_\tau u_k ,$$
$$y_{k+1} = C_0 x_k + D_0 u_k, \qquad (49)$$

$$C_0 = \begin{bmatrix} C & C\phi & . & C\phi^{N-1} \end{bmatrix}^T ,$$
$$D_0 = \begin{bmatrix} 0 & C\Gamma & . & C\sum_{j=0}^{N-2} \phi^j \Gamma \end{bmatrix}^T . \qquad (50)$$

Now design state feedback gain F such that $(\phi_\tau + \Gamma_\tau F)$ has no eigenvalues at origin and provides the desired closed loop behavior.

To realize the state feedback gain F through the control law (48) for the system (43), construct a fictitious, lifted system associated with (49) for which (48) can be interpreted as static output feedback. The measurement matrix of this fictitious system can almost always be made to have full column rank, so that any sampled data state feedback gain for the system (43) can be realized by the control law (48). For this state feedback one can define the fictitious measurement matrix as

$$C(F,N) = (C_0 + D_0F)(\phi_\tau + \Gamma_\tau F)^{-1} , \qquad (51)$$

which satisfies the fictitious measurement equation

$$y_k = Cx_k , \qquad (52)$$

then the feedback control (48) can be interpreted as static output feedback

$$u_k = Ly_k , \qquad (53)$$

for the system (49) with measurement matrix C . To realize the effect of F through L it must satisfy

$$x_{k+1}=(\phi_\tau+\Gamma_\tau F)x_k=(\phi_\tau+\Gamma_\tau LC)\,x_k\,, \qquad (54)$$

$$\text{so} \qquad \mathbf{LC}=\mathbf{F}\,. \qquad (55)$$

Now $N \geq \nu$; **C** has full column rank and any state feedback gain can be realized by fast output sampling gain **L** . If the initial state is unknown, there will be an error $\Delta u_k = u_k - Fx_k$ in constructing a control signal under state feedback. Then closed loop dynamics are governed by

$$\begin{bmatrix} x_{k+1} \\ \Delta u_{k+1} \end{bmatrix} = \begin{bmatrix} (\phi_\tau+\Gamma_\tau F) & \Gamma_\tau \\ 0 & LD_0 - F\Gamma_\tau \end{bmatrix} \begin{bmatrix} x_k \\ \Delta u_k \end{bmatrix} \qquad (56)$$

The system in (56) is stable if and only if F stabilizes (ϕ_τ, Γ_τ) and matrices $(\mathbf{LD_0}\text{-}F\Gamma_\tau)$ has all its eigenvalues inside the unit circle.

CONCLUSION

To represent the spatial instability a nodal model of large nuclear reactor is discussed here. A linear model is obtained by linearizing the nonlinear nodal model of the reactor. Three most promising techniques have been applied to design the spatial control for this Large Pressurized Heavy Water Reactor.

REFERENCES

1. W.M Stacey Jr. , Space *Time Nuclear Reactor Kinematics.* New York: Academics Press, 1969.
2. James J. Duderstadt, and Louis J. Hamilton, *NuclearReactor Analysis*, New York: John Wiley and Sons,Inc., 1976.
3. E. Hinchley, and G. Kuglar, "On - Line Control of the CANDU-PHW Power Distribution." In IAEA *Specialists' Meeting on Spatial Control Problems*, Studevik, Sweden, October 1974.
4. A.Höld and O. Lupas , " Real Time Simulation of the Transient Behavior of Local and Global PWR Core and Plant Parameters," in *ANS/ENS Proc of the Int. Topical meeting on Advances in Mathematical Methods for the solution of Nuclear Engg Problems*, April 27-29,1981, Munich , Germany.
5. A. P. Tiwari, B. Bandyopadhyay and H. Werner "Spatial Control of a Large PHWR by Piecewise Constant Periodic Output Feedback," *IEEE Trans. on Nuclear Science*, vol.47,pp. 389-402,2000.
6. A.P. Tiwari "Modelling and Control of a large Pressurized Heavy water Reactor," Ph.d. thesis, IIT Bombay, 2000.
7. S.S. Lamba and S Vittal Rao,"On Sub optimal Control Via the simplified model of Division" *IEEE Tras. Automatic Control* vol 19,pp 448-450,1974
8. A.B. Chammas and C.T. Leondes, "Pole placement by piecewise constant output feedback", *Int. Journal of control*, vol. 29,pp.31-38,1979.
9. H. Wernerand K. Furuta, "imulatneous stabilization based on output measurements," *Kybernetika*, vol.31, pp. 395-411,1995.

Distributed Control System to Fieldbus

M. D. Desai
Electrical Engineering Department, Nirma Institute of Technology,
Sarkhej Gandhinagar Highway, Tragad Patia, Post: Chandlodia
Ahmedabad- 382481,India
E-mail: nitahd@ad1.vsnl.net.in

Abstract

Industrial process control has a wide range of applications. It covers large number of process parameters. DCS is the soul of a large process plant. It tries to combine centralised and decentralised control. Various models by various companies are available .It also takes care about management aspects It has a operator station in the form of man machine interface. It facilitates engineering and operator changes in the process. Field control unit takes care of control aspects. Field monitoring unit collects and transmits the data collected from the process by transducers to the field control unit and operator station. It permits various modes of control with inbuilt redundancy. There is a provision of generating data useful for fault diagnosis. The present developments in the field bus may change the shape of DCS in future.

Key Words: DCS, Process Control, Control Modes, Data Communication, Protocols, Field bus.

INTRODUCTION

Industrial process control has a very wide range of applications. It includes large chemical, fertilizer, petrochemical, power plants, refinery and oil or gas supply systems. Large number of parameters like temperature, flow, level, pressure, PH, humidity, viscosity, force, velocity, acceleration, torque, chemical composition, etc. are to be closely controlled. Earlier analogue controllers were used. Later on single loop computerised controllers were used. Distributed control system is the soul of large process plant. For these processes physically scattered over a wide area of the plant computerised control system is used.

Present day process control systems is distributed among computing systems. It tries to reap the advantages of centralised and decentralised control systems. All over the world various distributed control systems (DCS) are manufactured and marketed by various companies in the form of different models. Yokogawa [1], Tata honey well [2, 3] Moore controls [4], CG- EL SAG Bailey [5], Fisher Rosemount [6] ,Johnson controls, Foxboro , MCS , ABB, Siemens Klockner Moeller , Robert Bosch , are some of the companies. Micro excel, [1]TDC 3000 [2, 3] Moore A PACS, [4,7] Freelance 2000, [5] Max 1000 GLS , Max 1000 DCS, [8] Plant web[9], and Delta V [6], are some of the common DCS models. Inspite of large number of companies and models the basic aim is to provide total plant automation along with redundancy.

There is some variation in details from brand to brand and model to model but the basic control strategy, capability and scope of applications are almost same. It necessitates high performance, compactness, modularity, friendly automation, easy Integration, easy operation and easy engineering and flexible control. It has to provide all the modes of control and allow analogue as well as digital signals.

DISTRIBUTED CONTROL SYSTEM

Distributed Control System is extensively used in medium and large industries. As the name indicates it has a distributed architecture. The process control as well as process management are distributed throughout the control room and throughout the process plant. Intelligence and hard ware both are distributed.[10] In earlier distributed control systems multi loop controller modules were either at the control room or in the field.

The DCS can be considered as inter connected control system with inter connected communication. A DCS has basically three major sections namely workstations or operation stations or operator stations, communication network, controller and input out put interfaces. [1,2,4,6].

Fig. 1 shows the schematic diagram for the DCs. The central block is a control unit and computer interface. The control section consists of control unit and communication cards. It receives signals from continuous, batch type and distributed process in the plant through transducers, programmable logic controllers and transmitters. The application part has operator stations dealing with engineers and operators for engineering and operational changes. Computer interface facilitates interaction with plant process on one side and production management on the other side. There is further interaction with the factory management for optimum utilisation of resources and efficient working of the plant.

A typical system configuration is as shown in Fig.2. The DCS is connected through high frequency bus to enhanced operator station. The enhanced operator station and other operator stations are connected through optical cable and optical adopters to control unit and field monitoring units. The process parameters are sensed by the transducers and sent to the field control units via signal conditioning units. Programmable logic controllers are directly connected to enhanced control units. I/O expansion units are also used to take care about large number of inputs and outputs. The inputs may be 4-20 mA signals, digital inputs may be from switching devices like position switches and control valves and direct operating field devices related to pressure and level variations. Digital outputs may be from DCS to field devices like alarms, solenoid valves, warning lights, motor contactors, output relays, etc. The control units can control processes scattered over 15 kms. At various levels redundancy is to be ensured some operator stations have printer and facility for colour hard copy. The operator stations are further connected to the supervisory computer through Ethernet.

OPERATOR STATION

Operator stations have 32 bit CPU, monitor, and are capable for large applications, multitasking functions and communication functions.Fig- 3. They have engineering and operator keyboards. Operator key board has alpha numeric, symbolic and function keys. They are connected to printer and colour hard copy unit. Operator panel system includes overview, control group tuning, alarm summary, operator guide, graphic, trend and other panels and user / message screens. Alarm summary panel gives status of each alarm with tag number, timing and associated process. Over view panel is helpful in monitoring the status of each process unit at a glance.

Control group panel displays face plate of number of feedback control instruments and switch instruments in bar graph and numerical form. Trend instrument panel displays instrument conditions. Tuning panel displays graphical and bar graph variation of parameters with respect to time during tuning. Instrument face plate panel displays parameter value on bar graph, tag, control mode and alarm status. Trend panel displays selected parameters variation graphically. Trends can be recorded. There is also a panel for guiding the operator. Graphic panel gives mimic diagram of selected process.

Actual process and components are inter connected and are visible in symbolic form. The process and parameter changes are visible. Message screen panel displays process alarms, operator guide messages and operation messages. Operation groups Are software defined. Operator station can belong to one operation group but control unit can belong to more than one group. Security function defines different access levels for operator, supervising operator and engineer. Operator stations and control units can exchange messages and data. Operator station can communicate with supervisory computer.

COMPUTER AND COMMUNICATION

The DCS requires number of software packages for carrying out various functions. Computer communication is essential component of any DCS. Process data acquisition and setting, interrupt messages for alarm, sequence, error, timer and control communications, file access and record and operator stations have specific communication requirement. Supervisory computer query also requires access to process data. Current process status can be displayed or printed out by process reporting functions. Operator and system utility functions are inbuilt. System maintenance functions display status of cards in control unit and status of the operator station.

FIELD CONTROL

Field control unit may be standard or enhanced. It has powerful control functions, wide range of Input/ Output cards, Input/ Output expansion unit and PLC support. Field control unit consists of processor, bus interface, power supply and set of Input/ Output cards. Enhanced field control unit can be connected to subsystem like PLC. Control unit processor card, power card and bus coupler are dual redundant. To meet all these requirements the control unit has large number of cards. The standard control unit

supports feedback control functions, sequence control functions and process database.

CONTROL UNIT

As shown in [Fig-4] Feed back control block can accept 1 to 5 V signal through I/O card and loop display unit., via loop connection. It is a PID controller. Inside this block 1-5 V signal passes through processing unit which may involve filtering or square root extraction or some other function. The other block takes care about calculation, compensation, etc. and sends the data to indicating controller. Batch status indicator provides interface between step sequence table and operator. Switch instrument indicates motor or valve conditions (On/Off) . Valve monitor packages are available which work independent of switch instrument. It monitors valve action with reference to output to valve , In case of abnormal function gives alarm.

Control unit software packages include valve monitor, PLC communication, control card for thermocouple or mV input, communication protocol, GPIB communication card, etc. PLC communication cards support various brands of PLCs. Arrangements are made for RS232, RS 422, GPIB and TV interface functions. Signal conditioner nests provided are capable of accepting inputs from RTD, potentiometer, mV, transmitter and pulse train cards. inputs from RTD , potentiometer ,mV, transmitter and pulse train cards.

FIELDING MONITORING

Field monitoring units [fig 5] receive direct voltage signal inputs from RTD and thermocouples, pulse train and contact signals, also checks alarms. Advance field monitoring units allows PLC and remote monitoring. It has multiplexer, signal conditioner, ADC, power supply, processor, etc, cards. Field control unit does input indication, and sequence control functions. Advance type does basic functions also. The scan period is 1 or 2 seconds. With operator station the system configuration is possible without control unit. Control unit builder allows control unit definition, instrument specifications, loop connection, sequence tables, operator guide messages, sequence messages, calculation, relational expressions, timers, counters, I/O , sequence instruments and annunciator messages. Operator station builder allows operator station system definition, scheduling, function key definition, definition of instrument constants, message request specification and graphic panel.

SOFT WARE

With CAD software on PC mouse operation can create source files of graphic panels. Standard instrumentation graphic symbols along with some geometric and other symbols allow graphic builder to develop mimic diagrams. Feed back control builder allows to visualise and set some control parameters. Control unit debugging tool permits testing of control units using virtual wiring on software.

CURRENT TRENDS

Process control for the plants requires special network for automation purpose. Different types of networks have been developed for this purpose. [10] open architecture necessitates open standards like Ethernet, TCP/ IP, OPC, object technology and open technologies like internet, web browsers, Eathernet hardware, java, Com/ Dcom, object model, active X, HTTP ,etc. Device network collects large number of small data units. It handles small number of messages, improves data carrying capacity and aims at saving of wire cost. It uses continuous scan cycle (1 ms to 100 ms.).

Enterprise network transfers larger units of information on irregular basis as in the case of email, web page down loading, SQL quarries, printing. The response time is up to 200 ms. In control network routine data scanning is mixed with on demand transfer of alarm status, controller and device programmes, batch reports, process recipes. e.g. profibus, world, FIP, Modbus plus, control net, foundation field bus, genius bus. Industrial intranet allows real time collection and analysis of plant data. Controllers, PLCs and ERP systems are able to access any sensor connected to the control system. In real time process control ethernet allows band width sharing. In full duplex mode provides 100-200 Mbps. The system becomes scalable.

Recently the development of field bus technology is in fore front. Profibus and foundation field bus are out to have lions share in the market. [11,12,13] Moreover regarding the operating system for the process control also Unix and NT are competing each other. [14] NT is cheaper but is considered to be less robust, less stable and less scalable compared to Unix.

CONCLUSION

Distributed control system is required for large process industries and manufacturing plants. It consists of operator stations, field control units, computers and communication units, field monitoring units and associated software and operating system. NT is trying to substitute Unix. In some cases hybrid systems are used. Field bus development is also very fast. The development of profibus and foundation field bus may change the basic nature of DCS it self. The current time is the transition time to DCS. The systems getting through the trial will survive and will be accepted by the users of tomorrow.

REFERENCES

1. Yokogawa, Micro excel Training Manual, AP. (1989)
2. Honeywell, History Module Specification and Technical Data HM03-400, Aug (1993)
3. Honeywell, Plant Network Module Specification and Technical Data, PN03-400, AP(1992)
4. Moore controls, Mycro Apacs Manual, May (1994)
5. C.G.Elsag Bailey, Free Lance 2000 Manual, Jan (1998)
6. Fisher Rosemount, Delta V: Ole for Process Control (OPC) Overview, Jan (1999)
7. Bader F.P. Re engineering the DCS, Tappi Journal, June (1995)
8. Max 1000 DCS Manual (1999)
9. Fisher Rosemount , Manual of 10. Plantweb, (1999)
10. Limaye CS, Integration of Instrumentation Technology with Information Technology, Intech (India Region), Feb.(2001)
11. Fieldbus News , Intech March (1999)
12. Bryant M.A., Defending Profibus; Intech AP. (1998)
13. Graube M. and Steinka F; Fieldbus Does Not Work As Defined in Standard- It works Much Better, Intech, AP (1998)
14. Leister MA and Prizon D; New Protocol widens Filed bus, Mar (1999)

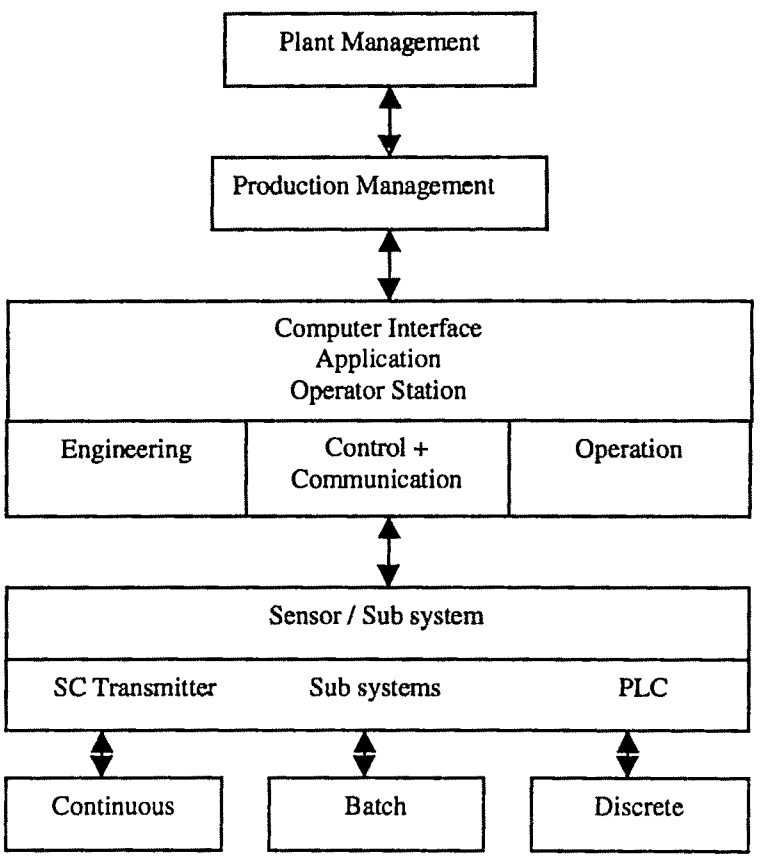

Fig 1 Block diagram of DCS

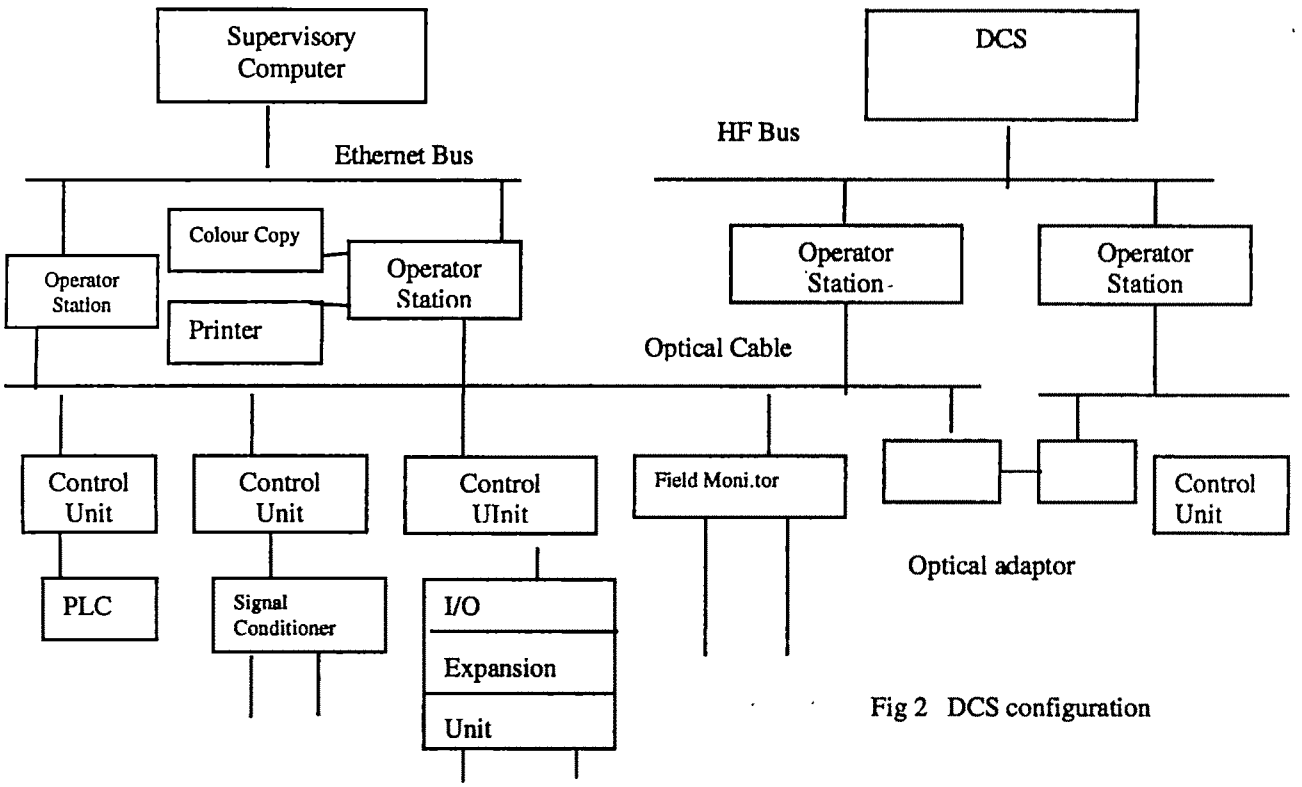

Fig 2 DCS configuration

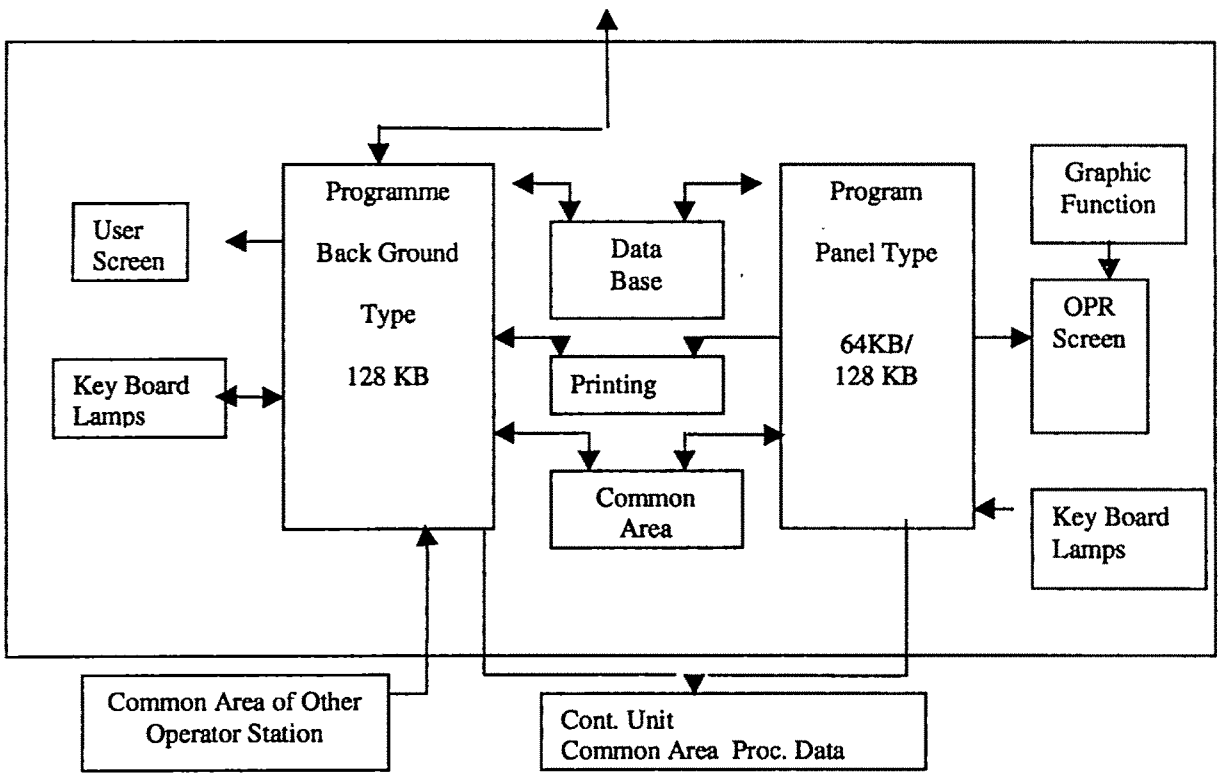

Fig 3 Operator Station Function

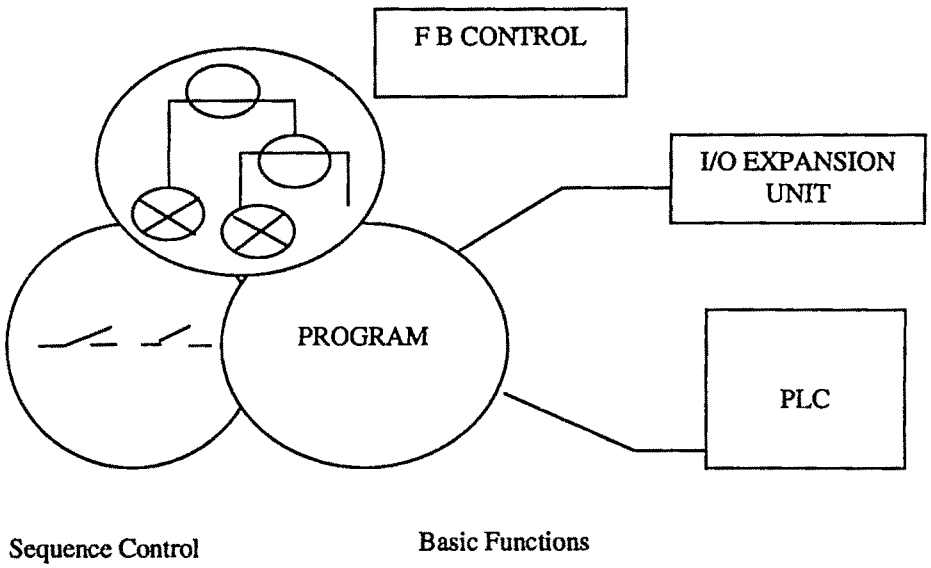

Fig 4 Field control Unit

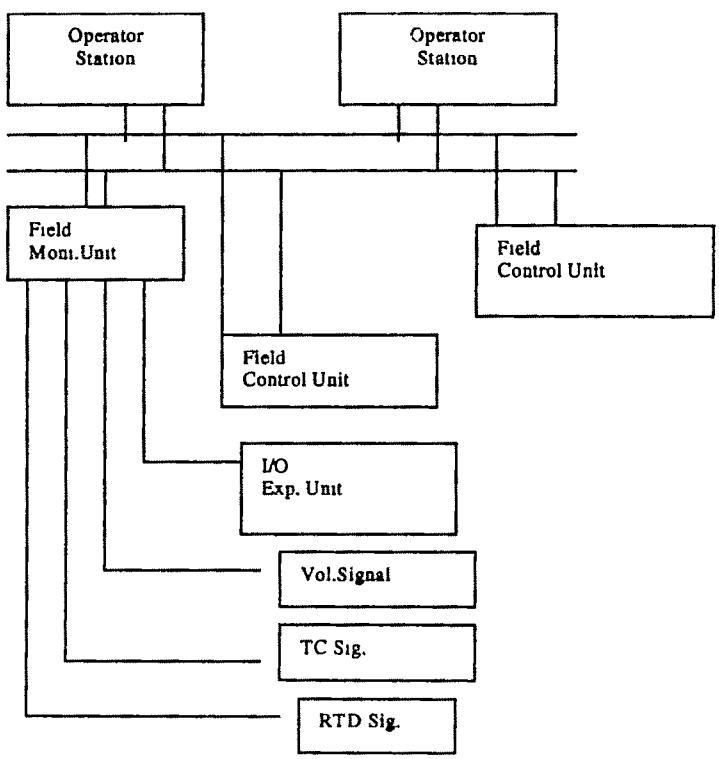

Fig 5 Field monitoring unit

Real Time Level Control Using Fuzzy Logic

R. Abdul Matheen[+], D. Najumnissa Jamal[+], and Abdullah*
[+]Department of Instrumentation & Control
*Department of Polymer technology
Crescent Engineering College, Vandalur, Chennai – 600 048, India.
Email: cec@giasmd01.vsnl.net.in.

Abstract

In a level process station, the control objective is to maintain the liquid level at a required height irrespective of the disturbances affecting the process. This paper presents the real time implementation of fuzzy logic control scheme to control the liquid level in a level process station. Investigations are carried out on the experimental setup. With the results obtained from open loop studies, a mathematical model of the liquid level system is formulated. A conventional fixed logic feedback controller is designed, which gives oscillatory controlled output. The knowledge of the PID controller then obtained is used to design and implement the FLC strategy. The superiority of FLC scheme over conventional feedback controller is highlighted.

Key words: PID – Proportional Integral Derivative, FLC – Fuzzy logic controller, ADAM Modules, Rule Base, Quantization Levels, Membership functions, Fuzzification, and Defuzzification

INTRODUCTION

Fuzzy logic control (FLC) technique has become an active area of research in the application of Industrial process which are not amenable to conventional control techniques. It attends to emulate human mind for monitoring the process parameters and to take decisions regarding the control action. The four principal components of FLC include Fuzzification interface, knowledge base, Decision making logic and Defuzzification interface.

Fuzzification:

Fuzzification converts the input data namely error e(t) and change in error ce(t) into suitable linguistic variables. A scale mapping is performed using triangular membership function, which transfer the range of input variables into corresponding universe of discourse.

Knowledge Base:

Knowledge base consists of data base and rule base. Database provides necessary definitions that are used to define linguistic control rules with syntax, such as: If < fuzzy proportion > then < fuzzy proportion > The IF part is called the antecedent and the 'THEN' part is called the consequent. In control applications the antecedents are 'error' and 'change in error' and the consequent is the 'control command'.

Decision Making Logic:

Decision making logic infers a system of rules through the fuzzy operators namely 'AND' and 'OR' and generates a single truth value which determines the outcome of rules (inferred fuzzy control action)

Defuzzification:

Defuzzification yields a crisp, non-fuzzy control action from an inferred fuzzy control action. In the present work the center of area method is used as Defuzzification strategy.

OPEN LOOP STUDIES

The fabricated level process station consists of process tank, differential pressure transmitter, controller, current to pressure converter, controlvalve, pump and ADAM interfacing modules and process computer. The differential pressure transmitter (DPT) used for the level measurement is connected to the bottom of the tank. This arrangement is equal to liquid height above the sensor multiplied by the specific gravity of the liquid. It is independent of volume (or) vessel shape. The level loop experimental setup is interfaced to the process computer, which acts as a direct digital controller, through signal conditioning module and control module as shown in figure1which consists of ADAM 4012A/D input module D/A output module and ADAM 4520 communication module. (which converts

RS485 protocol to RS232 protocol before being fed to the computer). The current to pressure transducer (I/P converter) accepts an electrical signal (4-20)mA and produces a proportional pneumatic output (3-15) psi for operating a control valve (or) positioner. The final control element is an equal percentage control valve, with a diaphragm pneumatic actuator. The actuator used is fail to close type, which enables the closure of valve in the event of an air failure that prevents the overflow of the tank. The valve positioner is a servo amplifier used with the valve actuator to assure that the control valve stem accurately takes the position that the input signal commands.

Open loop studies are carried out on the level process experimental set up as shown in figure3 .The Block diagram in figure1 shows the step change of 12mA to the I/P converter which converts the electrical signal into its equivalent 9psi pneumatic signal. This signal is applied to the control valve. The level then starts to rise monotonically and then gets saturated at some height, until the inflow into the tank equals outflow. The variation of the level is plotted on the screen as shown in figure2 .The level loop process parameters are calculated from the open loop response of the system obtained from the experimental data using reaction curve method [1]. The level process is modeled as a first order system with dead time as given in equation (1).

$$G_P(S) = \frac{K_P * e^{-\theta s}}{(\tau s + 1)} \qquad (1)$$

with Process gain, $K_p = 1.08$
Dead time, $\theta = 13$ Sec.
Time constant $\tau = 360$ Sec

PID CONTROLLER DESIGN

The PID controller is represented in the velocity from of discrete algorithm as given in equation (2).

$$\Delta U_n = K_c\,[1+T/T_R + T_D/T]\,e_n - K_c\,[1+2T_d/T]\,e_{n-1} + K_c\,\{T_D/T\}e_{n-2} \qquad (2)$$

The tuning of controller is carried out using ziegler Nichol's tuning rule. The controller settings of PI controller thus obtained are given as follows.

$$K_c = 0.9 * \tau / K_p * \theta \qquad (3)$$
$\tau = 360$ Sec
$\theta = 13$ Sec
$T_R = 3.33 * \theta$
$K_c = 15$; $T_R = 60$ .Sec

FLC DESIGN

During fuzzification [3] the fuzzy input variables namely error e(t) ranging from –70 to + 70 cms is converted into five linguistic levels namely error positive large (EPL) error positive medium (EPM), error zero (EZ), error negative medium (ENM), error negative large (ENL). Similarly the other fuzzy input variable namely, change in error; (c e(t)), ranging from –2 to +2 is converted into five linguistic levels namely (CENL) change in error negative large, (CENM) change in error negative medium, (CEZ) change in error zero ,(CEPM) change in error positive medium (CEPL) change in error positive large. The change in manipulated variable is also divided into five linguistic variables.The triangular membership function is used to perform the scale mapping. The membership functions of three fuzzy variables of the level loop system are shown in figure 9,10,11.

Rule Base:

The behaviors of the control surfaces are defined by the rules that tie together the fuzzy variables. In the present case 25 rules are framed. All the rules are represented in the form of a rule base matrix in table3.

In the matrix, the antecedents are the error and change in error. The consequents of the rules are the manipulated variables given in the box. The outcome of the rules namely the truth is obtained using max-min criteria.

The non-fuzzy crisp output from the FLC is obtained by carrying out defuzzification using the center-of-area method. The crisp output thus obtained is given in equation [4].

$$Z_o = \frac{\sum_{j=1}^{N} uz\,(wj)\,(wj)}{\sum \mu z\,(wj)} \qquad (4)$$

where j=1toN, the number of quantization levels Wj is the support value at which the membership function reaches the maximum value (μ_z (wj)) maximum value of membership function corresponding to the quantization level. The parameters of FLC then designed are given in table [1].

RESULTS AND DISCUSSION

PID Scheme Simulation:

After tuning the PID controller, its performance for setpoint tracking is studied. The closed loop response with the PID controller for set-point tracking is displayed in figure 4.The response shows overshoot .The oscillations before reaching the set-point would affect the life of the controller.

FLC Scheme simulation

After tuning the FLC, its performance for set-point tracking is studied. The closed loop response of the level process station with a fuzzy logic controller is given in Figure 8.

It can be seen from the response that liquid level of the tank reaches the setpoint without oscillations and overshoot. There is also improvement in rise time and setting time.

REAL TIME CONTROL OF LEVEL LOOP USING PID CONTROL

The PID control scheme is implemented on the level loop system. The controller output is given to the final control element through ADAM 4021 D/A output as shown in Figure1. The real time closed loop response of PID controller set-point tracking is shown in figure7. The corresponding error, change in error and controller output is shown in figure 5,6,7 respectively.

REAL TIME CONTROL OF LEVEL LOOP USING FLC

The FLC scheme is implemented on the level loop using 5-quantization level and 25 rules. Tuning is carried out by adjusting the membership values and rule sets. The real time closed loop response of the FLC scheme for set-point tracking is displayed in Figure 12. FLC performs well compared to PID controller. The closed loop response does not show overshoot and settles quickly without any oscillations. Also there is no offset in the closed loop response.

CONCLUSION

The present work brings out the potential advantage of applying FLC technique for liquid level control. The FLC performance has good set-point tracking. More over, because of their reliance on rules based on expert knowledge, they provide their environment, a higher machine intelligent quotient. The center of area method takes the center of gravity of final fuzzy space and produces a result that is sensitive to all the rules in particular. The results tend to move smoothly across the control surface. The comparison of closed loop performance of both the schemes show the superiority of FLC scheme over PID control. FLC can therefore be an effective control strategy for the liquid level control.

REFERENCES

1. P. Harriot, Process Control, Mcgraws-Hill, (1972, India.)
2. T. Thyagarajan, J. Shanmugam, R.C. Panda, M. Ponnavaikko, "Fuzzy controller for temperature regulation of dryer, "Proceedings of National Conference on Neural network and fuzzy systems, (Chennai, India, 1997) p 183-197.
3. Lee C.C, "Fuzzy logic controller part – 1, IEEE Transaction on systems Man and Cybernatics (1990) Vol. 20 (2), p 404 – 416.

Table. 1 FLC Parameter:

Parameter	Value
Input variable	2
Quantization levels	5
Rules	25
Membership function	Triangular
Defuzzification	Center of area method

Table. 2 Comparison Table of Performance Parameter

Performance listing	PI	FLC
ISE	307260358	27936.345
ITAE	16194.8655	14565.825
Maximum over shoot	1.8cm	0.1cm
Rise time	196s	170s
Settling time	240s	185s

Table 3 Rule based matrix controller output

Error Change in error	ENL	ENM	EZ	EPM	EPL
CENL	MVPL	MVPL	MVPL	MVPM	MVZ
CENM	MVPL	MVPL	MVPM	MVZ	MVNM
CEZ	MVPL	MVPM	MVZ	MVNM	MVNL
CEPM	MVPM	MVZ	MVNM	MVNL	MVNL
CEPL	MVZ	MVNM	MVNL	MVNL	MVNL

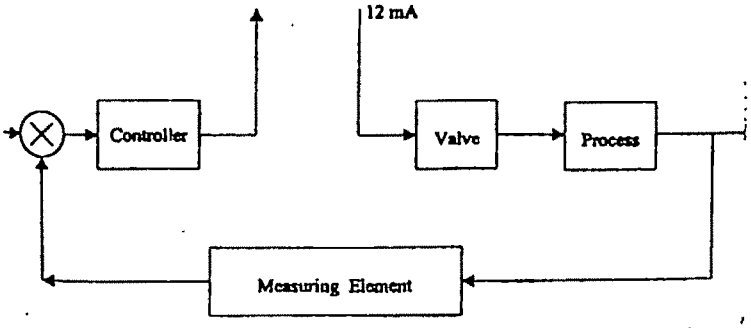

Fig.1. Block Diagram of Open loop setup

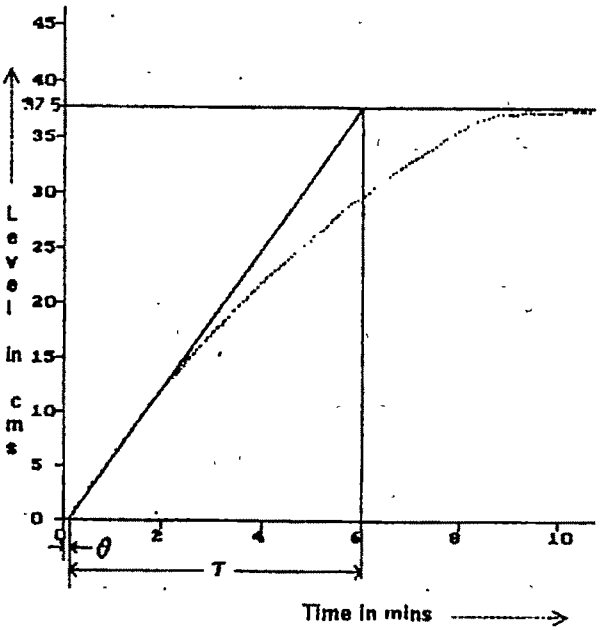

Fig.2. Open loop response curve of the system

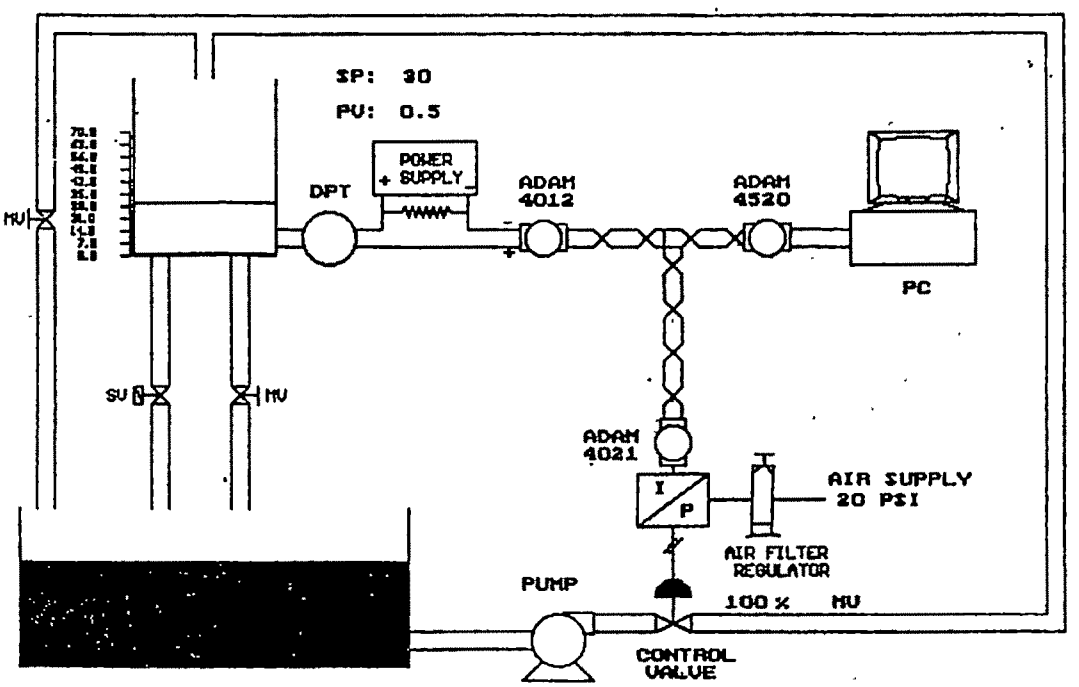

Fig.3. Schematic diagram of Level loop setup

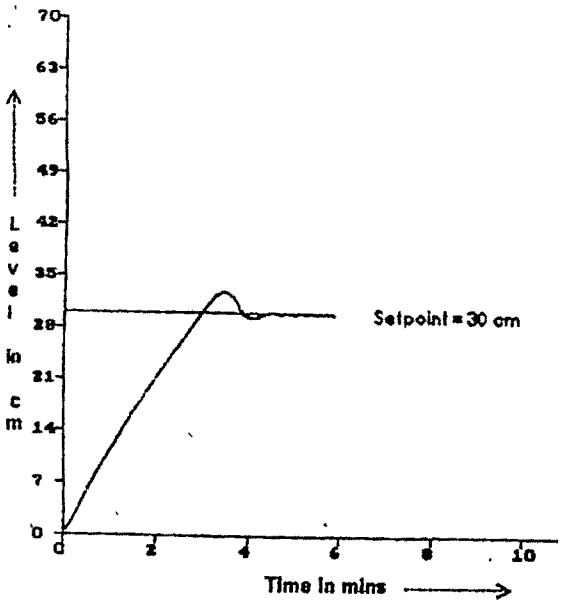

Fig.4. Closed loop response of Level

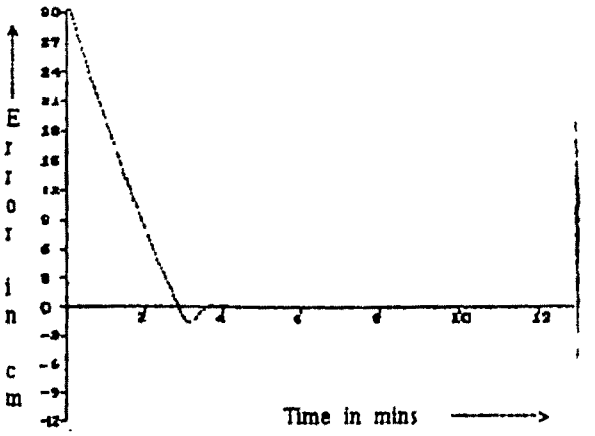

Fig.5. Error Curve

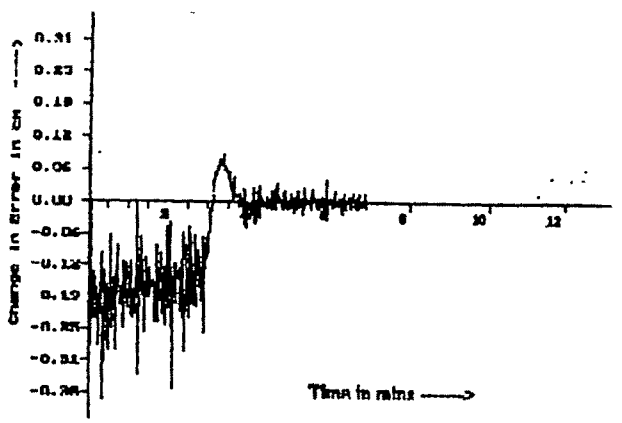

Fig. 6. Change in Error Curve

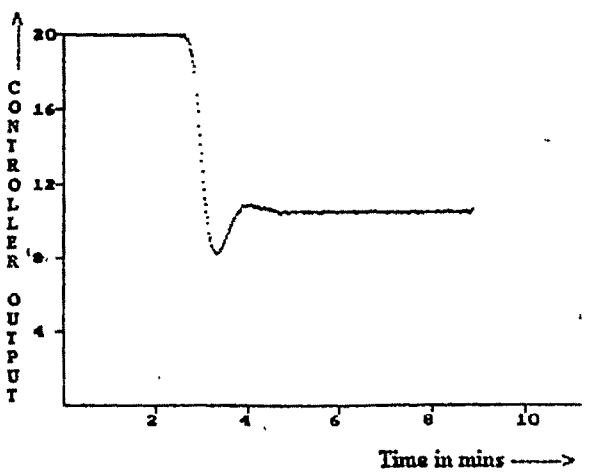

Fig. 7. Controller output curve

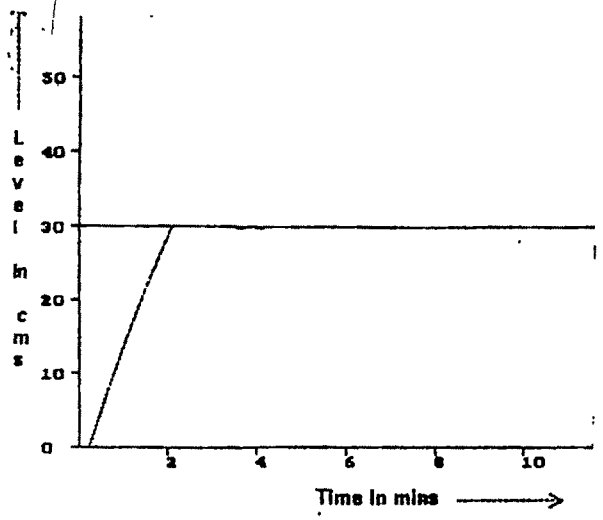

Fig. 8. Simulation of Level using FLC

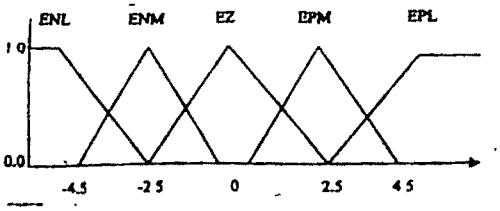

Fig. 9. Membership function of error e(t)

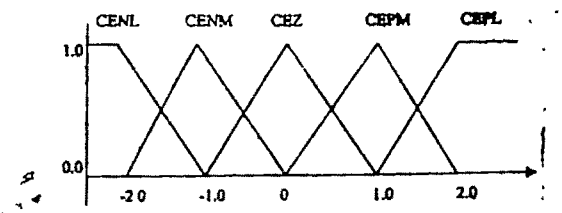

Fig. 10. Membership function of change in error ce(t)

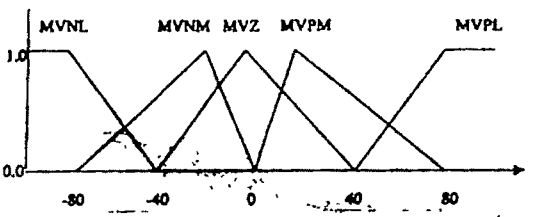

Fig. 11. Membership function for change in manipulated variable

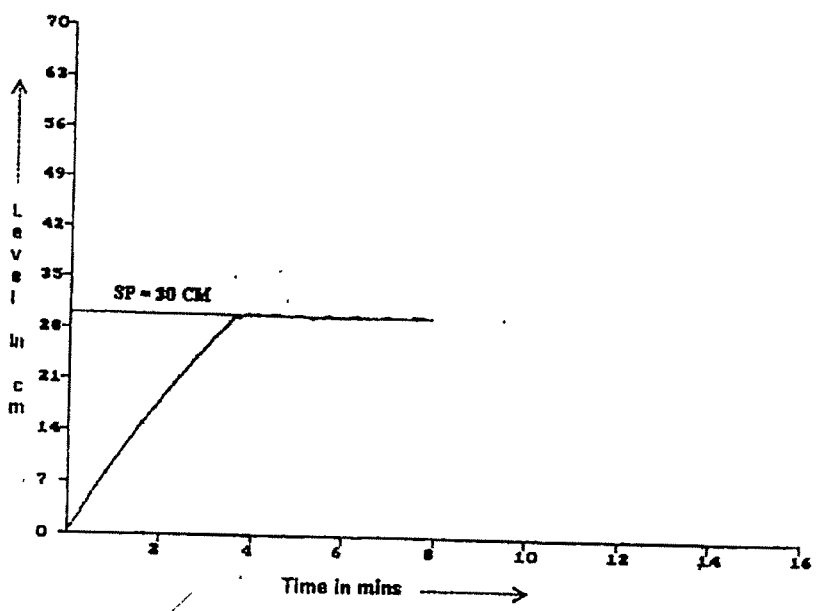

Fig. 12. Closed loop response curve of level using FLC

Nonlinear PI Controller For Buffered Acid Base System

A. Arvind Kumar[a], M. Chidambaram[a], V. S. R. Rao[a] and Rainer Pickhardt[b]
[a]Department of Chemical Engineering
Indian Institute of Technology, Madras, Chennai-600636, India
[b]Department of Electrical Engineering, Rhur University, Bochum, Germany

Abstract

The control of pH is one of the most difficult processes in the process industry because of the severe non-linearity and high precision required in manipulating the flow rate. Wiener model, which consists of linear dynamic element followed by non-linear static element, is used for representing such non-linear processes. Piecewise continuous polynomials are used for mapping the non-linear static gain accurately. The PI controller for the unity gain subsystem of the Wiener model is designed by the method of inequalities. The performance of the resulting nonlinear PI controller is compared with that of the state feed back and multiple model robust H_∞ controllers reported by Galan et al. (2000) for a buffered acid-base system through simulation study for a servo response. Regulatory response results of the nonlinear controller are also presented at different operating points to test the robustness of the controller.

Key words:PI controller, acid base system

INTRODUCTION

The pH control is one of the most difficult problems because of highly non-linear behaviour of the system. Gain scheduled PI controller was implemented by Chan and Yu [1]. The controller yielded good results for regulatory response around a fixed operating point. But it has to be re-tuned if there is any change in the operating point. In order to tackle severe non-linearities associated with the pH process, Wiener model based controllers have been used. A Wiener model consists of a linear dynamic element followed in series by a nonlinear static element Recently Galan et al.[2] have reported experimental results for buffered strong acid - strong based systems. A buffer is a salt of weak acid and strong base or vice versa.

The presence of a buffer in the acid-base system results in the flattening of the titration curve, i.e. the gain of the process is considerably reduced. An un-buffered strong acid - strong base system is very sensitive to the changes in the manipulated variable in the region of pH 4 to 11 i.e. a small change in the manipulated variable results in large change in the output (pH). The precision required in controlling such systems is very high. Buffering is important from the control point of view, because it reduces the sensitivity of the system to a large extent. But the buffer introduces additional differential equation relating the input and its state variable concentration in the model equations and the resulting pH will be a function of three state variables as compared to in the case of strong acid and strong base system. Galan et al.[2] proposed two methods of control of the above system (1) state feedback controller (2) multiple model robust H_∞ controller. The existence of state feedback controller provides useful information related to the internal stability and also defines the best performance achievable for the system. They assumed that all the state variables are available for measurement and implemented a simple inverse controller of the form $v = K_c(y_r - y)$ where K_c is the proportional gain, y_r is the set point and y is output of the process.

The multiple model robust H_∞ linear controller design methodology involves application frequency domain approach to design a controller k(s) for a plant such that the closed loop system satisfies the basic requirements of stability, performance and robustness. The details of the method are given in [2]. In this method the entire titration curve is divided into a number of zones based on the derivative criteria and the process is approximated as first order transfer function model in each of the zones. The local linear robust H_∞ controllers are designed based on these models. The global controller is then designed based on the multi-linear model structure.

The aim of this paper is to implement Wiener model based nonlinear PI control strategy for the buffered acid-base system. The method of inequalities is used to design PI

controller for the unity gain subsystem of Wiener model. This method takes into account the variations of parameters of the process in the design stage to obtain a single set of PI controller parameter, which gives satisfactory performance. The performance of the controller is compared with that of the state feed back and multiple model H_∞ controllers (reported by Galan et al. 2000) through simulation.

MODELING OF pH PROCESS

Consider a continuous stirred tank reactor of volume V. Let F_a be the flow rate of the feed stream consisting of strong acid (HCl). Let F_b be the flow rate of the titration stream consisting of strong base (NaOH) and a buffering agent ($NaHCO_3$) with dissociation constant K_b. Let C_a, C_{b1} and C_{b2} be the inlet concentrations of acid, base and the buffer. Let x_a, x_{b1} and x_{b2} be the state variable concentrations of acid, base and the buffer in the outlet. The values of the model parameters those reported by Galan at.el.[2] are given in Table 1. The mathematical model equations (and the model parameters) that describe the dynamic behaviour of the process are given in [2], where nonlinear algebraic equation (8) were used to carryout offline region identification. A derivative criterion is used to detect the change in the curvature of equation, which indicates the range when the linear approximation is becoming deficient, signaling a region change. The process is approximated as a first order system of the form $K_{p,i}/(\tau_{p,i}s+1)$ around the operating point. The values of the parameters used to obtain the linear models are outlined in Table 1.(from [2]).

NONLINEAR STATIC ELEMENT

The choice for the static element is governed by the fact that, the model used for control purpose must have an inverse. Polynomial models are usually employed to represent the non-linearities because they have an inverse by means of their roots. Odd order polynomials are preferred because they have atleast one real root. A single polynomial can be used to fit the entire steady state data but in most of the cases one has to go for higher order polynomials where coefficients are very sensitive. So, instead of going for higher order polynomials it is preferable to use lower order piecewise continuous polynomials. This allows us to map the non-linearities with lower order polynomials. The break points for piecewise polynomials are different from those of the linear models as discussed earlier. The accuracy of the piecewise polynomial fit for the actual nonlinear parameter values are shown in Table 2. The comparison of the steady state titration curve and the piecewise polynomial fit is shown in Figure 1. It can be seen that the polynomial fit maps the dynamic state titration curve very closely.

The implementation of Wiener model based PI controller is in two stages (refer Figure 2). In the first stage the intermediate state variable 'x' for the given setpoint and also the output is obtained by inverting the polynomial gain relation. Since the polynomial is of third order, there is possibility of three real roots. In actual implementation, that value of real root is chosen, which is closest to the operating point. In the second stage the difference in these values is fed to the controller, which will give a value for the manipulated variable (u). This 'u' will be given to the plant.

CONTROLLER DESIGN BY THE METHOD OF INEQUALITIES

The method of inequalities is a multi-objective formulation of the design problem. In this method, all the design specifications are directly expressed in terms of a set of inequalities known as the performance criteria. This method is called the method of inequalities because the performance criteria such as overshoot, steady-state error and the settling time are imposed as inequality constraints. More details about this method are given in Zakian and Al-Naib (1973) . In the design of the controller, the linear dynamic element, which is the first order transfer function of unity gain is used in a closed loop Simulink block diagram for each of the four zones (refer Table 2). The process is simulated for unit step change in each of the zone for randomly generated PI controller settings and the constraint satisfaction is verified.

The controller settings which give a minimum sum of ISE and γ times ISU in zone-1 (here the process has the largest time constant hence large ISE values and ISU), is taken as the optimal settings. The weighting factor (γ) for calculation of ISU is chosen by trial and error and it affects the maximum controller output for a unit step change. In the present case the value of γ used was 1/150. The algorithm for design of optimal PI controller by random search optimization is discussed by Zakian and Al_naib [3]. The constraints used in the design of controller are: Overshoot ≤ 0.2; Settling time $\leq$ 6 min & Steady state error ≤ 0.001. The initial guess for the controller parameters is obtained from the pole placement method. The average values of the time constant is taken ($\tau_{p\ avg}$ = 106.02) for design of PI controller with the poles placed at s=-.5 and s=-.5 respectively. The initial guess parameters obtained are: K_c = 1.75 &τ_I = 237.73. The optimal controller parameters obtained are: K_c = 2.45 &τ_I = 101.34

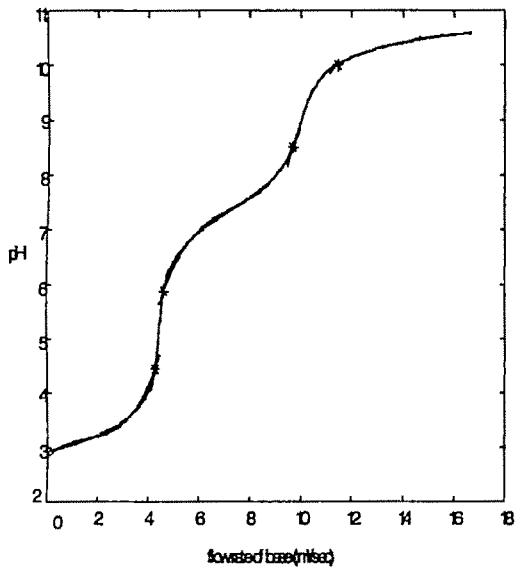

Fig 1. Piecewise polynomial fit of the steady state titration curve.--- Piecewise Polynomial fit;.... Actual titration curve ; * Break points

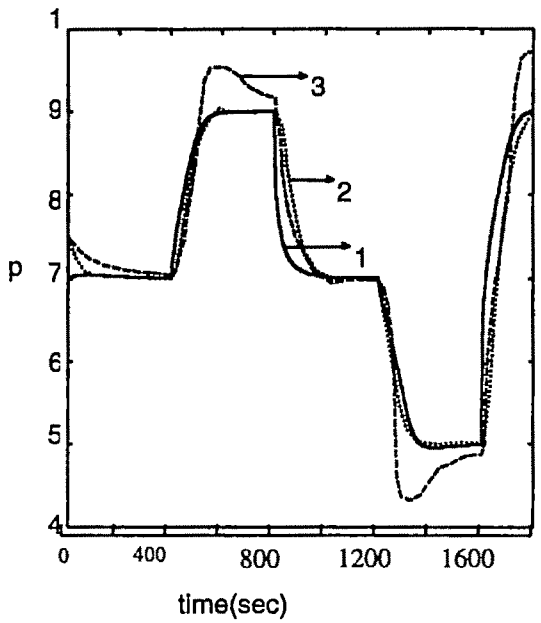

Fig 3 Simulation results of closed loop response for step change 1:Non-linear global PI controller 2: State feedback controller 3: Multiple model robust H_∞ controller

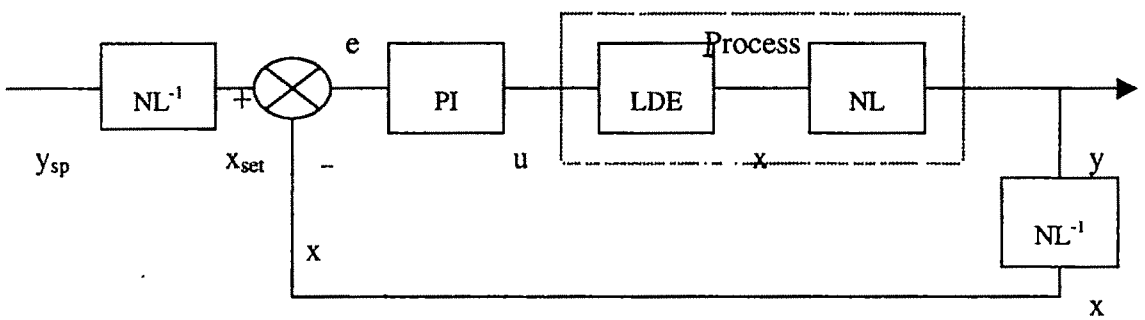

Fig 2. Block diagram of Wiener model based PI controller

SIMULATION RESULTS

The comparison of present nonlinear optimal PI, state feedback and multiple-model robust H_∞ controllers is presented for servo response. The nonlinear optimal PI controller is simulated on the nonlinear mathematical model. The responses of multiple model H_∞ controller and state feedback controller are plotted by obtaining data points for respective controller from Galan et al.[2] by using "digitizer" program in MATLAB. The data points are plotted and compared with the nonlinear optimal PI controller.

The state feedback controller defines the best achievable performance by a controller and hence forms the basis for comparison of the performance of other controllers. It can be seen from Figure 3 that the present nonlinear optimal PI controller shows as good a performance as state feed back controller, reaching the setpoint asymptotically in almost all the cases. The controller output is also within the limits of the final control element (0 to 20ml/sec), as can be seen from Figure 4. The multiple model robust H_∞ controller shows overshoot/undershoot in all the cases with a maximum overshoot of approximately 0.5 pH for step changes from pH 7 to 9, 7 to 5 and 5 to 9. Moreover it has higher settling time when compared to the nonlinear optimal PI controller. From the results it can be concluded that the nonlinear optimal PI controller shows superior performance in comparison to the multiple model robust H_∞ controller.

In the design of robust H_∞ controller, the variations in gain and time constant are considered for an equivalent local linear model. The performance, stability and robustness of the controller are ensured by minimizing the mixed sensitivity function for the system. However the choice of weighting (penalty) functions is not unique and requires several iteration in order to obtain them. Moreover the controller design involves a number of steps and is fairly complicated. In case of the state feed back controller, it is assumed that all the state variables are available for measurement. In case of the design of the nonlinear optimal PI controller, only the linear dynamic element is considered for controller design. The performance and the robustness of the controller are ensured by specifying the constraints on overshoot, settling time and steady state error directly in the time domain. The design procedure is simple and involves very few steps.

Model	U_{ss}	PH_{ss}	$K_{p,I}$ (pH min/l	$\tau_{p,I}$ (min)
1	0.14	3.3	3.89	131.25
2	0.26	5.0	101.62	118.55
3	0.45	7.4	5.24	103.52
4	0.60	8.6	25.95	94.23
5	0.82	10.4	1.76	82.58

Table 1 Linearization points and parameters for the local linear models

CONCLUSION

In the present work, nonlinear optimal PI controller is simulated for the buffered acid base system based on the Wiener model. The nonlinearity is represented by piecewise continuous polynomials and the linear dynamic element by transfer function of unity gain. The controller for the unity gain subsystem of the Wiener model is designed by the method of inequalities which takes into account the variation in the dynamic element. The robustness of the proposed controller was tested by comparing it with the state feed back controller and the multiple model robust H_∞ controller for servo response. From these results it was seen that the nonlinear optimal controller showed better response than the multiple model robust H_∞ controller and as good a response as the state feed back controller.

REFERENCES

1. Chan, H.C. and C.C.Yu (1995) Autotuning of gain scheduled pH control: An experimental study, Ind. Eng. Chem. Res., 34, 1718-1729.
2. Galan O., J. A. Romagnoli and A.Palazoglu (2000) Robust H_∞control of nonlinear plants based on multi-linear models: An application to a bench–Scale pH neutralization reactor, *Chem. Eng. Sci.*, 55, 4435-4450.
3. Zakian, V. and U.Al-Naib (1973) Design of dynamical and control system by the method of inequalities, IEE Proc. CTA-120,1421-1427.

A_0	A_1	A_2	A_3
5.399×10^{-2}	-2.546×10^{-1}	4.831×10^{-1}	2.822×10^{0}
-8.721×10^{0}	1.164×10^{2}	-5.142×10^{2}	7.556×10^{2}
4.517×10^{-2}	9.933×10^{-1}	7.515×10^{0}	1.211×10^{1}
3.707×10^{-3}	-5.332×10^{-1}	1.085×10^{1}	4.992×10^{1}
3.601×10^{-3}	1.683×10^{-1}	2.687×10^{0}	-4.087×10^{0}

Table 2. Values of coefficients of the equation $pH=A_0u^3+A_1u^2+A_2u+A_3$ for hydrochloric acid, sodium hydroxide and sodium bicarbonate system

Design Of Automatic Control System To Supply Fuel Gas With Suitable Calorific Value Utilizing The Available By-Product Gases In Iron And Steel Plant

G. Karmegam[1] and S. B. L. Saxena[2]
[1]E.C.E.Dept.,Kongu Engineering College, Erode-52, India
[2]Dept. of Electrical Engineering, Regional Institute of Technology., Jamshedpur, India.

Abstract

By-product gaseous fuels such as BF gas, CO gas and LD gas are generated from the processes at coke ovens, blast furnaces and BOF steel melting shops in the integrated iron and steel plant. The characteristics such as calorific value, specific gravity and composition of each by-product gas are different in nature and the stability of calorific value of fuel gas is of paramount importance in any heating process. This calls for properly designed control systems to be instituted so as to supply the fuel gases with stable calorific value to the various processes where the hot working is required to be carried out in the steel plant. This paper gives a brief account of the design of automatic control system to supply fuel gases with suitable calorific value utilizing BF Gas, CO Gas and LD Gas to the various production units in the plant.

INTRODUCTION

The Blast Furnace Gas is the by-product in Iron making process in the Blast Furnace and the calorific value of BF Gas is at the range of 850 to 900 Kcal/Nm3. The CO Gas is generated as a by-product fuel from the carbonization process of converting coal into coke to be used in Blast Furnaces as an input. This calorific value of CO Gas is in the range of 4000 to 4200 Kcal/Nm3. LD Gas is the by-product fuel from steel making process at LD converters and the calorific value is in the range of 1600 to 1800 Kcal/Nm3. The energy cost accounts for 30 to 35% of steel making cost. In order to achieve cost competitiveness, it is imperative to utilize the by-product gases to the maximum and reduce the quantity of purchased fuel to meet the heat demand in the various processes in the integrated steel plant. It is also important to mix the various by-product fuels depending on their availability to supply fuel gas to the various down- stream production units. The fuel gas should be supplied with stable calorific value so that the heating efficiency can be maximized and the chimney emission can be kept within the norms.

CONCEPT OF THE AUTOMATIC CONTROL SYSTEM

Different characteristics of by-product gases, hour to hour variations in availability of by-product gases and the heat demands required at the various furnaces are to be considered while designing the automatic control system for gas mixing and supply of fuel gas to the consuming unit. The plant fuel balance needs to be worked out to find out the various possibilities of mixing the available by-product fuel gases to achieve optimum usage of by-product gases in the plant. The net work pressure available in the by-product gas fuel net-works in the plant should be considered for the design, keeping the safety of the system in mind for selection of the equipments such as gas boosters, maximizing drums and associated pipeline networks. The objectives of the control system are (a) to utilize the available by-product gases – BF gas, CO gas, and LD gas and (b) to supply the fuel gas with the calorific value 2500 Kcal/Nm^3, stable within the permissible limits i.e., ± 2.5% band by mixing and boosting at desired pressure to meet the fluctuating demand by the furnace.

GAS MIXING AND BOOSTING

The BF gas is available in the plant network at pressure 300 to 800 mm wg and the CO gas is available in the plant network at a pressure of 600 to 1100 mm wg. It is essential to raise the BF gas pressure to the level of CO gas pressure to achieve desired mixing of these two gases for uniform and stable calorific value within the permissible limits. The BF gas is mixed with CO gas and boosted by boosters. The mixed gas is delivered to furnace at 1000 – 1200 mm wg.

The booster capacity designed to take care of the minimum gas demands of the furnace without sacrificing the calorific value control. As the gas sample may not be representative, the measurement of calorific value is not exactly matching with that of the main gas all the times. This may result in erratic behaviour of CV control system.. In addition to this, frequently the BF gas pressure used to be lower than the CO gas network pressure due to the fluctuations in generation of BF gas.. This resulted in cases of high CV of mixed gas being supplied to furnace.

MODIFICATIONS IN GAS MIXING STATION

The limitations experienced in gas mixing station are overcome by using a BF gas booster to a pressure of 1000 mm wg and the boosted BF Gas is supplied to the mixing stations. The BF Gas is injected in the mixing drum along with the CO Gas for uniform mixing, which will help in uniform calorific value in the mixed gas, which is being measured by calorie meter. The mixed gas is again boosted by the booster to deliver the mixed gas at a pressure of 1000 to 1200 mm wg to meet the gas demand of the re-heating furnaces at hot strip mill.

DESCRIPTION OF THE CONTROL SYSTEM

BF Gas and CO Gas are mixed in the ratio of 45% to 55% in order to achieve the calorific value of 2500 Kcal/Nm^3. A pressure control valve is installed to control the down stream pressure in BF Gas network at 400 to 500 mm wg and in CO Gas network at 500 to 600 mm wg. After mixing BF Gas with CO Gas the mix gas is boosted by the booster to export the gas to the Reheating Furnaces of Hot Strip Mill. The calorific value of the mix gas is measured and the signal is fed to the calorific value controller. The output of calorific value controller is transmitted to the ratio controller, the output of which is used to adjust the flow control valve in the BF gas main to achieve the calorific value of the mix gas at desired value.

The demand for the mixed gas at reheating furnaces is fluctuating in nature due to the operation of the hot strip mill. Any change in the mixed gas demand triggers the corresponding change in the set points of the flow controllers of CO gas and BF gas. The overriding control for adjusting the BF gas flow to be mixed with CO Gas is provided by the calorific value controller output.. The calorific value of mix gas is within the band of ± 2.5% of the set point i.e., 2500 Kcal/Nm^3.

MODIFICATION OF THE CONTROL SYSTEM

The modification was done to provide gas supply at stable pressure to furnaces irrespective of fluctuating demands. Before Modification, no export pressure control for mixed gas supply to HSM furnaces was provided which resulted in export pressure fluctuation with variation in mixed gas consumption at furnace end and leading to tripping of furnace. The export gas pressure used to vary from 1000 mm WC to 2000 mm WC depending on the gas consumption at furnace end. Necessary control philosophy was developed based on the study of the performance of mixed gas delivery pressure to ensure supply of mixed gas at constant pressure to the furnace. The suction damper of the booster was converted to control valve and controlled from the freelance 2000 distributed control system (DCS) based on the export gas pressure. Fig 1 and 2 show the variations in export pressure before and after modifications.

MODIFICATION TO CALORIFIC VALUE / WOBBE INDEX CONTROL LOOP

A stable pressure of mixed gas was ensured at the furnace end. When the availability of LD gas improved in the plant, it was necessary to consume LD gas by injecting into the BF gas network and this improved the CV of BF gas being injected at gas mixing station. The stability of CV of mixed gas was affected due to the varying quantities of LD gas injection and the varying CV of LD gas. Necessary modifications were carried out to overcome the problems. Fig 3 shows the system before modification and fig 4 shows the system after modification. Before Modification calorific value used to fluctuate because of the continuous variation in the gas consumption at the furnace end. CO: BF ratio was also affected because of LD gas injection in the main and resulted in varying Wobbe Index. CO gas flow control valve was not also present.

After Modification, dynamic variation of CO: BF ratio based on actual wobbe index has been incorporated in DCS to take care of LD Gas injection. CO gas flow control valve was put into auto operation for which necessary control philosophy has been developed. CO gas pressure control was improved. Variable ratio of CO : BF was implemented to take care of LD Gas injection. Calorific valve control, even when there is LD gas injection in the main, is not affected.

CONCLUSION

The control philosophy adopted to achieve stable CV of mixed gas to the reheating furnaces helped in maximum utilisation of the available byproduct gases namely BF gas, CO gas and LD gas. The varying characteristics of these byproduct gases decussated midcourse modifications to the original control system and the satisfactory results were achieved to supply mixed gas with stable CV in spite of the multivariable such varying gas pressures, gas plans calorific

valves of the gases influencing the controlled variable i.e. calorific value of the mixed gas.

Acknowledgement: The authors acknowledge with thanks for the support provided by the management of Tata Steel and Regional Institute of Technology, Jamshedpur. The author thanks their colleagues for their cooperation and help in preparing this paper.

Table 1 The composition and other characteristics of three gases (all units are % by volume) →

	B.F. Gas	C.O. Gas	L.D. Gas
CO_2	12 – 16	2.2 – 3.4	12.0 – 16.0
CmHn	-	2.4 – 4.2	-
O_2	0.8 – 1.2	0.4 – 1.0	1.2 – 2.2
CO	22 – 25	8.0 – 9.0	52.0 – 68.0
H_2	2.6 – 6	51.0 – 55.0	2.2 – 4.2
CH_4	-	21.0 – 25.0	-
N_2	Rest	Rest	Rest
CV	800 – 950	3800 – 4200	1600 – 1950
Sp. Gravity	1.01 – 1.03	0.45 – 0.50	1.05 – 1.15

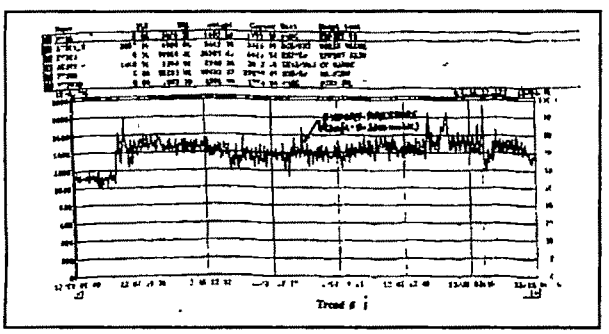

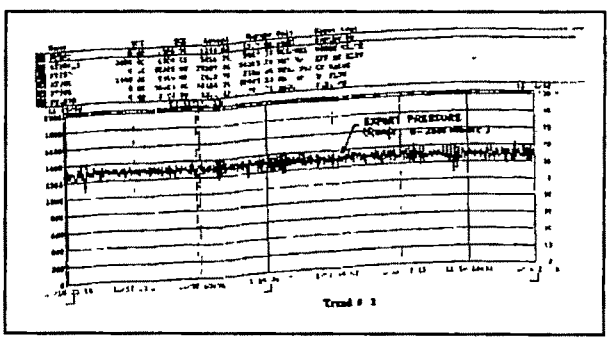

Variation of export gas pressure before modifications (Fig 1) and after modification (fig 2)

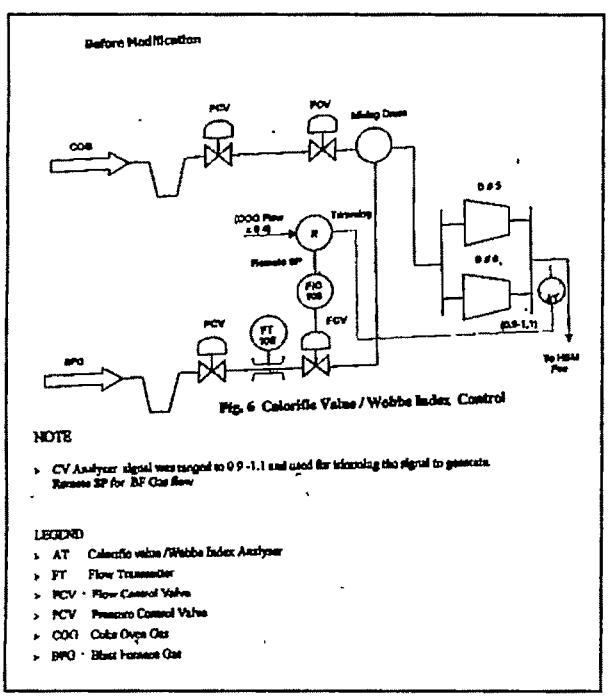

Fig. 6 Calorific Value / Webbe Index Control

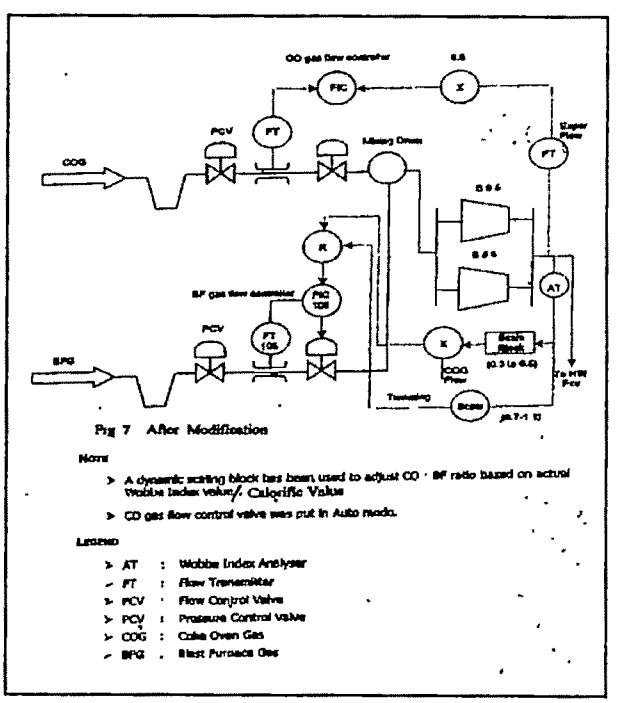
COG
PCV
FT
BFG
Scale Block
Tweaking
Note
A dynamic scaling block has been used to adjust CO : BF ratio based on actual Webbe Index value/ Calorific Value
CO gas flow control valve was put in Auto mode.
Legend
AT : Webbe Index Analyser
FT : Flow Transmitter
PCV : Flow Control Valve
PCV : Pressure Control Valve
COG : Coke Oven Gas
BFG : Blast Furnace Gas
Fig 7 After Modification

Calorific value / Webbe index control system before modification (fig 3) and after modification (fig 4)

Implementation Of A Suitable Process Controller Along With A Contamination Detector In A Novel 'See-Saw' Bioreactor For Achieving Very High Yield From Animal Cell Line Culture

Goutam Saha, Partha Sarathi Pal, Alok Barua and Satyabroto Sinha
Dept. of Electrical Engineering
Indian Institute of Technology Kharagpur 721302, India
E-mail: alok@ee.iitkgp.ernet.in

Abstract:

A novel bioreactor has been developed and fabricated in the laboratory, which is claimed better bioreactor than the conventional ones. It is a small volume bioreactor. Emphasis is on development a suitable control strategy so that more enzymes / metabolites, can be produced from this small volume bioreactor. A contamination detection algorithm has been developed which monitors the process and takes appropriate measures in case of contamination detection.

Keywords: *Biorector, See-Saw bioreactor, Contamination, Time Delay Control (TDC), Observer, Genetic Algorithm, Artificial Neural Network.*

INTRODUCTION

Now a day, to cope with various diseases- new or old - in terms of vaccination and improved variety of drugs production (for Cancer or AIDS), we have to go for animal cell line culture. The main difficulty of animal cell line culture is that the cell membranes are very thin and weak. For example, in case of Continuous Stirred Tank Reactor (CSTR) a substantial amount of animal cells will be destroyed by the impinging fan blades and the resultant shear force generated in the bioreactor. Many cells may also get destroyed because of entrapment in the air bubbles meant for aeration in air-bubble type reactor. In this bioreactor the above mentioned difficulties are absent. This novel bioreactor is named `See-Saw' bioreactor. The name has been derived from its underlying principle of operation. The working volume of the prototype bioreactor is small. But we cannot underestimate its importance, as the cost of the enzymes etc. produced from this animal cell line culture is very high. Moreover, the cost of the substrate used is also very high. It is not profitable to use commercial size bioreactors for the purpose. Rather, emphasis should be given to develop a suitable control strategy so that more enzymes/metabolites, can be produced from these small volume bioreactors. These are objectives, which are sought to be fulfilled in this investigation.

Designing a suitable bioprocess controller is to achieve maximization of the produce[14]. This is not easy because a bioprocess, in general, is a time-varying parameter, non-linear, undermodelled multivariable system plagued by uncertainties. The repeatability of a bioprocess is poor. The normal strategy for designing a controller for such system involves linearizing the non-linear process around a steady state operating point and then applying standard linear control theory to the small signal model. This type of controller may produce good result if the process is confined to the neighborhood of the operating point. But for the highly nonlinear process like bioprocess where the operating point is continually changing, this type of linearised controller produces poor result. They generally fail in scale-up conditions. For example, multiloop control (Seborg et al., 1959), adaptive control (Astrom and Wittenmark, 1988) do not produce expected results. The same is also true for fuzzy and neuro-fuzzy controllers. Though fuzzy controllers do not use standard process models, still the results are not encouraging because of the poor reproducibility of bioprocesses.

Efforts have been made to derive an expression for mass-transfer co-efficient of gaseous oxygen to liquid medium of the bioreactor with certain assumptions. Experimentations has been carried out to validate the expression[1].

The basic generalized mathematical model (unstructured and unsegregated), to describe the kinetics of fermentation has been formulated considering double substrate limitation. A controller has been designed which takes care of the non-linearities, non-stationarities of the parameters and the undermodelled dynamics of the bioprocess. The controller forces the states to track respective pre-defined optimal time trajectories by generating suitable control action. The optimal time trajectories are generated using genetic algorithms. A control strategy, namely time delay control (TDC), has been applied [2].

Here at every instant, depending on the input data, the control algorithm calculates the speed of various feed pumps and time period of oscillation of bioreactor fluid as control action.

Besides, environmental control for temperature and pH value of the bioreactor fluid, are done using separate controllers

Since the dissolved oxygen concentration is the only measurable variable, a suitable observer has been designed to estimate cell mass concentration, substrate concentration and product concentration. The observer acts as 'software sensor'.

Separately an algorithm has been developed for contamination detection. This has been achieved using an artificial neural network (ANN)[3]. This will help in saving manpower and costly material.

PROCESS MODEL

The generalized unstructured unsegregated model [4,5] obtained from mass balance equations in liquid condition is of the following form:

$$\frac{d\mathbf{m}(t)}{d(t)} = q_0(t)m_0(t) + q_4(t)m_4(t) - q_1(t)m_1(t)$$

where $g|\mathbf{m}(t)|$ = material accumulation and consumption rate that describe biological activities,

$q_0(t) = \frac{F_0(t)}{v(t)}$ = normalized inflow to the bioreactor,

$q_1(t) = \frac{F_1(t)}{v(t)}$ = normalized outflow from the bioreactor,

$q_4(t) = \frac{F_4(t)}{v(t)}$ = normalized recycle flow to the bioreactor

and

$\mathbf{m}(t)$ = bioprocess variables, dissolved oxygen content.

$v(t)$ = working volume of the bioreactor,

The unstructured and unsegregated model with double substrate limitation [8,12,13] is,

$$\frac{dx_1(t)}{dt} = \frac{\mu_m x_1(t)x_2(t)x_3(t)}{(K_s + x_2(t))(K_c + x_3(t))} - K_d x_1(t) + \frac{F_0(t)}{x_5(t)}X_{in} - \frac{F_1(t)}{x_5(t)}x_1(t)$$

$$\frac{dx_2(t)}{dt} = -\frac{\mu_m x_1(t)x_2(t)x_3(t)}{Y(K_s + x_2(t))(K_c + x_3(t))} - m_s x_1(t) - \frac{\alpha x_1(t)}{Y_p} - \frac{\beta\mu_m x_1(t)x_2(t)x_3(t)}{Y_p(K_s + x_2(t))(K_c + x_3(t))} + \frac{F_0(t)}{x_5(t)}S_{in} - \frac{F_1(t)}{x_5(t)}x_2(t)$$

$$\frac{dx_3(t)}{dt} = -\frac{\mu_m x_1(t)x_2(t)x_3(t)}{Y_0(K_s + x_2(t))(K_c + x_3(t))} - m_{s0}x_1(t) - \frac{\alpha x_1(t)}{Y_{p0}} - \frac{\beta\mu_m x_1(t)x_2(t)x_3(t)}{Y_{p0}(K_s + x_2(t))(K_c + x_3(t))} + \frac{F_0(t)}{x_5(t)}O_{in} - \frac{F_1(t)}{x_5(t)}x_3(t) + K_L a(O_2^* - x_3(t))$$

$$\frac{dx_4(t)}{dt} = \alpha x_1 + \frac{\beta\mu_m x_1(t)x_2(t)x_3(t)}{(K_s + x_2(t))(K_c + x_3(t))} + \frac{F_0(t)}{x_5(t)}P_{in} - \frac{F_1(t)}{x_5(t)}x_4(t)$$

$$\frac{dx_5(t)}{dt} = F_0(t) - F_1(t),$$

where

$x_1(t)$, $x_2(t)$, $x_3(t)$,$x_4(t)$ and $x_5(t)$= Cell mass, substrate, dissolved oxygen, product concentration respectively and volume of the bioreactor.

F_0 = Liquid feed – in rate, F_1 = Withdrawal rate

K_L = Oxygen mass transfer cofficient,

a = Surface area through which mass transfer of oxygen is taking place.

X_{in}, S_{in}, O_{in}, P_{in} = Influent cellmass, substrate, oxygen and product concentrations.

α & β are constants,

K_s, K_c = Saturation constants,

K_d = Biomass decay rate,

m_s, m_{s0} = Maintainence coefficient w.r.t. carbon and oxygen source for cellmass,

Y, Y_0 = Yield coefficient w.r.t. carbon and oxygen source for cellmass growth,

Y_p, Y_{p0} = Yield coefficient w.r.t. carbon and oxygen source for product formation,

O_2^* = Saturation value of oxygen in liquid medium of interest.

The bioreactor model equation can be written in the following matrix form:

$$\begin{bmatrix}\dot{x}_1(t)\\ \dot{x}_2(t)\\ \dot{x}_3(t)\\ \dot{x}_4(t)\end{bmatrix}=\begin{bmatrix}\mu\\ -(\frac{\mu}{Y}+\frac{\beta_\mu}{Y_p})\\ -(\frac{\mu}{Y_v}+\frac{\beta_\mu}{Y_{pv}})\\ \beta\mu\end{bmatrix}x_1(t)x_2(t)x_3(t)$$

$$+\begin{bmatrix}-k_d & 0\ 0\ 0\\ -(m_s+\frac{\alpha}{Y_p}) & 0\ 0\ 0\\ -(m_{s0}+\frac{\alpha}{Y_{p0}}) & 0\ 0\ 0\\ \alpha & 0\ 0\ 0\end{bmatrix}\begin{bmatrix}x_1(t)\\ x_2(t)\\ x_3(t)\\ x_4(t)\end{bmatrix}$$

$$+\begin{bmatrix}\frac{x_{in}}{x_5(t)} & -\frac{x_1(t)}{x_5(t)} & \frac{x_{11}}{x_5(t)} & 0\\ \frac{s_{in}}{x_5(t)} & -\frac{x_2(t)}{x_5(t)} & \frac{x_{12}}{x_5(t)} & 0\\ \frac{o_{in}}{x_5(t)} & -\frac{x_3(t)}{x_5(t)} & \frac{x_{13}}{x_5(t)} & (O_{sat}-x_3(t))\\ \frac{p_{in}}{x_5(t)} & -\frac{x_4(t)}{x_5(t)} & \frac{x_{14}}{x_5(t)} & 0\end{bmatrix}\begin{bmatrix}F_0(t)\\ F_1(t)\\ F_4(t)\\ K_La\end{bmatrix}$$

$$\dot{x}_5(t)=F_0(t)-F_1(t)$$

$$y(t)=c^T x(t)$$

where $c^T=[0\ \ 0\ \ 1\ \ 0]$,

$0\le x_1(t)\le 60 \qquad 0\le F_0(t)\le 1.6$

$0\le x_2(t)\le 100 \qquad 0\le F_1(t)\le 1.6$

$0\le x_3(t)\le 0.01 \qquad 0\le F_4(t)\le 1.6$

$0\le x_4(t)\le 0.15 \qquad 0\le K_{La}(t)\le 0.0168$

and volume of the bioreactor $x_5(t)$ varies within 10 to 15 litres.

μ is represented by MONOD's equation as follows:

$$\mu=\frac{\mu_m x_1(t)x_2(t)x_3(t)}{(k_s+x_2(t))(k_c+x_3(t))}$$

OPTIMIZATION USING GENETIC ALGORITHM

The aim is to find optimum time-profiles of F_0, F_1, F_4 and K_La under a particular operating mode [6,7] such that the yield, $(x_4(t))$, is maximized. Optimised time profiles of cell mass Conc. $x_1(t)$, substrate Conc. $x_2(t)$, Oxygen Conc. $x_3(t)$ and product Conc. $x_4(t)$ are obtained. These will be used as reference profiles for the purpose of control.

The optimisation algorithms are revisited in the form of flow charts in Figs 1 and 2 respectively.

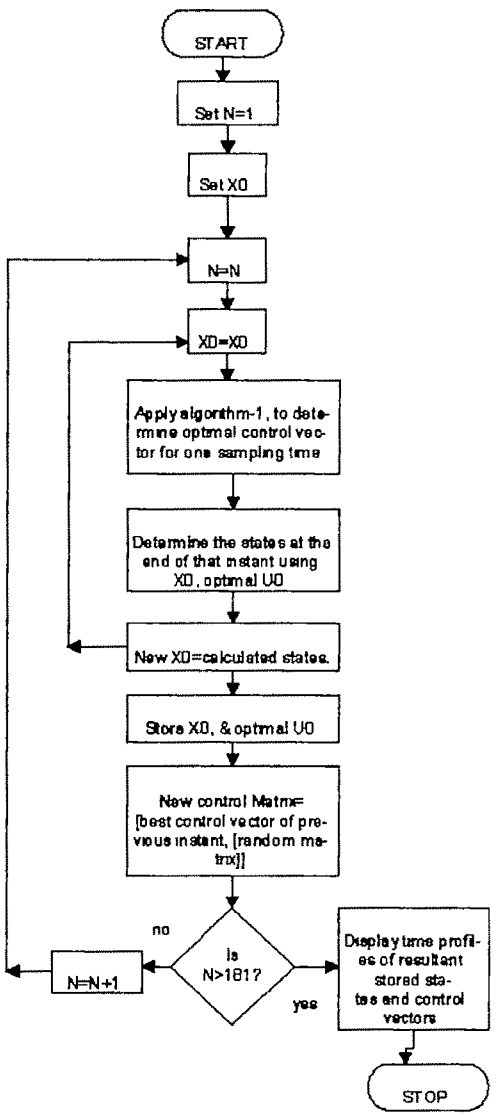
START
Set N=1
Set X0
N=N
X0=X0
Apply algorithm-1, to determine optimal control vector for one sampling time
Determine the states at the end of that instant using X0, optimal U0
New X0=calculated states.
Store X0, & optmal U0
New control Matrix= [best control vector of previous instant, [random matrix]]
Is N>181?
no
yes
N=N+1
Display time profiles of resultant stored states and control vectors
STOP

Fig.1: Flowchart of Algorithm2, the optimization algorithm.

TIME DELAY CONTROLLER AND OBSERVER

Time-delay control is a recent development[8,9]. It depends on estimation of a function representing the effect of uncertainties. This is done by assuming that the value of the

function representing the effect of uncertainties remains almost the same over an interval. The control law is derived assuming that the plant states follow certain prefixed reference trajectory. The control objective is to force the error (difference between the plant and model state vectors) to zero[2].

Adding the uncertainty factor, the plant model can be represented as below

$$\dot{\mathbf{x}}(t) = \mathbf{f}(\mathbf{x}, t) + H\mathbf{x}(t) + B(\mathbf{x}, t)\mathbf{u}(t) + \mathbf{h}(\mathbf{x}, t) + \mathbf{d}(t)$$

where

$\mathbf{h}(\mathbf{x}, t)$ is a four element non-linear vector representing unmodelled part of the plant dynamics and

$\mathbf{d}(t)$ is an unknown disturbance vector of dimension 4.

In order to estimate the effect of the term $\mathbf{h}(\mathbf{x}, t) + \mathbf{d}(t)$, it is considered in TDC that the value of the function $\mathbf{h}(\mathbf{x}, t) + \mathbf{d}(t)$ at the present time (t) is very close to that at time (t-L) in the past for a small time delay L, that is,

$$\mathbf{h}(\mathbf{x}, t) + \mathbf{d}(t) \cong \mathbf{h}(\mathbf{x}, (t\text{-}L)) + \mathbf{d}(t\text{-}L)$$

So, $\mathbf{h}(\mathbf{x}, t) + \mathbf{d}(t)$ is estimated by

$$\mathbf{h}(\mathbf{x}, t) + \mathbf{d}(t) \cong \dot{\mathbf{x}}(t-L) - \mathbf{f}(\mathbf{x}, t\text{-}L) - H\mathbf{x}(t\text{-}L) - B(\mathbf{x}, t\text{-}L)\mathbf{u}(t\text{-}L)$$

The TDC control law is derived as follows:

$$\mathbf{u}(t) = B^{+}(\mathbf{x}, t)[-\mathbf{f}(\mathbf{x}, t) - H\mathbf{x}(t) - \dot{\mathbf{x}}(t-L) + \mathbf{f}(\mathbf{x}, t-L) + H\mathbf{x}(t-L) + B(\mathbf{x}, t-L)\mathbf{u}(t-L) + A_m\mathbf{x}(t) + B_m\mathbf{r}(t)]$$

Since, TDC forces the plant dynamics to follow the reference model, which is essentially a LTI, model, a strategy for the observer design is to use the LTI reference model instead of the actual plant model. A Luenberger full order observer has been designed.

$$\dot{\mathbf{z}}(t) = A_m\mathbf{z}(t) + B_m\mathbf{r}(t) + \mathbf{f}\mathbf{c}^{T}(\mathbf{z}(t) - \mathbf{x}(t))$$

or, $\dot{\mathbf{z}}(t) = \dot{\mathbf{x}}_d(t) + A_m(\mathbf{z}(t) - \mathbf{x}(t)) + \mathbf{f}\mathbf{c}^{T}(\mathbf{z}(t) - \mathbf{x}(t))$

TDC control law finally takes the form:

$$\mathbf{u}(t) = B^{+}(\mathbf{z}, t)[-\mathbf{f}(\mathbf{z}, t) - H\mathbf{z}(t) - \mathbf{z}(t-L) + \mathbf{f}(\mathbf{z}, t-L) + H\mathbf{z}(t-L) + B(\mathbf{z}, t-L)\mathbf{u}(t-L) + A_m\mathbf{z}(t) + B_m\mathbf{r}(t)]$$

CONTAMINATION DETECTION ALGORITHM

The contamination detection algorithm has been developed using ANN [3,10]. It was developed using the fact that if the deviation is ±25% from the normal value for three consecutive instants, the process will be declared contaminated and the process will be stopped and regeneration may be started.

OXYGEN TRANSFER MODEL IN 'SEE-SAW' BIOREACTOR

Amount of oxygen deposited per unit volume per cycle in the bioreactor is given by *Gt/v* where *v* is the working volume of the bioreactor [1].

Average transfer rate (in gm/sec) is given by [1,11]:

$$Gt_a = \frac{Gt}{2t_c}$$

$$= \frac{8\sqrt{2}}{3}\pi r(Cai - Ca0)\sqrt{\frac{D_{ab}}{\pi t_c}u_s\, t_c} + 2\sqrt{2}\,\pi r^2(Cai - Ca0)\sqrt{\frac{D_{ab}}{\pi t_c}}$$

EXPERIMENTATION

Experimentation was done after completion of instrumentation part of the bioreactor. The result found was satisfactory.

The bioreactor looks like following:

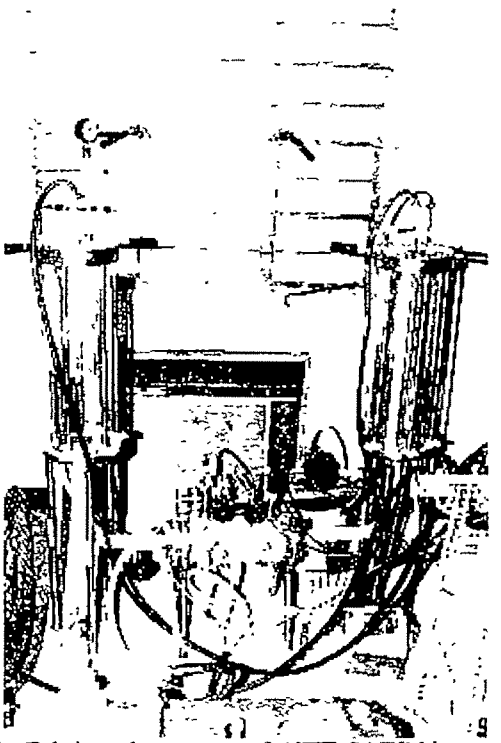

Fig. 3: Fabricated prototype of 'SEE-SAW' bioreactor

The instrumentation part was done as per following block diagram.

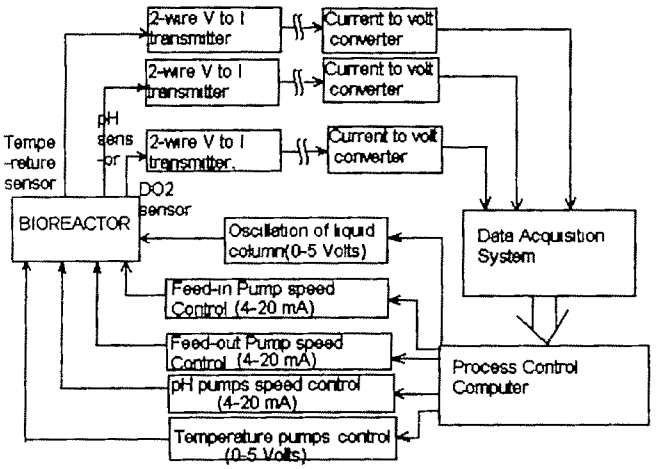
2-wire V to I transmitter
Current to volt converter
2-wire V to I transmitter
Current to volt converter
pH sens or
2-wire V to I transmitter
Current to volt converter
Tempe -reture sensor
DO2 sensor
BIOREACTOR
Oscillation of liquid column(0-5 Volts)
Data Acquisition System
Feed-in Pump speed Control (4-20 mA)
Feed-out Pump speed Control (4-20 mA)
pH pumps speed control (4-20 mA)
Process Control Computer
Temperature pumps control (0-5 Volts)

Fig.4: Block diagram of Instrumentation scheme

The experimentation was done with aerobic culture of yeast in this bioreactor. The product was to get maximum cell mass from the culture. The results obtained were highly satisfactory.

This experimentation could be extrapolated for other type of culture like different types of antibiotic production, animal cell line culture. The lab set up is now being upgraded to carry out further investigation in these areas.

BIBLIOGRAPHY

1. Goutam Saha, A.Barua, Satyabroto Sinha, B.C.Bhattacharya and S.Roy, 'Modeling of the Oxygen transfer Characteristics of a 'See-Saw' bioreactor', Chemical Engineering & Technology, Vol.-24, No.-1, pp 97 to 101, January 2001.
2. Kamal Youcef-Toumi, Osamu Ito, 'A time delay controller for systems with unknown dynamics', *ASME*, vol. 112/133, pp. 133-142, March 1990.
3. Ujjal Kr. Bhowmik, Goutam Saha, A.Barua and Satyabroto Sinha, 'On-line detection of contamination in a bioprocess using Artificial Neural Network', Chemical Engineering & Technology, Vol.-23, No.-6, pp 543 to 549, June 2000.
4. A.G.Fredrickson, R.D.Magee, H.M.Tsuchiya 'Mathematical models for fermentation processes', *Adv. Appl. Microbiol.*, vol. 13, pp. 419, 1979.
5. F.M.Williams,'A model for cell growth dynamics', *J. Theor. Biol.*, vol. 15, pp. 190, 1967.
6. Hiromu Ohno and Eiji Nakanishi, 'Optimum operating mode for a class of fermentation', *Biotechnology and Bioengineering*, vol.20, pp.625-636, 1978.
7. David E. Goldberg, 'Genetic Algorithms in Search, Optimization, and Machine Learning,'[bk], Addison-Wesley Publishing Company, New York, 1989.
8. Denis Dochain, 'On-line parameter estimation, adaptive state estimation and adaptive control of fermentation process' Ph.D. Thesis, Universite Catholique de Louvain, Belgium, 1986.
9. G. Bastin and D. Dochain, 'On line Estimation and Adaptive Control of Bioreactors', [bk], Elsevier Science, Amsterdam, 1990.
10. T.Chattaway, G.N.Stephanopoulos,'An adaptive state estimator for detecting contaminants in bioreactors', *Biotechnology and Bioengineering*, vol. 34, pp. 647, 1989.
11. Bird R.O., Stewart W.E. and Lightfoot E.N., 'Transport Phenomena' [bk], John Wiley and Sons, New York, 1960.
12. F.G. Bader, 'Analysis of double substrate limited growth', *Biotechtechnology and Bioengineering*, vol.20, pp.183-202, 1978.
13. C.G.Sinclair and D.N.Ryder,'Models for continuous culture of micro-organisms under both carbon and oxygen limiting conditions', *Biotechnology and Bioengineering*, vol. 17, pp. 375, 1975.
14. Reiner Luttmann, Gerhard Bitzer and Jens Hartkopf, 'Development of Control strategies for high cell density cultivations', *Mathematics and Computers in Simulation*, vol. 87, pp.153-164, 1994.

Fig. Flowchart of Algorithm1

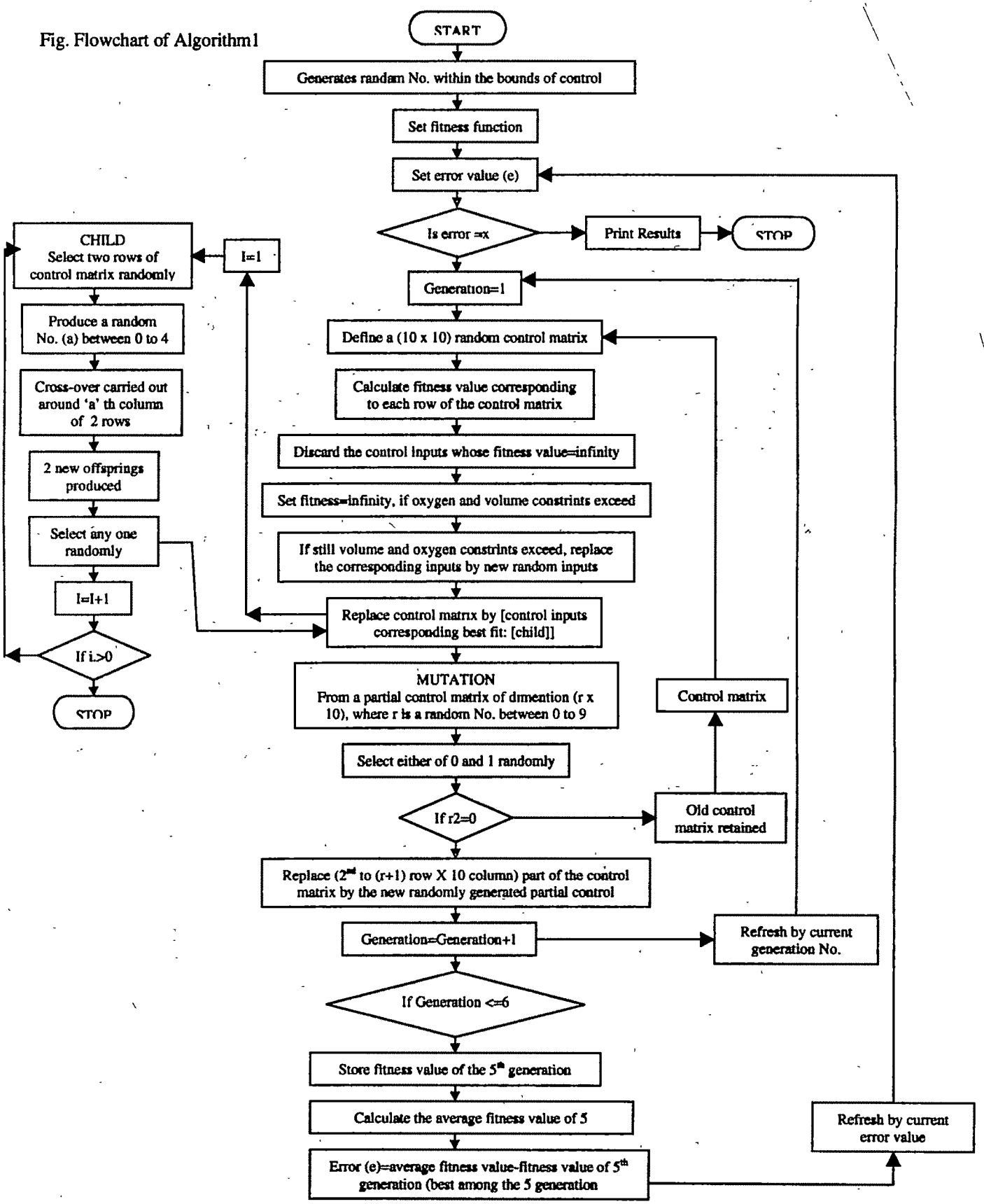
START
Generates randam No. within the bounds of control
Set fitness function
Set error value (e)
Is error =x
Print Results
STOP
Generation=1
Define a (10 x 10) random control matrix
Calculate fitness value corresponding to each row of the control matrix
Discard the control inputs whose fitness value=infinity
Set fitness=infinity, if oxygen and volume constrints exceed
If still volume and oxygen constrints exceed, replace the corresponding inputs by new random inputs
Replace control matrix by [control inputs corresponding best fit: [child]]
MUTATION
From a partial control matrix of dimention (r x 10), where r is a random No. between 0 to 9
Select either of 0 and 1 randomly
If r2=0
Old control matrix retained
Control matrix
Replace (2nd to (r+1) row X 10 column) part of the control matrix by the new randomly generated partial control
Generation=Generation+1
Refresh by current generation No.
If Generation <=6
Store fitness value of the 5th generation
Calculate the average fitness value of 5
Error (e)=average fitness value-fitness value of 5th generation (best among the 5 generation
Refresh by current error value
CHILD
Select two rows of control matrix randomly
I=1
Produce a random No. (a) between 0 to 4
Cross-over carried out around 'a' th column of 2 rows
2 new offsprings produced
Select any one randomly
I=I+1
If i>0
STOP

Design of Convex Controller for Insulin Delivery System with Optimization of Parameter λ

A. Sutradhar, G. C. Ray and A. S. Chaudhuri
Department of Electrical Engineering,
Bengal Engineering College (a Deemed University)
B.Garden, Howrah-711103, INDIA
asee1@rediffmail.com, aschaudhuri@hotmail.com

Abstract

The instrumentation and closed loop control of blood glucose concentration in diabetic patients have become very much important issue for the present day biomedical engineers. The present work describes an optimally convex controller for an automated insulin delivery system. The multivariable model of the micro-insulin dispenser system has been analyzed in algebraic framework. A method for selecting an optimal value of the parameter λ from a family of convex controllers has been presented. The controller thus designed has shown optimal performance in different patient conditions and the stability of the closed-loop system has been tested by using Kharitonov's criterion.

Key-words: Algebraic Framework, Insulin Dispenser, Convex Controller, Optimization, Kharitonov's Criterion.

INTRODUCTION

The fast life style pattern of patient and day-to-day advancement in medical instrumentation have forced the scientists and engineers to develop automated drug delivery systems in most long-term treatments. Diabetes Mellitus is one such disease where the drug (insulin) is to be administered frequently at different adjustable doses throughout the day for a very long period of time. Despite the varying demands of food, fasting and exercise, the Blood Glucose (BG) levels are closely regulated in the range of 3.5-8.0mmol/litre (63-144 *mg/dl*) to maintain *normo-glycaemia* in human body. In normal subjects, a sharp increase in insulin occurs after meals to counter the carbohydrate ingested. This is superimposed on a constant background of secretion. Insulin is to be injected externally in a patient suffering from type-1 or type-2 diabetes and has been in *ketoacidosis* (a state of uncontrolled catabolism associated with insulin deficiency) to counteract the glucose [1], [2].

The State-of-the-Art in closed-loop drug delivery system for controlling BG level is an automated microcomputer based insulin dispensing system described in several literatures [3], [4], [14], [15]. In [3], Cochin *et al* describe a micro-insulin dispenser system, which samples the BG level, patient conditions and automatically administers the prescribed dosage of insulin. The dosage of insulin is adjusted to fit the patient's lifestyle and needs by the experienced physicians from knowledge base or patient models [3], [11]-[15]. Concentration on the problem of establishing a normal operating state and optimum setting of the controller for insulin dispenser system is important. Cochin *et al* suggest a microprocessor based adaptive controller that switches between two control algorithms depending on the patient's active or resting conditions sensed by an accelerometer. An optimal 3-term controller has been suggested by the present author [17], [21] which operates in all possible patient conditions and thus eliminates the sensor to measure patient conditions. In their paper [22], the present authors discuss a method of designing a family of stable convex controllers for the insulin dispenser system for a restricted set of design specifications. In the present paper, the authors try to develop a method for finding an optimal setting of the parameter value (λ) for the convex controllers. Thus a single convex controller was sorted out to yield optimum time domain and frequency domain performances in all possible patient conditions. For this, the device was analyzed in algebraic framework and minimization of a Performance Index (PI), like integral squared error (ISE) has been applied on the design of convex controller. The controller thus realized has been tested for robust stability using Kharitonov's theorem [18], [19].

THE ALGEBRAIC FRAMEWORK

The micro-insulin dispenser, as shown in fig.1, operates on variable pumping rate principle. The basic components of this device are the storage capsule, the

micro pump, the accumulator, the pump return valve and necessary electronic control. Other sensing and controlling blocks are a chromatograph, an accelerometer, a pulse monitor and a microprocessor. The pump, return valves etc are all micro-systems controlled by electrostatic methods.

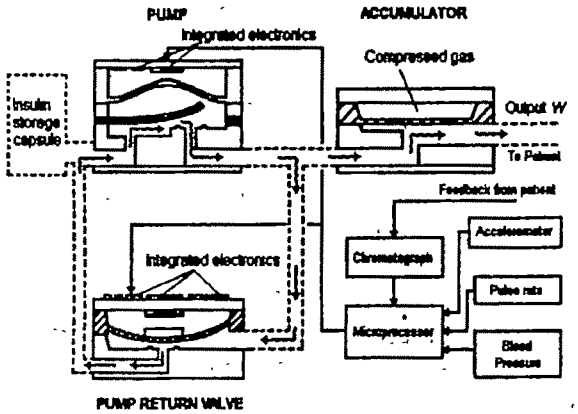

Fig. 1. Schematic Diagram of the Device

The block diagram of the micro-insulin dispenser system with reference insulin input (w_{ref}) and regulated output (y_p), is shown in fig. 2. The valve is non-linear both voltage-wise and fluid restriction-wise. The non-linearities in the system have been represented by a lumped step disturbance input in Pressure (P_d).

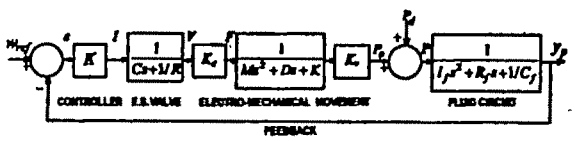

Fig. 2. The SISO Block Diagram of the Device.

Following the Desoer-Chan's model [16] with actuator and sensor noise signals, the closed-loop system in algebraic framework, with a controller of one degree of freedom, becomes as shown in Fig. 3. The

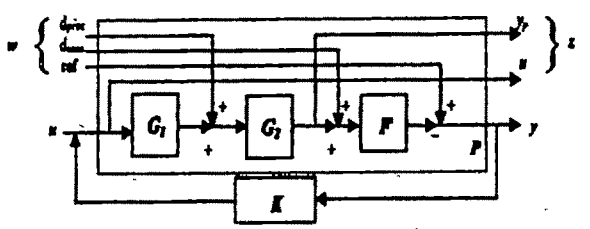

Fig. 3. The System in Algebraic Framework.

exogenous and actuator inputs, regulated and sensed outputs have been considered in separate groups to treat the system as a multivariable one. The plant can be described by the set of transfer functions from each of its *exogenous inputs* w or *actuator inputs* u to each of its *regulated outputs* z or *sensed outputs* y. The exogenous inputs w are process disturbance (w_1), sensor disturbance (w_2) and the reference input (w_3), actuator input is u and the regulated and sensed outputs are z $\{z_1, z_2\}$ and y. Closed loop transfer matrix from w to z is given by,

$$H = P_{zw} + P_{zu}K(I-P_{yu}K)^{-1}P_{yw} \qquad .....(1)$$

The closed-loop transfer matrix from the framework is

$$H = \begin{bmatrix} \frac{G_2}{1+G_1G_2FK} & \frac{-G_1G_2FK}{1+G_1G_2FK} & \frac{G_1G_2K}{1+G_1G_2FK} \\ \frac{-G_2FK}{1+G_1G_2FK} & \frac{-FK}{1+G_1G_2FK} & \frac{K}{1+G_1G_2FK} \end{bmatrix} \qquad .....(2)$$

where,

$G_1(s) = \dfrac{0.125}{s^3+12.5s^2+72.67s+33.335}$,

$G_2(s) = \dfrac{32}{s^2+24s+256}$ and $F(s) = 1$; have been calculated with the device parameters obtained from [3] as given below.

R =200MΩ C = 0.01μF M = 1e-6 kg D=12e-6 N.s/m
I_f = 0.03125 R_f = 0.75 C_f = 0.125 K_a = 1e-7
K = 66.67e-6 N/m K_v = 1.25e-8
W_{ref} = U_1 = 5e-5 step and
Pressure disturbance P_d = U_d = 0.3887 step

PROBLEM FORMULATION

For automated insulin administering device, the design specification demand for the controller varies widely [3] with patient conditions as per specifications given below.

$|\varepsilon_{ss}| \le 0.01$ PM ≥ 45°, GM ≥ 3dB, $\zeta \ge 0.5$
Patient resting:Overshoot ≤ 7.5%, Settling time,T_s≤60 s.
Patient active :Overshoot ≤ 16%, Settling time,T_s≤ 4.5s.

Hence the fundamental problem is to find a control law i.e. closed loop transfer matrix H that meets the design specification or determine that none exists.

The convex combination of a finite set of points x_1, x_2, ... x_n in n-dimensional or n-component Euclidean space vector $\mathcal{R}^n$ is a point given by $x = \lambda_1x_1+\lambda_2x_2+..\lambda_nx_n$, where $\sum\lambda_i = \lambda_1+\lambda_2+..\lambda_n = 1$, for i= 1, 2, ..,n and λ_i's real and ≥ 0 [5]-[8]. The design specifications can be expressed as sets. Let $\mathcal{H}$ be a vector space denoted by the set of all $n_{reg} \times n_{exog}$ transfer matrices, where n_{reg} and n_{exog} are the number of regulated outputs (z) and exogenous inputs (w) respectively. Each design specification $\mathcal{D}_i$ can be associated with a set of allowable transfer matrices $\mathcal{H}_i \subseteq \mathcal{H}$ [20]. If $\mathcal{H}_1$, $\mathcal{H}_2$... etc. correspond to specifications $\mathcal{D}_1$, $\mathcal{D}_2$ .... etc. respectively and $\mathcal{H}_1 \subseteq \mathcal{H}_2$, then specification $\mathcal{D}_1$ is stronger (tighter) than specification $\mathcal{D}_2$ and the set of transfer matrices satisfying all such design specifications is given by

$$\mathcal{H}_{spec} = \mathcal{H}_1 \cap \mathcal{H}_2 \cap ..... \qquad ....(3)$$

Most of the time domain and frequency domain specifications like overshoot, settling time, gain margin and phase margin etc. are closed-loop convex [20]. If two controllers K_1 and K_2 are found both of which stabilize the plant, then the convex combination of two closed-loop transfer matrices H_1, H_2 in 2-dimensional Euclidean space ($\mathscr{R}^2$) is a point $H_\lambda = \lambda H_1 + (1-\lambda)H_2$ for $0 \le \lambda \le 1$ and $\{H_1, H_2, H_\lambda\} \in \mathscr{H}$. We can obtain an infinite number of such controllers by varying only a single parameter λ which will stabilize the plant. For the present system, internal stability, time-domain and frequency domain design specifications along with optimization of a performance index (PI) [5], [17] have been considered. The convex controller is first obtained from the specifications following the equation (3). The optimal value of λ for the convex controller has been found out by imposing a stronger specification and minimizing the time domain PI like ISE.

CONTROLLER DESIGN

The closed loop stable system with a PI-type controller to produce 7.5% maximum overshoot, 4.5s settling time and frequency domain specs as mentioned in previous works [3] has been considered here.

According to Desoer's definition[16], the closed-loop system is internally stable if, all the closed-loop transfer matrices including those from disturbances to y_p and u are all stable. Thus internal stability is a closed-loop *convex* constraint. This prohibits a very small (bounded) actuator or sensor noise from producing large (unbounded) effect on u or y and hence z. Assumption is that P and K have no unstable hidden modes, i.e. mode uncontrollable from u or unobservable from y. A transfer function is stable and proper if it has number of zeros less than or equal to number of poles, and each pole has negative real part. A transfer matrix is stable if all of its elements are stable and proper transfer functions [16], [20].

First of all, a set of stable transfer matrices for some stabilizing controller K in the framework may be considered such that,

$$\mathscr{H}_{stab} = \{H \in \mathscr{H} | H = P_{zw} + P_{zu}K(I - P_{yu}K)^{-1}P_{yw}, \text{ for some } K \text{ that stabilizes } P\} \quad \ldots..(4)$$

$\mathscr{H}_{stab}$ is the set of possible closed-loop transfer matrices achieved with the controllers that stabilize the plant P. So the internal stability is a closed-loop *affine* and hence *convex* constraint. Design specifications thus must be closed loop convex i.e. the set of transfer matrices that satisfy it, is convex. Geometrically, it may be thought of a convex combination of two points on the line segment joined by the points [20]. If two controllers K_1 and K_2 both stabilize the plant P and yield closed-loop transfer matrices H_1 and H_2 respectively, then for each $\lambda \in \mathscr{R}$, there is some controller K_λ that also stabilizes P and yields convex combination of the closed-loop transfer matrices H_1 and H_2 as $H_\lambda = \lambda H_1 + (1-\lambda)H_2$ for $0 \le \lambda \le 1$. There are infinite number of such controllers, which will stabilize the system.

PERFORMANCE SPECIFICATIONS AS CONVEX CONSTRAINTS

Performance specifications can be considered as convex constraints. Primary purpose of a feedback system is to ensure that one of the regulated outputs, say z_i, be nearly tracking the command input say w_j. This is a tracking performance specification.

Let $s_{ij}(t)$ denote the unit step response from w_j to z_i. Some qualitative performance specifications on this step response may be defined. The time domain requirement satisfying both patient active and resting conditions are: maximum overshoot $\le$ 7.5% and settling time $\le$ 4.5s. So it is necessary that $s_{13}(t)$ settle exactly to the steady state value within the following limits as given in equation (5) and shown in Fig. 4.

$$s_{min}(t) \le s_{13}(t) \le s_{max}(t) \text{ for } t \ge 0 \quad \ldots.. (5)$$

The following sets of closed-loop transfer matrices define the time-domain specifications for the present problem within the constraints (5).

$$\mathscr{H}_{t1} = \{H \in \mathscr{H} | s_{13}(t) \le 1.075 \text{ or } s_{max}(t) \text{ for all } t \ge 0\} \ldots(6)$$

and,

$$\mathscr{H}_{t2} = \{H \in \mathscr{H} | s_{13}(t) \ge s_{min}(t) \text{ for all } t \ge 0\} \quad \ldots (7)$$

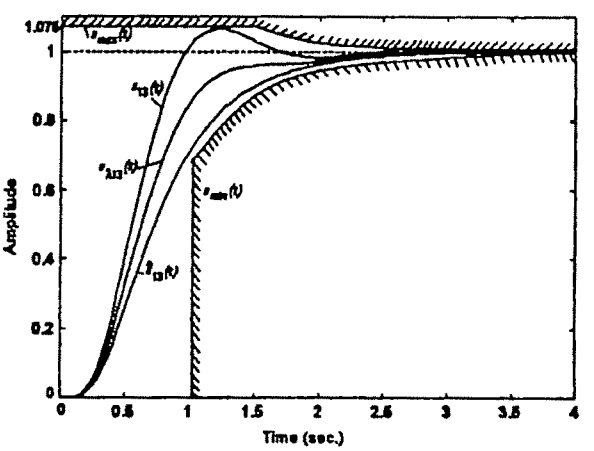

Fig. 4. The Step Responses with maximum and minimum constraints.

Now if H and $\hat{H}$ are transfer matrices corresponding to $s_{13}(t)$ and $\hat{s}_{13}(t)$ within the constraints (5) as shown in Fig. 4, then $s_{\lambda 13}(t) = \lambda s_{13}(t) + (1-\lambda)\hat{s}_{13}(t)$ for $0 \le \lambda \le 1$ also satisfies the constraint. Thus constraint (5) is closed-loop

convex. The same is true for tracking reference in frequency domain. Where the design specification is expressed by the sets of transfer matrices given in equations (8) and (9) and as shown in Fig. 5.

$\mathscr{H}_{t1}=\{H\in\mathscr{H}\mid |H_{13}(j\omega)| \le -3\text{dB for all } \omega\}$ ..... (8)

and

$\mathscr{H}_{t2}=\{H\in\mathscr{H}\mid \arg\{H_{13}(j\omega)\} \ge 45^{\circ} \text{ for all } \omega\}$ ..... (9)

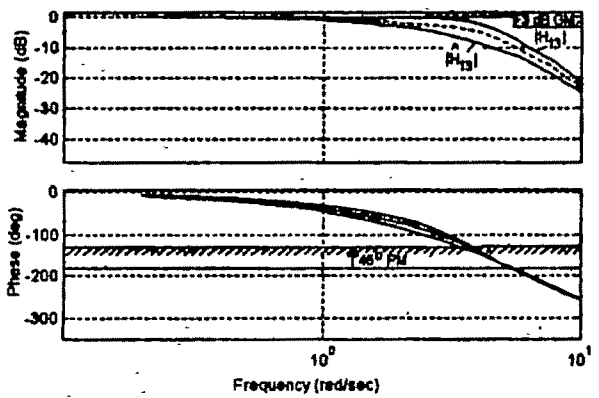

Fig. 5. Limits on Frequency Response

OPTIMIZATION OF PARAMETER λ

The convex controllers can be obtained from the intersection of all the sets of closed loop transfer matrices given by equations 4, 6, 7, 8 and 9. The set of transfer matrices satisfying all such specifications are given by

$$\mathscr{H}_{spec}=\mathscr{H}_{stab}\cap\mathscr{H}_{t1}\cap\mathscr{H}_{t2}\cap\mathscr{H}_{t1}\cap\mathscr{H}_{t2} \ldots.(10)$$

As the time domain performance specifications are closed loop convex and $\mathscr{H}_{spec}\subseteq\mathscr{H}$ the optimal value of the parameter λ will also produce a convex controller. The parameter λ is optimized by minimizing a time domain performance index, the ISE of $s_{13}(t)$ within the specification limits of $\mathscr{H}_{spec}$. Corresponding set of transfer matrices for optimal value of λ are represented as:

$$\mathscr{H}_{opt}=\{H\in\mathscr{H}_{spec}\mid \|e_{13}\| \text{ is minimum for all } t\ge 0\} \ldots.(11)$$

where, $\|e_{13}\|$, the norm of error of unit step response $s_{13}(t)$, represents the sum of square of the errors (SSE) for a discrete-time system which is same as the ISE in continuous time systems. The design of convex controller with an optimal value of λ is thus obtained from the specification $\mathscr{H}_{opt}$.

RESULTS AND DISCUSSION

In prototype system, two PI-type controllers with transfer functions $K_1(s)=(5000s + 2500)/s$ and $K_2(s) = (10000\ s + 8000)/s$ have been considered, both of which stabilize the plant P. The controller K_1 has critically damped response with high settling time and K_2 produces 30% overshoot and moderate settling time. The MATLAB instructions are used to compute all transfer matrices and their responses [8], [10]. The corresponding sets of $\mathscr{H}$ were verified to satisfy individual design specifications given in equations (4) through (10). The convex controller with different values of λ were tested for the specifications. The step responses of the transfer functions from w_3 to z_1 for the controllers K_1 and K_2 are shown in Fig. 6.

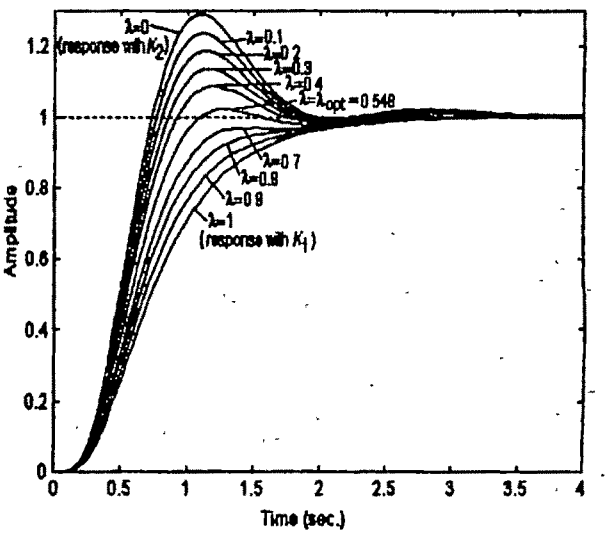

Fig. 6. Step responses of $H_{13}\in\mathscr{H}_{stab}$ for varying λ

The figure shows the responses with varying λ for convex controller in the full range of 0 and 1 on the basis of specification given in equation (4). The other specifications are stronger and hence subsets of $\mathscr{H}_{stab}$ and corresponding values of λ are also a subset of all real numbers between 0 and 1. The limiting values of λ are 0.4 and 0.9 for $s_{13}(t)$ and $\hat{s}_{13}(t)$ respectively in Fig. 4. The same range of λ also satisfies the frequency domain constraints given by equations (8) and (9).

Within the constraint $\mathscr{H}_{spec}$ the λ value is optimized according to equation (11). As the design specifications are made stronger and stronger the design value of λ converges to that given by equation (11). The MATLAB instruction `[y,t]= step(sys,[0,0.1,5])` has been used to get the sampled values of $s_{13}(t)$ at every 0.1 seconds interval up to 5 seconds. The discrete errors are stored in a column vector `e=[ones(51,1)]-y`. The norm $\|e\| = e^{T}e$ gives the sum of squared error (SSE). An algorithm written in MATLAB finds the optimal value of λ by minimizing the norm $\|e\|$ i.e. the SSE from the step response of H_{13}, within the overall constraints given by eqn. (10). This way search range of λ has been reduced. The optimal value λ_{opt} was found to be 0.548. Fig. 6 also shows the optimal performance step response of H_{13} for $\lambda=\lambda_{opt}$.

REALIZABLE CONTROLLER

The corresponding optimal convex controller $K_{\lambda\,opt}$ can be computed [20] as

$$K_{\lambda\,opt} = (A + \lambda_{opt}B)^{-1}(C + \lambda_{opt}D) \quad ....(12)$$

where, $A = I + K_2(I-P_{yu}K_2)^{-1}P_{yu}$,
$B = K_1(I - P_{yu}K_1)^{-1}P_{yu} - K_2(I - P_{yu}K_2)^{-1}P_{yu}$,
$C = K_2(I - P_{yu}K_2)^{-1}$,
$D = K_1(I - P_{yu}K_1)^{-1} - K_2(I - P_{yu}K_2)^{-1}$.

wherefrom, $K_{0.548}(s) =$

$$\frac{7260s^7 + 27e4s^6 + 47e4s^5 + 39e6s^4 + 16e7s^3 + 36e7s^2 + 79e6}{s^7 + 36.3s^6 + 626s^5 + 49e2s^4 + 19e3s^3 + 39e3s^2 + 22e3s}$$

The convex controller with $\lambda = \lambda_{opt}$ is a 7th order one, which is difficult to realize. The reduced order controller by eliminating four higher order states, the corresponding decomposition [9] of state matrices of the controller is The reduced order controller obtained by the MATLAB command `modred` [10], is a third order one having the transfer function

$$K_{0.548r}(s) = \frac{8490s^3 + 18356s^2 + 15470s + 4089}{s^3 + 2.038s^2 + 1.14s},$$

The step responses of all the closed loop transfer functions of H_{zw} with this realizable controller are shown in Fig. 7. It shows that all time domain specifications are satisfied.

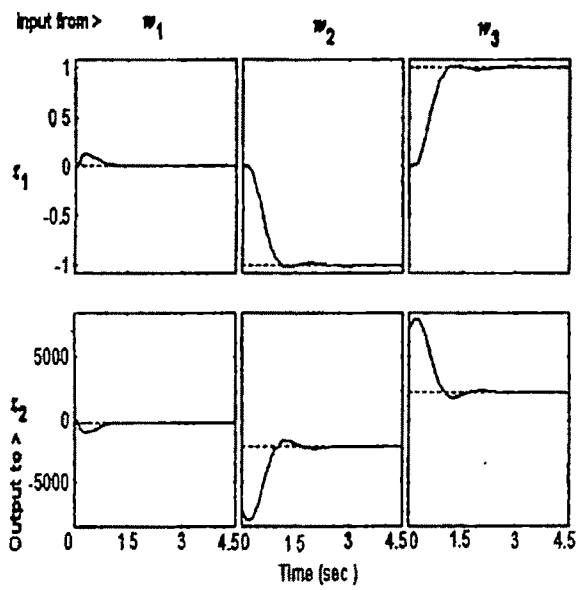

Fig.7. Step Responses of Transfer functions H_{zw}

Fig. 8. shows the Nyquist plot of H_{13}, which shows that the phase margin and gain margin are above the desired specification and hence satisfies frequency domain specifications also.

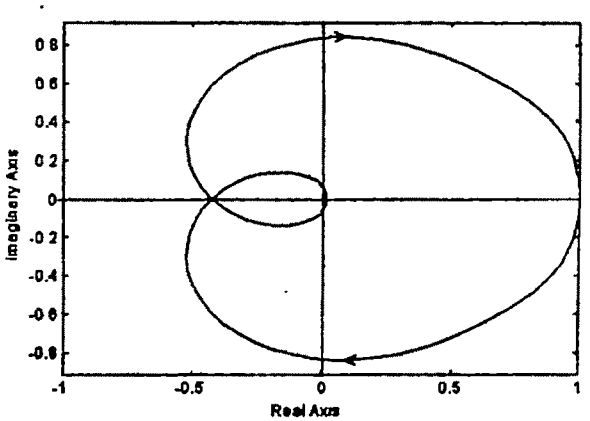

Fig. 8 Nyquist Plot of H_{13}.

STABILITY ANALYSIS

For stability analysis of the multivariable system, we use the Kharitonov's stability criteria. The characteristic equation for the closed loop system with reduced order controller for $\lambda_{opt} = 0.548$ is $s^8 + 38.54s^7 + 704.2s^6 + 6300s^5 + 30261s^4 + 87694s^3 + 112886s^2 + 71589s + 16355 = 0$, which is a monic polynomial. The four polynomials g_1, g_2, h_1 and h_2 [18], [19] giving $\pm 10\%$ perturbation to the coefficients of the characteristic polynomial (keeping the coefficient of the highest order term equal to one) are thus formed.

$g_1(s) = 14720 + 124175s^2 + 27349s^4 + 774.62s^6 + s^8$
$g_2(s) = 17991 + 101597s^2 + 33287s^4 + 633.78s^6 + s^8$
$h_1(s) = 64430s + 96463s^3 + 5670.0s^5 + 42.394s^7$
$h_2(s) = 78748s + 78925s^3 + 6930.0s^5 + 34.686s^7$

and the four Kharitonov's monic polynomials [18] $k_{kl}(s) := g_k(s) + h_l(s)$, for $k,l = 1,2$ are

$k_{11}(s) = 14720 + 64430s + 124175s^2 + 96463s^3 + 27235s^4 + 5670.0s^5 + 774.62s^6 + 42.394s^7 + s^8$
$k_{12}(s) = 14720 + 78748s + 124175s^2 + 78925s^3 + 27235s^4 + 6930.0s^5 + 774.62s^6 + 34.686s^7 + s^8$
$k_{21}(s) = 17991 + 64430s + 101597s^2 + 96463s^3 + 33287s^4 + 5670.0s^5 + 633.78s^6 + 42.394s^7 + s^8$
$k_{22}(s) = 17991 + 78748s + 101597s^2 + 78925s^3 + 33287s^4 + 6930.0s^5 + 633.78s^6 + 34.686s^7 + s^8$

As the first column of Routh's array of each of the four Kharitonov's polynomials above are all positive, they are Hurwitz [18],[19]. Thus it can be concluded that, the entire class of polynomials are Hurwitz. The controllers with λ_{opt} are also robust as Kharitonov's polynomials are all Hurwitz.

CONCLUSION

In the present work, the dynamics of micro-insulin dispenser device has been studied in algebraic framework. A linear convex controller has been designed with optimization of the parameter λ which can be applied satisfactorily in all possible patient

conditions. The unity feedback of the device has been considered to make all the entries of its closed loop transfer matrix proper and internally stable for a PI-type controller. It is useful to associate with each design specification, the set of transfer matrices that meet the design specification. All the design specifications as discussed here are closed-loop convex. An infinite number of such convex controllers can be designed for $0 \leq \lambda \leq 1$. Thus selection of λ between 0 and 1 has been a problem with the design of convex controllers, which is overcome by the present method. As the design specifications are made stronger and stronger the design value of λ converges to its optimal value, which gives the optimal performance within all time domain and frequency domain specifications. The overshoot and settling time could be brought down to appreciable level by the proposed controller as compared with the controllers already reported. Optimization of a single parameter for the convex controller is also much easier compared to other approaches to optimal controller design. The system with optimal controller thus derived has been tested for stability using Kharitonov's criteria and it satisfies the design specifications in all possible patient conditions. The present approach of designing the linear convex controller with an optimal value of parameter λ makes the insulin dispenser system less sensitive to the process and sensor noises, which is very much required in medical instrumentation. It has been shown rather heuristically that the criteria on robustness are concurrent with the design of convex controllers.

REFERENCES

1. H. Peter Chase, *Understanding Insulin Dependent Diabetes*., The Guild of Children's Diabetes Foundation. http://www.uchsc.edu/misc/diabetes/UIDDM.html.
2. P Kumar and M. Clarke, *Clinical Medicine*. 3e, ELBS publication, 1994.
3. I. Cochin and W. Cadwallender, "Analysis and Design of Dynamic Systems", 3e, Addison-Wesley, ©1997.
4. Insulin Pump: http://www.diabetesmonitor.com/pumps.htm.
5. M. Athans and P.L. Falb, Optimal Control: An Introduction to the Theory and its Applications, McGraw Hill Book Company, ©1966.
6. A.W. Roberts and D.E. Varberg, " Convex Functions", Academic Press, ©1973.
7. M. Artin, "Algebra", Prentice Hall of India, New Delhi,©1994.
8. M. Jamshidi, M. Tarokh and B Shafai, "Computer Aided Analysis and Design of Linear Control Systems", Prentice Hall, Englewood Cliffs, NJ, © 1992.
9. T. Glad and L. Ljung, Control Theory: Multivariable and Nonlinear Methods, 1e, Taylor & Francis, London and New York, © 2000.
10. MATLAB with SIMULINK User's Guide, Ver 5.2, The MathWorks, Inc., Mass.,©1998.
11. E.D. Lehmann and T Deutsch, "A Physiological model of glucose-insulin interaction in type-1 diabetes mellitus", J. Biomed Engg. Vol.14, May 1992, pp.235-242
12. E.D. Lehmann and T. Deutsch, "AIDA^2: A Mk. II automated insulin dosage advisor", J. Biomed. Eng. 1993, Vol.15, May 201-211.
13. E.D. Lehmann, "*The Diabetes Control and Complications Trial(DCCT): A role for computers in patient education?*", J. Diab. Nutr. Metab., Vol. 7, No.5,1994, *pp.*308-316.
14. R.S. Parker, F.J. Doyle III, K.L. Rabinovitch, and N.A. Peppas, *"Time and Frequency Domain Analysis of BG Regulation Algorithms"*, Proc. IEEE - Engg. in Medicine and Biology Society, 19th Annual International Conf., Chicago, IL, 1997.
15. R.S. Parker, F.J. Doyle III, and N.A. Peppas, "*Variable-rate Implantable Insulin Infusion Pumps – Closed loop Maintenance of Normoglycaemia Under Patient Variability for Type I Diabetes*", Proc. 11th World Congress, International Society for Artificial Organs, July, 1997.
16. C. A. Desoer and W. S. Chan, "The Feedback interconnection of Lumped Linear Time Invariant Systems", J. Franklin Inst., Vol 300, Nov-Dec, 1975. pp. 335-351.
17. A. Sutradhar and K. Ray, "Microcomputer based Adaptive controller using Parameter Optimization Technique", Journal of IE (I), Vol. EL-69, Oct,1988. pp.66-72.
18. B. Ross Barmishn, "A Generalization of Kharitonov's Four Polynomial Concept for Robust Stability Problems with Linearly Dependent Coefficient Perturbations", IEEE Trans. On Automatic Control, Vol AC-34, No. 2, Feb 1989, pp.157-165.
19. R. J. Minnichelli, J. J. Anagnost and C. A. Desoer, "*An Elementary Proof of Kharitonov's Stability Theorem with Extensions*", IEEE Trans. On Automatic Control, Vol AC-34, No. 9, Sep 1989, *pp.*995-998.
20. S. Boyd, C. Barratt and S. Norman, "*Linear Controller Design: Limits of Performance via Convex Optimization*", IEEE Proc. Vol.78 No. 3, March, 1990 , *pp.*529-574.
21. A. Sutradhar and A. S. Chaudhuri, " *Analysis and Design of an Optimal PID Controller for Insulin Dispenser System*", Presented in the Paper meeting and accepted for publication in the Journal of Institution of Engineers (I), (2001).
22. A. Sutradhar and A. S. Chaudhuri, " *Design and Analysis of an Optimally Convex Controller in Algebraic Framework for a Micro-insulin Dispenser System*", Communicated for publication in the Journal of AMSE, France, (2001).

Design Of Robust Controller For Robot Joint With Computed Torque

K. A. Gopal Rao
Department Of Electrical Engineering
A.U. College Of Engg., Visakhapatnam-530003, A.P, India

Abstract

Various techniques are studied for robot control in the literature. The one we consider comes under the joint motion control. One of the basic control schemes under this category is joint servomechanism. Since an industrial robot is highly nonlinear system i.e. the intertial loading, the coupling between joints and the gravity effects are all either position and/or velocity dependent terms, the above control scheme using constant gains to control a nonlinear system doesnot perform well under varying speeds and payloads. One solution to the problem is to use computed torque technique. In this paper we consider this concept in the joint servomechanism and derive the fixed feedback gains to control the joint under parameter variations and gravity.

INTRODUCTION

One of the major objectives of a robot is to move its manipulator from one point to another in an accurate and repeatable manner. It is obvious that as position is important, individual joints are controlled by a position servo. Given the dynamic equations of motion of a manipulator, the purpose of robot arm control is to maintain the dynamic response of the manipulator in accordance with some pre-specified performance criteria. For a multi-joint robot arm, development of suitable feedback control presents a substantial challenge, since the control problem is nonlinear and multivariable in nature.

The major emphasis in this paper is on closed-loop control of a robotic joint, because the over whelming majority of the robots currently available utilize such a control structure. It is important to understand that the term-closed loop as applied to robots does not mean that the loop is closed back to the master computer. In reality current control practice requires that the information about the axis motion be feedback only to the corresponding joint processor. That is to say, treat the robot arm as a simple joint servomechanism.

Various techniques are studied for robot control in the literature. These can be classified into three major categories: joint motion control, resolved motion control and adaptive control. The one we consider comes under the joint motion control

.One of the basic control schemes under this category is joint servomechanism. There are two loops for each joint control. The outer loop provides position error information and the inner loop with derivative feed-back to dampen the velocity variable. Both servo loop gains are constant and tuned to perform as critically damped joint system. Because of the fixed gains it does not have the capability of updating them under varying payloads. Since an industrial robot is highly nonlinear system i.e. the inertial loading, the coupling between joints and the gravity effects are all either position and/or velocity dependent terms. Thus, the above control scheme using constant gains to control a nonlinear system does not perform well under varying speeds and payloads. One solution to the problem is to the use of computed torque technique.

Given the Lagrange-Euler (L-E) or Newton-Euler (N-E) equations of motion of a manipulator, the control problem is to find appropriate torques/forces to servo all the joints of the manipulator in real-time in order to track a desired time based trajectory as closely as possible. The drive motion torque required to servo the manipulator is based on a dynamic model of the manipulator. The motor-voltage (motor-current) characteristics are modeled in the computation scheme and the computed torque is converted to the applied motor voltage (current). Because of the modeling errors and parameter variations in the model, position and derivative feedback signals will be used to compute the correction torques which, when added to the

torques computed based on the manipulator model, provide the correction drive signal for the joint motion.

In this paper we consider this concept in the joint servomechanism and derive the fixed feedback gain control the joint under parameter variations and gravity. We use the phase variable feed-back concept and design the controller. The selection of the feed-back gains is made so simple using the root-locus concept. With respect to speed signal this feed-back controller is nothing more than a PID controller.

MATHEMATICAL MODEL

Most industrial robots are either electrically, hydraulically or pneumatically actuated. Electrically driven manipulators are constructed with a D.C. permanent magnet, armature excited, continuous rotation motor incorporating such features as high torque-power ratios, smooth, low-speed operation, linear torque-speed characteristics and short time constants. Use of a permanent magnet field and D.C. power provide maximum torque with minimum input power and minimum weight. These features also reduce the motor inductance and hence the electrical time constant.

The block diagram of the system [1] under consideration is given by Fig.1. The parameter values are A=10, Ra=1.62, Kt=10.7, Ke=0.0754, La=3.39e-3, B=9, 55e-4, T=1/6280. In most of the cases load inertia of a robotic joint usually does undergo dramatic changes as a function of manipulator position. During design and control process this effect is simply ignored treating load inertia as constant. This is worst case approach, as motor and associated mechanical linkages and gears are selected for maximum load conditions. However, in this paper inertia is considered as a variable parameter.

Gravity torque produces disturbance to the system. This disturbance will cause the study state position to be in error. This can be eliminated increasing the amplifier gain. But this will make the system highly under damped in some cases. So a feedback controller is designed to effectively control the joint.

The fixed feedback gains, used to compute the signal equivalent to torque which control the joint under parameter variations and gravity, are derived using the phase variable feedback concept. The selection of the feedback gains is made so simple using the root-locus concept. With respect to speed signal this feed-back controller is nothing more than a P.I.D. controller.

SIMULATIONS AND RESULTS

Throughout the simulations we assume that the arm is initially at $\theta = 0$ (vertical position down) and the desired position is $\theta = \pi/2$ rad (horizontal position).

Simulation is first carried out with unity feed-back on linear and non-linear models. It is observed that the overshoot is above 45% and the error is very large in steady state. The P.I.D. controller is designed taking into consideration the computed torque concept and root-locus theory. The structure of the P.I.D. controller is $K_1+K_2s+K_3s^2$. The parameter values are $K_1= 1$, $K_2= 0.0095$ and $K_3= 0.0000456$. The overshoot is less than 2%. Simulations show that the steady state error in position is less than 0.001% at ts = 0.05sec when the gravity torques is present and/or absent and also when the arm is moving from horizontal position to vertical position (down).

CONCLUSIONS

In this paper studies are carried out on control of a servo driven robot arm with PID controllers. The studies are carried out using parameter variations and nonlinear model. The PID controller is designed using the concepts of computed torque and root- locus. The system behaviour with PID controller is satisfactory under all working conditions.

REFERENCES

[1] D.K. Richard, A.C. Thomas & N. Michael, 'Robotics Engineering: An integrated approach" Prentice-Hall international, 1989.

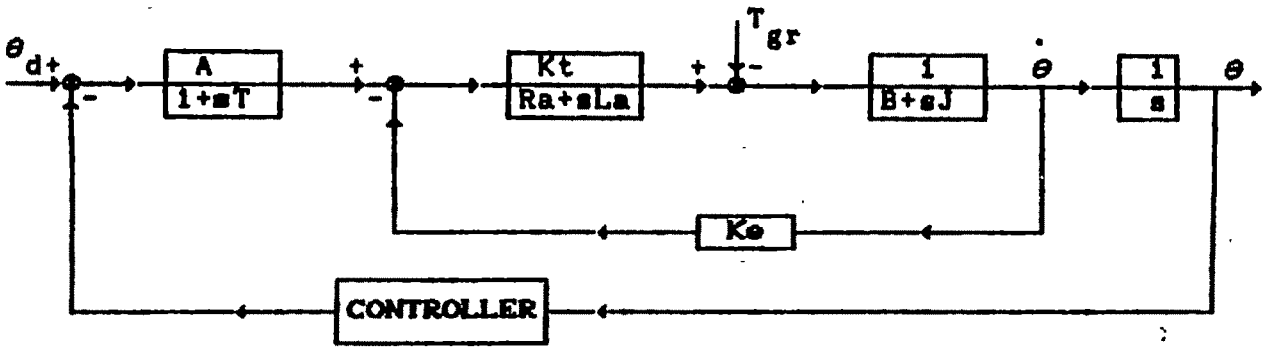

Fig. 1 BLOCK-DIAGRAM OF THE MODEL

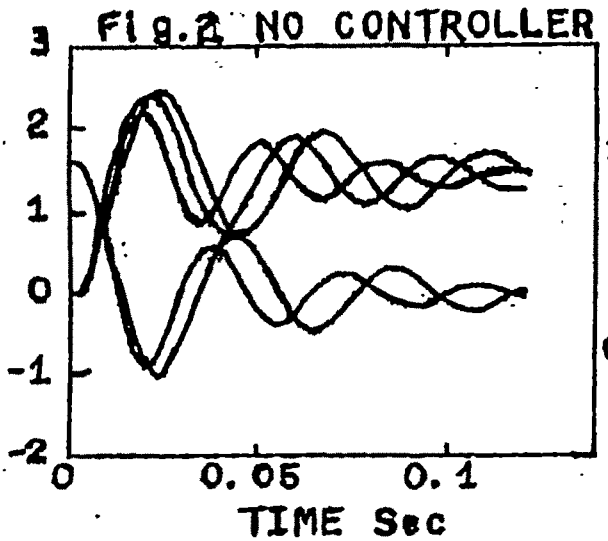

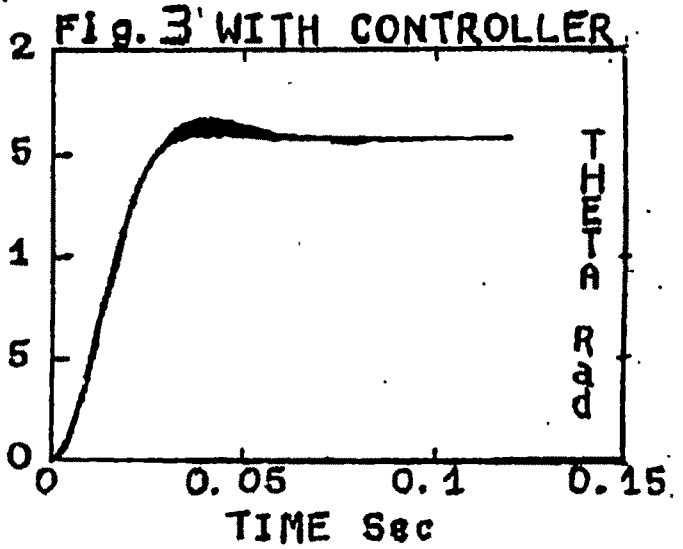

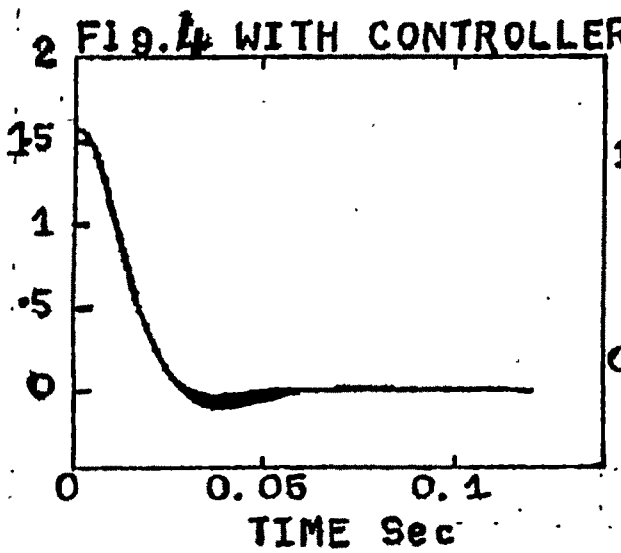

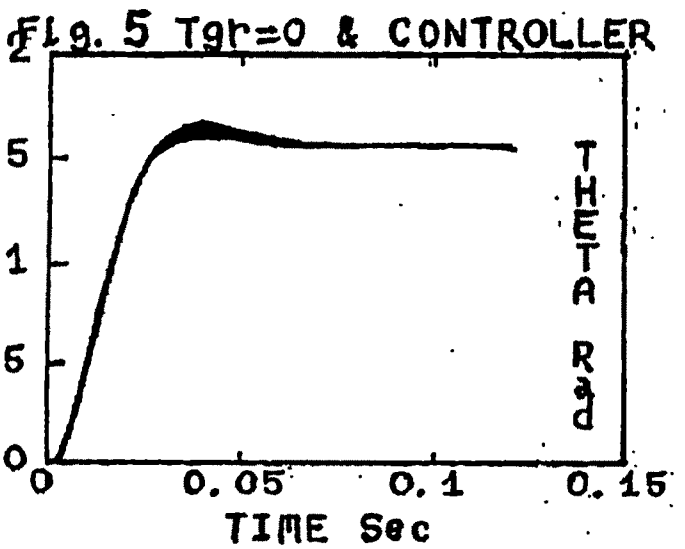

A New Lead Wire Compensation Method for Existing Two Wire Resistance Temperature Detectors (RTDs)

S. K. Sen
Department of Applied Physics
University of Calcutta
92 APC Road, Calcutta 700 009, India

Abstract

A new method of lead wire compensation technique is presented for existing two-wire resistance temperature detectors (RTDs). In existing two wire resistance temperature detectors that use bridge balance methods, the two lead resistances introduce appreciable error in measurements. The error so introduced is also dependent on environment temperature variations. The presented technique overcomes the effects of such lead resistances alongwith any temperature variation that the lead wires may be subjected to in industrial environments.

Keywords: Lead wire compensation, resistance temperature detectors, transducers.

INTRODUCTION

Resistance transducers, commonly known as resistance temperature detectors, are widely used for measurement of temperature. The common RTDs used are platinum, copper and nickel. The type of the RTD that is used depends on the particular application involved. RTDs used, viz., Pt 100, Pt 46, Cu 46 etc. are all referenced at 0°C.Thus the bridge circuit is balanced at 0°C and any unbalance bridge output is calibrated in terms of temperature of the process parameter. A further advantage of using RTDs allow very small temperature changes (–0.03°F) to be measured without much difficulty [1].

With temperature variation, the electrical resistance of the RTDs vary as per the standard formula, given by,

$$R_t = R_0 (1 + a_1 t + a_2 t^2 + a_3 t^3 + ... + a_n t^n) \qquad (1)$$

where,

R_0 = Resistance at 0°C, in ohms
R_t = Resistance at t°C, in ohms.
t = Unknown temperature, °C.
$a_1, ... a_n$ = Constants for the RTDs employed.

For most cases, only one constant, viz., a_1 is taken into consideration for finding out the unknown temperature t – this assumes a linear relationship between resistance and temperature, which is of course true only over a small temperature range. This assumption is obviously not true for use in resistance thermometry. For platinum RTDs, two constants are sufficient upto 650°C. This indicates a quadratic relationship between resistance and temperature and as such the linear relationship deviates by about 7 percent at the upper limit. For copper, the relationship is very linear upto 120°C and beyond this, three constants are generally used. A disadvantage with nickel is that its resistance temperature relationship is appreciably non-linear in nature.

Finding out the process temperature using RTDs as temperature sensors by employing normal bridge circuits has its own disadvantages. Firstly the bridge output varies in a non-linear manner with variation of temperature of the process parameter. Secondly, the resistance of the connecting leads add to sensor resistance, thereby introducing an appreciable error. This problem gets aggravated by temperature variations of the lead resistances in its passage from the transducer element upto the control room.

Researchers attempted at eliminating the nonlinearity factor by incorporating feedback in the bridge amplifier or by software means [2], but obviously at the cost of simplicity of the measurement circuit. But the second error, i.e., error due to lead resistance poses real problem. An

additional 5Ω resistance for a Pt 100 RTD results in approximately a 12°C deviation in temperature measurements [3] . In practice, the situation is even more compounded due to environment temperature variations. This results in an error which itself does not remain constant with time.

Three wire and four wire RTDs have been in use in industries to offset the effects of lead resistances. Four wire resistance measurements provide for the best accuracy, but only at the cost of two additional wires which may turn out to be quite costly. The situation gets compounded by the introduction of many four wire RTDs to measure process temperature at various locations. Thus in this case accuracy is derived, but only at the cost of considerable expenses.

A three-lead arrangement attempted at removing this cost factor but in this case the bridge output is dependent on R_l, the resistance of one lead length [4]. The bridge output for a three wire RTD follows like this:

$$V_o = (1/2)\, V_{ref} (R_S - R_B)/(R_S + R_B + 2R_l) \quad ...(2)$$

where, V_o is the bridge output, V_{ref} is the supply voltage to the bridge circuit.

R_S stands for the sensor resistance while R_B is the resistance element that balances the bridge. The effect of R_l is only absent in case $R_S = R_B$, otherwise the bridge output's dependence on R_l is evident from the above relationship. Although an apriori knowledge of R_l may be there, its dependence on temperature variation makes it more difficult to eliminate fully the effect of R_l on bridge output.

Since the RTD resistance changes by a factor of two or more, the error introduced by lead resistances would be a matter of great concern and must be eliminated for accurate temperature measurements.

PRINCIPLE OF OPERATION OF THE PROPOSED CIRCUIT AND SCHEMATIC DIAGRAM

A two wire RTD is depicted in fig. 1 in which R_S is the sensor resistance and R_l represents the resistance value of each lead wire, both supposedly equal. This assumption is realistically valid because each of the lead wires are to run through the same distance before terminating at the control room. The value of any one of the lead wire resistances can be found out by sending a known constant current through it and measuring the drop across it. Dividing the drop across R_l by the known constant current enables the measurement of R_l at any given temperature.

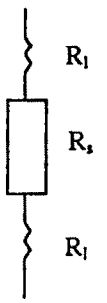

Fig. 1 Symbolic representation of a two-wire Resistance Temperature Detector

A resistance, having the value R_l is prepared and is of the same material as that of the lead resistances. This resistance is put just outside the control room and is shown by the resistance put across DE, shown in fig.2. In the same figure, the resistances R_s and two R_l's in series and put across AD represent the RTD alongwith the two lead length resistances. The resistance across DE placed outside the control room ensures that it is subjected to identical type of environmental temperature variations as that of the lead resistances.

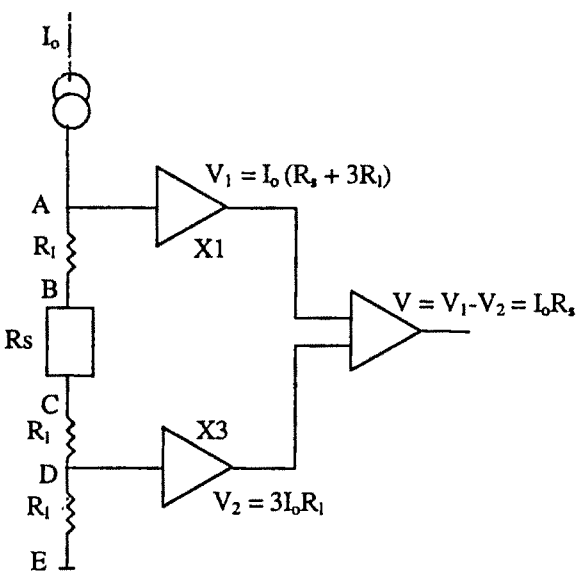

Fig. 2 Schematic diagram of the proposed circuit

A constant current source I_o is then fed along the line AE. Point A is now connected to an amplifier of gain 1 so that the output of this amplifier will be $V_1 = I_o (R_s + 3R_l)$. Point D is connected to another amplifier of gain 3 so that its output is $V_2 = 3I_oR_l$. These two outputs V_1 and V_2 are then fed to a differential amplifier so that its output is

$$V = V_1 - V_2 = I_o R_s$$

Thus the overall output of the circuit is totally independent of the lead wires. Since I_o is constant, thus the output voltage is dependent only on the variation of R_s, the sensor resistance. Assuming R_s to vary linearly with temperature changes, V can be straightway calibrated in terms of the unknown temperature.

The rationale behind putting Rl just outside the control room is justified because this resistance is subjected to the same kind of temperature variations as that of the lead wires.

CIRCUIT REALISATION

The scheme of the circuit is presented here in details in Fig. 3. A constant current source Io along the path AE is realised using op-amps and transistors.

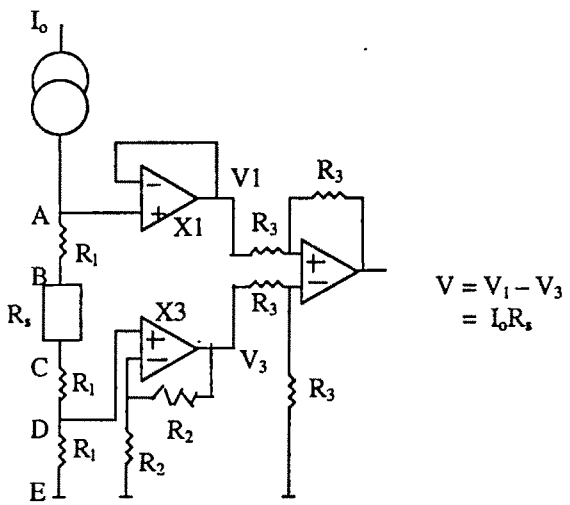

Fig. 3 Detailed diagram of Fig. 2

The X1 and X3 amplifiers as well as the differential amplifier are realised employing LM 324. The resistances R_2 and R_3 are all in the KΩ range. The circuit output is dependent on the constantcy of the current source I_o so that utmost care should be taken to ensure this.

CONLCUSION

A novel approach to the elimination of lead wire resistance effects in existing two wires RTDs is presented. The existing two wire RTD type of temperature sensors suffer from the flaw in that the lead wire resistances blur the accuracy of the measurement and it is also a fact that the amount of error is temperature dependent because with temperature variation, the lead wire resistances vary.

Space considerations and to certain extent cost considerations also, prohibit the replacement of existing two wire RTDs with three wire or four wire RTDs, because in that case one or two additional lead wire(s) is/are to be laid, as the case may be.

The presented technique eliminates the effects of lead wire resistances as well as its variations with temperature, so that the final output is directly proportional to the resistance variation of the RTD only. The accuracy limit in this case is only governed by the accuracy with which the constant current source can maintain its constancy of current.

Thus with very slight modification to the existing two wire RTDs, there will be complete elimination of lead wire effects. The designed circuit is cost effective, very easy to develop and implement and would occupy very less space.

One point to be noted is that the variations in the lead wire resistances due to temperature variations may not be exactly identical to the variations in the resistances put just outside the control room. Any error, if any, on this count may be offsetted by putting a somewhat higher value of lead wire resistances so that the percentage variation in the lead wire resistances with temperature is decreased to certain extent

REFERENCES

1. D P Eckman, *Industrial Instrumentation*, (1975)
2. F N Trofimenkoff and A E Nordquist, "Single amplifier resistance bridges with feedback linearization," IEEE Trans. Instrum. Meas., Vol. IM-33, pp. 60-63, Mar. 1984.
3. S Pradhan and S Sen, An improved lead compensation technique for three-wire resistance temperature detectors, IEEE Trans. Instrum. Meas., Vol. 48, pp. 903-905, October 1999.
4. H D Baker, E A Ryder and N H Baker, *Temperature measurement in engineering*, stanford, CT: Omega, 1975, Vol. 2, Ch.2, pp. 34-35.

Fault Tolerant Three Phase Real Power Measurement Using Microprocessor

S. Sengupta*, Gautam Sarkar*, Arghya Sarkar#, A.K.Mukhopadhyay*
*Department of Applied Physics, University of Calcutta, 92, A. P. C. Road, Kolkata-700 009
MCKV Institute of Technology, 243 G.T. Road (N), Liluah, Howrah-711204

Abstract

There are some disadvantages in measurement of power by conventional methods due to inductance and capacitance of coils and eddy current induced in the solid metal parts of the instruments by the alternating magnetic field of the current coil. Besides these, if a fault occurs in any of the PT secondary circuits, a conventional meter cannot detect it resulting in under-registration. In the present paper, a microprocessor based three-phase real power measurement system has been developed, which will display the power being fed to the load under normal condition. If any fault occurs in a PT secondary circuit, it will still show the actual three-phase power. The system has been tested in the laboratory and the results have been presented in the text.

Keywords: Power, Fault tolerant, Microprocessor.

INTRODUCTION

Electrical power is the key to industrial progress and efficient power management ensures it. To achieve this, accurate measurement of power is very important. The measurement of power by conventional meters has some problems in respect of inductance and capacitance of coils, eddy currents induced in the solid metal parts of the meters. Different methods have been suggested to reduce them [3], [4].

But if a fault occurs in any one of the PT secondary circuits, these meters cannot sense the fault and under-register the power flowing to the load.

With the advent of microprocessor, attempts were made to use it for measurement of power and energy [1], [2], [5] and [6] so that different disadvantage of conventional meters is reduced. But under-registration of such a meter for a fault in the metering circuits has not been considered as yet.

In this paper, a microprocessor based three-phase real power measuring unit has been developed that can sense the fault in the PT secondary circuit and always displays the actual power under both normal and faulty conditions. This developed scheme finds wide application in measuring three-phase real power accurately irrespective of the normal and faulty conditions of the PT secondary circuit provided the power circuit is healthy.

THEORETICAL DEVELOPMENT

The industrial programme of any country is based on modern technologies, in which electrical power acts as the prime mover. Measurement of electrical power is an important task in a power system.

The schematic diagram for measurement of power in three-phase four-wire system has been shown in Fig 1 whereas that for three-phase three-wire system has been shown in Fig.2. The vector diagram corresponding to Fig. 2 has been presented in Fig.3,

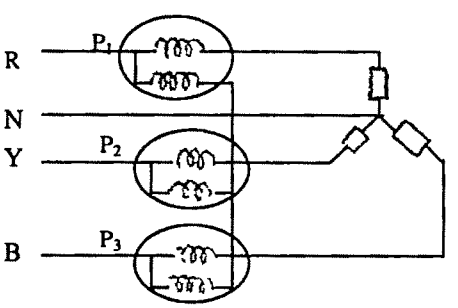

Fig. 1 Schematic diagram for measurement of power in three-phase four-wire system

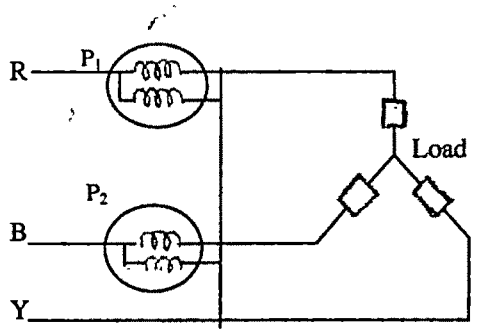

Fig. 2 Schematic diagram for measurement of power in three-phase three-

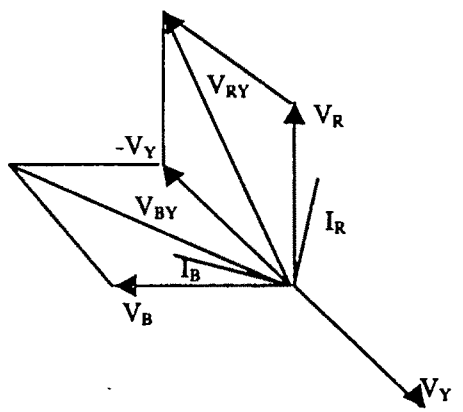

Fig.3 Vector diagram corresponding to Fig.2

The total real power flowing to the load is

$$P = V_{RY}I_R\text{Cos}(30^0+\Phi) + V_{BY}I_B\text{Cos}(30^0-\Phi) \qquad (1)$$

where V_{RY}, V_{BY} are the line voltages, I_B, I_Y are the line currents and CosΦ is power factor.

If the load is balanced, then $V_{RY} = V_{RB} = V_{BY} = \sqrt{3}V$ and $I_R = I_B = I_Y = I$ where V and I are phase voltage and current respectively.

Hence $P_{bal} = 3VI\text{Cos}\Phi \qquad (2)$

If any one of the PT fuses of the metering circuit is blown, the meter will show some reading which is less than the actual and can be corrected with the correction factors obtained as follows:

If the potential coil between R and Y phases is absent, $V_{RY} = 0$, (1) yields

$$P' = V_{BY}\,I_B\,\text{Cos}\,(30^0 - \Phi) \qquad (3)$$

Then the correction factors are obtained as

$$CT_{RY\text{-}unbal} = \frac{P}{P'} = \frac{V_{RY}I_R\text{Cos}(30^0+\Phi) + V_{BY}I_B\text{Cos}(30^0-\Phi)}{V_{BY}\,I_B\,\text{Cos}\,(30^0 - \Phi)} \qquad (4)$$

for unbalanced condition

$$\text{and } CT_{RY\text{-}bal} = \frac{\text{Cos}\,(30^0 + \Phi) + \text{Cos}\,(30^0 - \Phi)}{\text{Cos}\,(30^0-\Phi)} \qquad (5)$$

for balanced condition

Similarly for a fault in the PT secondary circuit between Y and B phases i.e. $V_{BY} = 0$, the correction factors are obtained as

$$CT_{BY\text{-}unbal} = \frac{V_{RY}I_R\text{Cos}(30^0 + \Phi) + V_{BY}I_B\text{Cos}(30^0 - \Phi)}{V_{RY}I_R\text{Cos}(30^0+\Phi)} \qquad (6)$$

for unbalanced condition

$$\text{and } CT_{BY\text{-}bal} = \frac{\text{Cos}\,(30^0 + \Phi) + \text{Cos}\,(30^0 - \Phi)}{\text{Cos}\,(30^0+\Phi)} \qquad (7)$$

for balanced condition

Thus it is seen that the correction factors are dependent on power factor of the load. In a conventional meter actual registration under this condition is not possible.

In this scheme, under faulty conditions the actual power is obtained as

$$P_{act\text{-}RY} = P'.CT_{RY\text{-}bal} \quad \text{for balanced load} \qquad (8)$$

$$= P'.CT_{RY\text{-}unbal} \quad \text{for unbalanced load} \qquad (9)$$

$$P_{act\text{-}BY} = P'.CT_{BY\text{-}bal} \quad \text{for balanced load} \qquad (10)$$

$$= P'.CT_{BY\text{-}unbal} \quad \text{for unbalanced load} \qquad (11)$$

On the occurrence of any fault in one of the potential circuits, the microprocessor calculates the three-phase power fed to the load using (8), (9), (10) and (11) and

also displays the actual three-phase power, which is transferred to the load.

PROPOSED SCHEME

The system block diagram has been presented in Fig. 4 in which the potential transformers PT_2 and PT_3 have been used for scaling down the line voltages and PT_1 has been used for measuring the power factor angle. Current transformers CT_1 and CT_2 scale down line currents. These signals have been fed to the microprocessor which, after executing the developed software, calculates and displays the total power under healthy and faulty conditions.

EXPERIMENTATION

Laboratory Set-up

The laboratory set-up for measurement of power has been shown in Fig. 5.

Measurement Techniques used in the Experiment

Measurement of line currents I_R and I_B

The line current has been scaled down by CT of 5/1 A ratio. The voltage drop across the burden gives the voltage corresponding to the line current which is converted to dc by peak detectors PD_1 and PD_2 and digitised by ADC based on 0809. ADC channels 1 and 2 have been selected corresponding to line currents I_R and I_B. The multiplication factor for current in this set-up is mfI_R and mfI_B.

Measurement of line voltages V_{RY} and V_{BY}

The line voltage V_{RY} (415V) is first scaled down by PT of ratio 415/5 V. The secondary voltage of PT is further scaled down by potentiometeric arrangement, converted to dc by peak detectors (PD_3 and PD_4) and digitised by ADC. Channels 3 and 4 of ADC have been utilised for digitising line voltages V_{RY} and V_{BY} respectively. The voltage-multiplication factor in this set-up is mfv_{RY} and mfv_{RB}.

Measurement of phase angle between V_R and I_R

Determination of proportional hex value of 180^0 i.e. N (180)

The instant the rising edge of voltage waveform of V_R is detected a counter is set. The counter is incremented at an interval of a very small delay till the voltage becomes low and the counter is stopped. This value of the counter, called the delay number, gives proportional hex value of 180^0 i.e. N (180).

If N be the delay number corresponding to Φ, the phase difference between V_R and I_R, then

$$\Phi \propto N$$

But $\quad 180^0 \propto N(180)$

$$\text{or,} \quad \frac{\Phi}{180} = \frac{N}{N(180)} \quad \text{(In degrees)}$$

$$\text{or,} \Phi = \frac{3.14 \times N}{N(180)} \quad \text{(In radian)} \qquad (12)$$

$$\text{or,} \quad 100\ \Phi = \frac{314 \times N}{N(180)} \quad \text{(In radian)} \qquad (13)$$

$$= \frac{13A_H \times N}{N(180)} \quad \text{(In Hex)} \qquad (14)$$

Evaluation of Cos (30° + Φ) and Cos (30°- Φ)

$$\frac{\pi}{6} \times 100 = 100 \times \frac{3.14}{6} = 52 = 34_H$$

Then $100 \cos (30° + \Phi)$

$$= \frac{1}{2}\left[C8_H - \left[34_H + \frac{13A_H \times N}{N(180)}\right]\right] \qquad (15)$$

Similarly, $100 \cos (30° - \Phi)$

$$= \frac{1}{2}\left[C8_H - \left[34_H + \frac{13A_H \times N}{N(180)}\right]\right] \qquad (16)$$

Evaluation of Three-Phase Power

The total power is given by

$$\frac{V_{RY}\, I_R\, 100\, \text{Cos}\,(30^0+\Phi)}{64_H} + \frac{V_{BY}\, I_B\, 100\, \text{Cos}\,(30^0-\Phi)}{64_H}$$

$$= \left| \frac{64_H\, mfv_{RY}\, V_{RYH}\, mf_{IR} I_{RH}\, \text{Cos}\,(30^0+\Phi)}{64_H} - \frac{64_H\, mfv_{BY}\, V_{BYH}\, mf_{IB} I_{BH}\, \text{Cos}\,(30^0-\Phi)}{64_H} \right| \times K \quad (17)$$

where,

$K = 1$ if $V_{RYH} \neq 0$ and $V_{BYH} \neq 0$ (18)

$$= \frac{64_H\, [\text{Cos}\,(30^0+\Phi)_H + \text{Cos}\,(30^0-\Phi)_H]}{64_H \text{Cos}\,(30^0-\Phi)_H} \quad (19)$$

if $V_{RYH} = 0$

$$= \frac{64_H\, [\text{Cos}\,(30^0+\Phi)_H + \text{Cos}\,(30^0-\Phi)_H]}{64_H \text{Cos}\,(30^0+\Phi)_H} \quad (20)$$

if $V_{BYH} = 0$

EXPERIMENTAL RESULTS

The experimental results have been presented in Fig 7, Fig 8, Fig 9, Fig 10 and Fig 11. Fig 10 and Fig 11 show that %error of reading of the developed meter remains within ±3%.

From the results and characteristics, the sources of errors in the experimentation can be identified as (a) difference in CT characteristics (b) difference in PT characteristics (c) difference in Peak detector characteristics and (d) in the software part, decimal part has been neglected in division resulting in errors in the final result.

SYSTEM SOFTWARE FLOWCHART

The system software flowchart has been presented in Fig.6.

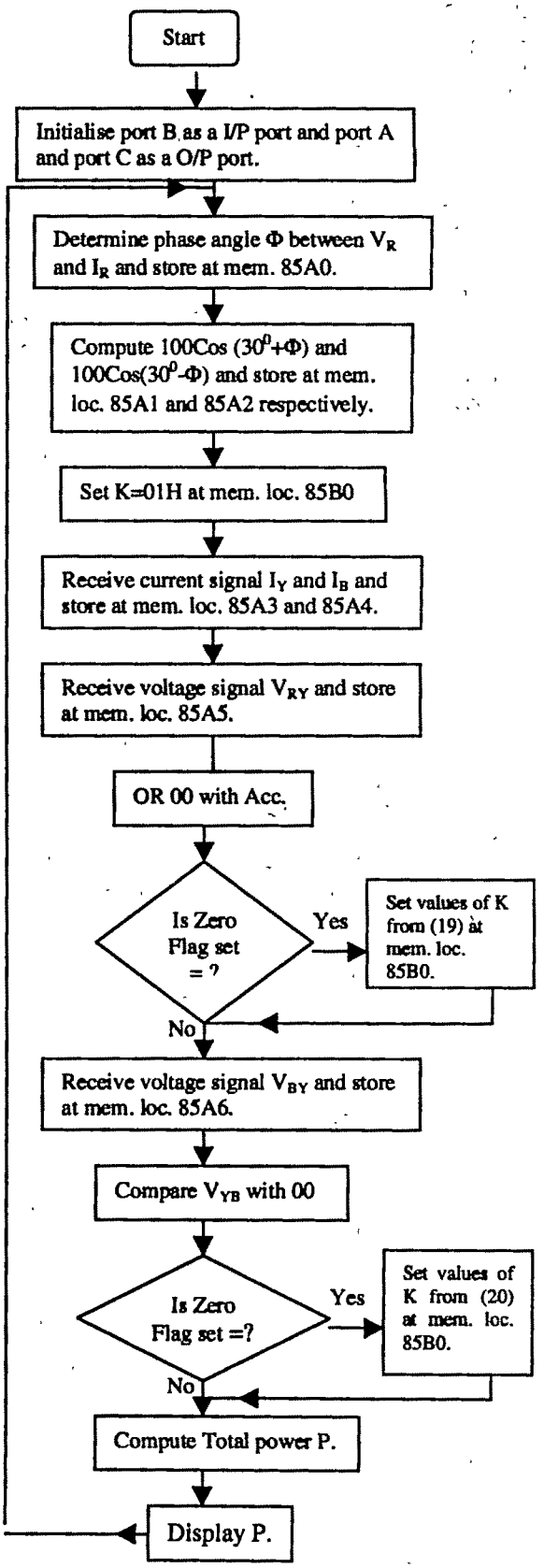
Start
Initialise port B as a I/P port and port A and port C as a O/P port.
Determine phase angle Φ between V_R and I_R and store at mem. 85A0.
Compute 100Cos (30⁰+Φ) and 100Cos(30⁰-Φ) and store at mem. loc. 85A1 and 85A2 respectively.
Set K=01H at mem. loc. 85B0
Receive current signal I_Y and I_B and store at mem. loc. 85A3 and 85A4.
Receive voltage signal V_{RY} and store at mem. loc. 85A5.
OR 00 with Acc.
Is Zero Flag set = ?
Yes
Set values of K from (19) at mem. loc. 85B0.
No
Receive voltage signal V_{BY} and store at mem. loc. 85A6.
Compare V_{YB} with 00
Is Zero Flag set =?
Yes
Set values of K from (20) at mem. loc. 85B0.
No
Compute Total power P.
Display P.

CONCLUSION

In this paper, a microprocessor based three-phase real power measuring unit has been developed that can sense the fault in the PT secondary circuit and always displays the actual power both normal and faulty conditions.
This developed scheme finds it wide utility in measuring three-phase power accurately irrespective of the normal and faulty conditions of the control circuit provided the power circuit is in healthy condition.

REFERENCES

1. G.S.Hope, O.P.Malik and J.Chang "Microprocessor Based active and reactive power measurements" Jour.Electric Power and Energy Systems, Vol.3, April 1981.
2. B. Djokic, P.Bosnjakovic and M.Begovic "New method for reactive power and energy measurement" IEEE Trans.Instru.Meas. Vol.41, P-280-285, April, 1992,
3. Electrical Measurements and Measuring Instruments - E.W.Golding and F.C.Winddies Wheeler Publishing, 5th Edition, 1991.
4. A course in Electrical and Electronics Measurement and Instrumentation - A.K.Swahney, Dhanpat Rai and Sons Publishing 11th Edition, 1994.
5. Textbook on Microprocessor Based Laboratory Experiments and Projects – A.K.Mukhopadhyay Wheeler Publishing, 2nd Edition 2000.
6. Microprocessor Architecture, Programming, and Applications with 8085 – Ramesh S. Gaonkar Penram International Publishing (India) 4th Edition 2000.

ACKNOWLEDGEMENT: Authors acknowledge the helps forwarded by K. N. Saha of Diamond Beverages (P) Limited, Kolkata in continuing this work.

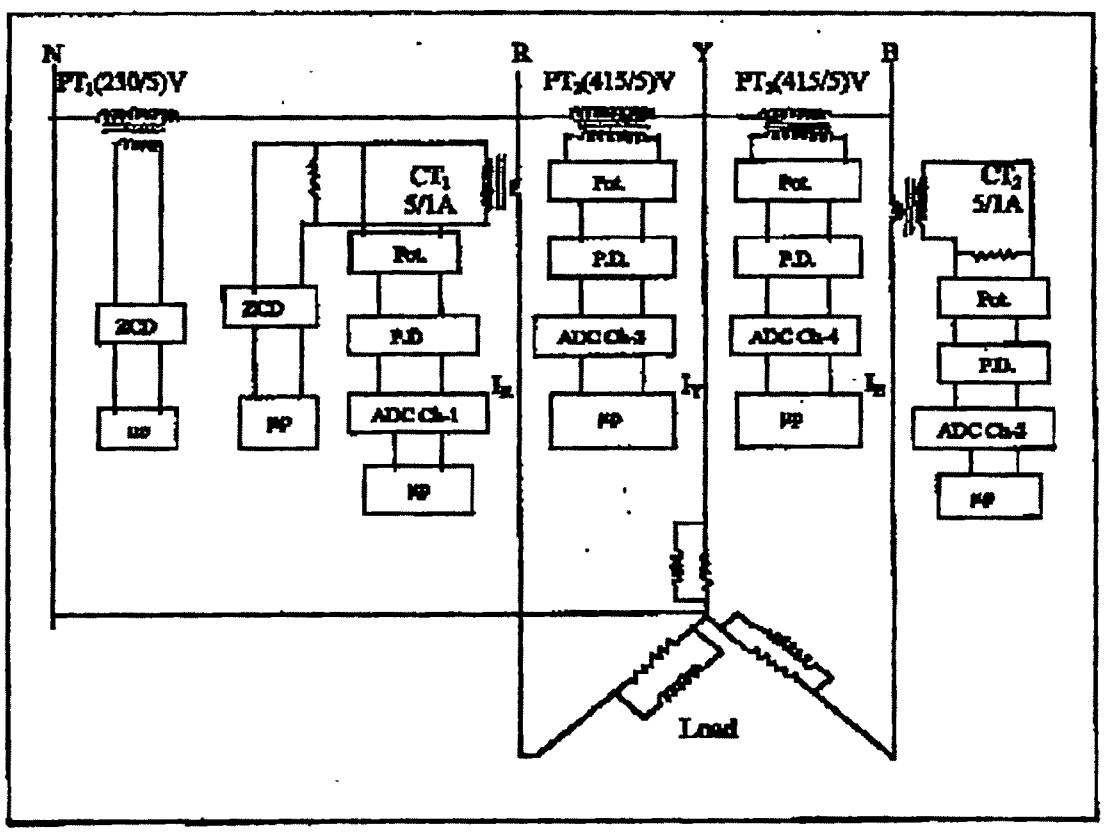

Fig. 4 Block diagram for Proposed Scheme.

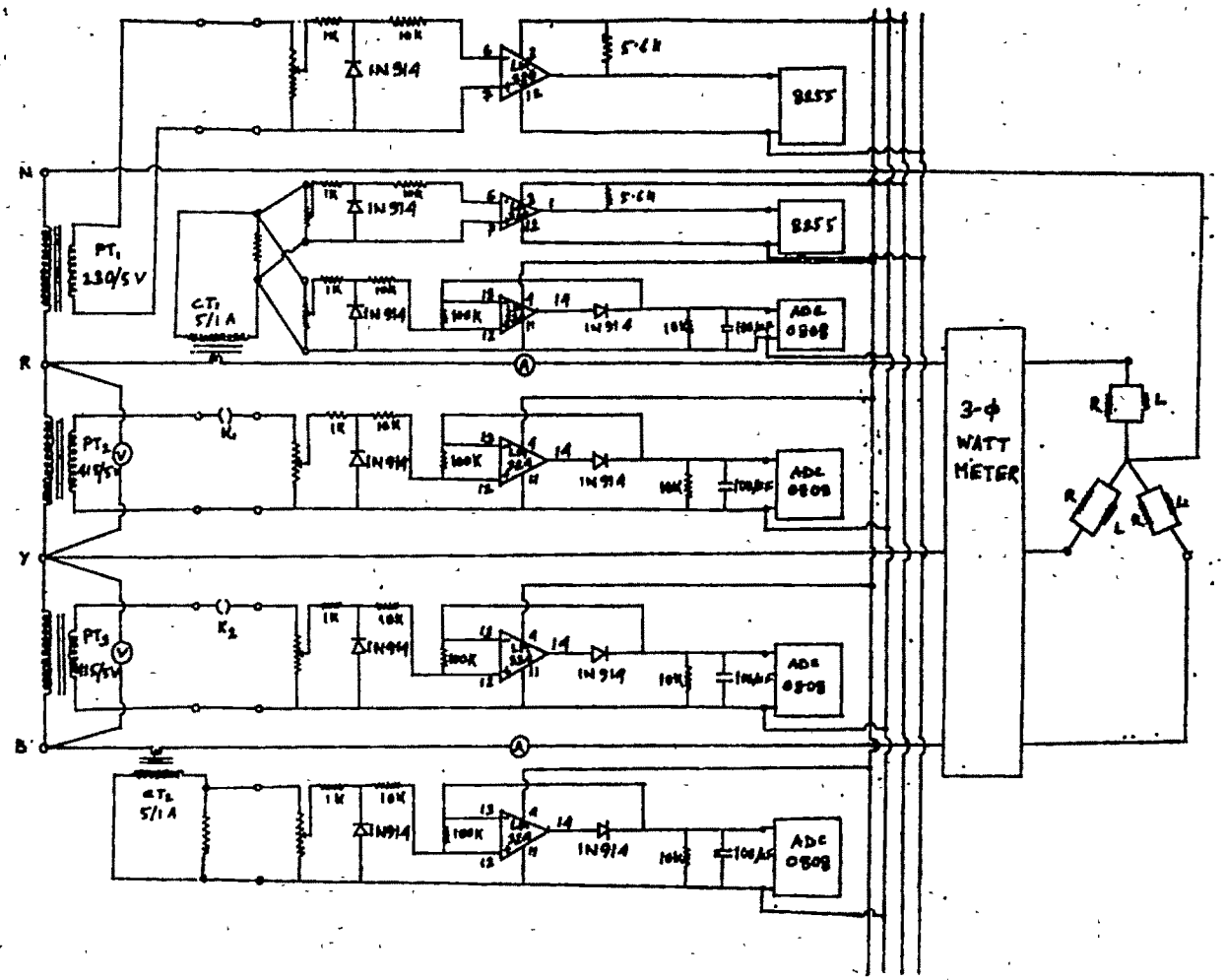

Fig.5. Details Circuit Diagram

Algorithm For Digital PID Redesign Of An Existing Analog Controller

S. K. Bharadwaj[1] and S. K. Nagar[2]
[1]Department of Electrical Engineering. MACT, Bhopal 462 007, India
email : sk_bharadwaj@indiatimes.com
[2]Department of Electrical Engineering
Institute of Technology, BHU, Varanasi 221005, India
e-mail: sknagar@banaras.ernet.in

Abstract

A method for the digital redesign of an existing analog controller is presented. The method is based on matching of time moments. The method leads to linear algebraic equations in terms of unknown parameters of discretized controller. The algorithm is fully implementable in ' MATLAB' which automatically computes the digital equivalent of an analog controller. The proposed controller gives good performance at higher sampling period also.

Index Terms—Analog controller,Digital Controller, Redesign.

INTRODUCTION

For simulation studies as well as the design and implementation of computer control systems, discretization of continuous time controller is often required. The digitalization problem has been considered by number of researchers {1-6}.

ALGORITHM

The block diagram of an existing continuous data control system has been shown in fig.(1). The continuous model as shown in fig.(1) can be digitized by inserting a sampler of duration T at the error input and replacing the continuous controller Gc(s) by a digital controller Dc(z) and a zero order hold as shown in fig.(2). The overall transfer function of the continuous and digital systems can be written from fig.(1) and fig.(2) respectively as given below:

$$\frac{C(s)}{R(s)}=M(s)=\frac{Gp(s).Gc(s)}{1+Gc(s).Gp(s)} \qquad (1)$$

$$\frac{C(z)}{R(z)} = Gd(z) = \frac{Dc(z).Gp(z)}{1+Dc(z).Gp(z)} \qquad (2)$$

where Gc(s) and Gp(s) are the transfer function of continuous controller and plant respectively; and Dc(z) and
Gp(z) are the transfer function of digital controller and plant preceded by ZOH respectively.

The design of the digital controller should be such that the steady state output of the digital control system follows the desired output of the continuous model for all sinusoidal inputs within the frequency range of the interest.

In the design method [1], the parameters of the digitized controllers are determined such that the open loop digital system Gp(z)Dc(z) approximates in the Pade sense with the open loop transfer function of their continuous time system.

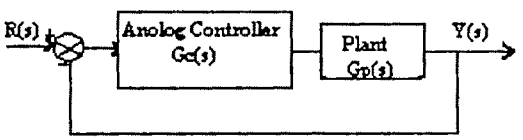

Fig.1. Continuous closed loop system

The open loop transfer function of the system shown in fig.(1) is given as The open loop transfer function of the system shown in fig.(1) is given as

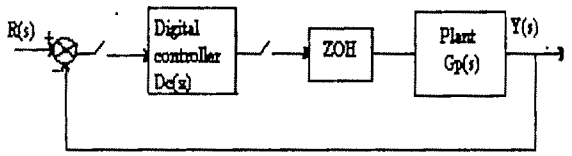

Fig 2 Discrete closed loop system

$$Mq(s) = \frac{M(s)}{1 - M(s)} \tag{3}$$

The design process starts by converting the open loop transfer function in fig.(2) to w domain.

The advantages of w' transformation are that the sampling and data hold operations are modeled exactly in the w domain regardless of the sampling rate employed and the w variable is analogous to the 's' variable in the sense that all familiar frequency domain design concept, procedures and interpretations are carried over directly [8].

Assuming Gp (w) and Mq (w) have formal power series expansion ,

$$Gp(w) = \sum_{i=0}^{\infty} g_i w^i \tag{4}$$

$$Mq(w) = \sum_{i=0}^{\infty} m_i w^i \tag{5}$$

The designed PID controller is designed by the T.F [7],

$$D(z) = K_P + \frac{K_I T(z+1)}{2(z-1)} + \frac{K_D(z-1)}{Tz} = \frac{C_0 z^2 + C_1 z + C_2}{z(z-1)} \tag{6}$$

where,

$$C_0 = K_P + \frac{K_I T}{2} + \frac{K_D}{T}$$

$$C_1 = -K_P + \frac{K_I T}{2} - \frac{2K_D}{T}$$

$$C_2 = \frac{K_D}{T}$$

The unknown parameters of the digital controller are obtained by

$$D(w) \cdot Gp(p) \overset{P}{=} Mq(w) \tag{7}$$

where D(w) is obtained by substituting, $z = \frac{1 + T/2.w}{1 - T/2.w}$ in D(z) and $\overset{P}{=}$ denotes equivalence in Pade sense.

Let, $D(w) = \frac{d_0 w^2 + d_1 w + d_2}{(1 + T/2.w)Tw}$, then from (7), we get

$$\frac{d_0 w^2 + d_1 w + d_2}{(1 + T/2w)Tw}(g_0 + g_1 w + g_2 w + \quad) = m_0 w^{-1} + m_1 w^0 + m_2 w^1 + \ldots\ldots$$

Computing the like powers of w ,we get

$$d_2 g_0 = m_0 T$$

$$d_1 g_0 + d_2 g_1 = m_1 T + m_0 \frac{T^2}{2}$$

$$d_0 g_0 + d_1 g_1 + d_2 g_2 = m_2 T + m_1 \frac{T^2}{2}$$

In matrix form,

$$\begin{bmatrix} g_0 & 0 & 0 \\ g_1 & g_0 & 0 \\ g_2 & g_1 & g_0 \end{bmatrix} \begin{bmatrix} d_2 \\ d_1 \\ d_0 \end{bmatrix} = \begin{bmatrix} m_0 T \\ m_1 T + \frac{m_0 T^2}{2} \\ m_2 T + m_1 \frac{T^2}{2} \end{bmatrix}$$

which can be solved for d_2 ,d_1 and d_0 .Thus controller D(w) is completely specified. Using the transformation $w = \frac{2}{T}\frac{z-1}{z+1}$, the controller D(z) can be obtained. Finally using (6),we can get the parameters of the digital PID controller.

ILLUSTRATIVE EXAMPLE

Consider the example chosen by Rattan[2], where the transfer function of the continuous controller and the plant are given by

$$Gc(s) = \frac{1+0.416s}{1+0.139s} \quad \text{and} \quad Gp(s) = \frac{10}{s(s+1)}$$

Following the algorithm given in [1] , the parameters of digital controller are as follows:

K_P =1.73913 , K_I =-9.855065 , K_D=0.3532551

A comparison of unit step response of analog and redesigned digital control system are shown in fig.(3). It may noted that present method gives good performance of the controller at a higher sampling period also.

CONCLUSION

An algorithm for digital redesign of an existing analog control system is given here. As the algorithm is fully computer aided,the controllers of different complexities can be tried and the best controller in terms of time & frequency response matching can be selected. Satisfactory results are also obtained for examples in [2-5].

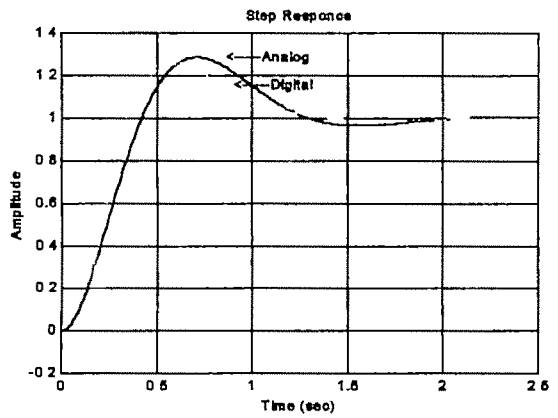

Fig.3 . (for T= 0.15 sec)

REFERENCES

[1] Jayanta Pal and S.K.Nagar, " A method for discretizing a continuous-time controller" Proc. Of 20th National Systems Conference NS.C.-96, Dec. 19-21, 1996, Vikram Sarabhai Space Center, Thiruvananthapuram.

[2] Kuldip S.Rattan, " Digitalization of existing continuous control systems", IEEE Trans. On Automatic Control, Vo.-29, No. 3, March 1984, PP282.

[3] Darriel Ravi V and W.Djaja,"Technique for enhancing the performance of discretized controller " IEEE Control System 1999, PP.52-57.

[4] R.A. Kennedy and R.J. Evans, "Digital Redisign of a continuous controller based on closed loop performance ", in Proc. 29th Conf. Decision Control, .PP 1898-1901,1990.

[5] Nadra Rafe , Tongwrn Chen and O.P. Malik,"A technique for optimal digital redesign of analog controller," IEEE .Trans.on Control System Tech. Vol-5, No-1,Jan-1997.

[6] Ye.N. Rosen Vasser,K.Yu. Polyakov and B.P Lampe, " Application of laplace transformation for digital redesign of continuous control system," IEEE Trans. on Automatic Control , Vol 4,No-4,April 1999.

[7] Houpis C H. & Lamont G.B. ,"Digital Control Systems," McGraw-Hill International Editions,1987.

[8] Philips C.L. and Nagle H T ," Digital Control Systems," Prentice Hall, 1990.

end

Analytical Structures For Fuzzy Controllers

J. S. Saini[†], M. Gopal[*] And A. P. Mittal[†]
[†]Electrical Engg. Dept., C.R. State College of Engg., Murthal, Sonepat – 131 039 (India)
[*]Electrical Engg. Dept., Indian Institute of Technology., Hauz Khas, New Delhi – 110 016 (India)
[†]Instrumentation & Control Engg. Dept., N.S.I.T., Sector 3, Dwarka, New Delhi – 110 045 (India)
Email of the corresponding author: mgopal@ee.iitd.ernet.in

Abstract

This paper derives analytical structures of a class of fuzzy controllers employing generalized membership functions with cross points varying from 0 through 1. Specific cross point variations are shown, analytically and through simulation, to have no impact on control surfaces. It also advances a rationale for scaling, along with some fresh perspectives on denormalization.

Key words: Fuzzy controllers, t-norms, s-norms, membership grade (mg).

INTRODUCTION

Since the time Zadeh proposed a theory of fuzzy systems [1,2], there was an increasing euphoria about having found fuzzy control as essentially a nonlinear map. However, this myth was exploded by the pioneering works of Mac Vicar-Whelan [3], Tang et.al .[4] and Ying [5] who proved some Fuzzy Logic Controllers (FLCs) to be linear PI controllers. Another result, though less rigorous, related fuzzy controller to multilevel relay control [6]. The initial euphoria started waning with more researchers contributing on similar lines [7-12].

Despite increased functional interpretability, structural obscurity of FLCs made it difficult to make out, precisely, analytically and objectively, the causes (nonlinearity and variable gains) of superior performance of FLCs with certain combinations of operators (t-norms, s-norms), membership functions (mfs), etc. The fundamental difficulty in fuzzy control is that analytical structure is unavailable even after FLC is constructed. Thus, FLCs are usually studied in an approximate manner and at best through computer simulations. Without unveiling their analytical structure, fuzzy control design largely proceeds on rules of thumb and thus more of an art, rather than in the spirit of conventional control design. Analytical exploration is thus necessary to convincingly support the claims that FLCs are more robust than the industrially dominant PID controllers or other types and also to provide definitive basis for design and analysis.

The main contribution of this paper is to derive analytical structures of an FLC with generalized mfs having variable cross points (CPs); besides advancing a rationale for scaling and some fresh perspectives on denormalization. Specific CP variations are shown, analytically and by simulation, to have no impact on control surfaces. This paper thus aims at generalizing the analyses presented in previous related research, as some impractical assumptions (such as uniformly distributed triangular mfs for input variables) made in earlier papers [7-11] have reduced their significance and applicability.

RATIONALE FOR NORMALIZATION AND DENORMALIZATION

The configuration of FLC has been well documented, refined and illuminated by several researchers, so a basic familiarity is assumed; however, the unfamiliar reader is referred to [13].

Normalization is the process of multiplying physical inputs with normalization factors so that inputs are mapped onto normalized input domain. Denormalization is the multiplication of defuzzified normalized control outputs with denormalization factors so that such outputs are mapped onto physical control output domain. The following example illustrates part of the rationale:

A level of 75m in a tank of 100m height may be classed as 'high' but the same level in a tank of 200m height would usually be classed as 'low' or "medium". However, such tanks can have same process dynamics (as determined by time constants, etc.) and hence controllable by same set of fuzzy control rules, even though physical Universes of Discourse (UODs) for the two tanks are different; [0, 100m] for the former and [0, 200m] for the latter. Without endangering the underlying linguistic meaning, broader shapes of similar fuzzy sets need be used for the latter case. However,

rather than altering the shape (in particular, base width) of fuzzy sets each time the FLC is applied to a smaller or bigger version of a problem, it is economical to use a common UOD, say [–L, L] or [0, 1]. Physical UOD can then be mapped onto normalized UOD with scaling factors. Thus fuzzification, inferencing and defuzzification can be designed independently of physical input and output domains, leading to better portability of FLCs – a major advantage of scaling.

Secondly, within the same problem, for several inputs spread over different physical UODs, a single fuzzy set (thus, a common UOD) can be used by choosing different input scaling factors, provided, of course, that shape of fuzzy sets for all inputs is same in all respects except for base-widths.

Let,

Scaled or Normalized Error, $E(n) = K_e\, e(n)$ (1)

Scaled or Normalized Rate, $R(n) = K_r\, r(n)$ (2)

Scaled/ Denormalized Control Output, $U(n)=K_u\, u(n)$ (3)

Here $e(n)\in[-l_e, l_e]$, $r(n)\in[-l_r, l_r]$, $U(n)\in[-l_u, l_u]$; square bracket terms represent physical UODs. $E(n)$ and $R(n)\in[-L, L]$, and $u(n)\in[-H, H]$; square bracket terms represent normalized UODs. Symbols take meanings as:

K_e = scaling factor for physical error variable e(n).
K_r = scaling factor for physical rate variable r(n).
K_u = scaling factor for normalized control output, u(n).
$K_{\Delta u}$ = scaling factor for incremental u(n) i.e. for $\Delta u(n)$.
l_e = max value of measured physical error.
l_r = max value of measured/computed physical rate.
l_u = max value of denormalized physical control action that can be exerted on actuators(s)/plant.
L = max value of normalized input variables.
H = max value of u(n) (defuzzified?). The question mark is addressed in 'further remarks on denormalization'.

Scaling involves a priori knowledge of input-output space. Physical input UODs need be so chosen that all permissible inputs be accommodated on them. Input scaling factors then should be such that all possible scaled inputs fall into corresponding scaled UODs. Thus we have: $K_e = L/l_e$ =(Range of normalized error)/(Range of physical error). $K_r=L/l_r$ =(Range of normalized rate)/ (Range of physical rate). On similar lines, $K_u=l_u/H$ =(Range of physical output)/(Range of normalized output). Note that there is no relation between H and L and, without loss of generality, each can be taken as 1.

Since input fuzzy sets are defined on scaled UODs, so scaling allows convenient manipulation of effective input fuzzification by altering scaling factors. Thereby, indeed weights given to particular variables are changed. Thus, although it seems that K_e, K_r etc. are constants based on maximum limits of UODs, yet these can be varied to certain extents to influence FLC's response. However, K_u variation runs a risk of exceeding physical UOD and if not properly selected/varied, it can lead to performance degradation, and also harm the actuators. Such risk for antecedents (by varying K_e, K_r etc.) although does not affect sensors etc., but if improperly selected/varied, can lead to performance degradation, as normalized UOD's full range is not utilized.

Further Remarks on Denormalization:

It is pertinent to address the following questions in denormalization's context:

a) Is it for a designer to spell out H first (before writing down rule base) or does it get known after inferencing?

b) Is normalized UOD for individual rule's consequent or for the defuzzified control action of all fired rules?

c) Defuzzified output is multiplied with K_u to get U(n) i.e. denormalized output,

$$U(n) = K_u * [\{\mu_1 u_1(n) + \mu_2 u_2(n) + \cdots + \mu_m u_m(n)\}/(\mu_1 + \mu_2 + \cdots + \mu_m)] \quad (4)$$

where m = number of rules fired at nth instant. Truly then, defuzzified normalized output (in square bracket) is mapped to physical UOD. On the other hand, one can not proceed without specifying UOD for individual rules' consequents before writing down rule base.

For a fuzzy rule, output fuzzy 'set' is always related to input fuzzy 'sets' in certain ways (depending upon experience/knowledge of the designer captured in the rule) i.e. normalized output $u(i, j) = V_{f(i, j)}$, where i, j are indices of fuzzy sets for antecedents and f(i, j) is index of fuzzy set for consequent. The designer has to express this function $V_{f(i, j)}$ himself, of course. A typical rule is:

$$\text{If } E(n) \text{ is } \tilde{A}_i \text{ AND } R(n) \text{ is } \tilde{B}_j \text{ then } u(n) \text{ is } V_{f(i, j)} \quad (5)$$

However, UOD for individual rule's consequent does not call for any relationship with input UOD (which implies that H is unrelated to either L or to l_e (or l_r etc.) permitting UOD for consequent of individual rules to be specified on pure convenience, say [0, 1]. So, input UOD has no numeric bearing on output UOD for individual rules. What is required is that this normalized UOD for individual rules be mapped to physical domain. But, what is being done is mapping of 'defuzzified' normalized output to the physical UOD. The controversy is resolved as:

Specification of output UOD for individual rules is more stringent than the one for defuzzified output. This is due to the fact that defuzzification only mellows the output, as defuzzified output $\leq$ max(contributions from individual rules) irrespective of defuzzifier algorithm. Observe that only in the case when input is extreme, just one rule is invoked, calling for extreme output bordering on UOD. Hence, it is sufficient to specify UOD for the consequent of

individual rules, even though it be the defuzzified output being multiplied with K_u to get denormalized value U(n).

INTRODUCING NONLINEARITIES IN FUZZY RULES

Asymmetry in fuzzy control table about either or both diagonals leads to nonlinear control, provided no other nonlinearity (e.g. in fuzzy set shapes or through cross points) exists, as otherwise two nonlinearities may counteract to produce overall linear control. Another method, although more global than table asymmetry, is to distribute output fuzzy sets asymmetrically over the output UOD. Observe that there are more free levers (entries in control table) to introduce nonlinearity in specific regions if similar output fuzzy sets are not combined through 'OR' operation.

GENERALIZED MEMBERSHIP FUNCTIONS

Define Cross Point (CP) as a point where $\mu_i(x) = \mu_{i+1}(x)$, where 'i' is index of fuzzy set. Note that CP is different from Cross Over Point (COP) which is defined in literature as a point where $\mu_i(x) = 0.5$. In most papers [5, 7-9], CP =0.5 =COP, allowing only a restricted characterization of mfs and resulting structures. To impart complete generality to mfs that allow CP-variation from 0 through 1 and also allow asymmetrical mfs through suitable choice of Left Top (LT), Left Foot (LF), Right Top (RT) and Right Foot (RF), we choose mfs of shapes shown in Fig.1; also shown is the division of E(n)-R(n) input space into different Input Combination (IC) regions, each affording a different analytical expression. CP variation can be had in one of the following four ways:

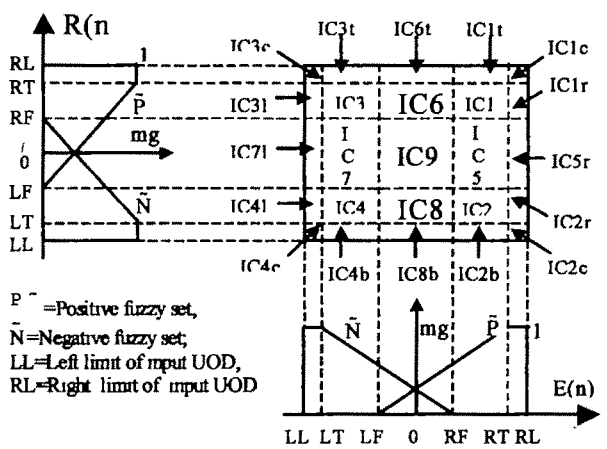

Fig. 1: Division of E(n)-R(n) input space into different Input Combination (IC) regions.

i. Fix LF & RF at LL & RL resp. and vary LT∈[LL,0] & RT∈[RL,0] implying CP∈[0.5,1];
ii. Fix LT & RT at LL & RL resp. and vary LF∈[0,LL] & RF∈[0,RL] implying CP∈[0,0.5];
iii. Fix LF & RF at values in the intervals ∈(LL,0] and ∈(RL,0] resp. and then vary LT∈[LL,0] and RT∈[RL,0] implying CP∈[x,1], where $0 \le x < 0.5$ depending upon LF & RF, but note that if LF=RF=0, then CP=0 and no variation in CP occurs even for full variation, as above, in LT & RT;
iv. Fix LT & RT at values in the intervals ∈(LL,0] & ∈(RL,0] resp. and then vary LF∈[0,LL] & RF∈[0,RL] implying CP∈[0,y], where $0.5 < y \le 1$ depending upon LT & RT, but note that if LT=RT=0, then CP=1 and no variation in CP occurs even for full variation, as above, in LF & RF.

Define the mfs as:

$\mu_{\tilde{P}}(E) = 0;$ $LL \le E(n) \le LF$
$= (K_e e(n)-LF)/(RT-LF);$ $LF \le E(n) \le RT$
$= 1;$ $RT \le E(n) \le RL$
$\mu_{\tilde{N}}(E) = 1;$ $LL \le E(n) \le LT$
$= (-K_e e(n)+RF)/(RF-LT);$ $LT \le E(n) \le RF$
$= 0;$ $RF \le E(n) \le RL$
$\mu_{\tilde{P}}(R) = 0;$ $LL \le E(n) \le LF$
$= (K_r r(n)-LF)/(RT-LF);$ $LF \le E(n) \le RT$
$= 1;$ $RT \le E(n) \le RL$
$\mu_{\tilde{N}}(E) = 1;$ $LL \le E(n) \le LT$
$= (-K_r r(n)+RF)/(RF-LT);$ $LT \le E(n) \le RF$
$= 1;$ $RF \le E(n) \le RL$

Next section takes up a specific configuration for deriving analytical structures for fuzzy controllers.

ANALYTICAL STRUCTURE OF FLC WITH PRODUCT 'AND', FOUR LINEAR RULES, AND CENTROID DEFUZZIFIER

Degrees of Fulfillment (DOFs) for this configuration are first computed (omitted here for space considerations). With singleton outputs, four linear control rules are:

Table 3 Linear Control Rules Table

E(n) \ R(n)	$\tilde{P}$	$\tilde{N}$
$\tilde{P}$	−H	0
$\tilde{N}$	0	H

$\tilde{P}$ and $\tilde{N}$ represent Positive and Negative fuzzy sets. The incremental control actions computed via equation:

$$\Delta U(n) = K_{\Delta u} \cdot [DOF1 \cdot (-H) + 0 + 0 + DOF4 \cdot (H)] / [DOF1+DOF2+DOF3+DOF4] \quad (6)$$

are listed below for different ICs. For sake of brevity, 'e' and 'r' replace e(n) and r(n).

CASE - I: $CP \in [0,0.5]$

IC1, IC1r, IC1t & IC1c: $\Delta U(n) = -K_{\Delta u} \cdot H$= constant (7)

IC2, IC2r, IC2b, IC2c, IC3, IC3l, IC3t and IC3c: $\Delta U(n) = 0$ = constant (8)

IC4, IC4l, IC4b & IC4c: $\Delta U(n) = K_{\Delta u} \cdot H$= constant (9)

IC5 & IC5r: $\Delta U(n) = K_p(r) \cdot r(n) + K_{vos}(r)$; (10)

where $K_p(r) = -K_{\Delta u}K_r H/[(K_r r-LF)+\{(-K_r r+RF)\cdot(RT-LF)\}/(RF-LT)]$ is variable Proportional (P) gain, varying with r(n). Since r(n) varies with time, so $K_p(r)$ is also called dynamic Proportional gain. $K_{vos}(r) = K_{\Delta u}H \cdot LF/[(K_r r-LF)+\{(-K_r r+RF)\cdot(RT-LF)\}/(RF-LT)]$ is variable control offset changing with r(n).

$\Rightarrow$ nonlinear P-controller + variable control offset.

IC6, IC6t: $\Delta U(n)=K_i(e)\cdot e(n)+K_{vos}(e)$; where $K_i(e)= -K_{\Delta u} \cdot K_e H/[(K_e e-LF)+\{(-K_e e+RF)\cdot(RT-LF)\}/(RF-LT)]$ is variable Integral (I) gain, varying with e(n). Since e(n) varies with time, so $K_i(e)$ is also called dynamic Integral gain. $K_{vos}(r)=K_{\Delta u}H \cdot LF/[(K_e e-LF)+\{(-K_e e +RF)\cdot(RT-LF)\}/(RF-LT)]$ is variable control offset changing with e(n).

$\Rightarrow$ nonlinear I-controller + variable control offset.

IC7,IC7l: $\Delta U(n)=K_p(r)\cdot r(n)+K_{vos}(r)$; where $K_p(r)=-K_{\Delta u} \cdot K_r H/[(-K_r r+RF)+\{(K_r r-LF)\cdot(RF-LT)\}/(RT-LF)]$; & $K_{vos}(r) = K_{\Delta u}H \cdot RF/[(-K_r r+RF)+\{(K_r r-LF)\cdot (RF-LT)\}/(RT-LF)]$.

$\Rightarrow$ nonlinear P-controller + variable control offset.

IC8,IC8b: $\Delta U(n)=K_i(e)\cdot e(n)+K_{vos}(e)$; where $K_i(e)=-K_{\Delta u}K_e \cdot H/[(-K_e e+RF)+\{(K_e e-LF)\cdot(RF-LT)\}/(RT-LF)]$; & $K_{vos}(r) =K_{\Delta u}H \cdot RF/[(-K_e e+RF)+\{(K_e e-LF)\cdot(RF-LT)\}/(RT-LF)]$.

$\Rightarrow$ nonlinear I-controller + variable control offset.

IC9: $\Delta U(n)=K_p(e, r)\cdot r(n)+K_i(e, r)\cdot e(n)+K_{vos}(e,r)$; where $K_p(e,r)=K_{\Delta u}K_r H\{(RF-LT)^2LF-(RT-LF)^2RF\}/Den$; $K_i(e,r) =-K_{\Delta u}K_e H[K_r r\{(RF-LT)^2-(RT-LF)^2\}-(RF-LT)^2LF+(RT-LF)^2RF\}/Den$; and $K_{vos}(r)=-K_{\Delta u}H\{(RF-LT)^2-(LF)^2 -(RT-LF)^2(RF)^2\}/Den$; & where $Den=\{(RF-LT)(K_r r-LF) +(RT-LF)(-K_r r+RF)\}\{(RF-LT)(K_e e-LF)+(RT-LF)(-K_e e+ RF)\}$.

$\Rightarrow$ nonlinear PI controller + variable control offset.

All above statements regarding FLC's behaviour in specific regions hold only in the general case of asymmetrical mfs placed asymmetrically, for in the particular cases some simplifications do emerge as noted ahead. Also, note from Fig.1 that CP and mf are not uniquely related in that a particular CP can be attained through several mfs e.g. a CP=0.5 is obtainable through any of following pairs of fuzzy sets: $[\tilde{N},\tilde{P}]$= [(LT,RF); (LF,RT)] =[-(100,100);(-100,100)] or [(-80,80); (-80,80)], or [(-10, 10);(-10,10)], etc. We term the first pair as full-variation (fv) mf and the rest of pairs as partial-variation (pv) mfs. Take H=100, $K_{\Delta u}=K_r=K_e=1$.

Observations & Simplifications (for $CP \in [0,0.5]$):

1. A global linear PI controller results with CP=0.5 but only if obtained by symmetrical fv mfs placed symmetrically. IC9 expands to occupy entire E(n)-R(n) space. So, expression for IC9 alone needs to be examined with LL=LT=LF; RF=RT=RL; RF=-LF:

$K_p(e,r)= -K_{\Delta u}K_r H/(RF-LF)=K_p$; $K_i(e,r)= -K_{\Delta u}K_e H/(RF-LF) =K_i$; $K_{vos}(r)=-K_{\Delta u}H(LF^2-RF^2)/(RF-LF)^2=0$ (11)

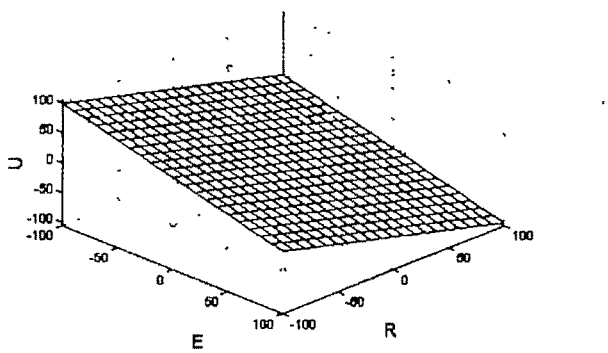

Fig. 2: Global linear PI control surface with CP=0.5; obtained by fv mf.

2. A piecemeal linear controller results with CP=0.5 but only if obtained by symmetrical pv mfs placed symmetrically. Inner linear region represents IC9, so equations in (11) are applicable except that $LF(=LT) \in (LL,0)$ and $RF(=RT) \in (RL,0)$, implying this region represents linear PI action but with constant offset (as $LF \neq -RF$). Regions IC1 to IC8 as such vanish, other regions merge, requiring analytical expressions only for IC5r, IC6t, IC7l, IC8b, IC1c,..., IC4c to be examined:

IC5r: $\Delta U(n) = -K_{\Delta u}K_r H \cdot r(n)/2RF - K_{\Delta u}H/2 = K_p r(n)+K_{os}$;

$\Rightarrow$ Linear P-controller + constant control offset.

IC6t: $\Delta U(n) = -K_{\Delta u}K_e H \cdot e(n)/2RF - K_{\Delta u}H/2 = K_i e(n)+K_{os}$;

$\Rightarrow$ Linear I-controller + constant control offset.

IC7l: $\Delta U(n) = -K_{\Delta u}K_r H \cdot r(n)/2RF + K_{\Delta u}H/2 = K_p r(n)+K_{os}$;

$\Rightarrow$ Linear P-controller + constant control offset.

IC8b: $\Delta U(n)= -K_{\Delta u}K_e H \cdot e(n)/2RF + K_{\Delta u}H/2= K_i e(n)+K_{os}$;

$\Rightarrow$ Linear I-controller + constant control offset.

IC1c to IC4c: $\Delta U(n)= -K_{\Delta u}H$, 0, 0 & $-K_{\Delta u}H$ respectively.

$\Rightarrow$ Constant control action surfaces.

3. For symmetrical mfs placed symmetrically, CP variation $\in [x,0.5]$ had by varying $LT \in [LL,LF]$ and $RT \in [RL,RF]$ but for fixed value of $LF \in [LL,0]$ and fixed value of $RF \in [RL,0]$ has no impact on control surface, for the rea-

son that expressions for this case are all independent of LT and RT. Thus, same piecemeal linear control surfaces are obtained (Fig.3) as the ones for particular values of LF and RF even when CP is varied as stated.

4. For symmetrical mfs placed asymmetrically, CP variation $\in$[x,0.5] had by varying LT$\in$[LL,LF] and RT$\in$ [RL,RF] but for fixed value of LF$\in$[LL,0] and RF $\in$[RL, 0] has no impact on control surface, as explained above, as RF-LT=RT-LF holds good for this case. So, same inferences hold as at sr. no. 3 above, except that piecemeal linear regions are placed asymmetrically w.r.t. (0,0,0) of UOD and same slope regions are of different areas.

5. For CP=0, FLC behaves as a multi-level relay.

CASE – II: CP $\in$(0.5,1]

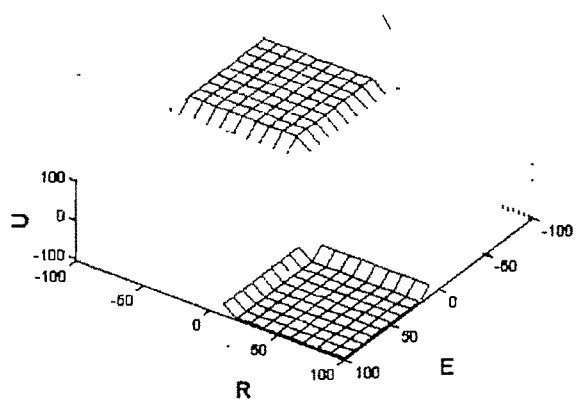

Fig. 3: Piecemeal linear control surface with CP=0 5; (same for CP$\in$[x, 0.5]) obtained by symmetrical pv mfs.

For obtaining this CP range, $|LT| < |LF|$, RT<RF; LF $\in$[LL,0); RF$\in$[RL,0); LT$\in$(LL,0]; RT$\in$(RL,0]. Incremental control actions computed for different ICs are:

IC1: $\Delta U(n) = K_p(e,r)\cdot r(n) + K_r(e,r)\cdot e(n) + K_{vos}(e,r)$: where $K_p(e,r) = -K_{\Delta u}K_rH\cdot RF/Den$; $K_r(e,r) = K_{\Delta u}K_eH(K_rr-RF)/Den$; $K_{vos}(r) = K_{\Delta u}H\{(RF)^2-(RF-LT)^2\}/Den$; & where Den= (RF-LT)(-$K_e$e-$K_r$r+3RF-LT)+(-$K_e$e+RF)·(-$K_r$r+RF).

$\Rightarrow$ nonlinear PI controller + a variable control offset.

IC2: $\Delta U(n) = K_p(e, r)\cdot r(n) + K_r(e, r)\cdot e(n) + K_{vos}(e,r)$; where $K_p(e,r) = -K_{\Delta u}K_rH\cdot(RF-LT)/Den$; $K_r(e,r) = -K_{\Delta u}K_eH\cdot(RT-LF)/Den$; $K_{vos}(r) = K_{\Delta u}H(RF\cdot RT-LF\cdot LT)/Den$; & where Den=(RT-LF)(RF-LT)+(K_rr-LF)(RF-LT)+(-K_ee +RF)(RT-LF)+(-K_ee+RF)(K_rr-LF).

$\Rightarrow$ nonlinear PI controller + a variable control offset.

IC3: $\Delta U(n) = K_p(e, r)\cdot r(n) + K_r(e, r)\cdot e(n) + K_{vos}(e,r)$; where $K_p(e,r) = -K_{\Delta u}K_rH\cdot(RT-LF)/Den$; $K_r(e,r) = -K_{\Delta u}K_eH\cdot(RF-LT)/Den$; $K_{vos}(r) = K_{\Delta u}H(RF\cdot RT-LF\cdot LT)/Den$; & where Den=(RT-LF)(RF-LT)+(K_rr-LF)(RF-LT)+(-K_ee+RF)(RT-LF)+(-K_ee+RF)(K_rr-LF).

$\Rightarrow$ nonlinear PI controller + a variable control offset.

IC4: $\Delta U(n) = K_p(e, r)\cdot r(n) + K_r(e, r)\cdot e(n) + K_{vos}(e,r)$ where $K_p(e,r) = K_{\Delta u}K_rH\cdot LF/Den$; $K_r(e,r) = -K_{\Delta u}K_eH(K_rr-LF)/Den$; $K_{vos}(r) = K_{\Delta u}H\{(RT-LF)^2-(LF)^2\}/Den$; & where Den = (RT-LF)($K_e$e+$K_r$r-3LF+RT)+($K_e$e-LF)·($K_r$r-LF).

$\Rightarrow$ nonlinear PI controller + a variable control offset.

IC1r: $\Delta U(n) = -K_{\Delta u}H(RF-LT)/(2RF-LT-K_rr)$;

$\Rightarrow$ nonlinear control varying with r(n) alone.

IC1t: $\Delta U(n) = -K_{\Delta u}H(RF-LT)/(2RF-LT-K_ee)$;

$\Rightarrow$ nonlinear control varying with e(n) alone.

IC1c: $\Delta U(n) = -K_{\Delta u}H$ = constant

IC2r: $\Delta U(n) = K_p(r)\cdot r(n) + K_{vos}(r)$; where $K_p(r) = -K_{\Delta u}K_rH/(RT-2LF+K_rr)$; & $K_{vos}(r) = K_{\Delta u}H\cdot LF/(RT-2LF+K_rr)$;

$\Rightarrow$nonlinear P-control + a variable control offset.

IC2b: $\Delta U(n) = K_r(e)\cdot e(n) + K_{vos}(e)$; where $K_r(e) = -K_{\Delta u}K_eH/(2RF-LT-K_ee)$; & $K_{vos}(e) = K_{\Delta u}H\cdot RF/(2RF-LT-K_ee)$;

$\Rightarrow$nonlinear I-control + a variable control offset.

IC2c: $\Delta U(n) = 0$ = constant

IC3l: $\Delta U(n) = K_p(r)\cdot r(n) + K_{vos}(r)$; where $K_p(r) = -K_{\Delta u}K_rH/(2RF-LT-K_rr)$; & $K_{vos}(r) = K_{\Delta u}H\cdot RF/(2RF-LT-K_rr)$

$\Rightarrow$ nonlinear P-control + a variable control offset.

IC3t: $\Delta U(n) = K_r(e)\cdot e(n) + K_{vos}(e)$; where $K_r(e) = -K_{\Delta u}K_eH/(RT-2LF+K_ee)$; & $K_{vos}(e) = K_{\Delta u}H\cdot LF/(RT-2LF+K_ee)$;

$\Rightarrow$ nonlinear I-control + variable control offset.

IC3c: $\Delta U(n) = 0$ = constant

IC4l: $\Delta U(n) = K_{\Delta u}H(RT-LF)/(RT-2LF+K_rr)$;

$\Rightarrow$ nonlinear control varying with r(n) alone.

IC4b: $\Delta U(n) = K_{\Delta u}H(RT-LF)/(RT-2LF+K_ee)$;

$\Rightarrow$ nonlinear control varying with e(n) alone.

IC4c: $\Delta U(n) = K_{\Delta u}H$ = constant.

Note: Above expressions of Case-II cannot be simplified further, however, following ones are simplified (under 'Simplification' headings) for symmetrical mfs placed symmetrically, using RF-LT=RT-LF and –LF= RF.

IC5: $\Delta U(n) = K_p(e,r)\cdot r(n) + K_r(e,r)\cdot e(n) + K_{vos}(e,r)$; where $K_p(e,r) = -K_{\Delta u}K_rH\cdot\{(RF-LT)^2+RF(RT-LF)\}/Den$; $K_r(e,r) = K_{\Delta u}K_eH(RT-LF)(K_rr-RF)/Den$; & $K_{vos}(r) = K_{\Delta u}H\{LF\cdot(RF-LT)^2 + RF^2(RT-LF)\}/Den$; and Den=($K_r$r-LF)(RF-LT)^2 +(-$K_r$r+RF)(RF-LT)(RT-LF) + (-$K_e$e+RF)($K_r$r-LF)· (RF-LT)+(-$K_e$e+RF)(-$K_r$r+RF)(RT-LF).

$\Rightarrow$ nonlinear PI controller + variable control offset.

Simplification: $\Delta U(n) = K_pr(n) + K_r(e)\cdot e(n) + K_{vos}(e)$; where $K_p = -K_{\Delta u}K_rH/2RF$ =constant; $K_r(e) = -K_{\Delta u}K_eH/2(2RF-LT-K_ee)$; $K_{vos}(e) = K_{\Delta u}H\cdot LT/2(2RF-LT-K_ee)$; $\Rightarrow$ linear P-controller+nonlinear I-controller +variable control offset.

IC5r: $\Delta U(n) = K_p(r)\cdot r(n) + K_{vos}(r)$; where $K_p(r) = -K_{\Delta u}K_rH\cdot(RF-LT)/Den$; $K_{vos}(r) = K_{\Delta u}H\cdot LF(RF-LT)/Den$; and Den

$=(K_r r-LF)(RF-LT)+(-K_r r+RF)(RT-LF)$; $\Rightarrow$ nonlinear P-controller + variable control offset.

Simplification: $\Delta U(n)=K_p r(n)+K_{os}$; where $K_p= -K_{\Delta u}K_r H/2RF$; $K_{os}=-K_{\Delta u}H/2$; $\Rightarrow$linear P-controller+constant offset.

IC6: $\Delta U(n)=K_p(e,r)\cdot r(n)+K_i(e,r)\cdot e(n)+K_{vos}(e,r)$; where $K_p(e,r)=K_{\Delta u}K_r H(RT-LF)(K_e e-RF)/Den$; $K_i(e,r)=-K_{\Delta u}K_e H\cdot\{(RF-LT)^2+RF(RT-LF)\}/Den$; $K_{vos}(r)=K_{\Delta u}H\{(LF(RF-LT)^2+RF^2(RT-LF)\}/Den$; and $Den=(K_e e-LF)(RF-LT)^2+(-K_e e+RF)(RF-LT)(RT-LF)+(-K_r r+RF)(K_e e-LF)(RF-LT)+(-K_e e+RF)(-K_r r+RF)(RT-LF)$; $\Rightarrow$nonlinear PI controller + variable control offset.

Simplification: $\Delta U(n)=K_p(r)\cdot r(n)+K_i e(n)+K_{vos}(r)$; where $K_p(r)= -K_{\Delta u}K_r H/2(2RF-LT-K_r r)$; $K_i= -K_{\Delta u}K_e H/2RF$; $K_{vos}(r) = K_{\Delta u}H\cdot LT/2(2RF-LT-K_r r)$; $\Rightarrow$ nonlinear P-controller + linear I-controller + variable control offset.

IC6t: $\Delta U(n)=K_i(e)\cdot e(n)+K_{vos}(e)$; where $K_i(e)= -K_{\Delta u}K_e H\cdot(RF-LT)/Den$; $K_{vos}(e)=K_{\Delta u}H\cdot LF(RF-LT)/Den$; $Den=(K_e e-LF)(RF-LT)+(-K_e e+RF)(RT-LF)$.

$\Rightarrow$ nonlinear I-controller+variable control offset.

Simplification: $\Delta U(n)=K_i e(n)+K_{os}$; where $K_i=-K_{\Delta u}K_e H/2RF$; $K_{os}=-K_{\Delta u}H/2$; $\Rightarrow$linear I-controller+constant offset.

IC7: $\Delta U(n)=K_p(e,r)\cdot r(n)+K_i(e,r)\cdot e(n)+K_{vos}(e,r)$; where $K_p(e,r)= -K_{\Delta u}K_r H\{(RT-LF)^2-LF(RF-LT)\}/Den$; $K_i(e,r) = K_{\Delta u}K_e H(RF-LT)(-K_r r+LF)/Den$; $K_{vos}(r)=K_{\Delta u}H\{RF(RT-LF)^2-(LF)^2(RF-LT)\}/Den$; and $Den=(-K_r r+RF)(RT-LF)^2+(K_r r-LF)(RT-LF)(RF-LT)+(K_e e-LF)(K_r r-LF)(RF-LT)+$ ~~$(K_e e-LF)(-K_r r+RF)(RT-LF)$~~; ~~$\Rightarrow$ nonlinear PI controller + variable control offset.~~

Simplification: $\Delta U(n)=K_p r(n)+K_i(e)\cdot e(n)+K_{vos}(e)$; where $K_p = -K_{\Delta u}K_r H/2RF$ =constant; $K_i(e)= -K_{\Delta u}K_e H/2(2RF-LT+K_e e)$; $K_{vos}(e)= -K_{\Delta u}H\cdot LT/2(2RF-LT+K_e e)$; $\Rightarrow$ linear P-controller+nonlinear I-controller+variable control offset.

IC7l: $\Delta U(n)=K_p(r)r(n)+K_{vos}(r)$; where $K_p(r)= -K_{\Delta u}K_r H\cdot(RT-LF)/Den$; $K_{vos}(r) = K_{\Delta u}H\cdot RF(RT-LF)/Den$; and $Den = (K_r r-LF)(RF-LT)+(-K_r r+RF)(RT-LF)$; $\Rightarrow$ nonlinear P-controller + variable control offset.

Simplification: $\Delta U(n)=K_p r(n)+K_{os}$; where $K_p= -K_{\Delta u}K_r H/2RF$; $K_{os}=K_{\Delta u}H/2$; $\Rightarrow$linear P-controller+constant offset.

IC8: $\Delta U(n)=K_p(e,r)\cdot r(n)+K_i(e,r)\cdot e(n)+K_{vos}(e,r)$; where $K_p(e,r)=K_{\Delta u}K_r H(RF-LT)(-K_e e+LF)/Den$; $K_i(e,r)= -K_{\Delta u}K_e\cdot H\{(RT-LF)^2-LF(RF-LT)\}/Den$; $K_{vos}(r) = K_{\Delta u}H\{(RF(RT-LF)^2-(LF)^2(RF-LT)\}/Den$; and $Den=(-K_e e+RF)(RT-LF)^2+(K_e e-LF)(RT-LF)(RF-LT)+(K_e e-LF)(K_r r-LF)(RF-LT)+(K_r r-LF)(-K_e e+RF)(RT-LF)$; $\Rightarrow$ nonlinear PI controller + variable control offset.

Simplification: $\Delta U(n)=K_p(r)\cdot r(n)+K_i\cdot e(n)+K_{vos}(r)$; where $K_p= -K_{\Delta u}K_r H/2(2RF-LT+K_r r)$; $K_i(e)= -K_{\Delta u}K_e H/2RF$; $K_{vos}(e)= -K_{\Delta u}H\cdot LT/2(2RF-LT+K_r r)$; $\Rightarrow$ nonlinear P-controller + linear I-controller + variable control offset.

IC8b: $\Delta U(n)=K_i(e)e(n)+K_{vos}(e)$; where $K_i(e)= -K_{\Delta u}K_e H\cdot(RT-LF)/Den$; $K_{vos}(r) = K_{\Delta u}H\cdot RF(RT-LF)/Den$; & $Den=(K_e e-LF)(RT-LF)+(-K_e e+RF)(RF-LT)$; $\Rightarrow$ nonlinear I-controller + variable control offset.

Simplification: $\Delta U(n)=K_i\cdot e(n)+K_{os}$; where $K_i= -K_{\Delta u}K_e H/2RF$; $K_{os} = K_{\Delta u}H/2$; $\Rightarrow$linear I-controller +constant offset.

IC9: $\Delta U(n)=K_p(e,r)\cdot r(n)+K_i(e,r)\cdot e(n)+K_{vos}(e,r)$; where $K_p(e,r = -K_{\Delta u}K_r H\{RF(RT-LF)^2-LF(RF-LT)^2/Den$; $K_i(e,r) = K_{\Delta u}K_e H\{(RT-LF)^2(K_r r-RF)-(RF-LT)^2(K_r r-LF)\}/Den$; $K_{vos}(r)=K_{\Delta u}H\{(RF)^2(RT-LF)^2-(LF)^2(RF-LT)^2\}/Den$; & $Den=(K_e e-LF)(K_r r-LF)(RF-LT)^2+(K_e e-LF)(-K_r r+RF)\cdot(RT-LF)(RF-LT)+(-K_e e+RF)(K_r r-LF)(RF-LT)(RT-LF)+(-K_r r+RF)(-K_e e+RF)(RT-LF)^2$.

$\Rightarrow$ nonlinear PI controller + variable control offset.

Simplification: $\Delta U(n)=K_p r(n)+K_i e(n)$; where $K_p=-K_{\Delta u}K_r\cdot H/2RF$; $K_i(e)= -K_{\Delta u}K_e H/2RF$; $\Rightarrow$linear PI-controller.

Observations (for CP$\in$(0.5,1]):

1. Constant control surfaces (ΔU= -100 or 0 or 100) appear only if LF and/or RF < |LL or RL|; size of these surfaces being affected only by LF and RF, and not by LT and RT.
2. LF and RF as well as LT and RT affect the nonlinearity of control surfaces (excepting that of IC9, as it represents linear surface for symmetrical mfs).
3. Degree of nonlinearity, excepting in constant ΔU surfaces, increases as CP is increased above 0.5 (Figs. 4, 5).
4. The control actions switch smoothly between different regions. This remark applies to Case-I too.

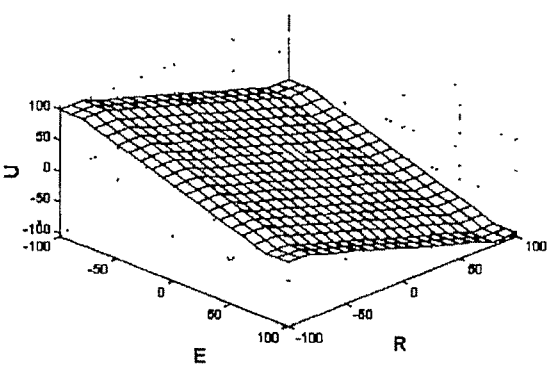

Fig. 4: Control surface with CP=0.67; obtained by symmetrical mfs placed symmetrically; (LT,RF)= (-40,80); (LF,RT)=(-80,40).

CONCLUSIONS

With the above mathematical analysis and the shown control surfaces, FLCs no more remain a black-box enigma. A simple yet powerful lever, in the shape of CP variation, has been introduced for FLCs, in that it yields a rich variety of control surfaces – from multilevel relay through linear to

nonlinear. Equivalence between FLCs and linear/ nonlinear P, I, PI controllers etc. has been established. Further, there is a word of caution for the case of symmetrical mfs placed symmetrically, as CP variation $\in$[x,0.5] had by varying LT$\in$[LL,LF] and RT$\in$[RL,RF] but for fixed value of LF$\in$[LL,0] and fixed value of RF$\in$[RL,0] has no impact on control surface, so if a Genetic Algorithm (GA) were designed to do CP variation through levers of LT or RT (besides others), it can fall into a deceptive saturation/termination condition.

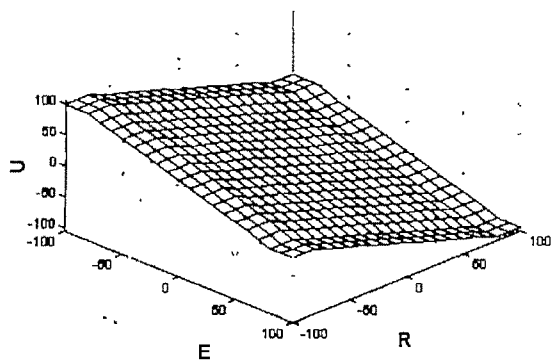

Fig. 5: Control surface with CP=0.89; obtained by symmetrical mfs placed symmetrically; (LT,RF)= (-10,80), (LF,RT)=(-80,10)

FUTURE DIRECTIONS

With the kind of generalized mfs introduced, behaviour of FLC under other combinations with different t-norms and s-norms needs to be explored. Control of processes with such FLCs needs to be evaluated in terms of time-domain specifications and other performance indices such as ISE, ITSE, etc.

REFERENCES

1. L.A. Zadeh, "Fuzzy sets," *Information and Control*, vol.8, pp.338-353, 1965.
2. L.A. Zadeh, "Outline of a new approach to the analysis of complex systems & decision processes," *IEEE Tr. on SMC*, vol.3, no.1, pp.28-44, 1973.
3. P.J. Mac Vicar-Whelan, "Fuzzy sets for man-machine interaction," *Int. J. Man Machine Studies*, vol.8, pp.687-697, Nov. 1976.
4. K.L. Tang & R.J. Mulholland, "Comparing fuzzy logic with classical controller designs," *IEEE Tr. SMC*, vol. SMC-17, no.6, pp.1085-1087, 1987.
5. H. Ying, "Analytical relationship between the fuzzy PID controllers and the linear PID controller," *Technical Report*, Dept. of Biomedical Engg., The Univ. of Alabama, Birmingham, Dec.8, 1987.
6. W.J.M. Kickert & E.H. Mamdani, "Analysis of a fuzzy logic controller," *Int. J. Fuzzy Sets & Syst.*, vol.1, pp.29-44, 1978.
7. J.J. Buckley & H.Ying, "Linear fuzzy controller: it is a linear non-fuzzy controller," *Information Sciences*, 51, pp.183-192, 1990.
8. A.E. Hajjaji & A. Rachid, "Explicit formulas for fuzzy controller," *Fuzzy Sets & Systems*, 62, pp.135-141, 1994.
9. H. Ying, W. Siler & J.J. Buckley, "Fuzzy control theory: a nonlinear case," *Automatica*, vol.26, no.3, pp.513-520, 1990.
10. H. Ying, "The simplest fuzzy controllers using different inference methods are different nonlinear PI controllers with variable gains," *Automatica*, vol.29, no.6, pp.1579-1589, 1993.
11. H. Ying, "Analytical structures of fuzzy controllers with linear control rules," *Information Sciences*, 81, pp.213-227, 1994.
12. C.-L. Chen et.al., "Theoretical Analysis of crisp-type fuzzy logic controllers using various t-norm sum-gravity inference methods," IEEE Tr. Fuzzy Syst.,vol.6, no.1, pp.122-136, Feb. 1998.
13. D. Driankov et.al., *An Introduction to Fuzzy Control*. N. Delhi: Narosa Pub. House, 1993.

Dynamics of driven Colpitts Oscillator

Prodyot Kumar Roy, Syamal Kumar Dana, *Member, IEEE*, Biswapriya Mukhopadhyay, Arijit Basuray, *Member, IEEE*

***Abstract*-The dynmics of Colpitts oscillator under the influence of sinusoidal forcing has been investigated here. Formation of torus and its breakdown to chaos has been observed when the Colpitts oscillator in periodically oscillating state is forced by external sinusoidal signal. The influence of amplitude and the frequency of the external signal have been stressed in this work. Results of both numerical and practical experiments are presented here.**

I. INTRODUCTION

For the past few decade physicists, mathematicians and engineers exerted great efforts on physical systems that exhibit complicated dynamics, called chaos. Electronic circuit is a rich source of such complex behavior of chaos.

In this paper, we focus on the working of a driven Colpitts oscillator. Colpitts oscillator is a well studied system as periodic oscillator in undergraduate studies. Development of such oscillators in chaotic regime and its synchronization is an active field of research in communication technology [1]. High frequency chaotic oscillators have immense potential for applications in secure communication. The Colpitts oscillator may produce periodic or chaotic oscillations [2] which depends upon the choice of circuit parameters. The circuit exhibits formation of torus and its breakdown to chaos under the influence of external periodic forcing, which again depend upon the amplitude and frequency of the forcing signal. In section II we have described the circuit scheme with its governing equations. Both the numerical and the experimental results are presented in section III&IV respectively. They are found in good agreement with PSPICE simulations. A summary is given, in the last section, with future prospects.

P.K.Roy is with Department of Physics, Presidency College, Kolkata 700073 (pkpresi@yahoo.com)
S.K.Dana is with Instrument Division, Indian Institute of Chemical Biology, Kolkata 700032, (sdana_ecsu@yahhoo.com)
B.Mukhopadhyay is with Jadavpur Vidyapith, Kolkata 700032
A.Basuray is with Neo Tele-Tronix Pvt. Ltd. (NTPL),Kolkata 700032 (ntpl@cal.vsnl.net.in)

II. DRIVEN COLPITTS OSCILLATOR

The driven Colpitts oscillator is shown in Fig.1. The inductor L with series resistance R is connected at the collector of the transistor. The emitter resistance R_1 is so chosen that the transistor is driven hard without damaging it. The capacitors C1 and C2 in the feedback path with the inductor L decide the frequency of the oscillator. The external periodic forcing is applied at the base of the transistor. The circuit equations are obtained, using Kirchoff's laws as given by,

$$C_1 \frac{dV_{C1}}{dt} = I_L - I_C \qquad (1a)$$

$$C_2 \frac{dV_{C2}}{dt} = I_L - I_C + I_E - I_R \qquad (1b)$$

$$L \frac{dI_L}{dt} = V_{CC} - V_{C1} - V_{C2} - I_R \qquad (1c)$$

where $I_E=I_s.\exp(V_{BE}/V_T-1)$, V_{BE} is the bas-emitter voltage and $V_T=KT/e$, e is the electronic charge and K is the Boltzman constant.

The effect of external periodic forcing is reflected in the base voltage as given by

$$V_{BE}=-V_{C2}+a.\sin(\omega t) \qquad (2)$$

The dimensionless form of the circuit equation is given as

$$\frac{dx}{d\tau} = Q k[z - \alpha\gamma \exp(-y'-1)] \qquad (3a)$$

$$\frac{dy}{d\tau} = Q(1-k)[z + (1-\alpha)\gamma \exp(y') - \rho(y + \frac{5}{V_T})] \qquad (3b)$$

$$\frac{dz}{d\tau} = -\frac{1}{Q}(x+y+z) \qquad (3c)$$

and $y' = (-y + a\sin(\omega_1\tau)/V_T)$

where $x=V_{C1}/V_T$, $y=V_{C2}/V_T$, $z=I_LR/V_T$ and $C=C_1k$, $k=C_2/(C_1+C_2)$, $\gamma=I_SR/V_T$, $\rho=R/R_1$, $t=\tau\sqrt{LC}$, $\omega_0=1/\sqrt{LC}$, , $\omega_1=\omega/\omega_0$, $Q=\omega_0L/R$ is the quality factor and ω_0 is the natural frequency of the oscillator.

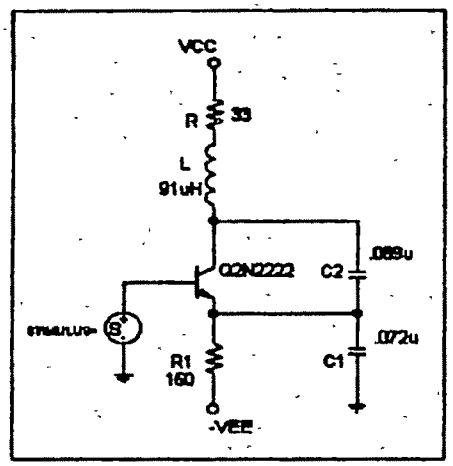

Fig.1 Experimental Circuit of Colpitts Oscillator

III NUMERICAL SIMULATION

For numerical simulations, 4th order Runge-Kutta algorithm is used with circuit parameters $L=120\mu H$, $R=33\Omega$, and $C_1=0.068\mu F$, $C_2=0.068\mu F$, $R_1=150\Omega$. A 2N2222A transistor is selected with base-emitter reverse saturation current $I_S=14.34\times10^{-15}$ and $V_T=27mV$. The Colpitts oscillator generates periodic oscillation without external forcing as shown in Fig.2a with its When a periodic forcing with amplitude $a=0.2$ and frequency $\omega_1=0.01$ is applied, the circuit shows a torus in the phase portrait in Fig.2b while it breakdown to chaos (Fig.2c) for sinusoidal amplitude $a=1.75$ at same frequency.

The Poincaré surface of section is taken at $y=-25$. The torus formation is confirmed by the $yp=f(xp)$ map in Fig.3a. xp and yp are the piercing points on the Poincaré surface of section. In Fig.3b breakdown to chaos is revealed by the random distribution of points in the Poincaré map.

IV EXPERIMETAL RESULTS

Experimental observations are presented here to verify the numerical results. The period-1 orbit without any external forcing is obtained as shown in the X-Y plot of CRO in Fig.4a. The

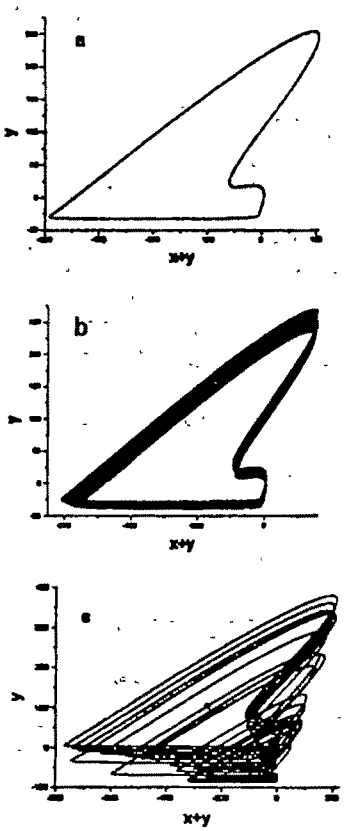

Fig.2 Phase portrait of x+y and x
(a) Period-1 (autonomous), (b) Torus Attractor (Forced), (c)Torus breakdown to chaos (forced)

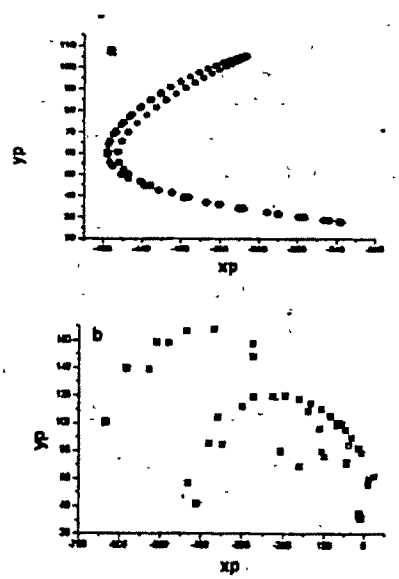

Fig.3 Poincaré map of xp and yp piercing of the attractor on the surface of section y= -25
(a) Torus formation (b) Breakdown to chaos

natural frequency of the autonomous oscillator has been measured as 86.2 kHz. When the circuit is forced by the sinusoidal signal with amplitude amplitude 0.2V and f=8.61kHz, the torus attractor is observed as shown in Fig.4b. Torus breaks down to chaos for changes in both the amplitude and frequency of the forcing signal. Fig.5a shows torus breakdown to chaos when the forcing frequency increased to 172.1kHz for the amplitude 0.2V. Torus attractor also breaks down to chaos even if the amplitude is increased to 1.75V keeping the forcing frequency unchanged at 8.6 1kHz as shown in Fig.5b.

a

b

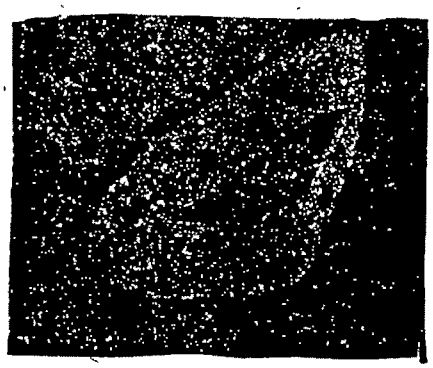

Fig.4 CRO X-Y Plots of emitter and collector voltage (a) Period-1 (b) Torus

V DISCUSSIONS

In real experiments, we have used commercially available components. The value of inductor is chosen as L=91uH with load resistance R=33ohm. The capacitors C_1=0.069uF and C_2=0.072uF and R_1=150ohm. The voltage at the emitter and collector of the transistor are taken as X-Y plots in CRO. The voltage at the collector is the sum of the voltages V_{C1} and V_{C2} across the capacitors C_1 and C_2 respectively,

a

b

Fig.5. CRO plot of Torus breakdown to chaos
(a) forcing amplitde=0.2V, frequency=172.1kHz
(b) forcing amplitde=1.75V, frequency=8.61kHz

which represents the x and y variables of the dynamical equations of Colpitts oscillator. The phase portraits in Fig.2 are thus plotted with x+y and y. Experimental observations are found in good agreement with numerical results except a kink that is present in the phase portraits of numerical results shown in Fig.2. The results are also checked with PSPICE circuit simulator and found perfectly in agreement with experiments.

REFERENCES

[1] L.M.Pecora, T.L.Carroll, G.A.Johnson, and D.J.Mar, Fundamentals of synchronization in chaotic systems, concepts, and applications, *Chaos*, vol.7, no.4, pp.520-543, 1997

[2] M.P.Kennedy, Chaos in Colpitts oscillator, *IEEE Trans. Ctr. Systs. CAS-I*, vol.41, no.11; pp.771-774, 1994

An Approach to the Design of a Low Cost PID Controller combined with Inverse Derivative Control Action

S. C. Bera and S. Chattopadhyay
Instrumentation Engineering Section, Applied Physics, University of Calcutta
92, Acharya Prafulla Chandra Road, Kolkata - 700 009
E-mail : sc0507@rediffmail.com

Abstract

A single PID controller in a process control loop may suffer from high frequency oscillations without offset or low frequency oscillation with offset. An inverse derivative control action can eliminate both these errors. In the present paper a low cost op.amp. based PID controller with inverse derivative control action has been described. Its transfer function has been derived and is found to be identical with the form already derived by other workers.It has been tested with a process plant analogue and the preliminary experimental results are reported in the paper.

Keywords : PID control, Inverse derivative control, Control parameters.

INTRODUCTION

In any process industry, the different process variables are maintained at the desired values by the operation of the different manual and automatic control loops in order to obtain the high quality product at lesser cost along with all the safety aspects of the plant operation and the PID controller [7],[8] is one of the most important components of any automatic control loop. The offset produced in the proportional controller due to load change is eliminated by the integral controller but this tends to increase the stabilisation time which may be minimised by the derivative control action. But in a very fast process the PI or PID control action may be excessively high enough which may lead to the high frequency oscillations of the process variable about the set point. This high frequency oscillation may be minimised by reducing the effective gain of the controller. In the case of a proportional controller the low frequency oscillation with offset may occur when a load change occurs in a process plant and this offset may be decreased by increasing the gain of the controller. The inverse derivative control action [1], [7] which is inversely related with the rate of change of deviation signal may be used in combination with P, PI or PID control action to achieve both these effects at high and low frequencies. Many works on the design and tuning of PID controllers are being reported. Isakson et. al. [5] have mentioned the non-functioning of derivative control action. W.L.Luyben has developed tuning methods with inverse derivative control action. In the present paper the design of a low cost IC based PID controller combined with inverse derivative control action has been reported. The transfer function of the whole network has been derived and is found to be identical with the standard form derived by the other workers [1], [7]. The function of this controller in an analogue process has been tested using a square wave signal. The preliminary experimental results are reported in this paper.

ANALYSIS

The inverse derivative control action is acheived along

with PID control action by means of an operational amplifier based circuit as shown in fig. 1 by using only two op-amps

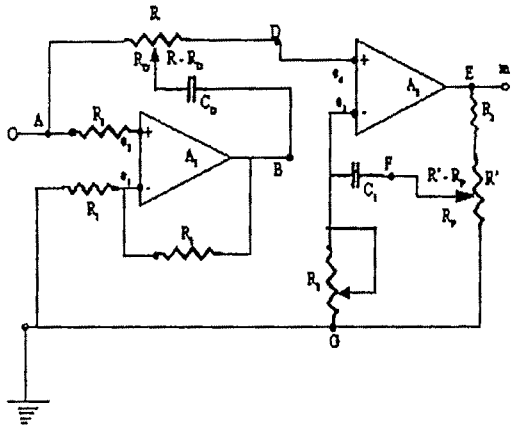

fig.1 : Circuit diagram of PID controller with inverse derivative control action.

If 'e' be the deviation signal at the input terminal A of the amplifier A_1 then the output signal 'V_B' at the output terminal B of the amplifier A_1 is obtained from the following analysis by the equation nos. (3) and (4).

Since the input impedance of the amplifier is high so the input signals 'e_1 ' and 'e_2' at the inverting and noninverting terminals respectively of the amplifier A_1 may be assumed to be identical.Again due to the high impedance negligible current passes through the input resistance R_1 from the input deviation signal. Hence the input signal 'e_2' at the noninverting terminal of A_1 will be almost equal to the input signal 'e'

$$\text{i.e.} \quad e_1 \approx e_2 \text{ and } e \approx e_2 \qquad (1)$$

Now,

$$e_1 = R_1 V_B / (R_1 + R_2) \qquad (2)$$

Hence,

$$e \approx e_1 = R_1 V_B / (R_1 + R_2)$$

$$V_B = (R_1 + R_2)\, e / R_1$$

$$\text{or} \quad V_B = \alpha\, e \qquad (3)$$

$$\text{Where } \alpha = (R_1 + R_2) / R_1 \qquad (4)$$

Hence the equivalent circuit of the network of amplifier A_1 between the terminals A & D may be as shown in fig. 2 and the Laplace transform of the circuit is given by

$$I(s) = [\, \alpha e(s) - e(s) \,] / (R_D + 1 / C_D s) \qquad (5)$$

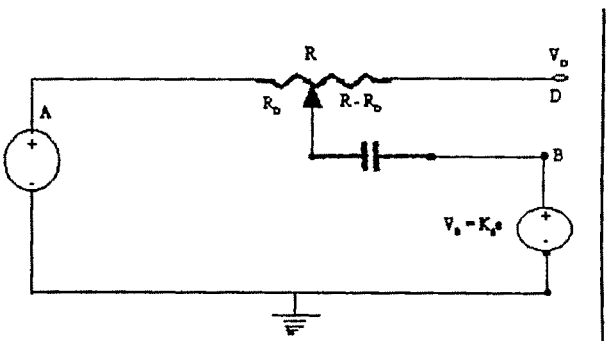

fig. 2 : Equivalent circuit of fig. 1.

Hence in the frequency plain the voltage signal at D will be given by

$$V_D(s) = e(s) + R_D I(s)$$

$$= e(s) + R_D [\, \alpha e(s) - e(s) \,] / (R_D + 1 / C_D s) \qquad (6)$$

or

$$V_D(s) = (1 + T_D s) / (1 + T_D s / \alpha) \qquad (7)$$

$$\text{Where } T_D = \alpha R_D C_D = (R_{12} + R_2) R_D C_D / R_1 \qquad (8)$$

Now this voltage signal is again input to the noninverting terminal of the second amplifier A_2 through the resistance R_D of the derivative potentiometer R. Since the current drawn by A_2 is negligbly small, so the voltage signal '$e_4(s)$' at the noninverting terminal of the amplifier A_2 will be approximately equal to $V_D(s)$.

$$\text{i.e.} \quad e_4(s) \approx V_D(s) \qquad (9)$$

Let the voltage signal at the output of the amplifier A_2 be 'm' and that at it's inverting input terminal be 'e_3'. Hence in the frequency plain, the voltage signal $V_F(s)$ at the point F of the circuit diagram as shown in fig.1 is given by

$$V_F(s) = R_p\, m(s)/(R_3 + R') = K\, m(s) \quad (10)$$

Where $K = R_p/(R_3 + R')$ (11)

This voltage is being discharged through R_I and C_I. Hence the voltage accross the capaciter C_I will be given by

$$V_F(s) - e_3(s) = V_F(s)/(1 + R_I C_I s)$$

or $$V_F(s) = [1 + 1/(R_I C_I s)]e_3(s) \quad (12)$$

From the equation nos. (9) and (11) we have the following equation (13).

$$K\, m(s) = (1 + 1/T_I s)e_3(s) \quad (13)$$

where $T_I = R_I C_I$ (14)

Now for the op-amp A_2 we have,

$$e_3(s) \gg e_4(s) \quad (15)$$

From the equation nos. (7), (9), (13) and (15)

$$K\, m(s) = (1 + 1/T_I s)(1 + T_D s)\, e(s)/(1 + T_D s/\alpha)$$

Thus the transferfunction of the controller circuit as shown in fig. 1 is given by

$$m(s)/e(s) = K_C (1 + 1/T_I s)(1 + T_D s)/(1 + T_D s/\alpha) \quad (16)$$

where $K_C = 1/K$

The above transfer function is identical with the transfer function of a PID controller with derivative control action derived by other investigators where the proportional constant 'K_C', integral action time 'T_I', derivative action time 'T_D' and dynamic gain a are given by

$$K_C = 1/K = (R_3 + R')/R_p, \quad T_I = R_I C_I,$$
$$T_D = \alpha R_D C_D \quad \text{and} \quad \alpha = (R_1 + R_2)/R_1. \quad (17)$$

EXPERIMENT

The preliminary experiment has been performed in order to test the operation of the controller as designed above. The control action signal has been passed through a series R-L circuit which is taken as a process plant analogue since it produces a time lag as in the case of an actual process plant. The signal obtained from the R-L circuit is compared with the input square wave signal to produced the deviation signal. This deviation signal is sent to the controller input. The controller output for the different values of controller parameters (K_C, T_I, T_D and α) are observed and the resulted waves are printed by a storage CRO. The preliminary waveforms are as shown in figs. 3(a)& 3(b).

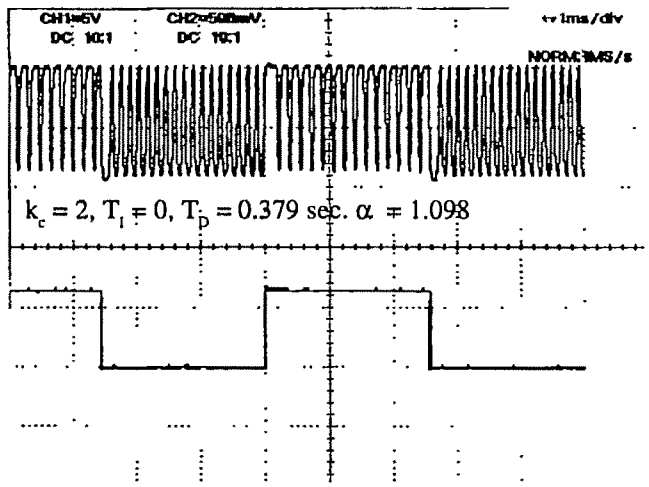

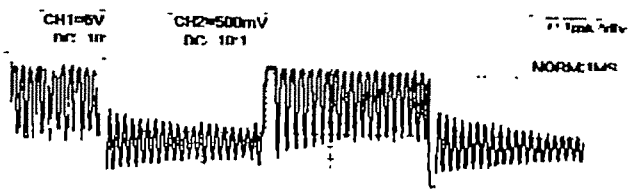

$k_c = 2$, $T_I = 1.841$ μ sec., $T_D = 0.379$ sec. $\alpha = 1.098$

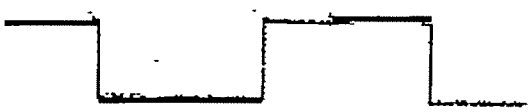

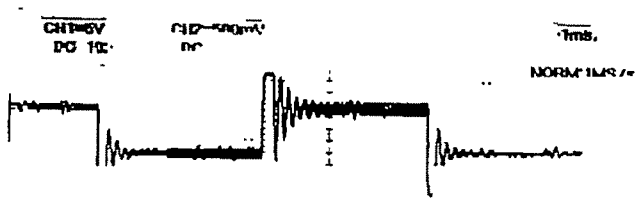

$k_c = 2$, $T_I = 2.367$ μ sec., $T_D = 0.379$ sec. $\alpha = 1.098$

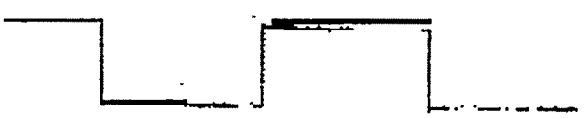

fig.3(a)

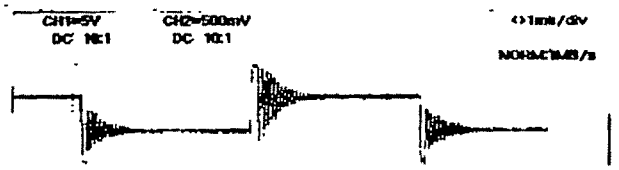

$K_C = 2$, $T_I = 0\mu$ sec, $T_D = 2.147$ sec, $\alpha = 1.15$

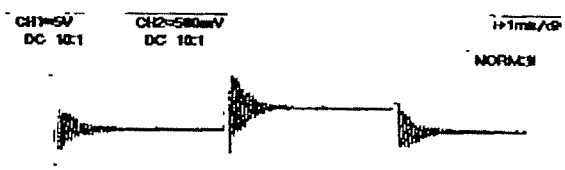

$K_C = 2$, $T_I = \mu$ sec, $T_D = 2.147$ sec, $\alpha = 1.2$

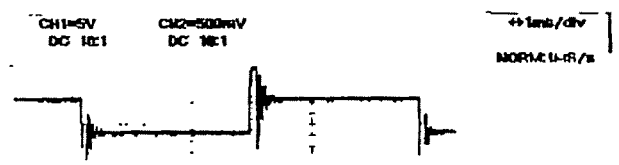

$K_C = 2$, $T_I = 0.263\mu$ sec, $T_D = 2.147$ sec, $\alpha = 1.15$

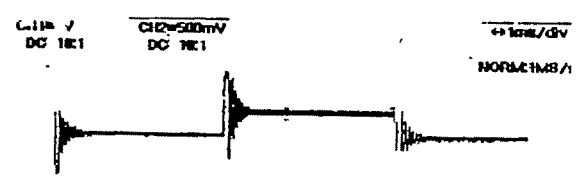

$K_C = 2$, $T_I = 0.131\ \mu$ sec, $T_D = 2.147$ sec, $\alpha = 1.2$

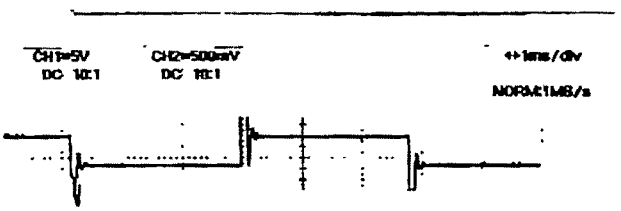

$K_C = 2$, $T_I = 1.315\mu$ sec, $T_D = 2.147$ sec, $\alpha = 1.15$

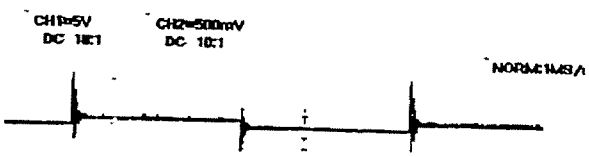

$K_C = 2$, $T_I = 0.131\ \mu$ sec, $T_D = 3.74$ sec, $\alpha = 2.0$

fig.3(b)

DISCUSSIONS

From the equation (17) it is found that the controller parameters K_C, T_I and $T_D$may be adjusted by the linear potentiometers R_P, R_I, R_D respectively and accordingly these parameter scales may be selected to be linear which will be easier to adjust the parameters during the tuning of the controller in a control loop in a process plant.The term '$1+T_Ds/\alpha$' in the denominator of the transfer function of the controller as shown in equation no (16) shows that this part of the transfer function of the controller is inversely related with the rate of change of deviation signal and hence it gives the inverse derivative control action.This term decreases the overall gain of the controller at high frequency and increases the overall gain of the controller at low frequency.Thus in a fast process where the process variable has a tendency to oscillate at a high frequency may be easily stabilised due to this decrease of overall gain by the inverse derivative control action. Similarly in a slow process where the low gain of a controller has a tendency to oscillate at a low frequency along with an offset, this inverse derivative control action may be used to reduce the offset since it increases the overall gain of the controller at low frequency.

From the equation no. (17) it is found that the adjustments of the controller parameters K_C, T_I and T_D by the potentiometer R_P, R_I and R_D for a given value of dynamic gain (α) are independent from each other.Hence it will be much easier to sellect any one or any combination of the control actions as demanded by a particuler process control loop. The cost of the controller will be very small since it involves only two operational amplifiers for all the modes of control action.

The experimental characteristic graphs of the controller as shown in figs. 3(a) & 3(b) reveal the satisfactory operation of the controller in process plant. A very good responce of the controller to the various parameters have been observed. Hence it may be concluded that the inverse derivative control action adjustable by the parameter (α) may be treated as an additional advantageous parameter of a controller so that the controller may be used in any type of process plant.It may be mentioned here that the experimental graphs as shown in figs.3(a) & 3(b) are arbitrarily selected only to show the performance of the controller and exact tunning analysis of the controller is under progress.

ACKNOWLEDGEMENT

The authors are thank full to the All India Council of Technical Education and MHRD, Govt. of India, since the present work is a part of the research project under the financial assistance of the AICTE (R&D) Project grant and MHRD (MODROB) Project grant and also the Department of Applied Physics for the facilities provided for the work.

REFERRENCES

1. William L.Luyben; ' effect of derivative algorithm and tuning selection on the PID control of Dead - time process ' Ind.Eng. Chem. Res. - 2001, vol. 40, no. 16, pp. 3605 - 3611.
2. Isaksson, A.J., Graebe, S.F., ' The derivative filter is an integral part of PID design.' presented at control system s 2000, Victoria, British, Coloumbia. May 2000.
3. Ziegler, T.E., Nichols, N.B., 'Optimum settings for automatic controller.' Trans. ASME. 1942.nov. 759.
4. Rivera, D.E., Morari, M., Skogestad, S., ' Internal model control. 4. PID controller design.' Ind.Eng. Chem. Process Des. Dev. 1986. vol. 25, pp. 252.
5. Marlin, T.E., 'Process Control.' McGraw - Hill, New york.1995.
6. Ogunnaike, B.A., Ray, W.H., ' Process dynamics, modeling and control.' Oxford University press. New york. 1994.
7. Bela, G. Liptak : ' Process measurement and Analysis 3rd edition, Butterworth Heinman Ltd., 1999.
8. Doglas M Considine, 'Process Instruments and Con trol hand Book', 2nd edition, *McGrawHill Company*, 1974.
9. M. Li, F. Wang, F. Gao, ' PID - Based Sliding Mode Controller for Nonlinear Processes.' Ind.Eng. Chem. Res. - 2001, vol. 40, no. 16, pp. 2660 - 2667.
10. R.A.Wright, C. Kravaris, N. Kazantzis, ' Model Based Synthesis of nonlinear PI and PID Controllers.'AIChE journal, vol 47, no. 8, 2001.
11. A. Visioli, ' Optical tuning of PID controllers for integral and unstable process.' IEE-Proce, Control Theo. Appli. vol.148,no.2 2001.

PC-Based Position Control System of a Motorised Valve in a Process Plant

S. C. Bera and J. K. Ray
Instrumentation Engineering Section, Applied Physics, University of Calcutta
92, Acharya Prafulla Chandra Road, Kolkata - 700 009
E-mail : jkroy_cal51@rediffmail.com

Abstract

In the modern PC based instrumentation system of a process plant the pnenumatic control valves are being replaced by motorised control valves. In the present paper a PC based position control system of a motorised control valve using ICON based Labtech Note Book Pro software has been described. The valve position has been calibrated and the results are reported in the paper. A linear behaviour of the angular position of the valve has been observed.

Keywords : Control valve, position feedback, PC based control, data acquisation software.

INTRODUCTION

In any modern process plant, the pneumatic control valves working as the final control elements[1,2] in a control loop are being replaced by the motorised valves [3] which can be directly operated by the digital control signal from a Personal computer[4]. In any control loop, it is required to position the control valve accurately at a location according to the set point signal[5], so that the process variable may be maintained at the desired value. This position control of a motorised valve may be obtained by using different techniques [6,7]. In a stepper motor type technique, the valve stem is driven by a stepper motor which can directly receive the digital signal from a digital controller or a PC-based controller with commonly available data acquisition and control softwares [8,9] and thus the position of the valve is maintained at the desired condition by using a suitable position feedback signal. In the present paper a unistep synchronous motor is used to drive a high quality teflon seated ball valve in a half inch line. The speed of the motor is reduced in 1 : 50 ratio by a gear box so that final speed of the valve is small (1 rpm) and the efficient control of the process variable is possible. To position the valve according to the set point signal, an icon based technique has been designed by using the Labtech Note Book Pro software. The position of the valve is calibrated using a dc set point signal generated in the Labtech Note Book Pro software. The control scheme along with the calibration curve of the motorised valve is presented in the paper. From the calibration curve it is found that the response characteristics of the valve with set point is almost linear and thus the performance of the designed circuitry may assumed to be quite satisfactory.

METHOD OF APPROACH

The motorised valve used in the present project is fabricated with a step synchronous motor at 10 Kg - cm torque to drive a teflon seated ball valve in a half inch line and with a speed reduction gear box of 50 : 1 ratio. The photographic view of the motorised control valve is shown in fig.1.
The rotor of the motor is a permanent magnet while the stator consists of two coils one of which gets direct supply and the other gets supply through RC circuits. Thus a rotating magnetic field is produced which drives the rotor in clockwise or anti clockwise direction depending on which coil is getting supply through RC circuit. This change of the direction of rotation of the rotor is obtained by means of the two bits digital signal obtained from PC through the output ports of its DAS card. The motor is stopped when this signal is '00' it runs in the forward direction when this pulse signal is ' 01 ' and in the reverse direction when the pulse signal is '10' .It again stops when this signal is '11'. An icon based software of Labtech Note Book Pro[10]. has been designed and is explained in the following section. In this software , the valve position signal obtained from a linear potentiometer attached with the valve shaft is subtracted from the set point signal in % produced in the display unit . The deviation signal thus produced is then converted into a two bit digital signal from the argument that when the deviation signal is positive the output is '01' and when it is negative, the output is '10' and in any other case the output is '00'. These digital signals are used to make ON or OFF any one of the two triacs by means of an opto isolator based diac driver network. Thus the motor rotates in one direction depending upon the command sig-

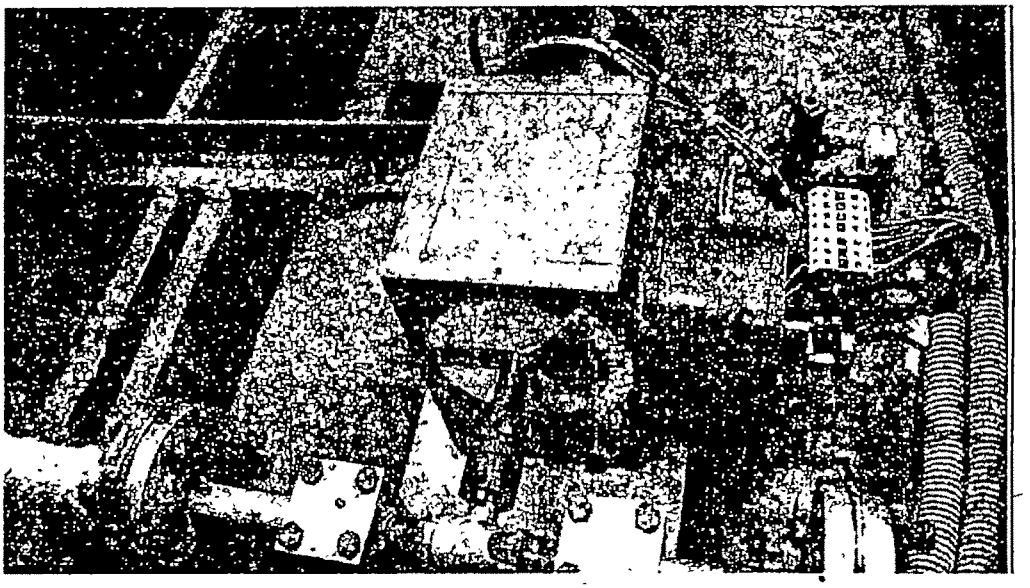

fig.1 : The photographic view of control valve

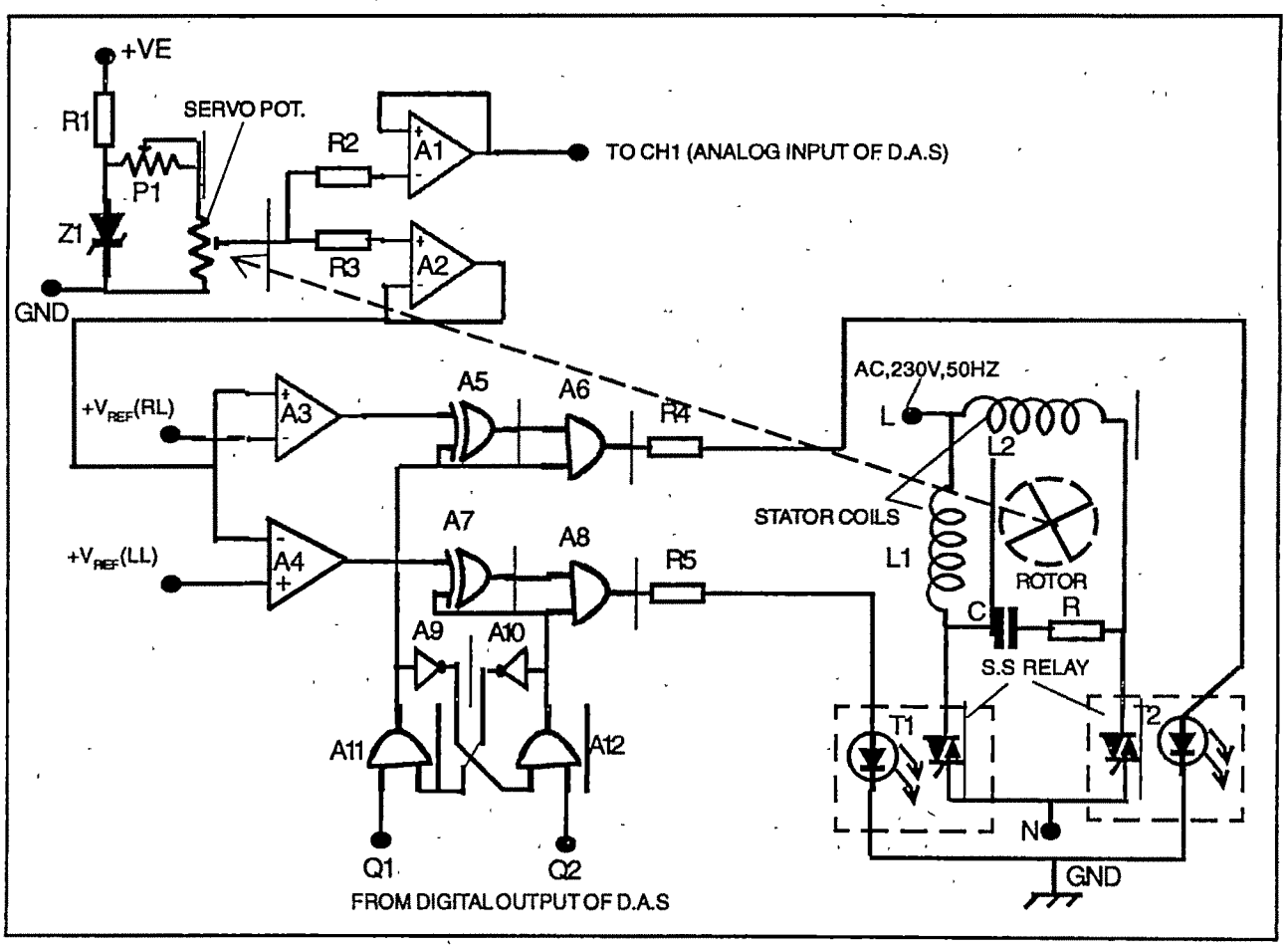

fig.2 : The interfacing electronic circuits for the control valve

nal and when deviation between the set point signal and the measured value of the valve position becomes zero it stops. If the set point is shifted to a new value then the corresponding digital signal changes and the valve rotates in the desired direction. The lower or upper limiting positions of the valve is selected electrically by means of two comparator circuits and the motor is stopped when these limiting positions are exceeded. The valve calibration data with set point are reported in the paper.

DESIGN AND FABRICATION

The Circuit diagram of the interfacing electronic circuit in between control valve and computer is shown in fig.2. A step sync Motor of 10kg.Cm torque is used to drive a 1/2" line stainless PTFE packed ball valve after speed reduction of 1:50 using a gear box. A servo potentiometer is also connected with the extended shaft of the main drive as feed back element. As the valve rotates the value of the resistance of the srvo potentiometer changes. This resistance value of the servo potentiometer is the indicator of the current position of the control valve. The step sync motor used with the control valve can rotate in forward and reverse direction which is depending on the phase of the ac voltage across the drive coil. There are two drive coils, one coil is connected parallel to the other coil via R.C circuit. Therefore a rotating magnetic field is generated inside the motor stator when an ac voltage is fed across the drive coil. The rotor is a permanent magnet and hence the interaction force between rotor and stator magnetic field generates a rotational force to drive the shaft of the control valve. The direction of rotation depends on the coil which gets the supply through the RC circuit. This is done using two solid state opto-isolated triac switches as shown in the circuit diagram. The position feed back signal from servo potentiometer has been buffered by OP.AMP A1 & A2. The output of A1 is fed to the comparator circuits for sensing thecontrol Right or Left limit of the valve position. The output of A2 is fed to analog channel 1 of the PC based data acquisation system for monitoring and controlling the valve position through computer. In the circuit diagram A3, A4 are other two comparator circuits which are monitoring the left and right limit values in terms of voltage.

Therefore if $V_{SP} > V_{refRL}$ then output of A3 goes high. When $V_{SP} < V_{refLL}$ then output of A4 also goes high. When $V_{refLL} < V_{SP} < V_{refRL}$ then output of A3 and A4 are both low.

The logic control circuit is formed using the exclussive OR gates (A5, A7) , AND gates (A6, A8), (A13, A14) and invereter gates (A11, A12) as shown in the circuit diagram of fig.2. Two digital output Q1 & Q2 from computer port are connected to the inputs of AND gates A11 & A12 . The logical state of Q1 is defined for forward rotation of the motor and Q2 is for reverse rotation. The logic 1 means motor will rotate and Logic "0" means motor stops.

If Q1 = Logic "1" then Q2 = Logic "0" and output of A3, A4 is Logic "1", then output of A6 is logic "1", Triac T1 will be switched ON. At this condition A8 will be logic "0" and T2 will be switched OFF, the motor gets power and it starts rotating. Let the motor in this situation is rotating in forward direction .

Now if Q2 = Logic "1" then Q1 should be in Logic "0" state then A8 is logic "1", T2 will be switched OFF and T1 is switched ON, then the Motor starts rotating in the reverse direction.

When Q1 & Q2 are in logic "0" state , T1 & T2 are switched OFF, and motor stops.

Inverter A9, A10 forcely pull output of A6 A8 to Logic "0" state when Input Q1 and Q2 are both accedentally logic "1" state,

Now the position control of the valve is being achieve by the computer using a ICON based software Labtech Note Book Pro, a data acquisation and control software package. The ICON based software modules and their interlink as developed for position control is shown in fig.3.

The set point for the valve position is given through the sliding potentiometer of the vission screen through a IPC block. The position feedback voltage from servo potentiometer of the valve is sample through the Analog signal module , The error signal is obtained from the difference block. This error signal is processed digitally through three different routes, which are created by various mathematical and logical blocks as shown in fig.3,

The route 1 consists of absolute and two AND blocks, the route 2 consists of moving average block, absolute block and upper limit block whereas the route 3 consists of sign block, NOT block and two AND blocks. By these three route the direction signal is converted to the digital output signals Q1 and Q2 when Q1 = logic '1' and Q2 = logic '0' when direction is positive , Q1 = logic '0'and Q2 = logic '1'the direction is negative.

The control software routine has been formed in build time window by dragging , dropping and connecting the Block ICONS as per diagram shown in Fig.3. The control desk is designed in a vission Window with a slide potentiometer element as set point terminal and a analog meter element for indicating control valve postion.The set point for the valve position can be given by setting the slider of the potentiometer through mouse.Each Block ICON has block dialog box having various setting through drop down list. All requisite parameters fordata acquisation, logical operation are defined through dop down list.

All requisite parameters for data acquisition, logical operation are defined through the block settings.

The analog meter module is connected with position feedback potentiometer through the block ICONS and therefore during RUNTIME the analog meter displays the current position of the motorised valve. When set value is greater than process value the error is positive, servo loop activates through software and motor starts to rotate the valve

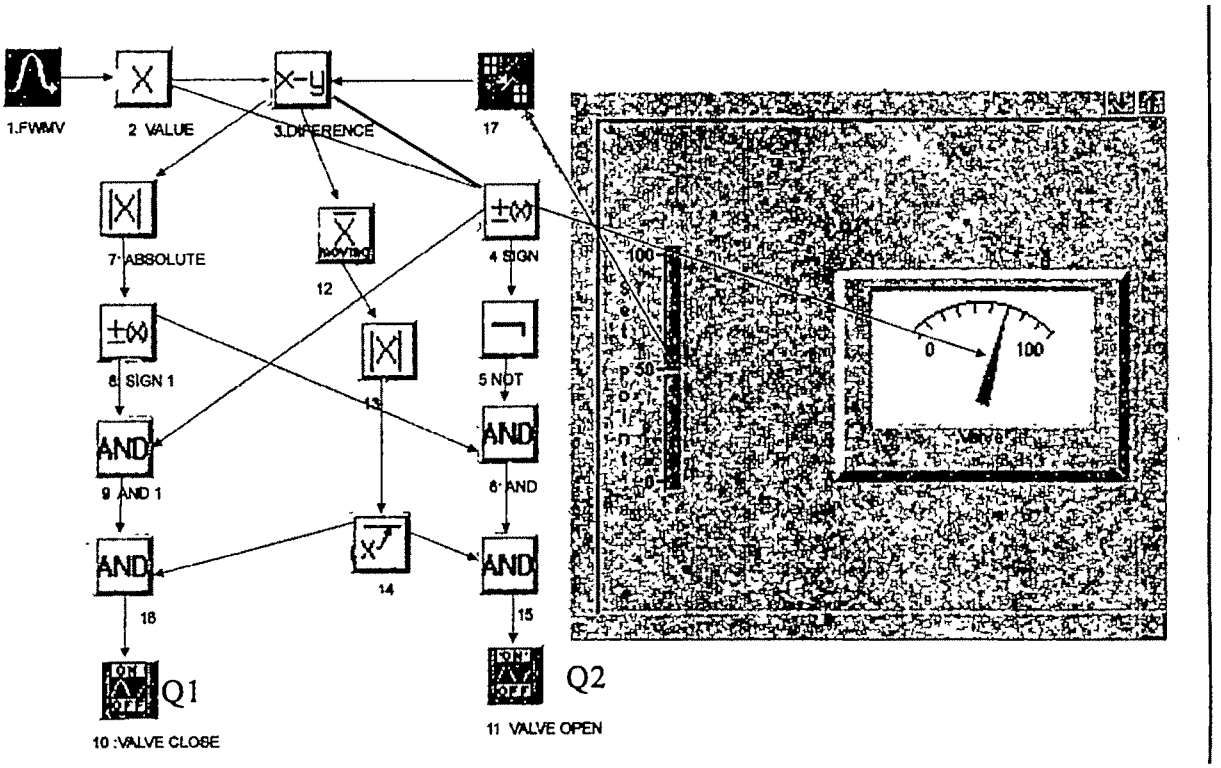

fig.3 : The ICON based software for digital control of the motorised valve

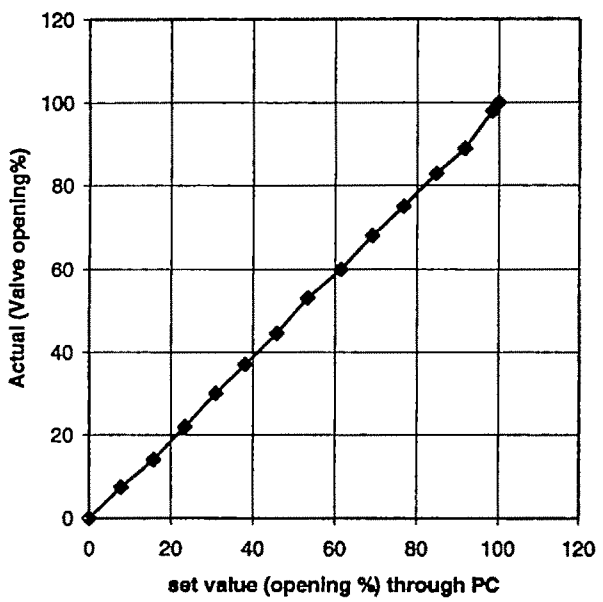

fig.3 : The static characteristics of the motorised valve

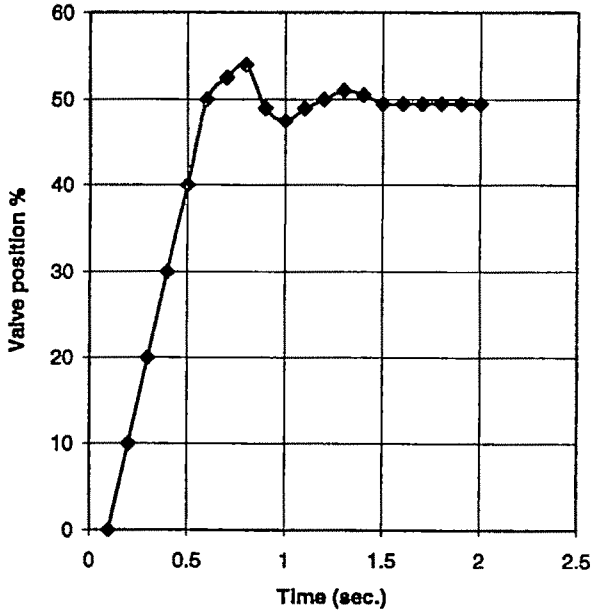

fig.4: Dynamic charracteristics of the motorised valve

to achive desire position. At desire position motor stops and error becomes zero.

A data LOG ICON is also connected with the analog position feedback module such that during a new set point operation, the control valve behaviour in the form of data can be logged for further analysis.

The developed interfacing electronic circuit is constructed on a 6cm x 8 cm glass epoxy printed circuit board. The triacs are mounted with heat sink for continious operation.

EXPERIMENTAL RESULTS

The experimental studies to evaluate performance of position control of the control valve were made in the following manner.

a) Analysis of logged data at various setpoints given in increasing and decraesing manner. The data plotted in the form of graph through EXCEL package of OFFICE 97

b) Repeatability and accuracy evaluation from the set of data.

The valve position charracteristics with set points is given in fig.4 and control charracteristics is shown in fig.5

CONCLUSION

From fig.5 and fig.6, it is found that the position control achieved from the developed ICON based digital control throgh computer is quite satisfactorily. The accuracy and repeatability are also within the acceptable range of industrial operation of any close loop control.

ACKNOWLEDGEMENT

The authors wish to acknowledge with thanks the Department of Applied Physics, C.U. for the departmental Laboratory facilities and to M.H.R.D and A.I.C.T.E for financing the project.

REFERENCES

1. Liptak, B.G.(Ed.), Instrument Engineers Hand Book, Vol.11, Sec.4.1, Pnenumatic-vs- Electronics, sec. 4.3, "Pneumatic Controllers", Chilton, Philadelphia, 1970.

2. Considine, D.M., " Process Instruments and Control hand book", 2nd.ed., Mc.Graw Hill Book Company, 19974.

3. Usry, J. D., " Stepping Motors for Valve Actuation", Instrum. Technol., Vol.24, No. 3, 1977, P-58

4. Hordeski, M.F., "Adapting Electric Actuators to Digital Control, Instrum Technol.,Vol.24, no.3, 1977, P-53

5. Baily, S. J., Stepping Controls Mature as Digital Actuators",Control Eng.,Vol.26, No.8, 1979,

6. Mei, T. X., and Goodall, R. M., " Position Control for a subsea pump system driven by a linear Motor", Control Engineering Practice, Vol.3, Issue.9, 1995, P-1209

7. Shila Ming- Chang and Tseng Shy-I, " Identification and position control of Servo pneumatic cylinder", Control Engineering Practice, Vol.3, Issue 9,1995, P-1209.

8. " The Secret of Success with LabVIEW", Instrumenta tion News Letter, National Instruments, Vol.8, No.4, 1996

9. " The ImagingBrings New Solutions to Production and Test", Instrumentation News Letter, National Instruments, Vol.8, No.4, 1996

10. Windows User's Guide "Labtech Data Acquisition and Process Control Software" 4/94 Release, Laboratory Tech nologies Corporation, USA, 1994.TP-381.

***

Design of a Novel Bridge type Flowmeter for a Conducting Liquid

S. C. Bera
Instrumentation Engineering Section, Applied Physics, University of Calcutta
92, Acharya Prafulla Chandra Road, Kolkata - 700 009
E-mail : jkroy_cal51@rediffmail.com

Abstract

The measurement of flow of a conducting liquid is generally made by using electromagnetic flow-meter which is available in the market at a comparatively higher cost. In the present paper a novel low cost bridge type technique of flow measurement of a conducting liquid has been described. The design aspects, theoretical analysis and calibration data are presented in the paper.The experimental charcteristic of the flow meter is found to follow the theoritical equation and has good repeatability over the entire operating zone.

Keywords : Lumped parameter bridge, conducting liquid, flow measurement

INTRODUCTION

The measurement of volume flow rate of a conducting liquid is generally done in the process industries by using electromagnetic flow meters [4], [5[, [6], [11] since this technique is very simple compared to the other methods. There are other techniques [4], [5], [6], [7] of this flow measurement like absorption type, turbine type, coriolis force type, target type, vortex type etc. But for the conducting liquid flow measurement, the electromagnetic flow measurement technique is much easier and less costly compared to the other measurements. In this technique an intense magnetic field is produced in the selected region of the flow tube by means of two coils excited from an ac or a dc source. Two sensing electrodes are placed on the diametrically opposite positions inside the tube in contact with the flowing liquid. The flowing liquid induces an e.m.f between the electrodes which is directly proportional to the flow. In the present paper a novel technique of measurement of flow of a conducting liquid has been described. In this technique no excitation coil is required. This technique consists of four metal electrodes inserted into the selected zone of the flow which are always in contact with the liquid and produce no obstruction to the liquid flow. This electrode system is excited from an a.c source and the output signal has been found to be linearly related with the liquid flow under streamline condition along with a small non-linear zone at turbulent condition. This output voltage has been amplified by an instrumentation amplifier and then rectified. The offset or zero adjustment network controls the offset of the rectified signal. This signal is then further amplified to voltage signal in the range of 0 - 5 volts and the non-linear zone is linearised by a microprocessor based piece wised linearisationtion technique. The digital output signal of microprocessor is converted into analog signal and is then converted into 4 - 20 mA current signal for transmission.The design of the flow head and thge calibration data before and after linearisation are reported in the paper. The experimental data are almost found to conform with the theoritical equations.

ANALYSIS

When two metal electrodes are immersed in a conducting liquid the polarisation effect [1],[3],[8],[9],[10], [13] at each electrode produces an electric double layer at each metal liquid interface across which there exists a difference in potential along with a polarisation impedance. If a very small value of sinusoidal voltage signal be applied across the electrodes then this ac voltage signal is superimposed with the half cell potential [8] at each electrode and accordingly the flow of ions from one electrode to the other is obtained. The electric current due to this flow ions may be opposed by the dc polarisation impedance and the ohomic impedance of the liquid between the two electrodes. Again if there is a flow of liquid from one electrode to the other then the flow of a liquid elements along with the ions may be opposed by the viscous effect of the liquid produced by the velocity gradient. Hence the net impedance between

the electrodes defined as the ratio of the supply voltage to the current may be assumed to be dependent on the electrode polarisation effect, ohomic effect and the velocity gradient of the liquid [8],[9],[10]. The dc polarisation effect non-linearly depends [9] on the electric current density and frequency of excitation and ohomic effect may be assumed constant for a particular system. When a liquid flows through a pipe line there exists a velocity gradient across the cross section of the pipe line which depends on the flow rate of the liquid if the polarisation effect and ohomic effect are assumed to be constant. In the present paper the effect of four electrodes inserted into a conducting liquid flowing through the pipe line with proper insulation at the diametrically opposite positions is studied. Since an impedance is always found to exist between any two of these electrodes, the four electrodes may be assumed to be equivalent to four lumped impedances as shown in fig. 1.

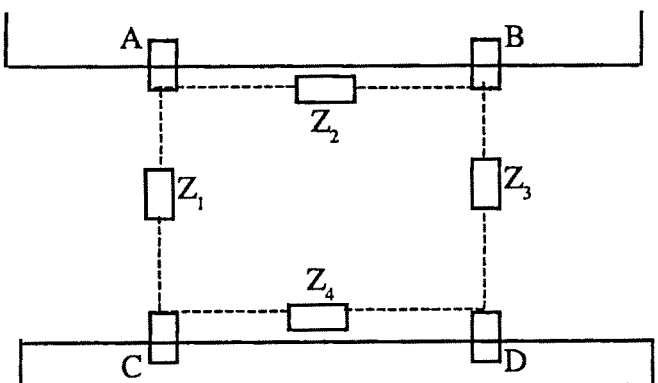

fig.1 : Lumped parameterequivalent impedance network between four electrodes.

Now when a conducting liquid flows through the horizontal pipe under the streamline condition it may be assumed to have no component of its velocity along any diameter since it is perpendicular to the length of the pipe line. Hence the lumped parameter impedance Z_1 between the diametrically opposite electrodes A & C and Z_3 between the similar electrodes B & D may remain constant but the effective lumped impedance Z2 between C & D or Z4 between A & B tends to change due to the velocity gradient among the liquid layers between the electrodes.

Hence if any two diagonally opposite electrodes be supplied from a very small value sinusoidal stabilised ac source then the output across the other two electrodes may change due to the flow of the conducting liquid following the Wheat stone's bridge network principle. So for a small value supply voltage V_s at a fixed frequency applied between A and D and for a very high input impedance of the measuring circuit the bridge output voltage signal V_o may be given by

$$V_o = (Z_2 Z_4 - Z_1 Z_3) / (Z_1 + Z_4)(Z_2 + Z_3) V_s \quad \text{---(1)}$$

For a very small value of ac voltage V_s and for the identical electrodes $Z_1 = Z_3$ and $Z_2 = Z_4$.

Let at any flow rate Qo of the liquid $Z_1 = Z_2 = Z_C$, $Z_2 = Z_4 = Z_o$ and at any other flow rate Q slightly different from Q_o the value of Z_o changes to Z_Q. Hence the Taylor series expansion of Z_Q may be given by

$$Z_Q = Z_o + \left(\frac{d}{dQ} Z_Q\right)_{Q_o} \Delta Q + \left(\frac{d^2}{dQ^2} Z_Q\right)_{Q_o} \Delta Q^2 + \ldots\ldots\ldots (2)$$

where $\Delta Q = Q - Q_o$

Let $\left(\frac{d}{dQ} Z_Q\right)_{Q_o} = \mu$ and $\left(\frac{d^2}{dQ^2} Z_Q\right)_{Q_o} = \beta$

Hence $Z_Q = Z_o + \mu \Delta Q + \beta \Delta Q^2 + \text{---------(3)}$

Under streamline conditions, the value of β and the coefficient of higher order terms may be assumed to be very small. Hence for very small change (ΔQ) of flow rate, Z_Q may be given by

$$Z_Q = Z_o + \mu \Delta Q \quad \text{---} \quad (4)$$

Hence putting $Z_1 = Z_3 = Z_C$ and $Z_2 = Z_4 = Z_Q$ in equation no. (1) the bridge output voltage for a liquid flowrate Q is given by

$$V_o = V_s [(Z_Q - Z_C) / (Z_C + Z_Q)] \quad \text{---} \quad (5)$$

From the equation nos (4) and (5) we get

$$V_o = V_s [(+ Z_o + \mu \Delta Q - Z_C) / (Z_C + Z_o + \mu \Delta Q)]$$

or

$$V_o = \{1 / (Z_C + Z_o)\} [(Z_o - Z_C) + \{2Z_C / (Z_o + Z_C)\} \mu \Delta Q - \mu^2 \Delta Q^2 / (Z_C + Z_o)^2] V_s$$

or

$$V_o = K_1 + K_2 \Delta Q + K_3 \Delta Q^2 \quad \text{---} \quad (6)$$

where

$$K_1 = [(Z_o - Z_C) / (Z_o + Z_C)] V_s \text{---} \quad (7)$$

$$K_2 = [2 \mu Z_C / (Z_o + Z_C)] V_s \text{ ---} \quad (8)$$

$$K_3 = [\mu^2 / (Z_C + Z_o)^2] V_s \quad \text{---} \quad (9)$$

Under the streamline conditions, the term $K_3 = [\mu^2 / (Z_C + Z_o)^2] V_s$ may be assumed to be very small and hence for a very small change ΔQ of flow rate, the equation no. (6) may be written as

$$V_o = K_1 + K_2 \Delta Q$$

or

$$V_0 = K_1 + K_2 (Q - Q_0) \quad \text{---} \quad (11)$$

Hence the bridge output voltage is linearly related with the incremental change in flow rate under the stream line condition. Under no flow condition $Q_0 = 0$ and for electrode separation along the pipe line equal to the pipe diameter, $Z_0 = Z_C$. Hence $K_1 = 0$ and the equation no. (11) is reduced to

$$V_0 = K_2 Q \quad \text{------} \quad (12)$$

Thus the bridge output voltage is linearly related with flow rate when the flow rate is very small and streamline.
Under the turbulent condition, the equation no. (3) may be given as

$$Z_Q = Z_0 + \mu \Delta Q + \beta \Delta Q^2$$

Hence from equation (5) the bridge output voltage is given by

$$V_0 = [(Z_0 + \mu \Delta Q + \beta \Delta Q^2 - Z_C) / (Z_0 + \mu \Delta Q + \beta \Delta Q^2 + Z_C)] V_s \quad \text{--------} \quad (13)$$

Hence under turbulent condition, the bridge output voltage may be non linearly related with the incremental change of flow rate. Therefore $Z_0 + Z_C >> \mu \Delta Q + \beta \Delta Q^2$. So the bridge output voltage under turbulent condition may be given by

$$V_0 = [(Z_0 - Z_C \mu \Delta Q + \beta \Delta Q^2) / (Z_0 + Z_C)] [1 - (\mu DQ + \beta D Q^2) / (Z_0 + Z_C)]$$

$$V_0 = K_1 + K_2 \Delta Q + K_3 \Delta Q^2 - K_4 \Delta Q^3 - K_5 \Delta Q^4 \quad \text{---} \quad (14)$$

where $K_3 = [(2Z_C \beta - \mu^2) / (Z_0 + Z_C)^2] V_s$ ----(15)

$$K_4 = [2\mu\beta / (Z_0 + Z_C)^2] V_s \quad \text{---} \quad (16)$$

$$K_5 = [\beta^2 / (Z_0 + Z_C)^2] V_s \quad \text{---} \quad (17)$$

Since μ and β are small so K_4 and K_5 may be negligible and hence the above equation no. (14) may be written as

$$V_0 = K_1 + K_2 \Delta Q + K_3 \Delta Q^2 \quad \text{--------} \quad (18)$$

Hence the relation between the bridge output voltage and the incremental change of flow rate may be assumed to be parabolic under some conditions of turbulent flow.

DESIGN

The design of the flow head is very simple as shown in fig.2. It involves only the selection of the electrode material which is chemically innert to the flowing liquid. In the present design, the flow rate of water through a one inch pipe line has been measured. Hence the electrode material is selected to be stainless steel. Since outside and inside diameter of the pipe are 25mm and 20 mm respectively so length of each electrode is selected to be 15 mm with 2 mm insertion depth. The diameter of each electrode is selected to be 4 mm. These selections are made on a trial basis so that the obstruction to the flow is minimum. Each electrode is covered with PVC sleeve and is fitted with a 2 mm terminal screw. Each electrode is then mounted on the flow head along its line of symmetry through a proper hole so that the electrode may be inserted with tight shut up condition and there is no water leakage at the operating pressure. The small gap is sealed with araldite. The length of the flow head is selected to be three feet with flange connections at both ends of internal diameter exactly equal to that of the pipe line. The flow head is connected with the pipe line through insulating gasket of teflon sheet.

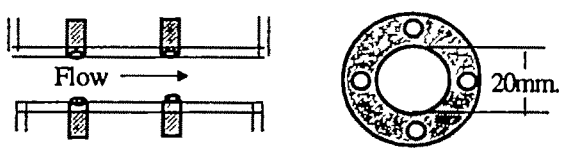

fig.2 : Flow head of the bridge flow meter

SIGNAL CONDITIONER

The lumped parameter bridge circuit formed by the four electrodes as shown in fig.(1), is supplied from a wein bridge oscillator at 1000 Hz. Any two diagonal electrodes are taken as the bridge supply nodal points and the other two diagonal electrodes as the bridge output nodal points. The bridge output voltage signal is first amplified by an instrumentation amplifier IC INA101KP as shown in fig.3. The gain of this amplifier is adjusted by the trimpot R_g. The amplified ac signal is converted to dc signal by a precision rectifier using IC4 and diodes D1 and D2 whereas the capacitor c1 and c2 and resistor R10 act as filter. The zero offset adjustment is obtained by the network consisting of IC5 whereas IC6 acts as buffer. The output of the buffer IC6 is input to the microprocessor through ADC. The digital output of the microprocessor is converted into the analog voltage by DAC and is then converted into current signal by voltage to current converter for transmission purpose. The transmitted signal is received across the load resistance to obtain the voltage signal for indication, control or other purposes.

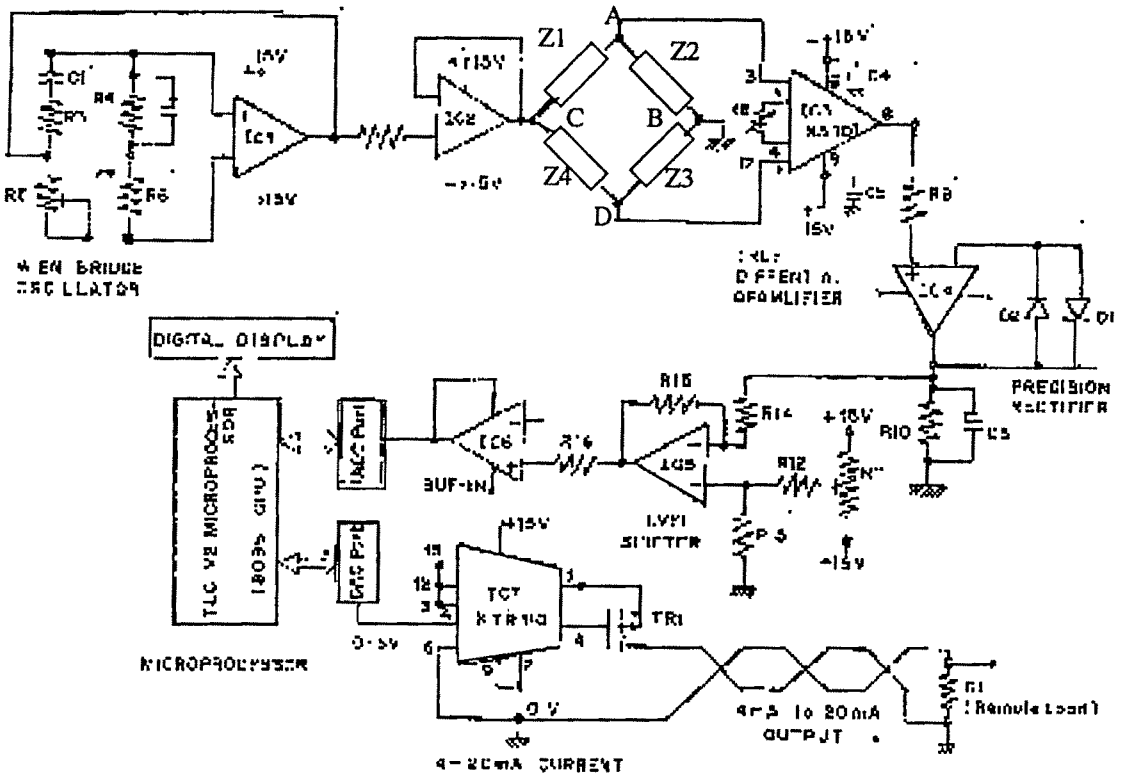

fig.3 : Signal conditiner circuit of the bridge type flow meter

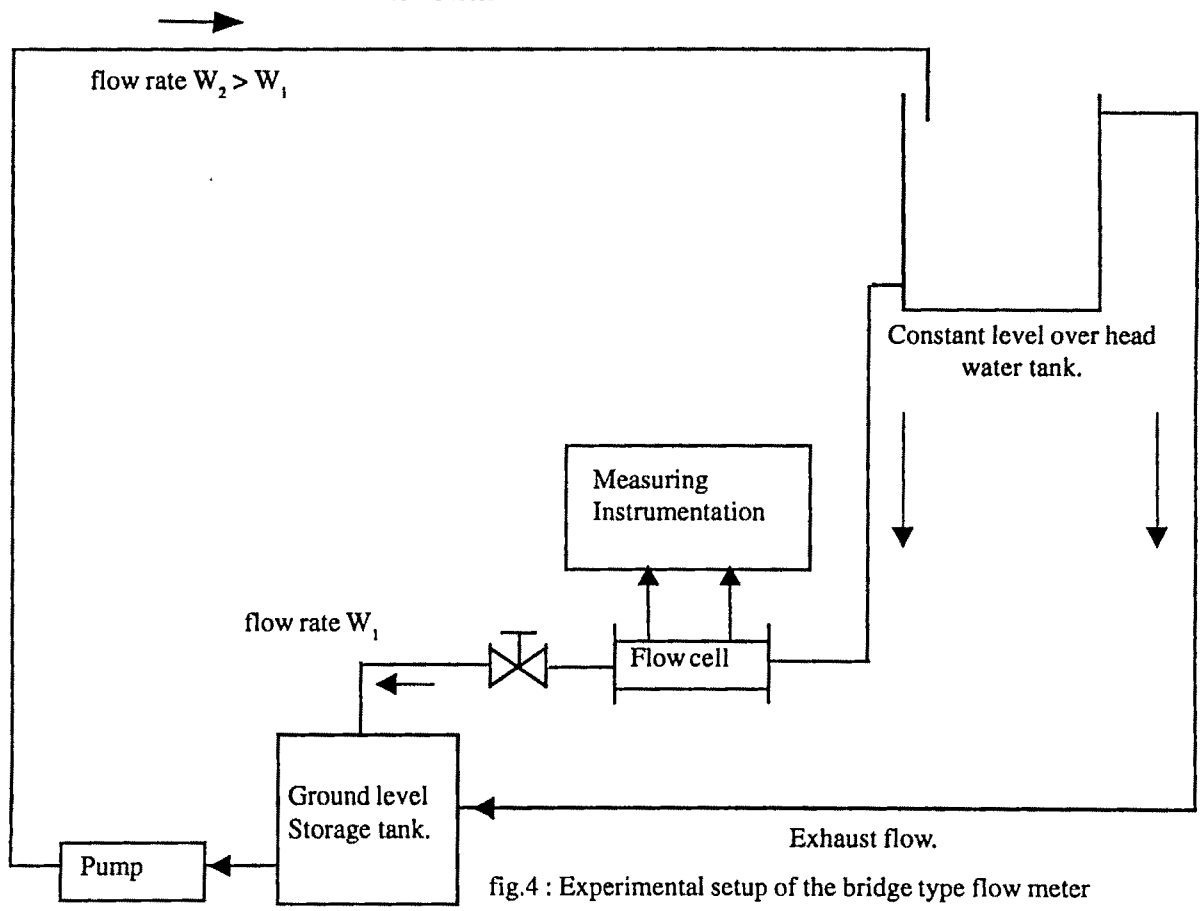

fig.4 : Experimental setup of the bridge type flow meter

LINEARISATION

The experimental graph as shown in fig.(5) is found to be non-linear with a linear zone over a large portion of the calibration characteristics of the flow transducer. It is linearised by using the piece-wise linearisation technique with the software programme by an ILCV2 8085 microprocessor. The software is designed according to a flow chart[11], where the characteristics curve is only devided into two linear pieces in which the 1st. linear part of the experimental graph is taken as the final linearise characteristics of the flow meter. From the experimental data this linear part is found to approximately satisfy the equation y = 0.67x +0.7 where y denotes the flowmeter output in volt and x denotes the flow rate in liter per minute and the data in the non linear zone of the experimental graph are converted into the corresponding data in the linear zone by the microprocessor. The linearised data are displayed in the microprocessor in liter/min.

EXPERIMENT

The experiment is performed by using tap water with the experimental set up as shown in fig.4.
The flow through the pipe line is increased in small steps and in each step the signal conditioner output and the microprocessor output are noted in both increasing and decreasing modes.The static calibration graphs obtained from the experiment for the signal conditioner output and microprocessor output after linearisation are as shown in fig.5.

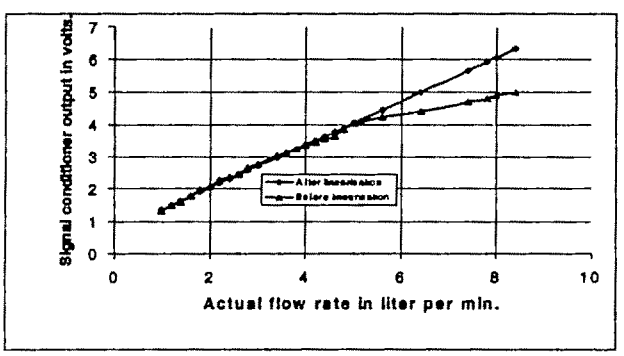

fig.5 : Calibration curve for bridge type flow meter before and after linearisation

DISCUSSION

The repeatability of the experimental data in the increasing and decreasing modes were found to be satisfactory.The calibration graph shown in fig.6 reveals that the nature of the graph is linear over large portion of the operating zone. The non-linearity may be due to the turbulence effect of flow .The nature of the graph appears to follow the theoretically derived equation (11) and (18). The technique is very simple and requires no magnetic excitation field coils as in the case of an electromagnetic flow meter and hence it is very low cost.

REFERENCES

1. P.C.Rakhshit : ' Physical Chemistry ' Scince Book Agency, 3rd Edition, 1973.
2. John Borer : ' Instrumentation and Control for the process Industries' Book, Elsevier Applied Science Publishers, 1st edition, 1985.
3. R. Bryon Bird, W.E. Stewart, and E.N. Lightfort, 'Trans port Phenomenon' Book. John Willy and Sons, 1994.
4. Bela, G. Liptak : ' Process measurement and Analysis 3rd edition, Butterworth Heinman Ltd., 1999.
5. Doglas M Considine, 'Process Instruments and Con trol hand Boók', 2nd edition, *McGrawHill Company*, 1974.
6. John P Bentley, 'Principles of Measurement Systems', 3rd.edition,LongmanSingapore Publishers(pte) Ltd,1995.
7. E. O. Doeblin. ' Measurement System application and Design' 4th. Edition, McGraw Hill Publishing Co., 1990
8. H.P. Schwan, : ' Linear and non-linear platinum electrode polarisation equivalence of frequency and time domain behaviour ', Medical and Biology eng. and comp. (GB) Vol.23, No.1, pp. 28 - 37, jan.1988.
9. R.W.Simson, J.G.Berberian, H.P.Schwan, ' Non-linear AC and DC polarisation of platinum electrodes ' IEEE Trans. on Biomed. Eng. Vol. BME27, No.3, pp.166 - 71, march,1980.
10. H.H.Sun, B. Oneral,: 'A unified approach to represent neutral electrode polarisation 'IEEE trans. on Biomed. Eng. Vol.BME30, No.7, pp. 309 - 406, july 1983.
11. J. K. Roy, K. Naskar & S. C. Bera, ' Low Cost Microprocessor based Liquid level Transmitter using inductive pickup'.,J. I.E. (I), Vol.80, May1999

Study of a Low Noise Head Mounted Temperature Transmitter

S. C. Bera and J. K. Ray
Instrumentation Engineering Section, Applied Physics, University of Calcutta
92, Acharya Prafulla Chandra Road, Kolkata - 700 009
E-mail : jkroy_cal51@rediffmail.com

Abstract

In the modern industries with computer based instrumentation system, the need of a head mounted transmitter is gaining importance in order to eliminate the effect of noise signal on the transducer characteristics. In the present paper the design of a low noise head mounted temperature transmitter using Bur-Brown ASIC Thermocouple amplifier AD595AQ has been described. The performance of the transmitter has been studied using a PC based monitoring unit and experimental report is presented in this paper.

Keywords : Thermocouple amplifier, temperature transmitter, PC based data acquisation.

INTRODUCTION

The accurate measurement and transmission of temperature is one of the essential requirements of any process industry [7]. There exists a number of sensors used for measurement of temperature[1,2,8]. Of these the thermocouples may be considered to be more economical and rugged with good stability. Because of their small size, they respond quickly and may be the good choices in applications where fast response is important. They function over temperature ranges from cryogenics to jet engine exhaust and have reasonable linearity and accuracy. A measurement of the thermocouple voltage combined with a knowledge of reference temperature can be used to calculate the junction temperature. The order of thermo emf generated by the thermocouple for each degree change in temperature is of the order of micro volt, so the amplification of this low value signal with temperature compensation requires highly reliable low noise DC amplifier and other signal conditioning circuits. The thermo emf generated by a thermocouple type temperature sensor is transmitted through a compensating cable . The noise voltage introduced in this compensating cable may introduce significant error in the measurement. The investigations on the linearisation of the temperature sensors, accuracy in the measurement, minimisation of noise, reduction of coast etc. are being reported by various workers [1, 2, 3]

In the present paper, the design of a low noise head mounted transmitter using the Bur Brown ASIC monolithic chip thermocouple amplifier AD595AQ integrally built in thermocouple amplifier and temperature compensator has been reported. The thermowell and head assembly is designed and fabricated for high pressure boiler temperature measurement. The performance of the designed temperature transmitter is tested by comparing it with a PT 100 temperature transmitter as well as a Hg-in-glass thermometer in a water bath. A PC based data acquisition system with icon based software has been used for this study.From the logged data the dynamic and static characteristics of the designed instrument are obtained to know the time constant and other parameters.

The experimental results are reported in the paper .From the experiment it is found that the dynamic and static error and time lag of the designed instrument appear to lie within tolerable limits. A prototype instrument thus developed has been installed in the running boiler drum of a miniature steam generation plant and has been found to work satisfactorily.

METHOD OF APPROACH

The basic principle of head mounted temperature transmitter using thermocouple as the sensing unit is that if the small value of thermocouple emf be amplified along with cold junction compensation at the thermowell head itself into a high value signal then the use of the costlier compensating cable may be avoided. Moreover the cold junction compensation for thermowell temperature instead of that for room temperature eleminates the error due to the effect of temperature gradients between the field points

and control room. Thus the high value signal of the head mounted transmitter may be regarded to be truly proportional to the temperature of the hot junction with minimum noise signal.

In the Present paper AD595AQ, an ASIC integrated circuit manufactured by BURBROWN is selected as thermocouple amplifier with cold junction compensator. As per manufacturer's data sheet shown in the block diagram fig.1 , it behaves like two separate differential amplifiers, the output of which are summed and the sum signal is used to control a high gain amplifier.

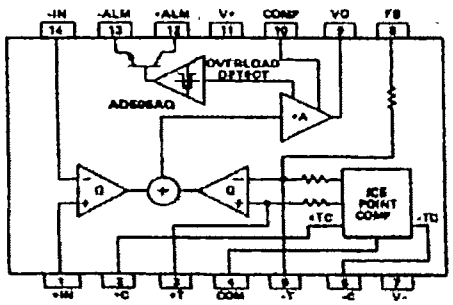

fig.2 : Schematic diagram of AD595AQ Integrated circuit.

The pins 1 and 14 of this I.C correspond to thermocouple input, The pin nos. 3 & 5 correspond to cold junction compensation circuit output proportional to Kelvin temperature, the pin nos. 2 & 8 correspond to the cold junction compensation circuit output proportional to Celsius temperature. the pin no. 9 corresponds to the resultant compensated amplifier output signal. Where as pin nos. 12 and 13 correspond to burnout indication signal of the thermocouple. The thermocouple signal is applied to the floating input stage at pin 1 and 14. Which is amplified by gain G of the differential amplifier then further amplified by gain A in the main amplifier. The output of the main amplifier is fed back to a second differential amplifier in an inverting mode. The feedback signal is amplified by this stage and is also applied to the main amplifier through a summing circuit. Because of the inversion, the amplifier causes the feed back to be driven to reduce the difference signal to a small value. The two differential amplifier amplifiers are made to match and have identical gain G. As a result, the feedback signal that must be applied to the right hand differential amplifier will precisely match the thermocouple input signal when the differential signal has been reduced to zero. The feedback network is trimmed so that the effective gain to the output pin 8 and 9 results 10mV/oC of the thermocouple excitation.

A cold junction compensation voltage is applied to the right hand differential amplifier. The compensation is a differential voltage proportional to the Celsius temperature of the AD595AQ. The compensation is applied through a gain scaling resistor so that the main output is also 10mV/oC. As a result the compensation voltage adds to the effect of the thermocouple voltage a signal directly proportional to the difference between 0°C and AD595AQ temperature. If the thermocouple reference junction is maintained at the AD595AQ temperature then it is equivalent to keep the thermocouple reference junction at ice bath. Hence if the IC AD595AQ may be mounted inside thermowell head enclosure maintained at a nearly uniform temperature of the atmosphere then the output signal obtained from the pin 9 of the IC will be directly proportional to the temperature of the hot junction in °C. This output signal is at 10mV/°C for the chromel-Alumel thermocouple output at 40.44uV/°C with a gain of 247.3. In the project this signal is further amplified by using the op.amp. LM358 in order to have the final output signal of 0 to 5V, for the temperature change of 0°C to 100°C. The circuit diagram is shown in fig.2.

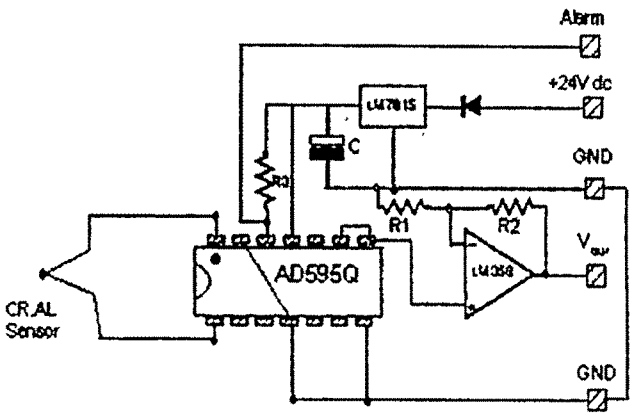

fig.2 : Circuit diagram of the head mounted temperature transmitter.

DESIGN AND FABRICATION

The chromel and alumel wires of 22 swg are used in a type K thermocouple wire. The glass sleeves are used to protect and insulate the thermocouple wires. The thermocouple junction is formed by welding together the thermocouple wire in an inert atmosphere. A small bead of 1mm diameter is formed at the welded tip of the thermocouple wires. This thermocouple is this inserted into a seamless SS316 one end closed thermowell as shown in fig.3 with MgO packing. Care has been taken to insulate thermocouple wires electrically with the thermowell. The MgO packing will help the transmission of heat from thermowell to the thermocouple tip. The other end of the thermowell is terminated to a threaded bush. This threaded bush is Argon welded with the thermowell for application to the steam service. This thermowell is fitted on a die cast aluminium housing with neoprene gasket seal such that the internal

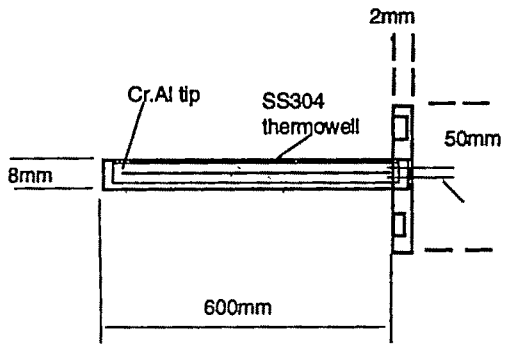

fig.3 : Design of the thermowell and its' die cast head

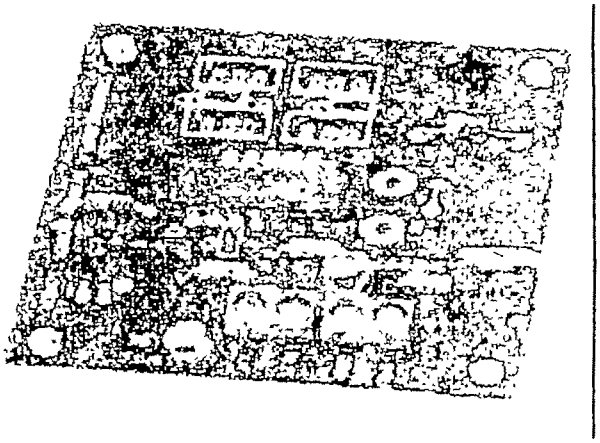

fig.4 : The fabricated printed circuit board of the temperature transmitter.

The thermocouple amplifier using AD595AQ along with other components as per circuit diagram given in fig.2 are assembled in small 30mm x 40mm size, double sided, PTH, glass epoxy printed circuit board as shown in fig.4. The thermocouple wires from thermowell are directly soldered to the input pins of the AD595AQ I.C. The output signal of the thermocouple amplifier, 24 volt DC supply and Alarm output are terminated to the PCB type screw terminal. The system is rugged that it can be fitted to the boiler drum of in a process tank with a temperature compensated output 0-5V dc proportional to temperature. This output can be fed to digital display unit , single loop or multi-loop process controller, PC based data acquisition system or in the analogue input of the PLC for control and monitoring. The output of the temperature transmitter does not require any compensating cable, which normally pick-up noise and reduce thermocouple signal and introduce error in the measurement. The photograph of the fabricated low noise head mounted temperature transmitter is shown in fig.5

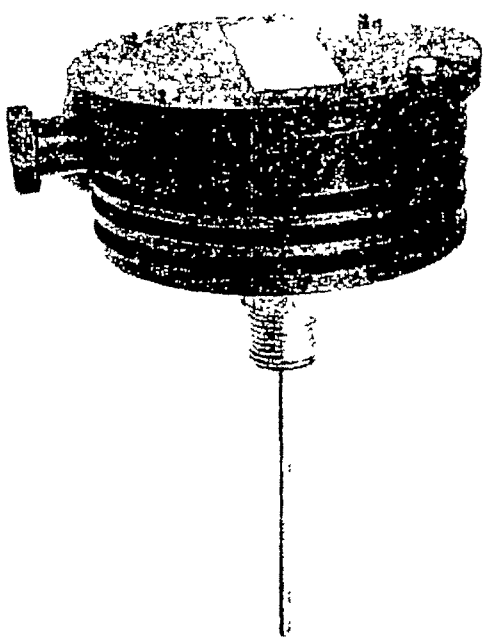

fig.5 : The photograph of the temperature transmitted fabricated in the present project.

EXPERIMENTAL RESULTS

The constructed temperature transmitter was tested in a temperature controlled water bath and its static and dynamic performance were evaluated with respect to a mercury in glass thermometer and a linearised Fisher Rosemount make P.R.T transmitter. A P.C based data acquisition system was designed for sampling of data, analysis and logging of data with the help of ICON based Labtech Note Book Pro software[4,5,6], Advantech make data acquisition PC add on card. The output of experimental Type K temperature transmitter and PRT transmitter are fed to channel 1 and channel 2 of the PC based data acquisition system. The sampling period was taken 10 sec. The temperature data with time were logged to a file of the computer are finally used for analysis and plotting of graphs. The schematic of the experimental setup is given in fig.5. The experimental results of static calibration curves for evaluation of performance are graphically shown in fig.7 and fig.8 and dynamic response for a ramp input and for a step input signals are shown in fig.9 and fig.10 respectively.

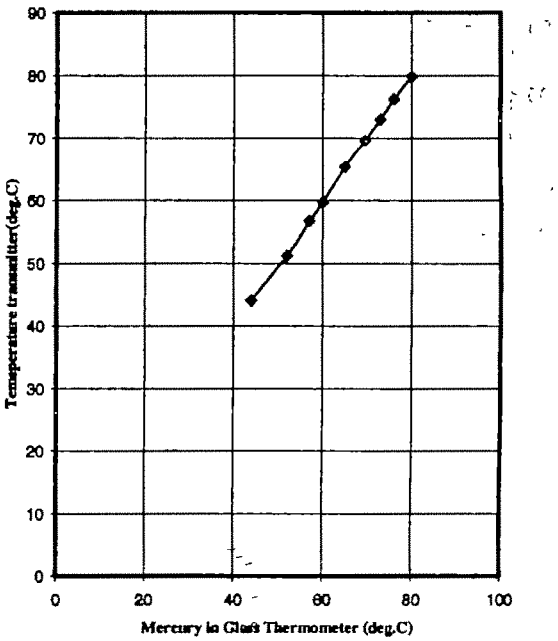

fig.7 : The Static response of the temperature transmit ter with Mercury in glass thermometer

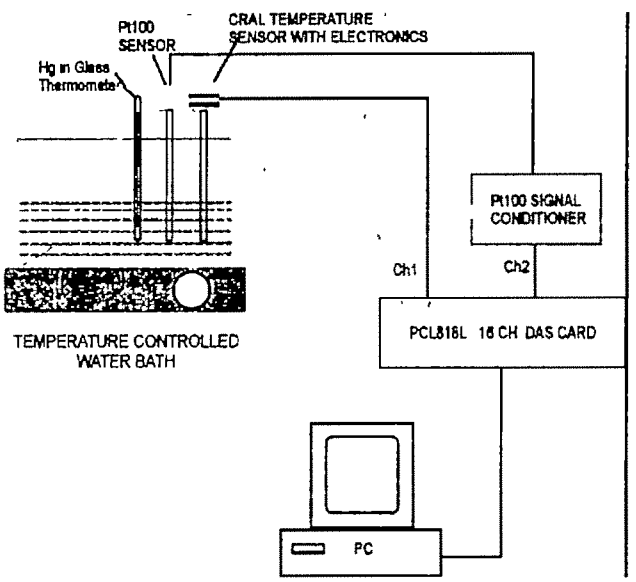

fig.6 : The schematic of experimental setup.

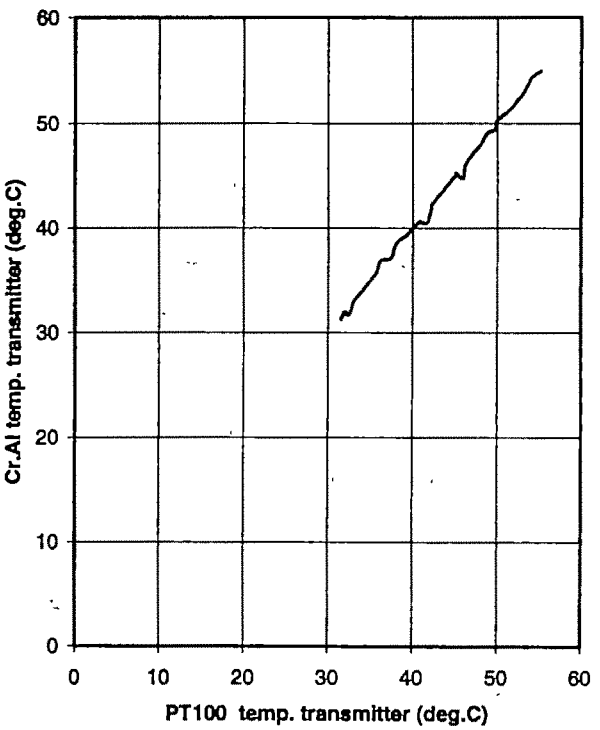

fig.8 : The Static response of the temperature transmit ter with PRT transmitter

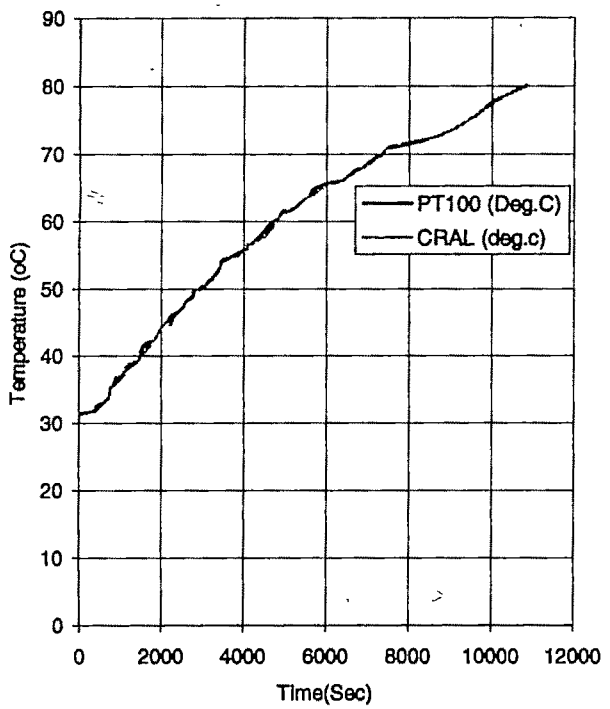

fig.9 : The comparative dynamic response of the temperature transmitter along with PRT temperature transmitter with ramp heat input.

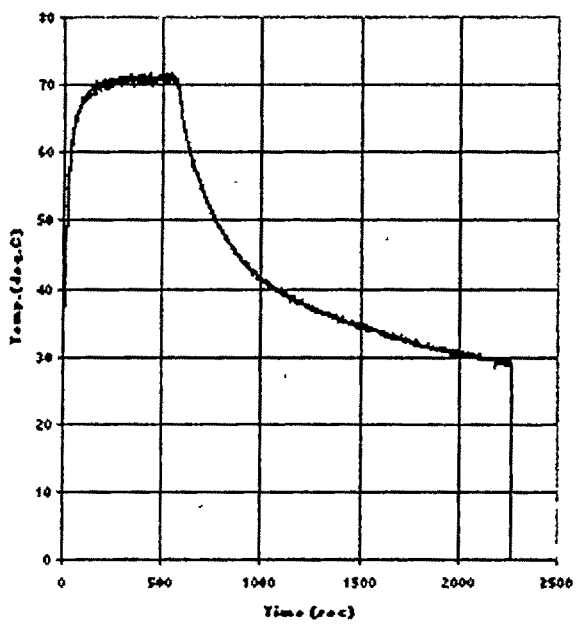

fig.10 : The Dynamic response of the temperature transmitter with step heat input

DISCUSSIONS

The calibration curves shown in fig.7 and fig.8 reveal that the designed transmitter has negligible errors with respect to the Hg-in- glass thermometer and PRT transmitter. The dynamic response curves in fig.9 and fig.10 reveal that the time lag of the transmitter is small within the tolerable limit. In the present project the transmitter is designed for voltage output but this transmitter can be designed for current output with little modification in the circuitry. It was revealed from the present study that this transmitter can be used to measure temperature in a pressured boiler drum or in any other process vessel for the accurate temperature measurement.

ACKNOWLEDGEMENT

The authors are thank full to the All India Council of Technical Education, M.H.R.D., Govt. of India, since the present work is a part of the research project under the financial assistance of the AICTE (R&D) and Dept. of Applied Physics, University of Calcutta for providing the laboratory facility for the work.

REFERENCES

1. Bodea, M. C. & Spanoche, 'A new precision and low cost temperature transducer',7th.Mediterranean Electrochemical Conference Proceedings, Antalya, Turkey, 12-14 April,1994, Vol.3, P-1208.
2. Raimundo Carlos, Silverio Freire, Sergio Daher and Gurdip Singh Deep, ' A highly linear p-n junction temperature sensor', IEEE transactions on Instrumen tation and Measurement, Vol.43, No.2, April 1994.
3. Augustin. S and Bernhard F.,'Numerical Calculation of static and dynamic parameters of industrial tem perature sensors' J. of the International Measurement Confedaration, Vol.17, Issue.4,1994, Pages 217-228.
4. Johnson, Gary W., 'LabVIEW Graphical Program ming', Practical Instrument Control, McGraw-Hill, 1994.
5. Graff, John., 'The Secret of Success with LabVIEW', Instrumentation News letter', Vol.8, No.4
6. Windows User's Guide, 'Labtech Data Acquisition and Process control Software'4/94 Release, Laboratory Technologies Corporation, USA, 1994
7. Considine, D.M., 'Process Instruments and Control handbook',3rd.ed., Mc.Graw Hill Book Company,
8. E.O. Doeblin, "Measurement system application & design", 4th. edition,Mc. graw Hill Publishing Com pany, 1990

MS–Excel Spreadsheet Simulation of Logic Functions Using Function–specific MSI Circuits

S. K. Sanyal and R. Nandi
Department of Electronics and Telecommunication Engineering,
Jadavpur University, Kolkata – 700 032, India.
E–mail : s_sanyal@ieee.org.

Abstract

This paper describes Ms–excel spreadsheet simulation of some combinational logic functions using function–specific MSI circuits like Multiplexers and Decoders. To achieve the desired outcome, spreadsheet simulations of fundamental logic functions like AND, OR and NOT and also EX–OR and EX–NOR functions have been carried out using the function toolbar. This low–cost and simplistic simulation approach makes it suitable as an engineering educational teaching aid for supplementing the learning of the course on logic design. Any change of inputs of logic circuits culminates in immediate change of logic output – a unique feature of spreadsheet analysis program. The details of the simulation have been incorporated.

Keywords : Spreadsheet, Simulation, Cells, Multiplexers, Decoders.

INTRODUCTION

With the advent of microcomputers and related technologies, the spreadsheet programs have become the part and parcel of modern PC based environment. Though originally developed and used for large–scale financial analysis, the spreadsheet is equally capable of performing scientific and engineering computations as reported in the literature [1–3]. The existence of Boolean functions in spreadsheet programs makes it possible to simulate the properties of logic gates and circuits. In this paper an attempt has been taken to simulate the basic logic functions like AND, OR and NOT functions followed by EX–OR and EX–NOR functions – a class of SSI circuits. A spreadsheet is basically a display of a grid of columns and rows identified by letters and nos. The intersection of columns and rows constitutes the 'cells' which can be used to store and display the logic variable. The logic gates/ circuits are represented by Squares/Rectangles with the inputs on the left hand side and the output on the right hand side. An attractive feature of spreadsheet is that if any input of the simulated logic gate/circuit is changed, the changed output is observed immediately thus the spreadsheet simulation exactly makes a replica of the logic gates/circuits implemented on breadboard in the laboratory. Thus this simulation technique can act as a very meaningful mode of imparting education in the course on logic design. The details of different simulations using MS–excel spreadsheet follow.

LOGIC GATE SIMULATION

A 4–input AND gate is simulated by MS–excel spreadsheet. The cells with identifiers A2, A3, A4 and A5 represent the four inputs. The output from the AND gate is logically computed according to the Boolean function, stored and displayed in cell C3. The relevant expression for the output from 4–input AND gate in cell C3 is = SUM (AND (A2, A3, A4, A5)). The 'AND' logical function is used from the toolbar using the paste function fx of the MS–excel spreadsheet. The above expression is typed on the formula bar. The requisite expression for the output from 4–input OR gate in cell H3 is =SUM(OR(F2, F3, F4, F5)). An interesting feature of spreadsheet is that if any input of the simulated logic gate is changed, the changed output is observed immediately on the screen. Thus the Truth Table of a particular logic gate can easily be verified by using the spreadsheet simulation program. For the simulation of NOT and BUFFER gates the logic function 'IF' from the toolbar is used. For the NOT gate the input cell is A23, while the output cell C23 utilises the Boolean expression = IF (A23 = 1,0,1) which stores a 0 in output cell C23 if the input cell A23 has a logic value of 1 otherwise a 1 will be stored in cell C23. This concept truly simulates a digital inverter or NOT gate. For the BUFFER gate the output cell H23 is logically equal to input cell F23. For the EX–OR logic gate the cells F30 and F33 represent the two inputs and the relevant expression for the output in cell H32 is = IF (F30 = F33, 0, 1) which means that if the two input cells are logically equal the output cell attains a

logical value of 0 otherwise 1. For the equivalence function the expression changes to = IF(A30 = A33, 1, 0).

For the simulation of 4–input NAND gate an intermediate cell K4 stores the result of 4–input AND gate with the input cells A12, A13, A14, A15 while the final NAND output in cell C13 follows the expression = IF(K4 = 1,0,1), the inversion of AND output. Similarly the NOR output in cell H13 is = IF(K9 = 1,0,1) where K9 represent the logical OR function of the input cells F12, F13, F14, F15). The simulation of all these very common logic functions are shown in Fig.1.

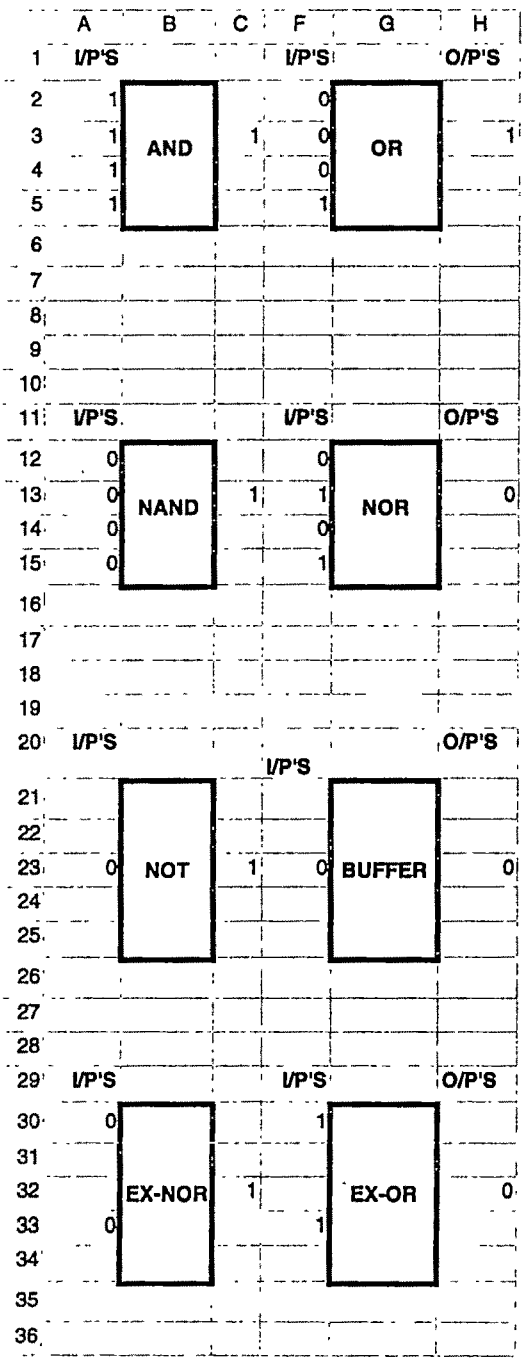

Fig.1 Excel simulation of logic functions.

The Truth Tables can be easily checked by changing the inputs and observing the change of outputs immediately.

SIMULATION OF MSI MULTIPLEXER

Multiplexer finds many applications in Digital systems design. This MSI device has three types of inputs namely Enable, Data and Select while the no. of output is only one. Because of some practical nesting limitation of the spreadsheet program, the simulation of 16x1 MUX is done by constructing a MUX tree structure using two 8x1 MUX and one 2x1 MUX. For a 16x1 MUX with S3(MSB), S2, S1 and S0 (LSB) as select inputs, the simulation scheme is shown in Fig.2.

The upper 8x1 MUX is activated for S3=E=0 stored in cell D20 while the lower 8x1 MUX is activated for E=1, i.e. the inversion of S3, stored in cell D38. The Enabled inputs are stored in D20 and D38 respectively.

The expression for the output from upper 8x1 MUX stored in cell H16 is

= SUM(AND(OR(AND(E9=0, F9=0, G9=0,
D11), AND (E9=0, F9=0, G9=1, D12),
AND (E9=1, F9=1, G9=1, D18)), D20=0)).

A similar expression is used for lower 8x1 MUX with output stored in H34. The outputs from two 8x1 MUXs are applied at the two inputs I23 & I24 of a 2x1 MUX with I25 as Enabled input and K24 as the output. Thus the cell K24 represents the single output of 16x1 MUX. For the 2x1 MUX the cell J21 = D20 acts as Enable input. The relevant expression the output of 2x1 MUX stored in cell K24 is

= SUM(AND(OR(AND(J21=0, I23)
, AND (J21=1, I24), I25=0))

Thus the simulation scheme as shown in Fig.2 fully obeys the Truth Table of 16x1 MUX.

SIMULATION OF BOOLEAN FUNCTION USING MSI MULTIPLEXER

The above simulation work has then been extended for the implementation of logic function using function–specific MSI multiplexer. The multiplexer based Boolean function implementation utilises the well known Shanon's Expansion Theorem [4]. As a case study, an attempt has been taken to implement the function F(A,B,C,D) = Σm(0,1,3,4,8,9,15) with A, B, C & D as input signals and F as output signal. To carry out Type–0 design [4] a 16x1 MUX which is simulated based on the scheme of Fig.2 has been utilised. The Type–0 simulation scheme is shown in Fig.3.

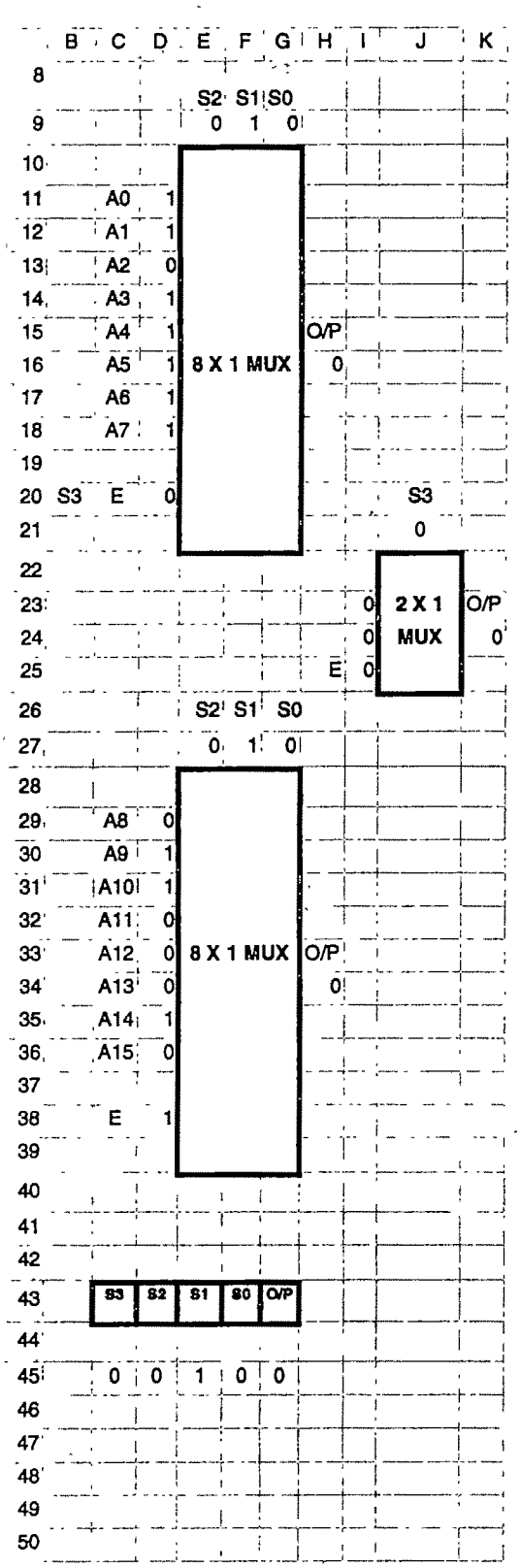

Fig.2 : Simulation scheme for 16 x 1 MUX.

In this simulation the cell F19 represents the Enable input and the cells G20, H20, I20 and J20 store the 4–bit select input with G20 as MSB. The cells F1 to F16 store the 16 data inputs. The functional output is stored in cell K10.

Now by utilising the concept of 'partitioning–off' of the input signals [4], the size of the multiplexer is reduced gradually from 16x1 to 8x1, then to 4x1 and finally to 2x1 thereby carrying out Type–1, Type–2 and Type–3 designs [4]. The Type–1 and Type–2 designs utilising the simulations of 8x1 and 4x1 Multiplexers are shown in Fig.4.

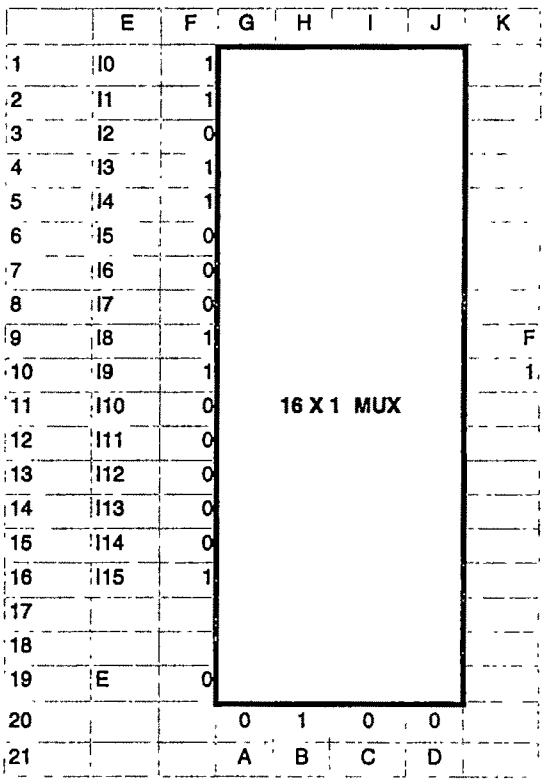

Fig.3 : Type–0 simulation scheme.

It is to be noted that the reduction of the size of the multiplexer invites the association of some SSI logic gates to complete the MSI design. Fig.5 represents the simulation scheme for Type-3 design using 2x1 MUX as basic building block.

SIMULATION OF BOOLEAN FUNCTION USING MSI DECODER

Since the Multiplexers have only one output, the implementation of many functions requires many multiplexers. To circumvent this problem, an alternative approach is adopted by using MSI Decoders. The simulation of 4 to 16 lines Decoder with enable facility is shown in Fig.6. Here the input variables D(MSB), C, B, A (LSB) are stored in the cells B19, B18, B17 and B16

while the Enable input is stored in cell B24. The 16 nos. of output lines D0 – D15 are stored in the cells F9 to F24. The expression for the output line D4 stored in the cell F13 is given by

=IF(AND(B19=0, B18=1, B17=0, B16=0, B24=0), 0, 1).

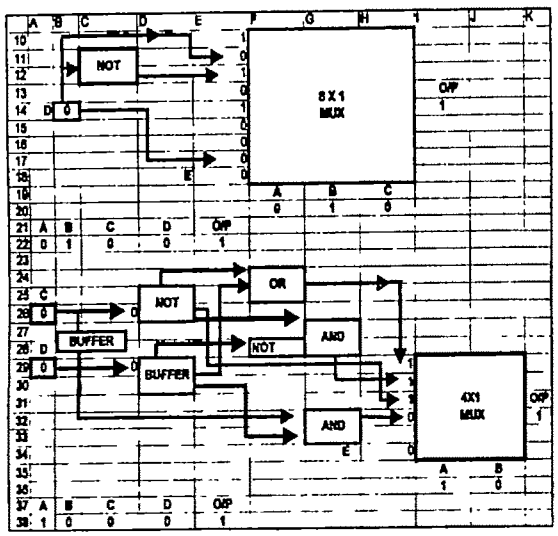

Fig 4 Excel simulation for type 1 and type 2 designs

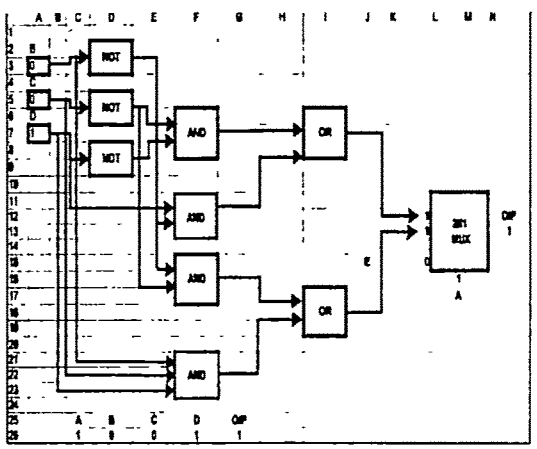

Fig 5 Excel simulation fro type 3 design

Following the procedure for Decoder implementation of Boolean function [4] an extended simulation scheme has been developed to implement the function F(A,B,C,D)=Σm(0, 1, 3, 4, 8, 9, 15) using the spreadsheet simulated 4x16 Decoder and a 7–input negated OR i.e. 7–input NAND gate. The 7–input NAND gate is simulated in which the cells H14 to H20 store the logical inputs of the 7–input NAND gates. The contents of H14 to H20 are derived from the output cells F9, F10, F12, F13, F17, F18 and F24 of the 4x16 simulated Decoder for those minterms for which the value of the function is 1. The relevant expression for the output function which comes from the output of 7–input NAND stored in cell J17 is given by = IF (SUM(AND(H14 : H20)=0, 1,0)).

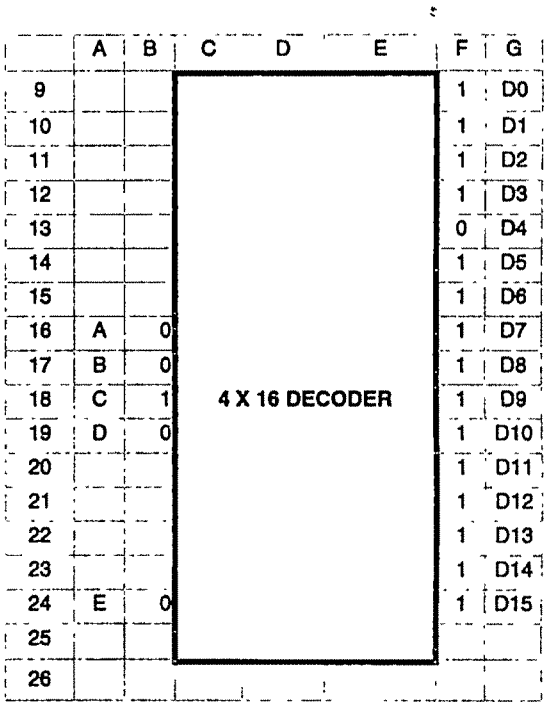

Fig.6 : Simulation of 4 x 16 Decoder.

The simulation scheme for the implementation of the above Boolean function using the simulated 4 x 16 Decoder and 7-input NAND gate is shown in Fig.7.

SIMULATION RESULTS

The Truth Tables of all the logic gates have been verified and the results are immediately available on the screen of the monitor. The Truth Table of the function in SOP form implemented both by Multiplexer and Decoder are also in conformity with the actual one. The effect of change of one input is immediately visible on the screen. The simulation scheme has been made much attractive to the student community as a user friendly laboratory educational teaching aid, where the successive design stages are clearly visible.

CONCLUSION

An Ms–excel spreadsheet simulation of fundamental and derived logic gates has been carried out. The approach is then extended to Multiplexer and Decoder based implementation of Boolean function. As a case study a particular function in SOP form has been taken. Different types of MUX design and Decoder implementation have

satisfactorily been carried out. The simulation scheme has brought about an excitement amongst the student community.

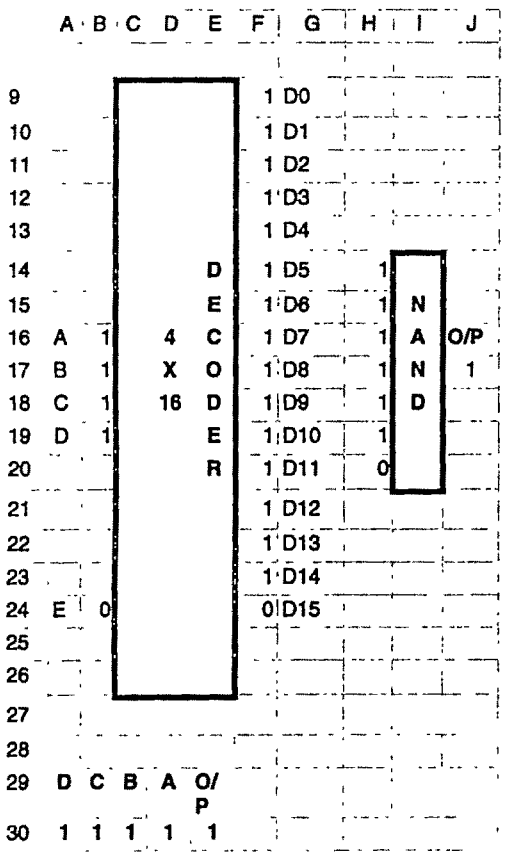

Fig.7 : Simulation of Boolean function using 4 x 16 Decoder & 7-input NAND gate.

It is concluded that the said low–cost, simple, user friendly and efficient spreadsheet simulation scheme can be considered as an alternative PC based teaching cum training tool for studying the course on logic design.

ACKNOWLEDGEMENT

The authors wish to acknowledge the UGC, New Delhi for its support behind this work in the form of Major Research Project entitled "Educational Development of Digital Functional System using MS–EXCEL Spreadsheet" at the Deptt. of ETCE, Jadavpur University, Kolkata–700032.

REFERENCES

1. L.P. Huelsman, Electrical Engineering applications of microcomputer spreadsheet analysis program, IEEE Transactions on Education (1984)., vol.E–27, No.2, May.
2. A. El–Hajj and K.Y. Kabalan, A spreadsheet simulation of logic networks, IEEE Transactions of Education (1991), vol.E–34, No.1, February.
3. A. El–Hajj, K.Y. Kabalan and M. Yehia, Simulation of a class of integrated circuits using spreadsheets, IEE Proceedings–G (1992), vol.139, No.5, October.
4. R.S. Sandige, Modern Digital Design, (Mc Graw–Hill, Singapore, 1990), p 331–P338.

Simulation of Fuzzy Combinational Functions Using Microcontroller

S. Chattopadhyay*, S. K. Sanyal, and R. Nandi****
*Department of Electronics and Telecommunication Engineering,
Netaji Subhas Engineering College, Techno City,
P.O. Panchpota Police Para, Garia, India.
**Department of Electronics and Telecommunication Engineering,
Jadavpur University, Kolkata – 700 032, India.
E-mail : s_sanyal@ieee.org.

Abstract

This paper describes the simulation of some fuzzy combinational functions like AND, OR, NOT, NAND, NOR, X-OR and X-NOR using 8031 microcontroller. This approach makes it possible the further extension in the simulation of different fuzzy combinational functions. The simulation is developed using the concept of Min/Max fuzzy operations as well as the negation operation. To simulate any fuzzy combinational function (except NOT) we need at least two inputs. These inputs are obtained by using a O-5V regulated dc power supply and a potential divider circuit. In this way five different voltages in the range of 1V-5V have been generated. For the purpose of the experiment, two voltages of magnitudes 2V and 4V are used as input to an A/D converter. These analog input voltages have been converted to digital codes by ADC 0808, a 8-bit 8 channel multiplexed A/D converter. The digital version of analog voltages are then applied to the 8031 microcontroller via Port A and Port C of 8155 PPI chip. A subroutine for the purpose of reading of the I/P analog voltages has also been developed which is called for the simulation of the said fuzzy operations. The result of these operations are obtained as 8-bit binary ward through Port-B of 8155 PPI chip.

Keywords : Fuzzy, membership function, Max, Min.

INTRODUCTION

The word 'fuzzy' means vague or not distinct. Vagueness is an aspect of uncertainty which is different from randomness [1]. Fuzzy logic is a mathematical way of looking at the intrinsic vagueness of the natural human language [1]. In other way we can say that fuzzy logic is a methodology for computing with words [7]. Computers do not understand vague human concepts; data have to be presented to a computer in simple binary logic. Most of human data, however, is not binary. For example, if we want to describe the 'speed' of a car then we do not want to divide the attribute 'Speed' into two well defined groups such as 'fast' and 'slow'. In our thinking, within the 'fast' group we get 'speed' which is really fast, and speed which is bordering on being 'slow', and a whole range in between. Extending this idea we can say that all things admit degrees in their description; these degrees are not random but rather deterministic, based on several factors such as the nature of the situation, experience etc. This is the basic idea of fuzzy sets as opposed to classical or crisp sets [1].

In classical set theory an object either belongs to a set or not; the speed of a car is either fast or slow. Classical set theory was the mathematical background for computer logic. In fuzzy set theory degree of belongingness to a set are introduced; the speed of a car can be, for example 80% in the 'fast' set and 40% in the 'slow' set, based on our experience and judgement. Fuzzy set theory is the mathematical background to capture the way people think [1].

The basic fuzzy operations are Min (AND), Max (OR) and Negation (NOT). An IEEE paper had already been published on 'Evaluation of Min/Max Instructions for Fuzzy Information Processing' [2]. This paper proposed the design of a fuzzy information processor using a quantitative approach. This quantitative approach was developed by

RISC (Reduced Instruction Set Computer) designers. Here 'Min' & 'Max' operations were implemented by expressing them in MIPS R3000A Assembly Language. These operations were also tested in an image processing application because of their usefulness in executing other fuzzy logical operations [2]. The present paper describes the simulation of some fuzzy combinational functions like AND, OR, NOT, NAND, NOR, X-OR and X-NOR using 8031 Microcontroller based on the definition of 'Min', 'Max' and 'Negation' operation.

BASIC CONCEPTS OF FUZZY SETS

A set is nothing but a collection of objects. A classical set or crisp set may be defined using membership function (MF). The MF assumes a value of 1 for elements that are members of the set, and assumes a value 0 for elements that are not members of the set. So we can define a classical set A as follows :

$\mu_A(X) = 1$ if $X \in A$
$= 0$ if $X \notin A$

If we consider universe of discourse U = {1,2,3,4,5,6} and A = set of even numbers, then we can write A as

{(1,0), (2,1), (3,0), (4,1), (5,0), (6,1)}

This concept has led to the two-valued Boolean logic, which is very natural for electronic systems based on switches, since a switch may assume one of only two possible values [3]. Such a system, however, is not applicable to human being's perceptions. So instead of considering two extreme values only we should also consider the intermediate values.

If 'I' is a collection of objects and X is its elements, then fuzzy set 'A' in 'I' is a set of ordered pairs such as

$A = \{X, \mu_A(X) \mid X \in I\}$

where $\mu_A(X)$ is the membership function of X in A. Elements with a zero membership are usually not listed [3].

Let us consider a fuzzy set A = 'integers close to 10' we can represent fuzzy set A as

A = {(7,.7), (8,.8), (9,.9), (10,1), (11,.9), (12, .8), (13, .7)}

In this example if the integer is 10, then it is most close to 10, so $\mu_A(X) = 1$. If the integer is 9 or 11, then it is not most close to 10 but also close to 10. So for integers 9 or 11, a membership function .9 has been assigned.

So by defining a fuzzy set we get a clear definition of an ambiguous statement. If we consider the previous example 'integers close to 10' then, before defining fuzzy set A it was an ambiguous statement. Once an ambiguous statement is defined somehow (by defining fuzzy set), it is no longer ambiguous, at least for the definer. So, we can say, there is nothing fuzzy about fuzzy sets [1].

In fuzzy logic application, three common operations are AND (intersection), OR (union), NOT (complement) [4]. The fuzzy AND of two fuzzy sets A & B is given by

$$A \text{ AND } B = A \wedge B = \min(\mu_A(X), \mu_B(X)) \quad \ldots(1)$$

where $\mu_A(X)$ and $\mu_B(X)$ are the MFs of element X in set A & B respectively. Similarly the fuzzy OR is defined as

$$A \text{ OR } B = A \vee B = \max(\mu_A(X), \mu_A(X)) \quad \ldots(2)$$

and fuzzy NOT is defined as

$$\mu_{\overline{A}}(X) = 1 - \mu_A(X). \quad \ldots(3)$$

SIMULATION PROCESS

The simulation process of some fuzzy combination functions like AND, OR, NOT, NAND, NOR, X-OR and X-NOR is explained clearly by the following diagram.

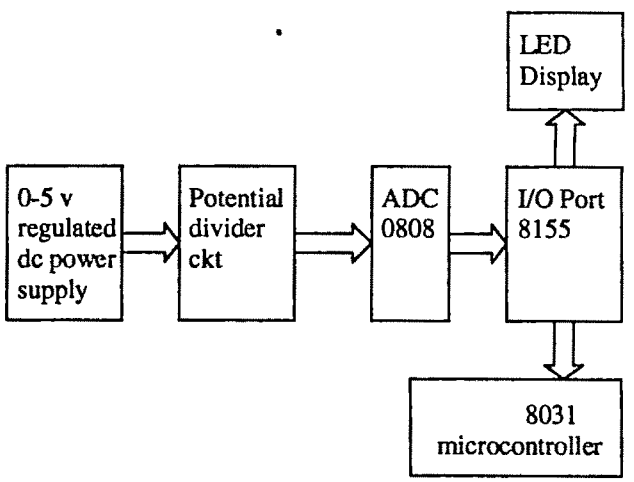

Fig.1 : Block diagram of simulation process

Any two input voltages 2v and 4v have been selected by potentially diving the 0 – 5v regulated dc power supply. These two input voltages have been converted to digital codes by ADC 0808, an 8 bit 8 channel multiplexed A/D converter. For this purpose channel 1 and channel 3 of ADC 0808 have been selected through proper programming of microcontroller. The codes enter the 8155 PPI chip via Port A and Port C respectively. The algorithms developed for above fuzzy operations being executed by writing suitable Assembly Language Programs for 8031 Microcontroller. An ADC read subroutine has been developed which is called repeatedly in the simulation process. The result of these operations have taken out through Port B of 8155 PPI which gives an 8-bit binary bit pattern. The flow chart for fuzzy AND operation has been shown in Fig.2 and Fig.3. Fig.2 shows the Flow Chart for ADC read subroutine which

is called in the main program for fuzzy AND, named as Fig.3 The 8031 Assembly Language Program for fuzzy OR operation has also been presented where Fig.4 is used for ADC read subroutine and Fig.5 for main program. The other fuzzy operations described in this paper will have same flowchart and assembly language program for ADC read subroutine, but the main program will change depending upon the particular operation.

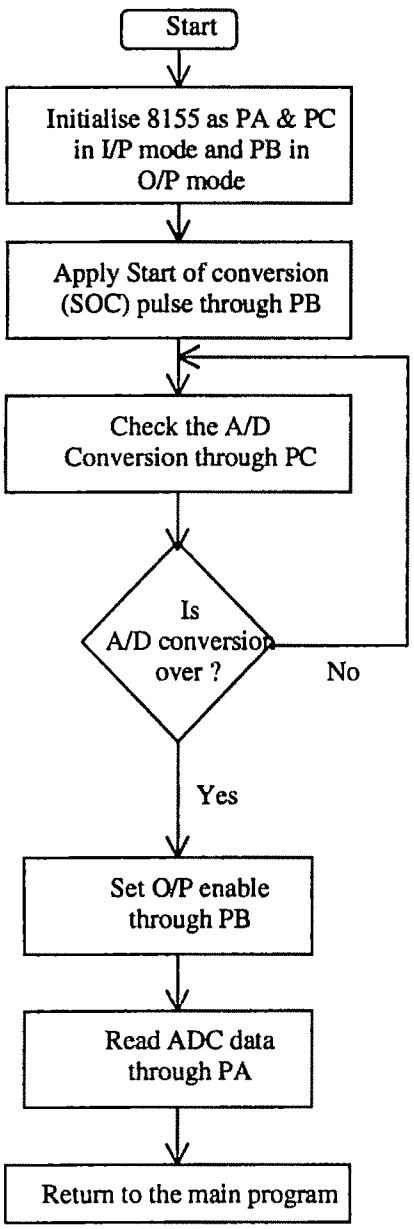
Start
Initialise 8155 as PA & PC in I/P mode and PB in O/P mode
Apply Start of conversion (SOC) pulse through PB
Check the A/D Conversion through PC
Is A/D conversion over ?
No
Yes
Set O/P enable through PB
Read ADC data through PA
Return to the main program

Fig. 2 : Flow chart for ADC read subroutine.

Fig. 3 : Flow chart for fuzzy AND operation. →

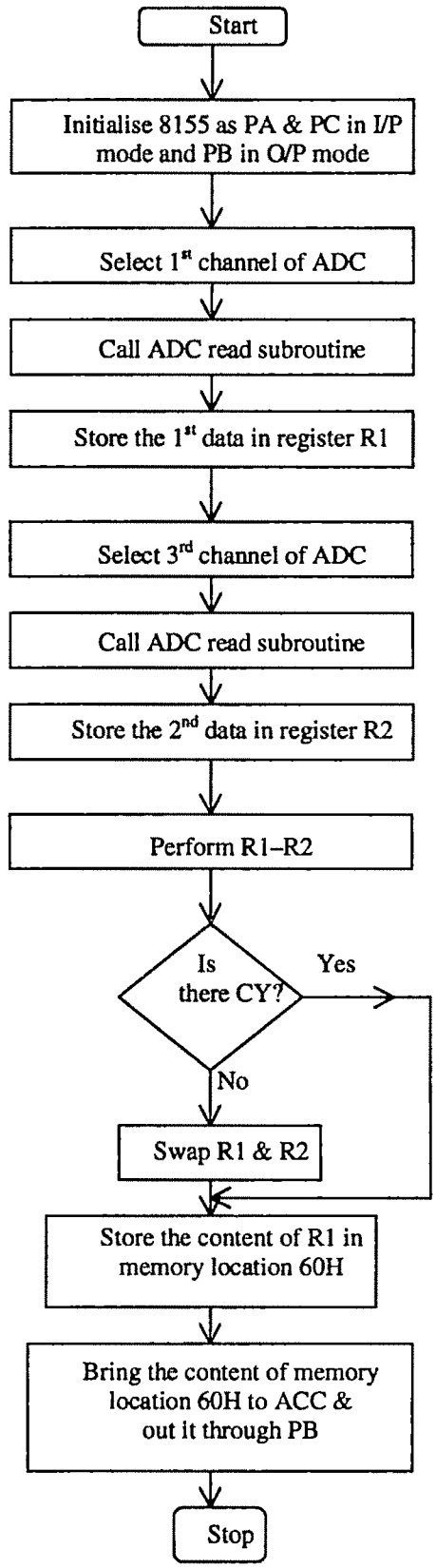
Start
Initialise 8155 as PA & PC in I/P mode and PB in O/P mode
Select 1st channel of ADC
Call ADC read subroutine
Store the 1st data in register R1
Select 3rd channel of ADC
Call ADC read subroutine
Store the 2nd data in register R2
Perform R1–R2
Is there CY?
Yes
No
Swap R1 & R2
Store the content of R1 in memory location 60H
Bring the content of memory location 60H to ACC & out it through PB
Stop

```
Label       Mnemonics

            ORL   A, # 08
            MOV   DPTR, # 0B802
            MOVX  @ DPTR, A
            ANL   A, # OF7
            NOP
            MOV   DPTR, # OB802
            MOVX  @ DPTR, A
            NOP
            NOP
LOOP1       MOV   DPTR, # 0B803
            MOVX  A, @ DPTR
            ANL   A, # 01
            JZ    LOOP1
            MOV   DPTR, # 0B802
            MOVX  A, @ DPTR
            ORL   A, # 10
            MOV   DPTR, # 0B802
            MOVX  @ DPTR, A
            NOP
            MOV   DPTR, # 0B801
            MOVX  A, @ DPTR
            RET
```

Fig. 4 : Programme for ADC read subroutine.

```
Label       Mnemonics

            MOV   A, # 02
            MOV   DPTR, # 0B800
            MOVX  @ DPTR, A
            MOV   A, # 00
            MOV   DPTR, # OB802
            MOVX  @ DPTR, A
            LCALL Program 1
            MOV   R1, A
            MOV   DPTR, # 0B802
            MOVX  @DPTR, A
            LCALL ADC read SR
            MOV   R2, A
            MOV   A, R1
            SUBB  A, R2
            JNC   L00P2
            MOV   A, R2
            MOV   R1, A
L00P2       MOV   60, R1
            MOV   A, 60
            MOV   DPTR, # 0B802
            MOVX  @ DPTR, A
L00P3       SJMP  L00P3
```

Fig. 5 : Main program for fuzzy OR operation

RESULTS OF SIMULATION

The simulation results for the different fuzzy functions described in this paper have been shown below in a tabular form. For this purpose, two input voltages of value 2V and 4V are used. The following table shows the bit pattern of PB of 8155 PPI chip where '0' represents OFF state and '1' represents ON state of LED respectively.

Table – 1 : Simulation results of different fuzzy functions

Fuzzy operation	Bit pattern observed from PB of 8155 PB_7 PB_6 PB_5 PB_4 PB_3 PB_2 PB_1 PB_0							
AND	0	1	1	0	0	1	0	0
OR	1	1	0	0	1	0	0	0
NOT	1	0	0	1	1	0	1	1
NAND	1	0	0	1	1	0	1	1
NOR	0	0	1	1	0	1	1	1
X-OR	1	0	0	1	1	0	1	1
X-NOR	0	1	1	0	0	1	0	0

CONCLUSION

The developed algorithms have been simulated using 8031 Assembly Language. The 8031 Microcontroller has been used because it is capable of providing some extra hardware facilities such as clock generator, RAM, ROM/ EPROM, Parallel and Serial I/O ports, timer/counter, A/D, D/A converters in addition to three basic units ALU, register unit and control unit. It is also known as single-chip microcomputer [5].

It is also possible to simulate different fuzzy combinational circuits such as adder, code converters, MUX, DEMUX, Encoder, Decoder etc. with the help of the developed algorithms described above. The advantage of implementing different combinational circuits using fuzzy logic rather than binary logic is quite straight forward. In case of TTL logic the range of voltage 0 – 0.4v (typical

0.2v) corresponds to logic '0' state and 2.4 – 5v (typical 3.5v) corresponds to logic '1' state [8]. The voltage ranging between the limits of logic '0' & logic '1' cannot be defined properly but using fuzzy logic any voltage in the transition region can be recognised properly by defining proper MF. Apart from the combinational circuits, this simulation idea can also be extended for different fuzzy sequential circuits live, flip-flop, register, counter etc.

REFERENCES

1. A. M. Ibrahim, Introduction to Applied Fuzzy Electronics (Prentice Hall of India, New Delhi, 1999). p 1-2, p 26-27.

2. H. Watanabe, D. Chen and S. Konuri, Evaluation of Min/ Max Instructions for Fuzzy Information Processing. IEEE Transactions on Fuzzy Systems, (1996), vol.4, August, p 369-374.

3. L.A. Zadeh, Fuzzy Logic, IEEE Computer (1998), p 83–89.

4. T. Terano, K. Asai and M. Sugeno, Fuzzy Systems Theory and Its Application, (Academic Press, NY, 1992), p 12–19.

5. ALS-SDA-31, 8031 system design aid – Users manual, (Advanced Electronic System, Bangalore, 1994), p 18–35.

6. S. Guo and L. Peters, Design and Application of an Analog Fuzzy Logic Controller. IEEE Transaction on Fuzzy Systems, (1996), vol.4, November, p 429.

7. L. A. Zadeh, Fuzzy Logic – Computing with Words, IEEE Transactions on fuzzy systems, (1996), vol.4, May, p 103.

8. M. M. Mano., Digital Logic and Computer Design. (Prentice Hall of India, New Delhi, 2000), p 63.

Digital Tuning of Analog Wave Processor

R.K. Nagaria*, P. Venkateswaran, S. K. Sanyal* and R. Nandi***
*Department of Electronics and Telecommunication Engineering,
Jadavpur University, Kolkata – 700 032, India.
**Department of Electronics and Telecommunication Engineering
Haldia Institute of Technology, Haldia–721657, India.
E–mail : s_sanyal@ieee.org

Abstract

Some new analog time–domain wave processing circuits (e.g. ramp, pulse, time–base etc.) based on integration / differentiation by using the new Current Feedback Amplifier (CFA) device are proposed. Digital tuning of the circuit parameter (e.g., time–constant) can be achieved by using a Switched Programmable R (or C) array, or by using a control voltage (V_c); in either case Port 1 of 8031 microcontroller has been used to achieve the digital tuning of the processing circuits. The variation of digital code or word is culminated in the variation in slope/output voltage in case of integrator/differentiator respectively. Satisfactory test results are obtained.

Keywords : Time–constant, Digital–tuning, Port.

INTRODUCTION

The Current Feedback Amplifier (CFA) device [1] is being widely used at present for the design of analog signal / wave processing circuits. The CFA has certain advantageous properties [2] e.g., improved AC performance with better linearity, flexibility of deriving current or voltage signal outputs at its two separate nodes, i.e. suitability of current or voltage mode designs, and accurate port transfer ratios equal to unity, i.e., low tracking errors ($\epsilon << 1$) implying low sensitivity design [3, 4].

We propose here some new novel active RC dual – input tunable integrator and differentiator circuits using the CFA; enhancement of time constant without requiring large spreads of passive components is obtainable. Both current mode and voltage mode versions are presented, whereas the previous Opamp versions [5, 6] were given for voltage mode applications. The analysis had been carried out using the practical CFA model (e.g., AD 844) with finite tracking errors ($\epsilon \neq 0$) and subsequent sensitivity figures had been derived.

The work is undertaken in two phases. The first phase of the work involves the design of some new integrator and differentiator circuits using the new CFA as the active device. The CFA is a current – mode amplifier with accurate terminal characteristics and wideband properties. Here two types of circuit configurations have been designed, viz. One having the time constant (τ) variable by one resistor or capacitor ; the other having a voltage variable τ– obtainable by utilizing a Multiplier (8013) element.

The second phase of the work involves the synthesis of digital tuning of τ. The single resistor (or capacitor) variation can be programmed in such a way that a desired resistor (a capacitor) value (hence a desired τ) can be switched from a weighted resistor (or capacitor) –array, the switch activation being done by a digital code (or word).

In case of voltage variable τ, the control voltage(V_c) is derived from a digital code by means of a R–2R ladder network element. A sequence of binary words generates a range of value of V_c, hence a sequential variation of τ – that finally yields a programmable waveshape for time–domain signals.

An interesting extension of such wave processing would be the design of digitally programmable sinewave generators based on double–integrator or double–differentiator loop networks. Here the component integrator / differentiator is the one as described above.

We have designed these wave processor / generator circuits in the laboratory by using the CFA device (AD 844) as the primary element in the analog portion, and a 8031 microcontroller as the tuning element in the digital portion. Suitable Assembly Langauge Programs have been

developed. The 4 bit binary codes (or words) are being connected to the analog circuit element through CD 4066 based switched Programmable Resistor / Capacitor Array. The digital variation in the binary codes manifests as the proportionate variation of slope, (output voltage) in integrator (differentiator) circuits.

ANALYSIS

The CFA device is characterized by the port relations $I_z = \alpha I_x$, $V_x = \beta V_y$ and $V_0 = \gamma V_z$, where $\alpha = 1 - \epsilon_i$, $\beta = 1 - \epsilon_v$ and $\gamma = 1 - \epsilon_0$. Usually the tracking errors are extremely small ($\epsilon << 1$) and for an ideal CFA these errors vanish ($\epsilon = 0$).

The proposed current mode configuration is shown in Fig. 1, where the output current (I_0) is

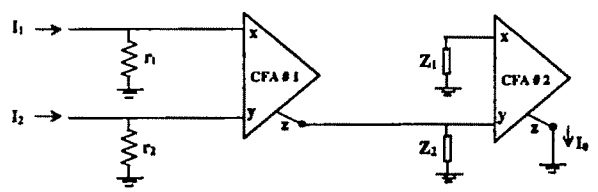

Fig.1 : Dual–input current mode ratio (Z_2/Z_1) function circuit.

$$I_0 = \alpha_1 \alpha_2 \beta_2 (Z_2/Z_1) \{\beta_1 I_2 (r_2/r_1) - I_1\} \qquad (1)$$

For a true differential input function, the realizability condition is

$$r_2 = \beta_1 r_1 = \{1 - \epsilon_{v1}\} r_1 \qquad (2)$$

Note that for ideal CFA ($\epsilon = 0$), eq. (2) becomes $r_2 = r_1$. With eq. (2) in eq. (1), one gets a ratio function (Z_2/Z_1) which yields a true differential integrator having a nominal time constant $\tau = CR$ with $Z_2 = 1/sC$ and $Z_1 = R$:

$$\frac{I_0}{I_2 - I_1} = \frac{1}{s\tilde{\tau}}; \qquad \tilde{\tau} = \tau / \alpha_1 \alpha_2 \beta_2 \qquad (3)$$

The modified time constant can be expressed as $\tilde{\tau} = \tilde{C}R$ where $\tilde{C} = C / \{1 - (\epsilon_{i_1} + \epsilon_{i_2} + \epsilon_{v_2})\}$ assuming error products are negligible since $|\epsilon| << 1$.

For a differentiator one selects $Z_1 = 1 / sC$ and $Z_2 = R$ yielding $I_0 / (I_2 - I_1) = s\tilde{\tau}$, where $\tilde{\tau} = \tilde{C}R$; $\tilde{C} = C\{1 - (\epsilon_{i_1} + \epsilon_{i_2} + \epsilon_{v_2})\}$. Both the functions are tunable by a resistance. The effects of the CFA errors can be corrected by a compensating capacitor (C_X) in series to C for integrator, and in parallel to C for the differentiator. The compensation design equations are

$$C_{Xint} = C / (\epsilon_{i_1} + \epsilon_{i_2} + \epsilon_{v_2})$$
$$C_{Xdiff} = C (\epsilon_{i_1} + \epsilon_{i_2} + \epsilon_{v_2}) \qquad (4)$$

Next the voltage mode configurations are shown in Fig.2. The results of the analysis and the pertinent design equations are presented in concise from in Table–1. The active sensitivities relative to the CFA

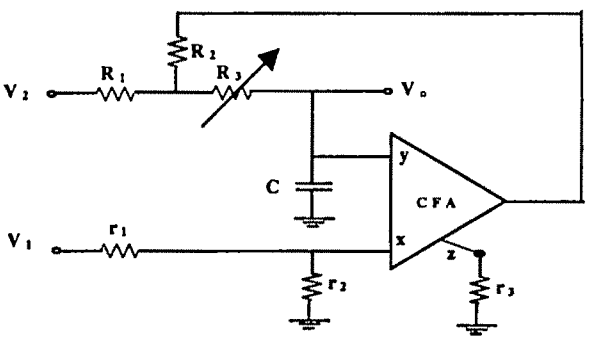

Fig.2(a) : Dual–input integrator using a CFA.

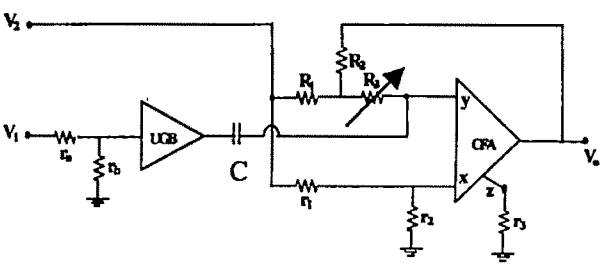

Fig.2(b) : Dual–input differentiator using a CFA and unity–gain buffer (UGB).

imperfections of the time–constant, calculated on the residues of the negative – real ($\tilde{\tau}$) pole/zero can be shown to be extremely low, i.e., $|s^{\tilde{\tau}} \epsilon| = \epsilon / (1 - \epsilon) << 1$ since usually $\epsilon_{i,v,0} << 1$. It may be observed that for both current /voltage –mode designs, τ_0 can be single tuned by a resistor. For the voltage mode circuits the tuning involves some enlargement factor, i.e., large spreads of component values are avoidable. The

integrator output is actually the capacitor voltage; a wideband buffer here would give voltage source output.

VOLTAGE CONTROLLED INTEGRATOR /DIFFERENTIATOR

The proposed analog voltage (V_c) controlled configuration is shown in Fig 3, wherein routine analysis based on CFA port properties yields the voltage transfer function

$$\frac{V_0}{V_i} = -\frac{(y_1 / y_2)}{(y_3 / \alpha\gamma y_2) + KV_c} \qquad (5)$$

where K is the multiplier constant usually K = 0.1 /volt for the 8013 element. Selection of appropriate RC components yields the desired integrator and differentiator function, the component choice and the pertinent design equations are listed in Table – 2.

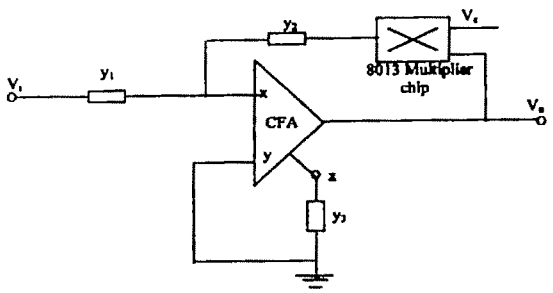

Fig.3 : Voltage (V_c) controlled integrator/differentiator using CFA and a multiplier element.

It may be observed in Table – 2 that τ_0 can be tuned manually by n (= RG_3; a resistor ratio) for the differentiator, and, by m (= C_3 / C; a capacitor ratio) for the integrator. In both functions, electronic tuning is obtainable by the control voltage V_c. With a nonideal CFA, the nominal time constant (τ) deviates slightly by a factor ($1 - \epsilon_i$).

The active sensitivity figures are seen to be quite low given by

$$\left|S^{\tau_0}_{\epsilon_{i,0}}\right| = \frac{\epsilon_{i,0}}{1-\epsilon_i} << 1$$

and $$\left|S^{\tau_0}_{\epsilon_v}\right| = 0$$

DIGITAL TUNING

To achieve digital tunability of the proposed networks a scheme has been developed involving Switched Programmable Resistor Array (SPRA) or Capacitor Array (SPCA) driven by Microcontroller. A scheme involving SPRA replacing R_3 of Fig. 2 is shown in Fig.4(a). The CMOS 4066 switches are driven by the internal Port 1 of 8031 microcontroller. This arrangement varies R_3 from 15R to R according to the binary code variation from 0000 to 1110 thereby varying the time-constant of the networks. Similar thing has been done with SPCA. The combination of SPRA and SPCA make a wider variation of time-constant associated with integrators and differentiators.

For the digital tunability of the network of Fig.3 a R-2R ladder type D/A converter is used. Port 1 of 8031 microcontroller drives the digital input side of the ladder network. The output of this network is connected to the control voltage terminal of 8013-multiplier chip. The arrangement is shown in Fig. 4(b).

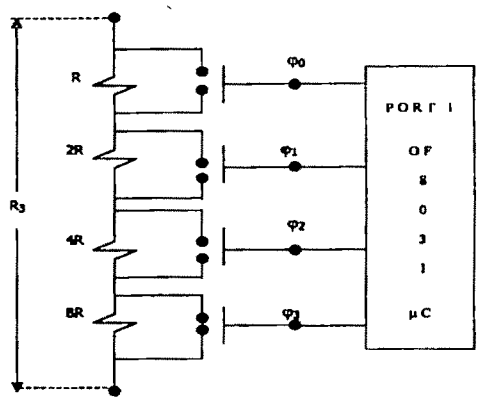

Fig.4(a) : Switched programmable register array.

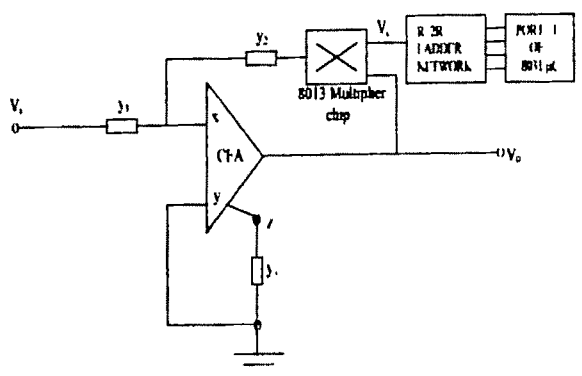

Fig.4(b) : Digitally tunable integrator/differentiator.

Table-1. Realization and design equations for voltage mode dual–input true integrator/differentiator

Fig. 2	Function	Transfer Equation	Simplified Design Equations		Transfer function & Time Constant
			Nonideal CFA	Ideal CFA	
a.	Integrator	$V_0[\delta sCR_1+\{1+x-(\alpha\beta\gamma)(1+m)x/\lambda\}] = V_2-\alpha\gamma(x/\lambda)V_1$ $x = R_1/R_2,\ n = R_3/R_1,\ m = r_1/r_2,$ $\lambda = r_1/r_3,\ \delta = 1+n+nx$	$R_1 = R_2 = R$ $r_3 = r_1(1+\epsilon_t+\epsilon_0)$ $r_2 = r_1/(1+2\epsilon_v)$	$r_1 = r_2 = r_3$	$\frac{V_0}{V_2-V_1}(s) = \frac{1}{s\tau_0}$ $\tau_0 = CR(2n+1)$
b.	Differen–tiator	$V_0(x+\alpha\delta u) = (sCR_1\delta p\beta)V_2-(sCR_1\delta k)V_1+\{\beta p(1+x)-1\}$ $x = R_1/R_2,\ n = R_3/R_1,\ u = r_1/r_3,$ $p = r_2/(r_1+r_2),\ k = r_b/(r_a+r_b),$ $\delta = 1+n+nx$	$r_1 = r_2 = r$ $r_a = r_b(1-2\epsilon_v)$ $R_1 = R_2 = (1+2\epsilon_v)$ $r_3 = r_1(1-\epsilon_i)$	$r_a = r_b$ $R_1 = R_2 = R$ $r_3 = r_1 = r$	$\frac{V_0}{V_2-V_1}(s) = \frac{1}{s\tau_0}$ $\tau_0 = (1+\frac{n}{1+n})\frac{CR}{4}$

Table-2. Realizability and design equations for the integrator/differentiator function in Fig.3.

Function	Components	Voltage Transfer Function $\frac{V_0}{V_i}(s)$	Time Constant	
			Ideal ($\epsilon = 0$)	Nonideal ($\epsilon \neq 0$)
Differentia–tor	$y_1 = sC$ $y_2 = 1/R$ $y_3 = G_3$	$\frac{-sCR}{RG_3(1-\epsilon_t)+KV_c}$ $\epsilon_t = \epsilon_i + \epsilon_o$	$\tau_0 = \frac{\tau}{n+KV_C}$ $\tau = RC$ $n = RG_3$	$\tilde{\tau}_0 = \frac{\tau}{\tilde{n}+KV_C}$ $\tilde{n} = n(1-\epsilon_t)$
Integrator	$y_1 = 1/R$ $y_2 = sC$ $y_3 = sC_3$	$-(sCR\,(m+KV_c)\}^{-1}$	$\tau_0 = \tau(m+KV_C)$ $\tau = RC$ $m = C_3/C$	$\tilde{\tau}_0 = (m+KV_C)\ \tilde{\tau}$ $\tilde{\tau} = \tau(1-\epsilon_t)$

The Assembly Language Program for the digital tunability is shown in Fig.4(c).

```
L00P1 : MOV  R0, # FFH
        MOV  R1, # 00H
        MOV  C, 90H
        MOV  94H, C
        MOV  C, 91H
        MOV  95H, C
        MOV  C, 92H
        MOV  96H, C
        MOV  C, 93H
        MOV  97H, C
        LJMP L00P1
```

Fig.4(c) : Assembly language program.

TEST RESULTS

Using the AD 844 type CFA tests both the current/voltage mode integrators and differentiators. First the circuits has been tested for anti phase sine wave inputs and satisfactory response up to about 48 KHz had been obtained with negligible phase error.

A typical test result with square waves of unequal-pace as the input to the proposed integrator configuration in Fig.2(a) is shown in Fig.5 for the component design of R = 10KΩ, C = 10 nF, n = 4.5, i.e., an enlargement factor of 10; the power level for the device has been set at 0 ± 9V.d.c. By replacing the chip randomly by another, it is observed that the wave response remained practically unaffected.

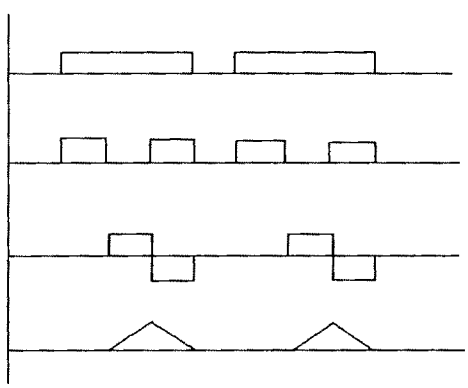

Fig. 5 : Experimentally observed response for dual-input integrator in Fig.2(a).

The digital tunability of both the networks of Fig.2 has been tested in the laboratory using both SPRA and SPCA and satisfactory test results have been obtained. The variation of binary word has been culminated in the variation of the slope and amplitude of the integrator and differentiator respectively. For the network of Fig.3, the slope variation has been found from 0.14 V/μs to 0.05 V/μs gain the binary word variation from 0000 to 1110 some of which has been shown in Fig.6.

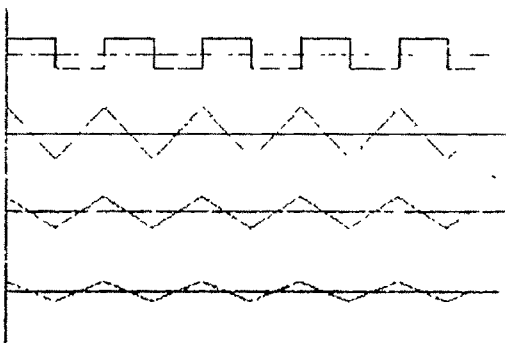

Fig.6 : Experimentally observed slope-variation from digitally tunable integrator. Upper trace : p-p amplitude 3.5V, frequency 5KHz. Lower trace : Trace 1 : slope 0.14 V/μs, Trace 2 : slope 0.08 V/μs, Trace 3 : 0.05 V/μs.

CONCLUSION

Some novel active-RC integrator and differentiator circuit design schemes using the CFA device are presented. Thorough circuit analysis using the generalized terminal properties of the CFA has been presented and the effects of the CFA imperfections ($\epsilon \neq 0$) have been derived. The advantageous features are differential input capabilities, single resistor / capacitor tunability with the possibility of enlargement of the nominal time constant, and, extremely low sensitivity. Some practical wave processing applications are shown in the experimental results. The networks have been coupled with SPRA/SPCA and microcontroller to achieve digital tunability.

REFERENCES

1. Analog Devices, Linear Products Databook, Norwood (MA, 1990).

2. C. Toumazou and J. Lidgey, Curerent feedback Opamps : A blessing in disguise ? IEEE Magazine Circuits & Devices, (1994), vol. 10, no.1, January, p 34–37.

2. A. Fabre, Insensitive voltage–mode and current–mode filters from commercially available transimpedance Opamps, IEE Proceeding–G. (CDS), (1993), vol. 140, no.5, May, p 319–321.

4. S.I. Liu, High input impedance filters with low component spread using current–feedback amplifiers, Electronics Letters, (1995), vol.31, no.13, June, p 1042–1043.

5. R. Nandi and S.K. Sanyal, A microprocessor controlled dual input integrator, European Transaction on Telecommunication (ETT); (1990), vol.1, August, p 509–511.

6. U.C. Sarker, S.K. Sanyal and R. Nandi, A high quality dual input differentiator, IEEE Transaction on Instrumentation and Measurement, (1990), vol.39, October, p 726–729.

DPLL – Operational and Circuit Simulation

Shubhra Verma & S. K. Kak

Electronics Engineering Department, Institute of Technology.
Banaras Hindu University. Varanasi – 221 005,India
E-mail:skkak@banaras.ernet.in

Abstract

This paper presents the operational and circuit simulation results of the DPLL for a normalized frequency. The DPLL operation was required to recover the system clock from the received Isochronous data stream available at receiver input. Simulation results have been shown for the lock-range and pull-in time variation for duty cycle change in the input frequency to DPLL. The paper also discusses the operational criticality of the parameters of the discrete digital devices available in spice model. The simulated DPLL block was found to satisfy the clock recovery requirement.

Key Words: DPLL, clock recovery, spice simulation

INTRODUCTION

In modern data transmission systems such as local area networks, telecommunication networks, and optical communication systems, information is transmitted or received in the form of either baseband or passband signals containing sequences of data bits. In these applications, only data signals are transmitted and separate clock signals needed for receiver local clock synchronization is not transmitted. Therefore the receiver has to extract the clock information from the received data stream using a clock recovery block, and decode the data using the extracted clock from a PLL or a PLL based recovery technique [1- 5].

For deriving synchronous multiples or locking two different free running oscillators, PLL has been widely used. It has also been used for extracting information from phase or frequency modulated signals as well as for realization of reference oscillator based frequency synthesizers which use stable sources for deriving highly stable and programmable frequency outputs. In the modern communication environment where digital and data communication are predominant as compared to analogue communication, a Digital Phase Lock Loop is of greater use and relevance than PLL. However, in the case of carrier modulation based data transmission, low noise and high speed AAPLL is used for low bit error rate and wide locking range requirements[6].

Digital Phase Lock Loop on the other hand is useful for high speed data transmission in both wired and wireless mode as well as in optical fiber based systems. To achieve rapid frame and bit synchronization in the presence of multiplexed data streams having high latency and jitter DPLL is of vital importance. Besides they are used in modern digital drives, storage and display systems. The available DPLL literature mostly talks of VHDL based realization or block diagram based analysis and results [7-12]. Thus the need arose of creating discrete digital devices based DPLL simulation to obtain operational and performance results for designing a receiver for isochroous data reception.

In the present simulation, all the functional blocks of the digital phase-locked loop system were implemented by MSI level TTL digital devices. The implemented DPLL block diagram is shown in Figure 1. The phase detector detects the difference in phase between its two input signals and can be implemented in various ways, including an XOR gate implementation, a J/K flip-flop phase detector, a digital multiplier, Nyquist-rate phase detector (NRPD), or a Hilbert transform phase detector. This simulation design uses an XOR gate implementation that outputs an error signal waveform as shown in fig. 2. The response of the I/D circuit is controlled by inputs like carry and borrow from the K-counter which thus either produces an increment or decrement in clock period by inserting or deleting a half pulse respectively, Fig. 3. The I/D circuit produces an output frequency equal to the one half I/D clock input whenever neither increment nor decrement is in process. Thus the DPLL continually adjusts the phase of f_{out} in this fashion so that in the lock condition a definite phase difference exists between f_{in} and f_{out}.

The lock state detection of DPLL is achieved by a D-flip-flop. Waveform in fig. 4(a) illustrates that if Q output

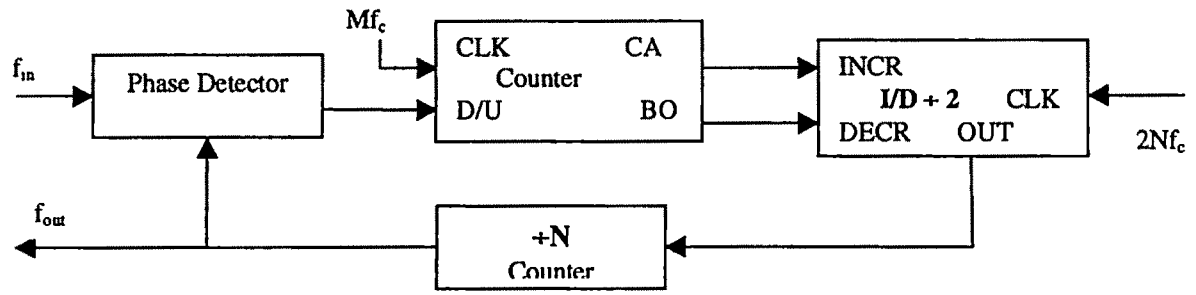

Fig1. First Order Digital Phase Lock Loop

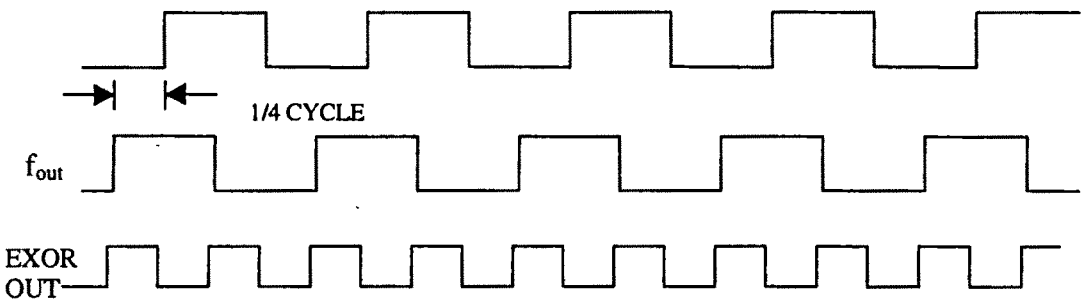

Fig2. Phase Detector Input Vs Output with zero Phase Error using EX-OR

is at a steady state level of 1 or 0 from D flip-flop, DPLL is in lock state, but if it shifts between either high or low, depending upon the phase difference between f_{in} and f_{out} an out-of-lock condition is illustrated as shown in fig. 4(b). In this condition, the D flip-flop will be in toggle mode.

FIRST ORDER DPLL EQUATIONS

The block diagram of a first order digital phase loop is illustrated in figure 1. Let the K-clock operate at a frequency of Mf_c and the I/D clock at a frequency of $2Nf_c$, where M is a constant, f_c is the loop center frequency, and N is the modulus of the divide-by-N counter. The I/D-clock, frequency and divide-by- N modulus will therefore determine the loop center frequency:

$$f_c = \text{I/D clock} \ / \ 2N \ \text{Hz} \qquad (1)$$

Equations for the K-counter and I/D circuits outputs will be:

$$K_{out} = (k_d \varphi_e Mf_c) \ / \ K \ \text{Hz} \qquad (2)$$

$$I/D_{out} = Nf_c + (k_d \varphi_e Mf_c) \ / \ K \ \text{Hz} \qquad (3)$$

where k_d is the phase detector gain, φ_e is the phase error, and K is the modulus of the K-counter.

The loop output is:

$$f_{out} = f_c + (k_d \varphi_e Mf_c)/2KN \ \text{Hz} \qquad (4)$$

From this equation, the tracking frequency range can be defined as Δf_{max} . At the limit of lock range, $k_d \varphi_e$ is ± 1. Therefore:

$$\Delta f_{max} = (f_{out})_{max} - f_c = Mf_c / 2KN \ \text{Hz} \qquad (5)$$

It is evident from the above equation that the lock range of the loop may be adjusted by adjusting K, the modulus of K- counter.

When the DPLL is in the lock condition, f_{out} equals f_{in}, and a definite phase error, φ_e, will exist between the two signals. From equation (4) we obtain:

$$\varphi_e = 2KN (f_{in} - f_c) / k_d \ Mf_c \ \text{cycles} \qquad (6)$$

which is the phase error between f_{in} and f_{out} under lock. This is illustrated in fig4. For a phase error of zero, f_{in} must equal the center frequency f_c.

OPERATIONAL CRITICALITY

As is well known for sequential logic the latency between clock and data can result in erroneous behavior hence the selection and proper data setup and hold times have to be ensured in the case of the simulation being presented in this paper. The timing parametric requirement of the used digital devices was satisfied by using Fast or Schottky types instead of LS type Flip -flops. Such TTL components are having stable output performance and thus can be cascaded without timing problems (this is true as long as the same families of TTL components and the

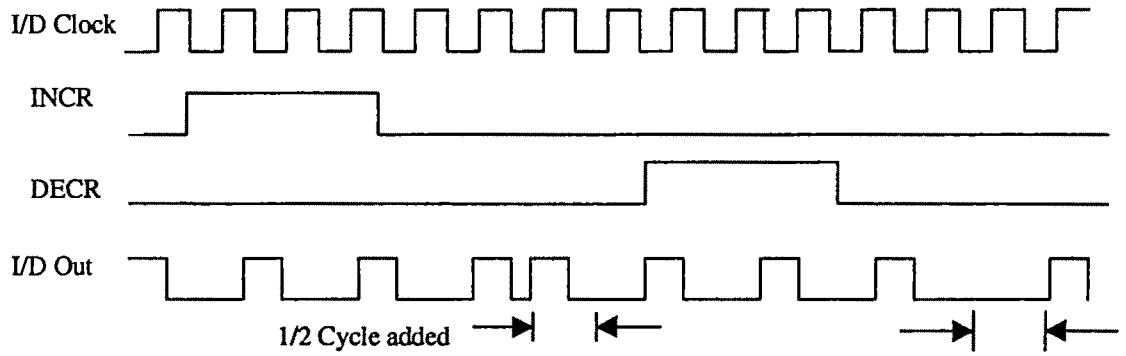

Fig3. I/D Circuit Waveform

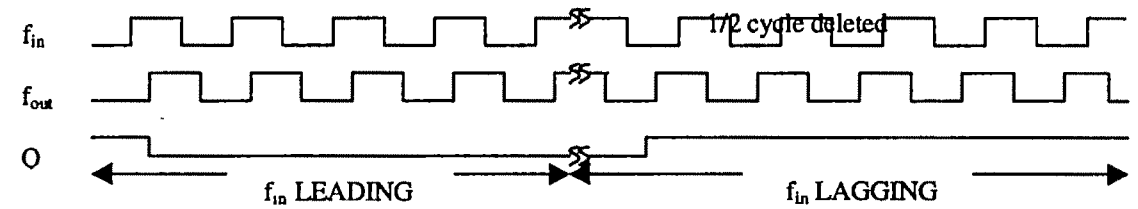

4(a) Lock Condition Waveforms

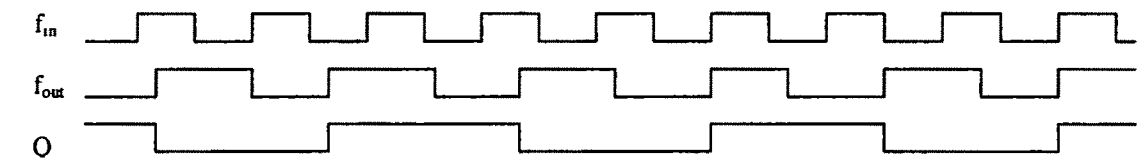

4(b) Out-of-Lock Waveforms

Fig 4. Lock Detection Waveform

same kinds of clocking events are used). It is very important that the inputs must be held stable for a setup time before and a hold time after the clock edge. For example the setup and hold times for 74LS74 positive edge-triggered flip-flop, are 20 ns and 5 ns, respectively. Further the propagation delay far exceeds the hold time, again in the 74LS74 case, the typical delay for a low-to-high transition is 13 ns. Therefore unless the clock signal to the second stage is delayed by more than 7 ns, the first stage cannot change its value and propagate it to the second stage before the hold time has expired which is necessary for the second stage to successfully latch the correct input value.

RESULTS & DISCUSSION

The digital phase locked loop implemented in this paper was simulated for K= 4, N = 4 and M = 16. This loop was tested for a I/D clock = 4 MHz and a center frequency of 128 KHz. As the input signal shifts around the center 128KHz frequency the DPLL is forced to follow the input and so long as it can track the input it is said to be in capture mode. The I/D frequency adapts by inserting or deleting a pulse to balance the phase and thus equals to the input frequency and then the DPLL is in the phase locked state. When phase locked, the loop tracks any change in the input frequency through this repetitive action. For the locked condition to be attainable, the frequency of the reference signal must be within a defined difference from the free-running or open loop frequency value of the oscillator, this is known as the pull-in range. Another important parameter is the lock range, which defines how large the frequency deviation can be between the two signals before they unlock. The amount of time required for the loop to acquire locked state is known as the pull-in time. These parameters can be strictly controlled by modifying the loop bandwidth of the DPLL as given by the equations above.

Fig5 shows simulation results and locking behavior of the first order DPLL up to initial 128 clock cycles. The DPLL was observed to be in lock between 80 KHz to 176 kHz. Fig 6. shows the simulation result to describe pull-in time performance of the DPLL. From the result, it is found that at the center frequency since the input and free running frequency are same hence the lock in time will always be zero and symmetrical on both sides of the shift in frequency for ± 6 KHz .

CONCLUSION

In this paper the operational and simulation results of a MSI based DPLL implementation using Pspice simulation is presented. Timing constraints and issues associated with DPLL have been discussed. The simulation results have proved that the behavioral DPLL model using standard LS & F TTL devices based spice

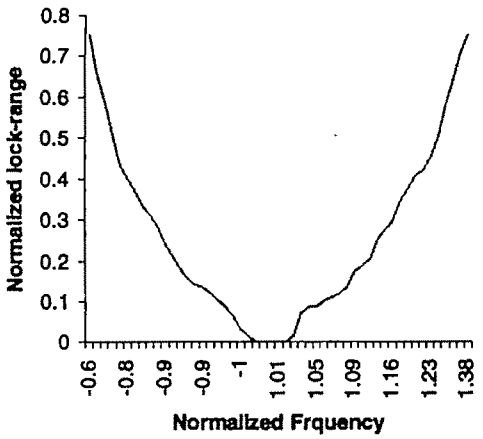

Fig5.Simulation Performance of the DPLL

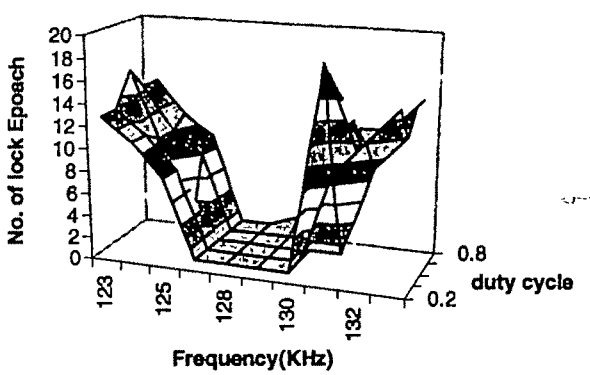

Fig.6:Effect of frequecy & pulsewidth on DPLL lock-range

model is realizable. The realized system gives satisfactory performance for even isochronous data for clock recovery circuit. Simulation results for the lock-range behavior and duty cycle effect on its performance have been presented that establish the system design stability over the required operational frequency range.

REFERENCES

1. Kyoohyun Lim, Seung Hee Choi, and Beomsup Kim, "Optimal Loop Bandwidth Design for Low Noise PLLApplications," IEICE Transactions on Fundamentals of Electronics, Communications and Computer Sciences, pp. 1979-1985, October 1997
2. Kyoohyun Lim, Chan-Hong Park, Dal-soo Kim, and Beomsup Kim, "A Low-noise ase-Locked loop Design
3. by Loop Bandwidth optimization", IEEE Journal of solid-State circuits, VOL.35, NO.6, June 2000
4. Joonsuk Lee, Beomsup Kim, "A 250MHz Low Jitter Adaptive Bandwidth PLL", IEEE International Solid-State Circuits Conference, San Francisco CA, February1999
5. Alain Blanchard, "Phase-Locked Loops: Application to Coherent Receiver Design", John Wiley & Sons publications
6. Jacob Klapper and John T.Frankle, "phase-Locked and Frequency-Feedback Systems: Principles and Techniques", Academic Press, New York
7. Joonsuk Lee and Beomsup Kim, "A Low-Noise Fast-Lock Phase-Locked Loop with Adaptive Bandwidth Control", IEEE Journal of Solid-State Circuits, VOL.35, NO.8, August 2000
8. CD74HC297 High speed CMOS Logic, Harris Semiconductor1997
9. Donald G. Troha, Digital phase lock loop design using SN74LS297 Texas instruments,1997
10. K. Lim, C. Park, B. Kim, "Low Noise Clock Synthesizer Design using Optimal Bandwidth", IEEE International Symposium on Circuits and Systems, Monterey CA, June 1998
11. Tae Hun Kim,and Beomsup Kim, "Dual-Loop Digital PLL Design for Adaptive Clock Recovery "ASP-DAC, Yokohama,Japan,Feb. 10-18,1998
12. Byungjin Chun, Yong Hoon Lee, and Beomsup Kim, "Design of Variable Loop Gains of Dual-Loop DPLL Based on Kalman Filtering Formulation," IEEE Transactions On Communications, December 1997.
13. Byungjin Chun, Seung H. Choi, Beomsup Kim, "A Digital Phase-Locked Loop with Variable Loop Gains Derived from RLS Method," IEEE International Conference on Communications, pp. 11-15, Montreal, June 8-12, 1997
14. Beomsup Kim, "Adaptive Carrier Recovery Using Dual Loop DPLL for Mobile Communication Applications," IEEE International Conference on Communications, Geneva, pp 1757-1761, May 23-26, 1993
15. Beomsup Kim, "Digital Carrier Recovery with Adaptive Dual Loop DPLL for Mobile Communication Applications," IEEE International Conference on Acoustics, Speeches, and Signal Processings, Minneapolis, April 28-30, 1993.

On Noise Segmentation and Filtering

P.Praveen[†*], Vinod Kumar[†]

[†] Department of Electrical Engineering. Indian Institute of Technology Roorkee, Roorkee-247667, India.

E-mail of corresponding author [*]: praveen_alp@yahoo.com,
puravuee@isc.rurkiu.ernet.in

ABSTRACT

In this paper, a neural network based method is proposed for restoration of images corrupted with mixed impulses. Impulse noise is suppressed by selectively filtering the contaminated signal regions only, thus minimizing distortion of clean passages and loss of high frequencies. A model was developed to segment the noisy pixels and to employ the multi-shell median filter (MMF) to these segmented regions. Neural network was used to take decisions on directing the filter. To support our proposed method, simulation results are also provided in this paper, which indicate that the filter is extremely useful for preserving edges or monotonic changes in trend, while eliminating impulses of short duration.

Key words: Impulse noise, Multi-shell Median Filter (MMF), Artificial Neural Network (ANN), Widrow-hoff learning rule.

INTRODUCTION

Standard broadcast TV signals are frequently contaminated with impulse noise arising from vehicle-engine or electrical-appliance interference. The image is corrupted with individual noisy pixels whose intensity significantly differs from the neighboring pixels. By noise, we refer to stochastic variations rather than deterministic distortions. While modern technology has made it possible to reduce the noise levels associated with various Electro-optical devices to almost negligible levels, one noise source can never be eliminated and thus forms the limiting case when all other noise sources are eliminated.

"Salt and Pepper" noises are generated from bit errors in the data stream and they occur as isolated impulses. The image is corrupted with individual noisy pixels whose brightness significantly differs from the neighboring pixels. Although it is widely known that non-linear filter like the median filter (MF) is useful for reducing random noise and periodical patterns, but direct median filtering have undesirable side effects such as smoothening of noise free regions, which results in loss of image detail and distortion of signal.

There are various alterations available in literature for reducing these drawbacks of the median filter. Jim Siu, Jimmy Li and Stefan Luthi, [1] proposed a multi-shell median filter (MMF) which is genuinely effective. C. J. Juan, [2] suggested a modification to the multi-shell median filter (MMMF) to decrease the processing time and to reduce unnecessary replacements Nevertheless, under certain specific conditions to be discussed in the following sections, MMMF fails to perform the desired filtering operation. The improved 2-D median filters developed by F. Ghani and E. Khan [3] suffers from the same drawback.

Under such conditions the performance of MMF, having no threshold factor was found satisfactory and hence was used. The approach used in this paper represents a substantive departure from the conventional unbiased approach of removing impulse noise. Essentially our contention is that the conventional filtering techniques are unsuited for dealing with impulse noises. Impulses should be removed only by selective identification and suppression [4]. This preserves discontinuities of sufficient duration while eliminating local roughness in the signal. Therefore, the essential factor is the identification of the noise and direction of the filter by using Neural Network. The reconstructed image is of significantly improved quality.

BACKGROUND

In this paper we have worked with images of size 256x256 and quantized to 256 different gray levels. The filter window size is taken to be an odd integer (2N+1)x(2N+1) for N=0,1,2,···. We define the following signal characteristics [5]:

1. An *edge* is a monotonic region between two constant neighborhoods of different value. The connecting

monotonic region cannot contain any constant neighborhood.

2. An *impulse* is a constant neighborhood followed by at least one, but no more than N points which are then followed by another constant neighborhood The two boundary points of these N points do not have the same value as the two constant neighborhoods.

There are several detectors, which are usually tuned for specific type of edge profiles. Although these detectors are genuinely effective, they cannot be used here because:

(a) They respond doubly to some noises in the image.

(b) They cannot distinguish between an edge and an impulse.

(c) They cannot be used if more than one pixel is corrupted in the same processing window.

While designing the filter for the noise detection process, there should not be any false detection, and pixels that are genuinely affected should be easily detected.

The method for isolating the noise was inspired from the similarity between the edge profiles of the impulse noise and that of objects having thin lines. Thin lines also correspond to pixels where the brightness function changes abruptly. A change of the image function can be described by a gradient (gradient-based methods) that points in the direction of the largest growth of the image function [6]

In this paper, we use weights that compare the central pixel with six of its nearest neighbors. Consequently, this method is robust and less sensitive to two or more corrupted pixels in the vicinity. We also show in Figure 8 that the selection of 6 nearest pixels is optimal.

If $p(x, y)$ is a continuous image and $p(i, j)$ be a discretized image of it. The partial derivative $\partial p(x, y)/\partial y$, can be approximated by the central difference [7] given by:

$$\frac{\partial^{r+1}}{\partial y^{r+1}} p(x, y+\frac{1}{2}) \leftrightarrow p_j^{r+1}(i, j+\frac{1}{2}) = [p_j^r(i, j+1) - p_j^r(i, j)] \quad (1)$$

Hence,

$$p_y^6(i, j) = [p_j^5(i, j+\frac{1}{2}) - p_j^5(i, j-\frac{1}{2})]$$
$$= [p(i, j-3) - 6p(i, j-2) + 15p(i, j-1) - 20p(i, j) + 15p(i, j+1) - 6p(i, j+2) + p(i, j+3)] \quad (2)$$

The scaling factors associated with the above equations have been omitted

If

$$p = [p(i, j-3), p(i, j-2), p(i, j-1), p(i, j), p(i, j+1), p(i, j+2), p(i, j+3)] \quad (3)$$

$$w = [1, -6, 15, -20, 15, -6, 1] \quad (4)$$

then,

$$\frac{\partial^6}{\partial y^6} p(x, y) \leftrightarrow p_j^6(i, j) = p \Theta w \quad (5)$$

where, Θ denotes 1D convolution.

The noise enhancement can be interpreted in the frequency domain as well. The result of the Fourier transformation is a combination of harmonic functions. The derivative of the harmonic function *Sin(nx)* is *nCos(nx)*; thus the higher the frequency, the higher the magnitude of its derivatives [6]. The impulse response of the weight w (4) is shown in the Figure 1.

NEURAL NETWORK MODEL

Neural Networks are composed of simple elements operating in parallel These elements are inspired by the biological nervous systems. To develop an artificial neural network (ANN), one develops a mathematical model that best describes the biological system's functionality.

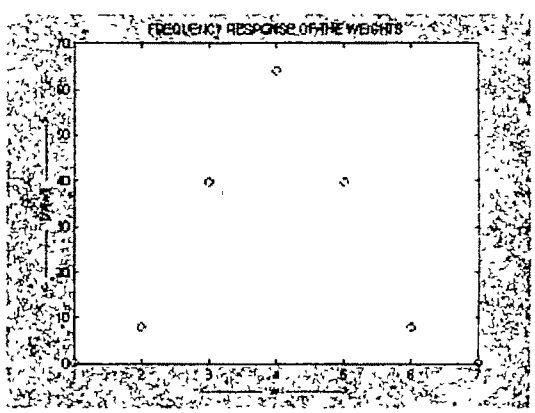

Fig. 1 Frequency Response of the weights.

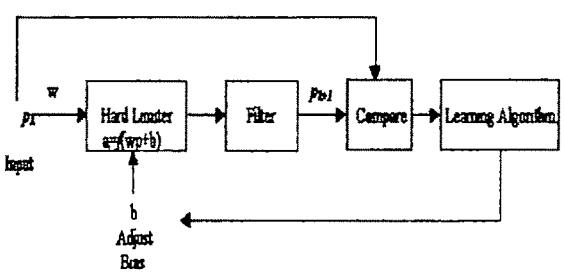

Fig. 2 Block diagram of the impulse noise suppression system.

Figure 2 gives an overview of the back-coupled error correction model that was designed. Three such cascaded neurons with distinct synaptic weights and parameters were used. The successive neurons are triggered only when the previous neuron transmits a stimulus and feed their output The output at the third neuron would give the final filtered image with minimum error and optimum result.

Weights (w):

For impulse noise detection, central difference value is given by:

$$\partial^6 P_n = P_{n-3} - 6P_{n-2} + 15P_{n-1} - 20P_n + 15P_{n+1} - 6P_{n+2} + P_{n+3} \quad (6)$$

where P_n is the intensity of the pixel under study, and P_i, i=(n-3) to (n+3) are the intensity of neighboring pixels

The weights from (6) are thus:

$$w = \{1, -6, 15, -20, 15, -6, 1\} \quad (7)$$

For pepper noise with no impulse characteristics,

$$\partial^6 P_n = P_{n-3} + P_{n-2} + P_{n-1} + 200P_n + P_{n+1} + P_{n+2} + P_{n+3} \quad (8)$$

The weights from (8) are thus:

$$w = \{1, 1, 1, 200, 1, 1, 1\} \quad (9)$$

Non-linear function (f):

The purpose of the nonlinear function is to ensure that the neuron's response is bounded. The actual response of the neuron is thus conditioned, or damped, as a result of large or small activating stimuli and thus is controllable. The non-linear function chosen was the 'Hard limiter'. It has a lower bound 'zero' and an upper bound 'one'. It has the characteristics shown in Figure 3.

The input to the function is $n = ((w^T p/100) + b)$. The paradigm that was designed had *seven* inputs (p), weights (w), and bias (b). n is the output of neuron prior to nonlinearity, and a is the output of the activation function.

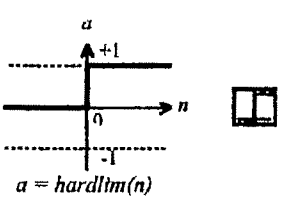

Fig. 3 The Hard limiter

The output from the hard limiter is

$$a = f((\frac{w^T p}{100}) + b) = 1, \quad \text{if } ((\frac{w^T p}{100}) + b) > 0$$
$$= 0, \quad \text{otherwise} \quad (10)$$

Error-correction learning rule:

Learning is the process by which the neural network adapts itself to a stimulus (p), and eventually (after making the proper parameter adjustments) it produces a desired response (T). If the two differ, then the neural network generates an ERROR signal (E) This is then used to calculate the corresponding parameter-correction term so that the two responses finally converge

This rule is used to reduce the mean square error (MSE) between the desired (or target) output value and the actual output value of a processing element by continuous adjustment of the network parameters. This is also known as the Widrow-Hoff learning rule or as the Least Mean Square rule [12].

Let a_{k-1} (x, y) represent an input image and a_k (x, y) denote a $_{k-1}$ (x, y) after an iteration. If their size is MxN, the root-mean-square error, e_{rms}, between a_{k-1} (x, y) and a_k (x, y) is the squared error averaged over the MxN array, given by:

$$e_{rms} = [\frac{1}{MN}\sum_{x=0}^{M-1}\sum_{y=0}^{N-1}[a_k(x,y) - a_{k-1}(x,y)]^2]^{\frac{1}{2}} \quad (11)$$

The objective is to reduce the error function, avoiding local minima and reaching the actual or global minimum

If the change of bias is proportional to a learning signal, then learning for the neuron is

$$\frac{\partial}{\partial t} b(t) =: E(p, T) \quad (12)$$

Since the bias is computed with a digital computer, Eq (12) is more useful in discrete-time form·

$$b(k+1) = b(k) + \cdot E(p, T) \quad (13)$$

where μ is the learning rate of the network, and k is the iteration step number

Thus, the rule for learning is expressed as:

$$b(k+1) = b(k) + (\text{bias correction term}) \quad (14)$$

$$b(k) = z^{-1}[b(k+1)] \quad (15)$$

Here z^{-1} is the unit-delay operator, and it represents a storage element. The choice of the initial bias term depends on the application. It is difficult to choose the bias optimally; some trial and errors are usually involved.

Learning is complete when the bias correction term is zero. The selection of the bias term, *b(k)* and the minimum number of iteration play a vital role in promoting stability, instability or a solution trapped in a local minimum.

FILTERING

Median Filtering:

Median Filtering is a special class of ranked order filters very useful in many signal processing applications. In median filtering, the input pixel is replaced by the median of the pixels contained in a window surrounding it.
That is, $v(m,n) = \text{median}\{y(m-k, n-l), (k,l) \in W\}$,
where W is a suitably chosen window [8].

The algorithm for median filtering requires arranging the pixel values in the window in increasing or decreasing order and picking the middle value. The window size is generally chosen so that N_W is odd. The nine-element processing window used for basic 2D-(3x3) median filtering is shown in Figure 4.

The efficiency of the median filter is poor when the number of noise pixels in the window is greater than half the number of pixels in the window [9].

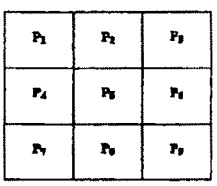

Fig. 4 A (3x3) Processing window.

Multi-shell median filter (MMF):

The following are the characteristic equations for the MMF [1]:
If

$$\begin{aligned} \text{Output}(x,y) &= \text{Max}(P_2, P_8), \text{ if } P_5 \geq \text{Max}[S] \\ &= \text{Min}(P_2, P_8), \text{ if } P_5 \leq \text{Min}[S] \\ &= P_5, \text{ if } \text{Min}[S] < P_5 < \text{Max}[S] \end{aligned} \quad (15)$$

$$S = \{P_1, P_2, P_3, P_7, P_8, P_9\} \quad (16)$$

Modified Multi-shell median filter (MMMF):

The following are the characteristic equations for the MMMF [2]:

$$\begin{aligned} \text{Output}(x,y) &= \text{Max}(P_2, P_8), \text{ if } P_5 - \text{Max}[S] \geq 16 \\ &= \text{Min}(P_2, P_8), \text{ if } \text{Min}[S] - P_5 > 16 \\ &= P_5, \text{ otherwise} \end{aligned} \quad (17)$$

The MMMF [2] suffers from a serious limitation. For regions in the image corresponding to low frequency signal and corrupted with a similar type of noise (negative impulse), the threshold equations are not satisfied. Under such conditions, this sort of noise is not eliminated as shown in Figure 6(a). We use the modified median filter, as there is no threshold value to control the filter.

SIMULATION RESULTS

Training the Neural Network and fixing network parameters:

Once the paradigm is designed, the next stage is testing the filter on different images corrupted with the "Salt & pepper" noise. The results of which have been recorded in Table 1. Testing done on images after training the neural network is tabulated in Table 2.

After training the neural network, the number of iterations k required to reach the global minimum is reduced considerably. However, a finite number of iterations are required even after training, if the amount of signal detail to be preserved or the noise density is more. The developed model is stable as it reaches the final global minimum position and its steady state, as soon as the error is minimized.

Layer 1 is designed for the 'Negative impulses among White Signal' regions ($P_n \leq 127$), Layer 2 is for the 'Positive impulses among Black Signal' regions ($P_n > 127$), and Layer 3 was for the 'Negative impulses among Black Signal' regions ($P_n \leq 127$).

The algorithm for isolation of the noise was tested and Figure 5 shows an enlarged view of the image before filtering, after isolation of noise, and finally after removing the noise. The output finally obtained at the Layer 3 of the filter is shown in Figure 7(d).

Evidence of functional improvement:

The performance improvement of the propounded method over the existing one is presented here. The evaluation of the performance is based on 'Subjective Fidelity Criterion'.

The suggested scheme is found to remove noises even from the edges of an image and preserve minor details (as shown in Figure 6(b)). Figure 6(a), shows a portion of the "Cameraman" image affected by impulse noise, after administering the MMMF. The white circles highlight the negative impulses left behind because of the threshold factor in the MMMF. While Figure 6 (b) shows the same portion after using the adaptive filter. It may not be possible to remove some noise even by repeated filtering if the root signal also has added noise [5].

Figure 9 and the Table 3 shows the difference in the Peak Signal to Noise Ratio (PSNR) for different noise densities, calculated using Eq. (18).

$$PSNR(dB) = 10\left[\log_{10}\left[\frac{\sum_{x=0}^{M-1}\sum_{y=0}^{N-1}(255)^2}{\sum_{x=0}^{M-1}\sum_{y=0}^{N-1}[I(x,y)-\hat{I}(x,y)]^2}\right]\right] \quad (18)$$

CONCLUSIONS

A new algorithm for noise detection is projected in this paper and a neural network based approach to filtering the data was used. The effectiveness of the proposed approach relies on the filter capability to detect the true noise configurations. The developed filter is adaptive and very sensitive to edges in the image. The optimal goal of the filter modeled is to improve the quality of the image by noise reduction. But as the complexity of the system increases, our ability to make precise and yet significant statements about its behavior diminishes until a threshold is reached beyond which precision and significance (or relevance) become almost exclusive characteristics.

REFERENCES

1. Jim Siu, Jimmy Li and Stefan Luthi, "A real time 2-D median based filter for video signals," IEEE Trans. Consumer Electronics, Vol. 39 (1993), p 115-121.
2. Chang Jung Juan, "Modified 2D median filter for impulse noise suppression in a real time system", IEEE Trans. Consumer Electronics, Vol. 41 (1995), p 73-81.
3. Farid Ghani and Ekram Khan, "Missing lines recovery and Impulse noise suppression using improved 2-D median filters," IEEE Trans. Consumer Electronics, Vol. 45 (1999), p 356-360.
4. Reinhard Bernstein, "Adaptive Nonlinear Filters for Simultaneous Removal of Different Kinds of Noise in Images", IEEE Trans. Circuits and Systems, vol. CAS-34 (1987), p 1275-1291.
5. Neal C. Gallagher, and Gary L. Wise, "A Theoretical Analysis of the Properties of Median Filters", IEEE Trans. Acoust., Speech and Signal Processing, vol. ASSP-29 (1981), p 1136-1141.
6. Milan Sonka, Vaclav Hlavac and R. Boyle, "Image Processing, Analysis and Machine vision", p 74-91.
7. Hilderban F. B, "Intr. to Numerical Analysis".
8. A.K.Jain, "Fundamentals of Digital Image Processing": Prentice Hall India.
9. Rafael C. Gonzalez, Richard E. Woods, "Digital image Processing": Addison-Wesley (2000).
10. Takis Kasparis and John Lane, "Adaptive Scratch Noise Filtering", IEEE Trans. Consumer Electronics, Vol. 39 (1993), p 917-922.
11. Jae S. Lim, "Two-Dimensional Signal and Image Processing": Prentice Hall Signal Processing Series, p 72-86.
12. Stamatios V. Kartalopoulos, "Understanding Neural Networks and Fuzzy Logic": IEEE Press, PHI (2000).
13. Alan C. Bovik, Thomas S. Huang, and David C. Munson, "A Generalisation of Median Filtering Using Linear Combinations of Order Statistics", IEEE Trans. Acoust., Speech, and Signal Processing, vol. ASSP-31 (1983), p 1342-1350.

Table 1: Training done on the network with an initial bias and learning rate. Layer 1:b=-50, μ = 10;Layer 2 :b=50, μ=0.1; and Layer 3:b=-3, μ =50.

Images (TIFF)	Layer 1 (Eq. 7)		Layer 2 (Eq. 7)		Layer 3 (Eq. 9)	
	k	Final b	k	Final b	k	Final b
Moon	83	33	18	68	2	-2.61
C'man	81	31	16	66	1	-2.77
Circuit	76	26	13	63	1	-2.86
Lena	74	24	15	65	1	-2.97
Pout	70	20	20	70	1	-0.97
Eight	69	19	06	56	0	-3.00
Paper	40	-10	06	56	0	-3.00

Table 2: Testing carried out after training the neural network. Layer 1:b= 54,μ= 1.1;Layer 2:b=70,μ=1.1; and Layer 3:b= -0.97,μ=1.1.

Image (TIFF)	Layer 1		Layer 2		Layer 3	
	k	Final b	k	Final b	k	Final b
Ash	5	94.48	6	125.29	1	-0.954
Beach	5	73.47	5	94.50	2	-0.956
Chateau	5	71.80	5	100.93	1	-0.968

Table 3: PSNR of original corrupted image, image filtered by a 3x3 MMMF, and after using the proposed approach for different Noise Densities.

% Noise Density	PSNR of Noisy Image (dB)	PSNR after using MMMF (dB)	PSNR after using the proposed filter (dB)
4	19.092	27.244	29.639
6	17.425	24.660	26.626
8	16.081	22.245	25.071
12	14.337	19.216	22.003
16	13.091	16.927	19.702
18	12.555	15.913	18.826
19	12.328	15.634	18.360
20	12.082	15.208	18.044
22	11.622	14.342	17.003
30	10.296	12.236	14.623
40	9.074	10.307	12.390
50	8.130	8.903	10.668

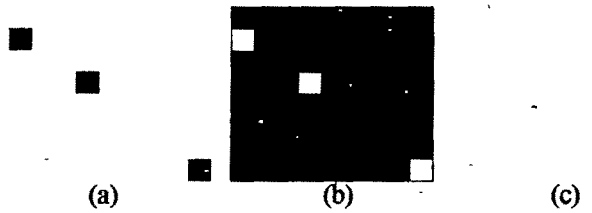

Fig. 5(a) The original image corrupted with impulse noise, (b) After isolating the noise, (c) After filtering the noisy image.

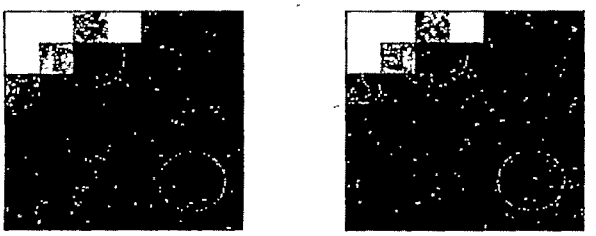

Fig. 6 (a) White circle shows the noise left behind by a 3*3 MMMF [2], (b) The circles now indicate the position where the noise was removed after using the proposed scheme.

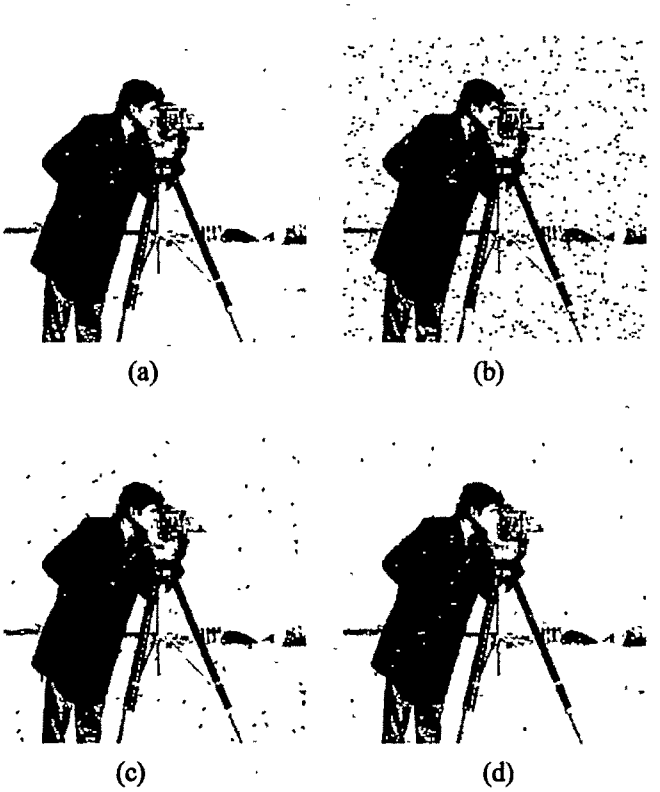

Fig. 7(a) Original image 'Cameraman', 256x256 scanned at 72 dpi & 8bits/pixel, (b) Image corrupted with noise (4%), (c) After MMMF filtering, (d) After filtering using proposed method.

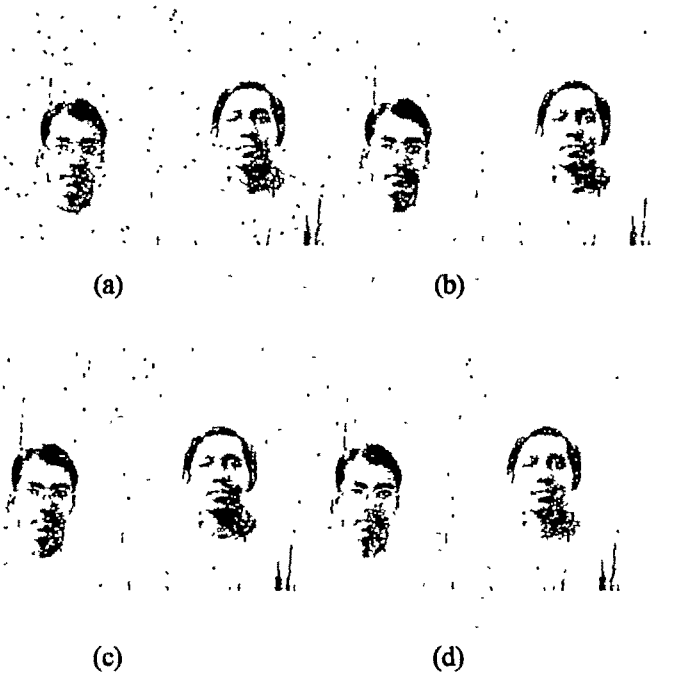

Fig. 8 (a) After MMMF filtering (28.1100 dB) on a corrupted image (scanned at 72 dpi & 8 bits/pixel, corrupted with 4% noise, 18.9625 dB), (b) After the proposed approach but with a variable weight window of 7x1 (32.1535 dB), (c) 5x1 (30.5636 dB), and (d) 9x1 (32.1538 dB).

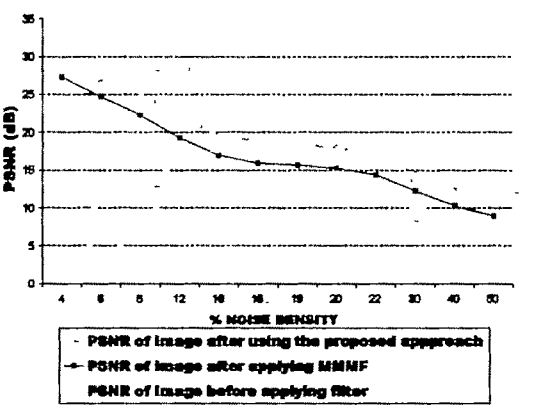
PSNR (dB)
% NOISE DENSITY
PSNR of image after using the proposed approach
PSNR of image after applying MMMF
PSNR of image before applying filter

Fig. 9 The improvement of PSNR in the proposed approach as against the original noisy image, and the noisy image filtered by a 3x3 MMMF.

A New Generation Microprocessor Based Interlocking Devices

R. Sarwoop[1], P. K. Sadhu[1], S. K. Mukherjee[1]. R Chakraborti[2] and B. M. Karan[1]
[1]Electrical and Electronics Engg. Dept, BIT, Mesra, Ranchi, India
[2]Electrical Engineering Dept, Jadavpur University, Calcutta 700 032, India

ABSTRACT

The microprocessor based system can be used for automatic interlocking system with alarm initiation device for banking security, railway wagon, personal vehicles at a high grade of modern security. The microprocessor is basically a small version of personal computer. Actually it is more cost saver than personal computer. It will maintain high grade of secrecy for the customer. In the market there are so many mechanical dialing locks and electrically operated dialing locks, but in this case if coding number are disclosed to anybody then there is a requirement to change the combination of numbers. That changing code is not an easy task for the general customers. In that case there is a recruitment of hardware personnel. Changed code in the existing system does not give the high grade of secrecy as because the changed code is known to the third person i.e. hardware personnel

INTRODUCTION

The aim of this project is to get a full security for bank locker system in automation using microprocessor. In the proposed microprocessor based or P.C. based interlocking device gives high grade of secrecy for the customers. Actually the changing of code is easily done by the customer by means of reset the password in software program only and this is very easy task. At the time of changing password there is no risk of electrocution. The microprocessor is programmed for setting password, time for solenoid coil energisation, alarm in case of decoity or any other tampering. In the proposed scheme interlocking will give another grade of protection for customer. In this device energy consumption is very less. Since the solenoid coil is not energized at locking period it is only energized at instant of opening for few seconds. On the otherhand all alarming circuits are taking power whenever tampering is offered. This proposed scheme will give high reliability to the customer for year after year because wear and tear of moving parts, electrical coils are very less due to minimum energisation. It is possible to provide different alarming system like local alarm, radio communication with police station, providing hidden video camera etc, for providing enhanced grade of security.

SALIENT FEATURES

- The system can be accessed 24 hrs.
- As interlocking system is used there is no chance of opening the door from outside.
- Power supply is required only at the time of opening the door by means of solenoid energisation.
- The system reduces human labour.
- The system offers full security for money and goods to customer.
- Programmability of password makes it more dynamic.
- It has wide range of applications.

SOFTWARE INTERFACE WITH REALTIME HARDWARE

Microprocessor is used for interfacing with real-time hardware. Password can be set in two registers and password can be entered from other two registers which is compared ,and signal is obtained from port(A) for opening the door. The time for which door should be opened can also be set in a register of microprocessor. The time calculation can be done by means of clock cycles.

model calculation

Internal clock frequency=3 MHZ

Time period for one T-state= 1/ Internal clock frequency = $1 / (3 \times 10^6)$

Numberof T-states for 0.5 sec=Required time delay/Time for one Tstate= $0.5 / (0.333 \times 10^{-6}) = 1500150$

The delay subroutine program has total T-states =24N +35

24N+35=1500150

N=(1500150-35)/24

N=F429

for example in case of 5 sec the subroutine with N=F429 is executed 10 times.

CIRCUIT DESCRIPTION

The signal obtained from port for opening the door is 5V with current in terms of milliamperes and hence it is connected to an electronic circuit for actuating the door lock.The signal is given to the optocoupler chip MCT 2E and the output from the chip is given to the pre amplifying stage consisting of operational amplifier(IC 741).The output from op-amp is given to a darlington transistor to actuate the relay.Relay is used to switch on/off the solenoid and hence the door interlock. The required supply is given to the solenoid coil and this circuit just acts as switch to actuate the relay and hence the solenoid plunger.

As per the solenoid valve is concerned when the supply voltage is applied it opens by pulling the plunger up due to magnetization of the coil and when the supply is cut off results in demagnetization and the closing of valve.

Similarly in case where wrong password is entered another signal is taken from port (B) to actuate the alarm .The above mentioned circuit can be used for this purpose.

OPERATION PROCEDURE

1)Reset the microprocessor.
RESET

2)Set the password in registers 8200,8201
SET
8200
INR
XX (1st 2digit password)
INR
XX (2nd 2digit password)

3)Set the time for which door should open in 8202
INR
XX (Time in seconds)

4)Enter the password in 8300,8301
RESET
SET
8300
INR
XX (1st 2 digit password)
INR
XX (2nd 2digit password)
RESET

5)Execute the program
RUN
8100 (Starting address of the program)
EXEC

3.FLOW CHART:

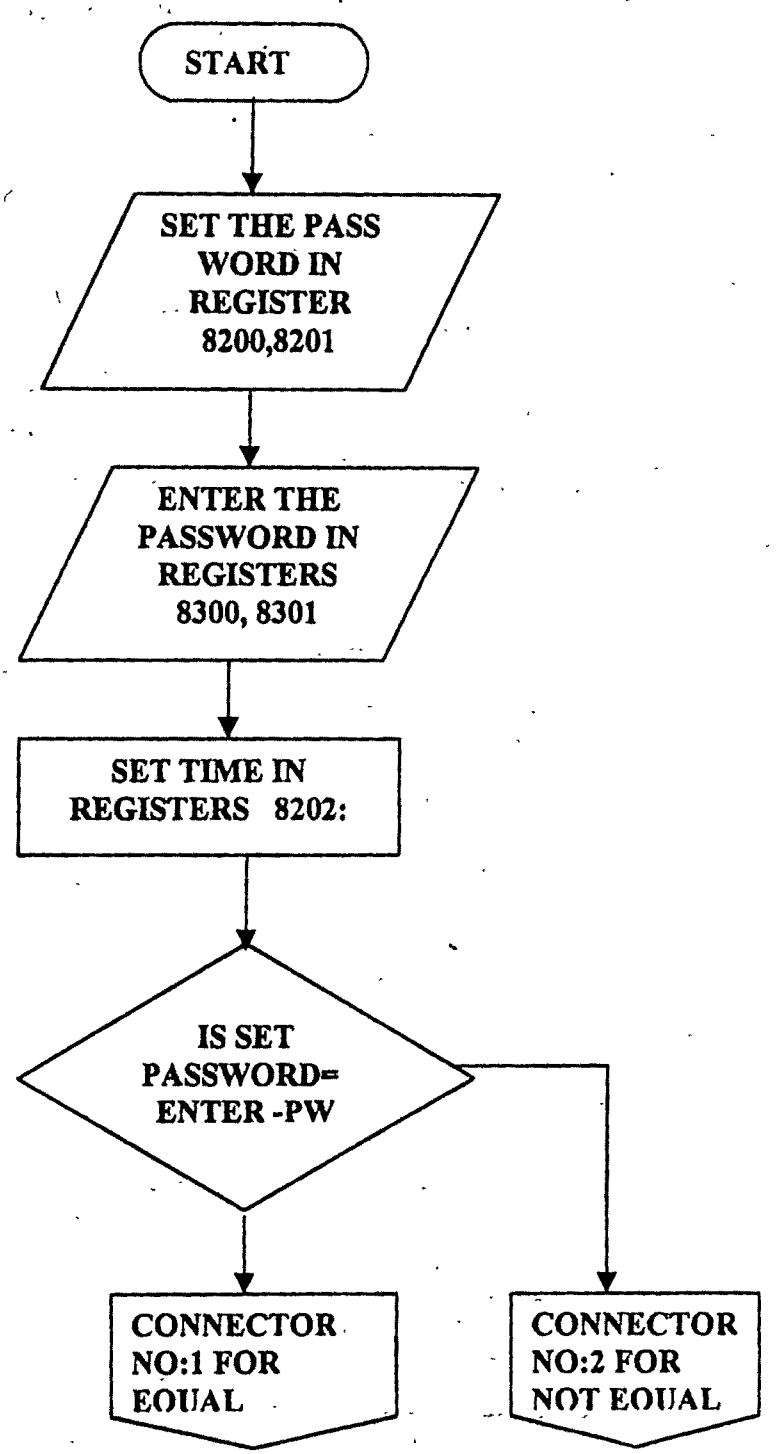
START
SET THE PASS WORD IN REGISTER 8200,8201
ENTER THE PASSWORD IN REGISTERS 8300, 8301
SET TIME IN REGISTERS 8202:
IS SET PASSWORD= ENTER -PW
CONNECTOR NO:1 FOR EQUAL
CONNECTOR NO:2 FOR NOT EQUAL

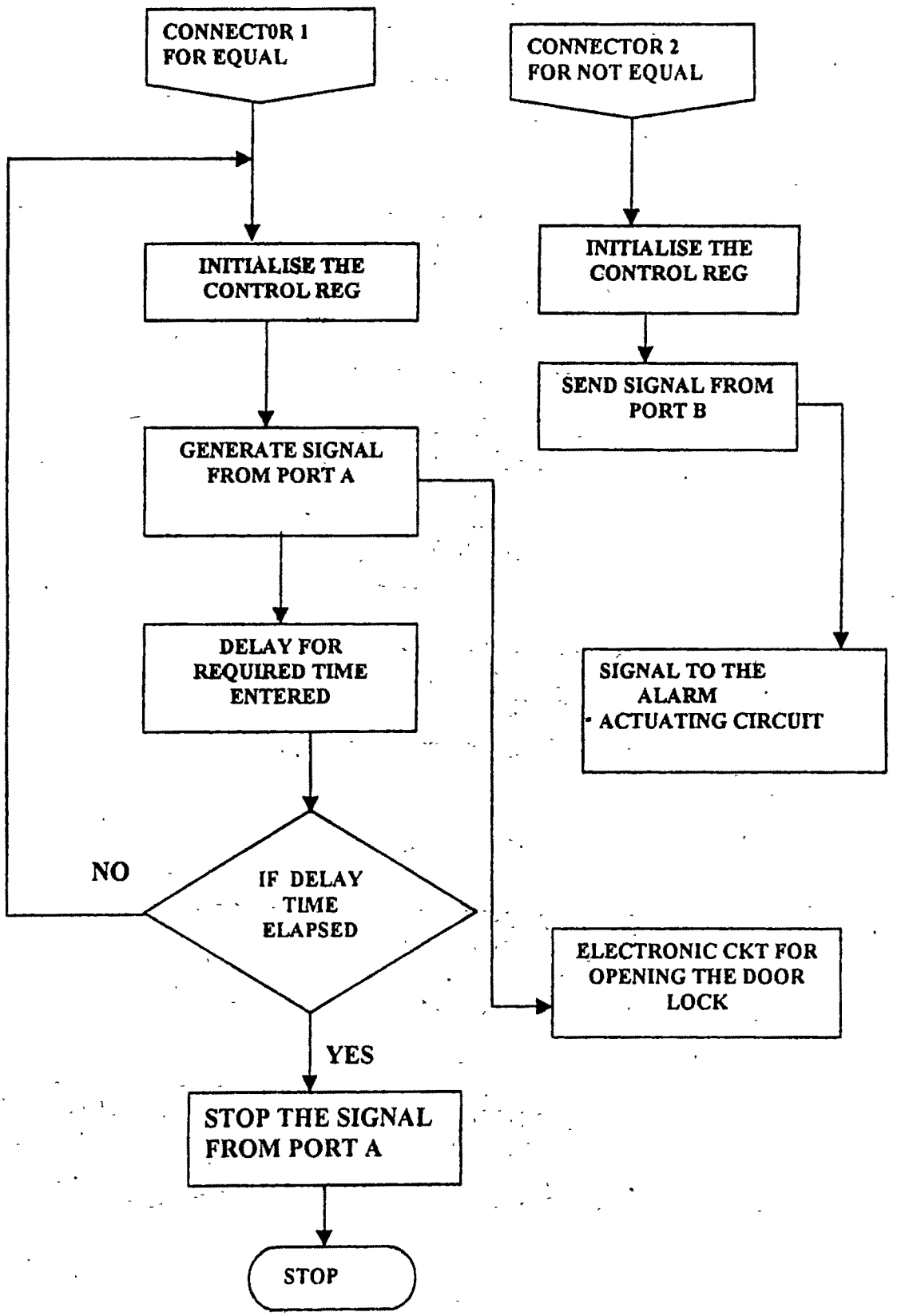
CONNECTOR 1
FOR EQUAL
CONNECTOR 2
FOR NOT EQUAL
INITIALISE THE
CONTROL REG
INITIALISE THE
CONTROL REG
SEND SIGNAL FROM
PORT B
GENERATE SIGNAL
FROM PORT A
DELAY FOR
REQUIRED TIME
ENTERED
SIGNAL TO THE
ALARM
ACTUATING CIRCUIT
NO
IF DELAY
TIME
ELAPSED
ELECTRONIC CKT FOR
OPENING THE DOOR
LOCK
YES
STOP THE SIGNAL
FROM PORT A
STOP

OPTOCOUPLER USING MCT-2E

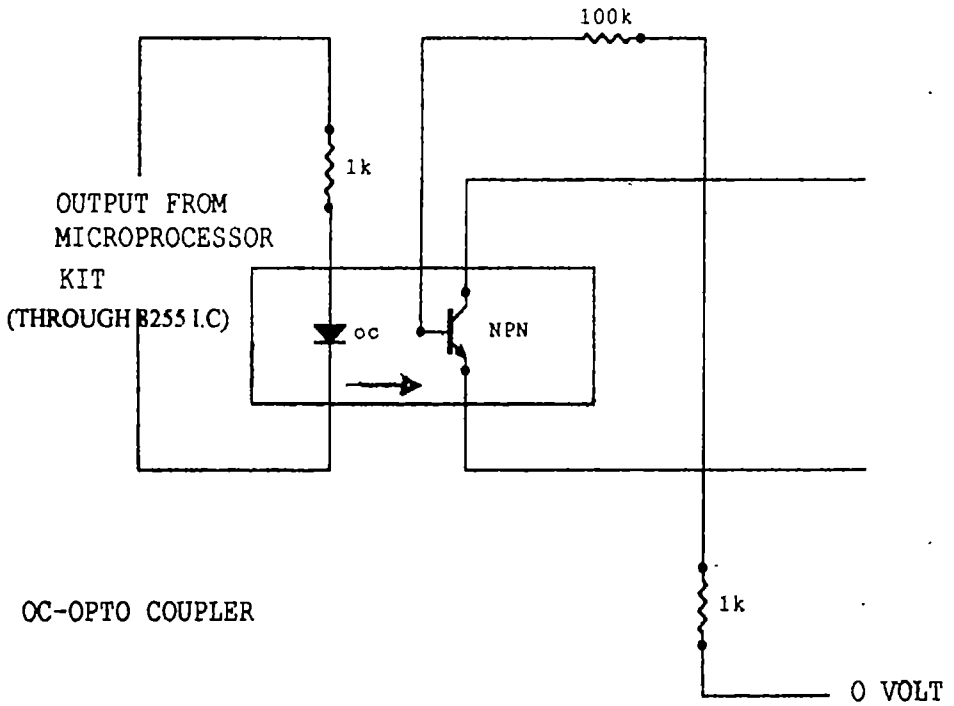

OC-OPTO COUPLER

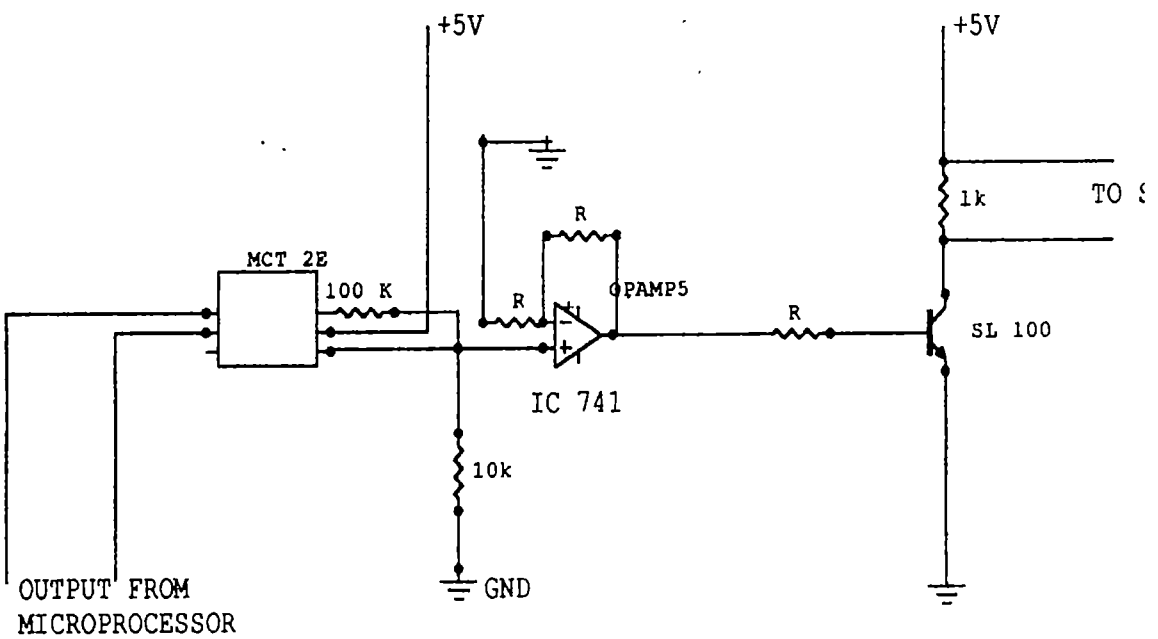

(THROUGH 8255 INTERFACING I.C)

CONCLUSION:

The program is entered in microprocessor .The microprocessor is interfaced with required electronic circuit .The hard ware parts are fabricated and implemented. The program is executed and the appropriate results are checked for realtime application.

REFERENCES:

- Microprocessor And its Applications By Mr.Nagoorkani
- Microprocessor And its Applications By Mr.Goankor
- H.Fujita, H.Akagi, "Pulse-density-modulation power control of 4KHZ Voltage-source inverter for induction melting applications"- IEEE Transaction on industry applications.

- J.Pforr, L.Hobon, "Resonant-switched mode preconverters for high-frequency induction heater"- Proceedings of power conversion international conference June 1991.

- Ogiwara, watanate. J. nakaoka, " Fixed frequency mode phesor- shifting power control ZVS high - frequency inverter for induction heating using Sidevices."- Volume 393-398 1997., Pub: Industrial electronics 1997 ISIE,97 USA

A Low Noise Multiplexed Analog Digital Signal Processor for Dimuon Spectrometer of ALICE

S. Sarkar [1], J. C. Santiard [2], V. Sharma [3], J. N. Roy [3], S. K. Sen [1]

[1]Electronic Science Section
Saha Institute of Nuclear Physics, 1/AH Bidhan Nagar, Calcutta 700 064, India
[2]Dics EP/MIC, CERN, 1211, Genese 23, Switzerland
[3]Semiconductor Complex Ltd, Phase VIII, SAS Nagar, Punjab 160 059, India
[1] Communicating author S Sarkar; e-mail: sandip@essgate.saha.ernet.in

Abstract

In this paper we present a low full custom, analog digital signal processor chip designed for use in nuclear physics experiments with gas detectors. It has sixteen input channels and one multiplexed output channel through which the output voltages corresponding to each channel are available serially. Each of these voltages are proportional to the incident charge to the corresponding channels. This chip has a input dynamic range of 500fC and exhibits very low noise of 640 e⁻ rms.

INTRODUCTION

Full custom ASIC CMOS Integrated Circuits are essential part for a variety of detectors used in the particle physics experiments [1]. The CMOS technology offers high compaction density, low power consumption and the combination of analog and digital circuits on the same chip which are often a critical constraint for these detectors with a large number of readout channels.

The ASIC design also has the flexibility to trade-off different design parameters to meet particular specifications. The Multiplexed ANAlog Signal-processor (MANAS) ASIC chip is one of these kinds.

It is fabricated in 1.2μm CMOS Double-Poly Double-Metal N-well process in Semiconductor Complex Limited in India. It is specifically designed for the frontend electronics of Cathode Pad Chambers (CPC) of Dimuon Spectrometer of ALICE, CERN, Geneve. This mixed analog-digital chip exhibits very low-noise of 640 e⁻ rms and high input charge sensitivity of 3.5 mV/fC. The maximum charge that it can handle is 500fC with ±2.5V power supply. MANAS has 16 channels that can be read serially via a multiplexer at an maximum speed of 10 MHz with TTL clock signals.

CHIP ARCHITECTURE

It has 16 input channels and one output channel. Input signals, after processing, are available at the output serially via a multiplexer. Outputs corresponding to each channel input are in form of voltage levels that are a measure of the amount of input charge to that particular channel. Each channel has a Charge Sensitive Amplifier (CSA), a Deconvolution Filter (DF), a Semi-Gaussian Shaper (SGS) and a Track-Hold (T/H) stage as shown in Figure 1 [1]. MANAS chip also has an Analog Multiplexer (M) that converts 16 parallel input to 1 serial output.

Charge Sensitive Amplifier

The Charge-Sensitive Amplifier (CSA) [3] is basically a feedback amplifier that integrates the total input charge (Q) onto its feedback capacitor (C_f=1pF). The amplitude of the output voltage is thus Q/C_f and is independent of the gain of the amplifier. To avoid charge build up from subsequent events, a reset mechanism is implemented by a active-feedback-resistor (R_f) of 20 MΩ. The resistor R_f is realised with the combination of 50 Ω silicon (diffusion) layer and a current divider of 400. This resistor together with the feedback capacitor C_f makes a decay time constant of 20μs which is kept much higher than the width of the input

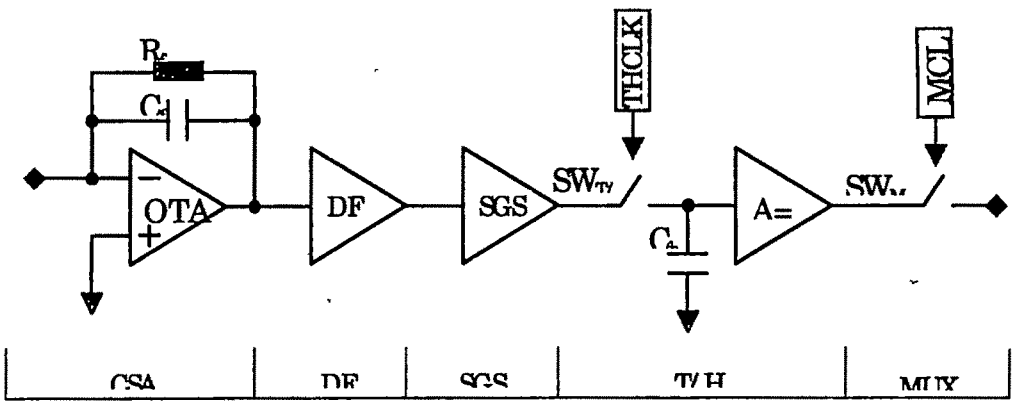

Figure 1 Operational schematic of a single channel of MANAS chip

current pulse in order to assure complete charge collection. The CSA then sees the input signal as a Delta function and the resulting output is then a slowly decaying step function with a peak amplitude Q/C_f. The essential building block of the CSA is an Operational Transconductance Amplifier (OTA) built around a folded cascode architecture.

Deconvolution Filter

The signal current in gas proportional Cathode Pad Chambers (CPC) is the result of the motion of the ions produced in the avalanche as they drift in the electric field towards the cathode. The shape of the current and charge waveforms for CPC can be approximated by the current and charge waveforms due to a point ionisation in a cylindrical geometry. The important feature of this charge waveform is that the a large fraction of the total charge is transferred in a very short time, a few t_o, the characteristic time constant for the given chamber which is of the order of 1ns and the signal continues for a much longer time, typically 50μs-100μs. This long tail hampers the processing of the signal in the following stages as well as the counting rates. The function of the Deconvolution Filter (DF) is to compensate for this long 1/t tail and prsent the next stage, which is a Semi Gaussian Shaper, a decaying step waveform where the decay is governed by the pole of the CSA

Semi-Gaussion Shaper

The Semi-Gaussion Shaper is built around the popular CR-$(RC)^2$ architecture and it consists of a low-pass filter and a band-pass filter. This combination transforms the input quasi-step function into a semi-gaussian shape with a peaking time of 1.2 us. The semi-gaussian shape is desirable for further processing for the following reasons; (a) its peaking time is independent of the amplitude of the input signal, (b) the peak amplitude is proportional to the input signal amplitude and is therefore is also proportional to the total input charge in the CSA stage, (c) the flatness of the semi-gaussian waveform around the peak amplitude allows some error in reading the peak amplitude without a considerable error in measurement (typically ±1% error in reading at peaking time ± 50ns), (e) the low-pass and high-pass filtration reduces the noise content that helps in low-noise design. A pole-zero compensation circuit is also included in this stage for canceling the pole originated in the CSA stage. This results in a very precise returns to baseline (± <1%) in 4.5 us which is necessary to avoid the problem of ballistic deficit in case of higher count rates.

Track and Hold Stage

Track and Hold Stage (T/H) stage reads the amplitude of the semi-gaussion waveform at the peaking time (i.e. the peak amplitude) and holds the value till it is read serially with the help of multiplexer. When an event occurs, the T/H capacitors (C_h) corresponding to hit channels charges up accordingly because the switches are closed in the operation mode. An HOLD signal is generated from an external trigger signal which is synchronous to the event. This HOLD signal is sent to all the T/H stages to disconnect the T/H stages from the channel by opening $SW_{T/H}$ at a time corresponding to the peaking time. Therefore the maximum amplitudes are stored for the hit channels and the pedastalvalues (default dc levels) are stored for those channels without any hit. As long as the HOLD signal is on, the charges are kept frozen in the T/H capacitors and are lost when the HOLD signal is released. The voltages stored in all the 16 hold capacitors are read serially with the help of an analog multiplexer (M) controlled by a TTL clock signal.

Layout Considerations

The layout of the 16 channel MANAS chip is shown in Figure 2. Each channel extends in the horizontal direction. Biasing blocks are placed in the edges near the corresponding pads. Digital control signals necessary for T/H and multiplexer (M) stages are laid well separated from sensitive analog blocks. Digital and analog power supplies are assigned separate pins to reduce coupling. The large input transistor in the CSA is laid in waffle iron topology to reduce parasitic resistance and capacitance. This also ensures proper value of g_m which otherwise gets modified in the presence of parasitic components.

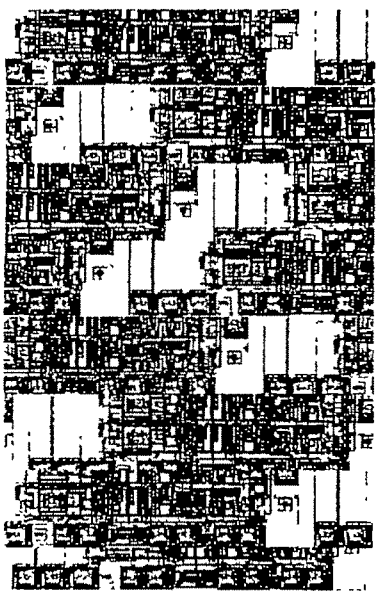

Fig 2 Layout of MANAS

PERFORMANCE TEST RESULTS

Characterisation have been performed on five chips coming from a single wafer. Chips with 44 PIN LCC ceramic package have been mounted on specially prepared test board to reduce parasitic effects during measurements. Test charge has been injected by a very stable precise voltage pulse through a known capacitor and to reduce power supply noise, the voltage sources with <1mV rms ripple have been chosen. To increase the accuracy all the measurements have been performed at a clock speed of 500kHz.

Noise and Input Capacitance

The noise measurement have been performed at a power consumption of 7mW/channel with 600μA bias current for the CSA and 1.2μs peaking time of the shaper. This resulted in a noise slope of 11.6 e- rms/pF as shown in Figure 3. The measured noise at each point includes the noise of the signal source as well as due to the capacitance connecting cables, test board and the 44 PIN LCC ceramic package

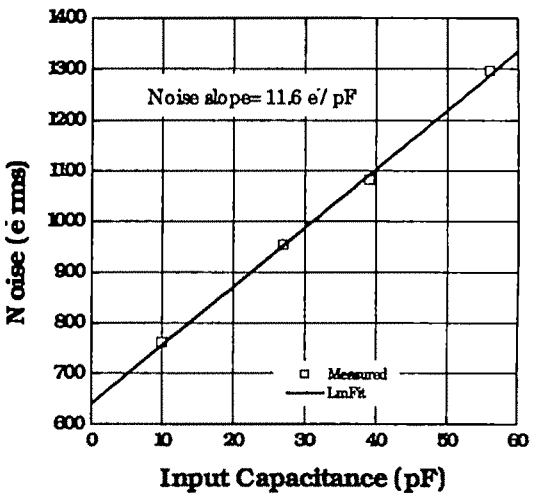

Fig 3 Change of noise with input capacitance

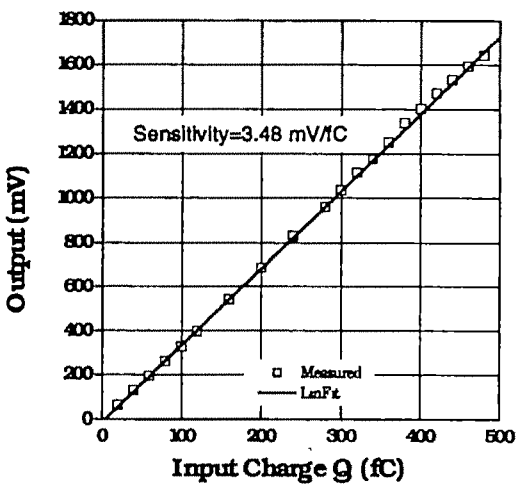

Fig 4 Output linearity

Dynamic Range and Linearity

The measured dynamic range for positive input signal is shown in Figure 4. The full input dynamic range is 480 fC with a sensitivity of 3.5 mV/fC as given by the gradient. The non-linearity error is ±4 fC from 0 to 375 fC. The input dynamic range for the –ve input signal is limited to 280 fC with a sensitivity of 3.27 mV/fC

Pedestal Distribution

Pedestal of a channel is defined as the output DC offset voltage level when there is no input signal. This level varies from channel to channel and also from chip to chip due to various reasons such as design parameter spread, threshold variation etc In Figure 5 the typical DC levels of all the 16 channels of a chip are shown. The comparatively high DC level of the first channel corresponds to the input to that particular channel and due to the absence of any input to other channels, they are at their pedestal levels.

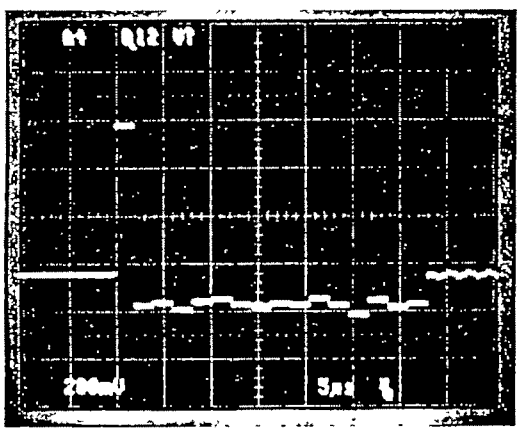

Fig 5 Typical pedestal distribution

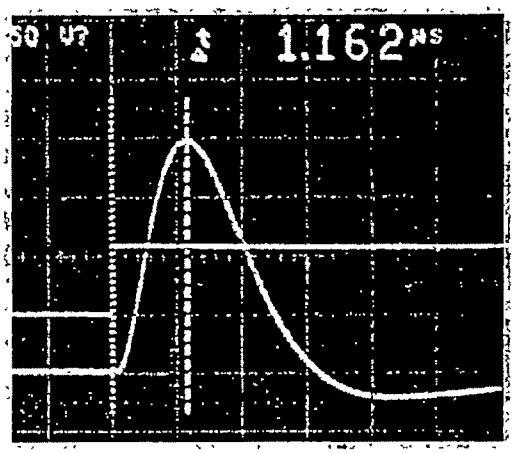

Fig 6 Typical shaper circuit

Semi-Gaussian Pulse Shaping

This is important to reduce noise as well as to reduce error in measuring the peak amplitude. Because of the flatness of the Gaussian peak the error in measuring the amplitude at peaking time±50ns is less than 1% compared to the amplitude at the peaking time. The Figure 6 shows the semi-gaussian shape of the shaped pulse superimposed on the input step voltage.

Temperature Dependence

We have observed practically no change in the pedestal levels for a change in temperature from T=27°C to 55°C on a oscilloscope with a 20mV/div scale. Only a few channels showed a little dependence that corresponds to a temperature coefficient of 0.03 mV/°C.

EXPERIMENTAL RESULTS &CONCLUSION

The measured parameters relevant for the gas detector application are given in Table 1.The measured performance of the first prototype of MANAS is well matched with the simulated results. The pedestal spread among the channels are due to the variation in design parameters, threshold etc. in the fabrication process which are difficult to control in the very first iteration but with the subsequent iteration these will improve.

Table 1: Measured specifications

Silicon area	2.7x4.7=12.42mm^2
Peaking time	1.2 µs
Noise at 0pF	640 e$^-$ rms
Noise slope	11.58 e$^-$ rms/pF
Dynamic range (+)	500fC
Dynamic range (-)	275fC
Sensitivity (+)	3.5mV/fC
Sensitivity (-)	3.27mV/fC
Readout speed	10 MHz (max)
Power consumption	7mW/channel
Temp. coefficient	0.03mV/°C

REFERENCES

1. E. Beuville, K. Borer, E. Chesi, E. Heijen, P. Jarron, B. Lisowski ans S.Singh, 'Amplex, A low noise, low power analog CMOS signal processor for multielement particle detectors,' Nucl. Instrum. Methods Phys. Res. A288 (1990) 157.
2. J. C. Santiard, W. Beusch, S. Buytaert, C. C. Enz, E. Heijne, P. Jarron, F. Krummenacher, K. Marent and F. Piuz, Gasplex a low noise analog signal processor for readout of gaseous detectors, CERN-ECP/94-17, 1994.
3. Z. Y. Chang and W. M. C. Sansen, 'Low-noise wide-band amplifiers in bipolar and CMOS technologies', Chapter 5, Kluwer Academic, 1991.R.
4. A. Boie, A. T. Hrisoho and P. Rehak, Signal shaping and tail cancellation for gas proportional detectors at high counting rates, Nucl. Instrum. Methods Phys. Res. 192 (1982) 365.
5. F. Krummenacher, 'Developpement d'un Filtre deconvolueur Pour Detecteurs a gaz Comte-Rendu de conception', Internal document, Smart Silicon Systems S.A. Lausanne, Switzerland.

An Automated Data Acquisition System And Frequency Response Of 12 Lead ECG Signals

M. Mitra[+] , Sucharita Mitra*
[+]Department of Applied Physics, University of Calcutta, 92 APC Road, Kolkata - 700 009
*Computer Vision and Pattern Recognition Unit, Indian Statistical Institute,203 B.T. Road, Kolkata 700 035
E-mail : susa68@hotmail.com

Abstract

A software based normalized ECG database is developed for both normal and abnormal ECG records for helping further processing, analysis, control and decision making application. After extracting pixel to pixel co-ordinate information of images of each signal of 12 lead ECG records the data are sorted to regenerate the signal . After calculating sampling period of each signal Discrete Fourier Transform (DFT) was performed to get frequency spectrum of them . Some interesting results have been observed in some typical cases which are discussed in this paper and help to prepare a normalized data base. Still the amplitude of first six harmonics of monopolar chest lead V6 are normalized to distinguish normal and abnormal ECG signals. In almost 99% cases we get accurate result.

Key Words : Electrocardiogram, database, harmonics, frequency diagram, confidence interval.

INTRODUCTION

This is the age of Information Technology. So, technology is used for storing, retrieving or processing of any kind of information regarding any field. Creation of database is the stepping stone to reach this information era. A completely computerized data extraction and processing system is much more acceptable today because of its wider application potential. This system also include some added advantages such as - flexibility of data processing , reduction of noise , improved precision to control , data management and other various additional capabilities. In this paper we concentrate to develop a purely computer based data extraction and processing system of 12 lead ECG signals. The ECG is a laboratory test only and is not a "sine qua non" of heart disease diagnosis. A patient with an organic heart disorder may have a normal ECG while a purely normal person may have a nonspecific electrocardiographic abnormalities. Therefore, a further analysis of ECG records should be done to get more specific observation and detection of cardiac abnormalities.

An instrumentation scheme using Computer Aided Design and Drafting (Auto CAD) application package is already being used to generate ECG database. Here, a single channel strip chart recorder and a digitizer with tablet attached to the RS 422/432 port of the computer are used as input device. The digital plotter/printer - plotter was used as output device [1].

This CAD based data acquisition system was used to study polar phase response property of monopolar chest leads (V_1 to V_6) ECG voltages. The spin harmonic constituent of ECG voltages are evaluated at each harmonic plane and the polar phase responses are studied at each plane[2].

Some systems were developed which can transfer wave data recorded on paper to a digital time data corresponding to those obtained by A/D converter [3.4].

The frequency characteristic of each segment of ECG signal was computed via Fast Fourier Transform (FFT) to identify the cardiac abnormalities [5].

Here, a high resolution flat based scanner is used to capture the image of each ECG signal recorded on a single channel chart recorder (Voltage in mili volts Vs. time in second). These images are then fed to a purely computer based software system developed by us to generate the raw database in ASCII format. These data are then sorted and another algorithm is developed to detect the sampling period of each signal. At present the sampling rate is confined to ~ 1261 samples per second in an average. The captured pattern is compared or checked with the original waveform by the help of the

regeneration module of our system. This database is then ported to DFT domain of the algorithm to determine the spin harmonic constituents of these data. The graphical representation of the amplitude or frequency diagram of each signal is obtained from the computer VDU display and hard copy can be obtained from printer or computer plotter. The result may reveal some interesting frequency response properties of 12 lead ECG voltages.

MATERIALS AND METHOD

To prepare the database of ECG signals we first collected 50 ECG reports of different patients. Out of these reports, 30 reports were of normal patients and rests were of patients suffering from some kind of heart disease. The ECG voltages of the usual twelve lead locations of the human body are obtained from the single channel chart recorder with a 25mm/sec paper speed and an average resolution of 10 mv/mm .

A flatbed scanner (HP ScanJet 4C model) of ordinary resolution (300 dpi) and 256 gray tone spectral resolution is used to scan those ECG reports with very high accuracy. After scanning those reports the images of ECG signals are fed to a Personal Computer (PC) having a system for extracting pixel to pixel co-ordinate information. For this purpose the following steps were involved:

Binarization of the image :-

This process converted a gray tone image into two tones or binary image after selecting a suitable threshold limit. After scanning we obtain images having pixel values which varied from 0-255 (for gray tone image). So to mark or detect only the black pixels (having 0-pixel value) a threshold value 1 is chosen. Hence all the pixels other than black got a value (say 0) and the rest i.e., the black pixels got another value 1 resulting in a two tone or binary image.

Raw Data Extraction :-

In this step the co-ordinate of each black pixel is extracted and then the values are calibrated according to the co-ordinate system of the chart. Electrocardiograph paper is a graph in which horizontal and vertical lines are represented at 1mm intervals. A heavier line represents 5mm interval.

Time is measured along horizontal lines where one smallest division i.e.1mm = 0.04 sec. Voltage is measured along the vertical lines and is expressed as mm (10 mm = 1 mv) . In routine cardiographic practice the recording speed is 25mm/sec. The usual calibration is a 1mv signal which produces a 10 mm deflection. To obtain this calibration in the detected co-ordinate values got a relation that 55.5 smallest divisions of actual ECG paper in horizontal direction is equal to 650 pixels of the image.

Similarly, we get that 12.7 smallest division of actual ECG paper in vertical direction is equal to 150 pixels of the image.

To standardize the ECG database this calibration part is essential. The most important parameter of ECG signal is patient's heart rate. Hence, for this purpose, we also include heart rate of each patient in each data file of this database.

Data Sorting and Re generation of the ECG Signal

Since the raw data are extracted from the image so they are arranged according to their ordinate value. But normally, the graphical data are arranged according to their abscissa value. A sorting routine is developed to sort the raw data according to their value of abscissa.

Now those sorted data are ported to the regeneration domain of the system for checking the captured pattern with the original wave shape.

Determination of Sampling Period

In this step the sampling period i.e, the number of samples per second is being computed. At first, the total number of samples occur in between two consecutive peaks of ECG signal is calculated.

After a thorough observation of ECG signals we find out that there is a very sharp transition of ECG voltage from baseline at every peak. Reminding this factor an algorithm is developed to capture two consecutive peaks of every ECG signal by assuming a predefined threshold value of transition . Our logic is :

IF (TRANSITION > PREDEFINED THRESHOLD)
CAPTURE THE PEAK ;

To calculate this predefined threshold we first search for both the maximum value(Max_Val) and minimum value (Min_Val) of voltage along vertical direction for every data set and then the predefined threshold is set to (Max_Val - Min_Val)/2. Following this method the peaks are captured very accurately with 98.6% success rate.

A counter is set to count the number of samples occurred between two consecutive peaks. From the heart rate the time period of ECG signal can be obtained. So, the sampling period can easily be computed for each signal.

Discrete Fourier Transform

After getting the sampling period , the generated database is used as input to the algorithm developed for Discrete Fourier Transform (DFT) to get frequency or amplitude diagram of every ECG signal. The algorithm is developed according to the Eqn. given below:

$$H(N/NT) = [\,T/(NT)] \sum_{k=0}^{N-1} h(kT)\; e^{-j2\pi nk/N}$$

Where NT is time duration and N sample values of h (kT) must represent exactly one complete period of the periodic function h(t); n is the number/order of

harmonics. All ECG signals are reproduced by inverse Fourier Transform operation.

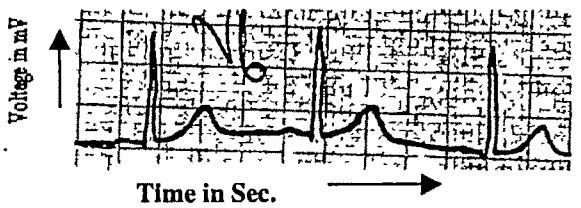

Fig 1 Original ECG signal from chart record

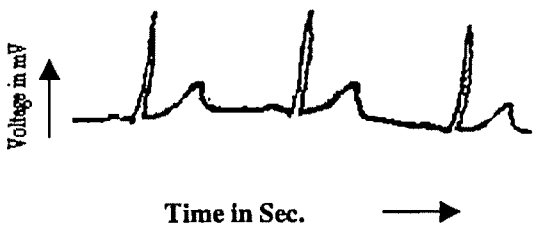

Fig 2 Reproduced ECG signal from Extracted database

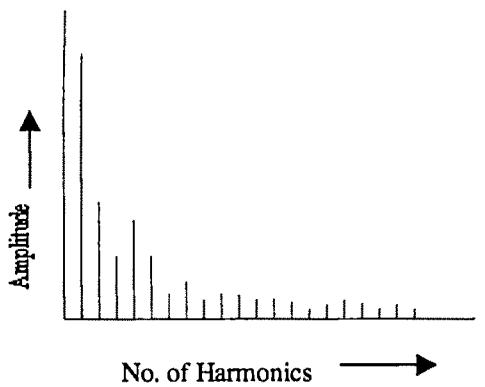

Fig 3 Frequency or Amplitude diagram of the ECG signal after DFT

RESULT

In the present investigation the analysis has been made for about 30 normal subjects and also for 20 abnormal subjects. The normal subjects were males in the age group 40 - 50 years. Here we normalized first six harmonics of normal subjects for the lead V6. We also estimate a confidence interval of each harmonic by calculating confidence limit of them because while the interval is determined, then in about 99% of the cases the interval will include the mean (μ) by selecting confidence coefficient 0.99. Though in table II we see that 2nd harmonic of patient2 (P2) and 6th harmonic of patient6(P6) are beyond the interval yet we see that ~99% cases the harmonics are within the range. The amplitude values of first 6 harmonics for 3 abnormal subjects mostly having Atrial Fibrillation with Partial RBBB are shown in table III where the values are widely varies from the confidence interval.

DISCUSSION

A software based ECG data extraction system is developed for both normal and abnormal subjects to obtain a normalized ECG database. For this purpose we analyze the frequency or amplitude diagram of each lead of each ECG wave for every normal and abnormal subjects. In this paper we give the normalized amplitude values of first 6 harmonics of ECG signal for chest lead V6 for normal subjects and we also calculate the confidence limit of each harmonic to obtain confidence interval of them and observe that most of the 99% cases the amplitude value of each harmonic is within this interval. On the other hand for abnormal subjects those values are much beyond that confidence interval. So we can conclude that our database can be used for better understanding of some biophysical properties of ECG signals also in some interesting clinical and diagnostic application.

REFERENCES

1. Goswami B, Mitra TK, Mitra M, Nag B, Basu S K, Basu D K, Data Base Generation from ECG Records using AutoCAD Application Package, IETE technical review, 1994,11: 67-69.
2. Goswami B, Mitra M, Nag B , Mitra T K, The Polar Phase Response Property of Monopolar ECG voltages using a Computer Aided Design and Drafting (CAD) Based Data Acquisition System, Int. J Biomed Comput, 1993, 33: 209 - 217.
3. Tezuka A, A study on transformation system of wave data recorded on paper into digital time data, Rec. Electr. Commun. Eng. Conversazione, 1989, 57 : 343 - 344.
4. Wideman LE and Freeman GL, A to D conversion from paper records with a desktop scanner and a microcomputer, Comp Biomed Res (USA), 1989, 22 : 393.
5. Abdulsada JW and Abbas HJ, Automatic diagnosis from electrocardiograms, Int J Syst Sci (UK) 1988, 19: 2157 - 2162.
6. Pahlm O and Sornmo L, Dataprocessing of exersize ECG, IEEE Trans Biomed, BME, 1987, 34 : 158-165.
7. Goon, A.M., Gupta, M.K., and Dasgupta, B, Fundamental of Statistics, 6th edn, 1993, 449 - 454. The World press Pvt. Ltd, India.

Table I

A PORTION OF EXTRACTED DATABASE IN ASCII FORMAT

Paper speed = 25 mm/s
Calibration factor = 10 mv/mm
No. of points = 1644
Heart rate = 65/min

X(Sec)	Y(mm)
0.000000	5.082000
0.085400	5.082000
0.170800	5.082000
0.256200	5.082000
0.341600	5.082000
0.427000	5.082000
0.512400	4.997300
0.597800	4.997300
0.683200	4.997300
0.768600	4.997300
0.854000	4.997300
0.939400	4.997300
1.024800	4.997300
1.110200	4.997300
1.195600	4.997300
1.281000	4.997300

Table III

A PORTION OF THE TABLE SHOWING AMPLITUDE VALUE OF FIRST SIX HARMONICS OF ABNORMAL SUBJECTS

For Lead V6

Harmonic No.	Amplitude value of abnormal subjects		
	A1	A2	A3
1	1	1	1
2	0.54106	0.74743	0.28226
3	0.20749	0.63035	0.48597
4	0.28517	0.30914	0.10561
5	0.09995	0.66818	0.45009
6	0.1205	0.18796	0.2461

A PC Based Bio-Feedback System For Correcting Paraplegia

Puvvada Ramesh
Department of Electronics, Communication and Instrumentation Engineering
GITAM, College of Engineering, Visakhapatnam 530 045, India

Abstract

A PC based biofeedback system for correcting paraplegia in partially paralyzed patients **is presented. This system consists apart from the PC, a set of surface electrodes, an instrumentation amplifier, a signal conditioner, an Analogue to Digital Converter and a Digital to Analogue Converter. The surface electrodes pick up the electro-myographic (EMG) signal from a muscle which can be activated by the patient. This signal which is normally weak, is amplified by a programmable gain instrumentation amplifier and is passed through a signal conditioner to filter the unwanted components. This signal is digitized and stored in the memory of the PC using an Analogue to Digital Converter. An on board Digital to Analogue converter, converts this signal back into analogue form to serve as bio-feed back signal, to activate the paralyzed part. The software necessary for EMG data acquisition and control is developed in assembly language using the macro-assembler MASM. Both hardware and software aspects of the problem are presented in this paper.**

1. INTRODUCTION

Many researchers have constructed inexpensive and powerful instruments for data acquisition and control using the readily available IBM PC and its clones[1-5]. These instruments, in general, consist of a transducer or sensor, an Instrumentation amplifier with a signal conditioner, an Analogue to Digital converter interface and a Digital to Analogue converter interface. The transducer converts the physical or physiological parameter of interest into an electrical signal which is normally very weak and buried in noise. The Instrumentation amplifier amplifies the weak signal to the desired level. The amplified signal is passed through a signal conditioner to limit the band width and to improve the signal to noise ratio. These signals are digitized and stored in the memory of the PC using an Analogue to Digital Converter Interface, installed in the expansion slot of the PC. This digital data is some times subjected to digital filtering to further improve the S/N ratio. Digital signal compression techniques are used to reduce the memory requirement for the data storage and for fast transmission to a distant specialist. The Digital to Analogue converter interface converts this digital signal back into analogue form for bio-feed back and control. An Instrumentation amplifier with an Isolation amplifier, a 12-bit Analogue to Digital converter interface and a 12-bit Digital to Analogue converter interface realized are presented in this paper.

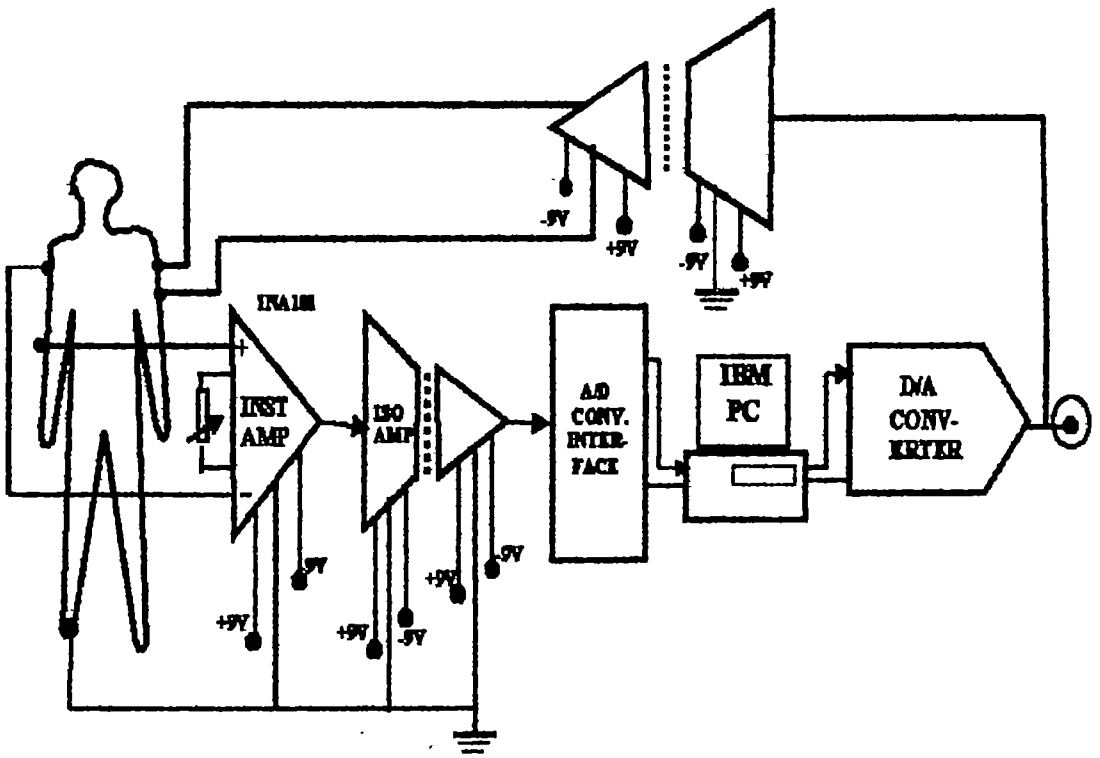

FIG. 1 PC BASED BOIMEDICAL INSTRUMENT

Software necessary for digitizing the electromyographic (EMG) signal and to convert it back into the analogue form for correcting paraplegia is developed in assembly language using macro assembler MASM. Both hardware and software realized around an IBM compatible PC are presented in this paper. The system can easily be adopted for several other applications with little or no modification.

2.MATERIALS AND METHODS

The PC based bio-feedback system for correcting paraplegia, as shown in Figure1. consists of an Instrumentation Amplifier, Isolation Amplifiers, an Analogue to Digital (A/D) converter Interface and a Digital to Analogue (D/A) converter Interface. The EMG signals which are normally weak (of the order of a milli volt or less) are picked up by the surface electrodes. The Instrumentation Amplifier (INA 101), the gain of which can be adjusted with a single potentiometer, amplifies these weak potentials to a few volts level. The Isolation amplifier (ISO 122) provides protection to the patient from electrical shock hazards. This signal is converted into a 12-bit digital code by an A/D converter (AD 574). This data is put simultaneously on the data bus of the D/A converter (AD7545A) to get back the analogue signal. This signal is

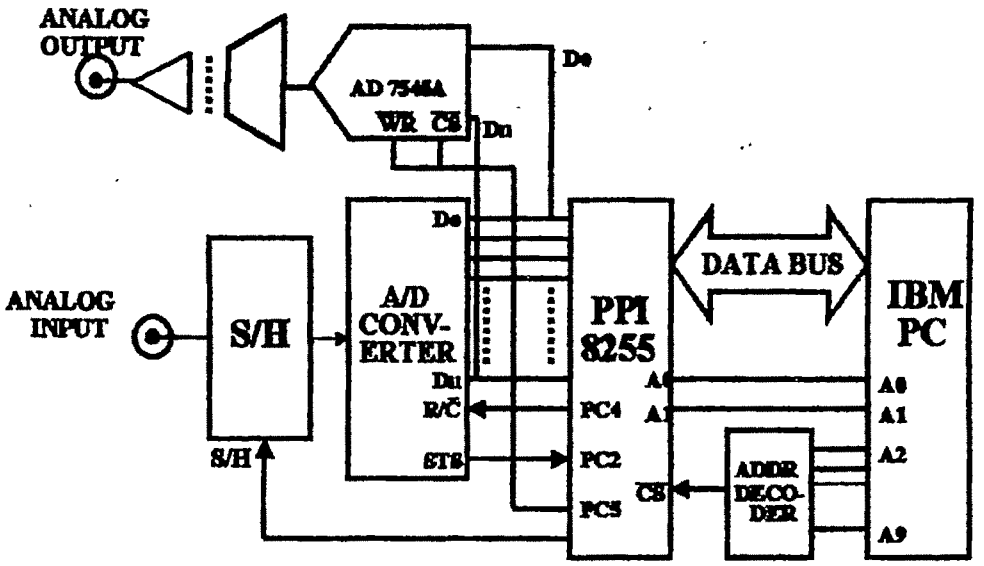

FIG. 2 A/D AND D/A CONVERTER INTERFACE

passed through an Isolation Amplifier (ISO 122) and is fed back to the patient for correcting paraplegia. The Instrumentation amplifier INA 101 and the isolation Amplifiers ISO 122 are energized by +9v and –9v batteries to provide safety to the patient. The rest of the circuits are energized by the ±12v and ±5v supplies available in the expansion slot of the PC.

3. A/D AND D/A CONVERTER INTERFACE

The Analogue to Digital (A/D) and the Digital to Analogue (D/A) converter interface as shown in Figure 2.[4, 5] consists of a Sample and Hold Amplifier (AD585), a 12-bit A/D Converter (AD574A), a Parallel Programmable Interface (PPI 8255A), a 12-bit D/A Converter (AD7545A) and the address decoding logic. Address decoding was done in such a way that the Port A, Port B, Port C and the Control Word Register (CWR) of the PPI are assigned hexadecimal addresses from 300 to 303 in the user reserved I/O space of the microprocessor, following the Intel norms.

The S/H amplifier takes about 3μs for sampling each data point before going into the hold mode. The Analogue to Digital converter takes about 20 μs to convert this analogue voltage into a 12-bit digital code. This 12-bit digital output is passed into the microprocessor's memory through Ports A and B of the PPI (8255A). Pin 6 of Port C (PC6) is used to activate S/H amplifier. Pin 4 of Port C (PC4) is used to command the conversion cycle of the A/D converter and Pin 2 of Port C (PC2) is used to test the end of conversion. This 12-bit digital output is also put on

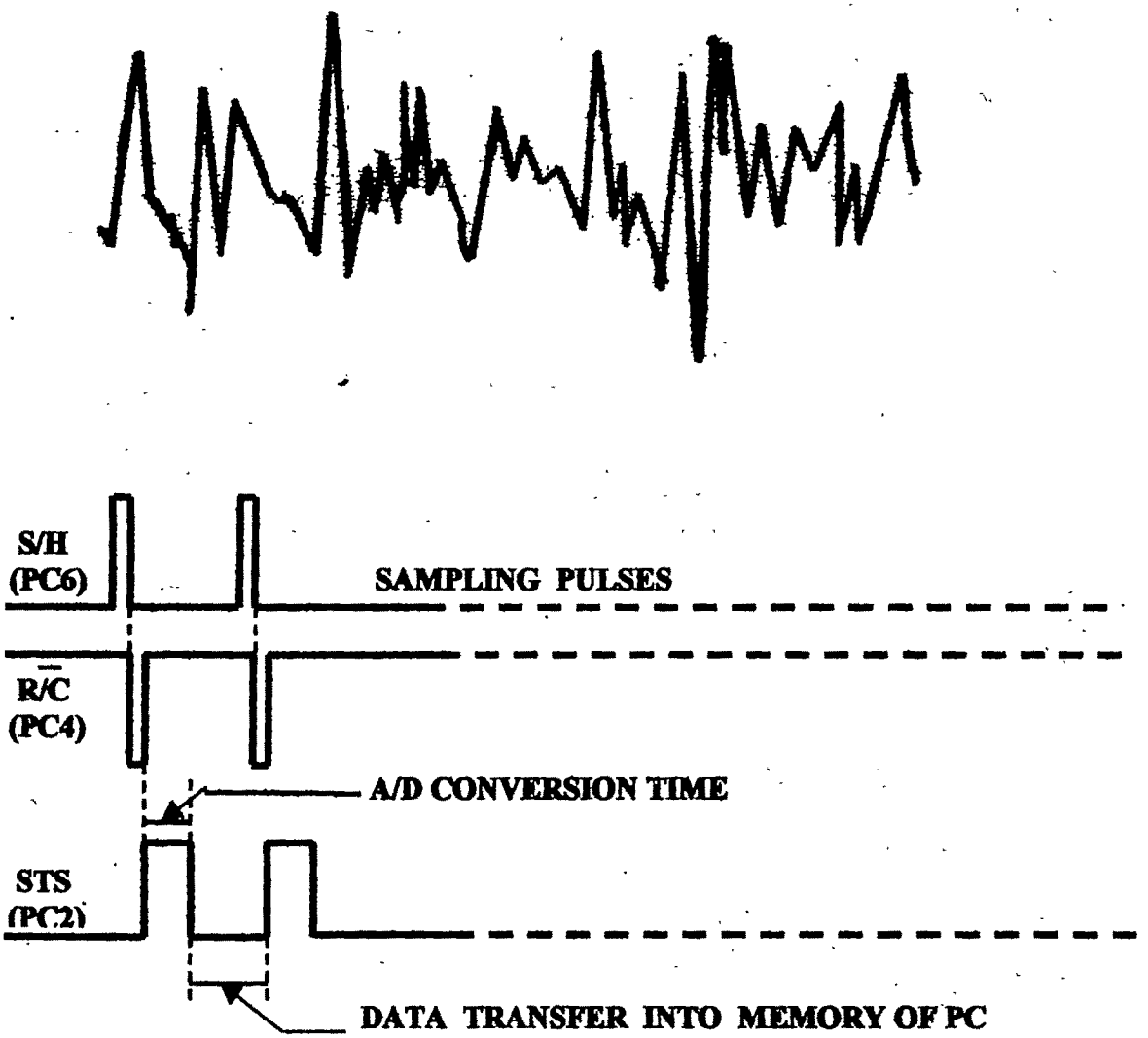

FIG.3 DIGITIZATION OF EMG SIGNAL

the data bus of the D/A converter (AD7545A) which is activated by the pin 5 of port C (PC5) of the PPI to get back the analogue signal for correcting paraplegia. This card goes into one of the expansion slots of the PC and is energized by the ±12V and ±5V available in the PC.

4. RESULTS AND DISCUSSION

A chronogram representing the various events for digitization using the A/D converter interface discussed, is presented in Figure 3. Generation of the

control pulses for sampling, activating the A/D and D/A converters was carried out with an assembly language programme. The digital data available at the Ports A and B of the PPI is simultaneously put on the data bus of the D/A converter for getting the analogue signal back for correcting paraplegia. 1024 data points acquired from the EMG signal during a period of 100 m sec are stored in the memory of the PC for further processing. (Assembly language source program will be supplied to the interested researcher on request). Work is in progress to test the capabilities of this instrument for correcting paraplegia in patients in the local King George Hospital Medical College Center.

ACKNOWLEDGMENTS

The author wishes to thank the University Grants Commission for providing financial assistance and the management of GITAM, College of Engineering for their help and encouragement.

REFERENCES

[1] W.J. Tompkins and I.G. Webster, "Interfacing sensors to the IBM PC", Prentice Hall , Englewood Cliffs NJ, 1988.

[2] P. Meller, "computer-assisted video microscopy for the investigation of monolayers on liquid and solid substrates", Rev. Sci. Instrum., Vol. 59, pp 2225- 2231, 1988.

[3] G. Shenhing and R.J. Patrick, "Personal Computer based Fourier Transform ion Cyclotron Resonance Mass Spectrometer", Rev. Sci. Instrum., Vol. 59, pp 2573-2576, 1988.

[4] R. Puvvada and S. Mekaoui, "A Microcomputer based Data Acquisition System for an NMR Pulse Spectrometer", Meas. Sci. Technol., Vol. 1, pp 647-650, 1990.

[5] R. Puvvada, S. Mekaoui and M. Chemloul, "A PC based Electronic System for the Generation of Magnetic Field Gradients", Meas. Sci. Technol., Vol. 1, pp 1247-1249, 1990.

LabVIEW Based Communication Protocol for Interfacing Spirometer with Personal Computer

A. Kandaswamy[#], C. Sathish Kumar[*1], and T. Vamsee Kiran[*]
[#]Dept. of Electronics & Communication Engineering, PSG College of Technology, Coimbatore
[*]Dept. of Electrical & Electronics Engineering, PSG College of Technology, Coimbatore
[1]*E-mail of corresponding author: c_sathish_k@yahoo.co.in*

Abstract

A communication protocol for the transfer of data between spirometer and Personal Computer has been developed using the software package LabVIEW. The protocol was formulated under the interface independent industry standard VISA (Virtual Instrumentation Software Architecture). It was tested by establishing a serial communication interface for transferring the patient details and lung parameters to the PC.

INTRODUCTION

The use of Personal Computers (PCs) for the acquisition and analysis of biomedical signals has been increased extensively in recent times [1]-[3]. Interfacing biomedical instruments to PC enable the medical practitioner to use advance techniques for the processing and data computing of biomedical signals. Apart from that, he will be able to use medical expert systems for the diagnosis and treatment of the respiratory diseases.

Disorders of the respiratory system is recognised as a major source of abnormal behaviour of human physiological system and hence a thorough investigation of respiratory system is essential. Spirometry is an essential pulmonary function test widely used in the diagnosis and management of respiratory system. In spirometry, the volume of air inspired and expired is measured as a function of time using the equipment called spirometer. Spirometry provides useful information about overall respiratory system that can be fundamental in categorizing and staging pulmonary diseases.

In this work, a communication protocol for interfacing a spirometer with Personal Computer (PC), is developed. The protocol has been developed using the software package LabVIEW (Laboratory Virtual Instrumentation Engineering Workbench) [4] under the interface independent industry standard, VISA (Virtual Instrumentation Software Architecture).

LabVIEW is one of the most popular and powerful computer tools available for the acquisition and analysis of electric signals. In contrary to other programming systems which use text-based languages to create lines of code, LabVIEW uses a graphical programming language, G, to create programs in block diagram form. It uses terminology, icons, and ideas familiar to technicians, scientists, and engineers, and relies on graphical symbols rather than textual language to describe programming actions.

DEVELOPMENT OF PROTOCOL

LabVIEW is a development environment based on the graphical programming language G. It is integrated fully for communication with hardware such as GPIB, VXI, PXI, RS-232, RS-485, and plug-in data acquisition boards.

VISA

VISA is a standard I/O Application Programming Interface (API) for instrumentation programming. VISA by itself does not provide instrumentation programming capability. VISA is a high-level API that calls into lower level drivers. The hierarchy of National Instruments-VISA is shown in the Fig. 1. VISA can control VXI, GPIB, or serial instruments, making the appropriate driver calls depending on the type of instrument being used.

CABLE CONNECTIONS

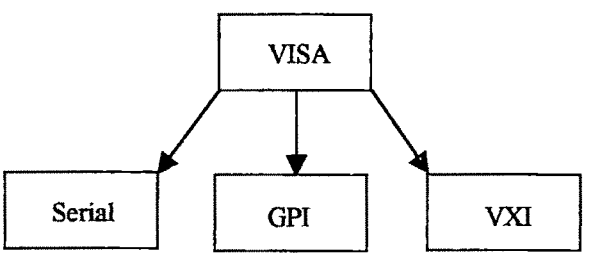

Fig.1 Hierarchy of National Instruments-VISA

An RS-232 cable has been modified such that both spirometer and PC act as Data Terminal Equipment (DTE) during communication [5]. Transmit Data (TD) and Receive Data lines of the spirometer are connected to the Receive Data (RD) and Transmit Data (TD) lines of PC. Each of the other lines of spirometer connector is connected to the corresponding line in PC.

PROTOCOL

In this work, a protocol was developed for serial communication between spirometer and PC under the industry standard VISA using LabVIEW. Spirometer SP-5000 from M/s Fukuda Denshi, Japan has been used in this application. The features of protocol needed for the communication between spirometer and PC is shown in Fig. 2 [6].

In response to the enquiry signal (Enq) from the spirometer, the PC issues an acknowledge (Ack) signal. On receiving the acknowledge signal, spirometer sends the header files which contains details such as logical block count, block length, language number, etc. Further sending and receiving of data is also controlled with the Ack signal. The data packet is transmitted in order of smaller block numbers. In case the data do not exist, the packet of the number will not be transmitted.

Front panel of the software showing the spirometric values obtained after the transfer of data from the spirometer to the PC is shown in Fig. 3. It acquires the patient data such as name, age, gender, height, weight and disease indications, and the various lung parameters. Apart from the patient data, the front panel shows the lung parameters: tidal volume (TV), inspiratory reserve volume (IRV), expiratory reserve volume (ERV), vital capacity

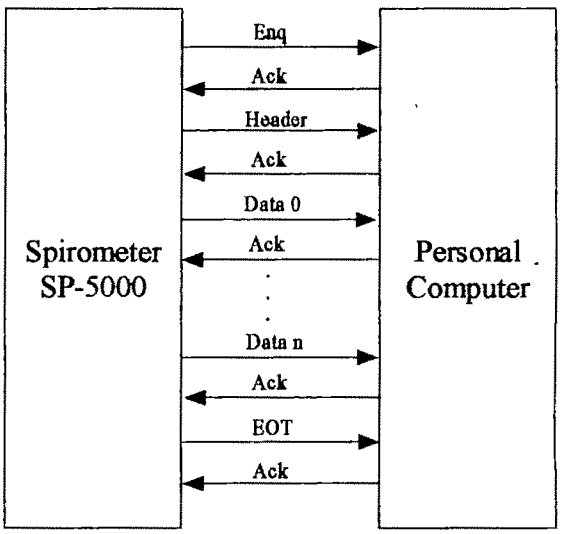

Fig. 2: Protocol for the communication between spirometer and PC

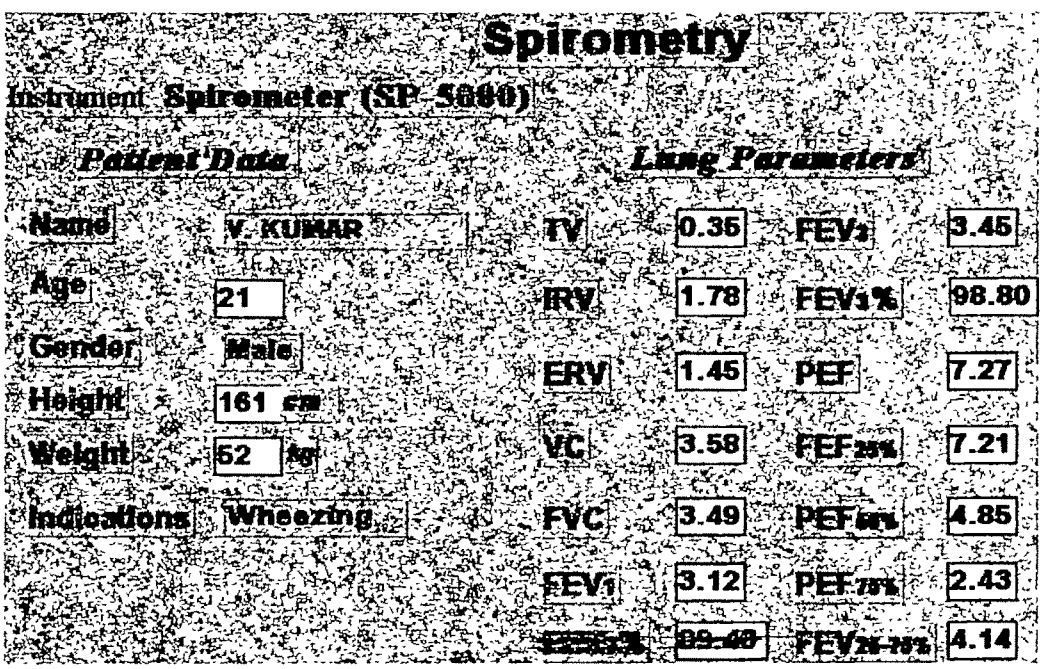

Fig. 3: Front panel of the software showing patient details and spirometric values

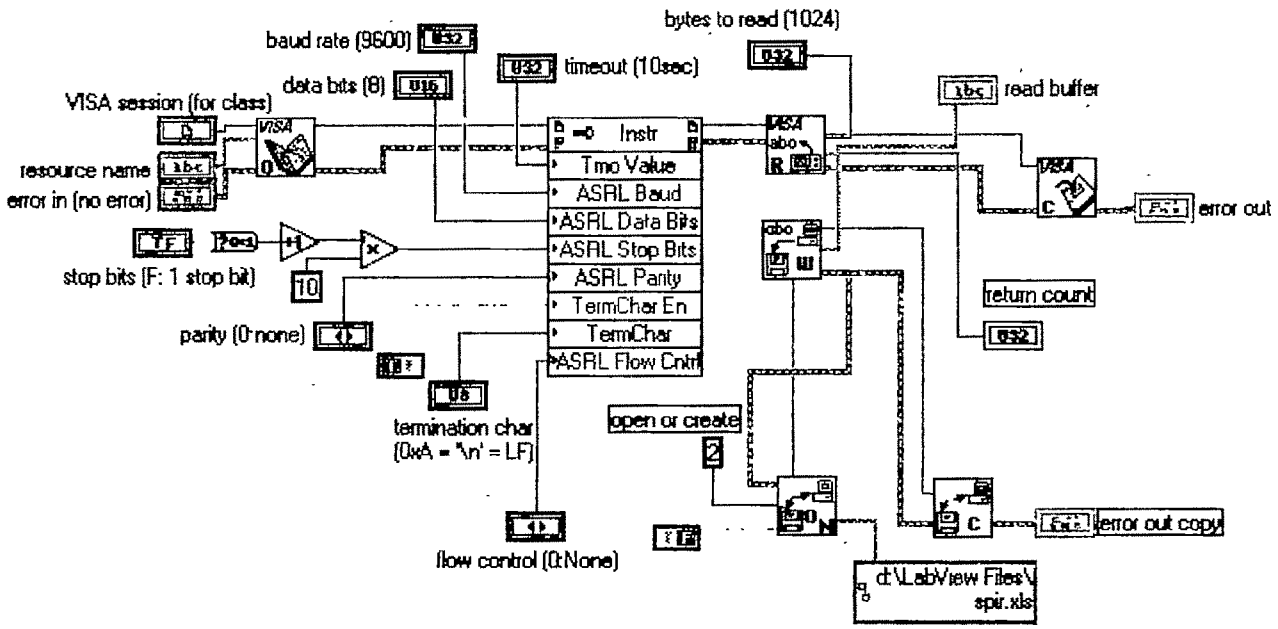

Fig. 4: The G-program for establishing communication link between spirometer and PC

(VC), Forced Expiratory Vital Capacity (FVC), Forced Expiratory Volume in 1 sec (FEV_1), FEV_1/FVC ratio in percentage (FEV_1%), Forced Expiratory Volume in 3 sec (FEV_3), FEV_3/FVC ratio in percentage (FEV_3%), Peak Expiratory Flow (PEF), Forced Expiratory Flow at 25% FVC ($FEF_{25\%}$), Forced Expiratory Flow at 50% FVC ($FEF_{50\%}$), Forced Expiratory Flow at 75% FVC ($FEF_{75\%}$), and Mean Forced Expiratory Flow during the middle half of the FVC ($FEF_{25-75\%}$).

The G-programme for establishing the communication link between the spirometer and PC is shown in Fig. 4. The diagram does not include the programs for front panel, and for separating the data packet into patient data and spirometric values and displaying them.

CONCLUSIONS

Establishing communication between spirometer and PC enable the physician to use various computer tools for the analysis of spirometric data. It also enables storage of data for further comparison.

VISA is the standard API for instrument drivers throughout the instrumentation industry. VISA uses the same operations to communicate with instruments regardless of the interface type. VISA is designed so that programs written using VISA function calls are easily portable from one platform to another. Thus this communication program developed is an industry standard API and it is interface independent and platform independent.

ACKNOWLEDGEMENTS

The authors wish to express their sincere gratitude to Mr. P. Sivakumar, Technician who extended full co-operation during testing. Thanks are also due to The Principal, PSG College of Technology, Coimbatore, India, Head of the Dept. (Electrical & Electronics Engg.), PSG College of Technology and the Mangement of PSG Institutions for providing the research facilities and encouragement.

This work was supported by Department of Science and Technology, Govt. of India vide Grant III.5(47)/96-ET.

REFERENCES

1. S. C. Cassidy and D. F. Teitel, "Left ventricular pressure and volume data acquisition and analysis using LabVIEW," *Comput. Biol. Med.*, vol. 27, pp. 141-149, 1997
2. B. Grinstead and M. E. Parten, "Biomedical signal acquisition using LabVIEW," *Eleventh IEEE Symp. Computer-Based Med. Sys.*, pp. 157–161, 1998.
3. M. L. Chugani, A. R. Samant, and M. Cerna, *LabVIEW Signal Processing*. Upper Saddle River, N. J.: Prentice Hall PTR, 1998.
4. User's Manual, LabVIEW ver 5.0, National Instruments Corporation, Texas, USA.
5. B. W. Putman, *RS-232 Simplified*. Englewood Cliffs, N. J.: Prentice Hall Inc., 1987.
6. Operation Manual, Spirosift SP-5000, Fukuda Denshi Co. Ltd, Japan.

DSP based Online Air-Gap Torque Monitor for Detection of Squirrel Cage Rotor Faults

Vinod V. Thomas, Krishna Vasudevan and V. Jagadeesh Kumar
Department of Electrical Engineering, Indian Institute of Technology, Madras
CHENNAI 600 036 INDIA
E-mail: krishna@ee.iitm.ernet.in

Abstract

This paper proposes a Digital Signal Processor (DSP) based implementation of online air-gap torque estimator for detection of squirrel cage rotor faults. Two non-invasive, computationally efficient methods for online air-gap torque monitoring are discussed. In both the methods the air-gap torque is computed from two stator voltages and currents and is cost effective when compared with the use of a conventional torque transducer. The online air-gap torque monitor has been implemented using TMS320C31 and tested on faulty cage rotors.

Key words: Air-gap torque estimator, rotor fault detection, DSP based air-gap torque monitor

INTRODUCTION

Online condition monitoring of induction machines has gained importance in recent years due to the need to reduce machine downtime in critical applications and enhance its reliability. An early detection of faults using modern signal processing techniques is a challenging task.

Traditionally, Motor Current Signature Analysis (MCSA) [1] has been used for non-invasive detection of electrical and mechanical faults of induction motors. MCSA provides direct information on the presence of various abnormal conditions, but the relationship between the fault severity and the magnitude of the characteristic spectral component is not well established [2]. This has motivated researchers to investigate alternative signals for condition monitoring such as air-gap torque and instantaneous power. These signals derived from multiple input voltage and current signals of the machine offer potential advantages over the one phase current spectrum.

As air-gap torque represents the combined effect of all the flux linkages and currents in both stator and rotor, it is highly sensitive to any asymmetrical operating condition [3]. Theoretically, next to rotor current, which is inaccessible for direct sensing, the air-gap torque is the diagnostic medium most affected by rotor faults [4].

Simulation studies have shown that a symmetrical machine model excited with motor variables for asymmetrical operating conditions can be used for monitoring air-gap torque for fault diagnosis [5]. In this paper, two efficient schemes for online estimation of air-gap torque for fault detection are identified. The scheme was implemented on dSPACE DS1102 DSP prototyping environment. The details of the implementation are discussed subsequently.

AIR-GAP TORQUE SPECTRUM

Air-gap torque spectra for both symmetric and asymmetric operation (rotor-bar breakage) at full load condition are given in Fig. 1. With broken rotor bars, frequency components are observed at characteristic

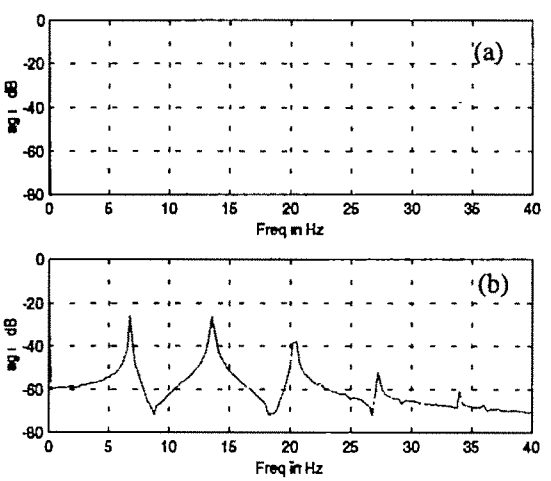

Fig. 1 Air gap Torque spectrum at full load (Normalised) a) Healthy Machine b) 3 rotor bars broken

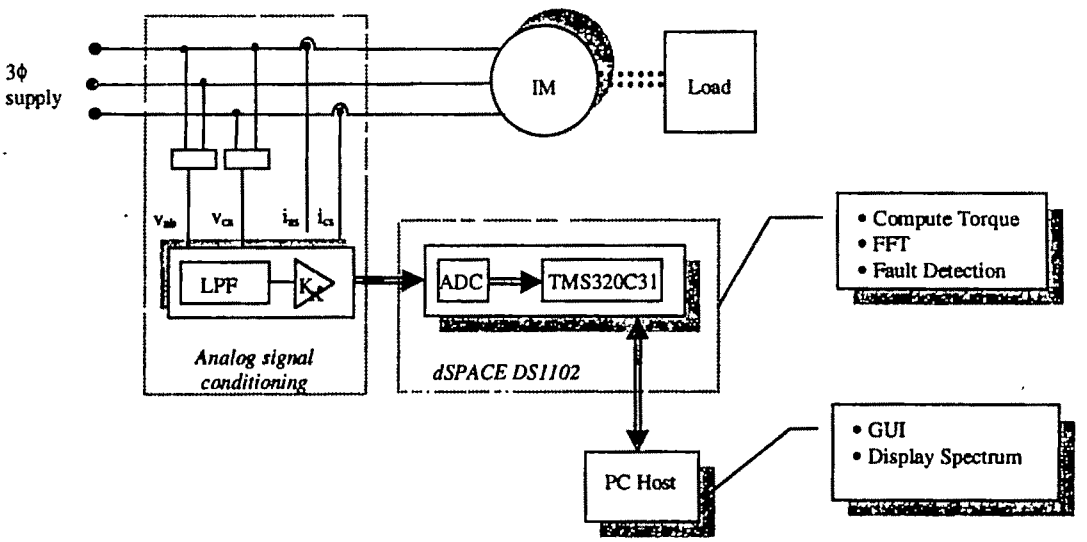

Fig. 2 Implementation of air-gap torque estimation (Scheme I)

frequencies,

$$f_c = f(2ks),\ k = 1,2,3.... \quad (1)$$

where f - *supply frequency* and *s- slip.*

In the case of air-gap torque spectrum, the characteristic frequencies are near dc. As air-gap torque is produced by the interaction of the flux linkages and the currents of a rotating machine, it is highly sensitive to motor faults [3]. Hence, it is obvious that air-gap torque spectrum is a potential signature that can be effectively used in online condition monitoring and fault diagnosis.

SCHEMES FOR AIR-GAP TORQUE ESTIMATION

Simulation studies have justified the use of healthy machine model excited with motor variables for asymmetrical operating conditions for estimating air-gap torque for condition monitoring [4]. Two non-invasive, computationally efficient and cost-effective methods for online air-gap torque monitoring are discussed. In both the methods the air-gap torque is computed from two stator voltages and currents and is cost effective when compared with the use of a conventional torque transducer.

Scheme I [2]

Air-gap torque for a symmetrical machine in terms of stator voltages and currents can be expressed as

$$T_{e\_hru} = \frac{p}{2\sqrt{3}}\left\{\begin{matrix}(2i_{as}+i_{cs})\int[v_{ca}-R_s(i_{cs}-i_{as})]dt- \\ (i_{cs}-i_{as})\int[v_{ab}-R_s(2i_{as}+i_{cs})]dt\end{matrix}\right\} \quad (2)$$

Simulation results have shown that characteristic frequencies are preserved in the air-gap torque spectrum computed according to (2) but for minor changes in magnitude.

Scheme II [6]

Another scheme for air-gap torque computation for symmetrical machines based on *qd* transformation is given by

$$T_{e\_pck} = 1.5\left(\frac{p}{2}\right)\left(\frac{1}{\omega_b}\right)\left(\psi_{ds}i_{qs} - \psi_{qs}i_{ds}\right) \quad (3)$$

where

$$\frac{d\psi_{ds}}{dt} = (v_{ds} - i_{ds}R_s)\omega_b \quad (4)$$

$$\frac{d\psi_{qs}}{dt} = (v_{qs} - i_{qs}R_s)\omega_b \quad (5)$$

Assuming stator reference frame the voltages and currents are transformed as

$$f_{qs} = f_{as} \quad (6)$$

$$f_{ds} = -(f_{as} + 2f_{bs})/\sqrt{3} \quad (7)$$

Both the schemes estimate air-gap torque with the same level of accuracy and their computational requirements are identical. The details of implementation of air-gap torque monitor based on *Scheme I* is discussed in the next Section.

IMPLEMENTATION

Block diagram of the digital signal processor based implementation of online air-gap torque monitoring scheme is given in Fig. 2. The various subsystems includes 3ϕ squirrel cage induction motor and load, analog signal conditioning, DSP add-on card (dSPACE DS1102), and a host PC

Induction Motor & Load

A 2.2 kW, 415V, 50 Hz, 3ϕ squirrel cage induction motor coupled to a dynamometer is used for testing the air-gap torque monitor. A set of additional cage rotors fabricated with the following faults – one rotor bar broken, three rotor bars broken, end-ring segment broken, and one rotor bar with 50% more resistance is used to test the performance of the air-gap torque monitor under faulted conditions. The parameters of the motor are given in Appendix.

Sensors

Hall effect closed loop current and voltage sensors are used for measuring i_{as}, i_{cs}, v_{ab}, and v_{ca}. These sensors are linear over a wide range of frequencies and also provide channel to channel isolation.

Analog signal conditioning

The voltage and current signals sensed are low pass filtered and then simultaneously sampled at 1kHz. Eighth order Butterworth switched capacitor filter with cut off frequency of 200Hz is used as anti-aliasing filters on each of the four input analog channels. The signals are amplified to the full range of the ADCs (±10V). The switched capacitor filter output offset voltage is in the range of 300mV/channel. Fig. 3 gives the details of the analog conditioning subsystem

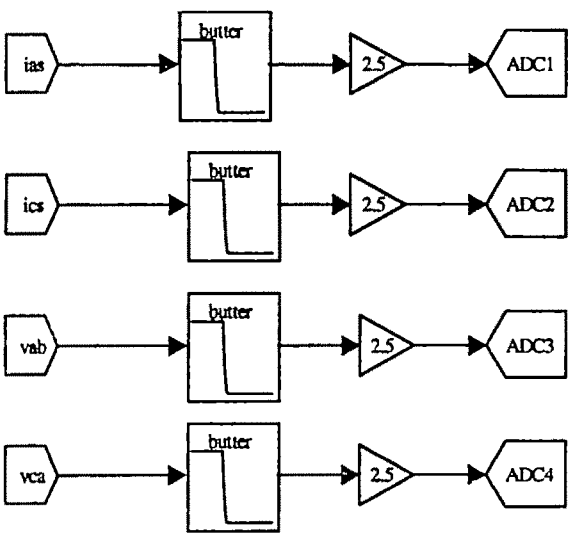

Fig. 3 Analog signal conditioning module

dSPACE DS1102 prototyping board

The DS1102 controller board is a compact PC-AT add-on card based on the Texas Instruments Digital signal Processor TMS320C31/40MHz. TMS320C31 is a 32-bit floating point processor capable of single cycle floating point multiply accumulate. It has 2Kx32 words of on-chip memory, two 32-bit timers, interrupt logic, serial port and DMA controller. High speed ADC and DAC hannels, incremental encoder interface and TMS320P14 based digital I/O subsystem are also available on the card. Of the four bipolar ADC channels, two are 16 bit ADCs and the other two 12 bit with conversion time 10µs and 3µs respectively. The TI TMS320P14, 16 bit microcontroller DSP, which acts as a slave processor provides digital I/O lines, timer driven event management capability and PWM generation. dSPACE real-time system consists of tools for rapid prototyping of DSP and control systems. Functional block diagram of DS1102 prototyping board is given in Fig. 4.

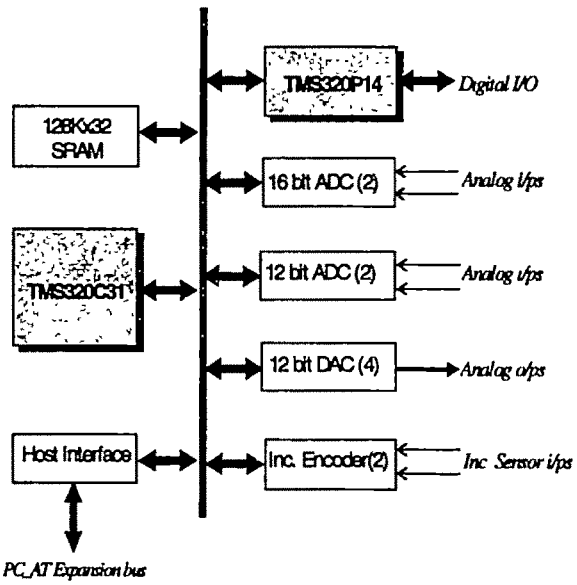

Fig. 4 Functional diagram of DS1102 prototyping board

Software organisation

Air-gap torque is computed from the digitised signals - v_{ab}, v_{ca}, i_{as} and i_{cs} - using equation (2). The torque computation and FFT are implemented on the TMS320C31 digital signal processor. The torque spectrum is computed with a frequency resolution of 0.25Hz. The host PC communicates to the DSP card using the host port interface reads in the spectrum and displays it on the monitor. A user friendly GUI is developed using MATLAB which serves as a control and display panel for the entire system. The Torque spectrum is updated every minute and it provides diagnostic information on the health of the machine.

The block schematic of the torque computation algorithm implemented on TMS320C31 is shown in Fig. 5. The highpass filters are used for removal of DC offsets. The DC offset in flux does not contribute to the air-gap torque. The highpass filter is implemented as a linear phase FIR filter – moving average filter of length 100 (fc=2.5Hz). To obtain a frequency resolution of 0.25Hz, 4096 samples of the computed torque are buffered and FFT of the windowed samples is computed.

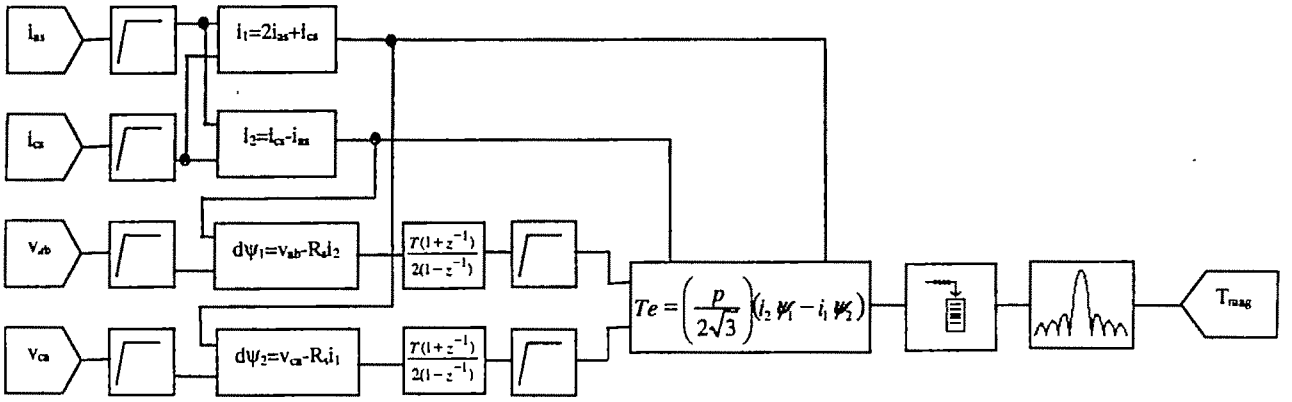

Fig. 4 Functional diagram of air-gap torque computation implemented on TMS320C31

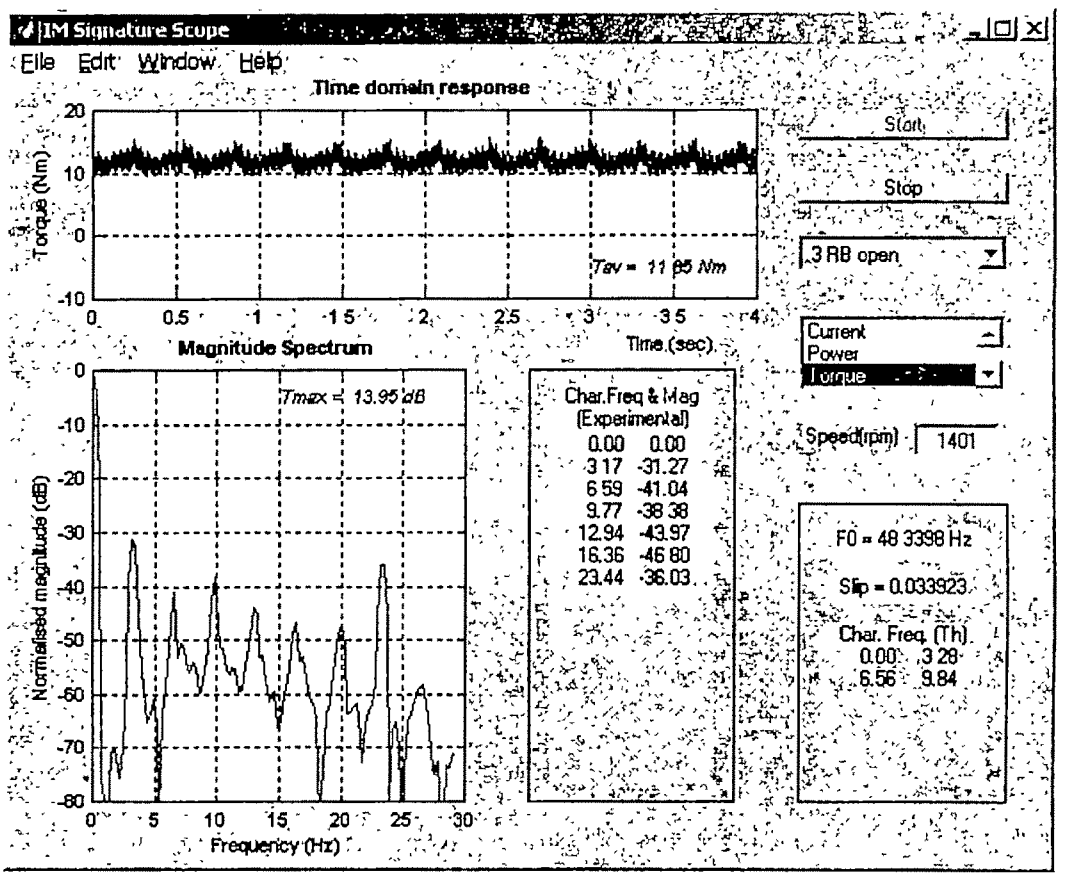

Fig. 5 Real-time graphical display of the Torque Monitor

Blackmann window was used for this implementation. The 4096 point FFT takes 7.27ms on DS1102/40MHz.

The GUI gives the user the option to choose the rotor type of the induction machine and whether to display Torque/ Current/Power Spectrum. The GUI initiates data acquisition and processing on the DSP using host-DSP interrupt on /INT3 of TMS30C31. The host monitors the processing done by TMS320C31 using real-time handshake signals and when the FFT computation is complete it reads in the data. The host processor carries out post-processing and display of results.

The speed of the motor is measured with a digital tachometer and given as input to the system. The spectrum, the fundamental frequency, and the slip are computed. The characteristic frequencies are measured from the spectral plot and are found to be matching with the theoretical characteristic frequencies computed according to (1).

Fig. 6 shows the display of the torque spectrum for the case of rotor with 3 rotor bars broken with 75% load. The experiment was repeated with rotors of different kinds of faults for various load conditions. In all the cases the characteristic fault signature was clearly distinguishable in the torque spectrum. In Fig. 6 the components are seen at 3.17Hz, 6.59 Hz and 9.77 Hz. The component at 23.44 Hz (f_r) corresponds to the angular velocity of the rotor (1401 rpm) and it is due to slight eccentricity present in the motor. The supply frequency during the test was 48.34 Hz.

CONCLUSION

Two non-invasive schemes for online air-gap torque estimation are identified. DSP based implementation of the above schemes are presented. The experiments have clearly demonstrated the effectiveness of air-gap torque spectrum in squirrel rotor fault identification. The algorithm is simple and is easily implementable on a DSP. DSP based controllers are now widely used in drive systems. The fault detection algorithm can be implemented in real time on the same DSP in a time-shared mode. Hence the additional hardware required for induction motor condition monitoring is reduced to minimum. The air-gap torque monitor discussed find application in condition monitoring and fault diagnosis of induction motors, field test for finding motor efficiency and as a substitute for expensive torque transducers in sophisticated drive systems.

APPENDIX

Machine data

2.2 kW, 50 Hz, 415V, 4 pole, 3ϕ cage IM with

$m_s = 36$	number of stator slots
n = 28	number of rotor bars
L=127e-3 m	length of stack
lg=0 4e-3 m	effective air-gap
r=47.9e-3 m	mean radius of air-gap
Ns=93	number of turns/phase
Rs = 2.772 Ω	stator resistance
Rb = 119.09e-6 Ω	rotor bar resistance
Lb = 0.44154e-6 H	rotor bar leakage inductance
Re = 1.59e-6 Ω	end ring segment resistance
Le = 0.0473e-6 H	end ring segment leakage inductance
J = 0.012kg-m^2	rotor inertia

REFERENCES

[1] W. T. Thomson and M. Fenger, "Current signature analysis to detect induction motor faults," *IEEE IA Magazine*. Vol. 7, pp.26-34, Jul./Aug. 2001.

[2] A. Bellini, F. Filippetti, G. Franceschini, C. Tassoni, and G. B. Kliman, "Quantitative evaluation of induction motor broken bars by means of electrical signal analysis," *IEEE-IAS 2000*, Rome, Oct. 2000

[3] J. S. Hsu, "Monitoring defects in induction motors through air-gap torque observations," *IEEE Trans. on Industry Applications*, vol. 31, pp. 1016-1021, Sep./Oct. 1995.

[4] A.M. Trzynadlowski and E. Ritchie, "Comparative investigation of diagnostic media for induction motors: A case with rotor cage faults," *IEEE Trans. Industrial Electronics*, vol. 47, pp. 1092-1099, Oct. 2000.

[5] V. V. Thomas, K. Vasudevan, V. Jagadeesh Kumar, "Use of air-gap torque for squirrel cage rotor fault identification", IEEE PEDS 2001, Bali, Indonesia.

[6] P. C. Kraus, *Analysis of Electrical Machinery*, MGH, 1987.

A Microprocessor Based Protection Scheme For The Alternator Rotor Winding

Konika Das (Bhattacharya), Debashis Ghosh, Dipten Dasgupta
Department Of Electrical Engineering , B.E.College (D.U.), Howrah - 711 103,India
E-mail of KonikaBhattacharya : poopoolee50@hotmail.com

Abstract

An 8086 microprocessor based automatic protection scheme for the alternator rotor winding has been devised. It requires only 1.5msecs for its operation, senses the occurance of the first fault, anunciates the fault location to the user and initiates trip at the second fault. Human dependence is reduced to the minimal in this scheme and the user-friendly protection scheme so devised can be installed in any large alternator.

Key words : Rotor insulation failure, protection, digital relay.

INTRODUCTION

When faults in an alternator are arranged according to the frequency of their occurrences and gravity of damages, the rotor earth fault does not precede the other major faults.On the occurrence of a double fault in the rotor winding tremendous vibrations affect the superstructure of the power station. This fault necessitates the development of a system which can detect the occurrence of the first insulation failure, locate it and ultimately trip the alternator in the event of the second insulation failure,giving anunciations and alarms at the right instants.

One of the conventional schemes [1] make use of the Wheatstone Bridge principle, which has the inherent immunity to sense fault at 50 percent of the winding. To overcome this insensitivity a periodic shifting of the bridge null-point is done by the operating personnel. The other relaying practices in use are the a.c and d.c biasing methods[2] which however fail to provide information regarding of the location of the fault in the winding, inspite of generation of trip at this fault. To counter the deficits in the afore- mentioned schemes, newer concepts [3,4,5,6] came into vogue, which were operational from microprocessor-based systems. Hence reliability and fastness of operation were ensured. The digital relays in use lack compactness and inspite of detecting the fault has the inability to locate the fault position.

In this work an attempt has been made to develop a digital relaying system, based on the conventional Wheatstone Bridge Principle. However, in effect automation has been introduced into the relaying scheme. The relay so developed is sensitive to the first rotor earth fault and will eventually initiate a trip at the onset of the second earth fault incident. The location of the two ground faults, the value of the exciter -voltage and the fault current at the time of occurrence of the fault are apparent by the execution of the relaying software. Human involvement which was necessary for ascertaining fault occurrence at 50% of the winding in the conventional Wheatstone Bridge method is no longer necessary.The supervisory algorithm of the Intel 8086 microprocessor-based protection scheme is executed in 1.5 msec. Structured on a modular design, the algorithm deftly handles 16 bit data manipulations, involving no floating point packages. For acquisition of the relevant signals and for processing them suitably for the digital environment, isolation amplifiers are used judiciously.

RELAYING LOGIC

The concept of the unbalanced wheatstone bridge is utilised to yield the fault location. In this scheme the inherent locational vulnerabilities that were existent in the previous methods[1,2] is eliminated. Referring to Fig.1, R is the resistance to rotor body from the midpoint of the shunt branch, comprising of resistance R_1 and R_1 in series.R_2 is to be switched periodically with the help of

switch S for sensing fault at 50% of the winding R_F represents the field winding and E is the excitation voltage. On closing the switch S, the bridge becomes unbalanced for a fault occurring at the mid-point of the rotor winding. Under this condition appearance of the voltage across R ensures an insulation failure at the mid-point of the field winding. On switching off S by the microprocessor in the split of a second, the circuit regains its configuration for sensing faults in the winding R, at any point other than the mid-point. The arc energy is a function of the winding shorted by the double rotor earth-faults. Therefore the detection of the first fault at any extreme point of the winding warrants immediate tripping, for the fear of grave damage due to a second fault at the other extremity.

The unbalance voltage V_R across the resistance R helps in determining the location of the first fault 'x' by equation (1) as follows

$$V_{R1} = \frac{-E[R_1 - 2xR_1]\,R}{[(R_1^2 + 2RR_1) - 2x(x-1)R_F R_1]} \qquad -(1)$$

where 'x' is the position of the first fault from the negative end of the exciter. Again any deviation from this recorded unbalance voltage helps to establish the onset the second fault. If V_{R1} has changed to V_{R2} then the equation (2) gives the value of 'y' which is the second fault location from the negative end of the exciter.

$$V_{R2} = \frac{-E[MR_1 - 2xR_1]\,R}{[M(R_1^2 + 2RR_1) - 2x(x-M)R_F R_1]} \qquad (2)$$

where M=x+1-y

HARDWARE DESIGN

Fig2 shows the hardware of the digital relay which comprises chiefly of isolation amplifiers which help interface the power signals with the Intel 8086 microprocessor. The voltage drop across R, V_R is the input variable to the isolation amplifier and the output from the opto-isolator V'_{opt} is made conformable for use with the analog-to-digital converter(ADC-0809) and varies linearly with V_R . The digitized versions of V'_{opt} and the exciter-voltage E (similarly processed by the opto-isolator) are further used by the microprocessor as input parameters for the algorithm.

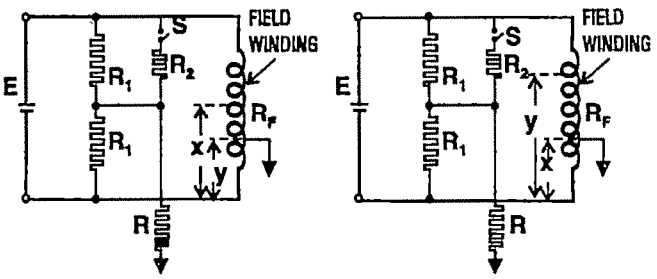

Fig. 1 : Additional arrangement in the excitation circuit for protection against insulation failure in the rotor winding

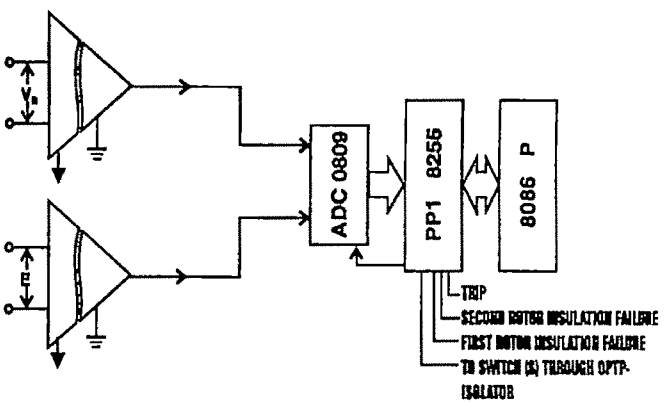

FIG. 2 : Schematic Layout of the Relaying Scheme.

RELAYING ALGORITHM

The dedicated algorithm working on an Intel 8086 microprocessor takes only 1.5msec, which can be further reduced by using a faster processor. While performing arithmetic operations it is meticulously emphasised that the large data handling does not result in improper results like overflowing or yielding negative values. At the start of the relaying algorithm, certain initialisations are made. V_{nf} is the no-fault voltage output from the opto-isolator., when V_R is zero. A counter Q is initialised to mark the instants of opening and closing of switch S (twice in every twelve hours). The flowchart as outlined in Fig.3 evolves around the central decisive element of whether $(V'_{opt} - V_{nf}) < 0.1V$. A negative conclusion indicates a fault. The path to be traced by the algorithm then depends upon the decisions of the two consecutive blocks A and B. Subroutines SR1 and SR2 aims to solve equations (1) and (2) to obtain x and y respectively.

TESTS AND ANALYSIS OF RESULTS

The tests are carried out on a simulated model of the alternator rotor. Faults are created at different points of the rotor, and keeping the excitation voltage constant, double insulation failures are created. The changes in V_R and V'_{opt} with first and second insulation failures are observed. Fault locations as a percentage of the field winding are deduced through an algorithm using the digital equivalent of V_R. The results are tabulated in Table I and conform well to theoretical values. In establishing equations (1) and (2) the transient effect of inductance in the field winding is neglected.

CONCLUSION

In this work a faster, reliable and sensitive digital relay functional on a simple algorithm is developed with facilities to inform the user on the types of fault. The relay also senses the acknowledgement of the first fault and then carries out the supervisory action for the second fault. Human intervention is therefore reduced to the minimum. Use of DSPs (Digital Signal Processors) instead of microprocessors will enhance speed, versatility and compactness of the scheme.

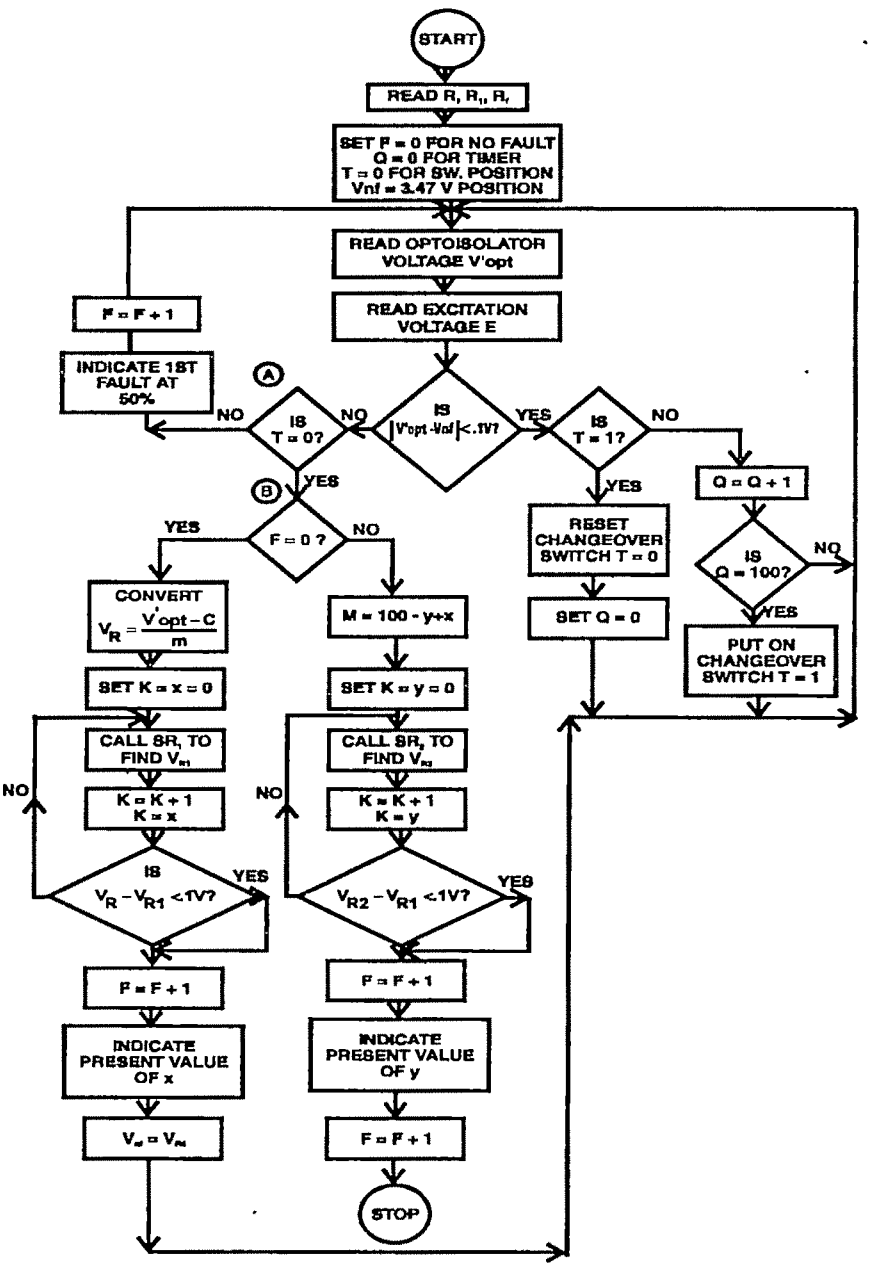

Fig. 3 Flowchart of the entire scheme

OCCURRENCE OF FIRST FAULT			OCCURRENCE OF SECOND FAULT			REMARKS *	
Position of the simulated fault from negative end of exciter (%)	V'_{opt} for 1st fault (Hex)	Position of the 1st fault as obtained by algorithm (%)	Position of simulated fault from negative end of exciter (%)	V'_{opt} for 2nd fault (Hex)	Position of 2nd fault as calculated by the algorithm (%)	No. of faults registered	Trip signal generated
0	4.96 V (FE)	0	-	-	-	01	NO !
25	4.17 V (D5)	24	0	4.96 V (FE)	0	02	YES
25	4.13 V (D4)	25	50	3.9 V (C7)	50	02	YES
25	4.13 V (D4)	25	75	3.47 V (B2)	74	02	YES
50	3.47 V (B2) #	50	25	3.75 V (BF)	25	02	YES
50	3.47 V (B2) #	50	75	3 V (99)	75	02	YES
75	2.74 V (BC)	75	25	3.47 V (B2)	26	02	YES
75	2.74 V (BC)	75	50	3.2 V (A3)	50	02	YES
75	2.74 V (BC)	75	100	2.15 V (6F)	100	02	YES
100	2.15 V (6F)	100	-	-	-	01	NO !

* Voltage after isolation amplifier is 12V representing proportional excitation voltage.

Fault at 50% detected by closing switch 'S' (Fig. 1)

! Sometimes it is necessary to generate TRIP signal for clearing of Fault.

REFERENCES

1. Modern Power Station practice, (Book) CEGB, Second and revised Edition, 1971, Vol.4, Electrical (Generator and Electrical Plant), Publ. Pergamon Press Ltd. Pp522-524.
2. C.Russel Mason, " The Art and Science of Protective Relaying," Ninth Wiley Eastern Reprint, April1992, pp218-22
3. C.Hargis, I.B Roberts, J.Sutton, J.Muhlhans, " turbogenerator Rotor Earth-Fault Monitoring and Protection," Presented at Sec. Intl. Conf. On Electrical Machines-Design and Application (Conf. Publ. No 2&4), London, England, 17-19Sept.'85, (London, England: IEE1985), pp6-10.
4. C.G Bright, P.J Turner, "Turbine-Generator Rotor Double Earth-Fault Analysis," presented at the Sixth Intl. Conf. On Electrical Machines and Drives (Conf. Publ. No.376), Oxford,U.K.,8-10 Sept.'93(London,U.K.,IEE1993),pp468-473.
5. H..K Verma, S.S Chhatja, " Microprocessor based relaying for Generator Protection on Stator Asymmetrical short-circuits, rotor over-heating and field-failure," Journal of Micro-Computer Applns(U.K),Vol. 11,N0-2, April'83,pp117-126.
6. V. Rajaraman," Recent Trends in Distributed Process Control Computers", International Federation of Automatic Control, Proc. Series No5.1988,pp 17-21.
7. K. Das (Bhattacharya), D. Ghosh and D. Dasgupta, "An Automatic Design Scheme for Protection of Alternator Rotor Winding", accepted for publication in The International Conference, EAIT 2001, Dec. 1 - 1 , IIT Kharagpur, India.

Application Specific Fuzzy Switching

Pradeep Chatterjee* Rajpal Singh† B.M.Karan† P.K.Sinha†
*TATA Engineering (on sponsored leave at B.I.T. Mesra, Ranchi) India
† Department of E.E.E, B.I.T. Mesra ,Ranchi, India
E-mail: pchats@ieee.org

Abstract

Application Specific Integrated Circuits (ASIC) has gained dominance in the recent technological developments which is even used to design switching logic for particular application. On the other hand fuzzy logic is a tool which introduces fuzziness to derive the best possible solution to a problem. This paper deals with the integration of fuzzy logic and ASIC leading to the development of an Application Specific Fuzzy Switching (ASFS) for optimal switching for induction motor control in A.C. drives.

INDUCTION MOTOR CONTROL

For the last two decades researchers are working on the development of A.C. drives to control speed and torque of induction motors. Their efforts in this field are justified, as induction motor is one of the cheapest and robust motors available to the industry today. Suitable design of A.C. drives for induction motor can transform the nonlinear torque-speed characteristics of induction motor to constant torque-speed characteristics similar to that of a D.C. motor. Development of A.C. drives for induction motors started with the variable frequency control followed by vector control and recently leading to direct torque control using space vector modulation. Here the Application Specific Fuzzy Switching is designed for direct torque control of squirrel cage induction motor, so space vector modulation for direct torque control shall be dealt in detail subsequently.

Variable frequency control is simple to design and implement and even offers the advantage of operating without an encoder. Control is generated by maintaining constant volts per hertz output used to drive a pulse width modulated (PWM) circuit. Since the torque and the flux are neither directly nor indirectly controlled it results in limited speed accuracy and poor torque control.

To overcome this limitation vector control used the concept of vectorizing the voltage and current into two orthogonal axes (d-axis and q-axis) so as to control the flux and torque independently similar to that of a D.C. motor control. This results in a good torque response and inclusion of an encoder increases the accuracy of speed and torque. The disadvantage being the mandatory inclusion of an encoder. Moreover the PWM modulator processes the voltage and frequency reference outputs of the vector control stage thereby creating a signal delay between the input reference and the resulting stator voltage vector produced. This limits achievement of very rapid flux and torque control.

DIRECT TORQUE CONTROL

Direct torque control uses the concepts of space vector modulation [1], [2] to optimally control the flux and torque of induction motor. The power circuit of direct torque control is as shown in fig1. A specific stator flux level can be achieved with a unique frequency of the inverter for a specific D.C. link voltage. As direct torque control uses the concepts of field oriented control it uses one of the six switching states (fig 2) to maintain desired torque and optimal flux level. The vector control uses the direct axis (d-axis) for flux control and the quadrature axis (q-axis) for torque control. If flux is to be increased switching state 1 is to be selected. Similarly if torque is to be increased and flux is to be reduced switching state 3 is to be selected. If torque is to be reduced and flux is to be increased then switching state 6 is to be selected.

Direct torque control combines field oriented control, digital signal processing and application specific integrated circuit. The control blocks associated are mathematical model of induction motor observer, hysteresis controller and ASIC for optimal switching.

The mathematical model of induction motor observer estimates the actual torque and flux of the motor from the current and voltage feedback. The reference/desired values of torque and flux are fed to the hysteresis controller as shown in fig 3. The torque and flux comparators in the hysteresis controller

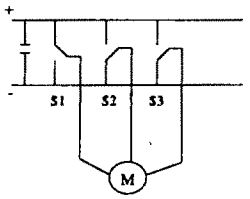

Fig 1. Power circuit for direct torque control

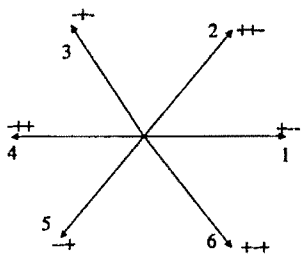

Fig 2. Stator Voltage Vectors

compares the actual torque and actual flux with their respective desired values. If the actual torque is below its differential hysteresis limit the torque status goes high and if it is above its differential limit the torque status goes low. Similarly flux status goes high or low depending on actual flux value is below or above it's differential limit. The torque and flux status are fed to the ASIC which decides the switching state to be selected and accordingly switches it.

The biggest drawback of the present scheme is that the ASIC switching is not optimal switching. This would be clear if we consider a particular case. Suppose the torque and flux levels are below their differential hysteresis limits. So switching state 2 is optimal selection so that both torque and flux increases simultaneously. At an instant of time torque reaches it's lower differential limit (which is supposed to be desired torque) but flux level is still below. Since the torque level has not reached the upper hysteresis limit the torque status has not yet changed and so switching state 2 continues to be selected. This results in unwanted increase in torque and partial increase in flux till actual torque reaches upper hysteresis limit. Instead switching state 1 would have been optimal selection of switching under such condition. There can be several such instances where optimal switching may fail with hysteresis controller and ASIC switching. In such cases fuzzy logic with its linguistic capability decides optimal switching states for better control.

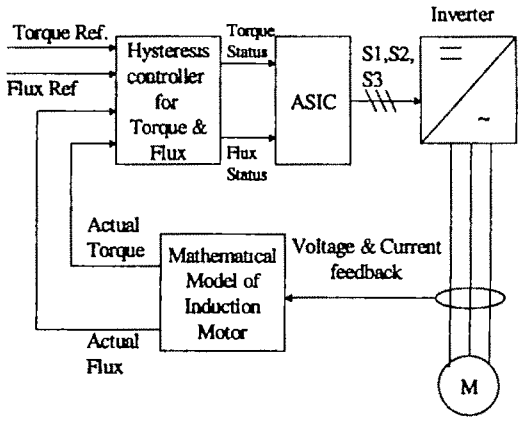

Fig 3. Direct Torque Control Scheme

APPLICATION SPECIFIC FUZZY SWITCHING

The direct torque control scheme using ASFS is as shown in fig 4.

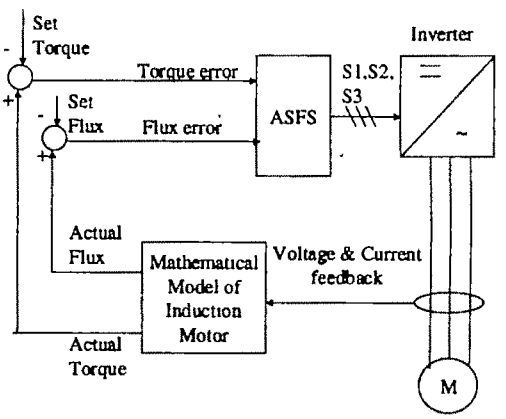

Fig 4. Direct Torque Control Scheme using ASFS

For designing ASFS two input variables are considered, the torque error and the flux error. Three membership functions are designed for each variable with the linguistics less error, zero error and more error. The zero errors have a range with membership value 1 corresponding to the variable which is considered to be within permissible error limit. The membership plots of the input variables are shown in fig 5 and 6. The output variable comprises of six membership functions to select the optimal switching state as shown in fig 7. The ASFS has been designed with a set of rules to select the corresponding switching state. In fact the set of rules does

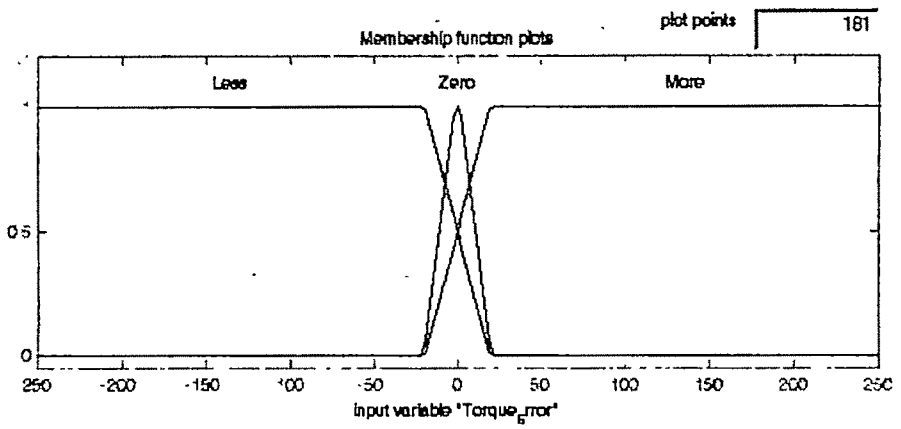

Fig 5. Membership Function of Torque Error

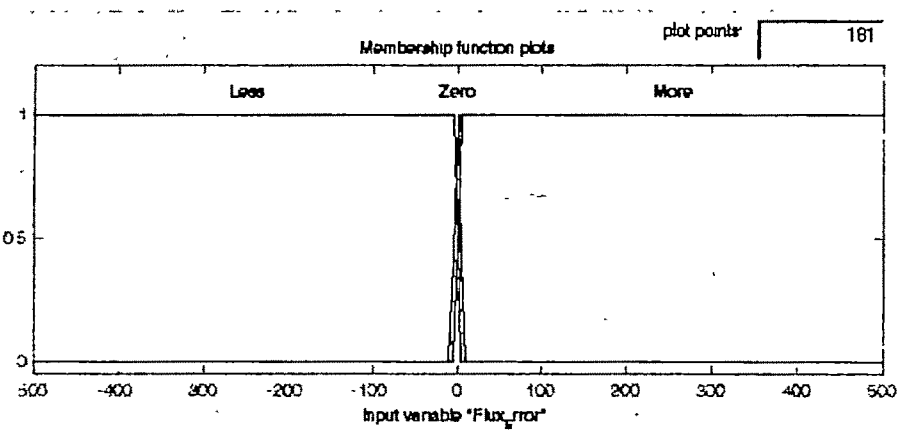

Fig 6. Membership Function of Flux Error

not specify the state to be selected when both flux and torque errors are zero. It has been observed that under such condition the ASFS switches to state 4 which results in optimal flux level thereby increasing efficiency of the motor. The ASFS has been tested with different values of torque and flux errors and some of the results have been shown in table1. The instantaneous torque error has been given a tolerance of ± 2 Nm and instantaneous flux error has been given a tolerance of ± 1.5 Wb. However the tolerance values can be set according to motor rating and desired performance. The results of simulation of switching states of an uncontrolled motor for torque and flux errors are shown in fig8.

CONCLUSION

The results of the ASFS proves to be very promising for optimal switching of direct torque control using space vector modulation of induction motor. This will result in elimination of PWM modulators thereby reducing heating of the motor and increasing its efficiency.

ACKNOWLEDGEMENTS

The authors are grateful to M/S TATA ENGINEERING for providing sponsorship for the project, AICTE, (grant no. 8017/RDII/R&D/DEG(613)/98-99) and BCST (grant no. BP/Y-06/97-98-308) for providing adequate funds to carry out the research activities.

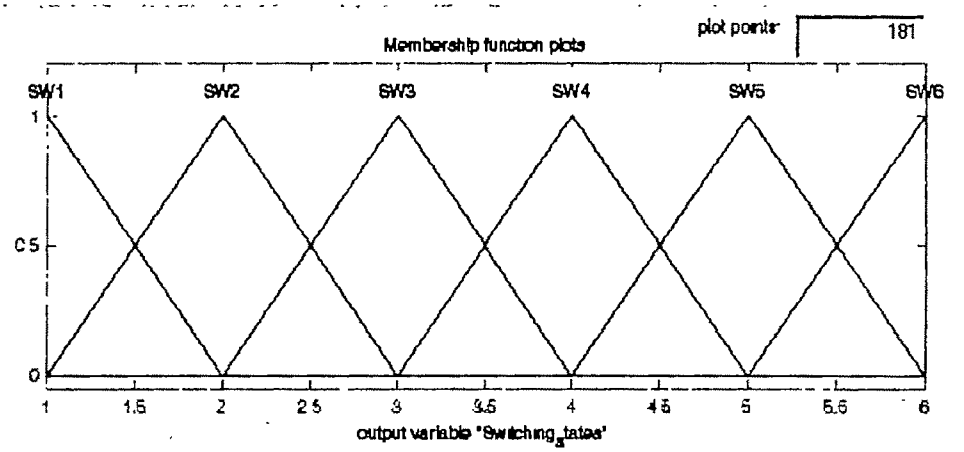

Fig 7. Member Function for Switching States

Table 1. Test Results for ASFS		
Torque Error (Nm)	Flux Error (Wb)	Switching State Selected
-10	1	3
-10	-4	2
10	-4	6
10	4	5
0	-4	1
0	0	4

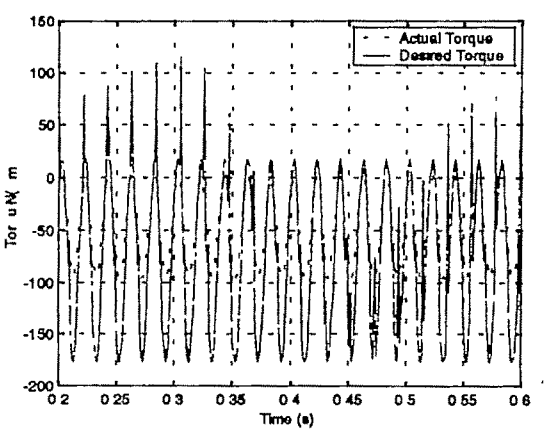

(a) Torque Comparasion

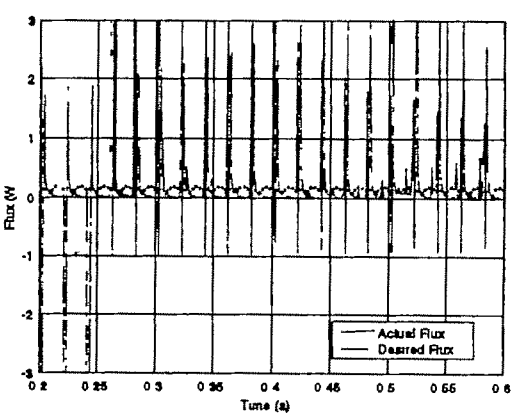

(b) Flux Comparasion

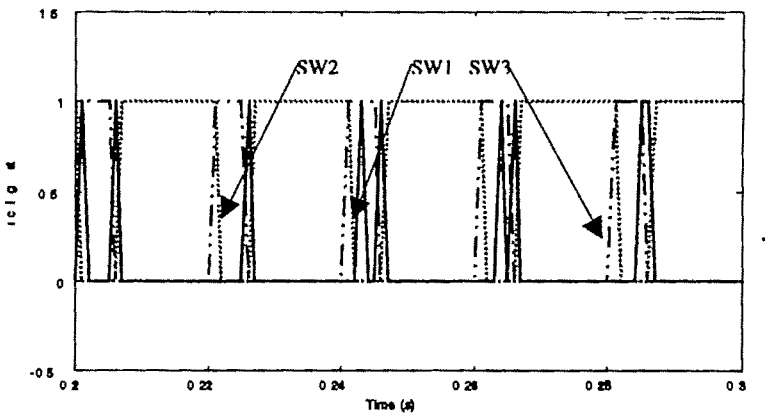

(c) Switching States selected by ASFS
Fig 8. Simulated results of ASFS

REFERENCES

1. M.Depenbrock, "Direct Self-Control (DSC) of Inverter-Fed Induction Motor", IEEE Transactions on Power Electronics, vol. 3, No. 4, October 1988
2. [2] James N. Nash, "Direct Torque Control, Induction Motor Vector Control Without an Encoder", IEEE Transactions on Industry Applications, vol. 33, No. 2, March/April 1997
3. [3] G.J. Klir, T.A. Folger, "Fuzzy Sets, Uncertainty, and Information", Prentice Hall, Englewood Cliffs, New Jersey, 1988

Soft Computing Pattern Recognition: Principles, Integrations and Data Mining

Sankar K. Pal

Machine Intelligence Unit
Indian Statistical Institute
Calcutta 700035, India
email: sankar@isical.ac.in

Abstract. Relevance of fuzzy logic, artificial neural networks, genetic algorithms and rough sets to pattern recognition and image processing problems is described through examples. Different integrations of these soft computing tools are illustrated. Evolutionary rough fuzzy network which is based on modular principle is explained, as an example of integrating all the four tools for efficient classification and rule generation, with its various characterstics. Significance of soft computing approach in data mining and knowledge discovery is finally discussed along with the scope of future research.

Keywords. Fuzzy logic, Neural networks, Genetic algorithms, Rough sets, Hybrid systems, Knowledge discovery

1 Introduction

Soft computing is a consortium of methodologies which work synergestically and provides in one form or another flexible information processing capabilities for handling real life ambiguous situations. Its aim is to exploit the tolerance for imprecision, uncertainty, approximate reasoning and partial truth in order to achieve *tractability, robustness, low cost solutions*, and *close resemblance to human like decision making*. In other words, it provides the foundation for the conception and design of high MIQ (Machine IQ) systems, and therefore forms the basis of future generation computing systems. At this juncture, Fuzzy Logic (FL), Rough Sets (RS), Artificial Neural Networks (ANN) and Genetic Algorithms (GA) are the principal components where FL provides algorithms for dealing with imprecision and uncertainty arising from vagueness rather than randomness, RS for handling uncertainty arising from limited discernibility of objects, ANN the machinery for learning and adaptation, and GA for optimization and searching [1, 2].

Machine recognition of patterns [3, 4] can be viewed as a two-fold task, consisting of learning the invariant and common properties of a set of samples characterizing a class, and of deciding that a new sample is a possible member of the class by noting that it has properties common to those of the set of samples. Therefore, the task of pattern recognition by a computer can be described as a transformation from the measurement space M to the feature space F and

finally to the decision space D. Depending on the type of input patterns, one may have speech recognition system, image recognition or vision system, medical diagnostic system etc.

In this article we first describe the relevance of different soft computing tools to pattern recognition problems with examples. Different integration among them are then described. As an example we explain an evolutionary rough fuzzy MLP, which has been designed based on modular concept for pattern classification and rule generation. Finally the significance of soft computing in data mining and knowledge discovery is discussed.

2 Relevance of Fuzzy Set Theory in Pattern Recognition

Fuzzy sets were introduced in 1965 by Zadeh [5] as a new way to represent vagueness in everyday life. They are generalizations of conventional (crisp) set theory. Conventional sets contain objects that satisfy precise properties required for membership. Fuzzy sets, on the other hand, contain objects that satisfy imprecisely defined properties to varying degrees. A fuzzy set A of the universe X is defined as a collection of ordered pairs

$$A = \{(\mu_A(x), x),\ \forall x \in X\}$$

where $\mu_A(x), (0 \leq \mu_A(x) \leq 1)$ gives the degree of belonging of the element x to the set A or the degree of possession of an imprecise property represented by A. Different aspects of fuzzy set theory including membership functions, basic operations and uncertainty measures can be found in [5, 6].

In this section we explain some of the uncertainties which one often encounters while designing a pattern recognition system and the relevance of fuzzy set theory in handling them. Let us consider, first of all, the case of processing and recognition of a gray-tone image pattern. Conventional approaches to image analysis and recognition [7, 8] consist of segmenting the image into meaningful regions, extracting their edges and skeletons, computing various features (e.g., area, perimeter, centroid etc.) and primitives (e.g., line, corner, curve etc.) of and relationships among the regions, and finally, developing decision rules and grammars for describing, interpreting and/or classifying the image and its sub-regions. In a conventional system each of these operations involves crisp decisions (i.e., yes or no, black or white, 0 or 1) to make regions, features, primitives, properties, relations and interpretations crisp.

Since the regions in an image are not always crisply defined, uncertainty can arise within every phase of the aforesaid tasks. Any decision made at a particular level will have an impact on all higher level activities. An image recognition system should have sufficient provision for representing and manipulating the uncertainties involved at every processing stage; i.e., in defining image regions, features and relations among them, so that the system retains as much of the 'information content' of the data as possible. If this is done, the ultimate output (result) of the system will possess minimal uncertainty (and unlike conventional

systems, it may not be biased or affected as much by lower level decision components).

In Short, gray information is expensive and informative. Once it is thrown away, there is no way to get it back. Therefore one should try to retain this information as long as possible throughout the decision making tasks for its full use. When it is required to make a crisp decision at the highest level one can always through away or ignore this information.

Let us now consider the case of a decision-theoretic approach to pattern classification. With the conventional probabilistic and deterministic classifiers [3, 4], the features characterizing the input patterns are considered to be quantitative (numeric) in nature. The patterns having imprecise or incomplete information are usually ignored or discarded from their designing and testing processes. The impreciseness (or ambiguity) may arise from various causes. For example, instrumental error or noise corruption in the experiment may lead to only partial or partially reliable information being available on a feature measurement F. Again, in some cases it may become convenient to use linguistic variables and hedges. In such cases, it is not appropriate to give exact representation to uncertain feature data. Rather, it is reasonable to represent uncertain feature information by fuzzy subsets.

Again, uncertainty in classification or clustering of patterns may arise from the overlapping nature of the various classes. This overlapping may result from fuzziness or randomness. In the conventional technique, it is usually assumed that a pattern may belong to only one class, which is not necessarily true in real life applications. A pattern can and should be allowed to have degrees of membership in more than one class. It is, therefore, necessary to convey this information while classifying a pattern or clustering a data set.

From the aforementioned examples, we see that the concept of fuzzy sets can be used at the *feature level* in representing input data as an array of membership values denoting the degree of possession of certain properties, in representing linguistically phrased input features for their processing, in weakening the strong commitments for extracting ill-defined image regions, properties, primitives, and relations among them, and at the *classification level*, for representing class membership of objects in terms of membership values. *In other words, fuzzy set theory provides a notion of embedding: We find a better solution to a crisp problem by looking in a large space at first, which has different (usually less) constraints and therefore allows the algorithm more freedom to avoid errors forced by commission to hard answers in intermediate stages.*

The capability of fuzzy set theory in pattern recognition problems has been reported adequately since late sixties. A cross-section of the advances with applications is available in [6, 2, 9, 10].

3 Relevance of Neural Network Approaches

Neural network *(NN)* models [11, 12] try to emulate the biological neural network/nervous system with electronic circuitry. *NN* models have been studied

for many years with the hope of achieving human-like performance (artificially), particularly in the field of pattern recognition, by capturing the key ingredients responsible for the remarkable capabilities of the human nervous system. Note that these models are extreme simplifications of the actual human nervous system.

*NN*s are designated by the network topology, connection strength between pairs of neurons (called weights), node characteristics and the status updating rules. Node characteristics mainly specify the primitive types of operations it can perform, like summing the weighted inputs coming to it and then amplifying it or doing some fuzzy aggregation operations. The updating rules may be for weights and/or states of the processing elements (neurons). Normally an objective function is defined which represents the complete status of the network and the set of minima of it corresponds to the set of stable states of the network. Since there are interactions among the neurons the collective computational property inherently reduces the computational task and makes the system fault tolerant. Thus *NN* models are also suitable for tasks where collective decision making is required. Hardware implementations of neural networks are also attempted.

Neural network based systems are usually reputed to enjoy the following major characteristics:

- *adaptivity*- adjusting the connection strengths to new data/information,
- *speed*- due to massively parallel architecture,
- *robustness*- to missing, confusing, ill-defined/noisy data,
- *ruggedness*- to failure of components,
- *optimality*- as regards error rates in performance.

For any pattern recognition system, one desires to achieve the above mentioned characteristics. More over, there exists some direct analogy between the working principles of many pattern recognition tasks and neural network models. For example, image processing and analysis in the spatial domain mainly employ simple arithmetic operations at each pixel site in parallel. These operations usually involve information of neighboring pixels (co-operative processing) in order to reduce the local ambiguity and to attain global consistency. An objective measure is required (representing the overall status of the system), the optimum of which represents the desired goal. The system thus involves collective decisions. On the other hand, we notice that neural network models are also based on parallel and distributed working principles (all neurons work in parallel and independently). The operations performed at each processor site are also simpler and independent of the others. The overall status of a neural network can also be measured.

Again, the task of recognition in a real-life problem involves searching a complex decision space. This becomes more complicated particularly when there is no prior information on class distribution. Neural network based systems use adaptive learning procedures, learn from examples and attempt to find a useful relation between input and output, however complex it may be, for decision-making problems. Neural networks are also reputed to model complex non-linear

boundaries and to discover important underlying regularities in the task domain. These characteristics demand that methods are needed for constructing and refining neural network models for various recognition tasks. ***In short, neural networks are natural classifiers having resistance to noise, tolerance to distorted images/patterns (ability to generalize), superior ability to recognize partially occluded or degraded images/overlapping pattern classes or classes with highly nonlinear boundaries, and potential for parallel processing.***

4 Genetic Algorithms for Pattern Recognition

Genetic Algorithms (GAs) [13, 14, 15, 16, 17] are adaptive computational procedures modeled on the mechanics of natural genetic systems. They express their ability by efficiently exploiting the historical information to speculate on new offspring with expected improved performance [13]. GAs are executed iteratively on a set of coded solutions, called *population*, with three basic operators: *selection/reproduction*, *crossover* and *mutation*. They use only the payoff (objective function) information and probabilistic transition rules for moving to the next iteration. They are different from most of the normal optimization and search procedures in four ways:

- GAs work with the coding of the parameter set, not with the parameter themselves.
- GAs work simultaneously with multiple points, and not a single point.
- GAs search via sampling (a blind search) using only the payoff information.
- GAs search using stochastic operators, not deterministic rules.

One may note that the methods developed for pattern recognition and image processing are usually problem dependent. Moreover, many tasks involved in the process of analyzing/identifying a pattern need appropriate parameter selection and efficient search in complex spaces in order to obtain optimal solutions. This makes the process not only computationally intensive, but also leads to a possibility of losing the exact solution. Therefore, the application of genetic algorithms for solving certain problems of pattern recognition, which need optimization of computation requirements, and robust, fast and close approximate solution, appears to be appropriate and natural [14].

5 Integration and Hybrid Systems

Integration of the individual soft computing tools help in designing hybrid systems which are more versatile and efficient compared to stand alone use of the tools. The most visible integration in soft computing community is that of neural networks and fuzzy sets [2]. Neuro-fuzzy systems has been successfully developed for decision making, pattern recognition and image processing tasks. The hybridization falls in two major categories: a neural network equipped with the capability of handling fuzzy information (termed fuzzy neural network) to augment its application domain, and a fuzzy system augmented by neural networks

to enhance some of its characterstics like flexibility, speed, adaptivility, learning (termed neural-fuzzy systems). Both the classes of hybridisation and their application to various pattern recognition problem are described in [2, 18].

There are some applications where the integration of GAs with fuzzy sets and ANNs is found to be effective. For example GAs are found sometimes essential for overcoming some of the limitations of fuzzy set theory, specifically to reduce the 'subjective' nature of membership functions. Note that the other way of integration, i.e., incorporating the concept of fuzziness into GAs has not been tried seriously. Synthesis of ANN architectures can be done using GAs as an example of neuro-genetic systems. Such an integration may help in designing optimum ANN architecture with appropiate parameter sets. Methods for designing neural network architectures using GAs are primarily divided into two parts. In one part the GA replaces the learning method to find appropiate connection weights of some predefined architecture. In another part, GAs are used to find the architecture itself and it is then evaluated using some learning algorithms. Literature is also available on integration of fuzzy sets, neural networks and genetic algorithms [2, 19, 20].

The theory of rough sets [21] has emerged as another major mathematical approach for managing uncertainty that arises from inexact, noisy, or incomplete information. It is turning out to be methodologically significant to the domains of artificial intelligence and cognitive sciences, especially in the representation of and reasoning with vague and/or imprecise knowledge, data classification, data analysis, machine learning, and knowledge discovery [22].

Recently, rough sets have been integrated with both fuzzy sets and neural networks. Several rough-fuzzy hybrid systems are discussed in [2]. In the framework of rough-neuro integration [23], two broad approaches are available, namely, use of roughs set for encoding weights of knowledge based networks [24], and designing neural network architectures which incorporate roughness in the neuronal level. Genetic algorithms have also been used for fast generation of rough set reducts from an indiscernibility matrix.

In the next section we describe, as an example, a methodology for integrating all the four soft computing tools, *viz.*, fuzzy sets, ANN, rough sets and GAs for classification and rule generation. Here rough sets are used to encode domain knowledge in network parameters of a fuzzy MLP. GAs are used to evolve the optimal architecture based on modular concept.

6 Evolutionary Rough Fuzzy MLP

The evolutionary rough fuzzy MLP utilises the concept of modular learning for better integration and performance enhancement [25, 26]. The knowledge flow structure of evolutionary rough fuzzy MLP is illustrated in Figure 1. Here each of the soft computing tools act synergestically to contribute to the final performance of the system as follows. Rough set rules are used for extracting crude domain knowledge, which when encoded in a fuzzy MLP not only results in fast training of the network, but also automatic determination of the network

size. The GA operators are adaptive and use the domain knowledge extracted with rough sets for even faster learning. The fuzziness incorporated at the input and outputs helps in better handling of uncertainties and overlapping classes. The nature of integration is illustrated in Figure 2.

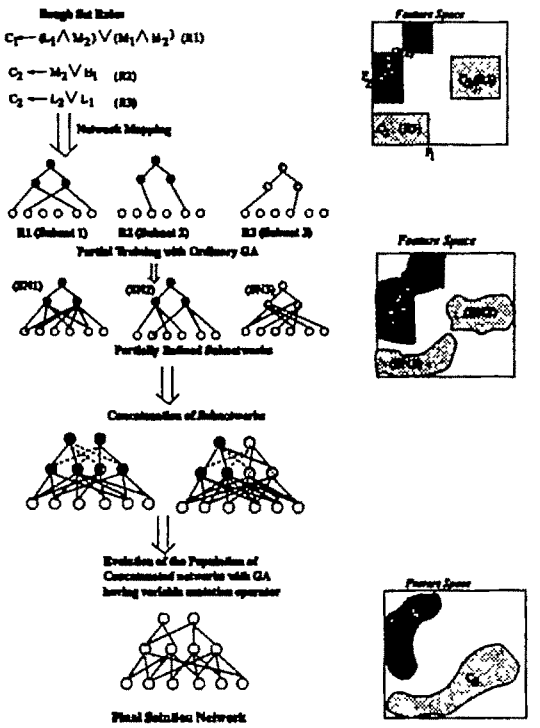

Fig. 1. Knowledge Flow in Modular Rough Fuzzy MLP

The evolutionary modular rough fuzzy MLP has been applied to a number of real world problems like speech recognition and medical diagnosis. In case of speech recognition [25], the system is found to correctly classify 84% of the samples, while the fuzzy MLP correctly classifies only 78% and the MLP only 59%. The system also gained in computation time significantly. For determining the stages of Cervical Cancer [25], the system provides results identical to that of medical experts in 83% of the cases. In other cases also the stagings were close. In addition to the above performance logical rules were extracted from the trained system. It was found that the rules coincided with the guidelines adopted by medical practicioners for staging. In the rough fuzzy MLP, the final network has a structure imposed on the weights. Hence, crisp logical rules can be easily extracted from the networks. This makes the system suitable for Knowledge Discovery in Databases. The rules obtained are found to be superior to those of several popular methods, as measured with some quantitative indices. For

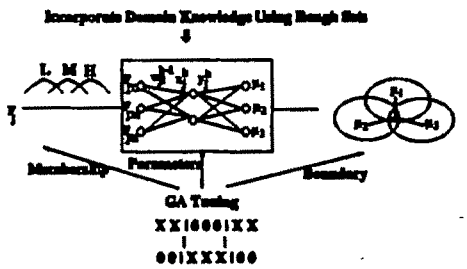

Fig. 2. Components of the Modular Rough-fuzzy MLP

example, on the speech recognition data, the rules obtained using the modular rough-fuzzy MLP have an accuracy of 81.02% with 10 rules, while the popular C4.5 rule generation algorithm have accuracy of 75.00% using 16 rules. Fraction of samples which are 'uncovered' by the rules obtained by us is only 3.10%, whereas the C4.5 rules have 7.29% uncovered samples. The 'confusion index' is also low for the proposed method (1.4) compared to C4.5 (2.0).

7 Data mining and knowledge discovery

In recent years, the rapid advances being made in computer technology have ensured that large sections of the world population have been able to gain easy access to computers on account of falling costs worldwide, and their use is now commonplace in all walks of life. Government agencies, scientific, business and commercial organizations are routinely using computers not just for computational purposes but also for storage, in massive databases, of the immense volumes of data that they routinely generate, or require from other sources. Large-scale computer networking has ensured that such data has become accessible to more and more people. In other words, we are in the midst of an information explosion, and there is urgent need for methodologies that will help us bring some semblance of order into the phenomenal volumes of data that can readily be accessed by us with a few clicks of the keys of our computer keyboard. Traditional statistical data summarization and database management techniques are just not adequate for handling data on this scale, and for extracting intelligently, information or, rather, knowledge that may be useful for exploring the domain in question or the phenomena responsible for the data, and providing support to decision-making processes. This quest had thrown up some new phrases, for example, *data mining* and *knowledge discovery in databases (KDD)*, which are perhaps self-explanatory, but will be briefly discussed in the next few paragraphs. Their relationship with the discipline of pattern recognition will also be examined.

The massive databases that we are talking about are generally characterized by the presence of not just numeric, but also textual, symbolic, pictorial and aural data. They may contain redundancy, errors, imprecision, and so on. KDD

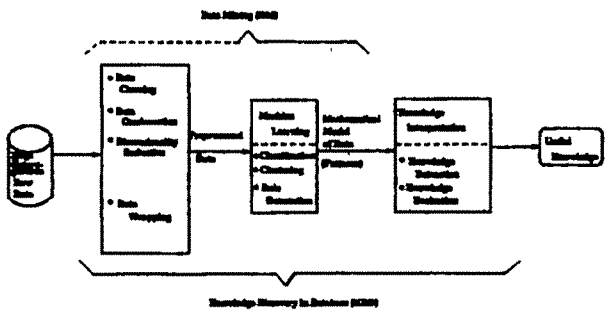

Fig. 3. Block diagram for Knowledge Discovery in Databases (KDD)

is aimed at discovering natural structures within such massive and often heterogeneous data. Therefore PR plays a significant role in KDD process. However, KDD is being visualized as not just being capable of knowledge discovery using generalizations and magnifications of existing and new pattern recognition algorithms, but also the adaptation of these algorithms to enable them to process such data, the storage and accessing of the data, its preprocessing and cleaning, interpretation, visualization and application of the results, and the modeling and support of the overall human-machine interaction. What really makes KDD feasible today and in the future is the rapidly falling cost of computation, and the simultaneous increase in computational power, which together make possible the routine implementation of sophisticated, robust and efficient methodologies hitherto thought to be too computation-intensive to be useful. A block diagram of KDD is given in Figure 3.

Data mining is that part of knowledge discovery which deals with the process of identifying valid, novel, potentially useful, and ultimately understandable patterns in data, and excludes the knowledge interpretation part of KDD. Therefore, as it stands now, data mining can be viewed as applying PR and machine learning principles in the context of voluminous, possibly heterogeneous data sets. Furthermore, soft computing-based (involving fuzzy sets, neural networks, genetic algorithms and rough sets) PR methodologies and machine learning techniques seem to hold great promise for data mining. The motivation for this is provided by their ability to handle imprecision, vagueness, uncertainty, approximate reasoning and partial truth and lead to tractability, robustness and low-cost solutions. In this context, case-based reasoning [20], which is a novel Artificial Intelligence (AI) problem-solving paradigm, has a significant role to play, as is evident from the recent book edited by Pal, Dillon and Yeung [20].

Some of the challenges that researchers in this area are likely to deal with, include those posed by massive data sets and high dimensionality, nonstandard and incomplete data, and overfitting. The focus is most likely to be on aspects like user interaction, use of prior knowledge, assessment of statistical significance, learning from mixed media data, management of changing data and knowledge, integration of tools, ways of making knowledge discovery more understandable

to humans by using rules, visualization, *etc.*, and so on. We believe the next decade will bear testimony to this.

References

1. L. A. Zadeh. Fuzzy logic, neural networks, and soft computing. *Communications of the ACM*, 37:77–84, 1994.
2. S. K. Pal and S. Mitra. *Neuro-fuzzy Pattern Recognition: Methods in Soft Computing.* John Wiley, New York, 1999.
3. R. O. Duda and P. E. Hart. *Pattern Classification and Scene Analysis.* John Wiley, New York, 1973.
4. J. T. Tou and R. C. Gonzalez. *Pattern Recognition Principles.* Addison-Wesley, London, 1974.
5. L. A. Zadeh. Fuzzy sets. *Information and Control*, 8:338–353, 1965.
6. S. K. Pal and D. Dutta Majumder. *Fuzzy Mathematical Approach to Pattern Recognition.* John Wiley (Halsted Press), New York, 1986.
7. A. Rosenfeld and A. C. Kak. *Digital Picture Processing*, volume 1-2. Academic Press, New York, 1982.
8. R. C. Gonzales and P. Wintz. *Digital Image Processing.* Addison-Wesley, Reading, MA, 1987.
9. J. C. Bezdek and S. K. Pal, editors. *Fuzzy Models for Pattern Recognition: Methods that Search for Structures in Data.* IEEE Press, New York, 1992.
10. S. K. Pal. Fuzzy image processing and recognition : Uncertainties handling and applications. *Int. J. Image Graphics*, 1(2):169–195, 2001. (Invited Paper).
11. D. E. Rumelhart and J. L. McClelland, editors. *Parallel Distributed Processing: Explorations in the Microstructures of Cognition*, volume 1. MIT Press, Cambridge, MA, 1986.
12. R. P. Lippmann. Pattern classification using neural networks. *IEEE Communications Magazine*, pages 47–64, 1989.
13. D. E. Goldberg. *Genetic Algorithms in Search, Optimization and Machine Learning.* Addison-Wesley, Reading, MA, 1989.
14. S. K. Pal and P. P. Wang, editors. *Genetic Algorithms for Pattern Recognition.* CRC Press, Boca Raton, 1996.
15. L. B. Booker, D. E. Goldberg, and J. H. Holland. Classifier systems and genetic algorithms. *Artificial Intelligence*, 40:235–282, 1989.
16. J. H. Holland. *Adaptation in Natural and Artificial Systems.* University of Michigan Press, Ann Arbor, 1975.
17. S. Bandopadhyay and S. K. Pal. Pixel classification using variable string genetic algorithms with chromosome differentiation. *IEEE Transactions on Geoscience and Remote Sensing*, 29(2):303–308, 2001.
18. S. K. Pal, R. K. De, and J. Basak. Unsupervised feature evaluation : A neuro-fuzzy approach. *IEEE Transactions on Neural Networks*, 11(2):366–376, 2000.
19. S.K. Pal, A. Ghosh, and M.K. Kundu, editors. *Soft Computing for Image Processing.* Physica Verlag, Heidelberg, 2000.
20. S.K. Pal, T.S. Dillon, and D.S. Yeung. *Soft Computing in Case Based Reasoning.* Springer Verlag, London, 2000.
21. Z. Pawlak. *Rough Sets, Theoretical Aspects of Reasoning about Data.* Kluwer Academic, Dordrecht, 1991.

22. R. Slowiński, editor. *Intelligent Decision Support, Handbook of Applications and Advances of the Rough Sets Theory*. Kluwer Academic, Dordrecht, 1992.
23. S. K. Pal, W. Pedrycz, A. Skowron, and R. Swiniarski (eds). Spl. issue on rough-neuro computing. *Neurocomputing*, 36(1-4), 2001.
24. M. Banerjee, S. Mitra, and S. K. Pal. Rough fuzzy MLP: Knowledge encoding and classification. *IEEE Transactions on Neural Networks*, 9(6):1203–1216, 1998.
25. P. Mitra, S. Mitra, and S. K. Pal. Staging of cervical cancer using soft computing. *IEEE Transactions on Biomedical Engineering*, 47(7):934–940, 2000.
26. S. K. Pal, S. Mitra, and P. Mitra. Rough fuzzy mlp : Modular evolution, rule generation and evaluation. *IEEE Transactions on Knowledge and Data Engineering*. (accepted).

Human Face Recognition Using Radial Basis Function Neural Network

M.V.Raghunadh, N.S.Murthy and K.Kishan Rao
Communication Systems Laboratory. ECE Department
Regional Engineering College, Warangal 506004
raghu@recw.ernet.in

Abstract

A neural network based face recognition system is presented in this paper. The system consists of two main procedures. The first one is face features extraction using Pseudo Zernike Moments (PZM) and the second one is face classification using Radial Basis Function (RBF) neural network. In this paper, some new results on face recognition are presented. Simulation results indicate that PZM with RBF neural network produce higher detection and lower missing rates than several existing state-of-the-art face detection systems, with an average false detection rate. Also experimental results show that high order degrees of PZM contain very useful information about face recognition process. The proposed system has been applied on face database of Olivetti Research Laboratory (ORL) with very good results.

INTRODUCTION

Automatic face recognition has received significant attention from the research workers in computer vision, neural network and signal processing [1]. The interest is motivated by applications in access control systems, model-based video coding, criminal identification and authentication in secure system like computer or bank teller machines. Although many face recognition systems by machines are available, it is still difficult to design an automatic system for the task because of problems associated with illumination and complex background. Also the visual angle and facial expression for face images are highly variable [1,2]. Several methods have been proposed for face detection including the techniques of graph matching [3], neural networks [4], and also some are geometric feature based [5].

Generally, two issues are central in the procedure of machine face recognition: (1) what features can be used to represent a face under environment changes and (2) how to classify a new face image, based on the chosen features, into one of the possibilities.

In first issue, many successful face feature extraction procedures have been presented and developed.

In this paper we used Pseudo Zernike Moment (PZM) based on central moments as face features. The advantages of considering PZM include the properties of shift, rotation and scaling invariance and robustness against noise. Also simulation results indicate that these features are very robust against change of face expression. PZM transform the input image into very low dimensional features vector. Allowing optimization of feature set. Therefore the designer may focus on complex and correct classifier. Classifier plays an essential role in the face detection process. In many face recognition systems, the Nearest Neighbor is widely used for classification. Neural network-based (NN) classifier has been proven to have many advantages for classification such as incredible generalization and good learning ability. The NN approach takes the feature vector as input and training a network to learn a complex mapping for classification and using of the NN for classification avoids the need for the simplification of the classifier.

In this work, face classifier is implemented via RBF neural network to take advantage of NN approaches. The organization of this paper is as follows: Section 2 describes the face feature extraction method. Face classifier technique is presented in Section 3. Experimental results are shown in Section 4 for comparing our system with other systems.

FACE FEATURES EXTRACTION

The invariance properties of moments of images have received considerable attention in recent years. The term invariant denotes an image feature remains unchanged if that image undergoes one or a combination of the changes such as: change of size (scale), change of position (translation), change of orientation (rotation), and reflection. Above properties of moments, occurred that moments have been proposed as pattern sensitive features in classification and recognition applications. In this paper Pseudo Zernike Moments (PZM) is proposed as facial features in face recognition system. PZM as statistical

features are very ease of use, computing and extraction, also the advantage of PZM is that they are very robust against noise. Also simulation results indicates that PZM as face features are very robust against change of face expression.

Pseudo Zernike Polynomials and Moments:

Zernike and Pseudo Zernike polynomials are well known and widely used in the analysis of optical systems. Pseudo Zernike Polynomials are an orthogonal set of polynomials of following form:

$$V_{nm}(x,y) = R_{nm}(x,y)\exp\left(jm\tan^{-1}\left(\frac{y}{x}\right)\right) \qquad (1)$$

where Vnm(x,y) denotes a complete set of complex- valued polynomials in two real variables x and y, which are orthogonal in the interior of the unit circle, n represents the degree of the polynomials, m represents its angular dependence,

Rnm(x,y) represents a real-valued set of polynomials inside the unit circle as follows:

$$R_{nm}(x,y) = \sum_{s=0}^{n-|m|} S_{n,|m|,s}(x^2+y^2)^{\frac{n-s}{2}} \qquad |m| \le n \qquad (2)$$

$$S_{n,|m|,s} = (-1)^s \frac{(2n+1-s)!}{s(n-|m|-s)!(n-|m|-s+1)!} \qquad (3)$$

The Pseudo Zernike Moments are defined as follows:

$$PZM_{nm} = \frac{n+1}{\pi}\sum\sum f(x,y)V_{nm}(x,y) \qquad (4)$$

From the above equations, it is obviously determined that $PZM_{n,m} = PZM^{*}_{n,-m}$ and these moments only computed for positive value of m.

PZM based on Central Moments

For remaining shift invariant property of moments, we used central and radial moments for computing PZM. This done as follows:

$$PZM_{nm} = \frac{n+1}{\pi}\sum_{(n-m-s)even,s=0}^{n-|m|} S_{n,|m|,s}\sum_{a=0}^{k}\sum_{b=0}^{m}\binom{d}{a}\binom{m}{b}\binom{K}{a}\binom{m}{b}(-j)^b CM_{2k+m-2a-b,\,2a+b} +$$

$$\frac{n+1}{\pi}\sum_{(n-m-s)odd,s=0}^{n-|m|} S_{n,|m|,s}\sum_{a=0}^{d}\sum_{b=0}^{m}\binom{d}{a}\binom{m}{b}\binom{K}{a}\binom{m}{b}(-j)^b RM_{2d+m-2a-b,\,2a+b} \qquad (5)$$

where k.= (n-s-m)/2 and d=(n-s-m+1)/2, $CM_{i,j}$ is the central moments and $RM_{i,j}$ is the radial moments.

For each face image these moments are computed as face features.

RBF NN-BASED CLASSIFIER

RBF neural networks have recently attracted extensive research interests in community of neural networks because: (1) they are universal approximations, (2) they have very compact topology, (3) their learning speed is very fast because of local-tuned neurons, (4) they possess the best approximation property. In this paper, RBF neural network is used as classifier in face detection system.

Structure of RBF Neural Network

Figure 1 shows the basic structure of RBF neural networks.

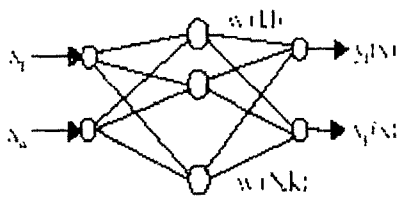

Fig 1 RBF Neural Network

The output of the i_{th} RBF unit is as follows:

$$R_i(x) = R_i\left(\frac{\|x-c_i\|}{\sigma_i}\right) \qquad I = 1,2,\ldots,n \qquad (6)$$

where x is an input feature vector with r dimensional, c_i is a r-dimensional vector named center of RBF node, n is the number of hidden nodes .

Typically, R(x) is chosen as a Gaussian function as follows:

$$R_i(x) = \exp\left(-\frac{\|x-c_i\|^2}{\sigma^2}\right) \qquad (7)$$

The jth output of RBF neural network is:

$$Y_j(x) = b(j) + \sum_{i=1}^{N} R_i(x) \times w_2(j,i) \quad (8)$$

where $w_2(j,i)$is the weight of the i_{th} RBF node to the jth output node and b(j)is the bias of the j_{th} output. The bias is not considered in this in order to reduce network complexity. Hence:

$$Y_j(x) = \sum_{i=1}^{N} R_i(x) \times w_2(j,i) \quad (9)$$

Classifier Design

For designing a classifier based on the RBF neural network, we set the number of input nodes in input layer of NN equal to the number of features that are determined based on number of PZM. The number of nodes in output layer is set to the number of image classes. The selecting RBF nodes we do following steps:

1. We initially set the number of RBF nodes equal to outputs.
2. For each class s, s=1,2,...,k, the center of RBF nodes is selected as the mean value of the sample feature belonging to the class, i.e.

$$C^k = \frac{\sum_{i=1}^{N^k} p^k(r,i)}{N^k} \quad (10)$$

where $p^k(r,i)$ is the ith sample with r-dimension (number of PZM is r) belonging to class k and N^k is the number of image in class k.

3. For any class *k*, compute the distance d_k from the mean to the furthest point p_f^k belonging to class *k*:

$$d_k = \left| p_f^k - c^k \right| \quad (11)$$

4. For any class *k*, compute the distance $d_c(k,j)$ between the mean of class *k* and the mean of other classes as follows:

$$d_c(k,j) = \left| c^k - c^j \right| \quad j=1,2,...,s, \quad j \neq k$$

Then find $d_{mm}(k,l) = \min(d_c(k,j))$and check the relationship between $d_{mm}(k,l)$ and d_k, d_l If $d_k + d_l \leq d_{mm}(k,l)$, then class k has no overlapping with other classes, otherwise class *k* has overlapping with other classes and misclassifications may occur in this case.

5. For all the training data, check how data are classified.
6. Repeat step 2 to 5 untill all the training sample patterns are classified satisfactorily.
7. The mean values of the classes are selected as the centers of RBF nodes. In this paper, a hybrid learning algorithm, which combines the gradient method and Linear Least Squared (LLS) method to adjust the parameters is used that presented in [6].

SIMULATION RESULTS

Experimental Studies are carried out on the ORL (Olivetti Research Laboratory) database image of Cambridge University. In this database the total number of images for each person is 10. None of the 10 samples are identical to each other. They vary in position, rotation, scale and expression. The change in orientation has been accomplished by rotating the person a few degrees (maximum 20 degree) in the same plane, and also each person has changed his face expression in each 10 samples. The change in scale has been achieved by changing the distance between the person and the video camera. Each image was digitized and presented by 112*92 pixel array whose gray levels ranged between 0 and 255. One sample of these images is shown in figure 2. Like the experiment of [7] and [8] we also use a database of 400 images of 40 individuals. A total of 200 images are used to train and another 200 are used to test, where each person has 5 images. In feature extraction step with Pseudo Zernike Moments, simulation has been done in three step based on degree of the Pseudo Zernike Polynomials (n). Experimental results are shown in Table 1 and Table 2 respectively. In Table 1 training data used as training images and testing data as testing images and in Table 2 testing data used as training images and training data as testing images.

We also define the average error rate as follows:

$$E_{ave} = \frac{\sum_{i=1}^{m} N'_m}{m N_t} \quad (12)$$

where m is the number of experimental runs, each being performed on random partition of the database into sets, N'_m is the number of misclassification for the i^{th} run, and N_t is the number of total testing images for each runs.

The comparison with Convolutional Neural Network (CNN) approach [7] and Nearest Feature Line (NFL) approach [8] using the same ORL database in terms of average error rate is shown in Table 3.

The lowest error rate achieved by our method is based on these condition: m=3, Number of PZM is 21. The way to partition the training set and query set is the same as that of [7] and [8]. For NFL method, the best error rate is the average of the error rates obtained on the condition: m=4, number of features is 40, and query set is the same as that of [7] and [8]. For NFL method, the best error rate is the average of the error rates obtained on the condition: m=4, number of features is 40, whereas the average error rate obtained by CNN in Table 3 is based on m=3.

REFERENCES

1. R. Chellappa, C.L. Wilson and S. Sirohey, " Human and Machine recognition of faces: A survey", Proc. Of IEEE, 83(5), 1995, pp. 705-740.
2. J.Daugman, "Face and Gesture Recognition: Overview."IEEETrans. On Pattern Analysis and Machine Intelligence, Vol. 19, No. 7, pp. 675-676, July 1997.
3. L. Wiskott, J. Fellous, N. Kruger and C.Malsburg, "Face Recognition by Elastic Bunch Graph Matching." IEEE Trans. On Pattern Recognition and Machine Intelligence, Vol 19, No. 7, pp. 775-779, July 1997.
4. H. A. Rowley, S. Baluja and T. Kanade, "Neural Network based Face Detection." IEEE Trans. On Pattern Recognition and Machine Intelligence, Vol. 20, No. 1, pp. 23-28, 1998.
5. G.Z. Yang and T. S. Huang, "Human Face Detection in Complex Background.", Pattern Recognition, 27: 53-63, 1994.
6. J-S. R. Jang, "ANFIS: Adaptive- Network-Based Fuzzy Inference System," IEEE Trans. Syst. Man. Cybern., Vol. 23, No. 3, pp. 665-684, 1993.
7. S. Lawrence, C. L. Giles, A. C. Tsoi and A. D. Back, "Face Recognition: A Convolutional Neural Networks Approach," IEEE Trans. on Neural Networks, Special Issue on Neural Networks and Pattern Recognition, Vol. 8, No. 1, pp. 98-113, 1997.
8. S. Z. Li and J. Lu. "Face Recognition Using the Nearest Feature Line Method," IEEE Trans Neural Networks, Vol. 10, pp. 439-443, 1999.

Table 1: Error rate and parameters

Features		Training		Test	
No. of PZM	PZM Order	No. of Epochs	RMSE(1)	No. of Misclass-ifications	Error Rate(2)
25	$0 \le n \le 5$	30 ~ 50	0.03 ~ 0.02	2	1 %
24	$6 \le n \le 8$	20 ~ 35	0.02 ~ 0.01	1	0.5%
21	$9 \le n \le 10$	15 ~ 22	0.04 ~ 0.03	0	0

(1) RMSE : Root Mean Square Error

(2) Error Rate = Number of misclassifications/ Number of total testing patterns

Table 2. Error rate and parameters

Features		Training		Test	
No. of PZM	PZM Order	No. of Epochs	RMSE(1)	No. of Misclassifi cations	Error Rate(2)
25	$0 \le n \le 5$	50 ~ 70	0.04 ~ 0.03	6	3%
24	$6 \le n \le 8$	45 ~ 50	0.02 ~ 0.01	5	2.5%
21	$9 \le n \le 10$	30 ~ 40	0.04 ~ 0.03	3	1.5%

Table 3: Error Rate in different methods

Methods	E_{ave} %
CNN	3.83
NFL	3.125
Our Method	1.2

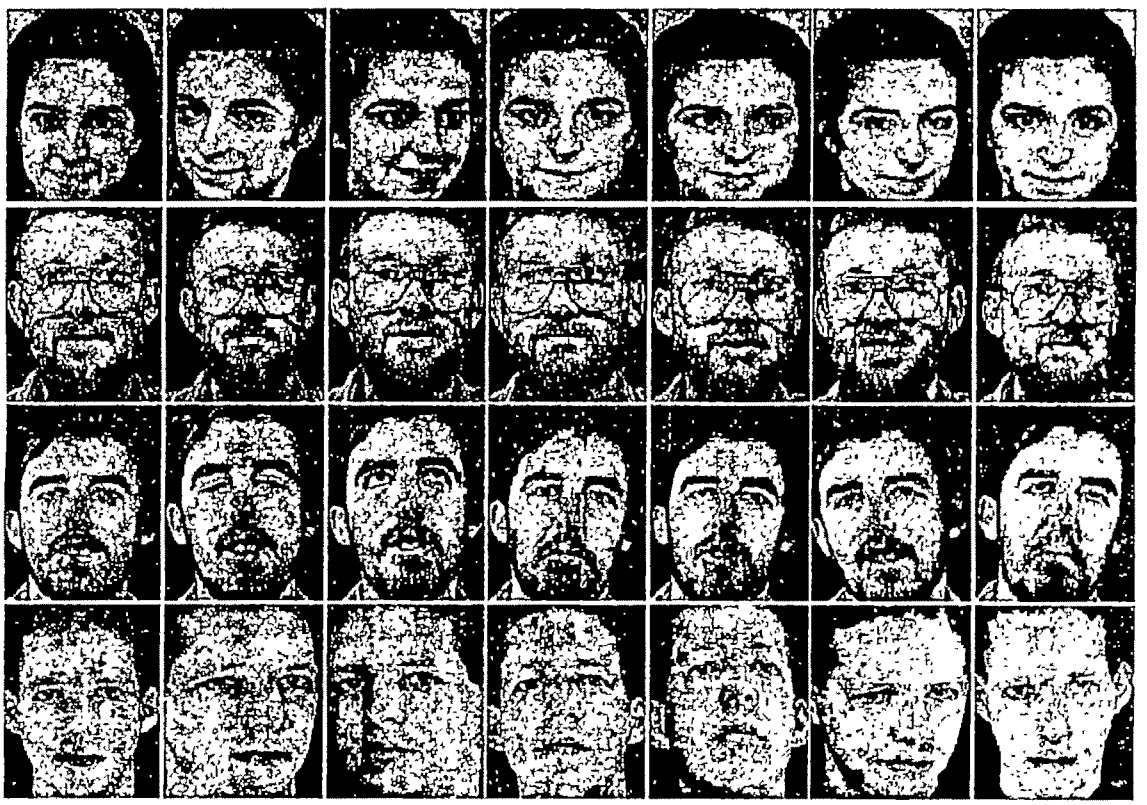

Figure 2. sample of face images on the ORL database.

Face Recognition using Fractal Measure on Color Images

U. R. Jena[*], M. Das Gupta[+], M. Mandal[◊], and A. K. Mandal[θ]
[*]On leave from El & TCE Dept. UCE, Burla, Orissa - 768018
[+]Department of Mathematics, Vidyasagar Evening College, Calcutta University, Kolkata
[◊]ETCE. Dept. Jadavpur University, Kolkata - 700032
[θ]ETCE. Dept. Jadavpur University, Kolkata - 700032 & Corresponding author
Email of the corresponding author: juetcakm@giacl01.vsnl.net.in

Abstract

A method for recognition of human faces using fractal measure on color images is presented. The concept of fractal dimension is used to define a multifractal measure of images, which is a global measure and hence is scale and orientation invariant. In our work the distribution of color intensities is sliced into various slices with respect to their dispersion. Then the distribution within a slice is used to calculate a fractal dimension as a measure of compactness, which is used as an element of the feature vector. A simple Euclidean distance is used to retrieve face images in a database. The orientation invariance property has been demonstrated by retrieving face images that are rotated through 90, 180 and 270 degrees thereby re-confirming the defining relation used for the fractal dimension of colour images used in this paper.

Keywords: face recognition, fractal dimension, feature vector, and metric space.

INTRODUCTION

Automated face recognition (AFR) is an important task in many applications such as security in public places like Airports, Rail and Bus stations; and authentication by automatic transaction machine (ATM), man - machine interface and criminal investigations.

In recent years, there has been a considerable progress in the area of face recognition, especially under stable conditions such as small variations in lighting, facial expression and pose. A detailed survey is available in Ref. [1]. The recognition problem is to find a similar face from the database of faces by some sort of similarity or dissimilarity measure between the test face and a face from database as in [2] - [4]. Many researchers have extensively investigated the recognition problem during the last few years. Some of the approaches adopted were segmentations and extraction of features such as eyes, mouth, etc for detection and recognition of a face in a given image. Use of wavelet decomposition for detection of faces in a domain is a recent development. Classical concepts like principal component analysis (PCA), also called as Karhunen-Loeve transform (KLT) based methods [5]-[8], singular value decomposition (SVD), Elastic Bunch Graph [9], Hidden Markov Model (HMM) [10], Radial Basis Functions (RBF), Isodensity Lines, etc. are still under refinement. The problem has gained dimension by the use of neural network classifiers, fuzzy classifiers, HMM-Based classifier, wavelet-based coefficient analysis and neuro-fuzzy classifiers as in [11], [12]. Most of the methods are too complicated and time consuming either in off-line trainings or in on-line recognition process. The proposed method provides a simple and faster method of image retrieval.

In this paper, we propose a method of retrieval of face image using fractal dimension on color distribution of the image. Each color image is divided in a number of segments around its' mean value and binary images are formed for each segment. The fractal dimension for each binary image is then computed to capture a global measure. The fractal dimensions are subsequently arranged as a vector D to be used as a metric to retrieve a test face from a set of faces called database or gallery. The paper is organised in five sections under the headings as fractal dimension, face recognition using multi-fractal dimension, performance measure of a similarity metric, results and conclusion.

FRACTAL DIMENSION

Fractal dimension of a set is a number that tells how densely the set occupies the metric space in which it lies. It is invariant of rotations and translations. Fractal dimensions are important because they can be defined in connection with real-world data, and they can be measured approximately by means of experiments. They can be attached to clouds, trees, coastlines, feathers, wrinkled surfaces of the sea during a storm, the colors emitted by the sun, etc. They provide an objective means for comparing fractals. They are attempts to quantify a subjective feeling we have about how densely the fractal occupies the metric space in which it lies [13-14].

There are many definitions for fractal dimension of fractal sets. The most commonly used fractal dimension was introduced by Hausdorff, based on the size variation of sets when measured at different scales. This is defined as follows:

Let $S \subset R^n$ be a fractal set. Let N (S,ε) denote the smallest number of circle with diameter ε that can cover S. Then the fractal dimension D of S is given by

$$D = \lim_{\varepsilon \to 0} \frac{\log N(S, \varepsilon)}{-\log \varepsilon} \qquad (1)$$

when this limit exists. Then the measure of S is

$$M = \lim_{\varepsilon \to 0} N(S, \varepsilon) = \lim_{\varepsilon \to 0} \varepsilon^{D}$$

So the fractal dimension is the limit of the ratio of log N (S,ε) and log ε as ε →0, where ε is the unit chosen to cover the fractal set.

PROPOSED FACE RECOGNITION USING THE CONCEPT OF MULTIFRACTAL DIMENSION

It has been observed that different types of pattern may sometimes give rise to the same fractal dimension value due to their common singularity distribution. In order to bring out the discriminating features in such cases, different intensity segmented binary images for a given image may be considered and fractal dimension for each such binary image may be evaluated. This type of multifractal measure [15-16] is found to be very useful for assessing similarity of texture images in ref. [17]. We have considered such a multifractal measure in this paper.

In the paper we have taken the color images, which are resolved into three-color components (red, green and blue); and each color component is treated as a separate image in the present context. The mean of the pixel values of an image is subtracted from each pixel values to obtain a zero mean image matrix A of size (b x b) pixels. Then we normalize the pixel values and segment it between (t+1) number of suitably chosen threshold values, based on the mean and deviation of the pixel values of the image. The segmentation of the image is done by considering $(k)^{th}$ and $(k+1)^{th}$ consecutive thresholds at a time (as shown in the Fig. 1) and converting the pixel values in between them, to unity (maximum) and the rest to zero (minimum). So t-number of binary images will be formed from a single face image of a person as illustrated in Fig. 2 and equal number of fractal dimensions will be computed using defining relation (1) in a way as discussed below:

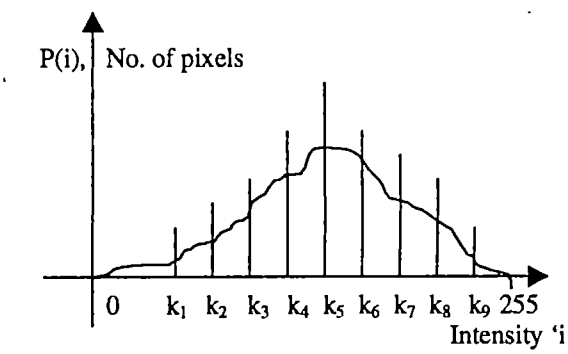

Fig. 1: Intensity of the image is sliced into 8-levels in between k_1 to k_9, where k_5 is the mean.

We take ε in relation (1) as a measure in pixel and N (S,ε) is the total number of covered boxes, that is the box having at least one non-zero pixel in the binary image according to box counting theorem [13]. Here the box sides are taken equal to ε.

For the computation of fractal dimension with a limiting value of a ratio, the unit ε is changed by the relation $\varepsilon = b/2^n$, for $n = 0, 1, 2, \ldots, s$, where $s=\log_2(b)$. When $n = 0$, then ε = b pixels, that is the whole length of the image is treated as unit for counting of N(S,ε) and when n = s , ε = 1 pixel. Hence, as n increases the size of box ε becomes b/2, b/4, . . . , until it coincides with the single pixel. Actually ε value lies between 0 and 1, which is obtained by considering b equal to 1.

Therefore, $-\log(\varepsilon) = -\log(b/2^n) = n \log(2)$,
where b = 1; and N(S, ε) = Number of covered boxes, i.e. boxes having at least one non-zero pixel. Substituting the above value of log (ε) in relation (1) we get

$$D(k) = \lim_{n \to \infty} \frac{N(S, \varepsilon)}{n \log(2)} \qquad (2)$$

So the fractal dimension D(k) can be computed for the binary image obtained between k^{th} threshold and $(k+1)^{th}$ threshold by using relation (2). The fractal dimensions thus obtained will form a vector D = [D(1) D(2) . . .D(t)] characterizing the face image This vector D will be a point in fractal dimension space. It is found that the threshold values based on the deviation, σ, for the present study of the individual face images, give good result if are uniformly spaced over the range from $-4\sigma/3$ to $4\sigma/3$.

PERFORMANCE MEASURE OF A SIMILARITY METRIC

In order to compare the effectiveness of a simple metric as a similarity measure, we use the recall and precision-measures of [18] which are computed based on the ranks of the retrieved images in response to a query.

Assume that $T_1^{(i)},..., T_m^{(i)}$ are the only images similar to a query image Q_i , i = 1 . . . n . Due to false matching, the image-querying algorithm may return this set of answers with various ranks. We use the following measures to evaluate the performance of various competing similarity metrics used in image querying.

Average recall-measure given by

$$r = 1/m \sum_{j=1}^{m} \text{rank}(T_j^{(i)}) \qquad (3)$$

Average precision for a query Q_i given by

$$p = (1/m) \sum_{j=1}^{m} 1/\text{rank}(T_j^{(i)}) \qquad (4)$$

where $T_1^{(i)},.....T_m^{(i)}$ are the answers for query Q_i in the order that they were retrieved.

It is obvious that a querying method is good if it has a low *r-measure* and a high *p-measure.*

EXPERIMENTAL RESULTS

We have carried out the experiment of face recognition problem in the Systems & Information Laboratory in the Electronics and Telecommunication Engineering Department, Jadavpur University. The photographs were acquired by the digital camera attached to the Silicon Graphics Interface workstation and processed by the Image Vision Library Development package. The images of frame size 64 x 64 were taken. From the result tables it is apparent that the success rate for recognition at first rank match is nearly 69% for gray images and nearly 89% for color images with 8-levels of threshold images and 73% for gray images and nearly 90% for color images with 16-levels of threshold images. Euclidean distance is used as a metric to retrieve a query face from the database of faces. It is to be noted that for gray images, 8-levels and 16-levels of threshold gives rise to, respectively 8 and 16-dimensional vectors in the metric space. The corresponding sizes of vector space for color images are 24 and 48 respectively, because of the three-color components considered. From the tables we find that the improvement from 8-levels to 16-levels of threshold for color images is not commensurate with the increase in dimension. It is also found from Table-2 that consideration of only red and green colors for the current database; with 16-levels of threshold (resulting in 32-dimensional vector) yields 90% correct recognition in 1^{st} rank. The result of correct match in first 3-ranks and first 9-ranks are also recorded in the same table, which are 95.7 % and 97.7 % respectively. We have also tested the technique for Olivetti Database containing 400 gray images (Fig. 3 shows a sample) and have tabulated the results of correct matches in 1^{st} rank, first 3-ranks and first 9-ranks with different threshold levels. The result is comparable to other methods and is presented in Table-3. In order to study the effect of database size on the result, the correct match in 1st rank are noted for variable database-size and the results are recorded in Table-4 and graphically displayed in Fig. 5. It is apparent from Fig. 5 that the recognition-rate using color components is much higher than the corresponding figure obtained from gray images. Fig. 6 shows the plot of percentage-recognition against the number of ranks (i.e., top n matches with which the query image is matched).

In an attempt to assess the performance of competitive search algorithms objectively, the recall (r-value) and precision (p-value) measures are computed by using relations (3) and (4), respectively. The values are given in the Table-5.

The main advantage of the proposed method is that it is independent of scale and rotation. We have studied the rotational invariance property and the result is given in the Table-1. As given in Fig. 4, we have experimented by taking 7-poses of each person from the database of 45 persons. The 5^{th} pose of each person of the same database is rotated through 90, 180 and 270 degrees, thus adding 3-images more to the above selected 7-poses to create a new database with 10-images per person of the first database. The new database is analysed for recognition of faces by the present method. The result is very good, since the Euclidean distance of the rotated images measured from the original one, is found to be zero; thus re-confirms the orientation invariant property of the proposed method.

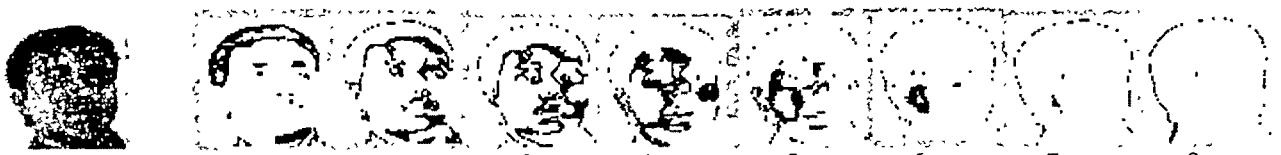

Fig. 2: An Image is sliced into eight binary images between nine consecutive threshold values of intensity.

Fig. 3: A sample of Olivetti database.

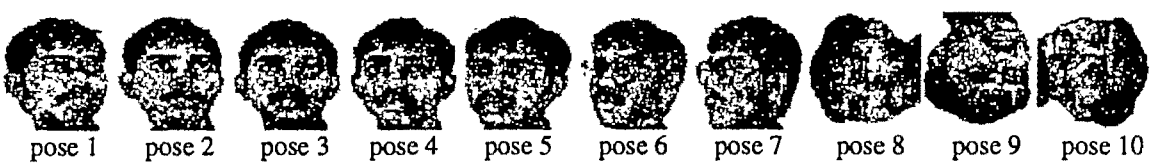

Fig. 4: A sample of created mixed database adding rotated images of faces from JU database.

Table 1 The percentage of correct match of a face in the JU database: (For 8 – levels of thresholds)

Image Type	Color Components used	1st – Rank match	First 3 – Ranks match	First 9 – Ranks match
Gray Image	Average of RGB	68.6	84	91.7
Color Image	All Components	89.1	94.8	97.3
	Red Component	77.3	89.3	95.3
	Green Components	70.4	85.1	94.4
	Blue Components	48.0	75.1	91.1
	Red and Green Comps.	87.3	95.3	97.7
Color Images with some rotated through 90, 180 & 270 degrees	All Components	91.5	94.6	97.1
	Red Component	85.1	92.6	97.3
	Green Components	82.6	89.1	94.2
	Blue Components	68.8	83.7	90.4
	Red and Green Comps.	91.1	95.5	97.7

Table 2 The percentage of correct match of a face in the JU database: (For 16 – levels of thresholds)

Different Images	Components Considered	1st – Rank match	3 – Ranks match	9 – Ranks match
Gray Image	Average of RGB	73.7	86.6	93.1
Color Image	All Components	89.5	95.7	98.2
	Red Component	84.2	92.8	97.5
	Green Components	78.4	89.1	96.4
	Blue Components	57.7	80.4	92.0
	Red and Green Comps.	90.8	95.7	97.7
Color Images with some rotated through 90, 180 & 270 degrees	All Components	92.6	95.7	98.2
	Red Component	90.8	96.0	98.0
	Green Components	83.7	92.2	95.7
	Blue Components	72.2	83.3	90.8
	Red and Green Comps.	93.3	97.1	98.4

Table 3 The percentage of correct match of a face in Olivetti Database (Gray Images) for different dimensions:

Dimension	1st – Rank match	First 3 – Ranks match	First 9 – Ranks match
8	82.5	93.5	98.0
16	88.0	94.7	98.0
20	91.0	96.0	98.5
24	87.5	94.0	97.0
32	80.2	92.7	96.7

Table 4 The percentage of correct match of a face for 1st rank match with database size:

Size of data-base	Percentage of match for gray images with 8-thresholded images measured in %	Percentage of match for gray images with 16-thresholded images measured in %	Percentage of match for color images with 8-thresholded images measured in %	Percentage of match for color images with 16-thresholded images measured in %
50	88.0	86.0	96.0	98.0
100	76.0	78.0	96.0	98.0
150	80.0	80.6	96.0	98.0
200	80.0	81.0	97.0	98.0
250	81.2	81.2	95.2	94.8
300	79.6	81.3	92.3	93.3
350	72.5	77.1	90.2	90.8
400	70.2	75.0	90.2	91.0
450	68.6	73.7	89.1	89.5

Table 5 Recall and Precision measures: (r-value and p-value)
(low r-value and high p-value imply better query method)

Sl. No.	Image No.	r-value	p-value	Sl. No.	Image No.	r-value	p-value
1	5.0000	9.7778	0.2602	11	105.0000	13.3333	0.2782
2	15.0000	57.3333	0.2074	12	115.0000	13.3333	0.1570
3	25.0000	16.2222	0.2587	13	125.0000	28.2222	0.0545
4	35.0000	6.2222	0.3063	14	135.0000	20.5556	0.1655
5	45.0000	100.7778	0.0753	15	145.0000	60.3333	0.2422
6	55.0000	35.2222	0.2273	16	155.0000	8.4444	0.2849
7	65.0000	65.7778	0.0175	17	165.0000	52.1111	0.1173
8	75.0000	33.1111	0.2716	18	175.0000	150.8889	0.1401
9	85.0000	75.3333	0.1952	19	185.0000	44.4444	0.2076
10	95.0000	109.7778	0.1308	20	195.0000	23.3333	0.2199

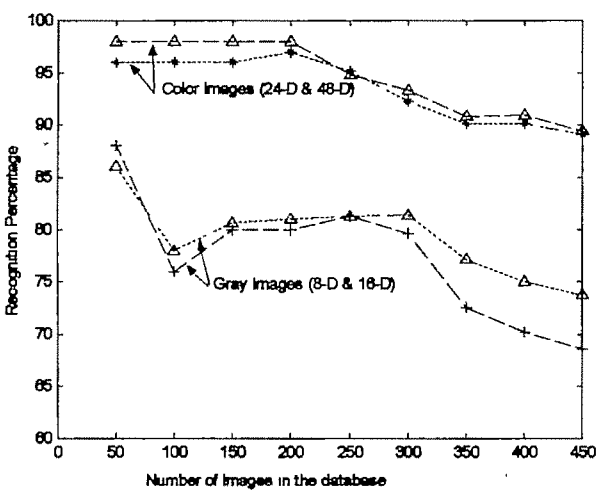

Fig. 5: A plot of recognition percentage versus size of the database.

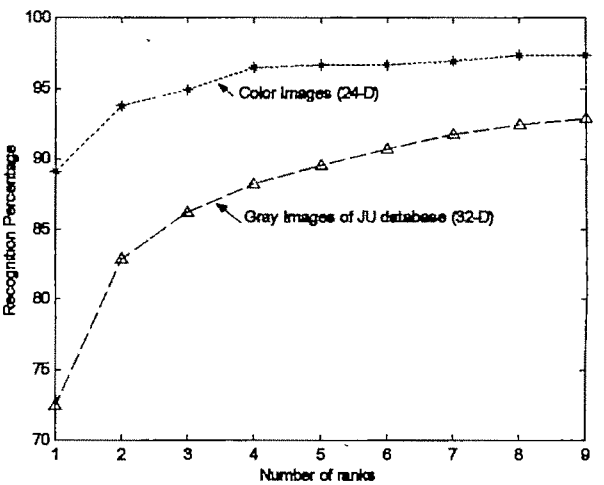

Fig. 6: A plot of recognition percentage versus number of ranks

CONCLUSION

In this paper we have described a computationally efficient face recognition method using fractal dimension as a global measure. A simple Euclidian distance metric is used to search a face database for a query face and the result is very encouraging. The most important feature of the technique is the success with which it can detect faces rotated through 90, 180, 270 degrees from the face database containing normal and rotated faces.

ACKNOWLEDGEMENT

The authors thankfully acknowledge the assistance of the postgraduate students working in the System and Information Laboratory, Electronics and Telecommunication Engineering Department Jadavpur University for creating the image database. Mr. U. R. Jena would like to thank AICTE for the sponsorship under QIP.

REFERENCES

1. R. Chellappa, C. L. Winson, and S. Sirohey, "Human and Machine Recognition of Faces: A Survey", *Proceedings of IEEE*, vol. 83, no. 5, may 1995
2. M. Mandal and A. K. Mandal, "Wavelet Metric for Matching Distorted Images", *Int. Conf. on Advances in Pattern Recognition and Digital Techniques*, pp. 499-503, ISI Calcutta, India, Dec 27-29 1999.
3. M. Mandal, T. Lahiri, U. R. Jena, M. Das Gupta, and A. K. Mandal, "Sub-region Fuzzy Features for Image Retrieval", *Journal of Science & Industrial Research*, vol. 59, Dec. 2000, pp. 1012-1022.
4. A. K. Mandal, M. Mandal, T. Lahiri, and U. R. Jena, "Applicability of Contrast Model in Assessing Similarity of Images", *ICARCV-2000*, (abstract in page-54, vol. 6, 2000).
5. L. Hong and A. K. Jain, "Integrating Faces and Fingerprints for Personal Identification", *IEEE Trans. Pattern Analysis and Machine Intelligence*, vol. 20, no. 12, pp. 1295-1307, Dec. 1998.
6. P. N. Belhumeur, J. P. Hespanha, and D. J. Kriegman, "Eigenfaces vs. Fisherfaces: Recognition Using Class Specific Linear Projection", *IEEE Trans. Pattern Analysis and Machine Intelligence*, vol. 19, no. 7, pp. 711-720, July 1997.
7. M. Kirby and L. Sirovich, "Application of K-L Procedure for the Characterization of Human Faces", *IEEE Trans. Pattern Analysis and Machine Intelligence*, vol. 12, no. 1, pp. 103-108, Jan 1990.
8. D. L. Swets and J. Weng, "Using Discriminant Eigen Features for Image Retrieval", *IEEE Trans. Pattern Analysis and Machine Intelligence*, vol. 18, no. 8, pp. 831-836, Aug. 1996.
9. L. Wiskott, J. -M. Fellous, N. Kruger, and C. von cer Malsburg, "Face Recognition by Elastic Bunch Graph Matching", *IEEE Trans. Pattern Analysis and Machine Intelligence*, vol. 19, no. 7, pp. 775-779, July 1997.
10. A. V. Nefian and M. H. Hayees, "A Hidden Markov Model for Face Recognition", *in ICASSP' 98*, vol. 5, pp. 2721-2724, 1998.
11. C. Garcia, G. Zikos, and G. Tziritas, "Wavelet Packet Analysis for Face Recognition", *Image Vision and Computing*, vol.18, no. *, pp. 189-297, 2000.
12. H. Wu, Q. Chen, and M Yachida, "Face Detection From Color Images Using a Fuzzy Pattern Matching Method", *IEEE Trans. Pattern Analysis and Machine Intelligence*, vol. 21, no. 6, pp. 557-563, June 1999.
13. Barnsley M. F, "Fractals Everywhere", Academic Press, Inc. 1993.
14. Mandelbrot B.B, "The Fractal Geometry Of Nature", W H Freeman Co. San Fransisco, 1988.
15. Mandelbrot B. B, "Fractals and Multifractals: Noise, Turbulence and Galaxies", 1988.
16. Fisher Yuval, "Fractal Image Encoding and Analysis", Springer 1998.
17. M. Das Gupta, M. Mandal, U. R. Jena, T. Lahiri and A. K. Mandal, "Texture Similarity by Fractal Measure" accepted for presentation in the IASTED International Conference (ATA), Sept 4-7, 2001, Spain.
18. Jing Huang, S. Ravi Kumar, Mandar Mitra, Wei-Jing Zhu "Spatial Color Indexing and Applications" *Proceedings of the 6th Int'l. Conf. on Computer Vision*, pp.602-607, IIT Bombay, India, Jan 4-7, 1998.

Face Recognition Using Eigenfeatures

Narottam Chand
Department of Computer Science & Engineering
Regional Engineering College, Hamirpur (H.P.) 177 005, India.
E-mail: nar@recham.ernet.in

Abstract

An automatic system that recognizes the person comparing characteristics of the face to those of known individuals have been developed. Principal Components Analysis (PCA) of face images, which is widely used in engineering approach to face identification, produces an inherently global representation. Here the faces are vertically oriented frontal view and normal expression variation is allowed. The face space is described by a set of eigenfaces. Each face is efficiently represented by its projection onto the space expanded by the eigenfaces and has a new descriptor. For better results the recognition is done at the face as well as at the feature level.

Keywords: Face, Recognition, PCA, Eigen, Feature.

INTRODUCTION

The problem of face recognition can be described as: given an image of human face, compare it with models in the database and report who it is if a match exists. Here the image is gray scale and normal expression variation is allowed.

Computational models of face recognition, in particular are interesting because they can contribute not only to theoretical insight, but also to practical applications. Computers that can recognize faces could be applied to wide variety of problems, including criminal identification, security systems, image & film processing, human-computer interaction, personal identification and face reconstruction [1, 2].

The possible applications of automatic human face recognition systems are in building security. A face recognizer could be used at the front entrance for automatic access control. They could be used to enhance the security of user authentication in ATMs by recognizing faces as well as requiring passwords. In the human or computer interface arena, workstations with cameras would be able to recognize users, perhaps automatically loading the user's environment when he/she sits down in front of the machine. Another example is in the criminal identification in the police department. Once a criminal is caught, the information needed can be obtained by asking the criminal to face a camera provided, without any need to open the manual file.

Eigen vectors (eigenfaces) are calculated from initial face image set. New faces are projected onto the space expanded by eigenfaces and represented by weighted sum of the eigenfaces. These weights are used to recognize the faces. Features (mouth, eyes, nose) are extracted manually from the given face image. Eigen vectors (eigenfeatures) are calculated from initial feature subimage set. Recognition results are verified using eigenfaces as well as eigenfeatures.

The test face to be recognized is projected onto the eigen space and reconstruction back onto the image space is done [3, 5]. If the reconstruction error turns out to be less than certain threshold then the test image belongs to the database and is identified as a person based upon the minimum Euclidean distance between the input face descriptor and each face model in the database.

If the algorithms results in no match then the face is termed as unidentified and system can be retrained by adding its description into the database.

PCA FOR FACE PROCESSING

A face which is an image, can be viewed as a vector. If the image's width and height are w and h pixels respectively, the number of components of this vector will be w*h. Each pixel is coded by one vector component. The construction

of this vector from an image is performed by a simple concatenation - the rows of this image are placed each beside one another.

The face vector belongs to a space called image space. All the faces look like each other. They all have two eyes, a mouth, a nose, etc. located at the same place. Therefore, all the face vectors are located in a narrow cluster in the image space. Hence the full image space is not an optimal space for face description. The task presented here aims to build a face space (eigen space) which better describes the faces. The basis vectors of this eigen space are called eigen vectors (eigenfaces).

PCA is a standard statistical technique for reducing the dimensionality of data while attempting to preserve as much of the information, in the form of variance, as possible [5]. PCA on a set of n faces can produce upto n components, each accounting for a decreasing amount of variance. If all n components are used, the representation is perfect, and the original face images may be recovered by multiplying through the coding vector with the eigenfaces. Typically, fewer eigenfaces are stored [6, 7].

EIGENFACE GENERATION

PCA computes the basis of a space which is represented by its training vectors. The basis vectors computed by PCA are in the direction of the largest variance of the training vectors. These basis vectors are computed by solution of an eigen problem, and as such the basis vectors are eigenvectors. These eigenvectors are defined in the image space. They can be viewed as images and indeed look like faces. Hence they are usually referred to as eigenfaces.

Each individual face can be represented as a linear combination of eigenfaces. Each face can also be approximated using only the "best" eignefaces – those that have the largest eigenvalues, and which therefore account for the most variance with in the set of face images. The best M eigenfaces span an M-dimensional subspace – facespace – of all possible images [7].

For better recognition of faces under large variations of facial expressions, a separate eigenspace is created for each expression class called eigenclass [4]. The input image to be recognized is mapped onto each eigenclass and is categorized on the basis of maximum match found.

Figure 1 shows schematically what PCA does for an eigenclass [4]. It takes the training faces from that expression class as input and yields the eigenfaces as output. Once this is done, the recognition can begin.

Let a face image I(x,y) be a two-dimensional N by N array of (8-bit) intensity values. An image may also be considered as vector of dimension N^2, so that a typical image of size 64 by 64 becomes a vector of dimension 4096, or equivalently, a point in 4096-dimensional space. An ensemble of images, then maps to a collection of points in this huge space.

First an initial set of training images $[\Gamma_1, \Gamma_2, \ldots, \Gamma_M]$ is prepared. The average face of the whole face distribution is

$$\Psi = (\Gamma_1 + \Gamma_2 + \ldots + \Gamma_M)/M$$

Then the average face is removed from each face,

$$\Phi_i = \Gamma_i - \Psi, \; i = 1,2, \ldots, M$$

Let X be the matrix containing Φ_is – each column representing a column vector for face. The dimensions of X is I (number of pixels of each face i.e. 4096) by M (number of faces in the training set). Usually the number of faces in a training set is smaller than the number of pixels contained in each face.

Hence, the dimension of matrix $X*X^T$ is I x I (4096 x 4096). However, its rank is M (if each training face is different from each other), and hence it has M eigenvectors. More efficient technique is to compute inner product X^T*X instead of the outer product $X*X^T$.

Let

- the matrix V be the inner product X^T*X,
- the matrix Q be the matrix of the eigenvectors of V,
- the matrix P be the matrix of the eigenvectors of the outer product, $X*X^T$, and
- the diagonal matrix Λ be the matrix of the eigenvalues of the inner product and of the outer product.

$$P = X.Q.\Lambda^{-1/2}$$

To check that P given above, is indeed the eigenvectors of $X*X^T$, the following equality has to be verified:

$$X*X^T*P = \Lambda*P$$

Provided that Q is the matrix of the eigenvectors of V:

$$X^T*X*Q = \Lambda*Q$$

Thus,

$$X*X^T*X*Q*\Lambda^{-1/2} = \Lambda*X*Q*\Lambda^{-1/2}, \text{ and}$$

$$X*\Lambda*Q*\Lambda^{-1/2} = \Lambda*X*Q*\Lambda^{-1/2}$$

The eigenvectors determine the linear combination of M training set face images to form the eigenfaces U_l.

$$U_l = \sum_{k=1}^{M} P_{lk}\Phi_k \qquad l = 1, 2, \ldots, M$$

FACE PROJECTION

Having the normalised eigen-vectors (in order that they fulfil the conditions of orthogonality and orhtonormality) the faces which constitute this base (or any other face) can be projected onto the eigenclass as follows:

$$Y = P^T * X$$

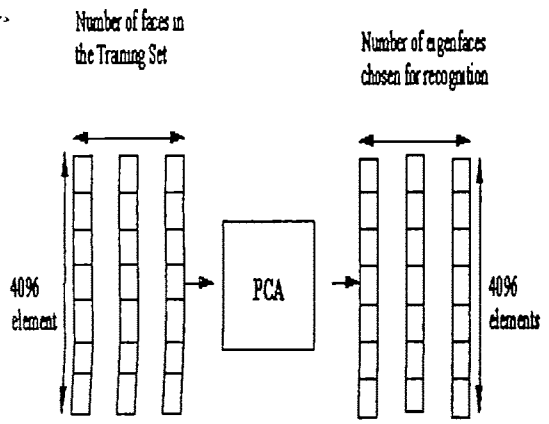

Figure 1: Eigenfaces generation process.

Being Y the matrix of components or the result of the X projection on P. For a particular facial image the vector in eigenspace (eigenclass) determines the weight of every eigen-vector on that image.

A new face Γ is transformed to its eigenface components by a simple operation,

$$W_k = P^T(\Gamma - \Psi) \quad k = 1, 2, ..., M \bullet$$

Where $M\bullet$ is the number of first eigenvectors of P, selected corresponding to largest eigenvalues.

For kth expression class weights form a vector

$$(\Omega_k)^T = [W^k_1, W^k_2, \quad ... \quad W^k_{M\bullet}]$$

RECONSTRUCTION

Once the eigenfaces has been computed for an eigenclass, each face in the image space can be viewed in the face space. The transformation from image space to face space is fairly simple.

Let

- E be the matrix of the eigenfaces, where the first column is the first eigenface and so forth,
- f_I be a face in the image space, and
- f_F be the same face in the face space

$$f_F = E^T * f_I$$

This is many-to-one transformation, since the dimensionality of the image space is far larger than the dimensionality of face space. Thus, the transformation introduces an error which can be seen by looking at reconstructed face. The reconstruction is performed by taking the inverse of above transformation.

$$f'_I = E * f_F$$

As an example, figure 2 shows a face along with its reconstruction.

Note the blurring of the reconstructed image. This can be simply explained. PCA puts each face of the training set on top of one another, and looks for variations. If the faces are not centred or are not at the same scale, the representation of the faces will be blurred [1, 4, 5]. Moreover half of the image constitutes background, and for PCA, a pixel belonging to the background has the same importance as a pixel belonging to the useful part of the image, the face.

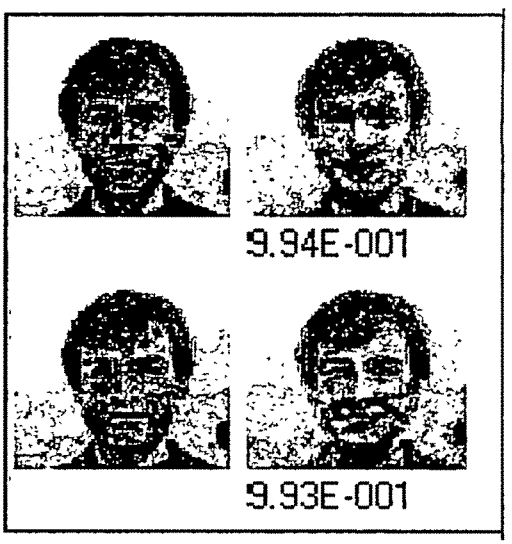

Figure 2: original face along with its reconstruction, the reconstruction error is shown below the reconstructed face.

The magnitude of the difference between the original face and its reconstruction, called the reconstruction error, is easily calculable. The Euclidean

distance between the original face f_I and reconstructed face f'_I is given as

$$\varepsilon = \bullet f_I - f'_I \bullet^2$$

Since a face is well represented by the face space, its reconstruction should be similar to the original, and the reconstruction error will be small [1, 2]. On the other hand, non-face images will have a large reconstruction error. This implies that the reconstruction error of faces should be within some threshold, •.

RECOGNITION PROCESS

Once the eigenfaces have been computed, the face space has to be populated with known faces [1, 5]. These faces are taken from the training set of particular eigenclass [4, 7]. Each known face is stored into the face space and its components stored in memory.

At this stage the recognition process can begin. An unknown face is presented to the system. The system projects it onto the face space and computes its distance from all the stored faces. The face is identified as being the same individual as the face which is nearest to it in face space.

The processing steps to recognize the test image are:

- Project the test image onto every eigenclass.
- Reconstruct the image from all the classes.
- For reconstructed image in a class find minimum error from all the images in that class. If minimum error turns out to be less than certain threshold then the test face belongs to the database of that class and the test image is identified as a person where this minimum error occurs. Repeat the process for all the expression classes.

Image is recognized of the person where maximum number of matches are found from the eigenclasses. For the same face the verification is done at the feature level.

If the algorithm results in no match then the face is termed as unidentified and system can be retrained by adding its description into the database.

EXPERIMENTS AND RESULTS

The face database is downloaded from WWW at: http://peipa.essex.ac.uk/ftp/ipa/pix/faces/manchester. These images are geometrically scaled down to size 64x64 from the original size 512x512. Also linear contrast stretch is performed over these images to add all 256 graylevels, whereas original database is having only 38 graylevels.

The eigenface based experiments are performed for face recognition. The faces are recognized with an accuracy of 90% to 93% depending upon the number of eigenfaces selected and the input test image.

The system works well for face recognition, but in some of the cases maximum number of failures are found.

Following observations are made:

- If there is major change in head orientation or change in face profile or due to spectacles or violation of normalization, convexity and illumination, the system is not able to recognize accurately.
- Four or five eigenfaces (eigenvectors) are sufficient to reconstruct the images. Number of eigenfaces should be as minimum as required for reconstruction and as maximum as there is no noise introduced.

CONCLUSIONS AND FUTURE SCOPE

The algorithm presented can recognize between 90% and 93% of faces in a set of 450 test images, with an acceptable number of false detections. Depending on the application, the system can be made more or less conservative by varying the arbitration heuristic or threshold used.

The main limitation of the current system is that it only operates over single static image. The method can be extended for image sequence.

REFERENCES

1 M. Turk and A. Pentland. Eigenfaces for Recognition. Journal of Cognitive Neuroscience (1991) vol. 3, no. 1, pp 71-86.

2 Rowley, Baluja and Kanade. Neural Network Based Face Recognition. PAMI (1998).

3 Quing Jiang. Principal Component Analysis and Neural Network Based Face Recognition. http://www.cs.uchicago.edu/~quingj/Thesis/index.html/

4 Narottam Chand. Analysis of Facial Expressions. M.Tech. Thesis, IIT Delhi (1998).

5 A. Pentland, B. Moghaddam, Thad Starner. View Based and Modular Eigenspaces for Face Recognition. Vision and Modeling Group. MIT.

6 Irfan Aziz Essa. Analysis, Interpretation and Synthesis of Facial Expressions. Media Arts and Sciences, MIT (1995).

7 Narottam Chand. Principal Components Analysis based Face Recognition. TIMA (2001).

3-Dimensional Fractal Measure For Texture Similarity

A.K. Mandal[1], M. Dasgupta[2], M. Mandal[3] and U. R. Jena[4]
Systems Information Laboratory, Dept. of Electronics & Telecommunication Engineering
Jadavpur University, Kolkata-700032, India
Email: juetcakm@giacl01.vsnl.net.in

[1]Corresponding author.
[2] Dept. of Mathematics, Vidyasagar Evening College, Calcutta University, Kolkata, India
[3] Dept. Electronics and Telecommunication Engineering , Jadavpur University
[4] On leave from the Dept. of El & TCE, UCE, Burla, Sambalpur, Orissa, India.

Abstract

A method of ranking similar texture images is presented using their multifractal self-similarity property. The concept of fractal dimension in a 3-dimensional space is used to define a multifractal measure of the images, which is a global measurement and hence is scale and orientation invariant. Fractal dimension for various intensity segmented images, for a single image, are used as the characteristic features for subsequent assessment of similarity of texture images by using the contrast model of Tversky [1]

Keywords: Fractals ,Fractal Dimension, Multi-fractal self-similarity, Texture analysis, Similarity Metric

INTRODUCTION

Multi-fractal analysis [2-5] is a tool for studying the self-similar measures of fractals and such an approach makes sense for "complex " images, in which the relevant structures are irregular in nature.

A pattern, which characterizes objects, is called a texture in image processing [6,7]. The measurement of Multifractal self-similarity will be employed here for comparing textures.

Mandelbrot [2] was the first to point out the abundance of multifractals in Nature .The concept of dimension is fundamental in the analysis of fractals and it provides an objective means for comparing fractals found in natural objects like clouds, trees, coastlines and images. The main objective of this paper is to find global features for the characterization of texture images, which would not depend on rotation and scale. The multifractal self-similarity [5] property is applied to extract suitable characteristic features from the texture images making the texture analysis problem reduced to the known task of extracting feature vectors. In this respect, fractal dimension, which is a global measurement of a multifractal [4], yields some fruitful result.

In this paper, an image is mathematically modeled as a graph of a function $z = f(x,y)$ which is a set in R^3 consisting of the points on the surface defined by f, $f(x,y)$ is the gray level of the pixel at position (x,y). For (b x b) pixel image, each pixel can take on any one of 256 levels of gray value. We scale the levels to b, That is

$$(x,y) \in \{ (u,v) : 0 \le u,v \le b \} \equiv I^2_b \text{ and}$$
$$f(x,y) \in I_b \equiv [0, b]$$

where I_b stands for the closed interval [0,b] and I^2_b stands for a square with side b .

The images are recursively partitioned into sub-cubes of various sizes and the number of cubes of corresponding size that cover the images, are counted. Fractal dimension[8] is then computed from the defining relation (2). The Fractal dimension is calculated for various intensity-segmented images for a single texture image. The intensity segmentation is done by suitably chosen thresholds based on the mean and standard deviation of each image. These Fractal dimensions are the characteristic features of the images, which are used effectively for assessing the similarity of textures.

In the next paragraph the similarity perception is explained which is based on the contrast model of Tversky [1] .

This is followed by the technique for computation of the fractal dimensions, which can be used by the similarity metric.

PERCEPTION OF SIMILARITY

In visual information systems, the emulation of human perception of similarity is of paramount importance [9-13]. Some models [14] assume that the perception of

human similarity is a measure of a distance in a psychological space. According to this model, visual stimuli are mapped as points in a perceptual space and by devising a suitable metric in psychological space, one can compare similarity in stimuli. However, some psychological experiment has established [1,15] that the stimuli does not satisfy metric axioms and can better be represented by sets of features. Jain [16] suggested fuzzy predicates to represent the visual stimuli and accordingly modified the contrast model of Tversky [1] for the computation of similarity of two dimensional face images. In [17-20] it has been shown that a Differential Distance Metric (DDM) derived from the wavelet coefficients is more effective in ordering the similar images taken from video sequence than the metric used in the contrast model itself [1, 11]. In this paper the similarity of texture images are compared with the feature vectors derived from the fractal dimensions of a 3-D image Model.

FRACTAL DIMENSION OF 3-D IMAGE MODEL

The most commonly used fractal dimension was introduced by Hausdorff , based on the size variation of sets when measured at different scales[3-4,21]. This is defined as follows:

Let $S \subset R^n$ be a fractal set . Let N(s) denote the smallest number of circle with diameter s that can cover S. The fractal dimension D of S is given by

$$D = \lim_{s \to 0} \frac{\log N(s)}{-\log (s)} \qquad (1)$$

when this limit exists, and the measure of set S is $M = \lim_{s \to 0} N(s)\, s^D$

Since fractal dimension is the limit of the ratio of log N(s) and log s as $s \to 0$, where s is the unit chosen to cover the fractal set , so we can use the defining relation (1) to compute fractal dimension for an image as follows:

For the computation of fractal dimension as a limiting value of a ratio, the unit s is changed by the relation $s = b/2^n$, for $n = j, j+1 \ldots, m$, where $m = \log_2(b)$. The lower limit j has been set to 2 in the present study since we are interested to capture the discriminating feature of each individual texture images while looking for similarities among them and for j= 0 and 1 yield identical fractal dimensions for densely packed texture images under consideration.

The upper limit m is chosen such that the size of the box becomes a single pixel. So we see that -log (s) equals $\log (2^n/b)$ and as $s \to 1$, $n \to m$.

The image is partitioned into non-overlapping blocks of size (s x s) pixels. The maximum intensity J_i in each block together with the corresponding location (x,y) is found. Here i varies from 1 to q where $q = (b/s)^2$ is the number of boxes of size (s x s) in the image.

According to the definition of Fractal dimension the number of boxes required to cover each sub-square is J_i/s and total no. of boxes $N(s) = \sum J_i/s$ where the summation is taken over all the q boxes. The fractal dimension can therefore be computed by relation (2)

$\therefore \log (s) = -\log (\frac{2^n}{b})$ for an image of size b x b

N(s) = Total Number of cubes of size s x s pixels

$$= \sum_{i=1}^{q} J_i/s \ , \ q = (b/s)^2 \text{ where } J_i = \max\{f(x, y)\}$$

in each sxs pixel boxes

$$\text{Therefore } D = \lim_{s \to 1, n \to m} \frac{\log \left(\sum_{i=1}^{q} J_i/s \right)}{\log (2^n/b)} \qquad (2)$$

In order to bring out the discriminating features in almost similar patterns, various intensity segmented images for a given image may be considered based on a particular threshold and fractal dimension for each such segmented images may be evaluated.

Relation (2) is used to compute the fractal dimension D(t) of the texture image at a particular threshold t. By using a number of thresholds (say p), based on the mean and standard deviations, various intensity segmented images for a single texture image can be obtained and their fractal dimensions will form a vector $D = [D(1) D(2). . . D(p)]^T$ characterizing the texture image. This vector D represents a point in the multifractal feature space.

The algorithm in Pseudo code is given at the end of the paper.

RESULTS

The vectors D of the multifractal space, have been computed with various threshold values (up to 20) for assessing the similarity between a video query and the target texture image. We submit any texture image as a query and retrieve twenty similar images from the database and display them in ranked order. A few sample results are shown in Figure1, where the leftmost image is the query followed by the similar textures in a database of 159 images.

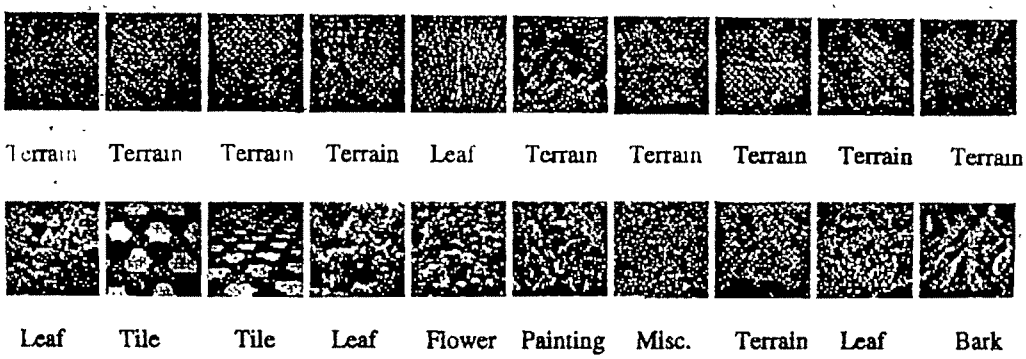
Terrain Terrain Terrain Terrain Leaf Terrain Terrain Terrain Terrain Terrain
Leaf Tile Tile Leaf Flower Painting Misc. Terrain Leaf Bark

(a) !0 Terrain Images out of 11 present in the image database as retrieved in 20 target images.

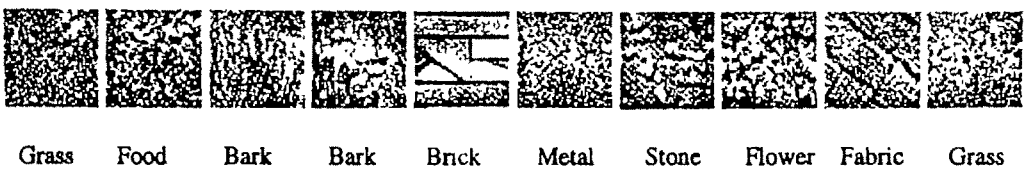

(b) 2 Grass images out of 3 present in image database as retrieved in 10 target images.

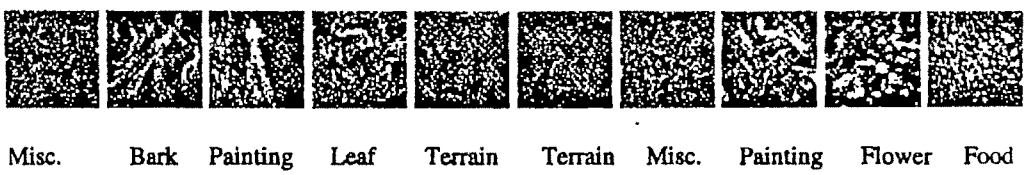

(c) 2 Miscellaneous images out of 4 present in the image database as retrieved in 10 target images

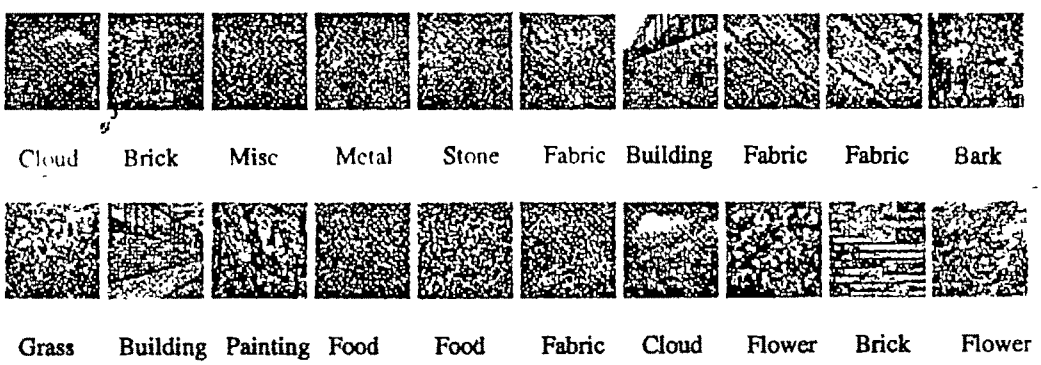
Cloud Brick Misc Metal Stone Fabric Building Fabric Fabric Bark
Grass Building Painting Food Food Fabric Cloud Flower Brick Flower

(d) 2 Cloud images out of 2 present in the image database are retrieved in 20 target images.

Figure 1: Retrieval of similar Texture images from a database of 159 images using 3-D fractal measure In each of the figures (a) to (d), the left most image is the query image while the retrieved images are arranged from left to right, top to bottom with increasing 'distance'.

ALGORITHM :

function rank (rs, kk)
for k = 1 to L
X_0 (k) = zero-mean gray level texture image matrix corresponding to image no k in the database size L
sz x sz_1 = size of X_0
σ = standard deviation of X_0
r = σ / 15 / (r = step of thresholds)
for t = 1 to p
$X=X_0 - r * t$ sign(X_0) / image after applying threshold step t
s=log2 (sz) (largest scale of box)
Normalize X_0 intensity to scale s
for n = s
$n_1=2^n$
nn=log10(n_1)
for j = 1 to n_1
win (n) = non-overlapping windows in scale n / in x - y image plane
A(N, n) = no of filled cubes in scale n / intensity value is the z dimension
end j
NN= log10(A(N,s))
end n
end t
d_t= slope of (nn, NN) plot / Fractal dimension at threshold t
D(k) = [d_1 d_2 d_t] / feature vector of the k th image
end k
for kk=1 to L
d_e (kk) = $D^T - D^Q$(kk) / D^T, D^Q are feature vectors for target texture image and query image respectively

rs(kk) = norm(d_e)
[rank, kk] = sort(rs) / Ranking of the images
end kk
end function

CONCLUSION:

The multifractal measure can capture the essential features of texture images and can be used as an effective tool for assessing similarity of images in video query . It has the added advantage that it is rotation and size invariant. The concept has also been verified in ordering color face images.

ACKNOWLEDGEMENT :

Mr. U.R. Jena would like to thank All India Council for Technical Education for financial Support under QIP programme, AICTE

REFERENCES

1. Amos Tversky "Features of similarity, Psychological Review, 84(4): July 1977, 327-352.
2. Mandelbrot B .B. 'The Fractal Geometry Of Nature ', W H Freeman Co. San Francisco 1988.
3. Mandelbrot B. B. 'Fractals and Multifractals : Noise , Turbulence and Galaxies ,1988.
4. Mallat Stéphane , 'Wavelet Tour of Signal Processing ', Academic Press, San Diego, USA 1999.
5. Fisher Yuval ,"Fractal Image Encoding and Analysis", Springer 1998.
6. Jähne Bernd ,'Practical Handbook on Image Processing for Scientific Application', CRC Press, New York, 1997.
7. Bigün, J., and J. M. H. du Buf, ' N-folded symmetries by complex moments in Gabor spaces and their application to unsupervised texture analysis', *IEEE Transactions, 1994.*
8. Barnsley M.F. "Fractals Everywhere", Academic Press Professional 1993.
9. W. Niblack, R. Barber, W. Equitz, M. Flickner, E. Glasman, D. Petkovic, P. Yanker, C. Faloutsos, and G. Tubing, The QBIC Project: Querying Images by Content Using Color, Texture, and Shape in Storage and Retrieval for Image and Video Databases ,

Proceedings of SPIE, SPIE, Vol. 1908, Bellingham, WA, 1993, pages 173-187.

10. H. Samet and A. Soffer. MARCO: Map Retrieval by Content. IEEE Transactions on Pattern Analysis and Machine Intelligence, 18(8):1996, 783-798.
11. Ramesh Jain and Amarnath Gupta. Computer vision and visual information retrieval . In Festschrift for Prof. Azriel Rosenfeld. IEEE Computer Soc.,1996.
12. Toshiaki Kondo and Hong Yan. Automatic Human Face Detection and Recognition under Non-uniform Illumination the 4th International Conference on Control, Automation,Robotics and Vision (ICARCV '96), Singapore, 3-6 , December,1996.
13. I. Craw, N. Costen, T. Kato, S. Akamatsu. " How Should We Represent Faces for Automatic Recognition?", IEEE on Transactions Pattern Analysis and Machine Intelligence, 21(8):1999, 725-736.
14. Roger N. Shepard Toward a universal law of generalization for physical Science, 237: 1988, 1317-1323.
15. Carol L Krumhansl. Concerning the applicability of geometric models to similarity data: The interrelationship between similarity and spatial density, Psychological Review, 85:1978, 445-463.
16. Simone Santini and Ramesh Jain ," Image Databases are not Databases with Images" Proceedings of the 9th Int. Conf, Vol. II, Florence, Italy , 1977, pp 38-45.
17. Carol L Krumhansl. Concerning the applicability of geometric models to similarity data: The interrelationship between similarity and spatial density, Psychological Review, 85:1978, 445-463.
18. Mandal Maya and Mandal Ajit K., 'Wavelet Metric For Matching Distorted Images', Proceedings of the 4th International Conference on Advances in Pattern Recognition and Digital Techniques (ICAPRDT,99), Indian Statistical Institute, Calcutta, December, 27-29, 1999, pp 413-417.
19. Mandal M., Lahiri T. ,Jena U. R. , Das Gupta M., and Mandal A. K., 'Sub-region Fuzzy Features for Image Retrieval', *Journal of Science & Industrial Research*, vol. 59, Dec. 2000, pp. 1012-1022.
20. Charles E. Jacobs, Adam Finkelstein, and David H. Salesin "Fast multi-resolution image querying" Proceedings of SIGGRAPH '95, ACM, New York, 1995, pages 277-286.
21. Fisher Yuval, 'Fractal Image Compression - Theory and Application' , Springer, New York 1996

Digital image Watermarking: A technique for secure transmission

Santi. P. Maity [a] and Malay K. Kundu [b]

[a] Electronics & Telecommunication Engg Dept.., Bengal Engineering College(D.U),
P.O.-Botanic Garden, Howrah-711103, (spmaity@yahoo.com).

[b]Machine Intelligence Unit, Indian Statistical Institute, 203, B.T.Road, Kolkata-700 035, India
(malay@isical.ac.in)

Abstract

The present paper describes a watermarking scheme where a watermark symbol (image) is first spread over a larger size using a Pseudo-random Noise (PN) sequence (key) and is then randomly embedded in the original image. Spatial mask of suitable size is used to hide visual data without perceptual degradation. Proposed scheme needs only the keys for watermark extraction. In absence of such keys, the complete decryption is almost impossible hence ensures security. Experimental result shows that the proposed scheme is resistant to common external attacks like mean & median filtering, image cropping, deliberate bit manipulation of pixel values and lossy (JPEG like) compression.

Key words: Digital Watermark, PN sequence, decryption, and JPEG compression.

INTRODUCTION

Digital representation of copyrighted material such as songs, photograph, movie and other form of information become available in the digital form. This offers advantages like the ease of access, portability, efficiency and accuracy of the information content along with the inherent disadvantages like possibility of large-scale unauthorized copying with violation of copyright and manipulation of the information content. The currently available formats for image, audio, image and video do not allow any kind of copyright or propriety protection.

One potential solution for claiming the ownership of an image is to use electronic stamps or signature known as digital watermark or watermark in short [1,2,3]. In some techniques, the watermarks are faintly visible, but in most of the current techniques they are completely invisible.

. Invisible watermarks can be classified as fragile watermarks and robust watermarks. Fragile watermark are susceptible to destruction by common external attacks while robust watermark is designed to withstand most of the attacks [4]. An ideal digital watermarking technique should have following properties [5].

Perceptually invisible i.e. watermark should not alter perceived quality and content of the digital image data.

Undetectable by hackers and difficult for decryption.

Robustness against various external attacks, like, mean & median filtering, D/A & A/D conversion, re-sampling /re-quantization, lossy compression, common geometric transformation (such as rotation, translation), cropping and scaling.

Resistant to insertion of other watermarks for rightful ownership (it is a maximal capacity requirement)[6].

Between two types of watermarking technique, spatial domain scheme is easy to implement but too fragile to withstand external attack while frequency or transform domain approach offers robust [7] watermarking with higher noise immunity but in most cases require higher computational cost. Apart from these attacks mentioned earlier, hidden data may be lost because of poor performance of the transmission channel when the watermarked image is transmitted. Under this situation to increase data reliability at the distant receiver, one popular scheme, used in digital communication is to repeat a bit pattern several times and then decision is made based on majority rule. Among the various watermarking schemes, private watermarking systems require the original image and a copy of the embedded watermark for extraction while public watermarking systems are those that require neither the original image nor the embedded watermark during the detection process. We propose a spatial domain public watermarking scheme with ease of implementation along

with a flavor of spread spectrum scheme [8]. Here a binary watermark symbol is spread over a larger size using a Pseudo-random Noise sequence (PN sequence) of suitable length to have its noise like structure.

WATERMARK INSERTION

The original image I may be a gray-level image of size N x N where $N= 2^p$ and digital watermark W is a two level image of size M x M where $M=2^n$ so that the original image I and digital watermark W may be expressed as $I= (i (x, y))$, $0\leq x <N$, $0\leq y <N$, where $i (x, y)\in \{0,1.....2^r -1\}$ is the intensity of pixel at (x, y) and r is number of bits used to represent each pixel. $W=\{w (x, y)\}$ where $0<x<M$, $0\leq y<M$ and $w (x, y)\in \{1,0\}$. About the values of p and n, $n<p$ and p is product of z and n where z is an integer number greater than one. In our case we consider a binary watermark of size (16x16) and (256x256), 8bits/pixel gray image as original image.

Step I.

First the original image is transformed to one dimensional sequence of the pixel by raster scanning and call the sequence a grayscale sequence .The grayscale sequence is expressed as $G=[g_0g_1g_2..g_{L-1}]^T$. Based on the size of the watermark symbol, a PN sequence(say PN1) of suitable length, say of length q, (in present case q =256 i.e. 2^8) is generated using "Linear Feedback Shift Register"[9] and then watermark is spread over the image size using this sequence (key) so that watermark image becomes dimensionally same to that of original image i.e. N x N= M x M x q. Watermark spreading is accomplished by considering bit wise X-OR operation of each watermark information with PN1.

Step II.

Another random sequence(say PN2) from 1 to N x N (in present case N=256) is generated & each bit information of spread watermark obtained in step I then replaces a particular bit in bit plane representation of pixels of the original image in a random manner according to the sequence generated in step II i.e. PN2. The selection of this particular bit in bit plane representation of gray value is fixed for a pixel but is not fixed for all pixels of the image. This way watermark information is inserted in the original image. Say any pixel after this operation has gray value W_1 and say watermark information is inserted in third Least Significant Bit (LSB) of bit plane representation of W_1

Step III.

To accommodate the effect of the possible attack like Low pass filtering and for possible survival of the embedded information the bit pattern is further manipulated according to some predefined norms by exploiting spatial masking effect of suitable size so that watermark information placed in the third Least Significant Bit of W_1 remain unchanged even after non destructive operation like mean and median filtering. The manipulation could be either overall increase or decrease of gray values of the pixel.

WATERMARK EXTRACTION

Our scheme requires neither the original image nor the watermarked image or watermark for its extraction, only except the keys (PN sequences) used to spread the watermark and for its random insertion in original image.

First the corrupted watermarked image is transformed to one-dimensional sequence of the pixel and gray value of each pixel is then converted in bit plane representation. Watermark information is picked up from the pixel number generated by PN2. The sequence of data thus formed is restored

With the help of PN1 used in step I. (inverse of spreading). This is accomplished by considering X-OR operation of each sequence of q binary data thus obtained with PN 1 used in step I and for the resultant string of length q, a decision is made based on majority rule. This inverse spreading process converts data sequence of length (2^p x 2^p) as a sequence of length 2^{2n} which is then converted into a matrix of size (2^n x 2^n). This is the watermark image inserted in the original image.

Similarity Measurement:

Since our data-hiding scheme uses an image (two level) pattern as watermark, visual degradation of extracted watermark may be compared with reference to the original watermark image. This subjective measurement and degradation of extracted watermark depends on viewer expertise, nature of non-destructive operation, sometimes may be structure of the watermark, local and global characteristics of image to be watermarked and the experimental conditions. A quantitative estimation of the extracted image quality may be done by measuring similarity between reference watermark W and extracted watermark W'. This is known as normalized cross correlation (NCC). and is expressed as (NCC) = $\sum_x \sum_y W (x, y) W' (x, y) / \sum_x \sum_y [W (x, y)]^2$ which is the cross correlation normalized by the watermark energy to make the maximum value of NCC to be unity.

RESULTS AND DISCUSSIONS

In the present work a binary image of size much Lower compared to that of image to be watermarked is used. Watermark insertion occurs randomly in suitable bit plane

based on image property & hence change in pixel values not always perceived by human eye. More over, spatial masking effect used in data manipulation also helps to make data hiding perceptually invisible on and average half the time. If we consider larger size of spatial mask, data insertion becomes perceptually invisible since we know the eye acts as a spatial low pass filter [10,11].

Figure.1 shows cameraman image of size 256x256 and 256 gray levels is used as original image (figure.1) and figure.2 is the corresponding watermarked image. The figure.3 is the binary watermark image of size 16x16. PSNR of the watermarked image compared to the original image is about 36.6174 dB. Therefore, quality degradations of the watermarked image are hardly perceivable to a human eye.

A. Image Filtering operation: Mean and Median Filtering:

To make this watermarking resistant to mean and median filtering, typical manipulation on bit planes are performed using some predefined norms such that the embedded watermark information is preserved even after mean filtering operation This process also helps in preserving watermark, even after several passes of median filtering of the watermarked image.

Figure.8 shows extracted watermark (NCC=0.994) from blurred version of watermarked image (after mean filtering) with PSNR 25.3763 dB. Water marked image after mean filtering is shown in figure 6.To reduce significantly the blurring effect, median filtering is applied on image. Figure 5 shows extracted watermark (NCC=1) from corrupted watermarked image (PSNR=26.70 dB after median filtering. Extracted watermark is exactly same to that of original watermark. Extracted watermark is fully recognizable even after five times median filtering of the watermarked image.

B. Image Cropping Operation:

Sometimes some rows and columns around the border of an image are deliberately cropped off by the hackers for possible removal of hidden watermark. If watermark is spatially spread all over the image before its insertion, it is really difficult for an outsider to detect or remove the watermark by cutting some part of the image. We have tested image cropping operation by removing 20 to 25 rows and columns from the border of the image and

Removed rows and columns of image are filled with arbitrary value (say 0). Experimental result shows if watermark is inserted in original sequence instead of in a pseudo-random fashion, data loss for extracted watermark is more. Figure. 11 shows extracted watermark after filling 20 rows and columns (10 from each side) by zero values.

C. JPEG Compression:

Watermark information is inserted in all pixels of the original image and each bit of watermark information is placed in multiple places. Since the energy of most natural images are concentrated on the lower frequency range, it is expected that watermark information placed in relatively low frequency zone of the original image might not be lost in the quantization operation of lossy data compression up to that extent till the watermarked image is not degraded severely due to high degree of compression. Figure.7 shows the extracted watermark (NCC=0.958) from JPEG compressed version of the watermarked image (PSNR=18.73 dB) with compression ratio (C.R)= 11.306. Figure.4 shows watermarked image after JPEG compression. As compression ratio increases, NCC value of the extracted watermark decreases and watermark is destroyed and become indiscernible. This is due to the fact that at high values of compression ratio both watermark as well as original image are degraded to such an extent so that processes of digital watermarking becomes less meaningful.

D. Deliberate Least Significant Bits manipulation:

Least Significant bit(s) for all randomly selected pixels in the watermarked image are complemented. The extracted watermark could be recognized unto to a certain level of bit alteration.

Table 1 shows test rest of digital watermarking for cameraman, lean and fishing boat images. For all three images watermarking scheme shows satisfactory result for all possible attack mentioned in this section. Figure.9 and figure.10 such two other test image lean and fishing boat respectively.

CONCLUSIONS

Proposed technique has been tested over large number of benchmark images as suggested by watermarking committee and for all images the watermark technique survive common external attack like mean and median filtering, JPEG compression, Image cropping operation and deliberate bit manipulation of pixels. Table.1 shows test result of digital watermarking for three such images like cameraman, Lena and fishing boat. The zoomed watermark image is found to be visually indistinguishable from the original image. The obtainable quality of the extracted watermark symbol as well as watermarked image in this method depends on the ratio of relative size of the original image to that of watermark symbol and of course on the nature of the original image.

Currently investigation are being carried out to make the proposed spatial domain watermarking technique resistant

other kinds of external attacks, such as the image re-sampling, flip and image rotation. Investigation is also being carried out to develop more robust but computationally less expensive frequency domain technique for watermarking.

Test Image	Attack	PSNR (dB)	Retrieval of logo NC value
Camera man	Nil	36.6174	Yes (1.0)
	Mean filter	25.37	Yes (0.994)
	Median filter	26.70	Yes (1.0)
	JPEG CR.11.3	187369	Yes (0.9583)
Fishing boat	Nil	36.78	Yes (1.0)
	Mean filter	24.83	Yes (0.89)
	Median filter	25.25	Yes (1.0)
	JPEG CR.9.10	17.4914	Yes (0.90)
Lena	Nil	36.39	Yes (1.0)
	Mean filter	27.13	Yes (0.81)
	Median filter	28.59	Yes (1.0)
	JPEG CR.11.2	17.915	Yes (0.85)

Table 1. Test result of the watermarking scheme

REFERENCES

[1] R. Anderson, ``Information Hiding'', Proceedings of the first Workshop on Information Hiding, LNCS-1174, Springer- Vela, New York, 1996

[2] N.F. Johnson and S. Jajodia, " Exploring steganography, seeing unseen," Computer, vol.31, pp. 26-34, 1998

[3] S. Katzenbesser and F. A .P Petitcolos, Information Hiding Technique for steganography and digital watermarking, Artech House, USA, 2000.

[4] E. T. Lin, Christine I. Podilchuk, Edward J. Delp,``Detaction of image alterations using semi-fragile watermarks" In Security and Watermarking of Multimedia Contents II, Ping Wash Wang, Edward J. Delp (Eds.), the proceedings of SPIE vol..3971, 2000.

[5] C- T. Hsu and J. L. Wu "Hidden Digital Watermarks in Images ", IEEE Transaction on Image Processing , vol. 8 , pp. 58-68, 1999.

[6] S. Suthaharan, S.W. Kin, H.K. Lee, S. Sathananthan,"Perceptually tuned robudt watermarking scheme for digital Images", Pattern Recognation Letters, vol. 21, pp.145-149, 2000.

[7] S. Jain,`` Digital watermarking Techniques:-Acase study in finger prints and faces'', Proceedings of the Indian Conference on Computer Vision, Graphics and Image Processing (ICVGIP-2000), pp.139-142, December 20-22, Bangalore, India.

[8] J. Cox, J. Kilian, T. Leighton, and T. Shammon,,``Secure Spread Spectrum watermarking for multimedia'' IEEE Transaction on Image Processing, vol. 6, pp. 1673—1687, 1997.

[9] B Sklar, Digital Communication, Prentice Hall, Englewood cliffs, N.J, 1998.

[10] F. W. Cambell, `` The Human Eyes as optical filter'', Proceedings of the IEEE , vol. 56, pp.1009-1014, 1968.

[11] J.L.Mannos and D.J. Sakrison ,.``The effect of a visiual Fidelity Criterion on the encoding of images'', .IEEE Transaction on Information Theory, vol.20, pp. 525-536, 1974..

Document Skew Detection Algorithm

M. V. Raghunadh, N. S. Murthy and K. Kishan Rao
Communication Systems laboratory, ECE Department
Regional Engineering College, Warangal 506004

Abstract

A document skew detection algorithm based on the hierarchical Hough Transforms is presented in this paper. It is capable of detecting the skew angle for various document images, including letter, hand written text, and barcodes. The algorithm is robust even when black-margins introduced by photocopying are present in the image and when the document is scanned at a low resolution of 50 dpi. The algorithm consists of two steps. In the first step, it quickly extracts centroids of the character. Then, a hierarchical Hough transform is applied to the selected centroids. The skew angle corresponds to the location of the highest peak in the Hough space. The performance of the algorithm is shown on a number of document images collected from various application domains. The algorithm is able to detect the skew angle with an accuracy of 0.1.

INTRODUCTION

A text line in document is defined as a group of characters, symbols, and words that are adjacent, relatively close to each other, and through which a straight line can be drawn. The dominant orientation shared by major text lines in a document determines the skew angle of that document. A document with a zero skew angle should have horizontally or vertically printed text lines, which are parallel to the respective edges of the paper. Figures 1(a), (b) and (c) show synthetic document images with zero skew angle, a skew of 45 0 , and non skew respectively. The conversion of paper document to electronic format is routinely performed for records management, archiving and many other applications. The principal stages in a document conversion system are scanning, binarization, region segmentation, text recognition and document analysis that includes steps for simple spelling checking process. If the document is not fed properly into the scanner, the text lines in the image would not be horizontal, and that may cause problems in segmenting the image to extract its layout structure. For example, in the most commonly used method of profiling [1], in the presence of skew there would not be valleys in the projection histogram and segmentation would not be possible. Skew detection and removal is a very important stage in document analysis.

Figure 1: A synthetic document image with (a) zero skew angle, (b) a skew angle of 45° , (c) a document image where text is not aligned along a straight line

Researchers for skew angle detection have developed several methods. It can be determined from document edges [2] or text again. Dengel [1] used the method of left margin search. The position of the first black pixel in each row of the image is stored in a vector. Using this vector, straight-line segments that describe left margin of layout objects (words, text lines, and blocks) are determined. The gradient of the straight line defines its angle with respect to the vertical orientation. But it does not provide an exact measure of the skew of the base line of text, particularly in presence of graphics region starting from the left margin.

Ciardiello have suggested a method using the projection histogram [3]. In this method, a sample region is rotated by pre-specified angles. The histogram of the horizontal projection of the region is evaluated for each angle. The skew angle corresponds to a rotation for which the mean square deviation of the histogram is maximized. In this method the rotation of the Cartesian grid has proved to be computationally expensive. Postl has proposed a method based on Fourier transform [4]. The direction for which the density in the Fourier spectrum is the largest gives the skew angle. However, computation of the Fourier transform may be quite time-consuming for large images.

As shown in Fig. 2, the skew detection algorithm presented in this paper consists of three steps. The first step quickly extracts the connected components based on a graph data structure, called Block Adjacency Graph (BAG). The second step is the selection of components based on the size of their bounding boxes by using the standard normal curve areas, that mean most of characters would be selected and exclude irregular characters (table, line, picture etc), and find the centroids of those components. And the last step is the skew detection by a Hierarchical Hough transform (HHT) algorithm, which performs the skew detection at two angular resolution levels, coarse and fine, with an improved HT.

EXTRACTING CONNECTED COMPONENTS

The information needed to determine the correlation of each character's blocks should include the closely blocks to large block that is boundary of character's block. Yu et al. [6] described the Block Adjacency Graph (BAG), which was used to extract the contours of the connected components in a binary image. This data structure can be created concurrently when the document is being scanned row by row. Processing steps such as contour extraction, vectorization and feature extraction are efficiently implemented based on this data structure [8].

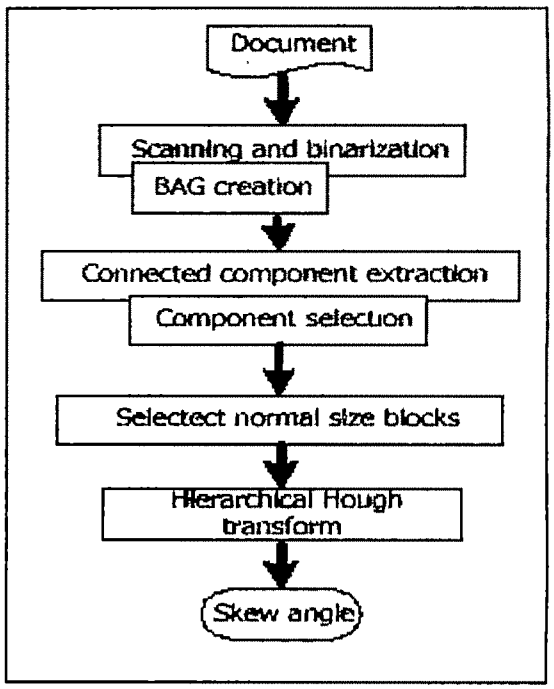

Figure 2: Block diagram of the skew detection algorithm

The binary image page is represented by P as a BAG which is defined as B= (N,∈), where N = $\{n_i\}$, is a set of block nodes and ∈ is $\{e(n_i, n_j) \mid n_i, n_j \in N\}$ is the set of edges indicating the connection between nodes n_i and n_j . Each node n_i is a block, which contains either one or several run lengths stacked together and aligned on the left and right seeds. Each node or a block is characterized by its upper left and lower right rectangular boundary coordinates $((X_u, Y_u),(X_v, Y_v))$where $X_u < X_v$ and $Y_u < Y_v$. The algorithm for creating a BAG from a binary image is given in Fig. 3. Note that BAG can be created as the image is scanned in a faster fashion.

SELECTION OF COMPONENTS BASED ON THE SIZE

The computational cost of BHT depends on the quantity of character's blocks, which have several sizes. There are many techniques for reducing the unnecessary block. In this approach, the standard normal curve area is introduced, that is method of statistic to separate some big or small blocks that are out of deviation is used.

The size of block is represented by $\lambda(n_{(X,Y)}) = (X_u - X_v) \times (Y_u - Y_v)$which acquires from the product of $(X_u - X_v)$ and $(Y_u - Y_v)$, mean (μ) and deviation of block's area(σ) are given by the following equations.

Each run length, r_i in the first row of the input image is regarded as a new block node n_i. For a new node, its geometric measure is the coordinates of its upper left and lower right vertices $((X_{ul}, Y_{ul}), (X_{lr}, Y_{lr}))$ initialized as X_{ul} $x_s(r), Y_{ul}$ $y(r)$ and X_{lr} $x_e(r)$, Y_{ul} $y(r)$, where $x_s(r), x_e(r)$ and $y(r)$ denote the beginning and ending column numbers are row number of run length r.

For the successive rows in the image{

For each run length r_c in the current row{

If r_c is 8- connected to a run length in the preceding row{

If r_c is 8- connected to only one run length r_l and r_l connects to only r_c below it and $x_s(r_c)$-$X_{ul}(n_l)$ $\leq T_a$ and $X_e(r_c)$-$X_{lr}(n_l)$ $\leq T_a$ then r_c is merged into the block node n_l, where n_l is the block node involving r_l. X_{ul} Average $r_k \in n_l$ $\{X_s(r_k)\}$, X_{lr} Average $r_k \in n_l$ $\{X_e(r_k)\}$ and Y_{ul} Y_{lr}.

Else, r_c is regarded as a new block node n_i.

initialized with edges $e(n_i, n_j)$ to those block nodes $\{n_j\}$ in which there is a run length 8- connected to r_c

}

Else, r_c is regarded as a new block node n_i.

}}

Figure 3: Algorithm for generating BAG data structure

$$\mu = \frac{1}{N}\sum_{n=1}^{N-1} \lambda(n) \qquad \text{and}$$

$$\sigma = \sqrt{\frac{1}{N}\sum_{n=1}^{N-1} (\lambda(n)-\mu)^2}$$

Assume that the distribution of block's area is Gaussian distribution, there can use the standard value and the standard normal curve area to find the cut off point for small and big block's area. The standard value is represent by Z , which controls the size of good blocks via the following formula:

$$Z = \frac{\lambda - \mu}{\sigma} \qquad \text{and} \qquad P(\lambda_z) = \int \frac{1}{\sqrt{2\pi}} e^{-\frac{z^2}{2}}\, dz$$

The suitable value of Z can be obtained from the Table of Normal Curve Areas, which give values of population of all blocks presented by $P(\lambda_z)$. Typically $P(\lambda_z)$ = 50% for all blocks, then Z=0.674 , so that the cut off small point and big point are given by $\lambda(n_s) = \mu - 0.674\,\sigma$ and $\lambda(n_b) = \mu + 0.674\,\sigma$ respectively, then this technique can reduce 50% computational cost, and noise for Hough transform method. The result of this step is shown in Fig. 4.

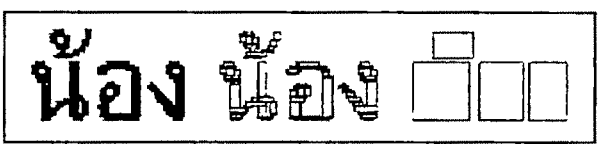

Figure 4: BAG representation of an image. (a) Binary image. (b) BAG (each rectangular block is represented as a node in the BAG). (c)Character blocks (integral closely node in the BAG)

SKEW DETECTION BY HIERARCHICAL HOUGH TRANSFORM

Hough Transform [7] is a well-known technique for detection lines and curves in an image. For line detection, a set of points in Cartesian space is mapped to sinusoidal curves in the Hough space $(\rho - \theta)$_ via the following transform:

$$\rho = x \cos\theta + y \sin\theta \qquad (5)$$

Each time a sinusoidal curve intersects another curve at a particular value of ρ and θ, the likelihood that a line corresponding to that (ρ,θ) coordinate value presents in the original image is increased by using an accumulator array

$H(\rho,\theta)$. The computational steps in the BHT are given in Fig. 5.

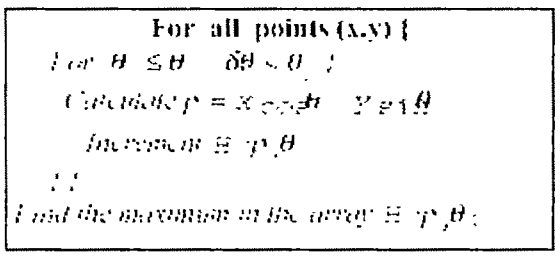

Figure 5 : Computational steps in basic Hough Transform

The computation cost of the BHT is represented by ξ_c (Nψ), where N is the number of points in Cartesian space and $\psi = \Delta\theta/\delta\theta$, where $\Delta\theta = \theta_2 - \theta_1$, $0^\circ < \theta_1$, $\theta_2 < 180^\circ$ and $\theta_1 < \theta_2$. The parameter $\delta\theta$ is the angular resolution, which controls the accuracy of the skew detection (orientation of the line). For computational reasons, most skew detection algorithms employing the HT, limit themselves to only a subset of (0° ,180°) that is possible angle of image. The computational cost can be decreased by reducing the number of point (X,Y) and $\Delta\theta$ or increasing the interval $\delta\theta$. Then, one can select a relatively large value of $\delta\theta$, say $\delta\theta_1$ to determine the skew angle θ in the desired angular range $\Delta\theta$. Then the BHT is implemented again with desired angular resolution $\delta\theta_0$ within the reduced range ($\theta - \delta\theta_1$, $\theta + \delta\theta_1$), $\delta\theta_0 < \delta\theta_1$. This method is called the hierarchical Hough transform (HHT). The computational complexity of HHT is ξ_c (Nψ$_1$) + ξ_c (Nψ$_2$) = ξ_c (Nψ$_H$), where

$$\psi_H = \psi_1 + \psi_2 = \frac{2\delta\theta_1}{\delta\theta_0} + \frac{\Delta\theta}{\delta\theta_1} \qquad (6)$$

Minimize the value of ψ_H , by using the derivative of Equation (2)

$$\frac{d\psi_H}{d\delta\theta_1} = 0$$

and solving for $\delta\theta_1$, so that the result is

$$\delta\theta_1 = \sqrt{0.5\Delta\theta\delta\theta_0} \quad \text{and} \quad \psi_H = \sqrt{\frac{8\Delta\theta}{\delta\theta_0}} \qquad (7)$$

For traditional HT, $\psi_T = \frac{\Delta\theta}{\delta\theta_0}$, Therefore

$$\frac{\psi_H}{\psi_T} = \sqrt{\frac{8\delta\theta_0}{\Delta\theta}} \qquad (8)$$

Equation 7 is used to determine the optimum value of $\delta\theta_1$ for given values of $\Delta\theta$ and $\delta\theta_0$. Typically, $\Delta\theta = 180^\circ$ and $0.05^\circ \le \delta\theta_0 \le 0.5^\circ$. If $\delta\theta_0 = 0.1^\circ$, then from eqn. (7), $\delta\theta_1 = 3.0^\circ$ and $\psi_H / \psi_T = 0.07$ are obtained. These values reduce the complexity of the HT from ξ_c(1800N) to ξ_c(120N)

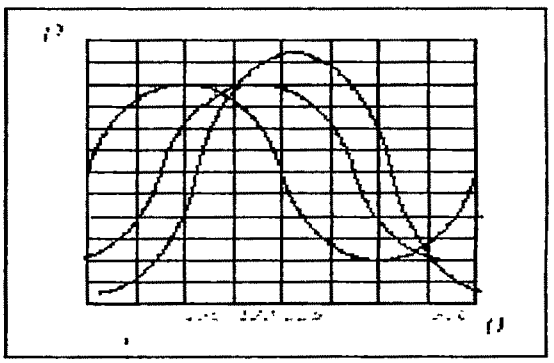

Figure 6 . The improved HT algorithm that finds the current peak at 135°

IMPROVEMENTS IN HOUGH TRANSFORM

To match the requirement of the hierarchical strategy for skew detection, the traditional HT as given in Fig 5 is improved in two respects. In the HT given in Fig. 5, the value assigned to a cell in the Hough space is the number of the sinusoid curves going through this cell. In order to avoid the possibility that the desired skew angle is not in the neighborhood of the angle θ obtained during coarse detection ($\theta - \delta\theta_1$, $\theta + \delta\theta_1$), one should use an integral of the sinusoid curve within a cell in the Hough space as the value assigned to it. For a simple example involving a two-point HT (see Fig. 6), the improved HT algorithm will find the correct peak at 135 o rather than at 180 o . Note that both the accumulator cells are assigned a value of 3 by the basic HT algorithm. The improved algorithm is show in Fig. 7.

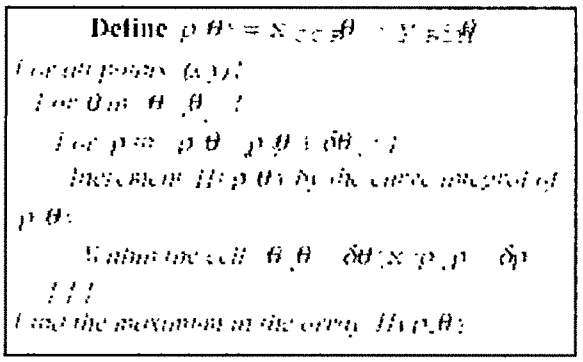

Figure 7: The improved basic Hough transform algorithm.

RESULTS

The skew detection algorithm proposed in this paper has been applied to several sizes and angles of document. For example input image show in Fig. 8 (a), (c), (e) and (g) respectively from the newspaper that was scanned with resolution 300 dpi. In our experiments, its performance is tested with $\delta\theta o = 0.1^0$, $\delta\theta = 180^0$. Therefore $\delta\theta_1 = 3^0$. The results are in Fig. 8 (b), (d), (f) and (h) respectively.

CONCLUSION

This research can be used for skew detection of document which is not fed properly into the scanner. Hough Transform (HT) can be applied to find the skew in the document but the computational cost is expensive. Therefore, selection of components based on the size by comparison with standard deviation and HT method be improved to hierarchical (HHT) in order to reduce the computational cost. The algorithm has been shown to be able to handle document image scanned at a resolution of 300 dpi which contains a little of character.

REFERENCES

1. A.Dengel, "ANASTASIL: A System for low-level and high-level geometric analysis of printed documents," in Structured Document Image Analysis, H. S. Baird, et al., Eds. New York: Springer-Verlag, 1992, pp 70-99.
2. B. Yu, X. Lin, Y. Wu, and B. Yuan, " Isothetic polygon representation for contours, " CVGIP: Image Understanding, vol. 56, pp. 264-268, 1992.
3. B. Yu,. "A method for automatic understanding of symbol connected diagrams", Proc. 3 rd Int. Conf. on Document Analysis and Recognition, (Montreal), pp. 803-806, 1995.
4. Rafael C. Gonzalez, Richard E. Woods, " Digital Image Processing", Addison - Wesley Publishing Company, Pearson Education, New Delhi, 2000.
5. G.J.Awcock and R.Thomas, "Applied Digital Image Processing", Macmillan Press, London, 1995.

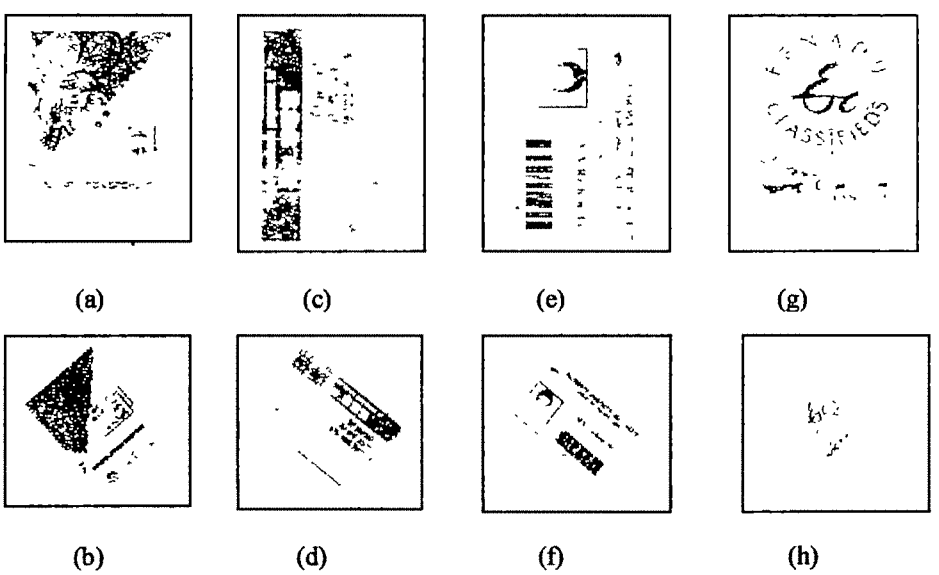

Figure 8 Experimental results

RLS Algorithm Based Sub-Band Decomposition And Application To Reduced Memory Image Compression

Suprava Patnaik
Electrical Engineering Department,
Regional Engineering College, Rourkela, India
E-mail: npatnaik1@vsnl.com

Abstract

In this paper a neural-network based recursive algorithm for computation of the principal component of a stationary vector stochastic process is discussed. Neurons of a network are trained sequentially, using recursive least square (RLS) algorithm to extract the principal components of the input process. The optimal criteria is to retain the maximum information contained of the input, so as to be able to reconstruct the network inputs from the corresponding outputs with minimum mean square error. In this paper a multi-stage principal component extraction (PCE) algorithm is proposed for sub-band decomposition. Though wavelet or sub-band coding of image has been shown to be superior to more traditional transform coding techniques, little attention has been paid to the important issue of whether both the wavelet transforms and the subsequent can be implemented in low memory without significant loss in performance. This paper addresses the problem of low memory image compression and proposes a block based, reduced memory PCE based, image compression algorithm.

Key words: RLS algorithm, sub-band coding, image compression

INTRODUCTION

Though Karhunen-Loeve (KL) transform is considered as the optimal transform, from efficient data compaction point of view, its conventional approach of evaluation requires the computation of input data covariance matrix. For large data sets, the dimensions of the covariance matrix grow significantly large making its computation and manipulation practically inefficient and inaccurate. As a result a method to evaluate most significant eigenvectors of the data covariance matrix without the need to form this matrix is required.

At first Oja[1] introduced a simple linear neuron model with constrained Hebbian type updating and proved the convergence of the weight vector to the principal component of the stationary input vector sequence. Sanger extended this to multi neuron case. Kung proposed a procedure for recursive computation of the principal components based on a sequential training. Recently, RLS learning based algorithms are presented [3,4] which, offer fast convergence without sacrificing the accuracy. This is achieved by using an adaptable step size or gain factor.

Recently wavelet based coder dealing with sub-band decomposition have been shown to outperform DCT based coders in terms of compression efficiency, but their implementations have not yet reached the stage of maturity as that of DCT based approach. Existing DCT as defined under JPEG standard are very efficient in their memory utilization because, if needed, they can operate on individual image blocks and thus the minimum amount of memory they require will be low. Memory efficiency is being one of the key issues to be addressed before a widespread deployment of, wavelet based sub-band decomposition CODEC technique takes place. It is currently one area of major research activity within the JPEG2000 standardization process. Thus there is a need of block based sub-band coding, which will retaining the beauty of wavelet based decomposition as well as making manipulation of a single image block possible if needed. Later part of the paper proposes a multi-stage PCE for sub-band decomposition for image compression, which works on image blocks and transformation based on this results sub-band decomposition analogous to multi-level wavelet transformation.

RLS ALGORITHM BASED PCE

The present method relies on the analogy between adaptive filter and neural network. In adaptive filtering, the RLS algorithm is typically an order of magnitude faster than the LMS algorithm. Since LMS is equivalent to the back-propagation (BP) algorithm in one-layer network, one can expect faster learning with RLS method. For a two layer auto-associative net-work with a single neuron at the hidden layer and with a constraint that $w_2 = w_1^t$, the performance index at time 'n' is equivalent to

$$J_1(n) = \frac{1}{n}\sum_{k=1}^{n} \varepsilon_1^t(k)\varepsilon_1(k)$$

$$= \frac{1}{n}\sum_{k=1}^{n} [d_1(k) - g(k)\, w_1(k)]^t\, [d_1(k) - g(k)\, w_1(k)]$$

where, $g(n) = w_1^t(n-1)\, x(n)$ w_1 and w_2 are the weight vectors connecting input neurons and output neurons to the hidden neuron respectively.

Assuming that current weight estimate $\hat{w}_1(n)$ is used in place of old weight $w_1(n-1)$, $k \in [0,n-1]$, the performance index can be minimized for $\hat{w}_1(n)$ by taking the partial derivative of $J_1(n)$ w.r.t $\hat{w}_1(n)$ and setting it to zero, which gives the normal equation

$$\sum_{k=1}^{n} g(k)[d(k) - g(k).\, w_1(k)] = 0$$

or, $$\sum_{k=1}^{n} w_1^t x(k)[d(k) - g(k).\, w_1(k)] = 0$$

which can be written in vector form as

$$r_n = R(n)\, w_1(n)$$

where, $$R(n) = \sum_{k=1}^{n} x(k)\, x(k)^t$$

$$= R(n-1) + x(n)\, x(n)^t$$

$R(n)$ is the correlation matrix and

$$r_n = \sum_{k=1}^{n} x(k)\, d^t(k) = r_{n-1} + x(n)\, d^t(n)$$

where r_n is the cross correlation vector.

Applying Matrix Inversion Lemma we get

$$P(n) = R^{-1}(n) = [1 - h(n)\, g(n)]\, P(n-1)$$

where $$h(n) = \frac{P(n-1)g(n)}{1 + g(n)^2 P(n-1)}$$

But $w_1(n) = R(n)^{-1} r_n$

$$= P(n)\, r_{n-1} + P(n)x(n)\, d^t(n)$$

$$= P(n-1)\, r_{n-1} - h(n)x(n)^t\, P(n-1)\, r_{n-1} + P(n)x(n)\, d^t(n)$$

$$= w_1(n-1) + h(n)\varepsilon(n)$$

and the estimated weight vector approaches the principal eigen vector of the input data space.

For m^{th} eigen vector estimation (network with m-hidden nodes), the mean of the input data space (image) is subtracted from each data vector to obtain zero mean training input space. $P(n)$ is initialised to 0.5 and weight vector to small random values. Network training is done sequentially , i.e. m^{th} neuron training is done assuming that m-1 previous neurons have already been trained and corresponding extracted principal components are $g_i(n) = \hat{w}_i\, x(n)$.

Learning algorithm for m^{th} neuron are as follows

$$g(n) = w_m^t\, (n-1)\, x(n)$$

$$h(n) = \frac{P(n-1)g(n)}{1 + g(n)^2 P(n-1)}$$

$$\hat{w}_m(n) = \hat{w}_m(n-1) + h(n)\varepsilon(n)$$

$$P(n) = [1 - h(n)\, g(n)]\, P(n-1)$$

where $$\varepsilon(n) = x(n) - \sum_{i<m} \hat{g}_i(n)\hat{w}_i - g_m(n)\hat{w}_m(n-1)$$

MULTI-STAGE RLS FOR SUB-BAND CODING

Keeping in mind the fruitful results obtained from multi-level wavelet transform present paper extends application of RLS to sub-band decomposition. For this purpose input image is partitioned into a series of non-overlapping blocks of size 'n x n'. By row or column ordering the pixel, we get a series of one-dimensional input vectors of size n^2. These are considered as training samples. The choice of the block size is a trade-off between the accuracy in estimating the principal components and the computational and architectural complexity of the algorithm. However in most of the real images though the neighbouring pixels are highly correlated, as the spatial distance increases the amount of correlation decreases substantially. This deteriorates the mean square accuracy. Blocks of, smaller size though not efficient from compression point of view improves accuracy of estimation with low computational complexity. As we know using wavelet transforms do not give rise to any compression at the transformation stage by itself but its beauty lies in the associated data classification in a time- frequency scale. Similarly RLS based sub-band decomposition with a block size 2 x 2 will also estimate the principal components more accurately and preserve the information content of input space efficiently though will not provide any compression at this stage. Detail of the network structure for n^{th} stage is shown in fig-1. Fig-2 shows the two-stage decomposed image block diagram.

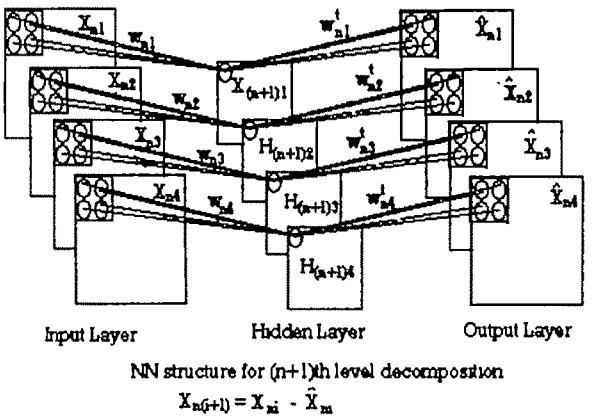

Fig 1 Network structure

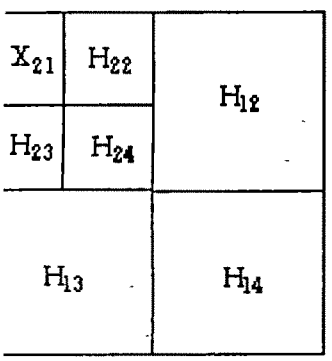

Fig 2 Image block diagram

Assuming the rank of a 2 x 2 matrix to be four at each stage network is trained for four eigen vectors which is equivalent to extract four principal components and requires four hidden nodes

At each stage decomposition is done using a three layer NN structure with four nodes in each layer. The network is trained to extract first four principal components. For the first stage input samples are taken from the image to be compressed, whereas for higher stages these are the output coefficients at the most significant hidden layer node of immediate lower stage network. The input image is partitioned into non-overlapping blocks of size 2 x 2 and the pixel values of these blocks are the four inputs to the NN. Thus for an image of size N x N we will get N/2 x N/2 no of samples. These four inputs are compressed by each hidden node to a single coefficient and replacing this coefficient with the corresponding input block of the input image, gives rise to an image of one fourth size at the hidden node outputs. The output coefficients (X_{n1}) at the most significant hidden layer node are associated with the first principal eigen vector. These are the transformed coefficients obtained by weight matrix 'W_{n1}', where 'n' stands for 'n^{th} – stage' decomposition and '1' is for most significant eigen vector. These coefficients trap maximum input entropy and captures significant amount of information which are usually low frequency components and hence can be compared with 'LL' sub-band coefficients of wavelet decomposition. These coefficients are used as input image for the immediate higher stage decomposition. The coefficients at the output of other hidden layer nodes (H_{n2}, H_{n3}, H_{n4}) are associated with next three higher order principal eigen vectors and are transformed using weight vectors W_{n2}, W_{n3}, W_{n4}. These coefficients capture edge information and can be correlated to the LH, HL, and HH sub-bands of wavelet decomposition. But unlike wavelet transforms these coefficients don't capture definite orientation information. Fig-3 shows the original and 3-stage decomposed image 'Lena'.

3-stage decomposed 'Lena'

Fig 3 Image block diagram of LENA

MULTI-STAGE PCE BASED REDUCED MEMORY CODING

Once network training is complete knowing the estimated weight parameters sub-band coefficients can be generated block by block for required number of levels instead of doing it for the full image space and then going to the next level. Therefore it will be useful to encode the data in the order it is generated. Obviously, buffering all the coefficients from a certain band before they are coded increases memory requirements and should be avoided. A modified embedded zero-tree coding algorithm for our low memory encoding is proposed.

1) For a block of size m x m (where, $m > n(2)^j$ where j is a natural number and n is the depth of decomposition), transformation is done using $W_{n1}, \ldots W_{n4}$. Restriction on the size of block ensures transformed sub-band at highest level will not vanish.

2) Embedded zero- tree (EZT) coding as proposed by Shapiro [2] is performed with a little modification in the tree structure. Instead of defining three different trees for different orientations as in case of wavelet based EZT here we can achieve same performance with a single tree with more descendants. Considering some pixel $P_{(m1, m2)}$ at i^{th} row and j^{th} as the parent node ,where 'm1' corresponds to level (scale) of decomposition and 'm2' stands for, depth of decomposition at level 'm1', all the elements present at same location of 'm1' level but at higher depths ($m_j > m_2$ and also the corresponding elements at lower decomposition levels ($m_i < m_1$) are considered as descendants.

3) At each stage coding performance is measured and if satisfactory, next block is considered for transformation and encoding with some 'end of block' code preceding it.

4) At the end weight parameter are entropy coded and transmitted.

EXPERIMANTAL RESULTS AND PERFORMANCE ANALYSIS

In table –1 PSNR results at different bits per pixel (bpp), for different test images along with comparisons with, Shapiro's result and JPEG (with arithmetic coding) are given. Though the proposed algorithm results are not always the best but are competitive at a fraction of the complexity and memory utilization. It is worth repeating that training is only one pass so has advantage over other neural network based techniques. The memory requirement depends upon the block size considered for decomposition. The encoder and decoder are responsible for handling the synchronization.

The proposed algorithm is based on the criteria that for an input of dimension 2 x 2 , the rank is four, and estimating first four principal components as discussed above, which seems to be enough to reconstruct the input. The network performance is based on minimising the variance. Sometimes there exits a wide gap between local variance and the global variance. This deteriorates the overall performance, which is more prominent for images like 'barbara' and 'mandrill' or those having more edge information. This can be improved by estimating more details locally, i.e. by extracting more eigenvectors for the blocks dealing with edges. Thus proposed algorithm provides wide flexibility for multirate data transmission.

Table-1: Comparison of proposed method with some standared algorithms.

Image	bpp	PSNR Shapiro	PSNR JPEG	PSNR proposed
Lena	0.25	34.13	31.96	34.20
	0.5	37.24	35.51	37.25
Barbara	0.25	27.57	26.42	27.52
	0.5	31.39	30.53	31.37
Goldhill	0.25	30.55	29.47	30.62
	0.5	33.12	32.12	33.32

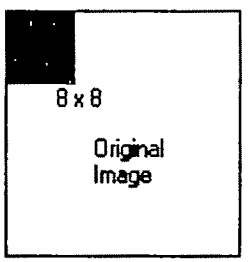

Fig 4 (a)

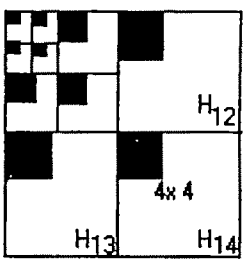

Fig 4 (b)

Peak signal noise ratio (PSNR) is considered as a performance measure. Each block is coded using embedded zero-tree coding algorithm proposed by Shapiro (2). Tree roots are selected gradually from highest level and lowest depth of decomposition to lowest level and highest depth. As shown in fig.-4, for a selected block of size 8 x 8, at maximum we can get three stage, decomposed image. The size of block reduces to 1 x 1 (a single pixel), at the highest level (fig-4b). The pixel at this level, are first considered as parent nodes with their descendants number increasing four times as we move through one level low.

CONCLUSION

In this paper a block based sub-band decomposition technique is developed. A modified zero-tree coding algorithm is implemented which provides low memory utilization, but wavelet compatible compression performance.

REFERENCES

1. E.Oja, 'A simplified neuron model as a principal component analysis' , J.Math.Biol., vol. 15, pp267-273, 1982.
2. Jerome M. Shapiro, "Embedded Image Coding Using Zerotrees of Wavelet Coefficients," IEEE Trans. on Signal Processing, Vol. 41, No. 12, pp. 3445-3460, Dec. 1993.
3. Shan Ouyang, Zheng Bao and Gui-Sheng Liao, "Robust Recursive Least Squares Learning Algorithm for Principal Component Analysis", IEEE Trans. on Neural Network, Vol. 11, No. 1, pp. 215-221, Jan. 2000.
4. Suprava Patnaik and R.N.Pal, "Image Compression using auto-associative neural network and embedded zerotree coding," Proceedings of Third IEEE Signal Processing Workshop on Signal Processing Advances in Wireless Communications ,Taiwan, March 20-23,2001.
5. Suprava Patnaik, R.N.Pal and A.K.Mohanty, "Image Compression Using PCE Based Decomposition and Fractal Coding", Accepted for publication in the proceedings of EAIT – 2001,Dec. 10-12, IIT, Kharagpur.

Vectored Image Encapsulation

Deepak Bhushan, S. K. Kak*
Department of Computer Science and Engineering,
*Department of Electronics Engineering
Institute of Technology, BHU, Varanasi.
e-mail: skkak@banaras.ernet.in

Abstract

A vector data structure is used to represent collection of images as a vector matrix. The algebra and permitted operations on this Vector Space are defined. Further vector wavelet transforms defined earlier helps in achieving faster processing and better compression for multiple images. Applying this technique on layers of colored images taken together and for stack of moving images, reduces the storage space needed. Results show that the processing time is halved, keeping all parameters same, the overall effect was to achieve a compression of 5 for 4 coloured frames at half the processing time with only 0.5 percent error, better than any other technique.

Key-Words: Image Processing, Vector Processing, Wavelet Processing, Image Compression, Vector data compression.

INTRODUCTION

Images are 2D array of tiny picture elements called Pixels that depict the nature and intensity of colour at that point in the image. The pixels can be represented using different data structures depending upon the depth of resolution of colours in the image. Such representation has got inherent redundancy. Data compression refers to the process of reducing or eliminating this redundancy, therefore reducing the amount of data needed for an exact or an approximate representation of total information of the image. Algorithms that restore exact or identical information of the image are called Lossless Compression Algorithms. Many such algorithms like Run-Length coding, Huffman coding and Delta encoding have been proposed and successfully implemented [1]. In contrast the Lossy compression algorithms are those, which produce degradation in the image quality at the time of restoration but this can be controlled up to a certain limit. Lossy techniques such as JPEG, wavelet based algorithm and MPEG are much more efficient than the Lossless techniques. JPEG uses discrete cosine transform of an array of pixel values and then approximates the insignificant coefficients to zero thus it concentrates the energy to a limited region of the histogram, so also the wavelet-based algorithms. The MPEG coding is applicable wherever linked moving images are to be coded. This coding removes the intraframe and interframe redundancy [2].

The transform-based technique (JPEG and wavelet based compression) is represented in Fig 1. The three steps A, B and C shown need processing and hence use CPU time t_A,t_B and t_C respectively. The faster algorithms try to minimize the total time T which is.

$$T = t_A + t_B + t_C$$

Therefore for N images of same dimension it would take NxT processing time for the same algorithm. If now multiple images are so represented that the three steps can be carried out simultaneouly then in such a case the time required for processing would be eploited. This is much less than NxT. This parallelism of operation is well known and used in various array and vector processing algorithms. However this implies SIMD implementation as per Flynn's Classification[3]. In this paper a new approach using Vectored Data structure representation of multiple images as a single vector image is being proposed, implemented and tested for optimizing image data processing, storage, and transmission time.The interframe redundancy due to the zero coefficients can further be used to achieve higher compression ratios in vectored form. The results of the vector representation implementation as presented in the paper support this hypothesis. The vector representation allows a structured and compact information representation. These vectored pixels demonstrate better compression results acording to Shannon's rate distortion theory, which

guarantee better results are always obtained when data is coded as vectors rather than scalars [4].

The first part of the paper defines a vector data structure, which is used to represent multiple images as a single vector image. Further it defines the algebra and the transform/ actions /operations that are in the Vector Space. The next part demonstrates how the vector wavelet transform defined earlier helps in achieving faster processing and better compression for multiple images. The same has been done for the multiple layers of coloured images taken together. The defined technique is also applicable for stack of moving (cine) images as a separate set and thus reduce the storage space needed for the same.

THE VECTOR SPACE

Let $\{v_1, v_2 \ldots v_n\}$ be a set of n orthogonal unit vectors. The representation at the pixel level is $\vec{I}(x,y) = \sum_{i=1}^{n} A_i(x,y)\vec{v}_i$ where $\vec{I}$ is the vector image and A_i is the i^{th} component image, x and y are the coordinates of the pixel and $\vec{I}$ becomes a 2D array of n dimensional vectors. Following equation can represent the vector image. $\vec{I} = \sum_{i=1}^{n} A_i \vec{v}_i$ The algebraic rules defined over the Vector space are given in table 1.

THEORY AND IMPLEMENTATION

The vector pixel defined as $\vec{I}(x,y) = \sum_{i=1}^{n} A_i(x,y)\vec{v}_i$ can be represented as a structure that contains the values as its components. Thus a set of multiple images becomes a 2D array of structures The operations defined on the vectors (table 1) are overloaded on the generic operators (+, -, *, /), which can be for either sequential algorithms or parallel algorithms to perform the operation separately for each component. As they offer a better data structure though if a higher complexity of operations which exploits parallelism of data and same set of sequence of instructions giving parallelized operation of the kind SIMD (single instruction multiple data) which can be used to save time required for processing the whole set of images. By changing the definitions of the generic operators in the context of the vectors those scalar algorithms can be reused for a set of images simultaneously when represented as a vector image. Another function is defined which calculates the norm of the vector. The definition of the norm was taken as maximum from the modulus values of the vector components so that it takes a minimum CPU time to calculate the norm. A null vector defined having all its components as zero. That is used in the sense that there are often a large number of vectors that can be approximated by this zero vector and thus a special short notation for it would be much economical to store.

RESULTS AND CONCLUSION

Multiple frames of monochrome, coloured and cine images were used each having NxM pixels dimension and intensity resolution of one byte per component. Using the definition of the structure for a vector pixel given above a 2D array I of structures was created such that $I[x,y].comonent_i = A_i(x,y)$ where x and y are the co-ordinates of the pixel. The vector discrete wavelet transform was calculated using the overloaded operators in the same algorithm as defined for the usual scalar transform. The subroutine was appropriately formed to accommodate the different data structure representing the image frame however the processing and calculation remains the same as they are overloaded on the generic operators as shown in the previous section. The results of the processing are as follows:

1) The monochrome processing of 5 images indicates that after the transformation 74 percent of the coefficient value in each image can be equated to the value in every other image as the values obtainable are nearly same resulting in generating a compression factor of 2 under lossless mode because of the use of vector encapsulation and wavelet transform. This compression can be further increased to a factor of 4 but at the cost of image quality or error penalty. The degradation is between 1 to 5% depending upon the complexity of the image. (Fig 2)

2) 4 cine coloured frames of 3-byte resolution and stored as 12 planes were processed using the above algorithm. It was observed that for each image the reconstructed output had an error less than 0.55 percent even at the compression factor of 5..(Fig 3)

The results for the processing time further show that it was also halved keeping all parameters the same the overall effect was to achieve a compression of 5 for 4 coloured frames at half the processing time with only 0.5 percent error. This result is better than other techniques used at present.

REFERENCES

1. A.K. Jain, " Fundamentals of digital image processing," Prentice-Hall, Englewood Cliffs, N.J., 1989
2. D.L. Gall, " MPEG: a video compression standard for multimedia applications," Communication of the ACM, Vol. 34, pp.46-58, Apr 1991
3. M V Jensen & B Nelsen, Department of Computer Science, Alborg, Denmark. "Real time layered video compression using SIMD computation." 4th ACPC conference proceedings, Salzburg, Austria 16-18 Feb 1999 p-377-387 .

4. M. Antonini, M. Barlaud, P. Mathieu and I. Daubechies, " Image coding using wavelet transform," IEEE Trans. Image proc. Vol. 1, pp. 205-220, Apr 1992

Table-1

Addition/Subtraction	$\vec{A} \pm \vec{B} = \sum_{i=1}^{n} (A_i \pm B_i)\vec{v}_i$
Multiplication with a Scalar	$c \times \vec{A} = \sum_{i=1}^{n} cA_i\vec{v}_i$
Vector Multiplication	$\vec{A} \otimes \vec{B} = \sum_{i=1}^{n} (\vec{A} \cdot \vec{v}_i)(\vec{B} \cdot \vec{v}_i)\vec{v}_i$
Convolution with a Scalar filter	$\vec{A} = \sum_{i=1}^{n} \vec{v}_i [(convolve(I_i, h(n)))]$
Convolution with a Vector filter	$\vec{A} = \sum_{i=1}^{n} \vec{v}_i [(convolve(I_i, h_i(n)))]$
Norm of vector	$\| \vec{A} \| = \max(\| A_i \|)$
Cosine transform of a vector:	$C[\vec{I}(t)] = \int_{-\infty}^{\infty} \vec{I}(t) \cos \omega t dt$ or, $C[\vec{I}(t)] = \sum_{i=1}^{n} \vec{v}_i \int_{-\infty}^{\infty} I_i(t) \cos \omega t \, dt$
Fourier transform of a vector:	$\Im[\vec{I}(t)] = \int_{-\infty}^{\infty} \vec{I}(t) e^{-i\omega t} dt$ or, $\Im[\vec{I}(t)] = \sum_{i=1}^{n} \vec{v}_i \int_{-\infty}^{\infty} I_i(t) e^{-i\omega t} dt$

Wavelet Transform		
Continuous Wavelet Transform	When the Scaling function $\phi(t)$ and the wavelet function $\psi(t)$ both are defined in the field **F** $\vec{W}(a,b) = \sum_{i=1}^{n} \vec{v}_i \int_{-\infty}^{\infty} I_i(t) \psi_{a,b}(t) dt$	When the Scaling function $\phi(t)$ and the wavelet function $\psi(t)$ both are defined in the field **F** $\vec{W}(a,b) = \int_{-\infty}^{\infty} \vec{I}(t) \otimes \vec{\psi}_{a,b}(t) dt$
Discrete Wavelet Transform	When the Scaling function $\phi(t)$ and the wavelet function $\psi(t)$ both are defined in the field **F** $\vec{A} = \sum_{i=1}^{n} \vec{v}_i [\downarrow (convolve(I_i, h_i(n)))]$ $\vec{D} = \sum_{i=1}^{n} \vec{v}_i [\downarrow (convolve(I_i, g_i(n)))]$	When the Scaling function $\phi(t)$ and the wavelet function $\psi(t)$ both are defined in the field **F** $\vec{A} = \sum_{i=1}^{n} \vec{v}_i [\downarrow (convolve(I_i, h(n)))]$

TRANSFORM BASED TECNIQUE

CALCULATION OF TRANSFORM COEFFICIENTS (A)	THRESHOLDING OF TRANSFORM COEFFICIENTS (B)	RUN LENGTH CODING OF COEFFICIENTS (C)

Fig 1

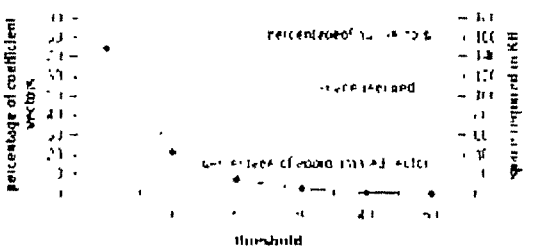

Fig 2(a)

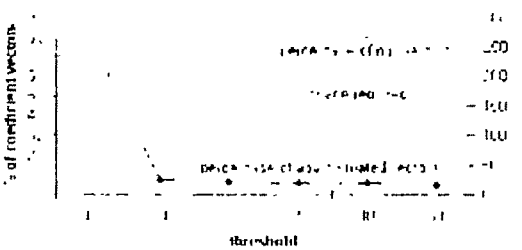

Fig 3(a)

Fig 2(b)

Fig 3(b)

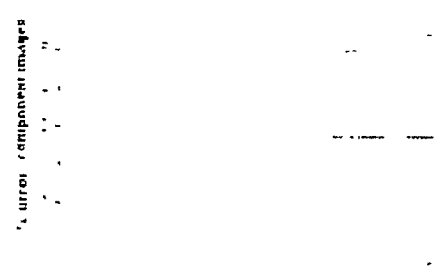

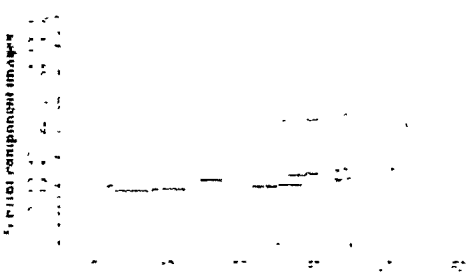

A Robust Edge Detector

B. L. Narayan and C. A. Murthy
Machine Intelligence Unit
Indian Statistical Institute, Kolkata 700 035, India
Email: murthy@isical.ac.in

Abstract

Edge detection algorithms, generally, perform a smoothing operation initially and a thresholding operation towards the end in order to suppress the responses of false edges. However, the thresholds being global, responses arising from weaker edges may also be suppressed. Here, we propose a simple scheme that provides large responses to true edges than to noise.

Keywords : Edge Detection, robust.

INTRODUCTION

An edge is the boundary between two regions with relatively distinct gray level properties [1].

Several approaches for edge detection can be found in the literature. Prewitt, Roberts and Sobel provided gradient based operators for edge detection [1], [2]. Marr and Hildreth [2],[3] had suggested that the zero-crossings of the convolution of the Laplacian of the two dimensional symmetric Gaussian with the image should be considered as edges. Canny [4], [5] found a filter that was optimal according to the criteria of good detection, good localization and a unique response to a single edge. This filter was found to be closely approximated by the first derivative of Gaussian. Usually, noise may be introduced into an image at the time of its creation or transmission. When noise is present in an image, the pixels corresponding to noise too output a non-zero response. Gene-rally, noise is random and some sort of local smoothing operation is performed over small windows around each pixel along the esti-mated edge direction at that pixel. This keeps the edge pixels largely unchanged while reducing the intensity of the noise. Noise removal is expected to be more for larger window sizes, but at the cost of image details. So, there needs to be a compromise between the window size for extr-acting true edges and that for noise removal. The weaker edge responses are then thresholded to suppress the responses arising from noise, *i.e.* all responses less than a threshold, say t_2, are made zero. During thresholding, some of the true edge responses may also be suppressed while some of the responses to noise may be retained. This problem is all the more evident when noise is prominent in an image, in which case, a significant number of edge responses arising from pixels corresponding to noise may be larger than those arising from edge pixels. Here, we propose a novel technique that is quite robust to noise. We shall first delve into the motivation behind our method.

MOTIVATION

The objective of any edge detection algorithm is to mark some pixels as edges and leave out the rest (hence implying that they are not edges). In this process, neither should the true edges be missed, nor the false edges be marked. So, an edge operator should be such that it produces a non-zero response only where there is an edge and a zero response everywhere else, so that all pixels corresponding to non-zero responses can be marked as edge pixels.

Despite the smoothing operation, the pixels corresponding to noise may still produce a non-zero, albeit weaker than before, response to the edge operator. These are then suppressed using a predetermined *global* threshold. The inherent assumption here is that, after smoothing, true edges produce stronger responses as compared to noise. When this is not the case, the operator fails to identify some of the true edges while declaring some false edges as edges. Thresholding with hysteresis, where pixels whose intensities are above another threshold, say t_1 ($t_1 < t_2$), are considered to be edge pixels if they are

connected to some pixel whose intensity is greater than t_2, leads to better detection of edge pixels but fails if the weak edges are not connected to strong edges.

In order to overcome this problem, an edge detection operator should provide larger values for true edges, however weak they be, while producing smaller values in response to noise, however strong they be. Let us note that a "large" absolute change in intensity values in the ~~neighbourhood of a pixel need not necessarily~~ mean ~~that~~ the pixel corresponds to an edge. Similarly, in the case of a weak edge, the absolute change in intensity values may be "small". In other words, the criterion needed to indicate an edge has to be chosen in a different manner than simply comparing the absolute differences of intensity values of neighbouring pixels.

Ideally, a step edge is the boundary between two distinct regions, each consisting of constant gray level values. Let the intensities of pixels in one of the regions be denoted by x_i, $i=1,2,...,m$ and those of the other region by x_i, i=m+1,m+2,...,m+n (assuming both regions have the same number of pixels). We have the following definitions:

$$TSS = \sum_{i=1}^{m+n} (x_i - \bar{x})^2, \text{ where } \bar{x} = \sum_{i=1}^{m+n} x_i .$$

$$WSS = \sum_{i=1}^{m} (x_i - \bar{x}_1)^2 + \sum_{i=m+1}^{m+n} (x_i - \bar{x}_2)^2, \quad \text{where}$$

$$\bar{x}_1 = \sum_{i=1}^{m} x_i \quad \text{and} \quad \bar{x}_2 = \sum_{i=m+1}^{m+n} x_i .$$

$$BSS = (\bar{x}_1 - \bar{x})^2 + (\bar{x}_2 - \bar{x})^2 .$$

The edges that are generally encountered form the boundary between two regions such that the two regions have small variation within them while maintaining a high variation between them (see Fig. 1), *i.e.*, they have a small within sum of squares (*WSS*) (or high between sum of squares (*BSS*)) as compared to the total sum of squares (*TSS*). When the fluctuation is solely due to noise, there are no two such distinctly uniform regions in the neighbourhood, *i.e. BSS* is relatively small as compared to *TSS*. Note that $TSS = BSS + WSS$.

For an ideal step edge, *WSS* would be close to *0* and the quantity $\frac{BSS}{TSS}$ would be close to *1*. If the pixel is not an edge pixel then the total variation would be largely accounted for by the within variation itself, thus making the quantity ~~$\frac{BSS}{TSS}$~~ small. Consequently, the quantity $\frac{BSS}{TSS}$ can be employed to discriminate between edges and noise. We shall consider this quantity to be the edge response at any pixel under consideration. We describe the proposed algorithm below.

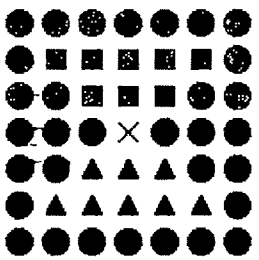

Fig. 1 : A neighbourhood for an ideal step edge (when edge orientation is horizontal). The neighbourhood consists of two distinct regions: one consisting of the triangles and the other consisting of the squares.

PROPOSED ALGORITHM

The structure of the proposed algorithm is similar to that of Canny's edge detection algorithm. Initially, edge directions are estimated and smoothing is performed in the estimated direction of the edge. The edge responses are then obtained at each pixel. For this purpose, the chosen neighbourhood is as illustrated in Fig. 1. When edge orientation is not horizontal (it may not be vertical either), the corresponding neighbourhood is obtained by rotating the one shown in Fig. 1. This is followed by non-maxima suppression and thresholding with hysteresis. Having attached larger responses to true edge pixels and smaller responses to pixels corresponding to noise, the chances of true edges, be they weak or strong, to be retained during the thresholding process are increased, thereby making this method robust to noise.

When *TSS* of a particular neighbourhood is quite small, say smaller than a threshold t_0, it means that there is little variation among the pixels in the neighbourhood. This indicates that there might not be an edge in that neighbourhood. Whenever *TSS* of a neighbourhood around a pixel is found to be less than t_0, we shall say that the pixel is not an edge.

RESULTS

The results on three artificial images and the image of Lena are provided here. About 5% of the pixels of the 'Circles' image (Fig. 2) and about 1% of the pixels in 'Bands-1' (Fig. 3) have been corrupted by *Uniform(-50,50)* noise [6]. In 'Bands-1', the pixels to be corrupted have not been chosen uniformly (the number of pixels corrupted

decreases as we proceed downwards). The top portion of 'Bands-2' (Fig. 4) has been corrupted by *Uniform(0,255)* noise. Gaussian noise has been added to the Lena image (Fig. 5). The results of Canny's algorithm have also been provided for the sake of comparison.

The figures in the parentheses provided beneath the images are

t_2 and $\frac{t_1}{t_2}$, respectively. For the results provided here t_0 has been fixed at *1* for the artificial images and at *25* for the Lena image.

We note that the output of the proposed algorithm on the Lena image is comparable to that of Canny's algorithm. The results on the artificial images depict the cases where our algorithm performs better than Canny's algorithm. Due to the type of noise involved in these images, the thresholding process in Canny's algorithm suppresses the responses corresponding to true edges but fails to suppress the responses from noise. The results reflect the ability of the proposed algorithm to effectively suppress the responses to noise while keeping the responses to true edges intact.

REFERENCES

1. C. R. Gonzalez and R. E. Woods, *Digital Image processing,* Addison Wesley Publication, India, 1992.
2. D. Marr, *Vision,* W. H. Freeman and company, New York, 1982.
3. D. Marr and E. C. Hildreth, Theory of edge detection, *Proceedings of the Royal Society of London,* B 207: 187-217, 1980.
4. J. F. Canny, *A computational approach to edge detection,* IEEE Trans. on Pattern Analysis and Machine intelligence, 8: 679-698, November 1986.
5. J. F. Canny, Finding lines and edges in images, Technical Report No. 720, Masachusetts Institute of Technology, 1983.
6. Jr. Arthur R. Weeks, *Fundamentals of Electronic image processing,* SPIE/IEEE series on Imaging Science and Engineering. SPIE and IEEE press, USA 1996

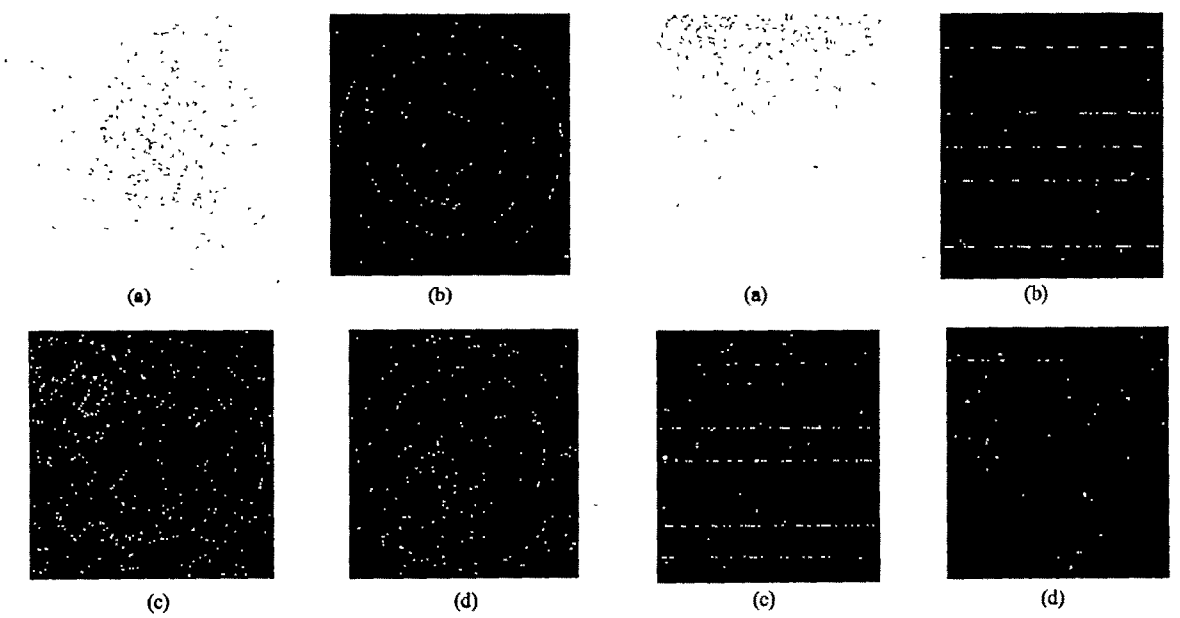

Fig 2 Test image circles (a) Original (b) proposed method (.97,.4) (c) Canny (.95,.4) (d) Canny (.98,.1)

Fig 3 Test image; Bands-I (a) Original, (b) Proposed method (.95,.4), (c) Canny (.9,.4) (d) Canny (.95,.4)

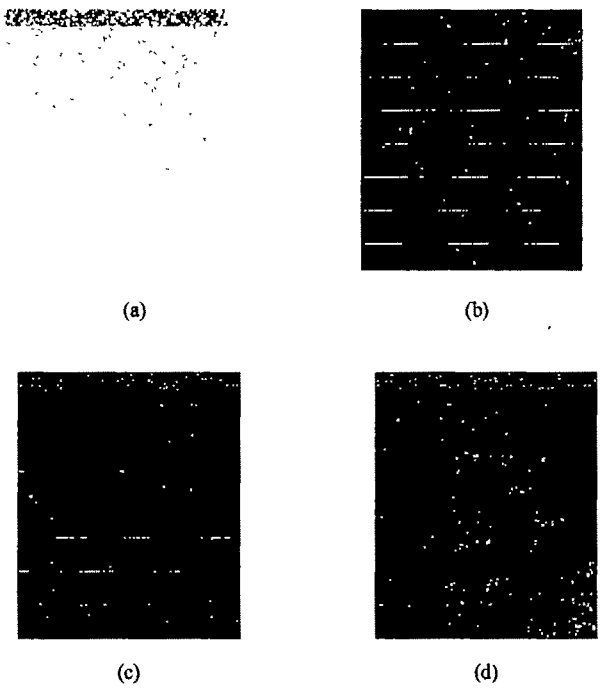

Fig 4 Test image; Bands-2 (a) Original, (b) Proposed method (.95,.4), (c) Canny (.9,.4) (d) Canny (.94,.4)

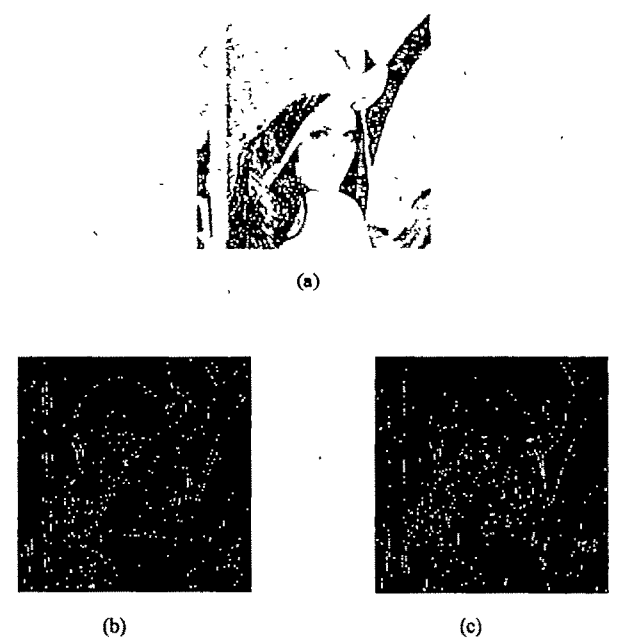

Fig 5 Lena (a) Original, (b) Proposed method (.9,.4), (c) Canny (.85,.4)

Speech Feature Extraction For Speaker Identification Using Artificial Neural Network

Anupam Shukla[1], A. S. Zadgaonkar[1] and Ritu Tiwari[2]
[1]Dept. of Electronics Engineering
[2]Dept of Computer Technology
Engineering College, Raipur. Chattish Garh, India.

Abstract

The work is mainly divided in to two parts i.e. to collect the speech data and extract the speech feature from the utterances of the speaker. The second part deals with the simulation of the computer model using Artificial Neural Network (ANN) for the identification the speakers. The detailed study has been done to determine the perceptual characteristic associated with the unvoiced and voiced speech sounds of the speaker and it is found that the pitch and formant frequency are the important features which are capable to identify the speaker. A four layer perceptron model of ANN is used to identify the speaker. The result shows that the variation of pitch along with the formant frequencies could be used effectively for the identification of the speakers.

INTRODUCTION

The problem of speaker recognition is complicated. If two speakers utter the same phrase in the same or even in the two different occasions there are only certain aspects of the sound which are the same. For different speakers, the anatomical features of the vocal track are different. Apart from the concrete semantic information a person speech carries information about his mood, his manner of speaking and his state of health. The individuality of voice manifests itself in these utterances in the specified context. Automatic identification of the speakers from their voice may have the potential application in many diversified fields. This technique could be used to provide controlled access to a facility or information to select the particular speaker. Speech is a non-stationary signal where amplitude, fundamental and the formant frequency vary with the time [5]. During any of these transient the speech signals contains information of the whole vocal tract. This speech features are very useful when the clues of the speaker's identity are either missing or highly ambiguous [2]. The parts that principally determine the spectra are the vocal cavities and the articulators, the characteristic of the vocal cords are reflected in the pitch information. The vocal cords play an important role in the production of the voiced sounds [1]. The sub-glottal air pressure and tension on the vocal cords are changing continuously during speech production to achieve the desired variation with time. In the present study we emphasise the importance of the pitch and the formant frequency together for the identification of the speaker. The most difficult problem is to decide which speaker is associated to certain area of the spectrogram and which feature is to be selected for the identification of the speaker. The feature selected should satisfy the two criteria that are consistency (low variation with in the speaker) and it differ markedly from one speaker to another. The complete study can be broadly classified in to two parts. First the recording of the speech and its analogue to digital conversion at the required sampling frequency to get the digitised files for the further processing to get the pitch and the formant frequency. Secondly the identification is achieved by the computer simulation model using neural network [3]. The network is trained and tested for the different speakers by the computer simulation model using neural network toolbox in MATLAB [4].

DATA ACQUISION, PREPROCESSING AND FEATURE EXTRACTION

The utterances in the present work is chosen on the basis that it should be of sufficient duration so that it consist of the entire variation of the speaker voice pattern. The code should consist of voiced and the unvoiced sounds and the utterances with the short vowel and consonant provide the most effective code word [6]. The utterances with the short vowels and consonant provides most effective code word

the basis of this words with vowels namely [a], [i] and [u] and the consonants were recorded. In the present work the code words are 'nam', 'sin ' and 'mum' which were recorded to satisfy the CVC context of the utterances. The analogue signal is recorded for 10 speakers on good quality audiotape and it is digitised at the sampling frequency of 10240 Hz. by using sound blaster card. Thus the entire data is stored in the floppy by separate file names to form a speech bank from which the speech feature pitch and the formant frequencies were acquired. The pitch extraction is done on the fundamental concept of estimating pitch by counting the number of pulses per seconds by tacking speech data at sampling frequency of 10240 using the software developed in Turbo C. The formant frequency F1 to F4 is acquired from the time dependent frequency analysis (SPECTROGRAM) using Signal-processing toolbox in MATLAB. The spectrogram computes the window discrete time Fourier transform of a signal using the sliding window. The sampling frequency used is 10240 Hz. and the FFT length is 512. The number of samples by which the segments overlaps is 475. The Kaiser window is used and its length is kept less than or equal to FFT length here it is kept 500. The spectrogram splits the signal in to segments and applies window parameter to each segment to compute the discrete Fourier transform of the each segment with length equal to FFT length. This produces the short-term frequency content of the signal specified by columns. [7].

SIMULATION MODEL FOR IDENTIFICATION

The neural network model with 4 layers having 5 neurones in the first layer and 10 neurons in the last layer and two intermediate layers of 10 neurones each has been used in this model for the computer simulation as shown in the figure 3(a). The ANN toolbox in MATLAB has been used in the present work. The network is trained by using LOGSIGMOID function as shown in the figure 3(b,c), which generates the output between 0 and 1. The training is done TRAINBPX, which uses both the momentum and adaptive learning rate to speed up the learning. The learning rate and the number of epochs are chosen to be .00001 and 8000 respectively, so as to get the desired error goal of 10 - 7 accurately.

RESULTS AND CONCLUSION

The average pitch and formant frequency for the speakers is determined from the speech signal with the help of the software developed in Turbo C and Speech Signal Processing Tool Box in MATLAB. The details are shown in the table number 1. The ANN output is shown in the Table No. 2, which shows the identification of the speaker. In the present study the attempt was made to use the perceptual features for the identification of the speakers. The analysis of the data reveals that pitch was strongest for young speakers and. Conversely, low pitch for the old speakers. The pitch itself is the sufficient feature to classify the speaker but along with the formant frequency of the speech signal gives the better score of identification up to 98 %. Hence it is concluded that the perceptual features of the speech can be used with confidence to identify the speakers easily by using ANN.

REFERENCES

1. A.S. Zadgaonkar and Anupam Shukla, " Hindi vowel recognition using ANN" , Jour. Of ASME, Vol.32, 95,pp. 48-53.

2. A.S. Zadgaonkar and Anupam Shukla, "Classification of Hindi consonants according to the place of articulation using ANN" International journal of electrical engineering education, Vol.32, No.3, July 95,pp.273- 275

3. R. P. Lippman, "A review of neural network for speech recognition" Jour. of Neural Computation, Vol 1

4. Manual of the MATLAB for Artificial Neural Network

5. B. S. Atal, "Automatic Speaker recognition based on pitch contours" Jour. Of Aco. Soc. Of America , Vol.52, No.6 (part2), pp.1686-1697.

6. Anupam Shukla, "Automatic speech recognition and speaker identification using ANN" Inter. Conf. Of Computational linguistics speech and document processing, ISI, Calcutta, Feb.18- 20, 1998.

7. Manual of Speech processing toolbox in MATLAB

Table 1 Speech feature as pitch and formant frequency

Sl. No.	SPEAKER	AVERAGE PITCH	FORMANT- FREQ F1	F2	F3	F4
1.	Speaker-1	152	600	1000	1700	3600
2.	Speaker-2	144	500	1100	1750	3500
3.	Speaker-3	148	700	1200	1800	3700
4.	Speaker-4	150	800	1400	1900	3650
5.	Speaker-5	142	900	1300	1950	3400
6.	Speaker-6	124	800	1200	2000	3600
7.	Speaker-7	122	950	1000	1950	3700
8.	Speaker-8	128	900	1250	1950	3850
9.	Speaker-9	121	1000	1600	1950	3900
10.	Speaker-10	120	900	1300	1850	3750

Table.2 ANN output to identify the speakers

SL. No.	Specification of Speaker	Target output of ANN	Actual output of ANN
1.	Speaker No. 1	0.10000	0.09989
2	Speaker No. 2	0.20000	0.19994
3.	Speaker No. 3	0.30000	0.29994
4.	Speaker No. 4	0.40000	0.39989
5.	Speaker No. 5	0.50000	0.49994
6.	Speaker No. 6	0.60000	0.59994
7.	Speaker No. 7	0.70000	0.649989
8.	Speaker No. 8	0.80000	0.79994
9.	Speaker No. 9	0.90000	0.89994
10.	Speaker No. 10	10.0000	0.99994

Neural Network Model Of Vertebrate Retina

Soumika Munshi and Asit K. Datta
Department of Applied Physics, Calcutta University
92 Acharya Prafulla Chandra Road, Calcutta 700 009, India
Email: akdatta@app-physics.org

Abstract

A neural network model of vertebrate retina is proposed. The vertebrate retina is thought to be composed of a two-dimensional array of variable-sensitivity photodetectors (VSPDs), where each photodetector is a combination of power dissipation resistance and capacitance in parallel, representing the membrane resistance and capacitance of the retinal neuron. Such a retina is termed as artificial retina. Any image incident on the retina gets transformed as variable voltage states depending on the grey values of the image. Current injected at any one of the nodes yields a spatially smoothed and filtered output voltage signal.

Keywords: Vertebrate retina, Artificial retina, Variable sensitivity photo-detectors, Computer vision

INTRODUCTION

Biological visual systems are able to master complex vision processing tasks with admirable ease through self-organizing networks. From a neuro-physiological point of view, processing capabilities of the vertebrate retina provides an example of feature extraction reducing the net processing load in the cortex and therefore offers abundant incentives for research, stimulating the idea of an efficient information processing technique. Attempts are therefore made to mimic the activities of the human visual system through the development of artificial retina which may feature on-chip sensing, processing, parallel data transfer and post processing for identification and other visual tasks [1-5].

The objective of this paper is to develop an electrical analog of the vertebrate retina, where an artificial retina represents the functioning of the retina. The electrical analogue is then modeled into an interconnected neural network and the response equations are established.

PHYSIOLOGICAL FUNCTIONING OF THE VERTEBRATE RETINA

The vertebrate retina consists of several layers of neuronal networks. Among the six principal cell types of neurons identified in the retina, each cell type is further classified into several subtypes. The retinal network contains two distinctive layers, consisting of the outer retinal circuit and the inner retinal circuit. Three major cell types identified in the outer retinal circuit are namely, photoreceptor array (gray), the horizontal cell (blue) and the bipolar cell (red). The neurons belonging to the same type are arranged in two-dimensional array in separate layers.

When an object is viewed through the eye, the light passes through the transparent portion of the retina to be projected on the photoreceptor array. Light-sensitive pigment present in the photoreceptor array chemically transducers the incident photon to a voltage response. The rods and the cones are two types of photoreceptors cells having varied sensitivities. The rod cells have a high sensitivity to light and operate at night, whereas the cone cells are much less sensitive to light and operate during daytime. With the increase in brightness of the incident illumination, the amplitude of responses of the photoreceptor cells increases, i.e., the response varies with the variation of intensity of different points of the incident image. The graded potential response of these cells has the advantage of integrating and averaging the incident light over time.

When the voltage signal reaches a nerve terminal called the synapse, neurotransmitter molecules secreted at the terminal transmit the signal from the pre-synaptic neuron to the post-synaptic neuron. The voltage signal reaching the receptor molecule of the membrane of the post-synaptic neuron changes the membrane conductance and hence the membrane potential. This voltage signal at the post-synaptic neuron is then transmitted to higher-order

neurons, which is then processed in successive stages, from one layer to the next. The interaction between these layers includes feedback connections from proximal to distal layers as well as feed-forward connections. Only neighbouring neurons are interconnected in the layered architecture. Since the voltage signal is transmitted only to neighbouring neurons, signal distortions are found to be very small.

The voltage signal is then transmitted to the horizontal as well as the bipolar cells. The horizontal cells show graded potential responses and exhibit large receptive fields. Neighboring horizontal cells are tightly coupled to each other, so that the response transmitted from the photoreceptor cells get propagated through the intensely coupled horizontal synapses to the bipolar cells. The bipolar cells exhibit a receptive field, where the receptive field surround antagonizes the receptive field center. It is widely believed that the narrow center response reflects the input from the photoreceptor, whereas the wide surround reflects the input from the horizontal cell. The behavior of the bipolar cells has the effect of smoothing a noisy image as well as enhancing the contrast of the image. Therefore the inner retinal circuit is mainly responsible for smoothening or filtering the input image.

Voltage output from the bipolar cell gets transmitted to the amacrine cells (white) and the ganglion cells (yellow) that comprise the inner retinal circuit. The analog voltage signals received by the ganglion cells give rise to action potentials to send the outputs to the brain for image identification. Another principal neuron type in the inner circuit is the interplexiform cell (light green) that provides a feedback pathway between the inner and outer layers.

ARTIFICIAL RETINA

Attempts are made to mimic the functioning of vertebrate retina by so called artificial retina. Artificial retina (sometimes called silicon retina) employs in general, a two-dimensional square, hexagonal or octagonal array of amorphous silicon based variable sensitivity photo-detectors (VSPDs). The photo-detectors may sometimes consist of a two-dimensional array of phototransistors followed by a logarithmic current to voltage converter or may be a fully resistive network. The resistive network performs spatial smoothening of the input signal. The device may have a logarithmic photo-response enabling it to operate over a wide range of light intensities and the capacitance of the device provides some amount of smoothing. Constant current termed the bias current is injected at each node. When a two-dimensional image is allowed to be incident on the surface of artificial retina, it is sensed by embedded photosensors at nodes in the array and then converted to voltages or currents. which drive the array.

Varieties of artificial retinas are fabricated, ranging from simple (20 x 20) CMOS VLSI chips to (256 x 256) GaAs based variable sensitivity photodetectors (VSPD) chips [6-10]. Mahowald and Mead's retina [11-12] is a two-dimensional resistive grid. Standley's chip[13] computes the moments of an image's brightness distribution to detect the relative position of an image in a dark background and also the orientation of the image. Bair and Koch's chip [14] uses two resistive chains in a CMOS VLSI chip that undergoes low-pass filtering to extract the edges of the input image.

Scientific investigations have revealed that when an image is incident on the biological retina, it initially performs a low-pass filtering of the input stimulus, followed by a logarithmic transformation and finally smoothening. The artificial retina also performs spatio-temporal smoothening of the input signal to produce a high-pass filtered output image. Both spatial and temporal edges are enhanced in the resultant high-pass filtered output signal.

PROPOSED MODEL OF ARTIFICIAL RETINA

Based on the physiological background, the proposed model of artificial retina attempts to functionally resemble the outer retinal circuit. It comprises of a network made up of a two-dimensional array of analog circuit components called photodetector cells as shown in fig. 1, where functioning of each photodetector cell approximates to that of a neuron. As seen from fig. 2, each photodetector cell is composed of a resistance and capacitance in parallel, which represent the membrane resistance and capacitance of a single neuron. This proposition is valid when one consider the semiconductor model of a photodetector. The biological evidence as elaborated below also suggests the validity of this electrical network. Every photodetector cell in the network is connected to its neighboring cells and interacts only with those cells. Currents flowing from a node to the neighboring node are ordinarily bi-directional, which suggests that the links or gap-junctions between neighboring cells provide a low-resistance pathway and can therefore be approximated by a resistor. This enable the voltage signals to be transmitted to neighboring cells without time delay through the gap-junctions. The analog circuit describing the single neuron type is endowed with the property of light intensity to voltage conversion, compact coupling between neighboring cells for smooth transmission of voltage signals, as well as filtering the input signal. This indicates that the same circuit is capable of performing the functions of the photoreceptor cells, horizontal cells as well as the bipolar cells.

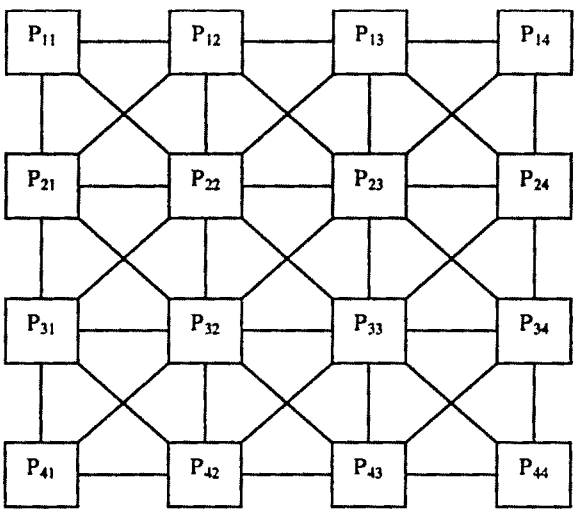

Fig. 1: Model of artificial retina using two-dimensional variable sensitivity photodetectors (VSPD).

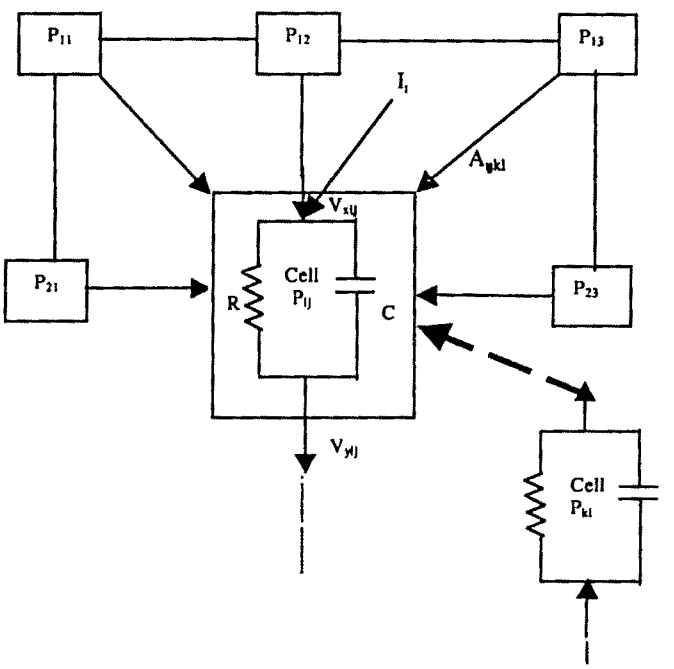

Fig. 2: Net current input to any VSPD cell P_{ij} through the neighbouring links as expressed in eqn. (5).

The relation between the voltage response and incident light intensity can be described by

$$V = V_{\max}\left(\frac{I}{I+\sigma}\right) \tag{1}$$

where $V_{\max}$ is the voltage response at saturation and σ is the intensity which gives a response of $(V_{\max}/2)$ and relates to the degree of light sensitivity.

When a grey image is incident on the proposed artificial retina, it gets translated as variable voltage states, as evident from eqn. (2), depending on the sensitivities of the photodetectors. Hence,

$$V_{ij}(t) = sX_{ij} \tag{2}$$

where V_{ij} (t) is the vector output at instant t, s is the sensitivity of the photodetector and X_{ij} denotes the gray level of the image projected on the photodetector chip P_{ij}.

Constant bias current I_{ij} is injected into the network at each node of the photodetector array by the application of a suitable input voltage U_{in}. With an input bias current injected at a single node, the potential drop at the nodes of the resistive links yields a symmetric output signal that peaks to U_{out} at the point of voltage application and then decays exponentially, as shown in fig. 4.

The ratio of the resistance of the vertical resistors to that of the horizontal resistors corresponds to smoothing or spatial low-pass filtering of the input signal. This spatial distribution of a particular voltage response gives the rate of response decay while the voltage conducts to the neighboring cell. The capacitances in the network provide some additional smoothing in the temporal domain. Effectively, injection of constant current at a node in a resistive chain results in a symmetrically decaying exponential function, thereby spatially smoothening out the input image, resembling the function of the bipolar cells in the outer retinal circuit.

NEURAL NETWORK MODEL

Setting up a neural network model of retina needs proper selection of circuit parameters of each variable sensitivity photo-detector in the array. Obeying Kirchhoff's law of current flow at any node, the current across photodetector cell P_{ij} for a one-dimensional array of photodetectors (for simplicity as shown in Fig. 3) can be expressed as

$$\frac{V_{xij}}{Z} = \frac{V_{xij} - V_{x(i-1)j}}{R_{ijkl}} + \frac{V_{xij} - V_{x(i+1)j}}{R_{ijkl}} + I_{ij} \tag{3}$$

where V_{xij} is the voltage applied at the ij-th cell, representing the membrane voltage of each neuron, Z is the impedance of each photodetector cell, representing the membrane impedance of each neuron and I_{ij} is the constant bias current at node ij. The current (V_{xij}/Z) across the photodetector can be expressed as

$$\frac{V_{xij}}{Z} = \frac{V_{xij}}{R_x} + C\frac{dV_{xij}}{dt} \tag{4}$$

The voltage response V_{xij} of the ij-th photodetector represented by eqn. (3) expresses the spatial distribution of voltage due to the incident input image and constant injected current I_{ij} at the ij-th neuron.

Generalizing eqn.(3) for a two-dimensional (M x N) array of photodetectors, the current equation takes the form

$$C\frac{dV_{xij}(t)}{dt} = -\frac{1}{R_x}V_{xij}(t) + \sum_{Pkl} A_{ijkl}V_{ykl}(t) + I_{ij} \tag{5}$$

where $A_{ijkl} = \frac{1}{R_{ijkl}}$ is the conductance of the link between neighbouring photodetector cells, and

$1 \le k \le M$; $k \ne i$
$1 \le l \le N$; $l \ne j$.

Eqn.(5) can be expressed in terms of a difference equation as,

$$\frac{C}{\Delta t}\{V_{xij}(t+1) - V_{xij}(t)\} = \left[-\frac{1}{R_x}V_{xij}(t) + \sum_{Pkl} A_{ijkl}V_{ykl}(t) + I_{ij}\right] \tag{6}$$

where Δt is a constant time interval and $V_{xij}(t)$ is the state of the cell P_{ij} at the t-th instant of time. Usually the time interval is assumed to be unity, i.e., $\Delta t = 1$. The resistance R_x and capacitance C and the conductance A_{ijkl} of the link between any two adjacent photodetectors (cells) are the parameters of the network. I_{ij} is the bias current of the cell P_{ij}

Evidently the A_{ijkl} is the interconnection weight of the neural network and is adjusted for processing of image falling on the retina.

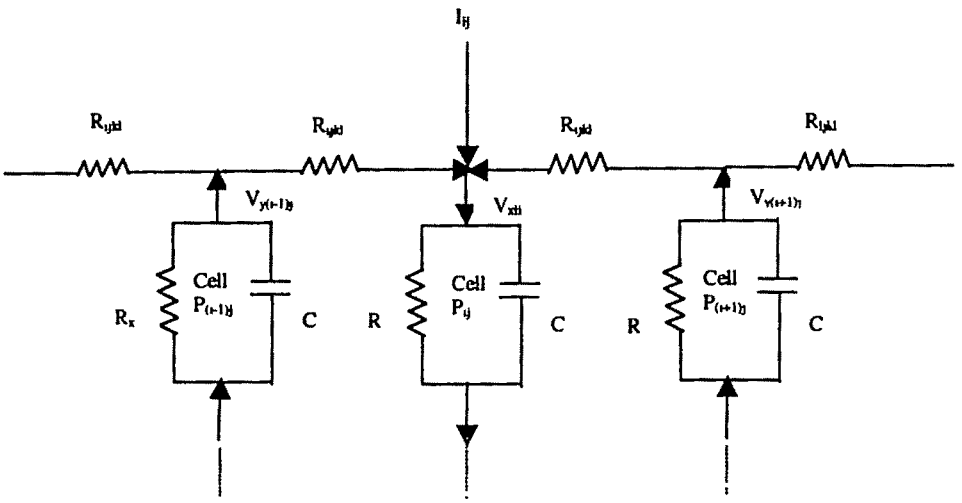

Fig. 3: One-dimensional array of receptors to demonstrate the current entering and leaving photodetector cell P_{ij}

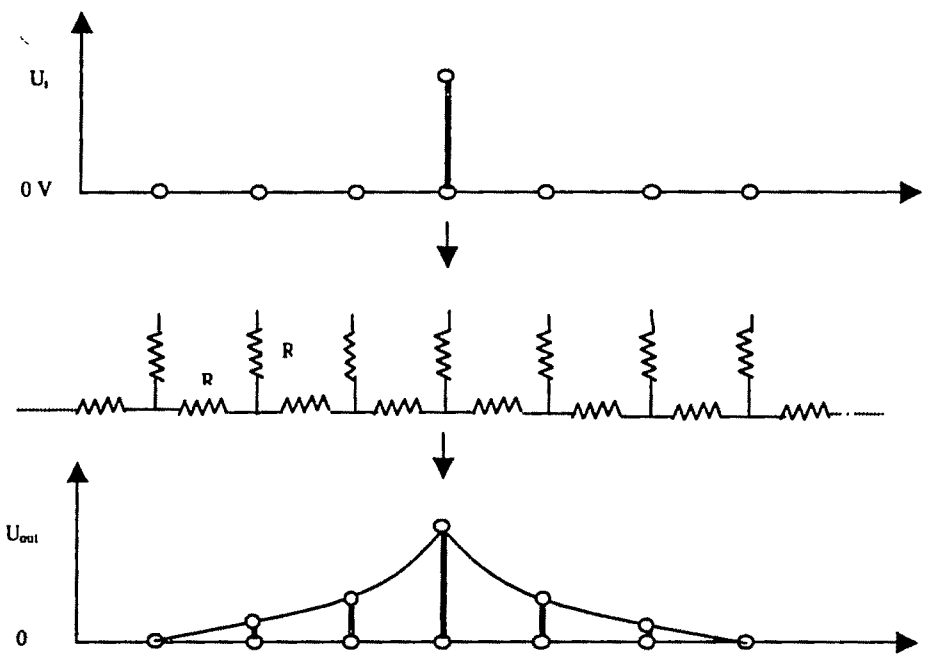

Fig. 4: Spatial smoothing of the input voltage signal when applied across a resistive chain.

The net input to any photodetector P_{ij} through the adjacent links have been approximated as a weighted sum of the voltage states V_{ykl} across the adjacent photodetectors and is represented as $\sum_{Pkl} A_{ijkl} V_{ykl}$, where A_{ijkl} serves as the interconnection weight between photodetectors P_{ij} and P_{kl}.

The output $V_{yij}(t)$ at any instant t of the cell P_{ij} is assumed to be a nonlinear ramp function of the input state $V_{xij}(t)$ of the cell, and is given by

$$V_{yij}(t) = f\{V_{xij}(t)\} = 0.5\left(|V_{xij}(t)+1| - |V_{xij}(t)-1|\right) \quad (7)$$

For a unit time step ($\Delta t = 1$), the eq. 6, can be written as:

$$V_{xij}(t+1) = V_{xij}(t) + \frac{1}{C}\left[-\frac{1}{R_x} V_{xij}(t) + \sum_{Pkl} A_{ijkl} V_{ykl}(t) + I_{ij}\right] \quad (8)$$

where $V_{xij}(t)$ represents the voltage state of any photodetector at the t-th instant, whereas $V_{xij}(t)$ represents the updated voltage state at the $(t+1)$th instant.

Therefore, with an image incident on the artificial retina that induces a voltage change as expressed by eqn. (1), the voltage response of the ij-th cell is the convolution of the light induced voltage with a spatially smoothed or spatially decaying exponential function.

Like in any neural network model, the interconnection weights A_{ijkl} between nodes here too, have to be optimized to attain an optimal output result.

The same principle is effective for all the cells of the photodetector array. The output from the photodetector array are updated and processed through a neural network until a stable state is reached and there occurs no further change in the voltage states of the network between two consecutive cycles. This gives the spatial distribution of the retinal cell response in the steady state (equilibrium point) and the image is said to be spatially smoothed and filtered.

CONCLUSION

The proposed model resembles much of the retinal functioning of the vertebrates. The vertebrate retinal network filters the input image with its dynamics. Since the basic component of the retinal circuit is a neuron, therefore the filtering properties of the retinal circuit can be implemented using the electrical properties of analog components. The networks perform fast analog computations based on Kirchoff's laws and are able to converge quickly to a stable voltage distribution in response to the voltages applied. The resistive-capacitive model in interconnected neural network is likely to resemble the functioning of the vertebrate retina, since biological investigations have revealed that the neuron membrane possesses an internal resistance as well as a capacitance.

REFERENCES

1. Mead, "Adaptive retina", *Analog VLSI Implementations of Neural Systems*, Boston, 239-246 (1989).
2. K. Kyuma, E. Lange, J. Ohta, A. Hermanns, B. Banish and M. Oita, "Artificial retinas – fast versatile image processors", Nature, 372 197 –198 (1994).
3. E.Lange, Y. Nitta and K. Kyuma, "Optical neural chips", IEEE Micro, 14, 29 – 41 (1994).
4. Koch and H. Li, "Vision Chips: Implementing vision algorithms with analog VLSI circuits", IEEE Computer Society Press, CA (1995).
5. Y. Nitta, J. Ohta, S. Tai, and K. Kyuma, "Optical learning neurochip with internal analog memory", Appl. Opt., 32, 1264 – 1274 (1993),.
6. J. L. Wyatt, Little known properties of resistive grids that are useful in analog vision chip designs, *Vision Chips*, IEEE Computer Society Press, 72 – 104 (1994).
7. Funatsu, Y. Nitta, Y. Miyake, T. Toyoda, K. Hara, H. Yagi, J. Ohta and K. Kyuma, "An artifical retina chip with a 256 x 256 array of n-MOS variable sensitivity photodetector cells", Proc. SPIE, 2597, 283-291 (1995).
8. R. G. Stearns and R. L. Weisfield, "Two-dimensional amorphous silicon array for optical imaging", Appl. Opt. 31, 6874 – 6881 (1992).
9. R. I. MacDonald and S. S. Lee, "Photodetector sensitivity control for weight setting in optoelectronic neural networks", Appl. Opt. 30, 176 – 179 (1991).
10. Y. Nitta, J. Ohta, S. Tai and K. Kyuma, "Variable sensitivity photodetector using metal-semiconductor-metal structure for optical neural networks", Opt. Lett., 16, 611 – 613, (1991).
11. M. A. Mahowald and C. Mead, "Silicon retina", *Analog VLSI and Neural Systems*, Addison-Wesley, MA, 257-278 (1989).
12. Mead, "Neuromorphic electronic systems", IEEE, 78, 1629-1636 (1990).
13. L. Standley, "An object position and orientation IC with embedded imager", IEEE J. Solid-State Circuits, 26, 1853-1862 (1991).
14. W. Bair and C. Koch, "An analog VLSI chip for finding edges from zero-crossings", *Advances in Neural Information Processing Systems*, 3, CA, 399-405 (1991).

Application Of Wavelet Transform Towards The Optimization Of Signal Parameters Of An Optical Wireless Local Access Network (WLAN)

N. Patnekar [1], G.C. Giakos [2], L. Fraiwan [1]
Optical Communications and Opto-Electronics Laboratory
[1] Department of Biomedical Engineering, The University of Akron, Akron OH, 44325, USA
e-mail: pninad@uakron.edu
[2] Department of Electrical Engineering, The University of Akron, Akron OH, 44325, USA
e-mail: gcgiakos@uakron.edu.

INVITED PAPER

Abstract

This paper is aimed to optimize the signal parameters necessary for designing an optical wireless local access network (WLAN), utilizing Wavelet Transform. The design of such a network is based on the specifications set by the IEEE 802.11 standard. A short range IR communication technique that is cost effective and requires less power considerations is used. Signals detected under line-of-sight point-to-point geometry are shown in this paper.

***Keywords**: Optical wireless, Wavelet Transform, WLAN, Infrared technique, noise reduction.*

INTRODUCTION.

The growing need for an optical wireless local access network has resulted from its attributes of being more secure, fast and immune to electromagnetic interference (EMI). This technology is utilized in large scale in developing portable personal computers, mobile communication, laptops, PDAs etc. These portable devices integrate computational power and mobility on a single platform and introduce the need for accessing communication networks without the restrictions imposed by cables [4]. The increasing interest in the wireless local access network gave way to the international standardization of this technology. In June 1997, a standard for WLAN for different technologies including radio and infrared set by the IEEE 802.11 committee was approved [4]. An essential characteristic of the IEEE 802.11 standard is that there is one single medium access control sub-layer for all the physical layers [4]. The medium access is based on a carrier sense multiple access with collision avoidance protocol (CSMA/CA)[2]-[4]. The physical layer deals with the actual transmission of the signal. This can be done either by radio or infrared. The infrared technology is very well suited for such a low-range application because of the following characteristics:

- Cost effective.
- High bandwidth for data transmission and hence is faster.
- More secure transmission.
- Low power requirements.
- EM interference free.

According to the specification the infrared physical layer can support two data rates: 1 Mb/s and 2Mb/s. The specification is aimed at allowing a smooth migration to higher data rates [4]. There is a different modulation scheme for each data rate: 16-PPM for 1Mb/s and 4-PPM for 2Mb/s. Other modulation schemes such as ASK and RZI (return to zero, inverted) can also be implemented. Lasers or light emitting diodes (LED) can be used as a transmitter. However, for an indoor environment LEDs are preferred as optical transmitters over lasers because they can produce substantial launch power and yet be Class 1 eye safe [1,6,7]. Infrared radiation has properties similar to light and hence indoor surfaces are good reflectors of infrared [4]. The system can be designed with two different geometries in consideration:

- Line-of-sight point-to-point
- Diffused geometry.

In line-of-sight geometry, an obstacle between the transmitter and receiver can introduce attenuation of the collected optical power which is typically called shadowing effect. In diffused geometry, there is a reduction in the collected optical power due to the multipath propagation of the signal. Propagation through multiple paths can give rise to time dispersion of the received pulses, which is called multipath dispersion. The bandwidth of the infrared link is determined by multipath dispersion [4]. Along with these interferences the system is also vulnerable to fluorescent and incandescent light that flickers on-off at 120Hz [9]. However, this noise can be eliminated by using signal processing algorithms.

DESIGN THEORY

A basic IEEE 802.11 architecture for WLAN is shown in fig.1. A group of stations that can have direct communication are called the basic service set (BSS) and the area occupied is called the basic service area (BSA). The basic service area can overlap or be totally disjoint. Different BSAs are connected by system called distributed system. A group of BSAs interconnected by a distributed system is called as an extended service system. The simplest IEEE 802.11 network is an independent BSS. The communication between the individual stations is based on the infrared technology. The IEEE 802.11 medium access layer is based on the carrier detect multiple access collision avoidance. When a station is ready to send data, it checks whether the channel if free. If the channel is free it starts the transmission immediately. If the channel is busy it keeps on checking the channel till it becomes free. The actual transmission is carried by using a transceiver. A transceiver is capable of communicating in both directions.

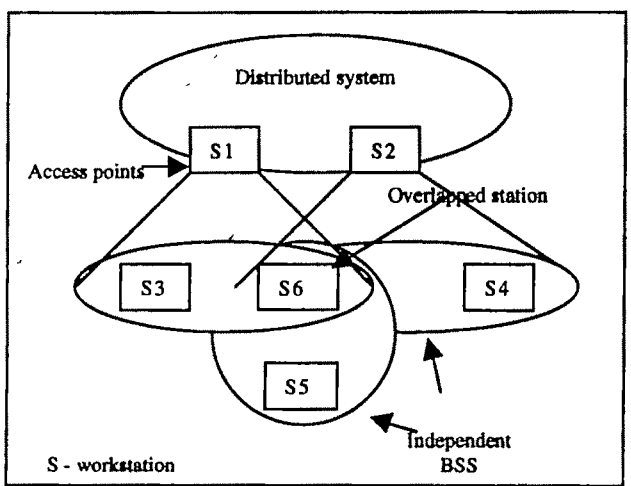

Fig 1 IEEE 802.11 Network architecture

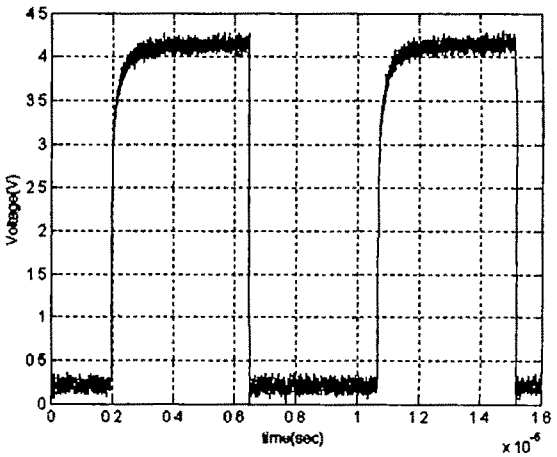

Fig 2 Unfiltered detected signal using LOS point to point geometry

WAVELET THEORY.

The signal received after transmission from a remote station is often contaminated by noise. The noise is further eliminated by using an appropriate signal processing algorithm. Wavelet transform is used in our case for removal of high frequency noise. A Haar transform is used to eliminate noise with appropriate thresholding up to level 6. Each level of transform gives us a trend, which is the signal and a fluctuation, which is the noise. All values of the fluctuations that are below the noise level are set to zero and a inverse transform is applied [5]. This technique gives a good approximation of the signal. Instead of a software filter, a hardware chip can be used that is programmed to give the output directly after taking the wavelet transform. Microcontrollers or DSP boards can be used which can perform such a dedicated function.

EXPERIMENTAL SETUP AND RESULTS

In this study two infrared transceivers HSDL-1100 from Agilent technologies have been used. The HSDL-1100 transceiver contains a high speed, high efficiency, TSAlGaAs 870 nm LED, a silicon PIN photodiode and a bipolar, silicon integrated circuit. The IC contains an LED driver that is set to drive the LED at a speed of 115.2 KHz. The receiver has high sensitivity to infrared signal and attenuates all signal outside the range. It also has an inbuilt lens that increases the effective field of view of the receiver and also contains a dye that absorbs visible light. The two transceivers are set up in a point-to-point line-of-sight geometry. Fig.2 shows the detected optical signal that was obtained under this transmission geometry. Further to

process the signal wavelet transform was applied to remove the noise component associated with the signal.

Haar wavelet was used to denoise the signal, as it is very efficient for 1-d signal. The filtered signal obtained after signal processing is shown in fig.3. And finally filtered noise components associated with the detected signal is shown in fig. 4.

CONCLUSION

In this paper, characteristics of the detected signal under indoor line-of-sight point-to–point geometry has been presented. By processing the data obtained with wavelet transform algorithms, a significant reduction of noise can be achieved. This paper forms a basis for the design of an Infrared Physical Layer for an Optical Wireless Local Access Network based on the IEEE 802.11 standards.

REFERENCES

1. G.C. Giakos, N. Patnekar, L. Fraiwan, S. Sumrain, N.Reddy, R. Nemer, K. Mehta, "Optimization of an Optical Wireless Communication System",
2. J.M. Kahn, and J.R. Berry, "Wireless Infrared Communications", Proc. IEEE, pp. 265-298, 1997
3. A. Moreira, R. Valadas, and A. Duarte,"Optical Interference Produced by Artificial Light", ACM Wireless Networks J., vol.3., pp. 131-140, 1997.
4. A. Moreira, R. Valadas, A Travares and A. Duarte, "the Infrared Physical Layer of the IEEE 802.11 Standard for Wireless Local Area Networks", IEEE Communication Magazine, December 1998, pp 107-112.
5. J.S. Walker, "Wavelets and their Scientific Applications", CRC Press, 1999.
6. J.R. Barry, "Wireless Infrared Communication", Boston, Klwster, 1994.
7. D. Heatley, D. Wisely, I. Neild and P. Cochrane," Optical Wireless: The Story So Far", IEEE Communication Magazine, December 1998, pp 72-82.
8. J.M. Elmirghani, and R.A. Cryan, "New PPM-CDMA Hybrid for Indoor Diffused Infrared Channels", Elect. Lett., vol. 30, no. 20, pp. 1646-1647, 1994.
9. H. Uno, K. Kumatani, H. Okuhata, I. Shirakawa, T.Chiba, " ASK digital demodulation scheme for noise immune infrared data communication.", Wireless Networks 3, 1997 pp 121-129.

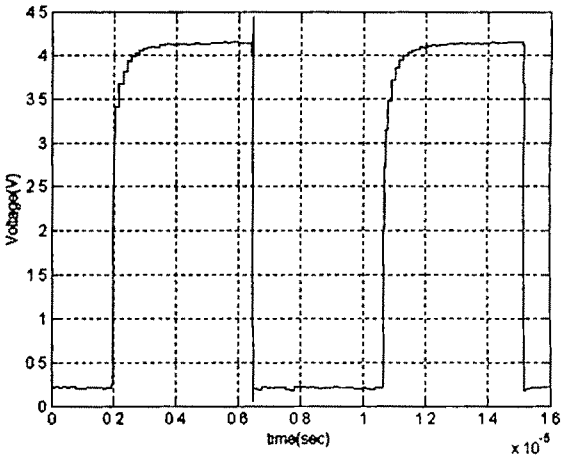

Fig 3 Unfiltered detected signal under LOS point-to-point parallel to surface optical link geometry

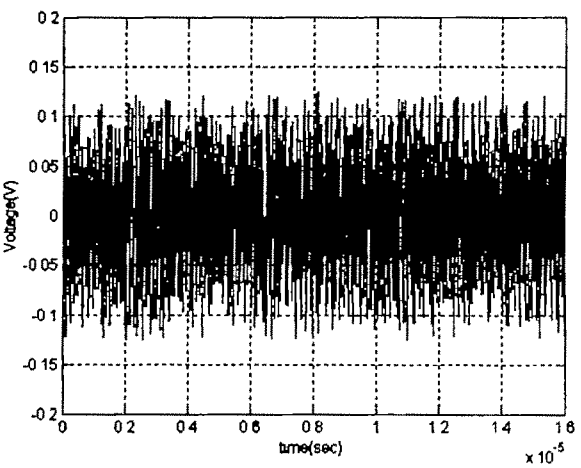

Fig 4 Removed noise under LOS point-to-point optical link geometry

Word Matching Algorithm in Information Processing

Vadali Srinivasa Murty and S. Raman
Dept. of Computer Science and Engineering
Indian Institute of Technology- Madras, Chennai, 600036,India.
smvadali@yahoo.com, raman@iitm.ernet.in

Abstract

Natural Language Processing (NLP) is required for numerous applications in the field of computer science. A large size of lexicon cannot be avoided in almost any NLP application. There are some time-critical applications like NLP interface to robot which require the speed of response to be very fast. This requirement can be met by using dedicated hardware solutions in the implementation of NLP tools. A preliminary study was made on dedicated hardware for NLP parser using modified string matching algorithm, which is based on parallel comparison with lexical entries. A comparative study was made between the performances of simulated hardware based on modified string matching algorithm and the software approach based on a traditional string matching algorithm [1]. An improvement of five times in speed was observed.

Key words: Information processing, word matching

INTRODUCTION

All NLP applications require parsing of the input sentence as a primitive operation. Parsing involves string matching which compares the input word with different lexical entries. Due to the usually large size of the lexicon, the process of string matching takes considerable amount of time, which is a limitation in some time-critical applications. This paper presents a technique of overcoming the limitation to some extent by having a dedicated hardware, which implements a modified string matching algorithm, which in turn, uses parallel processing techniques.

There are two approaches in handling the inflected words. One is by storing only the root words. In this approach, a morphological analysis is needed for matching the inflected words. The second approach is that of storing all the inflected words along with their respective root words in the lexicon. The former requires less amount of memory, but needs more time for processing. The later approach needs a little more memory compared to the former, but increases the speed of processing.

Raman and Shaji [1] have proposed an algorithm for string matching in which the lexicon is stored in alphabetical order and a sequential search is made on the lexicon. Only root words are stored in the lexicon, and morphological analysis is required for matching of inflected words. In the case of inflected words, all the words whose first character matches with the first character of the input word are taken into consideration. Some rules are framed depending on the type of root words. All these rules are applied on the selected lexicon entries in the process of matching the inflected words.

James J Hardwicke [2] proposes an algorithm for parallel access to an English dictionary. This algorithm also stores only root words in the lexicon and requires morphological analysis for inflected words. This algorithm divides the lexicon into different groups using alphabetical order. This algorithm uses upto five transputers and the dictionary is split over these.

Smith and Pierzchala [3] sketch an algorithm that uses a parallel and iterative technique for approximate string matching.

The above algorithms do not categorize the lexicon from the viewpoint of Part Of Speech (POS) tags. In this paper, we propose an algorithm, which categorizes the lexicon using the information of POS tags. All the inflected words along with their POS tags are stored at appropriate places in the lexicon. A simultaneous search is made among different categories of the lexicon because of which a considerable improvement in speed has been achieved. A comparative study was made between the simulated hardware based on modified string matching algorithm and the software approach based on traditional algorithm [1]. An improvement in speed of about 5 times has been observed.

MATCHING TECHNIQUE

The words in the lexicon are divided into different categories, and arranged in alphabetical order within each category. The lexicon is broadly divided into two categories as open class and closed class or high frequency words. Closed class or high frequency words are fixed in number. On an average, every sentence consists of about 30% [2] of words as high frequency words. Since these are less in number, improvement in string matching can be achieved by having them as a separate class. The open class words are again divided into four categories as Noun, Adjective, Verb and Adverb.

The match for the input word will be searched for first among high frequency words whose number is less. The search will be done as per the binary search algorithm. If the search is successful it will assign POS tags, which are stored along with each entry in lexicon, to the input word. If the match fails, a simultaneous search will be made on open class words, the size of which is usually large and may include new words. Since there are four categories in open class words, four comparator units are designed one for each category. In each comparator unit, there are three registers one for storing the starting address of that category, the second for the ending address, and the third one is for storing the result of comparison in that particular unit. These registers are called **start_cat, end_cat** and **compare_success** respectively. If comparison is successful in any unit, the **compare_success** register of that particular unit will be set. At the end of the comparison, values of **compare_success** registers of all the comparator units will be considered in assigning the POS tags to the input word. All the words of the input sentence with their POS tags are given as input to the top down chart parser, which parses the input sentence.

MATCHING ALGORITHM

The pseudo program of the matching algorithm is given below.

for (from start of high frequency words to end of high frequency words) **do**
begin
compare the input word with high frequency words using binary search algorithm with the first character of lexical entry as index
if (**comparesuccess**==1)
begin
assign POS tags to the input word and **exit** with status SUCCESS
end
else
begin
for (simultaneously from start to end of each open class category) **do**
begin
compare the input word with open class words in simultaneous manner using binary search algorithm with the first character of lexical entry as index
if any of the comparison unit's **comparesuccess** register is equal to one
begin
assign the pos tags to the input word depending on the value of the corresponding **comparesuccess** registers
exit with status SUCCESS
end
else
exit with status FAILURE
end

IMPLEMENTATION OF THE MATCHING ALGORITHM

The block diagram of comparator unit for high frequency words is shown in **Fig. 1**. Each word in the lexicon is stored in ASCII form. The ASCII value of first character of input word is compared with the first character of some random high frequency word in the lexicon. **Figure 1** shows an 8-bit comparator with A and B as inputs. A is the ASCII value of first character of input word and B is the ASCII value of first character of lexical entry. If comparison is successful the comparator unit will look for the matching of the remaining characters of the input word with lexicon. Otherwise the comparator unit will take the next high frequency word from the lexicon using the binary search algorithm. If all the characters of the input word match with those of a high frequency word in the lexicon, then POS tags of that high frequency word will be assigned to the input word. The comparator units for open class words are similar to the one we have discussed for high frequency words. All the input words with corresponding POS tags will be the inputs to the top-down chart parser, which parses the input sentence.

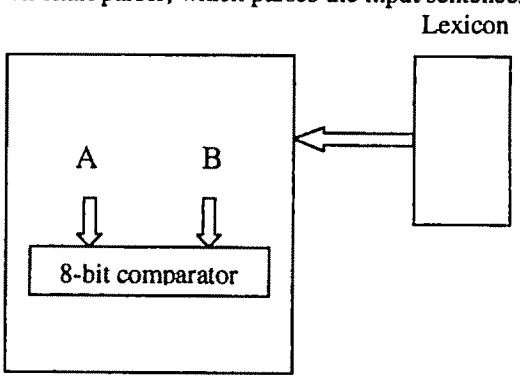

Fig 1: Comparator unit for high frequency words

MEMORY ORGANIZATION OF LEXICON

The format of each entry in the lexicon is as shown below.

The format of each lexical entry

Input word in ASCII code (104 bits)	Category in encoded form (4 bits)	Tense of verb in encoded form (3 bits)	Agreement register in encoded form (6 bits)

A maximum of 13 characters (8-bit each) are reserved for each word in the lexicon, thus requiring a total of 104 bits for storing an input word in ASCII code. Table1 shows the code for each of the 9 categories.

Table 1: Encoded form of categories

No.	Category	Code
1	Article	0000
2	Adjective	0001
3	Noun	0010
4	Verb	0011
5	Pronoun	0100
6	Preposition	0101
7	Primary auxiliary	0110
8	Secondary auxiliary	0111
9	Pronoun	1000

Table2 shows the code for each of the 6 verb forms.

Table 2: Encoded form of verb forms

No.	Verb form	Code
1	Base form	000
2	Present form	001
3	Past form	010
4	Present participle	011
5	Past participle	100
6	Not verb	101

Person ($1^{st}/2^{nd}/3^{rd}$) and number (Singular & Plural) agreements are registered in a 6 bit register as shown below:

1S	1P	2S	2P	3S	3P

where for instance 1S is for first person singular, and 2P stands for second person plural.

Every bit will be set or reset depending on the agreement information about the lexical entry. For example, if the lexical entry is an article 'a', then the register contents will be as shown below, corresponding only to Third person singular.

0	0	0	0	1	0

ARCHITECTURAL DETAILS

Block diagram is shown in **Fig. 2.** Each word from the input sentence will be sent to the input word register. It will be compared in the appropriate comparator unit associated with the PROM containing the high frequency lexical entries. If comparison is successful, the corresponding POS tags will be given to the input word in the assignment block. If comparison is not successful, then it will enable another input word register (buffer) which passes the input word to all the open class comparator units (1to4). The result of comparator units will be sent to the POS tag assignment block.

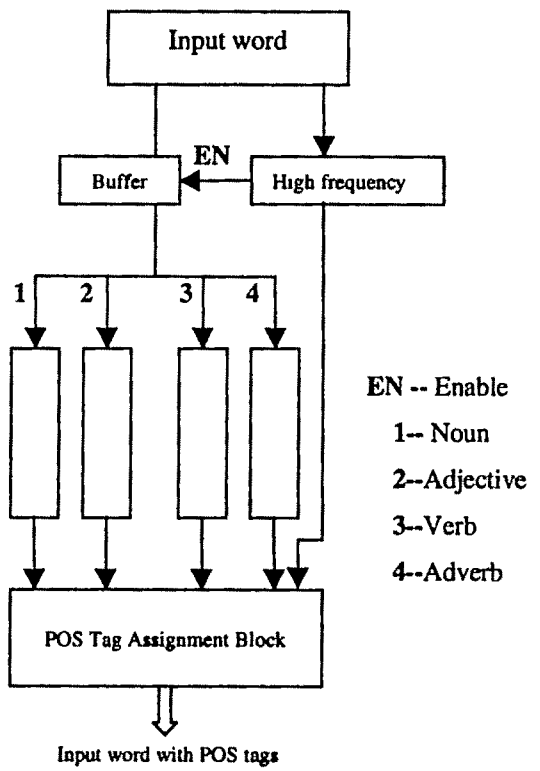

Fig 2: Block diagram of the matching unit

IMLPEMENTATION OF PARSER

All the words with POS tags of input sentence will be given as inputs to the top-down chart parser. In a Top-down chart parser, the input sentence is parsed by considering the rules of the specific grammar, one after another. If any of the input words is not matching successfully then that sentence need not be sent to the parser. For example, take a simplified grammar.

NP-> ART ADJ N
NP-> ADJ N
NP-> ART N
NP-> N
VP-> V NP
VP->V NP PP
VP-> V NP P PP

The encoded form of grammar is

NP-> 0000 0001 0010
NP-> 0001 001
NP-> 0000 0010
NP-> 0010
VP->0011 NP
VP->0011 NP PP
VP->0011 NP 0101 PP

All the input words along with their POS tags of the input sentence are parsed using the above rules.

RESULTS AND DISCUSSION

There are three different possible cases in the matching of the input word.

Case1: Input word is a high frequency word

If the input word is a closed class word, the expected worst-case time complexity by our algorithm is $\lceil \log_2 m \rceil$, where **m** is the number of high frequency words. With traditional string matching algorithm [1], the expected worst-case time complexity is $\lceil \log_2 n \rceil$, where **n** is the total number of entries in the lexicon. Since **n>>m,** the improvement in speed by our algorithm is significant in the case of high frequency words.

Case2: Input word is an open class word

If input word is an open class word the expected worst-case time complexity with our algorithm is $\lceil \log_2 ((n-m)/4) \rceil + \lceil \log_2 m \rceil$. Since **n >>m**, the time taken for the open class category can be approximated to $\lceil \log_2 (n/4) \rceil$. With the traditional algorithm [1], the expected worst-case time complexity is $\lceil \log_2 n \rceil$. Thus there is considerable improvement, in this case also.

Case3: Invalid words

In this case, the time complexity analysis is nearly similar to that for open class words, except that the result will not identify any specific lexical entry.

Given that every sentence consists of about 30% of high frequency words as inputs, the average time for matching an input word, by the two algorithms, is as follows.

Traditional algorithm: $\lceil \log_2 n \rceil$

Proposed algorithm: $0.3 * \lceil \log_2 m \rceil + 0.7 * \lceil \log_2 (n/4) \rceil$

From the above comparison, one can see that there is considerable amount of improvement in speed with the proposed algorithm. This has been due to parallel matching as well as to a prior classification of words based on their frequency of occurrence. Further, in the software approach there will be a large number of secondary memory accesses, necessitated by the large size of the lexicon, thus leading to more time in the process of matching. On the other hand, a dedicated hardware with the proposed string matching algorithm will significantly improve the speed of processing, both because of the algorithm and the implementation.

A basic parser for a restricted grammar was simulated in hardware. A comparative study was made between simulated hardware with proposed algorithm, and software approach with traditional algorithm. A speed up by a factor of nearly five was observed with simulated hardware. **Figure 3** shows the stabilization of the percentage improvement for increasing number of sentences. It may be seen that the improvement in speed stabilizes between the values of 4 and 5.

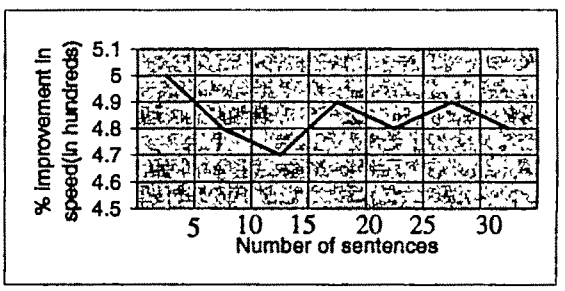

Fig 3: Percentage improvement in speed for increasing no. of sentences

DEVICE PROGRAMMING

Dedicated hardware for NLP parser was implemented using Verilog HDL using Altera MAX+plus10.0 FPGA tool. Details of logic cells, input /output pins, fan-in etc. of FPGA device used are given below.

Device used: EPF8282ATC100-2
FLEX 8000 configuration scheme: Active serial
Total dedicated input pins used: 4/4 (100%)
Total I/O pins used: 66/74 (89%)
Total logic cells used: 137/208 (65%)
Average fan-in: 3.45/4 (86%)
Total fan-in: 474/832 (56%)
Synthesized logic cells: 109/208 (52%)
Clock period: 15.3 ns
Frequency: 65.35 MHZ

FUTUTRE WORK

The predictive nature of the top down parser method can be exploited to optimize the matching algorithm in the sense that the knowledge of the expected category of the next token in the input system can restrict the search space to some specific lexical categories, thus pruning the search space. A token of an irrelevant category then

would imply a syntax error, and can make the parser exit. This is an issue worthy of future study.

REFERENCES

1. Raman, S and Shaji E R 'ASIC design of a matching unit' *Microprocessors and Microsystems* Vol 19 No 6 (July/Aug 1995) pp 327-340
2. Hardwicke, J J *et al.* 'Parallel access to an English dictionary' *Microprocessors and Microsystems* Vol 15 No 5 (July/August 1991) pp 291-298
3. Smith, D and Pierzchala, E 'An algorithm and architecture for approximate string matching' *Proc. Conf. 33rd Midwest symposium on circuits and systems* (1991) pp 736-739
4. Hall, P A V and Dowling, G R 'Approximate string matching' *Comput. Surv.* (December 1980) pp 381-402
5. Grossi, R 'A fast VLSI solution for approximate string matching' *Integration VLSI J.* Vol 13 No 2 (June 1992) pp 195-206
6. Morozov, S A *et al.* 'Hardware for character string matching ' *J. Computer System Science intern.* Vol 31 No 1 (January 1993) pp 71-81
7. Galil, Z and Park, K 'An improved algorithm for approximate string matching' *SIAM J. compute.* Vol 19 (December 1990) pp 989-999
8. Allen, J *Natural language understanding* Benjamin Cummings, Mento park, CA(1987)
9. Mano, M M *Digital Logic and Computer Design* Prentice-Hall, New Delhi (1989)
10. Palnitkar, *Verilog HDL* Sunsoft Press Prentice-Hall
11. *Altera MAX+plus 10.0 BASELINE* (FPGA Tool) Altera Corporation

Framing Strategy for Congestion Control in BISDN/ATM

S. K. Singhai, K. K. Saxena, N. P. Singh
Electrical Department, Government Engineering College, Bilaspur 495009, India

Abstract

The idea behind the framing strategy in packet switched networks is to confine packets entering into the network form any source within logical containers travelling through the network, called time frames. As long as the packets remain confined to their allotted time frames, the original smoothness of the admitted traffic stream can be maintained through the internal nodes of the network. As the packets of different frames cannot cluster together, cell loss can be eliminated if an upper bound is placed on the number of cells which can admitted within a time frame, and thus allowing the prediction of worst case queue sizes at each node. This paper reviews framing strategy to avoid it.

INTRODUCTION

The framing strategy is composed of two components: a packet admission policy imposed per connection at the edges of the network, and a particular service discipline at the switching nodes named stop-and-go queuing. Before discussing these concepts we introduce some formal notation. Let the network consist of N nodes j = 1,2.....N and L links I = 1,2,....., L with C_l being the transmission capacity of link l in bits/ sec. Let us denote the sum of the propagation delay of each link l plus the processing and switching time at the receiving and of I by T_l.

Central to both components of framing strategy is the notion of time frames. Let T_1 ,T_2 , ... T_G be a set of allowable time frames common to the whole network. For each time frame size T_g the time axis is divided into successive periods of length T_g called the type g frame. For each link of the network these frames may be defined independent of other links i.e. with reference to an arbitrary time- origin associated with that link. Over each link the corresponding frames of the link can be viewed as travelling with the packets from one end of the link to the other end and on to the processing and switching device at the receiving end, Therefore the frames at the receiving of link l, which will be called the arriving frames of l are T_l seconds behind the corresponding frames at the transmitting end called the departing frames of l.

ADMISSION POLICY

Packet admission policy is defined on a per connection basis. Connection *K* is defined as a stream of traffic going from a given source node i to a given destination node j over a fixed path and regulated according to given set of parameters. Each connection in the network is set-up in association with a frame Packets of a type g connection are referred to as type g packets. The type of a packet (the value of g) must be indicated in the packet header.

Before a connection k is admitted to the network a transmission rate r_k must be assigned to it. This assignment is done after allocating a transmission capacity equal to r_k on each link along the path to the destination. Denote the set of connection of type g that traverse link l by k (l, g) and the aggregate transmission capacity allocated to all connections k E k (l, g) by C_l^g

C_l^g = Sigma (r_k, g) , g =1 *thru* G, L=1 *thru* L

Capacity allocation over a link l is used to ensure that a constraint of the form,

Sigma (g=1 to G), where C_l^g is less than or equal to C_l

is satisfied by aggregate allocated capacity C_l^g . Note that the connections are multiplexed in a non-statistical manner and bandwidth is allocated on its peak rate requirement in order to eliminate cell loss.

Definition 1: A stream of packets arriving over a link I is defined to be (r, T_g) smooth if the aggregated length of packets received during each arriving type g frame of l is limited to r x T_g bits. Equivalently, if only packets of fix size Tee are encountered a stream of packets is (r, T_g) smooth if the number of received packets during each arriving type g frame is bounded by (1/ Tee) x r x T_g . In definition 1, a packet is considered as received during a

frame F if its last bit has arrived during F. Only an integral size T_g in which case it will be called a type g connection number of packets can be considered as received during each frame.

The packets admission policy and be stated as the following rule: once a connection k is set-up in the network its arriving packets stream over the corresponding access link is required to be (r_k, T_g) smooth where r_k is the allocated transmission rate and T_g is the associated frame size . Any arriving packet that violates this rule is not admitted into the network.

STOP-AND-GO QUEUING

Packet admission policy guarantees that the traffic stream of each type g connection k with an allocated rate r_k is (r_k, T_g) smooth upon admission to the network . If this property continues to hold as the packet stream of each connection arrives to the intermediate switching nodes then the problem of congestion is indeed solved. Unfortunately, this is not the case always. In case of conventional FIFO queuing, as the packets of a connection proceed to the destination node, this may cluster together and form bursts, violating the original smoothness property. Formation of long burst can cause serious degradation in delay and loss performance of the network and therefore must be avoided. The stop-and-go queuing solves this problem and preserves the original smoothness property of connection throughout the network.

To describe stop-and-go queuing, consider a node j with some incoming and out going links. Due to the arbitrary choice of time origins of the links and the arbitrary value of link propagation delays, the arriving frames of incoming links and the departing frame of outgoing links need not be synchronous. Few definitions in this paper establish a correspondence between pairs of arriving and departing frames of similar type over the incoming and outgoing links of j.

Definition 2: At a node n. an arriving type g frame F' of an incoming link l' and a departing type g frame F of an outgoing link l constitute an adjacent pair, if F is the first departing type g frame of l, that start after F' expires. l and l' can represent an internal link as well as an access link of the network.

Definition 3: At a node n, the phase mismatch of type g between an incoming link l' and an outgoing link l, denoted by Phl'lg is defined as the time between the end of an arriving type g frame of l' and beginning of the adjacent frame l. Clearly,

$$0 <= Thll'g < T_g$$

Stop-and-go queuing is based on the following three rules:

(a) Consider a node, an incoming link l', and an outgoing link l, and a packet of type g that has arrived during a type g frame F' of link l' and seeks service by link l. Let F be the departing frame of link l that is adjacent to the arriving frame F'. The packet does not become eligible for transmission by link l until the beginning of frame F and must be served before the end of F.

We see from this rule that new packets of a given type g are assigned as being eligible for transmission by a link l only at the beginning of type g departing frame of l. During a departing frame, the set of eligible packets of corresponding type constantly reduces in size, until the beginning of the subsequent frame, when new packets of that type become eligible.

(b). Any eligible type g packet, g=2,3...G has non-pre-emptive priority over eligible packets of type g'<g.

(c) A link should not stay idle while there is any eligible packet left in queue.

The stop-and-go queuing does not corresponds to any unique service discipline. The service discipline used here is FIFO since it enables sequenced delivery of packets at the destination. It is convenient from the user point of view and has simple hardware realization. This realization is called delayed FIFO queuing.

MAIN PROPERTIES

The crucial role of stop-and-go queuing is the prevention of packet clustering and the preservation of traffic smoothness. Traffic smoothness inside the network is essential for the provision of zero-loss and bounded-delay communication. These properties are articulated in a theorem. The theorem in detailed paper is stated without proof, for the special case where frame sizes are multiples of each other.

Theorem 1: Consider packet switching network N with the following assumptions:

1. Each frame size is multiple of smaller frame $T_g=I_g$ x T_{g+1}, g=1,2,.....G-1 for some integer I_g
2. The packet stream of each connection k of type g with the allocated transmission rate r_k is (r_k,T_g)-smooth over the access link to the network.
3. The stop-and-go queuing strategy described by rules a to c is practised at every network node.
4. The network initially contains no packets of any type g=1,.....,G.
5. The following constraint is satisfied by the aggregate allocated capacities C_l^g over each link l:

$SIGMA_{g=g0\ to\ G}\ C_l^g <= C_l - (\ Tee\ max\ /\ T_{g0})$, g0=2 to G and <=$C_l$, g0=1
where Tee_{max} is the maximum length of the packets in the network.

It then follows that:

a. Once a type g packet is designated as eligible for transmission by some link, it will receive service within T_g seconds, i.e.., before the current departing frame of type g expires.
b. The packet stream of each connection will maintain original smoothness property throughout the network.
c. At an outgoing link l of a node n, loss of packets of type g is eliminated by dedicating a buffer size,

   B_l^g=$Beta_l^g$ x C_l^g x T_g, $Beta_l^g < 3$ to the traffic of type g.

The possibility of loss free communication is established by part c of the theorem, while part a amounts to a bounded delay property, as will be discussed in the next sub section. According to part c., a total buffer space of size,

B_l= SIGMA (g=1 to G) $Beta_l^g$ x C_l^g x T_g

where $Beta_l^g$ < 3, g = 1 .....G is sufficient to eliminate buffer overflow at each link l, in regard to the traffic of any type g = 1,....G The actual value of $Beta_l^g$ depends on the transmission capacities and phase mismatches of type g of various incoming links l, relative to the outgoing link l. The properties of the framing strategy remain valid regardless of the changes in transmission speed and network size.

DELAY AND JITTER PERFORMANCE

The end-to-end delay of a packet is defined as the time between its arrival to the source node and its arrival to destination node. Consider a connection k of type g accessing the source node via access link l0 and traversing H internal links of the network denoted by l1, l2, ... lH.

The end-to-end delay of a packet p of the connection can be expressed as

$$D_k^g + d_p^g$$

where D_k^g defined as the connection delay, it is constant for all packets of the connection and dp^g, varies from packet to packet constituting a delay jitter term. This delay jitter is equal to the displacement of the packet as compared between the corresponding arriving frame to the source node and the corresponding arriving frame to the destination node and is therefore bounded by

$$-T_g < d_p^g < T_g$$

The connection delay D_k^g, itself can be broken into two parts:

$$D_k^g = Toe_K + Q_k^g$$

where Toe_K is the sum of end-to-end propagation and processing delays

$$Toe_K = SIGMA\ (h=1\ to\ H)\ Toe_l^h$$

where Q_k^g represents the total queuing delay of the connection Furthermore Q_k^g can be expressed as

$$Q_k^g = H\ x\ T_g + SIGMA\ (h=1\ to\ H)\ Theta^{g}_{lh-1,lh}$$

Finally Q_k^g is bounded by,

$$H\ x\ T_g <= 2\ x\ H\ x\ T_g$$

In summary as seen from above, the end-to-end packet delay of a connection k is constant except for a delay jitter between T_g and $-T_g$ The constant delay term D_k^g is the sum of the total propagation delay Toe_K and the total queuing delay Q_k^g where Q_k^g is between H x T_g and 2 x H x T_g

If the packet delay distribution in this scheme is compared to FIFO queuing, we observe that the delay associated with conventional FIFO queuing is smaller on the average, it is distribution over a much wider If the packet delay distribution in this scheme is compared to FIFO queuing, we observe that the delay associated with conventional FIFO queuing is smaller on the average, it is distribution over a much wider range creating considerable delay jitter The maximum delay resulting form conventional FIFO queuing can far exceed that provided by the framing strategy.

TRADE-OFF BETWEEN QUEUING DELAY BUFFER REQUIREMENTS AND GRANULARITY OF TRANSMISSION CAPACITY

There are three performance criteria that are affected by the choice of frame sizes: the end-to-end delay of the connections, the required buffer space and the granularity of the transmission capacity. The queuing delay of a type g

connection k traversing H links in the network Q_k^g is a fixed value between $H \times T_g$ and $2 \times H \times T_g$ we may express these quantities as

$$Q_k^g = \text{Alpha}_k^g \times H \times T_g$$

where Alpha_k^g is a coefficient between 1 and 2 depending on the phase mismatches between the pairs of adjacent frames of type g along the corresponding source destination path the required buffer space per link l for providing loss-free communication to the traffic of type g is

$B_l^g = \text{Beta}_l^g \times C_l^g \times T_g$, $\text{Beta}_l^g < 3$ to the traffic of type g.

Finally the transmission capacity can be allocated to the connections in the incremental steps of one packet per frame. Assuming that all packets in the network have a fixed length of Tee bits the incremental steps of rate allocation to a connection of type g would be

$\text{Delta } r^g = Tee / T_g$ Bits / Second

It is now clear that reducing the frame size T_g leads to an almost proportional reduction in the end-to-end delays as well as the buffer requirements for the corresponding traffic of type g. However it will also result in a proportional increase in the incremental steps of rate allocation i.e. reduced granularity of transmission capacity for that traffic type. Therefore the choice of the frame sizes involves a trade-off between the end-to-end delay and the buffer requirements on the hand, and the granularity of transmission capacity on the other hand. By combining above results the trade-off can be expressed as

$\text{Delta } r^g \times Q_k^g = \text{Alpha}_k^g \times H \times Tee$, $1 <= \text{Alpha}_l^g$,and

$\text{Delta } r^g \times B_l^g = \text{Beta}_l^g \times C_l^g \times Tee$, $\text{Beta}_l^g < 3$

This states that within a particular traffic type and for a given number of hops and a fixed packet size the increments of rate allocation and the queuing delay cannot be simultaneously decreased and a reduction in one would lead to a proportional increase of the other. A similar trade-off is also expressed between the buffer requirements for a given traffic type and the corresponding increments of rate allocation.

CONCLUSION

The realization of stop-and-go queuing at a node is particularly simple when either the arriving or the departing frames of the node are synchronous. The realisation aspect is not discussed here in detail however it has been established that while the framing strategy is very effective in eliminating congestion, it is wasteful in it's bandwidth allocation. Modified framing strategy is special case of framing strategy and proves beneficial in terms of network resource utilisation, when a bundle of virtual circuits originating from source, travel via the same path through the network to the destination.

REFERENCES

1. M. Iiyas and H.T. Mouftah,"Performance evaluation of congestion avoidance in BISDN", IEEE ICC, pp439-442, 1990.
2. Bijan Jabbari," A Bandwidth allocation technique for high speed networks" Ed.Turner J., *" The challenge of multipoint communication"*, 5th ITC seminar on traffic engineering for ISDN a design and planning, Lake Como, May 1987.
3. Gillian M Woodruff, R Kositpaiboon,"Multimedia traffic management principles for guaranteed network performance", IEEE JSAC Vol 8,No 3,pp 437-446, April 1990.
4. .Raj Jain," Congestion control in computer networks: issues and trends IEEE Network magazine, pp 24-29, May 1990.
5. G.M. Woodruff, R.G.H. Rogers, P.S. Richards," A congestion control framework for high speed integrated packetised transport", Conference record of IEEE Globecom'88, pp 203-207.

Performance Evaluation Of Handover Initiation Algorithm For Microcellular Systems

Brahmjit Singh* and K.K. Aggarwal**
* Electronics, Communication and Computer Engineering Department
Regional Engineering College, Kurukshetra-136119
** Guru Gobind Singh Indraprastha University, Delhi-110006
E-mail: pranjal_bjs@rediffmail.com

Abstract

Handover is the process that transfers an ongoing call from one cell to another as the mobile station moves through the coverage area of a cellular system. Due to random nature of the communication channel in mobile radio, it is difficult to determine the correct point for a handover. This paper presents simulation results of performance evaluation of handover initiation algorithm based on signal strength measurements. The handover decision depends upon the relative signal strength with threshold and hysteresis approach. Expected number of handovers and handover delay are used as the performance metrics. Based on the simulation study, the values of algorithm design parameters viz, hysteresis margin and length of averaging window are quantified for optimum trade-off.

Key words: Handover, Mobile Communication, Microcellular Systems.

INTRODUCTION

In the past few years, mobile communication industry has witnessed tremendous growth in the demand for high capacity wireless systems. Smaller cells are deployed to increase the traffic capacity in a limited spectrum allocation [1][2]. But as the cell size decreases, probability of crossing several boundaries between adjacent cells by a Mobile Station (MS) during a single call is increased. When a call is in progress, the network is required to maintain the call across the cell boundary. The continuity of the ongoing call is maintained by performing the call transfer to an alternate BS. Handover is the process whereby a MS communicating with one base station (BS) is switched to another BS during a call. Ongoing call transfer should be seamless to the mobile user to maintain the quality of service during the connection period. Figure (1) shows the handover of an ongoing call from one cell to another.

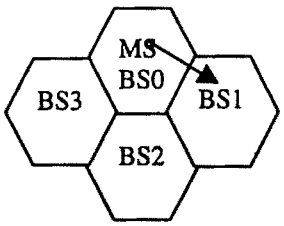

Fig 1. Handover from one cell to another in a cellular layout.

This process is especially important in microcelluar systems, where due to the reduced cell size (radius≤1Km), the mobile may travel several cells during a call. This increases the number of handovers per call. For this call transfer, the wireless network has to seek a new BS in the system for an existing call. This procedure requires network resources and therefore places an additional signaling and switching load on the system This also requires non-negligible amount of time for its implementation. It should be performed as infrequently as possible. Ideally one handover should take place per cell boundary crossing.

The decision to initiate the handover from one cell to another is based on the quality of communication link between the serving BS and MS. It is important to ensure that the drop in the link quality is not due to momentary fading and the MS is actually moving away from the serving BS. The parameters to evaluate the link quality include: Received Signal Strength (RSS), distance of MS from BS, Bit Error Rate (BER), and Channel to Interference Ratio (CIR), traffic load of the system and cell residence time. Voice quality of communication link is generally related to RSS. It is, therefore, a good indicator of call quality and has been the most commonly used criterion for making handover decision. In general, a MS is assumed to be served by the BS, which offers the strongest signal strength to the MS relative to other BSs of the cellular system. Rajiv Vijayan et. al [3] have developed a key

analytical model for evaluating the performance of handover algorithms based on relative signal strength measurements, i.e., the difference of signal strength from two BSs. However, it may happen that at the time of handover, RSS from the serving BS may still be adequate to support the call. Under this condition, relative signal strength approach will lead to unnecessary handovers, which is highly undesirable. Ning Jhang et. al [4] have extended the model given in [3] by including an additional criterion based on absolute signal strength in the handover decision algorithm. The absolute signal strength is the averaged value of RSS from the current serving BS measured by the mobile unit. This value has to be below a fixed threshold to initiate a handover. In this paper, the decision to initiate a handover is based on the criterion of relative signal strength measurements with hysteresis and threshold. Handover process is initiated only if the RSS from the serving BS drops below a fixed threshold and that from the target BS is stronger than the current one by a given hysteresis margin.

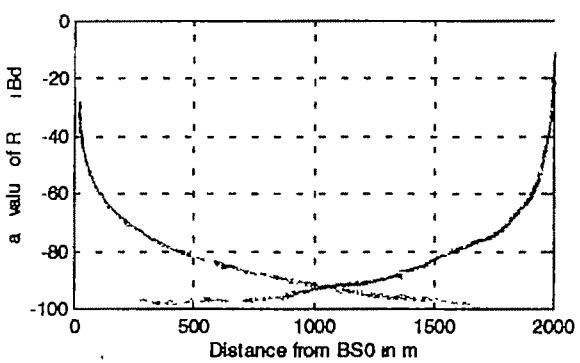

Figure 2. Profile of mean signal strengths from the two adjacent cells.

Figure (2) shows a MS moving from the serving BS_0 to the target BS_1. The quality of communication link between BS and MS is continuously monitored. As the MS moves away from the serving BS, communication link quality (and hence the call quality) degrades. When it drops beyond acceptable limit, it needs to be transferred from the serving BS to an alternate BS. The random nature of the communication channel in mobile radio makes it difficult to determine the correct point for a handover. Necessary handovers should be accomplished before a call is terminated due to poor signal level. But unnecessary handovers must be reduced. The frequency of unnecessary handovers is maximum near the cell boundary. These can be reduced by applying hysteresis margin. With the increase of hysteresis level, the number of unnecessary handovers decreases but it causes initiation delay. Unnecessary handovers can also be eliminated by applying an averaging window to the signal strength measurements. This also causes initiation delay, which may result in premature call termination. Continuation of a call depends on reliable detection and decision of handover initiation. It requires that the delay incurred in the decision process should be minimum. If we initiate the process too early, it will lead to ping- pong effect, that is, switching of MS back and forth between adjacent BSs. If delayed, call quality may degrade beyond an acceptable limit. These are two conflicting criteria. Improved call quality can usually be obtained only at the expense of an increase in the number of handovers. Thus a tradeoff must be made. This paper presents simulation results of the performance of handover initiation algorithm based on signal strength measurements using the criterion of relative signal strength with threshold and hysteresis. Expected number of handovers and handover delay are used as the performance metrics.

SYSTEM MODEL

We have considered a simple two-cell model. MS is moving from BS_0 to BS_1 on a straight line with constant speed. The measured signal strength has three components: path loss, which decays with distance from the BS, large scale fluctuations known as shadow fading, and small scale fluctuations referred to as multipath fading. Shadowing and fading of propagation environment will cause unnecessary handovers. which leads to increased traffic load of supervisory signals. The signal level the MS receives from each of the BSs is here considered to be the sum (in dB) of the mean signal strength due to path loss and shadow fading. Fluctuations due to fast fading are of small durations and their correlation distance is much smaller than the measurement interval for most cases of practical interest [5]. We assume that the received signal is passed through a low pass filter to average out the small-scale fluctuations. It is, therefore, neglected here as it gets smoothed out in the averaging process. The mean signal strength due to path loss has a log dependence of distance, while shadow fading is a zero mean Gaussian random process. In cellular systems, RSS measurements are done at discrete time interval, typically every 480 ms in GSM [6]. In the algorithm under study, signal strength measurement is taken every time the MS moves distance d_s, the sampling distance. RSS from BS_0 and BS_1 are sampled every kd_s distance, where k is a positive integer. The signal levels s_i (k), i=0,1, the MS receives from BS_i at k^{th} instance (at a distance of $k\,d_s$) in dB are given by

$$s_0(k)=K_1-K_2\log10(kd_s) + u(kd_s) \quad (1)$$

$$s_1(k)= K_1-K_2\log10\,(D-k\,d_s)+v\,(k\,d_s). \quad (2)$$

where u and v are zero mean stationary Gaussian random processes that model lognormal shadowing. D is the distance between BSs, K_1 is the signal strength at d=1 m, K_2 is 10η, where η is the path loss exponent. The path loss with respect to distance, that is, K_1-K_2log10 (kd_s) may be predicted by Hata –Okumara [7] and Walfisch-Ikegami empirical models [6]. The autocorrelation of the lognormal shadowing is assumed to be negative exponential as given by

$$E\{u(k_1 d_s)\, u(k_2 (d_s)\} = E\{v(k_1 d_s)\, v(k_2 d_s)\} = \sigma^2 \exp(-d_s \mid k_1 - k_2 \mid / d_0) \quad (3)$$

where d_o is the correlation distance which determines how fast the correlation decays with distance.

The composite received signal at MS can be taken as a random variable with lognormal distribution with probability density function such that

$$p(s) = \frac{1}{\sqrt{2\pi\sigma^2}} e^{-(s-\mu_0)^2/2\sigma^2}$$

where s=signal received in dB by MS from the serving BS, p(s) = probability density function of signal level received by MS, μ_o = averaged RSS due to path loss only evaluated from path loss model, σ = Standard deviation of shadow fading.

Estimate of link quality is derived generally from averaged levels over some averaging window length rather than the instantaneous values. The averaging of the RSS is achieved through an integration process over a suitable distance [8][9]. It smoothes out rapid fluctuations and estimates the local averaged value as given below:

$$s_0(k) = \exp(-d_s/d_{av}) s_0(k-1) + \{1 - \exp(-ds/d_{av})\} s_0(k) \quad (5)$$

$$s_1(k) = \exp(-d_s/d_{av}) s_1(k-1) + \{1 - \exp(-d_s/d_{av})\} * s_1(k). \quad (6)$$

where d_{av} is the averaging distance of the window, which determines how much weight is given to the past values of the signal. If d_{av} is too short, the fading fluctuations are not sufficiently smoothed out. If it is too long, handover decision may be too sluggish. Selection of averaging distance is, therefore, a tradeoff problem. The averaged values represented by equations (5) and (6) are taken as an implicit measure of call quality. The averaged signal strength difference is defined as

$$x(k) = s_0(k) - s_1(k) \quad (7)$$

Since s_0 (k) and s_1 (k) are Gaussian random variable, x (k) is also Gaussian.

HANDOVER INITIATION ALGORITHM

At the end of each distance, d_s, traveled along the MS trajectory, handover is initiated when:

1.The averaged signal strength from the serving BS drops below a fixed threshold T dB.

$$s_0(k) < T \quad (8)$$

It detects the need for handover. And

2. The averaged signal level from the target BS exceeds that from the current BS by a hysteresis margin h dB.

$$s_1(k) - s_0(k) > h \quad \ldots.(9)$$

Handover is commanded only when equation (9) is satisfied.

A handover may be initiated in the following two cases:

1. The MS communicates with BS_0 at $(k-1)^{th}$ instance, the beginning of the interval, but at k^{th}, the end of the interval, the relation $s_0(k)<T$ and $x(k) < -h$ are satisfied. This will cause call transfer from BS_0 to BS_1. Or

2. The MS communicates with BS_1 at $(k-1)^{th}$ interval but at k^{th} interval, the relation $s_1(k) < T$ and $x(k) > h$ are satisfied. This will lead to call transfer from BS_1 to BS_0

PERFORMANCE RESULTS

We simulate a scenario in which the MS traverses the distance D from BS_0 to BS_1.The specific simulation parameters are;

D =2000 m :Distance between two BSs
K_1=0dB & K_2=30dB: Constants for path loss
η = 3.0 : Path loss exponent
σ = 6 dB Standard deviation of shadow fading
d_s=1m Sampling distance
T= –94 dB fixed threshold

2000 realizations were used to estimate the number of handovers at each parameter setting. Plots in figure (3) shows the expected number of handovers versus hysteresis margin during a single trip from BS_0 to BS_1 for different averaging window lengths. The results are summarized as follows:

1. Number of handovers decreases as the value of hysteresis margin h, is increased from 0 to 16 dB. This implies that increasing the value of h can reduce the handover rate. The same observations were made in [3] and [4].

2. Using longer window lengths can also decrease handover rate. At lower values of hysteresis (h < 4 dB), value of d_{av} causes significant reduction in the number of handovers. But at higher values of h, hysteresis margin dominates the initiation decision.

3. Plots in figure (4) show the location of first handover on the path trajectory of the MS versus hysteresis margin for different settings of d_{av}. For h=0 dB and d_{av} =10m,first handover takes place at a distance of 1000m from BS_0. This is the exact geographical boundary between the two cells. As hysteresis margin is increased, the first cross over point shifts away from the cell border. For h=0 dB and d_{av} =20m, 30m and 40m,first handover occurs at 1064m, 1117m &1162m away from BS_0 respectively. A larger window length delays the handover and drags the crossover point into the coverage area of the target cell (BS_1). Moreover, as h is increased to 16 dB, crossover points are located at 1588m., 1643m and 1691m respectively. By now, the quality of service will degrade beyond acceptable limit and the ongoing call may be prematurely terminated due to poor signal level.

4. Hysteresis margin and length of averaging window both reduce the number of handovers but simultaneously increase the handover initiation delay. In real cellular systems, a handover delay more than 25% of cell radius is not acceptable. Handover area cannot exceed beyond 1250m from BS_0 for satisfactory call quality in our case.

5. For d_{av}=30m and h= dB, it is found that the expected number of handovers are 5 and the first handover takes place at a distance of 1245 m away, which is within acceptable limit. These are the optimum values of averaging window length and hysteresis margin for the handover initiation algorithm for the given system parameters.

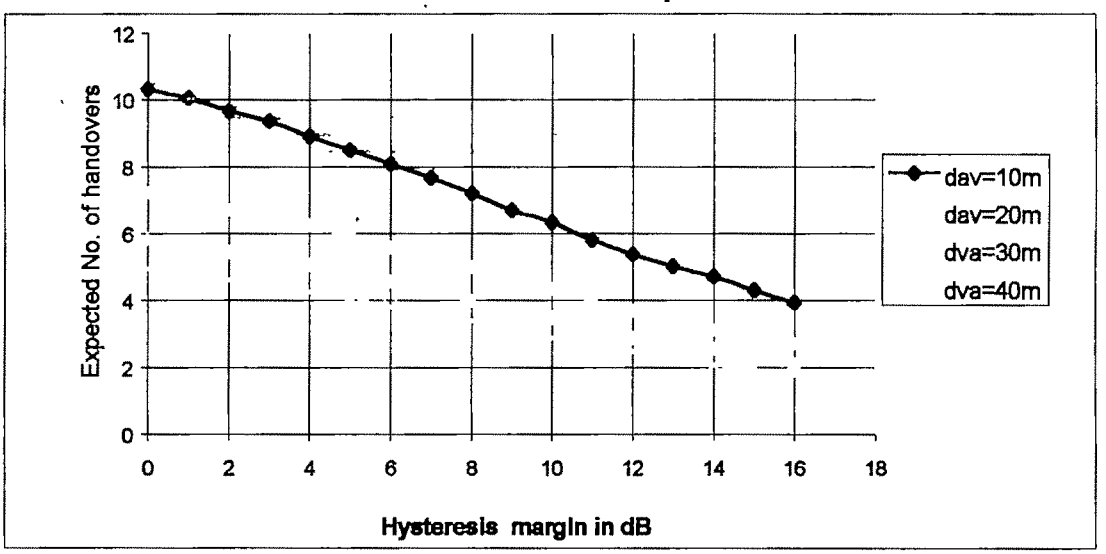

Figure (3): Expected number of handovers versus hysteresis margin

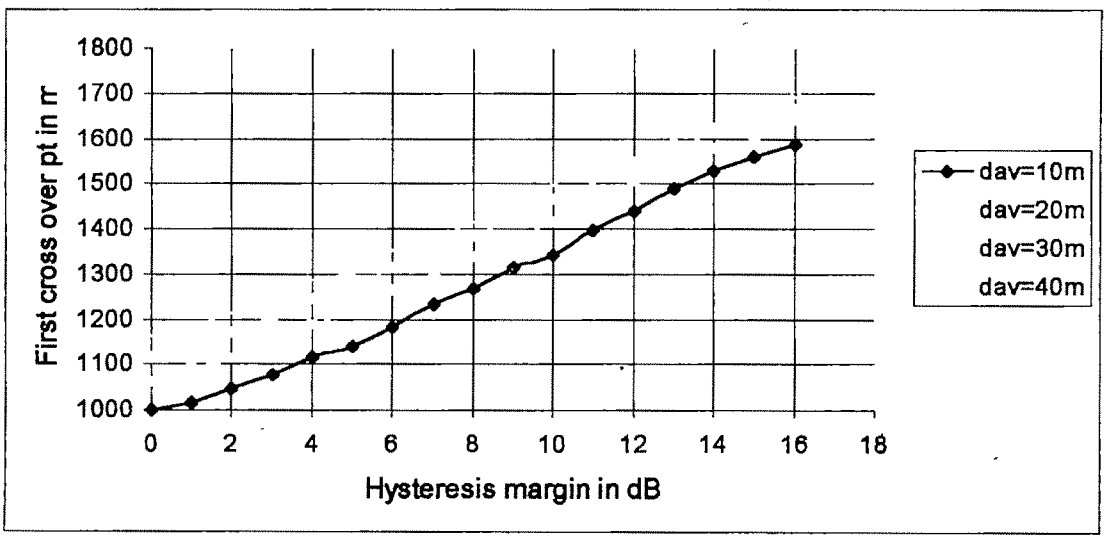

Figure (4): Location of first handover versus hysteresis margin

CONCLUSION

The performance of handover algorithm has been measured in terms of expected number of handovers and handover delay. These two are inversely proportional in the sense that increasing the hysteresis margin and/or averaging distance decreases the expected number of handovers but increases the delay. We have quantified these two conflicting requirements by choosing the optimum values of hysteresis margin and length of averaging window through case-by-case simulation studies. Given the propagation model and fixed system parameters, this simulation model can be used to evaluate the handover performance for simple microcelluar systems. The work is in progress to develop a simulation model for generalized multicelluar system. However, the trade off obtained here is good for given statistical parameters of propagation environment only. Since in mobile communication, the propagation environment is continuously changing, online estimate of standard deviation of shadow fading may produce consistent results. We are further working in this direction.

REFERENCES

[1] W. C. Y. Lee, " Smaller Cells for Greater Performance", IEEE Communications Magazine, 1991, pp. 19-23.

[2] Hakan Person, "Microcellular Structures and their Performance", IEEE Vehicular Technology Conference, 1992, pp. 413-418.

[3] Rajiv Vijayan and M. Holtzman,"A Model for Analyzing Handoff Algorithms", IEEE Transactions on Vehicular Technology, vol.42, No.3. August 1993.pp351-357.

[4] Ning Jhang and Jack M. Holtzman, "Analysis of Handoff Algorithms using both Absolute and Relative Measurements", IEEE Vehicular Technology Conference, 1994, pp. 82-86.

[5] Ramin Rezaiifar and Armand M. Makowski, " Optimal Control of Handoffs in Wireless networks", IEEE vehicular Technology Conference 1995, Pp. 77-81.

[6] Vijay K. Garg and Joseph E. Wilkes, "Principles and Applications of GSM", Prentice-Hall, 1999.

[7] Masaharu Hata, " Empirical Formula for Propagation Loss in Radio Systems", Electronics Letters 7th November 1991. Vol. 27. No. 23

[8] M. Gumundson, " Correlation Model for Shadow Fading in Mobile Radio Systems" Electronics Letters, November 1991,vol.27, pp. 2145-2146.

[9] W.C.Y.Lee and Y.S.Yeh, " On the Estimation of the second Order Statistics of Lognormal Fading in Mobile Radio Environment." IEEE Transactions on Communications, June 1974,pp869-873.

[10] Fortunato Santucci,Wei Huang and Vijay K. Bhargava, "A Framework for Analyzing the User Membership in Cellular CDMA Networks", IEEE Transactions on Comminicatiobs,vol.48,no.3.March 2000,pp442-454.

A Statistical Method For Characterizing Network Traffic

Narottam Chand[†], Ajay Guleria[†], D.R. Rana[*]
[†] Department of Computer Science & Engineering, Regional Engineering College
Hamirpur (H.P.) 177 005, India. E-mail: nar@recham.ernet.in
[*]Department of Electronics & Communication Engineering, Regional Engineering College
Hamirpur (H.P.) 177 005, India. E-mail: drr@recham.ernet.in

Abstract

The traffic behavior over the network is unpredictable. The task of monitoring the traffic on a large network is a daunting one. The problem addressed in this papers is the one of characterizing desired traffic, and recognizing and flagging undesired traffic. Clustering methods are proposed to network data. These allow the clustering of machines into activity groups, which consists of machines which tend to have similar activity profiles. The increasing complexity of both tele and data communication networks yields new demands concerning network security. This paper enumerates a variety of ways to extend statistical analysis techniques for solving security issues.

Keywords: Network, traffic, statistical, IP, clustering.

INTRODUCTION

Modern tele and data communication networks provide users with all kinds of services. In the future, the variety of available services will increase, ultimately offering any service anytime and anywhere [4]. The growing range of available services also increases the complexity of the underlying networks. Therefore, it is becoming increasingly difficult to detect, repulse and prevent misuse by both in and outsiders. Classical security mechanisms, i.e. authentication and encryption, and infrastructure components like firewalls cannot provide perfect security. The statistical analysis techniques to monitor and analyze TCP/IP packet streams that flow through network gateways for signs of malicious activity, nonmalicious failures, and other exceptional events may prove useful in handling the security related issues.

At a minimum, one needs to filter out all the undesired or uninteresting traffic in order to focus attention on those connections that are unusual or indicative of potential problem. Undesired can refer simply to those connection attempts that are considered abnormal and hence are disallowed by the firewall. Once a suspicious connection attempt has been detected, the traffic from that source can be pulled and perused to determine if allowed connections may have been used successfully to compromise the network [2].

The problem with this approach is that it can only catch those things one already knows about. Every network administrator has a bad ports list and a bad IPs list, and any connection matching one of these lists is scrutinized [2]. However, some connections are only bad if they are to certain machines, but are perfectly normal to others. For example, one may allow individuals to set up ftp servers, provided they follow certain guidelines to ensure relative security. So one may see a fair amount of ftp traffic in and out of the network to a (periodically changing) subset of machines. Suppose a machine that has never had ftp traffic suddenly starts to get ftp connections. An alert network manager might want to check to make sure that the system administrator for that machine has intended to set up an externally available ftp site, rather than someone taking advantage of a misconfiguration or vulnerability. This can be particularly important if the machine in question is an infrastructure machine, contains sensitive information, or is otherwise an important target for attackers. In fact, any traffic that is undesired for a given machine or class of machines should be flagged for further analysis.

The problem then is to determine what is desired and hence what is undesired for the network. This paper takes a pragmatic look at the issue of packet and/or datagram analysis based on statistical anomaly detection. The statistical data considered in this work consists of six

fields: date/time, source IP address, source port, destination IP address, destination port, and protocol (TCP/UDP).

MEASURING NETWORK TRAFFIC

The first and most obvious way to measure network activity is to keep count of the number of accesses to each port within a given time period (hourly, daily, etc.). When the count for a port on a given machine or set of machines is unusually high, this is an indication of a potential problem [2]. The determination of what constitutes *unusually high* can be made through studying the normal fluctuations of these quantities in historical data.

The incoming telnet sessions may be tabulated for the current day and compared with the activity for the previous few histories. The analyst can scan the list for daily counts that exceed the normal for the previous months, pull the traffic to that machine to determine who is making these connections, and, if warranted, pull additional traffic for the appropriate machines. Obviously this kind of analysis can only be done for a relatively small number of ports and machines, but for some of the most obvious services this can provide the analyst with considerable information about the traffic on the network.

The above idea can be extended to allow the consideration of all the ports in a natural way, by normalizing the counts by the overall traffic, thus obtaining a probability estimate, instead of a "connections per day" measure. So now one has an estimate of the probability of having an access to any given port for any given machine. This can then be used as above to determine whether the traffic for a given time period is undesired, or it can provide feedback for individual accesses. Port access attempts which have a low probability can be flagged as unusual and worthy of further investigation.

There are several risks and limitations associated with statistical analysis technology [1, 5]:

- Because user profiles are updated periodically, it is possible for an insider to slowly modify his behavior over time until a new behavior pattern has been established within which an attack can safely mounted.
- Determining an appropriate threshold for "statistically significant deviations" can be difficult. If the threshold is set too low, anomalous activities that are not intrusive are flagged as intrusive (false positive). If the threshold is set too high, anomalous activities that are intrusive are not flagged as intrusive (false negative).
- Defining user profiles may be difficult, especially for those users with erratic work schedule/habits.

STATISTICAL TRAFFIC ANALYSIS

The statistical system tracks subject activity via one or more variables called measures [3]. The statistical algorithms employ four classes of measures: categorical, continuous, intensity, and event distribution. *Categorical* measures are those that assume values from a categorical set, such as originating host identity, destination host, and port number. *Continuous* measures are those for which observed values are numeric or ordinal, such as number of bytes transferred. Derived measures also track the intensity of activity (that is, the rate of events per unit time) and the meta-distribution of the measures affected by recent events. These derived measure types are referred to as *intensity* and *event distribution.*

In the context of statistically analyzing TC/IP traffic streams, profiling can be derived from a variety of traffic perspectives, including profiles of

- Protocol-specific transactions (e.g., all ICMP exchanges)
- Sessions between specific internal hosts and/or specific external sites
- Application-layer-specific sessions (e.g., anonymous FTP sessions profiled individually and/or collectively)
- Discarded traffic, measuring attributes such as volume and disposition of rejections
- Connection requests, errors, and unfiltered transmission rates and disposition

Event records are generated either as a result of activity or at periodic intervals. In our case, activity records are based on the content of IP packets or transport layer datagrams. Our event filters also construct interval summary records, which contain accumulated network traffic statistics (at a minimum, number of packets and number of kilobytes transferred). These records are constructed at the end of each interval (e.g., once per N seconds).

The following sections provide examples for network activity that can be measured by statistical engine deployed to network gateways.

CATEGORICAL MEASURES

Categorical measures assume values from a discrete, nonordered set of possibilities. Examples of categorical measures include:

- Source/destination address: One expects, for example, accesses from head office to originate from a set of known host identities.
- Command issued: While any single command may not in itself be anomalous, some intrusion

scenarios give rise to an unusual mix of commands in the short-term profile.

- Protocol: As with commands, a single request of a given protocol may not be anomalous, but an unusual mix of protocol requests, reflected in the short-term profile, may indicate an intrusion.
- Errors and privilege violations: While some rate of errors is normal, a high number of exceptions in the recent past is abnormal. This is reflected both in unusual frequencies for abnormal categories, detected here, and unusual count of abnormal returns, tracked as a continuous measure.
- Malformed service requests: Categorical measures can track the occurrence of various forms of bad requests or malformed packets directed to a specific network service.
- Malformed packet disposition: Packets are dropped by a packet filter for a variety of reasons, many of which are innocuous (for example, badly formed packet header). Unusual patterns of packet rejection or error messages could lead to insight into problems in neighboring systems or more serious attempts by external sites to probe internal assets.
- File handles: Certain subjects (for example, anonymous FTP users) are restricted as to which files they can access. Attempts to access other files or to write read-only files appear anomalous Such events are often detectable by signature analysis as well.

CONTINUOUS MEASURES

Continuous measures assume values from a continuous or ordinal set. Examples include inter-event time (difference in time stamps between consecutive events from the same stream), counting measures such as the number of errors of a particular type observed in the recent past, and network traffic measures (number of packets and number of kilobytes). The statistical subsystem treats continuous measures by first allocating bins appropriate to the range of values of the underlying measure, and then tracking the frequency of observation of each value range. In this way, multi-modal distributions are accommodated and much of the computational machinery used for categorical measures is shared.

Continuous measures are useful not only for intrusion detection, but also support the monitoring of health and status of the network from the perspective of connectivity and throughput. An instantaneous measure of traffic volume maintained by a gateway monitor can detect a sudden and unexpected loss in the data rate of received packets, when this volume falls outside historical norms for the gateway. Continuous measures can also work in conjunction with categorical measures to detect excessive data transfers or file uploads, or excessive mail relaying.

MEASURING NETWORK TRAFFIC INTENSITY

Intensity measures distinguish whether a given volume of traffic appears consistent with historical observations. These measures reflect the intensity of the event stream (number of events per unit time) over time intervals that are tunable. Applied to raw event streams, intensity measures are particularly suited for detecting flooding attacks, while also providing insight into other anomalies.

Monitoring overall traffic volume and bursty events by using both intensity and continuous measures provides some interesting advantages over other monitoring approaches, such as user-definable heuristic rules that specify fixed thresholds. In particular, the intensity of events over a duration is relative in the sense that the high volume may reasonably be considered different.

EVENT DISTRIBUTION MEASURES

The event-distribution measure is a meta-measure that monitors which other measures in the profile are affected by each event. For example, an ls command in an FTP session affects the directory measure, but does not affect measures related to file transfer. This measure is not interesting for all event streams. For example, all network-traffic event records affect the same measures (number of packets and kilobytes) defined for that event stream, so the event distribution does not change.

CLUSTERING MACHINES

The above methods work well when dealing with a small number of machines. Once the number of machines on the network rises into the hundreds, one would like to aggregate machines based on activities. Intuitively, one would imagine that machines with similar functions should have similar normal activity. This is the case, although ones intuition as to which machines should be similar may not be entirely accurate. The idea is to do this aggregation in an automated manner. In the statistics literature this type of aggregation is called *clustering*. Hierarchical clustering is proposed to measure the network traffic. For details about clustering see [2, 6].

CONCLUSIONS

Much more extensive tests are needed to determine the best way to utilize these ideas. The optimal choice of the number of clusters is a difficult problem. Ultimately one must decide if it is necessary to cluster the machines into a small number of clusters instead of treating each machine as an individual. The latter should provide better accuracy while the former can require substantially fewer computations on a large network.

The main advantage to statistical systems are that they adaptively learn the behavior of users, they are thus potentially more sensitive than human experts. However there are a few problems with statistical approaches: they can gradually be trained by intruders so that eventually, intrusive events are considered normal, false positives and false negatives are generated depending on whether the threshold is set too low or too high, and relationship between events are missed because of the insensitivity of statistical measures to the order of events.

REFERENCES

1. A. Sundaram. An Introduction to Intrusion Detection. ACM Crossroads Magazine (1996).
2. David Marchette. A Statistical method for Profiling Network Traffic. In Proceedings of the USENIX Conference (1999).
3. P.A. Porras and Alfonso Valdes. Live Traffic Analysis of TCP/IP Gateways. In Proceedings of the 1998 ISOC Symposium on Network and Distributed Systems Security.
4. Dogan Kesdogan. Transaction-based Anomaly Detection.http://www.i4.informatik.rwth-aachen.de/
5. Mark Gerken. Statistical-Based Intrusion Detection (1997). http://www.research.att.com/
6. Pierre Michaud. Clustering Techniques. Future Generation Computer Systems 13(1997) 135-147.

A Mathematical Model for the specification of Sliding Window Protocol

Awadhesh Kumar Singh[†] & Anup Kumar Bandyopadhyay[+]
[†]ECCE Department, Regional Engineering College Kurukshetra-136119, India
E-mail : aksinreck@vsnl.net
[+]ETCE Department, Jadavpur University, Calcutta-700032, India
E-mail : anupbandyopadhyay@hotmail.com

Abstract

This paper presents a technique for proving correctness of a protocol. We have used first order logic for this purpose. Predicate to ensure correctness has been found on the basis of working of the protocol. Modeling is parallel to the communicating processes.

Keywords: Weakest precondition, Channel, Protocol, Non-deterministic selection

INTRODUCTION

A mathematical model for the specification of a data link layer protocol is proposed. We use Dijkstra's weakest precondition calculus [1] for this purpose. We have illustrated this technique by describing the sliding window protocol [2].

MATHEMATICAL MODEL

A system S is defined by a set S.P of processes, which can interact among them only through message transactions. A process P is defined by a set P.X of states and a set P.R of state transition rules. Assertion that a process P is in state P.x is made by the predicate expression in(P.x). Each process has a predefined initial state denoted by initial(P.x0). State SX of the system S is the collection of states of all the processes belonging to S.P.

A process can move from one state to the other by the action of a state transition rule. For a transition rule P.r and a post-condition Q there exist a weakest precondition wp(P.r, Q) such that if the system state satisfies this condition then the execution of P.r will eventually establish the truth of Q. This guarantee, however can not be given unless wp(P.r, Q) is true before the execution of P.r. We divide this condition into two parts. The first part is related to the process P itself, where the second part includes the co-operation requirements from other processes. With this idea we define two parts, [3] viz., (i) weakest self pre-condition denoted by wsp(P.r, Q) and (ii) weakest co-operation requirements, denoted by wcr(P.r, Q). The total weakest pre-condition is then given by

$$wp(P.r, Q) = wsp(P.r, Q) \wedge wcr(P.r, Q) \quad (1)$$

Since in this approach we have already considered the co-operation requirements, a separate proof of co-operation is not necessary [4].

A non-deterministic state transition rule P . r may include number of different sub-rules each of which requires a definite pre-condition to be satisfied for its execution . These pre-conditions will be called guards . Execution of a sub-rule will change the state of P as well as the state of one of the co-operating processes whose active co-operation is necessary for this execution. State transition in the co-operating process will be achieved by simultaneous execution of a state transition rule . If pre-condition for more than one sub-rules are satisfied then one of them is selected for execution. Selection procedure is non-deterministic and therefore, it is necessary to pass this information to the relevant co-operating process to produce the required state transition. The weakest pre-condition for a non-deterministic transition rule P . r is obtained as follows .

Let there be n number of sub-rules denoted by $P . r^i : i = 1 . . n$. On top of these sub-rules we assume a selector procedure, denoted by *select*, which makes the required non-deterministic selection .The post condition space for this procedure should therefore include a number of Boolean variables denoted by $s_i : i = 1 . . m$. At each invocation the selector makes one such variable true. If a sub-rule $P . r^i$ has a post condition Q_i then

$$s_i \Rightarrow wp(P . r^i , Q_i) \quad (2)$$

Let B_i denotes the required guard for $P . r^i$, then the truth of this condition should ensure the selectability of s_i , i.e. ,

$B_i \Rightarrow wr(select , s_i)$ (3)

where wr(select , s_i) is the weakest requirement that the procedure *select* may produce s_i . Using (2) and (3) the rule P . r is described as follows :

P .r : :
def $Q = \exists Q_i$;
$wp(P .r , Q) = (\exists k : B_k) \wedge$
$(\forall i \bullet B_i \Rightarrow wr(select , s_i)) \wedge$
$(\forall j \bullet s_j \Rightarrow wp(P . r^j , Q_j))$;
end of P . r ;

Next we consider a transition rule described by a collection of sub rules r^i, $1 \le i \le n$. Let us consider that the preconditions ω^i for these sub rules are same. The post conditions Q^i for these sub rules, on the other hand, are different. When ω^i is true, one of these sub rules is selected and the corresponding post condition is established. Selection procedure is non-deterministic in nature. This type of representation is necessary to model a noisy channel. For example, when a message is launched on a channel it may or may not be delivered at the far end depending on the noise condition during the transmission period.

The weakest pre-condition for such a sub rule $P.r^j$ is augmented as follows. Let there be n number of sub rules denoted by $P.r^j$: i=1..n. On top of these sub rules we assume a selector procedure denoted by *select*, which makes the required non-deterministic selection. The post condition space for this rule includes a number of Boolean variables, S^i : i=1..n. If sub rule $P.r^i$ has a post condition Q^i then

$S^i \Rightarrow wp(P . r^i , Q_i)$ (4)

and

$(\omega^i = \omega) \wedge (\omega \Rightarrow wr(select, S^i)$ (5)

Using (4) and (5) the rule P.r is described as follows:

P.r::
def $Q = \exists i : Q^i$;
$\forall i \bullet ((\omega^i = \omega) \wedge (\omega \Rightarrow wr(select, S^i))) \wedge$
$\forall j \bullet (S^j \Rightarrow wp(P . r^j , Q^j))$;
end of P . r ;

The operational model of a protocol can be described by state transition rules . These rules can be described completely by their weakest pre-condition, post condition pairs. However, operational specification may not be sufficient to ensure all the system requirements .One must also specify the system properties that must be maintained before and after each state transition. Best way to do this is to construct a condition Z related to the system states and the property requirements, and prove that

$\forall i \circ \forall m \bullet [\{wp(P_i . r_m , Q_{i , m}) \Rightarrow Z\} \wedge (Q_{i , m} \Rightarrow Z)]$

In other words a system invariant must also be specified. For a guarded command the system invariant Z must follow a similar condition which is given by

$\forall i \bullet (B_i \Rightarrow Z) \wedge (B_i \Rightarrow wp(P . r^i , Q_i)) \wedge (Q_i \Rightarrow Z)$

SPECIFICATION OF A NOISY CHANNEL [5]

We consider a noisy channel that accepts messages for transmission. Depending on the noise condition during the transmission time, the message is presented at the output or it may be lost. We describe this channel as follows. We define the following states for the channel.

STATE	SEMANTICS
Channel_idle	Channel is idle
Channel_launched	A frame has been launched on the Channel
Channel_produced	A frame is presented to the receiver

We can now describe the behavior of the channel as follows.

Process Channel ();
States : channel_idle, channel_launched, channel_produced;
Initial condition : in(channel_idle);
Transition rules
Channel . r_1
def Q=in(channel_launched);
wsp(Channel . r_1, Q)=in(channel_idle);
wcr(Channel . r_1, Q)=in(Ps . sent);
end of Channel . r_1;
Channel . r_2
def $Q=Q^1 \vee Q^2$
Q^1=in(channel_produced);
Q^2=in(channel_idle)
$(in(channel\_launched) \Rightarrow wp(Select, S^1)) \wedge$
$(in(channel\_launched) \Rightarrow wp(Select, S^2)) \wedge$
$(S^1 \Rightarrow wp(Channel . r_2^1, Q^1)) \wedge$
$(S^2 \Rightarrow wp(Channel . r_2^2, Q^1))$
end of Channel . r_2;
end of transition rules;

We assume a sender process Ps is running concurrently and moves to the state Ps . sent when it presents a message at the channel input. There exists another transition rule for the channel. When the receiver process receives the message the channel invokes another transition rule and moves to the idle state.

SPECIFICATION OF SLIDING WINDOW PROTOCOL

We consider the sliding window protocol to illustrate the application of the above mathematical model. Before presenting the formal specification using the proposed scheme we informally describe the protocol.

Informal Description

In sliding window protocol, each outbound frame contains a sequence number, ranging from 0 up to some maximum. At any instant of time, the sender maintains a fixed size buffer corresponding to set of frames, sent but yet not acknowledged, with their sequence numbers. This buffer is termed sending window. This storage is done for possible retransmission; since sent frames may ultimately be lost or damaged in transit. Since it has multiple outstanding frames, it maintains multiple logical timers, one per outstanding frame. Each frame times out independently of all the other once. Similarly the receiver also maintains a receiving window corresponding to the set of frames it is permitted to accept. The receiver has a buffer reserved for each sequence number within its window. Associated with each buffer is a bit telling whether the buffer is full or empty? Whenever a frame arrives, its sequence number is checked to see if it falls within the window. If so, and if it has not already been received, it is accepted and stored. An acknowledgement is sent also, if its predecessor frame has been acknowledged. Whenever the receiver has reason to suspect that an error has occurred, it sends a negative acknowledgement (NAK) frame back to the sender. Such a frame is a request for retransmission of the frame specified in the NAK. Sender retransmits a frame either on receiving NAK or on being timed out, whichever is earlier. Any frame falling outside the window is discarded without comment. The sender's window and receiver's window need not have the same lower and upper limits, or even have the same size. A frame buffer is released if buffer for its predecessor frame has already been released. Sender releases buffer after receiving acknowledgement while receiver does the same after sending acknowledgement. We define the states and transition rules for different processes of the system as given in appendix.

PROOF OF CORRECTNESS

In order to prove correctness of the protocol under reference we should prove that, for any frame, once acknowledgement has been sent and buffer has been released then receiver will not be ready to receive it again". In other words, any frame once received will never be received again. This will eliminate the possibility of receiving one frame for two different frames transmitted on the channel. Thus the predicate, which avoids duplicate frame reception will be

$$\{in(Pr\,.\,sent\_ack\_i) \wedge in(Pr\,.\,release\_buf\_i)\} \Rightarrow \neg in(Pr\,.\,rtr\_i)$$

Let us consider only two guards for the sake of simplicity. Since B1 is a guard and Q1 is post condition, thus selection of B1 will ensure the weakest precondition wpQ1 such that Q1 will be established. Thus we can write

$B1 \Rightarrow wpQ1$

similarly we have

$B2 \Rightarrow wpQ2$

also we have checked that guards are mutually exclusive in nature. Thus relationship between these two guards can be represented as follows.

$B1 \oplus B2$

from this we infer that

$B1 \Rightarrow \neg B2$

For the remaining proof of this predicate authors may please be contacted..

CONCLUSION

We have presented the use of weakest pre-condition approach to specify sliding window protocol. The goal was to formalize and prove its correctness. Although we have used First Order Logic, accuracy has not been compromised for the sake of simplicity. It shows the suitability of representation for evaluating the correctness of the protocol.

REFERENCES

1. E W Dijkstra,"A discipline of programming",Prentice Hall,1976.
2. A S Tanenbaum,"Computer Networks", 3/e, Prentice Hall of India, 1998.
3. A K Bandyopadhyay and J Bandyopadhyay,""on the derivation of a correct deadlock free communication kernel for loop connected message passing architecture from its user's specification"", Journal of System Architecture, vol 46(13), 2000, pp 1257-1261.
4. M Chandi and B A Sanders, "Predicate transformers for reasoning about concurrent computation", Science of Programming vol 24, 1995, pp 129-148.
5. A K Bandyopadhyay, " A mathematical model for the specification of data link layer protocols", Proc. COMNAM-2000, 21-22 December , 2000 , Jadavpur University, pp 109-114.

Nonuniform Sampling and On-line Estimation of Local Bandwidth of a Nonstationary Signal

Sumeet Goyal, Pradip Sircar

Department of Electrical Engineering
Indian Institute of Technology Kanpur
KANPUR 208 016, India

E-mail address of corresponding author: sircar@iitk.ac.in

Abstract

In this paper, an on-line strategy of nonuniform sampling is developed. The estimation of local bandwidth of a signal is achieved by a novel method based on orthogonal polynomial approximation. The presented scheme provides fast implementation of the nonuniform sampling strategy with accurate estimate of local bandwidth of a signal.

Keywords: Nonuniform sampling, Sampling strategy, Nonstationary signal, Local bandwidth

INTRODUCTION

Nonuniform sampling is an important step in processing a nonstationary signal whose bandwidth is a function of time [1]. Nonuniform sampling can be preferred over uniform sampling for sampling efficiency, higher signal-to-noise ratio (SNR), or for reasons like that a signal is non-band-limited or the signal sampling is ineffective over certain time durations due to intense interfering noise, and so on [2,3].

Nonuniform sampling can be implemented off-line or on-line. For the off-line method, the signal is first sampled at uniform spacings with the sampling frequency set to twice the maximum bandwidth of the signal. The entire data-set is then divided into several data-segments, consecutively each with different rate of variation of the signal. Next, we compute the power spectral density (PSD) of the signal over each data-segment, and a local estimate of the bandwidth is determined from the PSD computations. The number of sampled points to be retained over a data-segment is decided by this local estimate of the bandwidth, and the rest of the points are discarded. In this way, we can achieve a substantial reduction in the number of data points. The data compression so achieved can be advantageously used in data-storage or data-transmission purposes, and when needed, the entire data-set at uniform spacings can be reconstructed by employing orthogonal polynomial approximation technique. The off-line strategy of nonuni-

ON-LINE SAMPLING STRATEGY

In this paper, we address the on-line strategy of nonuniform sampling. The on-line strategy may be useful for sampling non-band-limited signals. The problem related to the on-line strategy can be stated as follows: Given the signal samples $\{s(t_1), s(t_2), \cdots, s(t_n)\}$ at time-instants $\{t_1, t_2, \cdots, t_n\}$ which are at nonuniform spacings, we have to find a local estimate of the signal bandwidth, and then utilize the "local" bandwidth to determine the sampling interval Δt and the time-instant $t_{n+1} = t_n + \Delta t$ where the next sample is to be measured.

Note that the bandwidth being a global signal parameter, only a local (averaged over some duration of time) estimate of the bandwidth can be determined when the bandwidth is time-varying. This implies that for a meaningful use of the local bandwidth, the time duration $t_n - t_1$, and hence the number of points, n should be properly restricted. This follows since in effect we are assuming quasi-stationarity for a nonstationary signal over a short duration of time.

In order to estimate the local bandwidth of the signal by employing some conventional method for computing the PSD, first, we need to reconstruct the signal values at uniform spacings over the time duration $t_n - t_1$. The reconstructed values can then be processed by some method based on Fourier-transform or time

the PSD values, we estimate the local bandwidth. The entire procedure as described above is computation - intensive and time-consuming, and hence, is not usually suitable for on-line estimation of local bandwidth.

ESTIMATION OF LOCAL BANDWIDTH

In this paper, we take an alternative approach based on parametric modelling for direct estimation of the local bandwidth of a signal. Assume that the signal for a short duration of time can be represented by the sinusoidal model [5],

$$s(t) = \sum_{i=1}^{m} a_i \sin(2\pi f_i t + \phi_i), \qquad (1)$$

where $f_1 < f_2 < \cdots < f_m$ are the frequencies of the constituent sinusoids, a_i are the corresponding amplitudes, and ϕ_i are the initial phases. The kth order derivative of the signal, assuming k even, is given by

$$\begin{aligned} s^k(t) &= \frac{d^k s}{dt^k} \qquad (2)\\ &= \sum_{i=1}^{m} (-1)^{k/2} a_i (2\pi f_i)^k \sin(2\pi f_i t + \phi_i), \end{aligned}$$

and the $(k+2)$th order derivative is expressed as

$$\begin{aligned} s^{k+2}(t) &= \frac{d^{k+2} s}{dt^{k+2}} \qquad (3)\\ &= \sum_{i=1}^{m} -(-1)^{k/2} a_i (2\pi f_i)^2 (2\pi f_i)^k \times \\ &\qquad \times \sin(2\pi f_i t + \phi_i). \end{aligned}$$

Under the assumptions that the integer k is reasonably large and a_i are of same order of magnitude, we obtain the following approximations for the higher-order derivatives,

$$s^k(t) \approx (-1)^{k/2} a_m (2\pi f_m)^k \sin(2\pi f_m t + \phi_m), \qquad (4)$$

and

$$\begin{aligned} s^{k+2}(t) \approx -(-1)^{k/2} a_m (2\pi f_m)^2 (2\pi f_m)^k \cdot \\ \cdot \sin(2\pi f_m t + \phi_m), \qquad (5) \end{aligned}$$

where f_m is the maximum frequency contained in the signal. Finally, evaluating the two higher-order derivatives at some point t_0 within the time span (t_1, t_n), we compute the maximum frequency contained in the signal as follows,

$$f_m = \frac{1}{2\pi} \left(- \frac{s^{k+2}(t_0)}{s^k(t_0)} \right)^{1/2}. \qquad (6)$$

Note that the above expression for f_m is valid when k is either even or odd.

For computation of the higher-order derivatives utilizing the signal values given at nonuniform spacings, we use the orthogonal polynomial approximation together with the minimum error-variance criterion [6]. The orthogonal polynomials $\{p_j(t)\}$ are generated by the use of recurrence relation:

$$\begin{aligned} p_{j+1}(t) &= (t - \alpha_{j+1}) p_j(t) - \beta_j p_{j-1}(t), \\ &\qquad j = 0, 1, \cdots \qquad (7)\\ \text{with} \quad p_0(t) &= 1, \quad p_{-1}(t) = 0, \end{aligned}$$

where

$$\begin{aligned} \alpha_{j+1} &= \frac{\sum_{i=1}^{n} w_i t_i [p_j(t_i)]^2}{\sum_{i=1}^{n} w_i [p_j(t_i)]^2}, \\ \beta_j &= \frac{\sum_{i=1}^{n} w_i [p_j(t_i)]^2}{\sum_{i=1}^{n} w_i [p_{j-1}(t_i)]^2}, \end{aligned}$$

and the polynomials $\{p_j(t_i)\}$ are orthogonal over the points $\{t_i\}$ with respect to the weight functions $\{w_i\}$.

The least-squares approximation for the sampled signal is given by

$$\begin{aligned} s_\ell(t) &= \sum_{j=0}^{\ell} b_j p_j(t) \qquad (8)\\ \text{with} \quad b_j &= \frac{\omega_j}{\gamma_j}, \\ \text{where} \quad \omega_j &= \sum_{i=1}^{n} w_i s(t_i) p_j(t_i), \\ \text{and} \quad \gamma_j &= \sum_{i=1}^{n} w_i [p_j(t_i)]^2. \end{aligned}$$

The degree of polynomial approximation, ℓ, is chosen such that the error-variance

$$\begin{aligned} \sigma_\ell^2 &= \frac{\delta_\ell^2}{n - \ell - 2} \qquad (9)\\ \text{where} \quad \delta_\ell^2 &= \sum_{i=1}^{n} w_i \left[s(t_i) - \sum_{j=0}^{\ell} b_j p_j(t_i) \right]^2 \end{aligned}$$

is minimum, or does not decrease appreciably any further with increasing ℓ.

The minimum-variance least-squares approximation method is known to have high noise-rejection capability which is essential to acquire reasonable accuracy in the computation of derivatives. The derivatives are computed employing the generating polynomials for the higher-order derivatives, and the entire process can be conveniently mechanised with the use of a computer.

The generating polynomials for the higher-order derivatives are given by the following relations:

$$p_{j+1}^1(t) = p_j(t) + (t-\alpha_{j+1})\,p_j^1(t) - \beta_j p_{j-1}^1(t), \quad j = 1, 2, \cdots \tag{10}$$

with $p_1^1(t) = 1, \quad p_0^1(t) = 0,$

and

$$p_{j+1}^k = k p_j^{k-1}(t) + (t-\alpha_{j+1})\,p_j^k - \beta_j p_{j-1}^k(t), \quad k = 2, 3, \cdots, \; j = 1, 2, \cdots \tag{11}$$

with $p_1^k(t) = 0, \quad p_0^k(t) = 0,$

where k is the order of derivative, and α_{j+1}, β_j are defined as in (7).

Note that while computing the maximum frequency f_m (6), we may employ the higher-order derivative - pairs computed at several points in the middle of the time span (t_1, t_n), and then calculate the average f_m for higher accuracy.

SIMULATION STUDY

For simulation study we utilize the lead-II electrocardiogram (ECG) signal, shown in Fig. 1, and the beta-rythm electroencephalogram (EEG) signal which is shown in Fig. 3. Both the ECG and EEG signals are known to be dominantly nonstationary in nature. In each case, 600 samples of the signal sampled at uniform spacings with the sampling frequency $f_s = 250Hz$ are employed.

To demonstrate the on-line nonuniform sampling strategy, we use a sliding window of $n = 22$ points for the ECG signal and a window of $n = 35$ points for the EEG signal. Initially, the n uniformly sampled points are taken at the sampling interval $T = \frac{1}{f_s}$. At the successive stages, the sampling interval Δt is chosen according to the local estimate of the signal bandwidth, and its value is set at $\Delta t = \ell T$, where ℓ is an appropriately chosen integer. The variations of the local bandwidth for the ECG signal are plotted in Fig. 2, and that for the EEG signal are plotted in Fig. 4.

The off-line estimates of local bandwidth of the ECG and EEG signals as determined by the autoregressive (AR) PSD computations are included in Figs. 2 and 4 respectively for comparison. While obtaining the orthogonal polynomial approximation, the error variance plot for a data-segment of the ECG signal is shown in Fig. 5. Similar plot for a data-segment of the EEG signal is shown in Fig. 6. Note that from Fig. 6, one can accept the degree of polynomial approximation to be either 6 or 26. However, it is verified that better accuracy of local bandwidth estimation is obtained by fixing the polynomial degree at 6.

CONCLUSION

The proposed method based on the orthogonal polynomial (OP) approximation calculates the estimate of local bandwidth of a signal with reasonable accuracy. The most desirable feature of the presented method is that the signal-samples at nonuniform spacings can be processed to extract the local bandwidth of the signal in one step. This feature makes the process fast, and the method provides a means for on-line implementation of nonuniform sampling.

REFERENCES

[1] J.J. Clark, M.R. Palmer, and P.D. Lawrence, "A transformation method for the reconstruction of functions from nonuniformly spaced samples", IEEE Trans. Acoust., Speech, Signal Processing, Vol. ASSP-33, 1985, pp. 1151-1165.

[2] P. Sircar and T.K. Sarkar, "System identification from nonuniformly spaced signal measurements", Signal Processing, Vol. 14, 1988, pp. 253-268.

[3] P. Sircar and A.C. Ranade, "Nonuniform sampling and study of transient systems reponse", IEE Proc., Pt. F, Vol. 139, 1992, pp. 49-55.

[4] R. Bose and P. Sircar, "On implementation of a nonuniform sampling strategy", in Proc. IEEE Region 10 Int. Conf. TENCON 98, New Delhi, Dec. 1998.

[5] R.J. McAulay and T.F. Quatieri, "Speech analysis / synthesis based on sinusoidal representation", IEEE Trans. Acoust., Speech, Signal Processing, Vol. ASSP-34, 1986, pp. 744-754.

[6] A. Ralston and P. Rabinowitz, A First Course in Numerical Analysis, McGraw-hill, Singapore, 1978.

[7] S.M. Kay, Modern Spectral Estimation: Theory and Application, Prentice-Hall, Englewood Cliffs, NJ, 1988.

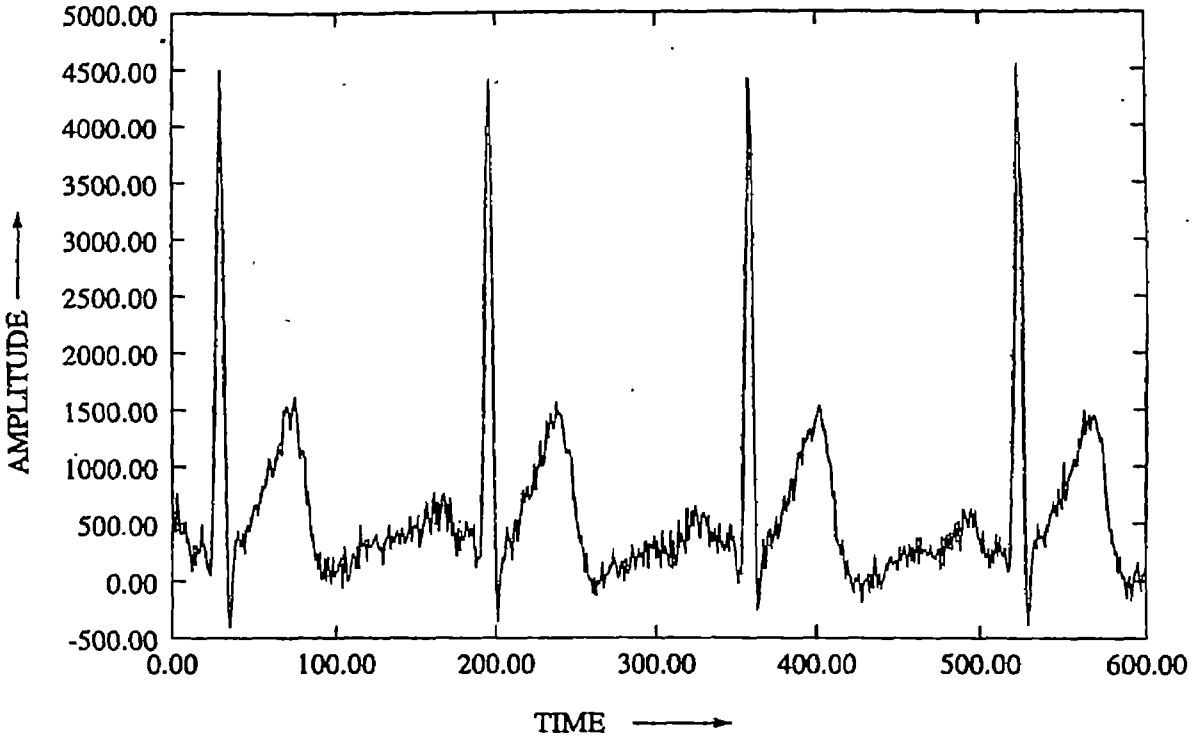

Figure 1: Electrocardiogram (ECG) signal

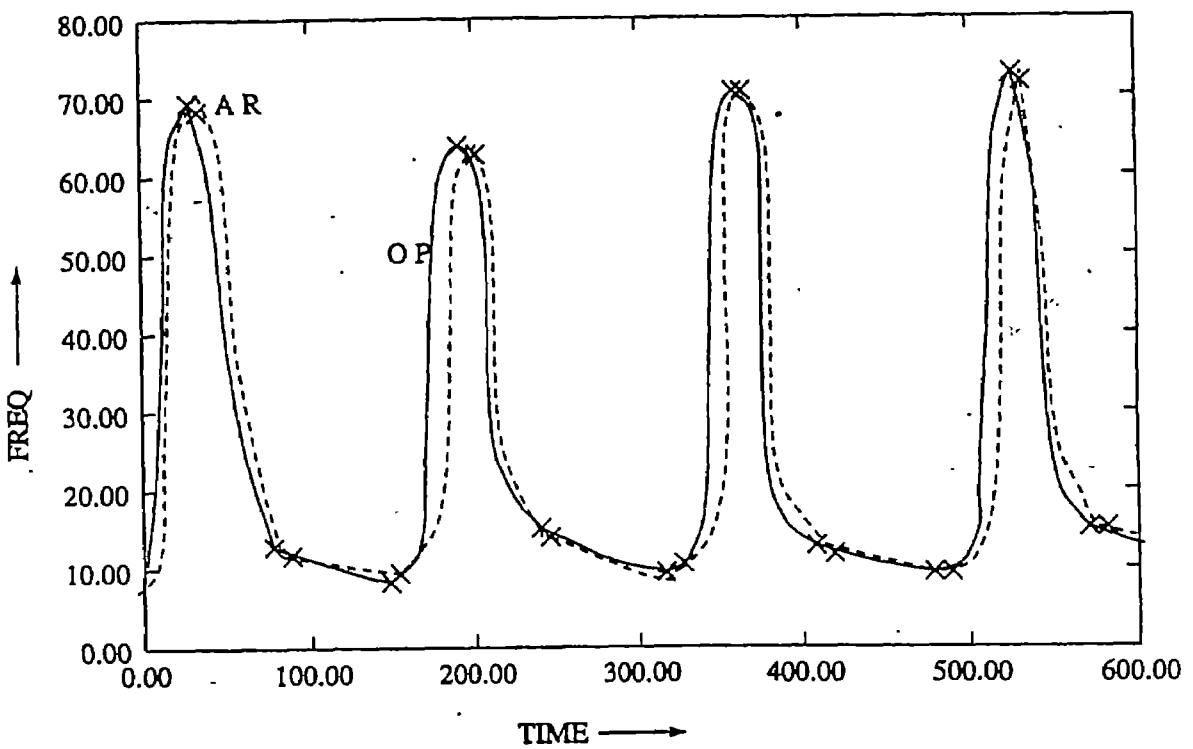

Figure 2: Local bandwidth estimation for the ECG signal by the methods based on the autoregressive (AR) PSD computations and the orthogonal polynomial (OP) approximations

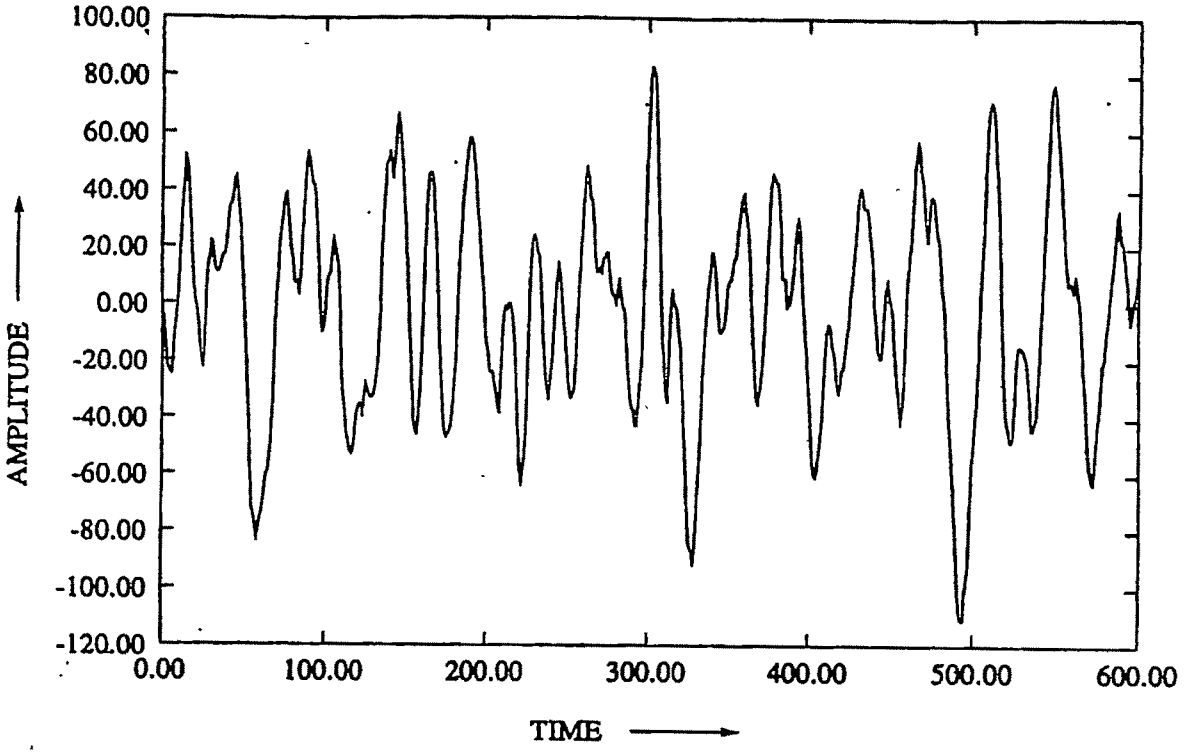

Figure 3: Electroencephalogram (EEG) signal

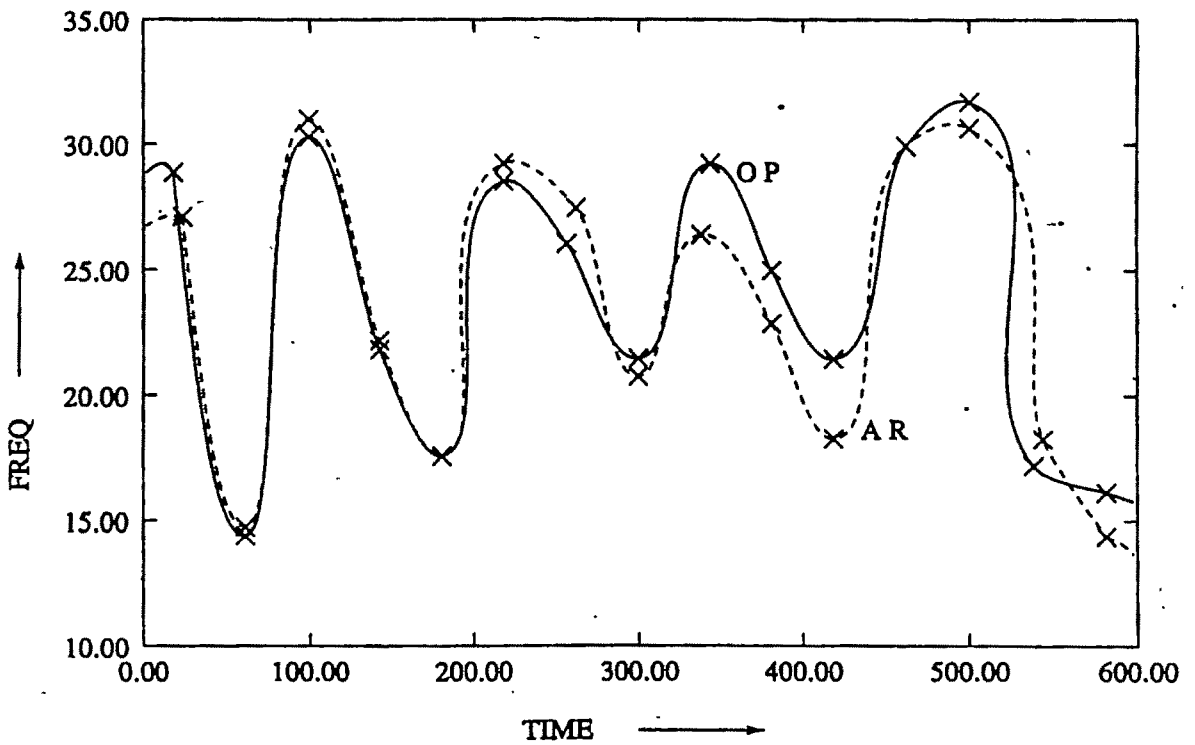

Figure 4: Local bandwidth estimation for the EEG signal by the methods based on the autoregressive (AR) PSD computations and the orthogonal polynomial (OP) approximations

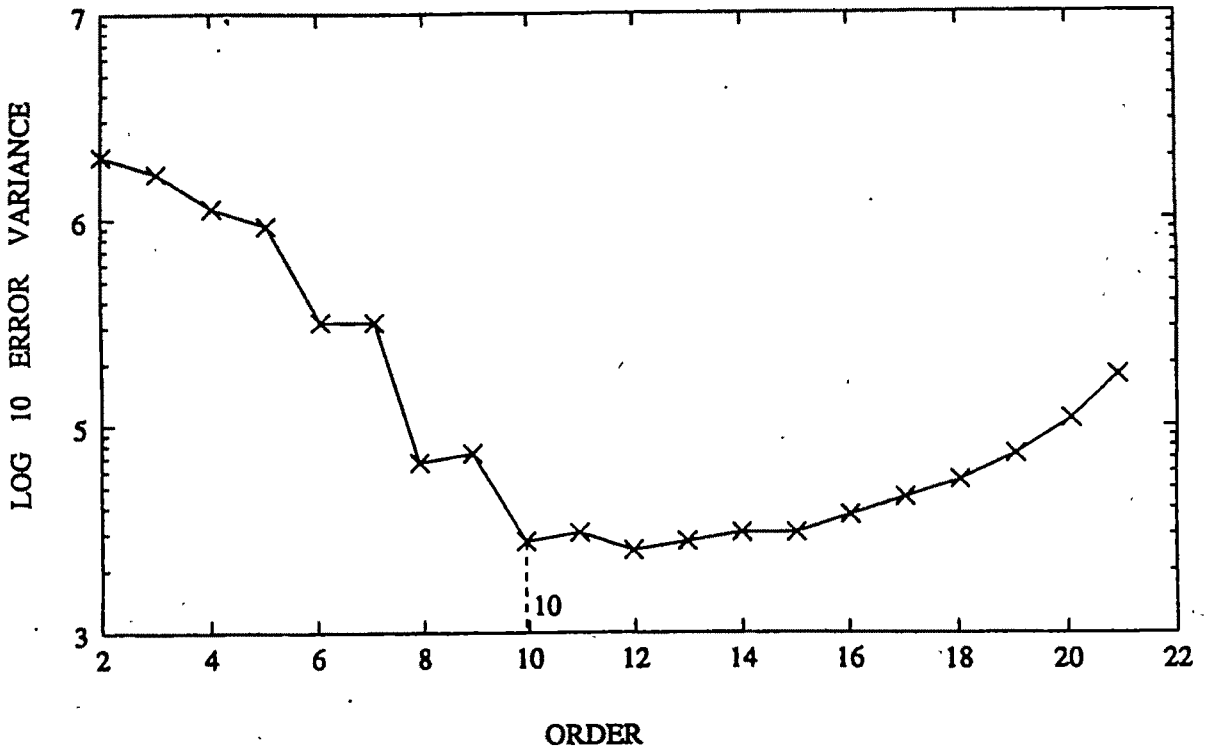

Figure 5: Error variance plot for the ECG signal (22 points)

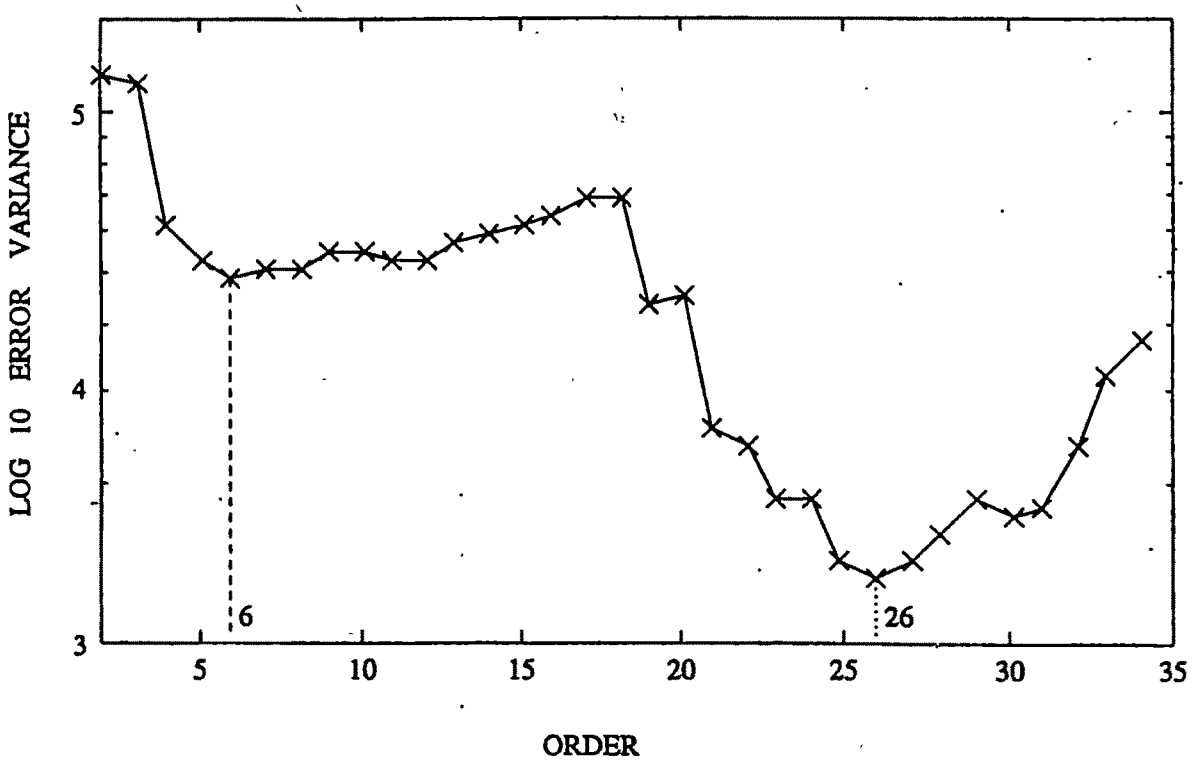

Figure 6: Error variance plot for the EEG signal (35 points)

Frequency Selective Rayleigh Faded HF Channel Using Multipath Propagation - A Model Based Approach

S. Sri Gowri[+], B. Prabhakara Rao[++], P. V. Subbaiah[+++]

[+]ECE Dept,V.R.S. Engg. College,Vijayawada-7, India, E-Mail: ssrigowri@hotmail.com

[++]ECE Dept ,J.N.T.U.C.E , Kakinada, India, E-Mail: prabhakarrao.b@hotmail.com

[+++]ECE Dept ,V.R.S .Engg .College Vijayawada, India, E-mail :PVS@hotmail.com

Abstract

In this paper the design and implementation of channel model over a frequency selective Rayleigh fading high frequency channel is dealt with. The proposed model is based on Quadrature phase Shift Keying (QPSK) modulation. When a complex-valued signal is transmitted through a frequency selective fading channel with complex low-pass equivalent, the time variant channel impulse response will have two components viz A direct component and a dispersive Rayleigh faded component. The received signal will consist of a number of time variant phasors which is the vector sum of different waves received after reflections by Ionospheric layers from a number of paths. It can be expected that due to randomly varying delays associated with different paths the received signal can be modeled as random process. QPSK is used for transmitting the bits in which information is encoded into phase according to the dibit transmitted. The demodulation is done by extracting inphase and quadrature phase components of received signal and inputing them to the decision making device yields the dibit at the receiver. The computer simulation of HF channel model using C showed good degree of accuracy between_input and output.. The signal to noise ratio increases with bit duration, but it is with in the limits for good_to worst channel conditions.

Key words: Frequency Selective Channel, Rayleigh Fading, Signal to Noise Ratio, Insertion Loss

INTRODUCTION

Communication using the High Frequency (HF) band between 2 and 30 MHz has been a primary means of beyond line of sight communication. Despite the advent of several other kinds of transmitting media such as satellite, optical fiber, coaxial cables etc., HF channel continues to be used extensively owing to the fact that it is economical and flexible. An accurate assessment of the performance of a newly developed HF radio system can be done through repeated tests of the system over an actual channel. When comparison is to be made between two or more systems over a real channel, they must all be tested simultaneously. Unlike cables, whose properties can be accurately defined and reproduced, Ionosphere channel properties can't be reproduced easily.

The channel's characteristics and transmission conditions vary uncontrollably. Hence tests can't be repeated at other times. Moreover, it is not possible to test a system repeatedly for the same channel conditions. The use of a channel simulator for evaluating the performance of a data transmission system offers several advantages. It is accurate and a large range of channel conditions can be produced in a controlled manner. It is possible to compare the performance of several systems under the same channel conditions using a channel simulator and tests can be repeated any number of times with consistent channel transmitting condition.

MODEL DESCRIPTION

Figure 1 shows the model of the data generation and transmission system using QPSK. The input to the system is the message of L number of characters. The model converts the given text in to ASCII code and supplies the bit stream to the QPSK encoder.

In quadrature PSK, set of two successive bits are mapped on to the four possible phases. When a pair of bits is encoded, say 0 1, the phase corresponding to the combination i.e., $5\pi/4$, is added to the previous bit interval, say $7\pi/4$, to give the phase shift in the present interval. Thus while in the previous bit interval a sinusoid of signaling frequency f_c with phase shift $7\pi/4$ was transmitted, in the present interval the sinusoid is transmitted with a phase shift $7\pi/4 + 5\pi/4 = \pi$. In doing so the effect of multipath, which causes phase errors will be reduced.

The general representation for the M-ary phase signaling waveform is

$$S(t)=U(t)\exp(j2\pi f_c t+\theta)$$

$$S(t)=\{U(t)\exp j(2\pi f_c t + 2\pi(m-1)/M+\theta)\}$$

$$0 \le t \le T \qquad (1)$$

where $m = 1,2,3,4.$

θ = Initial phase

U(t) is a rectangular pulse with amplitude A

$$S(t) = A\cos[2\pi f_c t+2\pi(m-1)/M+\theta] \qquad (2)$$

$$= A_{cm}\cos[2\pi f_c t] - A_{cm}\sin[2\pi f_c t]$$

If $=\pi/4$ and M=4,then $A_{cm} = A_{cm} = \pm A/2$

When $\theta>0$ is used, the signaling phase is shifted in every signaling interval , even when a long string of zeroes occur in the information.This results in a signaling spectrum with a width that is approximately equal to 1/T (T is a signaling interval).The spectral components above and below the carrier are used in maintaining synchronization at the receiver . Hence their presence in the received signal is important. Thus a non zero phase is used in such a case.

When s(t) is fed in to a single Rayleigh fading HF channel shown in figure1 above , the output would be

$$x(t)=s'(t)\,q1(t) + s\hat{}(t)\,q2(t) \qquad (3)$$

where q1(t) and q2(t) are random processes

The random processes have been generated by filtering the zero mean white Gaussian noise through a Bessel filter. The frequency and impulse response of a Bessel filter approaches Gaussian when the order of the filter is sufficiently large. While passing through the channel, the signal is modified as a result of random noise n(t) added to it . The noisy signal then passed through receiver filter C(t). The receiver filter's output is given by

$$y(t)= x(t) * C(t) + n(t) * C(t) \qquad (4)$$

The signal given to the demodulator is split in to I phase and Q phase components . The I channel input is given by

$$Y'(t) = \{ [x(t)*c(t)*d(t)] \exp(-j2\pi fct)\} + \{[n(t)*c(t)*d(t)] \exp(-j2\pi fct) \} \qquad (5)$$

DATA RECOVERY

The data is recovered from QPSK wave form by the demodulation, done by extracting inphase and quadrature phase components of received signal and inputting them to the decision making devise yields the dibit at the receiver.

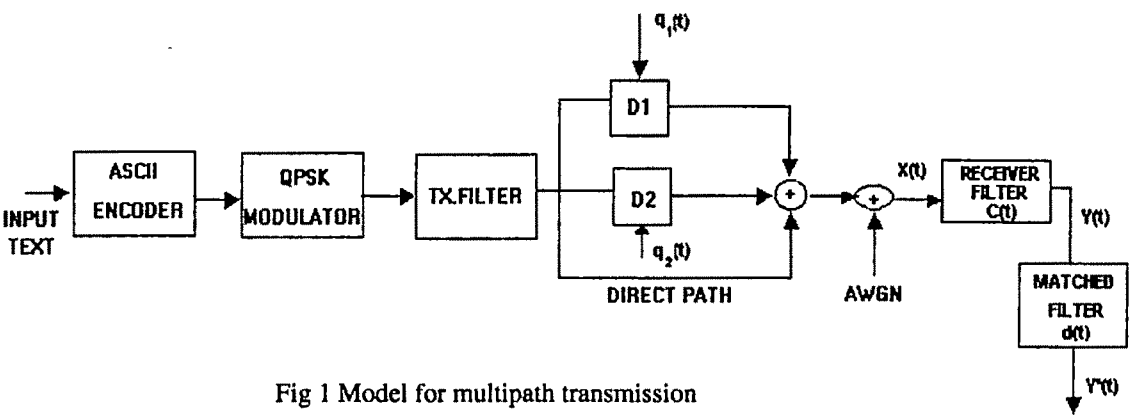

Fig 1 Model for multipath transmission

In the absence of the noise, in the Ith signaling interval, the received signal can be simply represented as

$$R_i(t) = \sin[2\pi f_c t+\theta+\varphi_i] \qquad (6)$$

The in phase (I) channel of demodulator gives

$$X_c = \int_{T_1}^{T_2} S_i(t)\cos(2\pi f_c t)\,dt$$

$= 0.5 \sin(\theta + \varphi_i)$ (7)

$X_p = X_{i-1} = X_c$ in the previous signaling interval $= 0.5 \sin(\theta + \varphi_{i-1})$ assuming path delay is constant for two successive signaling intervals. Similarly the quadrature phase component of the demodulator will give

$$Y_C = \int_{T_1}^{T_2} S_i(t) \sin(2\pi f_c t)\, dt$$

$$= 0.5 \cos(\theta + \varphi_i) \quad (8)$$

$Y_p = Y_{i-1} = Y_c$ in the previous signaling interval $= 0.5 \cos(\theta + \varphi_{i-1})$

The final outputs of the system are R and Q signals

$$R = X_C * X_P + Y_C * Y_P$$
$$= k \sin(\theta + \varphi_i) \sin(\theta + \varphi_{i-1}) + k \cos(\theta + \varphi_i) \cos(\theta + \varphi_{i-1}) \quad (9)$$

$$Q = X_C * Y_P - Y_C * X_P$$
$$= k \sin(\theta + \varphi_i) \cos(\theta + \varphi_{i-1}) - k \cos(\theta + \varphi_i) \sin(\theta + \varphi_{i-1}) \quad (10)$$

The decision is now made on the basis of the signs of R and Q signals as given under

R < 0 & Q < 0 01 ; R < 0 & Q > 0 00
R > 0 & Q < 0 11 ; R > 0 & Q > 0 10

SIGNAL TO NOISE RATIO

In the output signal the superimposed noise signal on the actual message is found by using

$$V_0(T) = 1/\tau \int_0^T [S(t) + n(t)]\, dt$$

$$= 1/\tau \int_0^T S(t)\, dt + 1/\tau \int_0^T n(t) dt \quad (11)$$

$$S(T) = 1/\tau \int_0^T V\, dt = VT/\tau = \text{signal power}$$

$$N_0(T) = 1/\tau \int_0^T n\, dt = VT/\tau = \text{noise power}$$

$$[S_0(T) / [N_0(T)]^2 = 2/\eta V^2 T \quad (12)$$

where, τ is time constant, T is the bit interval, V is the bit magnitude and $\eta/2$ = power spectral density of the white Gaussian noise.

Insertion Loss is given by $10 \log_{10}(p_0 / p_2)$ dB, where p_0 is the power delivered to the load by source (i.e., when the channel is removed) and p_2 is the Power delivered to the load by channel

CONCLUSIONS

The signal to noise ratio increases with bit duration but it is with in the limits for good to worst channel conditions. The SNR and insertion losses are varying exponentially with frequency and these losses are well with in +6.5 dB range of average value of 32.607 dB. Further the simulation of HF channel model exhibits excellent response viz. uniform response i.e the SNR AND INSERSION LOSS are constant with message of lengths of 1 to 140,000 characters.

The fig 2 shows that the noise added to the signal received is almost constant even if the length of the input to the model is increased and hence the SNR and ILOS is constant with input length

The figures 3 and 4 shows that the ILOS and SNR are varying exponentially with frequency. The maximum value of signal to noise ratio is about 59 dB and the maximum value of insertion loss is about 40 dB. The bit error rates can be decreased by employing the error correction / detection codes.

REFERENCES

1. Hariharan S. and Clark AP, 'Modeling of a Data Transmission System Over an H.F. Channel', Journal of IEEE on Digital Communications, vol. 36, Nos. 5 & 6, Sept - Dec 1990, pp. 406-417.
2. Yip K.W. & Ng TS, 'Discrete Time Model for Digital Communications Over Frequency Selective Rician Fading WISES Channel', IEE proc-commun, vol. 143, no 1, Feb.1996, pp. 37-42.
3. Yip K. W. & Ng TS, 'Efficient Simulation of Digital Transmission Over WSSUS Channels', IEEE Trans., 1995, COM - 43, pp 2907 - 2913.
4. CCIR, 'HF Ionosphere Channel Simulator', CCIR XIII th Plenary Assembly, Geneva, Vol. III, Report No. 549, 1974, pp. 66-75.
5. Smith WS, Wittke P. H. and Campbell, 'Error probabilities on Fading Channel With Inter Symbol Interference and Noise', IEEE Trans. 1993, IT - 39, pp. 1598 - 1607.
6. S Sri Gowri, S Venkateswarlu and Dr B Prabhakara Rao, 'Data Transmission over Rayleigh faded HF channel', Proceedings of ICORG2000, Vol. 2, pp 82-86

The input signal :

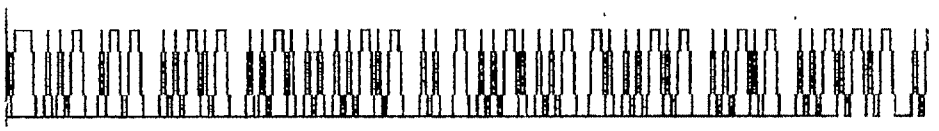

The received signal is :

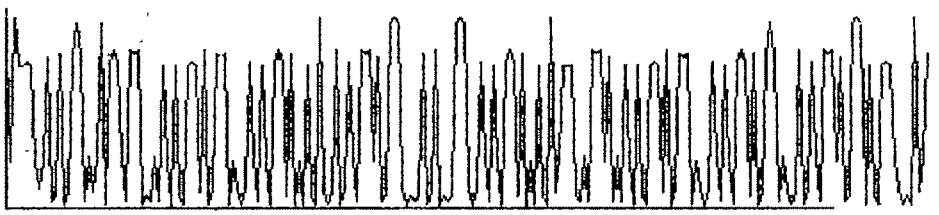

The noise introduced is (increased by a factor 40):

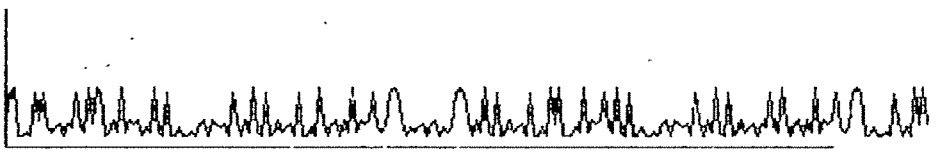

Fig 2 signal varying with the length of the input test

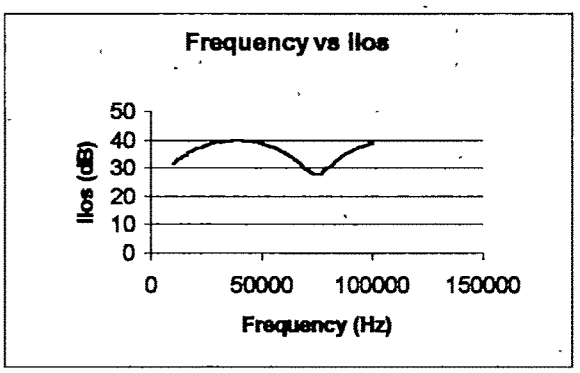

Fig 3 Frequency Vs ILOS

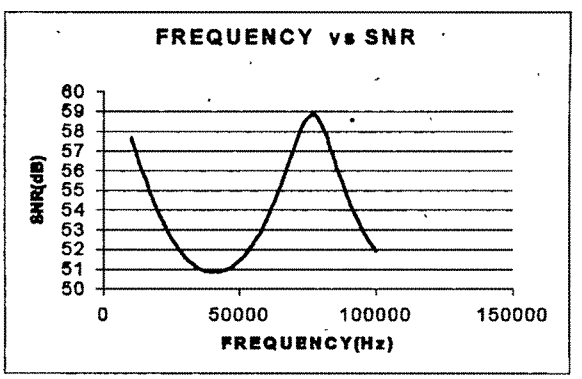

Fig 4 Frequency VS SNR

Some Studies On Open Slot And T-Junction Radiators

K. Chandra Bhushana Rao*, K. Padma Raju,[+], G. S. N. Raju[++], K. R. Gottumukkala**

*Department of Electronics and Communication Engg, GITAM Engineering College, Visakhapantam-530 045
[+] Department of Electronics and Communication Engg, JNTU College of Engineering, Kakinada-533 003
[++]Department of Electronics and Communication Engg, A.U. College of Engineering, Visakhapantam-530 003
**Department of Engg. Mathematics, A.U. College of Engineering, Visakhapantam-530 003, India.

Abstract

When the slots cut in one of the walls of the rectangular waveguide are used as open radiators coupling takes place from the waveguide to free space. Power also can be coupled to a T-Junction through the slot and T-arm radiates into free space. In the present work, intensive studies are made on coupling variations as well as on the effect of displacement of the slot on the admittance characteristics.

Key words: Slot, Self Reaction, Coupling, Displaced Slot

INTRODUCTION

Most of the reported literature contains the analysis of slots and wave-guide junctions towards obtaining only conductance. More over slots are assumed to be infinitesimally thin [1-2]. In fact, such slots do not exist. The assumptions are made only to obtain approximate analytical expressions for conductance. Watson [3] reported some data on coupling of a few typical junctions. But there is no information about its variation as a function of frequency.

The present work involves estimation of self-reaction [4-6] and discontinuity in modal current [9] in both the types of radiators. In the first case, self reaction is obtained using plane wave spectrum approach [7]. In the second case, the energy storage in both feed and coupled guides are considered and the self reaction is estimated. From the knowledge of self reaction and discontinuity in modal current normalized admittance is computed.

Considering the equivalent network of the radiators as an effective shunt element coupling is evaluated using transmission line matrix approach [8].

The analysis usually assumes the thickness of the wall to be negligibly small. However, the finite wall thickness has some influence on the coupling. Such effect is also estimated in the present work.

Several slot configurations as well as slot coupled junctions are reported in the literature by several authors [1-5]. However, the rectangular slot configuration whether longitudinal or inclined in the narrow wall of wave guide with a finite thickness is very common. In no occasion, a single slot is used as radiator. Instead, array of slot coupled T- junctions are commonly used. For the purpose of design of such arrays some techniques like empirical, analytical and perturbation are adopted. The first and third techniques are usually cumbersome and involves lot of approximations. Hence, the analytical techniques with the support of numerical evaluation is adopted in the present work. Main aim in the present work is to obtain the overall admittance characteristics and its dependency on the slot coupled T-junction.

The methodology involves intensive derivations for the self reaction [4-6] in the wave guide and discontinuity in modal current [9]. From the two expressions obtained normalized admittance is evaluated and the variation of both real and imaginary parts as a function of frequency is obtained for different displaced slot coupled T- junctions.

FORMULATION OF ADMITTANCE PARAMETER FOR THE RADIATORS

The expression for self reaction is obtained from the knowledge of equivalent magnetic current, transverse component of magnetic field and the electric field distribution in the aperture plane of the slot i.e.

$$< a, a > = - \iint \overline{H_t} . \overline{M} \; ds \; - \qquad (1)$$

where $\overline{M} = \overline{E_S} \times \overline{U}$

Following the formulation made in the expression for self-reaction is simplified and appears in the following forms.

$$< a, a > = \frac{4V_m^2}{\pi^2 \eta_0} \int_{\phi=0}^{\pi/2} \int_{\alpha=0}^{\pi/2} \left[\frac{Sin(ASin\,\phi\, Cos\,\alpha)}{ASin\,\phi\, Cos\,\alpha} \right]^2$$

$$\frac{[Cos(BSin\,\phi Sin\,\alpha) - CosB]^2}{(1 - Sin^2\,\phi Sin^2\,\alpha)} \; Sin\,\phi d\alpha\, d\phi$$

$$+ j\, \frac{4V_m^2}{\pi^2 \eta_0} \int_{\phi=0}^{\infty} \int_{\alpha=0}^{\pi/2} \left[\frac{Sin(ACosh\,\phi\, Cos\,\alpha)}{ACosh\,\phi\, Cos\,\alpha} \right]^2 .$$

$$\frac{[Cos(BCosh\,\phi\, Sin\,\alpha) - CosB]^2}{(1 - Cosh^2\,\phi\, Sin^2\,\alpha)} \; Cosh\,\phi\, d\phi\, d\alpha \qquad (2)$$

where $A = \frac{2\pi W_s}{\lambda}$ and $B = \frac{2\pi L_s}{\lambda}$

When the slot is displaced from the centre in a narrow wall of a waveguide the displacement is found to have considerable influence on the overall admittance characteristics. In this case the self reaction in the primary guide as well as secondary guide are evaluated and the final expression appear in the form of

$$<a,a> = \sum_m^\infty \sum_n^\infty \frac{4\varepsilon_m \varepsilon_n V_0^2 K^2}{j\omega\gamma_{mn} ab\mu_0 (K^2 + \gamma_{mn}^2)} Cos^2 m\pi$$

$$\cdot Cos^2 \frac{n\pi}{a}\left(\frac{a}{2} + dp\right) \cdot \left[\frac{Sin\left(\frac{n\pi W_S}{a}\right)}{\left(\frac{n\pi W_S}{a}\right)} \right]^2$$

$$\left[CosKL_S \left(\frac{\gamma_{mn}}{L_S} SinKL_S - CosKL_S + 2e^{-\gamma_{mn} L_S} \right) - 0.5\left(1 + e^{-\gamma_{mn} L_S}\right) \right]$$

$$+ \quad 2 \sum_m^\infty \sum_n^\infty \frac{1}{\pi^2} \left[\frac{ab}{(ma)^2 + (nb)^2} \right]^{1/2} \cdot$$

$$\cdot E_{max}^2 W_s^2 \left[\frac{2K}{K^2 - \left(\frac{m\pi}{b}\right)^2} \right]^2$$

$$\left[\frac{Sin\left(\frac{n\pi W_S}{a}\right)}{\left(\frac{n\pi W_S}{a}\right)} \right]^2 Sin^2 \frac{m\pi}{2} \left[Cos\left(\frac{n\pi}{a}\left(\frac{a}{2} + d\rho\right)\right)\right]^2 \cdot$$

$$\left[Cos\left(KL_S - Cos\frac{m\pi}{b} L_S \right)\right]^2$$

$$\left[\varepsilon_m \varepsilon_n \left(\frac{m\pi}{b}\right)^2 \frac{\gamma_{mn}}{j\omega\mu_0} + \frac{4j\omega\varepsilon_0}{\gamma_{mn}} \left(\frac{n\pi}{a}\right)^2 \right] \qquad (3)$$

The discontinuity in the modal current is obtained from [9] and appears in the following form

$$I_d = -2jY_{01} V_m \left(\frac{2}{ab}\right)^{1/2} \frac{\pi}{b\beta_{01}} \cdot \frac{K}{\beta_{01}^2 - K^2} \cdot$$

$$\cdot Cos(\beta_{01} L_S - CosKL_S) \qquad (4)$$

where $Y_{01} = \frac{\beta_{01}}{\mu_0}$ and

$$\beta_{01} = \left[K^2 - \left(\frac{\pi}{b}\right)^2 \right]^{1/2}$$

The admittance parameter is evaluated from

$$Y = - \frac{I_d . I_d}{< a, a >} \qquad (5)$$

Normalized admittance is obtained from Y/Y_{01}, where Y_{01} is characteristic admittance for the dominant mode.

Since the equivalent circuit of fig (1) of the slot is a shunt admittance, the transmission matrix of this parameter is given by

$$\begin{bmatrix} C_1^+ \\ C_1^- \end{bmatrix} = \begin{bmatrix} 1+Y/2 & Y/2 \\ -Y/2 & 1-Y/2 \end{bmatrix} \begin{bmatrix} C_2^+ \\ C_2^- \end{bmatrix} \qquad (6)$$

when the port of the primary guide other than the feed port is terminated in matched load, C_2^- becomes zero. The above matrix $Y = g_n + jb_n$

from the above matrix coupling dB is derived and is of the following form.

Fig. 1. Equivalent circuit seen from guide 1

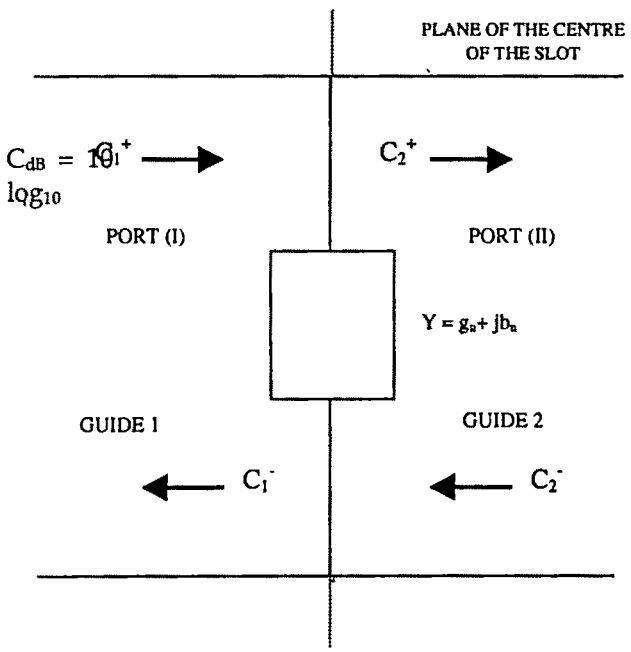

Fig 1 Equivalent circuit seen from guide 1

$$C_{db} = 10 \log_{10} \left[\frac{4 g_n}{(2+g_n)^2 + b_n^2} \right] - 8.686\, \alpha t \qquad (7)$$

where, $\alpha = [(\pi/2L)^2 - K^2]^{1/2}$, t is the thickness of the slot.

RESULTS AND CONCLUSIONS

From the data obtained of the normalized conductance coupling is evaluated as a function of frequency. The results on coupling for open slot radiator are presented in fig (2-3) for width of the slot 1.6 and theta is 5^0 and 10^0.

In the case of T-junction with the displaced slot from the centre of the narrow wall the variation of coupling is presented in fig (4-5) for displacements of 0.1mm, 0.2 mm and 0.3mm for slot widths equal to 0.2 cm and 0.4 cm respectively. From the results it is found coupling has a variation between–5to–15dB.

REFERENCES

1. H.Jasik, ed., Antenna Engg. Hand Book, New York, McGraw-Hill 1961.
2. R.S. Elliot, 'Antenna Theory and Design', New Delhi, PHI, 1981.
3. W.H. Watson, 'Resonant Slots', JIEEE, Vol. 93, part 3A, pp.747-777, 1946.
4. A.F. Stevenson, 'Theory of Slots in rectangular Wave Guide', J. Appl. Phys. Vol.19, pp.24-38, Jan 1948.
5. R.F. Harrington, Time-Harmonic Electromagnetic Fields, New York, McGraw-Hill, 1961.
6. V.H.Rumsey, 'The reaction concept in electromagnetic theory', Phys. Rev., Vol.94, No.6, pp.1483, June 15, 1954.
7. G.S.N.Raju, Ajoy Chakraborty, and B.N. Das, 'Studies on wide inclined slots in the narrow wall of Rectangular Wave Guide', IEEE Trans. on. A&P, Vol.38, No.1, Jan 1990.
8. R.E. Collin, Foundation for Microwave Engg. Tokyo, McGraw-Hill, 1966.
9. N.Marcuvitz and J.Schwinger, 'On the representation of electric and magnetic fields produced by the currents and discontinuities in wave guides", J.Appl. Phys., Vol.22, No.6, pp.806-819, June 1951.

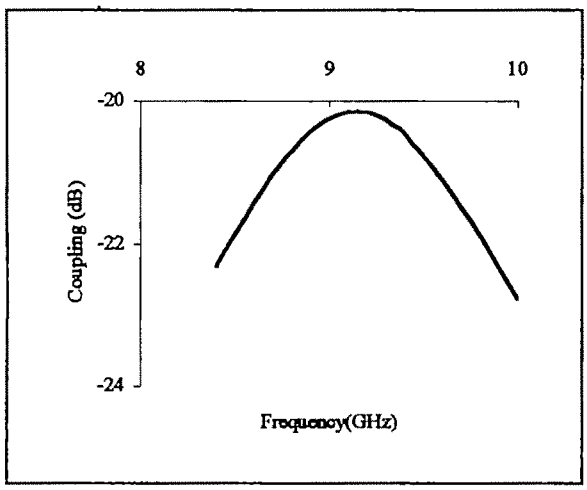

Fig.2. Variation of coupling with frequency for Theta = 5 degrees

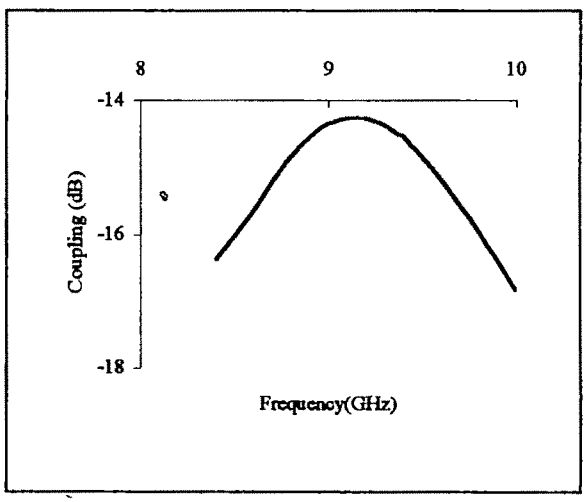

Fig.3. Variation of Coupling with frequency for Theta =10 degrees

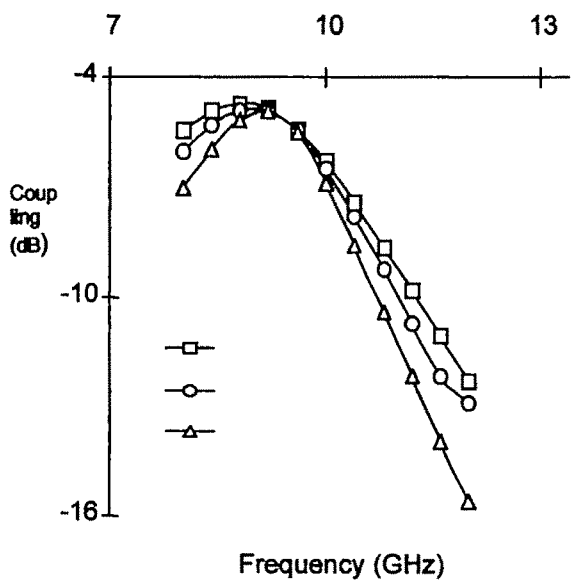

Fig. 4. Variation of coupling with frequency at resonant length and for slot width = 0.2 cm.

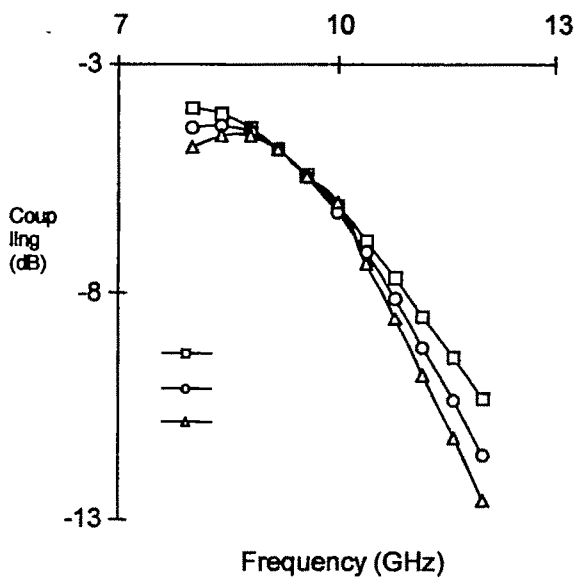

Fig. 5. Variation of coupling with frequency at resonant length and for slot width = 0.5 cm.

New approaches for implementing a robust synchronous optical CDMA Networks

Abhinav Roongta, Saurabh Sood, Subrat Kar

Deptt. of Electrical Engg.
Indian Institute of Technology, New Delhi - 110016
subrat@ee.iitd.ac.in

Abstract— **We propose an additional superposition constraint for codes used in S/CDMA networks to reduce the probability of error (PE) due to multiple access interference (MAI) to zero.**

I. Introduction

In this paper, S/CDMA is classified further into Synchronized Transmitters-CDMA (ST/CDMA) and Synchronized Transmitters & Recievers CDMA (STR/CDMA). In ST/CDMA the transmitters send OOCs in synnchronized fashion but no synchroniza-tion information in send to recievers. On other hand in STR/CDMA, synchronization information is send to recievers. This can be implemented either by reserving a particular OOC for maintaining sync or via Wavelength Division Multiplexing (WDMA). The deatails and effects of this implementation are not considered and ideal synchro-nization is assumed for the scope of this paper. Section 2 and 3 discusses ST/CDMA and STR/CDMA respectively.

II. Synchronized Transmitters CDMA (ST/CDMA)

In ST/CDMA, only transmitters are synchronized and no synchronization information is sent to the receivers. Thus receivers are not synchronized with the transmitters, however all transmitters send bit-synchronized data to the channel as shown in Fig. 1.

Since all users are synchronized the code of one user is never superposed on shifted version of other user. This results in modified system constraints for ST/CDMA for $(n, w, \lambda_a, \lambda_c)$ optical orthogonal code set C.

1. *The Autocorrelation Property:*

$$\sum_{t=0}^{n-1} x_t x_{t+T} \leq \lambda_a \tag{1}$$

for any $\mathbf{x} \in C$ and any integer T, $0 < T < n$. The autocorrelation constraint guarantees that each code is unlike cyclic shifts of itself. This property thus enables synchronization at the receiver end and is required because receivers are not provided any synchronization information. Thus same receivers as those used for asynchronous CDMA can employed here. Thus this is a necessary constraint.

2. *The Cross-Correlation Property:*

$$\sum_{t=0}^{n-1} x_t y_t \leq \lambda_c \tag{2}$$

for any $\mathbf{x} \neq \mathbf{y} \in C$ and any integer T.
The cross-correlation constraint guarantees that each code is unlike the other codes. This property thus helps multiple access communication. Note that in comparison to asynchronous case the synchronicity provided there is always maintained here. Also in synchronous CDMA one user code never interferes with the shifted version of any other code.

3. *The Superposition Property:* $\forall \mathbf{x} \in C$ such that $x_{j_0} = x_{j_1} = \ldots = x_{j_{w-1}} = 1$(as per notation in [7])

$$\sum_{\forall \mathbf{y} \in C, \mathbf{y} \neq \mathbf{x}} \sum_{i=0}^{w-1} y_{j_i} < w \tag{3}$$

The subscripts are reduced modulo n whenever necessary.The superposition property ensures that in absence of any particular code, superposition of all other codes will not result in an error for the absent code. The effect of this property on the probability of error due to MAI is discussed in section 2.2.

A. Design of OOC's for Synchronous ST/CDMA

We now present a modified Greedy Algorithm for constructing codes for the S/CDMA system.

A.1 The Greedy Algorithm for Constructing $(n, w, \lambda_a, \lambda_c)$ Codes for synchronous CDMA

Originally the code is empty. In ${}^nC_r$ steps, the algorithm examines all the binary n-tuples of weight w, one at a time. If an n-tuple satisfies the auto-correlation property, the cross-correlation *and the superposition* property with every codeword already included , it is added to the code set; otherwise, it is discarded. Computational and storage complexity of this algorithm is higher than that of the Greedy Algorithm for asynchronous DS-CDMA. The results of above Greedy Algorithm is shown in Table.I.

The number of OOCs generated can be compared with that of greedy algorithm for asynchronous On -Off CDMA [3]. It can be seen that number of users increase significantly as compared to asynchronous CDMA. Thus the number of users increase significantly at the cost of additional synchronization between the transmitters. Similarly if the receivers are also synchronized with the system then further increase in the number of users is expected.

n	w	Size of OOCs ST/CDMA	Size of OOCs On-Off CDMA
7	3	3	1
13	3	6	1
19	3	9	2
25	3	11	3
31	3	14	4
37	3	18	5
43	2	21	21
43	3	20	10
43	4	15	2
43	5	11	1
43	6	8	1

TABLE I
OOC'S GENERATED FOR ST/CDMA

B. Probability of Error in ST/CDMA

We note that the probability of error due to inter-user interference in synchronous ST/CDMA with threshold of receiver at w is zero.

III. Synchronized Transmitters and Receivers CDMA (STR/CDMA)

In ST/CDMA, all transmitters are in sync and the sunc information is send to receivers so that all receivers are also in sync with the transmitters. Thus whole system is in sync and it results in block diagram as depicted in Fig.2.

As in ST/CDMA, since all users are synchronized the code of one user is never superposed on shifted version of other user. Thus the cross-correlation constraint remains the same for ST/CDMA (eq. 2). Since synchronization between transmitters and receivers is obtained by external means, the auto-correlation constraint is not required here. Thus in STR/CDMA it is not required for a code to unlike the cyclically shifted versions of itself. The resulting system equations for STR/CDMA are as follows :

1. *The Cross-Correlation Property:*

$$\sum_{t=0}^{n-1} x_t y_t \leq \lambda_c \tag{4}$$

for any $\mathbf{x} \neq \mathbf{y} \in C$ and any integer T

2. *The Superposition Property:* $\forall \mathbf{x} \in C$ such that $x_{j_0} = x_{j_1} = \ldots = x_{j_{w-1}} = 1$(as per notation in [7])

$$\sum_{\forall y \in C, y \neq x} \sum_{i=0}^{w-1} y_{j_i} < w \tag{5}$$

The subscripts are reduced modulo n whenever necessary. An algorithm similar to the greedy algorithm of ST/CDMA can be used here with the modification that no auto-correlation constraint is required to be fulfilled here.

The probability of error due to MAI in synchronous ST/CDMA with threshold of receiver at w is zero. This can be shown quite similar to the facts presented for ST/CDMA . The results of greedy algorithm for STR/CDMA is shown in Table.II.

n	w	Size of OOCs (STR/CDMA)	Size of OOCs (ST/CDMA)
7	3	3	3
13	3	6	6
19	3	9	9
25	3	11	11
31	3	14	14
37	3	18	18
43	2	21	21
43	3	20	20
43	4	15	15
43	5	11	11
43	6	8	8

TABLE II
OOC'S GENERATED FOR STR/CDMA

As can be seen from comparing the size of OOCs for ST/CDMA and STR/CDMA, there is no increase in the size which was not expected beforehand, as we are relaxing a constraint. Qualitatively since the superposition constriant is infact a more stricter constraint and present in both ST/CDMA and STR/CDMA the size of OOCs for two systems are observed to be the same. Thus it can be concluded that as far as interuser interference and number of users is concerned there is no gain in imposing the synchronism in receivers and transmitters.

Similar to section 2 and 3 respectively the ST/CDMA with OHL and STR/CDMA with OHL is also evaluated. The conclusions are presented below

IV. Conclusion

S/CDMA is classified into synchronized transmitters CDMA (ST/CDMA) and syn-chronized trnsmitters & recievers CDMA (STR/CDMA). Also superposition constraint is proposed which makes probability of error (PE) due to MAI zero for these schemes. These schemes as expected can support more number of simultaneous users as coma-pared to asynchronous CDMA. However as far as number of users are concerned STR/CDMA showed no improvement over ST/CDMA. Thus sending the synchroniza-tion information to recievers and also maintaining zero PE due to MAI has no added advantages. The number of users are shown to be further increased by adding optical hard limiters (OHL) to above schemes.

References

[1] Fan R.K. Chung, Jawad A. Salehi, and Victor K. Wei, "Optical Orthogonal Codes: Design, Analysis, and Applications", *IEEE Transactions on Information Theory*, vol. 35, no. 3, May 1989.

[2] J.A. Salehi, " Code division multiple access techniques in optical fiber networks-part I: Fundamental Principles", *IEEE transactions on Communications*, pp. 824-833, August 1989.

3] J.A. Salehi and C.A. Brackett, " Code division multiple access techniques in optical fiber networks-part II: Systems performance and analysis", *IEEE transactions on Communications*, pp. 834-850, August 1989
4] P.R. Prucnal, M. A. Santoro, and S. K. Sehgal, "Ultra-fast all-optical synchronous multiple access fiber networks", *IEEE J. Select. Areas Commun.*, vol. SAC-4, pp. 1484-1493, Dec. 1986.
5] W.C. Kwong, P.A. Perrier, and P.R. Prucnal, "Performance comparison of asynchronous and synchronous code-division multiple-access tecnique for fiber-optical local area networks", *IEEE Transactions on Communications*, vol. 39, pp. 1625-1634, November 1991.
6] H. Walle, U. Killat, "Combinatorial BER Analysis of Synchronous Optical CDMA with Prime Sequences", *IEEE Transactions on Communications*, vol. 43, no. 12, December 1995.
7] G. C. Yang, "New Codes and New Approaches for Code Division Multiple Access on Optical Fiber Networks", *Ph.D. Theris Report*, University of Maryland, College Park, ch. 5, pp. 89-110, 1999.

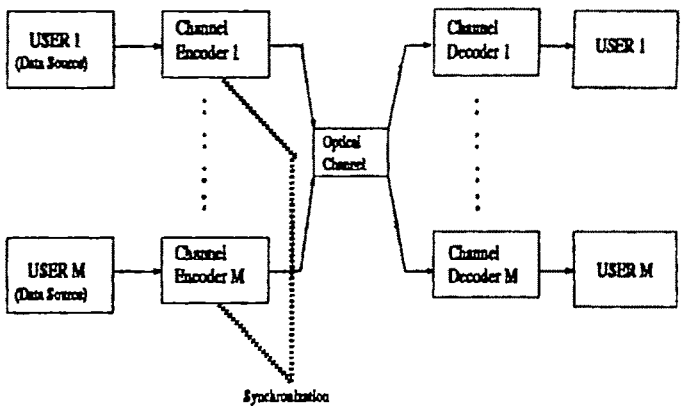

Fig. 1. A ST/CDMA scheme

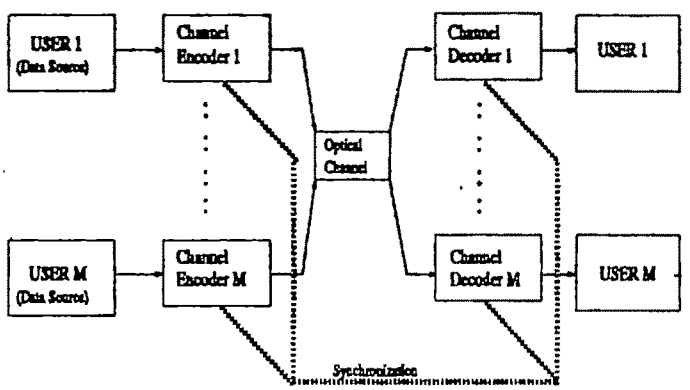

Fig. 2. A STR/CDMA scheme

Automatic Categorical Modularization Of Computer Network Protocols

A.K. Daniel
Computer Sc. & Engg. Department
M.M.M. Engineering College
Gorakhpur (UP)-273010

Abstract

Real World problems are often too difficult to be solved by a single monolithic system Many natural and artificial systems use modular approach to reduce the complexity of a set of sub-tracks by solving the overall problems satisfactorily. An evolutionary learning system is presented which automatically create a repertoire of specialized strategies for network protocols this reveals the human efforts of deciding how to divide and specialized the system.

INTRODUCTION

Many problems in machine learning are large and complex. To reduce this complexity a modular system uses specialized modules to solve the different aspects of the problem. The modular system often provide suitable performance. The separate part of the human brain deals with different aspects of images and the body neuron act as a neural network for image immolation. Modular system design in engineering however has relied on human expertise to manually divide a system into important specialized part often act in an ad-hoc way. Categorical modularization is significant in many control management systems (Environment) such as data communication, traffic load of a network system. The simplest problem for a learning (designing) computer network. Instead of load analysis of the user which are sending the different types of signals (voice image etc.) the most promising route is to decompose the solution into specialized part and deal with those aspects separately. Speciation can act as a modulating mechanism to perform this. A network configuration is also called a network topology. The network designer have the following major goals when establishing the topology of network. The topology should provide network reliability, least cost path between the users, should provide the best possible response and throughput. The topological goals are achieve with the help of different protocols. Modular system design in engineering, however, has relied on human expertise to manually divide a system into specialized parts. Often in an adhoc manner. Also manual modularization cannot be used on "Black box problems" or "Knowledge-lean problems" problems for which little human expertise exits. One way to decompose a solution is to create "modules" that serve very different functions, not different versions of the same function. The top-down structure of large software projects is an example each procedure has its own task. This goes by the label of functional modularization. Another way is where the "modules" perform different versions of basically the same job. We call this categorical modularization. Antibodies in the immune system are an example (i.e. they all locate and destroy infection). The body must maintain a repertoire of antibodies, each specializing (to some extent) against a different type of antigen. The aim is to survive any infection. i.e. transmission losses.

The requirement, to provide some protection against any possible attack is related to issues of generalization in system design. New network protocols and extensions to existing protocols are being deployed on the network (Internet). New functionality is being added to IP routers at a rapid pace. In the past, the main task of router was to simply forward packets based on a destination address lockup. Modern routers, however, incorporate several new services in addition to destination based forwarding such as

- Integrated services and differentiated services (e.g. bandwidth reservation);
- Enhanced routing functionality
- Security algorithms
- Enhancements to exiting protocols
- New core protocols

For the functional operation of a system we propose a software framework present an implementation, which address these requirements. Suitable software has been developed which having some of the following sub function (subroutines).

- Modularity: Implementation of specific algorithms cone in the form of modules, for plugins.
- Extensibility : New plugins can be dynamically loaded at run time.
- Flexibility : Instances of plugins can created configured and bound to specific flows.
- Performance: The system should provide for a very efficient data path, with no data copying, no context switching, and no additional interrupt processing. This overhead of modularity should not seriously impact performance.

SYSTEM DEVELOPMENT AND DESCRIPTION

The massage is passed from node to node till it reached destination. The massage is broken into smaller but optimal pieces called packet (frame) Consider unfortunately all-too-realistic situation for communication channel that makes errors during the transmission of information between nodes. The frames may be either damaged or completely lost. This protocol provides in which both senders and receivers have a variable whose value is remembered during noisy channel. The sender remembers the sequence number of the next frame to be sent, the receivers remembers the sequence number of the next frame excepted in arrival. After transmitting the frame the sender starts the timer running. If it was already running it will reset to allow another full time interval. The time interval must be chosen to allow enough for the frame to get at the receiver to process it in the worst case and for the acknowledgement frame propagate back to the sender that the information has not arrived. Only when the given time interval has elapsed, it is safe to assume that either the transmitted frame or its acknowledgement has been lost and to be sent a duplicate. After transmitting a frame and starting the timer the sender waits for following

(a) An acknowledgement frame arrives undamaged.

(b) A damages acknowledgement frame staggered.

(c) The timer go off.

If a valid acknowledgement comes in, the sender fetch the next packet and put it in the buffer, overwriting the previous packet. It also advance the sequence number. If the damage frame arrives or no frame at all arrives so the sequence numbers are not change so that a duplicate can sent. When a valid frame arrives at receiver it sequence numbers is checked to see if it duplicate or not if not it is accepted and an acknowledgement is generated and passed back to the sender.

ALGORITHM FOR SUMILITATION

For T=0 to Final-Time

BEGIN

Generate a message at each node and put them in corresponding queue

IF

Message is generated at each instant of time

THEN

Generate a source and destination node

IF

Source and destination nodes are same

THEN

Again generate destination node

ELSE

BEGIN

Find the shortest path between source and destination node find the next node matrix which gives the detail of intermediate nodes between source and destination.

END

Send a acknowledgement { channel acknowledgement }

IF

Noise in the channel

THEN

Wait for clear the noise

ELSE

DO { Loop for message transmission}

BEGIN

IF

Channel is empty at each instant of time for each link

THEN

Find the propagation time for message by using the delay count of the channel

ELSE

IF

Channel is busy at each instant of time for each link

DO

Set delay count=delay of the channel. Decrement the delay count by 1

IF

Delay count=0

Take out the message from the channel

THEN

The propagation time = delay count + delay of the channel

Find out the destination node for the message

/* Check noise after transmission during message acknowledgement */

IF

Noise in the channel

THEN

Wait for clearing the noise

ELSE

/*no noise in the channel */

IF

Message acknowledgement is true

THEN

Find out the destination node for the message

IF

Destination node is the node at where you reached

THEN

CONSUME IT; BREAK;

ELSE

Put it the proper queue by consulting next node matrix.

END

/* End of simulation Program */

EVALUATION FOR NOISE CHANNEL

Threshold value: 20

Simulation time :1000

Noise Level : 10

No. of Nodes : 5

Total number of jobs introduced at link 1=52

Total number of jobs terminated at link 1=42

Total number of jobs introduced at link 2=52

Total number of jobs terminated at link 2=33

Total number of jobs introduced at link 3=27

Total number of jobs terminated at link 3=27

Total number of jobs introduced at link 4=41

Total number of jobs terminated at link 4=31

Total number of jobs introduced at link 5=37

Total number of jobs terminated at link 5=37

Number of jobs introduced = 209

Number of jobs terminated =170

Percentage Throughput of the network=81.34%

EXPERIMENTAL RESULT AND CONCLUSION

The table 1 shows the performance against the users (nodes).

In this paper an attempt has been made to develop a Automatic categorical modularization of computer network protocols. Real World problems are often too difficult to be solved by a single monolithic system Many natural and artificial systems use modular approach to reduce the complexity of a set of sub-tracks by solving the overall problems satisfactorily. An evolutionary learning system is presented which automatically create a repertoire of specialized strategies for network protocols this reveals the human efforts of deciding how to divide and specialized the system.

REFERENCES

1. Computer Networks by Andrew S. Tenenbaum, third edition, Prentice Hall of India, ISBN 81-203-1165-5.
2. D.Dcasper, Zubin Dittia, Guru Parulkar, and bernhard Platters: Software Architecture for Next generation Routers, members IEEE 2000.

3. S. Deering and R.Hinden, " Internet Protocal, version 6 (Ipv6) specification, "rfc 1883 Dec. 1995",

4. IP Next Generation Overview.

http://playground.sun.com/pub/ipng/INET-IpngPaper.html

Table 1

TABLES FOR COMPARISION OF PROTOCOLS PERFORMANCE **Threshold value : 20** **Noise Level : 10** **Acknowledgement: 10**				
Simulation Time	1000	1000	2000	2000
Protocol/Nodes	5	8	5	8
Unrestricted / Simplex Protocol	100	100	100	100
Simplex Stop & Wait Protocol	91.39	94.51	88.71	88.04
Simplex Protocol for Noising Channel	**81.34**	87.13	91.93	89.28
Sliding Window Protocol	74.84	82.58	84.94	83.28

40 kHz Signal Amplitude in Relation to Solar Radio Emission at 2800 MHz

Barin Kumar De and Pinaki Pal
Department of Physics, Tripura University, Suryamaninagar 799 130, Tripura INDIA
E-mail of corresponding author : barin_de@yahoo.com

Abstract

The long distance 40 kHz radio signal has been observed to show good correlation with slowly varying component of solar radio flux at 2800 MHz. It has been observed that the zero-day (peak-day) of solar radio flux variation and that of 40 kHz amplitude variation superpose on each other in three cases, peak of radio signal leads the peak of solar radio flux in two case and in six cases peak of radio signal leads the peak of solar radio flux. The increase in conductivity parameter of wave guide mode propagation of LF wave in the earth-ionosphere cavity due to increase in solar ionizing radiation is responsible for the correlation.

Key words : Solar radio flux, Ionosphere, LF propagation

INTRODUCTION

The ionosphere is the region from about 60 km to 2000 km altitude where the solar irradiance produces a partially ionized plasma of mostly H^+ and He^+ above 1000 km, O^+ from 300 to 500 km, and molecular ion (NO^+, O_2^+, N_2^+) below 200 km. Total ion densities (=electron density) range from 10^8 to 10^{13} m^{-3}. Driven by neutral wind and electric fields the ionospheric electrons and ions move along geomagnetic field lines. Knowledge of ionospheric electron density is essential for a wide range of applications viz., radio telecommunication.

While the vast majority of telecommunication and broadcasting now take place in the HF, VHF and UHF portions of the radio spectrum, the frequency range between 10 kHz and 500kHz was once the dominant location of such activity. This was due to the abilities of these frequencies to provide reliable long distance communications under adverse conditions. Even during periods of intense solar flares when all other frequencies are unusable, a VLF-LF signal not only got through , but their propagation characteristics are improved. The spectrum below 100 kHz offers many interesting monitoring possibilities due to its unique characteristics. Here propagation is even more unusual because these frequencies have an additional characteristic of being able to travel long distance through solid rock. This has been used to great advantage by cave explorer and mining crews to keep in contact with different team members underground. The waves can also penetrate under the surface of ocean which normally blocks radio waves at higher frequencies. This has allows the navy to be able to transmit radio messages to submarines working at depths and at speed.

The wave guide formed between the lower ionosphere and earth's surface is good for very low frequency (VLF) and low frequency (LF) propagation round the earth. The conductivity parameter determining the status of the ionospheric radio propagation is controlled by the solar conditions. It is established [1,2] that the increase in intensity of L_α- and X-radiation are correlated with solar microwave radiation. Thus the spectral components of solar radiation controlling the electron density of lower ionosphere are related to 2800 MHz solar radio flux. It is then expected, the long distance propagation at 40 kHz in the earth-ionosphere wave guide is to bear some relationship with solar flux at 2800 MHz. In this paper we report the result of the study of amplitude of 40 kHz radio signal in relation to solar radio flux at 2800 MHz.

EXPERIMENTAL DETAILS

Transmitter: The 40 kHz radio wave (call sign: JG2AS/JJF-2) modulated by 1 Hz, is transmitted from Sanwa, Japan continuously with a power of radiation of 10 kW. The accuracy of transmitted frequency is $\pm 1 \times 10^{-11}$

Receiver: The receiving system consists of loop antenna feeding a number of OP AMPs used in tuned radio frequency mode. The output of AC amplifier is detected with a time constant 0.22s and the DC level is further amplified logarithmically. The DC gain has been used to adjust the receiver's sensitivity corresponding to the incoming signal which shows marked variation over the year. The DC output is used as the signature of amplitude of 40 kHz signal. The overall gain of the amplifier is 120 dB with a band width of 200 Hz. The time constant of the recorder is 7.5 s.

Propagation path: The great circle distance between Sanwa, ($36^0$11'N, $139^0$51'E) and Agartala (23^0N, 91^0E) is 4884 km. Considering the normal electron density profile, the daytime and nighttime ionospheric reflection heights are 70 and 90 km respectively.

OBSERVATIONS, ANALYSES AND RESULTS

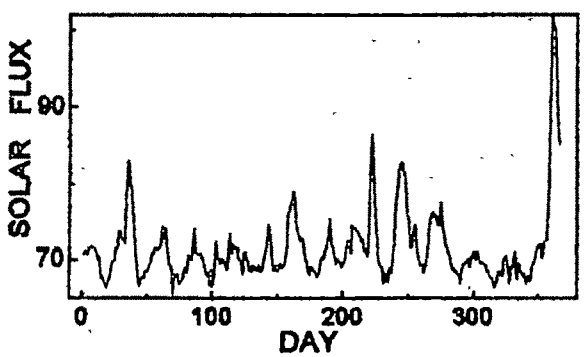

Fig.1. Day-to-day variation of solar radio flux at 2800 MHz from December 1995 to November 1996. The flux is in the unit of 10^{-22} $Wm^{-1}Hz^{-1}$

The amplitude of 40 kHz radio signal has been recorded in a diurnal basis in the Department of Physics, Tripura University. The amplitude of the recorded signal is larger at night than at day. The sunrise and sunset affects are characteristic features of the signal at the receiving station. The signal amplitude exhibits sudden enhancement (SES) during X-ray flares. Typical zigzag variations are also observed due to meteor shower. Quasi-periodic variations are observed during nights followed by high geomagnetic activity.

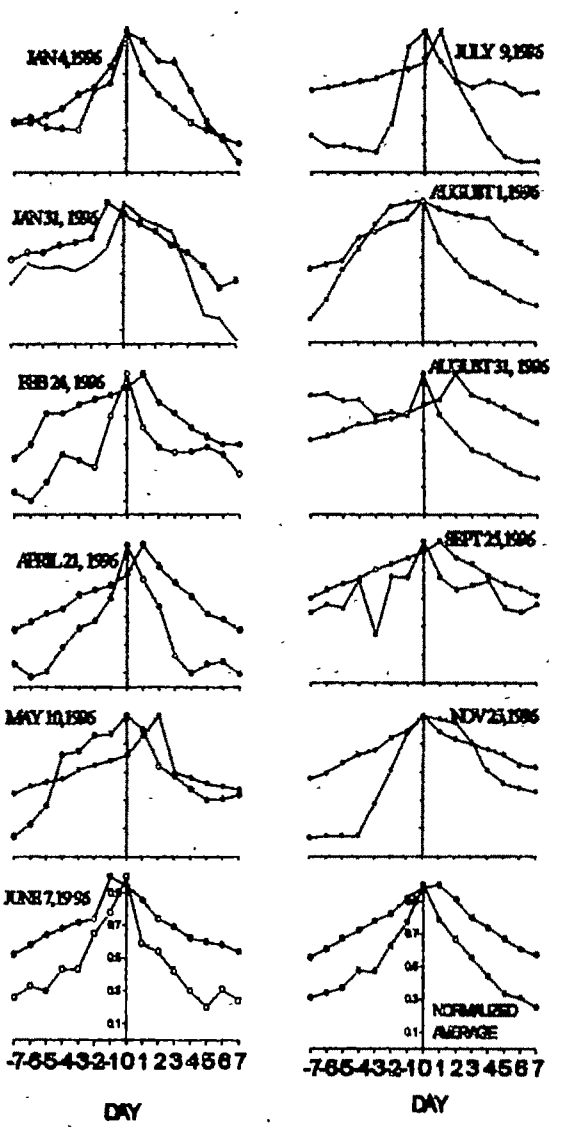

Fig.2. Variation of normalized values of 2800MHz solar flux and signal amplitude at 4okhzabout zero-day of solar flux.

The day-to-day variation of solar radio flux at 2800 MHz has been considered from Solar Geophysical Data Book, NOAA. The variation of flux with day has been plotted in Fig.1 for the period from December 1995 to November 1996.

We have selected 11 prominent peaks of this variation. The day showing the peak has been considered as zero-day. The normalized value of slowly varying components solar radio flux and the average value of amplitude of 40 kHz signal have been plotted for positive and negative days in Fig.2. The zero-day of solar radio flux variation and that of 40 kHz amplitude variation superpose on each other in three cases, peak of radio signal leads the peak of solar radio flux in two case and in six cases peak of radio signal leads the peak of solar radio flux.

DISCUSSION

The close correlation between solar radio flux and 40 kHz radio signal amplitude indicates a coupling between ionosphere and troposphere throughout the year. The increase in solar radio flux is an indication of enhancement of all kinds of solar ionizing radiation over the earth's atmosphere. It can cause an increase in ambient electron density in the D-region of theionosphere. The amplitude of 40 kHz radio wave in the spherical shell wave guide formed by the earth as a lower boundary and the lower ionosphere as upper boundary is dependent on conductivity parameter given by[3]

$$\omega_r = \omega_0^2 / \nu$$

where ω_0 is the angular plasma frequency and ν is the collision frequency of electrons.

The slowly varying component of solar ionizing radiation must give rise to a variation in ambient electron density in D- region. This, in turn, can control the overall attenuation of 40 kHz radio amplitude.

CONCLUSIONS

The slowly varying component solar radio flux may be used as index of long distance East-West LF propagation

REFERENCES

1. S. K. Sarkar, T. Chattopadhyay and M. K. Dasgupta. Sol. Phys. 40 (1975)411
2. F. Farnik, M. Karlicky and A. Tlamicha, Bull. Astron. Inst. Czech. 38(1987)36
3. J. R. Wait. Electromagnetic Waves in Stratified Media, Pergamon, Oxford (1982)

Propagation of ELF Radio Wave in Relation to Geomagnetic Storms

Barin Kumar De[+], Samarjit Sengupta*, and Pinaki Pal[+]
[+]Department of Physics, Tripura University, Suryamaninagar 799 130, Tripura, India
*Department of Applied Physics, Calcutta University, 92 APC Road, Kolkata 700 009
E-mail of the corresponding author: barin_de@yahoo.com

Abstract

Quasi-periodic (QP) variations in the atmospheric radio noise field strength (ARNFS) at 900 Hz during meteorologically clear nights exhibit a close correlation with principal geomagnetic storms having range of variation of earth's horizontal component of magnetic field as greater than 100γ. The periodicity of QP variation lies between 40 and 80 minutes. Precipitation of energetic particles in the polar atmosphere can give rise to the travelling of ionospheric disturbances towards equatorial belt. This, in turn, gives rise to periodic variation in conductivity parameter of wave guide mode of propagation of ELF radio wave in earth-ionosphere cavity.

Key words: Atmospherics, ionosphere, ELF radio wave, geomagnetic storm

BACKGROUND

The electromagnetic radiation of cloud discharge known as atmospherics or sferics is very much significant in regard to electric phenomenon going on in different types of cloud during meteorologically active periods. During clear period atmospheric radio noise field strength (ARNFS) measurement provides the study of ionospheric propagation. At Agartala we are in privileged position to study ARNFS from the local cloud discharge as well as from the distant sources of Australia, Japan and Africa. The variation of electric field ΔE can be expressed as Fourier transform:

$$\Delta E(d,t) = \int a(d,\nu) \exp(i\nu t)\, d\nu \qquad (1)$$

where the inverse FT is given by

$$a(d,\nu) = \int \Delta E(d,t) \exp(-i\nu t)\, dt \qquad (2)$$

gives the amplitude of Fourier component due to thunder electric pulse at a distance d. Previous experiments showed that the peak of the Fourier components lies in very low frequency (VLF) range. The extra-low frequency (ELF) component, though smaller in magnitude compared to VLF component, exhibits more variations in dB scale during ionospheric irregularities. The received Fourier component at frequency ν at distance d can be expressed as [1]

$$a_r(d,\nu) = G(\nu)\, W(d,\nu) \qquad (3)$$

where G(ν) is the function of spectral source function a(d,ν) and W(d,ν) is the wave guide transmission function.

W(d,ν) is dependent on the ionospheric conductivity parameter which is again dependent on electron density. Any periodic variation in conductivity parameter will result in periodic variation in attenuation, and hence will give rise to periodic variation in ELF noise field. We are interested in ELF atmospherics due to following reasons:

(i) Study of ELF atmospherics in North-East part of India is scanty.

(ii) The ELF-VLF spectrum between 50 Hz and 10 kHz is unusual in that sense that there is no broadcast transmitter in this range.

(iii) As long as the receiver is placed well away from unintentional short range electromagnetic interference, such as electrical power lines and electrical machinery, the spectrum is dominated largely by natural noise from cloud discharge.

(iv) No work has yet been reported on its propagation in relation to solar flare, meteor shower and geomagnetic activity.

We are recording atmospherics at 900 Hz in the Department of Physics, Tripuar University as a continuation of the experiment in Calcutta University since 1980.

INSTRUMENTATION

An `*inverted-L*' type antenna has been used to receive the predominantly vertically polarized ARNFS in the ELF band from near and far sources. The voltage induced at the antenna has been fed to the input of tuned radio frequency (TRF) receiver, the frequency of resonance being 900 Hz, through a low pass filter. The receiver consists of an AC amplifier and series resonance circuit. The AC output is detected, further amplified by a DC quasi-logarithmic amplifier. The DC output is the signature of field strength of ELF atmospherics at 900 Hz. An automatic gain control (AGC) has provided wide dynamic range.

ANALYSES AND RESULTS

The ARNFS at 900 Hz in the absence of local cloud activity is characterized by sunrise and sunset effects. In Fig.1, it is seen that diurnal pattern reveals higher and steady level at night than at day. This diurnal pattern is highly affected by local thunderstorms and cloud activity. The Fig.1 has been produced by taking average of the days which were locally clear in the month of August, 1997. During the clear nights ARNFS exhibits a steadiness in its level. But during 37 nights, in the one-year period from June 1997 to May 1998, we observed remarkable sinusoidal-like variations which we call quasi-periodic (QP) variations. Out of 37 events 31 are closely correlated with principal geomagnetic storms having the range of variation (ΔH) of horizontal component of magnetic field greater than 100 γ ($1\gamma = 1$ nanoTeslas).

We have considered the principal geomagnetic storms reported by obsevatories at Alibag, Hyderabad, Pondicherry, Shilong and Trivandrum. During the above period they reported 43 principal geomagnetic storms with $\Delta H > 100\ \gamma$. The QP variations in ELF ARNFS followed the commencement of 31 principal geomagnetic storms, the percentage correlation being 72%. The observed duration of a QP in a night is between 20 Hour to next 4 Hour in local time. The periodic times of QP variations have been observed between 40 to 80 minutes. The distribution of events in various range of periodic time has been shown in Fig.2.

Maximum number of events have been observed to exhibit periodic time between 60 and 70 minutes. The amplitude of QP has been found to vary with ΔH as shown in Fig.3. The amplitude of QP variations increases with increase of ΔH showing a tendency of saturation above 200 γ. In the diagram we have plotted the maximum value of ΔH reported by the stations as mentioned above.

DICUSSION

The ARNFS at a measuring station are the combined effect of the variation of source activity and the prevailing wave guide conditions. Due to small E-region losses, the atmospheric radio noise levels at night depends on sources up to 10,000 km. In our study we have recorded the integrated effect from all directions. The variation of sources and prevailing wave guide conditions are the factors governing the nighttime mean level. The QP variations over the mean level of ARNFS is expected to depend on the variation of electron density in the upper boundary of earth-ionosphere wave guide. In other words, occurrence of QP variations indicates the persistence of periodic disturbances in the lower ionosphere.

It is well accepted that occasionally distinct type of disturbances occur in the polar ionosphere and that they move horizontally polewards. They are called *travelling ionospheric disturbances* (TID). Large scale travelling ionospheric disturbances (LS TID) are characterized by (i) a direction of travel from polar to equatorial latitudes, (ii) little change in character over large distance, and (iii) correlation of their occurrence with magnetic activity. There are multiple evidences to indicate that the source of TIDs is in the evening sector of the auroral oval and that LS TIDs originate during polar magnetic storms. The TIDs originating there have periods from 30 minutes to a few hours. The wave front of TIDs may extend several thousands kilometers [2] in the East-West direction and travel from polar to the equator with a horizontal speed between 400 and 700 ms^{-1}. They are expected to create a periodic variation of electron density in the E-region of the ionosphere. These variations, in turn, can produce QP variations in the level of ELF atmospherics propagated over a large distance in earth-ionosphere wave guide.

During geomagnetic storms (under the influence of solar wind), the earth's upper atmosphere near the pole appears to become intermittently unstable. At such times, large amount of energies are suddenly released in to the polar atmosphere producing TIDs there. A number of simulations indicate that both Lorentz forces and Joule heating effect are important in producing gravity waves. During principal geomagnetic storms, LS TIDs are manifestation of atmospheric gravity wave and it may be understood from the following continuity equation of electron density, N:

$$\frac{\partial N}{\partial t} = Q - L - M \qquad (4)$$

where the rate of production and rate of loss per unit volume due to chemical processes are given by Q and L respectively; M being the transport term consisting of (i) the diffusion term M_d and (ii) the wave induced term M_w. The gravity wave obviously affects the wave induced term, M_w. We assume that the solution of equation (1) can be written as the sum of an unperturbed term, N_0, and a perturbed term N', the later being caused by gravity wave:

$$N = N_0 + N' \qquad (5)$$

The unperturbed term N_0 may undergo seasonal and diurnal variations which are slower than the time rate of variation of N' during geomagnetic storms because the later represents a variation due to gravity waves. The result is that over the seasonal and diurnal variations of electron density another rapid periodic variation is superimposed due to gravity wave. Consequently the conductivity parameter of wave guide mode of propagation varies periodically. The observed nighttime QP variation in ELF ARNFS is, therefore, the result of periodic variations in electron density in the E-region of the ionosphere. The observed range of periodicity is in good agreement with the that of gravity wave.

CONCLUSIONS

1. Long distant ELF ARNFS exhibit regular pattern in its variations.
2. The diurnal pattern is highly perturbed by local cloud activity.
3. Nighttime level is steady during meteorologically undisturbed days in the location of observation and is greater than daytime level on the average.
4. During principal geomagnetic storms of $\Delta H > 100\gamma$ nighttime level exhibits QP variations.
5. Periodicity of QP variation is concentrated about 60 minutes.
6. Amplitude of QP variation increases with the increase of range of variation (ΔH) of earth's horizontal component of magnetic field.

ACKNOWLEDGEMENT

The authors are grateful to Professor S. . K. Sarkar, Department of Physics Calcutta University for his constant encourage and suggestion in this work. The author is also thankful to Dr. D. Bhattacharjee for his continuous support in computer work.

REFERENCES

1. A. J. Smith and P. J. Jenkins. J. Atmos. Terr. Phys. 60(1998)263
2. L.A . Hajkowicz, Planet. Space Sci. 40(1992)1093
3. S.K. Sarkar and B. K. De. Ann. Geophysicae. 12(1994)1119.

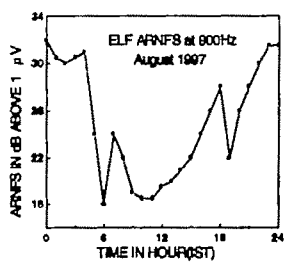

Fig 1 Diurnal variation of ELF ARNFS at 900Hz averaged over the days of observations in August, 1997. The ordinate represents the induced voltage at the input of the receiver in dB above 1 micro volt

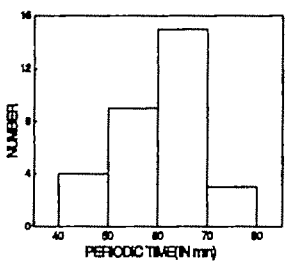

Fig 2 Distribution of events in various ranges of periodic times of QP variations of ELF ARNFS at 900 Hz

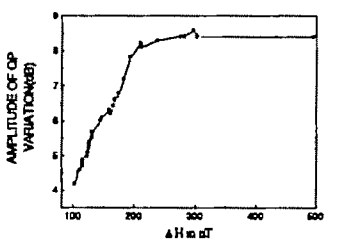

Fig 3 Amplitude of QP variations of ELF ARNFS at 900 Hz vs. range of variation (AH) of earth's horizontal components of magnetic field

Compression and Decompression of Information by using 2-D Cellular Automata

Amal K. Ghosh [1], Pabitra Pal Choudhury [2], Kajal Dihidar[2], Amitabha Basuray [3]

1. Electronics Test and Development Centre, West Bengal,4/2 B T Road, Kolkata-700 056, India.

2. Applied Statistics Unit,Indian Statistical Institute, 203, B. T. Road, Kolkata, 700 035, India

3. Dept of Applied Physics, University of Calcutta, 92, A P C Road, Kolkata 700 009, India.

Email : basuray@cucc.ernet.in /pabitra @isical.ernet.in

Abstract

In the present paper we have proposed a method where we can store the information within a minimum storage location as well as the stored information can be retrieved conveniently. This is a real state of the art problem of data compression and decompression in the context of multimedia in real time.

INTRODUCTION

The simplest form of 2D CA [1] consists of m rows and n columns i.e, total number of cells is mn and each cell contains either 0 or 1. Here all arithmetic addition, multiplication etc. are defined using modulo 2. The initial configuration of the array is known as the initial state. Assuming that the value of each cell of this array depends on its nearest neighbours for the next state, we can obtain the next state of this array. For 2D CA these nearest neighbours are 9 cells of 3x3 matrix centering that particular cell. Mathematically we can write (t+1)th state of (i,j)th cell, where the present state is (t)th state as follows:

$$s(t+1)=f(s_{i-1,j-1}(t),s_{i-1,j}(t),s_{i-1,j+1}(t),\ s_{i,j-1}(t),s_{i,j}(t),s_{i,j+1}(t),\ s_{i+1,j-1}(t),s_{i+1,j}(t),s_{i+1,j+1}(t))$$

But the value of each cell for the next state may not depend upon all 9 neighbours. The sum of the neighbouring cells on which each cell value is dependent is called the rule number of the 2D CA. The conventional method of defining a rule number for a linear rule in 2D CA can be explained in the following way:

64	128	256
32	1	2
16	8	4

The centre most box represents the current cell and other boxes are 8 neighbourhoods of that cell. There may be $2^9 = 512$ rules all of which are linear. Regarding the neighbourhood of the first and last cells we have two approaches. If we assume that the first and last cells are adjacent, then that particular case is known as periodic boundary condition and if we assume that the end points are fixed,the first and the last cells are not adjacent, equal to zero then that case is known as the null boundary condition. If the same rule is applied to all of the cells, then that CA is called as uniform or regular. Otherwise it is known as hybrid CA.

It is clear from the above that the Rule 33 & Rule 34 can be represented as follows:

Rule 33 : $Sn(t+1) = Sn-1(t) \oplus Sn(t)$

Rule 34 : $Sn(t+1) = Sn-1(t) \oplus Sn+1(t)$

These two rules are the most important rules in data compressions and decompressions.

APPLICATION OF RULE 33 AND RULE 34 IN COMPRESSIONS AND DECOMPRESSIONS

In fact the 2-D CA is also most important in cases where we want to store the information in the form of compression [2]. There are so many rules – we can use some of them for the purposes. Here we have used the Rule 33 & Rule 34 for the purpose. The compression and decompression may be shown by using the matrix algebra. In this case first we have formed the rule matrix, which can be used for compression of information and then we can retrieve the information by

multiplying the compressed information by the inverse rule matrix.

Suppose our binary information matrix is X and of order m x n. Then T be the rule matrix of order mn x mn such that

$$[T]\begin{pmatrix} X_1^T \\ X_2^T \\ X_3^T \\ . \\ . \\ X_m^T \end{pmatrix} = \begin{pmatrix} Y_1^T \\ Y_2^T \\ Y_3^T \\ . \\ . \\ Y_m^T \end{pmatrix}$$

where Y_{mxn} be the matrix obtained by applying rule on X_{mxn} and $Y_1, Y_2, \ldots\ldots Y_m$ be the row vectors of Y_{mxn} and $X_1, X_2, \ldots\ldots X_m$ be the row vectors of X_{mxn} .

We can obtain the rule matrix T in the following way:

At first we consider a null (0) matrix A of order mxn. Then put 1 at (1,1) position of that matrix and apply a particular rule no. on each of the mn cells to get 1st column of the rule matrix T. Then move the 1 of the matrix A to the (1,2)th position and same thing is repeated to get the 2nd column and this way is continued for all the cells of first row of A. Next apply same rule for all the cells of 2nd row of A,3rd row of A and so on to complete the rule matrix.

Let us first consider the Rule 33 – in this case the information in a particular cell in the next state(t+1) depends on the left neighbour and neighbour at that position in the previous state(t). The operation of rule matrix [T] of order 9x9 for the Rule 33 on the information 0 1 1 1 1 1 1 1 0 will be as follows:

$$\begin{pmatrix} 1&0&0&0&0&0&0&0&0 \\ 1&1&0&0&0&0&0&0&0 \\ 0&1&1&0&0&0&0&0&1 \\ 0&0&1&1&0&0&0&0&0 \\ 0&0&0&1&1&0&0&0&0 \\ 0&0&0&0&1&1&0&0&0 \\ 0&0&0&0&0&1&1&0&0 \\ 0&0&0&0&0&0&1&1&0 \\ 0&0&0&0&0&0&0&1&1 \end{pmatrix}\begin{pmatrix} 0 \\ 1 \\ 1 \\ 1 \\ 1 \\ 1 \\ 1 \\ 1 \\ 0 \end{pmatrix} = \begin{pmatrix} 0 \\ 1 \\ 0 \\ 0 \\ 0 \\ 0 \\ 0 \\ 0 \\ 1 \end{pmatrix}$$

It is to be noticed that if the concentration of 1s are more then it will be reduced to 0s i.e, the compression of information is possible. Now we can retrieve the original information from the compressed information by multiplying it with the inverse rule matrix as follows:

$$\begin{pmatrix} 1&0&0&0&0&0&0&0&0 \\ -1&1&0&0&0&0&0&0&0 \\ 1&-1&1&0&0&0&0&0&0 \\ -1&1&-1&1&0&0&0&0&0 \\ 1&-1&1&-1&1&0&0&0&0 \\ -1&1&-1&1&-1&1&0&0&0 \\ 1&-1&1&-1&1&-1&1&0&0 \\ -1&1&-1&1&-1&1&-1&1&0 \\ 1&-1&1&-1&1&-1&1&-1&1 \end{pmatrix}\begin{pmatrix} 0 \\ 1 \\ 0 \\ 0 \\ 0 \\ 0 \\ 0 \\ 0 \\ 1 \end{pmatrix} = \begin{pmatrix} 0 \\ 1 \\ 1 \\ 1 \\ 1 \\ 1 \\ 1 \\ 1 \\ 0 \end{pmatrix}$$

It is clear from the above that the retrieved information is nothing but the original one. Therefore, we may use this method for compression of information.

Same technique of compression and decompression can be demonstrated by using the Rule 34 also .

CONCLUSION

It is clear from the above discussion that we can compress the original information and retrieve it by using some rules in 2 Dimensional CA. One recent work [3] in data compression with long repeated strings is reported. But the novelty with our methodology lies in compressing and decompressing in real time i.e, in fraction of a nanosecond we can change the state of two dimensional information [4]

REFERENCES:

1. N.H.Packard and S.Wolfram, "Two dimensional Cellular automata", Journal of Statistical Physics 38(5/6), 901-946(1985).

2. A.R.Khan, P.P.Choudhury, K. Dihidar & R. Verma"Text Compression using Two –Dimensional Cellular Automata", Computers & Mathematics with Applications 37(1999) 115-127.

3. John Bentley, Douglon Mcllordy "Data compression with long repeated strings",Information Sciences135(2001) 1-11.

4. A.R.Khan, P.P.Choudhury, K. Dihidar , S.Mitra and P.Sarkar, "VLSI Architecture of cellular automata machine", Computers & Mathematics with Applications 33(5),79-94(1997).

MEMs / Porous Silicon-Based Smart Sensors And System-On-Chip

H. Saha
IC Design & Fabrication Centre
Department of Electronics & Tele-Communication Engineering,
Jadavpur University, Kolkata – 700032, INDIA
E-mail : juicc@vsnl.com

INVITED PAPER

INTRODUCTION

Microsensors have become essential element of process control systems and analytical instrumentations in various applications like industrial monitoring and automation, space and defense applications, automobiles, transportation, tele-communications, computer and robotics, environmental monitoring, biomedical instrumentations etc. With the development of microprocessors and application-specific integrated circuit (ASIC), signal processing has become precise, reliable and cheap. This stimulated research in sensor area and an explosive growth on sensor technology has taken place over the last few years [1]. The recent advances in micro machining technology have led to quantum jump in sensor technology and made possible the integration of sensing transducer with the dedicated signal processing circuit leading to the concept of SMART Sensors which has become a catchword in the field of process control and instrumentation in modern industrial and various other applications [2]. The concept is being presently further extended to develop a system-on-chip (SOC) that includes the micro actuator circuits and dedicated processor to implement sophisticated control algorithms as well as a display unit, preferably using porous silicon or any other compatible optoelectronic material [3].

MICROMACHINED ELECTROMECHANICAL SYSTEMS (MEMS)

Silicon transducers of Smart Sensors can be broadly divided into two categories (a) MEMS (Micromachined Electromechanical Systems) and (b) Porous Silicon. Micromachining technology enables the fabrication of various types of mechanical structures with very small dimensions in the micrometer range such as contilevers, cavities, nozzles, diaphragms and membranes, microbridges, resonators etc. [4]. Silicon has been proved to be an excellent material for MEMS usage since it has a yield strength two times higher than steel, Youngs modulus close to that of steel and yet a density which is one-third of the steel. Moreover, it does not deform plastically and does not show any hysterises. In addition, silicon is highly stress sensitive and demonstrates a significant piezoresistive effect [5].

Wet anistropic etching of silicon in preferential directions using antistrophic etchants like KOH, TMAH, EDP, Hydrazine and a complexing agent like isopropyl accohol in carried out in a controlled manner to develop unique structures not otherwise feasible [6]. The etch rate is strongly dependent on crystallographic orientation and composition and temperature of the etchant. Etch-stop mechanisms can be built-in the etchant processes by taking advantage of the fact the etch rates are also a function of silicon dopant concentration [7]. Sometimes electrochemically controlled Anistropic etching is used for better control [8].

POROUS SILICON

Porous Silicon is presently one of the most actively researched material for possible use in different types of devices such as electroluminiscent displays, sensors, optical filters and wave guides etc. [9]. Its extremely large surface to volume ratio ($>500m^2/Cm^3$) can be effectively utilized as an excellent sensing material and Porous Silicon based humidity sensors, vapour and gas sensors, have very high potential for commercial applications [10]. The nanopores of the Porous Silicon adsorb the vapour or gas molecules from the ambient and undergo significant change in its permittvity or conductivity. The structure and distribution of the nanopores can be easily controlled by varying the formation current density and the composition of the anodic etching solution during the formation of porous silicon

layer [11]. Further, the porous silicon layer behaves like a distributed R-C network having a strong piezoresistive properly. Any modulation of its resistance or capacitance consequent on sensing the desired entity may be mainfested in the form of a phase change which may be detected accurately and calibrated suitably for sensing purpose [12].

A very important properly of Porous Silicon is its room temperature electroluminiscence. It is possible in principle to fabricate a Porous Silicon based seven segment LED display and integrate it with the rest of sensing and signal processing circuit leading to the concept of a complete System-on-chip [13].

CMOS INTEGRATION

Both Silicon MEMS and Porous Silicon are compatible to CMOS IC processing technology [14,15]. The integration of these technologies can be divided in two distinctive steps : IC processing itself followed by micromachining as post processing step. The merger of CMOS process and micromachining adds to new possibilities of microfabrication utilizing the possibilities of anisotropic etching of silicon dioxide and silicon nitride films. Standard VLSI Cad Tools are used for designing the front and back end of the signal processing circuit. Recently developed MEMS software can be used for the post microfabrication processing [16].

SYSTEM-ON-CHIP (SOC) SENSORS

The CMOS integration of the micromachined or Porous Silicon sensor with CMOS signal processing unit may be ideally further extended to include (a) microactuator units and dedicated processors for implementing the sophisticated control algorithms and (b) display driver-decoder-latch coupled to Porous Silicon based electroluminiscent seven segment display for realizing a dedicated System-On-Chip for specific transduction and control or instrumentation [17]. Of course, the development of Porous Silicon based LED of acceptable efficiency and reliability is still in the embryonic stage.

TYPICAL APPLICATIONS

Pressure Sensors

The piezoresistive silicon pressure sensor is one of the most commonly used sensor in micro machining technology and smart sensors. It shows high sensitivity, good linearity and good stability. A typical fabrication process of a pressure sensor using direct wafer bonding technology is described [18]. The advantages of this type of pressure sensor are excellent control of thickness of the diaphragm which in turn determines the sensitivity and a dielectrically isolated piezoresistor which reduces the leakage and high-temperature operation (-20°C to 400°C).

Another variation of MEMS-type Pressure Sensor developed for the measurement of ambient pressure is fabricated by using a sacrificial layer resulting in the formation of a cavity interacting with ambient [19]. Porous silicon based pressure sensors are being developed utilizing the excellent piezoresistive property of porous silicon and its distributed R-C network nature [20].

Humidity and Gas Sensors

Porous Silicon based capacitive humidity sensor has been developed recently and is in the process of being commercially exploited [21]. The adsorbed water vapour condenses within the nanopores of the PS layer having dimensions less than the Kelvin radii and modulates the dielectric constant of the PS layer significantly resulting into the change of capacitance which can be precisely measured and correlated to the relative humidity of the environment. Gas sensors have been developed based on Porous Silicon for NO_2, CH_4 and Oxygen [22,23]. The gas detection is based on the principle of change in conductivity of PS layer caused by the modulation of the local field by the adsorbed gas molecules shifting the Fermi level with respect to the conduction band edge.

Bio-Sensors

Microsilicon biosensors are potentially one of the greatest possible applications in near future [24]. Silicon has already proved to be biofriendly and can be embedded inside the living cells without any toxic effect. A novel sensor consisting of two comb-electrode patterned on a free standing membrane has been reported for monitoring fermentation processes [25]. A multiple parameter blood sensor, capable of measuring blood pressure, blood flow velocity, oxygen saturation and temperature has been recently designed and fabricated. A system for localization and guidance of catheters inside the cardiovascular system is also being developed [26].

CONCLUSIONS

Micromachined and Porous Silicon based Microsensors integrated with CMOS signal processing technology are on the threshold of bringing a major revolution in monitoring, control and instrumentation in almost all application including biotechnology. In this presentation an attempt has been made to introduce the basic concept of micromachining and porous silicon formation for the fabrication of suitable sensors like pressure, temperature,

humidity, gas concentration and rate of fermentation. The integration of these sensors with CMOS signal processing technology leading to a Smart Sensor and finally with a display unit resulting with a complete system-on-chip has been discussed in some details.

REFERENCES

[1] Ljubisa Ristic ed., Sensor Technology and Devices, Artech House, Boston, 1994.

[2] S. Middlehock and S.A. Audet, silicon Sensors, Boston, Academic Press, 1989.

[3] S. Dey, A. Bagchi, J. Das and H. Saha, Development of a System on chip Integrating a Porous Silicon based humidity sensor with a Porous Silicon based seven segment display, Proc. XIth VLSI SOC Conf. Montpellier, 3-5 Dec., 2001.

[4] L. Csepregi "Micromechanics : A silicon microfabrication technology, Microelectronics Engg., 3, (1985) 221.

[5] L. Ristic, H. Hughes and F. Shemauskg, Bulk Micromachining Technology, in Sensor Technology and Devices, p.49 Artech House, Boston, 1994.

[6] K.D. Bean, "Anisotropic Etching of Silicon," IEEE Trans. Electron Devices, ED-25, (1978) p. 1185.

[7] J.W. Faust, Jr, E.D. Palik, H.F. Grag and R.F. Greene, "Study of Etch-stop Mechanisms in Silicon" – J. Electrochem Soc. 129 (1982) 2051.

[8] B. Koleck, S.D. Collins, N.F. Rooh and R.L. Smith, "Study of Electrochemical Etch-stop for High Precission Thickness Control of Silicon Membranes "IEEE Trans. On Elec. Dev. ED-36, (1989) p.663.

[9] L.T. Canham et.al., Nature 386, (1994) 133.

[10] Z.M. Rittersma, A. Splinter, A. Bedecker, W. Bencke, A novel surface surface micromachined capacitive porous silicon humidity sensor, sensors and actuators B 68 (2000) 210.

[11] J. Das, S.M. Hossain, S. Chakraborty and H. Saha, Role of Parasitics in humidity sensing by porous silicon, Sensors and Actuators, A 94, 1-2 (2001) p 44.

[12] H. Saha, J. Das, S. Dey and A. Bagchi, Development of Smart Humidity Sensor based Porous Silicon, Frontiers of VLSI Design and Test, Proc. VLSI Design and Test Workshop, August 16-18, 2001 p.233, Phonex Publishing House, 2001.

[13] S.M. Hossain, S. Chakraborty, S.K. Dutta and H. Saha, Metal Patterning for large area electroluminiscent porous silicon, Microelectronics Engineering 56, (2001) 303.

[14] Lj Ristic. CMOS technology : A Basu for micromachining, Microelectronics J, 20 (1989) 153.

[15] P.M. Fauchet, J. Von Behreu, K.D. Hirschman, L. Tyseskov, S.P. Duttagupta, Porous Silicon Physics and Device Applications; A status report, Phys. Status Solidi(a) 165 (1998) 3.

[16] Prof. S.K. Lahiri, IIT Khargapur (Private communication).

[17] H. Saha, S. Day, J. Das and S.M. Hossain, Development of a System on chip Integrating Porous Silicon Based humidity Sensor with Porous Silicon based seven segment display, Proc. XIth IFIP VLSI, SOC 2001.

[18] G.S. Chung, S. Kawahito, M. Ashiki, M. Ishida and T. Nakamura, Novel High Performance Pressure Sensors Using Double SOI Structure, Tech. Digest, Transducers'91, San Fransisco, (1991) p.676.

[19] A. Haberli, O. Paul, P. Malcovati, M. Faccio, F. Malobem and H. Baltes, CMOS integration of a Thermal Pressure Sensor System, IEEE (1996).

[20] Design, Fabrication and Testing of Porous Silicon based Integrated Smart Temperature and Pressure Sensor, - STC/IIT KGP Project, 2001.

[21] Z.M. Rittersma, W.J. Zaagman, M. Zetstra and W. Bencke, A monitoring instrument with capacitive porous silicon humidity sensors – Smart Mater. Structure 9 (2000) 351.

[22] C. Baratto et.al., A novel porous silicon sensor for detection of sub-ppm NO_2 concentration, - Sensors and Actuators B77 (2001), p. 62.

[23] T. Taliercio et.al., Porous Silicon membrane for gas sensor applications, Sensors and Actuators, A 46-47 (1995) 43.

[24] H. Lüth, M. Thust, A. Steffen, P. Kordis and M.J. Schönig, Biochemical Sensors with structured and porous silicon capacitors, Materials Science and Engineering B 69-70 (2000) p.104.

[25] T. Kalinowski, Z.M. Rittersma, W. Benecka and J. Binder, An advanced micromachined fermentation monitoring device, Sensors and Actuators B68 (2000) 281.

[26] J.F.L. Goosen, D. Tanase and P.M. Sarro, Miniaturisation of Sensors and Actuators for applications in Catheters, TU Delft/DIOC 9.

Development of System on Chip (SOC) Based on a Porous Silicon Humidity Sensor

H. Saha, S. Dey and J. Das.
IC Design and Fabrication Centre, Dept of ETCE
Jadavpur University, Kolkata 700 032, India
email: hsaha@vsnl.net

Abstract

Silicon based sensors ushered in the concept of smart sensors in which the sensing element and its signal conditioning part can both be integrated into a single device. Porous Silicon (PS), because of its large surface to area volume ratio (>500m^2 / cm^3), can be used as an efficient sensing element and PS based humidity sensors have been in limelight for quite some time now and some even have achieved near term commercial versions[1,2]. However smart humidity sensors that include both the PS based sensing element and the signal conditioning part integrated in a single chip is yet to be developed. We have not only designed the integrated sensor but also extended the design to the concept of a System on Chip (SOC) that integrates the sensor and its signal conditioning with a Porous Silicon based seven segment display and the associated display driver decoder latch circuit on the same device. The SOC may also include a simple microactuator unit for a specific control purpose or may contain a dedicated processor to implement sophisticated control algorithm.

INTRODUCTION

Porous Silicon is an excellent material for use as humidity sensor and vapour sensors, Pressure and Temperature sensor , Gas Sensors and Bio-sensors. Porous Silicon fabricated is compatible to standard CMOS technology and thus SMART Sensors integrating Porous Silicon with the CMOS signal processing unit is potentially attractive. For integration models of Porous Silicon needs to be developed both for sensor transducer application and also for electroluminiscent seven segment display and appropriate libraries formed so as to use VLSI CAD tools for design and development. ASIC Design and fabrication of a complete system on chip with Porous silicon as sensor CMOS silicon as signal processing and Porous silicon as seven segment display is an exciting and challenging activity in the field of recent VLSI design. We shall discuss the design of such a SOC (fig 1) in following sections.

FABRICATION OF POROUS SILICON HUMIDITY SENSOR

The device structure of Porous Silicon humidity sensor developed in this work has a membrane structure as shown in fig 2. The membrane structure has been realized using PS sacrificial layer. The PS absorbing layer was formed on the top surface by usual anodic etching method. Both contacts were taken from the top PS layer.

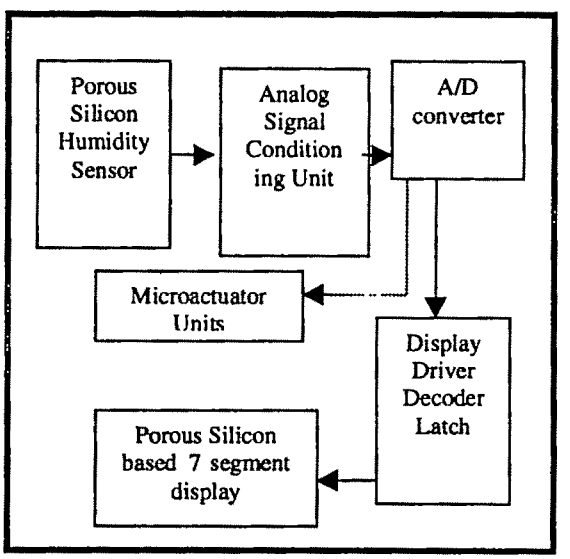

Figure 1 Block diagram of the system on chip

We chose the membrane structure rather than the sandwich structure, where one contact has been taken from the top PS layer and another from the bulk Silicon at the bottom[3]. Contacts on the top surface were formed by vacuum evaporation of a suitable metal and its subsequent annealing. The micro heater at the back side for resetting the device was also formed by vacuum evaporation technique of thin metal on the back of the membrane after sacrifice of the PS- layer through a patterned shadow mask.

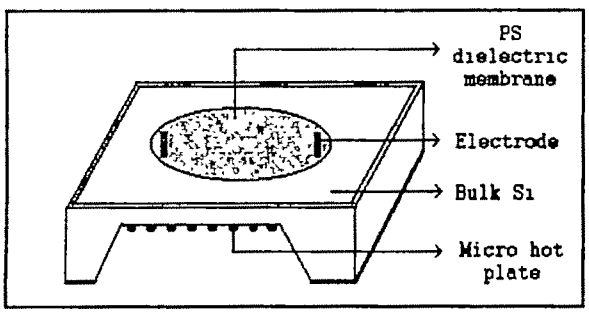

Fig 2. Basic Structure of the Humidity Sensor based on Porous Silicon dielectric membrane

SENSING PRINCIPLE OF THE POROUS SILICON HUMIDITY SENSOR

The Porous Silicon layer undergoes a change in its dielectric constant when exposed to humid ambient owing to adsorption of water vapour molecules in its micropores. When PS is exposed to humid ambient the pores get soaked with water vapour as vapour molecules diffuse in the pores until an equilibrium moisture content (EMC) inside the porous dielectric is reached. Water vapour condenses in all pores having radii less than Kelvin radius. The response time of the sensor is dependent on EMC which in turn depends upon the relative humidity(RH) and the pore radius distribution (morphology) of the PS layer. The effective dielectric constant of the PS-layer under this condition can be shown to change with relative humidity through φ_w , the volume fraction of pores filled with condensed water vapour in porous dielectric with pore radii less than Kelvin radii[4].

MEASUREMENT SCHEME : SIGNAL CONDITIONING UNIT FOR THE SENSOR

When PS layer is exposed to humid ambient water vapour is adsorbed on its surface and partly condensed inside the pores resulting in change of effective dielectric constant and hence the capacitance of the PS sensing layer. Thus the humidity can be measured by measuring the change in capacitance of the PS layer. Instead of earlier methods that used simple relaxation oscillator whose frequency measured depended on the capacitance of the PS layer we shall approach a novel phase detection technique. In this technique we shall measure the phase changed suffered by a sinusoidal signal when passed through the PS sensor . The phase change depends on the change in the capacitance of the porous layer and hence can measure the Relative humidity. The frequency detection approach used earlier necessitated that the sensor be ultimately interfaced to a micro-controller for proper calibration and linearity compensation. This approach necessarily leads to a hybrid sensor. The phase detection technique used by us however does not use any interfacing external circuitry and moreover it incorporates the linearity compensations and calibration techniques within the signal conditioning unit itself using techniques discussed later. Thus this leads to the concept of smart sensors in which the ASIC for the sensor signal conditioning and the Sensor device are all incorporated in a single Si wafer.

Refer to the block diagram (fig3) showing the basic scheme of the phase detecting signal processing circuit. The basic principle is that since Porous Silicon can be looked upon as a distributed RC network, where capacitance (C) of the PS is a function of the ambient humidity. Thus when a signal passes through the PS sample it suffers phase shift and attenuation depending on the values of its equivalent RC network which in turn depends upon the ambient humidity. The phase shift imparted upon the signal is a measure of the humidity. The parasitic components are usually much less sensitive to changes in relative humidity. These may dominate the equivalent lumped resistance and capacitance and thus reduce significantly the sensitivity of PS humidity sensor depending upon the choice of applied frequency of measurement. At low frequency range the lumped capacitance truly represents the active capacitance of the PS sensing device. Also relative changes of conductance at low frequency is negligible.

As shown in the block diagram (fig 3) we have first designed the signal conditioning unit as a separate discrete signal processing unit and measuring circuit. It contains a signal generator IC(ICL 8038) that generates a sinusoidal signal (5V, 625Hz) and a square wave in quadrature to the sine wave. The sinusoidal signal is amplified and then passed through the Porous Silicon sample which having a capacitive part of its impedance imparts a phase shift to the original signal. The phase shifted sine wave (after passing through PS is also rendered degraded and hence needs to be amplified) is now amplified and converted to a corresponding square wave using a sine to square wave generator which is in phase with it. The phase of this phase-shifted square wave is then compared with the phase of the

initially generated square wave, which is quadrature to the generated sinusoidal signal. Since, the PS layer is basically a distributed RC network, the sinusoidal signal will suffer a phase change less than 90° because of the resistive part, and hence it will not be in phase with the quadrature component. The difference in phase between these two square waves will thus be a measure of the capacitance of the sample.

The phase-shifted sine wave is then converted to a square wave by a comparator. The phase difference between the generated quadrature component square wave and the phase shifted (by the PS layer capacitor) square wave (converted from the phase-shifted sine wave) is detected by a conventional XOR gate (74LS136). A first order low pass Butterworth filter is used for the filtration of spurious high frequency signal from the circuit elements. The pulse width of the XOR gate output is dependent on the phase difference of the two square waves and hence depends upon the impedance of the sample and thereby the humidity. The output pulse width from the XOR gate is thus converted to a corresponding DC voltage. The filtered average DC output voltage is now properly scaled, zero and span adjusted and multiplexed using three different IC 324 chips before feeding it to an auto ranging circuit using LM339 chips for improving linearity

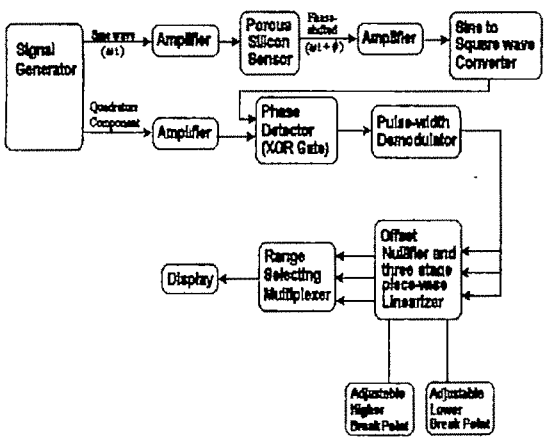

Fig 3 Schematic block diagram of the signal conditioning unit

The final output voltage can be digitized using an ADC for digital display and other interfaces. The auto ranging arrangement has been introduced to take care of the piece wise linearity of the response. The humidity response of our PS based humidity sensor was recorded by interfacing the output voltage of the signal conditioning part to a PC through a data acquisition module (ADAM 4017) and RS 485 interface for a wide range (15% to 95%) of relative humidity (Fig 4). We have measured different sensor parameters. Resolution and accuracy of the sensor are quite good. We have divided the entire range of the RH into three parts low (0-45%), medium (45%-75%) and high (75%-100%) respectively (fig 5)

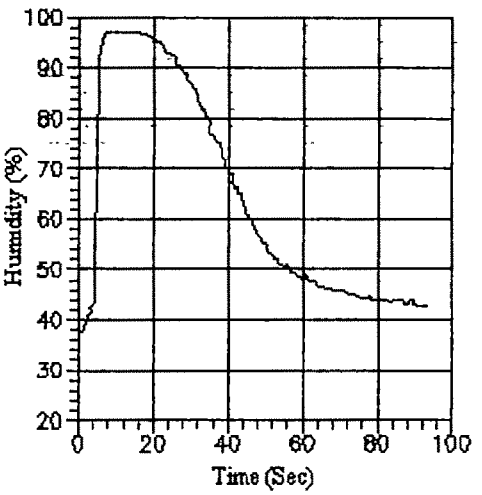

Fig 4. Response Time Characteristics of the Sensor

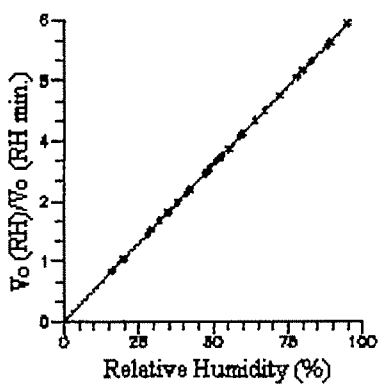

Fig 5.Linearized output from the signal conditioning unit

Accuracy near the transition region is ~2%, but otherwise it is better than 0.1%. We have provided the provision for complete compensation of the offset. Table 1 shows the various sensor parameters measured.

- Resolution : Better than 0.1%
- Accuracy 2%(Transition region of the piecewise regions), better than 0.1% (otherwise)
- Offset – 2V(Provision for complete compensation of offset)
- Dynamic Range: form minimum 15% to a maximum 98%RH.

Table 1 Different Sensor Parameters

INTEGRATION FOR SMART CHIP : ASIC DESIGN FOR SIGNAL CONDITIONING

The signal conditioning circuit using discrete IC chips by which the humidity is sensed has been discussed in the preceding sections. The same methodology will be used to design the ASIC for the signal conditioning circuit for the sensor. The main advantage of PS sensor is that, its signal conditioning circuit can be integrated with the sensor itself on the same chip so that the signal from the sensor device can be directly interfaced with a microactuator units or a display thereby giving a smart sensor.

In order to achieve the signal conditioning the Analog design for it has been done at the CMOS gate level using suitable VLSI CAD tools (TANNER TOOLS, T-SPICE, S-EDIT, L-EDIT). All these have been designed in the basic CMOS level. Central to the design of the signal conditioning circuit is the design of an operational amplifier. We have used for our purposes designed a basic two stage CMOS operational amplifier having the specifications shown in Table2.

Ao =55dB	GB= 4.5MHz	CMRR = 52dB
$\phi_{PHASE} = 60^0$	$I_{ss} = 25\mu A$	$C_C = 4pF$
$V_{DD} = 5V$	P = 0.25W	SR = 6V/μs

Table 2 : Design specification of OPAMP used for the signal conditioning circuit

We have attempted an alternative approach to designing an operational amplifier that focuses on identifying a minimal design parameter space emphasizing relevant design parameters rather than the natural design parameters[5]. A principal requirement needed for the ASIC design of the signal conditioning of the porous Silicon smart humidity sensor is a signal generator that would produce a sine wave and a square wave in quadrature with the sine wave. It is of much importance that the sine wave and square wave generated should be in quadrature to each other and the signal generator has to be designed accordingly. Also, to be kept in mind while designing the circuit, are the frequency requirements as PS shows best sensitivity in low frequency range (<1KHz). The operating frequency of the signal generator should be thus in this range. Keeping in mind the above considerations, a signal generator was designed using CMOS and simulation results were found to conform to the desired specifications. Fig.6 shows the designed CMOS equivalent circuit of the signal generator and Fig.7 shows the simulation results of the designed CMOS equivalent signal generator. One observes the designed phase quadrature between the square wave and the generated quasi sine wave from this simple design. The analog switch of Fig.6 has also been designed using CMOS transmission gates [6].

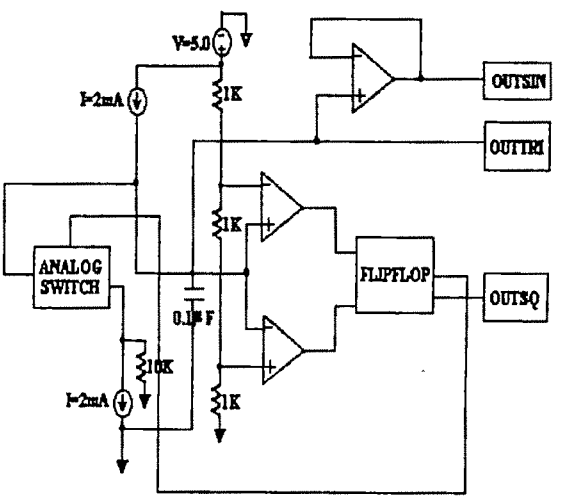

Fig 6. Signal Generator circuit scheme

As discussed earlier, the sinusoid generated is passed through the PS. For the simulation of PS and verification, we have developed a SPICE model of its equivalent capacitance and resistance at a given humidity. The PS model developed is essentially a macromodel the level of abstraction being mainly behavioral wherein the effects of the terminal current and voltages are incorporated based on the experimental results. The SPICE model is then implemented by forming an appropriate DLL. The phase

detector XOR gate is designed using CMOS. The output pulse-width of the XOR gate is dependent on the ambient humidity. Fig.8 shows the simulation results of (i) the designed CMOS sine wave generator, (ii) converted square wave by the designed CMOS comparator, (iii) quadrature square wave from the designed CMOS signal generator and (iv) the phase detected output from the designed CMOS XOR gate. For converting the pulse width from the XOR to a d.c. voltage, the required analog switch and a first order Butter worth active filter are also simulated and the resulting analog voltage varies with the equivalent capacitance and resistance of the PS at different humidity as expected. The experimentally measured resistance, capacitance vs humidity curves for the PS which are previously developed, are used for developing the PS model file for proper simulation.

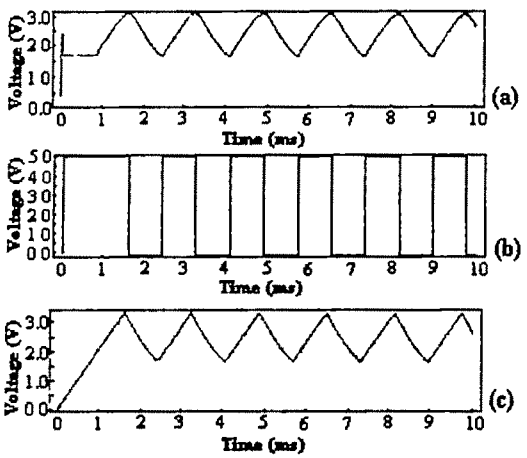

Fig 7. Simulation waveform of the signal generator (a) Sine wave (b) Quadrature Square Wave (c) Triangle Wave

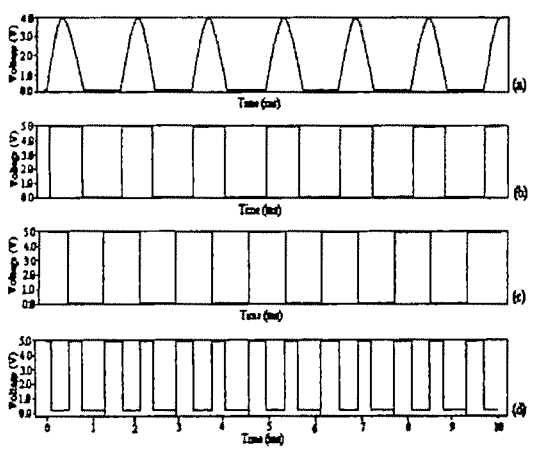

Fig 8. Simulation waveform showing Pulse width (d) depends on humidity

For all the simulation purposes we have used the Level 2 SPICE Models for 1.25μ MCNC CMOS process. The simulation results are found to be in well congruence with the experimental results. The analog voltage will now be digitized using a ADC. We have used a typical Successive Approximation type ADC commonly available. The design approach of the ADC is typical and as already known.

POROUS SILICON SEVEN SEGMENT DISPLAY: FABRICATION AND DISPLAY DRIVER DECODER DESIGN

Porous Silicon shows efficient tunable room temperature light emission at energies much above the silicon band gap.In order to fabricate a Porous Silicon based Seven segment LED we have proceeded in the following way: A p^+ layer is initially formed on the front side of the p-type wafer and then oxidized. It is then followed by masking for the seven segment using black ink. Selective etching of oxide follows and subsequently the ink is stripped keeping p-Si open for diffusion. n^+ layer is then formed by diffusion leading to n^+p^+ doped seven segment portion. Metal back coating is then done by Ag-Al paste and baking it at 110^0C. The front seven segment is now again masked using black ink so that the oxide portion is covered and Porous Silicon layer is formed on the n^+p^+ doped seven segment portion. This leads to a n-type PS and p-type Si junction that increases the quantum efficiency. Silver paste of about 30nm is then deposited for front contact. The contact being thin better luminescence is observed but with thin layer ohmic contact is not obtained so a double layer grid structure and carrier collection contacts are done on the seven segment[7]. The porous Silicon based seven segment display is seen to give stable luminescence and can be used for display.

The display driver decoder circuit is then designed and simulated at the basic CMOS level keeping in mind the particular requirements of the PS display. The design parameters and features of the unit are Latch Storage of Code and direct PS LED driving capability. The unit also has the capability to invert logic levels of the output combination. The circuit contains inverters Transmission gates, Nand Nor and Xnor gates, D-Flip Flop and also output buffer before they are connected to the LED

MICROACTUATORS AND ON-CHIP CONTROLLING OF HUMIDITY

One of the major advantages of the Porous Silicon Sensor is that it allows associated circuitry to be fabricated with it on the same device. Thus designing the ASIC for the microactuator to control the humidity in a process also

allows this unit to be fabricated along with the sensor and display on the same system on chip. Such applications are of much importance in the process industry where humidity serves as an important parameter typically, the Tea processing Industry. In those cases the output from the on-chip microactuators can be directly used to control the valves that open and close to draw in and draw out the humid air (by pumps). The output of the sensor can also be digitized so that programmable controller can be used which would also be on the same chip. For sophisticated controlling we can have a dedicated processor inside the SoC itself which implements the control algorithm(fig 9).

The same SoC can also be used as a humidity transmitter. The analog output voltage corresponding to the humidity from the sensor and further signal conditioning can be converted to a corresponding 4-20mA signal using V-I converters.

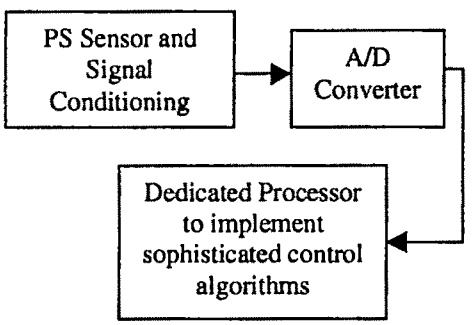

Fig 9. On chip control of humidity

CONCLUSION

A complete SOC integrating a PS based humidity sensor, mixed CMOS signal processing circuit and porous silicon based seven segment display has been proposed and designed using VLSI CAD tools. The porous Silicon based sensor the signal processing unit and the PS seven segment display has been discretely fabricated and tested successfully. The SOC we have so far discussed still needs a lot of improvement and improvisations . The layout and the physical design of the SOC is yet to be developed by us and issues related to the mixed signal design needs to be addressed. The floor planning of the sensor and the seven segment display is also to be designed. For layout of the Porous Silicon layer we need to associate the layout CAD files with appropriate DLLs so that the mask is appropriately formed. This has been a challenging job and we have designed the SOC with success and obtained results that are quite satisfactory but we still understand that it is only the beginning.

REFERENCES

1. Z.M. Rittersma, A. Splinter, A. Bdecker, W. Benecke, "A novel surface micromachined capacitive porous silicon humidity sensor" Sensors and Actuators B 68 (2000) 210-217.

2. G.M. O'Halloran, J. Groeneweg, P.M. Sarro and P.J. French, "Porous silicon membrane for humidity sensing applications " Proc. Eurosensors XII, 1998, 901-904.

3. J. Das, S.M. Hossain, S. Chakraborty, H. Saha, Role of parasitics in humidity sensing by porous silicon" Sensors and Actuators A (2001) (to be published).

4. Z.M. Rittersma and W. Benecke, "A humidity sensor featuring a porous silicon capacitor with an integrated refresh resistor" Sensors and Materials, 12 (1) (2000) 35-55.

5. Y. Chen, M.E. Schlarmann and R.L. Geiger "An improved design formulation for design and optimization of operational amplifiers" http//www.grove.ee.iastate.edu/docs/Papers/1999 0800.pdf.

6. H.Saha, J.Das, S.Dey, A.Bagchi, "Development of a Smart Humidity Sensor based on Porous Silicon", Frontiers of VLSI Design and Test., Proc. of VLSI Design and Test Wirkshops, August 16-18, 2001, pp233-238, Phoenix Publishing House, 2001

7. S.M. Hossain, S. Chakraborty, S.K. Dutta, H. Saha, "Metal patterning for large area electroluminescent porous silicon" Microelectronic Engineering (2001) (to be published).

Effects Of Structural Parameters On Threshold Current Density In VCSEL

M.C.Shrivastava[+] and B.D.Shinde[++]
[+]Dept. of Electronics and Instrumentation
Shri Govindram Sexaria Institute of Technology And Science, 23, Park Road, Indore-3.India
mcshrivastava@hotmail.com
[++]Dept. of Electronics, All India Shri Shivaji Memorial Society's College of Engineering,
Near R. T. O., Kennedy Road, Pune-1, India
bdshinde@hotmail.com

Abstract

A theoretical study has been made for the VCSEL device fabricated on GaAs and GaAlAs substrates by MOCVD. The threshold current density mainly depends on its structural parameter and carrier life time. The threshold current density Vs device diameter is evaluated and also threshold current density Vs number of wells has been plotted for given well thickness and the effects of above parameter on threshold current density has been studied. Comparison of VCSEL on two substrate shows that GaAlAs VCSEL is having low threshold current density has been studied. Comparison of VCSEL on two substrates shows that GaAlAs VCSEL is having low threshold current density of about 0.75 KA/cm^2 at diameter of 20μ m Material and design optimization is possible by such studies.

INTRODUCTION

VCSEL offers many advantages over their counter parts i.e. conventional edge emitted laser. They have circular output beams, low threshold current and operating voltages, high output power and high output speeds [1,2]. They are promising devices for parallel optical connections and processing.. Beside these advantages, they can be easily formed as laser arrays (VCSLA) [3] as a two-dimensional light source for optical parallel communication [2].

As reported in literatures these VCSEL's are fabricated on both GaAs and AlGaAs substrates using MOVCD [4]. There have been several reports on the threshold current density to keep it as low as possible at room temperature. In present work we have taken the model reported in literature [1,3] and modified considering the same average reflectivity of 0.996 for both substrates and the result are plotted in Fig. 1 & 2. If the crystalline quality of MOVCD is not same for two substrates then the threshold current density depends on surface recombination velocity Fig. 1. shows that the values of N_{well} and d should be optimized to keep threshold density at minimum [6].

THEORETICAL ANALYSIS AND MODELLING

As reported in literatures [2,3] relation for threshold density, J_{th} is given by,

$$J_{th} = N_{well}\, d\, n_{th}\, q\left[\frac{4s}{D} + \frac{1}{r}\right] \qquad (1)$$

where J_{th} is threshold current density, N_{well} is the number of wells, d is the well thickness, n the device diameter, S is the surface recombination velocity and r is the minority carrier lifetime.

The surface recombination velocity {S} is expressed by [7],

$$S = S_h\, V_{th}\, N_{st} \qquad (2)$$

where S_h is the hole trap, V_{th} is the Thermal Velocity of the carriers, N_{st} is the number of surface trapping centers per unit area at boundaries. Assigning the values to the variables from the curves and available data from literatures, we can obtain the threshold current density as low as 1.88923 KA/cm^2 for the threshold current of 6.5 mA

and voltage of about 2.5 V and surface recombination velocity of 2 cm/s for r = 2 nsec.

RESULTS AND DISCUSSIONS

The above computations indicates how the J_{th} varies with structural parameter after selection of material as well as it can be affected by surface recombination velocity. Fig. 1 shows the threshold current density versus number of wells(N_{well}) for given well thickness (d). The plot indicates that J_{th} varies almost linearly with both parameters. Fig. 2 shows the theoretical evaluation of Jth versus device diameter for two different substrates. It is seen from the figure that verification in both the cases is similar and this shows that the device characteristics deviated to a smaller value in GaAlAs material.

CONCLUSION

The results will indicate that optimization is required on structural parameters for keeping the threshold current density at minimum which also limits the pixel diameter to 20 to 21 , which will helpful for formulation of laser arrays dimensions. It has also been shown that the MOCVD provides good crystalline quality.

REFERENCES

1. R.S.Goel, B. L. Thibeault, S. W. Corzine, J.W..Scott and L.A. Coldern, "Design and characterization of $In_{0.2}Ga_{0.8}As$ MQW vertical cavity surface emitting lasers" IEEE Trans. Quant. Elec. Vol 29, No 12, Dec 1993
2. T. Tadokoro, H. Okamoto, Y. Kohama, T. Kawakami and T. Kurukawa, "Room temperature pulsed operation of 1.5 micron GAInP / InP vertical cavity surface emitting lasers", IEEE Photonics. Tech. Lett. Vol 4, No 5, May 1992
3. Y. Oshiso, Y. Kohama, S. Fukushima and T. Kurokawa, "8 independently addressable vertical cavity surface emitting laser diode arrays grown by MOVCD," IEEE Photonics. Tech. Lett. Vol 6, No 8, Aug 1994
4. Y. Oshiso, Y. Kohama and T. Kurukawa, "0.85 vertical cavity surface emitting laser array grown on GaAs / AlGaAs substrate by MOCDV" Jpn. J. Appl. Phys. Vol 34, No 11, Nov 1995
5. S. F. Yu,"Analysis and design of vertical cavity surface emitting lasers for self-sustained pulsation operations", IEEE Trans, Quant. Elect., Vol 34, No 3, March 1998
6. M. C. srivastava, A. E. Wagh," Effect of carrier density, well width and well number on threshold current density for InGaAs / gaAs strained QW laser", IE(I) J. -ET, Vol 79, March 1999
7. K. D. Choquett et. Al. "GaAs vertical cavity surface emitting lasers fabricated by reactive ion etching" IEEE Photon. Tech Lett., Vol 3, No 10, 1991

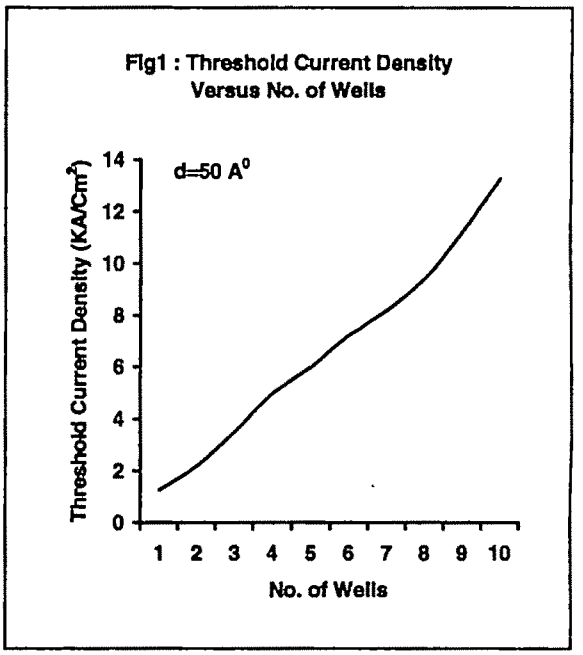

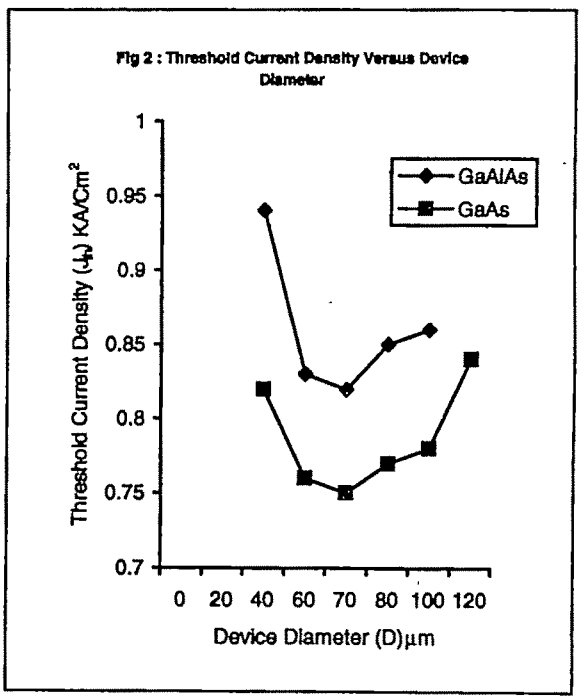

Optical Feedback Noise Reduction In Vertical Cavity Surface Emitting Lasers (VCSEL) Using Diffused Quantum Well Structure

M. C. Shrivastava[1] and B. D. Shinde[2]

[1]Dept of Electronics and Instrumentation, Sri Govindram Sexaria Institute of Technology and Science
23 Park Road, Indore 3, India

[2]Dept of Electronics, All India Shri Shivaji Memorial Society's College of Engineering
Kennedy Road, Pune 1, India

Abstract

The use of interdiffused quantum wells to improve the performance of VCSEL is studied theoretically. Self sustained pulsation is found to be enhanced which is very useful in reducing optical feed-back noise. Condition of self-sustained pulsation is obtained by considering band mixing effect

INTRODUCTION

Circular output beam with low divergence, high modulation speed, low threshold current and ease of fabrication in 2D array are the attractive features of vertical cavity surface emitting lasers VCSELs, for the application in optical interconnection, switching and optical computing[1].In order to use VCSELs for such applications it is required to reduce the influence of optical feedback is to employ the phenomenon of self sustained pulsation (SSP) in the VCSEL[3]. In this paper mechanism of SSP in VCSEL have been studied theoretically. In the present model the effect of band mixing due to impurity induced compositional disorder of quantum well of active region have been considered. Diffused quantum well (DFQW) in VCSEL have been proposed for high power, single longitudinal mode operation.

THEORETICAL MODEL

In order to analyze the performance of VCSELs the optical gain and refractive index of diffused quantum well under external carrier Injections are modeled by the k.p method[4]. The DFQW is approximated by an error function and the extent of interdiffusion is characterised by a diffusion length Ld. The optical gain G_λ, at a particular wavelength λ and L_d is calculated [3].

$$G(\lambda) = a(\lambda) \log (N/N_0) \quad (1)$$

$$\Delta n_r(\lambda) = d(\lambda) \log (N/N_r) \quad (2)$$

The condition of SSP is obtained by considering band mixing effect.

$$\eta = (G_{co} - G_{cl}) \frac{\partial \Gamma}{\partial N} +$$

$$\left[\Gamma_{co} \frac{\partial \sigma_{co}}{\partial N_{co}} - \frac{\sigma_{cl}}{\sigma_{co}} \Gamma_{cl} \frac{\partial \sigma_{cl}}{\partial N_{cl}} \right] - \frac{\partial \alpha}{\partial N} < 0 \quad (3)$$

Subscript co and cl stands for core and cladding region of the VCSEL. G and $\partial G/\partial N$ are equivalent optical gain and differential gain. N, Γ and α, carrier concentration, optical confinement factor and cavity loss respectively. $\partial\alpha/\partial N$ is equivalent differential cavity loss.

Calculated result of SSP instability condition is shown in Fig. 1 for five different values of L_d, $L_d = 0$ A $L_d = 5$ A, $L_d = 10$A, $L_d = 15$A, and $L_d = 20$A.

CONCLUSION

Use of DFQW structures in VCSEL to generate SSP is the precise control of overlap volume between the gain-absorber regions and lazing mode. However, controllability of using diffusion is limited by the precise diffusion well,

this requires precise variation in L_d which is practically not so easy. Therefore, with careful control of implantation energy and time of annealing, the desired performance can be obtained.

ACKNOWLEDGEMENT

The authors would like to thank to Dr. P.H. Waghodekar, Dr. A.E. Wagh and Dr. S.F. Yu (Hong Kong) for their encouragement through out this work as well as authors whose references have been cited.

REFERENCES

1. R.S. Geels, B.J. Thibeault, S.W. Corzine, J.W. Scott and L.A. Coldren. "Design and characterization of $In_{0.2}Ga_{0.8}As$ MQW vertical cavity surface emitting lasers", IEEE Journal of Quantum Electronics, Vol. 29, No. 12 Dec 1993.
2. K.P. Ho, J.D.Walker and J.M. Kahn, "External optical feedback effects on intensity noise of vertical cavity surface emitting lasers", IEEE Photon. Technol. Lett.,Vol. 5, 1993.
3. S.F.Yu, "Analysis and design of vertical-cavity surface- emitting lasers for self-sustained pulsation operation", IEEE Journal of Quantum Electronics, Vol. 34, No. 3, March 1998.
4. E.H. Li, B.L. Weiss, K.S. Chan and J. Micallef, "The polarization dependent refractive index of an interdiffusion induced AlGaAs/GaAs Quantum well", Appl. Phys. Lett., Vol. 62, 1992.
5. M. Yuri, J.S. Harris Jr., T. Takayama, O. Imafuji, H. Naito, M. Kume, K. Itoh and T. Baba, "Two dimensional analysis of self-sustained pulsation for narrow-stripe AlGaAs lasers", IEEE J. Select. Topics Quantum Electron., Vol. 1, 1995.
6. M. Yamada, "A theoretical analysis of self-sustained pulsation phenomena in narrow stripe semiconductor laser", IEEE J. Quantum Electron., Vol. 29, 1993.
7. S.F. Yu and E.H. Li, "Influence of lateral field on the relaxation oscillation frequency of semiconductor lasers", IEEE J. Quantum Electron., Vol. 32, 1996.

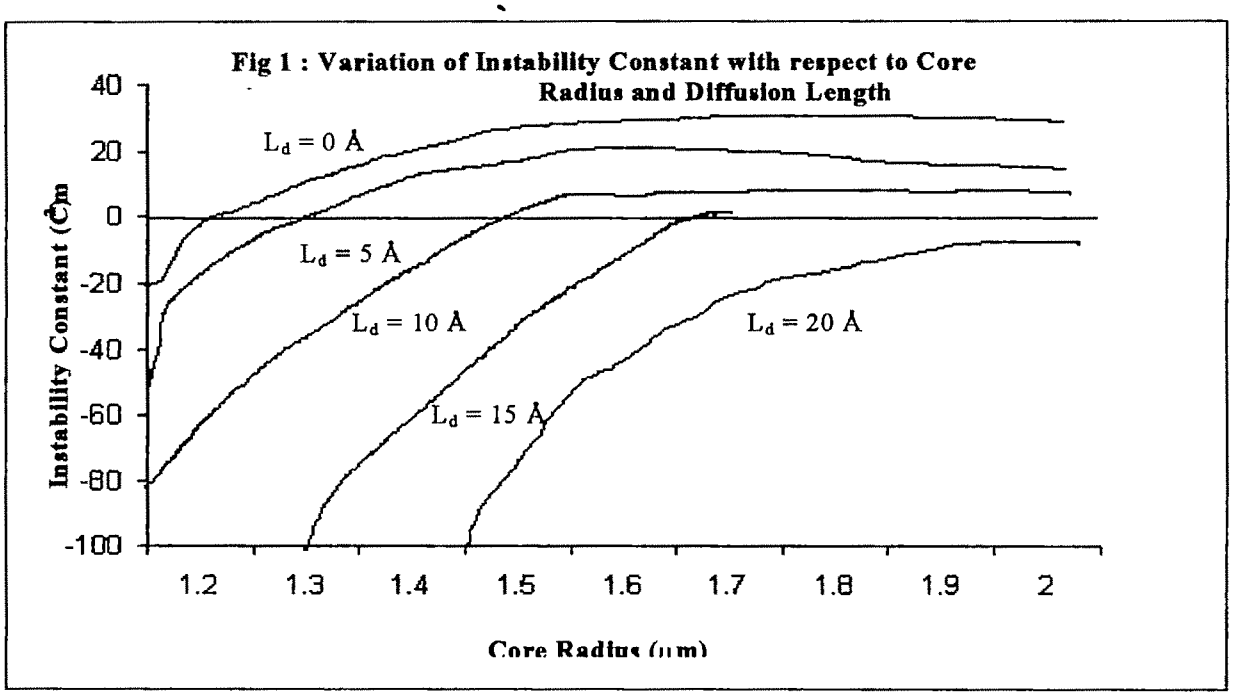

Wavelength Shift Evaluation In Fiber Bragg Grating For Strain Measurement

Y. K. Jain and Sanjeev Jain
Department of Electronics Engg
Samrat Ashok Tech. Institute, Vidisha (M.P.) 464 001, India.
E mail dr_sanjeevjain@hotmail.com

Abstract

Fiber Bragg grating (FBG) have been studied as optical sensors for different applications. They can be used for performing mechanical sensing, as we can obtain a relationship for direct transformation of the sensed parameter to a shift in reflected wavelength independent of the factors, which are responsible for distortion. The FBG used as strain sensor with a passive wavelength demodulation system facilitates the measurement of static longitudinal strain and dynamic longitudinal strain. The complete relationship for the strain versus wavelength variations due to the applied strain have been studied and a linear relationship has been obtained. This relationship has also been extended for tensile strain and compressive strain.

INTRODUCTION

The use of Fiber Bragg Grating (FBGs) is gaining popularity as an emerging technology in the telecommunication and instrumentation industry in the last few years as Optical fiber sensors [5] is due to its widespread applications. Fiber Bragg grating have been studied as an optical sensors for a variety of mechanical sensing applications, including condition monitoring of civil structures such as highways, bridges, buildings and dames; smart manufacturing and nondestructive testing of materials, remote sensing applications in oil reservoirs, and space stations; smart structures such as air plane wings, ship hulls, buildings.[6]The main advantages of FBGs for mechanical sensing is that they perform a direct transformation of the sensed parameter to a shift in reflected wavelength, independent of light level, connector or fiber losses or, operating at a different wavelength. It also provides potential for highly multiplexed operations. FBGs has a narrow bandwidth as compared to resistive foil strain gauges and can operate over a broad wavelength range that can be highly multiplexed i.e. allowing many of them to be used on a single fiber. Such gratings are small enough to be embedded or laminated. Because they are totally passive so there is no resistive heating. They are also non conductive, thus immune to electromagnetic interference. So in this paper we have studied the wavelength shift.

WAVELENGTH MEASUREMENT SYSTEM

Initially a non-reference FBG interrogation system is used for measurement of reflected wavelength. The major problems with this non referenced FBG interrogation set up include non linear response due to filter drift and stability from thermal coefficients of filters and other components, and the overall wavelength measurement involved in accuracy of several nanometers (several thousand times the resolution). Hence, to realize the potential of FBGs for mechanical sensing, a multi-wavelength – referenced FBG interrogation system has been used for rapid and accurate measurement of multiple FBG reflected wavelength. Use of these models has suggested that FBGs are very much suitable for strain sensor. These sensors are very much sensitive and accurate, gives precise results over conventional sensors.

The Grating on an photosensitive [4] germano-silicate optical fiber, which has been used in this work is made by exposing the fiber to an interference pattern of coherence two- beam ultraviolet (UV) light [8] [9]. As it provide us a means of measurement of strain by relating the shift in Bragg wavelength of the sensing region. The refractive index of the fiber is permanently raised by exposure to UV light, so that the fringe pattern is transformed into a refractive index pattern.

Fig.1 shows the grating written on the photosensitive optical fibers.

Characteristics of FBG : A fiber Bragg grating consists of a periodic stack of regions of higher and lower refractive index along an optical fiber. The center reflected wavelength on a grating is given by

Center reflected wavelength =
(2 x Period of grating) x Fiber refractive index

Three parameters that characterize the FBG are (a) Strength (b) Period (c) Length. The first two parameters can actually be made to vary along the grating and is done by selecting the appropriate grating profiles for these two parameters to suit to the different applications. The third, length of fiber Bragg grating is constrained by the size of the fabrication, which is normally limited to a few centimeters. This also limits, reflection bandwidth of the grating response. Because the reflection bandwidth of an grating is inversely proportional to its length.

As the periodic index modulation develops in the fiber core, a narrow peak appears in the transmission (reflection) spectrum. The center of the peak, occurs at the predicted Bragg Wavelength given by

$$\lambda_B = 2n \Lambda$$

where

Λ= Grating period
n = Effective refractive index

MODELLING OF FBG AS STRAIN SENSOR

Fiber Bragg grating is an excellent fiber optic sensing transducer element. Measurement of any physical quantity, which alters the optical constant of the fiber, can be measured by monitoring certain characteristics of the grating. Shift in grating wavelength may be used to sense the strain, strain affects the Bragg response directly through the expansion or contraction of the grating elements and through the strain optic effect. The fiber grating can be generic transducer element for any sensor types. The detectability of the Bragg response shift can be quite sensitive, using a wavelength demodulation technique.

The UV illumination method used to produce Bragg grating sensor as it allows the fiber to retain much of its intrinsically high compressive and tensile strain, if recoated properly after fabrication. Proper measurement of strain requires the accurate measurement of the Bragg grating center wavelength, and the ability to track rapid shifts in that wavelength i.e. ability of the system to track rapid shifts in the wavelength due to change in strain. With these sensors, recovery of signal information is accomplished by using optical instrumentation to detect, strain induced (changed) wavelength change of the FBG element. FBG elements used have been surface attached to provide direct measurement of strain by using the fiber laser strain sensor (FLSS) system [1] [7].

A remotely located sensing Bragg grating determines the wavelength of the fiber laser. In this measurement system, the Bragg grating wavelength is chosen to lie near the center of the fluorescent spectrum of an erbium-doped fiber, and forming one of the laser cavity end reflectors. This source / sensor combination provides improved interrogation efficiently increasing the signal to noise characteristics of the system. The integration of the Bragg grating tuned fiber laser with a passing wavelength demodulation system (WDS) [2] provides a practical, interrupt immune strain sensor system for the measurement of both static and dynamic strains.

MATHEMATICAL MODELLING OF STRAIN SENSOR SYSTEM

The basis for selective reflection of certain wavelength can be understood by referring to figure 2, which illustrates the reflection of an incident plane waves by a series of reflectors placed at distance d.In the case of X-ray diffraction that was considered by Bragg, these reflectors were the atomic planes of a crystalline lattice. However, the same effect is observed in the case of reflection from a corrugated grating formed. It is obvious that in order to maintain the coherence of plane wave-front (normal to the rays shown) and thereby avoid destructive interference, the path lengths for reflections from successive reflectors must differs by an integral number of full wavelength. So by geometrical consideration:

$$n\lambda = 2\, d \sin\theta$$

This is Bragg condition for grating.
where,
θ = Angle formed by the incident ray and the reflector
n = 1,2,3,4,5 - - - - - - (Integral number)
λ = Optical wavelength in medium
d = Spacing (i.e. period of grating)

To adopt the relation to the case of 180° reflection by grating, it is necessary that d equals to the grating spacing $\Lambda$and λ equals λ_B / n_{eff} , where n_{eff} is the effective index in the waveguide for the mode under consideration and θ = 90°. Then

$2\Lambda \sin 90° = n (\lambda_B / n_{eff})$
or

$2\Lambda = n (\lambda_B / n_{eff})$

The refractive index gets change as the strain is produced by an acoustic wave. As there is a change in the refractive index of the medium caused by the mechanical strain produced by an acoustic wave. As the strain varies periodically with the acoustic waves, the refractive index of the medium also varies periodically leading to a refractive index grating. When a light beam is incident on such a refractive index grating, diffraction takes place and this produce either multiple order diffraction or only single order diffraction. In the case of Bragg diffraction, only single mode is available i.e. n = 1.
Hence

$2\Lambda = (\lambda_B / n_{eff})$

The Bragg wavelength of a photo induced grating is expressed as

$$\lambda_B = 2 . n_{eff} . \Lambda \qquad (1)$$

where

λ_B = Bragg wavelength
n_{eff} = Effective refractive index of grating
Λ = Grating period.

The effective index of grating includes the refractive index of core (n_c) , and refractive index of cladding layer (n_{cl}). The effective refractive index increases since n_c and n_{cl} increases with strain.

So for an applied strain (ε), we have defined a change in Bragg wavelength as,

$$d\lambda_B/d\varepsilon = 2\, n_{eff} (d\Lambda/d\varepsilon) + 2\Lambda (dn_{eff}/ d\varepsilon) \qquad (2)$$

It can be also written as,

$$(1/\lambda_B) (d\lambda_B/d\varepsilon) = (1/\Lambda)(d\Lambda/d\varepsilon) + (1/n_{eff})(dn_{eff}/ d\varepsilon) \qquad (3)$$

So the change in Bragg wavelength ($\Delta\lambda_B$) for an applied strain ($\Delta\varepsilon$) is expressed as

$$(\Delta\lambda_B/\lambda_B) = [(1/\Lambda)(d\Lambda/d\varepsilon) + (1/n_{eff}) (dn_{eff}/ d\varepsilon)] \Delta\varepsilon \qquad (4)$$

We have considered n_{eff} and Λ as two analytic functions of strain, and it is possible to find the change in Bragg wavelength ($\Delta\lambda_B$) due to applied strain ($\Delta\varepsilon$) by using Taylor's expansion as

$$\begin{aligned}(\Delta\lambda_B/\lambda_B) = f (n_{eff}, \Lambda) &+ [(1/\Lambda)(d\Lambda/d\varepsilon) \\ &+ (1/n_{eff})(dn_{eff}/d\varepsilon)] (\Delta\varepsilon) \\ &+ [(1/\Lambda) (d^2\Lambda/d\varepsilon^2) \\ &+ (1/n_{eff})(d^2 n_{eff}/d\varepsilon^2)](\Delta\varepsilon)^2 \\ &+ \ldots\ldots\ldots \qquad (5)\end{aligned}$$

From the equation no. (5), it is clearly seen that the change in Bragg wavelength ($\Delta\lambda_B$) increases with increasing strain ($\Delta\varepsilon$). But for a large strain variations, the change in Bragg wavelength with strain is non linear. Hence we do not consider non linear variations. So change in Bragg wavelength can be defined as

$$(\Delta\lambda_B/\lambda_B) = [(1/\Lambda)(d\Lambda/d\varepsilon) + (1/n_{eff})(dn_{eff}/ d\varepsilon)] (\Delta\varepsilon) \qquad (6)$$

The first and second term on right hand side of the equation no. (6) is the change in grating period and change in refractive index of grating with strain change ($\Delta\varepsilon$) respectively. By strain optic tensor matrix solution, the photo-elastically induced change in refractive index of grating by applied strain ($\Delta\varepsilon$) (for longitudinal strain only) is,

$$(1/n_{eff})(dn_{eff}/ d\varepsilon) = - n^2_{core} / 2 [p_{12} - \nu(p_{11} + p_{12})] = -P_e \qquad (7)$$

where,

P_e = Effective photo-elastic constant
n_{core} = Refractive index of core
p_{11} & p_{12} = Constants of strain optic tensor
ν = Poisson's ratio

hence,

$$(\Delta\lambda_B/\lambda_B) = (1-P_e) (\Delta\varepsilon) \qquad (8)$$

In the proposed work we have taken a germano-silicate photosensitive fiber, so that

$p_{11} = 0.12$
$p_{11} = 0.27$
$\nu = 0.16$
$n_{core} = 1.46$
λ_B = center Bragg wavelength = 1550 nm.

So that

$P_e = 0.22126$ (for germano-silicate fiber)

Hence,

$(\Delta\lambda_B / \Delta\varepsilon)$ = 1.20 μm/ strain
Strain sensitivity = $(\Delta\lambda_B / \Delta\varepsilon)$ = 1.20 μm/ strain

It clearly exhibits a linear relationship between $\Delta\lambda_B$ and $\Delta\varepsilon$. It means that by the measurement of shift in Bragg wavelength we can obtain the applied strain. The wavelength demodulation system (WDS) is used to measure the wavelength of fiber Bragg grating used as strain sensor and tracked both static and dynamic strain. Since the center Bragg grating is linearly proportional to the longitudinal strain on the grating, so WDS will track the grating wavelength and can measures strain value

Table I

Tensile Strain (micro strain)	Bragg wavelength (nm)
0	1550.0
250	1550.3
500	1550.6
750	1550.9
1000	1551.2
1250	1551.5
1500	1551.8
1750	1552.1
2000	1552.4
2250	1552.7
2500	1553.0

Table II

Compressive Strain (micro strain)	Bragg wavelength (nm)
0	1550.0
-250	1549.7
-500	1549.4
-750	1549.1
-1000	1548.8
-1250	1548.5
-1500	1548.2
-1750	1547.9
-2000	1547.6
-2250	1547.3
-2500	1547.0

RESULTS

The Bragg grating allows the measurement of strain in tensile and compressive direction as shown in table I and II. The plot for the Bragg wavelength for the applied tensile strain and compressive strain is shown in figures 3 and 4 respectively.The plot shows that for tensile strain there is upward shift in Bragg wavelength with the applied strain and for compressive strain there is a downward shift in Bragg wavelength with the applied strain. It is very clearly seen from plots that there is a straight line relationship between applied strain and Bragg wavelength. It means that there is a linear relationship between Bragg wavelength and applied strain for given limits of strain.

CONCLUSION

In the present work, the FBG has been used as strain sensor for the measurement of strain. The fiber optic Bragg grating with passive wavelength demodulation system (WDS) facilitates the measurement of static and dynamic strain. This system provides a compact, rugged and high speed wavelength measurement of wide range of strain. Since the WDS tracked the grating center wavelength and therefore the strain on the cantilever beam, hence the characteristics of WDS will play role in deciding the measurement range and resolution of strain measurement. The many other parameters like pressure, flow, vibration, acoustics, acceleration, and certain chemical effects can also be measured through the interaction with strain on the FBG.

REFERENCES

1. Serge M.Melle, R.M.Measures, " A Bragg grating tuned fiber laser strain sensor system", IEEE photonics technology letters, vol. 5, no. 2, pp. 263-266, 1993.
2. Serge M.Melle, " A passive wavelength demodulation system for guided wave Bragg grating sensors", IEEE photonics technology letters, vol. 4, no. 5, pp. 516-518, 1992.
3. William W. Morey, Gary A. Balland, " Photo induced Bragg grating in optical fibers", Optics and photonics news, pp 8-14, 1994.
4. R.J. Campbell, Kashyap, "The properties and applications of photo sensitive germano-silicate fiber", International journal of optoelectronics, vol. 9, no. 1, pp. 33-57, 1994.
5. Thomas G. Giallorenzi, " Optical fiber sensor technology", IEEE photonics technology letters, vol. 18, no. 4, pp. 626-665, 1992.
6. Gang-Chih Lin, "Thermal performance of metal - clad fiber Bragg grating sensors" IEEE photonics technology letters, vol. 10, no. 3, pp. 406-408, 1998.
7. Faramarz Farahi, " Simultaneous measurement of temperature and strain: Cross-sensitivity considerations", Journal of light wave technology, vol. 8, no. 2, pp. 138-142, 1990.
8. G.Meltz, " Formation of Bragg gratings in optical fibers by a transverse holographic method", Optics letters, vol. 14, no. 15, pp. 823-825, 1989.
9. K.O. Hill, " Bragg gratings fabricated in monomode photosensitive optical fiber by UV exposure through a phase mask", App. Physics letters 62 (10), pp. 1035-1037, 1993.

Fig 1 Refractive index pattern

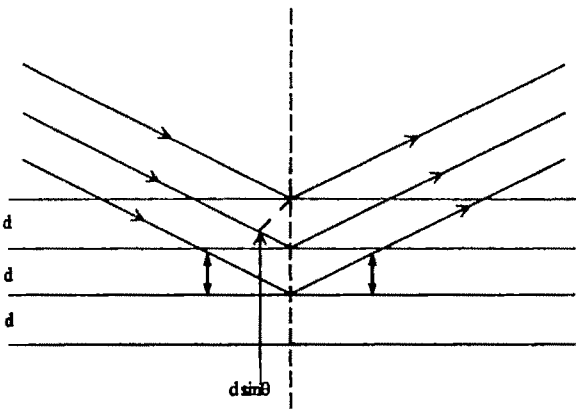

Fig. 2 Bragg reflection form a periodic structure

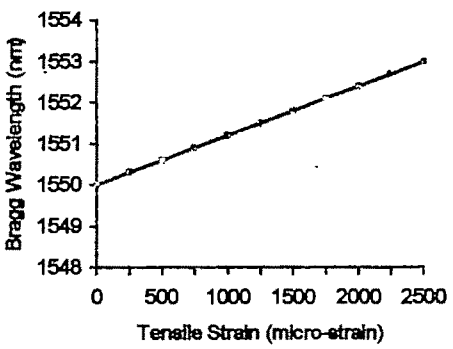

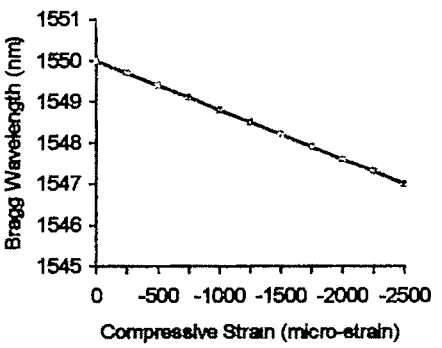

Improvement of Defocusing Error

Dola Roy Chowdhury, Kallol Bhattacharya and A.K.Chakroborty

Department of Applied Physics, Calcutta University
92, Acharya Prafulla Chandra Road, Calcutta-700009, India
E-mail: dolarc33@hotmail.com, dolarc4467@yahoo.co.in

Abstract

The axial irradiance distribution around the image of a point produced by a perfect lens zonally masked by polarizers is theoretically studied. It is observed that the point of maximum intensity of this irradiance distribution is not at the Gaussian focus. The shifted focus thus obtained is called the diffraction focus and this effect is termed as focal shift effect. In the present paper it will be shown that this focal shift can be controlled by changing the parameters of the object beam, or by changing the orientation of the zonal masks or by reorienting the output analyzer. The point spread function (PSF) of this masked lens at the diffraction focus is then compared to the point spread function of an ideal lens. The present study reveals that this polarization-induced focal shift can be fruitfully utilized in improving the defocusing error in critical and demanding situations. It has been shown that for a f/10 system with suitable polarization masking, a polarization induced focal shift of 220 μ m is achievable.

Key words: focal-shift, polarization

INTRODUCTION

Image formation at out-of-focus planes has been the subject of several papers because of interest in the focal-shift effect [1-2]; automatic focussing [3] and increasing the depth of focus [4-7]. In the absence of aberration, the principal maximum of the irradiance distribution lies at the Gaussian focus. Moreover, in the vicinity of the focal plane (a region of practical interest), the irradiance distribution is symmetric about it. But when aberrations are present, this will in general no longer be the case and we may call the point of maximum intensity the diffraction focus. We will refer to this as the *focal shift effect.* The amount of this focal shift depends upon the optical design, the Fresnel number and the f-number of the aperture.

The information gathered by an image-forming instrument is essentially limited by the size of its pupil. With a clear circular pupil of numerical aperture α and a radiation of wavelength λ, the lateral and longitudinal resolutions in the image space are $.61\lambda/\alpha$ and λ/α^2 respectively. It is nevertheless possible to change the imaging properties of the system by using different kinds of pupil mask. Extensive studies have been carried out in this direction [8-12]. The studies reveal that a system's imaging characteristics can be altered considerably by modifying its pupil function. It has also been recognized that the same effect can be achieved suitably oriented polarization masks on the lens aperture. The fact that the response of such a system can be continuously varied by changing the polarizing devices included in the system lends it the enhanced flexibility unobtainable by the use of conventional pupil masks [13-19]. The versatility of the method for modifying the imaging characteristics of the system stems from the fact that the polarization induced phase difference between the light emerging from the masking polarizers can be continuously varied either by changing the state of polarization of the incident beam or by reorienting the polarizers. Since a phase difference is introduced due to the masking, in effect we are deliberately introducing an aberration in the system by the process of masking. As a result there will be a shift of focus from the Gaussian image point. In the present paper we are proposing a masked aperture imaging system, where this shift of focus can be controlled just by changing the input beam parameters or by changing the orientation of the polarizers included in the system. In addition to that the quality of the image formed at the diffraction focus does not

vary considerably from that at the Gaussian focus. For a particular orientation of the output analyzer the depth of focus of the system also increases.

An expression for the intensity PSF of the proposed system with analyzer is derived in the next section. The expression for PSF is used to evaluate the axial intensity distribution for a number of cases. It is followed by some illustrations and the results of a comparative evaluation of images formed at the diffraction focus obtained with different orientations of the analyzer and also with different input beam to that formed at the Gaussian focus.

PROPOSED SYSTEM

As shown in Fig.1, the input to the imaging system under consideration is a polasrizer-quarter waveplate combination (PC), which renders the imaging beam elliptically polarized in general. F and S represent the fast and the slow axis of the compensator. The orientation of the transmission axis of the polarizer P and that of the fast axis of the compensator C with reference abscissa are θ and ϕ respectively. They determine the nature of the vibration ellipse of the elliptically polarized light incident on the mask M. The polarization masked lens aperture consists of two polarization- masked zones: a central circular zone and outer annular zone masked with linear polarizer P(α) and P(β) respectively, where α and β are orientations of the transmission axes of the polarizers with respect to the reference abscissa. This is followed by an analyzer P (γ) before the image plane S.

THEORY

Elliptically polarized light intercepted by the two zones of the polarization mask and emerges, in general, with a phase and relative attenuation between them. In what follows we have derived the expressions for this phase difference and attenuation factors in terms of the polarization parameters of the input beam and the orientations of the zonal masks. From ref [20], it is seen that, for a point source, the expression for the complex amplitude distribution at a point $P(x, y.z)$ near the geometrical focus of an aperture of radius a and of focal length f is given by,

$$U[P(x,y,z)]_0 = Kd^2 \int_0^1 \exp(-i\frac{1}{2}u\rho^2)\, J_0(v\rho)\,\rho d\rho \qquad [1]$$

where, $K = -\frac{2\pi iA}{\lambda f^2} e^{\frac{2\pi ir}{\lambda}}$

ρ is the radial co-ordinate of the pupil plane, A is the amplitude of the incident light, v and u, the reduced radial and axial co-ordinate at the plane of observation are given by,

$$u = \frac{2\pi}{\lambda}\left(\frac{a}{f}\right)^2 z$$
$$v = \frac{2\pi}{\lambda}\left(\frac{a}{f}\right) r = \frac{2\pi}{\lambda}\left(\frac{R}{f}\right)\sqrt{x^2+y^2} \qquad [2]$$

Similarly for an aperture of radius a' where $a' = \varepsilon a$, the amplitude distribution at the point considered is given by,

$$G_2(P) = K\varepsilon^2 d^2 \int_0^1 \exp\left(-i\frac{1}{2}u\rho^2\right) J_0(v\rho)\,\rho d\rho \qquad [3]$$

where,

$$u' = \varepsilon^2 u$$
$$v' = \varepsilon v \qquad [4]$$

As a consequence of Babinet's principle, the amplitude distribution $G_a(P)$ for the outer annular zone is simply the difference between equation [1] and [3], i.e.

$$G_a(P) = Ka^2\left[\begin{array}{l}\int_0^1 \exp\left(-\frac{1}{2}iu\rho^2\right) J_0(v\rho)\,\rho d\rho \\ -\varepsilon^2 \int_0^1 \exp\left(-\frac{1}{2}iu'\rho^2\right) J_0(v'\rho)\,\rho d\rho\end{array}\right] \qquad [5]$$

The term Ka^2, being common to G_c and G_a may henceforth be left out from subsequent analysis.The complex vector amplitude distribution due to the central circular region at the observation plane is given by,

$$Uc' = G_c P(\alpha)\begin{vmatrix} a \\ be^{i\delta} \end{vmatrix} \qquad [6]$$

and that due to the outer annular zone is

$$U_a' = G_a P(\beta)\begin{vmatrix} a \\ be^{i\delta} \end{vmatrix} \qquad [7]$$

where a and b are the two orthogonal components of the elliptical imaging beam subsequent to the polarizer quarter-waveplate combination along the two axes of an arbitrary Cartesian coordinate system and δ is the phase difference between them.

In the presence of an analyzer P(γ) before the image plane, the contribution from the two polarization masked zones are,

$$U_c = P(\gamma)U_c' \qquad [8]$$

and

$$U_a = P(\gamma)U_a' \qquad [9]$$

The intensity PSF in the neighborhood of focus is given by,

$$\left(\frac{2}{u}\right)^2\left[\left(U_1'^2+U_2'^2\right)\left(R_1^2+R_2^2\right.\right.\left.\left.-2R_1R_2\cos(\Delta_1-\Delta_2)\right)\right] +$$

$$\left(\frac{2}{u}\right)^2\left(U_1^2+U_2^2\right)R_2^2$$

$$+\left(\frac{2}{u}\right)^2\left[\begin{Bmatrix}U_1U_1'\cos ux-U_1'U_2\sin ux\\-U_1U_2'\sin ux+U_2U_2'\cos ux\end{Bmatrix}y\right.$$

$$\left.+R_1R_2\sin(\Delta_1-\Delta_2)\begin{Bmatrix}U_1U_1'\sin ux+\\U_1'U_2\cos ux\\-U_1U_2'\cos ux-\\U_2U_2'\sin ux\end{Bmatrix}\right] \qquad [10]$$

$$x=\frac{1-\varepsilon^2}{2}$$

$$y=R_1R_2\cos(\Delta_1-\Delta_2)-R_2^2$$

$$R_1=\cos(\gamma-\alpha)\left[a^2\cos^2\alpha+b^2\sin^2\alpha+ab\sin 2\alpha\cos\delta\right]^{1/2}$$

$$\Delta_1=\tan^{-1}\left(\frac{b\sin\alpha\sin\delta}{a\cos\alpha+b\sin\alpha\cos\delta}\right)$$

$$R_2=\cos(\gamma-\beta)\left[a^2\cos^2\beta+b^2\sin^2\beta+ab\sin 2\beta\cos\delta\right]^{1/2}$$

$$\Delta_2=\tan^{-1}\left(\frac{b\sin\beta\sin\delta}{a\cos\beta+b\sin\beta\cos\delta}\right) \qquad [11]$$

U_1, U_2, U_1' *and* U_2' are the Lommel functions. The eqn. [10] is the expression for the intensity PSF in the neighborhood of focus.

COMPUTATION

Since the shift of focus is associated with the aberration, so by changing the aberration or phase introduced by the mask, this focal-shift can be controlled. This is shown by the axial irradiance curves. The intensity PSF at the shifted focus is compared to that at the Gaussian focus. In some particular cases, the intensity PSF at the shifted focus does not appear to be significantly affected. It is almost similar to that at the Gaussian focus. In fig.2, The axial irradiance distribution for the masked lens is plotted for different values of the input beam parameter δ ($\delta = 0°, 45°, 90°, 135°, 180°$). It is seen that the axial distribution for the masked lens is symmetrical about the focal plane only when the input beam is linearly polarized. For other cases, the axial irradiance becomes asymmetric about the geometrical focal plane. So for this value of δ, the masked lens possesses two foci property. The nature of the intensity PSF at the two foci appears to be similar. It means that the images formed at the two focal planes are identical in all aspects for the particular value of δ. In addition to that the sidelobes are decreased in comparison to an ideal lens. So the shift of focus can be done just by changing the state of polarization of the input beam without touching the aperture itself and in this process the quality of the image is not much affected. In Fig.3, the axial irradiance is plotted for different values of γ ($\gamma = 0°, 30°, 45°, 90°, 135°$). $\gamma = 0°/90°$ lead to the case of either a reduced or an annular aperture. It is found that by reorienting the output analyzer, one can get different amount of focal shifts. For $\gamma = 90°$, the masked lens behaves as an annular aperture. The axial irradiance curve shows there is no focal shift in this case, but the depth of focus of the system increases. The resolution of the system also increases. This is shown in curve C of fig 3a. For $\gamma = 0°$, the system behaves as a reduced aperture. In this case also, the depth of focus of the system increases. This is shown by the curve A of fig 3. When $\gamma = 30°$, the shift is 4.583. The intensity PSF obtained at this point almost coincides with that of the ideal lens. This is shown in curve B of Fig 3a.

CONCLUSION

With a $f/10$ pencil for example ($f/a = 20$) and with light of wavelength $\lambda = 5.10^{-5}$ cm, the maximum focal shift obtained by our system is 0.22mm. This is calculated using eqn [2]. It is to be emphasized that the focal shift is achieved without translating the aperture plane or the image plane. The other attractive feature of our system is that the attainment of the focal shift is not at the cost of the quality of the image.

REFERENCES

1. .Li and E.Wolf, 'Focal shifts in diffracted converging spherical waves' Opt. Commun.39,211-215(1981)
2. Y.Li, 'Dependence of the focal shift on Fresnel number and f number', J.Opt.Soc.Am.72,770(1982)
3. G.Hausler and E.Korner, 'Simple focussing error'Appl.Opt.23, 2468-2471(1984)
4. J.Odeja-Castaneda, L.R.Berriel-Valdos, and E.Montes, 'Line spread function relatively insensitive to defocus'Opt.Lett.8,458(1983)

5. G.Indebetouw and H.Bai, 'Imaging with Fresnel zone pupil masks: extended depth of field' Appl.Opt.23,4299(1984)
6. C.Varamit and G.Indebetouw, 'Imaging properties of defocused partitioned pupils' J.Opt.Soc.Am.A2,799-802(1985)
7. D.A.Holmes, J.E.Korka and P.V.Avizonis, 'Parametric study of apertured focussed Gaussian beams' Appl. Optics11-14(1972) 565
8. P.Jaquinot and B. Roizen-Dossier,'Apodization' in Progress in Optics III, E.Wolf, ed,(North Holland, Amsterdam,1964),29-186
9. T.Asakura and S.Mishina,, "Diffraction by circular apertures with a ring shaped π phase change" Jpn. J.Appl. Phys.9.195-202(1970)
10. T.Asakura and H.Nagai, "Further studies of far field diffraction by modified annular and annulas apertures," Jpn.J.Appl. Phys. 10,879-885(1970)
11. M. .Mino and Y.Okano, "Improvement in the OTF of a defocused optical system through the use of shaded apertures,"Appl.Opt.10, 2219-2225(1971)
12. J.T.McCrickerd." Coherent processing and depth of focus of annular aperturre imagery," Appl. Opt. 10, 2226-2231(1971)
13. Ajay Ghosh, K.Murata and A.K.Chakroborty, "Frequency response characteristics of a perfect lens masked by polarising devices", J.Opt.Soc.Am.A.5, 277-284(1988)
14. K.Bhattacharya, Ajay Ghosh and A.K.Chakroborty," Vector wave imagery with a lens masked by polarisers",J.Mod.Opt.40,379-390(1993)
15. K.Bhattacharya, A.k.Chakroborty and Ajay Ghosh, "Simulation of effects of phase and amplitude coatings on the lens aperture with polarisation masks," J.Opt.Soc.Am.A.2, 586-592(1994)
16. Chakroborty AK, Mukherjee H: 'Modification of PSF by polarisation mask.' J.Opt.(Paris) 9(1978) 251-254
17. Ghosh A, Basu J, Goswami PP, Chakroborty AK, 'Frequency Response characteristic of a Perfect lens Partially masked by a Retarder.' J.Mod. Opt.34 (1978) 281-289
18. Ghosh A, Chakroborty AK, Murata K: 'Imaging characteristics of a perfect lens partially masked by a linear polariser.' Optik 76 (1987) 153-156
19. Datta SN, Ghosh A, Chakroborty AK: 'Imaging characteristics of a lens zonally masked by Polarizers and Retarder' Optik 100(1995)1-7
20. Born M,Wolf E: 'Principles of Optics', 6th ed. Pergamon, Oxford 1985

ACKNOWLEDGEMENT

D.Roy Chowdhury is thankful to the CSIR for the financial support provided to her for this study. The authors gratefully acknowledge the help of Dr. Ajay Ghosh during the course of this research.

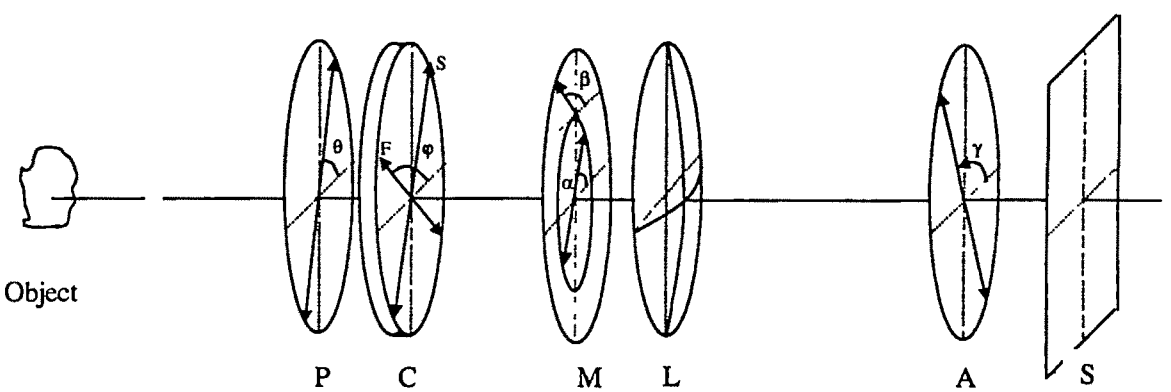

Fig 1. Schematic diagram of the proposed optical set-up, P-polariser, L-imaging lens, C-compensator, A-analyser, M-polarization mask, S-screen

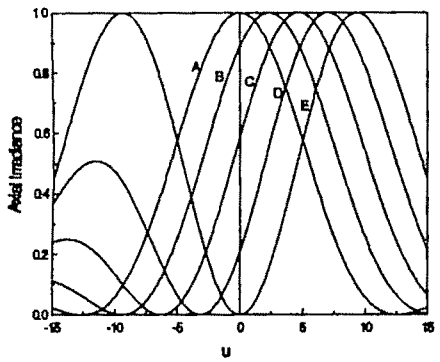

Fig 2. Axial Irradiance for different values of δ. For polarization masked lens aperture the polarization parameters are $\alpha=0^0$, $\beta=90^0$, $\gamma=45^0$,and a=b=1.Curve A, $\delta=0^\circ$,Curve B, $\delta=45^\circ$, Curve C, $\delta=90^\circ$, Curve D, $\delta=135^\circ$ Curve E, $\delta=180^\circ$

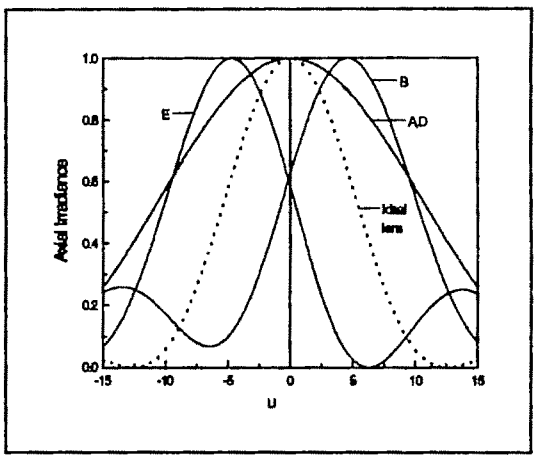

Fig 3. Axial Irradiance for different values of γ. For polarisation-masked aperture the polarization parameters $\alpha=0^\circ, \beta=90^\circ, a=b=1, \delta=90^\circ$. Curve A, $\gamma=0^\circ$ Curve B, $\gamma=30^\circ$ Curve D, $\gamma=90^\circ$ Curve E, $\gamma=135^\circ$

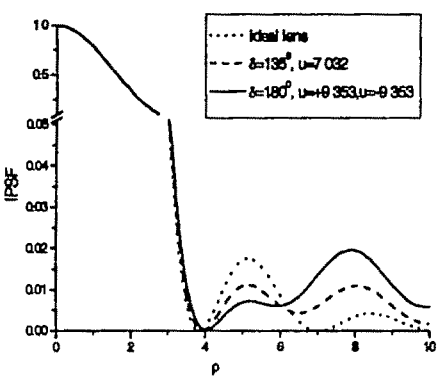

Fig 2(a). IPSF of the polarisation masked lens, and ideal lens for $\delta=135^\circ,180^\circ$ and other parameters as in Fig.2.

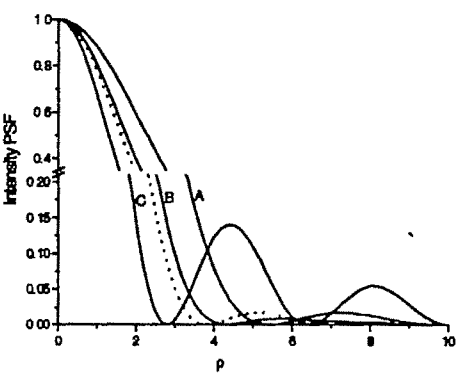

Fig 3(a). IPSF of the polarisation masked lens, and ideal lens for $\gamma=0^\circ,30^\circ,90^\circ$ and other parameters as in Fig.3. Curve A, $\gamma=0^\circ$ Curve B, $\gamma=30^\circ$ Curve C, $\gamma=90^\circ$

COLDII: A software package for computer optimisation of Lens Design

Jaya Basu and Lakshminarayan Hazra
Department of Applied Physics, University of Calcutta,
92, Acharya Prafulla Chandra Road,
Calcutta-700009.
Email: jbasuin@yahoo.com ; lnhazra@netkracker.com

Abstract

All general lens design procedures obtain aberrational information from a ray trace, that is calculating the geometrical path of rays through a system from object space to image space. Raytracing itself is a numerically intensive procedure, involving numerous algebraic, geometrical and trigonometrical equations, from which we arrive at the chosen aberrational information. The phenomenal 'number crunching' capabilities of digital computers has provided a fast and reliable ray tracing tool, as well as, a chance of exploring the possibilities of optimisation in specific problems. This essentially involves the solution of a multivariate nonlinear programming problem. The Gauss – Newton version of least squares and the damped least squares are two of the more widely used methods for optimisation, where the accurate evaluation of the aberration derivatives is one of the prerequisites for success of the particular method in use. COLDII is a computer software package developed by us for lens design optimisation. Three different least squares procedures are available in COLDII providing options to minimise stagnation problems. The present paper reports characteristic features of COLDII.

Keywords: lens design, computer software, lens optimisation.

INTRODUCTION

Computer aided lens design involves tackling of a constrained nonlinear multivariate optimisation problem [1]. It is usually an iterative procedure, that seeks to find a solution vector that will provide an optimum solution of the objective function, - also known as the merit function or defect function in optics, in the neighbourhood of the initial estimate.

The objective function in optical lens design is represented by a quadratic function over the search domain, and for such problems Newton's method is designed to achieve fast asymptotic convergence, when the first and second derivatives of the function are known[2]. Other optimisation strategies have been used elsewhere [3,4], but almost all optimisation packages for lens design tend to use some version of Newton's method as the key procedure. The evaluation/ calculation of the second derivative matrix in its entirety is a complicated and time consuming exercise, not yielding extra advantage over other methods [5]. Fortunately, for a large class of problems, a truncated Hessian matrix obtained after ignoring all the mixed second derivative terms in the original Hessian retains its usefulness in practical optimisation [6]. This technique of optimisation by least squares method using a truncated Hessian matrix is known as Gauss-Newton method in mathematical optimisation theory[7].

The damped least squares (DLS) method is a modification of the Gauss-Newton method, which has been found to be globally convergent. However, the rate of convergence is not entirely satisfactory for some cases and so new techniques for accelerating the convergence continue to be investigated [8].

The solution vector of the DLS method may be looked on as a change-direction vector in the hyperspace of the system variables. Too large a step in this direction is likely to violate the linearity assumptions, and it may lead to worsening the merit function instead of improving it. On the other hand, too small a step along the same direction is tantamount to unnecessarily restricting the possible improvement. An optimum step along this direction leading to the achievable minimum value of the merit function is what we are aiming at. This strategy is known as line search, and in optimisation theory, a line search following a direction search at each iteration is a well established technique for accelerating the convergence in almost all nonlinear optimisation procedures [9,10,11]

The DLS procedure reduces to the Gauss-Newton least squares when the damping factor tends to zero. In DLS, there is an inherent bias against small values of the damping factor; as, it is seen that the incorporation of the solution vector in its entirety often leads to worsening of the merit function, when only an appropriately higher value of the damping factor can provide a remedy by indirectly scaling down the solution vector. But a higher value of the damping factor yields a direction of search that is further away from the direction of superlinear convergence of the least-squares procedure. Obviously, a line search along the direction of a DLS solution vector is not likely to be as effective as one along the direction of the Gauss-Newton solution vector. This is why the modified versions of the Levenberg-Marquardt DLS procedure reported in the optimisation literature attempt to evolve strategies for using the basic Gauss-Newton method as much as possible [12,13,14].

Early works on semiautomatic optimisation include exploration of the basic Gauss-Newton method. These studies were essentially based on primary aberrations or a few finite aberration evaluations, so much so that one often came across situations where the number of nonlinear functions turned out to be less than the number of degrees of degrees of freedom of the system being optimised. The Gauss-Newton method of least squares is not applicable under such circumstances, and the damped least squares technique was the effective method to circumvent the problem.

Now we have immense and ever increasing computational power at our disposal, in terms of time and memory, and this allows us to choose and evaluate larger number of aberrations, so that, the total number of monochromatic and chromatic aberrations at different apertures and field points,- along with pseudo aberrations relating to the Gaussian requirements and boundary constraints is usually much higher than the available variable parameters during optimisation exercises. The use of damping is, therefore, no longer mandatory in most practical problems. Moreover, the convergence properties of the Gauss Newton method can be greatly enhanced by incorporating a line search at each iteration [10].

As no single optimisation technique can provide a panacea for lens design problems, COLDII has inbuilt options for choosing one among the three procedures, namely, Gauss-Newton approach, damped least squares approach and the total Hessian approach in the course of optimisation. The different types of problems which the program is capable of handling at present include all types of fixed focus lenses, such as camera lenses, telescopic systems, telecentric systems, systems with aspheric surfaces, diffractive or binary lenses and systems which require some of their parameters to be tied together during optimisation. After a brief restatement of the least squares optimisation procedures, the following sections present the characteristic features of COLDII..

LEAST SQUARES OPTIMIZATION

The merit function ψ is defined as the sum of squares of weighted defects, **f**. Each of the M defects f is a function of the N construction variables, **x**. Thus ψ is given by

$$\psi = \mathbf{f}^T\mathbf{f} \tag{1}$$

where $\mathbf{f}^T$ is the transpose of the aberration column vector **f**.

Using matrix representation, we have the column vectors **f** and **x** as

$$\mathbf{f} = \begin{bmatrix} f_1 \\ f_2 \\ . \\ . \\ f_M \end{bmatrix} \qquad \mathbf{x} = \begin{bmatrix} x1 \\ x_2 \\ . \\ . \\ x_N \end{bmatrix} \tag{2}$$

A Jacobian matrix is defined by

$$\mathbf{J} = \begin{bmatrix} \partial f_1/\partial x_1 & . & . & . & \partial f_1/\partial x_N \\ . & . & . & . & . \\ . & . & . & . & . \\ . & . & . & . & . \\ \partial f_M/\partial x_N & . & . & . & \partial f_M/\partial x_N \end{bmatrix} \tag{3}$$

The gradient of ψ can be written as

$$\mathbf{g} = \nabla\psi = 2\,\mathbf{J}^T\mathbf{f} \tag{4}$$

Further, let $\mathbf{T}_i$ be the Hessian matrix of f_i

$$T_i=\nabla^2 f_i=\begin{bmatrix} \partial^2 f_i/\partial x_1^2 & \cdots & \partial^2 f_i/\partial x_1 \partial x_N \\ \vdots & \cdots & \vdots \\ \partial^2 f_i/\partial x_N \partial x_1 & \cdots & \partial^2 f_i/\partial x_N^2 \end{bmatrix} \quad (5)$$

The complete Hessian matrix of ψ can be written as

$$\mathbf{G} = 2\mathbf{J}^T\mathbf{J} + 2\mathbf{S} \quad (6)$$

Where, S is defined as,

$$\mathbf{S} = \sum f_i \mathbf{T}_i \quad (7)$$

Let us now consider a change vector **p** given by

$$\mathbf{p} = \begin{bmatrix} p_1 \\ \vdots \\ p_N \end{bmatrix} \quad (8)$$

Using Taylor series expansion of the gradient of ψ at the point **x+p** in the hyperspace of the variables, we have

$$\mathbf{g(x+p)} = \mathbf{g} + \mathbf{Gp} \quad (9)$$

If the point **x + p** is to be a minimum of the function ψ, then **g (x + p)** must be zero, and we have

$$\mathbf{Gp} = -\mathbf{g} \quad (10)$$

Substituting from equations (4) and (6) we obtain

$$(\mathbf{J}^T\mathbf{J} + \mathbf{S})\,\mathbf{p} = -\mathbf{J}^T\mathbf{f} \quad (11)$$

For nonquadratic functions, **x + p** will not in general, be the minimum if **p** is given by equation (11), and the process has to be performed iteratively. Thus at the kth iteration, the normal equations are

$$(\mathbf{J}^T_k\mathbf{J}_k + \mathbf{S}_k)\,\mathbf{p}_k = -\mathbf{J}^T_k\mathbf{f}_k \quad (12)$$

In Newton's method, the above is used to determine change vector $\mathbf{p}_k$ at the kth iteration and the initial estimate for the (k+1)th iteration is

$$\mathbf{x}_{k+1} = \mathbf{x}_k + \mathbf{p}_k \quad (13)$$

Whereas equation (12) constitute the normal equations for the total Hessian approach, in Gauss-Newton method and the DLS method approximate forms of the normal equations are obtained respectively as

$$(\mathbf{J}^T_k\mathbf{J}_k)\,\mathbf{p}_k = -\mathbf{J}^T_k\mathbf{f}_k \quad (14)$$

and

$$(\mathbf{J}^T_k\mathbf{J}_k + \mu\mathbf{I})\,\mathbf{p}_k = -\mathbf{J}^T_k\mathbf{f}_k \quad (15)$$

where **I** is the identity matrix.

MERIT FUNCTION

The merit function ψ, is defined as

$$\Psi = \sum_\tau \omega_\tau^2 [\sum_i \omega_{im}^2 W_i^2 + \sum_i \omega_{ic}^2 (\delta W_i)^2 + \omega_d^2 (D - D_0)^2] + \sum_g \omega_g^2 (G_g - G_{0g})^2 + \sum_h P_h^2 \quad (16)$$

where the summations over τ, g and h indicate respectively the summations over the field points, the Gaussian controls and the penalty functions P_h for violations of the boundary conditions on the edge and center thicknesses, and on the range of glass types. The quantities ω_τ are the weights for image quality at the field points. For each field point, a set of rays are traced to calculate the monochromatic wavefront aberrations W_i and the Conrady chromatic aberrations δW_i together with the fractional distortion D; D_0 is the target value for fractional distortion at the same field point, and the associated weight is ω_d. Finally, ω_{im}, ω_{ic} are the weights for the monochromatic wave aberration and the Conrady chromatic aberration respectively for the i-th ray traced from the same field point. The Gaussian properties such as position and size of the image are controlled by setting a target value G_{0g} for each of the paraxial quantities; and G_g are the actual values obtained form the ray trace. The corresponding weights are ω_g. For effective operation, ω_g needs to be few orders of magnitude larger than the weightings on aberrations.

The scheme for tackling constraints like edge and axial violations, infeasible glasses etc. makes use of suitably formulated differentiable penalty functions P_h[10,15].

LINE SEARCH

As mentioned earlier, direct use of equation (13) for updating of the solution vector often leads to worsening of the merit function rather than improving it. This occurs as a result of nonlinearity of the constituent defect items f of the merit function ψ. This problem is circumvented by using a line search along the change vector as

$$\mathbf{x}_{k+1} = \mathbf{x}_k + \alpha_k \mathbf{p}_k \qquad (17)$$

where α_k corresponds to

$$\alpha_k = \min_{\alpha} \psi(\mathbf{x}_k + \mathbf{p}_k) \qquad (18)$$

Not only does this procedure leads to substantial acceleration of convergence, but also this holds the key to success with undamped least squares.

DAMPING FACTOR

The damping factor in our DLS procedure (15) constitutes a product of three factors:

$$\Lambda = \lambda_s [\lambda\lambda_g]_k \qquad (19)$$

Where λ_s has the same value in all iterations. It takes into account the large differences in absolute magnitudes of the various degrees of freedom. λ_g is termed as the global damping factor whose value is to be determined at each iteration and it has the same value for all variables. Values of the relative damping factor λ for the different variables are determined at each iteration; this makes use of the homogeneous second derivatives of aberrations.

PUPIL EXPLORATION

The shape and location of extraaxial entrance or exit pupils for most optical systems differ considerably from the Gaussian entrance and exit pupils. Larger the field, larger is this departure. Correct estimates for both the aberrations and illumination in extraaxial image points can only be obtained from a knowledge of the effective pupils. In order to ascertain the same, the effective location and shape of the vignetted entrance and exit pupils corresponding to an extraaxial object/image point are determined before the commencement of aberration computation for these points. This is done with the help of repeated finite ray tracing through the system from the extraaxial point and determining thereby the upper, the lower and the side rim rays.

CANONICAL COORDINATES

The vignetted pupils determined as above are approximated by an ellipse and subsequently scaled to a unit circle. Canonical coordinates for the pupil and the object/image points as suggested by H.H.Hopkins [17] are utilized for specification of the rays. The use of these coordinates within the program leads to greater efficiency, considerable simplification and the elimination of problems arising from systems having infinite conjugates or telecentric pupils.

ABERRATION DERIVATIVES

From equations (3) and (5) it may be noted that in each iteration MN number of first derivatives [and ½{MN(N-1)} number of second derivatives,, if total Hessian approach is adopted] need to be evaluated. Except for a few of these derivatives, the analytical forms of the aberration derivatives leads to unwieldy forms, that are not very convenient for use in optimisation algorithms. We, therefore, utilise numerical differentiation procedure [18,19]. The numerical forms of the first order derivatives, homogeneous second order derivatives and the mixed second order derivatives are as

$$\frac{\partial W_i}{\partial x_j} = \left[\frac{W_i(x_1,..,x_j+\delta x_j,..,x_N) - W_i(x_1,..,x_j-\delta x_j,..,x_N)}{2\delta x_j}\right] \qquad (20)$$

for the first order derivative.

The mixed second order derivatives are evaluated from

$$\frac{\partial^2 W_i}{\partial x_i \partial x_j} = \{[W_i(x_1,..,x_i+\delta x_i,..,x_j+\delta x_j,..,x_N) + W_i(x_1,..,x_i-\partial x_i,..,x_j-\delta x_j,..,x_N)] - [W_i(x_1,..,x_i+\delta x_i,..,x_j-\delta x_j,..,x_N) + W_i(x_1,..,x_i-\partial x_i,..,x_j+\delta x_j,..,x_N)]\}/(4\delta x_i \delta x_j) \qquad (21)$$

The homogeneous second order derivatives are obtained from equation (21) by simply substituting j by i.

$$\frac{\partial^2 W_i}{\partial x_i^2} = \{[W_i(x_1,..,x_i+\delta x_i,..,x_j+\ddot{a}x_j,..,x_N)+ W_i(x_1,..,x_i-\partial x_i,..,x_j-\ddot{a}x_j,..,x_N)]- 2[W_i(x_1,..,x_i+\delta x_i,..,x_j-\ddot{a}x_j,..,x_N)]\}/(\delta x_i^2) \quad (22)$$

It was found after extensive numerical checks that, $\delta x_j = 10^{-3}\, x_j$ i.e. 1% or 0.1% change in parameter gives consistently accurate values for aberration derivatives in most cases. Double precision arithmetic using 8-byte word has been used throughout.

RAYGRID SELECTION

Choice of the size of the ray grid and the location of the rays in the grid is a tricky issue; for it should be done in a manner that should adequately describe the aberrational image quality of the system with as few ray traces as possible. This is particularly so in the stage of design optimisation where the iterative procedure calls for many repetitions of the procedure. Indeed, it is contemplated that 75-80% of machine time of computation in lens design optimisation is taken up by ray tracing alone.
After several experiments, the process is economised by tracing only two rays from an axial point and six rays from each of the chosen extraaxial points.

In all three field points are chosen - the axial point, a point at the edge of the field, and the point at the edge of 0.707 of the field. Two finite rays are traced from the on axis point, one of which passes through the margin of the entrance pupil, while the other passes through the 0.707 zone of the entrance pupil. Six finite rays are traced from each off-axis point, four of which are tangential rays and the other two are sagittal rays. The four tangential rays comprise the upper and lower tangential rim rays and those 0.707 of the way to pupil rim. Sagittal rays on only one-half of the pupil need to be traced, and of the two sagittal rays, one passes through the edge of the pupil in the sagittal azimuth and the other passes through the 0.707 zone in the same azimuth. Values of distortions D at the extra axial points are obtained from the principal raytrace.

CONCLUDING REMARKS

COLDII is being designed to be used interactively giving the user both flexibility and ease of operation. It has been structured for operation on any IBM compatible PC. Work is currently in progress to include provisions for handling glass materials as variables. We have recently undertaken two experiments with the least squares optimisation of lens design. Whereas our trials with nonmonotone least squares have so far not yielded any significant advantage over the usual monotone procedure, trials with Broyden rank one updating of the Jacobian matrix during iterations seems to work well leading to substantial saving in machine time of computation. Several computer modules aiding structural design to obtain starting designs for COLDII have also been developed.

ACKNOWLEDGEMENT

Authors are indebted to the Department of Science and Technology, Government of India, for sponsoring a project during the tenure of which this work is done.

REFERENCES

1. R.R. Shannon, *The Art and Science of Optical Design*, (Cambridge University Press, Cambridge, 1997).
2. L.E.Scales, *Introduction to Nonlinear Optimization* , (Macmillan, London, 1981).
3. E.Glatzel and R. Wilson, *Appl. Opt.* **7** (1968) 265-276.
4. D.S.Grey, *JOSA* **53** (1963) 672-676, 677-680.
5. J. Basu and L.N.Hazra, *Journal of Optics* **26** (1997) 157-159.
6. H.H.Hopkins, *Opt.Acta* **13** (1966) 343-369.
7. P.E.Gill, W.Murray and M.H.Wright, *Practical Optimisation* (Academic, London, 1981).
8.J.Basu, *Acceleration of convergence of lens design optimisation*, Ph.D. thesis, University of Calcutta (1998).
9. P.N.Robb, *Appl.Opt.* **18** (1979)4191-4194.
10. H.H.Hopkins and A.Kadkly, *J.Mod.Opt.* **35** (1988) 49-74.
11. A.K.Rigler and R.J.Pegis, *The Computer in Optical Research*, Ed., B.R.Frieden, (Springer-Verlag, Berlin, 1980) p.210-285.
12. R.Fletcher and C.Xu, *IMA J.Numer. Anal.* **7** (1987) 371-389.
13. M.J.D.Powell, Numerical methods for nonlinear algebraic equations, Ed. P.Rabinowitz, (Gordon and Beach, London, 1970) p.76-89.
14. P.E.Gill and W.Murray, *SIAM J.Numer. Anal.*, **15**, (1978) p.977-992.
15.J.Basu and L.N.Hazra, *Optical Engineering* **33** (1994) 4060-4066.
16. J.Basu and L.N.Hazra, *Journal of Optics* **29** (2000) 95-104.
17. H.H.Hopkins, *Applied Optics and Optical Engineering*, Vol.IX, Eds., R.R.Shannon and C.G.Wyant, (Academic ,New York, 1983) p.375-440.
18. J. Basu and L.N.Hazra, *Journal of Optics* **25** (1996) 37-60.
19. J.Basu and L.N.Hazra, *Journal of Optics* **26** (1997) 157-159.

Near Field Diffraction of Gaussian Beams by Radial Walsh Filters

R.SenSarma and L. N. Hazra
Department of Applied Physics, University of Calcutta
92 Acharya Prafulla Chandra Road, Calcutta 700009, India
E-mail : ranas2k@rediffmail.com ; lnhazra@netkracker.com

Abstract

Walsh functions form a closed set of normal orthogonal functions over a given finite interval and take only the values +1 or –1, except at a finite number of points of discontinuity, where they take the value zero.This set provides a set of orthogonal binary phase filters for manipulating the amplitude and/or phase of an incident beam with a high transfer efficiency in energy.This paper reports over preliminary investigations on the near field diffraction properties of the radial Walsh filters for gaussian beam .

Key words: Near Field Diffraction , Walsh functions, Phase filtering, Gaussian beams, Laser beam shaping

INTRODUCTION

Walsh functions form a closed set of orthogonal functions over a given finite interval, each function taking merely one constant value (either +1 or –1) in each of a finite number of subintervals into which the entire interval is divided. This set provides a set of orthogonal binary phase filters for manipulating the amplitude and/or phase of an incident beam with a high transfer efficiency in energy. Walsh functions have been utilized to a great advantage in the field of signal coding and transmission and in allied problems of information processing [1-2]. Two dimensional Walsh functions in the usual rectangular coordinates have been used extensively in digital image processing applications, but for the treatment of problems of image formation for which one usually deals with some form of axial symmetry it is useful to develop Walsh functions in polar coordinates [3-4]. For systems with rotational symmetry about the axis, it is sufficient to deal only with radial Walsh functions. The latter have been developed as a special case of Walsh functions in polar coordinates, and have been found to be quite useful in the treatment of problems of apodization and the study of aberrated optical imagery [5-6]. In order to bring forth the potential of radial Walsh filters in imaging problems, far field diffraction characteristics of the first eight members of the set have already been investigated [7].

In nonimaging applications like beam shaping or energy concentrators, often one has to operate in the near field or Fresnel range of the diffracted wave field. These applications call for studies on axial resolution and/or transverse resolution achievable in the near field domains.

This paper reports on our investigations on the near field characteristics of radial Walsh filters when a Gaussian wave is incident on the same.

WALSH FUNCTIONS

A Walsh function [8] of a single variable x is represented as $W_n(x)$ where the subscript m refers to the order of the function. The functions take on values either +1 or –1 over a specified domain and the set of Walsh functions is orthogonal and complete in the interval. The order m of the function represents the number of zero crossings or phase transitions within the interval.

To define $W_n(x)$ of index $n \geq 0$ and argument x over the interval (0,1), it is first necessary to express the integer n in the form

$$n = \sum_{m=0}^{\tilde{n}-1} k_m 2^m \qquad (1)$$

where $\tilde{n}$ is determined so that $P = 2^{\tilde{n}} \geq n$. For all x in (0,1) , $W_n(x)$ is defined as

$$W_n(x) = \prod_{m=0}^{\tilde{n}-1} \operatorname{sgn}\{\cos(k_m 2^m \delta x)\} \qquad (2)$$

where
$$\begin{aligned} \operatorname{sgn} x &= +1, x > 0 \\ &= 0 \ , x = 0 \\ &= -1, x < 0 \end{aligned} \qquad (3)$$

Equation (2) can also be expressed as

$$W_n(x) = \sum_{j=1}^{P} H_{nj}\zeta_j^P(x) \quad (4)$$

$\zeta_j^P(x)$ are a set of zero-one functions, known as Block functions defined as

$$\zeta_j^P(x) = 1, x_j \le x \le x_{j+1}$$
$$= 0, \text{ otherwise} \quad (5)$$

where $x_j = (j-1)/P$ (6)

In the above H_{nj} are the elements of a $P \times P$ Hadamard matrix whose elements are +1 or −1. Radial Walsh functions [9] $\varphi_n(r)$ are useful in azimuth invariant two dimensional case. The relevant expressions are obtained by substituting $x = r^2$ in the expressions (1)-(6). Note that

$$r_j = [(j-1)/P]^{1/2} \quad (7)$$

Figure 1 below depicts the first four unidimensional Walsh functions and Table 1 gives the Hadamard matrix for $P = 2^2$.

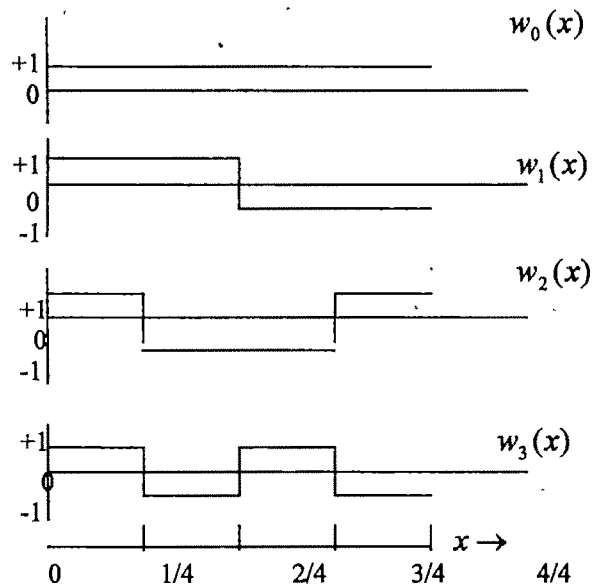

Figure1. Walsh functions in one dimension $W_n(x)$, $n = 0,1..,3$

Table 1. Hadamard matrix H_{nj} for $P = 2^2$

$$j \rightarrow$$
$$n \downarrow \begin{bmatrix} +1 & +1 & +1 & +1 \\ +1 & +1 & -1 & -1 \\ +1 & -1 & -1 & +1 \\ +1 & -1 & +1 & -1 \end{bmatrix}$$

EXACT DIFFRACTION ANALYSIS FOR NEAR FIELD PATTERNS

Consider a Gaussian beam propagating along the z axis (fig. 2). Let its waist be at the input plane P_1, $z = 0$.

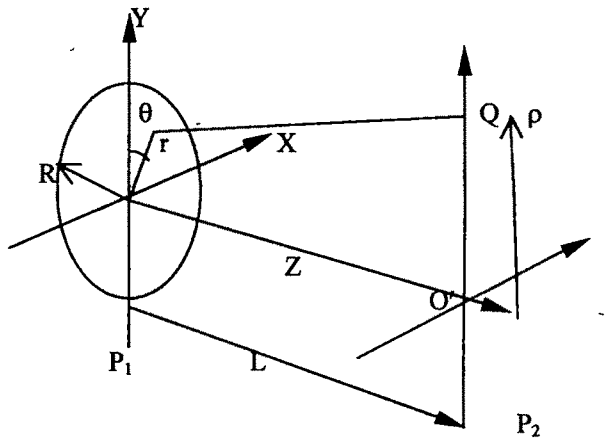

Figure 2. 3-D geometry of near-field exact diffraction analysis

The field at P_1 is

$$E(r) = \exp[-(\frac{r}{\omega_0})^2] \quad (8)$$

where ω_0 is the minimum spot size.

The transparency of the phase mask is given by

$$t(r,\theta) = \exp[i\phi(r,\theta)], \quad 0 \le r \le R$$
$$= 0 \quad , \quad r > R \quad (9)$$

where $R = \sqrt{2}\omega_0$

A phase mask H is placed over the beam at P_1. Complex amplitude at the point Q on the output plane P_2 at a distance L from P_1 is given by

$$F(\rho) = \int_0^R \int_0^{2\pi} \exp[-(\frac{r}{\omega_0})^2] \exp[i\ \varphi(r,\theta)] \frac{\exp[i\ \frac{2\pi}{\lambda} D(r,\theta)]}{D(r,\theta)} r\, dr\, d\theta \quad (10)$$

where,

$$D(r,\theta) = [(r\cos\theta - \rho)^2 + (r\sin\theta)^2 + L^2]^{1/2}$$

λ is the wave length of light.

It is a usual practice to make use of the Fresnel approximation theory for simplifying evaluation of the diffraction integral (10). However, some contradictions

between the results obtained thereby and the correct results by applying the rigorous Rayleigh Sommerfeld theory have recently been reported [10-11]. In our approach, we, therefore, decided not to make use of any approximation and take recourse to numerical evaluation. In the following, we present a convenient technique appropriate to the case of using radial Walsh functions as binary phase filters.

For binary phase filters corresponding to radial Walsh functions,

$$\exp[i\varphi(r,\theta)] \rightarrow \exp[i\varphi(r)] \tag{11}$$

Taking rotational symmetry of the phase filter into account and incorporating suitable substitution of variables, equation (10) becomes

$$\begin{aligned} F(\rho) &= 2\int_0^{R}\int_0^{\pi} \exp[-(\frac{r}{\omega_0})^2]\exp[i\varphi(r)]\frac{\exp[i\frac{2\pi}{\lambda}D]}{D} r\,dr\,d\theta \\ &= 2\int_0^{R}\int_0^{\pi} \exp[-(\frac{r}{\omega_0})^2]\exp[i\varphi(r)] \\ &\qquad \frac{\exp[i\frac{2\pi}{\lambda}\sqrt{r^2+\rho^2+L^2-2\rho r\cos\theta}]}{\sqrt{r^2+\rho^2+L^2-2\rho r\cos\theta}} r\,dr\,d\theta \\ &= \pi R^2 \int_0^{1}\int_0^{1} \exp[-2t]\exp[i\varphi(t)] \\ &\qquad \frac{\exp[i\frac{2\pi}{\lambda}D(t,\psi;R,\rho,L)]}{D(t,\psi;R,\rho,L)} dt\,d\psi \end{aligned} \tag{12}$$

where

$$D(t,\psi;R,\rho,L) = \sqrt{tR^2+\rho^2+L^2-2R\sqrt{t}\rho\cos(\pi\psi)}$$

$$t = \tilde{r}^2 = (r/R)^2$$

$$\psi = \theta/\pi$$

Let $F_n(\rho)$ be the complex amplitude at Q for a phase filter $\varphi(t) = W_n(t)$. Note that $W_n(t)$ in t space reduces to radial Walsh filter $\varphi_n(r)$ in r space.

$W_n(t)$ is given by

$$W_n(t) = \sum_{j=1}^{P} H_{nj}\zeta_j^P(t) \tag{13}$$

where

$P = 2^{\tilde{n}}$ $\tilde{n}$ is a positive integer so that $2^{\tilde{n}} \geq n$

$$\zeta_j^P = 1, \quad t_j \leq t \leq t_{j+1}$$
$$= 0, \quad \text{otherwise} \tag{14}$$

where

$t_j = (j-1)/P;$

$t_{j+1} - t_j = 1/P$

Thus the complex amplitude $F_n(\rho)$ may be obtained in a form

$$F_n(\rho) = \pi R^2 \sum_{j=1}^{P} H_{nj}\Gamma_j(\rho) \tag{15}$$

where

$$\Gamma_j(\rho) = \int_{t_j}^{t_{j+1}}\int_0^1 \exp[-2t]\frac{\exp[i\frac{2\pi}{\lambda}D(t,\psi,\rho)]}{D(t,\psi,\rho)} dt\,d\psi$$

Approximate form for $\Gamma_j(\rho)$ is calculated in the following manner

$$\Gamma_j(\rho) = \sum_{u=1}^{U}\exp[-2t_u]\sum_{v=1}^{V}\frac{\exp[i\frac{2\pi}{\lambda}D(t_u,\psi_v,\rho)]}{D(t_u,\psi_v,\rho)} \tag{16}$$

where

$$t_u = t_j + \frac{2u-1}{2UP} \quad \text{and}$$

$$\psi_v = \frac{2v-1}{V}$$

So that

$\Gamma_j(\rho) = \zeta_j(\rho)\exp[i\Omega_j(\rho)]$

The intensity at the point Q is given by

$$I_n(\rho) = \chi\sum_{j=1}^{P}\sum_{l=1}^{P} H_{nj}H_{nl}\zeta_j(\rho)\zeta_l(\rho)$$
$$\cos[\Omega_j(\rho) - \Omega_l(\rho)] \tag{17}$$

where

$$\chi = [\frac{2\pi\omega_0^2}{\lambda LPUV}]^2 \tag{18}$$

NUMERICAL RESULTS

Figures 3-9 give the variation of axial intensity with the distance from the filter for the phase filters based on the first eight radial Walsh functions $\phi_n(r)$, r=1,.....8, respectively. In the figure captions {Walsh n} ≡ $\phi_n(r)$. It may be noted that the magnitude of axial peaks increases with the order of the Walsh function. The numerical results presented here correspond to ω_0=1mm and λ=0.6328μm. The location of the axial peaks also gets separated with increasing order of Walsh function. Figure 11 shows the variation of axial intensity for $\phi_{15}(r)$. In order to show the light concentration at an axial peak, figure 12 shows the variation of light intensity with transverse distance ρ at the position of axial peak at L=65.8mm.

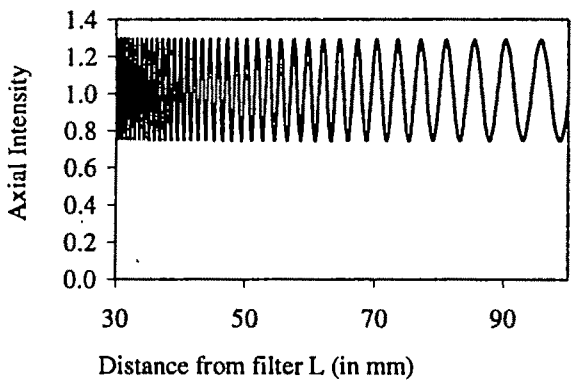

Figure 3. Axial Intensity Distribution Walsh 0

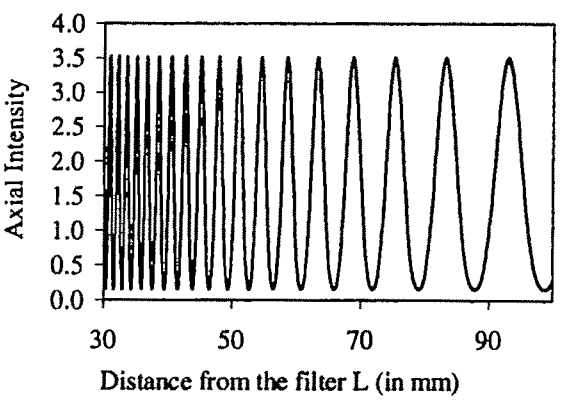

Figure 4. Axial Intensity Distribution Walsh 1

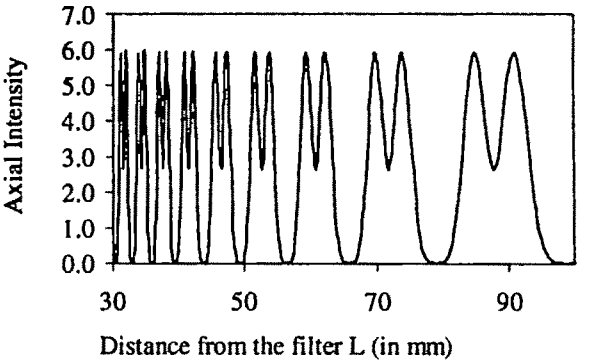

Figure 5. Axial Intensity Distribution Walsh 2

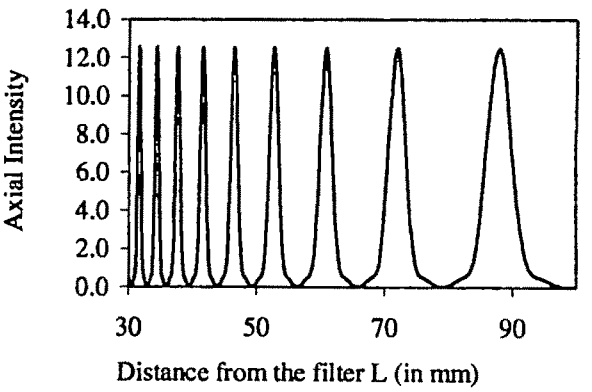

Figure 6. Axial Intensity Distribution Walsh 3

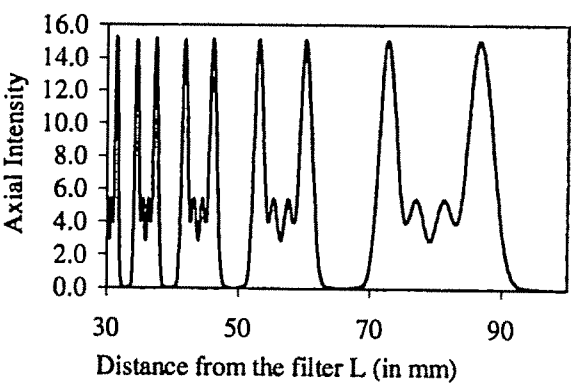

Figure 7. Axial Intensity Distribution Walsh 4

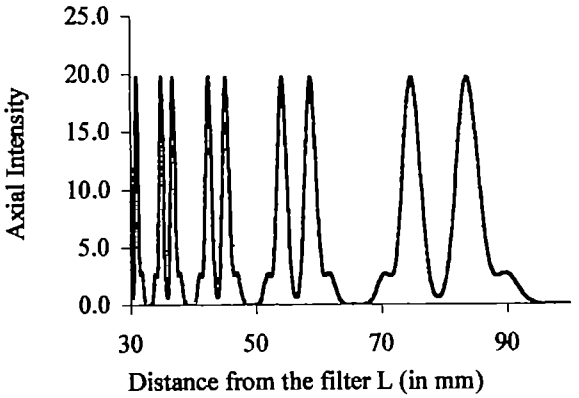

Figure 8. Axial Intensity Distribution Walsh 5

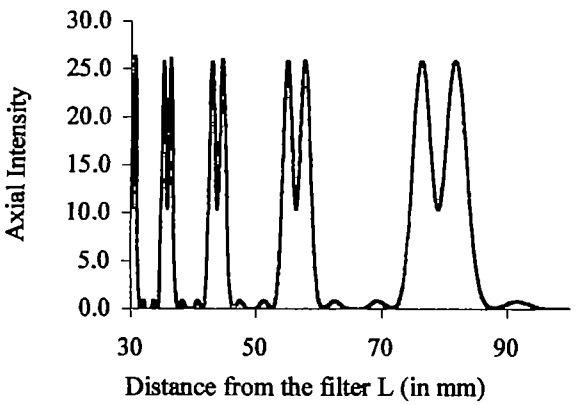

Figure 9. Axial Intensity Distribution Walsh 6

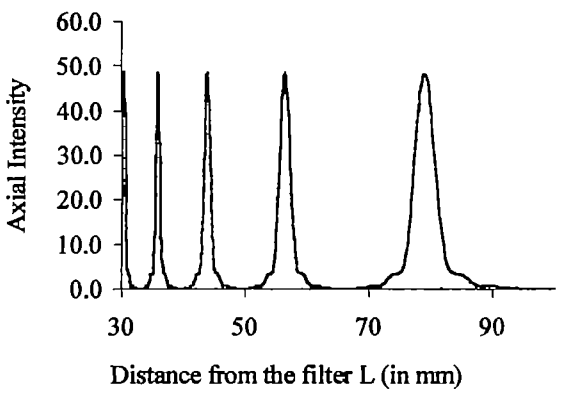

Figure 10. Axial Intensity Distribution Walsh 7

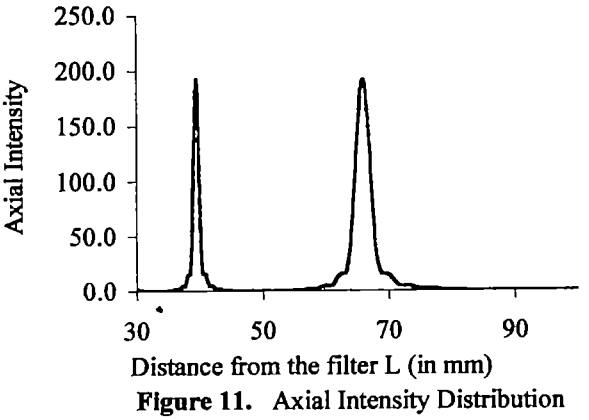

Figure 11. Axial Intensity Distribution Walsh 15

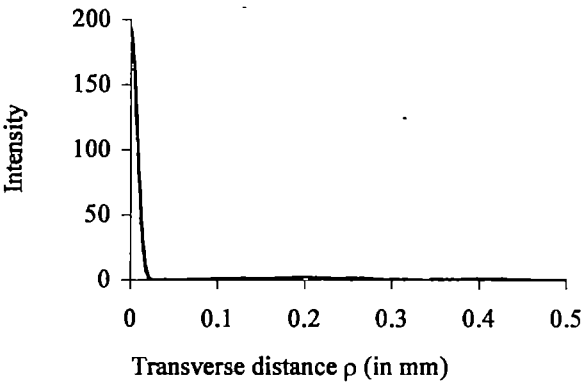

Figure 12. Variation of light intensity with transverse distance

CONCLUSION

Our exploration for direct implementation of radial Walsh functions as phase filters stems from the associated simplicity in practical realization of these binary filters. Also, the computational tools developed in course of this study set the tune for studying appropriate multistage phase filters in tackling involved beam shaping problems.

ACKNOWLEDGEMENT

The authors are indebted to the All India Council for Technical Education for sponsoring a project during the tenure of which the work is done.

REFERENCES

1. H.F.Harmuth, Transmission of Information by Orthogonal functions, Springer-Verlag, Berlin (1972).
2. K.G.Beauchamp, Walsh Functions and their Applications, Academic Press, New York(1985).

3. H.C.Andrews, Computer Techniques in Image Processing, Academic Press, New York (1970).
4. L.N.Hazra and A.Banerjee, 'Application of Walsh functions in generation of optimum apodizers', J.Opt, **5**, (1976)19-26.
5. L.N.Hazra, 'A new class of optimum amplitude filters'.Opt.Commn., **21**, (1977)232-236.
6. L.N.Hazra, P.K.Purkait and M.De, 'Apodization of aberrated pupils', Can.J.Phys, **57**, (1979) 1340-1346.
7. L.N.Hazra and A.Guha, 'Farfield diffraction properties of radial Walsh filters', J.Opt.Soc.Am. A, **3**, (1986) 843-846.
8. H.F.Harmuth, Sequency Theory : Foundations and Applications, Suppl.9 Advances in Electronics and Electron Physics (Academic , New York, 1977).
9. M.De and L.N.Hazra , 'Walsh Functions in problems of optical imagery' , Opt.Acta ,**24**, (1977)221-234.
10. C.J.R. Sheppard and M.Hrynevych, 'Diffraction by a circular aperture : a generalization of Fresnel diffraction theory',J.Opt.Soc.Am.A,**9** (1992)274-281.
11. L.M.Soroko , Meso-optics, World Scientific, Singapore(1996)

Application of Genetic algorithm in structural design of cemented triplets with prespecified aberration targets

S. Chatterjee & L. N. Hazra
Department of Applied Physics
University of Calcutta
92 Acharya Prafulla Chandra Road, Kolkata-7000009
email: chatterjee_d@hotmail.com; lnhazra@netkracker.com

Abstract

This paper presents a scheme for implementation of genetic algorithm in the structural design of cemented triplets according to a prespecified set of Gaussian characteristics and primary aberration targets. Contrary to the usual practice of heuristic preselection of glasses for the three elements of the triplet, our approach enables a treatment of actual glasses as design variables, providing thereby a through and effective exploration of the available configuration space of design variables. The primary goal is to locate the promising thin lens structural solutions that may be followed up to obtain practically useful designs.

INTRODUCTION

Traditional approaches for computer aided optimization of lens systems are essentially adaptations of different versions of gradient techniques in nonlinear optimization, so that the solution is a 'local' optimum in the neighborhood of a prescribed starting point in the constrained multivariate configuration space [1-3]. In practice, one has to take recourse to repeated trials with different starting points, for arriving at a 'workable' optimum. Fast, large memory computers has opened the doors of 'Global Optimization' strategies in lens design for large multivariate problems [4-6]. However, the 'curse of dimensionality' associated with the large number of variables severely precludes their practical implementation even for moderately complex problems[7-8].

In order to arrive at globally or quasiglobally optimal design solutions for multicomponent lens systems, an alternative strategy is being worked out. This essentially involves transforming a complex problem with large number of variables into a set of relatively simpler problems with lesser number of variables[9]; the subproblems in turn are tackled in a phased manner by making use of the principles of thin lens aberration theory and Gaussian optics. As the number of variables at the subproblem level are not very large, it is possible to utilize global optimization tools at this stage[10-14]. The nature of optimality of the design solution for the total problem obtained thereby, i.e., whether the achieved solution is globally optimum or not, is very difficult to ascertain. Nevertheless, in practice, this approach is highly likely to render better solutions than the ones obtained via conventional approach.

With this backdrop in view, the present paper addresses the problem of structural design of cemented triplets in accordance with a prespecified set of Gaussian characteristics and primary aberration targets. Cemented triplets constitute an important class of components in some objectives and widefield eyepieces. In our strategy of design, cemented triplets are explored to realize a particular component, whenever neither a singlet nor a cemented or broken contact doublet can satisfy the paraxial and primary aberrational requirements of the component. The next section presents an analytical formulation of the problem. It is followed by a section dealing with our adaptation of genetic algorithm for the purpose.

ANALYTICAL FORMULATION

In the case of a cemented triplet, there are only six design variables for thin lens configuration: shape variable X_1 for the first component; the glass variables glass1, glass2 and glass3 for the three elements of the triplets; and $\bar{k}_1$, the normalized power of the first element; $\bar{k}_2$, the normalized power of the second element.

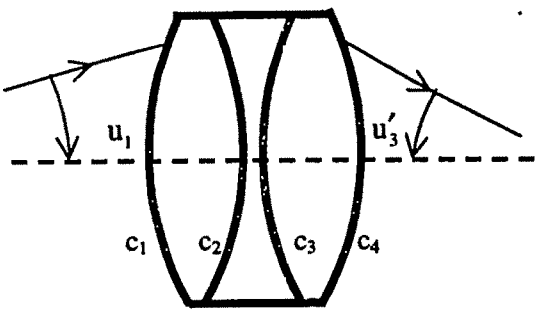

Fig.1a: A cemented triplet where c_1, c_2, c_3, c_4 are curvatures of the four interfaces.

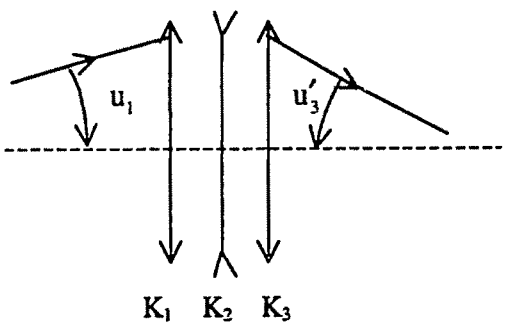

Fig 1b: Thin lens model for the cemented triplet assuming axial thicknesses to be zero. Total power $K=K_1+K_2+K_3$; u_1 : convergence angle for the ray incident on the first surface ; u_3' : convergence angle for the ray emergent from the last surface

We have $\bar{k}_1 = K_1/K$ and $\bar{k}_2 = K_2/K$, where K_1, K_2, K are the powers of the first element, second element and the triplet, respectively. Shape variable X for a thin lens element is defined as

$$X = \frac{c_1 + c_2}{c_1 - c_2} \qquad (1)$$

where c_1 and c_2 are curvatures of the first and second surfaces of the element.

As the three components of a cemented triplet have two common surfaces, there is effectively one shape variable available as a degree of freedom. Shape variable X_2 for the second element is given by:

$$X_2 = \left[\frac{\bar{k}_1(n_2-1)}{\bar{k}_2(n_1-1)}(X_1-1)-1\right] \qquad (2)$$

The shape variable x_3 for the third element is given by:

$$x_3 = \left[\frac{\bar{k}_1}{\{1-(\bar{k}_1+\bar{k}_2)\}}\frac{(n_3-1)}{(n_2-1)}(x_1-1)\right]$$

$$-\frac{2\bar{k}_2}{\{1-(\bar{k}_1+\bar{k}_2)\}}\frac{(n_3-1)}{(n_2-1)}-1 \qquad (3)$$

with X_1 given by

$$X_1 = \frac{c_1 + c_2}{c_1 - c_2} \qquad (4)$$

where $K_1+K_2+K_3=K$ and

$$\bar{k}_1 + \bar{k}_2 + \bar{k}_3 = 1 \qquad (5)$$

For each element of the triplet , the optical material or glass variable is allowed to take any integer value from 1 to a maximum value that indicates the maximum number of entries in the specified glass list .the glass list contains values for refractive index n measured at the operating wavelength and for the dispersion δn for different glasses.

FITNESS FUNCTION

In GA each individual in the initial population is assigned a unique fitness value, and the GA aims at maximizing this fitness in the subsequent generations.

$$\Phi = \frac{1}{1+\Psi} \qquad (6)$$

Fitness function Φ is inversely related to the optical merit function Ψ where optical merit function Ψ is defined as the sum of squares of Seidel aberrations. Ψ is given by

$$\Psi = \sum_{i=1}^{3} a_i^2 f_i^2 \qquad (7)$$

where f_i, i=1,.....3 is given by

$$f_i = [(\Gamma_i)_1 + (\Gamma_i)_2 + (\Gamma_i)_3 - (\Gamma_i)_t] \quad (8)$$

and ω_i are the corresponding weighting factors.In Eq.(7), Γ_i, I=1,2,3, correspond to the Seidel the central coma(S_{IIc}), and the longitudinal chromatic aberration (C_L), respectively. The subscript t is used to represent the target value of that particular aberration for the complete triplet.
$(\Gamma_i)_1$, $(\Gamma_i)_2$ and $(\Gamma_i)_3$ correspond to the first, second and third lenses, respectively , of the cemented triplet. $(\Gamma_i)_j$ have following significance:

$$(\Gamma_1)_j = (S_I/8)_j,$$

$$(\Gamma_2)_j = (S_{IIc})_j,$$

$$(\Gamma_3)_j = (C_L/2)_j, \quad (9)$$

where subscript j can take only three values,j=1,2,3, to denote the first, second, and third components, respectively, of the triplet. The corresponding numerical factors are incorporated in Eqs. (8) and forge a direct link between the Γ_i and the corresponding wave aberration coefficients.

For the j^{th} thin lens of the triplet in air with a stop on it, the Seidel coefficients for primary spherical aberration (S_I), the central coma (S_{IIc}), and the longitudinal chromatic aberration (C_L), are expressed in terms of the constructional parameters of the lens, namely, the shape, the power, the refractive index, and dispersion of the optical material of the lens and configurations of the imaging geometry. The exact expressions for these aberrations are

$$(S_I)_j = \frac{1}{4}h^4K^3(\bar{k}_j)^3\left\{\frac{n_j+2}{n_j(n_j-1)^2}\left[X_j - \frac{2(n_j^2-1)}{n_j+2}Y_j\right]^2 + \frac{n_j^2}{(n_j-1)^2} - \frac{n_j}{n_j+2}Y_j^2\right\}$$

$$(S_{IIc})_j = \frac{1}{2}h^2K^2H(\bar{k}_j)^2\left[\frac{n_j+1}{n_j(n_j-1)}X_j - \frac{2n_j+1}{n_j}Y_j\right]$$

$$(C_L)_j = K\left[\bar{k}_j\frac{(\delta n)_j}{n_j-1}\right] \quad (10)$$

where X_j is the shape variable, n_j is the refractive index at the operating wavelength, and (δn_j) is the dispersion value for the optical material of the jth element of the triplet. The expressions for Seidel aberrations as given by Eqs. (10) are also known as central aberrations, for the stop is assumed in contact with the thin lens.
Dispersion δn for a glass is defined as

$$\delta n = n_F - n_C, \quad (11)$$

where ($n_F - n_C$) is the difference between the refractive indices of the glass at the hydrogen F (486.1 nm) and the C(656.3 nm) lines.

As the triplet is thin and the three elements are in contact, the height of the paraxial marginal ray (semiaperture when the stop is placed on the lens), h, is same for all elements. Paraxial characteristic H is the optical, or Lagrange invariant for the lens system. K is the overall power of the cemented triplet. The variable $\bar{k}_j$ is the normalized power of the j^{th} element, and Y_j is the conjugate variable for the j^{th} element of the triplet.

Y_1, Y_2, and Y_3, the conjugate variables for the three elements of the triplet, can be expressed in terms of overall conjugate variable Y for the triplet and normalized power $\bar{k}_1$ and $\bar{k}_2$ for the first two elements. They are given by the following expressions:

$$Y_1 = \frac{Y - (1 - \bar{k}_1)}{\bar{k}_1}$$

$$Y_2 = \frac{Y - (1 - 2\bar{k}_1 - \bar{k}_2)}{\bar{k}_2}$$

$$Y_3 = \frac{Y + (\bar{k}_1 + \bar{k}_2)}{\{1 - (\bar{k}_1 + \bar{k}_2)\}} \quad (12)$$

Y represents the overall conjugate variable for the triplet lens and is given by:

$$Y = \frac{u_j' + u_1}{hK} \quad (13)$$

where u_1 and u'_3 are the convergence angles for the paraxial marginal ray in the object and the image spaces, respectively. Note that we follow the notation of Hopkins [15] and the sign conventions of Born and Wolf [16] in the definition of the Seidel coefficient and in writing all the subsequent relations.

GENETIC ALGORITHM

In genetic algorithm for optimization problems, the first generation is initialized at random within the available configuration space. The next generation is produced from the current generation via the use of genetic operators. This process is repeated until a suitable solution has been found. The system variables of each lens configuration are encoded as a chromosome and this is shown in fig II. We make use of binary coding of the variables.

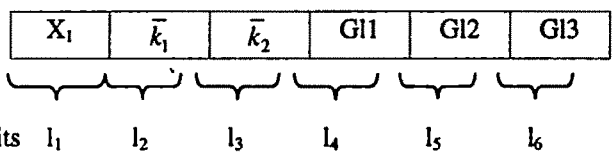

Fig. II: chromosome representation of variables

Steps followed in GA:

- Initialize the population ramdomly. Set a counter for generation number 1. Keep the copy of the best chromosome.
- Apply selection, crossover embedded with mutation to update the existing population.
- If the fittest among the new population is fitter than that of the previous generation, replace the best chromosome by the newly found best, else replace any individual of the new population with the best chromosome already found (elitism).
- The generation counter is increased by 1.
- If the generation counter exceeds a preset value for maximum number of allowed generations, then stop, otherwise go to next.
- Check for genetic diversity.
- Apply niching and then go to step 2.

Fig.III presents a flowchart for the procedure.

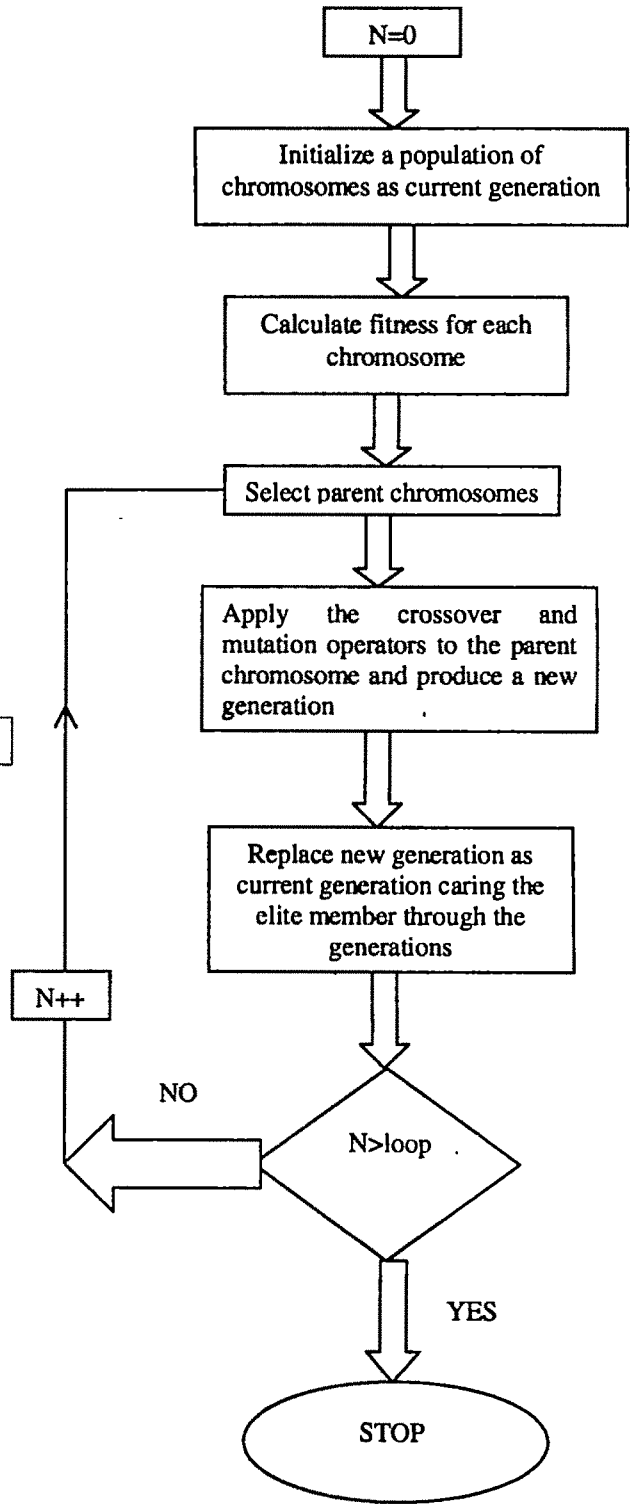
N=0
Initialize a population of chromosomes as current generation
Calculate fitness for each chromosome
Select parent chromosomes
Apply the crossover and mutation operators to the parent chromosome and produce a new generation
Replace new generation as current generation caring the elite member through the generations
N++
NO
N>loop
YES
STOP

Fig. III: Flow chart of genetic algorithm

CODING OF VARIABLES

The i^{th} variable, x_i is represented as a binary substring of length l_i, where l_i is given by :

$$l_i = \log_2 \frac{\left(x_i^{max} - x_i^{min}\right)}{\varepsilon_i} \quad (14)$$

where x_i^{max} --- upper bound of x_i
x_i^{min} --- lower bound of x_i
ε_i --- precision needed in x_i

For N variables the total length (L) of a chromosome:

$$L = \sum_{i=1}^{N} l_i \quad (15)$$

Any substring S_i decodes to a solution x_i as

where $DV(S_i)$ is the decoded value of the substring S_i

$$x_i = x_i^{min} + \frac{x_i^{max} - x_i^{min}}{2^{l_i} - 1} DV(S_i) \quad (16)$$

SELECTION

During selection operation usually highly fit chromosomes are selected for reproduction while less fit individuals are eliminated from the population. There are different selection schemes but we have used the probabilistic tournament selection technique. With tournament selection the selection pressure is constant over the generations and it is equal to the size of the tournament. For a tournament of size n_{tourny} the fittest among the n_{tourny} randomly chosen solutions from the population gets selected to the mating pool with a probability p_{tourny}. The value of p_{tourny} determines the selection pressure.

The selection process chosen does not guarantee selection of the fittest solution. Unless the fittest solution is much fitter than the rest of the population, it will occasionally not be selected and will die. This slows the rate of convergence and premature convergence may occur. The speed of the algorithm has improved by applying 'elitism'; which one may incorporate by making use of the results of previous search, e.g., by retaining the best, or elite member of the population through the generations.

CROSSOVER

We have applied uniform crossover operator in our algorithm because it has the maximum search power among all the crossover operators.

Crossover Mask:	1 0 0 1 0 1
Parent1:	1 0 1 1 0 0
Parent2:	0 1 0 0 1 1
Child1:	1 1 0 1 1 0
Child2:	0 0 1 1 0 1

Each bit in the child chromosome is created by copying the corresponding bit from one or other parent, chosen according to a randomly chosen crossover mask for each pair of parents. Where there is a 1 in the crossover mask, the bit is copied from one parent, and where there is a 0 in the mask the bit is copied from the other parent. The process is repeated with the bits and parents interchanged to produce the second child.

BIT MUTATION

Mutation is applied to each child after crossover to maintain diversity in the population. It randomly alters each gene from 0 to 1 or vice-versa with a very small probability.

$$00100 \Rightarrow 00000$$

In the above example , the third gene has undergone a change from 1 to 0, and creating a new solution.

GENETIC DIVERSITY

When genetic diversity is lost, crossover operation cannot produce new solutions. Then the tendency of the algorithm is to converge prematurely on the few highly fit individuals present in the population. Genetic diversity 'g' is given by,

$$g = \sum_{i}^{popsize} \frac{d_i}{(popsize)L} \quad (17)$$

where d_i is the Hamming distance of the i^{th} individual from the fittest individual. At each generation, the genetic diversity is calculated, and if it is smaller than a prespecified value, the best of the previous search is kept and the rest of the population is filled with randomly generated chromosomes.

SPECIATION

In Nature, different species find different combinations of environmental factors: different niches, which are

unsuitable for other species. As the number of individuals in a particular species continues to increase, the intraspecies competition for the same environmental resources increases. In the GA this competition may be artificially imposed by use of a fitness-sharing scheme. The idea of sharing is developed in such a way as to avoid crowding of individuals about one particular optimum, so the entire population is subdivided into groups that converge at different optima.

To implement the sharing scheme we employed a function of d_{ij}', the distance between the ith and the jth chromosomes in the design space, which is given by

$$Sh(d_{ij}') = [1 - (d_{ij}' / \sigma_{shar})] \qquad d_{ij}' < \sigma_{shar}$$

$$= 0 \qquad \text{otherwise.}$$

The shared fitness of the ith chromosome, Φ_i', is given by

$$\overline{\Phi}_i = \frac{\Phi_i}{m_i} \tag{18}$$

The niche count, m_i, for the i^{th} chromosome is given by

$$m_i = \sum_{j=1}^{popsize} sh(d_{ij}') \tag{19}$$

CONCLUDING REMARKS

The scheme for optimization of cemented triplets as presented above is adopted from our earlier experiments with genetic algorithm in structural design optimization of doublets [13-14]. However, a straightforward adaptation of genetic parameters does not yield an effective algorithm for the problem at hand. Further experiments on case specific modifications of the algorithm are in progress and will be reported subsequently.

ACKNOWLEDGEMENT

The authors are indebted to the Department of Science & Technology, Government of India, for sponsoring a project during the tenure of which this work is done.

REFERENCES

1. R.R. Shannon, The Art and Science of Optical Design, Cambridge Univ. Press, Cambridge (1997).
2. J.Basu and L.N.Hazra, 'Role of line search in least squares optimization of lens Design', Opt. Eng. 33(1994) 4060-4066.
3. W.J.Smith, Modern Optical Engineering, McGraw Hill, New York (2000)
4. A.E.W. Jones, "Global Optimization in lens design", Ph.D dissertation, Univ. Rochester, Rochester, New York(1992)
5. X.Chen and K.Yamamoto, "An experiment in genetic optimization in lens design", J.Mod. Opt. 44, 1693-1702(1997).
6. I.Ono and S. Kobeyashi, "Global and multiobjective optimization for lens design by real-coded genetic algorithms," in International Optical Design Conference, L.R.Gardner and K.P.Thomson, eds., Proc. SPIE 3482, 110-121 (1998).
7. 7.D.Sturlesi and D.C.O'shea, "Future of global optimization in optical design", in International lens design conference, Proc. SPIE, Vol.1354, 54-68(1990).
8. T.G.Kuper and T.I. Harris, "A new look at global optimization of optical design", Phot. Spectra, 151-160 (1992).
9. L.N.Hazra,"Structural design of multicomponent lens systems", Appl. Opt. Vol 23, 4440-4443(1984)
10. L.N.Hazra and A.K.Samui, "Design of the individual components of a multicomponent lens system: use of a singlet," Appl.Opt.25,3721-3730(1986).
11. S.Banerjee and L.N.Hazra, "Structural design of doublet lenses with prespecified aberration targets," Opt.Eng.36, 3111-3118(1997).
12. S.Banerjee and L.N.Hazra, "Simulated annealing with constrained random walk for structural design of doublet lenses", Opt.Eng.,vol37,3260-3267 (1998)
13. S.Banerjee and L.N.Hazra, "Genetic algorithm for lens optimization at structural design phase," in Optics and Optoelectronics, Theory,Devices, and Applications, O.P.Nijhawan, A.K.Gupta, A.K.Musla, and K.Singh, eds. (Narossa, New Delhi,1999), Vol1, pp.499-504
14. S.Banerjee and L.N.Hazra, "Experiments with genetic algorithm for structural design of cemented doublets with prespecified aberration targets", Appl.Opt., (2001) in the press.
15. H.H.Hopkins, Wave theory of Aberrations (Oxford U.Press. London, 1950).
16. M.Born and E.Wolf, Principles of Optics, Pergomon, Oxford(1980).
17. D.E.Goldberg, Genetic Aqlgorithms in Search, Optimization, and Machine learning (Addison-Wesley, New York, 1989).
18. D.E.Goldberg and K.Deb, 'A comparison of selection schemes used in genetic algorithms,' in Foundation of Genetic Algorithms,G.J.E. Rawlins.ed.Morgan Kaufmann, California, 1991), pp. 69-93.

Computerized Fringe Analysis for the Measurement of Refractive Index Profile of GRIN Glasses of Different Geometry

M.Ray (Shah), A. Datta, S.K.Sarkar and A. Basuray
Optics and Optoelectronics Section
Department of Applied Physics
University College of Science and Technology
92, A.P.C. Road
Calcutta–700 009, India
E-mail: minaray@cucc.ernet.in

Abstract

A software package is developed to analyze the fringes obtained in the interferometric set-up based on deflectometry principle for the measurement of refractive index profile of GRIN rods of different geometry. The fringe patterns both in presence and absence of the test samples are grabbed by a CCD camera and further processed by the software developed. Some experimental results are presented.

Key Words: Fringe Analysis, Interferometry, GRIN Glass, Refractive Index Profile

INTRODUCTION

There is a growing demand of gradient index (GRIN) rod lenses that find applications in wide field varying from copying machines, optical scanners to fiber optics light coupling systems [1]. But, unfortunately, its development is particularly handicapped by the non-availability of many kinds of GRIN materials as well as inability to produce large GRIN systems. Knowledge of variation of refractive index and the process involved in fabrication of GRIN rods is important in meeting recent demands for new optical systems. This calls for development of a moderately accurate and simple system for refractive index profile measurement.

Many interferometric systems are used for such measurements of which, Mach Zehnder interferometer is mostly used [2]. However, Mach Zehnder interferometer being a cyclic interferometer is much sensitive to vibrations and needs well-maintained sophisticated Laboratory facilities. Moreover, in such measurements a large number of fringe counts is required, which is time consuming as well as much involved.

An innovative simple technique has been developed by this group of workers using the combined effect of interferometry and deflectometry [3-5]. In the process, a set of optical fringes is generated by using a longitudinal interferometer (for circular GRIN geometry) and by transverse interferometer (for rectangular GRIN geometry). The fringe pattern so generated is then incident on the GRIN sample under test and the deviations of the fringes give a measure of the refractive index variation in the sample. The present report deals with the question of analyzing and processing the data using a computer. The necessary software for fringe analysis is developed. Some experimentally measured results on GRIN samples manufactured by M/S Graded Index Lens Corporation, USA, and NSG, Japan are also presented.

EXPERIMENTAL SET-UP

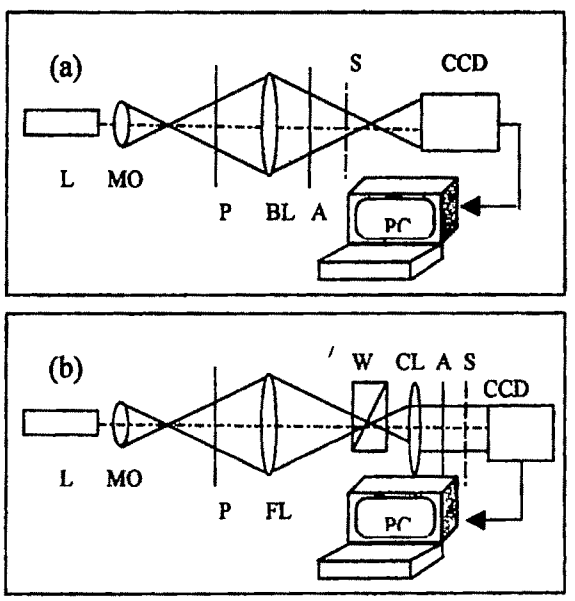

Fig.1 Set-up for (a) circular GRIN (b) rectangular GRIN L: He-Ne Laser, MO: Microscope Objective, P: Polariser, BL: Birefringent Lens, FL: Focusing lens, CL: Collimating lens, W: Wollaston Prism, A: Analyser, S: Sample Position, CCD: Camera, PC:

Fig. 1(a) shows the experimental set-up for the measurement of circular GRIN sample profile based on deflectometry principle using the interference pattern generated by a biregringent lens (BL). Fig. 1(b) shows the same for the rectangular geometry GRIN sample where, equidistant straight line fringes are generated with the help of a Wollaston prism. Presence of GRIN sample in the both cases modifies the fringe pattern according to the characteristics of the sample. Fringe patterns, both in presence and absence of GRIN sample are grabbed by a CCD camera and then processed using the image processing software and the fringe analysis is performed to get the refractive index profile of the GRIN sample.

MATHEMATICAL ANALYSIS

A birefringent lens has two refractive indices along x and y directions when the light propagates along z-direction. As a result, It has two foci for two orthogonal polarized incident light. Thus using an analyzer it acts as a longitudinal interferometer forming Newton's ring like fringes. Circular fringe intensity distribution for unit contrast is given by

$$I = 1 + \cos\left[\frac{2\pi}{\lambda}\Delta\left(\frac{1}{f}\right)r^2\right] \quad for\ \theta = \pi/4$$

and

$$I = 1 - \cos\left[\frac{2\pi}{\lambda}\Delta\left(\frac{1}{f}\right)r^2\right] \quad for\ \theta = -\pi/4$$

where θ is the angle between the analyzer and the optical axis, f is the focal length and r is the radial distance. Since this fringe system is not localized, the incident beam on a sample will diverge/converge according to the refractive index variation in negative/positive GRIN lens.
Using ray equation,

$$\frac{d}{ds}\left(n\frac{dr}{ds}\right) = \nabla n$$

Where, s is along the ray path. With paraxial approximation, it reduces to

$$\frac{d}{dz}\left(n\frac{dr}{dz}\right) = \nabla n$$

After passing through the sample of width 'd', change of angle will be

$$\int_{u}^{u'} d(u) = \frac{1}{n}\int_{0}^{d}\left(\frac{dn}{dr}\right)dz$$

Where, u and u' are the incident and refracted angles respectively. Neglecting the contribution due to sample thickness 'd', the change of refractive index at any point r_m, which corresponds, to the radius of the particular fringe will be

$$\Delta n_{(r=m)} = \sum_{m=1}^{n}\delta(r_m)/\delta(r_m - r_{m-1})$$

Where, m =1 represents the first central fringe.
For the rectangular geometry, the mathematical analysis is much simpler, as straight line fringes will be formed due to the lateral shift produced by the Wollaston Prism and the deviation of the straight line fringes after traversing the test sample will give the measure of the refractive index variation. The computation of the same may be made using the ray equation in Cartesian Co-ordinates.

FRINGE ANALYZER

A fringe analyzer is an image processing software that deals with the fringe systems. It provides with every minute details of the pattern and with some options even lets one modify the fringe pattern for better results. Although there exists many image processing software, none is specially suitable for some specific task such as refractive index profile measurement by analyzing the interferometric fringes as obtained in our case. In order to make the present system to operate in real time, it is necessary to develop the software specifically for this purpose so that it can be implemented for testing of GRIN samples even during fabrication process.

As a first step to achieve this goal, we have developed a fringe analyzer using Visual Basic and we have tested several fringe patterns with that.

DIFFERENT TASKS PERFORMED BY FRINGE ANALYZER

Various tasks performed by the developed software includes:

- Analyze both concentric circular type fringes and parallel straight fringes.
- Analyze multiple fringes together.
- Count the total number of fringes in a system.
- Find the location of the center of the symmetric type fringes (Flow diagram is shown in Fig.2).
- Measure the fringe width and inter fringe spacing of a particular fringe system(Flow diagram is shown in Fig. 3).
- Save the information of a particular fringe system in a text file(log file) that can be used later on.
- Make thinner fringes from a pattern of thick fringes without any alteration of the inter fringe distance.

- Convert an image to a monochrome one according to threshold value chosen by the user. After conversion, option is either to save it as new image or to restore to original image.
- Draw the color level profile of the picture. This can either be a RGB profile giving red blue and green values of color components, or a gray level profile giving only the average of the three color components.
- Zoom the fringe pattern according to user's choice for the better viewing of minute details.

FLOW – DIAGRAMS

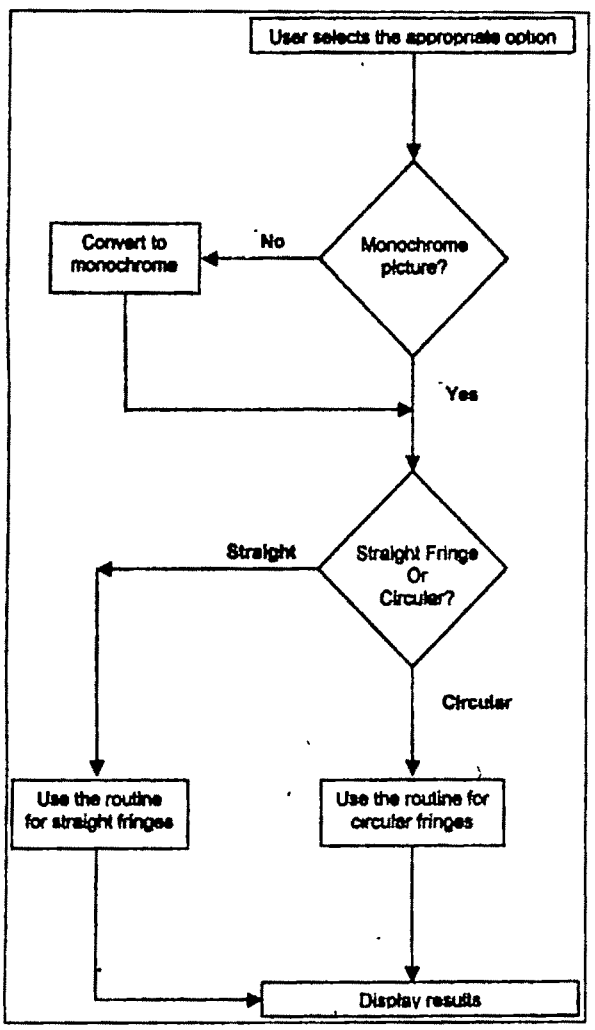

Fig. 2 Flow diagram for center-finding process

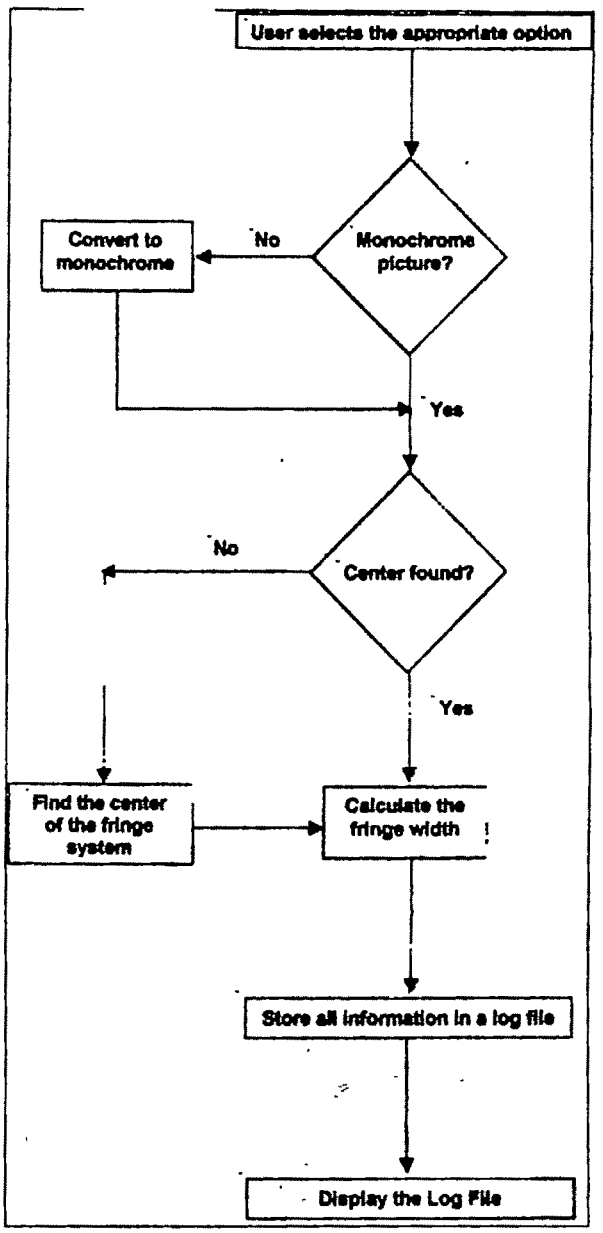

Fig. 3 Flow diagram for fringe-width calculation

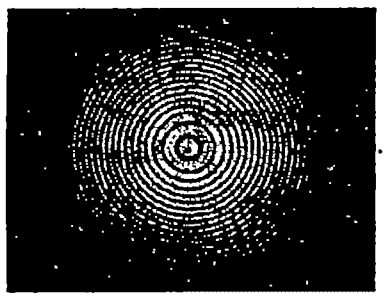

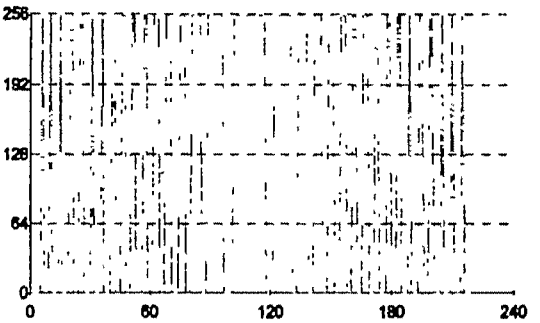

0f

(48, 117) to (267,117)

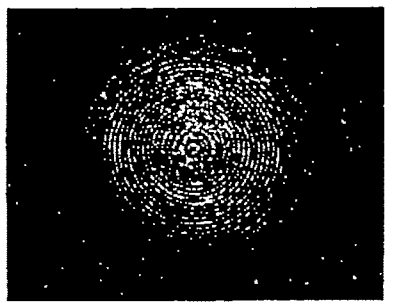

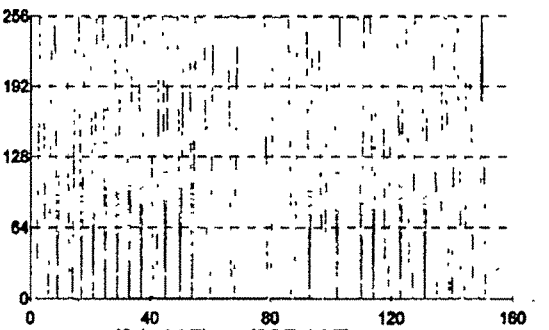

0n

(84, 117) to (237,117)

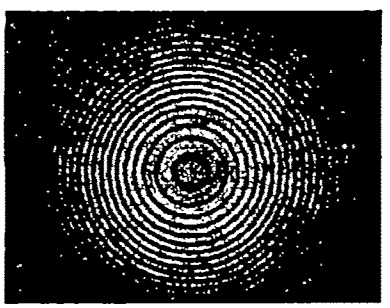

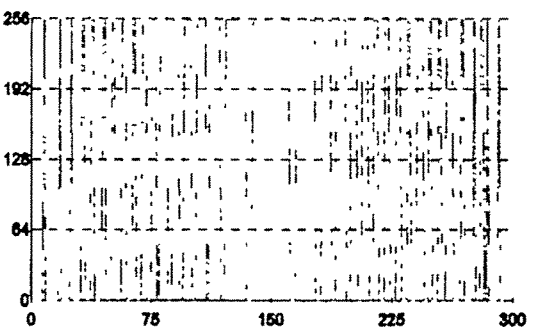

2f

(8,134) to (302, 134)

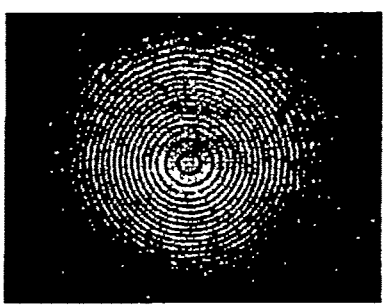

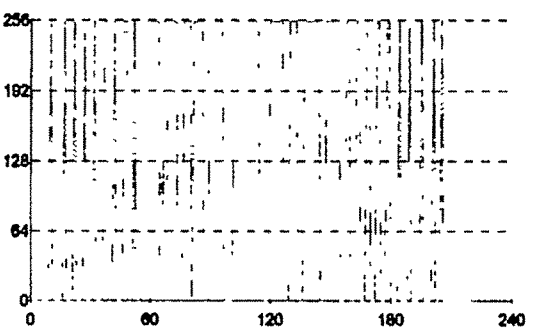

2n

(48,126) to (271, 126)

Fig.4 Fringe patterns along with their line profiles for different circular GRIN samples

RESULTS AND DISCUSSION

Fig. 4 shows the fringe patterns along with their line profiles for different GRIN samples and their respective refractive index profiles after fringe analysis and the necessary computation are depicted in Fig. 5. The comparison of the measured data for GRIN NO.3 with the supplied data shows very good agreement. Comparison for other two samples could not be shown due to the non-availability of the supplied data. It can be concluded that availability of the base glass data will further increase the accuracy of the results. Fig. 6 shows the fringe patterns of rectangular GRIN rods. Fig.7 gives the computer output of a typical circular GRIN samples using fringe analyzer software.

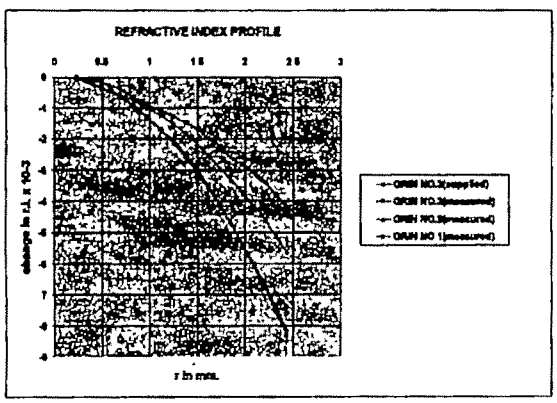

Fig.5 Refractive index profiles for different GRIN samples.

ACKNOWLEDGEMENT

Authors are thankful to the Council of Scientific and Industrial Research, Govt. of India for their financial support to carry out this work.

REFERENCES

1. D.T.Moore, Appl. Opt., 19, 7(1980) 1035-38.
2. J.B. Saunders, J. Nat. Bur. Stand., 73C(1969) 1-4.
3. N.Sood Biswas, S.K.Sarkar, A. Basuray, Opt. Engg., 35(1996) 407-15.
4. Mina Ray (Shah), S.K.Sarkar, A. Basuray and N. Sood Biswas, Int. Conf. On Fiber Optics and Photonics, Dec 18-20, 2000 , Calcutta, Vol..I, 59-62.
5. Md. A. Sekh, A. Basuray and N. Sood Biswas, Int. Conf. On Fiber Optics and Photonics, Dec 18-20, 2000 , Calcutta, Vol..II, 581-83.

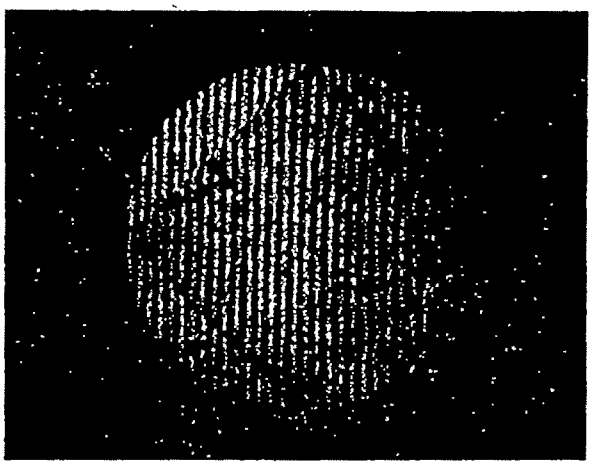

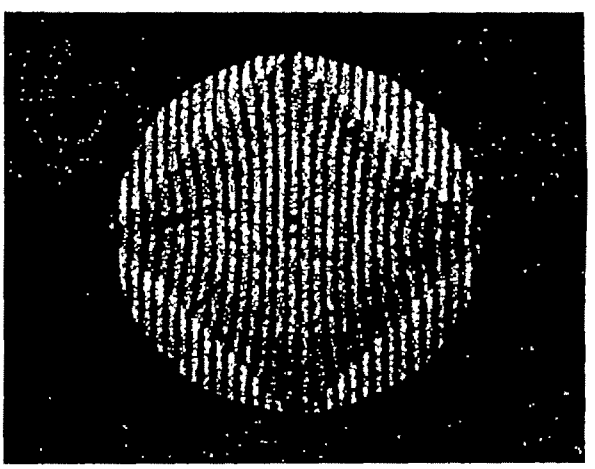

Fig.6 Fringe patterns of a rectangular GRIN rod

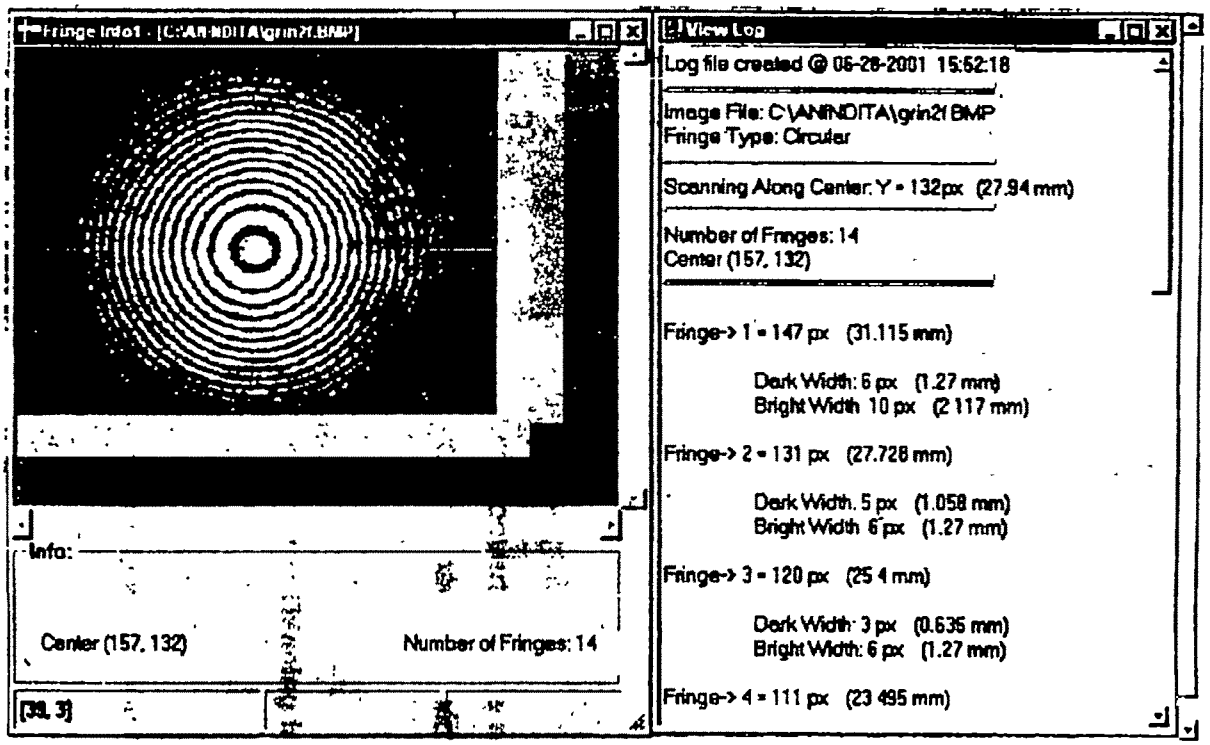
Fringe Info1 - [C:\ANINDITA\grin2f.BMP]
Info:
Center (157, 132)
Number of Fringes: 14
[38, 3]
View Log
Log file created @ 06-28-2001 15:52:18
Image File: C:\ANINDITA\grin2f.BMP
Fringe Type: Circular
Scanning Along Center: Y = 132px (27.94 mm)
Number of Fringes: 14
Center (157, 132)
Fringe-> 1 = 147 px (31.115 mm)
Dark Width: 6 px (1.27 mm)
Bright Width: 10 px (2.117 mm)
Fringe-> 2 = 131 px (27.728 mm)
Dark Width: 5 px (1.058 mm)
Bright Width: 6 px (1.27 mm)
Fringe-> 3 = 120 px (25.4 mm)
Dark Width: 3 px (0.635 mm)
Bright Width: 6 px (1.27 mm)
Fringe-> 4 = 111 px (23.495 mm)

Fig.7 Finding center and calculating fringe-width using fringe analyzer software

Indigenously Developed Optical Computer

Asit K. Datta and Soumika Munshi
Department of Applied Physics, University of Calcutta
92 Acharya Prafulla Chandra Road, Calcutta 700 009, India
email: akdatta@app-physics.org

Abstract

A unique optical computing architecture has been proposed and implemented that can perform arithmetic, logical as well as matrix-vector multiplication operations. The same architecture can be applied to perform some image processing operations like edge detection and skeletonization as well as identifying patterns from their noisy versions. The operation is completely digital and needs no analog to digital conversion. Because of parallel operation in two dimensions, the processing speed is greatly increased.

INTRODUCTION

Since early sixties, there has been considerable interest in the question whether optics could replace or complement electronic techniques in computing and signal processing. Performance of a computer depends very strongly not only on the algorithm but also on the hardware of interconnection capabilities. With the advent of sub-micron technology, the switching delays of a logic gate is likely to fall below 100 ps and clock speed close to few GHz. However it seems that the interconnection capabilities and the system bus technology appears to have reached a final limit. The reason being the physical limitation of the time-bandwidth product of the electronic wires, the topological limitations of the physical layout and the architectural limit known as Von-Neumann bottleneck.

Optics is viewed as an interconnection technology basically for its large bandwidth. The advantages of parallel processing gets multiplied several times when the possibility of interconnection in two or even three dimensions are considered. Optical imaging can provide very easily 1000x1000 parallel non-interactive channels or more. In fact, parallelism and the 2D interconnectivity of optical signal motivate much of the work.

A specific aspect of optical computing [1-5] is that the signal is transmitted not by electrons, but by photons. The presence of photon is taken as 1 and the absence as 0 in the digital logic system and the data can be represented in two or more dimensions. Since optical computations are inherently parallel and non-interactive, arithmetic operations have to be carry-less or symbolic substitution rules have to be evolved.

This paper proposes a unique optical computing architecture that can perform operations like arithmetic, logical, matrix-vector multiplication as well as can process images for pattern recognition. This has called for the development of a bipolar number system for carry-less computations as well as algorithms for image processing tasks like edge extraction and skeletonization and artificial neural network, which can be simulated and operated in such a architecture.

BASIC OPTICAL ARCHITECTURE

The optical architecture for arithmetic and logical operations are based on the shadow casting principle, as shown in fig. 1. Light from a two-dimensional array of sources project a shadow of the superimposed spatially coded input on the decoding mask. Light emerging from the decoding mask is the decoded output image, which is then scanned to obtain the result of desired operation. As shown in fig 1, operational kernels for desired basic operations, such as addition and / or logical operations are entered into the system by the on-off states of the light sources in the two dimensional source array. Data are entered into the system as two dimensional coded pattern according to evolved rules [6].

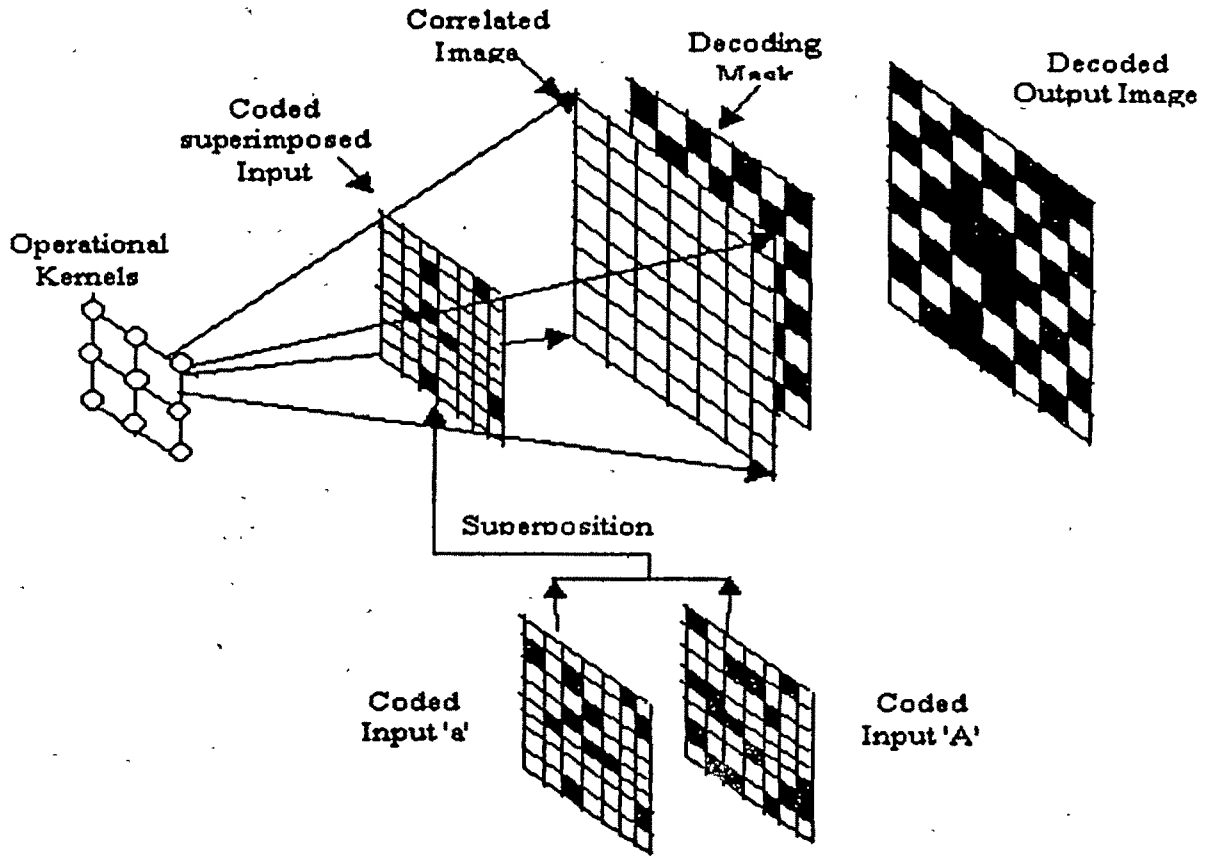

Fig. 1: Shadow casting principle.

On the other hand, matrix-vector multiplication follows the principle of convolution. The vector elements are entered by the on/off states of light sources, whereas the matrix elements are recorded on the input plane. The light from each source is line-imaged on each column of the matrix. The output image is then scanned to yield the convolution coefficients.

Carry-less Addition and Subtraction using Negabinary Number System

Since arithmetic operations need to be carry-less for optical computing, the representation of decimal numbers to other number systems is necessary. The number systems tried earlier are the modified signed-digit [7], mixed ternary number [8], quaternary number systems [9], residue number system [10]. However, these techniques require complex spatial encoding, multiple substitution rules, involve multiple-step algorithms during optical implementation and are less advantageous when multiple number crunching isnecessary. The negabinary carry-less arithmetic [11] however requires no substitution rules for its operation, but restrictions are still imposed on the speed of operation due to its multiple-step architecture.

A modified form of the negabinary number system termed the signed negabinary number system, having digits 0 and $\bar{1}$, has been proposed where a decimal number x has these following unique representation $x_{N-1}.....x_1x_0x_{-1}.....x_{-M}$,.

$$x = \sum_{l=-M}^{N-1} x_l (-2)^l, \qquad x_l \in \{0,\bar{1}\} \tag{1}$$

One of the operands, say A is converted to its equivalent (in 0 and 1's) in unsigned negabinary number system and the other operand, say a is converted to its signed negabinary form (in 0 and $\bar{1}$'s). Addition operation is performed at each bit position in parallel, resulting in four input combinations, $(0+0)$, $(\bar{1}+0)$, $(0+1)$ and $(\bar{1}+1)$.

Since the negabinary and signed negabinary number systems inherently represent negative numbers, subtraction is achieved by addition only. Thus $a - A = a + (-A)$ or $a -$

(-A) = a + A or (-a) - A = (-a) + (-A) or (-a) - (-A) = (-a) + A, where *a* and *A* are positive numbers

Spatial encoding of input data and decoding principle of the result

Since optical computing is done by the manipulation of two dimensional images, spatial encoding of input data is necessary. Fig. 2 shows the spatial coding of the inputs and the possible superimposed input combinations. Fig. 3 represents the on/off states of light sources serving as the operational kernels for desired operation, that project the image of the coded superimposed input on the decoding mask plane, where a decoding mask of the form as shown in fig. 4 is placed. The decoding is done as follows: presence of light in the cell (2,3) is interpreted as 1, presence of light in the cell (3,2) is interpreted as $\bar{1}$, whereas absence of light in any of the cells is 0.

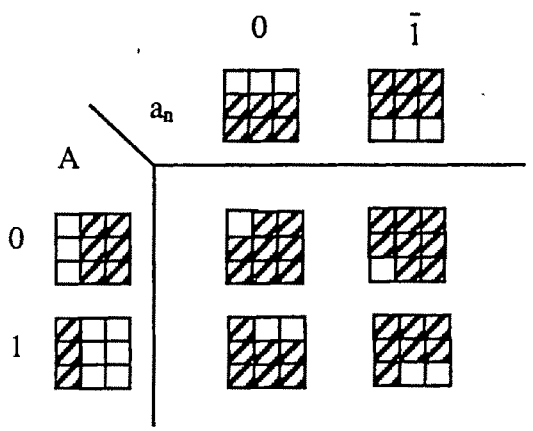

Fig. 2: Spatial encoding of inputs and their superposed patterns

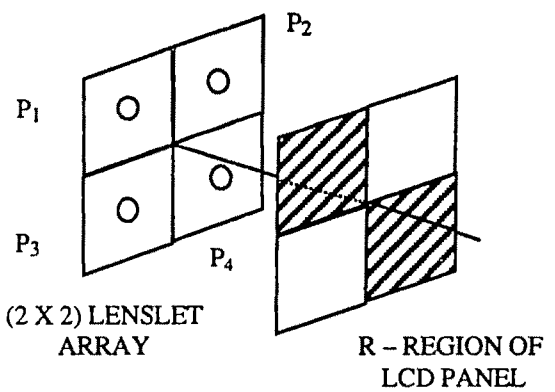

Fig. 3: Cell design on LCD in front of lenslet array.

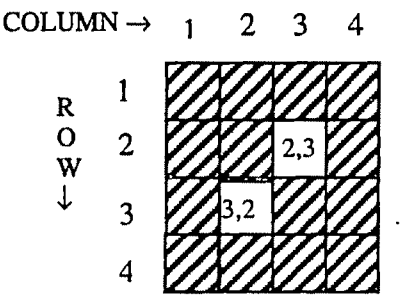

Fig. 4: Decoding mask for arithmetic operations.

The results are obtained in the mixed negabinary form comprising of 1, 0, $\bar{1}$. The mixed negabinary number can be converted back to decimal number system by multiplying the coefficients ($\bar{1}$, 0 or 1) with the corresponding negabinary radix and finally adding up the coefficients.

Logical Operations Using the Signed Negabinary Number System

For logical operation, the input operands *a* or *A* can take on values either 0 or 1 in the decimal number system. Possible input combinations in the decimal form are 00, 01, 10 and 11. Both 0 and 1 are converted to two-bit signed negabinary number forms as 00 and $\bar{1}\,\bar{1}$ respectively. The negabinary forms of the two operands are spatially coded and then superimposed. The superimposed patterns of the input combinations are depicted in fig. 5. On/off states of the sources for logical OR, AND and Ex-OR are shown in fig. 6. Light from the source array projects a shadow of the superimposed coded input over the decoding mask, which is taken of the form as shown in fig. 7. Decoding is done as follows: presence of light in any of the cells (2,2), (2,3), (3,2) or (3,3) is interpreted as $\bar{1}$ and absence of light in any of the cells is 0. The decoded results are multiplied by the corresponding negabinary radices to obtain the final result.

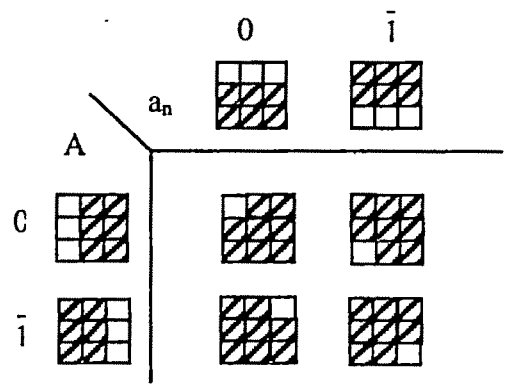

Fig. 5: Spatial coding of inputs and superposed (3x3) bit pattern of the operands 'a' and 'A'.

Logical Function	Source Pattern
A+B	● ○ / ○ ○
A.B	● ● / ● ○
A ⊕ B	● ○ / ○ ●
DON'T CARE	○ ○ / ○ ○

Fig. 6: Source patterns of some logical operations

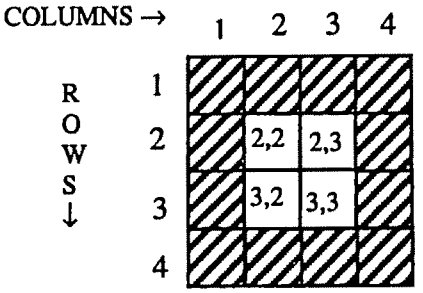

Fig. 7: Decoding Mask for Logical Operations.

The rules for logical operations in signed negabinary number system are

$$0+0=0;\ \ 0+\bar{1}=\bar{1};\ \ \bar{1}+\bar{1}=\bar{1};\ \text{(OR operation)}$$
$$0\bullet 0=0;\ \ 0\bullet\bar{1}=0;\ \ \bar{1}\bullet\bar{1}=\bar{1};\ \text{(AND operation)} \quad (2)$$
$$0\oplus 0=0;\ 0\oplus\bar{1}=\bar{1};\ \bar{1}\oplus\bar{1}=0.\ \text{(Ex-OR operation)}$$

Negabinary number based Matrix-Vector Multiplication

Several digital techniques were proposed for matrix-vector multiplication in which the technique of so-called 'digital multiplication by analogue convolution' (DMAC) techniques [12] is utilized for optical computation. The binary technique [13] utilizes sign-bits for bipolar number representation. The proposed negabinary number based digital matrix-vector multiplier does not use sign bits for negative number representation and eliminates A/D conversion and successfully achieves the demanded accuracy at the expense of long processing time.

Realized through convolution operation using the unsigned negabinary number system, the product h of two L digit numbers a and A, expressed in base S is represented by,

$$h = aA = \sum_{i=0}^{L-1}\sum_{j=0}^{L-1} a_i A_j (-2)^{(i+j)} \quad (3)$$

where, $a = \sum_{i=0}^{L-1} a_i (-2)^i$ and $A = \sum_{j=0}^{L-1} A_j (-2)^j$ (4)

The convolution coefficients $a_n A_n$ can only take on values as 0 and 1.

No carry is produced when multiplication is carried out by DMAC procedure with a mixed representation (i.e., decimal weight factor h_n and negabinary radix $[-2]^n$) as indicated. For example, multiplication of (-4) and (-5) results in 01222100 which when multiplied by the corresponding negabinary radix yields the value 20.

UNIFIED ARCHITECTURE FOR ARITHMETIC, LOGICAL AND MATRIX-VECTOR MULTIPLICATION

Fig. 8 shows the unified optical architecture that can perform arithmetic, logical, matrix-vector multiplication. Use of a single liquid crystal panel (LCD) and folding of optical path in the proposed architecture has reduced the cost and complexity to a large extent with regard to spatial tolerance. Moreover the use of a single LCD panel serves the double purpose of introduction of operational kernels as well as input data.

Light ray follows the path $M_1M_4RB_2M_3SM_5M_6T$ for arithmetic and logical operations based on the optical projection or shadow casting principle as seen from fig. 8. As seen, light from a laser source is incident on a (2x2) lenslet array LA_2, which acts as point sources. The lenslet array in combination with the addressable opaque and transparent cells on the R region of the LCD panel introduces operational kernels in the architecture. The spatially encoded bits of the two operands are superimposed and the resulting pattern is recorded in the input plane at the location S of the LCD. An angular projection of this superimposed pattern is formed at location T on the LCD panel, which is then decoded and processed to obtain the result.

For matrix-vector multiplication light takes the path $M_1B_1QM_2M_3SM_5M_6T$ based on the principle of convolution operation. The unsigned negabinary equivalents of the vector elements are entered by the on/off states of light sources. The matrix in unsigned negabinary form is recorded on an electrically addressed LCD panel. The partial products are recorded on a two-dimensional detector array and added in a computer to yield the convolution coefficients. As seen, light from the same laser source is transformed as a horizontal line-image using CL_1 and then focused as a one-dimensional array of eight sources by means of a lenslet array LA_1. The light transmitted from the

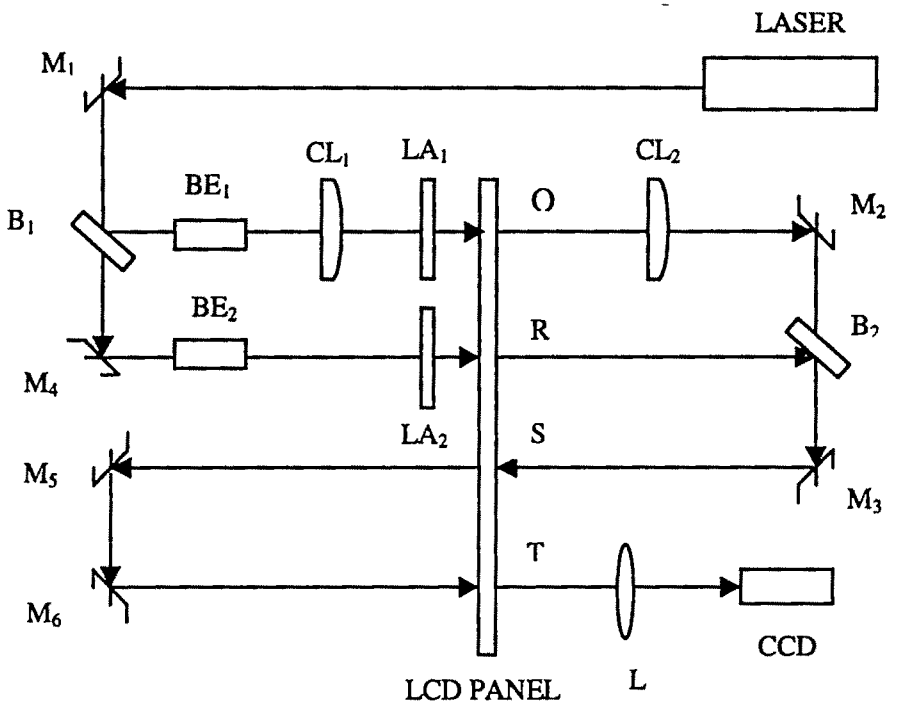

Fig. 8: Composite optical arrangement for implementing arithmetic, logical and matrix-vector operations. $M_1, M_2, \ldots M_6$: Mirrors; BE_1, BE_2 : Beam Expanders; B_1, B_2: Beam Splitters; LA_1, LA_2 : Lenslet Arrays; CL_1, CL_2: Cylindrical Lens; L; Condensing Lens; Q,R,S,T: Regions on the LCD panel.

sources is modulated through the location Q of the LCD panel in accordance with the negabinary equivalents of the elements of the vector. The cylindrical lens CL_2 transforms the light from each light source into a line-image, parallel to the axis of the cylindrical lens, which is incident on each column of the line-image recorded at the location S of the LCD. The line-image recorded at location S of the LCD represents the negabinary equivalents of each element of a row of matrix. Light signal from the LCD after convolution is passed undisturbed through location T of the LCD, condensed by condenser lens L onto the CCD camera. The captured image is scanned and processed to obtain the results of multiplication.

APPLICATIONS OF THE DEVELOPED OPTICAL COMPUTING ARCHITECTURE IN IMAGE PROCESSING

The developed optical computing system is capable of undergoing some low level image processing as well as pattern recognition tasks. Implementation of optical morphological operation can be carried out for edge extraction and skeletonization with the help of the developed system. Furthermore, since the basic principle underlying artificial neural networks is a matrix-vector multiplication operation, so pattern recognition can also be done using this architecture.

Edge-detection and Skeletonization using Morphological Transformation

Edge extraction and skeletonization can be obtained by morphological operations in an optical architecture by suitably modifying the algorithm using the technique of angular shift.

If $P|N;N|_{ij}$ is the state of i,j-th cell in the edge detected image, $\overline{A}\,|N;N|$ is the inverted input image A, $C|N;N|$ is the morphologically dilated image of A by structuring element B, represented by $(A \oplus B)$, then the state of the edge extracted image is

$$P|N;N| = \overline{A}|N;N| \bullet C|N;N| \qquad (5)$$

where " $\bullet$ " denotes logical *AND* operation.

The complete skeleton is the union $\bigcup_n$ (or logical *OR* operation) of all the n skeletal components of A and can be represented as

$$S = \bigvee_{n} [(A \ominus B)|_n - \{(A \ominus B)|_n \circ B\}] \quad (6)$$

where $(A \ominus B)|_n$ represents n-times erosion of A by structuring element B, $\{(A \ominus B)|_n \circ B\}$ represents n-times erosion of A, followed by morphologically opening (opening of an image is the erosion operation followed by dilation of the image) the eroded image by B and "-" computes difference of two images.

Optical array logic architecture is basically an optical morphological processing technique, where the structuring element is in the form of an array of point sources. Based on the angular projection principle, an easy method for edge-detection as well as skeletonization has been proposed. Based on the optical array logic architecture, methods have been evolved where edges of images can be detected optically by shift operation of input image in two-dimensional space [14]. Techniques for skeletonization [15] that have already been proposed result in shape distortions.

The technique involves some basic dilation and erosion operations. The partially overlapped optical projections of the input image (white object in a dark background) projected by a (2x2) source array results in dilation, whereas the partially overlapped optical projections of the inverted input image results in erosion. Light follows the same path as that for arithmetic or logical operations as shown in Fig. 8. All the sources in the source-array are kept at 'on' state. The (2x2) source-array casts four shifted optical projections of the input image (white object in a dark background and the reverse for skeletonization) recorded at S portion of the LCD panel. The overlapped projections are then projected at the T portion of the LCD panel. Light transmitted through this portion is condensed into a CCD camera.

For edge detection, the input image is recorded at S region of the LCD panel. The partially overlapping projections results in a dilated image, which when superimposed with the complementary input image, recorded at T portion of the LCD panel, produces the edge-image that is recorded by a CCD camera. The technique for edge extraction in case of binary images involves a single step process.

Whereas for skeletonization, the source-array casts four partially overlapped angular projections of the inverted input image, recorded at the S region of the LCD panel. The T region of the LCD panel is kept transparent. Hence the light that passes undisturbed through this region is recorded by the camera and then negated. This overlapped eroded image is again eroded and then dilated, producing an opened image, which is again recorded. The difference of the eroded and opened image is then computed, resulting in a skeletal image. This procedure of obtaining the skeleton is repeated till the difference-image becomes zero. Skeletonization is therefore an iterative process.

The system has the advantage of single instruction parallel processing of image. The techniques have been tested both for binary and grey images. The grey images are thresholded at all possible grey levels and then edges or skeletons extracted at all these thresholded values. Results of edge extraction and skeletonization of images are shown in Figs. 9(a) and 9(b).

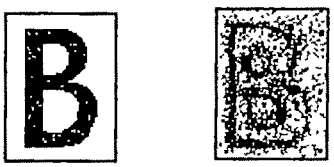

Fig. 9(a): Alphabet "B" and its experimentally obtained edge-image.

Fig. 9(b): Simulated edge image and skeleton of hand-written "6".

Winner-take-all Neural Network for Associative Pattern Recognition

Neural network [16] is an extensively useful class of network that utilizes an associative memory retrieval process for pattern recognition. The process of recognition comprises of 'training or learning phase' followed by the 'recall' phase of the learnt pattern, provided that the presented unknown pattern matches any of the trained pattern.

The entire process of training followed by the process of recall can be represented by a process of multiplication of the inputs (in the form of vectors) to the network with the weight factors (in the form of matrices) of the interconnection strengths. The n inputs (S^n), of dimension (p x q), are presented to the network for training through a set of q input nodes. The weight determines the interconnection strength between the input and output nodes. If the weight matrix is w_{nq}, it is formed by taking the same row (say p-th row) of each of the training patterns. Thus a total number of p training matrices are created. The output Y_n is given by the weighted sum of the inputs X_q as,

$$Y_n = \sum w_{nq} X_q \quad (7)$$

The highest output vector element is designated as 1, i.e., winner and the rest as 0. The selection of the maximum element of the output vector is justified because the

autocorrelation between the unknown input pattern and one of the trained patterns is maximum when the two patterns match. The corresponding row of the training matrix, which has produced this 1, is the correct match and the corresponding pattern is the correctly recalled pattern.

Since a matrix-vector multiplication process is the core element of the model, optical implementation of the matrix-vector multiplication [17] has been studied. Training matrices are recorded on electrically addressed spatial light modulator, where each matrix is composed of the same row of each pattern that the network is being trained with. After training, if an unknown pattern is presented to the network in the form of a vector, the output vector is obtained by the element that has the highest magnitude through a winner-take-all algorithm. Pattern can be recognized even if the input is noisy and distorted.

Since this pattern recognition process basically involves matrix-vector multiplication operation, so the light rays in Fig. 9 follows the said path as described above. Each row of the unknown input binary pattern is presented to the network as on/ off states of light sources representing one/ zero of the binary pattern. The source array LA_1 in combination with the control at the region Q of the LCD panel serves the purpose of introduction of the unknown binary pattern. The training matrix is recorded at the S portion of the LCD panel. The output transmitted through the T region of the LCD panel is condensed onto a CCD camera, scanned to yield the winner. All the rows are similarly processed to decide on the winning pattern. Patterns recognized from their distorted versions by the proposed system are shown in Fig. 10.

Noisy Input Pattern | Target Pattern | Recognised Pattern

Fig. 10: Patterns recalled from their distorted

CONCLUSION

This paper reports the evolution of an optical computing system built and tested for carry-less arithmetic, logical and matrix-vector multiplication on 8 and 16 bit data. Photographs of the developed optical computing setup are shown in fig. 11. The technique and implementation issues have shown the parallel processing capabilities of the free space interconnection along with the bipolar data handling capability of the system. The optical computing system is then utilized for image processing operations such as skeletonization and edge detection of input image. The technique of optoelectronic matrix vector multiplication architecture has been utilized as the basic building block for realizing artificial neural networks for pattern recognition.. It has been shown that the proposed technique is capable of identifying image from its partial and distorted input.

ACKNOWLEDGEMENT

The author (S.M.) is grateful to DST (GOI) and CSIR for funding to carry out the work.

REFERENCE

1. D. Smith and D. Miller, "Computing at the speed of light," New Scientist, Vol. 85, p 554, 1980.
2. E. Abraham, C. T. Seaton and S. D. Smith, "The optical computer," Scientific American, Vol. 248, p 63, 1983.
3. Sawchuk, and T. C. Strand, "Digital optical computing," Proc. IEEE, Vol.72, p 785, 1984.
4. Huang, "Optical Computing: Is concept becoming reality?", SPIE, 78 (1990).
5. J. Shimada,"Optical Computing: pros and cons", *Optical Computing in Japan*, Nova Science, Commak (1990).
6. J. Tanida and Y. Ichioka, "Optical logic array processor using shadowgrams", J. Opt. Soc. Am. 73, 800 (1983).
7. R. P. Bocker, B. L. Drake, M. E. Lasher and T. B. Henderson, "Modified signed-digit addition and subtraction using optical symbolic substitution", Appl. Opt., 25, 2456-2457 (1986).
8. A.K. Datta, A. Basuray and S. Mukhopadhyay, "Arithmetic operations in optical computations using a modified trinary number system", Opt. Lett., 14, 426-428 (1989).
9. M. S. Alam, K. Jemili and M. A. Karim, "Optical higher-order quaternary signed-digit arithmetic", Opt. Eng. 33, 3419-3426 (1994).
10. S. Mukhopadhyay, A. Basuray and A, K, Datta," New technique of arithmetic operation using positional residue system". App. Opt. 29, 2981-2893, (1990).
11. G. Li, L. Liu, L. Shao and Z. wang, "Negabinary arithmetic algorithms for digital parallel optical computation", Opt. Lett. 19, 1337-1339 (1994).

12. D. Psaltis, D. Casasent , D. Neft and M. Carlotto, "Accurate numerical computation by optical convolution", Proc. SPIE 232 (1980) 151.
13. S. Bandyopadhyay , A. K. Datta , S. S. Bawa , A. M. Biradar and S. Chandra, "Realization of digital optical matrix-vector multiplication", J. Phys. D: Appl. Phys. 28 (1995) 7-11.
14. K. Datta and M. Seth, "Cellular processing for edge detection in an optical shadow casted architecture", Optics and Laser Technology, 26 (1994) 297.
15. R. He, H. Yan and J. Hu, "Skeletonization algorithm based on cross segment analysis", Opt. Eng. 38(4), (1999) 662-671.
16. J. J. Hopfield, D. W. Tank, "Neural computation of decision in optimization problems", Biol. Cybern., 52, (1985), 141-152.
17. Soumika Munshi, Nabendu Saha and Asit K. Datta, "A negabinary number based optical matrix-vector multiplier", Optik, 110, (1999), 378-382.

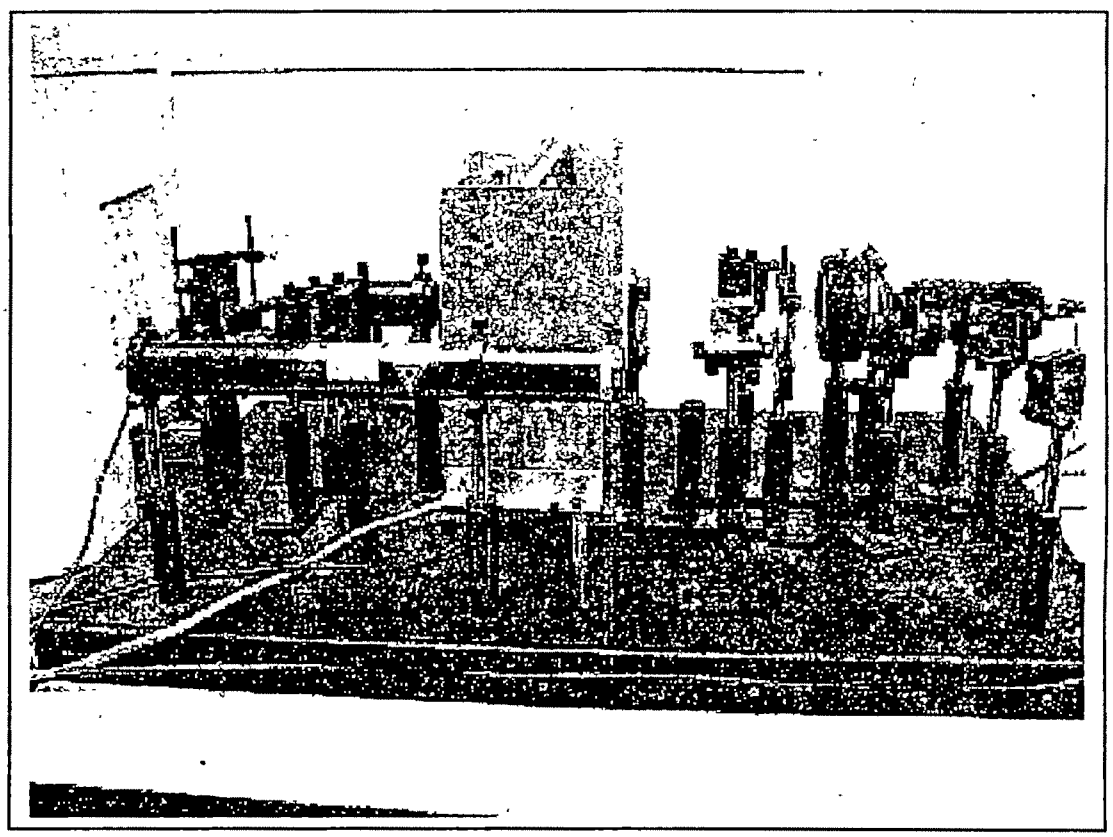

Fig. 11: Photograph of the developed unified optical computing architecture

Laser Beam Shaping using Phase-Only Filter at Fractional Fourier Transform Plane

K. N. Dey*, S. Sanyal* and Ajay Ghosh*
*Department of Computer Science, *Department of Applied Physics
University of Calcutta, 92, A.P.C.Road, Calcutta 700009, India
E-mail : ajay_ghosh@hotmail.com

Abstract

The present paper reports a technique for laser beam shaping using phase-only filters at fractional Fourier transform plane. Fresnel transform has been used for analyzing the system and the corresponding computer software is developed for simulating the performance of the setup. The same has been tested and experimentally verified for a periodic grating as object. The possibility of achieving the effect of spatial frequency filtering by using suitable mask function at fractional Fourier transform planes has been explored. It has been found that the proposed filters are well suited for shaping of laser beams. The results are presented and discussed.

Keywords : Laser Engineering, Optical Design, Beam Shaping

INTRODUCTION

The output profile of the most of the conventional laser resonators is Gaussian in nature. In the recent past a number of beam-shaping techniques has been reported for converting the gaussian profile to any profile useful for some specific applications [1-4]. A commonly used technique is to truncate the beam by an aperture. A neutral density filter having suitable transmittance profile may also be used for getting a flat top profile, which has many important applications in optical processing, laser micro-fabrication and laser surgery. Unfortunately, all these techniques suffer from a serious limitation of having very low energy efficiency. Another reported technique is to use binary diffraction gratings [5-6]. This technique is also associated with limited diffraction efficiency. Aspheric reflective mirrors or aspheric lenses have also been used for redistributing energy of a gaussian beam and are highly energy efficient. But fabrication of these elements is very difficult and the applications are limited to only circular beam shaping geometry [7-8]. A phase-only filter in this respect is highly effective and its theoretical energy efficiency may approach 100%. Phase-only filters belong to a class of absorption-less optical elements, which can change the phase profile of any incoming beam, which, in turn, changes the intensity profile at the focal plane of a lens placed after the filter. The present communication reports of using such a filter at the fractional Fourier transform plane with the intention to change the profile of the laser beams. This may remove certain limitations associated with the conventional spatial filtering setup, which uses an architecture capable of performing only linear space invariant operations, i.e., the operations that can be expressed as a convolution of the input function with a space invariant impulse response. The manipulation of the spatial frequency spectrum also requires delicate and sophisticated setups due to its utmost fineness and minute localization of the spectrum.

Based on the pioneering work of Namius [9], McBrid *et.al.* [10] gave the mathematical foundation of the fractional Fourier transform (FRT). Apparently their work could not attract much interest until Ozaktas and Mendlovic [11-13] suggested different techniques for optical implementation of FRT based on a physical definition utilizing the propagation of light beams through the graded index medium. They also established relations of FRT with Radon-Wigner, chirp and wavelet transforms [14-16]. A definition of FRT based on Wigner distribution function was suggested by Lohmann [17]. He along with other scientists later proved the equivalence of both the definitions [18]. Several scientists implemented FRT in the Fresnel domain using free space propagation. Bernardo [19] used ABCD matrix formalism as a tool for derivation of

FRT results. We refer to Lohmann *et.al.* [20] for an excellent review of FRT and its applications in optics.

In what follows, the field distribution at the half transform plane is obtained using Fresnel transform as the analyzing tool [21]. The same setup is simulated using computer. Some of the computed results obtained so far have been verified experimentally. Finally the effects of spatial filtering at the half transform plane is simulated and presented to show the utility of such filters in laser beam shaping.

MATHEMATICAL FORMULATION

Let us consider that $\psi(x_1,y_1;0)$ is the wave amplitude distribution in $(x_1,y_1;0)$ plane of a monochromatic light wave propagating along Z-axis of a reference coordinate system. It is well known that the wave amplitude distribution $\psi(x_2,y_2;z_1)$ at any parallel plane at a distance z_1 is the result of a convolution operation with an appropriate Fresnel function

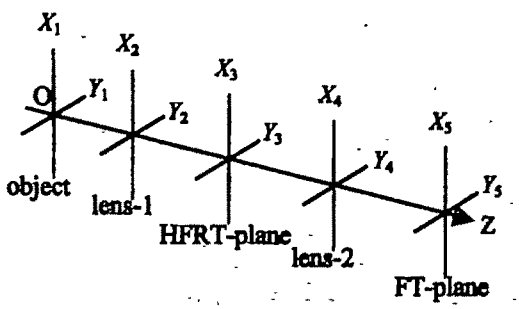

Fig. 1 A schematic diagram of the FRT setup

which may be expressed as

$$f_z^{\lambda}(x,y) = \frac{i}{\lambda z}\exp[-\frac{i\pi}{\lambda z}(x^2+y^2)] \qquad (1)$$

The operation may be written in usual notations as follows,

$$\psi(x_2,y_2;z_1)=\psi(x_1,y_1;0)\otimes f_{z_1}^{\lambda} \qquad (2)$$

The subscript 2 is used to indicate that the plane of investigation is a different plane parallel to the plane denoted by subscript 1. Now, ignoring the finiteness of the lens aperture the complex amplitude transmittance of a thin convex lens is given by,

$$L(x,y) = \exp[\frac{i\pi}{\lambda f}(x^2+y^2)] \qquad (3)$$

where, f is the focal length of the lens. If the lens is considered to be ideally thin then the wave amplitude distribution $\psi_L(x_2,y_2;z_1)$ just after the lens may be expressed as

$$\psi_L(x_2,y_2;z_1) = \psi(x_2,y_2;z_1)L(x_2,y_2) \qquad (4)$$

So, the wave amplitude distribution $\psi(x_4,y_4;z_1+z_2)$ at a distance z_2 from the lens may be obtained in a similar fashion, i.e.,

$$\psi(x_4,y_4;z_1+z_2) = \psi_L(x_2,y_2;z_1)\otimes f_{z_2}^{\lambda} \qquad (5)$$

Proceeding accordingly, the final form of the wave amplitude distribution at the output plane of the optical system shown in figure-1, i.e., at the plane at a distance z_3 from an identical second lens may be shown to be given by

$$\psi(x_5,y_5;z_1+z_2+z_3)= [\psi(x_4,y_4;z_1+z_2)\,L(x_4,y_4)]\otimes f_{z_3}^{\lambda} \qquad (6)$$

Writing explicitly

$$\psi(x_5,y_5;z_1+z_2+z_3)= \frac{i}{\lambda z_1}\frac{i}{\lambda z_2}\frac{i}{\lambda z_3}\exp[\frac{i\pi}{\lambda z_3}(x_5^2+y_5^2)] \iiint\iiint \psi(x_1,y_1;0)\exp[-\frac{i\pi}{\lambda z_1}(x_1^2+y_1^2)] \exp[\frac{i\pi}{\lambda}\{\frac{x_2^2+y_2^2}{K_1}+\frac{x_4^2+y_4^2}{K_2}\}] \exp[\frac{2i\pi}{\lambda}\{\frac{1}{z_1}(x_1x_2+y_1y_2)+\frac{1}{z_2}(x_2x_4+y_2y_4)\}] \exp[\frac{2i\pi}{\lambda z_3}(x_4x_5+y_4y_5)]dx_1dx_2dx_4dy_1dy_2dy_4 \qquad (7)$$

where the limits of the integrations are extended from $-\infty$ to $+\infty$. After proper substitutions and using the following standard relation of Fresnel function

$$\frac{i}{\lambda z}\int_{-\infty}^{\infty}\int\exp[-\frac{i\pi}{\lambda z}(x^2+y^2)]\exp[2\pi i(ux+vy)]dxdy = \exp[i\pi\lambda z(u^2+v^2)]$$

(7) will be reduced to

$$\psi(x_5,y_5;z_1+z_2+z_3)=$$
$$\frac{iK_2K_3}{\lambda z_1 z_2 z_3}\exp\left[-\frac{i\pi}{\lambda z_3}\left(1-\frac{K_2}{z_3}-\frac{K_2^2K_3}{z_2^2 z_3}\right)(x_5^2+y_5^2)\right]$$
$$\int_{-\infty}^{+\infty}\int_{-\infty}^{+\infty}\psi(x_1,y_1;0)\exp\left[-\frac{i\pi}{\lambda z_1}\left(1-\frac{K_2}{z_1}\right)(x_1^2+y_1^2)\right]$$
$$\exp\left[2\pi i\left(\frac{K_2K_3x_5}{\lambda z_1 z_2 z_3}x_1+\frac{K_2K_3y_5}{\lambda z_1 z_2 z_3}y_1\right)\right]dx_1\,dy_1 \qquad (8)$$

where,
$$\frac{1}{K_1}=\frac{1}{z_2}+\frac{1}{z_1}-\frac{1}{f}$$
$$\frac{1}{K_2}=\frac{1}{z_3}+\frac{1}{z_2}-\frac{1}{f} \qquad (9)$$
$$\frac{1}{K_3}=\frac{1}{K_1}+\frac{K_2}{z_2^2}$$

In the above analysis it is assumed that different orders of FRT lie between the object plane and the Fourier transform plane. This is actually a necessary consequence of Huygen's principle. Since the dual action of focusing and propagation are not interleaved in this system, the exact placement of different orders will be difficult to find out. If the system is centrally symmetric along the direction of propagation, then according to the above logic, the half-order FRT will be present at the central plane [22]. It can be shown that the condition to get the half-order FRT is

$$z_1=f(1-1/\sqrt{2}) \qquad (10)$$
$$z_2=f(2-\sqrt{2}) \qquad (11)$$
$$z_3=f(1-1/\sqrt{2}) \qquad (12)$$

So, in fig.-1 if z_1, z_2 and z_3 follow the conditions given by (10), (11) and (12) respectively, then at a distance $z_2/2$ from the first lens, i.e., in the (x_3,y_3) plane, one gets the half-order FRT.

Using the above conditions the wave amplitude distribution at the half order FRT plane may be written as

$$\psi[x_3,y_3;2p]=[\{\psi(x_1,y_1;0)\otimes f_p^{\lambda}\}\,L(x_2,y_2;f)]\otimes f_p^{\lambda} \qquad (13)$$

where $p=(1-1/\sqrt{2})f$.

Writing (13) in a similar manner the half order FRT of any function $\psi(x_1,y_1;0)$ may be written as

$$FRT_H\left[\psi(x_1,y_1;0)\right]=$$
$$\left(\frac{i}{\lambda}\right)\left(\frac{2}{f}\right)\exp\left[\frac{i\pi\sqrt{2}}{\lambda f}\left(x_3^2+y_3^2\right)\right]$$
$$\int_{-\infty}^{\infty}\int_{-\infty}^{\infty}\psi(x_1,y_1;0)\exp\left[\frac{-i\pi\sqrt{2}}{\lambda f}\left(x_1^2+y_1^2\right)\right]$$
$$\exp\left[\frac{i4\pi}{\lambda f}\left(x_3x_1+y_3y_1\right)\right]dx_1\,dy_1 \qquad (14)$$

Substituting

$$\left.\begin{aligned}X_1&=x_1/\sqrt{\lambda f/2}\\Y_1&=y_1/\sqrt{\lambda f/2}\\X_3&=x_3/\sqrt{\lambda f/2}\\Y_3&=x_3/\sqrt{\lambda f/2}\end{aligned}\right\} \qquad (15)$$

(14) reduces to

$$FRT_H\left[\psi(x_1,y_1;0)\right]=i\exp\left[\frac{i\pi}{\sqrt{2}}\left(X_3^2+Y_3^2\right)\right]$$
$$\int_{-\infty}^{\infty}\int_{-\infty}^{\infty}\psi(X_1,Y_1;0)\exp\left[\frac{-i\pi}{\sqrt{2}}\left(X_1^2+Y_1^2\right)\right]$$
$$\exp\left[2i\pi\left(X_3X_1+Y_3Y_1\right)\right]dX_1\,dY_1$$
$$=i\exp\left[\frac{i\pi}{\sqrt{2}}\left(X_3^2+Y_3^2\right)\right]$$
$$\text{F.T.}\left[\psi(X_1,Y_1;0)\exp\left\{\frac{-i\pi}{\sqrt{2}}\left(X_1^2+Y_1^2\right)\right\}\right] \qquad (16)$$

The result is in the reduced coordinate (X_3,Y_3). The actual distribution in (X_3,Y_3) plane may be obtained using conversion relations given in (15).

From the above relation it may be concluded that half-order FRT of any function is a product of Fresnel function and the Fourier transform of the product of the given function in a specified reduced coordinate with another Fresnel function. Hence, well-developed fast algorithms of conventional Fourier transforms can be used for computations of half-order FRT in order to exploit the vast potential of FRT in different fields of optics.

RESULTS AND DISCUSSIONS

Based on the above analysis computer software is developed to simulate the fractional Fourier transforming optical system and visualize half order FRT of any object function. The same is tested with a grating as the object. It has been found that the

experimental result and that obtained using computer are same.

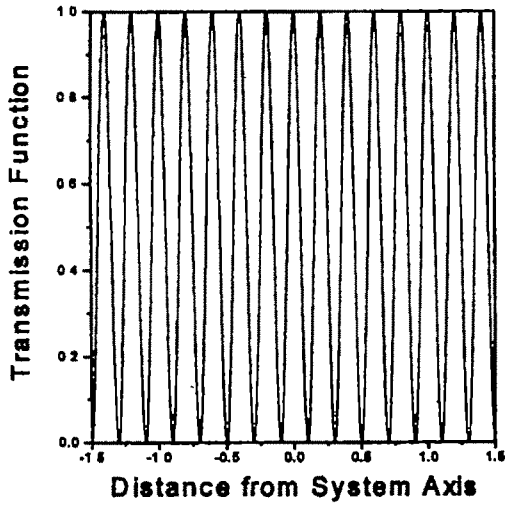

Fig. 2(a) The object function ; a sinusoidal grating

Figures - 2(a, b, c) show the object function, its half transform and the Fourier transform respectively obtained using computer. It may be recalled that the results are similar to that obtained by Lohmann *et.al.* using Wigner distribution approach [17]. But a close comparison reveals that it is easier to interpret the results in terms of the coordinates of the object plane and that of FRT plane while classical Fresnel diffraction theory is used for analysis. Figure – 3(a, b) shows the image of grating and its half transform respectively. The grating used for practical demonstration is a square-top one.

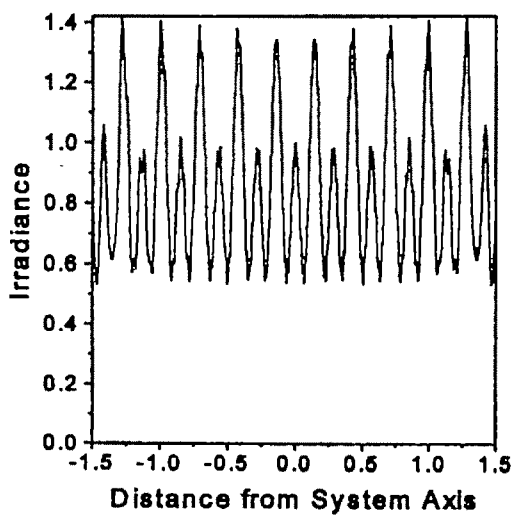

Fig. 2(b) The half-order FRFT of the object function shown in fig.-2(a)

Hence the result has some difference with the theoretical one. It should be noted that the frequency of the grating formed at half transform plane is exactly 1.4 times in both the cases

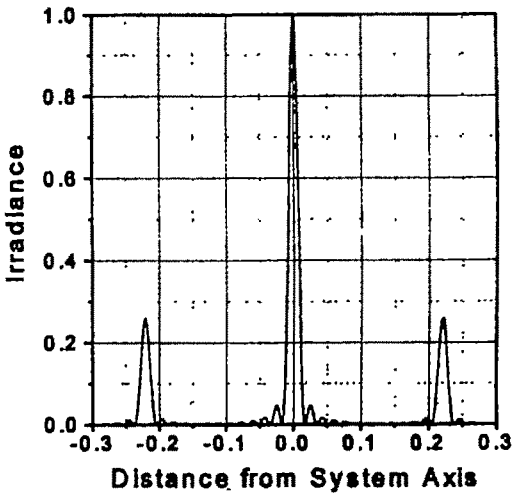

Fig. 2(c) The Fourier transform of the object function shown in fig.-2(a)

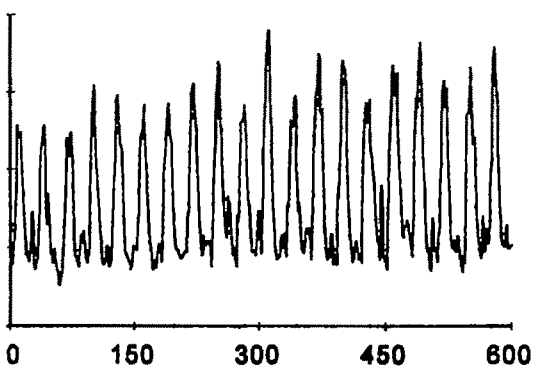

Fig. 3(a) Experimentally obtained intensity transmittance of a grating

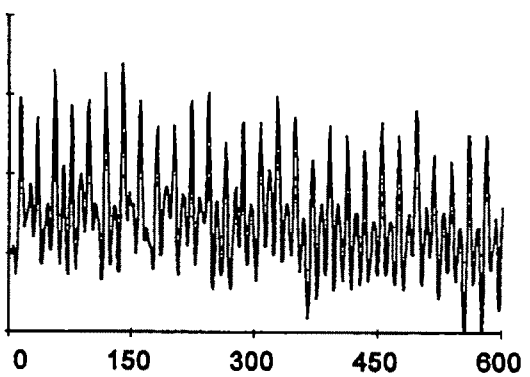

Fig. 3(b) Experimentally obtained intensity transmittance of the same grating at half transform plane

Figure – 4 shows a Gaussian profile of the input function and its profiles at half-transform and full-transform plane.

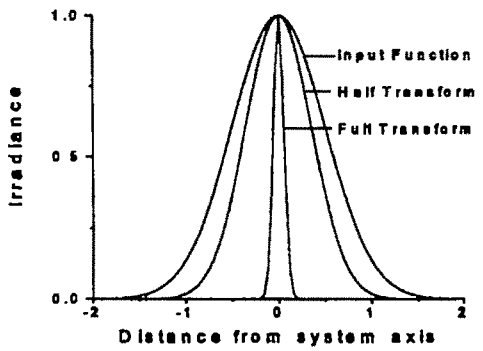

Fig. 4 Gaussian profile, its half transform and full transform

The technique is extended for spatial filtering using a mask at half transform plane. A computer simulated

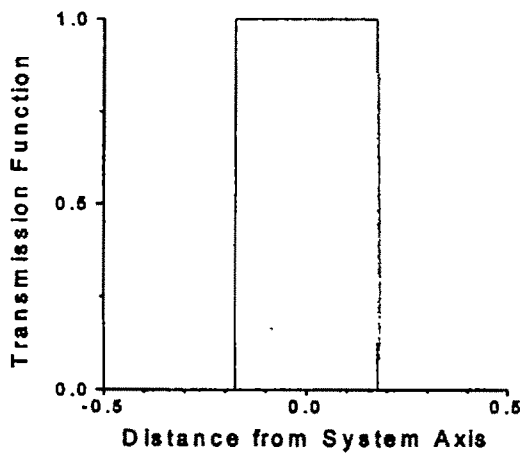

Fig. 5(a) The object function : a slit

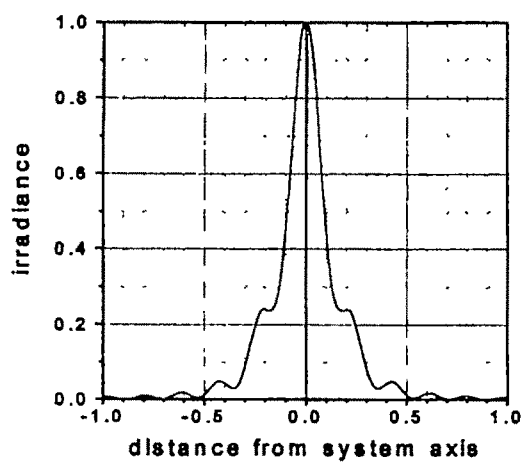

Fig. 5(b) The half-order FRFT of the slit shown in fig.-5(a)

experiment clearly indicates that a band pass π -phase mask at half transform plane can extract edges of a slit placed at the object plane (see fig-5 (a,b,c,d,e)).

Figure-5(a) shows the input object while fig.-5(b) and fig.-5(c) are its half transform and Fourier transform respectively. Figure -5(d) depicts the mask function and its position with respect to the half transform obtained and fig.-5(e) represents the filtered output. It is to be noted that unlike Fourier transform plane where the input function is totally resolved into its frequency components, FRT planes composed of information of both the spatial characteristics and the frequency characteristics of the input function. Naturally any physical filtering operation will affect both the functions.

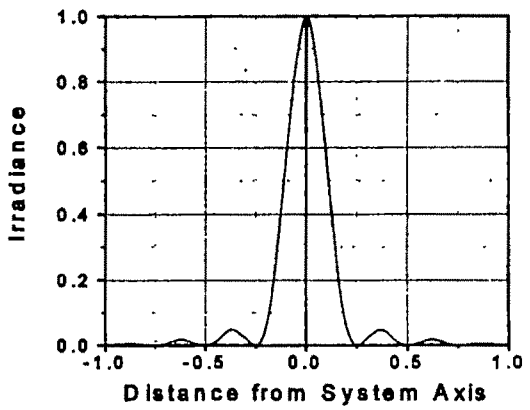

Fig. 5(c) The Fourier transform of the slit

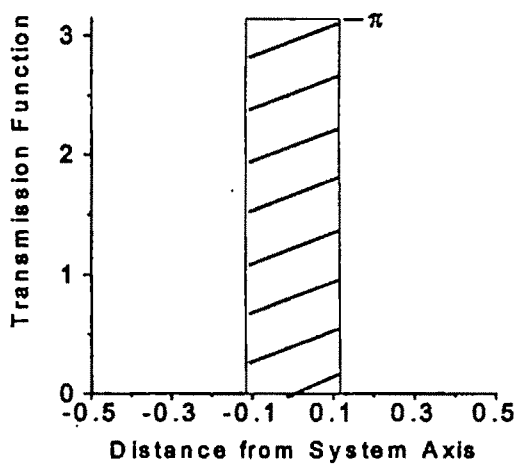

Fig. 5(d) The filter function with respect to the same coordinate axis as the half transform

It may be concluded from the above discussion that the filtering at fractional order planes is a nonlinear

operation and depends on the input object information. In other words, the filters so designed are

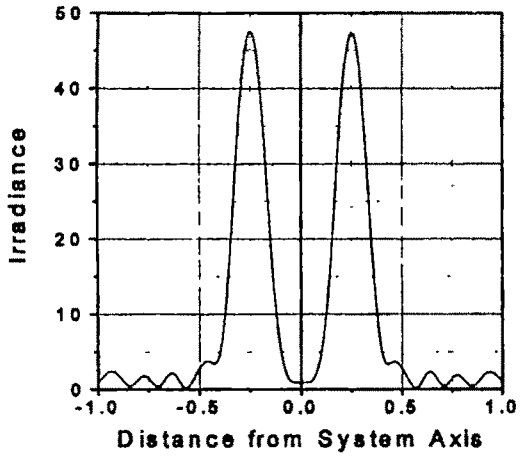

Fig. 5(e) The filtered output of the slit function used

dedicated in nature. From what is obtained so far it seems that a new class of filters may be generated which can be used at FRT planes for laser beam shaping and so on.

ACKNOWLEDGEMENT

This work is funded by Armament Research Board, Ministry of Defence, Govt. of India.

REFERENCES

1. V.V.Kotlyar, I.V.Nikolsky and V.A.Soifer, "Adaptive iterative algorithm for focusators synthesis", Optik, 88 (1991) 17.
2. P.M.Dickey and S.C.Holswade, "Gaussian laser beam profile shaping", Opt.Eng., 35 (1996) 3285.
3. S.Kawakami and O.Ogawa, "Light beam redistribution using computer generated phase plates", J.Lightwave Tech., 7 (1989) 1412.
4. R.M.Stevenson et al, "Binary-phase zone plate arrays for the generation of uniform focal profiles", Opt.Lett., 19, (1994) 363.
5. M.Kuittinen, P.Vahimaa, M.Honkanen and J.Turunen, "Beam shaping in the nonparaxial domain of diffractive optics", Appl.Opt., 36, (1997) 2034.
6. X.Tan, B.Gu, G.Yang and B.Dong, "Diffractive phase elements for beam shaping : a new design method", Appl.Opt., 34, (1995) 1314.
7. T.J.Suleski and D.C.O'Shea, "Gray-scale masks for diffractive optics fabrication", Appl.Opt., 34, (1995) 7501.
8. W.W.Simmons, G.W.Lappelmeir & B.C.Jony, "Optical Beam Shaping Devices Using Polarization Effects", Appl.Opt., 13 (1974) 1629.
9. V.Namius, "The Fractional Fourier Transform and its Application to Quantum Mechanics", J. Inst. Maths Applics, 25 (1980) 241.
10. A.C.Macbride and G.F.Roach, Fractional Calculus (Pitman, Boston, 1985).
11. H.M.Ozaktas and D. Mendlovic, "Fourier Transforms of Fractional Order and their Optical Implementation", Optics Communications, 101 (1993) 163.
12. D. Mendlovic and H.M.Ozaktas, "Fractional Fourier Transforms and their Optical Implementation : I", J. Opt. Soc. Am. A, 10 (1993) 1875.
13. D. Mendlovic and H.M.Ozaktas, "Fractional Fourier Transforms and their Optical Implementation : II", J. Opt. Soc. Am. A, 10 (1993) 2522.
14. H.M. Ozaktas, B. Barshan, D. Mendlovic and H. Urey, "Space-Variant Filtering in Fractional Fourier Domains", Inst. Phys. Conf. Ser. 139 (1994) 285.
15. A.W. Lohmann and D. Mendlovic, "Fractional Fourier Transform : Photonic Implementation", Appl. Opt., 33 (1994) 7661.
16. H.M.Ozaktas and D. Mendlovic, "Fractional Fourier Optics", J. Opt. Soc. Am. A, 12 (1995) 743.
17. A.W. Lohmann, "Image Rotation, Wigner Rotation and the Fractional Fourier transform", J. Opt. soc. Am. A, 10 (1993) 2181.
18. D. Mendlovic, H.M.Ozaktas and A.W. Lohmann, "Graded-Index Fibers, Wigner-Distribution Functions and the Fractional Fourier transform", Appl. Opt., 33 (1994) 6188.
19. L.M. Bernardo, "ABCD Matrix Formalism of Fractional Fourier Optics", Opt. Eng., 35 (1996) 732.
20. A.W.Lohmann, D.Mendlovic and Z.Zalev-sky, "Fractional Fourier Transforms in Optics" , Progress in Optics, vol-38, Ed.E.Wolf, (North Holland, Amsterdam, 1998) 265.
21. L.Savigny and M.De, "Fresnel Transform in Optics", Bull.Opt.Soc.India, 2 (1968) 52.
22. A.K.Chakraborty, D.Roychoudhury, S.Bandyopadhyay, S.Sanyal and A.Ghosh, "Spatial Filtering at Fractional Fourier Transform Plane" Optics and Optoelectronics – Theory, Devices and Applications, vol-1, Editors O.P.Nijhawan, A.K.Gupta, A.K.Musla and K.Singh (Narosa, New Delhi, 1998) 69.

Network Sensitivity relations from Dee Bee's Invariant Product Theorem

D. Basu and Bhaskar Bhattacharyay
Instrumentation Engineering Section
Department of Applied Physics, University of Calcutta
92, Acharya Prafulla Chandra Road, Kolkata- 700 009

Abstract

Sensitivity is a very important factor in precise measurements, calibration, standardisation and in many other aspects. The authors in this paper have developed some sensitivity relations for electrical networks from his Invariant for electrical networks from his Invariant Product theorem. The relations are simple, interesting, unique and independent of circuit configuration. They involve two or three constants which can be determined practically by the same approach for all circuits without knowing the values of circcuit parameters. The relations can be used for testing sensitivities of electrical measuring networks and process control circuits using Impedence transducers. They are also useful to study the nature of variations of active and reactive components of currents and voltages with impedence variation in power system networks.

NOTATIONS

$Z_f = R_f + jX_f$ = Self impedence of fth. branch of a network.

$i^d = i^d_a + j\, i^d_r$ = Current in the dth. branch of the network.

$Z^{\infty}_i = R^{\infty}_f + j\, X^{\infty}_f$ = value of the Z_f for which i^d is infinite valued. It is independent of Z_f

$if^d_{\infty} = I^d_{a\infty} + j\, i^d_{r\infty}$ = Value of i^d when Z_f is infinite valued. It is also independent of Z_f

$W_d = A_d + jB_d$ = A complex constant independent of Z_f, R_f and X_f

$Wdz = W_d \times Z_d$ = Constant when Z_d is constant.

INTRODUCTION

In electrical measuring circuits sensitivity plays an important role in it's degree of precision and accuracy. Coventionally the sensitivity can be pre-determined by knowing the circuit configuration as well the values of the circuit parameters. The method of determination is labourious if the circuit is bit complicated and the sensivity formulae is different for different networks. The authors in this paper have developed some sensitivity relations from his Invariant product Theorem[1] which are simple in nature, which can be easily applied to determine different sensitivity values when the constants of the relations are known. The methods are unique in approach and are independent of circuit configuration. Further the method seems to be free from errors which generally creep in the theoretical values of the parameters due to jointings, lead resistances, contact resistances etc. and also due to ageing effects which makes the results by conventional methods erroneous.

THE SENSITIVITY RELATIONS

1) Current Sensitivity

From Invariant product Theorem we have,

$$(i^d - i^d_{f\infty}) (Z_f - Z_l^{\infty}) = W_d \quad \text{--- (1)}$$

or

$$(i^d - i^d_{f\infty}) = W_d / (Z_f - Z_f^{\infty})$$

therefore

$$\delta i^d / \delta Z_f = - W_d / (Z_l - Z_f^{\infty})^2$$

$$= -(i^d - i^d_{f\infty}) / (Z_l - Z_f^{\infty}) = \lambda + j\mu \text{ , (say)} \quad \text{--- (2)}$$

Now when R_f is variable and X_f is constant then,

$$\delta i^d / \delta R_f = (\delta i^d / \delta Z_f).(\delta Z_f / \delta R_f)$$

or

$$1.\ (\delta i^d / \delta Z_f) = - W_d / (Z_f - Z_f^{\infty})^2 = \lambda + j\mu \quad \text{--- (3)}$$

therefore, $\delta i^d_a / \delta R_f = \lambda$ and $\delta i^d_r / \delta R_f = \mu$

Again when X_f is variable and R_l is constant

$$\delta i^d / \delta X_f = (\delta i^d / \delta Z_l).(\delta Z_f / \delta X_f)$$

$$= -jW_d / (Z_f - Z_f^{\infty})^2 = -\mu + j\lambda \quad \text{--- (4)}$$

therefore, $\delta i^d_a / \delta X_f = -\mu$ and $\delta i^d_r / \delta X_l = \lambda$

Note:

1) The reactance sensitivity is j times the resistance sensitivity and vice versa as reflected from the equations (3) & (4).

2) In case of DC equation (2) can be written as

$$\delta i^d / \delta R_f = - W_d / (R_f - R_f^{\infty})^2 \quad \text{--- (5)}$$

where W_d and R_f^{∞} are real constants,

3) Equation (5) can be written as

$$\delta i^d / \delta R_f = 1 / (a.R_l^2 + bR_f + C)$$

or

$$\delta R_f / \delta i^d = a.R_f^2 + bR_f + C$$

Which is the equation of a parabola. This shows that Inverse of DC sensitivity varies parabolically with variation of R_l.

2) Voltage Sensitivity

The voltage across dth. branch,

$$v^d = i^d . Z_d$$

$$\therefore\ \delta v^d / \delta R_f = (\delta i^d / \delta R_f). Z_d = - W_d.Z_d / (Z_f - Z_f^{\infty})^2$$

$$= - W_{d'} / (Z_f - Z_f^{\infty})^2 \quad \text{--- (6)}$$

and

$$\delta v^d / \delta X_f = (\delta i^d / \delta X_f). Z_d = - jW_d.Z_d / (Z_f - Z_f^{\infty})^2$$

$$= - jW_{d'} / (Z_f - Z_f^{\infty})^2 \quad \text{--- (7)}$$

Note:

1) Here also reactance sensitivity is j times resistance sensitivity and vice versa.
2) DC sensitivity $\delta v^d / \delta R_l = - W_{d'} / (R_f - R_f^{\infty})^2$ and its inverse is a parabola with R_f

3) Magnitude Sensitivity

We have

$$i^d = i^d_a + j i^d_r = W_d / (Z_f - Z_f^{\infty})^2 + i^d_{f\infty}$$

$$= \alpha + j\beta \quad \text{... (8)}$$

$$\delta i^d / \delta R_f = \delta i^d_a / \delta R_f + j\delta i^d_r / \delta R_f$$

$$= -W_d / (Z_f - Z_f^{\infty})^2 = \lambda + j\mu \quad \text{[Vide Eqn (3)]}$$

Now $|i^d|^2 = (i^d_a)^2 + (i^d_r)^2 = \alpha^2 + \beta^2$

$$|i^d| = \sqrt{(\alpha^2 + \beta^2)}$$

$$\delta |i^d|^2 / \delta R_f = 2\, i^d_a (\delta i^d_a / \delta R_f) + 2 i^d_r (\delta i^d_r / \delta R_f)$$

$$= 2\alpha\lambda + 2\beta\mu \quad \text{... (9)}$$

Again

$$\delta |i^d|^2 / \delta R_f = 2 |i^d| . \delta i^d / \delta R_f$$

$$\text{or } \delta |i^d| / \delta R_f = (1 / 2|i^d|)\, (\delta |i^d|^2 / \delta R_f)$$

$$= \{1 / (2\sqrt{(\alpha^2 + \beta^2)}\}.(2\alpha\lambda + 2\beta\mu)$$

$$= (\alpha\lambda + \beta\mu) / \sqrt{(\alpha^2 + \beta^2)} \quad \text{... (10)}$$

The expressions for $\delta|i^d|^2 / \delta X_l$ and $\delta|i^d| / \delta X_f$ can be obtained similarly.

DETERMINATION OF SENSITIVITY VALUES

It is seen that all the sensitivity values with respect to R_f or X_f of Z_f can be easily determined from equations (3), (4), (5), (6), (7) (9) and (10) provided the values of the three constant W_d, $i^d_{f\infty}$ & Z_f^{∞} (and hence the values of α, β, λ, μ) are known. The values can either be evaluated preactically with the help of equation (1) by taking three sets of reading for i_d corresponding to three known values of Z_f or theoretically by knowing the circuit parameters.

REFERENCE

1. Basu. D, ' Invarient Product and Ratio Theorems for Linear Networks ', J. of the Institution of Engineers(I), vol.66, pt EL3 &4, Dec.1985-Feb86

Simulation and Performance Analysis of FDDI based Network Designed for Movement of Trains in Sections

Vikas Jain and Vinod Chandra
Department of Electrical Engineering, Indian Institute of Technology, Delhi-110016
vikaas_jain@yahoo.com, vchandra@ee.iitd.ernet.in

Abstract

FDDI based network has been proposed for application in movements of trains in railway sections. Performance analysis of protocol designed for this application has been carried out. Simulation software is developed to find suitability of FDDI protocol for railways signaling applications as well as to study the performance under fault conditions. Graphs are plotted to find the optimum performance of ring under the various constraints that are encountered practically in data transmission for our required application.

INTRODUCTION

With increase in Railway traffic, control of signals and regulation of traffic is becoming more complex. Suitable network is required for the purpose of interconnecting different railway stations for the purpose of communication and centralized train control. FDDI is 100Mbps network consisting of dual ring topology with optical fiber as medium as shown in Figure1. The dual counter rotating rings are designated as primary and secondary rings. FDDI can support large number of stations, which can cover a long section length[1,2]. The important fault tolerant features are automatic switch over to the alternative ring and decentralized operation of the fragmented loops in the event of multiple faults. Various prioritization schemes can be implemented for incoming data.

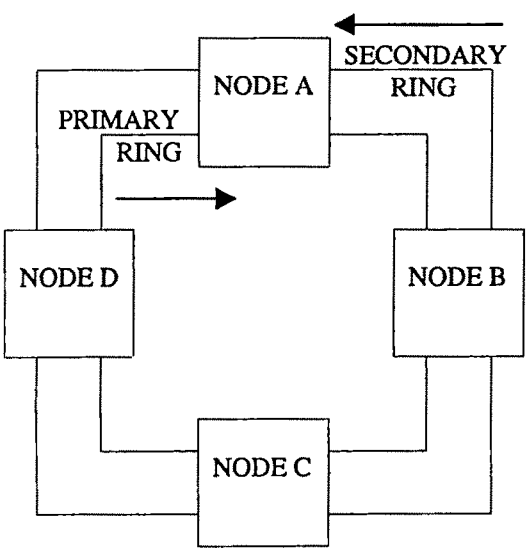

Fig 1: Dual ring topology of FDDI with primary and secondary ring.

FDDI network is capable of transmitting both synchronous as well as asynchronous traffic. All these features make it suitable for Railway applications where yard status, time table, train delay, arrival time, train speed and location and signaling information is needed to be communicated from one station to another. It also acts as high-speed backbone for use in interconnecting low speed LANs at each station.

FDDI SPECIFICATIONS

The standard for FDDI is specified by the X3T.9 working group of ANSI. Data can be transmitted with the bit error rate of 1 bit in $2.5X10^{10}$. The token is 19 bytes long and has a typical transmission time of 0.88μs and the maximum frame size allowed is 4500 bytes with a typical transmission time of 0.36 ms. The ring latency with these values will always be greater than 1.73ms and the effective Target Token Rotation Time (TTRT) lies between 4ms to 165ms[1]. Total number of stations allowed is up to 1000 for single attached stations (SAS) and up to 500 for dual attached stations (DAS). Total fiber path between stations allowed is 200 km for SAS and 100 Km for DAS. For the present application dual attached stations have been used in the FDDI ring.

FAULT TOLRENCE

FDDI provides a number of fault tolerance features due to its dual ring topology. During normal conditions, the primary ring is used for data transmission. There are two types of faults encountered. One fault is break in the fiber path and other is node failure. In the event of a single failure in primary path, the secondary path is used to retain the connectivity on the ring. In the case of breakage in either the dual paths or a node failure the dual ring is automatically wrapped, the dual ring topology becomes single ring topology[1,3]. Data continues to be

transmitted on FDDI ring during wrap condition in the path as shown in Figure 2 and 3. There may be certain multiple fault conditions in which communication becomes fragmented yielding smaller ring segments.

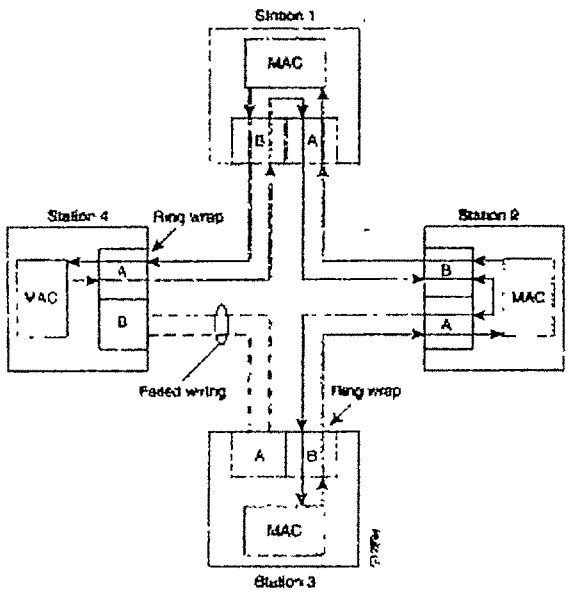

Fig 2: Wrapping up under path failure

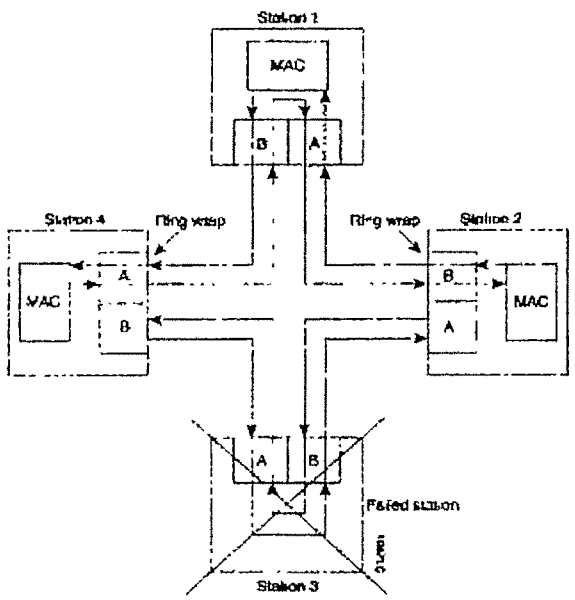

Fig 3: Wrapping up under node failure

TIMED TOKEN ROTATION PROTOCOL

Token rotation time (TRT) is the time that token takes to make one round trip on the network. Token holding time (THT) is the time for which a node holds the token. FDDI ring is initialized or reinitialized by claim token process. During the claim token process the target token rotation time (TTRT) is assigned to the ring based on expected traffic known as operational value. Ring's TTRT value is set to a large default value of 165ms in the claim frame, which is placed in the ring for circulation. The media access control layers (MAC's) of all the nodes compare the value of TRT in the received claim frame with their own TRT. MAC's receiving claim frame with higher bid value than itself modifies the frame by replacing previous bid value with its own value while those receiving lower bid value relays the frame without modification to downstream station. This process continues until any of the MAC's receives the claim frame that it has transmitted. That value of TRT is set as operational value. If TRT expires on any MAC during claim process then the claiming process will abort and Beacon process is initiated as it indicates that previous process failed to initialize the ring. Entry to Beacon state indicates a major break or reconfiguration of ring. A MAC entering the Beacon state continuously sends the Beacon frame to downstream node. All MAC's receiving the Beacon frame from upstream stations are required to yield so that when ring is restored a MAC eventually will receive its own Beacon frame and will be able to initiate the claim token process. If the token returns back earlier than the operational value then it indicates light load on network and allows MAC to commence transmission of asynchronous frame in the remaining time after sending synchronous frame. A late arriving of token represents a heavy load on the network, and the MAC may only transmit synchronous frames. In this manner the unused capacity builds up for the benefit of downstream stations. If a station transmits data for all the allowable time then downstream station needs to wait for one complete rotation before transmitting data. The timed token protocol adheres to two fundamental properties:

1) The average token rotation time is at most equal to operational time.

2) The maximum token rotation time is at most twice the operational value.

PRIORITIZATION SCHEME

One feature of token ring network is the need for a prioritization scheme to ensure that stations with important traffic have a chance to obtain control of token. Two types of traffic are allocated to FDDI bandwidth, synchronous and asynchronous class of traffic [4,5]. Synchronous traffic must have guaranteed bandwidth and must be transmitted during certain prescribed time period whereas asynchronous traffic is allowed only in bandwidth that exceeds this minimum that is allocated to synchronous traffic.

Asynchronous traffic is further classified in two classes, restricted and non-restricted class. Restricted tokens are used when a station decides to use full asynchronous bandwidth exclusively to communicate with other particular station for a longer period. Entry in to restricted dialogue is usually done with control of Station Management (SMT). The station initiating the restricted dialogue captures the standard non-restricted token and transmits the frame to destination station. The two

stations can then exchange restricted tokens and maintain the exclusive dialogue. All other asynchronous communication is prevented during the dialogue. The SMT monitors the restricted dialogue time and terminates it after some upper time value exceeds, if not self terminated within that period of time. A non-restricted asynchronous capacity allocation supports eight levels of priority level from 0 to 7 with 7 is having the highest priority.

PREFORMANCE PARAMETERS

There are two types of parameters that can be varied to monitor the performance and behavior of FDDI timed token rotation protocol, fixed parameters and configurable parameters. Fixed parameters include extent of network, number of stations, station interface delays like transmission time, token processing time etc. that cannot be varied after the installation of network and do not vary with time. Configurable parameters include those which change frequently due to changes in user application requirements. Altering these parameters can significantly affect the performance of the network. These parameters include offered asynchronous load, synchronous traffic and the value of TTRT as well as frame size. The effect of all these parameters should be taken in to account when constructing a network in order to ensure that the network throughput and response time are within reasonable limits for the required applications. Incorrect setting of the TTRT or an over allocation of synchronous bandwidth leads to lower throughput of asynchronous data. Transmission of asynchronous data requires certain minimum value of TTRT given by the equation below.

$$TTRT \bullet \bullet SA_i + F_{max} + D_{max} + Tokn\_tim \qquad (1)$$

- $\bullet SA_i$ Sum of synchronous allocation of all the Stations
- F_{max} Time taken to transmit a maximum length Frame
- D_{max} Delay for maximum ring length (includes Propagation delay along the fiber length as Well as sum of token processing time at all the Nodes.
- Tokn_tim Transmission time for a token

If the operational value is less than latency of the ring, the token will not arrive until after TRT time expires and the ring eventually will enter the claim process.

SIMULATION DETAILS

Fixed as well as configurable parameters can be varied and can be fed as input parameter in the program to calculate their effect on the system throughput and their contribution to various type of losses that occur under certain constraints such as limited buffer size, variable frame size, time expiry of the information packets. In this simulation, number of nodes can be varied up to 10 nodes along with inter nodal distances with some typical values of station interface delays. For calculation of results, sum of synchronous allocation of all the station is taken as 10ms. Algorithm of program works as follows:

sim_time	Simulation time.
real_time	Instantaneous time considered during Simulation.
Pkt_allowed	Maximum number of valid packets to be send by the node.
unused_time	Remaining time from the allowed time which is not utilized for sending the data by previous node.
send_pkt_time	Transmission time for packets.
send_packet	Number of packets sent by any node in Single frame.
send_node	Node which sends the packet.
present_node	Node which is having token or frame.
dest_node	Node for which frame has data.

```
main ()
{
status=token;
input_para();      //input the values of parameters
pkt_gen();         //generates inter-arrival time for packets
pkt_info();        //assigns destination, priority, Expiry
                   //time of each arrived packet
token_path();      //token path is decided under normal
                   //and fault conditions
while(sim_time>=real_time)
{
next_node();       //finds the next node in token path
node_TRT();        //TRT of present node is calculated
update_time1();    //updates real time
if(status==token)
{
open_file(node); //read the details of packets at present
                 //node
expired_pkt(real_time);    //Mark the expired packets
buffer_loss(real_time);    //mark the overflowed packets
                           //from the limited size buffer
pkt_allowed(node_TRT, prev_unused_time);
                           //calculates the maximum
                           //numbers of valid packets that
                           //that are in queue at this node.
if(pkt_allowed==0)
{
continue;
}
send_packet(real_time, pkt_allowed);
                           //calculates the number of
                           //packets send
unused_time=unused time-send_pkt_time;
if(send_packet==0)
{
break;
}
```

```
update_time2(real_time,pkt_send); //updates real time
                                  //further by
                                  //adding transmission time
status==frame;
send_node==present_ node;
}
if(status==frame&&dest_node==present_node)
{
status=acknowledge;
}
if(status==acknowledge&&send_node==present_node)
{
status=token;
}
close_file(node); //closes the data files of all the nodes.
}
sum_total_pkt();          //Sum of total packets
                          //generated in all the nodes.
sum_pkt_send();           //Sum of total packets send by
                          //the nodes
sum_buffer_loss();        //Sum of packets lost due to
                          //overflow of buffer at all the
                          //nodes.
sum_time_expired_pkt(); //Sum of total time expired
                        //packets at all the nodes.
display_result(); //Displays the data calculated.
}
```

FDDI RING PERFORMANCE

The lower value of TTRT reduces the efficiency of the ring. When TTRT approaches the minimum value as given by equation (1) throughput for asynchronous traffic becomes zero and only synchronous traffic is delivered by the ring [1,4]. If TTRT is increased, each node gets more time to transmit its asynchronous data. Ideally if a node has much asynchronous data to transmit throughout the time it gets the opportunity, then throughput keeps on increasing with increase in TTRT. However, under certain conditions node can not transmit data at all the times, even if it has opportunity to transmit the data. So, along with the allowed time to transmit, some other factors also determine the frame length and these are discussed below.

1) Arrival rate of data.
2) Length of data to be transmitted to single destination.
3) Limited buffer size.
4) Finite time for the validity of information content.

With increase in TTRT the access delay at each station will increase. If the arrival rate of information is such that the data overflows from the limited size buffer while waiting in the queue before getting the opportunity for being transmitted, then it will contribute to the loss of information. Due to long access delay if the data inside the buffer remains for a period longer than the time for which its information contents were valid, then also larger values of TTRT will contribute to loss of data packets. Fig 4 shows the effect of buffer size on throughput at different arrival rates. Throughput of the system improves with increase in buffer size and for the same buffer sizes the low arrival rate gives the better throughput. Information length also effects the throughput of the system. All the packets in an information have the common destination node. It is also not necessary that two

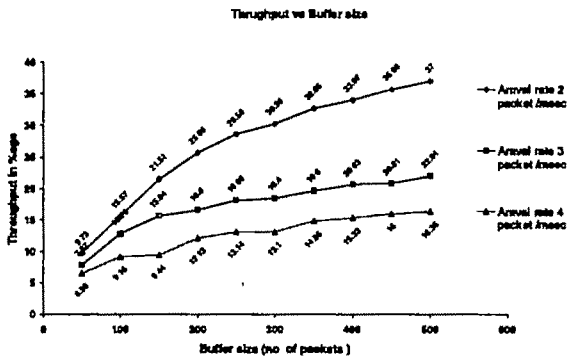
Throughput vs Buffer size
Throughput in %age
Buffer size (no of packets)
Arrival rate 2 packet /msec
Arrival rate 3 packet /msec
Arrival rate 4 packet /msec

Fig 4: Plot of Throughput Vs Buffer size for different arrival rate of asynchronous traffic.

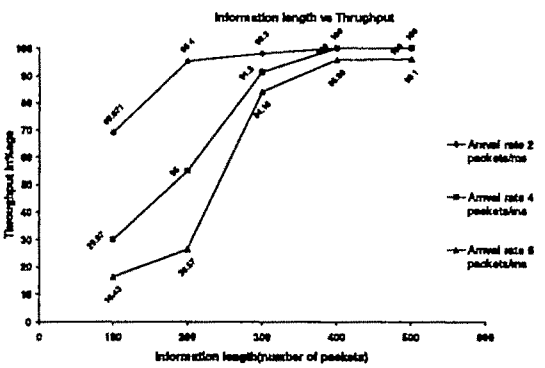

Fig 5: Plot of throughput Vs information length for different arrival rate of asynchronous traffic.

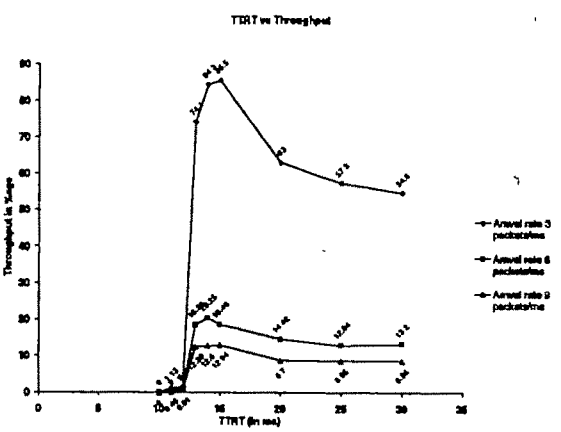

Fig 6: Plot of throughput Vs TTRT for different arrival rate of asynchronous traffic.

consecutive information may have common destination node. Also, the frame contains data for single destination

at a time so the length of frame depends on information length and hence effects the throughput. When the node acquires the token for transmission of smaller information length, data can not be transmitted for the remaining time available to the node for transmission so the buffer will not get cleared at the faster rate. Incoming data keeps on filling the buffer leading to lower throughput of the system. Figure 5 shows the variation of throughput with different information length of packets. In figure 6 it can be seen that the throughput of the system improves at a high rate initially when the TTRT increases from the minimum possible value. If TTRT is further increased the access delay increases to such an extent that it causes buffer loss and expiry of valid time period of information packets which leads to decreased throughput of the system.

If the number of nodes are less then access delays will also be lesser as token has to pass through lesser number of nodes which contribute for the delay due to token processing and transmission time. The effect of lesser number of active nodes can be seen in figure 7 where system throughput is compared for different nodes by keeping all other parameters constant.

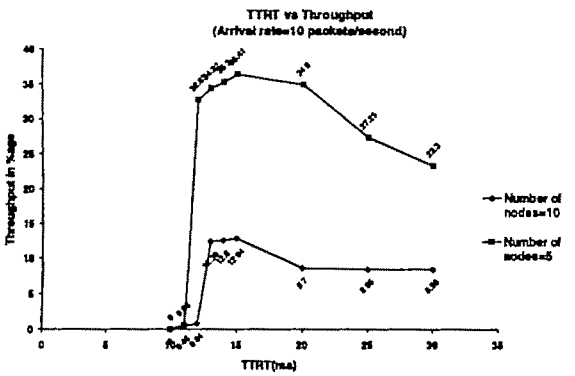

Fig 7: Plot of throughput Vs TTRT for different arrival rate of synchronous traffic.

REFERENCES

1. Sonu Mirchandani and Raman Khanna, FDDI Technology and Applications, John Wiley & sons, inc. (1993)
2. R. Jain, FDDI current issues and future plans, IEEE Communication Magazine vol. 31, issue 9 (Sept 1993) pp. 98-105
3. Biao Chan, Karnat S., and Wei Zhao, Fault tolerant, Real time communication in FDDI based Networks, Computers, Vol. 30, issue 4, Apr 1997, pp. 83-90.
4. Albert B., Jayasumana A. P., Performance Analysis of FDDI LANs using numerical methods, Computers and Digital Techniques, IEEE proceedings vol. 144, issue 3, May 1997 pp. 149-154
5. Warahera P. N., Jayasumana a. p. FDDI: throughput evaluation with multiclass traffic, IEEE Transactions on Communications, vol. 42, issue2, part I, Feb- Apr 1994 pp. 499-510.

Virtual Wavelength Path Algorithm for Design of WDM Network Exploiting Combined Wavelength and Optical Code Conversion

(Invited Talk)
R.Gangopadhyay
Department of Electronics and Communication Engineering,
Indian Institute of Technology, Kharagpur - 721 302;
Tel.:+91-3222-78028, Fax:+91-3222-55303,
Email:ranjan@ece.iitkgp.ernet.in

Abstract – The capacity, scalability and performance improvement of wavelength-routed optical network can be augmented by additional features of wavelength conversion and optical code conversion. The present work provides for the first time virtual wavelength path algorithm for the design of WDM networks exploiting combined wavelength conversion and optical code conversion.

1. INTRODUCTION

In a wavelength division multiplexing (WDM) network, the setting up of calls between every pair of nodes is achieved by lightpaths (wavelength path) through dynamical wavelength routing and wavelength assignment. A lightpath [1] is an all optical transmission path between two network nodes implemented by the allocation of the same wavelength throughout the path. As such it does not require any wavelength conversion or electronic conversion at the intermediate nodes. However, for a given network, the limited number of wavelengths, the limited number of transceivers per node and the channel constraints limit the maximum number of lightpaths that can be established.

The concept of virtual wavelength path (VWP) ie. an optical path provisioning based on wavelength conversion at the intermediate nodes, ensures improved network performance and network scalability. In this case the wavelength for a VWP is allocated link by link and the path is composed of several wavelength paths (WP) governed by the wavelength conversion. From the point of view of wavelength resources, VWP approach to wavelength allocation is more efficient than the WP approach[2].

In a high capacity optical network using WDM and optical code division multiplexing (OCDM), virtual optical code path (VOCP) provides another design option for optical path layer provisioning. As in VWP, the optical code for each VOCP is allocated link by link; the optical path is decomposed into several optical optical code paths governed by the optical code conversion.

When both wavelength conversion and optical code conversion are utilized in the transport layer of a WDM network conjointly, it is possible to enhance the network scalability without significant drain of the wavelength resource.[3,4]

The channel allocations of OCDM/WDM along with WDM are schematic ally shown in Fig.1.Let us roughly estimate the number of channels. The processing gain of OCDM becomes 30 for 10 Gbit/s when the chip pulse width is assumed to be 3 ps. The theory shows four codes are available for BER in the case of the bipolar gold code. By taking into account that the Fourier-transform limit chip pulse of 3 ps occupies the bandwidth of 100 GHz, there are 38 wavelength channels within the EDFA gain bandwidth of 30 nm. The overall number of channels of OCDM/WDM becomes 150. To maintain the same number of WDM channels, the frequency spacing must be as small as 25

GHz. In comparison, in a more moderate WDM with channel spacing of 50 GHz, the spectrum efficiency of OCDM/WDM could be twice as much as with WDM.

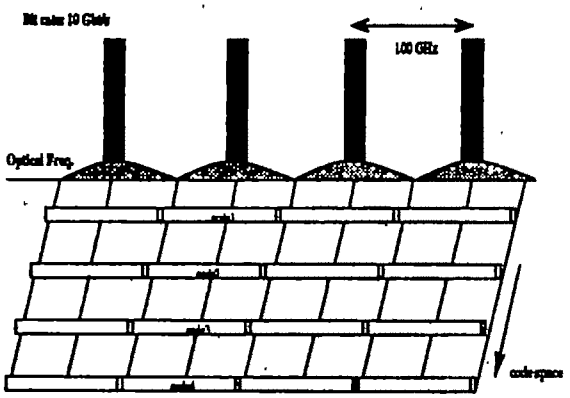

Figure 1: *Channel allocations CDM/WDM*

2. MULTIHOP OCDM NETWORKS

As an example, consider a 8-node multihop WDM network configured as a linear bus topology. This will require 16 wavelengths for establishing any node to any node connectivity as shown in Fig.2. However, one can introduce additional design option by adopting a hybrid (OCDM/WDM) to multihop networks for network scalability as well as optimum network resource utilization.

In the later case each transmitter operates at a wavelength and optical code unique to the transmitter; each receiver is tuned to a unique wavelength and an optical code unique to that receiver.

Assuming that each node is equipped with 2 transceivers and signifying $OC_{i,j}$ represents the optical code j on the wavelength λ_i (e.g. OC_{12} represents the optical code 2 used on wavelength channel λ_1), Fig.3 simply represents the same 8-node multihop linear bus based on the combined strategy of OCDM/WDM. One can notice that the number of wavelengths W' required in the absence of code conversion and the number of wavelengths W required in the presence of code conversion, with number of optical codes C per wavelength, must satisfy W'=WC.

For the WDM network design the possible trade-off between the number of wavelengths and

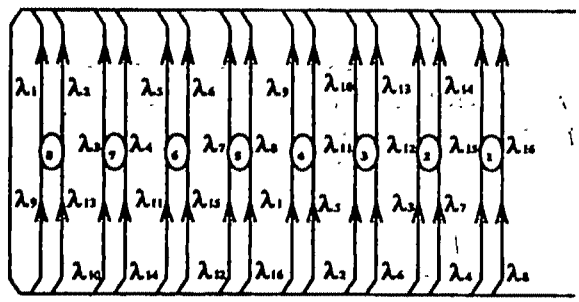

Figure 2: Eight-node multihop linear bus WDM network.

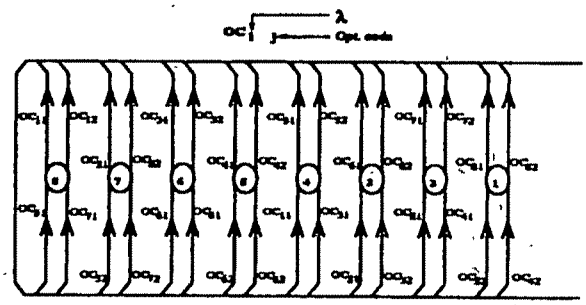

Figure 3: Eight-node multihop linear bus optical using OCDM/WDM multihop principle.

the number of codes that could be used in a network to achieve the required network performance is an important issue. In the present work we have exploited the wavelength path design algorithm for WDM network performance evaluation exploiting combined wavelength routing, wavelength conversion as well as optical code conversion.

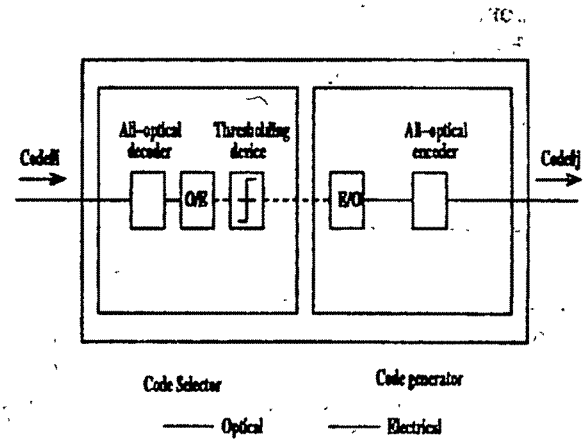

Figure 4: *Configuration of the optical code converter*

2..1 Optical code conversion

OCC at a node is crucial to the successful use of the VOCP concept. One particular configuration for the OCC is shown in Fig.4, consisting of a code selector and generator. To perform conversion from code OC_i to OC_j , the selector is controlled to select only OC_i from the input signal; the selection is based on matched filtering between the incoming and the locally assigned code. The output is detected by the photo detector, and the electrical signal drives the code generator to output OC_j . The code generator regenerates the desired optical code only when the code selector is triggered by the auto correlation output of the matched filter. Note that all-optical conversion without electrical-to-optical (EO) conversion is desirable in order to maintain network transparency. In order to regenerate the optical code without EO conversion, optical thresholding in the optical code selector is required. Although all-optical thresholding devices are not yet routinely available, a semiconductor saturable absorber would be a strong candidate.

2..2 OCC based cross-connect switch

A possible architecture for an OCC-based cross-connect switch, exhibiting the VOCP's functionality, is depicted in Fig.5, configured so that OCC is performed after wavelength conversion. Since OCDM decoding is insensitive to the wavelength variation of the light source, in OCDM/WDM demultiplexing the wavelength channel selection has to be made first, followed by the OCDM decoding. As shown in the inset of Fig.5, there are three possible paths through the wavelength converter and OCC cascade. After wavelength conversion and/or optical conversion, the input signal is presented to the optical matrix switch for routing to the appropriate output port. The wavelength converters, OCC's, and matrix switches are controlled by electrical signals. Add/drop multiplexing can also be carried out at the selected input (for adding the signal from the node) and output ports (for dropping the signal to the node).

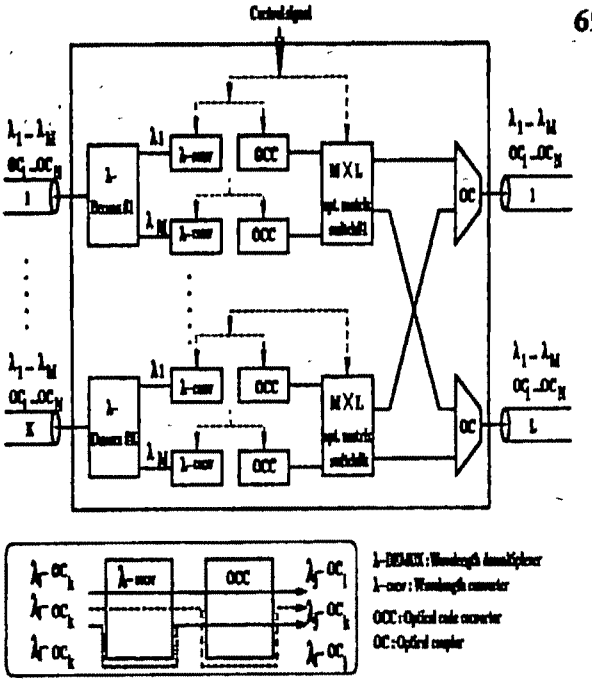

Figure 5: *Architectures of optical cross-connect switch with the optical code converter (OCC) and the wavelength-to-code converter*

3. VIRTUAL WAVELENGTH PATH ALGORITHM

The virtual wavelength path (VWP) algorithm achieves fast routing of lightpath and semilightpaths between a given source and destination by minimizing the overall cost function that accounts for link cost (wavelength on a link) and wavelength/code conversion cost (doing wavelength/code conversion at a node when necessary). Essentially, the following steps are involved:

1. Construct the wavelength graph (WG) of the network which defines the node-to-node link connectivity of the physical network and the connectivity among nodes residing in virtual wavelength layer and code layers. For example, Fig. 6 gives the WG of a 5-node unidirectional ring network using only wavelength conversion.

2. Find a shortest path between the source and the destination using the shortest path algorithm for WG (SPAWG)

3. Map the found path back to the network to obtain the minimum cost semilightpath(VWP).

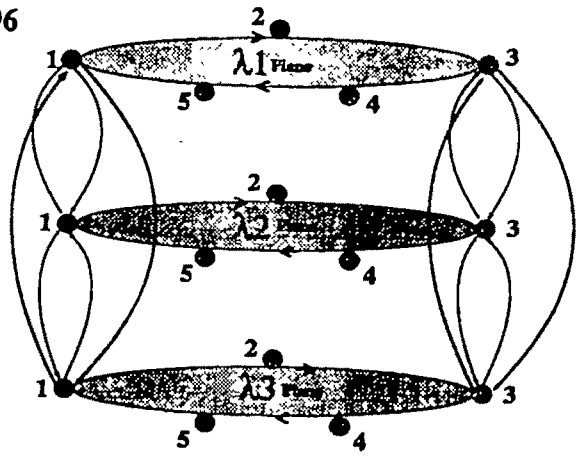

Figure 6: Wavelength graph of a 5-node unidirectional ring with full wavelength converters placed at nodes 1 and 3.

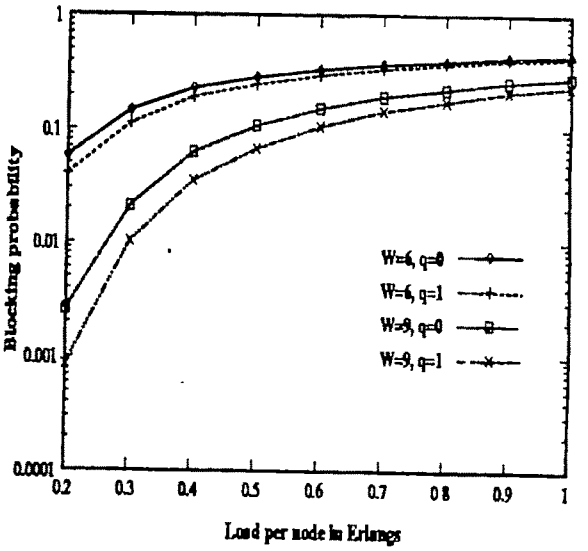

Figure 7: Blocking probability versus load per node (Erlangs) for 20 node ring network with W=6 and 9 wavelengths with/without wavelength converters.

The SPAWG algorithm [1,5] for finding the shortest path between two given vertices of the WG is presented. For easy notation the vertices of the WG are simply labelled by the numbers 1,..,N and the weight of edge (i,j) is denoted by a_{ij}. If the edge does not exist then it has infinite weight. If two vertices, say i and j, are either in the same column or in the same row, this relation is denoted by $i \sim j$. In the algorithm, three sets of numerical variables are used : a variable u_i, associated to each vertex; a variable R_i, associated to each row and a variable C_j, associated to each column. The variables $\{R_i, C_j\}$ will represent the row and column minimum values respectively. For simplicity, the start-point of the searched path is labelled by one. Also, the set-valued variables P and T for permanently and tentatively labelled vertices, respectively (permanently labelled vertices are those for which the computation has already terminated, that is, the variable u_i contains the weight of a shortest path from 1 to i. For the tentatively labelled vertices the computation is still going on).

SPAWG Algorithm

Step 1 (Initialisation)

1. $u_1 = 0$;
2. *If* $i \sim 1$ *then* $u_i := a_{ij}$ *else* $u_i := \infty$ $(\forall\ i)$
3. $R_i := min\ \ u_j : j$ *is in the ith row,* $j \neq 1$, $(\forall\ i)$
4. $C_j := min\ \ u_i : i$ *is in the jth column,* $i \neq 1$, $(\forall\ j)$
5. $P := 1$; $T := 2,...,N$

Step 2 (Designation of a new permanent label)

1. *Find the minimum of* R_i, C_j $(\forall\ i,j)$
2. *Find an* $h \in T$ *with the minimum* u_h *in the row or the column which gave the minimum above (ties are broken arbitrarily)*
3. $T := T - h$; $P := P \cup h$
4. *If* $T = \emptyset$ *then STOP*

Step 3 (Updating row and column minimum)

1. *If h, found in Step 2, is in row i and column j*
2. *then* $R_i := min\ \ u_j : j$ *is in the ith row,* $j \in T$
3. $C_j := min u_i : i$ *is in the jth column,* $i \in T$
4. *The minimum over an empty set is taken to be* ∞.

Step 4 (Revision of tentative tables)

If h, found in Step 2, is in row i and column j, then for all $l \in T$ *in row i and in column j, set* $u_l := min\ \ u_l, u_h + a_{hl}$. *Go to Step 2.*

Algorithm SPAWG, like Dijkstra's algorithm, computes the minimum weight distance from the root 1 to all other vertices. In the network simulations carried out with SPAWG algorithm a dynamic traffic scenario is considered in which each node receives call requests which are Poisson distributed with mean arrival rate α and exponentially distributed call holding times with mean $1/\mu$. The destination nodes are chosen uniformly at random.

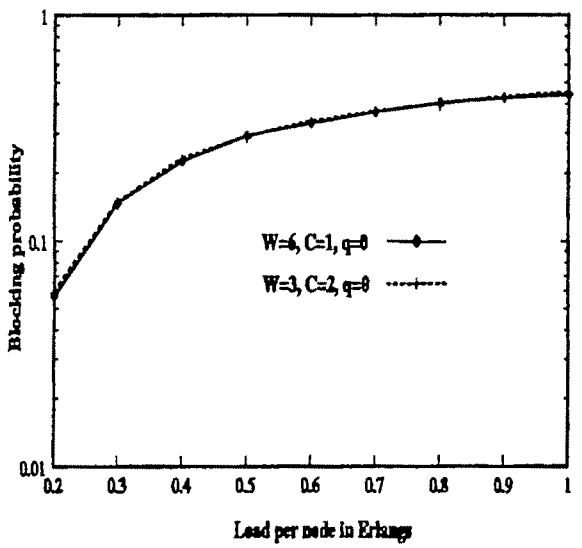

Figure 8: Blocking probability versus Load per node(Erlangs) for 20 node ring network with W=6, Codes(C) = 1 per wavelength, q=0.

In order to accommodate virtual code path, one needs to introduce C rows corresponding to each wavelength layer in the wavelength graph if C number of codes are used on each wavelength. The virtual wavelength path algorithm (SPAWG) described above is therefore suitably modified accordingly to obtain the minimum cost path depending on the prescribed edge cost, wavelength conversion cost and the code conversion cost.

4. RESULTS

The performance evaluation of a 20-node unidirectional WDM network has been carried out by simulation using SPWAG algorithm for routing and wavelength/code allocation. Figure 7 shows the blocking probability performance versus the traffic load (Erlangs) per node with the number of wavelengths, W=6 and 9 without wavelength conversion (conversion density q=0) and with full wavelength conversion(q=1) at every node.

The benefit of wavelength conversion as well as the improved network performance with higher value of W is evident. Figure 8 depicts the blocking performance of the same ring network versus the load for two situations: a) W=6, C=1, q=0 and b) W=3, C=2, q=0 indicating that there is no significant change between the blocking performance of the network working with W' wavelengths without any code conversion and with W wavelengths and C number of codes per wavelength such that W'=WC. This suggests that by using optical code conversion one requires less wavelength resources compared to a situation where code conversion is not used. Finally, the improved network performance with larger number of signature codes per wavelength as well as with full wavelength conversion facility for a 20-node ring network is shown in Fig.9.

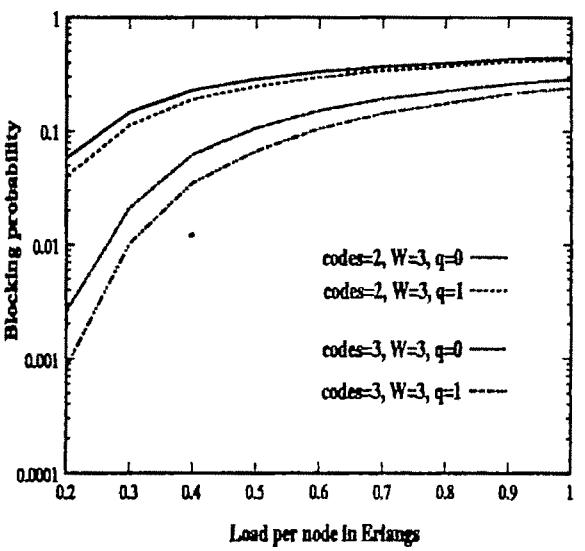

Figure 9: Blocking probability versus load per node for a ring network of 20 nodes with/without code conversion.

5. CONCLUSION

In conclusion the virtual wavelength path algorithm provides a versatile simulation tool for the optimum design and performance evaluation of both regular and irregular WDM network incorporating wavelength routing, wavelength assignment with/without wavelength conversion as well as optical code conversion. In particular,

optical code division multiplexing(OCDM) multihop network has been shown to provide an efficient way of scaling existing WDM networks without further cost to the wavelength resource.

REFERENCES

[1] I.Chlamtac,A.Farago and T.Zhang, "Lightpath (Wavelength) routing in large WDM networks", *IEEE Journal of Selected Areas in Communications*, vol. 5, pp. 909-913, 1996.

[2] C. Chen and S. Banerjee, "A new model for optimal routing and assignment in WDM optical networks", *Tech. Report. CS-9507, Stevens Institute of Technology*, 1995.

[3] G. Vanmuaci, "Combining frequency-division and code-division multiplexing in a high-capacity optical network," IEEE Network, pp. 21-30, March 1989.

[4] Ken-ichi Kitayama, "Code division multiplexing lightwave networks based upon optical code conversion", IEEE SAC, vol.16, pp. 1309-1319, 1998.

[5] R. Gangopadhyay and S. Saha, "Semilightpath approach for optimal placement of wavelength converters in WDM networks", International Conference on Fibre Optics and Photonics, New Delhi, India, December 1998, vol. 3, pp. 787-790.

System Design Of Night Vision Devices

P. K. Datta

Instruments Research and Development Establishment, DRDO
Raipur Road, Dehra Dun 248 008, India

Abstract

There are many defence applications of night vision devices like, infrared homing, infrared fuse, infrared surveillance and reconnaissance. One other major area of application envisaged for FPA's is in IR imaging seekers for 'Fire and Forget' type missiles in anti-armour role. Besides defence applications, thermal imagers are also being intensively used in Medical Science (eye research, cancer research, cardiac imaging), physical sciences (ranging and laser fusion), space astronomy, industrial process control and forest fire control. Under the above framework of reference, this paper presents various options in the system design of night vision devices of various types and generations. Two types of systems are mainly elaborated. They are, (a) those utilise the available photons reflected off the target i.e. image converter (IC), image intensifier (II) or TV based systems, and, (b) those which make use of the temperature and emissivity of the target i.e. thermal imaging systems.

INTRODUCTION

Although human eye is one of the most versatile and adaptable optical sensors, it suffers from some major drawbacks at low light level like poor sensitivity and thereby degraded visual acuity, low quantum efficiency, spectral limitation, etc. To counter these drawbacks, a host of photoelectronic sensors sensitive at different bands of the electromagnetic spectrum and capable of converting input signal photons to an electric current or to stored electronic charge pattern has gradually been developed. Based on these sensors, varieties of photoelectronic imaging devices viz. image converters, image intensifiers and vidicon tubes, intensifier charge coupled/injected devices and thermal imagers of various generations have been invented to provide vision during night. The prime driving force behind these inventions has been to equip the military with night vision and night shooting capabilities.

The technology of direct view image tubes i.e., image converters and image intensifiers began in 1934 with the development of a proximity focused image converter, known as zero generation image tube employing S-1 type of photocathode. This makes use of an illuminating IR source and conversion of the IR image into a visible image. Because of its inherent limitations of very low quantum efficiency (≈1%) and the illuminating source being liable to be very easily detected, first and second generation image tubes employing S-20 and S-25 photocathodes were developed. The sensitivity of these photocathodes is 250 μa / lumen and quantum efficiency 25%. Employing negative electron affinity (NEA) photocathode like GaAs, Cs, CsO, third generation image tubes having sensitivity more than 1000 μa / lumen, 45% quantum efficiency and improved longer wavelength threshold upto 900 nm have been developed. Also, super generation image tubes using super generation tri-alkali photocathode providing luminous sensitivity better than 600 μa / lm and 100 times less dark current as compared to third generation tubes have been invented. These devices are being used not only for various military operations, but also for a variety of other applications, like astronomical observation, study of nocturnal behaviour of animals, industrial process control, medical diagnostics, etc. Further development on the photocathode has led to the invention of fourth generation photocathodes employing InP, GaAsP, InGaAs and the like, having much better longer wavelength threshold upto 1500nm and better photocathode sensitivity and quantum efficiency. The main problem with these photocathodes is the simultaneous increase in thermionic emission and as such its use is restricted unless the photocathode is cooled [1,2]. Recently, work has been initiated at various Institutes for the development of solid state image intensifier using II-VI group of emitters. However, its overall gain is poor because of narrow spectral sensitivity and a major breakthrough is needed before this could be used for application oriented devices.

Low light television (LLTV) system is an extension of an image intensifier based device and utilises a TV tube coupled to the output of an image intensifier photocathode. The advantages of a LLTV system over their contemporary II tube based devices are:

i) Sighting with greater comfort and less fatigue
ii) Freedom of head position
iii) Multi display facility
iv) Recording of image possible
v) Adjustment of brightness and contrast
vi) Image processing possible

Depending on the type of photo sensitive transducers, two basic families, namely vidicon family of tubes employing photoconductors as transducers and orthicon family (including SEC camera tube and SIT) employing photoemissive photocathodes as transducers, have been developed.

LLTV based systems are now finding major applications not only as night vision systems but also as Optronic Director for naval ships/ground anti-aircraft batteries in support of radar. The target is tracked automatically using either of edge tracking, centroid tracking and correlation tracking methods. The Optronic Director is immune to jamming and is of immense use in support of radar, particularly at lower height where radar detection is limited because of ground clutter.

The chief drawback of TV camera system for low light application lies in the bulky appearance and heavy weight. This can be conveniently overcome by coupling a third generation/super generation image intensifier tube to an area array CCD image sensor by demagnifying fibre optics [3]. Such a camera offers performances equivalent to a classical low light level camera while presenting a greatly reduced size. This considerably broadens its range of applications, as follows:

i) It is possible to obtain high gain over the spectral range from X-ray to near IR
ii) Electronic gating to a few nano seconds
iii) Low light level imaging (analog) or photoelectron counting (digital)
iv) Several arrays can be coupled to obtain more pixels

For better capabilities under conditions of haze and mist, thermal imagers have been developed utilising the radiating infrared energy emitted by different substances. By examination of terrain through the infrared region, the sensor derives information not obtainable by optical cameras, radars and in some cases II based or LLTV camera based systems. However, IR radiation cannot propagate through the atmosphere because of high attenuation in the spectral region other than 3000-5000nm and 8000-14000nm wavebands.

Thermal radiations are relatively low energy quanta as compared to visible radiations and therefore use of most of the detectors suitable for the visible region cannot be extended to the thermal region. Thermal detectors have very low S/N at room temperature and as such have to be cooled to a very low temperature to improve the performance. Thermal detectors are classified according to the detector array configuration and the type of scene dissection employed. In the first generation system, the scene is scanned by an opto-mechanical scanner. There are five variations of the complete 2-D coverage of the total FOV, which are as given below:

i) Parallel scan with steps
ii) Parallel scan with or without interlace
iii) Serial scan
iv) Serial parallel scan
v) Serial parallel scan using SPRITE (Signal processing inside the element)

Increasing the number of elements in the detector simplifies the requirement of opto mechanical scanner and also improves the S/N as the square root of the number of elements in the array.

Second and third generation systems employing linear and staring focal plane arrays (FPA's) respectively essentially consist of 2D arrays of infrared sensitive elements in conjunction with a CCD signal processor. The 2D mosaic array in the third generation covers the entire FOV of the system and thus does away with the cumbersome opto-mechanical scanning. Detector elements in the array have one to one correspondence with picture elements in the scene and a high density with 1000 to 10000 detector elements are necessary to meet the requirement of resolution and sensitivity in most practical applications. The CCD signal processor stores the charge from detector elements in a 2D array of potential wells and transfers the charge packets in parallel to an on-chip multiplexer, which then shifts out the column of information in the form of video lines.

Some unique features of staring FPA's which make them particularly attractive for application in IR imaging missile seekers are:

i) Electronically scanned with no moving parts.
ii) Elimination of opto-mechanical scanner
iii) Near unity scan efficiency (FPA's integrate signal from every picture element at a time).
iv) Suitable for degraded weather conditions because of much improved sensitivity.

There are many upkeeping defence applications of thermal imaging, like, infrared homing, infrared fuse, infrared surveillance and reconnaissance. One other major area of application envisaged for FPA's is in IR imaging seekers for 'Fire and Forget' type missiles in anti-armour role. Besides defence applications, thermal imagers are also being intensively used in Medical Science (eye research, cancer research, cardiac imaging), physical sciences (ranging and laser fusion), space astronomy, industrial process control and forest fire control.

For low range applications, uncooled thermal detectors like Pyroelectric Vidicons or Micro-Bolometers are being utilized for developing devices in the hand held mode. Laser gated imaging technique has been utilized not only to enhance the performance of image intensifier based cameras so as to find an economically viable alternative to costly thermal imaging systems [4], but also to significantly improve undersea surveillance capability which has widespread applications in defence and commercial arenas.

SYSTEM DESIGN OF NIGHT VISION DEVICES

Under the above framework of reference, it may be interesting to study the system design approaches of Night Vision Devices of various types and generations.

Night Vision systems are of two types: (a) Those which utilise the available photons reflected off the target i.e. image converter (IC), image intensifier (II) or TV based systems, and, (b) Those which make use of the temperature and emissivity of the target i.e. thermal imaging systems. We would consider the system design of these two separately.

(A) IC/II/TV based systems: One of the major factors limiting the performance of an optical system at low light level is the noise in the signal. The noise to signal ratio is inversely proportional to the square root of the number of photons reaching the image plane. Hence, a large entrance pupil is required in these systems to ensure collection of more signal photons and consequent enhancement of the signal to noise ratio. Further, to enhance the image illumination, the speed of these systems should be considerably high. As such both high speed and large aperture are the essence of low light level imaging systems. The limiting resolution of sensors like IC tube, II tube or LLTV systems seldom exceeds 50 lines/mm. To match this, the objective lens design has to be optimised to perform the highest modulation transfer in the frequency range 0-50 lines/mm.

IC/II based devices comprise objective, IC/II tube and eyepiece or magnifier. Though the design of objective is of prime importance, great care has to be exercised in the design of the eyepiece of magnifier for its optimum performance. Generally a magnifier for viewing the tube image using a single eye is designed by adopting any standard form of eyepiece having the same optical properties such as magnification and field of view. While fixing the magnification of the eyepiece or magnifier, considerable thought must be given taking into account the sensor and eye resolution. For sustained observation, as in the case of night driving equipment, a binocular type of eyepiece is needed. It is a large diameter lens system through which both the eyes can observe the magnified image of the single output.

For objective lens used in low light level systems, both dioptric and catadioptric systems can be used. Catadioptric systems are shorter in length due to folding of rays and as such are preferred to dioptric systems when a long focal length and a high aperture system is required, despite the fact that the central obscuration reduces both the transmittance and MTF of the device. The aberration correction in this case is normally achieved with the help of a pair of afocal correctors placed inside the focus of the primary mirror based on a design suggested by Becker. The afocal correctors help in controlling spherical aberration and coma, and a field lens placed near the image plane corrects astigmatism. Three-lens corrector with slightly overall positive power would give still better corrections at higher speeds. For making the device light and compact, the Mangin mirror concept is introduced. This consists of a refracting front and reflecting back surface and spherical aberration is corrected by suitably designing the curvature of the refracting surface. The large over-corrected chromatic aberration is compensated by using a positive corrector element in the object space of the system. A doublet used as a field lens corrects the astigmatism as well as lateral colour. The chief drawback of this system is the presence of ghost image in the image plane due to Fresnel reflection from the refracting surface of the thick mirror. In low light level applications, the ghost image can considerably reduce the final image MTF. Hence it is imperative that the refracting surface be given high efficiency broad band antireflection coating over the complete spectral band passing through the system.

For objectives of night vision goggles and driving equipment where field of view of more than 40 degrees is required, Double Gauss System or its variants are employed.

At low light level, the performance of the devices would not only be governed by the aperture and speed of the objective lens, but also, by (a) object size, its brightness, its reflectivity, its reflectivity contrast with respect to the back-ground, (b) intervening medium between the object and the imaging system, (c) overall transmission through the optical system, (d) luminous and radiant sensitivities of the photocathode, (e) integration time of the ultimate

receptor i.e. eye, and, finally (f) observational criterion. Out of these parameters, some are fixed by nature (like, brightness of object depending on ambient light condition, object reflectivity, intervening medium); some by physiological condition (like, integration time of eye); some by basic requirements (like, size of the object, desired range performance, observational criterion) and some by judicious optical and thin film design (like, aperture and speed of input objective lens, overall transmission). There are, however, some other parameters which could be suitably controlled in order to arrive at an optimised system design of the imaging system, as explained below.

When the ambient light level is poor, image intensifier based night vision systems become contrast limited and its range capability in detecting, say, a green painted vehicle against green vegetation is seriously affected. Using the fact that the reflectivity contrast between green paint and green vegetation reverses its polarity three times in the visible wavelength upto 650 nm [5], a study [6,7] has been made to enhance the image contrast and thereby the range capability of the systems by optical filtering of contrast reversal bands. It has been observed that a substantial improvement in range, e.g., of the order of 50% in case of S-25 photocathode under starlit condition over no cut-off filter takes place if a low pass filter cutting off wavelengths upto 660 nm is used. As such from the transmission point of view the system design can be optimised [8] by specifying a high efficiency wide band antireflection coating over the spectrum from 660 nm to 900nm.

The choice of the II tube is made depending on the particular application for which the night vision device is being designed. Special features and applications of different types of II tubes are given in the following Table1.

B. II based systems: All bodies, day and night, radiate thermal energy in the IR wave band as functions of their absolute temperature and emissivity. By examination of terrain through IR region, the sensor reveals information not obtainable by optical cameras or radar. Camouflage netting and foliage do not conceal heat and most military activities produce detectable radiation.

Present day thermal imaging systems essentially consist of:

i) IR optics module
ii) Opto mechanical scanner
iii) IR detector package alongwith its associated cryogenics
iv) Noise free pre-amplifiers
v) Signal processor
vi) Display module

The optical design considerations in case of thermal imaging are quite different from those pertaining to visible systems because of requirement of not only spatial resolution but also thermal resolution. For a given detector size, spatial resolution improves with increased focal length, whereas a better thermal resolution is achieved by increasing the aperture of the objective. As such it often becomes necessary to design thermal optical systems with relative aperture as low as f/0.8.

The required aberration corrections also need special mention. The spatial resolution becomes optimum when the spot size, as obtained form spot diagram analysis, is reduced to $1/5^{th}$ of the detector size. The objective could be either catadioptric or dioptric. The catadioptric systems are completely free from chromatic aberrations, although they suffer from central obscuration and short back focal length. The performance also deteriorates rapidly at off axis, with coma predominating, thus limiting the field to 1^0 or 2^0, although excellent correction is obtained on the axis.

The dioptric systems are more common due to availability of good materials. From optical design point of view, these systems have advantages because high refractive indices and low dispersions of the materials (e.g., germanium) enable better correction.

The optics design is very much linked up with the type of scanning mechanisms. There are two type of scanners: convergent beam scanners and parallel beam scanners. A convergent beam scanner operates in a part of the optical system where rays are converging or approaching a focus. A convergent beam scanner typically is placed between the innermost focussing refractors and the rays are parallel or collimated. If the scanner is located in front of the optical system, the term object plane scanner applies. A parallel beam scanner may also be placed between a relay lens pair. The type of scanner preferred for a particular application depends on what trade-offs can be made. A convergent beam scanner generally requires fewer elements in the optical design and ends in a light and compact system. However such a scanner introduces varying aberrations and distortions with its movement, and these have to be continuously corrected. A parallel beam scanner requires more complicated optics, but is free from the requirement of continuous correction of aberrations with the movement of scanner.

The temperature difference between the target and the background, that gives rise to a signal of the detector output equal to the detector noise, is known as the noise equivalent temperature difference (NETD) and is related [9,10] to the relative aperture of the objective lens, noise equivalent band width of the system, detector pixel size, number of detector elements in series, detectivity of the detector, optics transmission co-efficient and differential change in radiant emittance with differential change in temperature. The minimum resolvable temperature different (MRTD) at any given frequency is related to NETD in terms of scanning frame rate, angular frequency, modulation transfer function

(MTF) of the system at the same angular frequency, instantaneous field of view of the system and the integration time of the eye. Thus the expression of MRTD of thermal imaging system takes into account the effects of noise, resolution, temporal integration, spatial integration and spurious image defects. The values of MRTD at different angular frequencies would represent the minimum temperature difference between the target and the background, demanded by the thermal imaging system to resolve the target at these frequencies. The overall system MTF, on the other hand, takes care of the effects of the optics, as well as of the detector, electronic amplifier, video processor and video monitor. The values of MTF at different angular frequencies would indicate the modulation produced by the thermal imaging system at these frequencies. The intersection of the MRTD vs angular frequencies and MTF vs angular frequencies would denote the limiting angular frequency of the complete system. From the value of the limiting angular frequency, the range capability of the thermal imaging system for any type of target can be easily estimated [11] using Johnson's criterion [12].

The IR detector array converts the incident radiant energy into proportional electrical signal output. Mercury Cadmium Telluride (MCT) cooled to 77 K is now universally accepted as the best detector material for 8000-13000 nm spectral band. Presently available IR detectors comprise large number of discrete detector elements arranged in a variety of configurations, to suit system design requirements and they are mounted on a suitable dewar for cooling to 77 K. Joule Thomson cryostat and stirling engine coolers are two viable options for field applications.

The IR detector arrays cover only a portion of the FOV at an instant of time. Opto-mechanical scanner moves the image across the elements of detector array so as to get the complete 2-D coverage of the total FOV in real time. It is possible to visualise different types of scan mechanisms which may be incorporated in a thermal imager. A plane oscillating mirror is the simplest of all these mechanisms. A rotating polygonal mirror also acts as a scanner in more or less the same way as a plane oscillating mirror. Other scan mechanisms include rotating eyeball lens scanners, refracting polygonal prism scanners and contra rotating wedge scanners. As the latter categories are quite expensive and sometimes may introduce extra aberrations in the system, the most commonly used scanning mechanisms are plane oscillating mirrors and rotating polygonal mirrors. Any scanning arrangements in a thermal imager must include both line scanning (horizontal) and frame scanning (vertical). Sometimes, both polygonal mirror and oscillating mirror are to be employed to get scanning in both planes. In other cases, the same scanning unit can be designed in such a way so that it performs both the tasks.

Electrical signal output from IR detectors is of the order of nanovolts only. Low noise, high gain preamplifiers located close to detector amplify the detector output for further processing. Preamplifier outputs are further amplified by post amplifiers which boost up the signal level, compensate for responsivity variations across the elements of the array and provide optimum filtering to limit the electronic system band-width. For low speed scanning systems such as parallel scan systems, the detector frequency response well exceeds the system requirement and single stage RC low pass filter serves the purpose. However, for high speed scanning systems, viz. series parallel scan systems, the electronic response function of the post amplifiers must compensate for amplitude drop of detector output at higher frequencies. In both the cases, the lower cut off frequency has to be selected to minimise i/f noise without sacrificing image quality.

After post amplifier stage, different design routes have to be adopted for the type of display i.e. LED display (Direct view) or CRT display (Indirect view).

In LED display, the signal outputs from post amplifiers are fed to elements of a LED array identical in configuration to detector array through LED driver stage which converts the voltage output to proportional current. The image on the LED array is scanned by the same scanner as used for scanning the IR image across the detector array, and, viewed through a suitably designed optical system. Since, single line video is not available for such systems, the gains of all the post amplifiers have to be switched simultaneously and uniformly to vary the contrast in the display. Similarly, to change the image brightness level, a DC current above the signal current has to be superimposed simultaneously and uniformly for all the channels by a single control knob.

In CRT display, the outputs from the serial elements are first converted into a single channel output using time delay and integration (TDI) circuitry. The resulting parallel channel outputs are again required to be converted into a single line video output for display on CRT. This is carried out by electronic multiplexing wherein post amplifier outputs are fed to an electronic switch which samples each parallel channel in sequence and repeats the process periodically. The sampling rate is governed by the system requirements and may typically be of the order of a few mega Hertz. The electronic switch has to be sufficiently noiseless, transient-free and fast.

For generation of horizontal and vertical sweeps for display of imagery on CRT monitor, scan position pick off sensors are incorporated in the scanner assembly. Suitably designed logic circuitry, which accepts the scan encoder output as also the multiplexer drive control output, ensure

that multiplexed video output is displayed at appropriate point on the display screen, which is in synchronisation with the scan position and the channel being sampled at that instant of time. Brightness and contrast control and video polarity reversal are standard requirements of CRT display. In addition, a movable electronic cross-hair is to be generated on CRT to facilitate boresighting.

In some of the systems, the Imager output is made compatible with standard TV display monitor using digital scan conversion. This requires two sets of memories which are sequentially used for digitised video storage and readout. While the image output is written on the first memory, the second one is readout at TV rate, sync. pulses introduced and output displayed on the monitor. For the next frame, the role of the two memories is reversed and the process is repeated.

CONCLUSION

The present trend is to develop an all-time, all-weather and all-environment imaging system as intensive research work all over the Globe in the areas of Automatic Target Recognition and Tracking, Multi-Sensor Fusing and Through-the-wall Imaging has opened up possibilities for realisation of such a system. It would probably consist of the combination of CCD/ICCD camera, long range Thermal Imager, Millimetric Wave Imager, Ultra Wide Band (UWB) and Mircowave Radar and Acoustic Sensors. This would, no doubt, post a very challenging job to the system designers, but, nevertheless, days are not very far off when one would be able to use such a system for satellite applications.

ACKNOWLEGEMENT

The author wishes to thank Mr JAR Krishna Moorty, Director, IRDE for his kind permission to present this work.

REFERENCES

[1] G.O. Towler, "Review of Image Intensification and Conversion", in Advances in Electronics and Electron Physics, vol.52,pp 150-152, 1979.

[2] P.K. Datta, P.Dasgupta, O.P. Nijhawan, and R.Hradaynath, "Influences of Temperature on the MTF of Cascaded Image Intensifier Tubes", Appl Opt , 23, pp 1967-1971, 1984.

[3] P.Girard, Y.Beauvais, and P De groot, "Night Vision with Generation III Image Intensifiers", in proceedings of the International Symposium on Opto-Electronics Imaging, New Delhi, Dec 2-5, 1985, pp 89-100.

[4] P.K. Datta and E David, "Effect of Atmospheric Attenuation on the Performance of Image Intensifier Based Devices and a Possible Solution by Gating Technique", in Proceedings of International Conference on Fibre Optics and Photonics (Photnics-2000), Calcutta, Dec 18-20, 2000, pp. 329-332.

[5] E.A. Richards, "Contrast Enhancement in Imaging Devices by Selection of input Photosurface Spectral Response', in Advances in Electronics and Electron Physics, vol 28B, pp:661, 1969.

[6] O P. Nijhawan, P K Datta, and P.Dasgupta, "Contrast Enhancement in Night Vision Devices by Filtering Contrast Reversal Bands', In proceedings of the International Symposium on Opto-electronics Imaging, New Delhi, Dec 2-5, 1985, pp. 161-165.

[7] P.K. Datta, R K. Suri, M.S. Azad, and O P Nijhawan, "Range Prediction of Image Intensifier Tube Based Night Vision Devices and Improving Capability by Filtering Techniques', SPIE, 813, pp. 215-216, 1987

[8] P K. Datta, and O.P. Nijhwan, "Threshold Parameters in Low Light Level Imaging for Optimisation of Performance", in proceedings of Conference on Emerging Opto-electronic Technologies, Bangalore, Dec 16-20, 1991. pp 383-389.

[9] J.A. Ratches, "Static Performance Model for Thermal Imaging System", Opt. Eng. vol, 15, pp. 525-530, 1976.

[10] J.M. Lloyd, "Thermal Imaging System", 5 3-5 6, Plenum Press, New York 1975.

[11] P.K. Datta, Ajay Kumar, O.P. Nijhawan, and D.R. Poddar, "Range Estimation of Thermal Imaging System from MRTD and MTF Measurement", Optik, 1, p-3, 1994

[12] J Johnson, "Analysis of Image Forming Systems', in proceedings of Image Intensifier Symposium, pp 249-273, 1958.

Table 1

TYPE OF TUBE	SPECIAL FEATURES	APPLICATIONS
First Gen 3- State Cascaded	High gain, high S/N at the cost of increased size and weight	Long range observation (both military and non-military), astronomical and medical observations
Second Gen MCP inverter tube	High gain, reduced S/N, lower size and weight	Weapon mounted devices, medium range observation devices, hand held night vision binocular, study of nocturnal animal behaviour
Second Gen and Third Gen/Super Gen Wafer	Low gain, S/N equivalent to MCT inverter, very low weight	Night vision goggles
Demagnification type MCP inverter tube	High gain, S/N equivalent to MCT inverter, high field of view	Night driving
Magnification type MCP inverter tube	Lower gain, S/N equivalent to MCP inverter, high resolution	Night photography
Hybrid tube	High gain, high S/N medium size and weight, gated image tube	Electronic shutters

AN ELECTRIC FIELD INDUCED SINGLE MODE FIBER OPTIC POLARIZATION CONTROLLER

S. Chakraborty, Dr. S. K. Ghosh, * Dr. S. K. Sarkar
E. E. Department, Jadavpur University, Kolkata - 700 032
*** Applied Physics Department Calcutta University**
e-mail : santanu5@vsnl.net

Abstract

Here, we are reporting a new type of fiber optic polarization controller. The state of polarization at the output of the fiber can be changed by varying the voltage of the electric field in which fiber is placed. The electrostriction and Kerr effect are responsible for that change. The experimental study has been made to establish the viability of electric stress induced single mode fiber optic polarization controller and the result can be demonstrated with the help of Poincare sphere. The developed controller removes the problem of stringent alignment in existing polarization controller.

1.0. Introduction :

A single mode fiber optic electrometer for the measurement of the electric field has been reported earlier by the authors [1,2]. The basic concept is that electric field can be used to directly strain the optical fiber causing the relative phase change at the output with respect to input and it is observed by polarimetric arrangement. The electrometer has been designed by placing sufficient length of single mode fiber (50 m.) which is spirally bonded in single layer over one of the circular aluminium plates used as electrodes. The applied field between two circular plates changes the dimension of the single mode fiber and ultimately change the state of polarization of the output beam due to electrostriction and electro-optic Kerr effect.

Single mode fiber optic controllers are popular now-a-days[3] to control the state the polarization (SOP) of output laser for coherent detection. In conventional polarization controllers, the polarization is controlled by mechanical twisting or micro-bending, so that their alignment among the fibers should be maintained too precisely such that any mechanical disturbance may prove hazardous[4]. The experiment is conducted by coupling polarized laser beam to the single mode fiber-optic electrometer and the output beam is then analyzed. The change of SOP intensities are recorded for different direct voltages or altermating voltages and the spacing between two electrodes of the electrometer. The experimental observation reveals that the SOP is a complex dependence of voltage and spacing between two plates and they are independent of each other. The experimental results can be represented by Poincare Sphere[5].

The study shows that the variation of SOP is the joint effect of electrostriction and Kerr, where electrodes are separated by minimum allowable distance whereas Kerr effect is prominent when the sufficient spacing is allowed in between the electrodes. The experimental and theoretical results both support the fact that the azimuth change is very prominent rather than change in ellipticity when we perform the experiment allowing some spacing between the electrodes. Whereas change in ellipticity is dominant with less change in azimuth at closest distance between the plates. Hence transformation of state of elliptic polarized beam to linearly polarized beam and vice versa with little change in azimuth, is possible with this polarization controller. Similarly considerable change in azimuth is possible with small change in ellipticity. SOP of controller can be changed by varying the electric field and/or the separation between two electrodes. The advantage of this controller is that, it is easy to control the SOP whereas in conventional controller alignment among the fiber elements are critical. So far our developed controller is concerned, the dynamic range is limited.

2.0. Theory :

Single mode fiber which is normally isotropic in nature becomes birefringent under the application of electric field [1,2]. For the developed polarization controller, due to elongation in length in the transverse direction and compression in length in the direction perpendicular to it as the electric pressure is built up in the system for the application of direct or alternating voltage, the corresponding change in polarization is :

$$\Delta\phi = 2\pi\, n_{co}\, \frac{\Delta l}{\lambda} \qquad \text{.....(1)}$$

Where, $\Delta l = \dfrac{\varepsilon l \times V^2}{\sigma Y (2d^2)}$

n_{co} = Core refractive index for silica glass.
Fiber = 1.452
l = length of fiber winding
λ = He-Ne Laser wavelength = 633mm
V = impressed voltage on electometer
d = separation between two plates.

Kerr effect is the electo-optic effect for application of voltage, due to which laser beam faces an increment in refractive index in a particular direction when guided through the single mode fiber. This in turn produces a change in polarization of magnitude.

$$\Delta\phi_{Kerr} = \frac{2\pi\, Klv^2}{d^2} \quad \text{.....(2)}$$

Where :

K = Kerr constant of silica glass $=.17\times10^{-14}$ m/v^2 .
L = Total length of wound single mode fiber in m.
V = Voltage impressed on the eletrometer in volts.
d = Seperation between two plates.

From theoretical points of view, the output polarization changes its phase due to conbinational effect of electrosfriction and kerr effect,

$$\Delta\phi = \Delta\phi_{elec} + \Delta\phi_{Kerr}$$
$$= 2\pi\left(n_o \frac{\Delta\phi}{\lambda} + \frac{Klv^2}{d^2}\right) \quad \text{.....(3)}$$

It is evident from theoretical study that when the separation between two plates is 0·227 mm, a phase change of π radian, (for 50 m single mode fiber) may be realised for 230 V d.c. Voltage. With large spacing between two plates, only 15° change of phase is introduced due to birefringence at 250 V d.c.

2.1. Control of birefringence by Photoelastic straining :

A material is deformed, when it is placed under a field of elastic stress. As the local density gets modify its optical property is also changed. If a elastic stress, electrostriction, is applied to a linear anisotropic medium, when no torsion is present, its effects are directly rendered by a modification of the index ellipsoid of the materials [3]. This small modificaion of ellipticity of polarized laser beam propagating through the single mode fiber under elastic stress (σ) may be utilised for controlling birefringence.

The change in index of ellipsoid is given by.

$$\frac{1}{n_{ij}^2} = \frac{1}{n_{ij}^2}\bigg|_{\delta=0} + \Delta\left[\frac{1}{n_{ij}^2}\right] \quad \text{.....(4)}$$

The variation $\Delta\left[\frac{1}{n_{ij}^2}\right]$ is a function of the components of the stress tensor which is delineated as[3] :

$$\Delta\left[\frac{1}{n_{ij}^2}\right] = \pi_{ijkl}\sigma_{kl} \quad \text{.....(5)}$$

Where, π_{ijkl} = Forth order piezo-optical tensor.

The typical value of different components of π for silica glass is of the order 10^{-12} m^2/n^{-1}.

From theoretical calculations it can be shown that a change from elliptic polarization to linear polarization and again change to elliptic polarization is rendered with 50 m. of S.M. fiber with a spacing of 0·227 mm betweeen two electrodes under potential difference of 170 volts to 190 volts.

3.0 Controller Design :

Fifty metres of single mode fiber is wound spirally in single layer between two annular shaped aluminum electrodes. The inner hole of the alumium electrode has a diameter of 4 cm which is designed to minimize micro-bending effect, and the outer diameter of the electrode is 20 cm. to accommodate 50m. of S.M. fiber. The spacing between two plates can be changed by using micropositioner arrangement. The bonded fiber coil attached to one of the plates is fixed in position and the movement of the other plate can be varied by micro-positioner displacement.

The minimum increment in separation between the plates can be controlled by an amount of 0·001 mm (which is the least count of the micrometer).

4.0 Experimental set-up and procedure :

The experimental set-up is shown in Fig (1) He-Ne laser is first passed through a polarizer and then focused by the microscope objective to the single mode fiber for efficient coupling. The laser output beam is passed through an analyser and detected by a photodetector for measurement of optical power. We used the low noise power meter for recording the data.

Following adjustment of the coupling optics, the polarizer and analyser are positioned in crossed condition and adjusted to minimise the deceted signal. After application of voltage to the fiber optic controller, linealy polarized input beams become elliptically polarized at the out put.

The phase change in polarization i.e. azimuth can be determined by rotation of the analyzer in the direction of major axis. At the same time by measuring the power in orthogonal direction or in minor axis, ellipticaty can be determined. The ellipticity is precisely the ratio of power carried through two axis.

In order to measure the contribution of electrostriction and Kerr effect, we performed the experiment with varing voltages and spacing between

the electrodes of the polarization controller. We used the micro-positioner controller to vary the spacing between the plates. In this experiment we tried to maintain the input and output optics free from strain to avoid influencing the measurement with their own birefringence.

5.0 Results & Discussions

The results for experiment performed with the developed polarization controller is given in Table - 1, Table -2 and Table -3. From experimentation we may conclude that output polarization changes with applying voltage between the plates as well as the separation between the plates for fixed voltage. Actually, the phase variation is related to square of the applied voltage [1]. The experimental observation relates to the theoretical back ground . It may be projected that for experiment minimum separation between two electrodes both effect of electrostriction and Kerr effect are responsible for change in polarization, of which electrostriction effect is prominent [1,2]. Both of these effects obey the square law dependance of electric field between two electodes to change the phase. When the spacing between the two electrodes of the polarization controller increases, the change of phase is small compared to the previous case, which is also evident from Table-1 which indicates the change in azimuth of polarized light beam for different voltages between the electrodes separated by a distance of ·249 mm. The effect of electrostiction causes the photoelastic straining and ellipticity of the Laser beam is found to change for a direct voltage variation from 170 volts to 190 volts. At the same time when we investigate the ellipticity of the output beam with increase of applied voltage, the ellipticity disappers at certain voltage i.e . it becomes linearly polarized and with further increase of voltage elliptical polarized light again reappears. For our experimental investivation, within the voltage range 170 volts - 190 volts the output beam changes from elliptical polarization to linear polarization and again to elliptical polarization and the crossover voltage is 180 volts. Table - 2 shows the change in ellipticity of polarized beam for different D.C. voltage between the electrodes with the electrodes separated by a distance 0·227 m.m, a fiber distance. For experiment with variable separation between two electrodes i.e. the electrode with fiber winding does not touch the other electrode, the electrostriction effect is absent and only Kerr effect is porminent. We also observe such SOP change is absent when spacing between the two electrodes is sufficiently large. From table-1 and table-3 we may conclude that Kerr effect contributes little to the change in ellipticity and more to the change in azimuth of the polarized laser beam. Table-3 shows the change in azimuth and ellipticity of polarized beam with variable separation between electrodes at 150 volts d.c.

Direct Voltage (Volts)	Power Carried through major axis (μw)	Power Carried through minor axis (μw)	Rotation of axis of Analyser	Remarks
20	2·5	·8	7°	0
50	2·43	· 78	8°	0
75	2·42	· 77	10°	0
100	2·41	· 75	14°	0
125	2·4	· 74	20°	0
150	2·42	· 76	28°	0
175	2·39	· 75	38°	0
200	2·37	· 73	50°	0

Table 1 : Change in Azimuth of polarized light for different d.c. voltage between the electodes separated by a distance of 0·24 mm.

Direct Voltage (Volts)	Power Carried through major axis (μw)	Power Carried through minor axis (μw)	Rotation of axis of Analyser	Remarks
170	2·31	1·2	5°	0
172	2·65	· 91	6°	0
174	2·73	· 62	7°	0
176	2·92	· 19	7· 5°	0
178	3·25	· 05	8°	1
180	3·49	· 15	8°	0
182	3·37	· 31	9°	0
185	3·15	· 6	9°	0
188	2·9	1·0	10°	0

Table 2: The change in ellipticity of polarized light for different d.c voltage between the electrodes separated by a distance of 0.227 mm.

Direct Voltage (Volts)	Separation between electrodes (mm)	Power Carried through minor axis (μw)	Power Carried through major axis (μw)	Rotation of axis of Analyser
150 Volts	·2	2·5	·1	5°
	·205	2·47	·9	8°
	·21	2·5	·9	12°
	·215	2·6	·8	17°
	·22	2·5	·9	22°
	·225	2·4	·1	28°
	·23	2·5	·1	35°
	·24	2·6	·8	45°
	·245	2·5	·1	55°

Table 3 : Change in Azimuth and ellipticity of polar ized beam with variable spacing between the electrodes at 150 volts d.c

5.1 Poincare sphere Representation of the working of polarization controller :

Proper characterization of optical polarization controller needs the change of state of polarization to be represented with the help of Poincare sphere notation. By usual practice of polarization measurement by Poincare sphere is a helpful diagram to explain the SOP of any output beam. In view of that we have seen in our experiment the traversing of the state of polarization point through the meridian circle is achieved by changing direct voltage impressed on the controller in the range 170 volts to 190 volts, minimum spacing between its two electrodes (Fig.2). In this case change in ellipticity corresponds to little change in azimuth. Similar change in azimuth is obtained (path 'B' in Fig.2) by varying the spacing between two electrodes in the range 0·200 mm 0·245 mm with a fixed voltage of 150 volts in between the electrodes. In other words the Poincare sphere representation can be extended for indicating the SOP with respect to applied voltage over the sphere.

Conclusion :

An humble study has been reported in this paper for the induced polarization and control of birefringence in the developed fiber-optic controller with the help of direct voltage on the electrodes of the controller and/or changing the separation between two electrodes. So far from experimental point of view, only the polarization changes from elliptic to linear and again to elliptic within the range of D.C. voltage (170 V- 190 V) for a particular set-up. This voltage range is unique for the present set-up because below this range of voltage the SOP change is not prominent and above this range the change in SOP is associated with considerable amount of phase change. Finally to get any desired polarization from the polarization controller, it can be calibrated with the help of Poincare sphere represented with voltage for particular set-up.

Reference

1) Ghosh S. K, Sarkar S. K., Chakraborty S,'Studies of Electostriction and Kerr effects on a Fiber Optic Direct Voltage Operated Electrometer, Comm. In Inrumentation (CSIO-CSIR) Vol.8, No. 1, Jan - March 2001.

2) Ghosh S. K., Sarkar S. K., Chakraborty S, ' To study Electrostriction and kerr effects in a Proposed Fiber Optic Electrometer With A.C. Excition, 'Accepted in CII (CSIO-CSIR) April 2001.

3) Lefevre H.C., ' Single - Mode Fiber Fractional wave Devices and Polarization Controller, 'Elec. Lett, Vol.20, pp-253-254, August 1980

4) Imai T., Nosu K., Yamaguchi, ' Optical Polarization Control Utilising and Optical Heterodyne Detection Scheme, 'Elect Lett, Vol. 21, pp-52-53, 1985

5) Ulrich R., 'Polarization Stabilization in Single Mode Fiber, 'Applied Phys. Lett. 35(ii) pp-840-842, Dec 1979

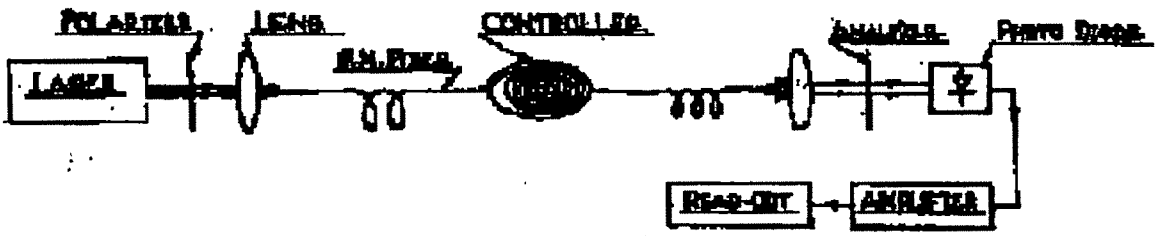

FIG-1 : EXPERIMENTAL SET-UP.

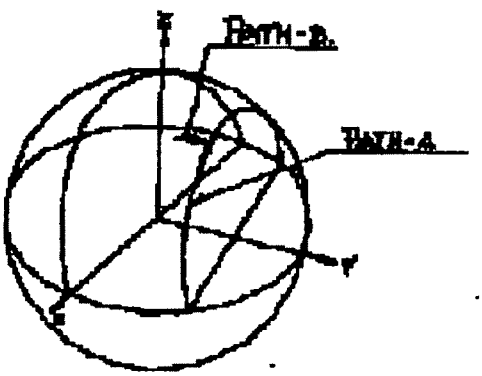

FIG-2: POINCARE SPHERE REPRESENTATION OF POLARIZATION TRANSFORMATION.

STUDY OF A FIBER-OPTIC NON-CONTACT ROTATION SENSOR FOR CALIBRATION OF ENERGY METER

S. K. Ghosh, A. Rakshit, S. Chakraborty and S. Mondol
E. E. Department, Jadavpur University, Kolkata - 700 032
e-mail : santanu5@vsnl.net

Abstract

The support software for a fiber optic noncontact rotation sensor based on the laser intensity modulation induced by the reflection of a rotation surface, has been described in the present paper. As the acquisition of the reflection beam is affected by pseudorandom and random noises, this work enables the calculation on through autocorrelation of the results to get rid of the effects of noise. As the work includes floating point arithmatic it is favourable to interface the measuring set up with a PC Online, after converting the intensity variation of the laser beam to it's digital form with ADC and communicating these results to PC with the help of the printer port. During analog to digital conversion adaptive sampling is introduced with proper software, design of which is delineated here. The Software is written in "C" language and with suitable implementation of the system the method provides uniform resolution at all speeds of the rotation surface within a wide working range.

1.0. Introduction :

Optical fiber sensor system is more suitable in modern days due to its greater immunity to EMI, EMC noises and corrosion. Noncontact type speed measuring method is feasible in situations where the measurement is mechanically inaccessible or the case is not suitable for contact type measuring arrangement[1]. In earlier works noncontact type speed measuring techniques have been developed where there are no special marking on the surface[1]. The fiber optic sensor system is employed for capturing the circumferential irregularities of the rotating surface under measurement. The principle is that for a steady speed of the surface, irregularities on the surface repeats at regular intervals and a pseudo-random data is generated by sensing these irregularities. The autocorrelogram has been computed from these electrical data which are the replica of its intensity modulated optical form and the speed of the surface is calculated by detecting the interval between successive global peaks [1,2].

In this work laser light falls on the surface, and is reflected back and is captured and it's intensity is converted to an electrical signal which after sampling and A/D conversion is supplied to the PC by printer port communication, and the data is stored in hard disk file[2]. Reading data from the file, the autocorrelogram is produced in which the repeatation of the global maxima gives the speed of the surface directly. The use of laser beam, instead of noncoherent light beam to illuminate the surface, causes an improved signal to noise ratio (S/N) for the system [3,4]. It has been found that the guided mode of collection of laser beam required around 10 μw power to be coupled to the fiber. A multimode fiber is used and the experimental study reveals that the measuring system works with resolution of 0.1% over a wide range of speed from a very low value 1000 r.p.m.

In the present work the signal to noise ratio is greatly improved for such a noncontact speed measuring system with the noise elimination by adaptive sampling and calculation of autocorrelation[5] of the results by floating point arithmatic. The hardware and software details for such a method for non contact type speed measurement is included in this paper.

2.0. Theory :

The basic idea behind this non-contact type rotation sensor is that there remains a signature of irregularities, which are repeated at regular interval when the rotation surface is at constant speed, of rotation . The signature of these irregularities in the optical signal is pseudo-random in nature with a particular form repeats itself after a complete period of revolution. The autocorrelogram is computed from this pseudo-random data and revolution period is determined by realizing the repeatation of global peaks through zone search[6] method.

2.1. Autocorrelogram Computation :

The autocorrelogram function for a finite real discrete pseudo-random event is delineated as [6].

$$R_{xx}(T) = \frac{1}{N} \sum_{K=0}^{N-1} \chi(t_k)\, \chi(t_k+T) \quad \text{... eqn. (1)}$$

Where,

t_k = KT; T is the sampling interval.

N = Number of discrete samples.

$\chi(t_k)$ = discrete sample value at time t_k.

The computation of the autocorrelogram function involves a large number of real floating point multiplications for moderately large value of N.

The Wiener - Khintchine theorem[6] provides an alternative way to compute the autocorrelogram function. According to this theorem the computation of autocorrelogram function may be given as :

$$R_{xx}(T) = \frac{1}{N} \sum_{n=0}^{N-1} S_{xx}(n) e^{j2\pi n/(NT)} \quad \text{... eqn. (2)}$$

Where $S_{xx}(n)$ is the discrete power density specturm computed as :

$$S_{xx}(n) = \frac{1}{N} \sum_{n=0}^{N-1} x(n) \times *(n) \quad \text{... eqn. (3)}$$

Where $\chi(n) = \sum_{n=0}^{N-1} x(k) W_n^{nk}$ ... eqn. (4)

for n = 0,1,2 ..... (N-1);

χ^* (n) is conguate of χ(n).

And, discrete Fourier transform (D.F.T.) of χ(k) is χ(n).

N = Number of discrete samples.

n = harmonic number.

The simplification achieved by the D.F.T. technique, specially for large value of N is so great that even this complex computational method (by Wiener Khintchine theorem) gives significant advantage over real-time autocorrelation.

2.2. Peak detection algorithm by zone search method :

The autocorrelogram for a particular speed of the rotation surface is given in fig. (1). The figure reveals that there is global peaks accompanied by local peaks due to noise in the signal. The global peaks are the signature of the irregularities and period of the global peaks is essential to calculate the speed of the rotation surface. Hence a special peak detection technique is employed for searching the global peaks in the authocorrelogram. This method is efficient and termed as zone search method. This method is comprised of searching of maximum value i.e. the peak itself over a limited zone in which the peak is expected to occur. Proper selection of limited zone is obtained with the help of following considerations. The time interval between successive global peaks is essentially constant, hence it is estimated from the autocorrelogram of a preliminary estimate (T_{estm}) of correct time interval. The zone of search of the maximum value is selected between points (fig.1) z_1 and z_2 where $z_1 = {}^1/_2\, T_{estm}$ and $z_2 = {}^3/_2)\, T_{estm}$. From the estimated locations of z_1 and z_2, direct search for maximum value is made between these two points . This maximum value corresponds to the location of P_2. The number of data points between P_1 and P_2 corresponds to the actual speed of the shaft.

3. Hardware Requirement

3.1. Fiber optical sensor system :

The fiber optic sensor set-up is shown in Fig. 2. He-Ne laser is coupled to multimode fiber (core diameter = 123μm, clad diameter = 400 μm) with the focussing help of a lens and the multimode fiber tip is placed with respect to the surface in such a way that it illuminates small portion of the surface. The laser beam reflected from the surface is collected by another similar strip of multimode fiber, and the guided laser beam illuminates the base of a photo-transistor. The converted electrical signal is amplified and placed at the input of the sampler.

3.2. Sample and Hold Circuit :

The sample and hold circut is shown in Fig. - (3). A narrow pulse at the input G_1 opens the FET switch (sampling) and Vin, which is the electrical conversion of optical wave carrying the signature of measurand variable, charges the capacitor C untill there is a narrow pulse at G_2 of the discharge FET switch. The capacitor C discharges through the FET discharge switch and the circuit is ready for another sampling sequence. The narrow (50 ns.) pulses for sampling and discharging action is generated through software programming. The sampling rate may be controlled by repeating the sample and hold pulses at G_1 and G_2 with a software controlled repeatation rate. For an initial estimate of sampling interval, a lower limit of speed is specified. After creating the autocorrelogram by using this sampling interval to the software on a priority basis, the sampling interval for the next sequence of event is calculated. This process is an adaptive way of reaching the exact sampling rate[7]. The useful interative equation for this method is expressed as :

$$(T_{samp})\, n+1 = \frac{T_{fn}}{(N/4)} \quad \text{... eqn. (5)}$$

Where, T_{fn} is the time period computed at the end of the n^{th} interation.

N = Number of discrete samples.

3.3. A/D Conversion and data interfacing with PC via printer port :

The pin-out diagram of DB-25 printer port connector (LPT-1) shown in Fig. (4). The DB - 25 connector is connected to three eight bit registers on the PC bus side. These three registers are designated as Data output register, status input register and command output register. The addresses assigned to three registers are Base address + 0 , Base address + 1 and address + 2, respectively. On the other side rather than PC, four user defined data input lines are selected through pin number : 10, 12, 13, 15 of the DB-25 connector. Pins 2 and 3 are used to control G_1 and G_2 lines of the sample and hold circuits. The other pins of the DB-25 connector are intended to carry the data byte for control of DAS (0808) and A/D converter, such that (1) start conversion (pin 3), (2) End conversion (pin no.11), (3) ALE, ADC, ADB, ADE (pin Nos. 4,5,6,7 respectively) are used. The Hardware arrangement also provides convenient four byte data interfacing of PC with A/D converter. The sampled output is connected to pin no. 26 of the Data Acquisition System (DAS 0808) such that pin no. 26 is input 0 where input 0 is the only input that is enabled by selection of ADC=0, ADB = 0, ADE = 0. The ALE output from the PC latches the data with the DAS 0808. The DAS performs the first stage of A/D conversion and the output is eight bit digital word. The data output from the DAS is then converted to its analog form and this analog signal is again converted to 4 bit digital word by a four bit A/D converter. These four output lines from A/D converter are connected to the Data Input pins of the DB-25 connector. A schmitt trigger circuit generates 300 K.Hz. clock pulse is used to drive the DAS 0808. This 300 K.Hz clock pulse is related to DAS conversion time, which is 3.3 μs. The conversion time of the available D/A and four bit A/D converters are 50 μs and 22 μs respectively. At last the output pin ADC of the DB-25 connector supplies the start conversion pulse.

3.4. Timing Diagram :

The timing diagram for different activities performed by the PC interfaced system is shown in Fig. (5). At first the DAS goes to Reset mode and ALE pin is high after 50 ns. with the pin remains high for 2.5 μs. The sampling gate is strobed at the same instant and new data is place at Input 0 of the DAS 0808. After a delay of 2.5 μs from the moment DAS is strobed, the start conversion pin of the DAS 0808 is held high. A software then polls the end conversion pin, if held high it indicates that the A/D conversion of the sampled data is over. The data read software which is installed in the PC starts polling for the data at this point of time and this polling continues for a time span of 100 μs. After successful capturing of digital word the autocorrelogram starts and continues including software delay for 2.5 ms. It is time when the hardware is reset and another cycle starts.

4.0 Software :

A program in 'C' language is written to handle properly. The salient features of the program may be delineated as :

1. To generate strobe pulses for different hardware devices in tune with the timing diagram.
2. To store data in a hard-disk file.
3. To compute the autocorrelogram for the data stream.
4. To include delay between two actions.
5. To generate graphics with the results obtained from autocorrelogram.

The instructions 'import' and 'outport' with proper command line arguments such as register address of input registers, are used to make access to a input and output device respectively. Masking and demasking techniques of eight bit data stream, are solutions to make a particular line of communication on or off. The software delay is introduced with 'delay' instruction available in 'C' language, with argument specifying a particular time interval. A hard disk file is created and opened with both reading and writing attributes to store the data stream from the A/D converter. Reading the integer value of the binary data stream from the file, the complex domain analysis of the data stream is generated to achieve the Fast Fourier Transform (F.F.T.) of the data stream. The floating point arithmatic is important to maintain the integrity of the adopted F.F.T. technique. After the successful completion of the First Fourier Transform, the autocorrelogram is calculated. The zone search method i.e. the global peak detection algorithm subroutine is written in 'C' language. The plot of the autocorrelogram output with respect to time is achieved with the interaction contained in graphics.h header file. The different subroutines to carry out different projects, which are written in 'C' language, are amalgumated as a single library function rotation.lib under the header file rotaion.h.

5.0 Calibration of Energymeter :

The data required energymeter calibration are : (a) Meter constant (b) Load current (c) power factor (d) Full load current and (e) line voltage .

Experimental tests have been performed for different load currents. Repeatability tests performed over 10 hour interval has given an accuracy of the same order of magnitude.

The calibration curve of the energy meter performed by conventional method is shown in Fig (6). It is seen that if the calibration performed by the conventional method is supposed to be correct, then the accuracy of the present method is within 1%.

4. Conclusion :

An optical fiber sensor system for measuring speed of rotation surfaces has been described. This sensor system doesn't make use of reference channel but typical light intensity variation externally induced, such as fibre losses or source intensity fluctuation, result in changing only the amplitude of the response curve and hence the target searched by signal is not affected by such intensity fluctuations. The speed of the measurand surface is also not affected by the measument process so that the speeds of very low power rotating devices can be accurately measured. Due to this reason the system can be faithfully used as a tool for calibration of energy meter. Accuracy achieved in the present investigation is 1%.

REFERENCES

1) Mukherjee A., Rakhit A., Bhatterjee S.N,' A Novel PC based speed monitoring system,' JI of Institu tion of Engineers,' Pt. EL., Vol. 75, pp-88-90, November 1994.

2) Mukherjee A,' Development of a software package for GPIB compatible automatic test systems,' MEE Thesis, Jadavpur University, 1990

3) Senior J.M., Cisworth S.U., Burrow N.G,' An extrinsic optical fiber sensor employing partially reflecting mirror,' SPIE, vol. 522, pp.204-210, 1995

4) Johnson M,' Fiber displacement sensor for metrology ad control,' Opt. Eng., Vol. 24, no.6, pp-961-965, 1985.

5) Papopoulis A,' Probability, random variables and stochastic processes,' McGraw Hill, 1985.

6) Ghosh S.K., Rakshit A., Dutta J.C., Mandal S., Chakraborty S., 'Development of a Fiber-optical Non-contact Rotation Sensor for calibration of Energy meter,' Accepted for publication in the Journal of Institution of Engineers', April - 2001

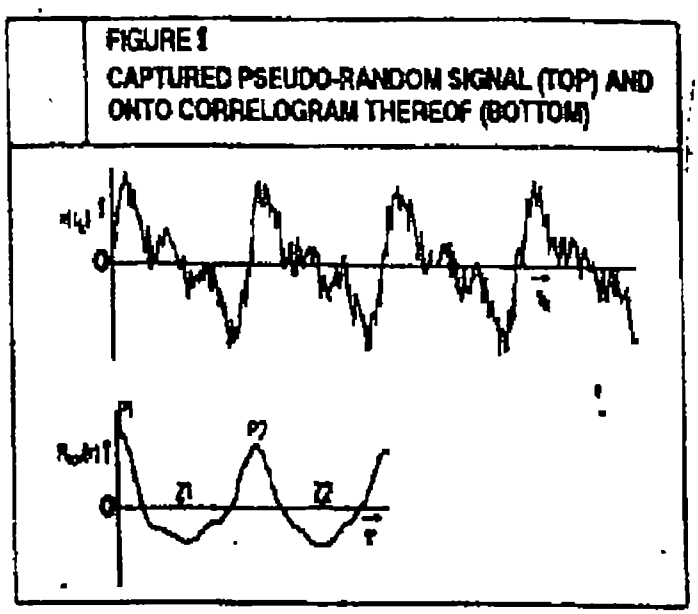

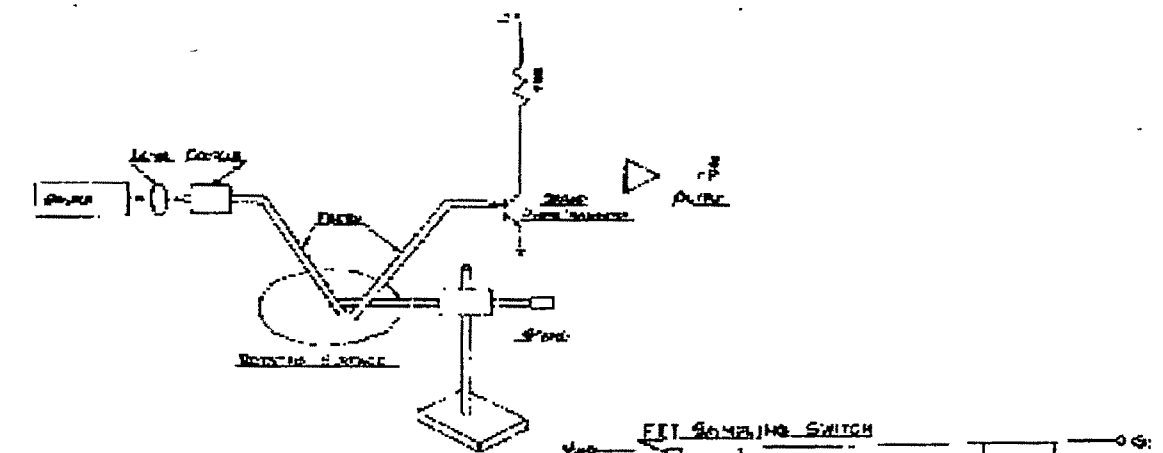

FIG-3: SAMPLE AND HOLD CIRCUIT

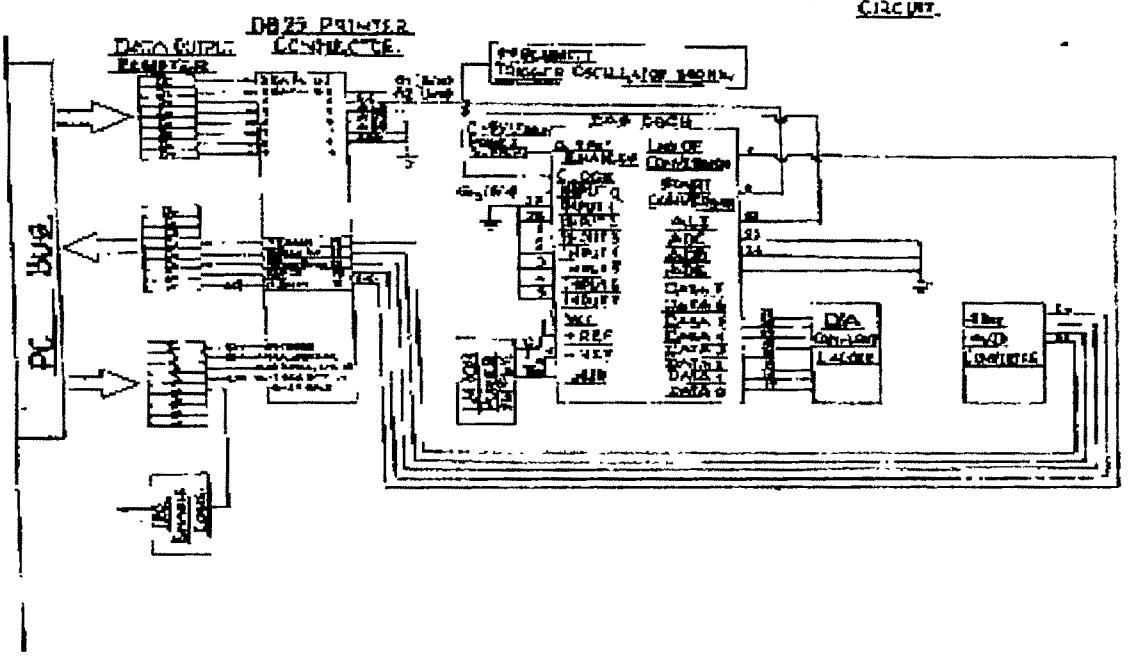

FIG-4: HARDWARE DETAILS.

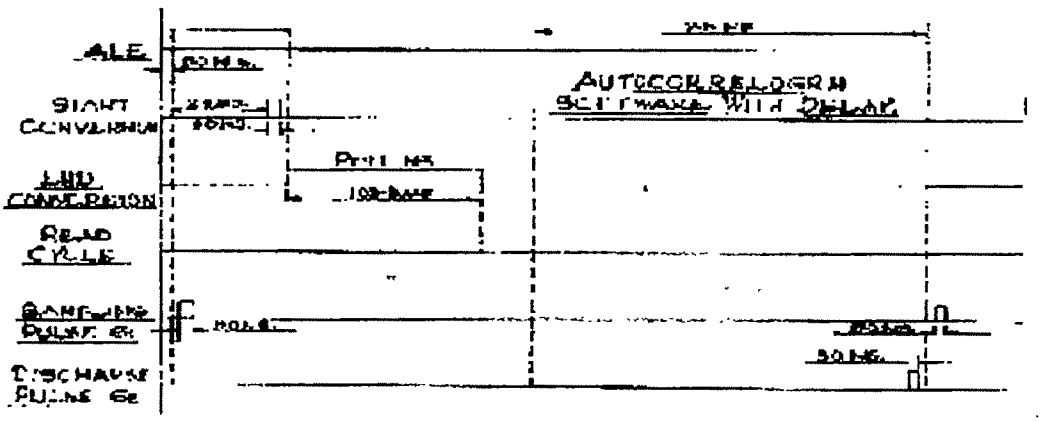

FIG-2 : TIMING DIAGRAM.

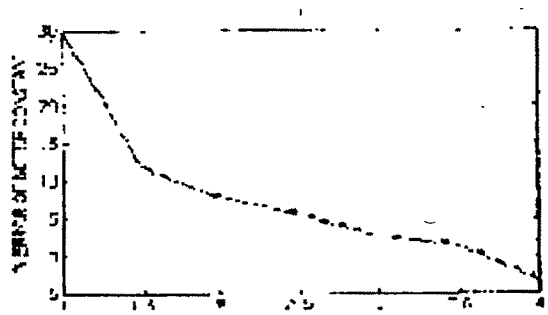

FIG-3 : CALIBRATION OF THE ENERGY PROBE

Control And Communication For The Power Grid In A Restructured Power Industry

Anjan Bose
College of Engineering & Architecture
Pullman, WA 99164-2714, USA

Abstract

The restructuring of the electric power utility industry all over the world has caused a reexamination of the planning and operation of the power grid. At the same time, great advances in communication and computer technology have made more sophisticated control of the power grid possible. We present here a closer look at how new computation, communication and control can be applied to the power grid for better security and economy of the power supply. We also make clear how this structuring of the power industry to bring more competition among the energy suppliers is made possible by these new technologies.

We first examine the existing control and operation of the power grid. Then we look at the new structures proposed in various parts of the world and how that affects power grid operation. The new relevant computation and communication technologies are presented next together with the new power grid control that these technologies can enable. Finally, we show not only how these new technologies can operate the power system better but also how they enhance the operation of the energy markets in a restructured industry.

A New Approach To Designing PID Controller

S. P. Bhattacharyya
Texas A & M University
College Station, TX 77845, USA

Extended Abstract

The Proportional-Integral-Derivative (PID) controller is the workhorse of the control industry and is used in the world in motion control, process control, manufacturing and aerospace applications. It is therefore a surprisingly severe drawback of control theory that modern (H_2) and postmodern (H_∞) methods of synthesis and design are inapplicable to PID controller.

In this talk we present recent results aimed at remedying this situation. Specificcally, we present procedures by means of which the entire set of PID controllers stabilizing a given linear time invariant (LTI) plant can be constructively calculated. This result is applicable to both continuous time systems as well as discrete time or digital systems. By "constructively" we mean that the solution procedure involves the computation of solutions of linear equations and linear inequalities.

We also show how it is possible to determine, constructively, subsets of the stabilizing set attaining various performance objectives. These performance criteria include robustness, nonfragility, optimality, loop shaping and model matching. Illustrative examples are included as well as future research and development directions

Author Index

A. A. Ghatol, 19
A. Arvind Kumar, 351
A. Basuray, 665
A. Chakrabarty, 161
A. D. Kulkarni, 121, 139, 203
A. Datta, 665
A. Gupta , 155
A. K Chakraborty, 641
A. K. Daniel, 607
A. K. Gupta, 179
A. K. Mondal, 509, 521
A. K. Mukhopadhyay, 161, 191, 243, 379
A. K. Pradhan, 187
A. K. Singh , 231
A. Kanadaswamy, 299, 472
A. P. Mittal, 389
A. P. Tiwari, 331
A. Rakshit, 711
A. Routray, 187
A. S. Chaudhuri, 173, 365
A. S. Zadgaonkar, 551
A. Srinivasa Rao, 279
A. Sutradhar,365
Abdullah, 345
Abhinav Roongta, 603
Abhishek. Sharma, 65
Ajay Ghosh, 679
Ajay Guleria, 581
Ajit K. Chattopadhyay, 249
Alok Barua,359
Amal K. Ghosh, 619
Amitabha Basuray, 619
Anindita Dasgupta, 81
Anish Deb, 81
Anjan Bose,705
Anup Kumar Bandyopadhyay, 585
Anupam Shukla, 551
Arabinda. Das, 191
Arghya Sarkar, 379
Arijit Basuray, 397
Asit. K. Datta, 555, 671
Awadhesh Kumar Singh, 585
B. B. Pati , 41
B. Bandyopadhyay, 13, 331
B. Bhattacharya, 293
B. D. Shinde, 631, 633
B. K. Dubey , 273
B. L. Narayan , 547
B. M. Karan, 109, 285, 453, 485
B. Prabhakara Rao, 595
Barin Kumar De, 511, 615
Bhaskar Bhattacharya, 685
Biswapriya Mukhopadhyay, 73, 397
Brahmjit Singh, 575
C. A. Murthy, 547
C. Christober Asir Rajan, 101, 133
C. K. Chanda, 161
C. Sathish Kumar, 472
Chakravarthini M. Sajj, 13
D Najumnissa Jamal, 345
D. Basu, 685
D. Das, 97
D. P. Kothari, 9, 91, 149
D. Patranabis, 315
D. R. Rana, 581
D. K. Mohanta, 109
Debashis Ghosh, 481
Deepak Bhushan, 641
Dipten Dasgupta, 561
Dola Roy Choudhury, 365
G. C. Gaiskas, 355
G. C. Ray, 365
G. Karmegam, 355
G. Raja Rao, 57
G. S. Kalyan, 51, 61
G. S. N Raju, 599
G. V. K. R. Sastry, 51, 57, 61
Ganti Prasada Rao, 1
Gautam Saha, 359
Gautam Sarkar, 81, 379
H. Saha, 621, 625
I. Alam, 115
J. C. Santiard, 459
J. Das, 625
J. J. Barve , 67
J. K. Ray, 407, 419
J. N. Roy, 459
J. S. Saini, 389

Jaya Basu , 647
José Luis Rodríguez Marrero, 259
K. A. Gopal Rao, 209, 371
K. Aadhi Vairava Sundaram, 25
K. B. Madhu Sahu, 51
K. C. Patra, 41
K. Chandra Bhushana Rao, 599
K. K. Aggarwal, 575
K. K. Saxena, 143, 571,
K. Kishan Rao, 503, 531
K. L. Barui , 293
K. Manivannan, 101, 133
K. N. Dey, 679
K. P. Detroja, 67
K. Padma Raju, 595
K. R. Gottumukkala, 599
Kajal Dihidar, 619
Kallol Bhattacharyya, 641
Konika Das (Bhattacharya), 481
Krishna Vasudevan, 475
L. Fraiwan, 561
L. N. Hazra, 653, 659
Lakshminarayan Hazra, 647.
M. C. Srivastava, 631, 633
M. Chidambaram, 37, 351
M. D. Desai, 339
M. Dasgupta, 509, 521
M. Gopal, 389
M. J. Nigam, 25
M. K. Patel, 187
M. Mitra, 463
M. Mondal, 509, 521
M. R. Mohan, 101, 133
M. R. Vikraman, 299
M. Ray (Shah), 665
M. S. Nagaraj, 121, 139, 203
M. V. Raghunadh, 503, 531
Mahadev S. Patil, 303
Malay K. Kundu, 527
N. Ahmed, 31
N. Nagendra, 121, 139
N. P. Singh, 571
N. Patnekar, 561
N. S. Bhuvaneswari, 167
N. S. Murthy, 503, 531
Narendra Kumar, 179
Narottam Chand, 517, 581
Netai Pal, 243
O V Ramana Murthy, 31
P. K. Satpathy, 97.
P. Anbalagan, 215
P. B. Dutta Gupta, 97, 199
P. K. Datta, 699
P. K. Sadhu, 285, 453
P. K. Sinha, 485
P. Mallikarjuna Rao
P. N. Das, 161
P. Praveen , 447
P. S. Bimbhra, 269
P. V. Subbaiah, 595
P. Venkataramu, 203
P. Venkateshwaran, 437
Pabitra Pal Choudhury, 619
Partha Sarathi.Pal, 359
Pinaki Pal, 611, 615
Pradeep Chatterjee, 485
Pradip Sarkar, 589
Prodyot Kumar Roy, 73, 397
Puvvada Ramesh, 467
R. Abdul Matheen, 345
R. C. Bansal, 91
R. C. Jha, 109, 115
R. Chakraborti, 453
R. Gangopadhyay, 693
R. K. Manimozhian, 215
R. K. Nagaria, 437
R. K. P. Bhatt, 31
R. N. Chakrabarti, 285
R. N. Mahanty , 199
R. Nandi, 425, 431
R. P. Singh, 227
R. Padma Sree, 37
R. S. Mahajan, 143
R. Sen Sarma, 653
R. Swaroop, 453
Rainer Pickhardt, 351
Rajat Bhattacharjee, 311
Rajpal Singh, 485
Ramnarayan Patel, 149
Ritu Tiwari, 551
S. Agrawala, 231
S. B. L. Saxena, 273, 355
S. B. Shivakumar, 121, 139, 203
S. C. Bera, 401, 407, 413, 419
S. C. Konar, 173
S. Chatterjee, 659
S. Chattopadhyay, 401, 431
S. Chakraborty, 705, 711
S. Dey, 161, 625
S. G. Bhirud, 237
S. K. Bharadwaj, 385

S. K. Ghosh, 711, 705
S. K. Goswami, 115
S. K. Kak, 443, 531
S. K. Mukherjee, 285, 453
S. K. Nagar, 65, 385
S. K. Sanyal , 425, 431, 437
S. K. Sarkar, 665, 705
S. K. Sen, 375, 459
S. K. Singhai, 571
S. Kumar,155
S. Mondal, 711
S. Nagarajan, 167
S. P. Bhattacharyya, 707
S. P. Choudhury, 285
S. Raman, 565
S. S. Salankar, 19
S. Santthosh Babu, 215
S. Sanyal, 679
S. Sarkar, 459
S. Sengupta, 243, 379
S. Sri Gowri , 595
S. V. Dudul, 19
Salil Kr. Jain, 65
Samarjit Sengupta, 615
Sanjeev Jain, 635
Sankar K. Pal, 491
Santi P. Maity, 527
Satyabroto Sinha, 359
Saurabh Sood, 603
Shubhra Verma, 443
Sishaj P. Simon, 127
Smarajit Ghosh, 219, 223
Soumika Munshi , 555, 671
Subrat Kar, 603
Sucharita Mitra, 463
Sudip K. Majumder, 263
Sumeet Goyal, 589
Suprava Patnaik, 537
Sushil Kumar Gupta, 179
Syamal Kumar Dana, 73, 397
T. Ananthapadmanabha, 121, 139, 203
T. Aruldoss Albert Victoire, 127
T. Ghosh, 109, 115
T. K. Basu, 237
T. K. Sengupta, 191
T. Mohanta, 109
T. R. Rangaswamy, 167
T. S. Bhatti, 91, 149
T. Vamsee Kiron, 472
Thomas Joseph, 127
U. R. Jena, 509, 521
Utpal Maji, 243
V. Jagadeesh Kumar, 475
V. R. Mankar, 19
V. S. R Rao, 351
V. Sharma, 459
V. Vasantharathna, 215
Vadali Srinivasa Murty, 565
Victor P. Sundarsingh, 303, 307
Vikas Jain, 687
Vinayak N. Shet, 303, 307
Vinod Chandra, 687
Vinod Kumar, 447
Vinod V. Thomas, 475
W. M. Shivakumar, 121, 139, 203
W. M. Wonham, 321
Y. K. Jain , 635
Y. Singh , 269